UNCLASSIFIED

AD NUMBER

AD887478

NEW LIMITATION CHANGE

TO

Approved for public release, distribution unlimited

FROM

Distribution authorized to U.S. Gov't. agencies only; Test and Evaluation; 01 APR 1971. Other requests shall be referred to Office of Naval Research, Arlington, VA 22203-1995.

AUTHORITY

USNASC ltr, 11 Apr 1972

THIS PAGE IS UNCLASSIFIED

CPIA PUBLICATION 214

UTEC CE 71-089

Handbook for the Engineering Structural Analysis of Solid Propellants

AD887478

MAY 1971

Prepared by

J. Edmund Fitzgerald

William L. Hufferd

Under Contract N0O014-67-A-0325-0001

With the University of Utah

Sponsored by

OFFICE OF NAVAL RESEARCH AND
NAVAL WEAPONS CENTER CHINA LAKE

DDC
RECEIVED
SEP 1 1971
D

AD No.
DDC FILE COPY

CHEMICAL PROPULSION INFORMATION AGENCY

THE JOHNS HOPKINS UNIVERSITY • APPLIED PHYSICS LABORATORY • SILVER SPRING, MD.

Distribution limited to U. S. Gov't agencies only; test and evaluation; 1 April 1971. Other requests for this document must be referred to the Office of Naval Research, Code 439, Arlington, Virginia 22217.

Best Available Copy

Best
Available
Copy

AD-887478L

The following pages are purposely left blank:

2.58

3.88

3.90

4.30

4.32

5.88

6.20

6.22

7.12

8.26

9.30

9.32

10.22

10.24

11.134

11.144

F.58

DDC-TCA
24 Sep 71

CPIA PUBLICATION 214 UTEC CE 71-089

Handbook for the Engineering Structural Analysis of Solid Propellants

MAY 1971

Prepared by

J. Edmund Fitzgerald

William L. Hufferd

Under Contract NOOO14-67-A-0325-0001

With the University of Utah

Sponsored by

OFFICE OF NAVAL RESEARCH AND

NAVAL WEAPONS CENTER CHINA LAKE

CHEMICAL PROPULSION INFORMATION AGENCY

Operating under Contract N00017-63-C-0651

THE JOHNS HOPKINS UNIVERSITY • APPLIED PHYSICS LABORATORY • SILVER SPRING, MD.

Unclassified
Security Classification

DOCUMENT CONTROL DATA - R & D

(Security classification of title, body of abstract and indexing annotation must be entered when the overall report is classified)

1 ORIGINATING ACTIVITY *(Corporate author)* University of Utah	2a. REPORT SECURITY CLASSIFICATION Unclassified 2b GROUP

3 REPORT TITLE

Handbook for the Engineering Structural Analysis of Solid Propellants

4 DESCRIPTIVE NOTES *(Type of report and inclusive dates)*

Handbook

5 AUTHOR(S) *(First name, middle initial, last name)*

J. Edmund Fitzgerald
William L. Hufferd

6 REPORT DATE	7a. TOTAL NO OF PAGES	7b. NO OF REFS
May 1971	908	

8a. CONTRACT OR GRANT NO.	9a. ORIGINATOR'S REPORT NUMBER(S)
Contract N00014-67-A-0325-0001 b. PROJECT NO	UTEC CE 71-089
c.	9b OTHER REPORT NO(S) *(Any other numbers that may be assigned this report)* CPIA Publication No. 214
d.	

10 DISTRIBUTION STATEMENT

Distribution limited to U.S. Gov't. agencies only; Test and Evaluation (III R[illegible]) (3) Oct. 1971. DDC 540[illegible] dtd 23 Jun[illegible] applied Apr 71. Other requests for this document must be referred to Naval Air Systems Command, Code [illegible], Naval Weapons Center, Code 605[illegible], or Office of Naval Research, Code 42[illegible].

11. SUPPLEMENTARY NOTES	12. SPONSORING MILITARY ACTIVITY
	(1) Office of Naval Research, Arlington (2) Naval Weapons Center, China Lake

13 ABSTRACT

The Handbook presents a review and discussion of some of the refinements and improvements that have been incorporated into the methods of determining the grain structural integrity of solid rocket motors during the past fifteen years. The Handbook has been written primarily for the solid propellant grain designer/analyst.

[No items on this DD Form 1473 are subject to the document distribution statement.]

DD FORM 1 NOV 68 1473 (PAGE 1)
S/N 0101-807-6811

Unclassified
Security Classification

A-31408

14 KEY WORDS	LINK A		LINK B		LINK C	
	ROLE	WT	ROLE	WT	ROLE	WT
Solid Propellants						
Solid Propellant Grain Design						
Solid Propellant Rocket Motors						
Structural Integrity						
Viscoelasticity						
Nonlinear Viscoelasticity						
Aging						
Stress-Strain Analysis						

FOREWORD

This timely and comprehensive volume was prepared under the joint sponsorship of the Structural Mechanics Program of the Office of Naval Research and the Polymer Science Branch of the Naval Weapons Center, China Lake, through ONR Contract N00014-67-A-0325-0001 with the University of Utah, for the below indicated reasons.

In the structural integrity analysis of solid rocket propellant motors, intrinsic material and geometric complexities, such as interrelated time, temperature and shape dependent grain response, have dictated many simplifying assumptions which are becoming increasingly incompatible with rising performance requirements. While over the years propellant mechanics research has resolved many of these obstacles, the current trend toward higher solid filler content is greatly aggravating the seriousness of those remaining. Accordingly, there is now a rapidly growing need for a sound and comprehensive survey and collation of inadequately exploited research gains, and for their proper integration into grain design technology. The purpose of this present bold but sound effort to achieve these formidable goals is twofold. The first is to provide in fact just such a needed guide for immediate design utilization. The second is to provide an authoritative advance document to serve as the basis for a scheduled joint Air Force-Navy sponsored engineering review and, where appropriate, a supplemental expansion of its contents, by the various specialists in the Government-Industry solid propellant community who serve on the Joint Army-Navy-NASA-Air Force Structural Integrity Committee for solid rocket motors.

The willingness of the authors, Professors J. Edmund Fitzgerald and W. L. Hufferd, to undertake such a dual purpose mission is commendable. The fact that the effort had the concurrence of all the prospective reviewers on this very effective Committee is indicative of the professional respect and acknowledged leadership they enjoy among their colleagues in this technically aggressive and highly competitive community. An initial review of the draft of this "basic" document by the undersigned reveals that both objectives of the undertaking are admirably met and that the confidence placed in these authors is indeed well founded.

Assuredly, this integration of present knowledge with its planned supplementation will greatly assist our solid rocket engineers to provide the requisite structural integrity in critical propellant grains of our solid rocket motors. In view of the viable, dynamic nature of defense technology, however, our continuing adequacy in this vital area of solid rocketry can be insured on even a minimum basis only by the effective implementation of the further research and development requirements identified in this and future amendments to this timely and authoritative handbook.

March, 1971

John M. Crowley
Structural Mechanics Program
Office of Naval Research

PREFACE

This Handbook represents an attempt to present an accurate report and evaluation of the current state-of-the-art of solid propellant grain structural integrity. Major emphasis is given to the requirements for meaningful material characterization, structural analysis and failure analysis of solid propellants. The Handbook has been written primarily for the designer/analyst.

In preparing this Handbook, we have relied heavily on the published and unpublished works of many of our colleagues from the solid rocket community. In addition, conversations with technical personnel of various solid rocket motor companies were carried out for the purpose of obtaining accurate information on current structural integrity practices. For their generous cooperation, we are particularly grateful to:

Aerojet Solid Propulsion Company
Atlantic Research Corporation
Hercules Incorporated
Lockheed Propulsion Company
Mathematical Science Corporation
Rocketdyne
Thiokol Chemical Corporation
United Technology Center

We wish to acknowledge the Structural Mechanics Program of the Office of Naval Research which jointly sponsored this effort under Contract N00014-67-A-0325-0001 with the Naval Weapons Center. Special thanks are due to Mr. John Crowley for his inception of the handbook concept as well as his constant efforts toward bringing this Handbook to fruition. In this regard, the effective assistance and support of Dr. Arnold Adicoff of the Naval Weapons Center and Mr. Irving Silver of the Naval Air Systems Command is also appreciated.

We are also indebted to Mrs. Merle Bryner, Mrs. Marilyn Harris, Mrs. Kaye Bowen and Mrs. Johanna Broadbent for their devotion and skill in the task of typing this manuscript.

J. Edmund Fitzgerald
William L. Hufferd

February, 1971

TABLE of CONTENTS

INTRODUCTION

1.1 General

This Handbook presents a review and discussion of some of the refinements and improvements that have been incorporated into the methods of determining the grain structural integrity of solid propellant rocket motors during the past fifteen years. Major emphasis is given to discussions of the current state-of-the-art practices along with a critical appraisal of the accuracy and range of applicability of structural analysis methods. The necessity and importance of experimental verification of grain structural integrity is similarly stressed.

A grain structural integrity analysis is an evaluation of the ability of a solid propellant rocket motor to perform satisfactorily throughout a specified environment, and is comprised of two parts: a grain structural analysis and a failure analysis. A grain structural analysis is the determination of the stresses, strains, deflections and deformations a solid propellant grain may be subjected to during its lifetime. A structural analysis, when coupled with appropriate failure data of the component materials through a failure analysis, defines the limiting environment in which a solid rocket motor may be expected to perform satisfactorily. Most often, however, the environment of a rocket motor is specified by the prime contractor or the sponsoring government agency to the propulsion system subcontractor. Thus, a coupled structural and failure analysis, or equivalently a grain structural integrity analysis, instead of defining

an operational environment, serves to determine a minimum margin of safety for satisfactory motor operation throughout the specified service life of the motor.

In determining a minimum margin of safety, consideration must be given not only to the statistical variations inherent in the experimental determination of material property data, but also to the loads encountered by the motor (e.g., vibration, acceleration, pressurization, etc.), the physical environment of the motor (e.g., aging conditions, humidity, temperature, etc.), and the inaccuracies inherent in the analysis methods or artificially introduced through simplifying assumptions. The margin of safety determined through proper consideration of these factors is an indication of the overall system reliability. If these factors were precisely known, there would only be required a margin of safety greater than zero. Inasmuch as this is not the case, and quite often assumptions or approximations must be made regarding specific information which is unavailable, arbitrary restrictions are placed on an acceptable minimum margin of safety. These restrictions reflect an ignorance factor associated with the structural analysis, the loading conditions, propellant behavior and failure analysis as well as the physical environment and mission requirements. The degree of arbitrariness of these restrictions has been somewhat lessened by the motor experience gained throughout the industry during the past decade. This experience has been gained in all aspects of grain structural integrity and has resulted in generally acceptable engineering approximations and assumptions regarding failure data, aging behavior, structural analysis and minimum margin of safety which are valid for the most part for engineering analysis purposes. Within this context,

approximations and simplifying assumptions are normally introduced for, say, material property data for which data is available for a similar material, or for a motor design for which experience exists with a similar configuration. The validity and usefulness of these assumptions and approximations are discussed herein, cautioning that in reality there is no satisfactory substitute for the actual information required. In the case of vastly different materials or design configurations, the required information must, of necessity, be obtained through more sophisticated analyses, more extensive laboratory testing; and if necessary, determination of grain structural integrity may ultimately require verification through full-scale motor tests. In any case, simplifying assumptions and approximations require substantiation through past experience or appropriate analyses and experimentation.

1.2 Loading Environment

This chapter serves as an introduction to the subject by considering the loading conditions to which a solid rocket motor is likely to be subjected. Temperature, dynamic, acceleration, pressurization and combined loadings are discussed in terms of their origin and relative severity in conventional motor designs. These loadings are discussed in some detail in this chapter so that future chapters on analysis methods will not be unduly repetitive in describing the loading environments.

This chapter also considers the influence of the physical environment which a solid propellant rocket motor experiences during its lifetime. This is a most difficult and significant problem facing the structural integrity engineer. Of the factors producing adverse effects which serve to reduce

the operational service life of a solid rocket motor, the normal aging of propellants and liners, and relative humidity level during storage are generally accepted as being the most critical. Proper evaluation of the effect of these storage conditions on the structural integrity of a solid rocket motor requires consideration of the physical, chemical and physiochemical changes of all age-sensitive system and sub-system components.

1.3 Preliminary Design Analysis Methods

This chapter is the first of two chapters dealing specifically with the methods of performing a grain structural analysis. Preliminary design configuration analysis methods are discussed here and final design analysis methods are dealt with in the following chapter.

A preliminary design analysis of a prospective candidate motor configuration determines if a given grain design has merit and possibly gives qualitative or semi-quantitative indications of how the design may be structurally improved. At this state in the analysis of a solid propellant grain approximations and simplifying assumptions in the analysis methods are warranted. Design data sheets and approximate engineering formulas are recommended for the analysis of conventional motor designs. Extensive numerical analyses at this level are unwarranted. The additional accuracy gained from using a computer analysis is often unjustified in view of possible approximations made regarding, say, material properties or failure data, and also, the uncertainty of the final design configuration does not justify the expense of computer analyses. An exception may exist in the case of new or novel grain designs, in which case computer analyses may be required. In these cases, and particularly in the case of radically new grain designs, development of new analyses coupled with

experimental subscale motor tests is recommended in place of relying on computer analyses of questionable applicability.

In this chapter, approximate engineering analysis methods are given for the loading conditions discussed in Chapter 2. The approximate methods consist of formulas for calculating stresses, strains and deflections for thick-walled hollow cylinders. Empirically derived relationships for determining stress concentration factors for slotted and star configurations, and curves of finite length end correction factors are included. The presentation of this material has been parameterized in terms of web fractions and length to diameter ratios. Because of the approximate and preliminary nature of the analysis methods discussed in this chapter, only the expressions used for determining maximum values of stress, strain and deflection are given. These values are sufficient for a preliminary design analysis. Profiles of stress, strain and deformation as a function of length for finite length hollow cylinders have been obtained by means of numerical solutions to the equations of elasticity.

The analysis methods presented are based on infinitesimal linear elasticity theory. Indications of how time and temperature effects may be incorporated are also discussed. For the most part, because of the preliminary nature of a preliminary design analysis, these modifications are not called for at the preliminary design stage.

1.4 Final Design Analysis Methods

This chapter considers the methods of conducting final design analyses. Preliminary design analysis methods were discussed in the preceding chapter.

The final stage of a grain structural analysis is performed after a preliminary design analysis has indicated the potential adequacy of a given

grain configuration. Whereas a preliminary design analysis normally investigates loads and regions of a propellant grain generally thought to represent critical structural integrity parameters, under simplifying assumptions and approximations, a final design analysis usually encompasses the total loading environment and the entire propellant grain, normally under less restrictive assumptions and approximations.

The level of sophistication required in the final analysis and design stage is determined by the complexity of the grain configuration and the severity of the loading environment. Presently, the final stage of a grain structural analysis involves extensive use of approximate numerical techniques. Few closed-form analytical solutions are obtained during the final analysis stage because of the complexities of the problems involved and the relative ease of developing numerical analysis methods for obtaining approximate solutions. A brief description of the numerical techniques commonly used throughout the solid propellant industry is presented here along with a discussion of current industry practices.

1.5 Special Design Considerations

Several areas of grain structural integrity analyses require special consideration. Particular theoretical and experimental investigations have been carried out for

- TRANSITION REGIONS
- GRAIN TERMINATIONS

The results of some of these studies are summarized in this chapter. In some cases the results are quite qualitative and, at best, are only suited for preliminary design analysis efforts when coupled with competent

engineering judgment. Considerable detail is presented to illustrate design and analysis procedures.

1.6 Experimental Stress Analysis Methods

Experimental stress analyses may serve as the primary analysis tool or confirmatory experimentation of other analysis techniques. Experimental methods are frequently used as the main analysis tool for complex grain configurations when the validity of the results of analytical and numerical analyses is seriously questioned. Experimental methods are also employed for confirmation of analysis and failure predictions with subscale and prototype motor tests used as ultimate verification of grain structural integrity. Properly used, experimental stress analyses represent powerful tools for the designer/analyst, complementing analytical and approximate numerical analysis techniques.

Presently, experimental methods make considerable use of photoelasticity, displacement measuring devices and Structural Test Vehicles (STV's), which model the essential features of production delivery motors. These topics are discussed in this chapter.

1.7 Failure Analysis Methods

A failure or strength analysis comprises the final stage of a grain structural integrity analysis. The results of a strength analysis are expressed as a factor of safety or margin of safety. Determining a minimum safety factor requires consideration of the statistical variations inherent in the experimental determination of material property data, the loads encountered by the motor (e.g., vibration, acceleration, pressurization, etc.), the physical environment of the motor (e.g., aging conditions,

humidity, temperature, etc.), and the inaccuracies inherent in the analysis methods or artificially introduced through simplifying assumptions. The margin of safety determined through proper consideration of these factors is an indication of the overall system reliability. If these factors were precisely known, there would be no real requirement for a margin of safety greater than zero. Inasmuch as this is not the case, and quite often assumptions or approximations must be made regarding specific information which is unavailable, arbitrary restrictions are placed on an acceptable minimum margin of safety. These restrictions reflect an ignorance factor associated with the structural analysis, the loading environment, propellant behavior and failure criteria as well as the physical environment and mission requirements.

1.8 Material Characterization Methods

The material characterization of highly filled solid propellants constitutes one of the major problems to be resolved before proper structural integrity analyses can be made.

There exist at present several, essentially standard, test specimen geometries for the above purpose. These are generically

- Uniaxial specimens of several varieties
- Biaxial strip specimens
- Torsion, single and double-lap shear
- Triaxial (poker-chip) specimens
- Diametral specimens.

The specifics of sample preparation are well covered in the ICRPG Solid Propellant Mechanical Behavior Manual, CPIA Publication No. 21,

September 1963, including its various additions and revisions. This sample preparation aspect is, therefore, not discussed herein.

In addition to methods and specifications for sample preparation, the CPIA Manual presents specific test procedures to be followed when using the above specimens. This area occupies the discussions of this chapter. The published procedures are based upon the use of a linear viscoelastic constitutive equation and the Moreland-Lee reduced time integral, using an experimentally determined time-temperature shift factor. The deficiencies of the test procedures center primarily upon the validity of the above assumptions.

1.9 Linear Viscoelasticity

This chapter summarizes the equations of linear viscoelasticity and also contains a discussion on the eigenvalue interpretation of linear viscoelasticity, which provides a rapid means of conducting "pseudo" nonlinear analyses.

1.10 Thermoviscoelasticity

The analysis associated with problems in thermoviscoelasticity ranges from the simplicity of linear viscoelastic analysis to the complexity of nonlinear viscoelasticity.

The reason for this wide range of complexity lies in the physical assumptions relative to the effect of temperature upon the material behavior. A discussion of these assumptions and present methods of thermoviscoelastic analysis are presented in this chapter.

1.11 Nonlinear Viscoelasticity

The ability to predict analytically the mechanical response of a structure requires as a prerequisite the characterization or mathemati-

cal description of the mechanical response of each of the materials in the structure. These mathematical descriptors of the constituent material response, or constitutive equations as they are called, together with a knowledge of the applied surface loads and displacements and the field equations of engineering mechanics, comprise a system of equations whose solution yields the state of stress and strain for every point within the body. To predict the success or failure of a grain design requires comparing the calculated stress or strain states within the body to some failure criterion. One therefore finds that an analysis of a structure is only as good as the constitutive equations defining material response and also that a failure analysis is of little consequence if the predicted state of stress is largely in error. Also, the determination of general failure criterion for three-dimensional states of stress generally requires the calculation of the stress state in laboratory samples subjected to multiaxial loading conditions. Thus, the determination of appropriate failure criteria is also dependent on the constitutive equations defining material response.

While the sequence constitutive equation, loads definition, structural analysis and failure definition are obviously totally interrelated, and the final usable answer to a performance prediction is equally dependent upon the accuracy of each of the above elements in a design, the discussion of this chapter is concerned mainly with the development of acceptable constitutive equations.

1.12 Appendices

A number of appendices are included to supplement the text material.

Appendix A summarizes the equations of linear elasticity.

Appendix B presents a further discussion of finite element computer programs from the user's point of view. A typical computer program is listed along with descriptions of required input and output data Three sample problems are solved to illustrate the use of finite element computer programs.

Appendix C contains parametric design curves for preliminary design analysis of cylindrical grains with various end conditions and subjected to thermal, pressure and acceleration loads.

Appendix D presents photoelastic test data for evaluating star valley stress/strain concentration factors.

Appendix E presents a sample motor structural integrity analysis to illustrate the design and analysis procedure for the novice designer/analyst.

Appendix F presents a compendium of motor experience gained throughout the solid propellant industry during the past decade. Motor failures and subsequent corrective action taken are discussed in the hope that such information might benefit the entire industry in preventing similar type failures in the future. Inasmuch as the greatest effort has been made to avoid compromising the proprietorship of the various companies or causing any embarrassment to any company or presenting material of a classified nature, these discussions take on a rather general form in which the specific details relating to motor programs, mission objectives and propellant type are for the most part omitted. It is still felt, however, that this material will benefit the new engineer entering the solid propellant industry.

II. LOADING AND ENVIRONMENTAL CONDITIONS

2.1 INTRODUCTION

The loads encountered by a solid rocket motor are normally classified as two types: specified loads and induced or derived loads. Specified loads are fixed by mission requirements demanded by the prime contractor or sponsoring government agency in RFP or motor specification documents. These loads are typically the operational temperature environment, acceleration, vibration, shock, transportation and handling loads, and the physical environment (e.g., aging conditions, humidity, etc.). Induced loads arise from a particular selection of the propellant, processing techniques and grain configuration satisfying the mission objectives of the motor. Induced loads are typically cure shrinkage, pressure, flight and certain combined loads.

The origin and severity of these loads and environments are discussed in this chapter. Suggestions for minimizing adverse effects of these loads through variations in material properties or design configurations are given. A section dealing with manufacturing and processing considerations is also included.

2.2 SPECIFIED LOADS

2.2.1 THERMAL LOADS

The most severe temperature loading is most often low temperature cycling. The critical areas of analysis are typically the inner bore in internally perforated grains and the case-grain termination points (i.e., grain ends).

Thermal stresses and strains arise because of the difference between the coefficient of thermal expansion of the propellant and the motor case.

The coefficient of thermal expansion of propellants, liners, and insulation materials is typically an order of magnitude larger than that of motor case materials. Thus, upon cooling to temperatures lower than the motor cure temperature, thermal stresses and strains are induced in a propellant grain due to the restrained shrinkage of the propellant, liner and insulation buffer materials. The difference in linear coefficients of expansion for composite propellants with a steel or fiberglas case is typically 5×10^{-5} $(°F)^{-1}$; with an aluminum case this difference is about 4×10^{-5} $(°F)^{-1}$. This difference typically ranges between 8×10^{-5} and 10^{-4} $(°F)^{-1}$ for double-base propellants and a steel or fiberglas case. The magnitude of thermally induced loads depends upon the propellant and grain design selected to satisfy the motor requirements, inasmuch as this selection determines the propellant cure shrinkage which is equivalent to a prescribed temperature loading. Cure shrinkage stresses and strains are discussed further in §2.3.1. The operational temperature range is normally specified in an RFP or motor specification document.

In performing thermal stress and strain analyses, the calculations may be referred to the propellant cure temperature and cure shrinkage stresses and strains superposed, or the calculations may be referred to the zero stress/strain temperature of the propellant, T_1. This temperature is defined to be the temperature at which thermally induced stresses and strains vanish. As noted in §2.3.1, because of propellant shrinkage during cure, the stress free temperature will usually be higher than the cure temperature. The cure process for conventional cast double-base propellants, described in §2.3.1, usually results in a stress free state at ambient temperatures, however.

The temperature T_1 may be conveniently determined by several techniques. One method is to subtract the equivalent temperature decrease associated with the cure shrinkage from the propellant cure temperature,

$$T_1 = T_c - \frac{1}{3\alpha_p} \left. \frac{\Delta V}{V_o} \right|_{t \to \infty} = T_c + \frac{\alpha}{3\alpha_p} \qquad (2.1)$$

where T_c is the propellant cure temperature, α_p is the propellant linear coefficient of thermal expansion and α is the net volumetric cure shrinkage. The net volumetric shrinkage of polybutadiene propellants is typically 0.2% and that of slurry cast double-base propellants 0.5%. The shrinkage of conventional cast double-base propellants is substantially lower.

Alternately, the zero stress/strain temperature may be determined from analog or subscale motor tests. In these tests the temperature of the cured motor is slowly raised above its cure temperature and measurements of the internal configurations versus temperature are recorded. The temperature at which the internal geometry of the motor coincides with the original mandrel configuration is then defined to be the stress free temperature. Measurements made in this manner indicate that T_1 is typically 15°F higher than the propellant cure temperature for polybutadiene propellants and 22°F higher for slurry cast double-base propellants [1].

Thermally induced stresses and strains may be minimized by reduction of the zero stress-strain temperature or through design optimization. Minimization of the zero stress-strain temperature is accomplished by reducing the propellant cure temperature or introducing a complicated cure cycle as discussed in §2.3.1. Design optimization procedures are currently based on engineering intuition of the analyst gained through past motor experience and on parameterized computer analyses.

At grain termination points, bond stresses are reduced by introducing intentionally released areas called *flaps* or *boots*, or by the use of stress-relief grooves, fillets, wedges, etc. Stress relief flaps are composed of materials which have strength and elongation characteristics greater than the propellant throughout the anticipated temperature range of the motor. They are also selected to have insulative capabilities consistent with the motor ballistic requirements. Silica or silica-asbestos filled buna-n rubbers typically fulfill these requirements.

Inner bore hoop stresses and strains are minimized through design considerations which will become evident in subsequent discussions of grain analysis methods in Chapters 3 and ..

Aerodymamic heating effects have become important in recent years with the development of supersonic aircraft and sophisticated air-launched attack missiles. The structural problem which results from aerodynamic heating arises when a solid rocket motor, which has been in storage at a low temperature, or externally attached to a high-flying aircraft for a length of time sufficient to allow the major portion of the propellant grain to reach equilibrium, is then subjected to the thermal barrier which results from a supersonic dash of the aircraft. The temperature of the boundary layer and that of the missile skin is raised appreciably because of the dissipation of energy generated in the boundary layer at high speeds and the shearing work done on the fluid by the viscous stresses within the boundary layer at high velocities. The result is that temperature gradients will exist within the motor case and the propellant.

Since the major portion of the propellant grain doesn't have time to react to the temperature gradient caused by aerodynamic heating, bond

stresses in addition to those already present due to thermal cooling are induced. As a general rule, the magnitude of this additional stress is small, on the order of a few psi. This component of thermally induced stress normally acts for only a short period of time before expansion of the insulation or liner buffer materials (which expand an order of magnitude more than the case) induces a compressive stress component which results in an overall net reduction of bond stresses. One sees, then, that the structural problem associated with aerodynamic heating is a decline in the strength properties of the propellant-liner-insulation-case bond system due to the rapidly rising temperature field. This problem reaches catastrophic proportions when the temperature rise at the propellant-case interface is such that the bond stress capabilities at this interface decrease more rapidly than the bond stresses decrease. This behavior is described schematically in Detail 1 below.

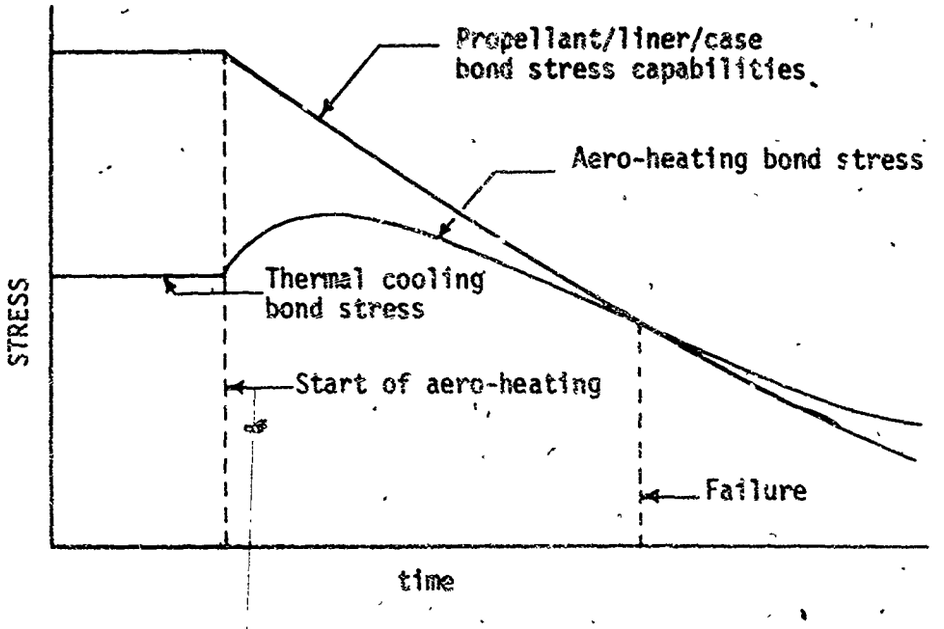

Detail 1. SCHEMATIC REPRESENTATION OF AERODYNAMIC HEATING EFFECTS

Upon aerodynamic heating, the net bond stresses initially increase in magnitude slightly, and then decrease with time. The propellant-case interfacial bond stress capabilities decrease monotonically with time during aero-heating. If at some time during this process, the interfacial bond stress capabilities decay to the point where they are less than the induced bond stresses, then failure will ensue.

A normal procedure for minimizing adverse effects of aero-heating is to insulate the external surface of the motor case with cork or some other good light-weight insulation material which has a heat transfer coefficient comparable to that of the propellant. This insulation inhibits the magnitude of the temperature differential between the case and the propellant, and decreases the temperature flux. Another method for decreasing adverse effects, which is currently being researched by a number of companies throughout the country, involves the use of high temperature curing adhesives, elastomers and propellants. The use of these materials minimizes degradation through imporvement of the high temperature physical properties of the component material. These materials have not been developed sufficiently to be considered state-of-the-art as yet, however.

2.2.2 ACCELERATION LOADS

This section presents a brief discussion of two classes of acceleration loading conditions:

(i) storage slump

(ii) launch and manuvering

Transportation of a solid rocket motor normally induces acceleration loads of the order of $\pm$ 3 g's or less. Because of the load reversal during transportation, this type of acceleration loading is better described under dynamic loadings and will be considered in a subsequent subsection.

AXIAL ACCELERATION

Axial, or longitudinal acceleration loads occur under vertical storage, transportation and launch conditions. During vertical storage of a solid rocket motor, the propellant grain is subjected to a one gravity body force. Normally a 1 g load is not sufficient to produce a critical shear stress along the case-propellant bond interface. An exception to this occurs in the case of large solid rocket motors in which inadequate grain terminations are provided, since bond shear stresses are proportional to the motor diameter. In this situation it is not unusual for grain end unbonding to occur. The major problem associated with vertical storage, however, is the occurence of large propellant deformations, or slump. Slump can be a critical design factor for storage above ambient temperatures (i.e., 70°F). At lower temperatures, the stiffness of the propellant usually lessens the magnitude of deformations.

Grain deformations under axial storage conditions are proporti al to the square of the motor diameter; thus, slump of a propellant grain is particularly pronounced in the case of long term vertical storage of relatively large solid motors, as for example, in a silo. This condition may also become critical in smaller motors when propellant slump provides gas flow restrictions not accou. ed for in the ballistic design of the motor. An example of this is a motor with a submerged nozzle or radial slots.

Slump characteristics of a solid propellant are controlled by the creep properties of the propellant. Thus, increasing propellant stiffness will reduce the magnitude of slump deformations; however, the adverse effects associated with increasing the propellant stiffness, in particular, the reduction in propellant elongation capabilities, usually overshadow any benefit. Thus, axial slump is most often dealt with through design

procedures which allow for large deformations. Stress relief flaps, or boots, provided at grain terminations to prevent grain end unbonding during temperature cycling, are usually also adequate for preventing grain end unbonding during axial storage.

During launch of a solid rocket motor, high shear stresses are induced at the case propellant bond interface. These stresses are a maximum at the forward end grain terminations, and are directly proportional to the acceleration magnitude and motor diameter. The maximum shear stresses normally occur near the time of maximum acceleration, rather than immediately upon launch. Axial acceleration stresses are more severe in an unpressurized motor, such as in a second stage vehicle, than one which is internally pressurized. Pressurization induces a hydrostatic compressive field which tends to enhance propellant strength capabilities and lessen somewhat the effects of body forces. High temperature acceleration is more severe than low temperature acceleration because of reduced propellant case bond strength capabilities. Axial launch and inflight accelerations are the more important acceleration loads for high acceleration motors.

Axial acceleration stresses may be minimized by maximizing the extent of bonded area, in particular grain end support, and through design of grain terminations in such a manner as to minimize stress concentrations at grain case singularities.

TRANSVERSE ACCELERATION

Transverse, or lateral accelerations occur under horizontal storage, transportation, and maneuvering during free flight. Horizontal storage at moderate temperatures, like vertical storage, can produce significant propellant deformation. In addition to providing gas flow constrictions

from star points or longitudinal slots closing together, there is the more severe problem of case ovality in flight weight motors. This latter problem is corrected by providing stiffening rings to prevent the case from becoming oval during storage. All of the above effects are minimized, or at least compensated for, by periodically rotating the motor ninety degrees. In the case of long, thin starpoints, startup deflections are often limited by providing consumable styrofoam supports for the individual starpoints.

Inflight maneuvering normally does not induce significant acceleration loads. For very high acceleration motors bending of the motor case due to sharp maneuvers may occasionally result in grain cracking or grain end unbonding. Normal design practices for other loading conditions, however, generally result in adequate structural capabilities during free flight maneuvering.

2.2.3 DYNAMIC LOADS

VIBRATION

Vibration of solid rocket motors is generally recognized as a potential structural integrity problem for applications in which severe or sustained vibration environments are encountered because of significant propellant damping. Vibration effects are most severe during ground and inflight transportation. Free flight vibration is not normally damaging to the propellant grain because of the relatively short burn times of solid rocket motors. Resonant burning, however, may lead to significant structural problems, particularly in the case of thin unsupported grain webs (e.g., thin starpoints, wagon-wheels, etc.). The high aluminum content of most modern solid propellants tends to reduce somewhat the problem of

combustion instability. For certain combustion conditions, gas flow conditions and internal grain configurations, acoustic instability may result in pressure waves of sufficient magnitude to cause propellant fracture and subsequent catastrophic motor failure.

A critical problem associated with vibration is that of generating local temperature increases sufficient to cause either spontaneous ignition of the propellant or severe mechanical degradation. The rate of energy dissipation into heat for a linear viscoelastic material is proportional to the frequency of vibration, material stiffness and the square of the magnitude of the deformation. Thus, the vibration problem is typically most severe for conventional motors under the low frequency, first resonant mode, at high temperatures. In this situation the propellant stiffness is a minimum for vibration conditions, and the motion of free surfaces (e.g., a starpoint) is greatest, resulting in maximum energy dissipation into heat. The problem is further complicated by the characteristically strong temperature dependence of propellant mechanical properties. This temperature dependence makes the energy dissipation very sensitive to temperature variations so that a continuing periodic forced motion gives use to substantial temperature increases.

At low temperatures the propellant behaves more nearly elastically so that motion and energy dissipation are reduced. Also, the heat generated is more readily conducted away from sources of heat generation at low temperatures than at high temperatures.

Another problem occurs for sustained vibration of very high mass fraction motors. During sustained vibration, the temperature increase

associated with energy dissipation causes the propellant grain to expand to fill available free volume. If insufficient free volume is provided, propellant-propellant or propellant-case contact may be made. This contact may result in local temperature increases an order of magnitude, or more, higher than average temperature increases; or it may cause structural failure due to degraded propellant mechanical properties.

In the event that temperature increases are not sufficient to cause autoignition, there still exists the possibility of inducing sufficient degradation of material properties, as a result of cyclic loading, to cause chemomechanical breakdown of the propellant or propellant-liner-case bond. Examples of propellant flow and propellant depolymerization during extended cyclic loading have been presented by Tormey and Britton [2].

The vibrational capabilities of solid rocket motors are currently determined from full scale motor tests. The specific nature of the test environment is dictated by the applicable military specification. A typical specification will require vibration testing in each of three mutually orthogonal directions (transverse, vertical, and longitudinal) at input amplitudes of 0.100 inch double amplitude displacement or 5 g's peak acceleration intensity at frequency ranges between 2 and 500 cps and 5 to 2000 cps. In addition, a certain portion of the test is carried out under sinusoidal oscillation while continuously varying the frequency or under broad band random excitation. Most military specifications now require 30 minutes dwell time at each of the resonant frequencies between 2 and 500 cps. Table I presents a comparison of some measured vibration levels with vibration specifications.

In the past, numerous inquiries have been made regarding the question of how realistic are the vibration specifications. These inquiries

TABLE I. COMPARISON OF SOME MEASURED VIBRATION LEVELS WITH VIBRATION SPECIFICATIONS [3]

MODE OF OPERATION	MEASURED VIBRATION LEVELS	SPECIFIED ENVIRONMENT
I. TRANSPORTATION AND HANDLING		
A. Shipment by Common Carrier		Part 1. Sinusoidal resonance search: 2 to 500 cps Part 2. Sinusoidal resonance dwell: 1.3 to 5.0 g(peak) for 30 min. at each resonance (2 to 500 cps) Part 3. Sinusoidal upder sweep frequency: 1.3 to 5.0 g(peak) for 45 min in each axis (sweep rate = 15 min. for each 5-500-5 cps cycle)
1. Truck		
a. paved road	0.35g(peak(max at 4 cps)	
b rough roads (20-25 mph)	1.7 g(peak)(max at 10 cps) 2.1 g(peak)	
c. cross-country (1 to 10 mph)	5.0 g(peak)	
2. Tractor-Trailer	3.7 g(peak)(max in 240-350 cps region)(occurred less than 1% of time)	
3. Railroad		
a. over the road (50 to 70 mph)	0.8 g(peak)(max at 1000 cps) 2.2 g(peak)(max value noted 93% of vibration was less than 0.75g) 2.0 g(peak)(predominant frequencies in 2.5 to 7.5 and 50 to 62 cps regions)	
b. switching shack (transient)	35 g(peak) with 8 mph impact	
4. Aircraft, propeller-driven with reciprocating or turbo engine	5.0 g(rms)(max at 490 cps) 5.0 g(peak)(1 to 250 cps)	
5. Aircraft, jet engine	2.8 g(rms)(max at 800 cps)	
6. Helicopter	7.0 g(rms)(max at 400 cps) 1.0 g(peak)(3.5 to 35 cps)	
7. Ships		
a. calm seas	0.08g(peak)(max's at 1.5 & 15 cps)	
b. rough seas	0.8 g(peak)(max's at 0.1 and 15 cps)	
c. emergency manuevers	3.0 g(peak)(max's at 2.5, 12 and 45 cps)	
B. Shipment by Special Transporters		
1. Minuteman Stage III/Boeing Transporter	0.6 g(peak(10 times more peaks noted in the 0.25 to 0.5 g range than in the 0.5 to 0.75 range)	
2. Nike I (storage-to-launcher)	1.0 g(peak)--longitudinal 1.5 g(peak)--lateral 3.0 g(peak--vertical	
3. Titan III Segment/tractor Trailer Transporter	1.3 g(peak)--fore-aft 1.0 g(peak)--lateral and vertical	
II. AIR LAUNCHED ROCKETS		
A. Captive Flight (tactical aircraft)		Part 1. Sinusoidal Resonance Search: 5 to 50 cps or 5 to 2000 cps. Part 2. Sinusoidal Resonance Dwell: 5 or 10 g(peak) for 30 minute at each resonance. Part 3. Sinusoidal Sweep Frequency: 5 or 10 g(peak) for 2 hours in each axis (sweep rate = 20 min. per 5-2000-5 cps cycle)
1. Carried in bay (doors open) (q = 1480 psf)	4.3 g(rms)--longitudinal 9.3 g(rms)--lateral 11.8 g(rms)--vertical (spectrum covers 20 to 2000 cps with a maximum in the 500 to 1000 cps region)	
2. Externally Carried	4.7 g(rms) for Mach 1.7 at 35,000 ft. 6.3 to 9.0 g(rms) for 600 knots at 5,000 ft. altitude 3.0 g(peak)(7 to 180 cps)	
B. Powered, Free-Flight	0.86 to 2.8 g(rms)	Part 1. Sinusoidal Sweep Frequency. 5 to 20 g(peak) for 2 hours in each axis (sweep rate = 20 min. for each 5-2000-5 cps cycle). Part 2. Random: 0.04 g^2/cps (7.4 g-rms) for 30 min. in each axis. (100 to 1000 cps with 6 db/octave roll on each end to 50 and 2000 cps respectively).

TABLE I. (continued) COMPARISON OF SGNF MEASURED VIBRATION LEVELS WITH VIBRATION SPECIFICATIONS [3]

MODE OF OPERATION	MEASURED VIBRATION LEVELS	SPECIFIED ENVIRONMENT
III. GROUND LAUNCHED ROCKETS		Part 1. Sinusoidal with Sweep frequency: 5 to 50 g(peak) for 30 min. in each axix (sweep rate = 20 min. each 5-2000-5 cps cycle)
A. Launched from Stationary Site	4.5 g(rms)(max PSD noted was 0.007 g^2/cps at 1200 cps)	Part 2. Random: 0.02 g^2/cps (5.30 g-rms) to 1.5 g^2/cps (46.3 g-rms) for 30 min. in each axis (100 to 1000 cps with 6 db/octave roll off each end to 50 and 2000 cps respectively)
B. Launched from Mobile launcher		
1. Captive Transportation, Tracked Vehicle (30 to 35 mph)	1.65 g(peak) at 76 cps-longitudinal 1.04 g(peak) at 80 cps-lateral 1.95 g(peak) at 80 cps-vertical 2.73 g(rms)(PSD spectrum peaks at 100 cps)	
IV. SHIP LAUNCHED ROCKETS		
A. Captive Transportation (Tactical Ships)		
1. Destroyer	5.0 g(peak)(17 to 170 cps)	
2. PT Boat	6.0 g(peak)(10 to 140 cps)	
3. Submarine	2.0 g(peak)(15 to 160 cps)	
B. Powered, Free Flight	8.3 g(rms)(max. PSD noted was 0.037 g^2/cps in 700 to 1400 cps region)	

resulted in a recent study being conducted to compare available motor data with current vibration specifications [8]. The major objection to current specifications is that the resonace dwell requirements are an unrealistic facsmile of the actual motor vibration environment. Wagner [3] recommended that resonant frequency tests be abandoned and replaced by random sweep vibration tests since these are more representative of the actual environment of a solid rocket motor.

It is easily demonstrated that the maximum internal heat generation in a solid propellant grain occurs during vibration at resonance; and also that as the temperature of the propellant increases, the resonant frequency of the motor initially decreases. Most current specifications require that during resonance dwell tests the input motor vibration frequency be varied to follow changes in the resonant frequency of the motor which results from the temperature increasing. This environment is more severe than the vibration environment a solid rocket motor actually encounters during its lifetime.

Questions have also been raised regarding the requirement that input acceleration intensities (usually $\pm$ 5 g's) be monitored at fixed motor/shaker attachment points. Amplification factors frequently result in $\pm$ 10 g's acceleration occurring at antinodes. This loading situation is intended to simulate aircraft vibrational loading of an externally mounted rocket motor. In practice, however, the vibrational loading is due mainly to air and wind buffeting loads. The result is that the motor, in fact, is a main source of vibration loading for the aircraft. This condition is not simulated in present vibration tests.

Some improvement in present vibration testing and specifications are expected to result from the captive flight tests of instrumented bomb dummy units in a program sponsored by the Air Force Rocket Propulsion Laboratory, and from Condor Motors, presently instrumented and being monitored during captive flight by Rocketdyne.

SHOCK

Shock loads normally occur when a solid rocket motor is dropped or subjected to a severe mechanical jolt during handling or transportation. The various blast waves of nuclear explosions are also an important source of shock loads. The time averaged magnitude of these loads, excluding shock waves from nuclear explosions, is normally in the range of one to five g's. Peak local intensities range between 25 and 75 g's.

Peak shock load intensities act for a very short time during which propellant normally behaves essentially as an elastic material with a glassy modulus. As a consequence, the propellant grain itself is usually undamaged. The major damage that occurs is usually bending or warping flight weight rocket motor cases. Possible damage inflicted on a propellant grain as a result of shock loads may be either propellant-liner-case unbonding, or the development of a shock wave with sufficient energy to cause detonation.

Case-grain unbonding is most likely to occur at intermediate to low temperatures either in the immediate area of the point of application of the shock load, or at case-grain terminations. At high temperatures the propellant is more compliant and can better withstand large deformations. The compliant, high-strength, elastomeric end-release flaps employed at critical grain-terminations interfaces to relieve thermal stresses also serve to reduce the probability of peel failure at these locations during shock loading of a motor.

Detonation of propellants is a complicated process which is still not completely understood. Some of the possible initiation mechanisms are adbabatic heating of compare gases within void areas, friction between

the solid particles in the propellant, fracture of energetic solid oxidizer particles and viscous heating of the propellant binder [4-10]. There are indications that the energy release due to viscous damping is not sufficient to initiate detonation of propellants [10,11]; however, this question has not yet been completely resolved.

In the absence of quantitative analyses, laboratory and full scale motor tests are routinely conducted to determine the shock sensitivity of peopellants and loaded motors. Laboratory tests generally consist of impact sensitivity tests in which physical impact is caused by a falling weight such as in the ERL test; or shock sensitivity tests, in which the initiating shock is generated by a donor explosive, as in the gap test; or by high velocity impact, by a projectile. References 5, 6 and 8 contain further discussions of laboratory methods of determining and evaluating shock sensitivity of propellants. An analytical model which qualitatively relates the experimental conditions of shock pressure, shock impulse and accepter diameters in regard to initiation of detonation has been discussed by Pratt [7].

TRANSPORTATION AND HANDLING

Some of the loads arising from transportation and handling of rocket motors have been discussed briefly in the previous sections. The magnitude and vibrational frequency of transportation loads vary somewhat depending upon the carrier. Some measured vibration levels for transportation are shown in Table I. Specifications typically require 30 minute resonance dwell tests at each resonance between 2 and 500 cps at peak input accelerations between 1.3 and 5 g's, and sinusoidal sweep tests from 5 to 500 cps at 1.3 to 5 g's peak input acceleration.

During handling of a solid rocket motor damage is most likely to be inflicted upon the motor case. This damage may consist of bending of the motor case or nozzle, dents in flight weight cases, bending or denting attachment or handling lugs, etc. Grain unbonding in the area of the dent is also likely to occur.

Full scale motor tests usually consist of dropping motors, unpackaged and packaged in protective shipping containers, from various heights in various attitudes onto concrete or steel slabs. Visual inspection and non-destructive tests, such as X-ray inspection and ultrasonic inspection of critical bond regions are used to determine the severity of the damage. Some specifications require simply that the motor not detonate, whereas others require that it operate satisfactorily after drop tests. Common tests for shock sensitivity have been mentioned above. Usually dropping a flight weight motor which is not encased in a protective container will result in irreparable damage to the motor case.

2.2.4 SPECIAL LOADS AND ENVIRONMENTS

Occasionally a solid rocket motor will be required to operate successfully in a special environment. The spin environment has probably had the greatest attention, although little has been published in the open literature on the structural behavior of a spinning propellant grain. It is possible that the spin rate may induce appreciable inertial stresses and deformation within the grain. Star-shaped grain geometries are usually avoided, since the deformations of starpoints will normally be excessive. The spin environment frequently leads to eratic burning characteristics; the most noteworthy of which is errosive burning. Strong coupling between the burning characteristics and structural behavior is to be expected.

Other loads and environments, which will not be discussed in detail in this handbook, result from requirements for heat sterilizable propellants for space application, resistance to radiation and special environments peculiar to nuclear explosives. Generally, particular propellants are developed and tailored specifically to survive in these environments.

2.3 PROPELLANT AND DESIGN INDUCED LOADS

The induced loads, as mentioned in Sec. 2.1, arise from a particular selection of the propellant, processing techniques and grain configuration satisfying the motor mission objectives. These loads typically consist of cure shrinkage, pressure, flight and certain combined loads.

2.3.1 CURE SHRINKAGE

Cure shrinkage stresses and strains are induced during propellant cure when the propellant is transformed from a highly viscous fluid-like material into a solid. The majority of propellant cure shrinkage takes place prior to the initial point of propellant solidification (i.e., gel); however, cure shrinkage stresses develop only after gel, inasmuch as propellants display fluid properties prior to gelaton and cannot support substantial shear stresses. The shrinkage that takes place between propellant gel and completion of cure is restrained by the motor case. As a result, shrinkage or residual stresses exist in a solid rocket motor upon completion of cure. For propellants which gel at an early stage of the cure process, the possibility of developing shrinkage stresses which are greater than the stress capabilities of the partially cured propellant exists. The result is that a motor may exhibit cracks or unbond regions immediately upon removal from cure. These effects are most evident in high mass fraction,

composite propellant motors and slurry cast high energy double base propellants which are cured under conditions leading to undesirable nonuniform temperature fields. Under certain conditions, however, as it shall be seen, curing in a nonuniform temperature field leads to a reduction in cure shrinkage stresses and strains.

The amount of shrinkage that takes place during cure of a solid rocket motor is a consequence of the particular choice of propellant and processing techniques selected to satisfy a given motor s temperature environmental requirements. Conventional composite propellants are cured by a polymerization process which is generally accompanied by a volume shrinkage which is proportioal to the binder volume present. Because of propellant shrinkage during cure, the zero stress/strain temperature will be higher than the cure temperature. Composite propellant rocket motors are typically cured between 130°F and 145°F. The cure shrinkage that takes place is equivalent to a 15°F temperature drop [1]. Thus, the zero stress/strain temperature, which is normally taken to be the reference temperature for thermal stress and strain calculations, ranges between 145°F and 160°F for most conventional composite propellants. The stress free temperature for slurry cast double base propellants is typically 22°F higher than the cure temperature [1]. These propellants are typically cured between 115°F and 140°F.

The cure of conventional cast double-base propellants is basically a mutual diffusion process between casting powder and casting solvent with no chemical reaction occurring until the final stages of the cure process [12]. Casting powder granules, consisting primarily of nitrocellulose with metal fuel, oxidizer, ballistic modifiers and stabilizers incorporated to improve motor performance, are loaded into an empty motor chamber by a

pneumatic conveyor. The casting solvent which is a high energy liquid containing nitroglycerin with diluents to increase plasticization and reduce sensitivity, is then added under pressure. This pressure causes the liquid to flow into interstices in the powder granules until voids have been replaced by casting solvent. The solvent is absorbed by the casting powder which in turn swells the powder into interstices formerly occupied by the absorbed liquid. Mechanical displacements are often applied to the propellant by means of rams to aid grain consolidation. After the casting powder and solvent have combined to form a single phase material the temperature is raised to about 120°F and the propellant cure completed. Propellant containment by the rams is maintained at the 120°F cure temperature. Thus, cure shrinkage in cast double-base propellants results essentially from bed settling and collapse of micro-voids in the casting powder granules during ambient temperature mixing of solvent and powder, and is not chemical in nature. Some chemical shrinkage does occur during completion of cure at the elevated cure temperature; however, because of the partial cure at ambient temperature a decreased net shrinkage relative to composite propellants results. Furthermore, because of the compressive loading on the propellant grain during the entire cure process, an essentially stress free condition exists in the grain when it is returned to ambient temperature.

The volumetric cure shrinkage of most composite polybutadiene propellants can be adequately described by the relation

$$\frac{\Delta V}{V_o} = -\alpha\{1 - \exp(-\beta t)\} \qquad (2.2)$$

where α and β are experimentally determined constants. The constant α represents the net volumetric shrinkage, and the product $\alpha\beta$ represents

the initial rate of shrinkage. The net volumetric shrinkage α is usually not explicitly temperature dependent, however, the shrinkage rate $\alpha\dot{\xi}$ is strongly temperature dependent since polymerization, in general, is a thermally activated process which is usually adequately described by first order kinetic theory. Procedures for performing cure shrinkage tests are not readily available in the open literature, however, a common technique makes use of a mercury dilatometer submerged in a constant temperature bath. The rise of the mercury column in a capillary is monitored using a cathetometer. More direct techniques for measuring the stress free temperature were discussed in §2.2.1.

Determination of cure shrinkage stresses in a solid rocket motor represents a diffucult task which is not easily carried out. Thacher [1] has analyzed recently the double-base manufacturing process, and Cost [13] introduced an analytical approach which may prove to be worthwhile for determining shrinkage stresses in composite propellants. In this report Cost treated ouring polymers under isothermal and steady-state thermal conditions, and formulated the basic governing differential equations in terms of differential operators. The material properties were treated as functions of space, time, temperature and degree of cure. Indications of how material behav may be related to molecular parameters were given, based on Bueche's theory of molecular viscoelasticity. Such a theory may serve as a guideline for future developments in this area; however, lacking experimental verification, these developments should be considered to be of a preliminary nature. Development of analysis techniques for cure shrinkage stresses will likely be necessary in the future with the evolution of more complicated and more highly constrained grain configurations.

Several techniques have been successfully used for minimizing cure shrinkage stresses and reducing the stress free temperatures. One method is to use propellant binders and ingredients which undergo minimum shrinkage during polymerization. Unfortunately, the resultant propellants seldom meet motor performance requirements. Another effective means of reducing shrinkage stresses is to cure the propellant at a lower temperature for a longer period of time. Still another alternative is to step cure the motor starting at an intermediate temperature and gradually increasing the cure temperature in steps at various stages of the cure process. This process produces a nonuniform temperature field which in some situations results in a more favorable strength distribution during cure. Step cure cycles are usually determined empirically by performing propellant cure shrinkage tests at a number of different temperatures. A step cure has been successfully used by Lockheed Propulsion for polysulfide, polycarbutene and slurry cast double base propellants. Double-base propellants are often cured in a nonuniform temperature field.

Auxilliary benefits are derived from both the step cure and the longer term low temperature cure. These methods of propellant curing reduce the stress free temperature and thereby reduce the stresses and strains resulting from temperature cycling. These curing methods also tend to produce a more fully cured propellant and thus reduce aging degradation due to propellant post curing.

2.3.2 PRESSURIZATION LOADS

Pressurization loads arise during ignition of a solid propellant rocket motor and act until motor burnout. Ignition pressurization induces a compressive hydrostatic pressure throughout the grain with superimposed tensile hoop components of stress and strain at the inner bore. The

pressurization loads imposed on a solid rocket motor are determined by the propellant properties (e.g., bulk compressibility, burn rate, pressure exponent, temperature sensitivity, etc.), the grain configuration and the stiffness of the motor case. The ballistic properties of the propellant determine the grain configuration and the motor operating pressure. Low modulus case materials such as fiberglas cases typically give rise to more severe pressurization loads because of their lower stiffness.

The hoop strain at the inner bore and the stresses and strains at grain terminations are usually the critical design parameters for pressurization loading, particularly for low temperature firings where the propellant has less elongation capabilities than at high temperatures. Design considerations which lead to a reduction of thermally induced stresses and strains also tend to reduce pressurization stresses and strains.

2.3.3 FLIGHT AND COMBINED LOADS

Certain combined loads are of more significance in determining the structural integrity of a solid rocket motor than the individual loads applied separately. The most significant combined loading is normally that of low temperature firing. A low temperature firing of a solid rocket motor superimposes the stress state resulting from ignition pressurization upon the existing stress state due to thermal cooling. As in the individual loadings, the critical strain field occurs at the inner bore. The bond stresses at grain terminations are also of major importance. Thermal strains are usually higher than pressurization strains with the possible exception of fiberglas case motors in which pressurization strains of 20% are not uncommon. Thermal strains are also induced at a slow loading rate, the motor cooling rate, whereas pressurization strains are

induced at a higher loading rate. Propellant strength and elongation capabilities are higher under a hydrostatic pressure so that thermal cycling will usually dominate design considerations. There is some evidence which indicates that if a motor has not failed during low temperature cycling it is not likely to fail upon firing [14]. There is additional evidence that suggests existing flaws or cracks may enlarge and propagate leading to catastrophic failure during firing [15].

Launch of a solid rocket motor superposes the stress states due to pressurization, thermal cooling or cure shrinkage and axial acceleration. The addition of launch acceleration loads in considering low temperature firings is usually not required inasmuch as the propellant stiffness and strength capabilities are substantially higher at low temperatures than at high temperatures. At high temperatures, on the other hand, thermal stresses and strains are inconsequential and launch acceleration stresses dominate design considerations because of the reduced propellant strength and stiffness.

The above, combined loading situations, and others which may occur, require considerations of cumulative damage effects in assessing motor structural integrity.

2.4 AGING AND HUMIDITY

The influence of the physical environment which a solid propellant rocket motor experiences during its lifetime is a most difficult and significant problem facing the structural integrity engineer. Of the factors producing adverse effects which serve to reduce the operational service life of a solid rocket motor, the normal aging of propellants and liners, and relative humidity level during storage are generally

accepted as being the most critical. Motors are also frequently required to be impervious to salt spray resulting from shipboard storage and transportation, and biological attack (e.g., fungus growth in tropical climates). These latter environments are not discussed herein, however. Some of the factors which influence aging behavior are described in Table II. Proper evaluation of the effect of these storage conditions on the structural integrity of a solid rocket motor requires consideration of the physical, chemical and physiochemical changes of all age and environment-sensitive system and subsystem components. Some of the more important factors influencing operational service life as well as current practices of establishing and verifying service life predictions are discussed in the following subsections. For convenience, the effects of relative humidity level are discussed separately from other aging degradation mechanisms.

General surveys of environmental and aging effects have been presented by Fishman [16], Bills, Fishman and Myers [17] (§7.0, "Applications of Mechanical Property Testing for Surveillance"), and Kelley [18]. These articles contain rather extensive reference up to about 1966. Hence, the references cited herein refer, for the most part, to more recent literature on this subject. Of the recent literature, references 19 through 29 pretty well reflect the current state-of-the-art.

2.4.1 RELATIVE HUMIDITY

The presence of moisture severely degrades the mechanical and chemical properties of most solid propellants [16, 17, 19-25, 30-32]. This degradation is typically manifest as swelling of the binder matrix, reduction in modulus and retardation of propellant ignition, often leaching of surface

TABLE II. FACTORS INFLUENCING PROPELLANT DEGRADATION DURING AGING [18]

FACTOR	MANIFESTATION	FAILURE MODE
Change of Chemical State	Hardening, embrittlement, gassing, accumulation of degradation products, viscous flow enhancement, change of adhesivity.	Increased tendency to crack during storage, ignition, or temperature cycling; possible burning rate change, impulse loss, ignition problems, and linear separation.
A. Chemical reactivity of propellant components singularly or in combination		
B. Chemical interaction with environment	Same as A; in addition, nonhomogeneity of propellant at surfaces and within bulk.	Same as A
1. Atmosphere		
a. Moisture		
b. Gaseous or solid decomposition products (autocatalysis)		
c. Air (oxygen, ozone, contaminants in air)		
2. Other materials in motor (liner, metals, etc.)	Same as A	Same as A
C. Factors which may influence rate of change	Time scale of degradation	
1. Temperature		
2. Stress state		
D. Irradiation	Polymer crosslinking or degradation	Same as A
1. Background		
2. Induced		
E. Bacteriological action	Surface changes	Unknown
Change in Physical State		
A. Reversible physical changes		
1. Phase changes which depend on time and temperature	Hysteresis of temperature-dependent physical properties	Increased tendency to crack during storage, ignition, or temperature cycling.
2. Recoverable strains	Probably minor	Probably minor
3. Diffusion of materials	Nonhomogeneity of propellant properties; oxidizer-poor surfaces, porosity, shrinkage.	Crack development, increased tendency to crack during storage, ignition, or temperature cycling.
a. Gases		
b. Plasticizer		
c. Moisture		
B. Irreversible physical changes	Cracks at fillets, liner separation, viscous deformation, dewetting (blanching)	Increased burning areas and rates.
1. Strain beyond reversible limit caused by:		
a. Gravity		
b. Acceleration (during transport)		
c. Thermal gradients		
d. Environmental temperature		

oxidizer particles is observed. The mechanism of this degradation is primarily a reversion process in which chemical scission of polymer network cross-links and consequent reduction in modulus is caused by hydrolytic attack at cross-link sites. Epoxide cured propellants are relatively insensitive to hydrolytic attack. Imine cured propellants have varying degrees of susceptibility. Double-base propellants are usually less influenced by moisture than composite propellants.

Moisture enters a solid propellant or liner-propellant interface through a diffusion process. The depth of penetration appears to be controlled by the relative humidity level, the ratio of volume to surface area exposed and the duration of exposure. Inasmuch as moisture is stored to a large extent in the binder matrix, reduced strength and increased elongation capabilities of the propelllant are observed at ambient temperatures and above; whereas at low temperatures significantly reduced elongations are observed, probably due to moisture embrittlement or freezing-in water which restricts polymer chain motion. The strength of the liner-propellant bond is reduced at all temperatures due to moisture diffusion at high relative humidity levels.

Available information suggests that the effects of high moisture content are more severe for propellant in a strained state than in an unstrained state. This attribute may lead to particularly acute problems during temperature cycling of a solid rocket motor due to breathing of the propellant or rocket motor interior with the external environment. In this situation frost and water may condense on the propellant surface and accumulate in subsequent temperature cycles, eventually leading to structural failure of the propellant in areas of high stress concentration.

Inasmuch as moisture induces drastic and rapid degradation of propellant and propellant-liner bonds, exposure of a solid propellant grain to high humidity levels must be avoided since it is not always possible or practical to select propellant polymers in which water is not soluble. Fortunately the humidity level in a solid propellant grain may be maintained at an acceptable low level relatively easily through proper implementation of hermetic seals and dessication. Past experience has indicated that short and probably even long term exposure to relatively low humidity levels produces no effect directly attributable to the level or duration of exposure. It is generally accepted that at levels below about 30% RH no effect is observed.

The effects of relative humidity have also been observed to be reversible to a certain extent. The original properties of a propellant grain which has been inadvertently exposed to a high humidity level, but which has not yet structurally failed, are substantially recovered by dessication of the grain. As a general rule, the drying recovery time is the same as the exposure time to moisture. Dessication of un-aged propellants also tends to remove moisture introduced during mixing, casting and curing operations.

2.4.2 AGING

In addition to being sensitive to moisture levels, solid propellants experience changes due to normal aging during long term storage. These changes are reflected in changes in the chemical and physical properties of the propellant and liner-propellant bond. Unlike the effects of moisture, however, the effects of aging are irreversible. Most propellants typically exhibit between 25 and 50 percent degradation during aging. The discussion here is restricted to chemorheological aging. Mechanical aging degradation

results from sustained or cyclic application of the loads discussed previously and is normally handled through cumulative damage considerations.

Several factors are known to influence the aging characteristics of propellants which in turn effect the shelf-life of a solid rocket motor. The dominant aging mechanisms affecting propellant behavior, which normally occur simultaneously, are continued post-curing, oxidative cross-linking and polymer chain scission [16-18,20-23,30,31]. Additional consideration must also be given to surface versus bulk aging characteristics [17,25-27,30-38] and migration effects [17,20,23-25,33,35,37,39,40]. The influence of these factors is dependent to a greater or lesser extent upon the propellant polymer and cure system, cure cycle, cure catalysts, ballistic modifiers and aging temperature.

Post-cure curative reactions result from the slow continuation of reactions not driven to completion during the normal cure cycle. These reactions result in an increase in the propellant modulus due to the formation of additional network cross-links.

Oxidative cross-linking is primarily a surface phenomenon which results from free-radical attack at double bonds in the polymer chain backbone. This mechanism also results in an increase in stress and decrease in the strain properties of solid propellants.

Chain scission is largely determined by the cure system and results in softening of the propellant. This phenomenon, as mentioned before, is accentuated by the presence of moisture; however, Hydroxy-terminated (HTPB) and Carboxy-terminated polybutadient (CTPB) propellants frequently display this reversion process during high temperature aging. Polyurethane propellants also undergo chain scission during aging due to splitting of functional linkage.

Distinct differences between the surface and bulk aging characteristics of propellants have been noted primarily due to surface oxidation of the propellant. This surface oxidative cross-linking results in a considerably stiffer propellant surface. Surface skin effects, notably hardening of the grain inner bore, has been observed to a depth of one-half inch in some cases [34,36,38,40]. Significant variations in the aging behavior of propellant aging in sample cartons and propellant aged in rocket motors has also been observed [24,34,36,38]. These variations have been attributed in part to the fact that motors are characteristically cured at a higher temperature than the oven temperature because of internal exothermic reactions. Cartons, on the other hand, are cured at a temperature more nearly equal to the oven temperature.

Migration of soluble species is of major concern at the propellant-liner-insulation bond interfaces [17,20-23,25,37,39,40]. Soluble species such as low molecular weight polymer, burning rate catalysts, plasticizers, moisture and degradation products may migrate across bond interfaces causing both chemical and physical changes. An exact relation between ingredient migration and the physical and chemical changes is not presently known. Such a relation is influenced in a complicated manner by time, temperature, concentration and relative solubility of the migrating species. The predominant physical effect of all migratory species is degradation of the adhesive bond between the liner and propellant or liner and insulation or case. In addition, the propellant and the liner of insulation may harden or soften either separately or jointly. Typically, migrating species from the propellant into the liner or insulation act as plasticizers causing the liner or insulation to soften and swell and the propellant to harden and shrink resulting in high localized stresses and strains at the bond

interface as well as a weakened adhesive bond. Plasticizer migration from certain elastomeric insulations into the propellant, on the other hand, normally softens the propellant. In other situations, such as a curative imbalance between the liner and the propellant, a hardening of either or both the propellant and the liner may result. Cross migration of other ingredients may have similar results depending on the particular ingredients and concentrations involved. It suffices to observe that migration invariably degrades the adhesive bond system.

Migration in composite propellants has been observed to be particularly critical in CTPB propellants, which have a notorious history of difficult bonding problems to begin with; and for propellants employing liquid alkylferrocene ballistic modifiers. Migratory behavior has also been observed of dioctyl azelate (DOZ) and circo light oil. The primary migrating species of double-base propellants is the energetic plasticizer nitroglycerine. Diethylene glycol dinitrate (DEGDN), triethylene glycol dinitrate (TEGDN), trimethylethylene trinitrate (TMETN), dibutyl phthalate (DBP) and triacetin are also known to migrate when used in CMDB propellants. Isodecyl Pelargonate (IDP) demonstrates migratory behavior in both double-base and composite propellants. An additional concern with double-base propellants is the decomposition of certain ingredients to form products which increase the sensitivity or stability of the propellant.

The storage or aging temperature influences the rate at which the above processes occur, the relative severity of degradation, and, to a certain extent, if a given aging mechanism will occur. In general, increasing the aging temperature accelerates the rate at which degradation takes place. It is also noted that the degradation in propellant and

liner-propellant properties observed during high temperature aging is significantly greater than the degradation observed during ambient temperature aging, even for prolonged periods of time [17,18,25,27-35,41-44]. Post-cure curative reaction rates are accelerated by increasing the storage temperature. In this situation, high temperature aging completes the normal cure process. Migration rates and the relative degradation of the liner-propellant adhesive bond due to migration are significantly increased at high temperatures.

Surface hardening due to oxidative cross-linking also appears to be accentuated at elevated temperatures. On the other hand, propellant softening due to excess chain scission over continued post-cure cross-linking, noticeably absent under ambient temperature storage conditions, has been observed in CTPB, HTPB and polyurethane propellants during high temperature aging.

For the most part, the processes discussed in the previous paragraph are de-emphasized under low temperature storage conditions. However, an alternate problem may be introduced for composite propellants containing liquid alkylferrocenes which may crystallize during low temperature storage. Crystallization has been observed to be most severe for propellants containing n-butyl ferrocene liquid burn rate catalyst at temperatures below about -40°F [25]. This phenomenon has been attributed to the existence of n-butyl ferrocene in a supercooled state which undergoes a change of phase to a crystalline state due to shock conditions induced by temperature excursions or mechanical loading. Substantially reduced propellant elongations are obtained as a result

of crystallization. Of equal importance is the possibility of propellant detonation. Since n-butyl ferrocene is a highly energetic plasticizer any severe mechanical jolt, such as a low temperature firing, may fracture n-butyl ferrocene crystallites thereby releasing sufficient energy to initiate and propagate detonation mechanisms resulting in catastrophic motor failure.

In addition to the primarily physical effects discussed previously, aging also affects the ballistic properties of solid propellant grains. The normal ballistic changes are changes in burn rate, pressure and temperature sensitivity of burn rate and igniteability caused primarily by hardening of the propellant and evaporation and migration of volatile catalysts [20,21,23,25,35,37,43].

MINIMIZATION OF ADVERSE AGING EFFECTS

The problem of controlling and minimizing aging effects has only been partially solved by the propellant chemist. The problem facing the propellant chemist is that of formulating completely stable solid propellants which undergo insignificant changes in all aging environments. This goal has effectively been attained only for polybutadiene-acrylnitrile acrylic acid terpolymer (PBAN) propellants [38], which typically undergo about a 25% decrease in strain properties during the first few months of aging and then remain stable thereafter.

Continued post-cure cross-linking is exhibited by all composite propellants to a greater or lesser extent. One effective means of controlling post-cure reactions has been to extend the cure cycle to assure completion of all normal cure reactions. This technique,

although effective in minimizing continued cross-linking during storage, may frequently result in undesirable, and unacceptable unaged propellant physical properties. Alternatively, the propellant chemist may explore different curative/polymer ratios to obtain a given degree of polymerization meeting design target physical properties. The most desirable method of controlling the effects of post-cure reactions is to maintain a balance between post-cure cross-linking and chemical scission of polymer chains. For this situation the aging behavior obtained from conventional aging of bulk samples is indistinguishable from the unaged properties inasmuch as polymer chains are broken and new cross-links are formed in an unstressed state. In a composite solid propellant grain under ambient storage conditions, the polymer chains that are broken are in a strained state; however, the new cross-links formed are still in an unstrained state. This observation has important and significant implications which are seldom recognized or considered in conducting grain structural analyses. Namely, forming new cross-links in an unstrained state in propellant which was previously strained de-emphasizes the importance of the effects of previous loadings. In essence, the propellant has no memory for prior loadings. Such an effect would significantly enhance the low temperature resistance to, say, inner bore cracking of an aged propellant grain, for example; which would not be evident from the aging behavior of bulk samples.

Oxidative cross-linking is primarily a surface phenomenon which is suppressed to a certain extent, but not eliminated by the presence of antioxidants in the propellant prepolymer. This effect is further

minimized by sealing the rocket motor interior in an inert gas environment. A positive internal pressure is often maintained to circumvent breathing of the motor during environmental changes. This procedure has effectively reduced the problem associated with oxidative cross-linking to an inconsequential level.

Migration effects may be reduced to tolerable levels through consideration of the equilibrium concentrations of migrating species and the use of migration barriers. Primarily, effort has been directed toward the elimination or reduction of the degradation of adhesive bonds attributed to plasticizer migration. For composite propellant applications, liners and insulations have been developed which are resistant to absorption of migrating plasticizers [25,45]. Non-functional plasticizers have also been introduced into elastomeric insulations intended for low temperature applications. Conventional powder-embeddment case-bond systems used with double-base propellants are reasonably resistant to plasticizer migration; however, the high glass transition temperature of the epoxy in which the casting powder granules are embedded in, precludes use of this system at low temperatures [20,46-48]. Adequate low temperature behavior has been demonstrated using a double-layer bonding concept [47]. One layer, selected to resist plasticizing and plasticizer migration, is used as a coupling layer to bond a propellant bonding layer to the case or insulation. The propellant bonding layer is attached to the propellant through mutual diffusion and chemical interactions.

SERVICE-LIFE PREDICTIONS

Presently, the prediction of aging degradation is largely based on past experience with similar propellants, and on fairly extensive surveillance

test programs. As noted in a subsequent subsection, however, surveillance testing is an inadequate means of making initial service-life predictions and is best suited for revising service-life predictions during the lifetime of the motor and as a terminal measure of ultimate service-life.

In an effort to obtain an indication of the aging degradation of new propellant formulations or new liner-propellant bond systems due to long term storage at ambient temperatures short term accelerated aging tests are conducted at elevated temperatures. Accelerated aging test data are then related to ambient temperature aging conditions assuming that the rate of aging degradation obeys the classical Arrhenius equation

$$k' = A \exp(-E_A/kT) \qquad (2.3)$$

where

k' = rate of reaction at temperature T

E_A = activation energy, assumed constant

A = constant

k = Boltzmann's constant

Equation (2.3) is used to predict propellant physical property degradation by treating the rate of reaction k' as an average rate associated with some change, Δ, in a pertinent mechanical property. Thus,

$$k' = \frac{\Delta}{t} \qquad (2.4)$$

Defining Δ has the critical change signifying the end of useful service life, (2.4) and (2.3) may be combined to yield an estimate of the service life

$$t = A' \exp(E_A/kT) \qquad (2.5)$$

in which A' is a new constant equal to Δ/A. Equation (2.5) indicates that a plot of log t versus 1/T should be linear. This behavior has been observed for some propellants as shown in Detail 2 which presents data for polyurethane propellants where Δ was taken to be doubling of the initial strain at maximum stress or the decrease to one-half of the initial maximum nominal stress. (It should be recalled that polyurethane propellants frequently undergo a reversion, e.g., softening under high temperature aging. Most polybutadiene propellants, on the other hand, will harden under high temperature aging).

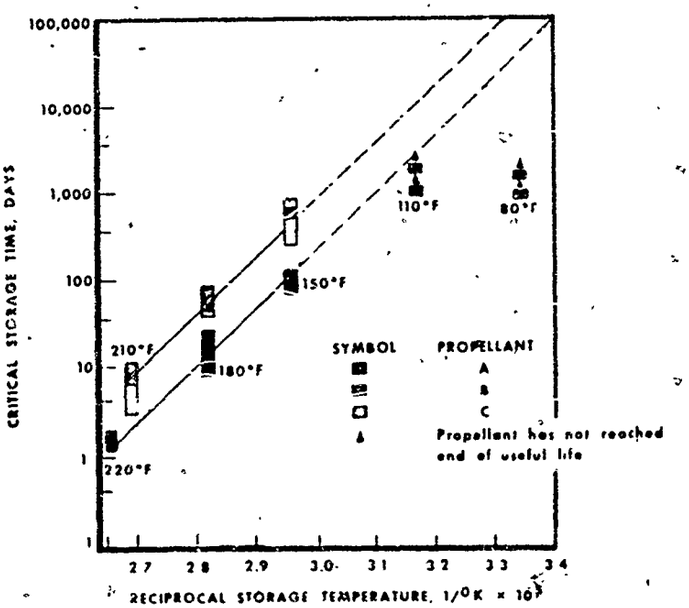

Detail 2.

Another Arrhenius type relation has been used for some propellants in which the degradation of a given physical parameter is a linear function of the logarithmic storage time with an increasing degradation rate with increasing storage temperatures. This behavior shown in Detail 3 for a CTPB propellant. In these circumstances the curves at different storage

temperatures may be cross plotted as a function of aging temperature as shown in Detail 4. A curve of this type may be used for interpolating aging degradation at other storage temperatures.

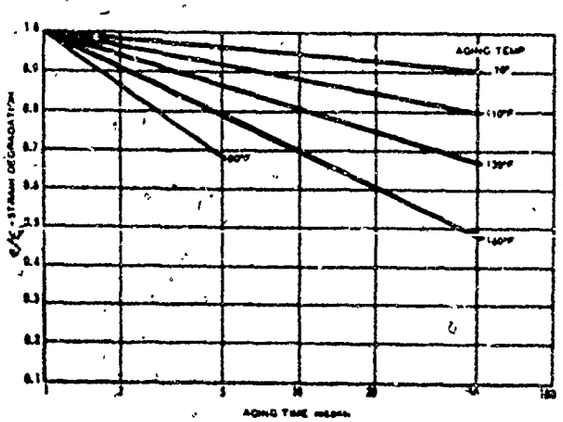

Reduction in Strain Capability

Detail 3.

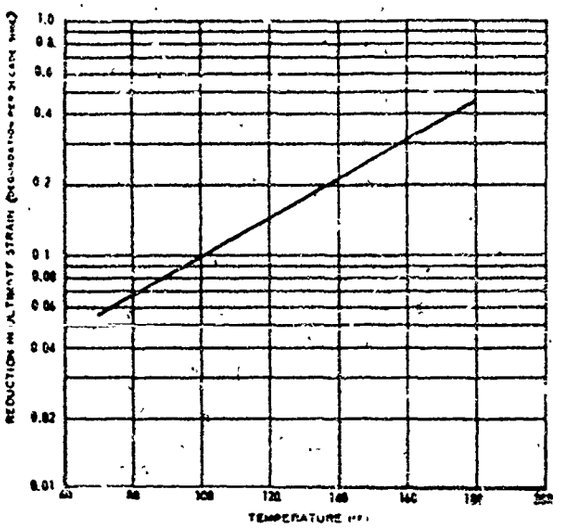

Reduced Strain Degradation

Detail 4.

The validity of the above kinetic approach is based on the assumption that the same processes occur over the range of storage temperatures and times; the only effect of the increased temperature is assumed to be an increase in the rate of reaction. This assumption leads to the well known rule-of-thumb that a ten-degree increase in temperature approximately doubles the rate of reaction. This behavior has been observed to a certain extent for some propellants. In general, however, caution must be exercised when using the straightforward Arrhenius type relations to make service-life predictions inasmuch as the assumption of a constant, temperature independent activation energy is not valid; and processes which do not occur, or are at least of little consequence at ambient

temperatures are initiated at elevated temperatures. The activation energies for competing processes (e.g., hydrolytic chain scission and oxidative cross-linking) are most probably different. Typically the degradation predicted from accelerated aging tests is substantially larger than that observed at lower storage temperatures. Thus, the common rule-of-thumb that 5 and 10 weeks aging at 160°F is equivalent, respectively, to 5 and 10 years ambient storage can be seriously misleading, and may result in eliminating propellants from consideration which are adequate for the actual storage environment.

Despite the inherent deficiencies associated with accelerated aging tests such tests are required on new propellant formulations in order to obtain even some indication of the aging characteristics of the propellant; even though such information is difficult to interpret at this time. Improvements in the methods of analyzing and interpreting accelerated aging test data are required, if this type of data is to be successfully used for quantitative service-life predictions in the future. Some indications of possible extensions of present analysis methods are described in the following paragraphs. Further improvements in service-life predictive capabilities will be forthcoming from the extensive chemical aging program being sponsored by the Air Force Rocket Propulsion Laboratory. This study is aimed specifically at relating chemical changes during aging to mechanical property changes.

Temperature dependence of the activation energy E_A may be introduced in a straightforward manner by considering the Van't Hoff equation from which Arrhenius obtained (2.3) [49],

$$\frac{d \log k'}{dT} = \frac{E_A}{kT^2} \tag{2.6}$$

As an initial point of departure, there is evidence (e.g., [50]) that the activation energy for fracture of viscoelastic materials is linear in temperature. There are also indications that the activation energy for some chemical reactions is also linear in temperature [49]. Thus, as a first approximation one may take $E_A = E_o - E_T$, where E_o is the activation energy at absolute zero. Substituting this expression in (2.6) and carrying out the implied integration,

$$k' = A(T)^{E/k} \exp(-E_o/kT) \tag{2.7}$$

The analogue of (2.5) is then

$$t = A' T^n \exp(E_o/kT) \tag{2.8}$$

where $n = k/E$. Equation (2.8) incorporates temperature dependence into the activation energy E_A; however, it is still based on the assumption that either only one process is occurring or that all processes have the same activation energy. If multiple aging mechanisms are occurring, which undoubtedly happens, then one may write (2.8) after the suggestion of Ree and Eyring [51] in the form

$$t = \sum_i A_i(T)^{n_i} \exp(E_{o_i}/kT) \tag{2.9}$$

where $n_i = k/E_i$. Equation (2.9) may lead to fruitful results if one considers a separate activation energy for each of the concurrent processes of chain scission, oxidative cross-linking and continued post curing. These activation energies may be related to changes in, say, cross-link

density in an effort to relate molecular parameters to observed mechanical behavior.

Mechanical properties (2.9) enter only through the damage index Δ in the coefficients A_i. It will be recalled that Δ is defined as the critical change in a particular parameter which signifies the end of useful service life. Inasmuch as the stress state during aging has a strong influence on aging behavior, as noted previously, it may be desirous to introduce a more direct dependence on the stress state. This may be accomplished by rewriting (2.9) as

$$t = \sum_i A_i (T)^{n_i} \exp[(E_{o_i} - W)/kT] \qquad (2.10)$$

where W is the work done in the stress state of interest. Within the usual context of the kinetic theory of the strength of solids W is taken to be $1/2\ \sigma\varepsilon$, (i.e., the strain energy associated with uniaxial tension on molecular bonds). However, inasmuch as we are not attempting, or suggesting, that this approach be interpreted molecularly in the context of the classical kinetic theory of solids, a more general expression may be considered from a phenomenological point of view. From this point of view, W, for example, may be taken to be the energy of a linear viscoelastic material as noted in [52]

$$W = \int_{vol} \int_{-\infty}^{t} \sigma_{ij}(\tau)\, \dot{\varepsilon}_{ij}(\tau)\, d\tau\, d\,vol \qquad (2.11)$$

corresponding to the loading history experienced by an aging propellant grain.

It may be possible to introduce temperature dependence into W in an ad hoc manner through the assumption of thermorheologically simple material behavior.

While the above approach is probably somewhat more general than present methods of analyzing accelerated aging test data, it does not account for the fact that certain processes occur at elevated temperatures which are of no importance under ambient temperature storage conditions. This behavior may be accounted for possibly by introducing a threshold temperature for a process in the expression for the activation energy for the process. This temperature may also be incorporated into the expression of a W and a shift factor relating storage-temperature and time with degradation deduced. Clearly much more work is required to quantitatively define the relationship between ambient and elevated temperature storage. Our intention here is only to point out a possible approach and hope that it will stimulate further study on this complex problem.

Direct development of constitutive equations for aging viscoelastic materials is another approach to the problem of predicting the aging behavior of solid propellants. For an aging, linear viscoelastic material a general differential constitutive equation may be written in the form

$$\left[\frac{d^n}{dt^n} + p_1(t)\,\frac{d^{n-1}}{dt^{n-1}} + \cdots + p_n(t)\right]\sigma = \left[q_0(t)\,\frac{d^n}{dt^n} + \cdots + q_n(t)\right]\varepsilon \tag{2.12}$$

Lubliner [53] has pointed out, however, that selection of a model for representing a time varying material requires more care than for a time invariant one. It is also noted that the solution of (2.12) becomes complicated except for the most simple models.

An alternate approach to the differential operator representation is to introduce a time dependent kernel (i.e., relaxation function) into

the common Boltzmann integral of linear viscoelasticity,

$$\sigma(t) = \int_{-\infty}^{t} k(t,\tau)\ \dot{\varepsilon}(\tau)d\tau \qquad (2.13)$$

In time-invariant linear viscoelasticity, $k(t,\tau)$ is simply the relaxation function $E(t-\tau)$. Several forms may be chosen for the aging kernel $k(t,\tau)$. Rabotnov has discussed two forms of $k(t,\tau)$,

$$k(t,\tau) = h(\tau)\ \phi(t-\tau) \qquad (2.14)$$

$$k(t,\tau) = g(t)\ \phi(t-\tau) \qquad (2.15)$$

Equation (2.14) has been used to describe creep in concrete, and (2.15) is frequently encountered in solving problems in the theory of hereditary elasticity with boundary conditions given on a variable boundary. Substituting (2.14) into (2.13) gives

$$\sigma(t) = \int_{-\infty}^{t} \phi(t-\tau)\ h(\tau)\ \dot{\varepsilon}(\tau)d\tau, \qquad (2.16)$$

whereas the function $g(t)$ in (2.15) can be extracted from the integral to give

$$\sigma(t) = g(t) \int_{-\infty}^{t} \phi(t-\tau)\ \dot{\varepsilon}(\tau)d\tau \qquad (2.17)$$

The functions $h(\tau)$ and $g(t)$ characterize the aging behavior of the material and may be determined experimentally from tests of aged samples.

Aging effects may also be treated within the framework of reduced variable concepts in the same manner that temperature is under the normal assumption of thermorheologically simple material behavior. Fulmer [54,55] has successfully treated environment as a reduced variable

in investigations of the creep failure of polymers. Stauffer and Wineman [56] recently suggested a more formal approach which represents an extension to the thermorheologically simple theory. Their study suggests an aging constitutive equation of the form

$$\sigma(t) \int_{-\infty}^{t} E\left[t-\tau, \psi_{s=-\infty}^{t}(s)\right] \dot{\epsilon}(\tau)\, d\tau \qquad (2.18)$$

where the functional $\psi_{s=-\infty}^{t}(s)$ is the reduced variable characterizing the effect of environment on the relaxation modulus. It is clear that the same considerations can be introduced into (2.16) or (2.17) and also into the previous kinetic approach if a technique, such as the idea of a threshold temperature, can be successfully derived for separating mechanisms which occur at elevated temperatures but not at lower temperatures.

The relaxation function E is determined in the presence of the environmental history ψ for the entire time interval $(-\infty,t]$. Supposing, for discussion purposes, that the relaxation modulus is determined for a series of aging times at constant temperature. Then a series of curves as depicted in Detail 5 would result.

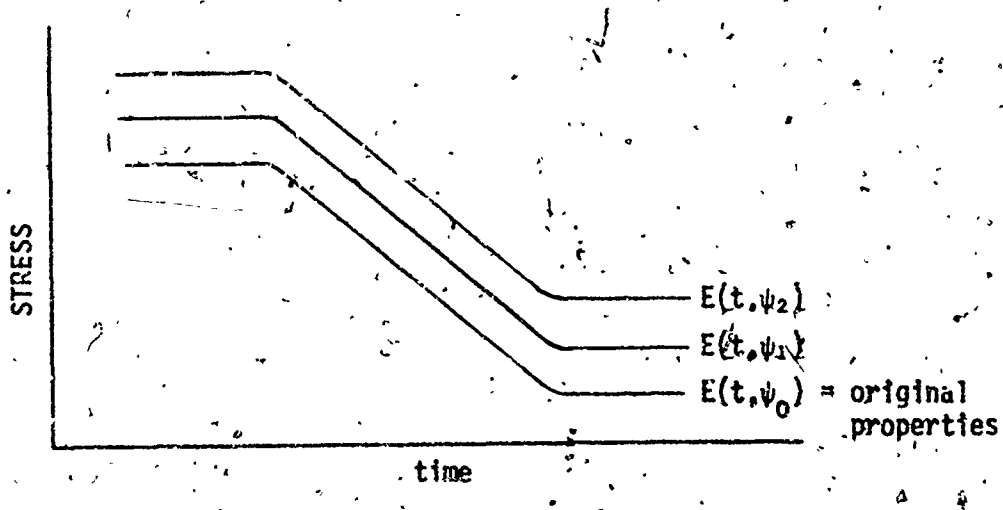

Detail 5. DEPENDENCE OF RELAXATION FUNCTION ON AGING TIME AT CONSTANT TEMPERATURE.

Changes in glassy and rubbery response may be accounted for simply through scale changes. If the slopes through the transition regions are identical for all aging times then a shift function may be determined relating aging time to relaxation response. If a relation between elevated and ambient temperature aging can be developed, than a master temperature-time curve for aging may be constructed in the identical way that a master relaxation modulus curve is constructed. If the slopes through the transition region vary with aging time or temperature, which they will do, then a more complicated reduced variable must be introduced. In principle, it should be possible to do this in a manner analogous to the construction of strain and temperature dependent shift factor (i.e., by vertical as well as horizontal translations). Rotations may also be required, however.

The reduced variable approach for studying the effects of aging is appealing for several reasons. First, the approach is quite general. It is equally well suited for studying the influence of other environments, such as humdidity, irradation, biological contamination, etc. Secondly, the approach is also suited for assessing damage inflicted by mechanical aging. By introducing a slightly different notation and a more general interpretation, (2.18) may be cast in the form similar to the equations discussed in Chapter II for describing the permanent memory behavior of solid propellants. Thus, by combining various aspects of the reduced variable approach to aging and environmental effects discussed here with the developments of Chapter II, it is not too difficult to see now a general nonlinear constitutive theory for solid propellants including the effects of aging and environment may be developed.

The reduced variable approach to aging may also afford a more direct opportunity for relating chemical changes during aging to observed mechanical behavior from the molecular viewpoint of Kelley and Williams [57,58]. Chemical changes may be characterized by their influence on a reduced variable. For example, the equilibrium modulus E_e, from rubber elasticity theory, is related to the crosslink density ν_e;

$$E_e = 3\nu_e kT \tag{2.19}$$

Thus, the vertical scale changes in E_e, shown in Detail 5 above, are related to changes in crosslink density. Observing changes in crosslink density through changes in the modulus in swelling with aging time then supplies the information for determining a vertical scaling shift factor for E_e. Aging temperature effects can be incorporated as discussed previously. Changes in other molecular parameters with aging time and temperature can be used in a similar manner. Chain scission may be determined from changes in binder molecular weight. The combined effects of concurrent chain scission and cross-linking can be separated to a certain extent and measured by continuous stress relaxation and intermittent stress measurement techniques. Dielectric and dynamic properties can also be used to measure changes in internal structure (e.g., molecular weight, degree of crystallinity, dewetting, crosslink density, conformational changes, etc.). Oxidative cross-linking may be measured by techniques which determine amounts of free and bound oxygen in propellant. Determination of these and other kinds of chemical changes during aging and establishment of their relationship to mechanical behavior should lead to a better understanding of aging degradation and a more realistic approach to service-life predictions. An important consideration in studies of this

type is that only changes in mechanical properties which are relevant to a motor structural integrity determination should be sought; extrapolations of propellant properties which do not enter directly into a structural integrity analysis can be seriously misleading.

The length and breadth of the discussion here on service-life prediction is indicative of the importance and severity of this problem. While this presentation has not considered present methods of making service-life predictions in detail, several approaches have been described which remove certain deficiencies from current service-life prediction methods. Some combination of the approaches described above, coupled with the information forthcoming from the Air Force sponsored Chemical Aging program, should lead to improved service-life predictive capabilities. Current techniques for making service-life predictions are adequately treated in References 17, 28, 33, 42, 44 and 59 through 67.

SURVEILLANCE PROGRAMS

In recent years, due to a general lack of confidence in service-life predictive capabilities, massive surveillance programs supposedly aimed at maximum cost effectiveness are initiated with each new motor program [17, 26-29, 38, 42-44, 61]. While it is not our intention to fully review past surveillance programs, some of the more important factors which contribute to a meaningful surveillance program will be briefly discussed. It will be seen that surveillance programs achieve maximum effectiveness when they function as a terminal measurement of ultimate service life.

Following an initial service-life prediction based on analysis of accelerated aging test data by some means such as those mentioned previously,

propellant samples, subscale-prototype motors and full-scale motors are placed in storage under service conditions 12 to 18 months before the first delivery of production motors. Periodically, subscale and full-scale motors are test-fired to determine ballistic changes. Physical property tests are also conducted to evaluate degradation of particular parameters which are determined to be important to the determination of grain structural integrity. These tests should typically involve selected uniaxial, biaxial and triaxial bond adhesion tests at various temperatures under loading environments carefully designed to simulate the motor loading environment. Recently determination of the cohesive fracture energy has been added to the list of relevant parameters [68]. An assessment of damage accumulation may be provided by conducting combined and repeated loading tests making use of cumulative damage concepts [17, 27, 28, 59, 60, 66, 67, 69]. Because of the significance of the differences observed between surface and bulk aging, carton and motor aging, and aging in a strained versus a stress-free state prototype subscale motors should be aged and periodically tested to failure under a critical loading environment, such as, for example, low temperature cycling. Occasional dissection of full-scale motors allows correlation of the behavior observed from carton storage with that observed from motor storage, evaluation of aging in a stressed state, and evaluation of surface and interface effects in the full-scale motor [24, 33, 34, 36, 39, 40, 69]. Miniature test specimens have been developed for determining propellant properties near the inner bore surface and the case-grain interface [33, 36, 39, 40, 70, 71]. As these tests are evaluated service life predictions may be continuously updated. Contingency samples should be provided in an aging surveillance program such as this to substantiate that a first failure does indeed

represent a deterioration of motor service life and to obtain statistical data for predictions of mean service life and probable distribution of failures. Extreme value statistics may be used for predictions of a first failure. By allowing 12 to 18 months lead time on controlled aging of motors and propellant samples, sufficient time is provided from the first indication of motor age-out to determine an appropriate course of action for the motors remaining in the field.

A comprehensive surveillance program, such as that outlined in the previous paragraph, is effective in evaluating the ultimate service-life of a solid rocket motor; however, the greater usefulness of such a comprehensive aging program is the rational basis it provides for extending the useful service-life of a solid rocket motor beyond contractor requirements or objectives. The value of this capability is readily recognized when it is recalled that in Southeast Asia, as in Korea, it has been necessary to use weaponry which has gone substantially beyond the predicted storage life.

NON-DESTRUCTIVE TEST TECHNIQUES

The comprehensive aging program outlined in the previous section has one serious drawback; namely, the high costs involved. Testing of propellant samples aged in cartons is not too expensive; however, structural testing of aged STV's and full-scale motors, and dissection of full-scale motors for propellant samples is quite expensive. Furthermore, when discrepancies exist between the controlled aging environment and field service conditions, or when uncertainties exist about actual field conditions, it is frequently necessary to remove motors from field storage for structural testing if a meaningful evaluation of motor service life is to be made. Removing motors

from the field can also be quite expensive. Thus, considerable attention has been given to the development of Non-Destructive Test (NDT) techniques which are applicable to solid propellant surveillance and which are adaptable to field use.

Some of the NDT techniques in use throughout the industry are summarized in Table III. Not all of these techniques are readily usable for field inspection of in-service motors, however. Also, these NDT inspection techniques are usually adequate for determining if failure has occurred in the form of cracking, unbonding, etc.; but they are, for the most part, not directly applicable to an assessment of propellant or case/grain bond degradation due to aging. For these reasons, recent efforts have been directed toward development of NDT methods for recording changes in physical properties which are relevant to structural integrity determination. Hardness relaxation measurements have been suggested as a means of evaluating surface aging[72].

Embedded gages have also been suggested for monitoring changes in propellant properties. The instrumentation required for monitoring internal stresses and strains in a propellant grain is not available within the present state-of-the-art technology, however. This instrumentation problem is difficult and complex. Satisfactory solution requires a knowledge of the stress-state existing in the motor and complete characterization of the propellant response.

The Air Force Rocket Propulsion Laboratory is sponsoring the development of an embedded gage for monitoring changes in propellant properties due to aging in a solid rocket motor. This instrumentation is vitally needed; however, progress on this difficult problem will most likely be slow and the development of reliable instrumentation will probably take several more years' research.

TABLE III. NON-DESTRUCTIVE TESTING FOR SOLID PROPELLANTS [18]

CONDITION	DETECTION TECHNIQUE	FOR DETECTION OF	OTHER CONSIDERATIONS
Chemical State	Radiation Reflection or Diffraction		
	Infrared attenuated total reflectance (ATR)	Chemical structural groups; quantitative compositional changes	
	Infrared reflectance	Same as above	Poorer than ATR
	Ultraviolet spectroscopy	Same as above	
	X-ray diffraction	Appearance of crystalline degradation products	Frequency of crystalline products occurrence unknown
	Resonant Response		
	NMR	Chemical structure and compositional changes	
	EPR	Free radical concentration	Secondary effect; occurence or correlation not established
	Evolved Gas Analysis		
	Mass spectrometer	Quantitative gases up to mol. wt. of C_6 hydrocarbons	
	Gas chromatography	Same as above	
	IR transmission		
	Film sensors		
	External sample analysis	All components	Does not measure grain
Physical State			
A. Propellant Surface Condition	Visual (Photographic) Observation	Surface cracks; migration products; roughness; accumulation of degradation products, oxidizer concentration owing to moisture; localized dewetting	Subjective observation.; travel-mechanisms required
	Boroscope		
	Miniaturized T. V. Microscope		
	Radiation Reflectance or Diffraction	All surface and sub-surface changes that effect reflected density	
	Photocell (visible)		
	X-ray diffraction		
	U. V. reflectance spectroscope		
	γ-ray back-scatter		
	Scintillation read out		
	Infrared reflectance		
	Radiation emission	All physical changes of surface or sub-surface that effect local rate of heat transfer	
	Infrared scan		
B. Dimensional Stability	Profilometer	Slump, liner separation, sub-surface voids, surface cracks	Requires internal traveling mechanism
C. Propellant Homogeneity and Density	Radiation Transmission	Porosity (dewetting) voids, cracks	
	X-ray		
	γ-ray		
	Scintillation read out		
	Low Frequency Sonic Transmission or Scatter	Porosity (dewetting) voids, cracks	
	Microwave transmission or reflection	Same as above	
D. Propellant Physical Properties	Hardness and Hardness Relaxation	Propellant modulus and relaxation rate changes caused by chemical changes or compositional changes owing to migration or absorption	Good potential to provide monitoring of propellant condition at selected points on surface; semi-non-destructive
	Sonic Transmission Reflection or Scatter	Propellant modulus	Establishment of correlation required
	Propellant Samples in Perforation or External to Motor	All physical properties	Correlation not established
	X-ray Diffraction Microwave	Crystallinity changes	Occurrence and correlation of crystallinity not established
E. Adhesive Interface Integrity	Ultra Sonic Reflection or Transmission	Modulus	At low temperature except for metal cases
	Low Frequency Sonic Reflection or Transmission	Liner separations	Developed system
	Infrared Emission	Liner separations	
	Radiation Transmission		Very high energies required for large grains
	X-ray		
	γ-ray		
	Microwave transmission or reflection		

2.4.3 CLOSURE

From the previous discussions it can be seen that complex problems are associated with aging and the exposure of a propellant grain to the environment. The solution to these problems is only partly complete at the present time. Adverse effects of exposure to the environment may be controlled by not allowing the propellant grain to come directly in contact with the environment. The problems associated with aging are more complex, however. The ultimate solution to problems associated with aging, of course, is the development of propellants and propellant-liner bond systems which do not age. This objective represents a difficult task requiring control of migration and balance of post cure reactions with chemical scission. These undertakings, as noted previously, have only been partially successful thus far. Several studies are presently underway which should result in an improved understanding of the mechanisms of aging and ultimately in the control of aging degradation. These programs have been discussed in the previous subsection. Because of the complexity of the aging problem, however, several more years of intensive research are required for obtaining a solution to the problems associated with aging.

2.5 MANUFACTURING AND PROCESSING CONSIDERATION

In the authors' opinion most motor failures do not result from a design deficiency, but rather, are the result of some obvious defect in processing that could have been avoided through thoughtful consideration of the processing methods and controls required to maintain the structural integrity of a solid propellant grain. To overcome the occurrence of motor failures attributable to processing errors it is necessary that the structural integrity engineer be familiar with the actual methods of motor

manufacture, the processing controls that are feasible in a plant operation and the controls that are necessary to maintain motor structural integrity. Thus, the purpose of the discussion herein is to acquaint the practicing engineer with some of the more important manufacturing and processing considerations which are related to motor structural integrity. The emphasis here, is given to the bond systems existing in rocket motors since bond failures represent the majority of all motor failures.

The integrity of any bond in a solid rocket motor is directly related to the processing methods. Good processing methods lead to reliable bond systems, whereas bad processing methods lead to poor bond systems which invariably result in costly repairs, and in some instances, even in motor rejection. In fabricating a stress relief flap, caution must be exercised to ensure the bond integrity between the flap and the motor case, within the flap, and between the flap and the propellant.

The bond between the flap and the motor case is the strongest of all interfacial bond systems and will represent an area of concern only if improper bonding techniques are used. The best bonding procedure is to vulcanize the flap in place using uncured or only partially cured rubber stock. An alternate, equally acceptable method is to use a high temperature (300°F) adhesive system to secondarily bond a cured rubber flap to the case. In this case, it is necessary to determine any detrimental effects the high temperature post cure of the rubber flap may have on the strength and compliance characteristics of the flap or on the propellant - liner - flap bond capability. In the event that the high temperature cure does result in a serious degradation of the flap material, acceptable results may be frequently obtained with a low temperature cure (160°F) secondary bond. In this case, as in the above cases, proper processing methods and

controls with regard to cleaning and surface preparation of the case and the flap, and the aging conditions of the adhesive are a prerequisite for obtaining acceptable bonds. The quality of this bond is normally determined from single lap or double lap shear tests.

The integrity of the flap is assured only through vulcanization of uncured rubber into a continuous one-piece flap. In this process, it is desirable to vulcanize the flap to the motor case simultaneously, if possible, to avoid the use of secondary bonds. Secondary bonds within the flap itself are usually not recommended. The potential savings, when compared with costs in time and money of extensive repairs, are not sufficient to justify secondary bonds in this critical region. The quality of this bond is determined through small angle and large angle (180°F) peel tests. The small angle tests are probably more representative of actual motor conditions. The interpretation of the results of either test is, at best, only qualitative.

The integrity of the propellant-liner-insulation (i.e., flap) bond is also, to reiterate, related to processing methods. The quality of this bond is normally determined through bond-in-tension and peel tests of the propellant-liner-insulation interface. The acceptance criteria for bond-in-tension tests is that the interfacial bond strength in tension be at least as great as the propellant strength, and that the observed failure mode be a cohesive failure on the propellant.[1]

Peel tests are routinely obtained from small angle, 90° and 180° angle

[1] The question of when a failure is or is not a cohesive failure is still unresolved. As a general rule-of-thumb, however, one may interpret a cohesive failure as one in which at least 1/16 inch of propellant remains on the liner surface. The primary requirement of a good bond system is that the strength of the bond be as great as or greater than the strength of the weakest component of the system, however.

peel tests. In these tests, as in the bond in-tension test, it would be desirable to have a cohesive failure in the propellant, liner, or even in the insulation. Unfortunately, the failure mode, and of course, the failure load, is greatly influenced by the angle of peel, the particular type of peel specimen being used, and the rate of the test. The result is that peel test data are extremely difficult to interpret quantitatively. Most present peel analyses do not indicate what the peel capability of a particular bond system under a given load environment should be, nor for that matter, do they assess the correspondence between peel angle in a motor and angle of peel during a laboratory peel test. Thus, these tests are only qualitative and are of most use in comparison of adhesive systems or evaluation of processing studies.

More quantitative results of adhesive bond systems may be obtained from the blister peel test [73,74]. The results of this test may be applied directly to assess the integrity of a given propellant/liner/insulation/case bond system. However, these tests are not conducted on a routine basis yet. Also, with the single exception of the blister peel test, there are no analyses available.

In the previous paragraphs major emphasis was placed on obtaining cohesive propellant failures. The justification for requiring this type of failure is based on the heuristic argument that past experience with solid rocket motors has indicated that grain unbonding at grain terminations is much less likely to occur when laboratory tests of the bond system have resulted in cohesive propellant failures. In the event that laboratory tests predominantly result in adhesive failures between the propellant and liner or the liner and insulation, corrective measures should be taken prior to manufacturing a motor, almost irrespective of the failure loads.

There are several means of improving a bond system to avoid adhesive failures. Usually only minor modifications are required. It is a generally accepted fact that the majority of all adhesive failures in laboratory specimens and full scale motors may be attributed to poor processing procedures. Thus, the methods of manufacturing the laboratory specimens should first be reviewed to ensure that proper consideration was given to surface preparation of all bonding surfaces, and that adhesives, liners and propellant were cured in the correct manner. The age and storage conditions of liner, propellant and adhesive ingredients should also be evaluated since most polymers and adhesives are greatly influenced by these factors, and they have a definite, restricted shelf-life. Another factor worthy of serious consideration is the storage environment of laboratory test specimens prior to their testing. It is well known that the storage environment is a major influence of bond strength and failure mode. Hence, early consideration should be given to restrictions on the relative humidity level and the atmosphere during specimen handling prior to testing and curing testing. In this regard, the use of solvents in storage and test areas should be avoided.

In the event that adhesive failures or low strength bonds still predominate after considering the factors in the previous paragraph, extensive processing studies may be employed for improving a bond system. Liner-propellant failure strengths increase as the liner thickness is increased. The failure mode also tends toward a cohesive propellant failure as the liner thickness increases. Thus, one significant processing study is to determine the liner-propellant strength and failure mode as a function of liner thickness. Liner cure or precure prior to propellant casting also

influences liner-propellant bond strength and failure mode. Hence, bond studies may be performed to determine the optimum liner cure or precure. Various different surface preparation techniques are also worth considering. Typically, the best bonds are obtained with rubber surfaces which have been sandblasted and loose particles removed by dry inert gas flow, or by acid etching. Ultrasonic cleaning methods appear to be a reliable means of cleaning hard surfaces such as metals and plastics. In the case of sandblasted surfaces, care should be exercised in choosing the grit size to avoid damage to the insulation and in maintaining a dry gas flow for removing loose particles. Vapor degreasing after sandblasting is not recommended unless the part has been exposed to the atmosphere for some time, in which case, care must again be exercised to make sure only clean solvents are used and no solvent remains on the part. Acid etching generally results in excellent bonding surfaces. The precaution that must be taken here is to control the depth of chemical attack. Acid etching is undesirable for small rubber parts as it is very easy to seriously degrade the bulk rubber properties.

It is worth mentioning that similar precautions should be taken with regard to obtaining good insulation flap-to-case bonds and flap-to-flap bonds. In these instances, processing studies similar to those mentioned above may be undertaken to improve a particular bond system. An additional consideration here is that of the pressure environment during cure of the adhesive. Maintaining a uniform pressure of sufficient magnitude is of particular importance when dealing with pressure-sensitive adhesive films.

In all laboratory processing studies, only those processing methods which can be carried over into plant manufacturing operations, with due regard for costs involved, should be considered.

2.6 NOMENCLATURE

A	=	Constant
E	=	Activation energy, constant
E_A	=	Activation energy at temperature T
E_o	=	Activation energy at absolute zero
E_e	=	Equilibrium modulus
g	=	Acceleration of gravity
$g(t)$	=	Aging function
$h(\tau)$	=	Aging function
k'	=	Rate of reaction
k	=	Boltzmann's Constant
$k(t,\tau)$	=	Kernal function
a	=	k/E = Constant
T	=	Temperature
T_1	=	Zero stress/strain temperature
T_c	=	Propellant cure temperature
ξ	=	Dummy time
t	=	Time
V	=	Volume
W	=	Work
α	=	Net volumetric cure shrinkage
α_p	=	Linear coefficient of expansion of propellant
β	=	Constant
Δ	=	Change in a physical property
ε	=	Strain
$\phi(t-\tau)$	=	Relaxation function
$\psi(s)$	=	Reduced variable for environment
σ	=	Stress
τ	=	Dummy time
ν_e	=	Crosslink density

2.7 REFERENCES

1. Lockheed Propulsion Company, "Engineering Methods for Grain Structural Integrity Analysis," Combined Final Report Contracts No. AF04(611)-8013 and DA-04-495-ORD-3260, May 1963.

2. Tormey, J. F. and Britton, S. C., "Effect of Cyclic Loading on Solid Propellant Grain Structures," AIAA Journal, Vol. 1 No. 8, August 1963.

3. Wagner, F. R., "Solid Rocket Load Definition Study: The Vibration Environment," Solid Rocket Structural Integrity Information Center, College of Engineering, University of Utah, AFRPL TR-68-149 (Contract No. F04611-67-C-0042), November 1969.

4. Bowden, F. P. and Yoffee, A. D., Initiation and Growth and Explosions in Liquids and Solids, Cambridge University Press, 1952.

5. Cook, M. A., The Science of High Explosives, Reinhold Publishing Corporation, New York, 1958.

6. Irwin, O. R., Salzman, P. K., Elwell, K. B., and Valor, N. H., "Shock Sensitivity of Solid Composite Propellants," 5th Seminar on the Sensitivity of New Materials (U), CPIA Publication No. 150, July 1967.

7. Pratt, T. H., "Initiation of Detonation in Solid Propellants," Technical Report S-177, Rohm and Haas Company, November 1968.

8. Napadensky, H. S ; "Sensitivity of Explosive Systems to Detonation and Subdetonation Reactions," ITT Research Institute, Chicago, Illinois, 1968.

9. Eriksen, T. A. and Tulis, A. J., "Shock-tube Sensitivity Testing," 5th Seminar on the Sensitivity of New Materials (U), CPIA Publication No. 150, July 1967.

10. Secor, G. A. and Williams, M. L., "Dynamic Measurement of Shock Intensity in Viscoelastic Materials," Final Report to USAMC, Redstone Arsenal, Alabama for Contract No. DAAH 01-67-C-1441, University of Utah, October 1969.

11. Secor, G. A., "Dynamic Fracture of Simulated Solid Propellant," in "The Chemistry and Mechanics of Combustion with Application to Rocket Engine Systems," UTEC TH 70-204, University of Utah, November 1970.

12. Thacher, J. H., "Structural Analysis of a Portion of the Cast-Double-Base Manufacturing Process," Bulletin of the 5th Meeting of the ICRPG Working Group on Mechanical Behavior," CPIA Publication No. 119, Vol. I, pp. 457-471, October 1966.

13. Cost, T. L., "Analytical Methods for Determining the Shrinkage Stresses in Polymeric Materials During Cure," Technical Report S-72, (Contracts No. DAAH01-67-6-0947 and DAAH01-68-C0891), December 1968.

14. Williams, M. L. and Jacobs, H. R., "The Study of Crack Criticality in Solid Rocket Motors," AFRPL TR 71-21, (UTEC DO 71-041), College of Engineering, University of Utah, (Contract No. F04611-70-C-0006), January 1971.

15. Bills, K.W., Jr., et al, "Applications of Cumulative Damage in the Preparation of Parametric Grain Design Curves and the Prediction of Grain Failures as Pressurization," Report 1341-26F, Aerojet-General Corporation, (Contract No. N00017-69-C-4423), August 1970.

16. Fishman, N., "Environmental Effects on Solid Propellants," Feature Article, Solid Rocket Structural Integrity Abstracts, Vol. 3, No. 1, pp. 1-22, January 1966.

17. Anonymous, "ICRPG Solid Propellant Mechanical Behavior Manual," CPIA Publication No. 21, 1963.

18. Kelley, F. N., "Solid Propellant Mechanical Properties Testing, Failure Criteria and Aging," Advances in Chemistry Series, Number 88, "Propellants, Manufacture, Hazards and Testing," pp. 186-243, American Chemical Society, 1969.

19. Colodny, P. C. and Ketchum, G. F., "Humidity and Temperature Effects on the Creep Behavior of Solid Propellants," Bulletin of the 4th Meeting of the ICRPG Working Group on Mechanical Behavior, CPIA Publication No. 94U, Vol. I, pp. 135-140, October 1965.

20. Dickinson, L. A., Atschuleo, M. H., McClay, R. E., and Tice, H. B., "Case Bonding Technology - A Review of Selected Applications (U)," Proc. of the Insulation and Case-Bonding Symposium (U), CPIA Publication No. 159, pp. 143-152, November 1967.

21. Stensen, R., "Chemical and Physical Factors Governing the Storage Life of Solid Propellant Rocket Motors," AIAA Paper No. 68-526, ICRPG/AIAA 3rd Solid Propulsion Conference, Atlantic City, New Jersey, June 4-6, 1968.

22. Kim, C. S., "Mechano-Chemical Effects in Propellant Binder Aging (U)," Bulletin of the 7th ICRPG Mechanical Behavior Working Group Meeting (U), CPIA Publication No. 177, pp. 303-314, October 1968.

23. Mosher, I. P., "Aging Mechanisms in CTPB Propellants (U)," Bulletin of the 7th ICRPG Mechanical Behavior Working Group Meeting, (U), CPIA Publication No. 177, pp. 291-302, October 1968.

24. Hart, W. D., Briggs, W. E. and Franz, W. K., "Experimental Investigations to Define the Effects of Aging Upon the Mechanical Properties of PBAA, PBAN, and CTPB Propellants," Bulletin of the 8th JANNAF Mechanical Behavior Working Group Meeting," CPIA Publication No. 193, Vol. I, pp. 227-238, March 1970.

25. Fife, W. B. and Epstein, R. H., "A Critique of Factors Affecting the Shelf Life of Motors Containing Polybutadiene Propellant Systems," Bulletin of the 8th JANNAF Mechanical Behavior Working Group Meeting, CPIA Publication No. 193, Vol. I, pp. 239-254, March 1970.

26. Button, S. C., et al, "Engineering Analysis of System Surveillance Programs," Bulletin of the 8th JANNAF Mechanical Behavior Working Group Meeting, CPIA Publication No. 193, Vol. I, pp. 297-318, March 1970.

27. Thacher, J. H., et al, "Structural Evaluation and Characterization of Materials, Subsystems, and Systems in a Solid Rocket Surveillance Program," Bulletin of the 8th JANNAF Mechanical Behavior Working Group Meeting, CPIA Publication, No. 193, Vol. 8, pp. 319-330, March 1970.

28. Leeming, H., et al, "Service Life Prediction and Verification," Bulletin of the 8th JANNAF Mechanical Behavior Working Group Meeting, CPIA Publication No. 193, Vol. 8, pp. 331-342, March 1970.

29. Myers, J. L., et al, "Organization and Management of Aging and Surveillance Programs," Bulletin of the 8th JANNAF Mechanical Behavior Working Group Meeting, CPIA Publication No. 193, Vol. I, pp. 343-356, March 1970.

30. Leeming, H., et al, "Solid Propellant Structural Test Vehicle, Cumulative Damage and Systems Analysis," Final Report No. AFRPL-TR-68-130, Contract F04611-67-C-0100), Lockheed Propulsion Company, Redlands, California, October 1968.

31. Leeming, H., et al, "Solid Propellant Structural Test Vehicle and Systems Analysis," Final Report No. AFRPL-TR-70-10, Contract No. F04611-69-C-0002, Lockheed Propulsion Company, Redlands, California, March 1970.

32. Oberth, A. E. and Bruenner, R. S., "The Cause of Moisture Embrittlement in Solid Propellants," Bulletin of the 5th ICRPG Mechanical Behavior Working Group Meeting, CPIA Publication No. 113, Vol. III, pp. 43-52, March 1967.

33. Olds, R. M. and Thompson, A. R., "Comparison of Operational Motor and Accelerated Aging Sample Propellant Properties," Bulletin of the 5th ICRPG Mechanical Behavior Working Group Meeting (U), CPIA Publication No. 158, Vol. I, pp. 1-14, October 1967.

34. Bennett, S. J. and Layton, L. H., "Aging Effects on Solid Propellant in Laboratory Samples and Full Scale Motors (U)," Bulletin of the 7th ICRPG Mechanical Behavior Working Group Meeting (U), CPIA Publication No. 117, pp. 339-350, October 1968.

35. Pickett, M. F., "Characterization of C-55A Propellant," NAVWEPS Report 9013 (NOTS TP 3997), U. S. Naval Ordnance Test Station, China Lake, California, April 1966.

36. Hart, W. D. and Briggs, W. E., "Experimental and Theoretical Correlation of Aging Effects Between Laboratory and Analog Motors," AIAA Paper No. 68-527, ICRPG/AIAA 3rd Solid Propulsion Conference, Atlantic City, New Jersey, June 4-6, 1968.

37. DeWitt, I. L., "Determination of Concentration Gradient of Ingredients in Aged Propellants," Presented at the 25th ICRPG Meeting of the Working Group on Analytical Chemistry, Picatinny Arsenal, New Jersey, June 1968.

38. Anonymous, "Service Life Improvement Program," Final Report TASK 5, TWR-2984, Contract No. AF 04(694)-926, Thiokol Chemical Corporation, Wasatch Division, Brigham City, Utah, 20 August 1968.

39. Miller, W. H. and Fulbright, J. L., "Variation of Propellant Mechanical Properties Near Propellant/Liner, Restrictor, Insulation Interfaces," (U), Proc. of the Insulation and Case Bonding Symposium (U), CPIA Publication No. 159, pp. 153-172, November 1967.

40. Fulbright, J. L. and Miller W. H., "Failure Analysis of Solid Propellant Grains Based on Dissected Motor Properties," Bulletin of the 6th ICRPG Mechanical Behavior Working Group Meeting, CPIA Publication No. 158, Vol. 1, pp. 377-392, October 1967.

41. Lohr, J. J., Wilson, D. E., Hamaker, F. M., Stewart, W. J., "Accelerated Testing of the Mechanical and Thermal Integrity of Polymeric Materials," J. Spacecraft Rockets, Vol. 5, No. 1, pp. 68-74, 1968.

42. Moon, E. L., "Samsonov, A., and Myers, J. L., "Revised Minuteman Service Life Estimating Procedure," TRW 12138-6002-RO-00, Contract F04701-68-C-0327, TRW Systems Group, San Bernardino, California 31 March 1969.

43. Francis, E. C. and Carlton, H., "A PBAA/AN Propellant Surveillance Report (U)," Bulletin of the 7th ICRPG Mechanical Behavior Working Group Meeting (U)," CPIA Publication No. 177, pp. 327-338, October 1968.

44. Veit, P. M., "Surveillance Program for Stage II Minuteman," Bulletin of the 8th JANNAF Mechanical Behavior Working Group Meeting, CPIA Publication No. 193, Vol. 1, pp. 255-266, March 1970.

45. Fife, W. B. and Wells, R. D., "Improved Insulation for Advanced Weapon Systems (U)," Proc. of the Insulation and Case Bonding Symposium, CPIA Publication No. 159, pp. 21-42, November 1967.

46. Whelan, W. P., Jr., Van Buskuk, P. R. and Kiley, L. Y., "New Materials for Solid Propulsion Combustion Chamber Insulation (U)," Proc. of the Insulation and Case-Bonding Symposium (U), CPIA Publication No. 159, pp. 3-20, November 1967.

47. Greever, W. L., "An Extended Temperature Range Case Bond System CMDB Propellants (U)," Proc. of the Insulation and Case Bonding Symposium, CPIA Publication No. 159, pp. 117-128, November 1967.

48. Vriesen, C. W. and Schloss, H. R., "Adhesive Study - Case Bonding Solid Rocket Motors (U)," Proc. of the Insulation and Case Bonding Symposium, CPIA Publication No. 159, pp. 129-142, November 1967.

49. Eyring, H. and Eyring, E. M., "Modern Chemical Kinetics," Reinhold Publishing Corp., New York, 1963.

50. Bartenev, G. M. and Zuyev, Yu. S., "Strength and Failure of Viscoelastic Materials," (translated by F. F. and P. Jaray), Pergamon Press, New York, 1968.

51. Ree, T. and Eyring, H., "Theory on Non-Newtonian Flow, I. Solid Plastic System," J. Appl. Phys., Vol. 26, pp. 793-809, 1955.

52. Fitzgerald, J. E., "Thermomechanics of Nonlinear Polymers under Non-equilibrium Processes," Presented at the Winter Meeting, Soc. Rheology, February 1971 (submitted for publication in Proc. Soc. Rheology).

53. Lubliner, J., "Rheological Models for Time-Variable Materials," Nuclear Engineering and Design, Vol. 4, pp. 287-291, 1966.

54. Fulmer, G. E., "Environment, in Addition to Stress, Temperature and Molecular Weight as a Reduced Variable in Environmental Stress Cracking," Pol. Eng. Sci., pp. 280-294, 1967.

55. Fulmer, G. E., "Kinetics of Environmental Stress Cracking," Proceedings of the Fifth International Congress on Rheology, Kyoto, Japan, 1968.

56. Stouffer, D. C. and Wineman, A. S., "Constitutive Representation for Linear Aging Environmental-Dependent Viscoelastic Materials," Paper presented at the Winter Meeting of the Society of Rheology, University of Utah, Salt Lake City, 1-3 February 1971.

57. Kelley, F. N. and Williams, M. L., "The Engineering of Polymers for Mechanical Behavior," Rubber Chem. and Tech., Vol. 42, pp. 1175-1185, 1969.

58. Williams, M. L. and Kelley, F. N., "Application of the Interaction Matrix Method to Solid Rocket Design," Bulletin of the 8th Meeting of the JANNAF Mechanical Behavior Working Group, CPIA Publication No. 193, Vol. I, March 1970.

59. Briar, H. P., "Relationships Between Propellant Failure Times in Various Modes of Failure," Bulletin of the 6th Meeting of the ICRPG Mechanical Behavior Working Group (U), CPIA Publication No. 158, Vol. II, pp. 137-148, March 1968.

60. Wiegand, T. H., "Prediction of Motor Life and Failure from Laboratory Test Data (U)," Bulletin of the 7th ICRPG Mechanical Behavior Working Group Meeting, (U), CPIA Publication No. 177, pp. 315-326, October 1968.

61. Myers, J. L., and Moon, E. L., "Service Life Prediction Programs for the Minuteman LAM 30 Propulsion System," Bulletin of the 8th JANNAF Mechanical Behavior Working Group Meeting, CPIA Publication No. 193, Vol. I, March 1970.

62. Briar, H. P. and Wiegand, J. H., "A Statistical Approach to Failure Criteria," Bulletin of the 3rd Meeting of the ICRPG Working Group on Mechanical Behavior, CPIA Publication No. 61U, Vol. I, pp. 455-468, October 1964.

63. Maiti, I. A., Morrill, L. G. and Bersche, C. V., "Predicting Propellant Storage Life by Superposition," Bulletin of the 5th ICRPG Mechanical Behavior Working Group, CPIA Publication No. 119, Vol. I, pp. 39-64, October 1966.

64. Planck, R. W., "Another Look at Predictions of the Service Life of Propellant Grains from Laboratory Test Data on Aged Specimens," Bulletin of the 6th ICRPG Mechanical Behavior Working Group Meeting, CPIA Publication No. 158, Vol. I, pp. 1-14, October 1967.

65. Chappell, R. N., Jensen, F. R. and Burton, R. W., "Statistical Service Life Prediction: Minuteman Third-Stage Propellant Grain," J. Spacecraft Rockets, Vol. 5, No. 1, pp. 42-44, 1968.

66. Bills, K. W., Jr. and Steele, R. D., "Effects of Chemical Change and Time-Dependent Response and Failure Properties on Grain Storage Life (U)," Bulletin of the 7th ICRPG Mechanical Behavior Working Group Meeting (U), CPIA Publication No. 177, pp. 351-358, October 1968.

67. Majerus, J. N., Buai, H. P. and Wiegand, J. H., "Behavior and Variability of Solid Propellants and Criteria for Failure and for Rejection," J. Spacecraft Rockets, Vol. 2, pp. 883-845, 1965.

68. Layton, H. L. and Bennett, S. J., "A Fracture Mechanics Approach to Surveillance," Bulletin of the 8th JANNAF Mechanical Behavior Working Group Meeting, CPIA Publication No. 193, Vol. I, pp. 209-226, March 1970.

69. White, B. B., "Case Cutting Techniques for Rocket Motor Dissection," Bulletin of the 6th ICRPG Mechanical Behavior Working Group Meeting, CPIA Publication No. 158, Vol. I, pp. 307-528, October 1967.

70. Briggs, W. E. and Hart, W. D., "A Special Miniature Specimen for evaluating Propellant," Bulletin of the 8th JANNAF Mechanical Behavior Working Group Meeting, CPIA Publication No. 193, Vol. I, pp. 435-438, March 1970.

71. Robinson, C. N., Graham, P. H. and Sturms, C. E., "A Microtest Specimen for Evaluation of Propellant Tensile Properties," Bulletin of the 5th ICRPG Mechanical Behavior Working Group Meeting, CPIA No. 119, Vol. I, pp. 65-82, October 1966.

72. Leeming, H. and Anderson, G., "Nondestructive Relaxation Modulus Measurement," Bulletin of the 8th Meeting of the JANNAF Mechanical Behavior Working Group, CPIA Publication No. 193, Vol. I, March 1970.

73. Jones, W. R., Jr., "Cohesive and Adhesive Polymer Fracture Investigation," Ph.D. Thesis, University of Utah, June 1970.

74. Williams, M. L., "The Continuum Interpretation for Fracture and Adhesion," J. Appl. Pol. Sci., Vol. 13, pp. 29-40, 1969.

III. PRELIMINARY DESIGN ANALYSIS

3.1 INTRODUCTION

A preliminary design analysis of a prospective candidate motor configuration determines if a given grain design has merit and possibly gives qualitative or semi-quantitative indications of how the design may be structurally improved. At this state in the analysis of a solid propellant grain approximations and simplifying assumptions in the analysis methods are warranted. Design data sheets and approximate engineering formulas are recommended for the analysis of conventional motor designs. Extensive numerical analyses at this level are unwarranted. The additional accuracy gained from using a computer analysis is often unjustified in view of possible approximations made regarding, say, material properties or failure data, and also, the uncertainty of the final design configuration does not justify the expense of computer analyses. An exception may exist in the case of new or novel grain designs, in which case, computer analyses may be required. In these cases, and particularly in the case of radically new grain designs, development of new analyses coupled with experimental subscale motor tests is recommended in place of relying on computer analyses of questionable applicability.

In the following sections, approximate engineering analysis methods are given for the loading conditions discussed in Chapter 2. The approximate methods considered in this chapter consist of formulas for calculating stresses, strai and deflections for thick-walled hollow cylinders. Empirically derived relationships for determining stress concentration factors for slotted and star configurations, and curves of finite length end correction factors, are included. The presentation of this material has been parameterized in terms of web fractions and length to diameter ratios. Because of the approximate d preliminary nature of the analysis methods discussed in this chapter only e expressions used for determining maximum values of stress, strain and deflection are given. These values are sufficient for a preliminary design analysis. Profiles of stress, strain and deformation as a function of length for finite length hollow cylinders have been obtained by means of finite difference solutions to the equations of elasticity formulated in terms of Southwell stress functions. These results are contained in the form of parametric curves in references 1, 2 and 3.

Extensive parametric curves which significantly simplify preliminary design analyses are presented in Appendix C.

The propellant is assumed to be incompressible. The influence of Poisson's ratio on stress and strain response is discussed in a subsequent chapter.

The analysis methods presented here are based on infinitesimal linear elasticity theory. The pertinent equations of elasticity are summarized in Appendix A to this handbook. Indications of how time and temperature effects may be incorporated are also discussed. For the most part, because of the preliminary nature of a preliminary design analysis, these modifications are not called for at the preliminary design stage.

3.2 TEMPERATURE LOADINGS

Thermal stresses and strains, as discussed in Chapter 2, result from a difference in linear and bulk coefficients of thermal expansion between the propellant and the motor case. Typical values of the "reduced" coefficient of (linear) thermal expansion for polybutadiene and double base propellants for various case materials are listed below:[1]

REDUCED COEFFICIENT OF THERMAL EXPANSION, α_R

Case Material	Propellant: Polybutadiene	Propellant: Double Base
Steel	$.5 \times 10^{-5}$ $(°F)^{-1}$	$.8 \times 10^{-5}$ $(°F)^{-1}$
Aluminum	4×10^{-5}	7.4×10^{-5}
Fiberglas	5×10^{-5}	9.5×10^{-5}
Nylon 66	$\sim 0.9 \times 10^{-5}$	3.7×10^{-5}

These values of α_R are representative of many propellants in these two classes of propellants. The use of the above values is recommended when thermal expansion data on the particular propellant being considered is unavailable. Most propellants will not have reduced coefficients of thermal expansion which vary more than ± ten percent from the above values.

In performing thermal stress and strain analyses, the calculations may be referred to the propellant cure temperature and cure shrinkage stresses and strains superposed, or the calculations may be referred to the zero stress/strain temperature of the propellant, T_1. This temperature is defined to be the temperature at which thermally induced stresses

[1] The "reduced" coefficient of thermal expansion occurs frequently in thermal stress and strain analyses and is defined by the relation $\alpha_R = \alpha_p - [(1 + \nu_c)/(1 + \nu_p)]\,\alpha_c$.

and strains vanish. Because of propellant shrinkage during cure, the zero stress/strain temperature will be higher than the cure temperature. It is often more convenient to take the zero stress/strain temperature as the reference for thermal stress analysis.

The temperature T_1 may be conveniently determined by several techniques. One method is to subtract the equivalent temperature decrease associated with the cure shrinkage from the propellant cure temperature

$$T_1 = T_c - (1/3\ \alpha_p)\ (\Delta V/V_0)\Big|_{t\to\infty} = T_c + (\alpha/3\alpha_p)\ , \quad (3.1)$$

where T_c is the propellant cure temperature, α_p is the propellant linear coefficient of thermal expansion and α is the net volumetric cure shrinkage. The net volumetric shrinkage of polybutadiene propellants is typically 0.002 and that of slurry cast double base propellants 0.005. The shrinkage of conventional cast double base propellants is considerably less as indicated in the previous chapter. These values are sufficiently representative to be valid in a preliminary design analysis.

Alternatively, the zero stress/strain temperature may be determined from analogue or subscale motor tests. In these tests the temperature of the cured motor is slowly raised above its cure temperature and measurements of the internal configuration versus temperature are recorded. The temperature at which the internal geometry of the motor coincides with the original mandrel configuration is then defined to be the zero stress/strain temperature. Measurements made in this manner indicate that T_1 is typically 15°F higher than the propellant cure temperature for polybutadiene propellants and 22°F higher for double base propellants [4,5]. These temperature increases are in close agreement

with those calculated using equation (3.1) and the values given above for typical volumetric cure shrinkage of these propellants. These values can be safely used in preliminary design analyses since there is little variation for a large number of propellants.

3.2.1 SHRINKAGE DUPING CURE

The volumetric cure shrinkage of most polybutadiene propellants and some double base propellants can be adequately described by the relation

$$\Delta V/V_0 = -\alpha[1 - \exp(-\beta t)], \qquad (3.2)$$

where α and β are experimentally determined constants. The constant α represents the net volumetric shrinkage, and the product $\alpha\beta$ represents the initial rate of shrinkage. The net volumetric shrinkage α is usually not explicitly temperature dependent, however, the shrinkage rate $\alpha\beta$ is strongly temperature dependent since polymerization, in general, is a thermally activated process which is usually adequately described by first order kinetic theory. Procedures for performing cure shrinkage tests are not readily available in the open literature, however, a common technique makes use of a mercury dilatometer submerged in a constant temperature bath. The rise of the mercury column in a capillary is monitored using a cathetometer.

Determination of cure shrinkage stresses in a solid rocket motor represents a difficult task which is beyond the current state-of-the-art capabilities. Recently, however, Cost [6] introduced an analytical approach which may prove to be worthwhile in the future for determining shrinkage stresses. In this report, [6] Cost treated curing polymers

under isothermal and steady-state thermal conditions, and formulated the basic governing differential equations in terms of differential operators. The material properties were treated as functions of space, time, temperature and degree of cure. Indications of how material behavior may be related to molecular parameters were given, based on Bueche's theory of molecular viscoelasticity. Such a theory may serve as a guideline for future developments in this area, however, lacking experimental verification, these developments should be considered to be of a preliminary nature. Development of analysis techniques for cure shrinkage stresses will quite likely be necessary in the future with the evolution of more complicated and more highly constrained grain configurations.

For the present state-of-the-art motor configurations, adverse effects of cure shrinkage can, for the most part, be avoided in preliminary and final design analysis phases through experience and engineering judgment based on the guidelines outlined in Chapter 2.

3.2.2 THERMAL COOLING AND TEMPERATURE CYCLING

The most severe loading experienced by a solid rocket motor is typically repetitive low temperature cycling. For conventional motor configurations, the critical areas of analysis are the inner bore and the case grain termination points.

In the case of very high mass fraction motors, the radial component of the case-grain interfacial stress at the motor midplane may be the limiting design parameter.

Normally, when considering temperature cycling effects, the stresses and strains are determined only for a low temperature soak of the grain. Cycling effects are then accounted for in the failure analysis using some cumulative damage rule. This is the procedure adopted here for preliminary design analysis.

In performing thermal strain or thermal stress analyses, a number of simplifying assumptions are normally introduced. First, the grain geometry is idealized to an infinite length hollow cylinder. Correction for internal geometry and finite length are introduced as multiplicative factors. It is also typically assumed that the case is infinitely rigid. Physically, this assumption is equivalent to assuming that the ratio bE_p/hE_c is negligible compared to one, where b denotes the outer grain radius, h the case thickness and E_p and E_c are Young's Moduli of the propellant and the case respectively. One also normally assumes a uniform temperature distribution throughout the grain. This is equivalent to assuming that the grain is very slowly cooled. The last assumption typically made is that the propellant is incompressible (i.e., $\nu = 1/2$).

The assumption of mechanical incompressibility normally leads to an inconsistency when Poisson's ratio, ν, the elastic modulus E and linear coefficient of expansion α (or equivalently the bulk modulus K and bulk coefficient of expansion 3α) are treated as independent quantities. For incompressible materials, thermodynamic restrictions require that α vanish. Thus, the development of thermal stresses and strains in incompressible material is excluded. In this case one typically makes the ad hoc assumption that as $\nu \to \frac{1}{2}$ the bulk modulus K becomes infinite, but the quantity $E = 3K(1-2\nu)$ remains finite and α is also assumed to be

nonzero. These inconsistencies can be removed most easily by reformulating the basic thermoelastic equations with the ad hoc introduction of a Grüneisen relation. Specifically, the limit

$$\beta = \lim_{\substack{\nu \to \frac{1}{2} \\ \alpha \to 0}} \left(\frac{\alpha_p E_0}{(1-2\nu)} \right) = \lim_{\substack{\alpha \to 0 \\ K \to 0}} 3\alpha_p K \qquad (3.3)$$

is assumed to approach a finite value as $\nu \to \frac{1}{2}$ and $\alpha \to 0$ concurrently. For crystal lattice structures, the quantity β (= constant) is known as the Grüneisen constant, and its existence is demonstrated through consideration of the nonlinear volume dependence of the frequency of a lattice vibration of specified wave vector. [7,8] The existence of the limit (3.3) for amorphous materials is based on thermodynamic arguments [9]. The usefulness of the relation (3.3) in performing thermal stress analyses has been suggested by Freudenthal [10] and Fitzgerald [11].

It is worth noting that the aforementioned inconsistencies do not exist in current finite element computer programs which incorporate Herrmann's reformulation [12]. This is due to the fact that Poisson's ratio is not taken to be 1/2 in these programs. Instead, the assumption is made that $\lambda >> 2\mu$ where λ and μ are the Lame constants, and a mean pressure function $H = 3\theta_1/2\mu(1+\nu)$ is introduced as additional unknown at each element, where θ_1 is the first stress invariant. In the limit as $\nu \to \frac{1}{2}$, Herrmann's reformulation can be shown to be equivalent to (3.3) [9].

The use of the relation (3.3) in performing thermal stress analyses of solid rocket motors is discussed in greater detail in a later section of this handbook. In the following sections, for the most part, the

results will be based on the asumptions of incompressibility and a non-zero coefficient of expansion α. Although inconsistent, these assumptions have led to results which have been proven reasonably adequate in the past for preliminary design purposes.

HOLLOW CYLINDER

Under the assumptions stated above, the maximum inner bore hoop strain is independent of material physical properties and is given by [4,5,13,14,15]

$$\varepsilon_\theta(a) = \log_e\{1 + \varepsilon'_\theta(a)\}, \tag{3.4}$$

where

$$\varepsilon'_\theta(a) = (3/2)\ \alpha_R\ \lambda^2\ \Delta T, \tag{3.5}$$

and

α_R = $\alpha_p - 2/3(1+\nu_c)\ \alpha_c$ = propellant reduced coefficient of linear expansion

$\lambda = b/a$ = Ratio of grain outer radius to inner bore radius

$\Delta T = T_1 - T$ = Temperature decrement from zero stress/strain from zero stress/strain temperature T_1.

The natural logarithm of the hoop strain has been introduced in equation (3.4) for calculation of the actual hoop strains since measurements on cooled analogue motors have indicated that the hoop strain is better described in terms of natural strain [4,5,13]. The relationship between $\varepsilon_\theta(a)$ and $\varepsilon'_\theta(a)$ is shown in figure 1, where it is seen that the

deviation associated with using equation (3.5) reaches about 10 percent at a hoop strain of 10 percent. For small strains, the difference between (3.4) and (3.5) is negligible.

In arriving at equation (3.5) a condition of plane strain has been assumed. If a condition of so-called "generalized" plane strain is assumed[2], equation (3.5) becomes

$$\epsilon_\theta^i(a) = (3/2)\ (\alpha_R\lambda^2-\alpha_p)\ \Delta T \quad . \qquad (3.6)$$

The maximum hoop strain at low temperatures predicted for conventional grain geometries by (3.6) is typically on the order of ten percent less than that given by (3.5). Equations (3.4) and (3.5) are recommended for preliminary analyses, since they tend to produce conservative results, and the condition of "generalized" plane strain is unrealistic and can lead to an overly optimistic opinion of a motor's capabilities.

Equation (3.5) is applicable for long, circular port grains. The relation between λ and grain length-to-diameter ratio L/D for which equation (3.5) is valid, based on numerical analyses [1,16], is shown in figure 2. All points to the right of the curve correspond to geometries for which (3.5) is applicable. Values of λ and L/D corresponding to points to the left of the curve represent geometries for which finite grain length correction factors must be applied. Finite length correction factors are discussed in a subsequent section of this chapter.

In addition to finite length correction factors, corrections for concentration factors for star perforated grains must also be applied

[2] By "generalized" plane strain is meant a condition of constant (nonzero) axial strain.

FIGURE 6 Grain Radius Ratio Versus Length-To-Diameter Ratio for Progressive Burning Grains

to equation (3.5). This correction is also discussed in a later section of this report.

Under the assumption's leading to equation (3.5), the maximum radial component of the stress is the case-grain interfacial bond stress given by

$$\sigma_r(b) = E_p \alpha_R (\lambda^2 - 1) \Delta T \quad . \tag{3.7}$$

The inner bore hoop stress is given by

$$\sigma_\theta(a) = 2\lambda^2 \alpha_R E_p \Delta T \quad . \tag{3.8}$$

SOLID CYLINDER

The previous equations have been developed for hollow cylinders under a condition of plane strain. To calculate thermal stresses and strains arising in an incompressible, infinite length solid cylinder, rigidly restrained, the basic thermoelastic equations must be modified if meaningful results are to be obtained, since mathematically infinite stresses are developed for even an infinitesimal temperature change in a rigidly restrained, infinite length hollow cylinder. This result is due to the aforementioned inconsistent assumption of the independence of the bulk coefficient of thermal expansion and the bulk compressibility. There are two methods by which an incompressible solid cylinder can be handled in a preliminary analysis. First, as in the case of the infinite length hollow cylinder, Poisson's ratio may be taken to be one-half and and nonzero linear coefficient of thermal expansion assumed with the rigid case replaced by a flexible thin case. Under these conditions the maximum radial bond stress is given by

$$\sigma_r(b) = \frac{3hE_c\alpha_R\Delta T}{2(1-\nu_c^2)b} \quad . \tag{3.9}$$

For a steel case with a grain radius to case thickness of 100 and a typical value of α_R taken from the table on page 2, this equation represents a bond stress of 25 psi/°F. The radial strain for this condition is constant independent of material physical properties and radial position and is given by

$$\varepsilon_r(r) = (3/2)\,\alpha_p \Delta T \qquad (3.10)$$

An alternate approach to this problem is to reformulate the basic thermoelastic equations with the ad hoc introduction of the Grüneisen relation (3.3). In this case a rigid case may be treated with the maximum radial bond stress given by

$$\sigma_r(b) = \beta\sigma_R\,\Delta T/\alpha_p \qquad (3.11)$$

where β is treated as a material constant. In the case of a flexible thin case the maximum bond stress is given by

$$\sigma_r(b) = \frac{\beta\alpha_R\Delta T}{\alpha_p}\left\{\frac{1}{1+\frac{2(1-\nu_c^2)b}{3\,hE_c}\,\frac{\rho}{\alpha_p}}\right\} \qquad (3.12)$$

The radial strain is again independent of the radial coordinate and material physical properties, and is given by

$$\varepsilon_r(r) = (3/2)(\alpha_p-\alpha_R)\,\Delta T \qquad (3.13)$$

For a typical composite propellant with bulk modulus K = 500 ksi and linear coefficient of expansion $\alpha_p = 5.6 \times 10^{-5}$ (°F), the Grüneisen constant β is determined to be 84 psi/°F. Using this value for β

equation (3.11) gives a bond stress of 75 psi/°F for a rigid case, and equation (3.12) gives a stress of 23 psi/°F for a flexible thin steel case with b/h = 100. It is seen that equations (3.9) and (3.12) give equivalent results for the case of a flexible thin case, as they should. The results for a rigid, or very thick case, are seen to be about three times greater than that for a thin case.

The strain represented by equation (3.13) is about one-tenth that given by equation (3.10). This is to be expected, however, since the assumption of a rigid case severely limits deflections.

From the above discussions, it is apparent that for geometries which can be analyzed using either classical techniques or through introduction of a Grüneisen relation, the results will not be significantly different. The introduction of a Grüneisen constraint, however, places the equations of thermoelasticity on an admissible thermodynamic basis. The greater use of a Grüneisen constraint will be for highly confined geometries; that is, very high mass fraction motors with relatively stiff, or thick cases. Before extensive use can be made of a Grüneisen constant, however, further investigation is required to verify that β is indeed a constant. In particular more accurate determinations of the bulk modulus of propellants and the behavior of the coefficient of thermal expansion in multiaxial stress states must be obtained.

The analysis described here for solid cylinders is useful for the preliminary analysis of, say, cartridge-loaded end-burning grains.

END-BONDED HOLLOW CYLINDER

The remaining grain geometry that is readily handled in a preliminary analysis is the finite length hollow cylinder with both ends bonded subjected to a uniform temperature decrease.

As in the previous cases a number of simplifying assumptions can be introduced. First, uniform end effects are assumed with no bending. The case is also treated as being rigid, and Poisson's ratio is taken to be 1/2 with a nonzero coefficient of expansion. Based on these assumptions the pertinent stresses and strains are given by [14].

$$\sigma_r(b) = (\alpha_p-\alpha_c)(1-\lambda^2) E_p \Delta T , \tag{3.14}$$

$$\sigma_\theta(a) = -2\lambda^2 (\alpha_p-\alpha_c) E_p \Delta T , \tag{3.15}$$

$$\sigma_z(r) = -(\alpha_p-\alpha_c)(1-\lambda^2) E_p \Delta T , \tag{3.16}$$

$$\epsilon_r(a) = (\alpha_p-\alpha_c)(1+3\lambda^2) \Delta T/2 , \tag{3.17}$$

$$\epsilon_\theta(a) = (\alpha_p-\alpha_c)(1-3\lambda^2) \Delta T/2 , \tag{3.18}$$

$$\epsilon_z(r) = -(\alpha_p-\alpha_c) \Delta T . \tag{3.19}$$

These equations can also be modified to include a Grüneisen constraint, however the resulting equations, to a linear approximation, yield results which agree quite well with the stresses and strains predicted by equations (3.14) through (3.19). For most applications, the results will differ by less than one percent.

3.2.3 AERODYNAMIC HEATING

Aerodynamic heating stresses and strains can be handled in a relatively easy manner in a preliminary design analysis. The conservative approach is to assume that the propellant grain undergoes a step radial displacement corresponding to a step temperature increase at the motor case. The resultant stresses and strains induced in the propellant grain are then superposed with thermal cooling stresses and strains. Temperature gradients through the case and propellant-case interface and expansion of insulation or liner materials are neglected in this approximation. Under these loading conditions and assuming plane strain conditions the maximum radial bond stress due to only aerodynamic heating is given by

$$\sigma_r(b) = 2(\lambda^2-1)\,\alpha_c\,E_p\,\Delta T_c/(3+\lambda^2)\ ,$$

and the inner bore hoop strain is given by

$$\varepsilon_\theta(a) = 4\lambda^2\,\alpha_c\,\Delta T_c/(3+\lambda^2)\ , \tag{3.21}$$

where ΔT_c denotes the step temperature increase at the motor case. Equations (3.20) and (3.21) may be added to equations (3.6) and (3.5) respectively to obtain the bond stress and bore hoop strain in a cooled propellant grain subjected to aerodynamic heating:

$$\sigma_r(b) = (\lambda^2-1)\,E_p\,\{\alpha_R\,\Delta T + 2\alpha_c\,\Delta T_c/(3+\lambda^2)\}\ , \tag{3.22}$$

$$\varepsilon_\theta(a) = 3\alpha_R\,\lambda^2\,\Delta T/2 + 4\lambda^2\,\Delta T_c/(3+\lambda^2)\ . \tag{3.23}$$

It can be seen, from a comparison of equations (3.20) and (3.21) with (3.22) and (3.23), that the magnitude of the stresses and strains

induced by aerodynamic heating will usually not be significant. The critical factor under this loading is the rapid decline of the propellant-case interfacial bond stress capabilities caused by the rapid temperature increase at the propellant case interface. The magnitude and the time scale of the temperature increase at the propellant case interface is usually minimized through the use of external insulation, such as cork, on the motor case which ablates and transfers the energy absorbed as heat back into the air flow.

In obtaining the above results, the heat transfer problem was neglected by imposing constant time and spatial variation of the temperature. This problem is complicated by the fact that for high velocity flow, the aerodynamic heating of the boundary layer affects the heat transfer and the friction appreciably. Further complications are introduced when the temperatures become so high that the gas dissociates or ionizes (an unlikely prospect for solid rocket motors), or for very high altitude high velocity flight where the mean free path of the molecules becomes of the order of the boundary layer thickness and the continuum treatment is no longer valid (also unlikely for solid rocket motors). At subsonic velocities aerodynamic heating is usually negligible, whereas at high speeds, on the other hand, the rate of heat flow to the missile skin increases roughly in proportion to the flight velocity (if the surface is maintained at constant temperature).

The approximations introduced above are undoubtedly sufficient for preliminary design purposes. Refinements which include introduction of time and spatial distribution of temperature are discussed in the following chapter on final design analysis techniques.

3.3 DYNAMIC LOADS

Dynamic loads are not treated extensively at the preliminary design stage since determining the dynamic response of a solid rocket motor involves solution of a coupled thermomechanical problem, which is not easily solved analytically. Simple problems, such as stan point deflections, and in some cases axisymmetric geometries can be dealt w th through the introduction of simplifying assumptions.

3.3.1 SHOCK LOADS

Shock loads occur when a solid rocket motor is subjected to a severe mechanical jolt such as dropping during handling or shipping. Since these loads act over a short period of time, the propellant normally responds as an elastic material with a glassy modulus. The most severe damage likely to occur is unacceptable inelastic deformation of the case. Damage to the propellant grain is usually minimal, although the possibility does exist for grain unbonding at low temperatures caused by large deflections of the case. Stresses and strains in the propellant grain can be estimated through an approximate conversion of the shock loads to an equivalent gravity loading, and subsequently treating shock loading as an acceleration loading.

For a motor subjected to an axial shock, the shear stress at the propellant-case interface is given by [15]

$$\tau_{rz} = \rho\, n{\cdot}g\, b\, (\lambda^2-1)/2\lambda^2 \qquad (3.24)$$

where inertial effects due to straining have been neglected and

ρ = Propellant Density

$n{\cdot}g$ = Equivalent Acceleration in Gravities.

Typically a multiplicative factor of 3 is applied to equation (3.24) in an attempt to account for stress concentrations at grain termination points [4]. Because of the short loading duration, grain deformations will be small and can be neglected under axial shock loadings. A lateral, or transverse shock, however, can produce significant grain deformations. The maximum inner bore hoop strain for a rigidly incased, incompressible cylindrical grain subjected to a lateral shock is given by [15]

$$\varepsilon_\theta(a) = 3/4 \; \frac{a \rho \, n \cdot g}{\xi_p} \; \frac{(\lambda^2-1)^2}{\lambda^4+1} \qquad (3.25)$$

under plane strain conditions.

Equations (3.24) and (3.25) can be used for geometries other than cylindrically perforated grains. In using (3.24) an equivalent circular port radius can be estimated, or more simply, the product of the total propellant weight and the equivalent acceleration loading can be divided by the total bonded area to give an average shear stress. In the case of star perforated grains a multiplicative strain concentration factor may be applied to equation (3.25) for estimating bore strains.

Modifications, introduced due to partial head end bonding are discussed in a subsequent section of this chapter.

Lateral shock loading of star perforated grains can be treated in a similar approximate manner. Assuming incompressibility and treating the star point as a cantilevered plate of uniform thickness the stress at the point of support is given by [15]

$$\sigma = 3 \; n \cdot g \; \rho \; \ell^2/h \; , \qquad (3.26)$$

where

ℓ = length of starpoint,

h = average starpoint thickness

Normally a factor of 2 is multiplied into (3.26) to account for the stress concentration at the point of support. The deflection of the innermost point of the star tip may be estimated from the relation [15]

$$\Delta = 3 \frac{n \cdot g \rho \ell^4}{E_p h^2} \quad . \tag{3.27}$$

The results of this section may be used to estimate the gross behavior of solid rocket motors subjected to shock loads, however, these results must be regarded as approximate since the true dynamic problem has not been considered.

3.3.2 VIBRATION

Vibration of solid rocket motors is generally recognized as a potential structural integrity problem for applications in which severe or sustained vibration environments are encountered. For example, possible effects of cyclic loading of solid propellants have been vividly shown by Tormey and Britton [17]. They reported on an extreme amount of dissipative heating and grain damage which occurred in vibration tests of solid propellant rocket motors.

Vibration is not dealt with extensively at the preliminary design stage, and in fact, it has only been recently that finite element computer programs have been available for considering vibration in final design analyses. Simple geometries, however, such as star points

subjected to lateral vibrations and circular port grains subjected to axial shear vibrations can be dealt with in an approximate manner. In the following paragraphs approximate formulas are given for estimating amplitude ratios and dissipation. A brief general discussion is also provided.

While the analysis problem has not as yet been completely solved for the complex grain geometries of practical motor systems (see references 18 and 19 for current status and extended bibliographies), analytical solutions have been obtained for simple systems which seem to agree well with experimental data (references 20 through 24). Such information, while not capable of providing quantitative information for motor design and analysis purposes, can provide valuable insight into material property and grain design characteristics which are advantageous for applications.

In addition to the usual difficulties encountered in uncoupled thermoviscoelastic analyses, the characteristically strong temperature dependence of propellant mechanical properties makes the dissipation or heat generation resulting from cyclic loading very sensitive to temperature variations, and hence leads to a strongly nonlinear heat source term. Moreover, in rocket motor vibration, energy is coupled into the propellant grain from the vibrating case by the inertial reaction of the mass of the propellant grain to the accelerating case. Disregarding inertia and material property degradation, large temperature increases are encountered whenever the applied stress or strain exceeds a certain critical value. The combination of temperature-dependent properties and inertia leads to the possibility of temperature and displacement jump instabilities which are similar to the phenomena observed in a nonlinear

spring-mass system in which the spring softens with increasing displacement.

In considering the vibration response of solid rocket motors, two propellant physical property parameters are of particular significance. These are the log-log slope of the reduced relaxation modulus in the time-temperature region of interest (slope of the curve log modulus versus log reduced time) and the slope of the log shift factor, a_T, versus the temperature range of interest. The amplication factor at resonance (with or without jump instability effects) which, along with the acceleration level, determines the peak strains imposed on the propellant is a function of the relaxation modulus slope only. As this slope decreases (i.e., as the propellant becomes more elastic and less viscoelastic) damping decreases and the propellant strain amplitude at resonance increases. Conversely, as the slope increases, corresponding to an increase in viscous response, the strains at resonance decrease and the resonance broadens. Clearly, with all other factors equal, a propellant with a large slope would be subjected to smaller deformations at resonance.

The slope of the shift factor versus temperature curve is a measure of the temperature sensitivity of the viscoelastic properties of a propellant. Since the mechanical property temperature sensitivity along with inertial loading conditions produces the nonlinear jump instability effect, it follows that for otherwise identical conditions, the jump stability effect will be most predominant for propellants which have a large shift factor versus temperature slope.

The above discussion has been concerned only with what might be called "reversible" thermomechanical effects resulting from the propellant

thermoviscoelastic properties and cyclic loading conditions. "Irreversible" effects which include fracture, degradation or decomposition effects and autoignition which can be the result of the combined high temperature and cyclic strain conditions of the vibration environment have not been accounted for. These phenomena are, of course, also of paramount importance, however the establishment of a failure criterion for the thermal-vibration environment is a difficult task. Experience has shown that for the conditions usually encountered in solid rocket motor vibration, fracture or severe degradation will usually precede and prevent temperature rises to levels at which autoignition will occur. Propellant susceptibility to fracture under prescribed vibration conditions is a significant factor in practical situations, however, and is found to vary significantly from propellant to propellant as well as for various transient loading conditions.

The problems of physical or chemical degradation for the combined thermomechanical environment is undoubtedly the most difficult and least understood of the failure mechanisms known to be significant for vibration of solid propellant. Degradation of CTPB propellant under sustained vibration has been shown by Tormey and Britton [17]. Degradation of other composite propellant formulations has also been shown [24]. Experience indicates that there is not a gross difference in the vibration behavior of double base and composite propellants.

As mentioned above, the dynamic behavior of simple geometries can be approximated in a relatively easy manner using lumped parameter single degree of freedom models. In the following paragraphs the isothermal steady-state sinusoidol vibration behavior of starpoints and the

case-grain interface under lateral vibration modes, and the propellant grain under an axial vibration mode are discussed. The presentation of this material essentially parallels the development in reference 15.

LATERAL VIBRATION OF A STARPOINT

The star point under a lateral mode of vibration is idealized as a massless cantilevered plate with a concentrated, equivalent mass at its free end. The model is shown in figure 3A. The dimension in the z direction is assumed sufficiently large so that end effects may be neglected. The model is excited at the fixed end.

The equation of motion governing the elastic response of the model is

$$M_e \ddot{v}_m + k v_m = k v_b, \tag{3.28}$$

where

M_e = effective mass of the lumped mass systems,

v_m = lateral displacement of the mass,

v_b = lateral displacement of the base support,

k = spring constant of the model,

and the superior dots indicate differentiation with respect to time t. The viscoelastic response of the model is obtained in a straightforward manner from the corresponding elastic solution by replacing the elastic spring constant of the model, k, by a complex spring constant k*:

$$k \rightarrow k^* = (k' + ik'')\,\omega^n \quad , \tag{3.29}$$

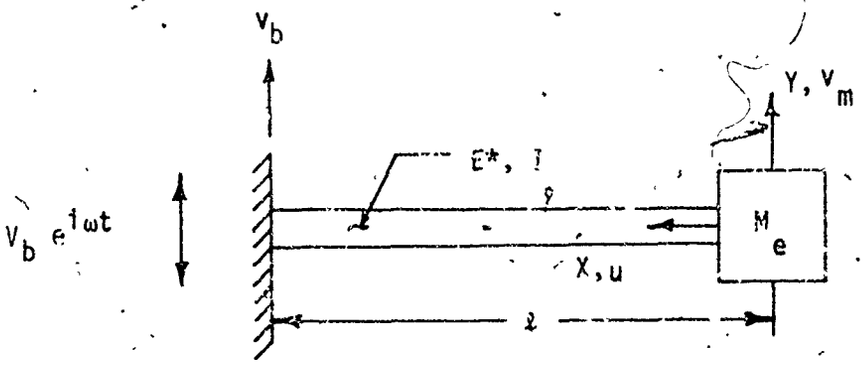

A. LUMPED MASS MODEL OF SLENDER STAR POINT UNDER LATERAL EXCITATION.

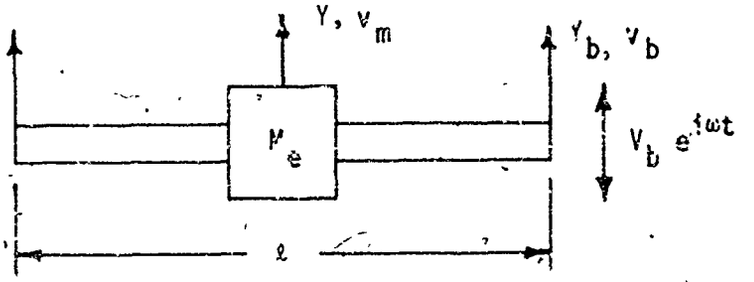

B. LUMPED MASS MODEL OF CASE AND GRAIN UNDER LATERAL EXCITATION.

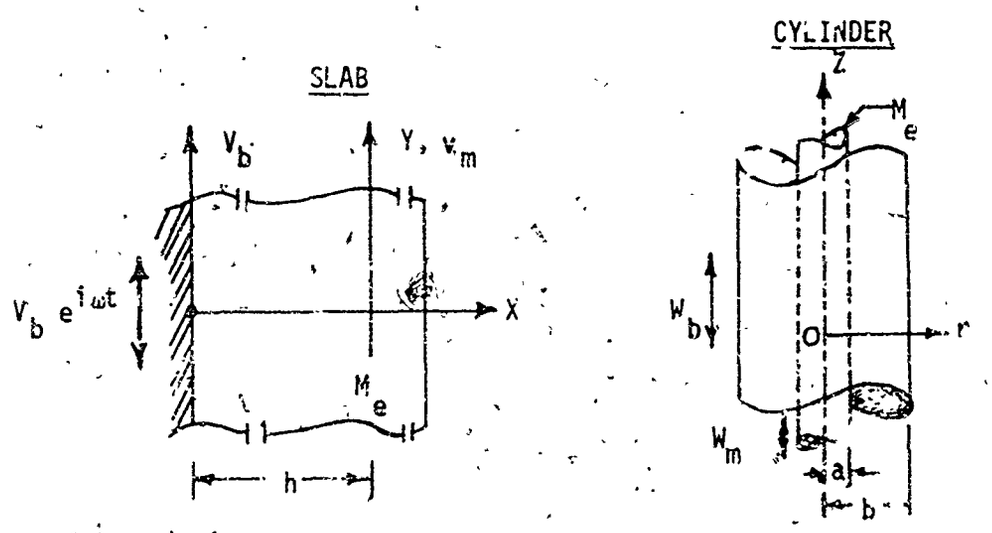

C. LUMPED MASS MODEL OF INFINITE SLAB AND CASE-BONDED GRAIN.

FIGURE 3 Vibration Models

where

ω = circular excitation frequency

n = slope of relaxation modulus versus reduced time curve, assumed constant,

and a power law representation of the complex spring constant of the material has been assumed. For the case of steady state sinusoidal vibration, the excitation v_b and the response v_m are assumed to be of the form

$$v_b = V_b \exp(i\omega t) \quad , \tag{3.30}$$

$$v_m = V_m \exp[i(\omega t - \alpha)] \quad , \tag{3.31}$$

where

V_b = magnitude of excitation

V_m = magnitude of response

α = phase angle

Substituting (3.29), (3.30) and (3.31) into (3.28), the equation of motion governing the viscoelastic behavior of the model is obtained;

$$-M_e\omega^2 V_m + (k' + ik'')\,\omega^n V_m = (k' + ik'')\,\omega^n V_b e^{i\alpha} \tag{3.32}$$

From this equation the amplitude ratio of the response to the excitation is readily determined to be

$$\left| \frac{V_m}{V_b} \right| = \frac{(1 + \beta)^{\frac{1}{2}}}{((1 - M_e\omega^{2-n}/k')^2 + \beta^2)^{\frac{1}{2}}} \quad , \tag{3.33}$$

where the loss tangent β is defined through the relation

$$\beta = k''/k' \quad . \tag{3.34}$$

Equation (3.33) can be simplified through introduction of a natural frequency

$$\omega_n^{2-n} = k'/M_e \quad , \tag{3.35}$$

and a reduced frequency ratio

$$\Omega = (\omega/\omega_n)^{2-n} \quad . \tag{3.36}$$

Substituting (3.35) and (3.36) into (3.33) a simpler expression for the amplitude ratio is obtained;

$$\left| \frac{V_m}{V_b} \right| = \frac{(1 + \beta^2)^{\frac{1}{2}}}{[(1 - \Omega)^2 + \beta^2]^{\frac{1}{2}}} \quad . \tag{3.37}$$

The behavior of the amplitude ratio as a function of the frequency ratio Ω is shown in figure 4 for several values of β. Clearly, the amplitude ratio is a maximum when the excitation frequency is equal to the natural frequency of the model; that is, when $\Omega = 1$,

$$\left| \frac{V_m}{V_b} \right|_{max} = \frac{(1 + \beta^2)^{\frac{1}{2}}}{\beta} \tag{3.38}$$

The phase angle by which the response lags the excitation may also be determined from (3.32);

$$\tan \alpha = \frac{\beta\Omega}{(1 - \Omega) + \beta^2} \quad . \tag{3.39}$$

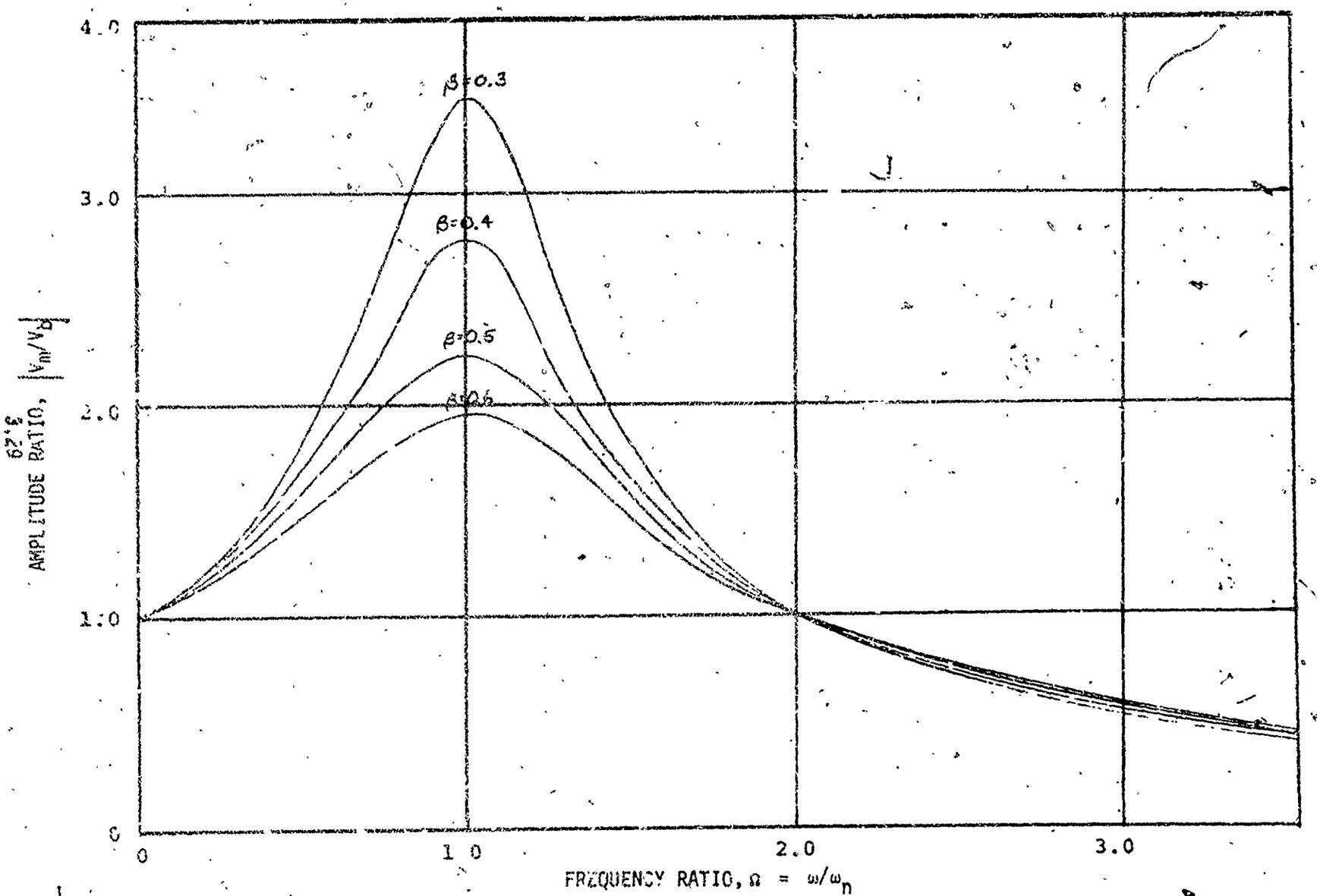

FIGURE 4 Amplitude Ratio Versus Frequency Ratio

It is seen that at maximum amplification, the phase angle is simply related to the loss tangent; viz.,

$$\alpha = \tan^{-1} (1/\beta) \quad . \tag{3.40}$$

From (3.38) and (3.40) it is seen that the maximum amplification factor and the phase angle lag of the response can be estimated knowing only one propellant physical property, namely the slope n of the log-relaxation modulus versus reduced time curve. Knowing n, the loss tangent β is determined using the relation

$$\beta = \tan (n\pi/2) \quad . \tag{3.41}$$

This relation exists theoretically for linearly viscoelastic materials, however for nonlinear, highly solids loaded propellants this relation has been shown to be in error [23]. Nevertheless, equation (3.41) is an acceptable approximation for preliminary design purposes when the dynamic behavior of the propellant is unknown.

Although the complex stiffness of the model, or propellant, is not required for estimating the response for an excitation frequency equal to the natural frequency of the model, this information is needed for determining the response for any other frequency. The effective mass M_e and the spring constant k^* are readily determined to be [25]

$$M_e = (33/140)\ (w\ell/g), \tag{3.42}$$

and

$$k^* = (1/3)\ (h/\ell)^3\ E^* = (1/3)\ (h/\ell)\ (E' + iE'')\omega^n, \tag{3.43}$$

where

w = linear density of cantilevered plate,

ℓ = length of cantilevered plate,

g = acceleration of gravity ,

h = plate thickness = average thickness of starpoint,

E^* = complex modulus,

$E'\omega^n$ = storage modulus,

$E''\omega^n$ = loss modulus.

$\beta = E''/E'$ = loss tangent

Before considering the lateral vibration of a cylindrical port propellant grain it should be noted that the maximum amplification ratio (3.36) is also valid for acceleration forced vibration. Also, although it appears that a high loss tangent β implying a large amount of internal damping would serve to decrease the amplification factor, an increase in internal damping significantly increases internal heat generation, and hence temperature rise, at frequencies away from resonance since the resonance is broadened. It should also be noted that the simple theory presented here applies only to Euler-Bernouilli beams. When the thickness of the beam (i.e., starpoint) is such that shearing deformations becomes significant. (roughly when the height approaches the length), then Timoshenko beam theory must be used to determine the response [26, 27] Finally, it should also be remembered that only a simple single degree of freedom model has been employed in the idealization of the starpoint geometry. Any real continuum, of course, possesses an infinite number of degrees of freedom, however this approximation should be valid for the lower modes of vibration.

LATERAL VIBRATION OF A CIRCULAR PORT GRAIN

The lateral vibration of an infinite length cylindrical port grain is idealized by the pin-ended model shown in figure 3B. The amplitude ratio (3.33) is also applicable for this model, however, new and different values of β, k^* and M_e are required. For the geometry of this model, the effective mass is given by

$$M_e = (29/70)\ (w_e \ell/g), \tag{3.44}$$

where

$$w_e = \rho_c bh + \rho_p \pi(b^2-a^2)\ , \tag{3.45}$$

with

w_e = linear density of the beam,

ℓ = length of beam,

ρ = density,

h = motor case thickness,

$2b$ = grain O.D.,

$2a$ = grain I.D.,

and the subscripts c and p refer to case and propellant properties respectively. For this model, the frequency terms are absorbed in the real and imaginary parts of the complex spring constant,

$$k^* = k'(\omega) + ik''(\omega) \tag{3.46}$$

where

$$k' = \frac{48}{\ell^3}\{E'\omega^n\pi(b^4-a^4)/4 + E_c b^3 h\} \simeq \frac{48}{\ell^3} E_c b^3 h\ , \tag{3.47}$$

$$k'' = \frac{48}{\ell^3}[E''\omega^n\pi(b^4-a^4)/4]\ ; \tag{3.48}$$

and the loss tangent is given by

$$\beta = k''\ell^3/48\ E_c b^3 h. \tag{3.49}$$

Assuming $\beta << 1$, the approximate expression for the amplitude ratio at $a = 0$ is obtained;

$$\left|\frac{V_m}{V_b}\right|_{max} \simeq 4E_c h/E'' \pi\omega^n b \ . \qquad (3.50)$$

It can be seen here that high amplification factors may be observed for lateral vibration because of the strong influence of the case stiffness.

The natural frequency at resonance is approximately given by

$$\omega_n^{2-n} = \frac{(70)(48)E_c b^3 h g}{(29)\ \ell^4\ w_e} \ . \qquad (3.51)$$

AXIAL VIBRATION

In a manner similar to that above, the axial vibration of a case-bonded cylindrical grain cay be treated by lumping its mass at the center as shown in figure 3C. The slab which is also shown in figure 3C is mathematically equivalent to the cylinder and is used in the following section in discussing thermomechanical coupling and heat generation. As before, the grain is assumed sufficiently long so that end effects may be neglected.

As before, the amplitude ratio is also given by (3.37) with a new definition of the natural frequency ω_n. For this geometry it is more convenient to work with a nondimensional effective mass M_e^* defined by

$$e^* = \frac{g\ M_e}{\pi\rho_p b^2} = \frac{\lambda^4}{2}\{(\lambda^2-1)/\lambda^2 \log_e\lambda + 2(\log_e\lambda - 1)\ , \qquad (3.52)$$

The effective mass versus λ is shown in Figure 5.

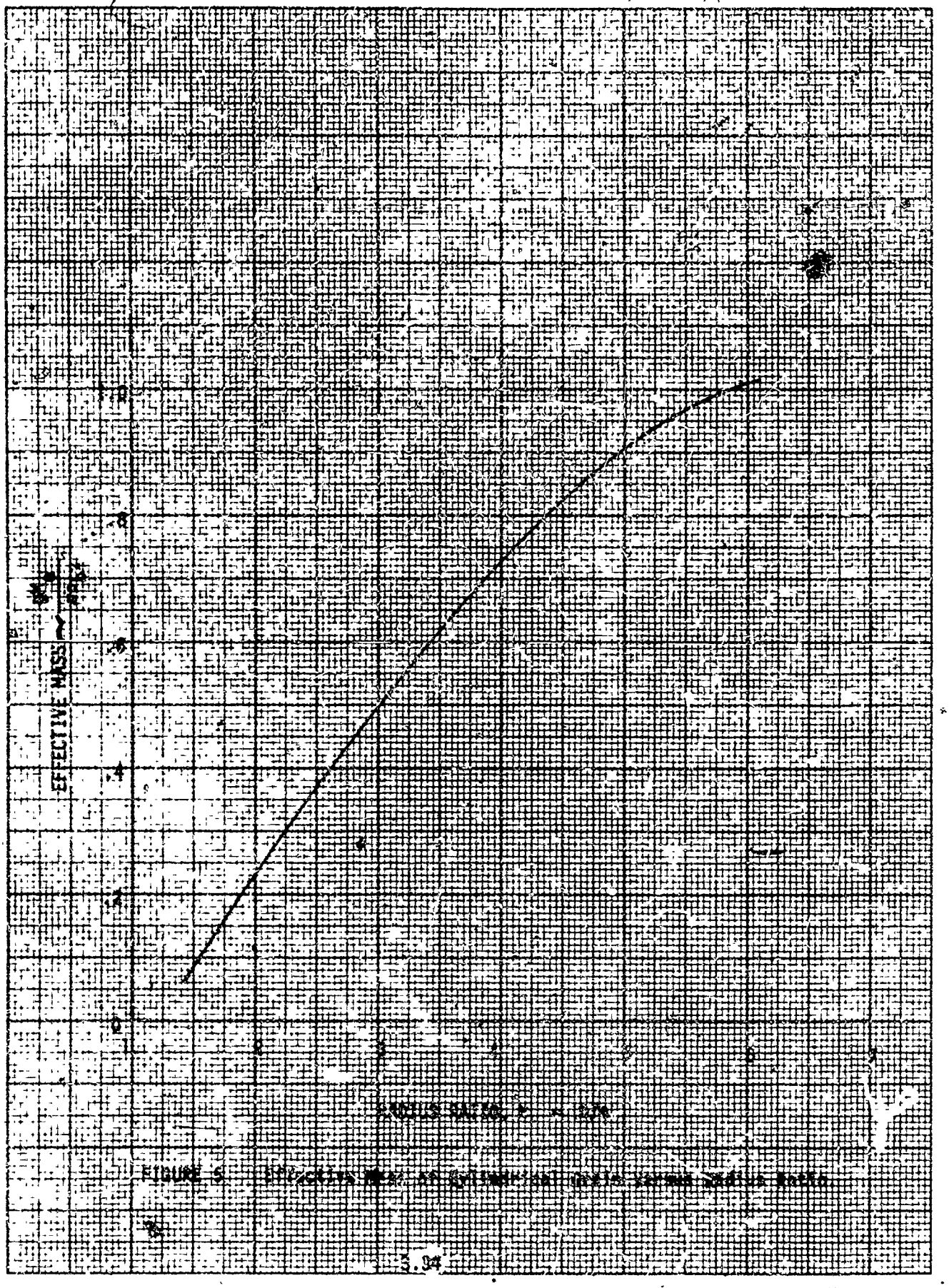

FIGURE 6 [illegible] AS A FUNCTION OF [illegible] RADIUS RATIO

The spring constant is also modified from that given above;

$$k^* = 2\pi G^*/\log_e\lambda = (2\pi/\log_e\lambda)(G' + iG'')\omega^n , \qquad (3.53)$$

assuming a power law representation for the shear modulus. The loss tangent β is now given by..

$$\beta = G''/G' \qquad (3.54)$$

Finally, the natural frequency is redefined to be

$$\omega^{2-n} = 2\pi G'/m_c \log_e\lambda , \qquad (3.55)$$

so that the amplitude ratio is indeed given by (3.37) with the maximum value given by (3.38).

THERMOMECHANICAL COUPLING AND HEAT GENERATION

As mentioned before, sustained vibration of a solid rocket motor can lead to substantial internal dissipative heating, particularly in the vicinity of regions of high local strains. The resulting high local temperatures can produce significant mechanical or chemical degradation of the propellant, and conceivably even cause autoignition of the propellant.

The nature of the thermomechanical coupling problem has been studied for slabs under lateral vibrations and for cylinders under axial shear vibrations, (see references (15, 20 through 24, and 28). The slab shown in figure 3C is dynamically equivalent to the long solid rocket motor under axial vibration, which is also shown in figure 3C. This slab geometry has been treated for one-dimensional [15, 20, 23] and two-dimensional [22, 28] heat transfer conditions. The specific details of these studies are not presented here however, the general results are discussed.

For a shear mode of vibration the rate of mechanical dissipation D is given by

$$D = \omega G'' \left|\gamma_{xy}\right|^2/2 \qquad (3.56)$$

where γ_{xy} is the shear strain. Thus, dissipation and hence, heat generation is seen to be proportional to the square of the strain magnitude. This points out the significance of the aforementioned high local strains. The strain amplitude is determined using the ratio of output motion amplitude to input amplitude and the phase relation. A relation similar to (3.56) also exists for stresses indicating high local stresses also significantly influence heat generation. It can also be seen from (3.56) that the maximum dissipation occurs at the natural frequency $\omega = \omega_n$, since G" is a maximum at this frequency.

The nature of the dynamic response of the viscoelastic slab under steady state thermal and vibration conditions is shown in figures 6 and 7 where the amplitude ratio and maximum temperature rise in the slab are presented as a function of the frequency ratio ω/ω_n. In figure 7 the actual temperature rise is 56°F times the reduced temperature, ϕ_1. The normalizing factor H in these figures is a thickness parameter which has the dimension of length and is defined by

$$H \equiv \omega_n^{-\frac{(n+1)}{2}} \frac{2k_1 K}{\beta a} , \qquad (3.57)$$

where,

K = Propellant conductivity, assumed constant ,

β = Propellant loss tangent ,

n = slope of relaxation modulus curve ,

ω_n = natural frequency ,

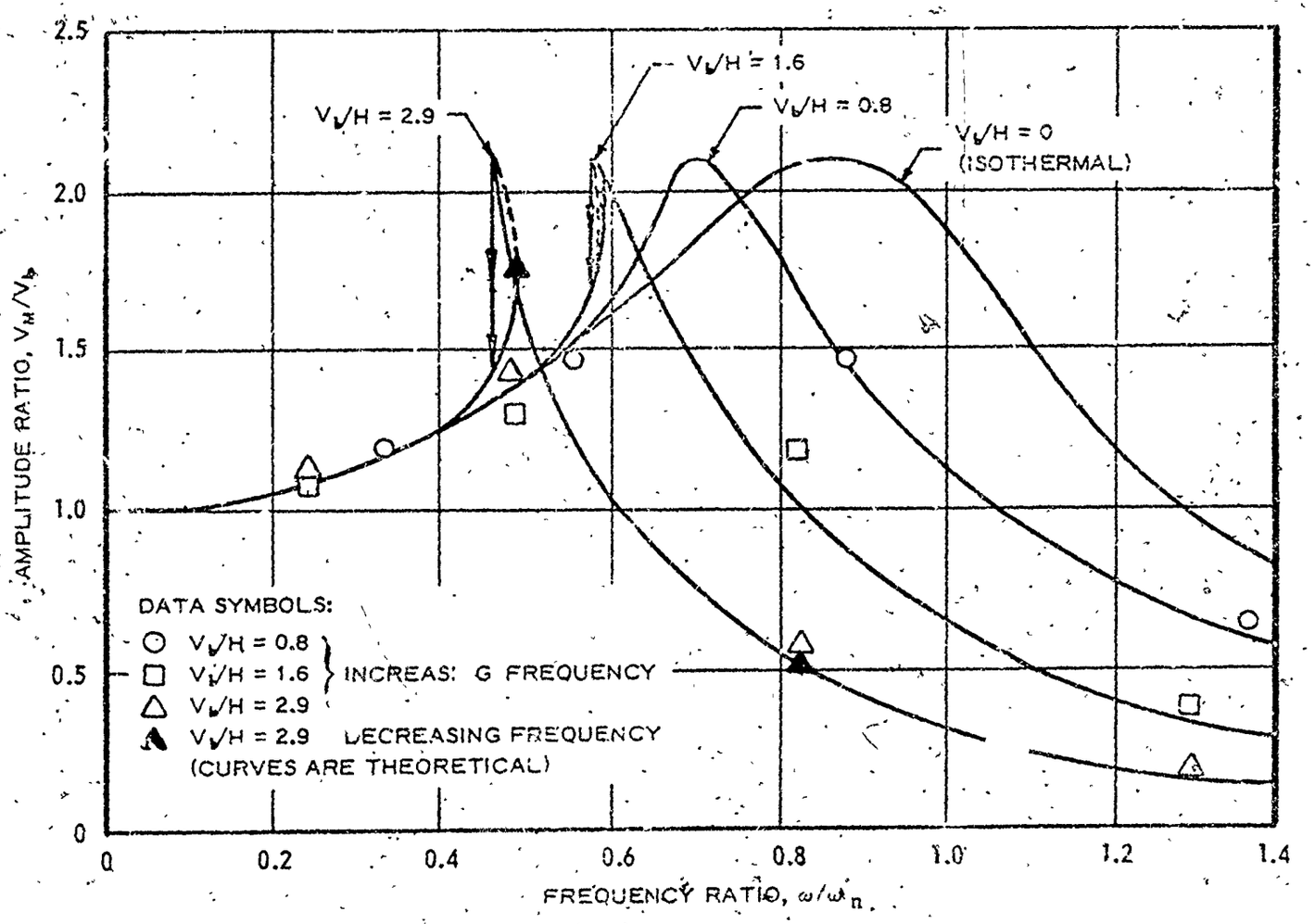

FIGURE 6 Steady-State Displacement Amplitude Ratio For Inertial Loading.

and k_1 and a are constants defined by

$$J^* = (J' - iJ'') = (k_1 - ik_2)\,\omega^{-n}\,e^{a\theta} \quad . \tag{3.58}$$

The relation (3.58) has been found to well approximate the complex compliance of some composite propellants over a wide range of frequencies and temperatures [21, 28]. In (3.58) θ is the temperature difference above a reference temperature. The constant a can be determined from the shift factor versus temperature curve.

The aforementioned studies have also included random-loading processes. The equations for thermomechanical response to stationary random-loading processes have been shown to be similar to those for harmonic loading [23, 28].

VIBRATION DESIGN ANALYSIS SUMMARY

Before closing this discussion on vibration, some of the pertinent results will be summarized for easy access.

The amplitude ratio for forced displacement and forced load vibration is given by (3.37) for the laterally vibrating starpoint and slab and axial shearing vibrations of the circular cylinder;

$$\left|\frac{V_m}{V_b}\right| = \frac{(1+\beta^2)^{\frac{1}{2}}}{[(1-\Omega)^2+\beta^2]^{\frac{1}{2}}} \quad . \tag{3.37}$$

It is also observed that for steady state (and adibatic) conditions the maximum amplitude ratic depends on only the loss tangent; viz.

$$\left|\frac{V_m}{V_b}\right|_{max} = (1+\beta^2)^{\frac{1}{2}}/\beta \quad , \tag{3.38}$$

and occurs at the frequency $\omega = \omega_n$ where

$$\Omega = (\omega/\omega_n)^{2-n} = 1 \quad , \tag{3.39}$$

and the phase angle

$$\alpha = \tan^{-1} \beta^{-1} \quad . \tag{3.40}$$

The loss tangent β can be estimated from (3.41),

$$\beta = \tan (n\pi/2) \tag{3.41}$$

in the event that actual propellant data is unavailable, although errors on the order of 20 percent are common when using (3.41) for highly solids loaded propellants. A typical value of β is about 0.5 for composite propellants. This value of β gives a maximum amplification factor of 2.25. The slope n of the stress relaxation modulus curve typically ranges between 0.2 and 0.3 for composite propellants, and is somewhat lower for double base propellants.

The maximum dissipation is given by (3.56);

$$D = \omega G'' |\gamma_{xy}|^2/2 \quad , \tag{3.56}$$

which points up the importance of minimizing strain (or stress) concentrations. Significant temperature rises were seen to occur at frequencies equal to about one-half the natural frequency. Results have also shown that an increase in slab thickness (i.e., an increase in grain web thickness) will increase the steady state temperature, assuming strain is unchanged. The equilibrium temperature is related to $\omega G'' h^2 |\lambda_{xy}|^2/2K$, where h is the slab thickness. Disregarding the temperature dependence of G", doubling the slab thickness (grain web thickness) results in a four-fold increase in the steady state temperature. The ratio of the output amplitude along with the phase relation determines the strain amplitude needed for estimating dissipation and the equilibrium temperature.

3.4 ACCELERATION LOADS

Acceleration loads can be treated in the same manner as shock loads. In most cases normal acceleration loads will produce negligible stresses and strains. The exceptions to this rule are the large diameter solid rocket motors undergoing 1 g vertical or horizontal storage slump, and some tactical missiles which are subjected to very high launch accelerations.

Storage slump of large solid motors in which inadequate grain terminations have been provided can be a critical design factor for storage above ambient temperatures. The result is that grain unbonding may occur at the grain ends. In large diameter motors in which adequate grain terminations have been provided, large deformations of the grain can serve to constrict the gas flow resulting in errosive burning, particularly in the area of a submerged nozzle or radial slots. At low temperatures, the propellant stiffness significantly reduces slump deformations. Parametric curves for determining storage slump deformations are presented in Appendix C.

3.4.1 AXIAL ACCELERATION

The shear stress at the propellant-case interface is given by equation (3.24) for axial acceleration;

$$\tau_{rz} = \frac{3}{2}\rho \, ng \, b \, (\lambda^2-1)/\lambda^2 \, , \qquad (3.59)$$

where a stress concentration factor of 3 has been introduced to account for stress concentrations at the forward grain termination point, and inertia effects due to straining have again been neglected. For irregular configurations, the shear stress may be calculated from the simple formula

$$\tau_{rz} = 3 \, n \cdot g \, W/A \, , \qquad (3.60)$$

where

W = total propellant weight,

A = total bonded area.

Head end bonding of the propellant grain to the case serves to reduce acceleration stresses by lessening the propellant weight supported in shear by the motor case. The ratio of load carried by a full head end bond to the total load for Poisson's ratio $\nu = 1/2$, is shown in Figure 8 as a function of length-to-diameter ratio, and in Figure 9 as a function of the grain radius ratio, λ[2]. For a value of Poisson's ratio less than 1/2, the ratio of the load carried by the head end bond is decreased. This influence of Poisson's ratio is discussed in a following chapter.

Although full head end bonding serves to significantly reduce acceleration stresses and slump deformations, as indicated in Figures 8 and 9, the low temperature storage and firing capabilities of the motor may be severely compromised. Head end bonding effectively doubles the length of the propellant grain in thermal stress and strain calculations.

The axial deflection at the port of an axial accelerating propellant grain is given by [14]

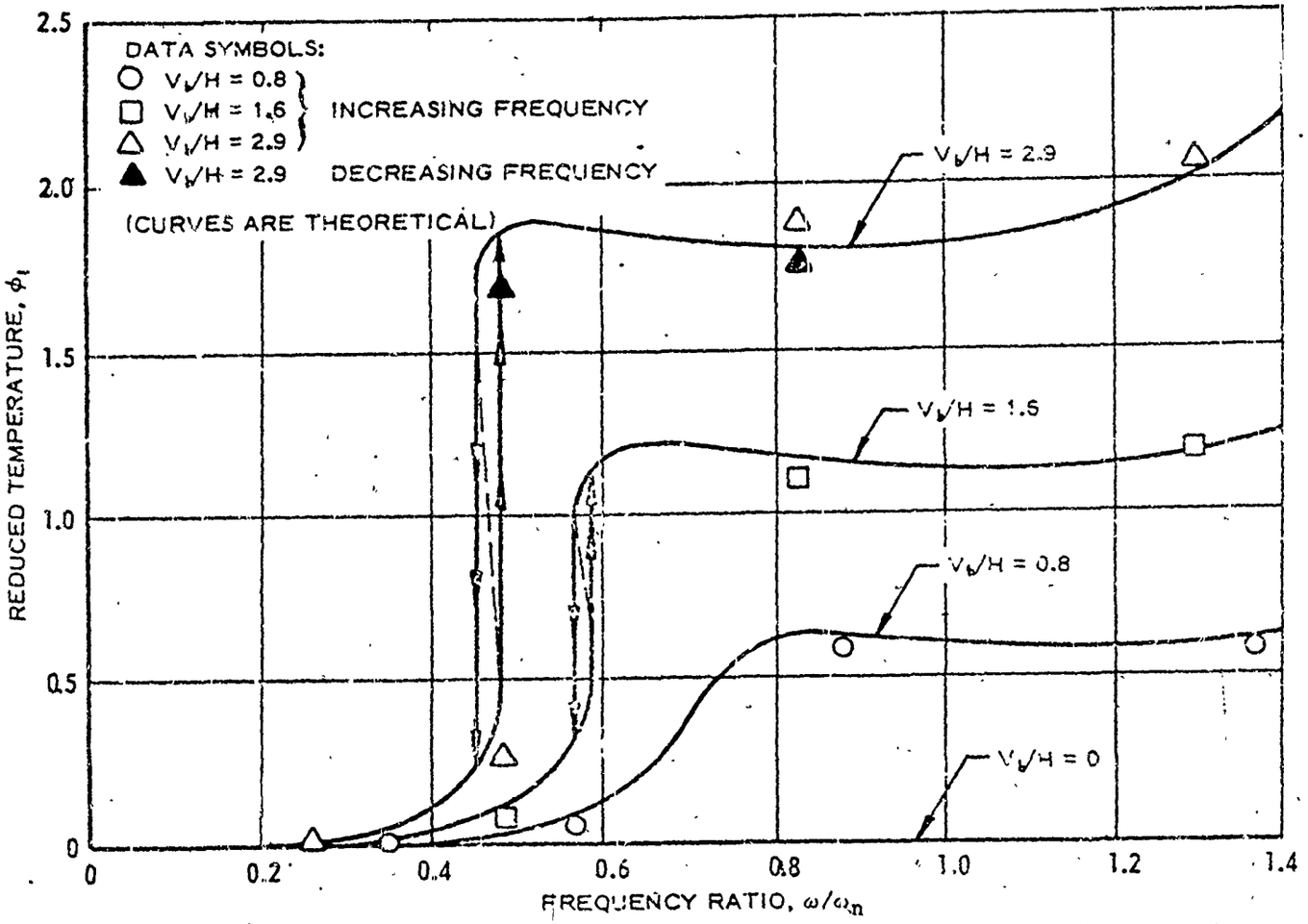

FIGURE 7 Steady-State Reduced Temperature At Insulated Boundary For Inertial Loading.

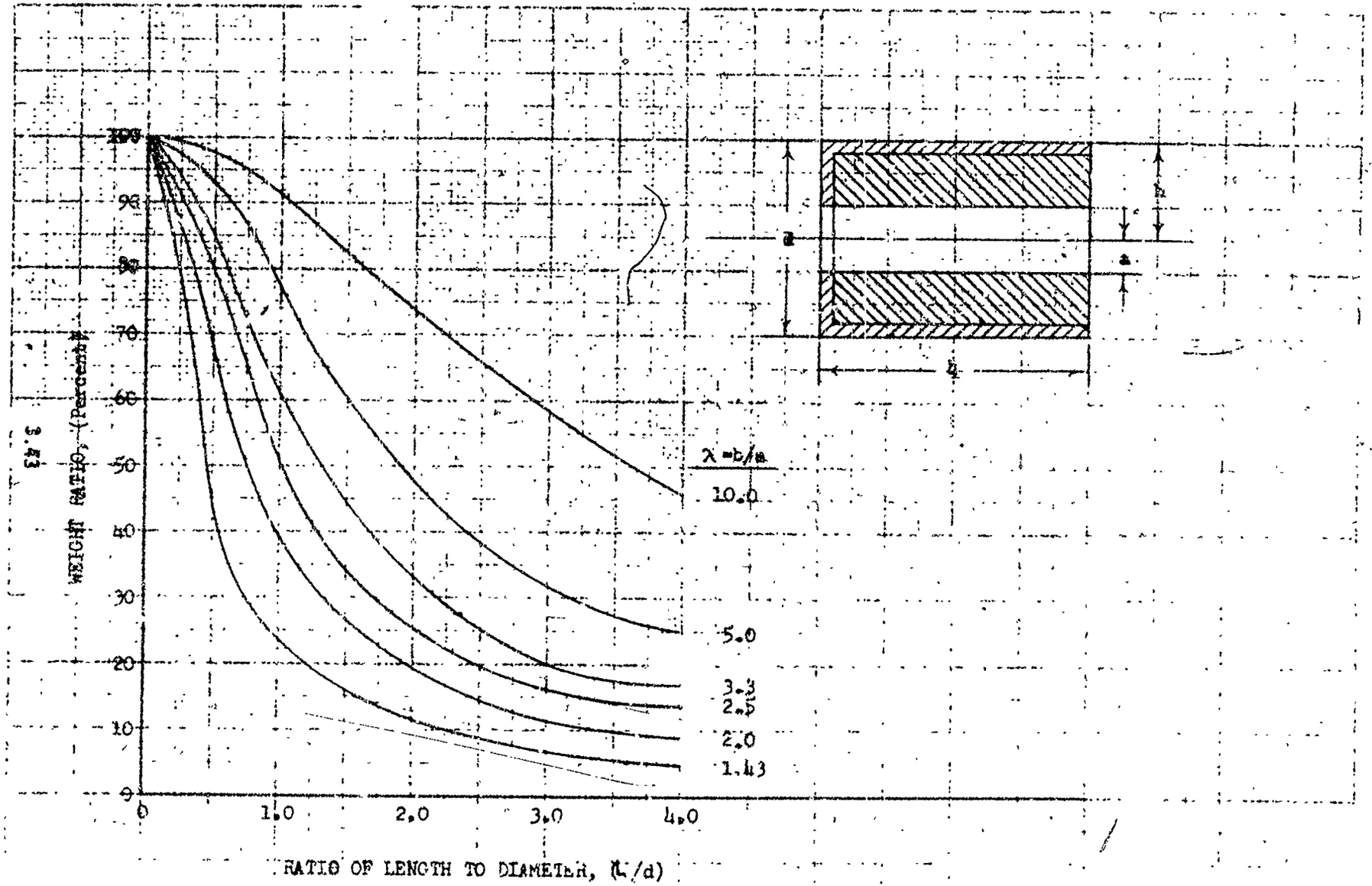

FIGURE 8 Ratio Of Load Carried By End Bond To Total Load. Axial Acceleration, $\nu = 0.5$

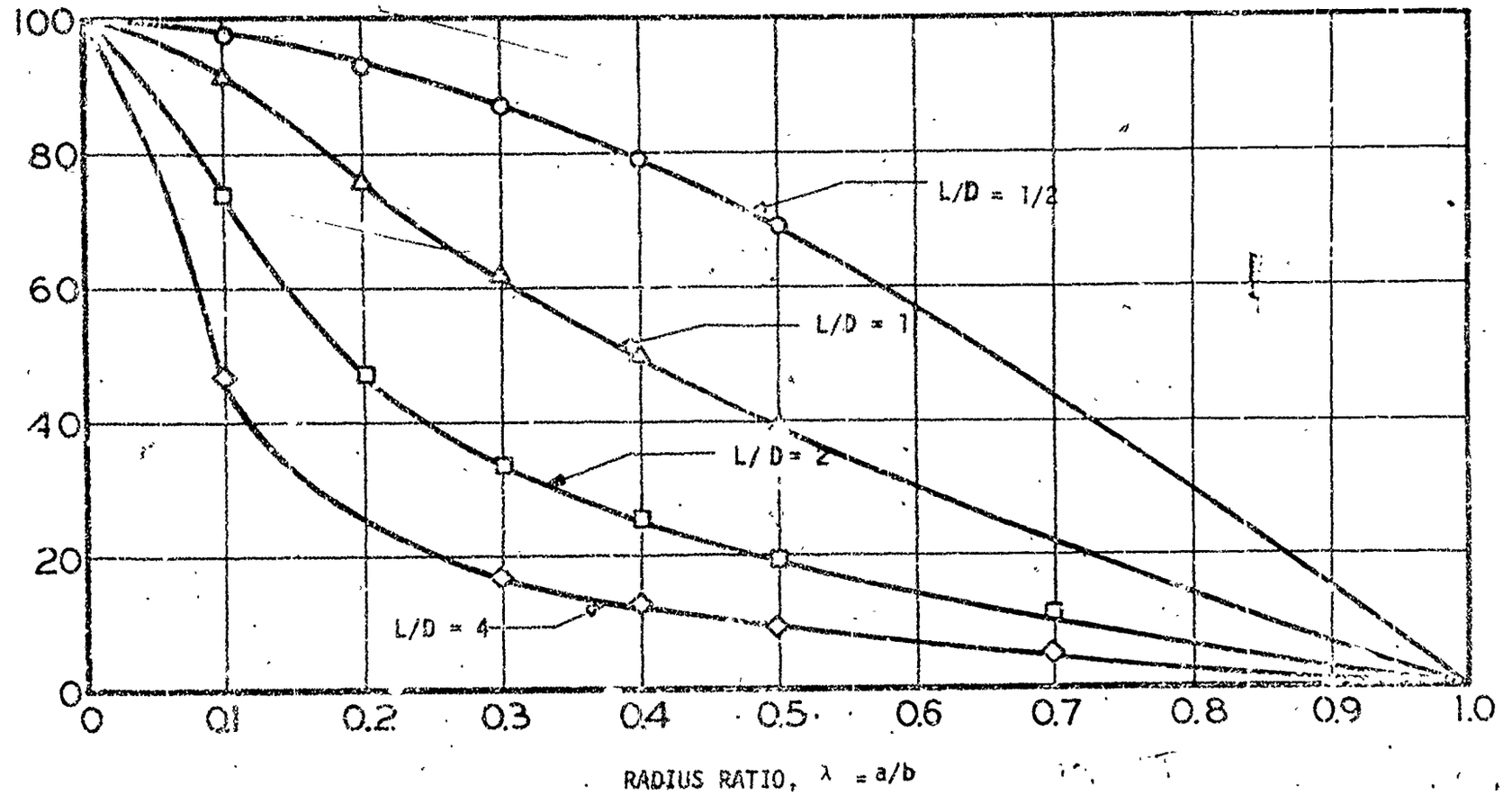

3.44

FIGURE 9 - Ratio Of Load Carried By End Bond To Total Load, Axial Acceleration, b = 0.5

$$w = \frac{3}{2}\frac{n\cdot g}{a^2}\frac{\rho}{E_p}\left\{\frac{\lambda^2-1}{2} - \log_e \lambda\right\}, \qquad (3.61)$$

assuming propellant incompressibility. This relation can also be used to calculate axial storage slump deflections by setting n·g = 1.

3.4.2 LATERAL ACCELERATION

The maximum inner bore hoop strain for a rigidly encased, incompressible cylindrical grain subjected to a lateral acceleration loading is given by (3.25) ; viz.,

$$\epsilon_\theta(a) = \frac{3}{4}\, a\, \rho\, \frac{n\cdot g}{E_p}\, \frac{(\lambda^2-1)^2}{\lambda^4+1} \qquad (3.25)$$

assuming plane strain conditions. The strains in a star perforated grains can also be estimating using (3.25) and the stress-strain concentration factors discussed in a subsequent section.

Treating the star point as a thin cantileved plate of uniform thickness h and assuming propellant incompressibility, the stress at the base support (i.e., case-grain interface) is given by

$$\sigma = 6\, n\cdot g\, \rho\, \ell^2/h, \qquad (3.62)$$

where a stress concentration factor of 2 has been included. The deflection of the star tip can be determined approximately using relation (3.27);

$$\Delta = 3\,\frac{n\cdot g}{E_p}\,\rho\,\frac{\ell^4}{h^2} \qquad (3.27)$$

A somewhat better approximation than that given by (3.27) can be obtained by considering the nonuniform cross-section of the star point. Treating the star point geometrically as a truncated triangular section

(Figure 10), the deflection at the tip of the star point is given by [4]

$$\Delta = n \cdot g \frac{\rho \ell^2}{E} \left\{ 1.38 \, (\ell/H)^2 + (1.13) \frac{h_o}{H} \left[\frac{1}{4} + 2(\ell/H)^2 \right] \right\} \qquad (3.63)$$

for $h_o/H < 0.1$, where h_o, ρ and H are defined in Figure 10. This result can also be used for estimating the storage slump deflection of a star point by setting $n \cdot g = 1$ g.

3.5 PRESSURIZATION LOADS

Pressurization loads occur during firing of a solid rocket motor and normally act for a short duration of time. In conventional geometries, the hoop strain at the inner bore is the critical design parameter, particularly under low temperature firings where the propellant has less elongation capabilities than at high temperatures. These strains are most critical when low modulus materials, such as fiber reinforced phenolics, are used for case materials since pressurization strains are inversely proportional to the case modulus.

3.51 HOLLOW CYLINDER

Assuming plane strain conditions and treating the propellant grain as an incompressible material, the maximum inner bore hoop strain due to ignition pressurization is given by [14]

$$\varepsilon_{\theta_p}(a) = \frac{b \, \lambda^2 (1-\nu_c^2)}{h E_c} P_i \qquad (3.64)$$

where

ν_c = Poisson's ratio of the case,

P_i = ignition pressure.

For a grain with free ends the pressurization strain is approximately given by [4]

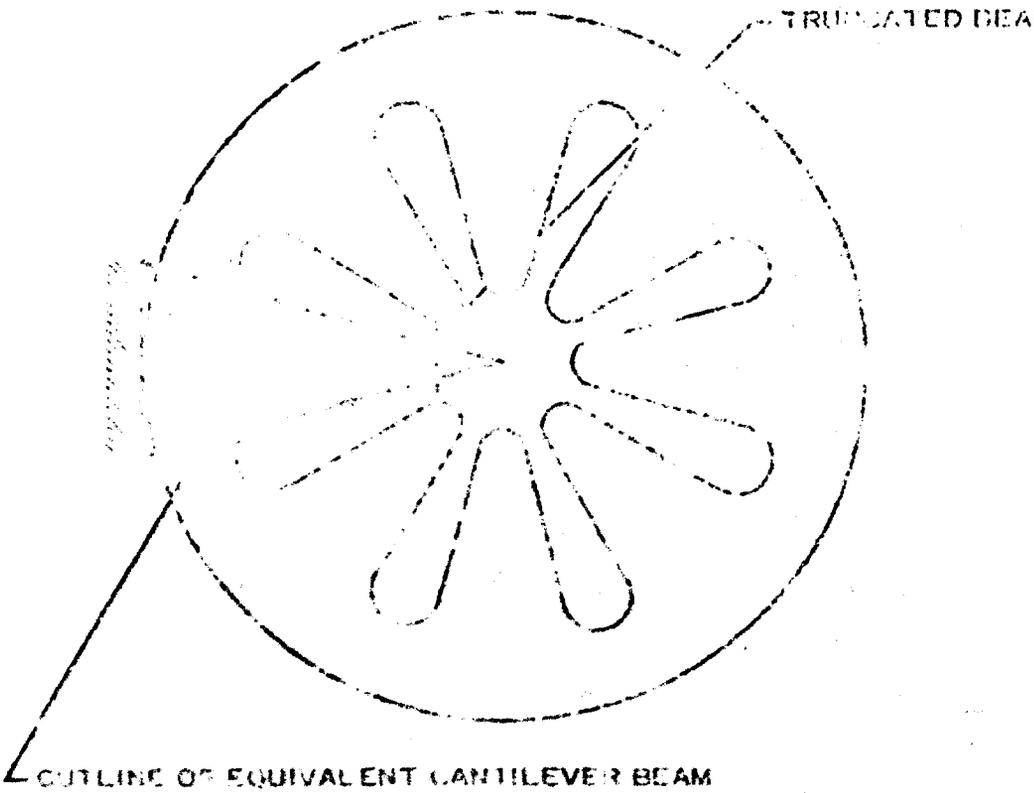

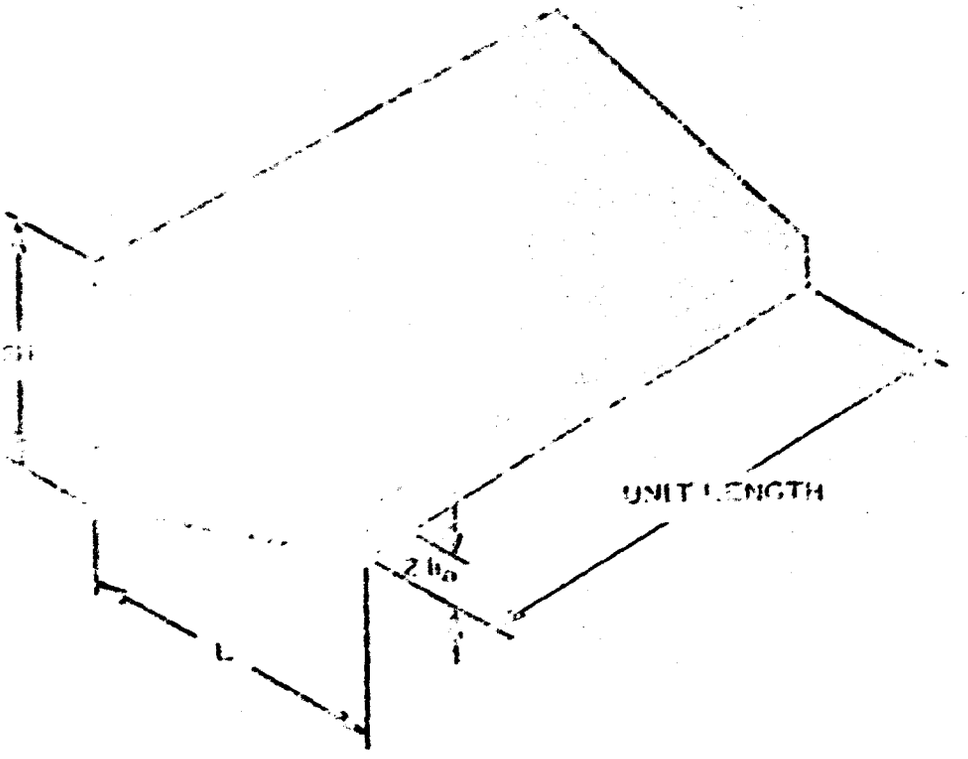

Best Available Copy

FIGURE 10 Truncated Star Point Geometry.

$$\varepsilon_{\theta_p}(a) = \frac{3.4\, b\, \lambda^2}{(3+\lambda^2)\, hE_c} P_i \qquad (3.65)$$

Equations (3.64) and 3.65) can serve to bound the pressurization strains in a finite length grain.

The hoop stress at the inner bore is most easily expressed in terms of the ratio of the case-grain interfacial pressure P' to the operating pressure P_i. Under plane strain conditions and propellant incompressibility, this ratio is given by [14]

$$\frac{P'}{P_i} = \frac{1}{1 + \frac{2}{3}\frac{(\lambda^2-1)(1-\nu_c^2)}{\lambda^2}\frac{bE_p}{hE_c}} \qquad (3.66)$$

The inner bore hoop stress is then given by

$$\sigma_\theta(a) = \frac{1 + \lambda^2(1-2P'/P_i)}{\lambda^2 - 1} P_i \qquad (3.67)$$

It can be seen that for a very stiff or thick case, (e.g., $bE_p/hE_c \ll 1$) the hoop stress $\sigma_\theta(a)$ is approximately equal to the applied pressure. It is also seen that the ratio P'/P_i decreases as the case modulus E_c decreases. Hence larger bore stresses and bore strains are obtained for propellant grains with low modulus case materials, such as fiberglas.

3.52 STAR PERFORATED GRAIN

Equations (3.64) and (3.65) can also be used for determining pressurization strains in star perforated grains by applying a star valley stress/strain concentration factor.

Alternatively, empiral relationships derived from photoelastic tests may be used to estimate pressurization stresses and strains in star perforated grains [29, 30]. These results are given in terms of the maximum hoop stress at the star valley σ_θ^s to the applied external pressure P_o;

$$H \equiv -\left(\frac{\sigma^{s}_{\theta(a)}}{P_o}\right)_{P_i = 0} = N^{-1/3}\sqrt{\frac{1+\lambda}{\lambda}}\left[1 + 2\sqrt{a/\rho}\right] , \qquad (3.68)$$

where

a = radius to star valley,

$\lambda = b/a$,

N = number of star points, $(2<N<8)$,

ρ = star valley fillet radius, $(a/\rho>4)$.

For an internally pressurized grain without a case, the hoop stress at the star valley is related to (3.68) by the relation

$$-\left(\frac{\sigma^{s}_{\theta(a)}}{P_i}\right)_{P_o = 0} = 1 + H . \qquad (3.69)$$

Denoting by P' the external pressure due to motor case restraint, the bore hoop stress is finally given by

$$-\left(\frac{\sigma^{s}_{\theta(\alpha)}}{P_i}\right) = 1 - H\left(1 - P'/P_i\right) . \qquad (3.70)$$

The pressure ratio P'/P_i is evaluated using equation (3.66) by replacing the radius ratio by an equivalent ratio λ_e defined by [29]

$$\left(\frac{1}{\lambda_e}\right)^2 = \left(\frac{1}{\lambda_w}\right)^2 - 0.2\left\{\left(\frac{1}{\lambda_w}\right)^2 - \left(\frac{1}{\lambda_A}\right)^2\right\} , \qquad (3.71)$$

Where the subscript W indicates equal web fraction (a thick walled cylinder with web fraction equal to that of the star perforated grain) and the subscript A indicates equal area (a thick walled cylinder with a web fraction determined such that the cross-sectional area of the cylinder is equal to that of the star perforated grain). A further discussion on the expression for calculating an equivalent cylinder, (eq. (3.71)), is presented in section 3.7.7 of this chapter.

The strain at the star valley, assuming plane strain conditions and propellant incompressibility, is given by

$$\left(\frac{\varepsilon^{s}_{\theta(\alpha)}}{P_i} \right) = \frac{3}{4E_p} H \left(1 - P'/P_i \right) \quad (3.72)$$

Comparison of the stress given by (3.70) and the strain given by (3.72) with finite element computer solutions has demonstrated that these expressions are adequate for predicting pressurization stresses and strains in star perforated grains.

3.6 FINITE LENGTH END CORRECTION FACTOR

The results presented in the previous sections are based on the assumption of plane strain conditions. The range of length - to - diameter ratios and grain radius ratios for which this assumption yields valid results has been previously shown in figure 2. The corresponding results for finite length grain geometries can be obtained by applying numerically obtained end correction factors. For example, the hoop strain in a finite length hollow cylinder under uniform thermal cooling can be written in the form

$$\varepsilon'_{\theta}(a) = \frac{3}{2} \alpha_R \lambda^2 \bar{P}_{\varepsilon} \Delta T \,, \quad (3.73)$$

where $\bar{P}_{\varepsilon}$ is the finite length end correction factor defined as the ratio of the strain (displacement) at the center of the cylinder of finite length to the strain in an equivalent cylinder of infinite length. Curves of $\bar{P}_{\varepsilon}$ obtained through numerical calculations are presented in figure 11 as a function of length - to - diameter ratio for various values of the grain radius ratio λ, and in figure 12 as a function of λ for several length - to - diameter ratios. [1, 4, 16]

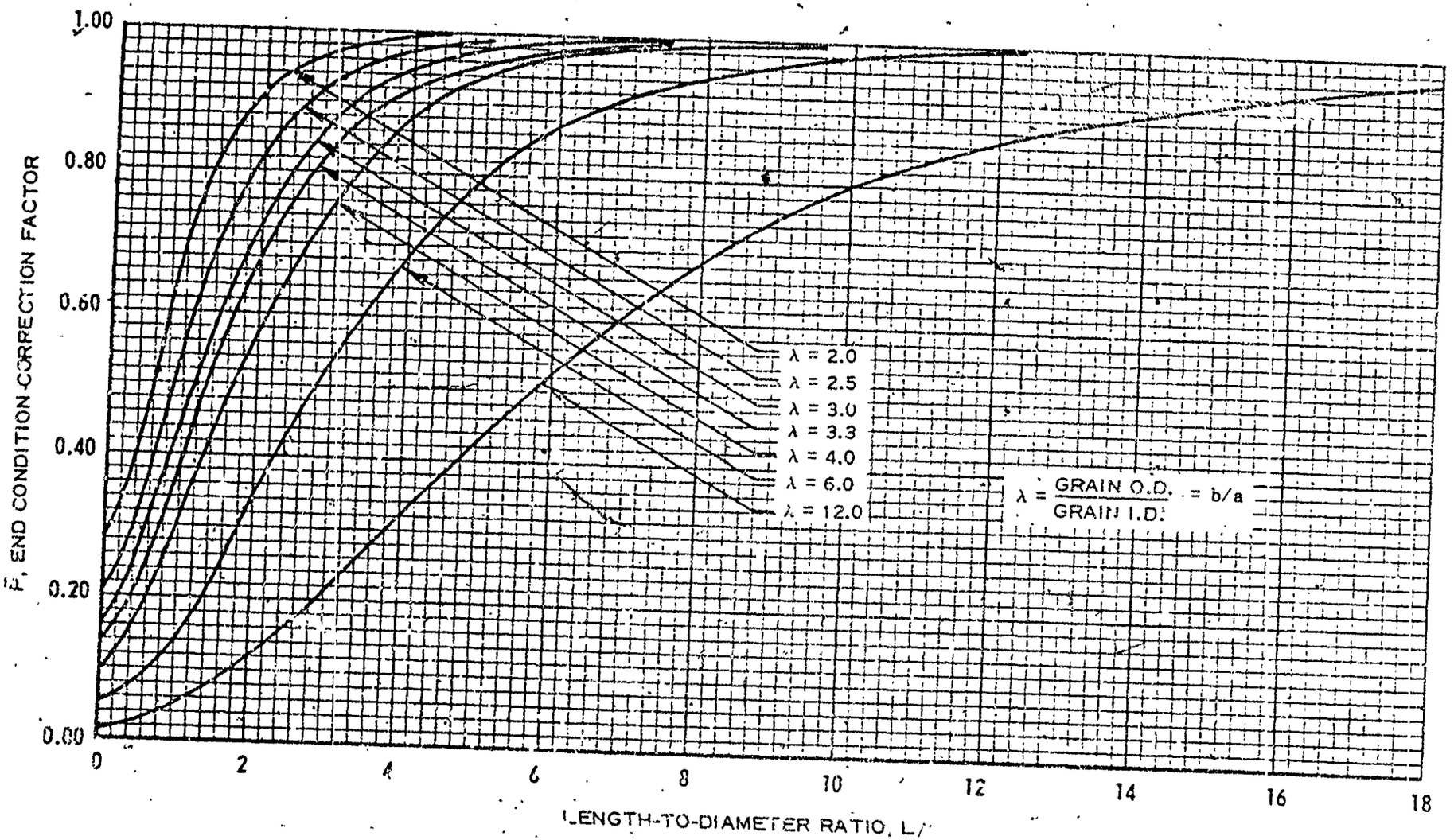

Figure 11 Parr End Condition Correction Factor for Finite Length Grains, $\bar{P}$ versus L/D

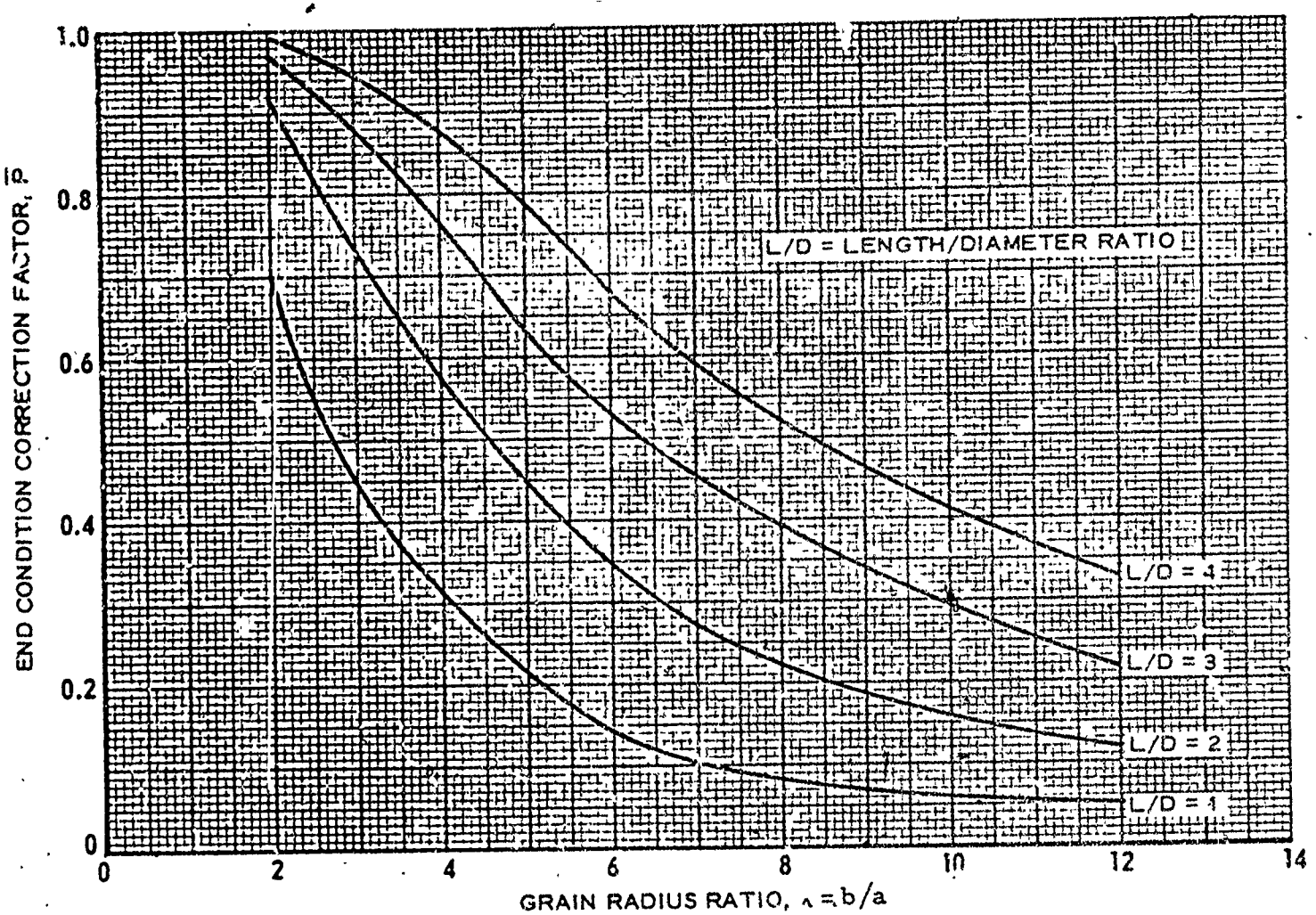

Figure 12 Parr End Condition Correction Factor for Finite Length Grains, $\overline{P}$ versus λ

In a similar manner, the hoop stress at the inner bore can be written in the form

$$\sigma_\theta(a) = 2\lambda^2 \alpha_R E_p \bar{P}_\theta \Delta T \ , \tag{3.74}$$

and the radial bond stress at the case grain interface represented by

$$\sigma_r(b) = \alpha_R E_p (\lambda^2-1) \bar{P}_r \Delta T \ , \tag{3.75}$$

Where $\bar{P}_\theta$ and $\bar{P}_r$ are the respective finite length correction factors. Curves of $\bar{P}_\theta$ and $\bar{P}_r$ versus λ are shown in figures 13 and 14 respectively for several values of the length - to - diameter ratio.

3.7 STRESS/STRAIN CONCENTRATION FACTORS FOR STAR PERFORATED GRAINS

In addition to correcting for finite length geometries all of the previous expressions obtained for hoop stresses and strains or the inner bore of a hollow cylindrical grain can be used in analyzing star perforated grain geometries by applying a star valley stress/strain concentration factor K_t. Numerous photoelastic investigations have been conducted to evaluate K_t experimentally for numerous geometries. The studies discussed here were conducted by Fourney and Parmerter [29] and dealt with simple slot grain geometries, the effect of slot width, positive and negative wedge angles and elliptical slot tips. These results have been parameterized in terms of the number of star points, web fraction, slot width ratio and fillet radius ratio. Parametric curves of these test results are presented in appendix D.

In the present section, empirical relationships which were developed during the course of the aforementioned photoelastic studies for quickly calculating concentration factors are discussed. These relations have been demonstrated to be adequate for estimating star valley concentration factors. [29]

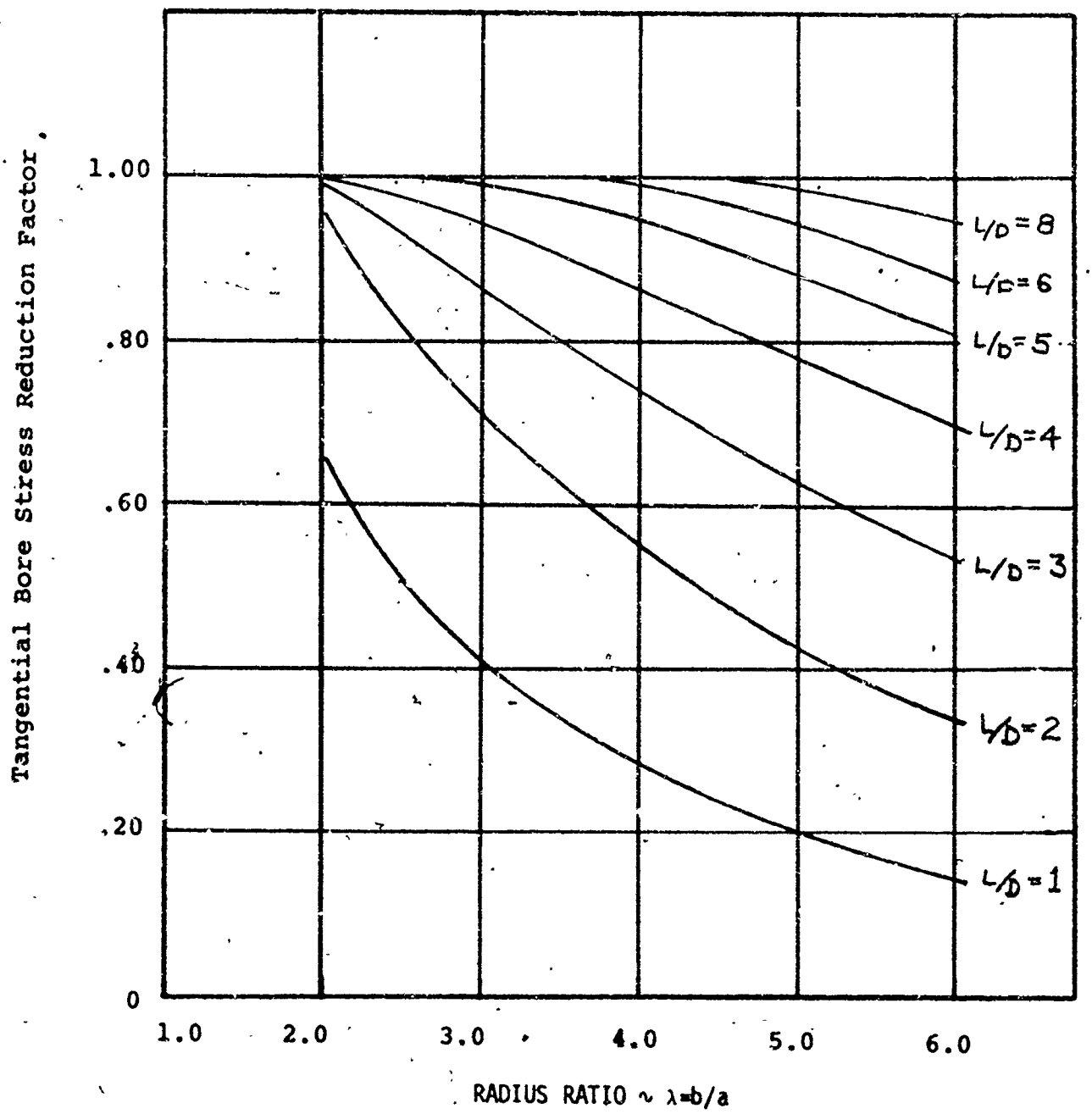

FIGURE 13 Tangential Bore Stress Reduction Factor for Flat End Cylinders of Finite Length Versus Radius Ratio

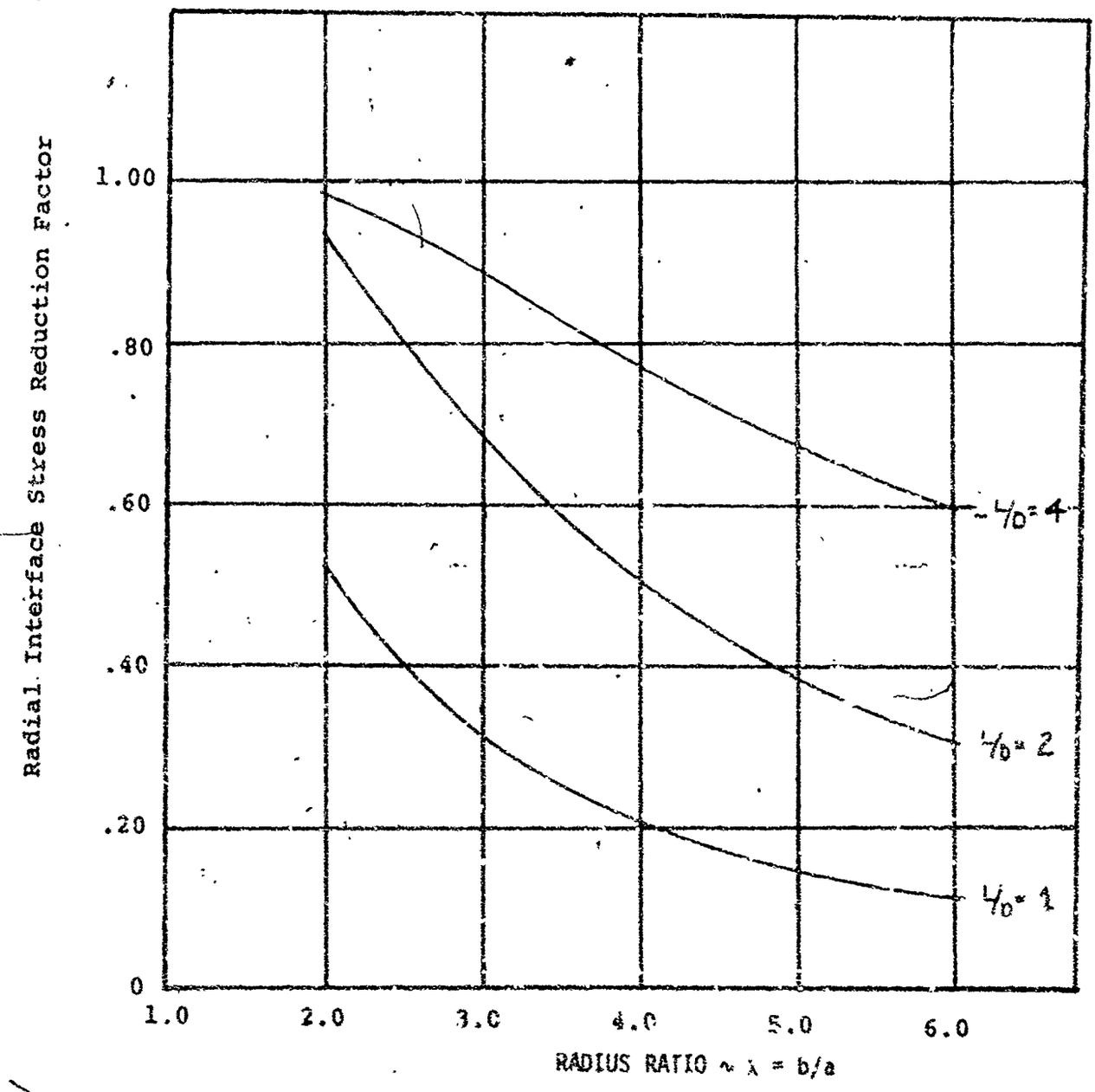

FIGURE 14 Radial Interface Stress Reduction Factor for Flat End Cylinders of Finite Length Versus Radius Ratio.

In the course of conducting experimental photoelastic grain stress analyses the stress concentration parameter

$$H = -\sigma^{s}_{\theta(a)}/P_o \qquad (3.76)$$

is directly measured, where

$\sigma^{s}_{\theta(a)}$ = star valley hoop stress,

P_o = externally applied pressure.

The stress/strain concentration factor K_f used in performing grain structural analyses is related to the photoelastic parameter H through the following relation:

$$K_f = \frac{\lambda^2-1}{2\lambda^2} H \qquad (3.77)$$

The behavior of the normalizing factor $(\lambda^2-1)/2\lambda^2$ as a function of λ is shown in figure 15. This factor approaches an asymptotic value of $\frac{1}{2}$ for large λ.

3.7.1 SIMPLE SLOT GRAIN GEOMETRY

One quite simple relation for estimating strain concentrations in simple slotted grain configurations makes use of the simple geometric relationship [31]

$$K_f = \frac{2\theta_2-\theta_1}{2(\theta_2-\theta_1)} \qquad (3.78)$$

where the angles θ_1 and θ_2 are defined in figure 16. A plot of K_f versus the ratio of θ_1/θ_2 is also shown in figure 16. Equation (3.78) is unofficially reported to produce results which are in close agreement with actual bore strain measurements of MINUTEMAN-WING II and POLARIS A3 motors.

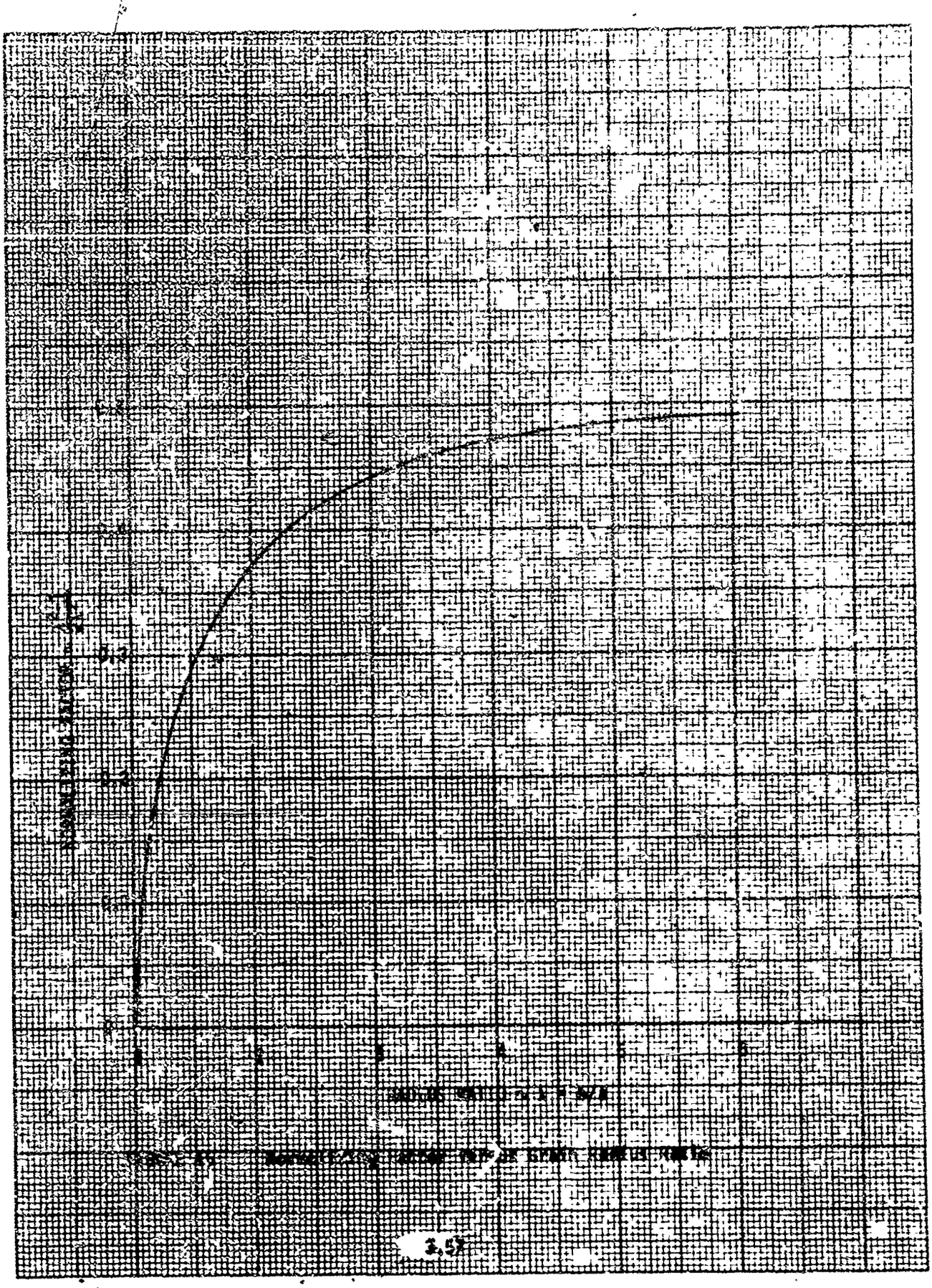
ACCELERATION
1
2
3
4
5
6

3,55

The results of fairly extensive testing by Fourney and Parmeter have shown that the test data obtained for the simple slot configuration (figure 17) may be represented by the empirical equation (3.68), which may be written in the alternate form,

$$H = N^{-1/3} \sqrt{\frac{a+b}{b-a}} \left[1 + 2 \sqrt{a/\rho}\right] \qquad (3.79)$$

where

N = number of star points,

α = radius to slot tip,

b = outer grain radius,

ρ = slot tip fillet radius.

This expression has been shown to provide an adequate prediction of the concentration factor for geometries with two to eight starpoints, except near the limit point $a/\rho \to 1$. For any value of N, $a=\rho$ implies a circular port grain in which $K_t = 1$ or $H = 2\lambda^2/(\lambda^2-1)$, irrespective of N. The validity of (3.79) for a larger number of star points has not been demonstrated, however, the excellent agreement obtained for values of N between two and eight intuitively indicates that this expression should be adequate for preliminary design analysis purposes.

Modifications to the simple slot geometry typically introduced by the structural analyst to reduce star valley concentration factors include increasing the slot width, introducing positive or negative wedge angles of the star slot or introduction of an elliptical slot tip. Typical photoelastic test results for these geometries for N = 4 are discussed in the following paragraphs. More extensive results are presented and discussed in Appendix D.

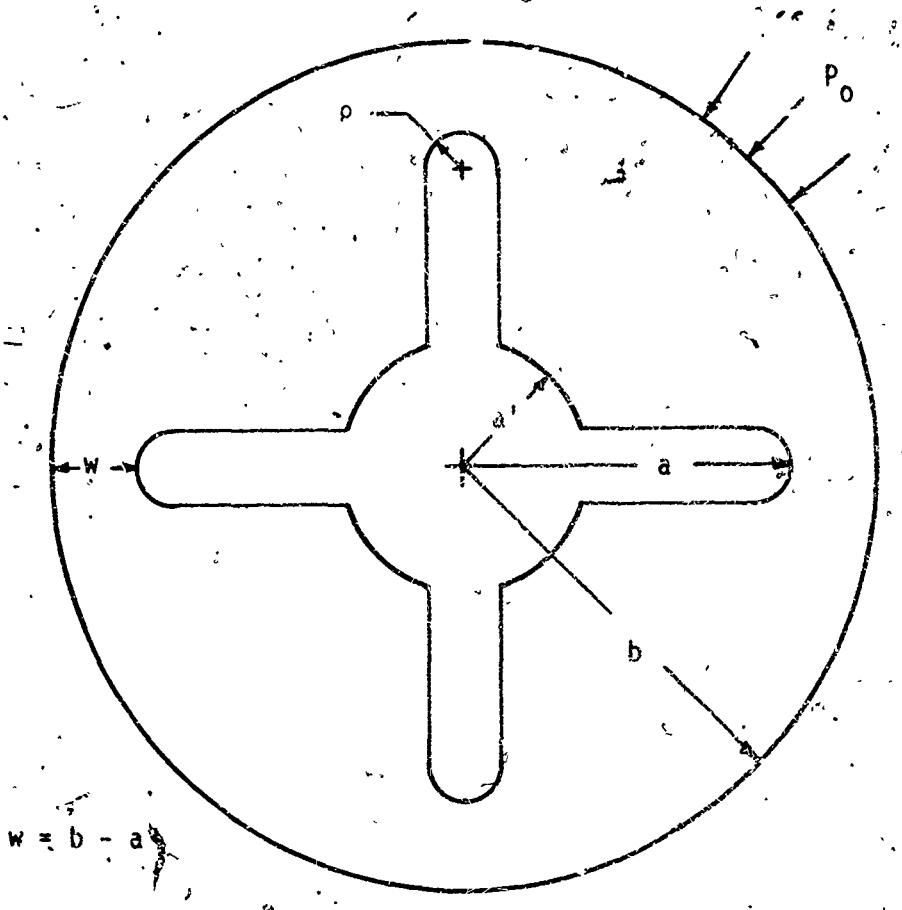

FIGURE 17. Geometry of Typical Cross-Section, Simple Slot Configuration

3.7.2 SLOT WIDTH EFFECT

The influence of the slot width geometry (figure 18) on the photoelastic parameter H is shown in figures 19 and 20. It is to be noted that the parameter H is significantly reduced for values of the slot width factor $d/2\rho > 1$. This result indicates the strong desirability of avoiding semi-circle slot tips whenever possible. It is also noticed that a minimum value of H is obtained. The exact value of $d/2\rho$ where this minimum occurs however, is seen to be a function of the port-fraction a/b and the fillet radius ratio a/ρ.

3.7.3 POSITIVE WEDGE ANGLE GEOMETRY

Typical results for the positive wedge angle geometry shown in figure 21 are presented in figure 22 as a function of the wedge angle α for a fixed $a/\rho = 8$ and N = 4. The limit line at $\alpha = 90°$ corresponds to a circular port grain. The values of H at $\alpha = 0$ correspond to the simple slot geometry (figure 17). It is observed that for moderate positive wedge angles (e.g., $\sim 30°$) significant decreases in the stress (strain) can be obtained.

3.7.4 NEGATIVE WEDGE ANGLE GEOMETRY

Typical test results for the negative wedge angle geometry (figure 23) are presented in figure 24 as a function of the wedge angle β. In this case the limit line at $\beta = 90°$ corresponds to a square with a finite radius of curvature ρ at the corners. The limit $\beta = 0$ again corresponds to the simple slot configuration (figure 17). It can be seen from this curve that the variation of H as a function of β is negligible for angles

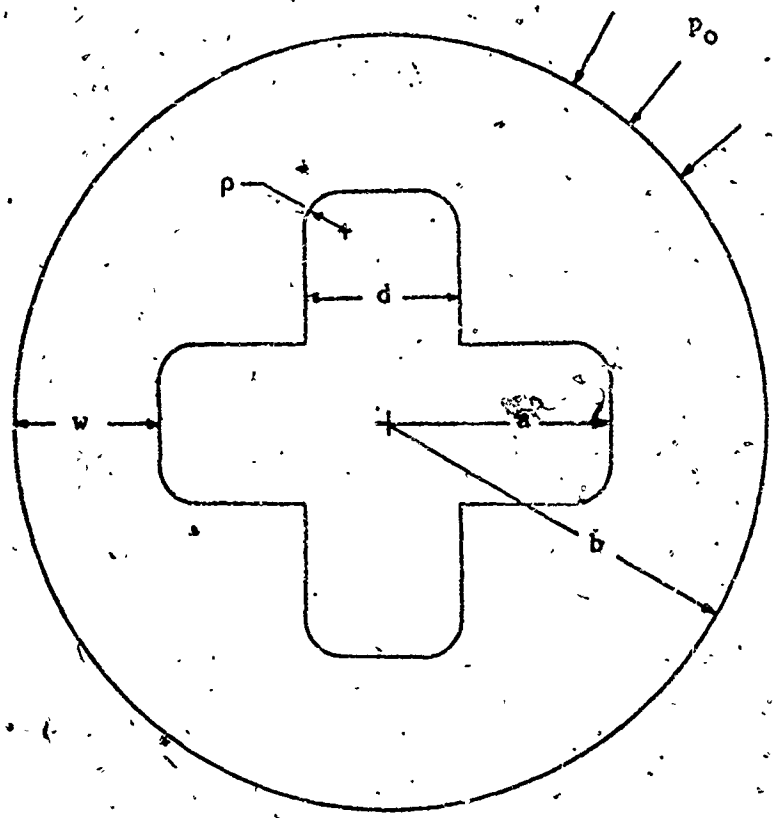

FIGURE 18. GEOMETRY OF TYPICAL CROSS SECTION FOR SLOT WIDTH EFFECT TESTS

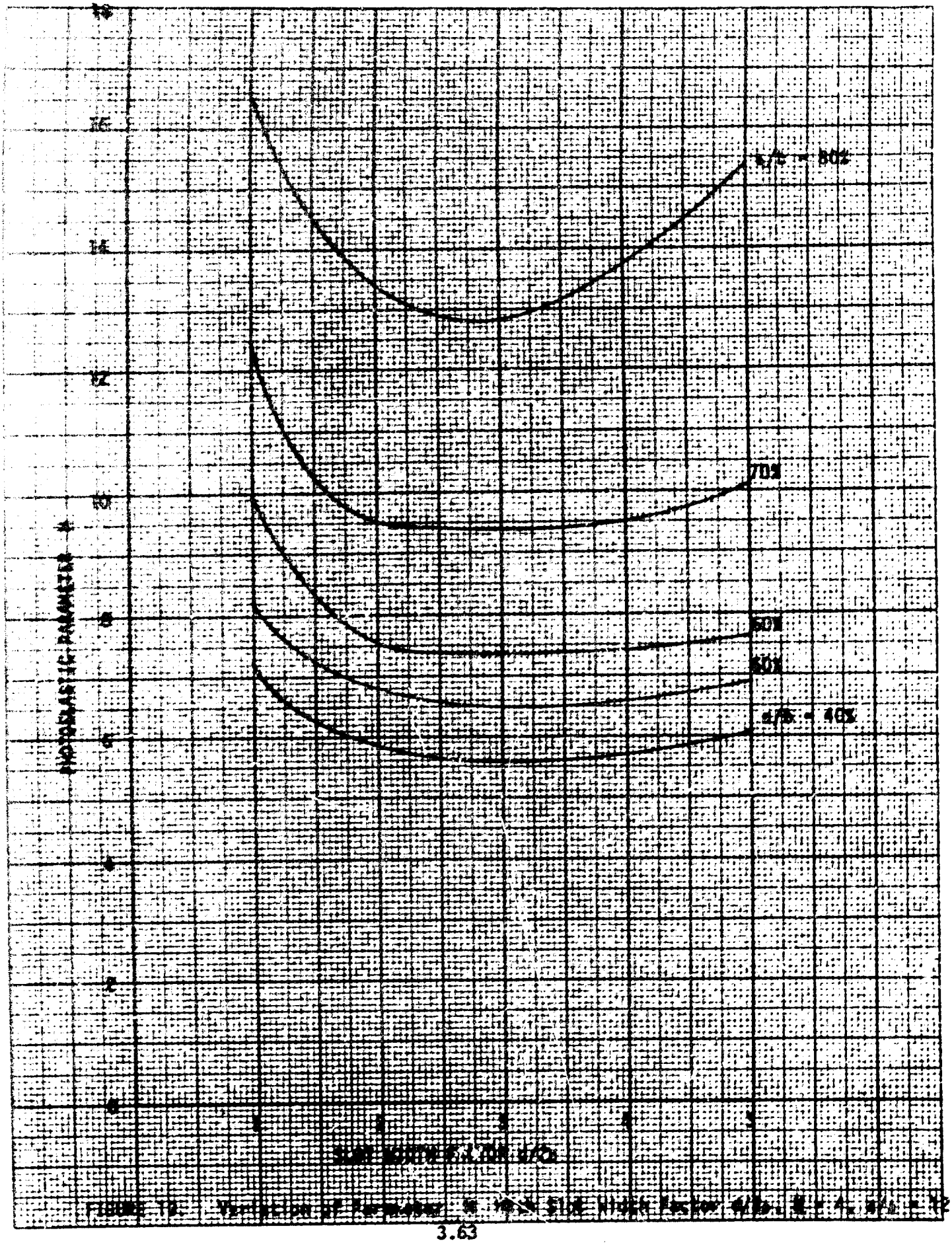

FIGURE 19. Variation of Parameter [illegible] with Stress Intensity Factor $K/\sigma\sqrt{a}$, $E = 4$, $a/b = 1/2$.

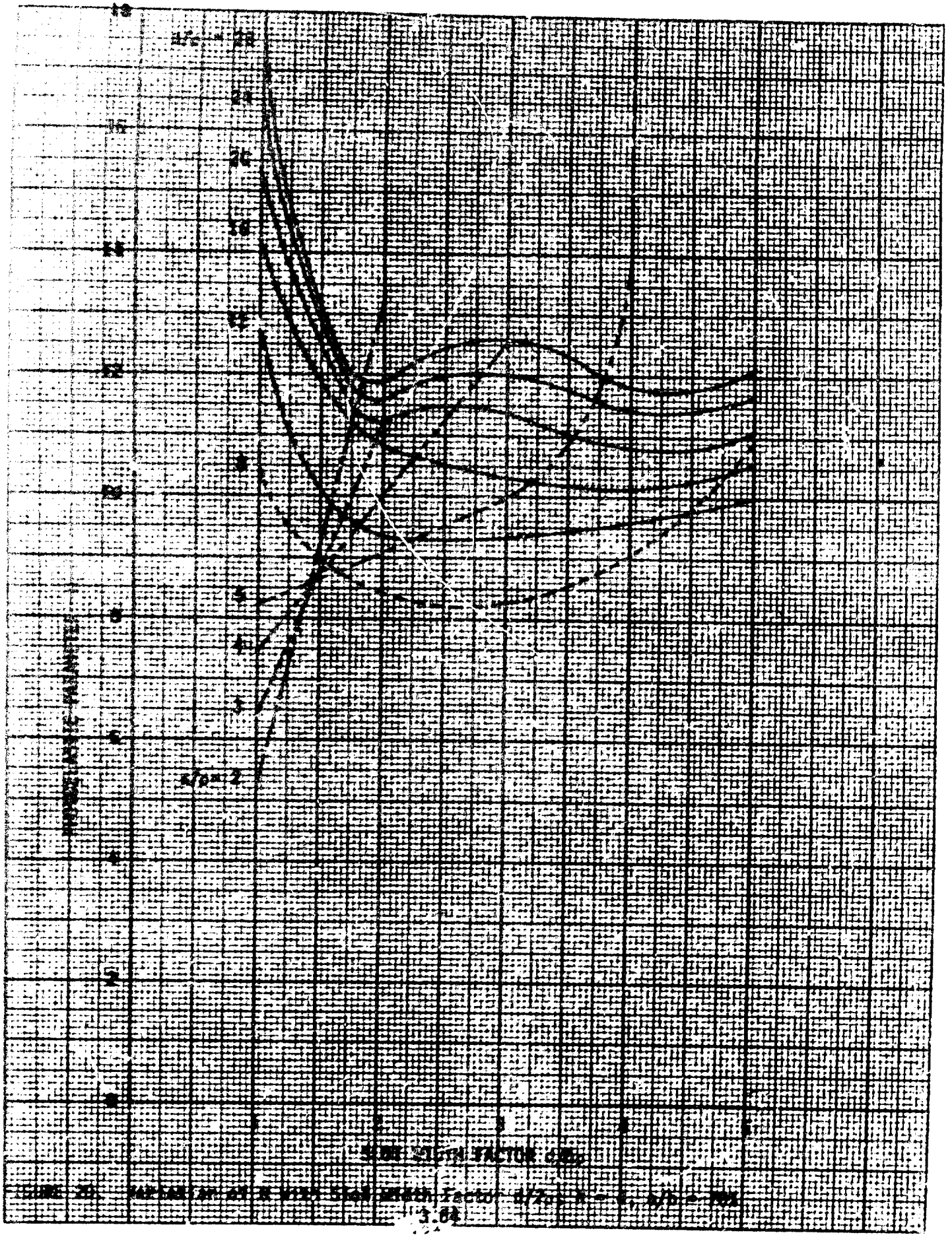

FIG. 20 FACTOR M_1 OF A PLATE WITH SIDE CRACK; depth factor $d/2c$; $h = \infty$, $a/b = 0$

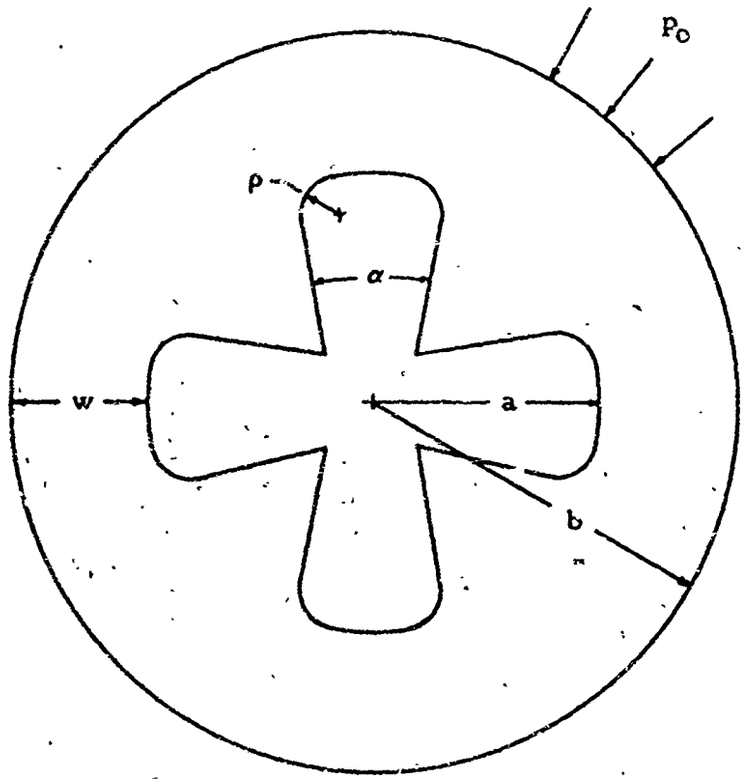

FIGURE 21. GEOMETRY OF TYPICAL CROSS SECTION FOR POSITIVE WEDGE ANGLE TESTS

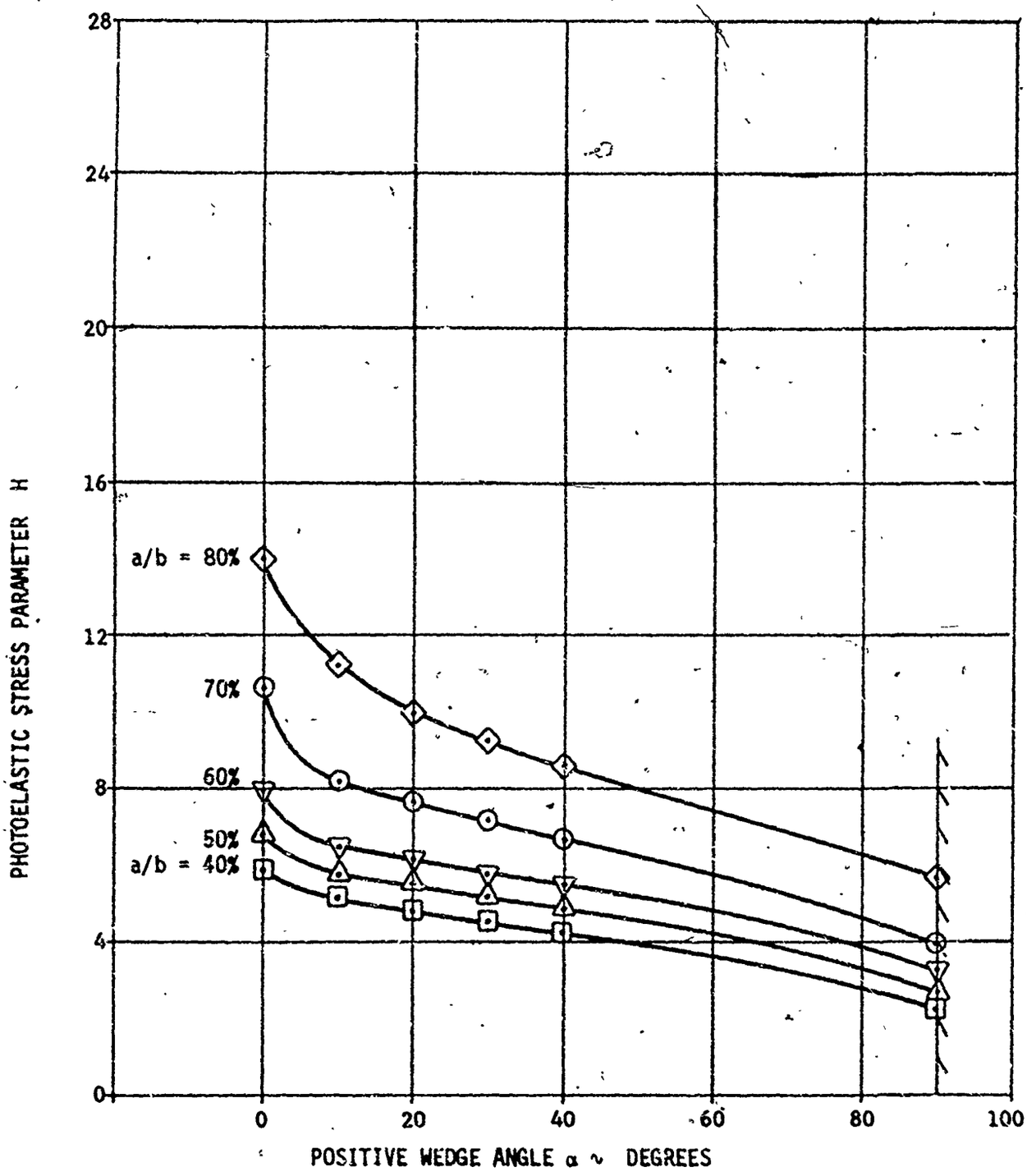

FIGURE 22. Positive Wedge Angle Test Results, N = 4, a/ρ = 8

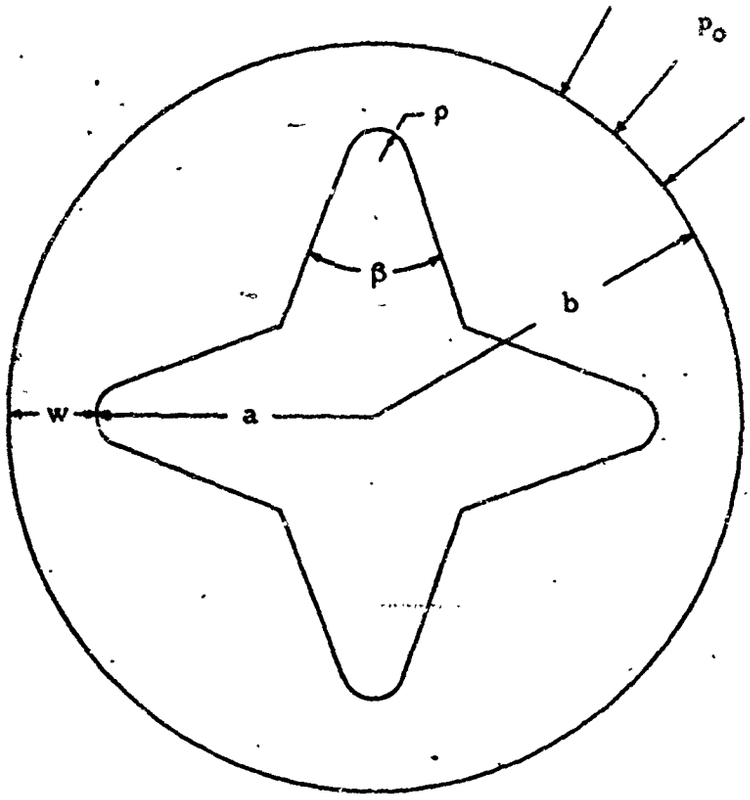

FIGURE 23. GEOMETRY OF TYPICAL CROSS SECTION FOR NEGATIVE WEDGE ANGLE TESTS

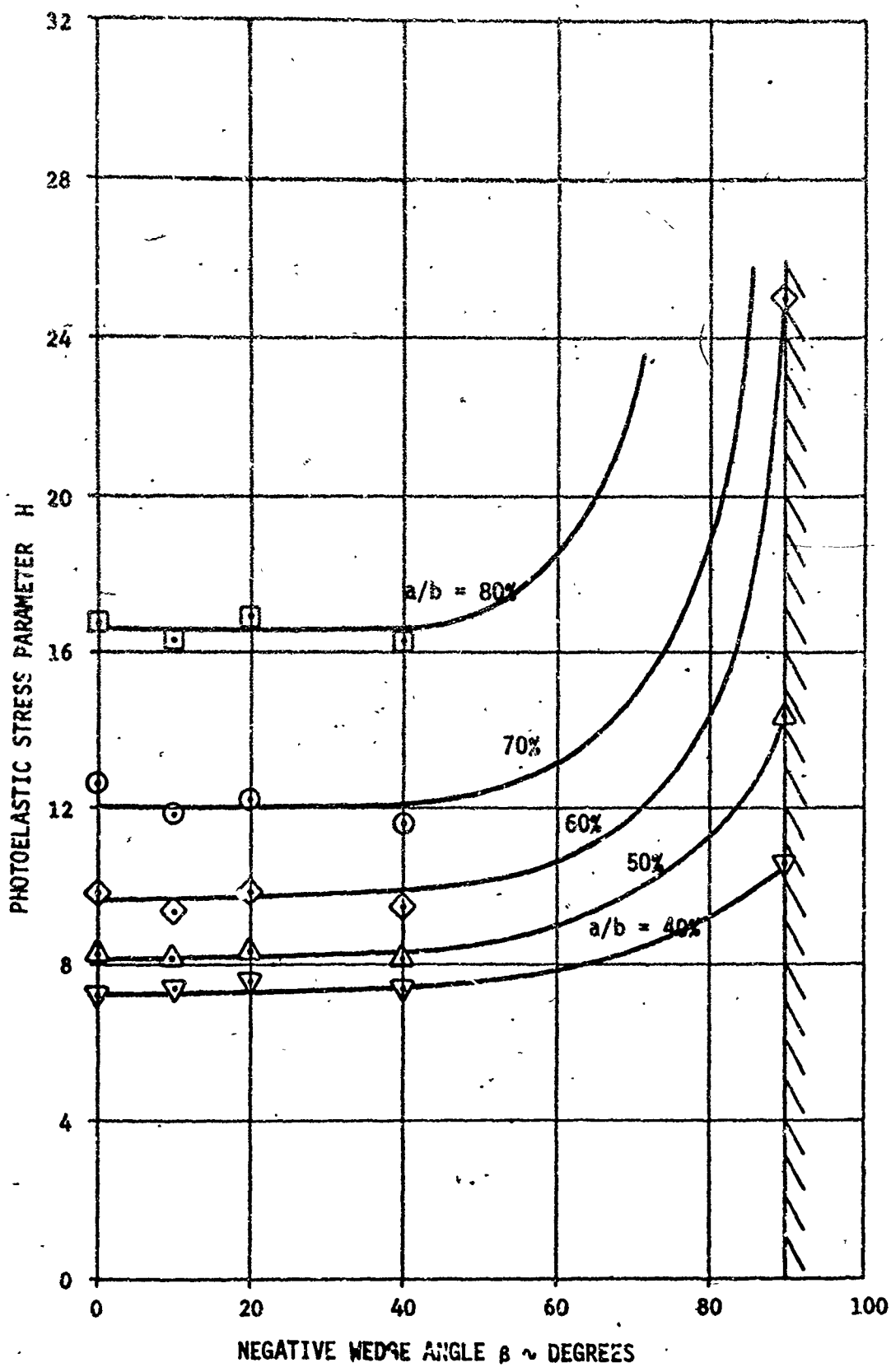

FIGURE 24. NEGATIVE WEDGE ANGLE TEST RESULTS, N = 4, a/ρ = 12.

up to 45 degrees. This result indicates that most practical star perforated geometries with negative wedge angles may be treated as simple slotted grains.

3.7.5 ELLIPTICAL SLOT TIP GEOMETRY

The last geometry modification studied extensively by Fourney and Parmerter was that of the elliptical slot tip shown in figure 25. The parameter ϵ in these tests is the ratio of the minor axis of the ellipse to the major axis of the ellipse. A value of $\epsilon = 1$ corresponds to a semi-circle slot tip and hence a particular type of simple slotted configuration. When ϵ is small ($\epsilon \to 0$) the slot tip resembles the type used in the slot width effect tests. Since the semi-circle slot tip has one point of stress concentration and the geometry used in the slot width effect tests has two points of concentration, it is intuitively felt that at some intermediate value of ϵ a transition from one point of concentration to two points of concentration must occur, and that at this transition the stress should be uniformly distributed around the tip. One also feels that this transition will represent a minimum stress configuration. Fourney and Parmerter found that this was indeed the case. A configuration of minimum stress occurs for a value of ϵ in the range $0.35 < \epsilon < 0.70$, and at a value of ϵ where the transition from one concentration point to two concentration points is occurring. The behavior of the stress factor H as a function of ϵ is shown in figure 26 for a fixed $a/\rho = 12$ and $N = 4$. The shaded region in this figure indicates the value of ϵ at which a minimum H occurs.

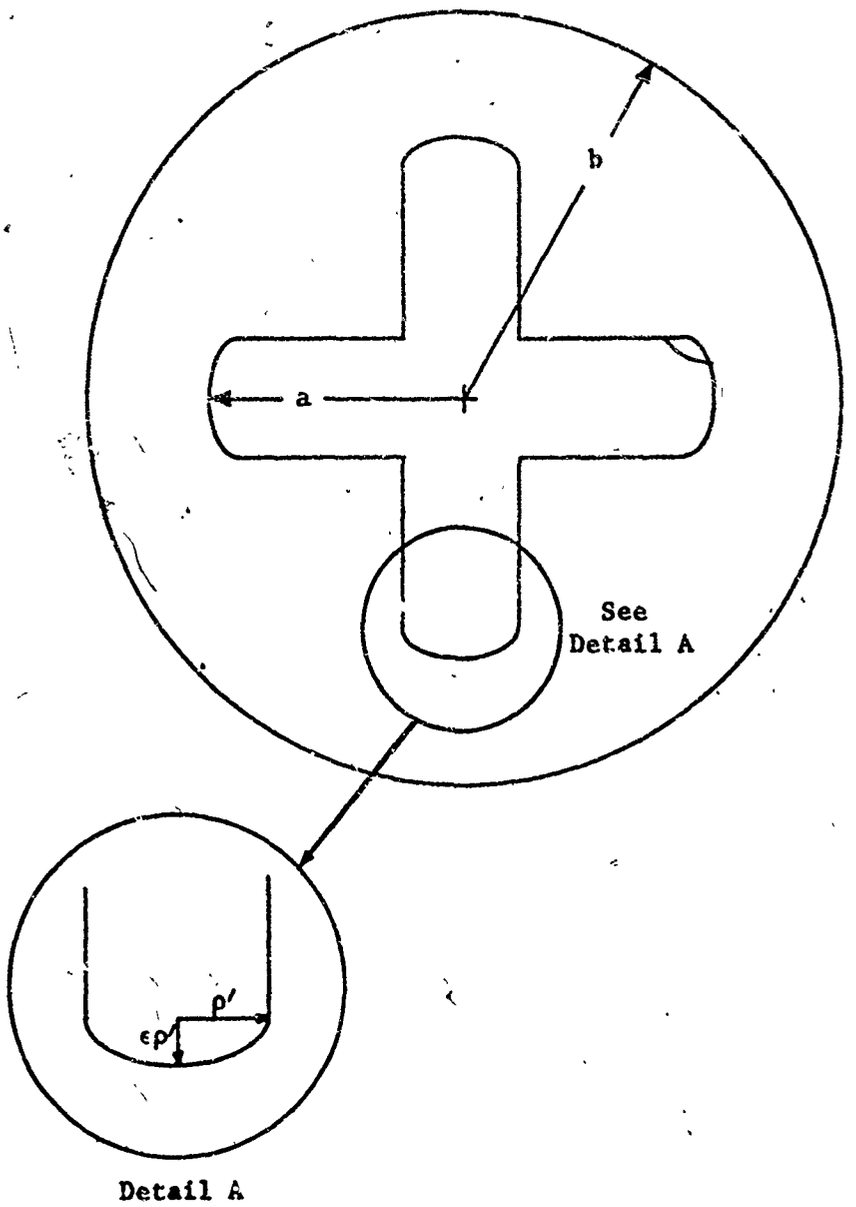

FIGURE 25. GEOMETRY OF TYPICAL CROSS SECTION FOR ELLIPTICAL SLOT TIP TESTS

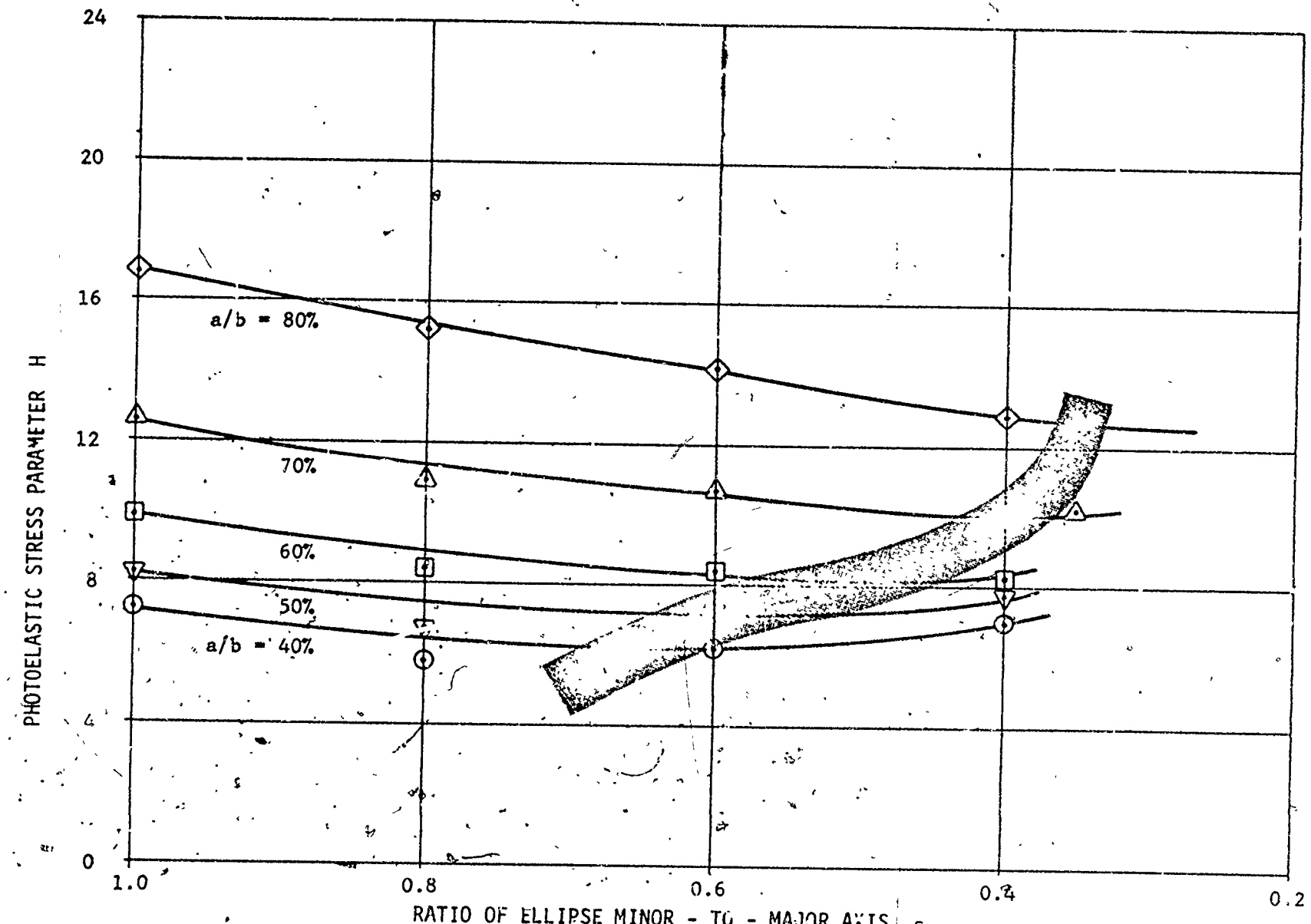

FIGURE 26 - ELLIPTICAL SLOT TIP TEST RESULTS, N = 4, a/ρ = 12.

3.7.6 EXTENSION OF PHOTOELASTIC TEST RESULTS

In the previous paragraphs only the photoelastic test results for four-slotted grain configurations have been presented. These results can be extended quite easily, however, to any reasonable number of star points. In the experimental investigations it was found that for the five geometric configurations defined in figures 17, 21, 23 and 25, the stress parameter H was inversely proportional to the cube root of the number of starpoints (i.e., $H \propto N^{-1/3}$) for values of N between 3 and 8. This fact allows the stress concentrations presented in figures 19, 20, 22, 24 and 26 to be extended to grain geometries with $N \neq 4$ by multiplying the stress factor H by $\sqrt[3]{4}$ and dividing by $\sqrt[3]{N}$ for the particular number of star points in the geometry under consideration. This extension is valid for values of N between 3 and 8, and can quite likely be extended to higher values of N with proper engineering judgment.

Fourney and Parmerter's investigation also demonstrated that in all cases other than the slot width tests the functional dependence of the stress factor H on the fillet radius is linear with a/ρ. This behavior is illustrated in figures 27 through 29 for the positive wedge angle tests, the negative wedge angle tests and the elliptical slot tip tests. These curves can be used to scale the previously presented results in figures 22, 24 and 26 to the particular fillet radius ratio a/ρ being analyzed.

In geometries in which slot width is important in reducing the stress concentrations, the results presented in figures 19 and 20 must be used in scaling the dependence of H on a/ρ for the particular port fraction a/b and slot width parameter $d/2\rho$ for the grain being analyzed.

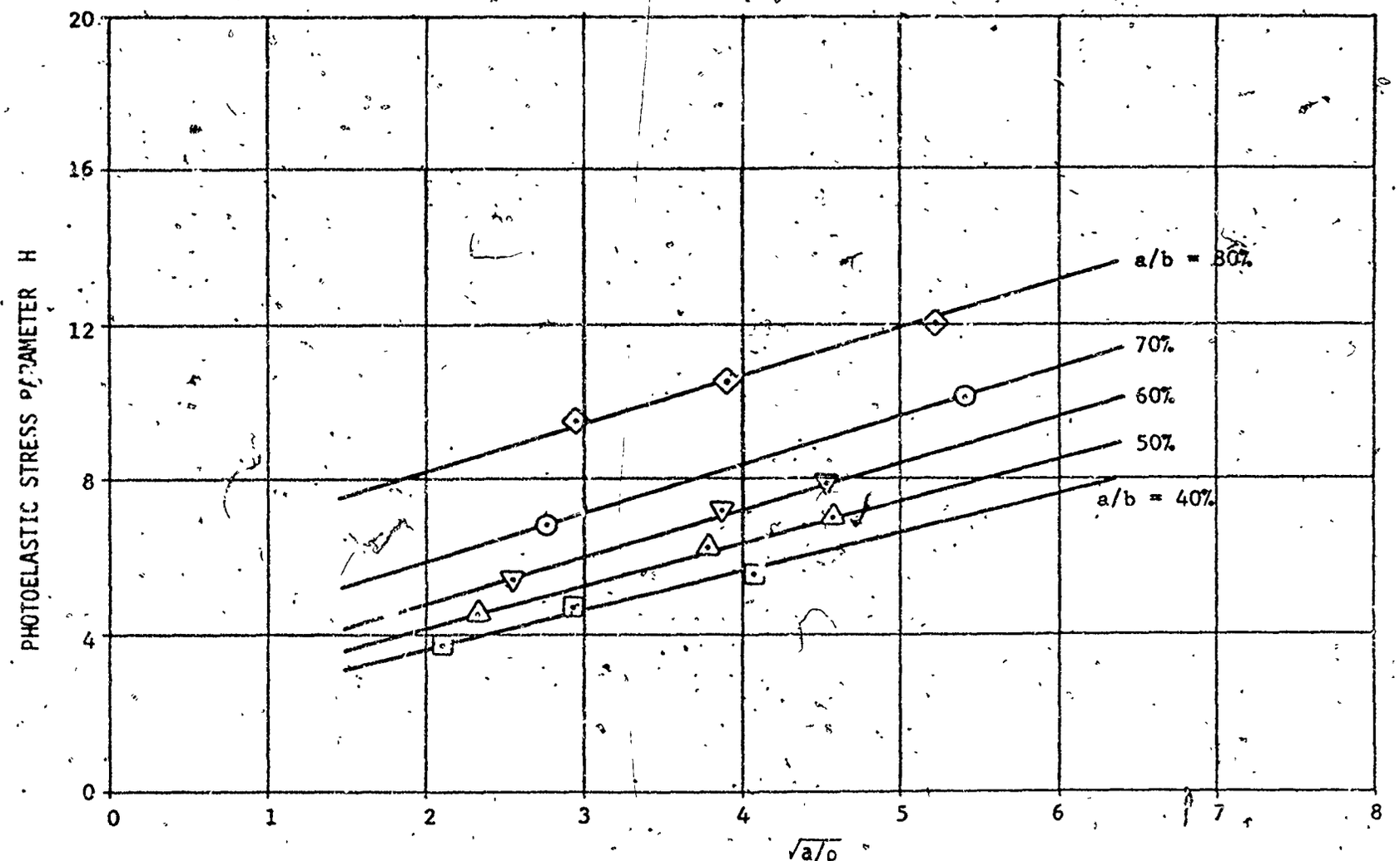

3.73

FIGURE 27. VARIATION OF PARAMETER H WITH FILLET RADIUS RATIO a/ρ FOR POSITIVE WEDGE ANGLE TESTS, N = 4, α = 30

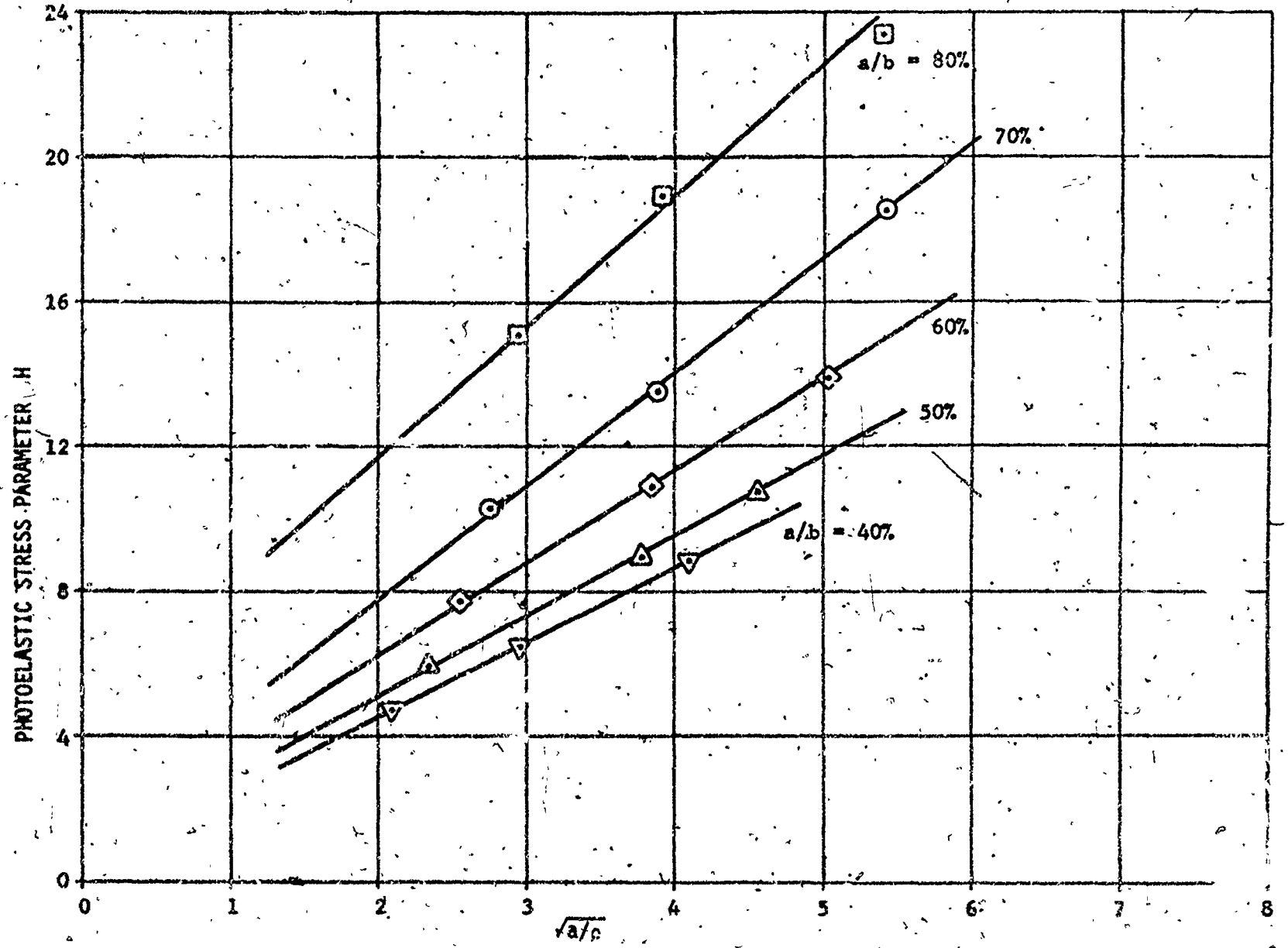

FIGURE 28. Variation of Parameter H With Fillet Radius Ratio a/ρ For Negative Wedge Angle Tests, N = 4 β = 20.

3.74

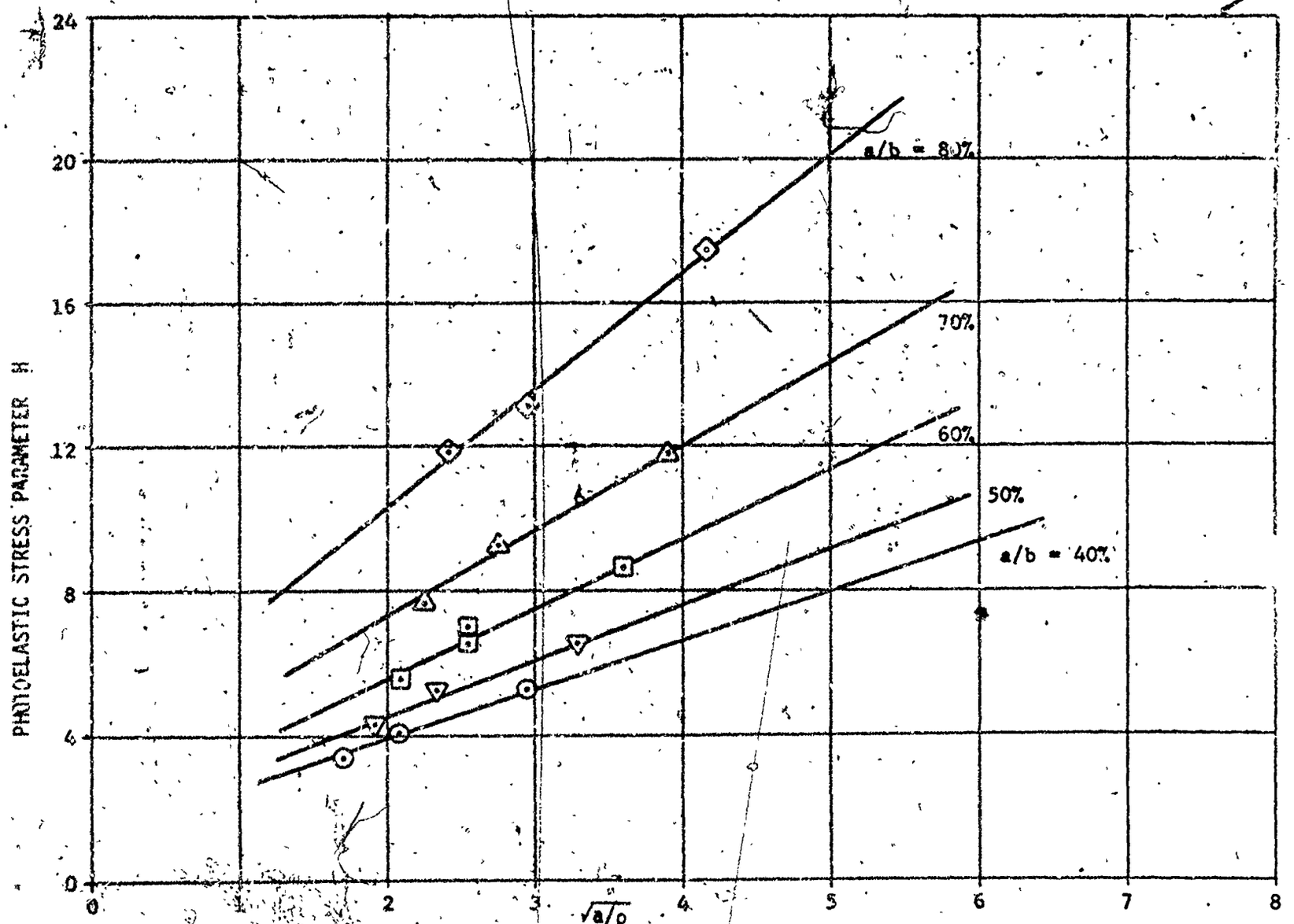

FIGURE 29. Variation of Parameter H With Fillet Radius Ratio a/ρ For Elliptical Slot Tip Tests, N = 4, ε = 0.8.

The dependence on the number of starpoints, as mentioned above, however, obeys the $N^{-1/3}$ rule.

The maximum deviation between experimental data and results calculated using the above scaling rules was found to be less than 7% for values of N between 3 and 8. This deviation is, of course, quite acceptable for a preliminary design grain structural analysis.

3.8 DESIGN ANALYSIS PROCEDURE SUMMARY

Before continuing further the procedure one follows in estimating the stress/strain concentration factor for a given star grain geometry is briefly summarized. The most rapid technique for estimating concentration factors is, of course, to use the simple equation (3.78) or figure 16. This method is what has become to be known classically as a "back-of-the envelope" calculation, and is most often carried out (and incidentally, recommended) while the structural analyst is peering over the shoulder of the grain designer and being asked to comment on the structural adequacy of a motor design.

In cases where more time is available, or slightly more sophisticated results are desired equations (3.79) and (3.77), and the results discussed in the previous sections are recommended for estimating concentration factors. The photoelastic test model which corresponds to the given grain configuration is selected from figures 17, 18, 21, 23 and 25.

In the case of simple slotted grain geometries and geometries with negative wedge angles in which the half-angle is less than roughly 25 degrees, the photoelastic parameter H is calculated directly using equation (3.79) and the stress/strain concentration factor K_t calculated using (3.77).

For geometries in which the slot has been widened to reduce concentrations, the port fraction a/b, the fillet radius a/ρ and the slot width factor $d/2\rho$ are determined for the particular grain geometry. The value of H for $a/b = 70\%$ for the particular values of a/ρ and $d/2\rho$ is then determined from figure 20. This value of H is then scaled using figure 19 to the appropriate port fraction. The resulting value of H is next scaled for geometries in which $N \neq 4$ by multiplying this value by $\sqrt[3]{4}$ and dividing by $\sqrt[3]{N}$. The concentration factor K_t is then finally determined from equation (3.77) where the normalizing factor $(\lambda^2-1)/2\lambda^2$ may be determined directly from figure 15.

In geometries which have positive wedge angles (figure 21), the pertinent geometric parameters are the included wedge angle α, the port fraction a/b, the fillet radius ratio a/ρ and N, the number of star points. Knowing a/b and a/ρ for the given grain geometry, a value of H is selected from figure 27 for $N = 4$ and $\alpha = 30°$. For wedge angles which are other than 30°, this value is scaled using figure 22 to correct to the proper wedge angle. In case $N \neq 4$ the final result is again obtained by multiplying this last value of H by $\sqrt[3]{4}$, dividing by $\sqrt[3]{N}$ and using equation (3.79) or figure 15 to determine K_t.

The identical procedure to that suggested in the previous paragraph now using figures 28 and 24 is used in obtaining the concentration factors for grain geometries with negative wedge angles in which the included angle is greater than 50 degrees. As mentioned above, the concentration factor for geometries with wedge angles less than 50° can be calculated directly using equations (3.79) and (3.77).

For geometries with elliptical slot tips, a similar procedure as that suggested in the previous paragraphs is used, with figures 29 and 26 treating e, the ratio of the minor to major axis of the ellipse as the variable quantity. When it is ballistically feasible, it is recommended that the value of e be selected which gives the minimum H for the particular port fraction a/b required.

In earlier investigations Fourney and Parmerter also studied the influence of the inverse star point on the stress factor H [32] Although only a limited number of tests were conducted, the results suggest that for values of the ratio a'/a (see figure 7 for definition of a') up to 60% no apparent difference from the results obtained for simple slot configuration is noted. At a value of a'/a = 80%, however, significant reductions in the stress concentration H are obtained. These results imply that for grain geometries with thick webs and short starpoints, concentration factors obtained by the methods discussed in the preceding paragraphs will lead to overly conservative predictions of the stresses and strains in the grain. For these geometries, the appropriate stress/strain concentration factor must be obtained from photoelastic tests of the actual geometry.

3.9 EQUIVALENT HOLLOW CYLINDER

In considering problems which involve a thickwalled hollow elastic cylinder bonded to a thin elastic casing and subjected to an internal pressure or thermal load, the classical Lame solution can be used by replacing the case by an equivalent uniform pressure P'. For a thick walled infinite length cylindrical grain subjected to an internal pressure, the interface pressure is given by [14]

$$\frac{P'_p}{P_i} \equiv \frac{P_{Pressure}}{P_i} = \frac{1}{\left\{1 + (1-2\nu_p)\lambda^2 + \left[(\lambda^2-1)\,\frac{(1-\nu_c^2)}{(1+\nu_p)}\,\frac{bE_p}{hE_c}\right]\right\}\frac{1}{2(1-\nu_p)}}, \quad (3.80)$$

where allowance has been made for a compressible grain. It can b seen that for an incompressible grain ($\nu \to \frac{1}{2}$) and a thin case ($bE_p/hE_c \ll 1$), the interface pressure P'_p is approximately equal to the applied internal pressure P_i. The maximum inner bore hoop stress $\sigma_{\theta_p}(a)$ and hoop strain $\varepsilon_{\theta_p}(a)$ are then given in terms of P'_p by the relations

$$\frac{\sigma_{\theta_p}(a)}{P_i} = \frac{(\lambda^2+1)}{(\lambda^2-1)} - \frac{2\lambda^2}{(\lambda^2-1)}\,\frac{P'_p}{P_i} \quad (3.81)$$

and

$$\frac{\varepsilon_{\theta_p}(a)}{P_i} = \frac{1}{E_p}\left\{\left[\nu_p + \frac{\lambda^2+1}{\lambda^2-1}\right] - \frac{2\lambda^2}{(\lambda^2-1)}\,\frac{P'_p}{P_i}\right\}. \quad (3.82)$$

The problem of a hollow elastic case bonded cylinder subjected to thermal loads also admits the classical Lame solution by determing the equivalent case-grain interfacial pressure P'_T required for compatible case and grain deflections. For uniform cooling, the interface pressure P'_T is given by

$$P'_T \equiv P'_{Thermal} = \frac{\alpha_R E_p(\lambda^2-1)\,\Delta T}{1 + (1-2\nu_p)\lambda^2 + (\lambda^2-1)\,\frac{(1-\nu_c^2)}{(1+\nu_p)}\,\frac{bE_p}{hE_c}} \tag{3.83}$$

The maximum inner bore hoop stress, $\sigma_{\theta_T}(a)$, hoop strain $\varepsilon_{\theta_T}(a)$ and case-grain interface bond stress $\sigma_{r_T}(b)$ are given in terms of P'_T for uniform cooling by the relations

$$\sigma_{\theta_T}(a) = -\frac{2\lambda^2 P'_T}{(\lambda^2-1)}\ , \tag{3.84}$$

$$\varepsilon_{\theta_T}(a) = -\frac{2(1-\nu_p^2)\lambda^2 P'_T}{E_p(\lambda^2-1)} + (1+\nu)\,\alpha_p\,\Delta T\ , \tag{3.85}$$

and,

$$\sigma_{r_T}(b) = -P'_T\ . \tag{3.86}$$

These expressions, (3.80) through (3.86), can be used for determining pressurization and thermal stresses and strains in long case-bonded hollow cylindrical grains. The end correction factors discussed in section 3.6 can also be applied to account for finite length effects. The validity of the above equation for determining the interface pressures in star perforated grains, however, is in doubt when the web becomes thin. If the web is thin the external pressure will not be uniform and shear transfer between the case and grain may be appreciable. Equations (3.80) and (3.83) may still be used to determine P' however, by choosing a value of λ which properly represents the star grain as an "equivalent

thickwalled cylinder."[4] Intuition clearly indicates that the equivalent cylinder lies between an equal web fraction grain cylinder and an equal area cylinder. Calculations based on an equal web fraction equivalence yield a lower bound to the stresses while an equal area equivalence yields an upper bound.

Recently Fourney and Parmerter [29] have compared computer solutions for case-bonded and free star grains obtained by Becker and Brisbane [33] for thermal and pressure loads with their photoelastic test results. They found excellent agreement for the free grain for both stress and strain. For the case-bonded grains however, the maximum stress calculations showed good agreement when the equivalent pressure P' was calculated using an equal web fraction equivalent whereas appreciable error developed in the strain calculations, particularly for large values of the stress concentration parameter H and values of $\nu \approx 0.5$. Using the examples reported by Becker and Brisbane and sample numerical calculations of their own, Fourney and Parmerter hav derived tentative rules for finding a better equivalent cylinder. The comparisons of Fourney and Parmerter showed that the correct equivalent is much closer to equal web fraction than to equal area, indicating that the star grain material inside an equal web fraction cylinder is not effectively utilized in profiding hoop stiffness. The area of this ineffective material is proportional to $[(1/\lambda w)^2 - (1/\lambda_A)^2]$ where λ_w refers to an equal web fraction equivalent and λ_A refers to an equal area equivalent. The results of Fourney and Parmerter indicated that considering this area to

[4] This thickwalled cylinder is equivalent in the sense that the pressure P' calculated using (3.80) or (3.83) with the chosen value of λ is equal to the average value of the normal stress the case exerts on the actual star grain.

be 20% effective in increasing hoop stiffness, considerable improvement in the accuracy of strain calculations is obtained. They proposed that for the purpose of calculating the interface pressure P', an equivalent cylinder be calculated using equation (3.71); viz;

$$\left(\frac{1}{\lambda_e}\right) = \sqrt{\left(\frac{1}{\lambda_W}\right)^2 - 0.2\left\{\left(\frac{1}{\lambda_W}\right)^2 - \left(\frac{1}{\lambda_A}\right)^2\right\}} \quad . \tag{3.71}$$

Based on comparative examples it was found that when λ_e was used to calculate P', the maximum error in stress was less than 10% and the maximum error in strain was less than 15%. These results are adequate for preliminary analysis purposes and represent a considerable improvement over results obtained using λ_W or λ_A for calculating P'.

When dealing with star perforated grains the interface pressures P_p' and P_f' are calculated directly using (3.80) and (3.83) with the equivalent grain radius ratio λ_e defined by (3.71). In calculating the appropriate stresses and strains, however, expressions (3.81) and (3.82), and (3.84) and (3.85) must be modified to include the star valley stress/strain concentration factor K_f or equivalently the photoelastic parameter H. These modifications have been introduced previously for pressure loading of a long incompressible grain, and resulted in equations (3.70) and (3.72) for determining pressurization stresses and strains; i.e.,

$$-\left(\frac{\sigma_{\theta_p}^{s(a)}}{P_i}\right) = 1 - H(1 - P_p'/P_i) \quad , \tag{3.70}$$

and

$$\left(\frac{\varepsilon_{\theta_p}^{s(a)}}{P_i}\right) = \frac{3}{4E_p} H(1 - P_p'/P_i) \quad . \tag{3.71}$$

Similar results for uniform cooling of an incompressible star grain are easily obtained from equations (3.84) and (3.85) by applying the stress concentration H; viz;

$$\varepsilon'_{\theta_T}(a) = \frac{3}{4E_p} H P'_T \quad , \tag{3.87}$$

and

$$\sigma_{\theta_T}(a) = - H P'_T \tag{3.88}$$

These results are equivalent to equations (3.5) and (3.7) when these latter equations are multiplied by the factor $K_i = 2\lambda^2/(\lambda^2-1)$. The radial bond stress $\sigma^s_{r_T}(b)$ is given by (3.86) and is only sensitive to the effective radius ratio λ_e.

It can be seen that equations (3.70), (3.71), (3.87) and (3.88) are quite sensitive to the interface pressure P' and hence to the propellant compressibility and case stiffness. It has already been pointed out that for a very stiff base ($bE_p/hE_c \ll 1$), $P'_p \to P_i$ as $\nu \to \frac{1}{2}$. For stiff, but not rigid cases, and nearly incompressible propellants better results can be obtained by expanding the interface pressures P'_p or P'_T in a truncated finite series expansion. Noting the similarity between (3.80) and (3.83) and defining,

$$\delta \equiv (1-2\nu_p)\lambda^2 + (\lambda^2-1)\frac{(1-\nu_c^2)}{(1+\nu_p)}\frac{bE_p}{hE_c} \quad , \tag{3.89}$$

one can write

$$= \frac{P'_p}{2(1-\nu_p)P_i} = \frac{P'_T}{\alpha_R E_p(\lambda^2-1)\Delta T} = \frac{1}{1+\delta} \tag{3.90}$$

Carrying out the expansion of (3.90) for $\delta<1$, one obtains,

$$= 1 - \delta + \delta^2 - \delta^3 + \cdots \; . \qquad (3.91)$$

Now only those terms which are significant compared to unity need to be retained in calculating and hence P_p' or P_T'. This procedure should lead to a better estimate of the stresses and strains in a solid propellant rocket motor grain. The influence of Poisson's ratio can also be considered in an ad hoc manner by letting $\nu = \frac{1}{2} - \Delta$ where $\Delta << 1$, and retaining only first or second order terms in Δ.

Since inner bore hoop strains are usually the critical design parameter for conventional motor designs, and also since treating the case as being rigid and the propellant as incompressible leads to conservatively high prediction of these strains, the modification of the previous paragraph need not be considered in a preliminary design analysis unless the design is found to be marginally safe* using conservative analysis techniques. In these cases, however, a cautious interpretation of the improved result is strongly recommended in view of possible variations in the propellant physical property or environmental response.

3.10 CLOSURE

This chapter has presented a summary and discussion of the recommended techniques commonly employed throughout the solid propellant rocket industry for conducting preliminary design analyses of solid propellant rocket motors. As mentioned in the introduction these analyses are carried out to determine only if a particular grain design has merit and to obtain qualitative recommendations for structural improvements.

The techniques discussed in this chapter are applicable to conventional grain designs. These methods are not directly applicable to, say, full slotted grains, cartridge loaded grains, strip bonded grains or grains with geometrical transitions (e.g., star geometry to circular port transition). Techniques for analyzing motors in a spin environment have also not been include

The influence of Poisson's ratio, consideration of finite deflections and further discussion on the applicability and usefulness of a Grüneisen relation are also presented in a subsequent chapter. The sensitivity of analysis results to Poisson's ratio indicates further studies on the effects of stress state, strain and time on Poisson's ratio and the bulk response of propellant need to be carried out. Introducing a Grüneisen relation, even in ad hoc manner, serves to remove the sensitivity of analysis results to Poisson's ratio, however a much better characterization of the bulk response of propellants is required for universal acceptance of such a relation.

Finite deflections also become important in the pressurization of motors with low modulus case materials, such as fiberglas, where strains on the order of 20% are not uncommon.

The methods presented here have all been based on linear elasticity theory with indications given of the means of extending these results to include linear viscoelastic response. It is generally accepted that solid propellants are not linear elastic materials, nor, for that matter, linear viscoelastic materials. Unfortunately, an adequate nonlinear constitutive theory has not yet been formulated. Application of even the most simple nonlinear constitutive theory suggested to date

introduces significant computational difficulties and requires extensive characterization testing for the particular propellant involved. Because of the limited objectives of a preliminary design analysis, these considerations are not required and one is well justified in using linear theories at the preliminary design stage. A discussion of nonlinear material behavior and the inclusion of nonlinear constitutive theories in more refined final design analyses is presented in Chapter II.

In presenting analysis methods, often more than one approach has been given. In general the alternate approaches will give slightly better results. For example, equation (3.27) gives the approximate deflection of a star point tip subjected to a lateral acceleration when the star point is treated as a cantilever beam of uniform thickness whereas equation (3.63) gives the same result treating the star point as a cantilivered beam with a truncated triangular cross-section. Pressurization strains in star perforated grains may be obtained by simply applying concentration factors to equation (3.64) and (3.65) or they may be determined from (3.72) when the case-grain interfacial pressure is determined using an equivalent hollow cylinder. Similarly, star valley stress/strain concentration factors may be determined quite simply using equations (3.78) or (3.79), or the results in figure 18 through 29 can be used to give a better estimate. The criteria for deciding which of the alternate approaches should be used involves consideration of the time and funds given the structural analyst to carry out the required task, the complexity of the grain geometry and the severity of the load environment. Another significant factor in making

this decision is past experience with similar grain geometries under similar loading conditions.

Finally it should be mentioned that the analyses discussed here need not be carried out in detail in every preliminary design analysis. Clearly, one need not consider dynamic or acceleration loading of a motor which is only going to be subjected to static firing. For conventional geometries with typical total use environments the critical design parameter is the inner bore hoop strain under combined low temperature storage and ignition pressurization. High temperature acceleration and shock loadings only become the controlling design factor for sophisticated high acceleration air launched attack missiles or surface-to-air anti-ballistic missiles. Vibration effects will also be insignificant except in the case of a star perforated grain with long thin star points, or highly confined high mass fraction motors where the volume expansion due to the temperature rises associated with sustained vibration result in significant case-grain interfacial shear stresses. Aerodynamic heating effects will almost always be negligible when the motor case is externally insulated.

3.11 NOMENCLATURE

a = Grain Inner Radius
b = Grain Outer Radius
D = Motor Diameter
E = Tensile Modulus
h = Case Thickness
H = Mean Pressure Function
K = Bulk Modulus
K_f = Stress/Strain Concentration Factor
k = Spring Constant
k^* = Complex Spring Constant
L = Motor Length
ℓ = Length of Starpoint
M_e = Effective Mass
N = Number of Starpoints
n = Slope of Relaxation Curve
P = Pressure
$\bar{P}$ = Finite Length Correction Factor
T_1 = Zero Stress/Strain Temperature
t = Time
v = Displacement
V = Volume

α = Phase Angle
α = Coefficient of Linear Expansion
α,β = Constant
β = Loss Tangent
β = Grüneisen Parameter
Δ = Deflection
ε_θ = Hoop Strain
ε_r = Radial Strain
ε_z = Axial Strain
λ = b/a = Grain Radius Ratio
λ = Lamé Constant
θ_1 = First Stress Invariant
ρ = Propellant Density
ρ = Star Valley Radius
σ_θ = Hoop Stress
σ_r = Radial Stress
σ_z = Axial Stress
τ = Shear Stress
μ = Lamé Constant
ν = Poisson's Ratio
ω = Circular Frequency
Ω = Normalized Frequency

3.12 REFERENCES

1. Rohm & Haas Company quarterly progress report on Engineering Research, Report No. P-61-17, June 25, 1962; Redstone Arsenal Research Division, Huntsville, Alabama, (Contract DA-01-021-ORD-5135).

2. Rohm & Haas Company quarterly progress report on Engineering Research, Report No. P-62-21, April 19, 1963; Redstone Arsenal Research Division, Huntsville, Alabama, (Contract DA-01-021-ORD-11878).

3. Messner, A. and Schliessmann, D., "Parameter Calculations of Simple Propellant Grains for Temperature Cycling, Pressurization and Acceleration"; Appendix C in support of Study of Mechanical Properties of Solid Rocket Propellants, Aerojet General Report No. 0411-10F, March 1962; Aerojet General Corporation, Solid Rocket Plant, Sacramento, California, (Contract AF 33(600)-40314 S.A. No. 1).

4. Lockheed Propulsion Company, "Engineering Methods for Grain Structural Integrity Analysis," LPC Report No. 578/556-F-3, May 1963, Redlanss, California, (Contracts AF 04(611)-8013 and DA-04-495 ORD-3260).

5. Jones, J. Fitzgerald, J. E., and Francis, E., "Thermal Stress Investigation of Solid Propellant Grains: Volume 1 - Theory and Experiment," LPC Report No. 578-F-1, May 1963, Lockheed Propulsion Company, Redlands, California, (Contract AF 04(611)-8013).

6. Cost, T. L., "Analytical Methods for Determining the Shrinkage Stresses in Polymeric Materials During Cure," Technical Report S-72, December, 1968, Rohm & Haas Company, Redstone Research Laboratories, Huntsville, Alabama,(Contracts DAAH01-67-6-0947 and DAAH01-68-C0891).

7. Kittel, Charles, "Introduction to Solid State Physics," Third Edition, 1966, John Wiley & Sons Inc., New York.

8. Tobolsky, A. V., "Properties and Structure of Polymers," John Wiley & Sons, Inc., New York, 1960.

9. Hufferd, W. L., "On the Existence of a Grüneisen Relation for Incompressible Elastic Solids," forthcoming in the International Journal of Solids and Structures.

10. Freudenthal, A. M., "Thermal Stress Analysis and Grüneisen's Relation," J. Appl. Physics, Vol. 31, No. 2, 1960 (p. 434).

11. Fitzgerald, J. E., "Revised Computer Program for Stress Analysis Utilizing a Grüneisen Constraint; Technical Note: Submitted for publication in the AIAA Journal.

12. Herrmann, L. R., "Elasticity Equations for Incompressible and Nearly Incompressible Materials by a Variational Theorem," AIAA Journal, Vol. 3, No. 10, 1965.

13. Francis, E. C., and Cantey, D., "Structural Integrity of Propellant Grains (U)," LPC Report No. 556-F, Volume 1, January 1963, Lockheed Propulsion Company, Redlands, California, (Contract No. DA-04-495-ORD-3260).

14. Williams, M. L., Blatz, P. J. and Schapery, R. A., "Fundamental Studies Relating to Systems Analysis of Solid Propellants," GALCIT SM 61-5, (Thiokol Report No. 23-61), February 1961. Guggenheim Aeronautical Laboratory, California Institute of Technology, Pasadena, California, (Contracts DA-01-021-ORD-11919 (780), DA-01-021-ORD-2314, NOD. 7, and AF 33(600)-36514).

15. Hoekel, T. and Schapery, R. A., "The Structural Design of Solid Propellants," Report No. 2123, January, 1967, Emerson Electric of St. Louis, Electronics and Space Division, St. Louis, Missouri, (Contract No. N0D600-67-C-0081).

16. Parr, C. H., "End Effects Due to Shrinkage in Solid Propellant Grains," Bulletin of the 20th JANAF PANEL ON PHYSICAL PROPERTIES OF SOLID PROPELLANTS, Volume I, November 1961.

17. Tormey, J. F. and Britton, S. C., "Effect of Cyclic Loading on Solid Propellant Grain Structures," AIAA Journal, Vol. 1, No. 8, August 1963.

18. Achenbach, J. D., "The Structural Dynamics of Solid Propellant Rockets," Applied Mechanics Reviews, Vol. 21, No. 6, June 1968.

19. Baltrukonis, J. H., "The Dynamics of Solid Propellant Rocket Motors," Mechanics and Chemistry of Solid Propellants (Edited by A. C. Eringen, H. Liebowitz, S. L. Koh and J. M. Crowley), Pergamon Press, 1967, pp. 297-332 (NASA CR-658)

20. Schapery, R. A., "Effect of Cyclic Loading on the Temperature in Viscoelastic Media with Variable Properties," AIAA Journal, Vol. 2, No. 5, May 1964.

21. Schapery, R. A., "Thermomechanical Behavior of Viscoelastic Media with Variable Properties Subjected to Cyclic Loading," Bulletin of the 3rd Meeting, ICRPG Working Group on Mechanical Behavior, Vol. 1, October 1964.

22. Clemmer, L. E., "Thermomechanical Response Studies of A Viscoelastic Cantilever Plate, "School of Aeronautical, Astronautical, and Engineering Sciences, Purdue University, June 1965.

23. Schapery, R. A. and Cantry, D. E., "Thermomechanical Response Studies of Solid Propellants Subjected to Cyclic and Random Loading," AIAA Journal, Vol. 4, 1966, p. 255.

24. Lockheed Propulsion Company, "Solid Propellant Structural Integrity Investigations: Dynamic Response and Failure Mechanisms", AFRPL-TR-64-141, Vol. I, LPC Report No. 667-Q-1, October 1964, Contract.

25. Den Hertog, J. P., "Mechanical Vibrations", McGraw-Hill Book Company, Inc., New York, 1947.

26. Snowdon, J. P. "Vibration and Shock in Damped Mechanical Systems", John Wiley & Sons, Inc., New York 1968.

27. Chen, Y., "Vibrations: Theoretical Methods", Addison-Wesley Publishing Company, Inc., Reading, Mass. 1966.

28. Lockheed Propulsion Company, "Solid Propellant Structural Integrity Investigations: Dynamic Response and Failure Mechanisms", AFRPL-TR-65-171, LPC Report No. 667-F, November 1965, Contract No.

29. Fourney, M. E. and Parmerter, R. R., "Parametric Study of Rocket Grain Configuration by Photoelastic Analysis," AFSC Report No. AFRPL-TR-65-52, March 1966, Mathematical Sciences Corporation, Seattle, Washington, Contract No. AF 04(611)-1052a.

30. Fourney, M. E. and Schmidt, W. F. "Extension of Photoelastic Design Data to Case-Bonded Grains and Axisymmetric Geometries", AFSC Report No. AFRPL-TR-68-136, September 1968. Mathematical Sciences Corporation, Seattle, Washington, Contract No. F04611-68-C-0013.

31. Sampson, R. C., "Development of Equations Suitable for Calculations of Stresses and Strains at the Bore of Solid Propellant Motors", Aerojet-General Structures Technical Memorandum 211 SRP, February, 1963.

32. Fourney, M. E., and Parmerter, R. R., "Stress Concentrations for Internally Perforated Grains", NAVWEPS Report 7758, 1961.

33. Becker, E. B. and Brisbane, J. J., "Application of the Finite Element Method to Stress Analysis of Solid Propellant Rocket Grains", Rohm and Haas Report No. S-76, November 1965.

IV. FINAL DESIGN ANALYSIS

4.1 INTRODUCTION

The final stage of a grain structural analysis is performed after a preliminary design analysis has indicated the potential adequacy of a given grain configuration. Whereas a preliminary design analysis normally investigates loads and regions of a propellant grain generally thought to represent critical structural integrity parameters, under simplifying assumptions and approximations, a final design analysis usually encompasses the total loading environment and the entire propellant grain, normally under less restrictive assumptions and approximations.

The level of sophistication required in the final analysis and design stage is determined by the complexity of the grain configuration and the severity of the loading environment. Presently, the final stage of a grain structural analysis involves extensive use of approximate numerical techniques. Few closed-form analytical solutions are obtained during the final analysis stage because of the complexities of the problems involved and the relative ease of developing numerical analysis methods for obtaining approximate solutions. A brief description of the numerical techniques commonly used throughout the solid propellant industry is presented here along with a discussion of

current industry practices. A detailed summary of the application of numerical methods to structural integrity problems has been presented by Parr [1,2]. The application of the finite element method to grain stress analysis problems has been reviewed by Anderson [3]. The summary of the finite element method presented below is supplemented by a more thorough development in Appendix B.

4.2 NUMERICAL TECHNIQUES

The first applications of numerical methods to the structural analysis of solid propellant grains involved use of finite difference techniques [4-8]. The finite difference method requires replacement of the governing field equations by a set of finite difference equations using Gaussian elimination or successive over-relaxation methods [9]. The finite difference technique is particularly well suited for solution of equations of Laplace or Poisson type, and thus finds greatest use in the solution of steady-state heat conduction or torsion problems. The method is not particularly well suited, however, for problems involving several materials, irregular shaped boundaries or mixed boundary conditions although Steyer [10] has proposed a more flexible theoretical development of the finite difference approach to treat these situations.

In the past few years the finite element method has almost entirely replaced finite difference routines since irregular shaped boundaries are more easily handled, and greater freedom in material properties is allowed. Materials can be anisotropic as well as isotropic, and bodies of several materials can be analyzed quite easily.

The finite element method is a numerical discretization procedure which represents an extension of the techniques originally used in the

structural analysis of ordinary framed systems. The impetus for the use of finite element techniques in analyzing continuum structures came from Turner, Clough, Martin and Topp [1] who pointed out that a continuum structure could be treated as a collection of elements such that the deformation of every element was completely determined by the nodes bounding it, and that the addition of element stiffness could be reduced to a routine procedure if the components of the displacement at every node were referred to a common coordinate system. The method offers tremendous versatility, and with each new generation of computers increasingly more complex and more sophisticated analyses are routinely carried out. It is noted however that the results are subject to some uncertainty, as will become apparent in subsequent discussions. The accuracy and reliability of the finite element method is directly proportional to the intelligent use of the method and interpretation of the results. Caution must be exercised in posing the problems to be solved and in modeling the problems for computer analysis. Properly used and interpreted, the finite element method is as satisfactory an analysis tool as any other analysis method.

Finite element solutions normally begin with the statement of a variational principle. A functional is defined which has the relevant physical variables of the problem as its arguments. A variational theorem is then developed which shows that the particular functions from a certain class of admissible functions which minimize the functional are those which satisfy the governing differential equations of the problem. The displacement formulation of the finite element method, also known as the (direct) stiffness method, has found the most use in

linear elasticity problems[1]. In this case the Theorem of Minimum Potential Energy [12], which states that the potential energy assumes an absolute minimum for those displacements satisfying the equilibrium equations, provided that the classes of admissible displacement functions are restricted to those satisfying compatibility and the displacement boundary conditions, is employed.

The above minimization process is systematized by noting that certain features of the direct stiffness finite element technique may be interpreted as applications of the Rayleigh-Ritz Method[2]. The Rayleigh-Ritz procedure consists of assuming a trial family of solutions which depend upon a number of arbitrary parameters. The unknown parameters are determined in such a manner as to minimize the functional (e.g., Potential Energy). In this procedure the best solution within the original class of admissible functions is obtained, and, under certain completeness and continuity restrictions, the minimization process tends monotonically to the correct answer as the number of elements increases. The finite element analysis using non-conforming elements (i.e., elements for which some or all continuity requirements are violated on element interfaces), is not a simple form of the Ritz

---

[1] Variational theorems have been developed for complementary energy and mixed energy formulations; however, these are not extensively used since they require selection of element stresses satisfying the equations of equilibrium. In addition, the flexibility or redundant force method, which is equivalent to the complementary energy formulation, is more difficult to program and execute on a computer since the composite flexibility matrix is not formed by direct addition of the corresponding components of the element flexibility matrices as is the situation in the stiffness formulation.

[2] For this reason the finite element method is often called the *extended Ritz Method*.

procedure since the energy density on element interfaces is infinite. The analysis is usually performed by evaluating the necessary integrals as a sum over the elements ignoring the interface contributions. The discretized equations do not define a minimum but a stationary condition, in general, and the finite element solutions generated by element subdivision do not constitute a minimizing sequence for the energy.

The finite element method requires approximation of the body being analyzed by a number of subregions or elements. These elements are usually a collection of triangles which are combined into quadrilateral elements during execution of the program in order to minimize stress oscillations. In the displacement formulation displacements are approximated in each element by a function which introduces the nodal point displacements as the unknowns. The potential energy is minimized over each element yielding a system of algebraic equations for the unknown displacements. The solution of this system is the displacement field from which the stresses are calculated. The displacement functions are normally assumed to be linear within each triangular element in order to guarantee inter-element compatibility. In areas where the actual displacement field is linear, a linear approximation is adequate with large elements. In areas where the displacements are progressively more nonlinear, such as case/grain termination points, the elements must be made progressively smaller in order to approximate the actual displacements. In addition, errors in the displacement approximation produce even

larger errors in stress calculations since the stresses are related to the derivatives of the displacements.

4.3 OUTLINE OF THE FINITE ELEMENT METHOD

Presently the finite element method is commonly used for two-dimensional (i.e., plane stress, plane strain, axisymmetric), quasi-static linear elastic stress analysis. Extensions to three-dimensional geometries, linear viscoelasticity and thermoviscoelasticity and dynamic phenomenon in both elasticity and viscoelasticity have been made; however, these more sophisticated analyses are not used on a routine basis as yet in the structural analysis of solid rocket motors, mainly because such programs are quite expensive to run.

The approach commonly employed throughout the rocket industry involves modeling three dimensional behavior by a series of two-dimensional problems. Shell elements are frequently introduced to model the motor case. Considerable lattitude is available in the specification of boundary conditions and material properties. Forces or displacements may be prescribed in either coordinate direction at boundary nodal points. Distributed shear and pressure loads along any portion of the boundary may also be prescribed with the programs internally converting these to concentrated nodal point forces as required. Internal generation of body forces such as centrifugal forces or accelerations is also allowed. Provision is also made for different element temperatures. The internal grid network is often automatically generated using a linear interpolation or Laplacian scheme to simplify computer input.

As mentioned above the propellant may be treated as an orthotropic material in most programs if desired. Nonlinear propellant behavior is also handled quite easily and many programs are routinely equipped to handle bilinear behavior.

INCOMPRESSIBLE REFORMULATION

A problem arises using the displacement formulation of the finite element method for materials for which Poisson's ratio, ν, approaches one-half indicating incompressibility in infinitesimal deformation theory. The theorem of minimum potential energy is equivalent to the Navier displacement formulation of the classical elasticity field equations, and it is well known that the Navier displacement formulation is not valid for incompressible materials. Since solid propellants exhibit incompressible or nearly-incompressible material response ($\nu > 0.49$), the displacement formulation of the finite element method does not give acceptable solutions to problems involving these materials. As Poisson's ratio approaches one-half significant errors are introduced in the finite element solution for the displacement field due to the appearance of the term of $1-2\nu$ in denominators of the governing equations. Even more serious inaccuracies occur in the stresses, since the stresses are related to the strains through the constitutive laws, and the strains must be obtained from numerical differentiation of the displacement field. This normal ill-conditioned behavior is relieved considerably using Herrmann's reformulation [13,14] or overlapping elements [15,16]. There is still a tendency for some oscillation of stresses however, in problems of high restraint and values of Poisson's ratio near one-half. There is some indication that highly

constrained problems may be amenable to meaningful solution by introducing the Grüneisen ratio as an independent material property [17].

The incompressible reformulation most in use throughout the solid propellant industry is attributed to Herrmann and considers only mechanically incompressible materials. These are materials for which stress produces no volume changes, but temperature induced volume changes are allowed. In treating mechanically incompressible response, Herrmann introduces a new mean pressure function H as an additional unknown. In the earliest reformulation Herrmann and Toms [13] related the mean pressure function H to the mean pressure σ by the relationship

$$H = \frac{3}{2(1+\nu)} \tag{4-1}$$

Later, in connection with a modified Reissner Variational principle Herrmann took this relationship to be in the non-dimensional form [14]

$$H = \frac{3\sigma}{2\mu(1+\nu)} \tag{4-2}$$

In the development of a variational theorem for incompressible orthotropic elasticity Taylor, Pister and Herrmann [18] took the mean pressure function H to be simply the mean pressure σ independent of Poisson's ratio. Key [19] has proposed a reformulation for anisotropic elasticity which appears to be less sensitive to numerical inaccuracies since the volume strain occurs only in the common constitutive law relating the mean pressure and the volume strain. His

equations of equilibrium involve only the deviatoric components of strain and the gradient of the mean pressure. A comparison of some of the reformulations for incompressible elasticity has been presented by Yeh [20]. For definiteness, the later definition of H introduced by Herrmann and given by (1) will be used in the following discussion. In this form H is the mean pressure σ in the limit of Poisson's ratio equal to one-half. Completely equivalent results can be obtained using any of several definitions for H.

The classical theory of coupled thermoelasticity requires the solution of the 16 equations [21]

$$\tau_{ij},_j + f_i = \rho\ddot{u}_i$$

$$\varepsilon_{ij} = \frac{1}{2}(u_i,_j + u_j,_i)$$

$$\tau_{ij} = \lambda e\delta_{ij} + 2\mu\varepsilon_{ij} - \beta\Delta T\ \delta_{ij}$$

$$KT,_{ii} = \rho c_v\dot{T} + \beta\dot{e}T\ .$$

for the 16 unknowns u_i, ε_{ij}, τ_{ij} and the temperature T, for small excursions from the reference temperature T_o such that the material response functions are essentially constant, independent of temperature. Using (1) as a definition for H, it is observed from 4 that

$$\sigma = \frac{\tau_{ii}}{3} = (3\lambda+2\mu)(e-3\alpha\Delta T)$$

or

$$e - 3\alpha\Delta T = \frac{3}{2\mu}\frac{(1-2\nu)}{(1+\nu)}\sigma = (1-2\nu)H$$

Thus, using (6), (4) may be written

$$\tau_{ij} = 2\mu[\varepsilon_{ij} - \alpha\Delta T\delta_{ij} + \nu H\delta_{ij}]$$

The reformulated displacement equilibrium equations then have the form

$$H_{,i} + \mu\, u_{i,jj} + f_i + \alpha\mu T_{,i} = 0$$

Equations (6)-(8) are now valid for all admissible values of Poisson's ratio ($0 \leq \nu \leq \frac{1}{2}$), and (6) and (8) form a system of four simultaneous equations from which the unknown displacements U_i and the mean pressure function H are determined.

Following this reformulation, Herrmann developed a variational principle [14] to be used in conjunction with the Ritz method and the finite element formulation. The displacements u_i are assumed to be linear within each element and hence continuous across element boundaries, and the mean pressure function H is assumed to be constant within each element. The nodal point displacements and element values of H are treated as unknowns. Hughes and Allik [22] have conducted a study which indicates computational efficiency may be improved by

assuming a linear variation of the mean pressure function H across each element. Anderson [3] further discusses this reformulation.

In Herrmann's reformulation, and in the performance of thermal stress analysis of elastic materials in general, the elastic modulus E, Poisson's ratio ν and the linear thermal expansion coefficient α are tacitly assumed to be independent of each other. For supposedly incompressible materials this assumed independency leads to a physical inconsistency. Focusing our attention on (6) it is normally assumed that $\nu \to \frac{1}{2}$ while $\lambda \to \infty$; however, the quantity $\mu = \lambda(1-2\nu)/2\nu$ remains finite such that $e = 3\alpha\Delta T$. This inconsistency can be removed if one considers that the three constants E, α and ν are not independent but are related through the Grüneisen relation.

$$\beta = \rho C_v \gamma = (3\lambda+2\mu)\,\alpha \qquad (4\text{-}9)$$

The Grüneisen ratio γ may be defined through statistical arguments [23] or, as a thermodynamic derivative which can be expressed in terms of other thermodynamic quantities [24]. For many solid propellants it may be adequate to assume β to be a constant since the product ρC_v is essentially constant. Surland's compressibility experiments [25,26], although limited in number, suggest that γ should be reasonably constant.

Typical composite solid propellant data indicate that β should range between 68 and 100 psi/°F. Although this variation appears to large, it should be noted that this variation is inherent in any propellant grain stress analysis because of the difficulties associated

with precise experimental determination of the bulk propellant physical and thermal properties required for a grain stress analysis. The particular form of the parameter β given here by (9) was first suggested by Freudenthal [27,28] in connection with thermal stress analysis of metals with inelastic stress-strain behavior. The potential usefulness of such a relation in conducting solid propellant grain stress analyses was pointed out by Fitzgerald in reference 29. The theoretical foundations and physical interpretations of the Grüneisen ratio have been explored by Fitzgerald and Hufferd [17].

Using (9), equation (6) can be written in the form

$$e - \frac{3\beta\Delta T}{(3\lambda+2\mu)} = \frac{3}{2\mu}\,\frac{(1-2\nu)}{(1+\nu)}\,\sigma = \frac{1-2\nu}{\mu}\,H \qquad (4.10)$$

From (10) it is seen that as $\nu \to \frac{1}{2}$, $(3\lambda+2\mu) \to \infty$ and now $e = 0$, rather than $e = 3\alpha\Delta T$. It is also noted that the factors associated with one-dimensional restraint, $\alpha E = \beta(1-2\nu)$, and two-dimensional restraint, $\alpha E/(1-\nu) = \beta(1-2\nu)/(1-\nu)$, vanish for $\nu = \frac{1}{2}$ while the factor associated with three-dimensional restraint, $(3\lambda+2\mu) = \alpha E/(1-2\nu) = \beta$, remains bounded instead of becoming infinite. Thus the usual inconsistencies encountered in the conventional formulation of incompressible thermoelasticity are removed when β is introduced as an independent constant rather than α. Although Herrmann's reformulation considers only mechanical incompressibility, the introduction of a Grüneisen, parameter β allows consideration of true isochoric response in what appears to be a logically consistent manner. The assumption of incompressibility is now clearly associated with the vanishing of thermal stresses

except in the limiting case of complete three-dimensional restraint. The parameter β represents the hydrostatic stress associated with a temperature change of 1°F under conditions of three-dimensional restraint. This result is physically appealing. Many materials, including solid propellants, have a value for Poisson's ratio which is very nearly equal to one-half, although these materials do not have a vanishing thermal expansion coefficient, nor for that matter, an infinite bulk modulus. As a result these materials are typically idealized as mechanically incompressible materials with the embarrassing result that the predicted infinite stresses do not develop for even finite temperature changes of a completely restrained body. The parameter β allows for the more reasonable development of finite stresses under these conditions.

Anderson has explored the use of overlapping tension and shear elements which avoid the necessity of reformulation for $\nu = 1/2$. Alternating elements carry normal and shear stresses respectively and overlap to cover the complete structure. Using these elements no displacement constraint effect occurs for nearly incompressible materials, and experience has also indicated the absence of stress oscillation. Continuity of displacements along element boundaries is not obtained with these elements; however, experience has shown that finite element analysis using nonconforming or incompatible elements may give good results in some cases [30]. Apparently completeness of the assumed displacement functions is more important than continuity in demonstrating convergence of the solution [30-32]; however, the convergence will not necessarily be monotonic. Lack of completeness destroys convergence.

DEVELOPMENT OF BASIC EQUATIONS

The essential equations for the determination of any element stiffness are

$$\{e\} = [B]\{u_i\} \tag{4.11}$$

and

$$\{\sigma\} = [D](\{e\} - \{e_T\}) \tag{4.12}$$

in which

$\{e\}$ = column matrix of strains at a point in the element,

$\{e_T\}$ = column matrix of initial strains due to temperature changes, chemical shrinkage, crystal growth, etc.;

$\{u_i\}$ = matrix of nodal displacements;

$[B]$ = transformation matrix relating strains and displacements;

$\{\sigma\}$ = column matrix of stresses

and

$[D]$ = material property matrix.

For an isotropic material,

$$[D] = \begin{bmatrix} \lambda+2\mu & \lambda & \lambda & 0 & 0 & 0 \\ \lambda & \lambda+2\mu & \mu & 0 & 0 & 0 \\ \lambda & \lambda & \lambda+2\mu & 0 & 0 & 0 \\ 0 & 0 & 0 & \mu & 0 & 0 \\ 0 & 0 & 0 & 0 & \mu & 0 \\ 0 & 0 & 0 & 0 & 0 & \mu \end{bmatrix}$$

Generally a polynomial displacement function is assumed so that the displacements, $\{u\}$, at a point in the element are given by

$$\{u\} = [M]\{\alpha\} \tag{4.13}$$

in which

$\{\alpha\}$ = matrix of the coefficients of the polynomial (i.e., the generalized displacements);

and

$[M]$ = transformation matrix relating $[u]$ and $\{\alpha\}$.

The relationship between strain and displacement at a point is

$$\{e\} = [\Delta]\{u\} \tag{4.14}$$

where $[\Delta]$ is a matrix of differential operators. The relationship between strain and displacement is therefore

$$\{e\} = [\Delta][M]\{\alpha\} \tag{4.15}$$

The nodal point displacements follow from (13) as

$$\{u_i\} = [M_i]\{\alpha\} \tag{4.16}$$

in which $[M_i]$ is obtained from $[M]$ by substituting the coordinates of the nodes. Summarizing,

$$\{\alpha\} = [M_i]^{-1}\{u_i\} \tag{4.17}$$

$$\{u\} = [M][M_i]^{-1}\{u_i\} \tag{4.18}$$

$$\{e\} = [\Delta][M][M_i]^{-1}\{u_i\} \tag{4.19}$$

from which the matrix $[B]$ of (11) is determined to be

$$[B] = [\Delta][M][M_i]^{-1} \tag{4.20}$$

This procedure works well for simple elements. However, for complex elements it is desireable to avoid inverting $[M_i]$, by obtaining the interpolation relation (18) directly as

$$\{u\} = [\phi]\{Y_i\} \tag{4.21}$$

in which $[\phi]$ is a matrix of interpolation functions from which the displacements, $\{u\}$, at any point can be found directly from the nodal displacements, $\{u_i\}$. These interpolation functions can be written down directly for quite complex cases provided a coordinate system which is *natural* to the element being considered is used.

As mentioned before the governing equations can be developed using the principle of minimum potential energy. Letting U represent the strain energy of a structure subjected to the surface tractions v_i and body forces f_i, the potential energy V may be written

$$V = U - \int_{S_\sigma} u_i \bar{T}_i dS - \int_V u_i f_i dV \tag{4.22}$$

where

$$U = \int_V W dV \tag{4.23}$$

in which W is the strain energy density. For an elastic material

$$W = \frac{1}{2}\ \sigma_i e_i \tag{4.24}$$

with σ_i is given in matrix form by (12). Using matrix notation, (22) may be written

$$V = \frac{1}{2} \int_V (\{e\}^T - \{e_T\}^T)[D](\{e\} - \{e_T\})\ dV$$

$$- \int_{S_\sigma} \{u\}^T \{T\} ds - \int_V \{u\}^T \{f\}\ dV \tag{4.25}$$

Substituting (11) into (25), and regarding the modal displacements as constants with respect to integration over the element volume

$$V = \frac{1}{2} \left\{ \{u_i\}^T \left[\int_V [B]^T [D][B] dV \right] \{u_i\} \right.$$

$$- 2\{u_i\}^T \int_V [B]^T [D]\{e_T\} dV + \int_V \{e_T\}^T [D]\{e_T\} dV$$

$$\left. - \{u_i\}^T \int_{S_\sigma} [\phi]^T \{\bar{T}\}\ ds - \{u_i\}^T \int_V [\phi]^T \{f\}\ dV \right\} \tag{4.26}$$

Now applying the theorem of minimum potential energy,

$$\delta V = 0 = \delta\{u_i\}^T \left\{ [K]\{u_i\} - \{F\} \right\} \tag{4.27}$$

in which [K] denotes the element stiffness

$$[K] = \int [B]^T [D]\, [B] dV \tag{4.28}$$

and {F} denotes the load vector

$$\{F\} = \int_V [B]^T [D]\{e_T\}\, dV + \int_{S_\sigma} [\phi]^T \{\bar{T}\}\, dS + \int_V [\phi]^T \{f\}\, dV \tag{4.29}$$

The first integral in (29) represents the nodal forces arising from temperature changes or chemical shrinkage; the remaining integrals represent nodal forces arising from surface tractions and body forces respectively. For (27) to hold for arbitrary $\{u_i\}$ it is both necessary and sufficient that

$$\{F\} = [k]\, \{u_i\} \tag{4.30}$$

The analogy between the finite element analysis of continua and the stiffness method of analysis of structures is evident from (30).

In order to consider incompressible and nearly-incompressible material behavior, (12) is rewritten in terms of the mean pressure function H.

$$\{\sigma\} = [\bar{D}]\,(\{e\} - \{e_t\}) + \{Q\}\,H \tag{4.31}$$

where

$$[\bar{D}] = \begin{bmatrix} 2\mu & 0 & 0 & 0 & 0 & 0 \\ 0 & 2\mu & 0 & 0 & 0 & 0 \\ 0 & 0 & 2\mu & 0 & 0 & 0 \\ 0 & 0 & 0 & \mu & 0 & 0 \\ 0 & 0 & 0 & 0 & \mu & 0 \\ 0 & 0 & 0 & 0 & 0 & \mu \end{bmatrix}$$

and

$$\{Q\}^T = 2\mu\nu\{111000\}$$

for an isotropic elastic material. Using (31), Herrmann's variational functional, $I(u_i,H)$, may be written

$$\begin{aligned} I(u_i,H) = {} & \frac{1}{2}\{u_i\}^T\left[\int_V [\delta][\bar{D}][B]\,dV\right]\{u_i\} \\ & - \{u_i\}^T\int_V [B]^T[\bar{D}]\{e_T\}\,dV \\ & + \frac{1}{2}\int_V \{e_T\}^T[\bar{D}]\{e_T\}\,dV + \{u_i\}^T\int_V [B]^T\{Q\}H\,dV \\ & - \int_V \{e_T\}^T\{Q\}H\,dV - \int_V \mu\nu(1-2\nu)\,H^2\,dV \\ & - \{u_i\}^T\int_{S_\sigma} [\phi]^T\{\bar{T}\}\,ds - \{u_i\}^T\int_V [\phi]^T\{f\}\,dV \end{aligned} \tag{4.32}$$

Treating H as a constant over the element and setting the first variation of (32) with respect to the nodal point displacements u_i and the mean pressure function H equal to zero leads to the result

$$I = \delta\{u_i\}^T([\bar{K}]\{u_i\} - \{\bar{f}\} + \{k\}H)$$

$$+ \delta H(\{u_i\}^T\{k\} - f' + k'H) = 0 \qquad (4.33)$$

where

$$[\bar{K}] = \int_V [B]^T[\bar{D}][B]\, dV$$

$$\{f\} = \int_V [B]^T[\bar{D}]\{e_T\}\, dV + \int_{S_\sigma} [\phi]^T\{\overset{\nu}{T}\}\, ds$$

$$+ \int_V [\phi]^T\{f\}\, dV$$

$$\{k\} = \int_V [B]^T\{Q\}\, dV$$

$$f' = \int_V \{e_T\}^T\{Q\}\, dV$$

$$k' = -\int_V 2\mu\nu(1-2\nu)\, dV$$

Equation (33) will hold for arbitrary δu_i and δH only if

$$[\bar{K}]\{u_i\} - \{\bar{f}\} + \{k\}H = 0 \qquad (4.34)$$

and

$$\{u_i\}^T\{k\} - f' + k' H = 0 \qquad (4.35)$$

Equations (34) and (35) represent a system of four equations to be solved for the unknown displacements u_i and the mean pressure function H. The strains are then determined from (11) and (21), and the stresses calculated using (31). In practice, the above stiffness matrix, nodal point displacement and force vectors, derived here for one element, are directly combined for all nodes in the body.

A variational principle is readily developed using the Grüneisen ratio; however, such a principle has not been incorporated as yet into existing finite element computer routines. A difference in behavior is expected for incompressible or nearly incompressible materials using the Grüneisen parameter formulation, since the dilatation vanishes in this approach, as required physically, instead of becoming equal to the volume thermal strain $3\,e_T$.

The application of the equations developed in this section to the element configurations most used throughout the solid propellant industry is discussed in a subsequent section of this chapter.

SOLUTION OF EQUATIONS

The basic equations for the finite element analysis of continua have been summarized in the previous section. The composite stiffness matrix is formed directly by combining the element stiffness matrices requiring continuity of displacements between elements and equilibrium of nodal point forces:

$$[K]\{r\} = \{R\} \tag{4.36}$$

in which $\{r\}$ here denotes the unknown nodal point displacements (and the element mean stresses in Herrmann's reformulation) and $\{R\}$ denotes the nodal point forces. This set of linear algebraic equations must be solved for computation of the element stresses.

The total number of equations is twice the number of nodal points for plane and axisymmetric problems, and three times the number of nodal points for a general three-dimensional structure; plus the number of elements when considering an incompressible body with a constant value of the mean pressure function H for each element. For most problems which require the use of a large number of elements, direct matrix inversion is not practical. Since some of the diagonal terms are zero for incompressible materials, the system is also unsuitable for the usual Gauss-Seidel iteration scheme.

Various solution schemes which take advantage of special characteristics of the stiffness coefficient matrix have been successfully used in finite element computer codes. For example, the banded character of the coefficient matrix has been exploited by the

application of modified elimination techniques, and likewise, the sparseness of the coefficient matrix.

The choice of the solution method is arbitrary to some extent, however, the choice of the solution scheme must be made during development of the computer program since different solution techniques require that the large amount of information that represents the system of equations be organized and stored in different forms. The arrangement of nodal points, and hence elements, in a regular way through the body is of great assistance in the efficient utilization of any solution scheme and also reduces the amount of information which must be input stored and processed by the computer.

Several solution techniques have been used throughout the solid rocket industry. The more popular methods have included straightforward Gaussian elimination, tridiagonalization partition, and Grout (or Cholesky) reduction.

Once the stiffness matrix has been computed for all elements and added to the total stiffness matrix, the stiffness is complete Consequently, the equations can be modified for all of the nodal displacements which are known (at least one axial displacement must be specified for axisymmetric problems and three displacements, not collinear, for plane problems so that rigid body motion of the entire structure is prevented). Proper ordering then produces a banded stiffness matrix.

The solution of the modified banded matrix is efficiently accomplished for many problems using the Gauss elimination method without pivots or equilibration of the matrix. If the standard

displacement method is used in the formulation, the resulting stiffness matrix after modification for boundary conditions is symmetric and positive definite. For this situation it is not necessary to use pivots or scale the matrix prior to beginning the elimination procedure. For an incompressible problem the resulting stiffness matrix is symmetric but not positive definite. With proper ordering of the equations numerical difficulties usually do not result when using the Gaussian elimination procedure without pivots. The elimination or reduction procedure leads to an upper triangular matrix from which the solution is affected by back substitution.

When the stiffness matrix is not so well-conditioned (e.g., a long cantilever beam subjected to transverse loading in which most of the displacement of each node produces only rigid body element translation while a small fraction produces deformation), round-off errors can be reduced by pivoting. Pivoting involves interchanging rows and columns so that the largest numbers are on the diagonal. If only row interchanges are made, the method is known as partial pivoting.

Gauss elimination is performed on the stiffness matrix by blocks. In this process only the stiffness matrix of part of the structure is required at each stage of computation. In the tridiagonalization technique, a banded matrix is reduced to tridiagonal form by Gauss elimination and the solution obtained by back substitution. The application of the tridiagonalization method to structural systems involves operating upon each nodal point consecutively beginning with the first nodal point. Handling the nodal points serially allows the operations to be performed over a specified narrow band with a width

much less than the rank of [K]. This results in an upper triangular banded system of equations which may be solved by back substitution.

The Cholesky or Grout reduction is still another variant of the Gauss elimination method. The symmetrical stiffness matrix is decomposed into the product of a lower and upper triangular matrix. A feature of this method is that it yields smaller round-off errors and economization of storage space. Slightly more computation time is required with the Cholesky variant, however, due to the square root evaluations required.

The direct methods discussed above have serious limitations which restrict their application to three-dimensional problems. For example, Gaussian elimination for symmetric band matrices is restricted to relatively small band widths (on the order of 400 on a 32,000 word computer). Thus, iterative methods have been explored.

An important feature distinguishing iterative methods from elimination methods is that the former tend to be self-correcting due to their repetitive structure. This feature is often credited with minimizing round-off errors. The magnitude and effectiveness of this self-correction is strongly dependent on the conditioning of the system being solved. For very ill-conditioned problems a meaningful solution by direct or iterative techniques may be unattainable.

Iterative schemes involve the application of a simple algorithm that consists mainly of the accumulation of inner products and the subsequent multiplication by the inverse of a single number or of a small matrix. Round-off error may be introduced, however, during the

accumulation of inner products and in the subsequent matrix division. Block iterative methods are generally more susceptible to round-off error than are point iterative methods since they involve the direct solution (by elimination or by matrix inversion) of lower-order systems. Block iterative methods, for positive definite symmetric matrices, on the other hand, converge much faster than point methods. The convergence of Gauss-Seidel and over-relaxation (accelerated Gauss-Seidel) methods can be hopelessly slow for large systems of equations. In general it is found that round-off problems are not the decisive factor in choosing between point and block methods.

Present three-dimensional finite element computer programs [33-35] employ the alternating component iterative method developed by Rashid [37,38] This solution scheme belongs in principle to the general class of block iterative methods in the sense that one deals with iteration on subvectors and the direct solution of lower order systems, although it differs in certain basic ideas. The application of the method involves the direct solution of block-tridiagonal systems of order (1/m)th of the total system. In practice the order of these subsystems may exceed 5000, and round-off errors will be present. Rashid [37,38] has discussed convergence of the method and a correction procedure for reducing rounding errors.

4.4 INDUSTRY PRACTICES

The approach commonly employed throughout the rocket industry involves modeling three-dimensional behavior by a series of two-dimensional problems. Shell elements are frequently introduced to model the motor case behavior. Current analyses make use of the programs developed in references 39 through 43 or some variant thereof for the most part.

Several refinements are introduced into the normal analysis procedure as the need requires. Specialized computer codes have been developed for analyzing axisymmetric geometries subjected to nonaxyisymmetric loadings [44-46] and transverse accelerations [47] of solid rocket motors. Three-dimensional analyses may be required for particular problems with complex geometries; however, these analyses are used infrequently due to the relatively high costs involved. Transient heat conduction analyses [48,49] may be conducted to determine temperature distributions in a solid rocket motor during thermal cooling or aerodynamic heating. Temperature dependent material properties may then be input and analyses conducted at various time intervals to obtain an indication of propellant viscoelastic response. More direct viscoelastic [50-53] and thermoviscoelastic [29,54-59] analyses are performed using programs with internal time marching schemes assuming linear, thermorheologically simple propellant behavior. Additional programs have been developed to handle dynamic analyses [29,55,56,60,61], and some progress is being made in the development of computer codes to model observed kinematic [62,63] and material nonlinearities [64-66].

The above refinements are normally introduced, in the final design and analysis progess to supplement results obtained from two dimensional analyses only when the grain geometry is quite complicated and there is insufficient experience on which to base design decisions. In this situation it is necessary to also supplement more refined analyses with experimental confirmation using full size motors or STV's inasmuch as many of the recently developed computer codes are still open to some questions regarding the range of applicability and accuracy.

4.5 FUTURE DEVELOPMENTS

Although the rocket industry has the capability for performing rather sophisticated stress analyses several inadequacies throughout the industry are reflected in the results of current numerical analyses. Of primary importance is the determination of meaningful descriptions of propellant behavior. There is industry wide recognition that the current descriptions of propellant behavior are inadequate. The development of highly solids loaded propellants in the past few years for the more sophisticated high performance, high mass fraction solid rocket motors has resulted in significant errors between observed response and the response predicted by common analysis methods due to the marked nonlinear behavior of highly solids loaded propellants. This nonlinear behavior is most significant under combined mechanical and thermal loads. It has been observed that for the two loading conditions of primary importance, pressurization and thermal cooling, deflections and strains throughout a propellant grain are usually weakly influenced

by the response characteristics of propellant so that seemingly crude viscoelastic approximations are usually adequate for predictions of strains and displacements, whereas, the marked nonlinear viscoelastic behavior of most modern propellants results in meaningless linear viscoelastic predictions for stresses. This result has, of course, given rise to almost universal adoption of the STV a means of experimental determination of grain structural integrity.

Other refinements being developed involve introduction of newly developed elements into existing finite element computer programs, determination of optimum time steps in routines which handle viscoelastic behavior using a time marching procedure, and consideration of the non-deterministic nature of the statistical variations in material properties and the loading environment history in stress analysis routines. Development of codes more highly user oriented is also deemed necessary to reduce input errors.

4.6 NOMENCLATURE

B = Transfer to Matrix Relating Strains and Displacements

e_v = Specific Heat

D = Material Property Matrix

E = Modulus

e = $\varepsilon_{11} + \varepsilon_{22} + \varepsilon_{33}$

e = Strain

p_T = Thermal Strain

f_i = Body Force

H = Mean Pressure Function

k = Thermal Conductivity

k = Stiffness

T = Temperature

u = Displacement

V = Potential Energy

w = Strain Energy Density

α = Coefficient of Linear Expansion

β = $\frac{3\alpha E}{(1-2\nu)}$

δ_{ij} = Kronecker Delta $\begin{cases} 1 , & i = j \\ 0 , & i \neq j \end{cases}$

ε_{ij} = Strain

λ = Lamé Constant

γ = Grüneisen Ratio

ρ = Density

σ = $\tau_{11} + \tau_{22} + \tau_{33}$

τ_{ij} = Stress

ν = Poisson's Ratio

μ = Lamé Constant

4.7 REFERENCES

1. Parr, C.H.: "The Application of Numerical Methods to the Solution of Structural Integrity Problems of Solid Propellant Rockets", Solid Rocket Structural Integrity Abstracts, Vol. 1, No. 2, October 1964.

2. Parr, C.H.: "The Application of Numerical Methods to the Solution of Structural Integrity Problems of Solid Propellant Rockets II", Solid Rocket Structural Integrity Abstracts, Vol. 4, No. 1, January 1967.

3. Anderson, J.M.: "A Review of the Finite Element Stiffness Method as Applied to Propellant Grain Stress Analysis", Solid Rocket Structural Integrity Abstracts, Vol. 6, No. 4, October 1969.

4. Parr, C.H.: "End Effects Due to Shrinkage in Solid Propellant Grains", Bulletin of the 20th JANAF Panel on Physical Properties of Solid Propellants, Vol. I, November 1961.

5. Parr, C.H.: "Deformations and Stresses in a Case-Bonded Solid Propellant Grain of Finite Length by Numerical Methods", Rohm & Haas Company Quarterly Progress Report on Engineering Research, Report No. P-61-17, June 25, 1962; Redstone Arsenal Research Division, Huntsville, Alabama, (Contract DA-01-021-ORD-5735).

6. Parr, C.H.: "Deformations and Stresses in Axially Accelerated Case-Bonded Solid Propellant Grains of Finite Length", Rohm & Haas Company Quarterly Progress Report on Engineering Research, Report No. P-62-27, April 19, 1963; Redstone Arsenal Research Division, Huntsville, Alabama, (Contract DA-01-021-ORD-11878).

7. Messner, A.M.: "Propellant Grain Stress Analysis", Bulletin of the 17th Meeting of the JANAF-ARPA-NASA Solid Propellant Group, Vol. II, May 1961.

8. Messner, A.M. and Schliessman, D.: "Parameter Calculations of Simple Propellant Grains for Temperature Cycling, Pressurization and Acceleration". Appendix C of Study of Mechanical Properties of Solid Rocket Propellants, Aerojet-General Corporation Report No. 0411-10F, March 1962.

9. Allen D.N. deG.: Relaxation Methods in Engineering and Science, McGraw Hill Book Co. Inc., New York, 1954.

10. Steyer, C.C.: "A Comparison of Finite Difference and Finite Element Methods for Grain Structural Analysis", Bulletin of the 4th Meeting of the ICRPG Working Group on Mechanical Behavior, Vol. I, CPIA Publication No. 94U, October 1965.

11. Turner, J.J., Clough, R.W., Martin, H.C., and Topp, L.J.: "Stiffness and Deflection Analysis of Complex Structures", Journal of Aero. Science, Vol. 23, No. 9, September 1956.

12. Fung, Y.C.: "Foundations of Solid Mechanics," Prentice-Hall, Inc., Englewood Cliffs, N.J., 1965.

13. Herrmann, L.R. and Toms, R.M.: "A Reformulation of the Elastic Field Equations, in Terms of Displacements, Valid for all Admissible Values of Poisson's Ratio", J. Appl. Mech., Vol. 31, pp. 148-149, 1964.

14. Herrmann, L.R.: "Elasticity Equations for Incompressible and Nearly Incompressible Materials by a Variational Theorem", AIAA Journal, 3, No. 10, 1965.

15. Anderson, J.M.: "A Finite-Difference Method Based on Energy Principles for Stress Analysis of Elastic Solids", AIAA Paper No. 65-175, February 1965.

16. Anderson, J.M. and Christiansen, H.N.: "Behavior of the Finite Element Stiffness Method for Nearly Incompressible Materials", Bulletin of the 6th Meeting of the ICRPE Working Group on Mechanical Behavior, Vol. I, CPIA Publication No. 158, October 1967.

17. Hufferd, W.L. and Fitzgerald, J.E.: "A Reformulation of the Thermoelasticity and Elasticity Field Equations for Incompressible Materials", to be submitted for publication.

18. Taylor, R.L., Pister, K.S. and Herrmann, L.R.: "On a Variational Theorem for Incompressible and Nearly-Incompressible Orthotropic Elasticity", Int. J. Solids Structures, Vol. 4, pp. 875-883, 1968.

19. Key, S. W.: "A Variational Principle for Incompressible and Nearly Incompressible Anisotropic Elasticity", Int. J. Solids Structures, Vol. 5, pp. 951-964, 1969.

20. Yeh, G.C.K.: "A Comparison of Various Elasticity Formulations Valid for all Admissible Values of Poisson's Ratio", Astronautica Acta, Vol. 19, pp. 317-326, 1969.

21. Boley, B.A. and Wiener, J.H.: "Theory of Thermal Stresses," John Wiley & Sons, Inc., N.Y., 1960.

22. Hughes, T.J.R. and Allik, H.: "Finite Elements for Compressible and Incompressible Continua", Application of Finite Element Methods in Civil Engineering, ASCE, 1969.

23. Kittel, C.: "Introduction to Solid State Physics", John Wiley & Sons, Inc., N.Y., 1966.

24. Rice, M.H., McQueen, R.G. and Walsh, J.N.: "Compression of Solids by Strong Shock Waves", in Solid State Physics, Vol. 6, Academic Press, Inc., N.Y., 1958.

25. Surland, C.C.: "Compressibility of Elastomers with Crystalline Fillers and Microvoid Inhomogeneities Related to Various Empirical Equations of State for Liquids and Solids", J. Appl. Polymer Sci., Vol. 11, pp. 1227-1229, 1967.

26. Surland, C.C.: "Compressibility and Other Thermodynamic Properties of Polymers", J. Appl. Polymer Sci., Vol. 12, pp. 1423-1437, 1968.

27. Freudenthal, A.M.: "Thermal Stress Analysis and Grueneisen's Relation", J. Appl. Physics, Vol. 31, p. 434, Februaty 1960.

28. Freudenthal, A.M.: "Thermoelastic Equations and Grueneisen's Relation", J. Appl. Physics, Vol. 32, p. 801, 1961.

29. Leeming, H., et.al.: "Solid Propellant Structural Test Vehicle, Cumulative Damage and Systems Analysis", Final Report AFRPL-TR-68-130, Lockheed Propulsion Co., October 1968.

30. Zienkiewicz, O.C.: "The Finite Element Method in Structural and Continuum Mechanics", McGraw-Hill Book Co., N.Y., 1967.

31. Avantes E. Oliveira, E.K. de: "Theoretical Foundations of the Finite Element Method", Int. J. Solids Structures, Vol. 4, pp. 929-952, 1968.

32. Irons, B.M., Zienkiewicz, O.C. and Avantes, E. Oliveira, E.K. de: "Comments on the Paper: Theoretical Foundations of the Finite Element Method", Int. J. Solids Structures, Vol. 6, pp. 695-697, 1970.

33. Cook, W.A.: "Three-Dimensional Stress Analysis of Solid Propellant Motors Using the Finite Element Method", Thiokol Chemical Corporation, Wasatch Division, TWR-3387, Brigham City, Utah, May 1969.

34. Rashid, Y.R.: "Three-Dimensional Analysis of Elastic Solids", Gulf General Atomic, Report GA-7011, LaJolla, California, February 1968.

35. Cornell, D.D., Jadhau, K.B., and Rashid, Y.R.: "A Computer Program for the Three-Dimensional Stress Analysis of Composite Structures", Report GA-7855, General ATOMIC Division of General Dynamics, LaJolla, California, February 1968.

36. Becker, E.B., Brisbane, J.J. and Schkade, A.F., Jr.: "Investigation of Techniques of Three-Dimensional Finite Element Stress Analysis", Tech. Report S-250. Rohm & Haas Company, Redstone Research Laboratories, March 1970.

37. Rashid, Y.R.: "Three-Dimensional Analysis of Elastic Solids-I: Analysis Procedure", Int. J. Solids Structures, Vol. 5, pp. 1311-1331, 1969.

38. Rashid, Y.R.: "Three-Dimensional Analysis of Elastic Solids-II: The Computational Problem", Int. J. Solids Structures, Vol. 6, pp. 195-207, 1970.

39. Becker, E.G., and Brisbane, J.J.: "Application of the Finite Element Method to Stress Analysis of Solid Propellant Rocket Grains", Rohm & Haas Co. Report S-76, November 1965.

40. Pister, K. S., Taylor, R.L. and Dill, E.H.: "A Computer Program for Axially Symmetric Elasticity Problems", Mathematical Sciences Corporation Report No. 65-21-3, December 1965.

41. Cook, W.A.: "A Finite Element Formulation for Axisymmetric Bodies Having Incompressible and Near Incompressible Materials", Thiokol Chemical Corporation, Wasatch Division, Report TWR-1749, March 1966.

42. Black, B.L., Webb, L.D. and Daly, J.M.: "Solid Propellant Grain Structural Analysis Using the Direct Stiffness Method", AIAA 6th Solid Propellant Rocket Conference, Washington, D.C., No. 65-176, Feb. 1965.

43. Wilson, E.L.: "Structural Analysis of Axisymmetric Solids", AIAA Journal, Vol. 3, pp. 2269-2274, 1965.

44. Brisbane, J.J. and Becker, E.B.: "Finite Element Analysis of Axisymmetric Bodies Under Non-Axisymmetric Loads" Bulletin of the 6th ICRPG Meeting of the Working Group on Mechanical Behavior, CPIA Publication 158, Vol. 8, October 1967.

45. Dunham, R.S. and Taylor, R.L.: "Analysis by a Finite Element Method of Orthotropic Axisymmetric Solids Subjected to Arbitrary Loads", Bulletin of the 6th Meeting of the ICRPG 158, Vol. 8, October 1967.

46. Dunham, R.S. and Nickell, R.E.: "Finite Element Analysis of Axisymmetric Solids with Arbitrary Loading", Report 67-6, Univ. of California, Berkeley, June 1967.

47. Brisbane, J.J. and Becker, E.B.: "Stress Analysis of Solid Propellant Grains Under Transverse Acceleration Loads", Report No. S-116, Rohm & Haas Company, Redstone Research Laboratories, March 1967.

48. Wilson, E.L. and Nickell, R.E.: "Application of the Finite Element Method to Heat Conduction Analysis", Nuclear Engineering and Design, Vol. 4, pp. 276-286, October 1966.

49. Becker, E.B. and Parr, C.H.: "Application of the Finite Element Method to Heat Conduction in Solids", Report S-117, Rohm & Haas Company, Redstone Research Laboratories, November 1968.

50. Chang, T.Y.: "Approximate Solutions in Linear Viscoelasticity", Structural Engineering Laboratory Report No. 66-8, University of California, Berkeley, July 1966.

51. Herrmann, L.R. and Peterson, F.E.: "A Numerical Procedure for Viscoelastic Stress Analysis", Bulletin of the 7th Meeting of the ICRPG Working Group on Mechanical Behavior CPIA Publication No. 177, October 1968.

52. Webber, J.P.H.: "Stress Analysis in Viscoelastic Bodies Using Finite Elements and A Correspondence Rule with Elasticity", J. Strain Analysis, Vol. 4, pp 236-243, 1969.

53. Bills, K.W., Campbell, D.M. and Steele, R.D.: "Failure in Grains Exposed to Rapid Changes of Environmental Temperatures" Aerojet-General Corp. Report 1236-81F, September 1969.

54. Taylor, R.L. and Chang, T.Y.: "An Approximate Method for Thermoviscoelastic Stress Analysis", Nuclear Engineering and Design, Vol. 4, pp. 21-28, 1966.

55. Nickell, R.E.: "Stress-Wave Analysis in Layered Thermoviscoelastic Materials by the Extended Ritz Method", Report S-175, Rohm & Haas Company, Redstone Research Laboratories, October 1968.

56. Dunham, R.S.: "Dynamic Stress Analysis of One-Dimensional Thermorheologically Simple Viscoelastic Solids with Nonlinear Heat Conduction Analysis", Report No. RK-JR-70-13, U.S. Army Miss. 6 Command, Redstone Research Laboratories, July 1970.

57. Cost, T.L.: "Thermomechanical Coupling Phenomena in Non-Isothermal Viscoelastic Solids", Report S-226, Rohm & Haas Company, Redstone Research Laboratories, August 1969.

58. Taylor, R.L., Pister, K.S. and Goudreau, J.L.: "Thermomechanical Analysis of Viscoelastic Solids", Int. J. Num. Methods. Eng., Vol. 2, pp. 45-59, 1970.

59. Leeming H., et al.: "Solid Propellant Structural Test Vehicle and Systems Analysis", Final Technical Report AFRPL-TR-70-10, Lockheed Propulsion Company, March 1970.

60. Anderson, J.M.: "Adaptation of the Finite-Element Stiffness Method to Viscoelastic Steady-State Sinusoidal Vibration Solutions", Bulletin of the 5th Meeting of the ICRPG Working Group Mechanical Behavior, CPIA Publication No. 119, Vol. 1, October 1965.

61. Baker, W.E. and Daly, J.M.: "Dynamic Analysis of Solid Propellant Grains Using the Finite Element Method (Direct Stiffness Method)", Bulletin of the 5th Meeting of the ICRPG Working Group on Mechanical Behavior, CPIA Publication No. 119, Vol. 8, October 1966.

62. Herrmann, L.R.: "A Nonlinear Two-Dimensional Stress Analysis Applicable to Solid Propellant Rocket Grains", Bulletin of the 4th Meeting of the ICRPG Working Group on Mechanical Behavior, CPIA Publication No. 94U, Vol. I, October 1965.

63. Peterson, F.E., Campbell, D.M. and Herrmann, L.R.: "Nonlinear Plane Stress Analysis Applicable to Solid Propellant Grains" Bulletin of the 5th ICRPG Meeting of the Working Group on Mechanical Behavior, CPIA Publication No. 119, Vol. I, October 1966.

64. Wilson, E.L.: "A Digital Computer Program for the Finite Element Analysis of Solids with Nonlinear Material Properties", Aerojet-General Corporation Report TM-23, July 1965.

65. Bills, K.W., et al.: "Applications of Cumulative Damage in the Preparation of Parametric Grain Design Curves and the Prediction of Grain Failures on Pressurization", Aerojet-General Corporation Final Report 1341-25F, August 1970.

66. Dong, R.G., Pister, K.S. and Dunham, R.S.: "Mechanical Characterization of Nonlinear Viscoelastic Solids for Iterative Solution of Boundary Valve Problems", Metal Mechanics, Vol. 9, pp. 36-48, 1970.

V. SPECIAL DESIGN CONSIDERATIONS

5.1 INTRODUCTION

Several areas of grain structural integrity analyses require special consideration. Particular theoretical and experimental investigations have been carried out for

- TRANSITION REGIONS
- GRAIN TERMINATIONS

The results of some of these studies are summarized in this chapter. In some cases the results are quite qualitative and, at best, are only suited for preliminary design analysis efforts when coupled with competent engineering judgment. Considerable detail is presented to illustrate design and analysis procedures.

5.2 TRANSITION REGIONS

A propellant grain with a transition from a star perforated to circular port geometry is often used to obtain a particular ballistic trait desired. Certain combinations of cylindrical port grains, which burn progressively, and star grains, normally regressive, give rise to neutral burning. Such grain geometries are frequently employed in sounding rockets and rocket motors for sled track use. Other combinations result in geometries used in tactical applications requiring pulse or boost and sustain phases.

The transition from a star to circular port geometry is a complex three dimensional boundary value problem for which few, if any, results are available from three dimensional analyses. In the absence of theoretical or experimental analyses, some indication of the expected response can be obtained under simplifying assumptions to gain insight into the design problem [1].

Hoekel and Schapery[1] have used Sampson's rigidity coefficient[2] to obtain an approximate design tool. Alternatively, one can use Parmeter and Fourney's relations given in Chapter 3; however, the resulting expressions are more complicated. Assuming

$$\lambda^3 >> \lambda^2 - \lambda + 1$$

and requiring the product

$$\frac{1}{a\sqrt{\rho}}$$

to be a constant, Hoekel and Schapery suggested using the approximate relation

$$\rho = \left(\frac{r}{a}\right)^2 \tag{5.1}$$

as an approximate design tool for the transition region. As the radius to the star point, a, becomes smaller, the fillet radius ρ increases as the square of the reciprocal of a. Thus, the slot width must widen through the transition region as indicated in Fig. 1. This result requires that the mandrel for this region must be equipped with some collapsible feature. For many applications with only limited temperature extremes, such as sounding rockets or sled rocket motors, experience indicates acceptable transition regions can be designed, however, without recourse to collapsible mandrels. In such instances, the curvature through the transition zone is maintained at as near a full radius as ballistically allowed, and the fillet radius of the star valley is kept constant or slightly decreasing to facilitate easier mandrel removal.

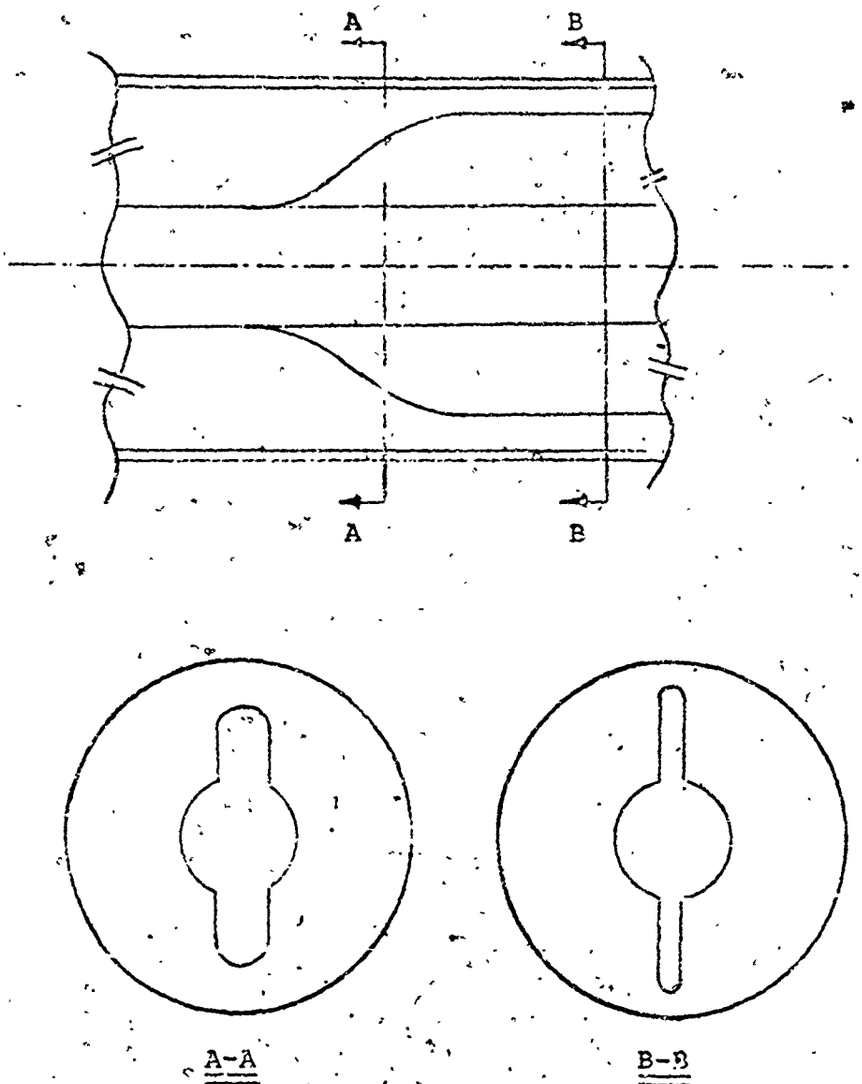

$$(a^2\rho)_A = (a^2\rho)_B$$

FIGURE 1. TRANSITION BETWEEN A STAR AND CYLINDRICAL PORT GEOMETRY [1]

The above design guidelines are only qualitative and under normal circumstances will lead to reasonable design configurations for preliminary design purposes. For motors subjected to extreme temperature and/or pressure environments, and at all times during a final design analysis phase, such practices are not recommended. In these situations acceptable solutions to the problem at hand can only be obtained through three dimensional computer analyses or three dimensional photoelasticity investigations followed by verification testing of structural test vehicles.

5.3 GRAIN TERMINATIONS

The problem of the design of the configuration of the case-grain end termination of a case-bonded solid propellant rocket motor in order to minimize stress concentrations at the propellant-case interface has received considerable attention in recent years.

It is well known that very high local stresses occur at the case-grain junction and in a number of instances have been responsible for motor failures. These high stresses arise because of the order-of-magnitude difference between the coefficients of expansion of the case and grain which acts as a loading or forcing function during low temperature cycling and because of geometric discontinuities which may exist in the grain design. When the included angle of the case-grain termination is less than 135°, as illustrated in Fig. 2, the elastic solution has a mathematical singularity and the stresses become infinite.

The problem of grain unbonding is of most concern for large diameter solid rocket motors under 1-g axial storage (slump) conditions, certain

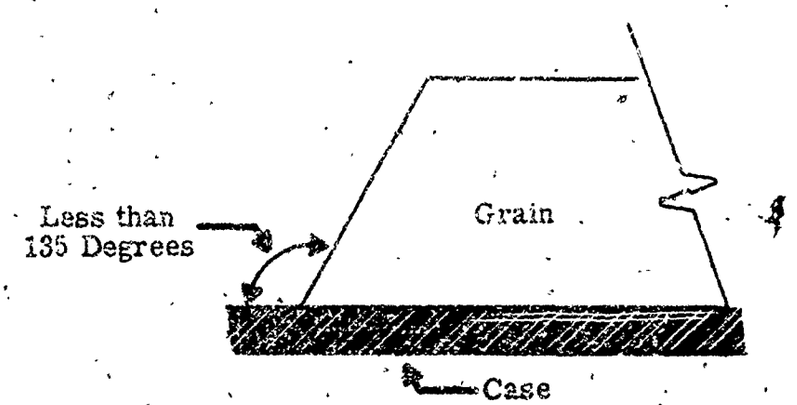

FIGURE 2. UNDESIRABLE CASE-GRAIN TERMINATION JUNCTION

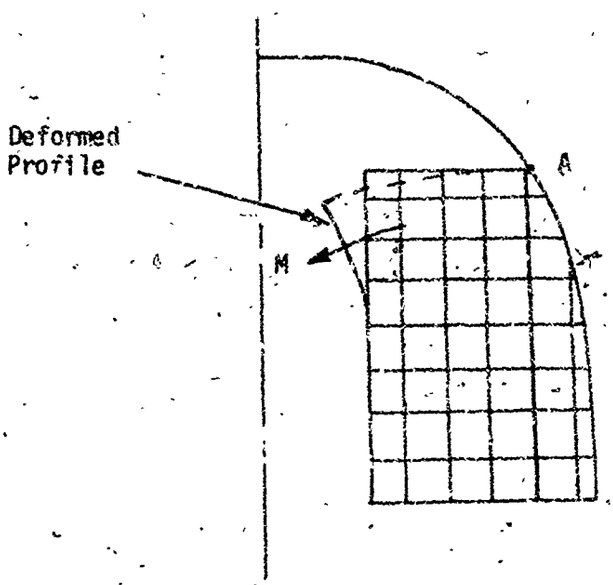

FIGURE 3. SLUMP DEFORMATIONS[4]

high acceleration motors and thermal cycling of moderate to high web fraction motors (WF>50%) with length to radius ratio greater than about 3. The action of gravity during storage or acceleration causes the propellant near the forward end to slump downward as well as inward (Fig. 3). Excessive inward displacement changes the contour of the inner bore which may adversely affect ballistic performance. Opening of a crack between the motor case and grain may allow burning there, leading to failure of the case, and the inertia loads during firing may cause the initial crack to propagate, also leading to case failure or nozzle ejection. Low temperature cycling produces similar effects.

The mathematically infinite stresses occurring at case-grain termination points may be relieved by introducing elastomeric relief "flaps" or "boots", or by contouring the grain-end configuration. Design guidelines for these two methods of minimizing bond stresses at case-grain terminations are discussed in the following paragraphs. The discussions are presented in some detail in the hope that such information will aid the designer in making appropriate design decisions.

5.3.1 RELIEF FLAPS

Relief flaps (Figs. 4 and 5) allow the propellant to deform as it would otherwise while allowing the designer to control the length of the crack unbond. Relief flaps are composed of materials which have higher strength and elongation than the propellant throughout the total use environment of the motor; and insulation characteristics compatible with ballistic requirements. Silica or silica-asbestos filled buna-n rubbers typically fulfill these requirements. Occasionally, particularly in the case of large solid rocket motors, the head-end flap is backfilled with rubber insulation, as indicated in Fig. 5 , as added insurance against possible burning within the flap.

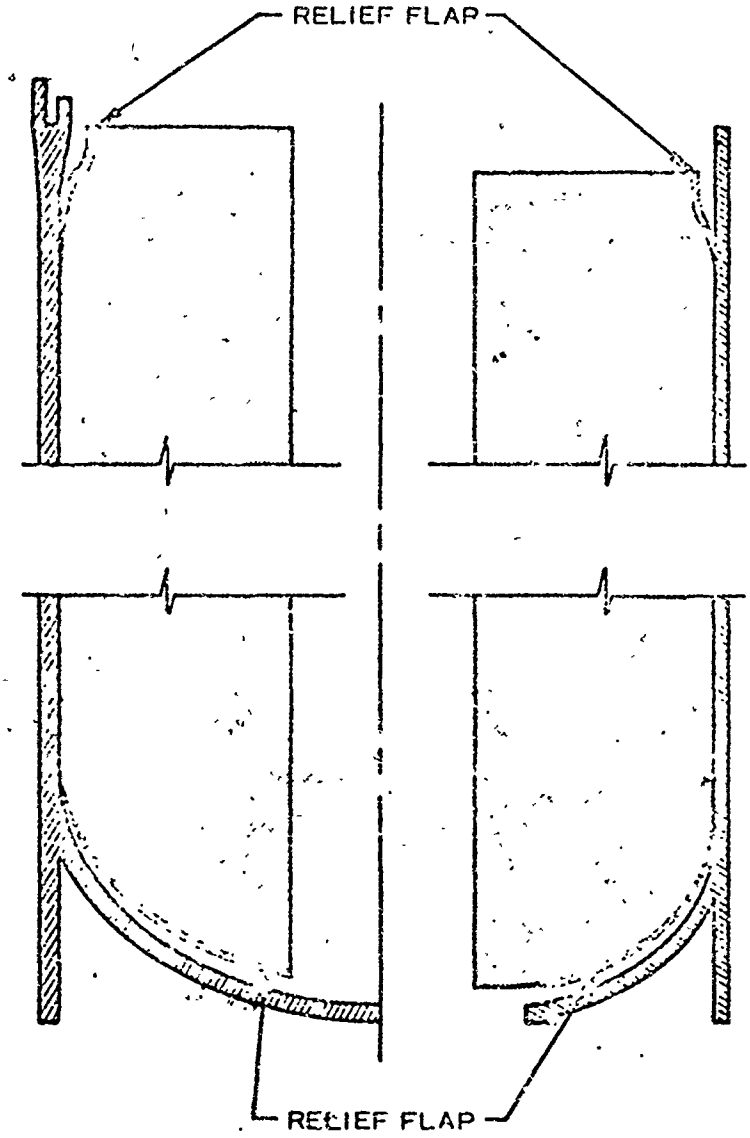

FIGURE 4. TYPICAL CASE-GRAIN TERMINATION STRESS RELIEFS[3]

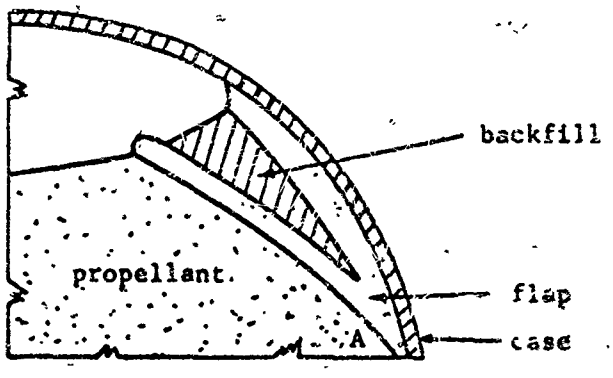

FIGURE 5. CURRENT DESIGN PROCEDURE FOR LARGE DIAMETER SOLID MOTORS[4]

Basically, a relief flap removes the mathematical singularity and resultant high local stresses from a region of low stress capability (the propellant or propellant-liner case interface) to a region of higher compliance and strength characteristics (the rubber flap). Caution must be exercised in designing the relief flap to ensure that the rubbery material of the flap, absorbs and dissipates the high local stresses. If too thin a flap or a flap with insufficient filler radius or material is used, high local bond stresses may still occur at the propellant flap interface near the point of highest concentration in the flap, leading to unbond cracking away from the end of the grain.

SIMPLE PRELIMINARY DESIGN PROCEDURE

A simple procedure for the design of stress relief flaps which has proven adequate for large solid motors and preliminary design purposes in other situations has been presented by Lockheed Propulsion Company[3] based on observed grain end unbonding in motors without release flaps ranging in size from 4 to 120 inches in diameter.

Observed grain end unbonding during thermal cooling of motors without relief flaps has suggested that the depth of the unbond is proportional to the motor web fraction, for web fractions in excess of about 50%, motor diameter, and to a lesser extent, motor length-to-diameter ratio. An empirical curve derived from actual failures of motors with web fractions near 50% and L/D ratios between one and three is shown in Fig. 6.

The procedure recommended for using Fig. 6 in designing an end relief flap is to estimate the depth to which an end unbond will propagate, and then to introduce a stress relief flap equal to twice this depth. This technique has been used with a high degree of success at LPC for motors ranging in size from 4 inches to 156 inches.

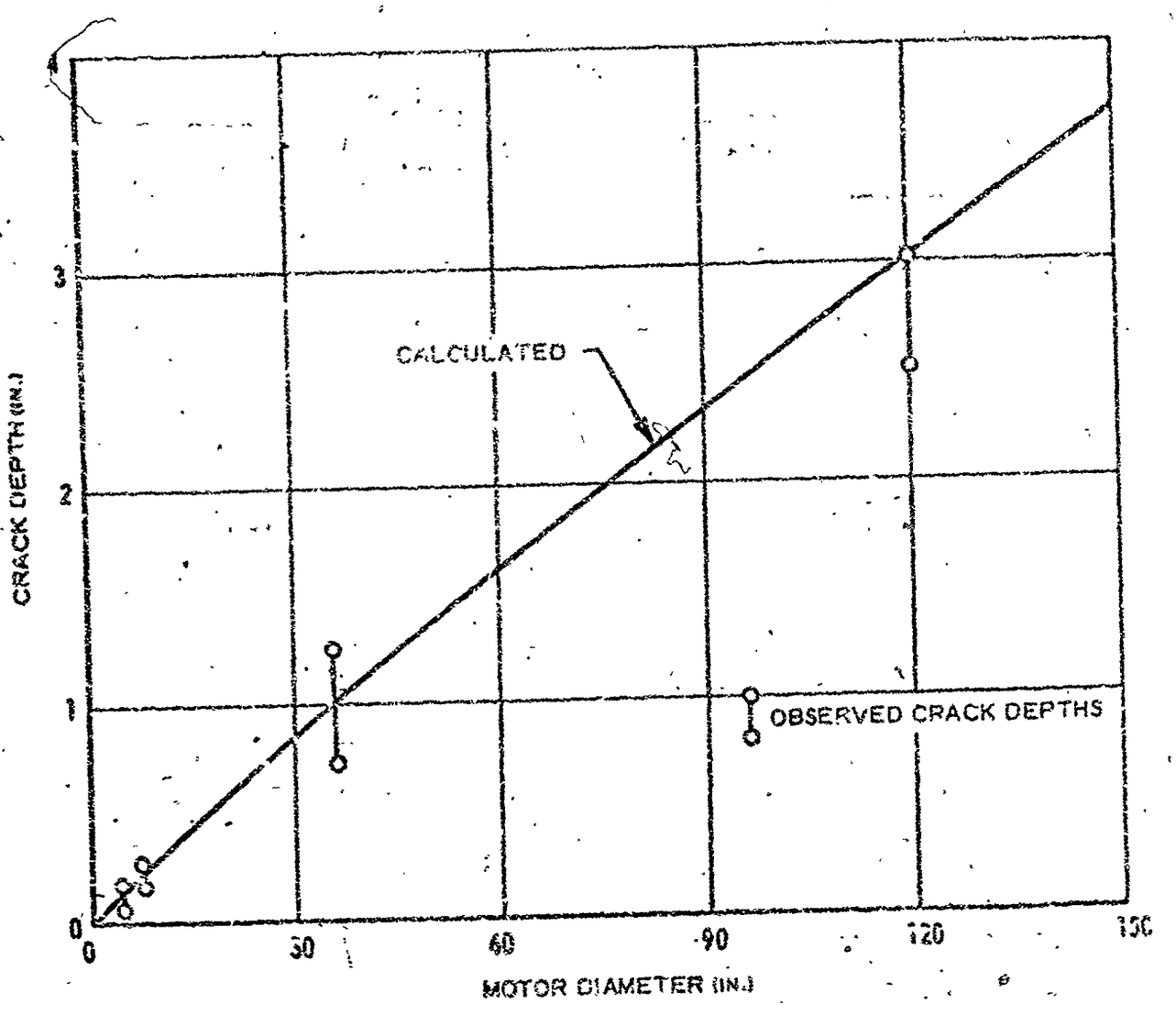

FIGURE 6. GRAIN TERMINATION CRACK DEPTH VERSUS MOTOR DIAMETER[3]

It must be recognized, of course, that the above technique is only a "rule-of-thumb" which experience indicates is adequate for large solid motors and preliminary design purposes. The final design analysis of stress relief flaps for tactical motors and ABM's which experience considerably more severe thermal and acceleration environments requires a more quantitative approach. Numerical and analytical solutions have been obtained by Dill, Doak and Schmidt[4], and Noel and Webb [5-7] have obtained design guidelines using fracture mechanics considerations.

SINGULAR BEHAVIOR OF CASE-GRAIN TERMINATIONS

Dill, et al[4] investigated the nature of the singularity at the case grain termination assuming a circular inner bore and a rigid case. The solution away from the termination was obtained numerically. The axially symmetric stress distribution near the point A in Fig. 7 was determined analytically introducing local polar coordinates as shown in Fig. 7. If the case is regarded as rigid then the stress distribution near the point A (i.e., for small ρ) is the same as that for plane strain since the circumferential displacement and strain are zero at point A. For a state of plane strain, the solution near the corner yields stresses and displacements that have the form

$$\sigma_r, \sigma_\theta, \tau_{r\theta} \text{ proportional to } r^k$$

$$u, v, \text{ proportional to } r^{k+1}$$

where

$$-1 < k < 0 .$$

That is, the displacements are finite, but the stresses are infinite. The fact that infinite stresses are predicted by infinitesimal linear theory is normally interpreted to mean that a nonlinear theory would give

high stresses at that point. The parameter k, which characterizes the behavior of the singularity, depends upon the boundary conditions along the edges near the corner (Point A), upon Poisson's ratio, and upon the angle between the propellant surface and the case.

The particular solution is interpreted in the following manner. It is supposed that the actual solution to the complete problem could be expressed in a series of terms r^{λ_n}, n = 1, 2, ... The coefficients of the series and the parameters λ_n are chosen so as to satisfy the differential equations and the boundary conditions on the edges. Away from the corner this solution would agree with that determined numerically; sufficiently near the corner, all of the terms in the series solution would be negligible except that term giving rise to infinite stresses. Thus, the solution obtained by Dill et al[4] is presumed to apply sufficiently close to the corner.

If the case is rigid and the propellant surface is not restrained, there will generally be a singularity in the stress as is evident in Figure 6. The angle β is defined in Fig. 7.

The extent of the singularity can only be determined by solving the complete boundary value problem. This was done for the plane stress problem using photoelasticity. It was found that the singularity is of a very localized nature and in all cases the stress concentration was negligible beyond 0.25 inches from the corner.[1]

[1] The dimensions of the Hysol 4485 models used in this investigation were approximately 2" by 4" by 1/4" thick.

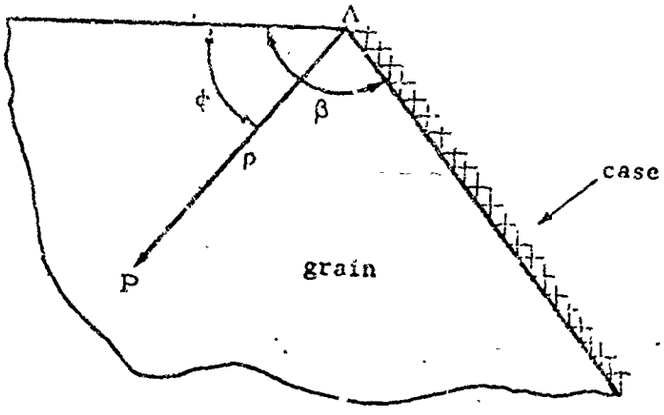

FIGURE 7. LOCAL COORDINATES[4]

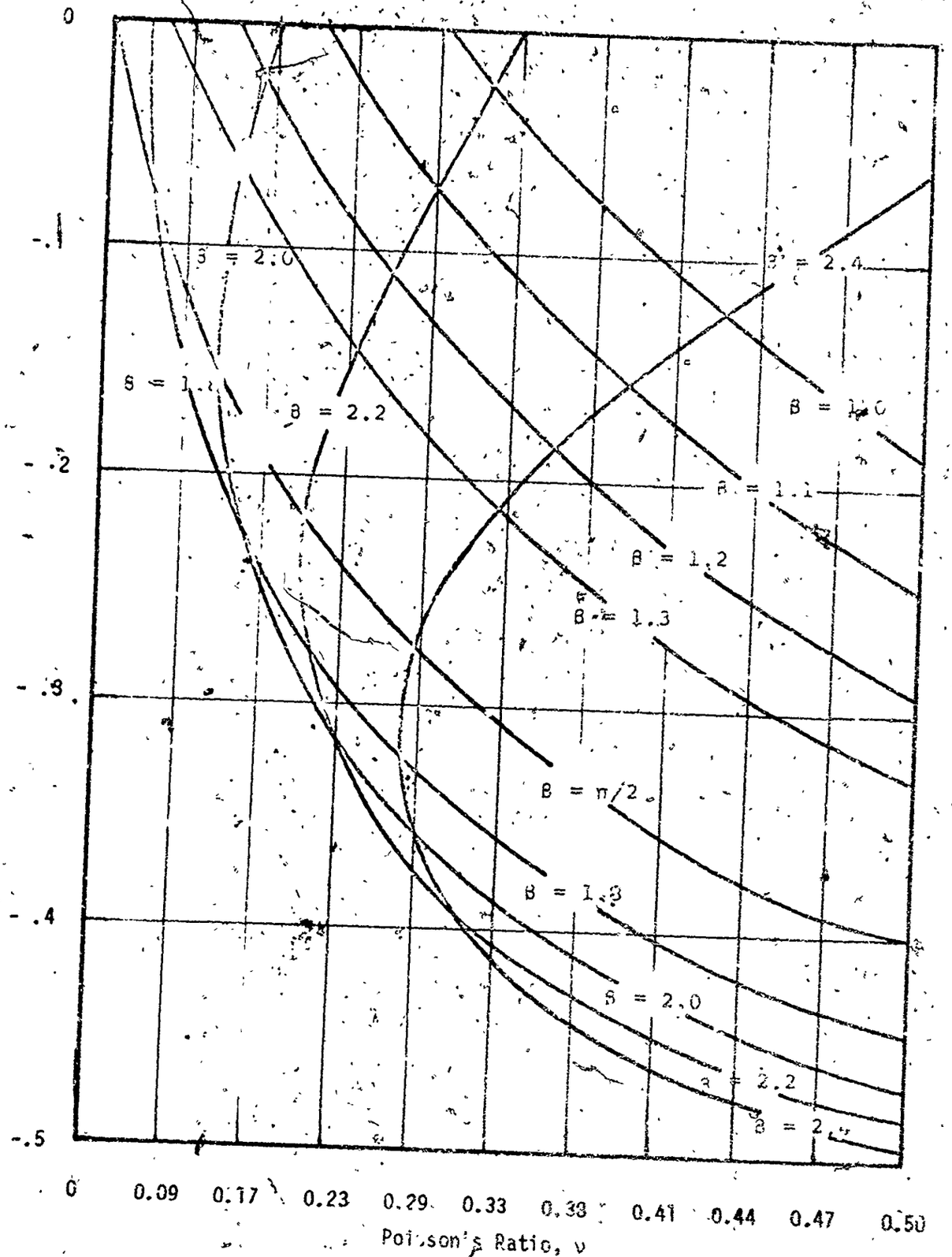

FIGURE 8. REAL ROOTS OF THE CHARACTERISTIC EQUATION FOR A FREE-FIXED WEDGE[4]

It is noted that for each value of Poisson's ratio, ν, there is a particular angle β_0 such that no singularity exists if the juncture angle is less than β_0. For plane strain conditions β_0 is determined from the relation

$$\sin^2\beta_0 = 1 - \nu \tag{5.2}$$

Some of these values are shown below:

Plane Strain	
ν	β_0
0.50	45°
0.40	51°
0.30	57°

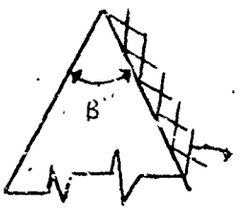

No singularity if $\beta<\beta_0$.

Dill, Nesk and Schmidt[4] also considered the situation corresponding to the use of a membrane bonded to the surface as reinforcing (Fig. 9). The membrane is regarded as allowing no tangential displacement (i.e., inextensible) while offering no resistance to bending. The results are shown in Fig. 10.

There also exist singular solutions for certain angles β and certain values of Poisson's ratio. The critical angle is, however, much larger than for the preceeding problem, and in fact, there is no singularity if $\beta < \pi/2$.

An ideal design achieved by the cylindrical bore cylindrical case with an inextensible membrane bonded to the flat end is shown in Fig. 11. For this design, the stress state under an axial load is pure shear and the displacement is axial. The singularity at point A does not occur, and, moreover, the shear stress is uniform along the case and therefore the smallest possible.

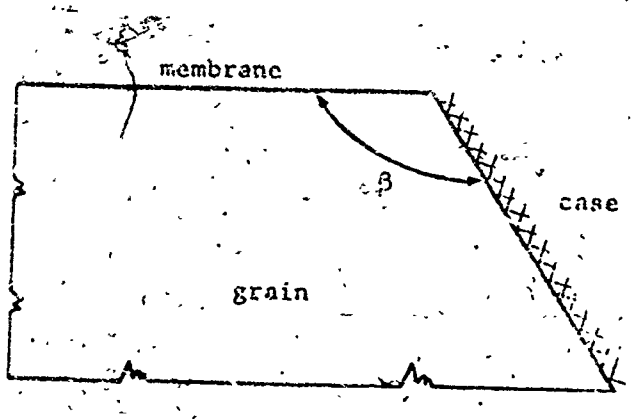

FIGURE 9. END MEMBRANE REINFORCING[4]

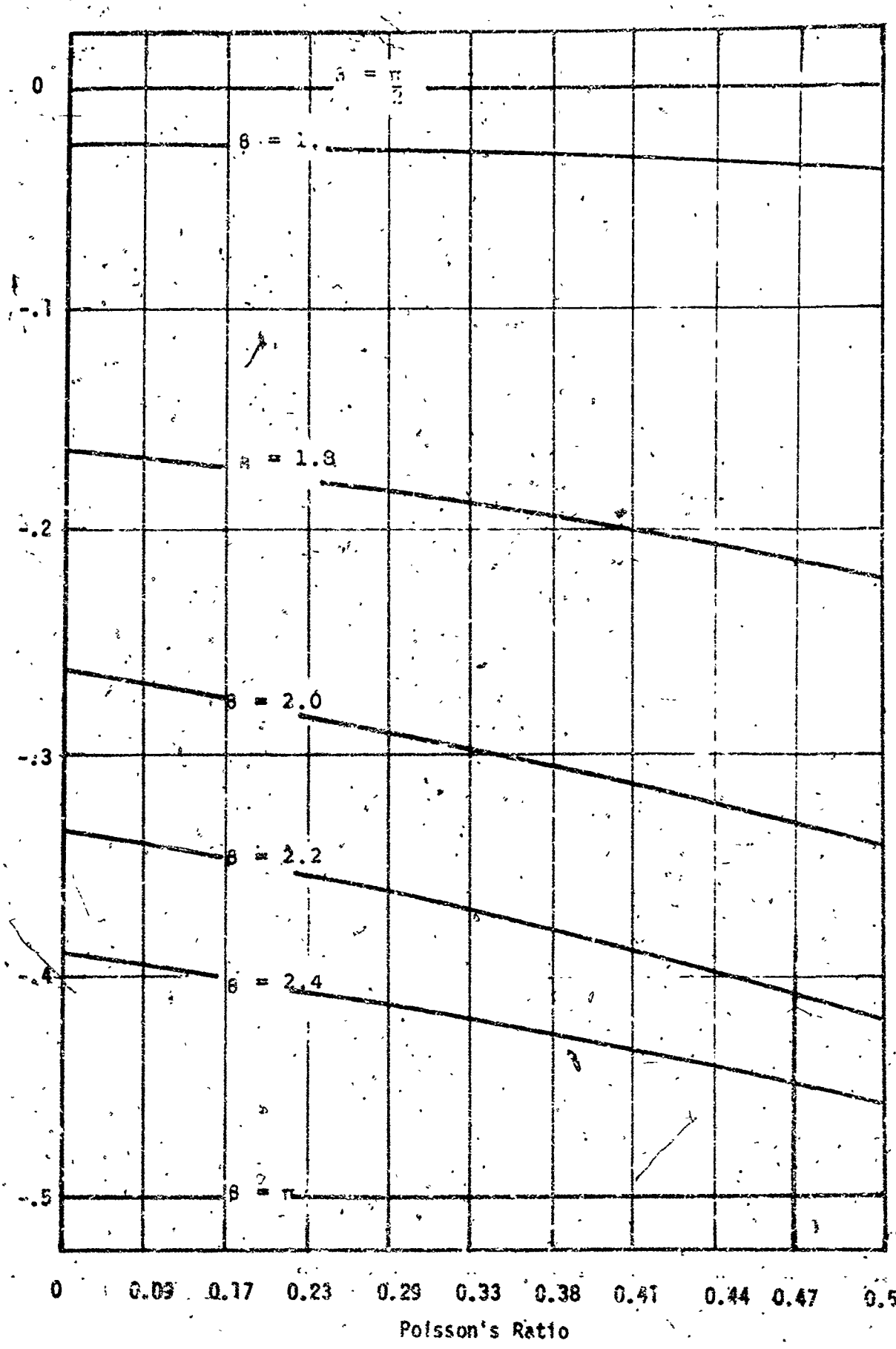

FIGURE 10. REAL ROOTS OF THE CHARACTERISTIC EQUATION FOR A MEMBRANE-FIXED WEDGE[4]

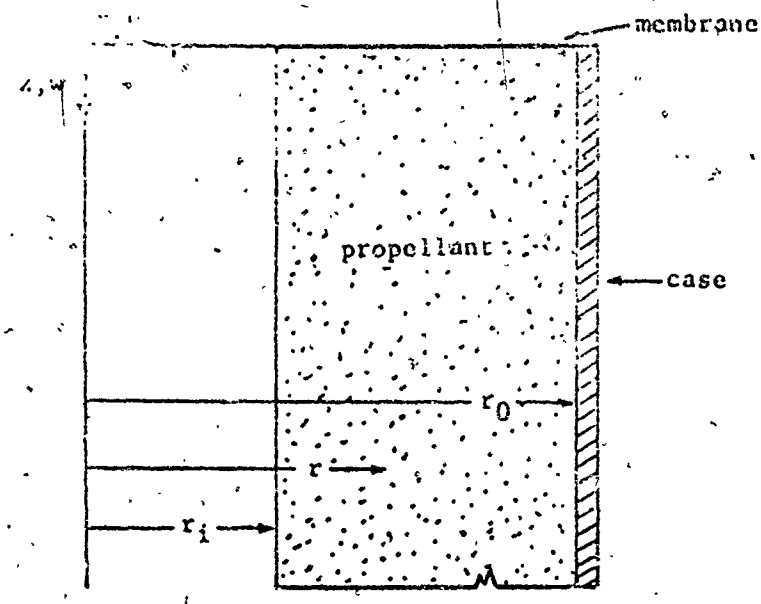

FIGURE 11. IDEAL DESIGN[4]

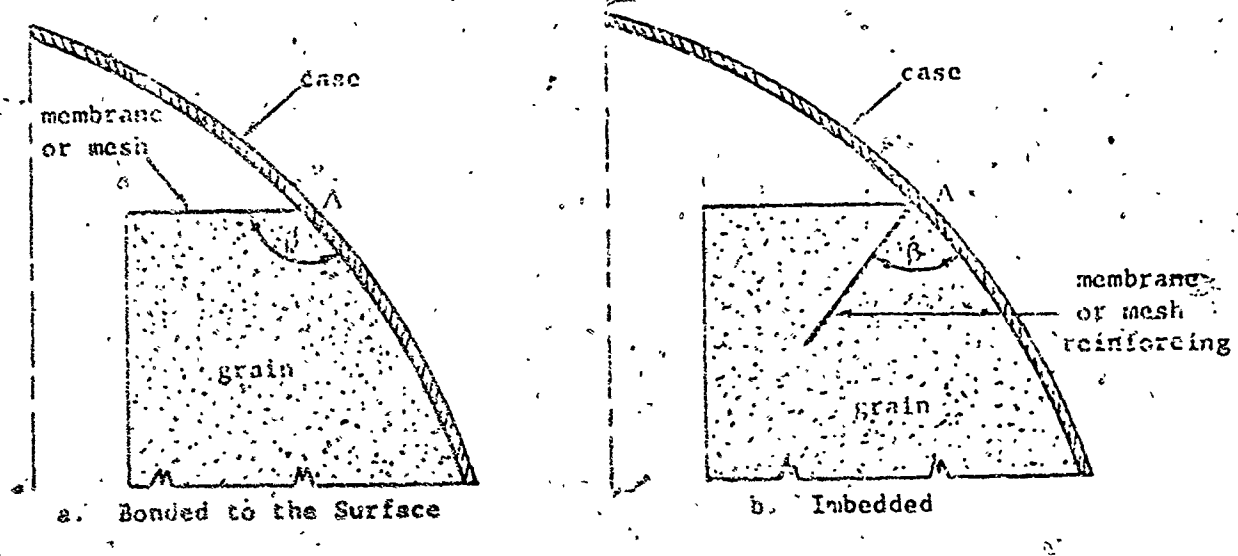

FIGURE 12. POSSIBLE USE OF REINFORCING[4]

Two possible uses of reinforcing for a curved case-grain termination are shown in Fig. 12. A membrane bonded to the end will inhibit inward displacement (Fig. 12-A). There will, however, be a stress singularity at point A because the included angle β is greater than 90°. Thus, unbonding may occur between the membrane and the case at A. This singularity can be avoided by imbedding the reinforcing along a cone which is normal to the case (Fig. 12-B). Although this situation was not analyzed the included angle β is less than 90° and finite stresses are expected at A. In effect, the reinforcing is acting more efficiently by preventing displacement normal to the case and by relieving the normal stress on the boundary. Hence design (B) is considered superior to design (A).

ENERGY BALANCE APPROACH

Fracture mechanics considerations have also been applied to the problem of designing case-grain terminations [4-11]. While the details of the fracture mechanics approach is delayed until the discussion of failure theories in Chapter 7, the basic features of the approach as applied to the problem of grain-case unbonding are presented here.

The fracture mechanics approach is based on the exchange between the energy stored in a strained body and the energy expended in the formation of new surface area. When the rate of change of stored energy is greater than the rate at which energy is used in forming new surface area fracture ensues. This approach has been applied to both adhesive and cohesive failure. These failures are similar from the fracture mechanics point of view; the essential difference being the interpretation of the energy required to create new surface. For the particular problem at

hand the interfacial surface energy, γ_a, describes the amount of energy released by the grain as a crack extends along the case-grain interface. The surface energy γ_a is a material property which is determined from laboratory tests such as the blister peel test described in a later section of this handbook and in references 9 and 10. Although, the adhesive fracture energy, γ_a, as well as the cohesive fracture energy, γ_c, are both time and temperature dependent, considerable insight into the problem can be gained through consideration of the linearly elastic problem discussed herein. Extensions to viscoelastic behavior have been suggested elsewhere [10,11].

For linearly elastic systems, the balance between the change in strain energy and the energy required for fracture provides the relationship for numerically predicting the onset of bond separation:

$$-\frac{\partial U}{\partial A}(c)\Big|_u \geq \gamma_a \qquad (5.3)$$

where

U = Strain energy

A = Fracture surface area

c = The current value of the varying crack dimension.

The subscript u implies that the derivative is to be evaluated with boundary displacements specified. The term on the left will increase until it equals γ_a, at which time fracture occurs.

From Appendix A the strain energy U is given by

$$U = \int_{vol} W \, dvol$$

where

W = strain energy density

$$= \frac{1}{2}[\lambda+2\mu)e^2-4\mu e_2] - (3\lambda+2\mu)\alpha(T-T_0)e$$

and

e = first strain invariant = e_{11}

e_2 = second strain invariant = $\frac{1}{2}\sum_{p_q}^{15} \delta_{p_q} e_{p_i} e_{p_j}$

λ = Lame Constant = $\frac{\nu E}{(1+\nu)(1-2\nu)}$

μ = Lame Constant = $\frac{E}{2(1+\nu)}$

Parametric curves have been generated in references 5 to 11 for several solid rocket motor configurations. These results may be used to obtain comparative information on the susceptibility of interfaces to debond by comparing the rates of energy release. The greater the numerical value of $\partial U/\partial A\big|_u$, the more susceptible the grain is to bond failure.

Finite element stiffness programs were used to evaluate the rate of energy change with isothermal temperature changes[2]. The procedure is to calculate the strain energy density for each element, multiply by the element volume and then sum to find the total energy.

---

[2] Although this discussion is concerned only with temperature changes, a similar approach readily applies to pressure and acceleration loadings.

Considering isothermal temperature changes, Eq. (5.3) may be nondimensionalized by dividing the lengths by the outside grain radius b and the strain energy density by the combination of parameters $E(\alpha\Delta T)^2$, so that the total energy may be expressed as

$$U = E(\alpha\Delta T)^2 b^2 \bar{U} \tag{5.4}$$

where the superior bar indicates a normalized total energy. Similarly, by replacing A by $b^2\bar{A}$, Eq. (5.3) may be rewritten as

$$E(\alpha\Delta T)^2 b \left(\frac{\partial \bar{U}}{\partial \bar{A}}\right)\Big|_u \geq \gamma_a \tag{5.5}$$

This equation relates the critical temperature drop (i.e., incipient cracking) to the surface energy and the released surface area. Comparative results can be obtained by solving (5.5) for T_{cr}:

$$\alpha\Delta T_{cr}\sqrt{\frac{Eb}{\gamma_a}} = \left(-\frac{\partial \bar{U}}{\partial \bar{A}}\Big|_u\right)^{-\frac{1}{2}} \tag{5.6}$$

Here, the term ΔT_{cr} is interpreted as the maximum temperature drop that can be imposed without failure.

As remarked earlier, the modulus E and the fracture energy γ of solid propellants are both time and temperature dependent. However, there is increasing evidence that the time and temperature dependent behavior of E and γ are essentially similar. In this situation it may turn out that although E and γ individually vary substantially with loading rate and temperature, the ratio (E/γ), is essentially constant over much of the temperature range of interest. Thus, (5.6) provides a valid means for estimating quasi-viscoelastic fracture.

Equation (5.6) also indicates that the critical temperature is dependent upon the size of the motor. More specifically, ΔT_{cr} varies as the inverse square root of the grain radius b. Thus, a larger diameter motor can withstand a smaller temperature decrement before the onset of failure than can a smaller motor of similar geometry with the same material properties and energy release rate.

Parametric curves have been generated by Noel [6,11]. The model of the grain used in reference 6 is shown in Fig. 13. The outside radius, modulus of elasticity, coefficient of thermal expansion and the temperature change were all normalized to unity. The base value used for Poisson's ratio was 0.485. Incremental values of the bond separation length (measured as shown in Fig. 13), s, were input defining a region of stress free boundary. Zero displacements were prescribed for the portion of the boundary remaining bonded. The axially symmetric model was given a plane of symmetry at the midpoint of its length. The progressive separation, as programmed, simultaneously enlarged at both ends; first along the radius until s=b and then along the outer surface toward the plane of symmetry.

The computer results provided the ordinates for the plot of strain energy - versus - released areas shown in Fig. 14-A. The individually computed ordinates were then used as pivotal points for numerical computation of the derivatives of the energy with respect to released area shown in Fig. 14-B. An abrupt discontinuity of the slope was always found as s/b = 1.0, reflecting a difference in the rate of change of strain energy between the crack approaching the corner of the cylinder

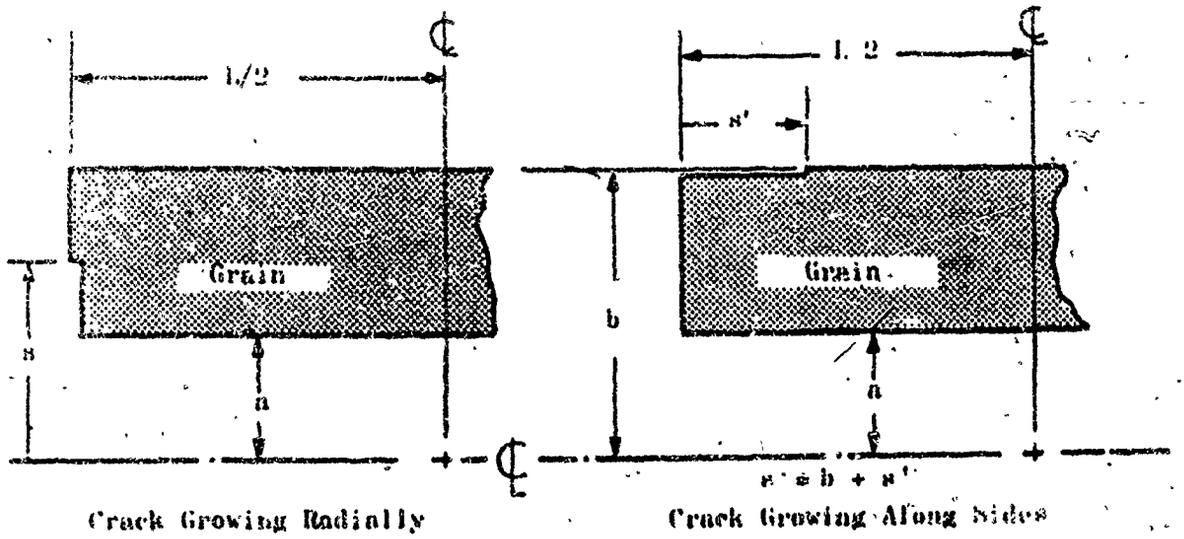

FIGURE 13. BOND SEPARATION[7]

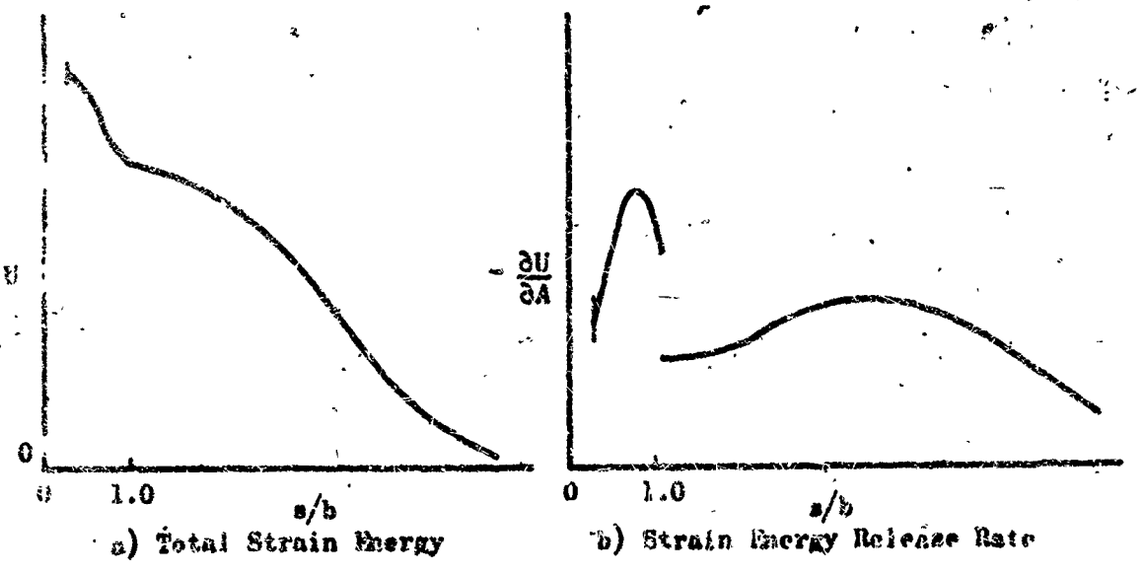

FIGURE 14. RESULTS OF NUMERICAL ENERGY CALCULATIONS[7]

and leaving the corner. The reciprocal of the square root of the absolute value of this rate, then, provides the ordinates for a plot of (5.6) against the released length s/b.

The results of computations for three different grain designs with web fractions of 60%, 80%, and 100%, are shown in Fig. 15. Each was assigned a length-to-radius ratio, L/b, of 12 and a Poisson's ratio, ν, of 0.485. Generally, the allowable drop in temperature, ΔT_{cr}, is found to be smaller for the higher web fractions. However, as the bond separation, s, approaches zero, the maximum temperature drop prior to bond failure for the solid cylinder becomes very large. This is explained by the lack of a stress singularity is a fully bonded solid cylinder since the stresses are everywhere uniform and hydrostatic. In fully bonded circular port grains on the other hand, large stresses develop near the inner bore-case intersection for any temperature drop, however small. This is reflected by the finite ΔT_{cr} indicated when no bonded surface is released.

Valleys or minimums are in evidence at two locations on each curve of Fig. 15, one in the region where $s < b$ and the other where $s > b$. These minimums indicate that for the given geometry there may be points of instability. That is, there may exist configurations such that when the maximum (critical) temperature drop is felt then a separation will grow in an unstable manner across the valley of the curve.

A shorter cylinder with a length-to-radius ratio of 4 and an 80% web fraction was used to investigate the influence of L/b on ΔT_{cr}. The results are compared with the cylinder whose L/b is 12 in Fig. 16. The behavior in the region where $s < b$ is only slightly changed; however, as

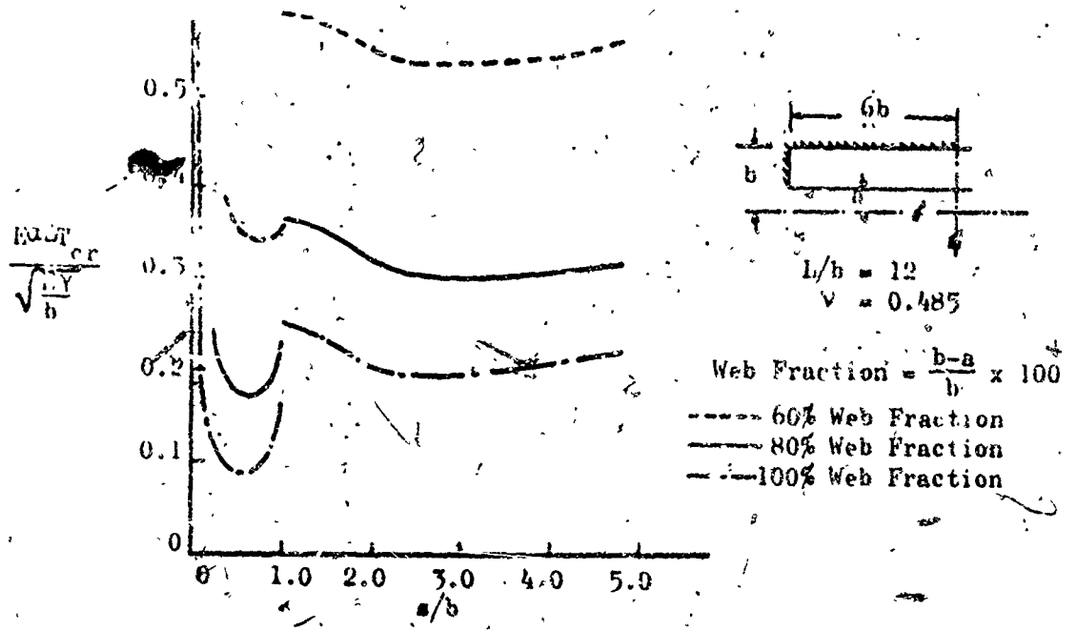

FIGURE 15. INFLUENCE OF WEB FRACTION[7]

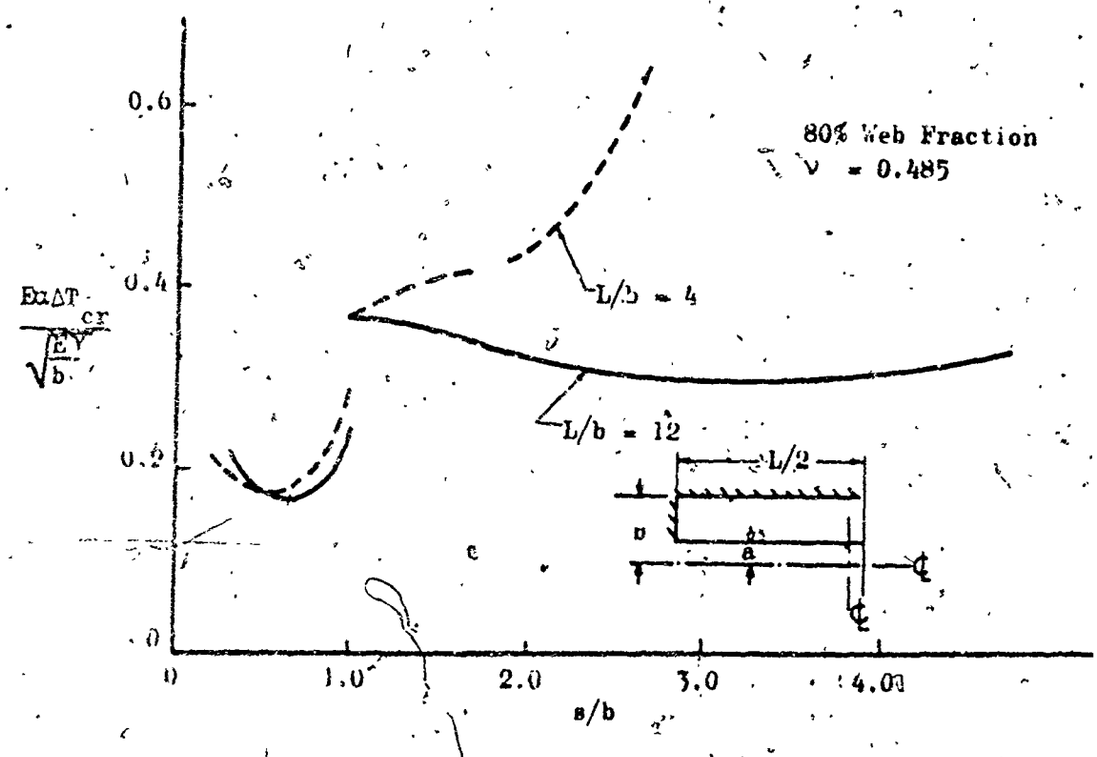

FIGURE 16. EFFECT OF LENGTH-TO-RADIUS RATIO[7]

the bond separation proceeds down the sides of the cylinder, end effects apparently become dominant, resulting in a curve without the minimum evident in the longer grain.

The significance of a change in the Poisson's ratio used for the calculations is indicated in Fig. 17. The maximum allowable temperature drop decreases as Poisson's ratio increases; however, the general curve shape is relatively unchanged.

The influence of a curved end dome and relief grooves and conicyls was also considered by Noel. The shape of the dome and the resulting ΔT_{cr}'s are shown in Fig. 18.

The two relief groove geometries considered are shown in Fig. 19 along with curves of ΔT_{cr}. One configuration has a shallow conicyl or toroidal indentation on the inner bore next to the fixed head and the other has a valley in the flat free end next to the cylindrical case. The web fraction was 80% and the L/b ratio 12 for both geometries. It is seen that nearby conicyls or valleys in the propellant free surface are quite significant in their ability to reduce the critical temperatures. In addition to influencing the initiation of fracture they also greatly reduce the tendency for fracture to propagate, once it is initiated.

A third configuration consisting of a deep conicyl at the longitudinal centerline was also studied by Noel. This design was found to have little effect on cleaving near the ends. It was concluded that conicyls lose their effectiveness in increasing the critical temperatures as they are moved away from the locale of the cleaving.

Noel [11] has also investigated grain case unbonding of the specific motor designs in the Air Force sponsored STV program. In this investigation

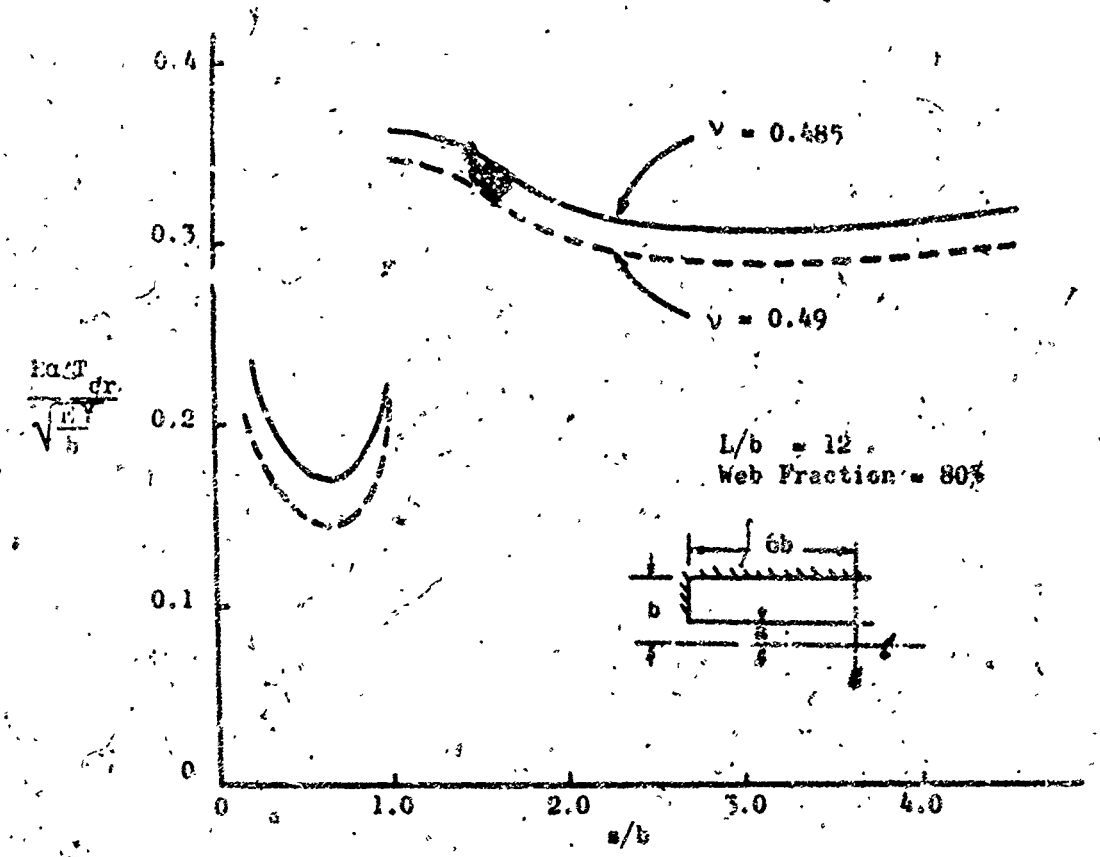

FIGURE 17. INFLUENCE OF POISSON'S RATIO CRITICAL TEMPERATURE ΔT_{cr} [7]

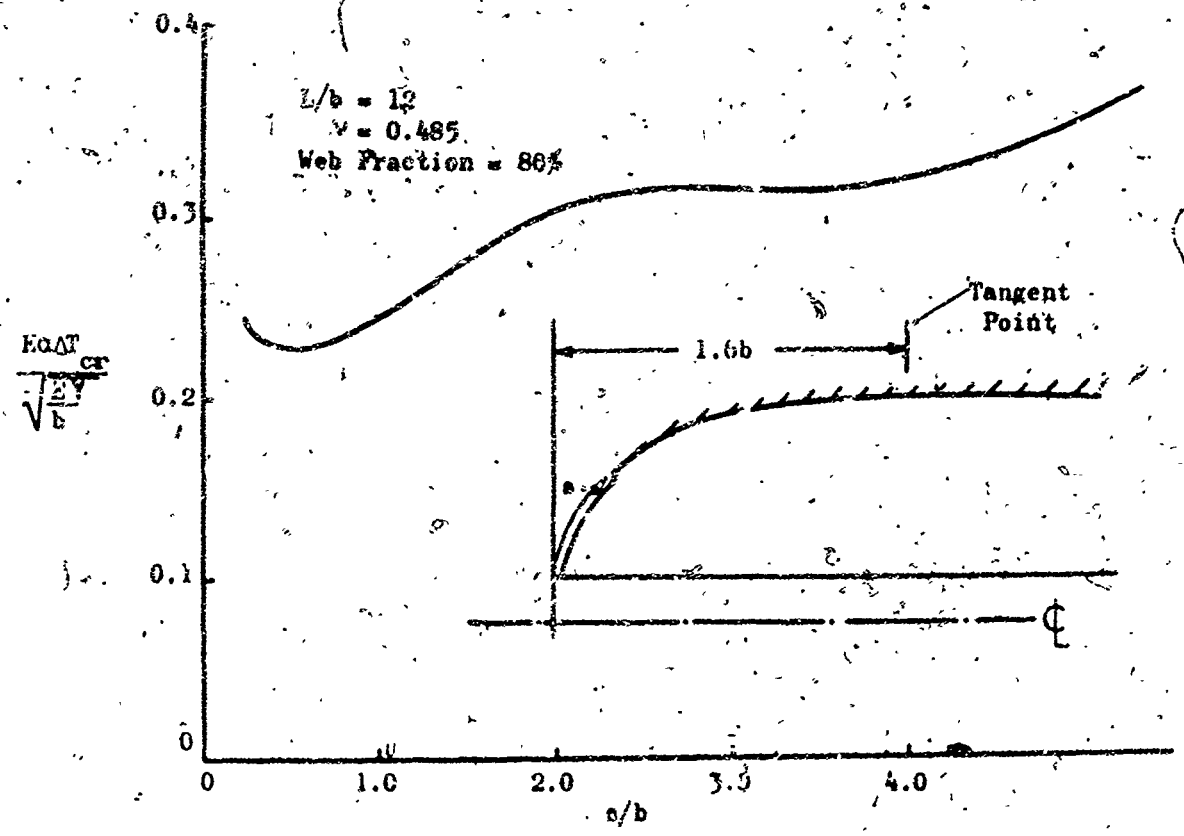

FIGURE 18. INFLUENCE OF DOME SHAPE ON CRITICAL TEMPERATURE ΔT_{cr} [7]

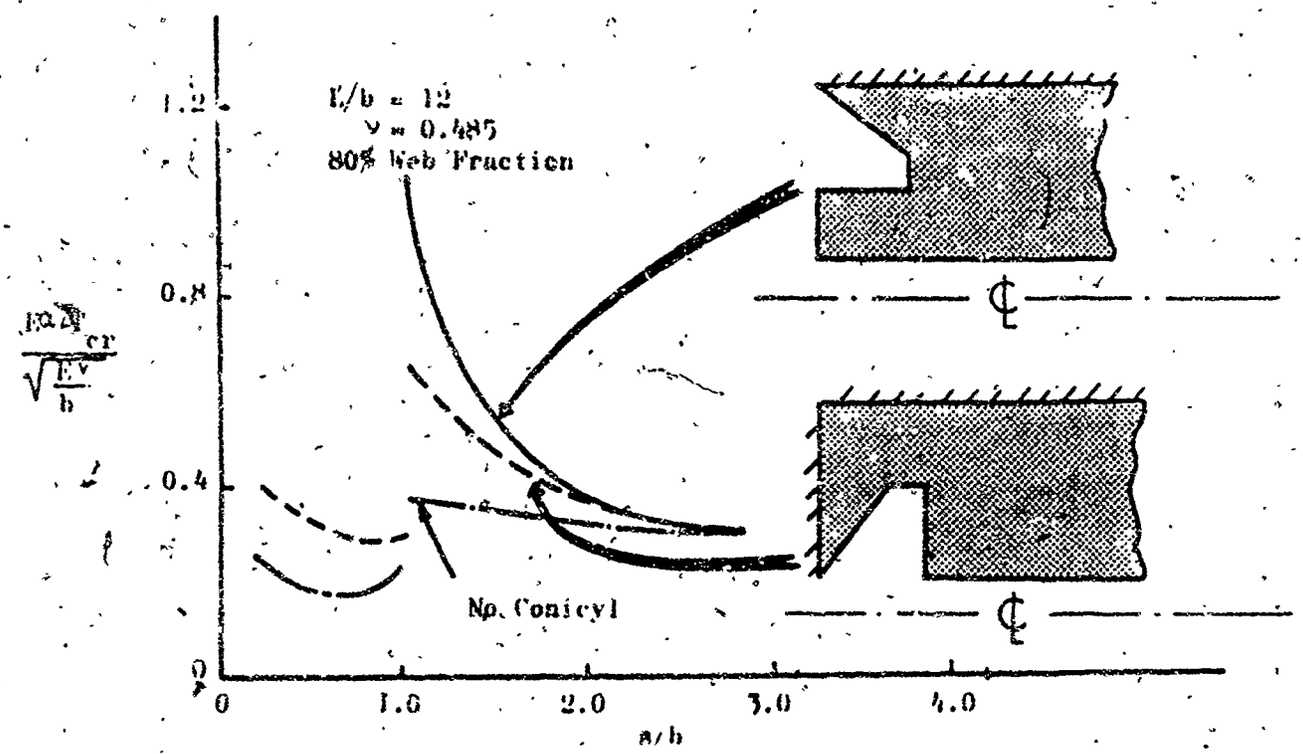

FIGURE 19. EFFECT OF GRAIN END CONICYLS ON CRITICAL TEMPERATURE ΔT_{cr} [7]

the rate of change of energy were normalized with respect to $E_g(\alpha_g \Delta T)^2 b$ where the subscripts g refer to the grain. Numerical values were input for the ratios E_c/E_g, α_c/α_g, t_c/b and the web fraction where t_c denotes the motor case thickness. The crack dimension s is measured from the end of the grain for axially symmetric unbonding and from the axial center of the grain for radial cracks. Thus, there is no crack until s becomes larger than the inner bore radius a.

In order to use the energy balance approach for geometries not initially precracked requires assumptions to be made concerning the flaws inherent in the material. Over the spectrum of rates and temperature covered by the LPC [11] tests for γ and the cumulative damage tests for ϵ_a/a_o, it appeared that the size of the inherent flaw was approximately 0.02 inches in radius for the STV propellant. With $s_o = 0.02$ and normalized on the STV case radii, then

7-inch STV's, $s_o/b = 0.006$

4-inch STV's, $s_o/b = 0.01$

The results for the 4-inch STV are shown in Fig. 20 and results for the 7-inch STV in Fig. 21.

Comparison of the unbonding curves suggests that the concentric-type unbond will cause the initiation of adhesive-type failures for both the 4-inch and 7-inch STV's, but that the shape will soon degenerate into the circumferential type. This effect has also been observed in tests of polyvinyl chloride in glass beakers [7].

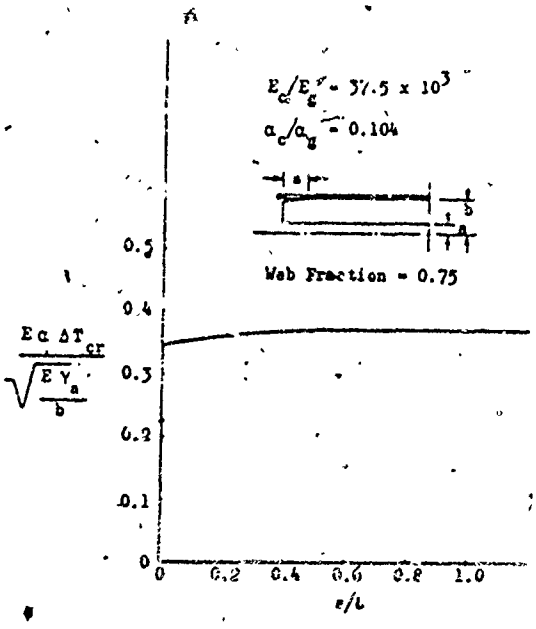

Figure a. Axially Symmetric Unbond

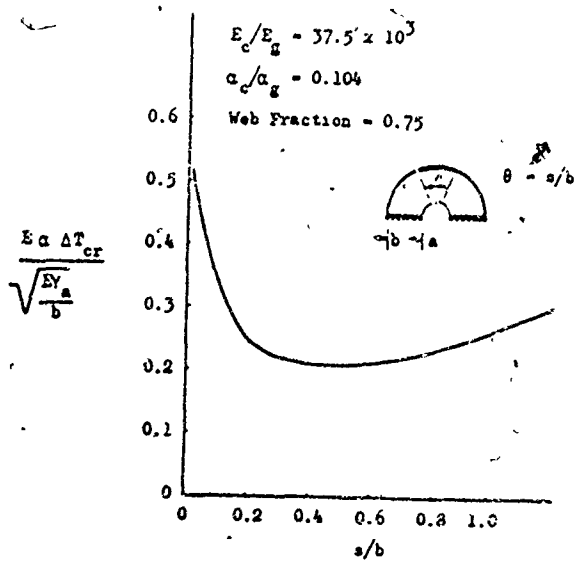

Figure b. Plane Strain "New Moon" Unbond

FIGURE 20. CRITICAL TEMPERATURE CURVES FOR 4-INCH STV'S BASED ON ENERGY BALANCE (t/b = 0.1875)[11]

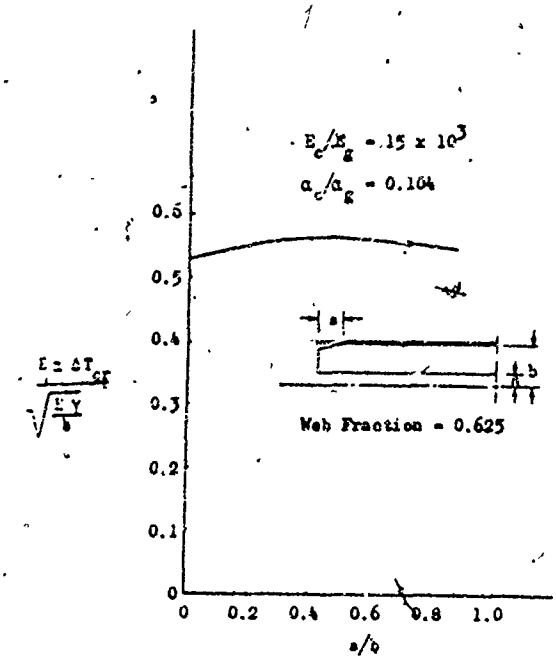

Figure a. Axially Symmetric Unbond

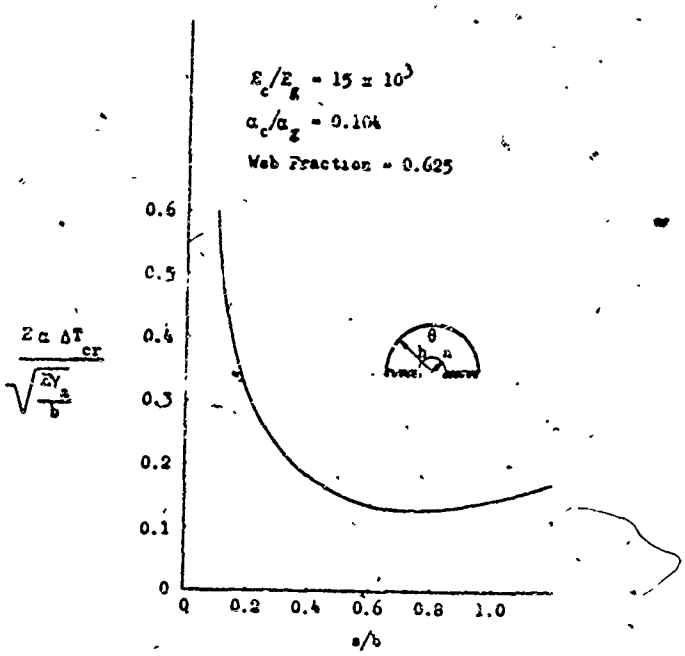

Figure b. Plane Strain "New Moon" Unbond

FIGURE 21. CRITICAL TEMPERATURE CURVES FOR 7-INCH STV'S BASED ON ENERGY BALANCE (t/b = 0.107)[11]

5.3.2 GRAIN END CONTOURING

In addition to employing stress relief flaps, local stress concentrations may be minimized by contouring the grain end configuration. This approach offers some advantages over the use of stress relief flaps. The most important one is increased overall grain reliability due to elimination of the bonded interfaces between the propellant, flap and case. Removal of this bond substrate reduces the probability of failure due to manufacturing anamolies and uncertainties in the anticipated loads environment.

One example of grain end contouring has been presented in Fig. 19 and discussed in connection with the use of energy balance concepts for designing case-grain terminations.

Dill, et al[4], investigated the use of a fillet at the grain end to prevent cracking. The tensile reaction corresponding to the inward motion M in Fig. 3 can be distributed by a fillet, reducing the tensile stress to an allowable level. Their analysis indicated that the stress will be finite if the fillet angle β shown below is less than 45°.

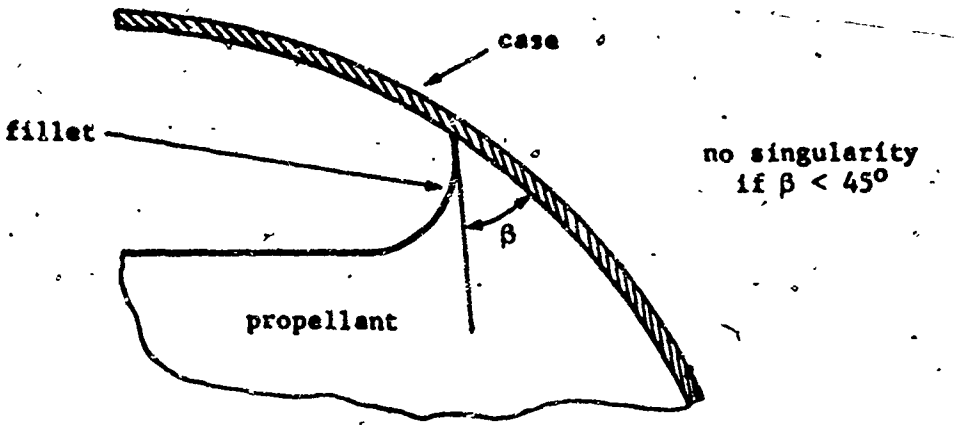

DETAIL 1. Fillet Design

Durelli and co-workers [12-22]have conducted extensive studies of the stress concentrations at the ends of solid propellant grains using two-and-three photoelasticity. Some of the more recent of these studies have been reported by Robinson, Graham and Moore[23] Some of the results reported in references 12, 13, 15 and 23 will be summarized herein. These results provide guidelines for rocket motor design.

Durelli, et al[12], conducted a study on the propellant grain geometry shown in Fig. 22. The grain was assumed to be subjected to a uniform shrinkage while bonded partially or totally to a rigid shell. Although both two- and three-dimensional photoelastic analyses were carried out for the models shown in Fig. 22 and on models designed with various modifications, only those results applicable to the design of case-grain terminations will be discussed here. (Their results for investigations of the effect of the slot geometry are presented in Appendix D.)

The two-dimensional results reported here are given in terms of a normalized shear stress concentration factor K, defined as

$$K = \frac{\max\ (\tau_{max})}{E\alpha} \tag{5.7}$$

where

$\max\ (\tau_{max})$ = maximum shear stress

E = Young's Modulus

α = Shrinkage that would have occurred if the model were not bonded (free shrinkage).

The factor K also gives the shear strain since

$$\frac{\tau_{max}}{E} = \frac{\gamma_{max}}{2(1+\nu)} \tag{5.8}$$

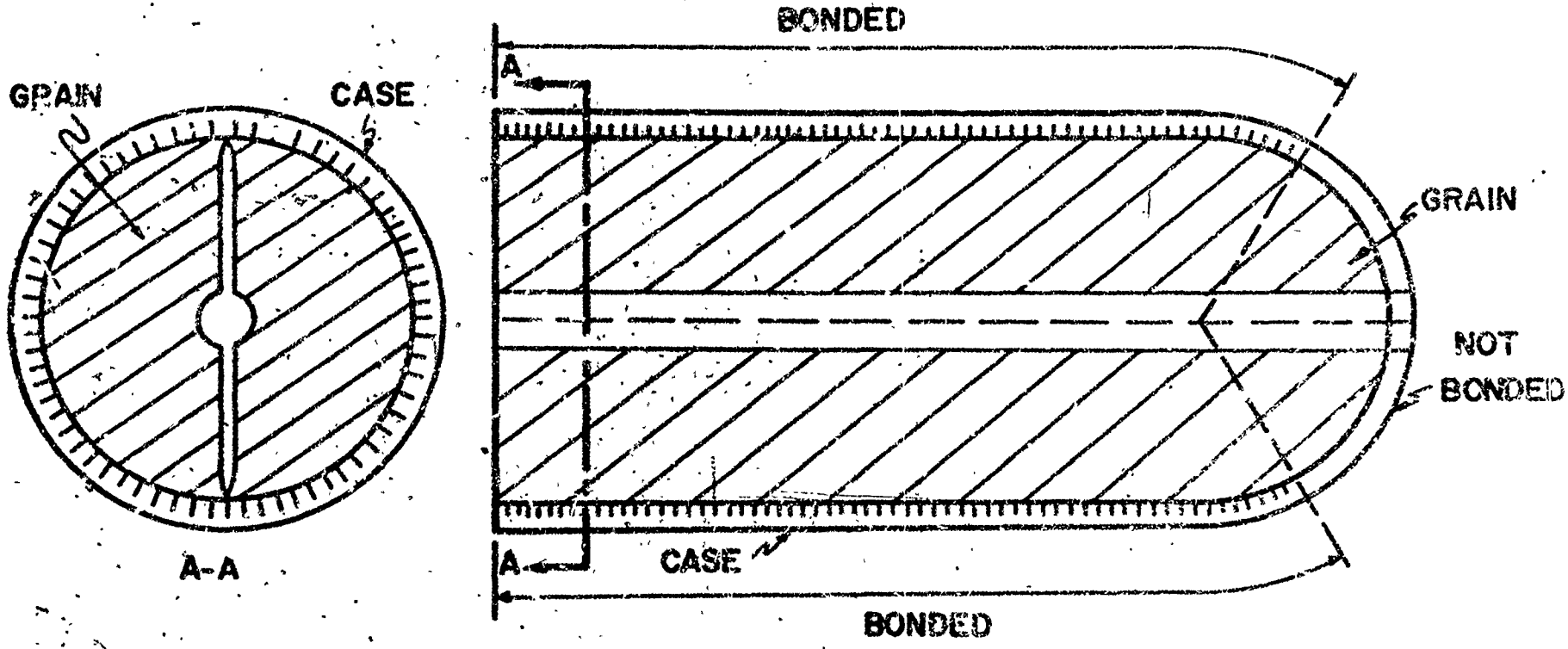

FIGURE 22. SKETCH OF THE ESSENTIAL FEATURES OF THE GRAIN TO BE SIMULATED IN THE MODELS [12]

Thus,

$$\max (\gamma_{max}) = 2(1+\nu)K\alpha \tag{5.9}$$

On free boundaries, the shear stress is one-half the normal stress tangent to the boundary, and so

$$\max (\sigma_{tan}) = 2KE\alpha \tag{5.10}$$

Also, on a free boundary, the tangential strain can be written in terms of K;

$$\max (\varepsilon_{tan}) = 2K\alpha \tag{5.11}$$

The concentration factor for the three-dimensional models is defined as

$$k = \frac{\max (\tau_{max})}{E\alpha^*} \tag{5.12}$$

*It should be noted that care must be exercised in applying the two-dimensional results to the three-dimensional counterparts. The stresses at any point in plane stress or plane strain models can be described by σ_x, σ_y, τ_{xy}, and σ_z and the strains by ε_x, ε_y, γ_{xy}, and ε_z. In the plane stress models subjected to restrained shrinkage, the boundary condition is $\varepsilon_x = \varepsilon_z = \alpha^*$. It follows from these boundary conditions that the shear stress in the central region of the plane stress models bonded on one side is $1/2\ E\alpha$, whereas the shear stress in the corresponding region of the plane strain model is $2(1-\nu)E\alpha^*$ (or $E\alpha^*$ for $\nu = 1/2$). Thus, the normalized shear stress reported for the plane stress model is $\tau_{max}/E\alpha = 1/2$, but for the plane strain model, the corresponding normalized shear is $\tau_{max}/E\alpha^* = 1$.

Where

$\max(\tau_{max})$ = maximum shear in the plane containing the particular slice under analysis.

α^* = longitudinal strain in the model, at the interface of the model and shell at the grain midplane (origin of coordinate system).

The variation of the peripherical groove length around the head end dome was one of the factors studied. A series of two-dimensional models of the meridian cross-section which were bonded everywhere at the boundary except for a region between the axis of the model and a given angle $\pm\ \theta$ measured from the axis as shown in Fig. 23. The stress concentration factor associated with the geometric corresponding to angles from 0° to 84° is also shown in Fig. 23. The curve has been extrapolated to 90° since there is little variation at 84°. It is seen that K is smallest for small values of θ.

The variation of radius at the end of the dome unbonded boundary was studied using a meridian model made with an unbonded boundary in the dome section, terminated at each knuckle point (90° from the axis) by a hole with a diameter 1/20 of the model width. Assuming that the slot width is not significant, except as it determines the radius at the end of the bond, then the K factors as a function of the ratio of the radius at the end of the bond to model width were determined as shown in Fig. 24. It can be seen that decreasing the radius at the end of the slot or groove increases the concentration factor K in an asymptotic manner.

A meridian model with a completely unbonded dome area was built with an elliptical hole at the junction of the dome and the straight part of the plate as shown in Fig. 25. The concentration factor K is 2.6.

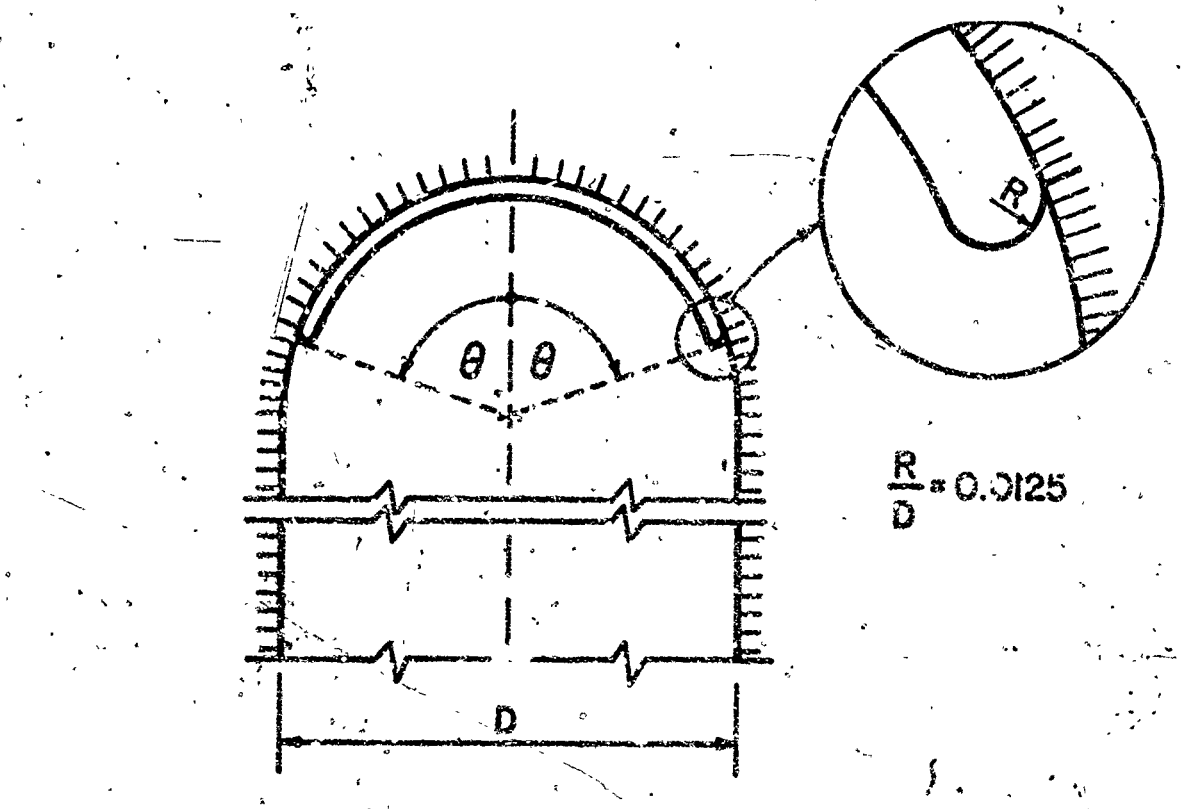

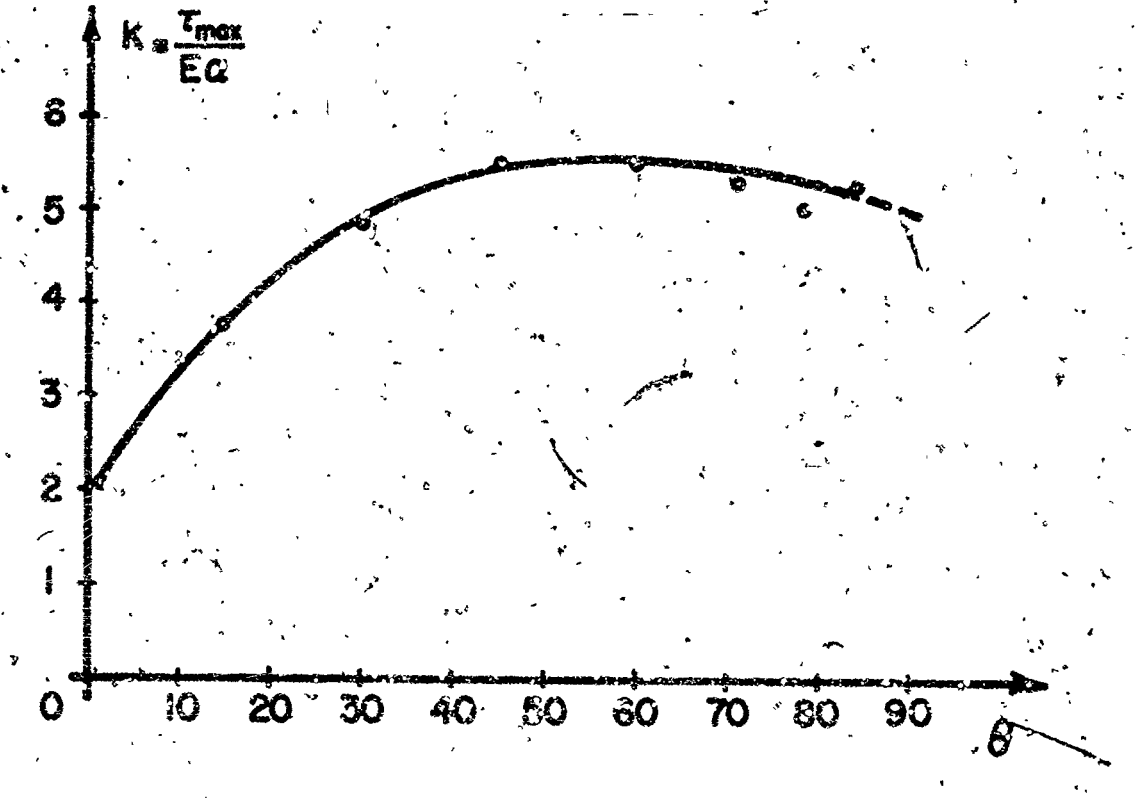

FIGURE 23.

STRESS CONCENTRATION AT THE END OF A PERIPHERICAL GROOVE SEPARATING THE BONDED FROM THE UNBONDED BOUNDARY OF A PLATE PARTIALLY RESTRAINED FROM SHRINKAGE [12]

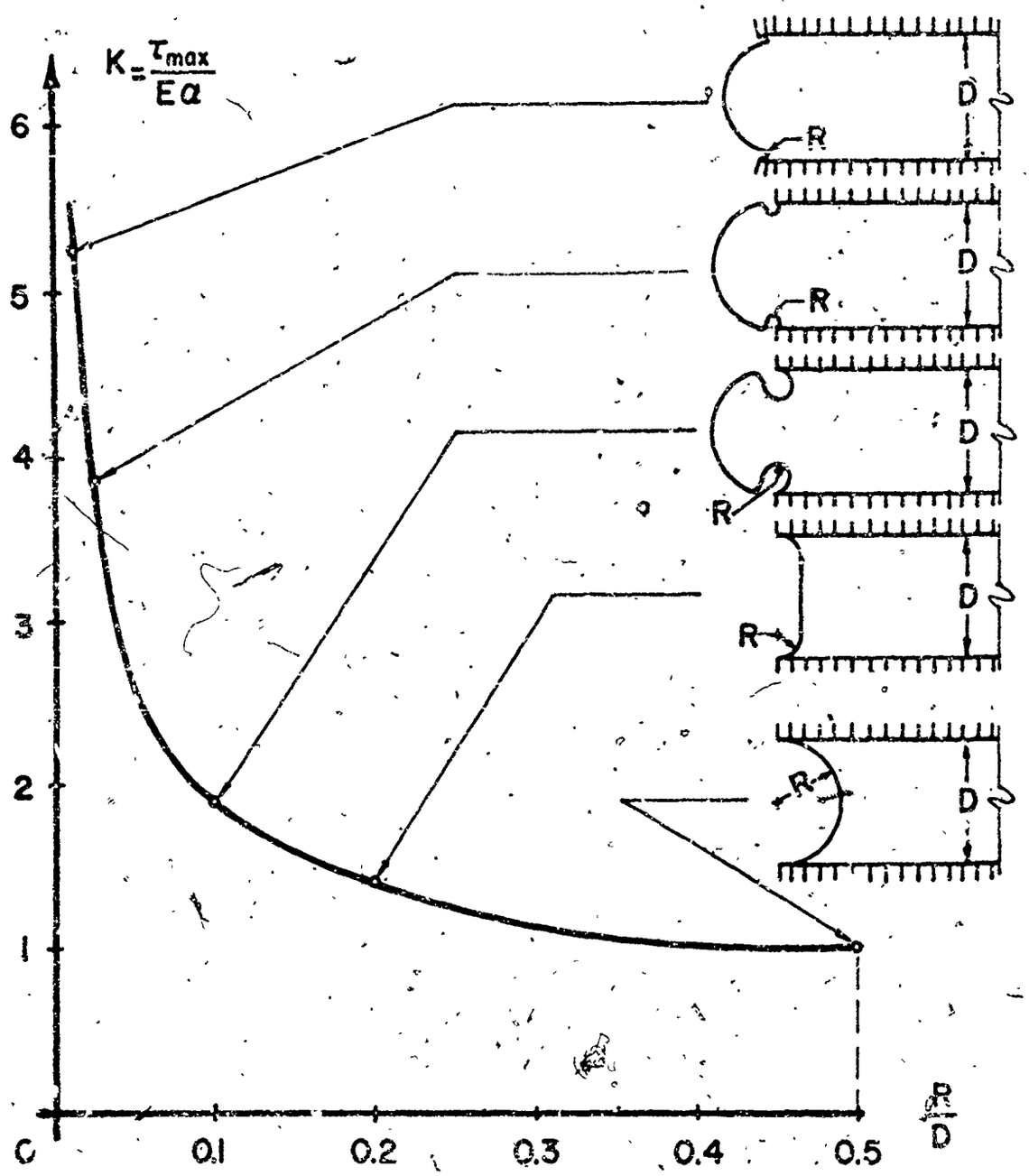

FIGURE 24.

STRESS CONCENTRATION IN PLATES WITH DIFFERENT END CONFIGURATION, BONDED ON TWO SIDES, AND SUBJECTED TO BIAXIAL RESTRAINED SHRINKAGE [12]

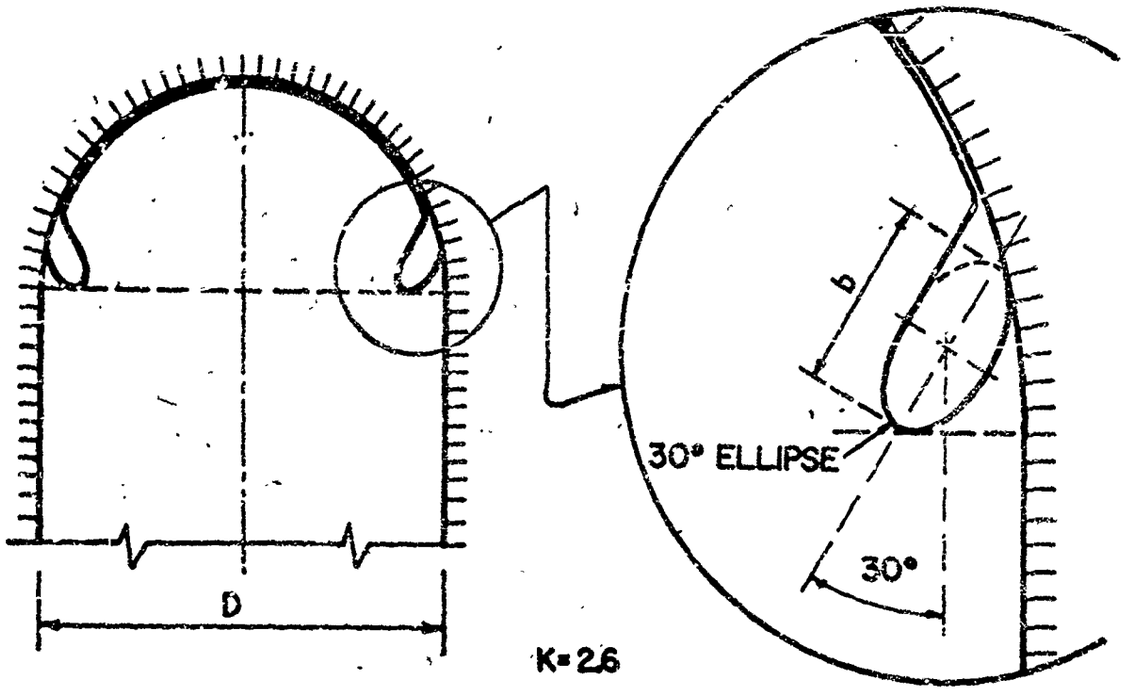

FIGURE 25.

ELLIPTICAL HOLE AT THE POINT OF DISCONTINUITY BETWEEN BONDED AND UNBONDED BOUNDARIES, IN A PLATE PARTIALLY RESTRAINED FROM SHRINKAGE

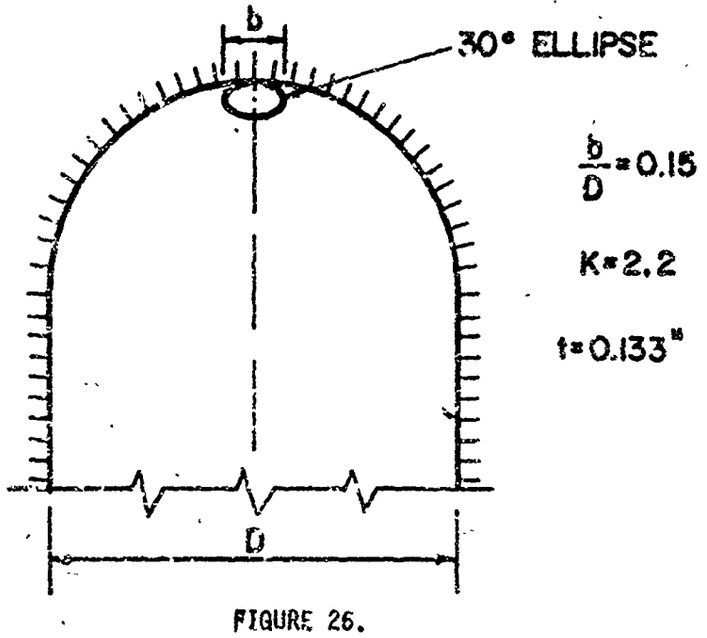

FIGURE 26.

ELLIPTICAL HOLE CLOSE TO THE APEX OF THE SEMICIRCULAR END OF A PLATE SUBJECTED TO RESTRAINED SHRINKAGE[12]

Another model was built with an elliptical hole near the apex of the dome. Fig. 26 shows the geometry and a stress concentration factor of 2.2

To estimate the influence of length of the concentration factor K two models which had an original length of six times the width were both reduced to three times the width and two times the width successively. The length is measured from the apex of the dome to the other end in each model. One model was similar to that shown in Fig. 23 with $\theta = 84°$ and the other was one of those depicted in Fig. 24 with $R/D = 0.025$. The K factors for the original length as well as the two shortened lengths are stated below. It is seen that the K values decrease only slightly as the length-to-width ratio is reduced.

Plate Length-to-Width Ratio	$\pm$ 84° Slot at Dome	$\frac{R}{D} = 0.025$ at $\pm$ 90° at End of Slot at Dome
6	5.2	3.9
3	4.9	3.8
2	4.7	3.7

The geometry of the model used by Durelli, et al[12], in part of the three-dimensional studies is shown in Fig. 27. The concentration factors for the meridianal slices as defined by (5.12) are given in Fig. 28.

A second three-dimensional model, shown in Fig. 29, was also investigated. The plan of slicing for the three-dimensional photoelasticity tests is shown in Fig. 30. The stress concentration factors as defined by (5.12) are shown in Fig. 31.

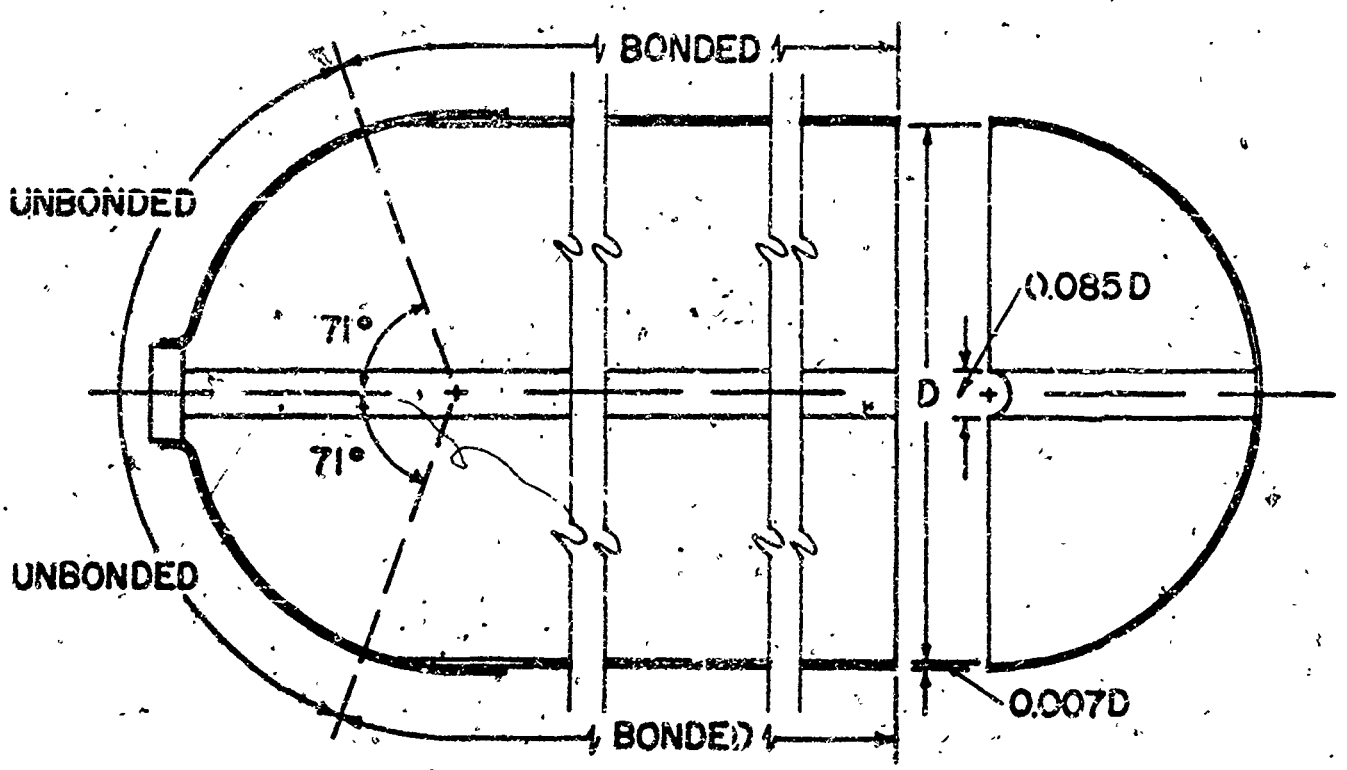

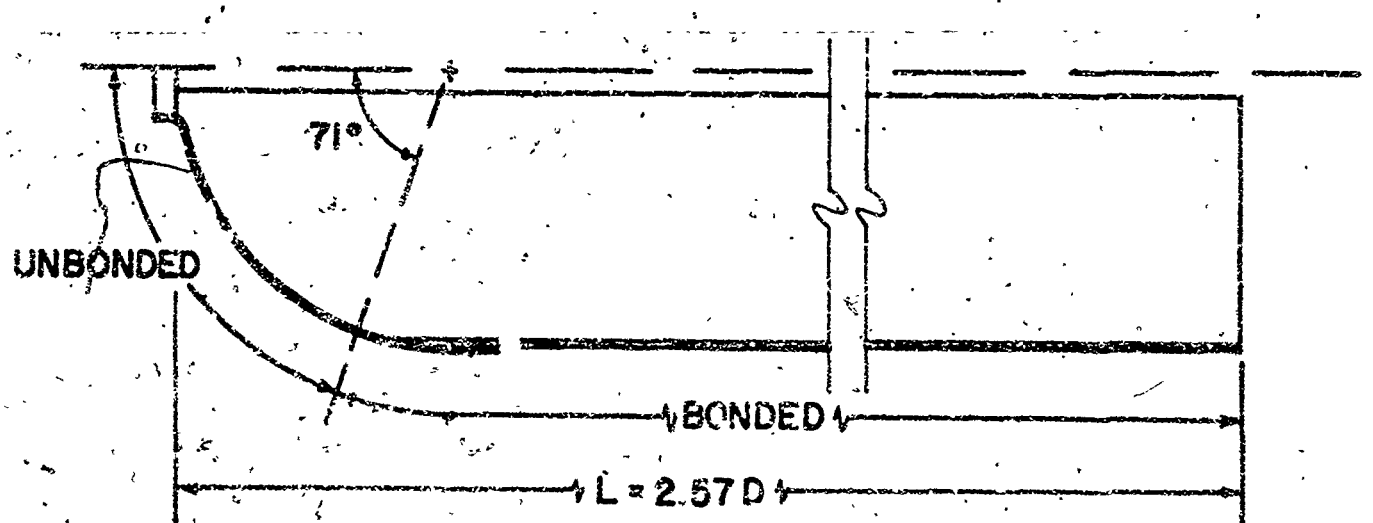

FIGURE 27. THREE-DIMENSIONAL MODEL[12]

SLICE NO.	LOCATION	$K = \frac{\text{slice}(\tau_{max})}{E\alpha^*}$
2, 2A	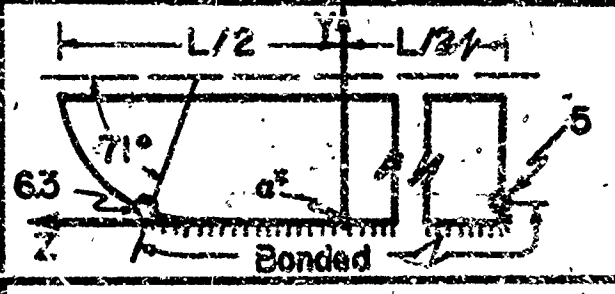	6.3 5
4, 4A	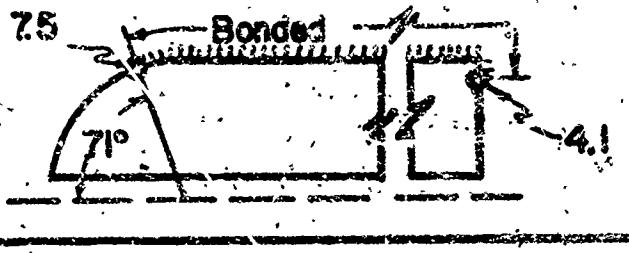	7.5 4.1

$$\epsilon_x\Big|_{x=y=z=0} = \bar{\epsilon}_z = \alpha^*$$

The stress concentration takes place at the points marked by a dot.

FIGURE 28. STRESS CONCENTRATION FACTORS FOR THE GEOMETRY OF THE ROCKET GRAIN[12]

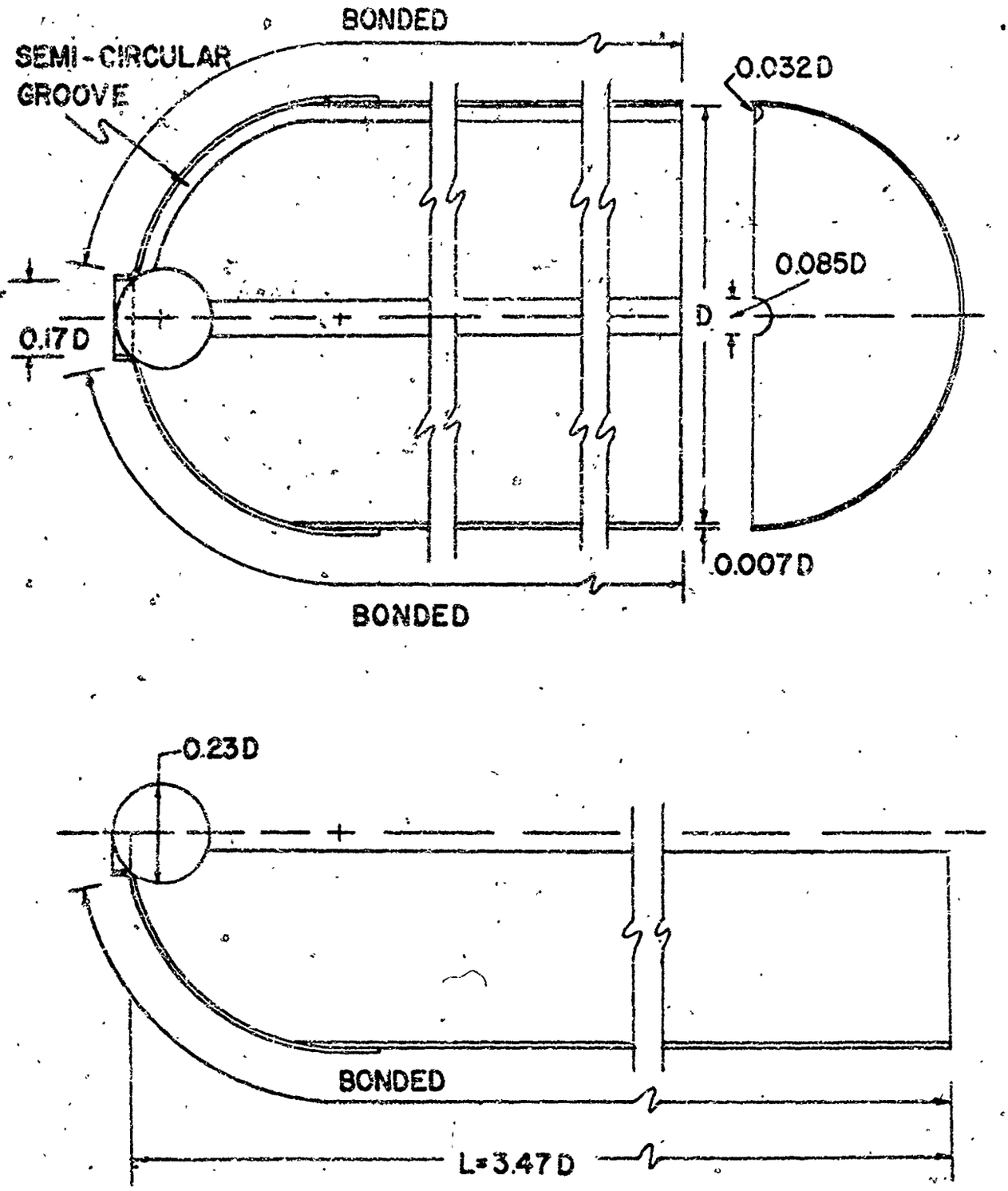

FIGURE 29.

GEOMETRY OF THE THREE-DIMENSIONAL MODEL WITH MODIFICATIONS TO REDUCE STRESS CONCENTRATIONS[12]

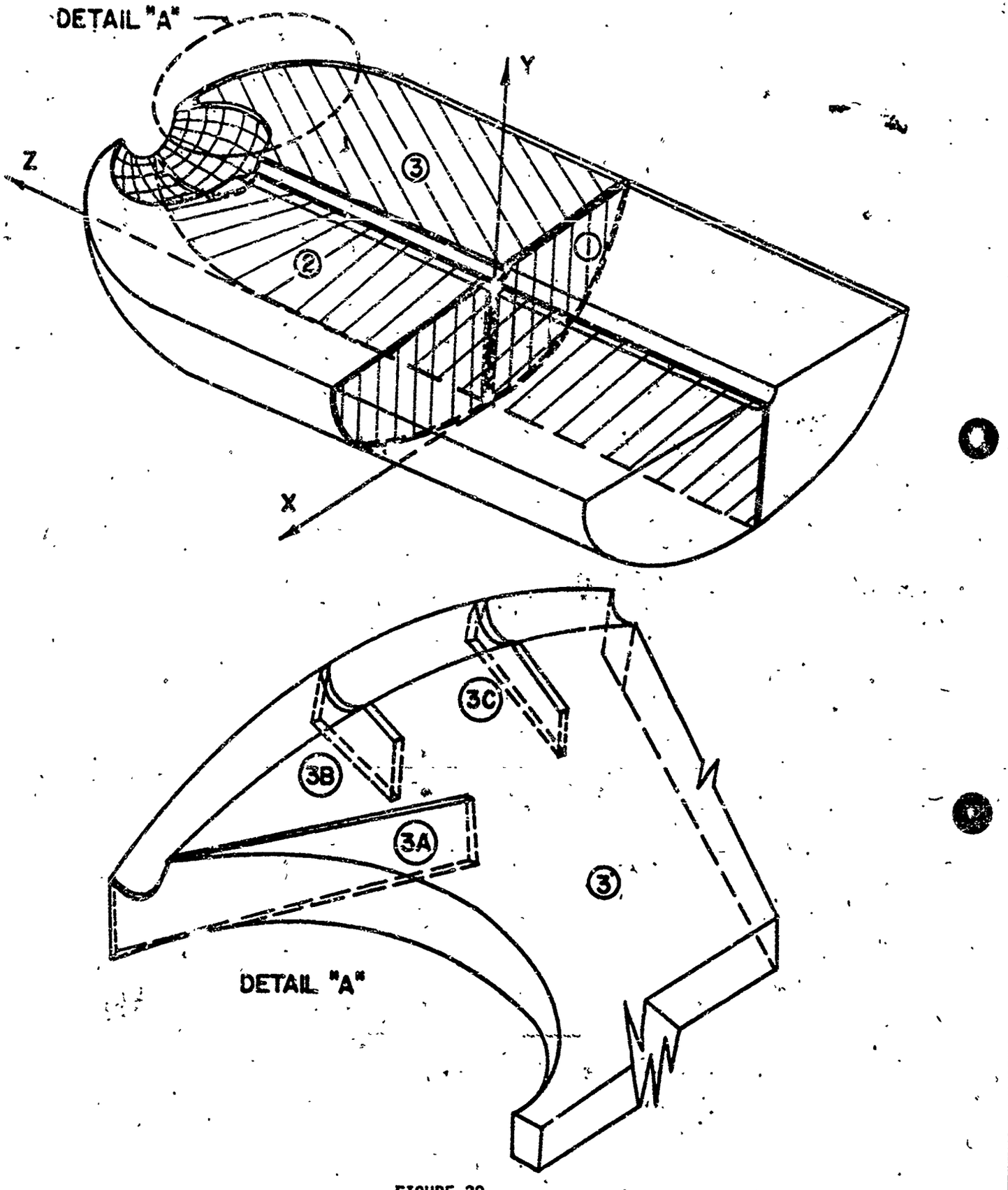

FIGURE 30.

PLAN OF SLICES FOR THE THREE-DIMENSIONAL MODEL CORRESPONDING TO THE MODIFIED GEOMETRY OF THE GRAIN [12]

SLICE NO.	LOCATION	$K=\frac{\text{slice}(\tau_{max})}{E\alpha^*}$
1	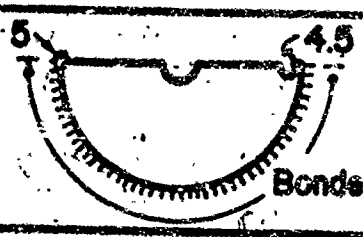	5 4.5
2		3
3	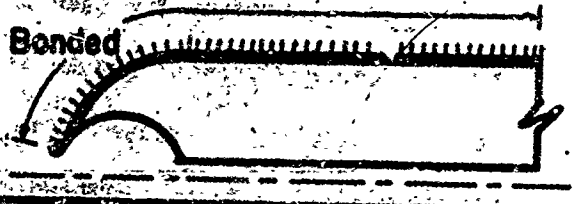	2.7
3A	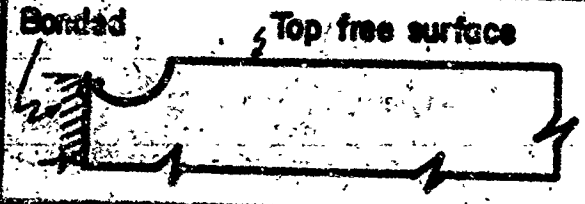	2.5
3B	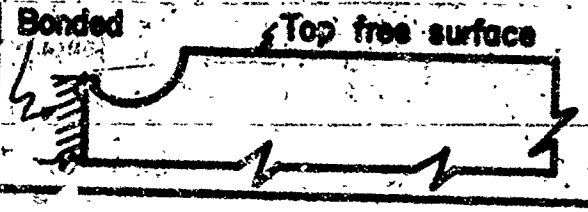	2.4
3C	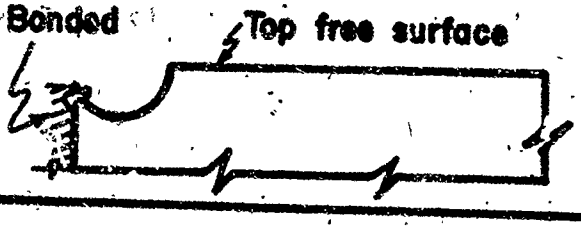	2.5

$$\epsilon_z\big|_{xyz=0} = \bar{\epsilon}_z = \alpha^*$$

The stress concentration takes place at the points marked by a dot.

FIGURE 31.

STRESS CONCENTRATION FACTORS FOR THE MODIFIED GEOMETRY OF THE ROCKET GRAIN [12]

Comparing Figs. 28 and 31, it is seen that the stresses in the model depicted in Fig. 29 are considerably lower than those of the model in Fig. 27. The essential features of these two designs which are chiefly responsible for the difference in stress levels of the two models are shown in Fig. 32 for illustrative purposes. Design A has a square corner along one edge and a reentrant corner along the other edge of the bonded interface as shown in the figure. Although analysis of both the square and reentrant corner are limited by the same difficulties discussed in the following chapter for the analyses of cracks in two-dimensions, it is clear that both corners show high stresses, and at the junction of the two edges, the stresses will be some combination of these two high stresses.

Design B is characterized by outward corners at the interface edges as shown in Fig. 32. These corners show lower stresses than the square reentrant corner. Besides this, since the maximum stresses of the outward corners do not occur on the edges, the junction of the edges becomes less critical.

The above discussion and limited parametric data present some of the considerations that a designer may put to use to minimize high local stresses at case-grain terminations.

The results of several other experimental investigations by Durelli and his co-workers are also available for use in making design decisions relating to case-grain terminations. In other studies, Durelli, et al [13-15,18,19,22,23], investigations involved the use of two- and three-dimensional model analyses. The two-dimensional models were of two types: (i) strips bonded on one side, and (ii) rectangular plates bonded on both

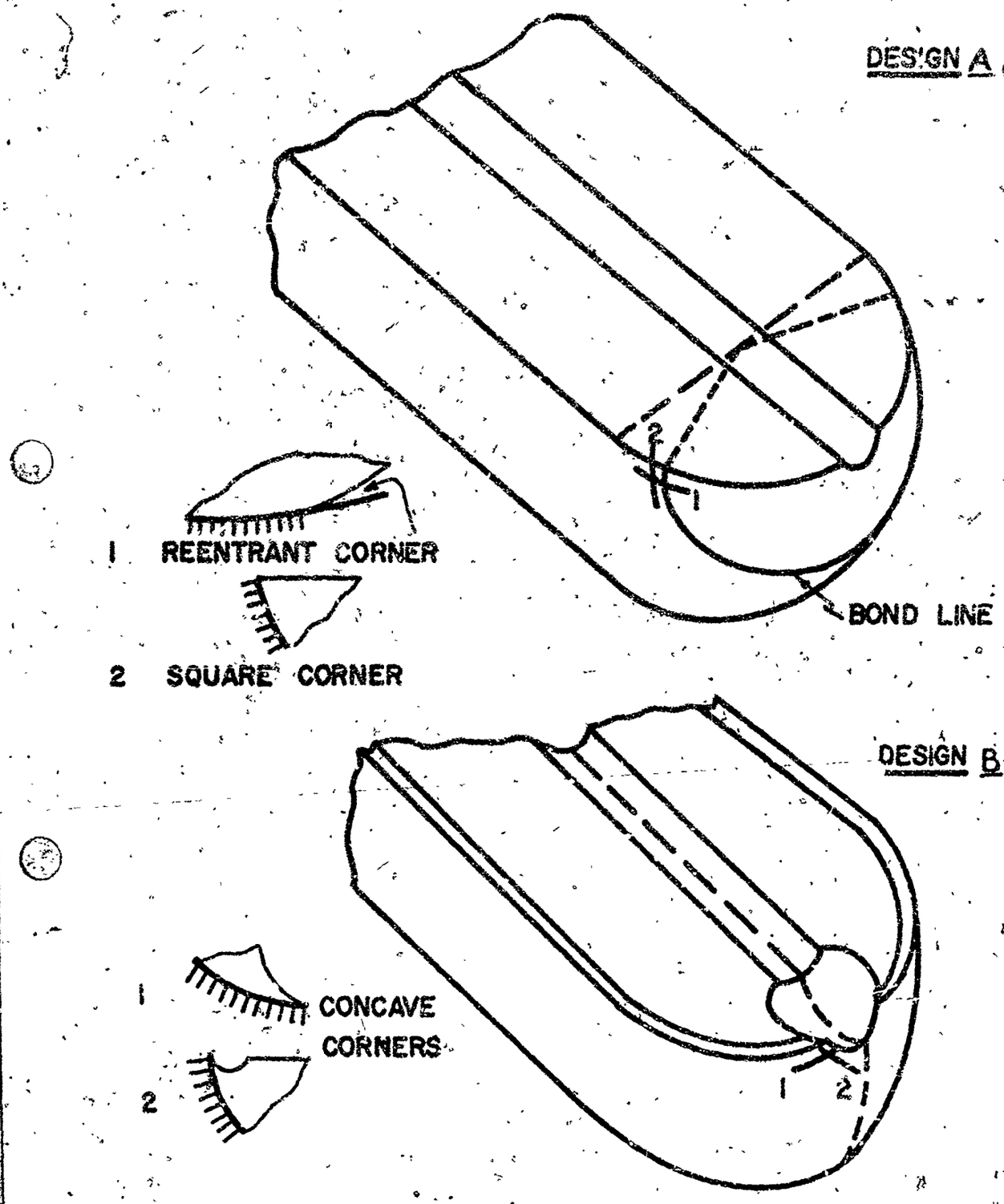

FIGURE 32. COMPARISON OF DESIGNS[12]

longitudinal sides. The first type simulates the meridian plane in thin web grains, and the second type simulates the meridian plane near the interface of thick web grains. The three-dimensional models were also of two types: (i) an idealized slab bonded on one face, and (ii) hollow cylinders bonded to shells. The central cross-section of the first type of specimen has a central region which simulates the meridian cross-section in axisymmetric thin web grains. The second type of specimen reproduces closely the geometry of simple rocket motors. Fig. 33 illustrates both the two- and three-dimensional simulations. The loading is produced by restrained shrinkage of the stress.

Fig. 34 presents the stress concentration factors in plates bonded along one edge with different fillet configurations. This figure shows that an increase in the radius of curvature of an end fillet, decreases the stress concentration; however, little is gained if the radius is larger than one-half the height of the strip (or web of the grain).

In another study[15], the three models shown in Fig. 35 were used to analyze the stress distributions associated with seven different geometries of junctions of bonded and free boundaries. The length-to-width ratio was about six, however, from a previous table (page 5.40) the concentrations obtained are expected to vary little for different length-to-height ratios.

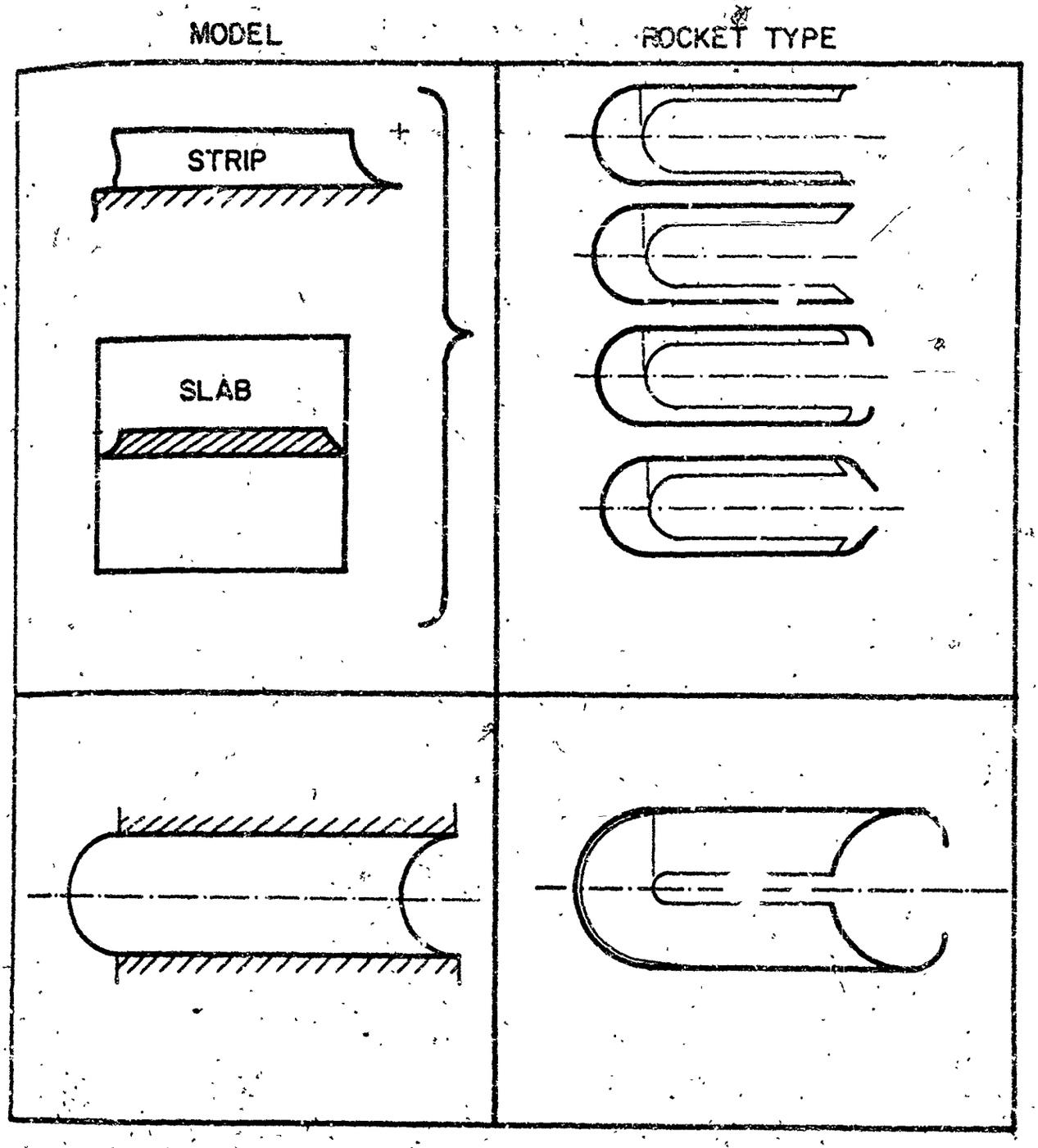

FIGURE 33.

TWO AND THREE-DIMENSIONAL SIMULATIONS OF SOLID PROPELLANT ROCKET GRAIN ENDS[13]

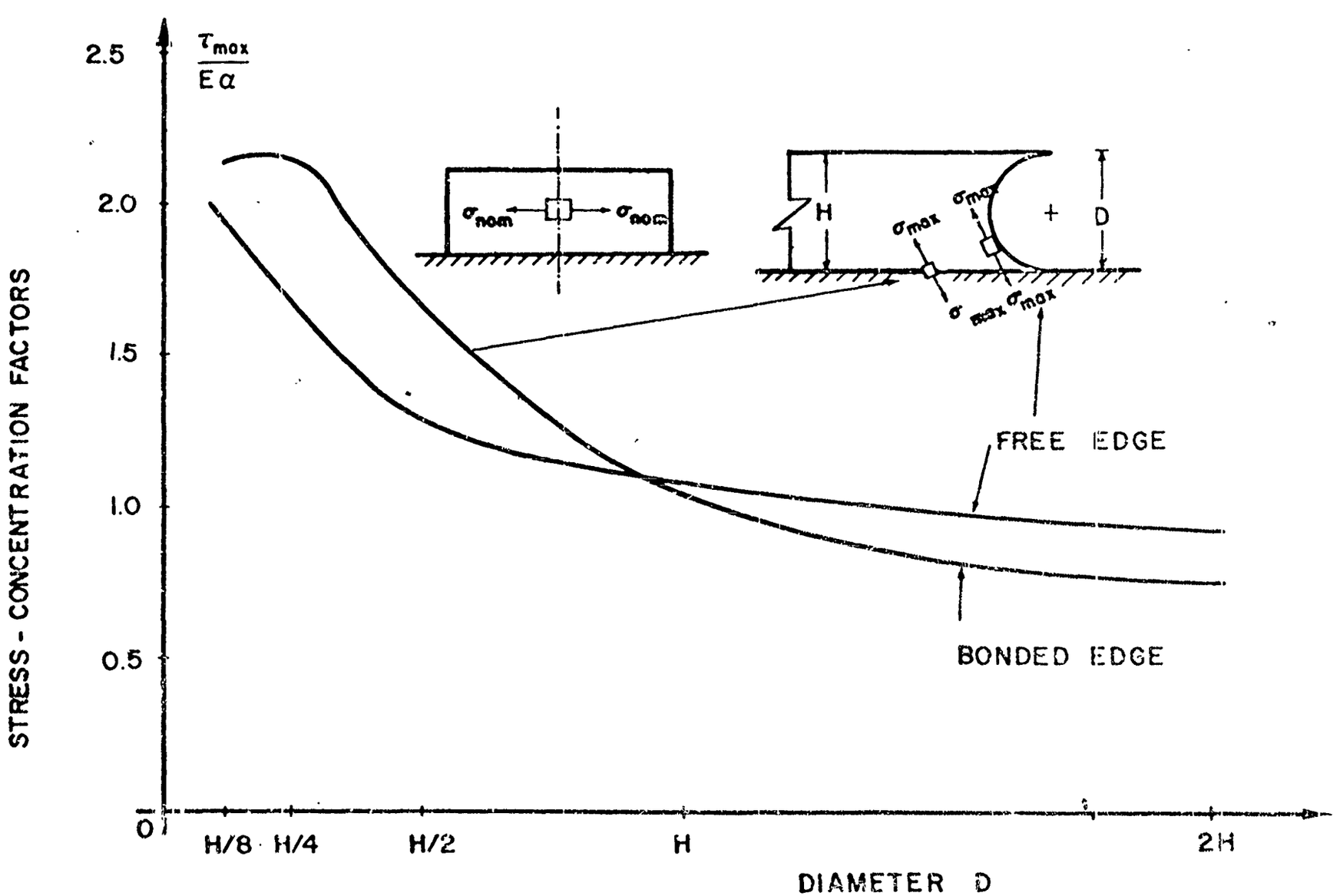

FIGURE 34.

PLANE - STRESS - CONCENTRATION FACTOR IN PLATES BONDED ALONG ONE EDGE[13]

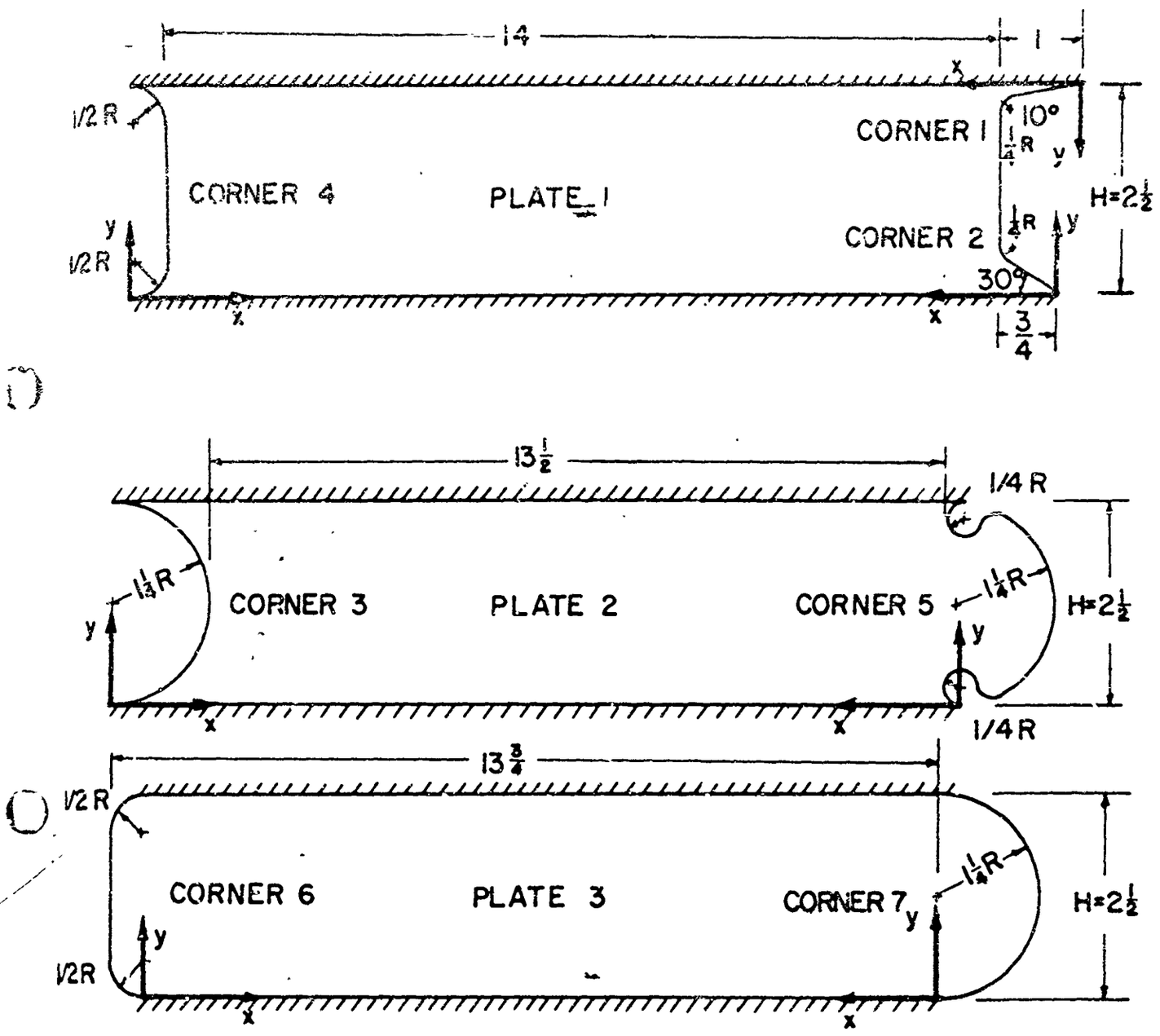

FIGURE 35.

DIMENSIONS OF THE THREE MODELS USED TO ANALIZE THE STRAINS ASSOCIATED WITH 7 DIFFERENT GEOMETRIES OF JUNCTIONS OF BONDED AND FREE BOUNDARIES[15]

Two types of shrinkage loading conditions were analyzed. In one type of test the long edges of the plates were restrained longitudinally, but allowed to move freely, one toward the other. This restraint is called "longitudinal restraint" here. In the other type of test, the two long boundaries were held apart so that there was restraint both along and between the boundaries. This situation is called "biaxial restraint". The restraint between the boundaries does not have the same value as the restraint along the boundaries.

Figure 36 shows schematically the two loading conditions studied. This figure also shows the loading obtained by subtracting those two loading conditions from one another. In this figure u and v denote the components of displacement in the x and y directions, respectively; a bar is added to specify a displacement applied to a boundary.

The subtraction (in a tensorial sense) of the two loading conditions used in the tests permits the determination of stresses associated with

*The "biaxality ratio", k, is determined in the following manner. If the stresses along the transverse axis obtained from the shear difference method are put in the form of $\sigma_x/E\alpha$ and $\sigma_y/E\alpha$, then from Hooke's Law the normalized strain ε_y/α can be obtained all along the transverse axis. The average value of ε_y/α times the height is the displacement of the top edge with respect to the bottom. The average value of ε_y/α along the transverse axis is then the biaxiality ratio k. For the three models shown in Figure 35, k was found to be

MODEL	BIAXIAL RESTRAINT RATIO k
1	0.73
2	0.80
3	0.73

PROCEDURE TO OBTAIN TRANSVERSE RESTRAINT

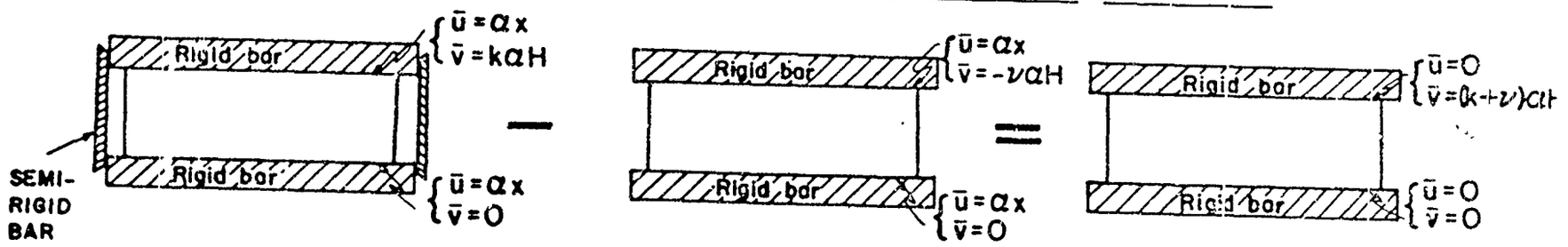

BIAXIAL RESTRAINT (photoelastic analysis)

LONCITUDINAL RESTRAINT (photoelastic analysis)

TRANSVERSE RESTRAINT

EXTENDED ANALYSIS TO OBTAIN VARIOUS BIAXIAL RESTRAINTS

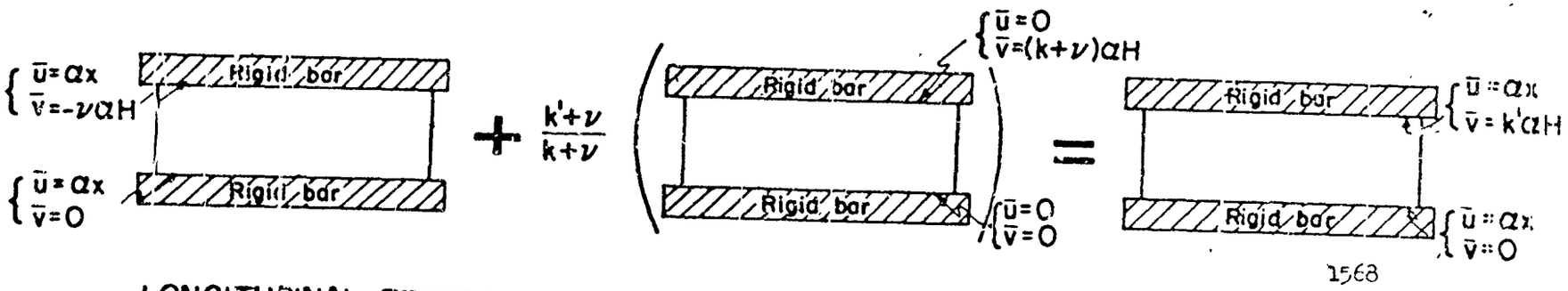

LONGITUDINAL RESTRAINT (photoelastic analysis)

TRANSVERSE RESTRAINT (above analysis)

VARIABLE BIAXIAL RESTRAINT (any value of k')

1568

FIGURE 36. SCHEMATIC DIAGRAM INDICATING THE PROCEDURE TO OBTAIN ANY RATIO OF BIAXIAL RESTRAINED SHRINKAGE [15]

a variety of other biaxial conditions. The difference itself (labeled transverse restraint in the figure) corresponds to the loading of a plate bonded to two rigid edges without shrinkage and then subjected to an applied displacement normal to the two edges. If this third loading condition (transverse restraint) is combined with the longitudinal restraint in different proportions, any ratio of biaxial restraint can be produced. Figure 36 shows the procedure used to obtain a loading condition with a biaxial restraint ratio k'. Stresses and strains can be combined following the same procedure. For example, the tangential stress along the free boundary for a value of biaxial restraint of, say, k' can be obtained by multiplying the value of the tangential stress associated with the transverse restraint by $(k'+\nu)/(k+\nu)$ and adding the result to the value of the longitudinal stresses associated with the longitudinal restraint. Durelli, et al, [13] present several representative examples of transverse restraint for the models shown in Fig. 35.

Peak values of τ_{max} and τ_{xy} are given in Figures 37 and 38. In the case of five of the corners, the peak value of τ_{max} did not appear on the interface, but occurred instead on the free boundary. These figures indicate that concave and outward corners are associated with more favorable stress conditions than convex, square or reentrant corners.

Stress concentrations were determined in another study [19] for slabs with different edge geometries bonded on one face and shrunk using three-dimensional photoelasticity. The results for five different geometries are presented in Fig. 39. These results supplement the earlier discussion of the analytical results of Dill, et al. [4].

CORNERS WITH PEAK τ_{max} ON INTERFACE		
TYPE OF CORNER	PEAK VALUE OF $\tau_{max}/E\alpha$	PEAK VALUE OF INTERFACE SHEAR $\tau_{xy}/E\alpha$
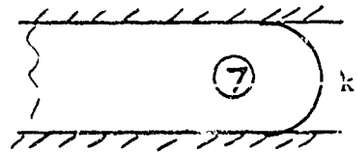	2.9	2.7
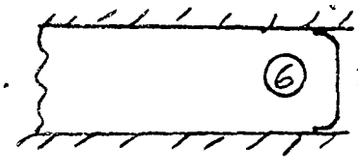	2.2	2.1

CORNERS WITH PEAK τ_{max} ON FREE BOUNDARY	
TYPE OF CORNER	PEAK VALUE OF $\tau_{max}/E\alpha$
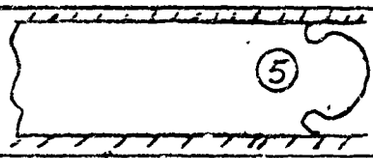	1.9
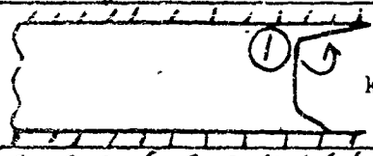	1.8
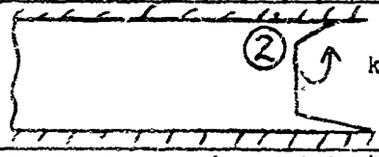	1.5
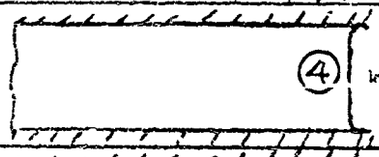	1.4
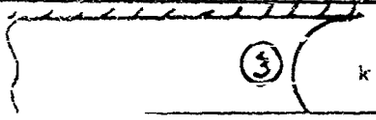	1.0

FIGURE 37. COMPARISON OF STRESSES IN THE NEIGHBORHOOD OF CORNERS IN PLATES SUBJECTED TO BIAXIAL RESTRAINT[15]

CORNERS WITH PEAK τ_{max} ON INTERFACE		
TYPE OF CORNER	PEAK VALUE OF $\tau_{max}/E\alpha$	PEAK VALUE OF INTERFACE SHEAR $\tau_{xy}/E\alpha$
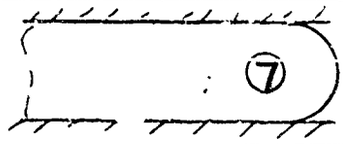 ⑦	1.6	1.0
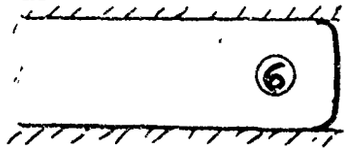 ⑥	1.7	1.4

CORNERS WITH PEAK τ_{max} ON FREE BOUNDARY	
TYPE OF CORNER	PEAK VALUE OF $\tau_{max}/E\alpha$
 ⑤	1.0
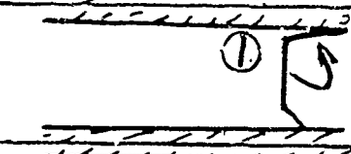 ①	0.9
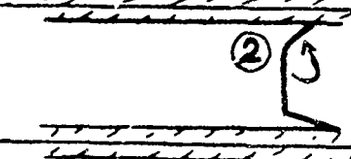 ②	0.6
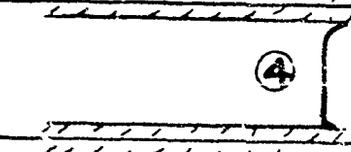 ④	1.0
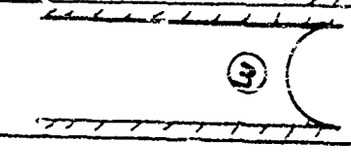 ③	0.6

FIGURE 38. COMPARISON OF STRESSES IN THE NEIGHBORHOOD OF CORNERS IN PLATES SUBJECTED TO LONGITUDINAL RESTRAINT[75]

GEOMETRY	$K = \max \tau_{max} / E\alpha$
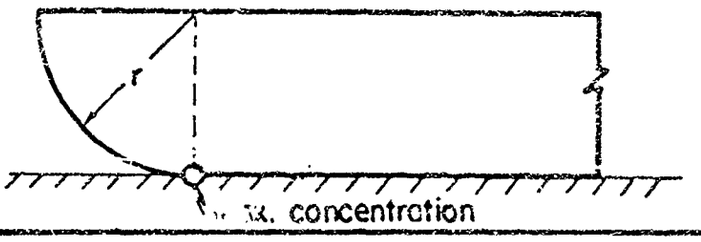	3.4
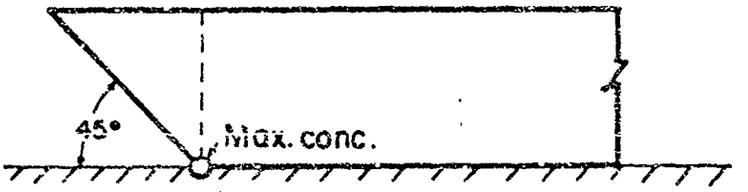	3.3
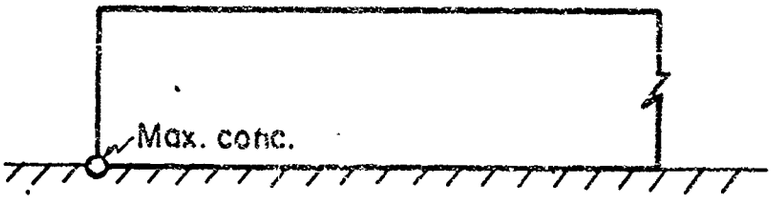	3.0
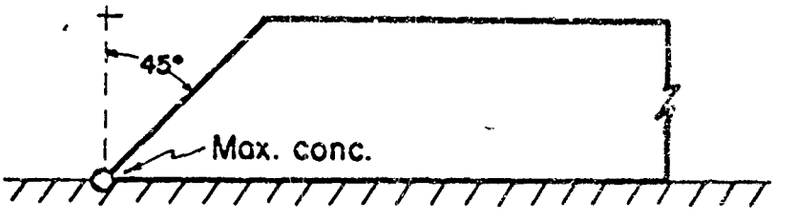	1.9
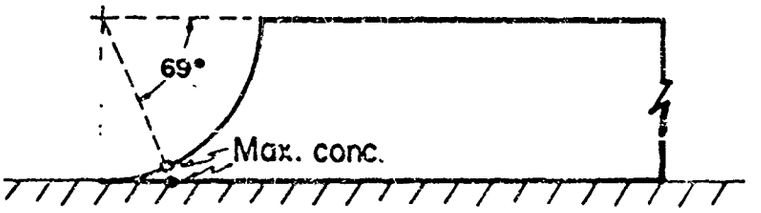	1.7

FIGURE 39.

STRESS CONCENTRATION FACTORS IN THE CENTRAL CROSS-SECTION OF SQUARE SLABS BONDED ON ONE SIDE AND SHRUNK (PLANE STRAIN) [19]

The stress concentration factors in three cylinders of revolution bonded to shells and shrunk are shown in Fig. 40 [22]. The shells were made of fiberglass reinforced epoxy, and three dimensional photoelasticity and the Moire method were used in the analysis. The results of this investigation indicated that the flexibility and anisotropy of the rocket motor case may have a significant effect on the stress distribution in the propellant grain models.

Complementing their earlier studies, Durelli and co-workers determined the stress concentration associated with the end of a strip bonded on one side, when the end has the shape of a wedge and the angle of the tip is varied from 0 to 180 degrees, under a subcontract to Atlantic Research Corporation [23]. Stress concentration factors for the end angles are shown in Fig. 41 for corner radii of 0.125, 0.03125, and < 0.0001 inches. The peaks of stress concentration occur at approximately $\phi = 90°$ as well as $\phi = 0$. The optimum acute angle appears to be in the neighborhood of 60°. For reasonably controlled radii, it is seen that the stress does not change significantly for angles below 90°. It is also noted that the position of maximum stress is not located at the interface, but somewhere above. This position changes as the angle ϕ changes; however, the location is essentially constant for angles below 120° as Fig. 42 shows for $R = 0.125$ inches.

Under the same subcontract long plates having a semi-circular end were bonded both partially and totally to rigid frames, and elliptical holes were located near the boundary either at the apex or at the transition between the straight and circular boundaries. The stress concentrations around the elliptical holes were determined when the plate

GEOMETRY	max $\frac{\tau_{max}}{E\alpha^*}$
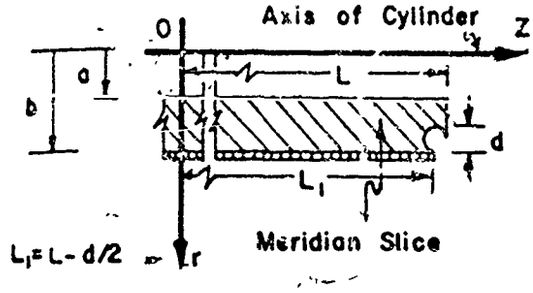 $\frac{2l}{2b} = 2.60, \frac{b}{a} = 2.70, \frac{d}{b-a} \approx 0.25$	6.6
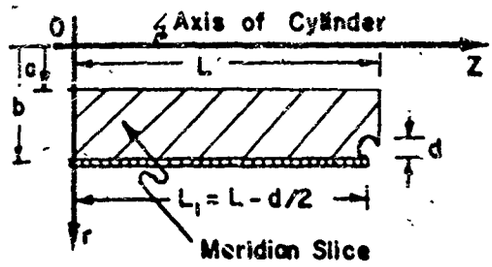 $\frac{2L}{2b} = 1.25$, $\frac{b}{a} = 2.40$, $\frac{d}{b-a} \approx 0.33$	5.
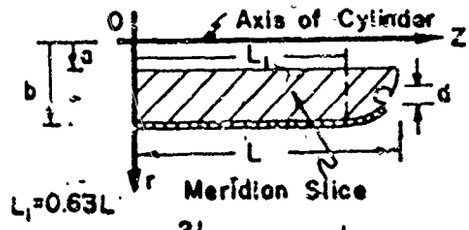 $\frac{2L}{2b} = 1.29$ $\frac{b}{a} = 2.33$ $\frac{d}{b-a} \approx 0.29$	4.0

FIGURE 40.

STRESS CONCENTRATION FACTORS IN THREE CYLINDERS OF REVOLUTION BONDED TO SHELLS AND SHRUNK .[22]

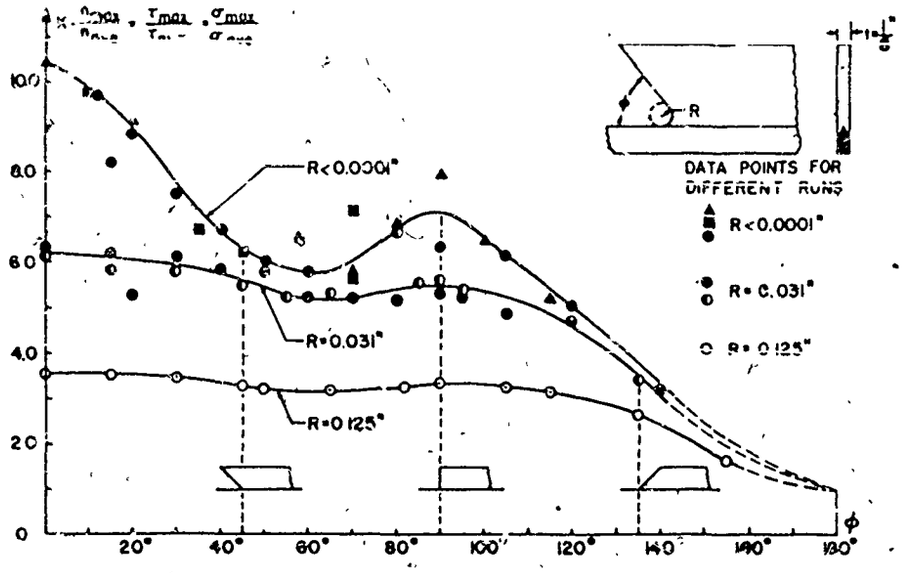

FIGURE 41. PARAMETRIC STRESS CONCENTRATION FACTORS FOR VARIOUS ANGULAR CORNERS[25]

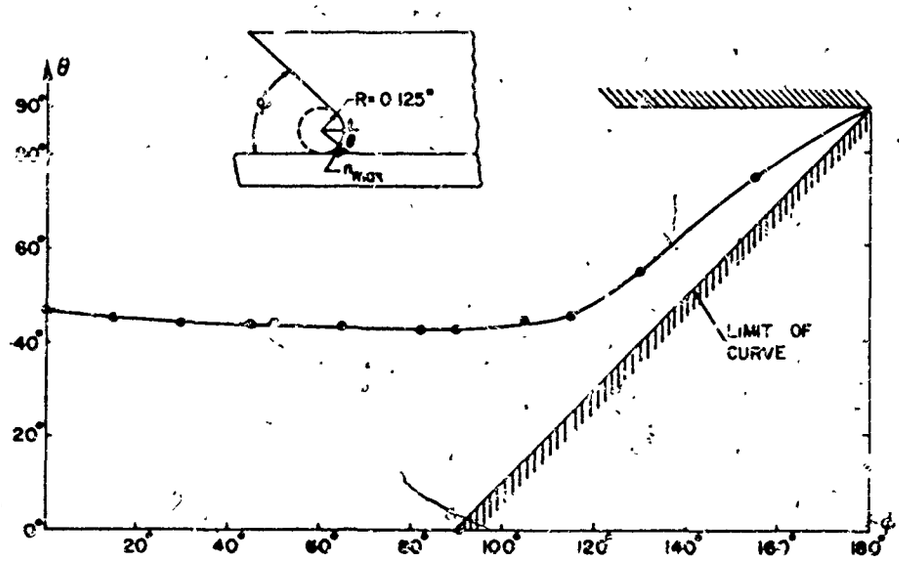

FIGURE 42. POSITIONS OF MAXIMUM STRESS AT VARIOUS ANGULAR CORNERS[23]

was subjected to restrained shrinkage. These concentration factors are shown in Figures 43 and 44. It is seen that the maximum stresses associated with the ellipse which has its major axis parallel to the longitudinal directions are smaller than the stresses associated with the ellipse which has its major axis parallel to the transverse direction. In both cases the peak values of the stress concentration factor takes place at a/D = 0.3.

In the case of the elliptical holes located at the point of discontinuity between bonded and unbonded boundaries, (Fig. 44) the relative value of stress concentration factors for the two positions of the ellipses is opposite to the previously mentioned result. The maximum stresses in the elliptical hole with its major axis in the transverse axis was found to be smaller than those at the hole with its major axis in the longitudinal direction.

By plotting stress concentration factors against the dimensionless area of the hole, another set of curves can be obtained. Those are shown in Figures 45 and 46, respectively, for the case of various elliptical holes tangent at the apex, and the case of various elliptical holes tangent at the discontinuity of bond. The stress concentration decreases in both cases when the elliptical hole becomes a circular hole. This may also be observed from a family of curves obtained by expressing concentration factors in terms of the ratio of the ratio of major to minor axis of the ellipse as given in Fig. 47. All curves have minimum values as a/b approaches unity.

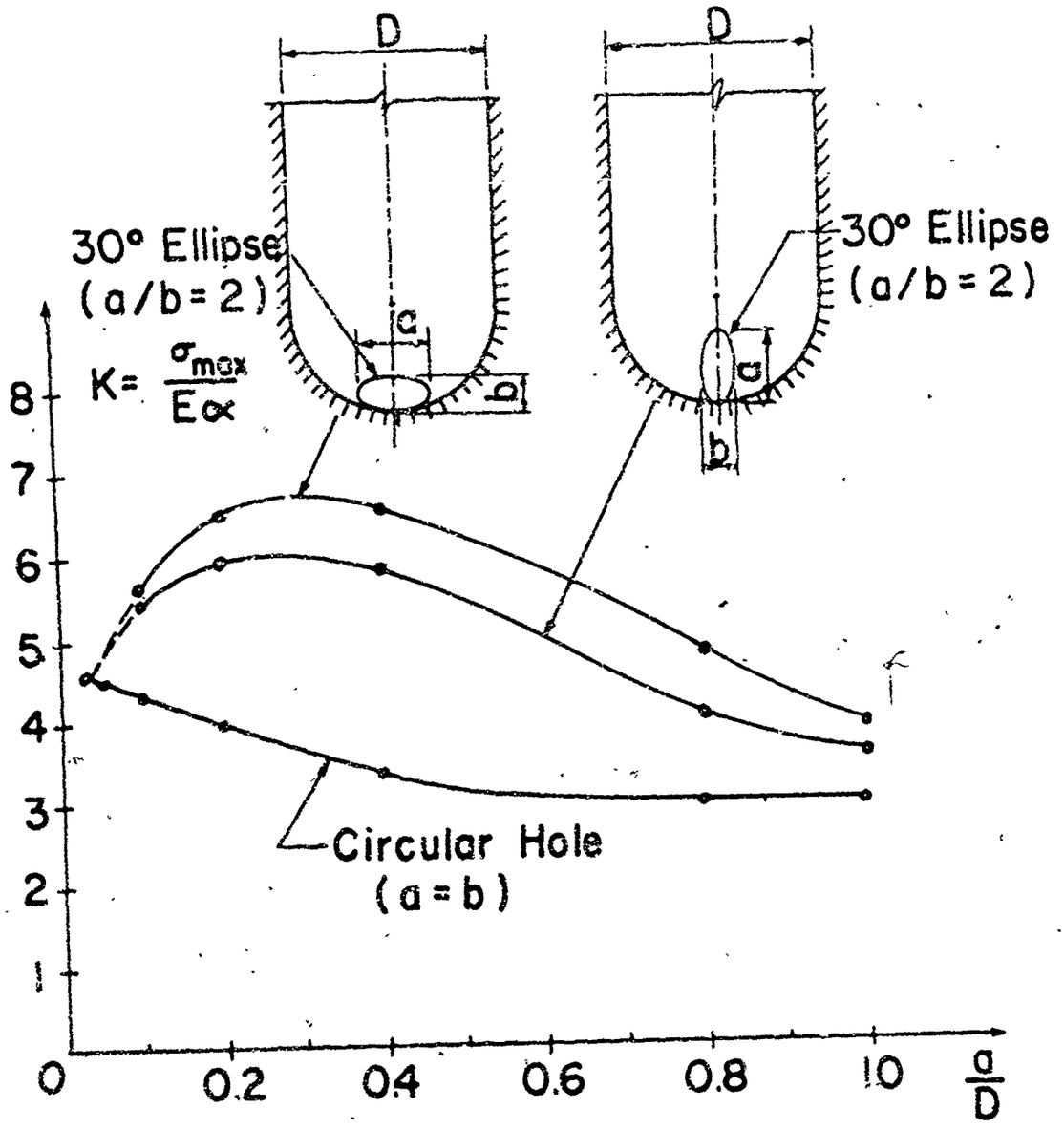

FIGURE 43.

PARAMETRIC STRESS CONCENTRATION FACTORS FOR VARIOUS ELLIPTICAL HOLES TANGENT AT THE APEX, IN THE PLATE SUBJECTED TO RESTRAINED SHRINKAGE [23]

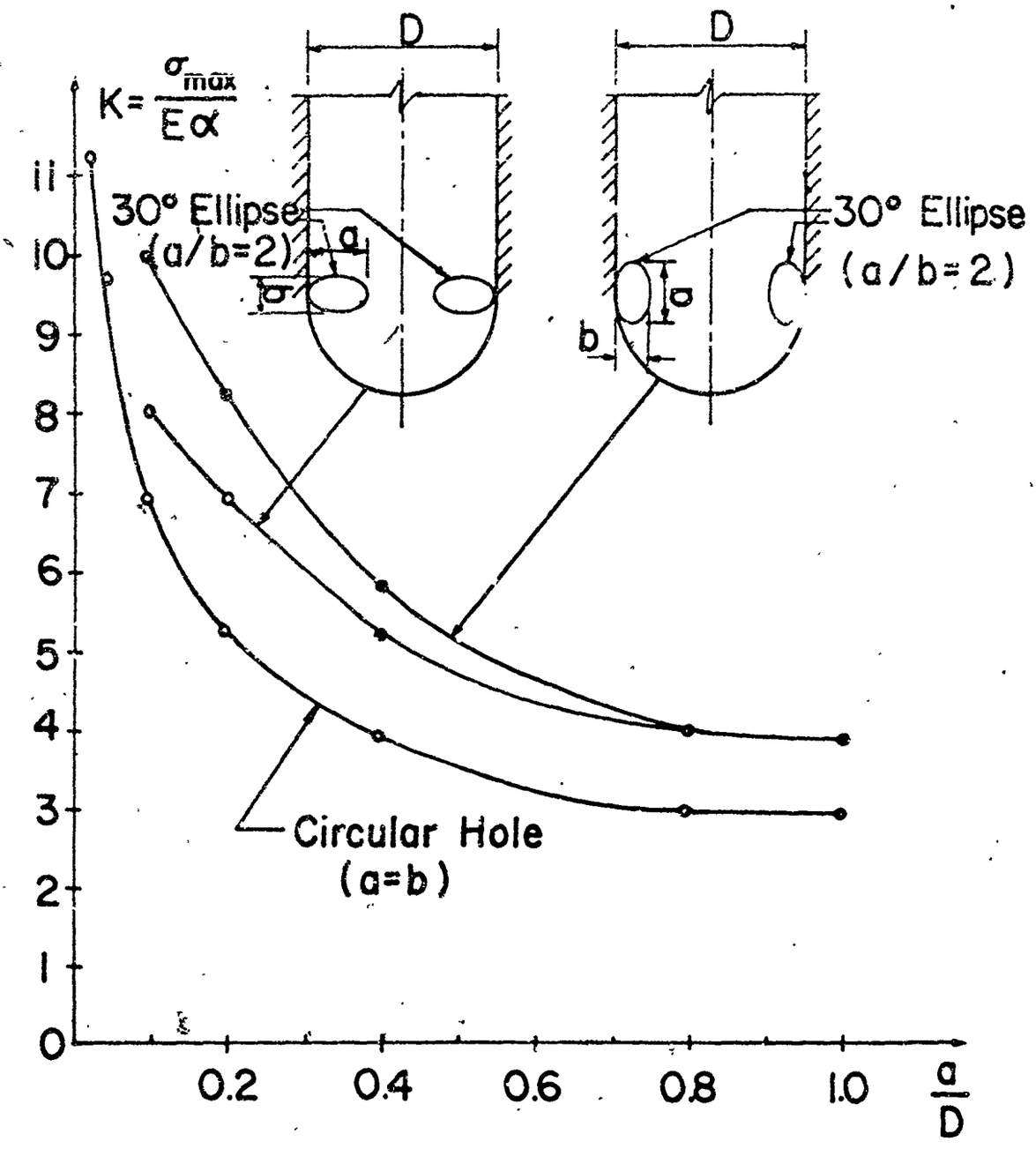

FIGURE 44.

PARAMETRIC STRESS CONCENTRATION FACTORS FOR VARIOUS ELLIPTICAL HOLES TANGENT AT THE DISCONTINUITY OF BOND, IN THE PLATE SUBJECTED TO RESTRAINED SHRINKAGE [23].

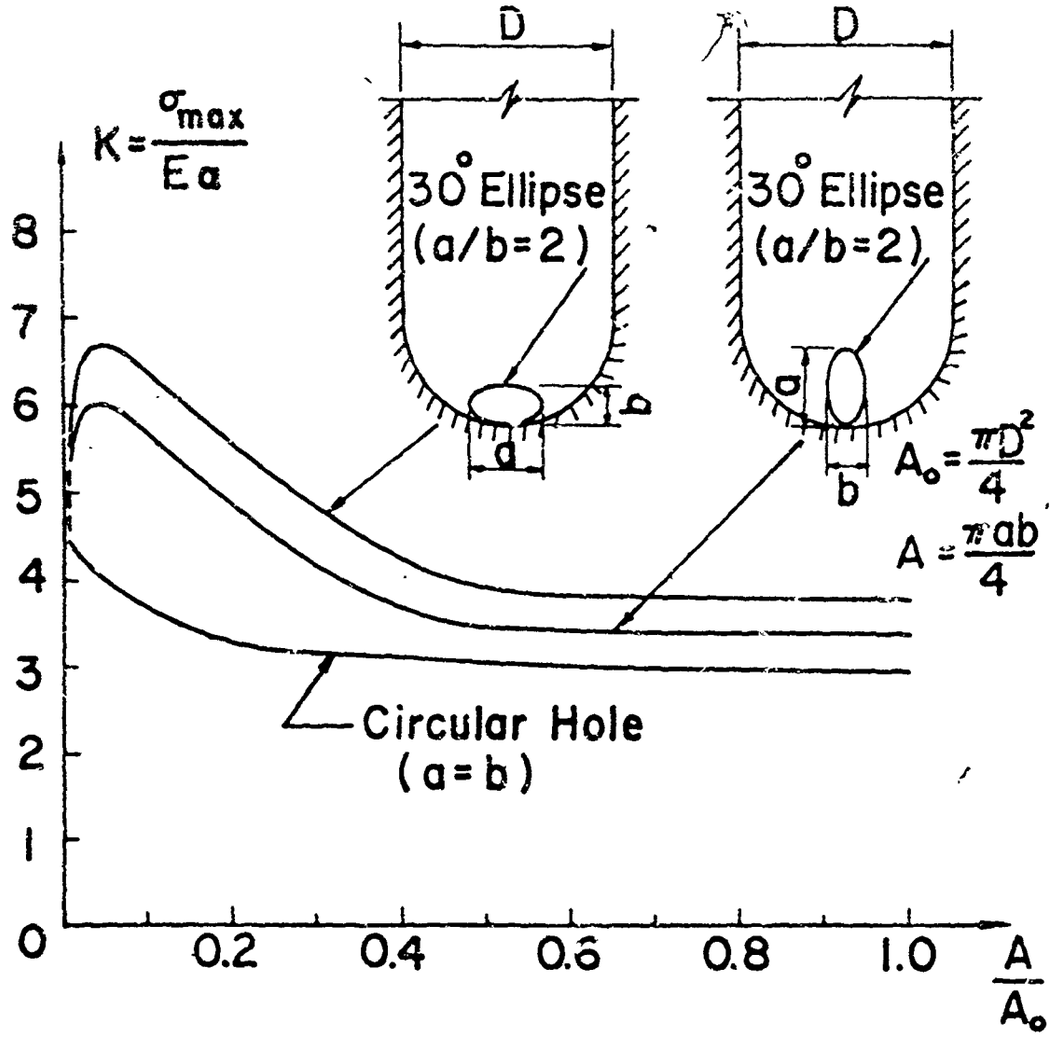

FIGURE 45.

PARAMETRIC STRESS CONCENTRATION FACTORS FOR VARIOUS ELLIPTICAL HOLES TANGENT AT THE APEX, IN THE PLATE SUBJECTED TO RESTRAINED SHRINKAGE [23]

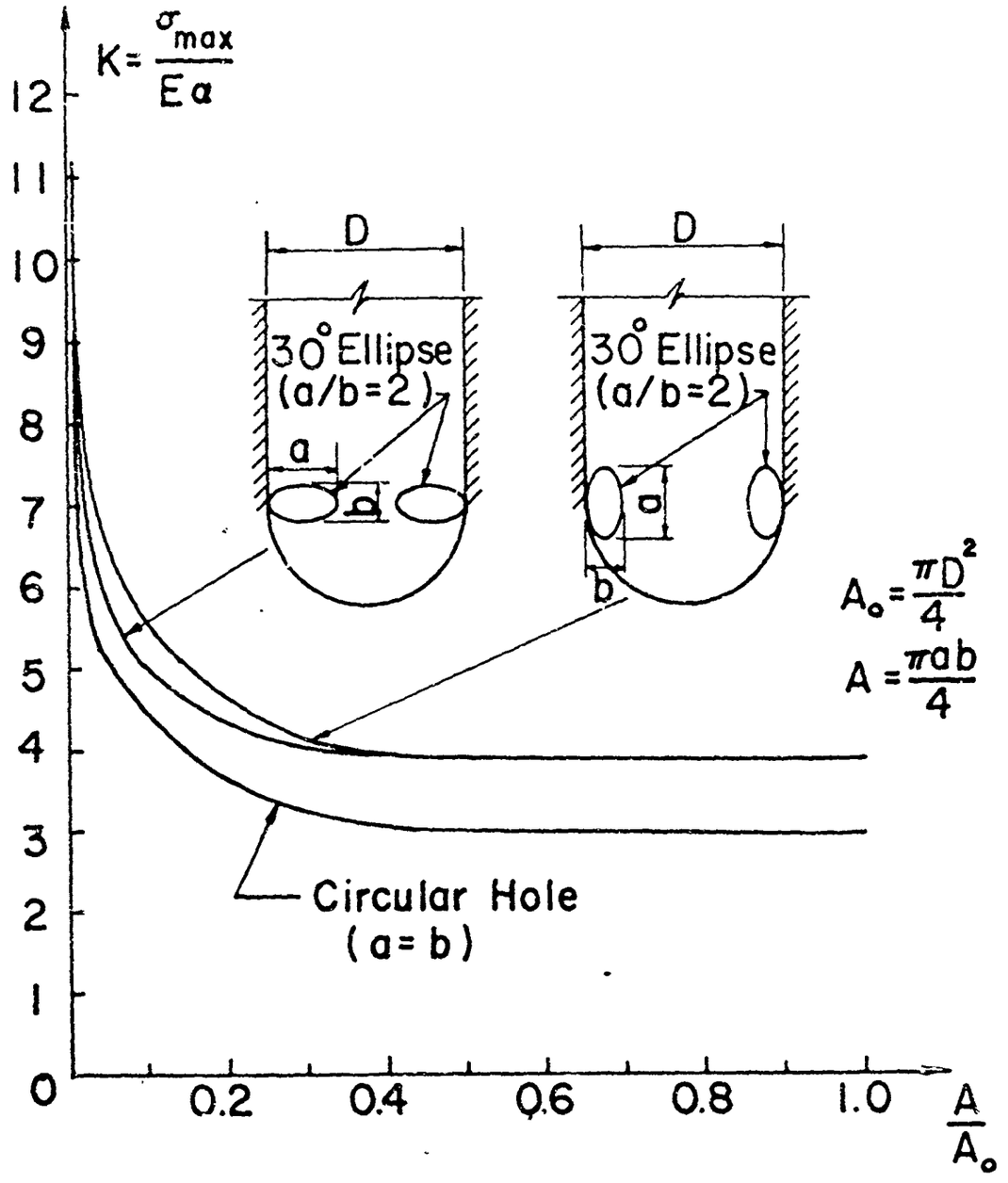

FIGURE 46.

PARAMETRIC STRESS CONCENTRATION FACTORS FOR VARIOUS ELLIPTICAL HOLES TANGENT AT THE DISCONTINUITY OF BOND, IN THE PLATE SUBJECTED TO RESTRAINED SHRINKAGE[23]

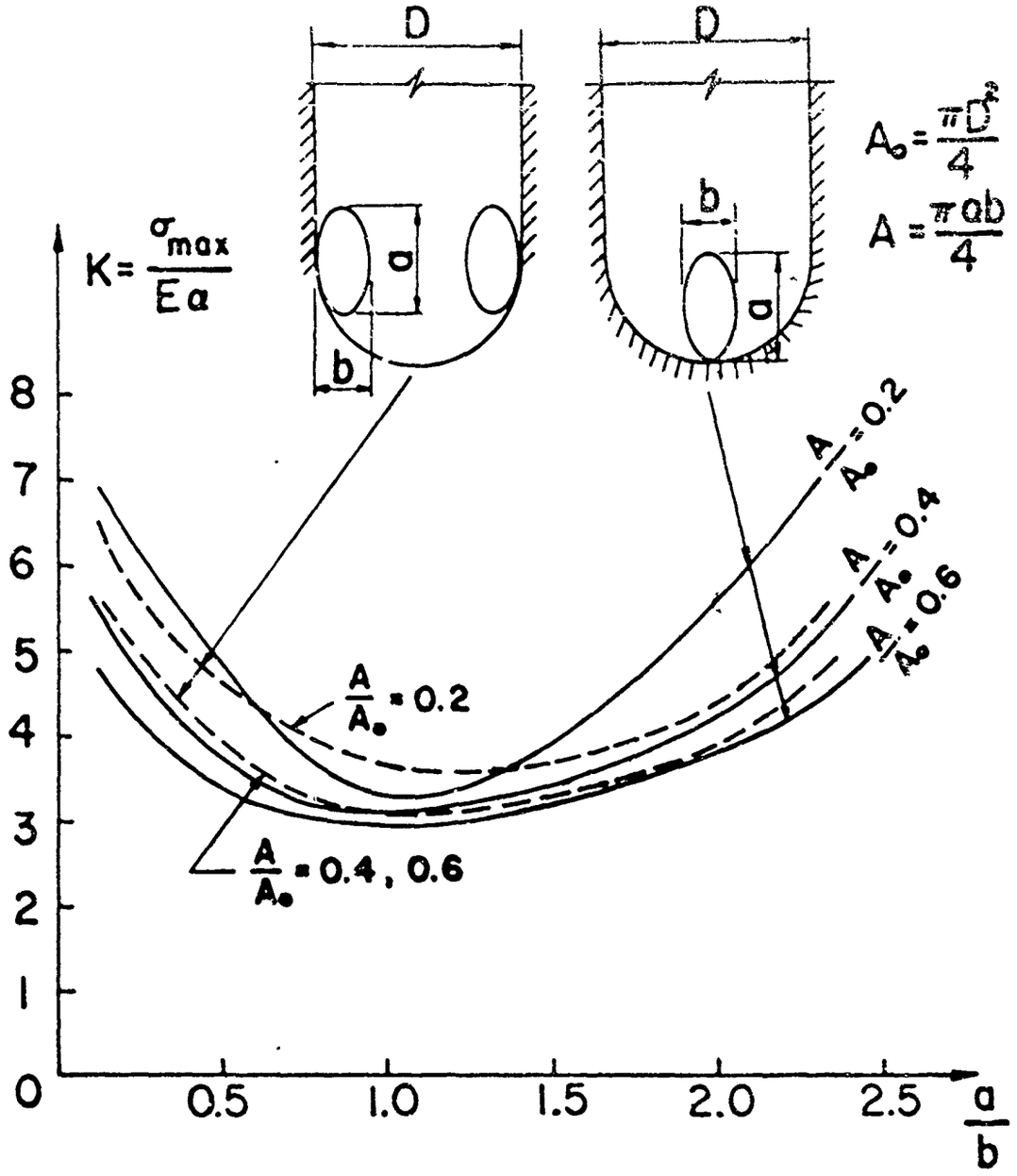

FIGURE 47.

PARAMETRIC STRESS CONCENTRATION FACTORS FOR VARIOUS RATIO OF ELLIPTICAL PERFORATIONS IN THE PLATES SUBJECTED TO RESTRAINED SHRINKAGE[23]

Additional two-dimensional studies were conducted to evaluate the effects of multiple notches (in the form of circular holes) along the case-propellant interface in the vicinity of the grain ends. The results obtained indicate that additional stress relief notches beyond the first one do not offer any significant advantage over the single circular fillet as may be seen from Fig. 48.

Based on available photoelastic data, Atlantic Research Corporation [23] conducted an experimental evaluation program using analogue motors with the aft-end grain shapes shown in Fig. 49. The square corner was selected as a reference.

A parametric stress analysis was first conducted for circular fillets in order to better evaluate the effect of various parameters upon the state of stress at the propellant grain end termination. The geometry of the fillet is shown in Fig. 50. The numerical solutions obtained for three web fractions and three fillet radii at each web are presented in Figures 51 through 56. The quantity δ is the differential linear thermal strain between the case and the propellant and E is the equivalent elastic modulus of the propellant. The other quantities in the figures are defined as

σ_f^* = Maximum Effective Fillet Stress

σ_b^* = Plane Strain Effective Bore Stress

σ_t = Tangential Fillet Stress

σ_r = Radial Stress at Grain-Case Interface

τ_{rz} = Shear Stress at Grain-Case Interface

$K_F = \sigma_f^*/\sigma_b^*$ = Stress Ratio at Fillet.

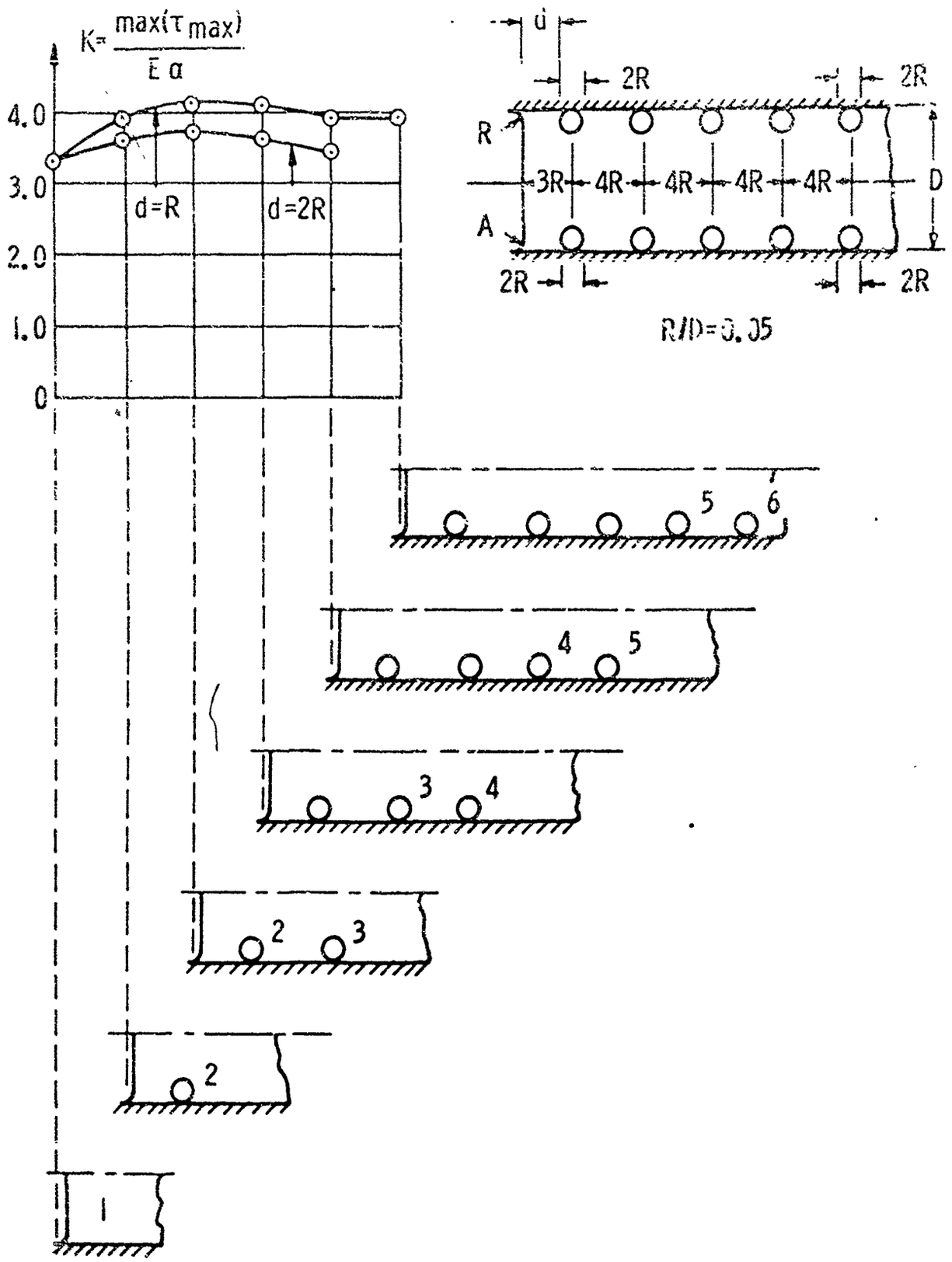

FIGURE 48.

STRESS CONCENTRATION IN RECTANGULAR PLATES WITH ROWS OF HOLES ALONG TWO BONDED BOUNDARIES, SUBJECTED TO RESTRAINED SHRINKAGE[23]

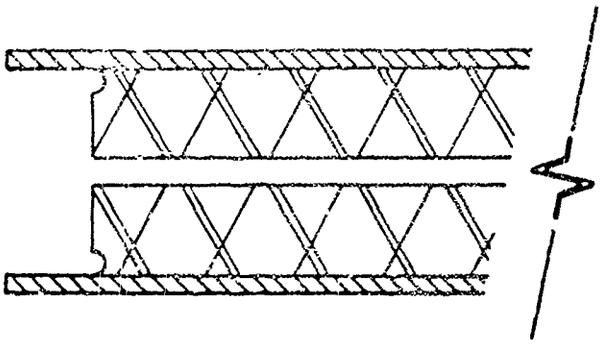

a. Semi-Circle

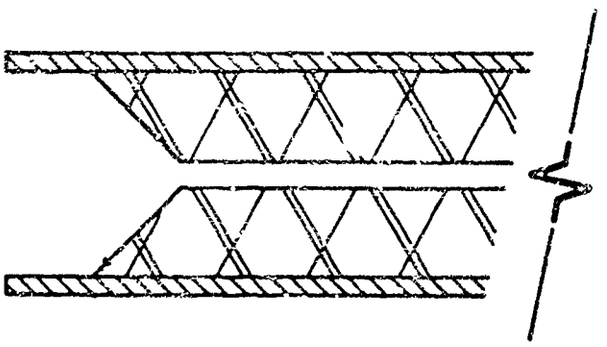

b. 45-Degree Angle

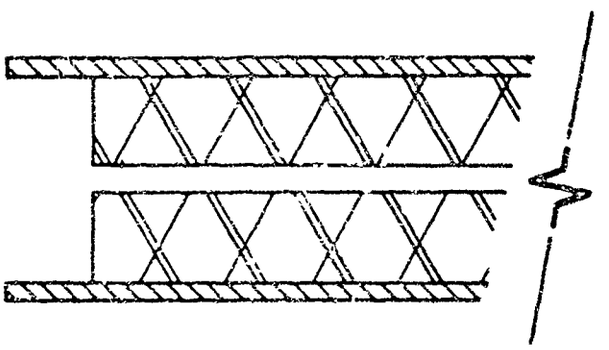

c. Square Corner (Reference)

FIGURE 49. SHAPES FOR PROPELLANT MODEL STUDIES BASED ON PHOTOELASTIC STUDY[23]

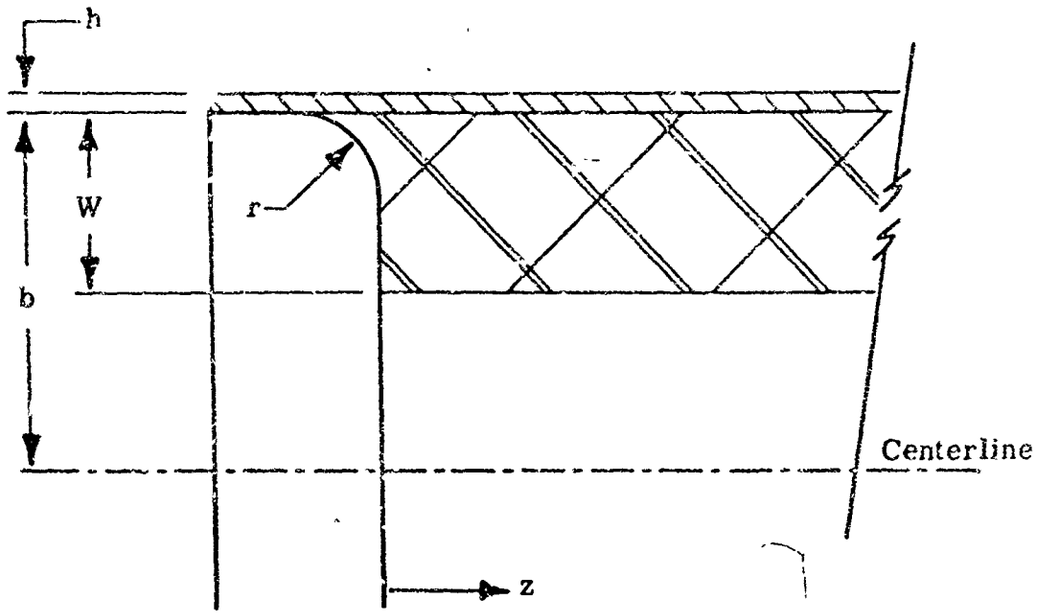

FIGURE 50. TYPICAL FILLET GEOMETRY[23]

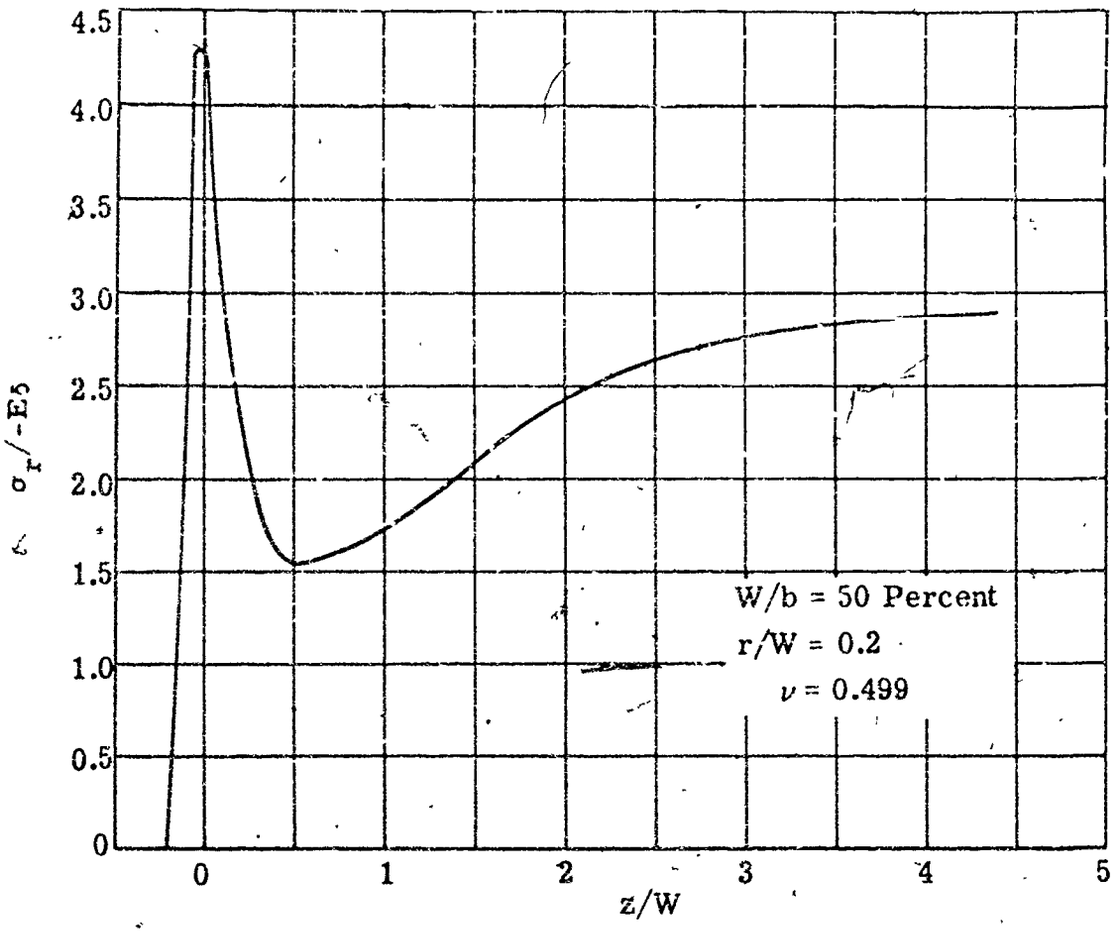

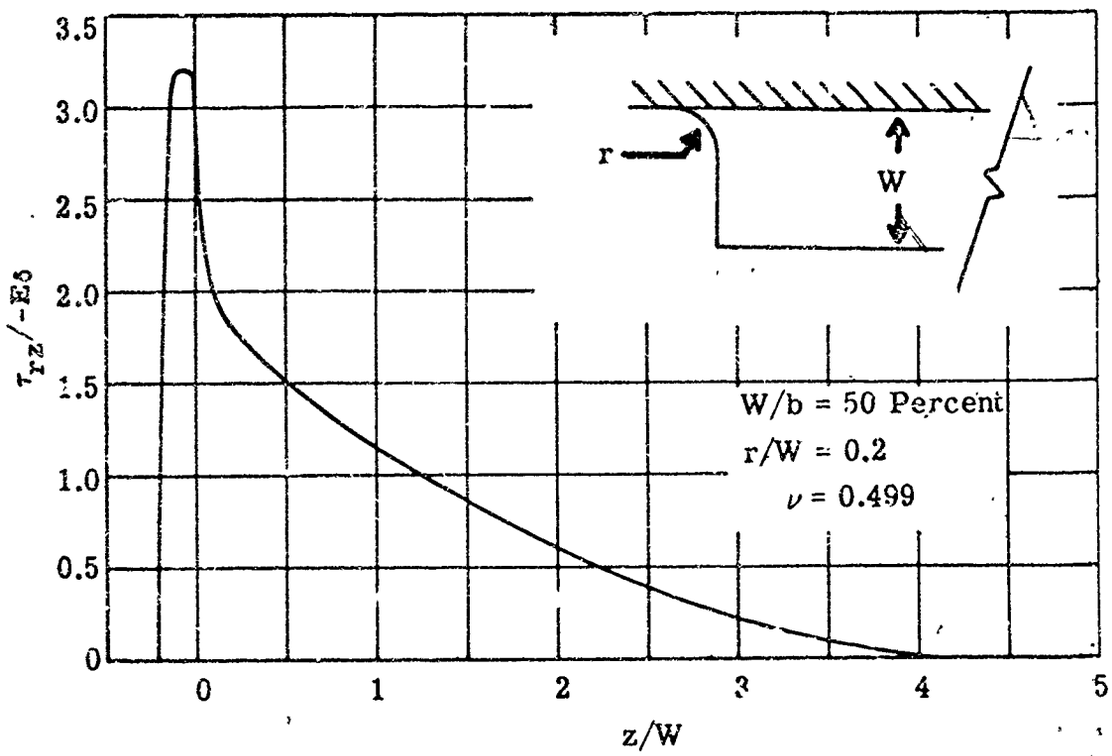

FIGURE 51. STRESS DISTRIBUTION AT THE CASE-GRAIN INTERFACE[23]

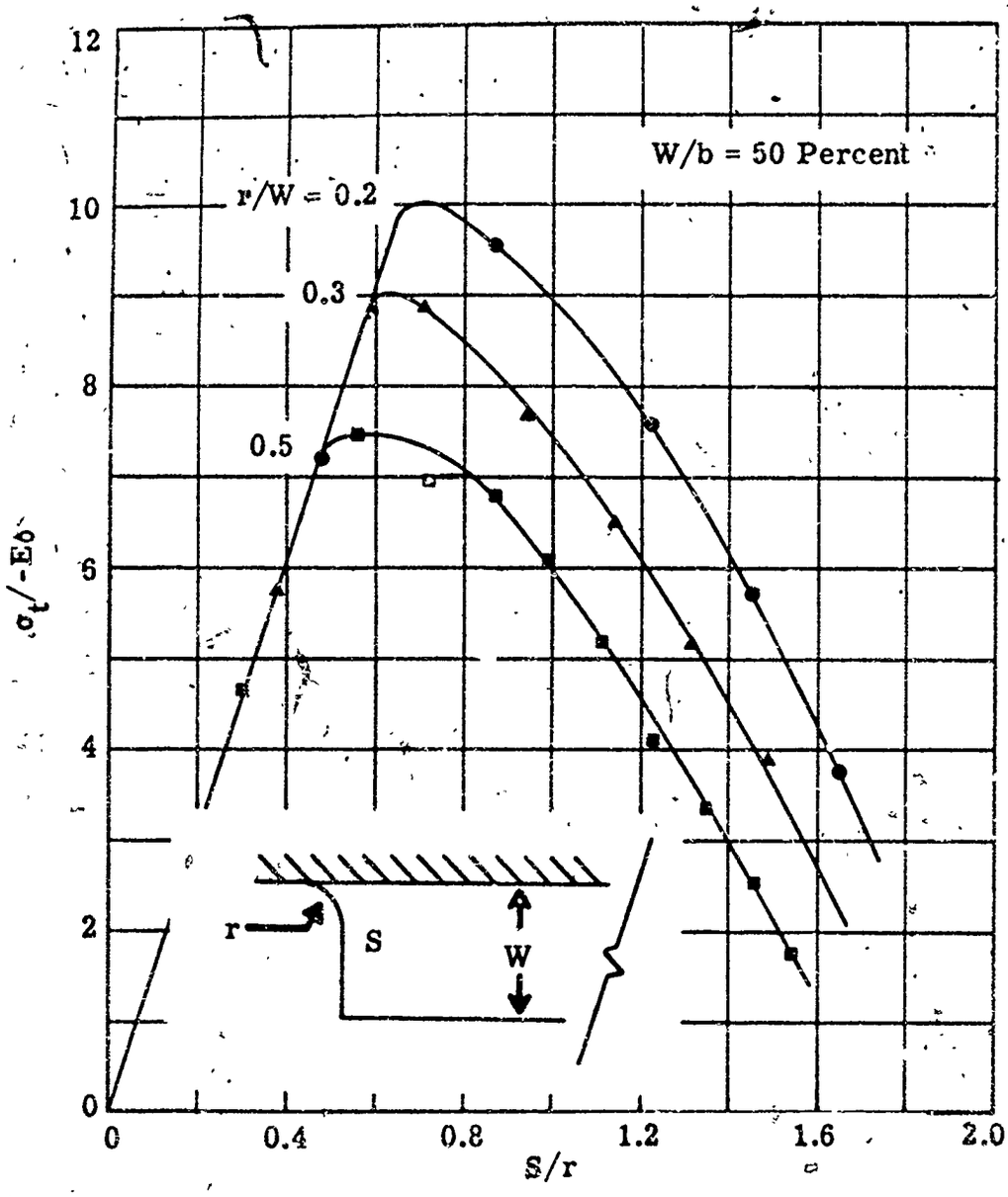

FIGURE 52. TANGENTIAL STRESS AT THE CONICAL FILLET[23]

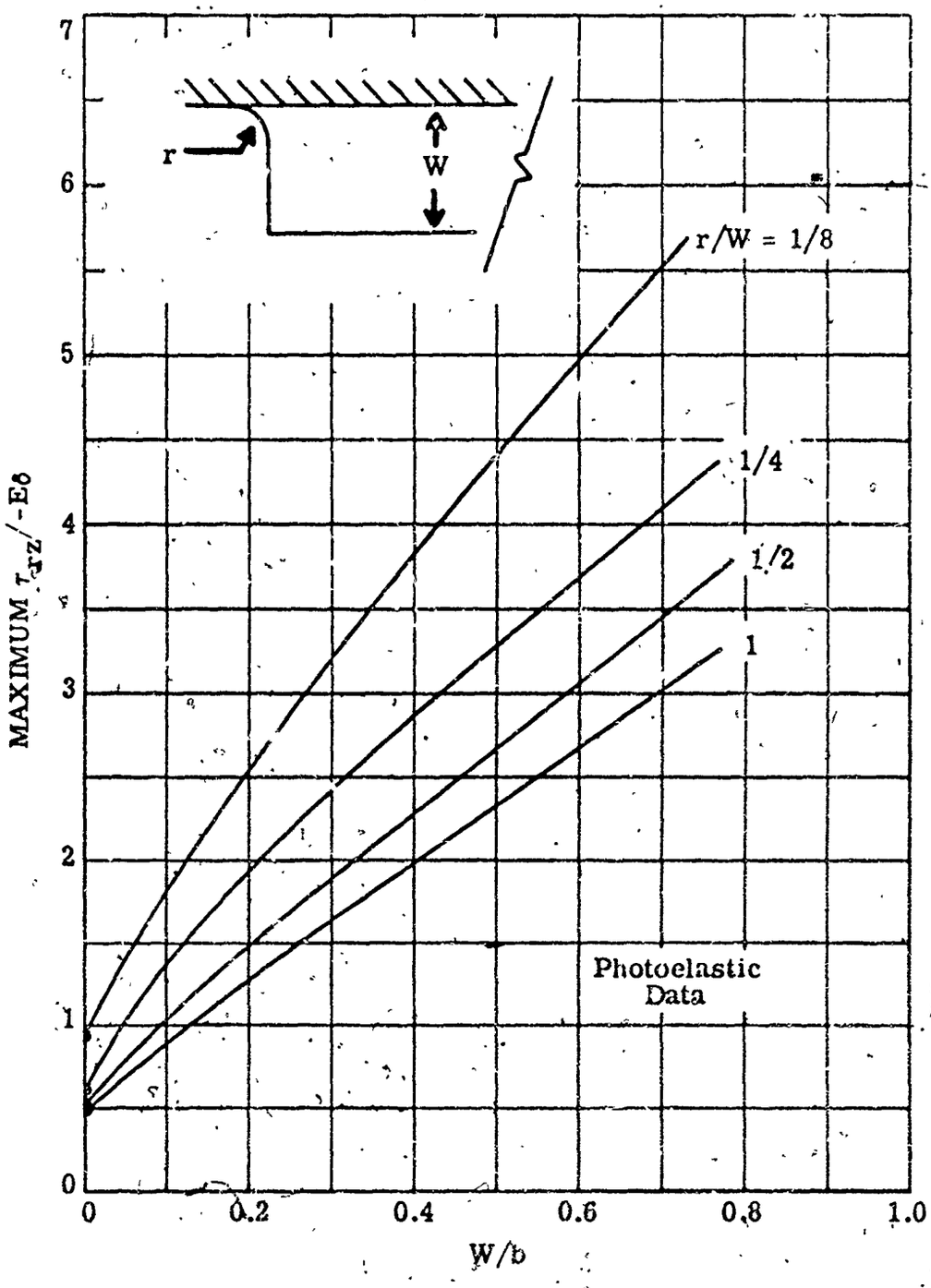

FIGURE 53. MAXIMUM INTERFACE SHEAR STRESS AT THE CIRCULAR FILLET[23]

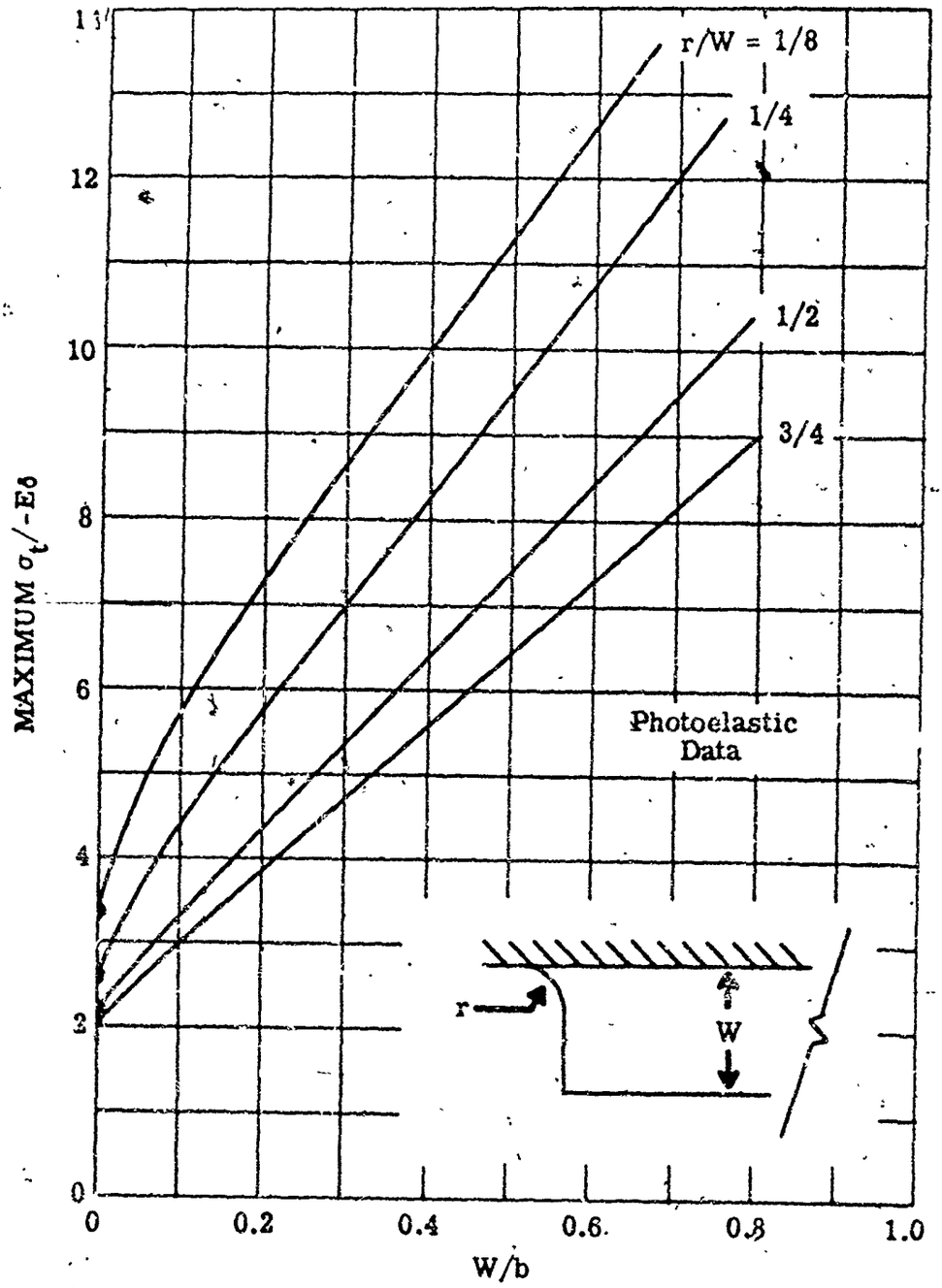

FIGURE 54. MAXIMUM TANGENTIAL STRESS AT THE CIRCULAR FILLET[23]

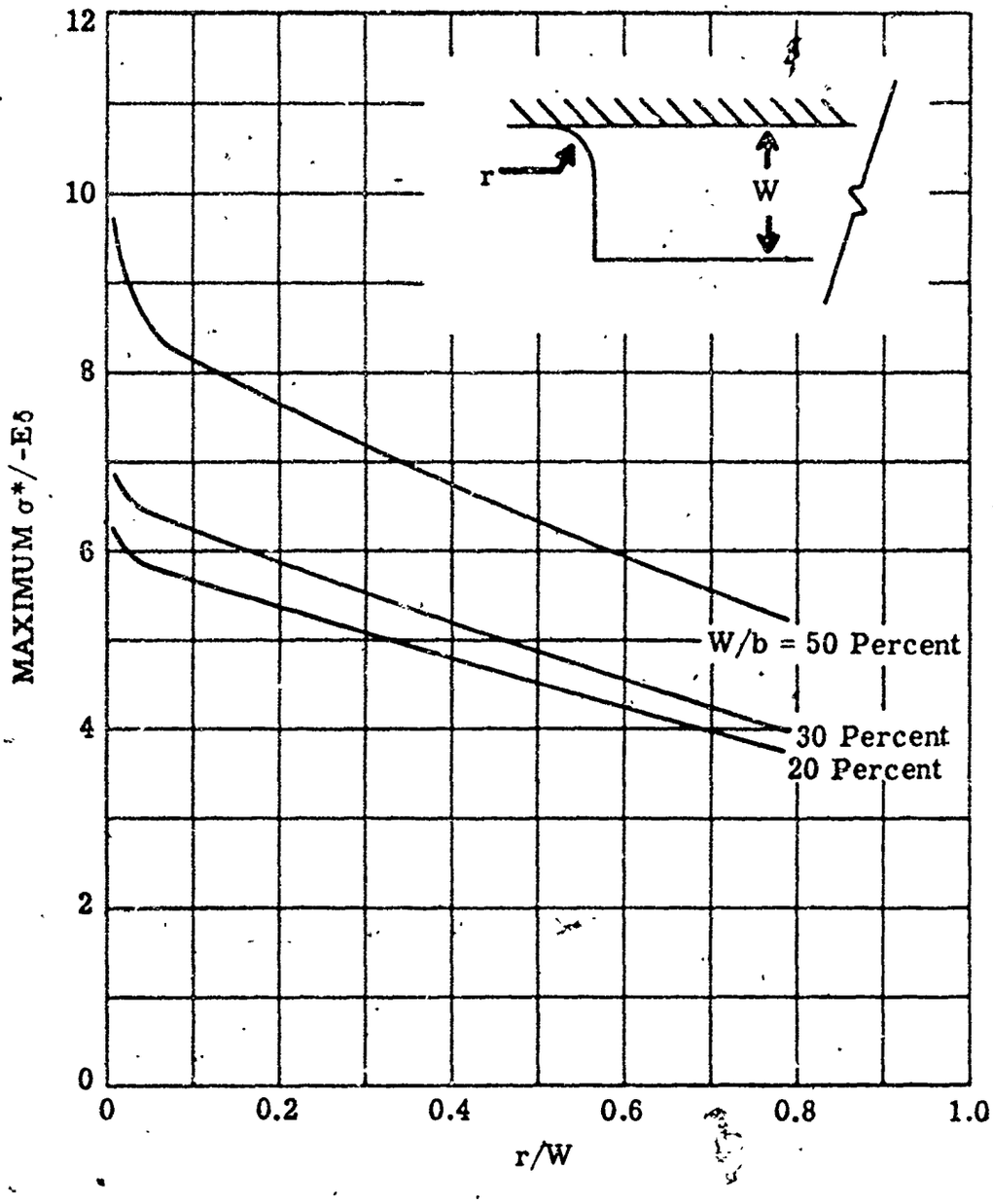

FIGURE 55. MAXIMUM EFFECTIVE STRESS AT THE CIRCULAR FILLET[23]

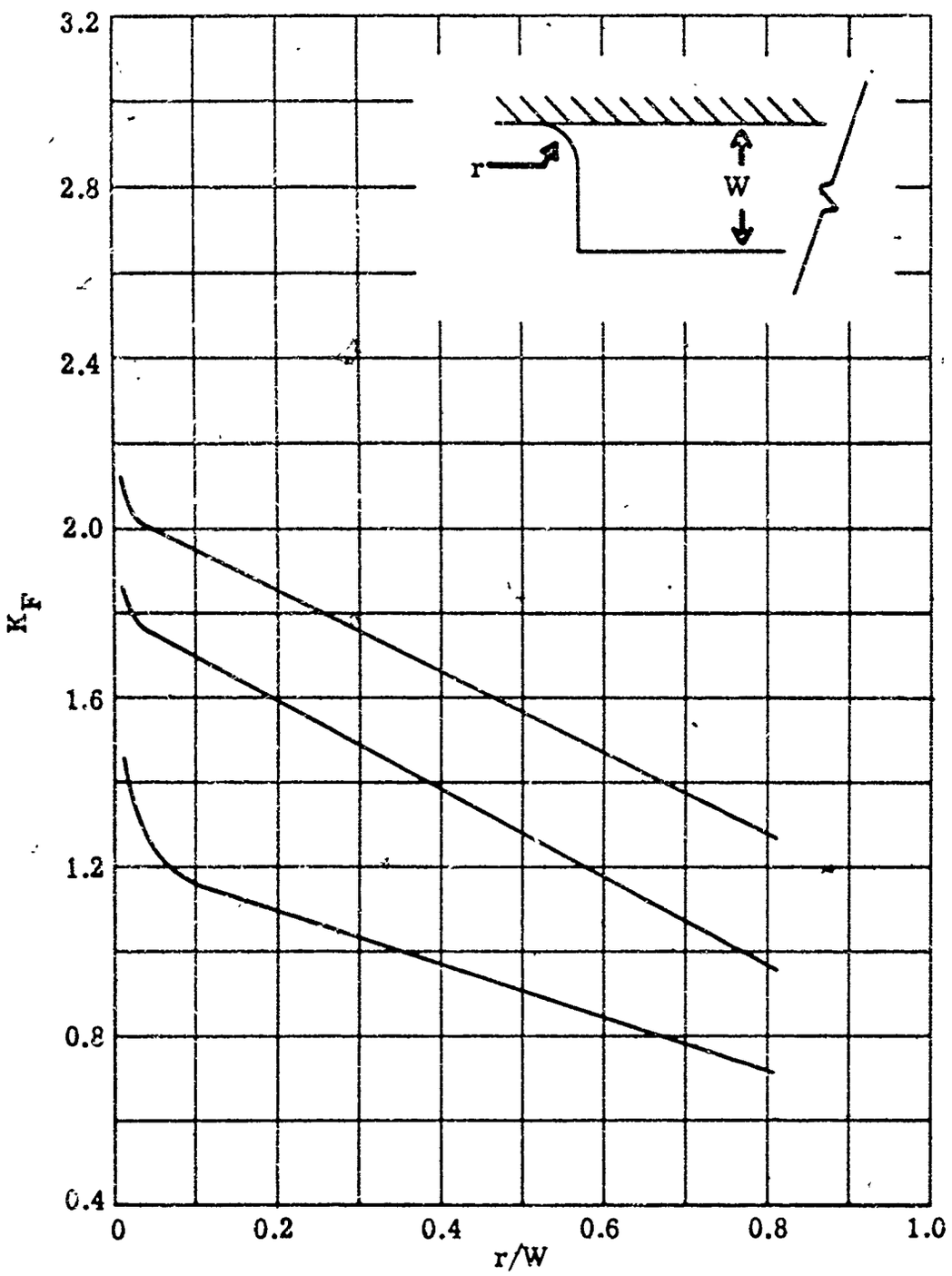

FIGURE 56. MAXIMUM STRESS RATIO AT THE CIRCULAR FILLET[23]

The effective stress in this study was used to compare the state of stress in the motor with uniaxial tensile data, and is given by

$$\sigma^* = \frac{1}{\sqrt{2}} [(\sigma_r-\sigma_\theta)^2 + (\sigma_\theta-\sigma_z)^2 + (\sigma_z-\sigma_r)^2 + 6\tau_{rz}^2]^{\frac{1}{2}}$$

The results show that the stress ratio, K_F, increases with decreasing fillet radius and/or decreasing web fraction. To have failure at the fillet rather than at the inner bore, the stress ratio must be greater than one. Although decreasing the web fraction increases the probability of failure at the fillet, it is observed that the actual stress magnitude is lowered, and hence, a lower temperature is required for failure.

Besides the circular fillet analogue motors, three conical end terminations and a square end reference motor were made and tested. The analysis parametric curves for these geometries are shown in Fig. 57 through 59. The 45° partial cone or partial ramp results presented are for an end configuration designed to displace the same propellant volume as the 0.20 inch fillet radius.

Analogue motor tests were also conducted by Robinson, et al, to compare actual failure data with photoelastic and analytical investigations. The motors consisted of ten-inch long, fifty percent web fraction grains, case-bonded in four-inch diameter, heavy wall aluminum tubes. A PBAN propellant formulation (ARCADENE 212) was selected. The motor configurations are shown in Fig. 60. Several motors were made with each configurations and thermally cooled until failure was observed by radiographic inspection. Failure data are shown in Fig. 61. All failures occurred at the contoured end in the form of circumferential cracks. The predicted failure temperatures shown in Fig. 61 were

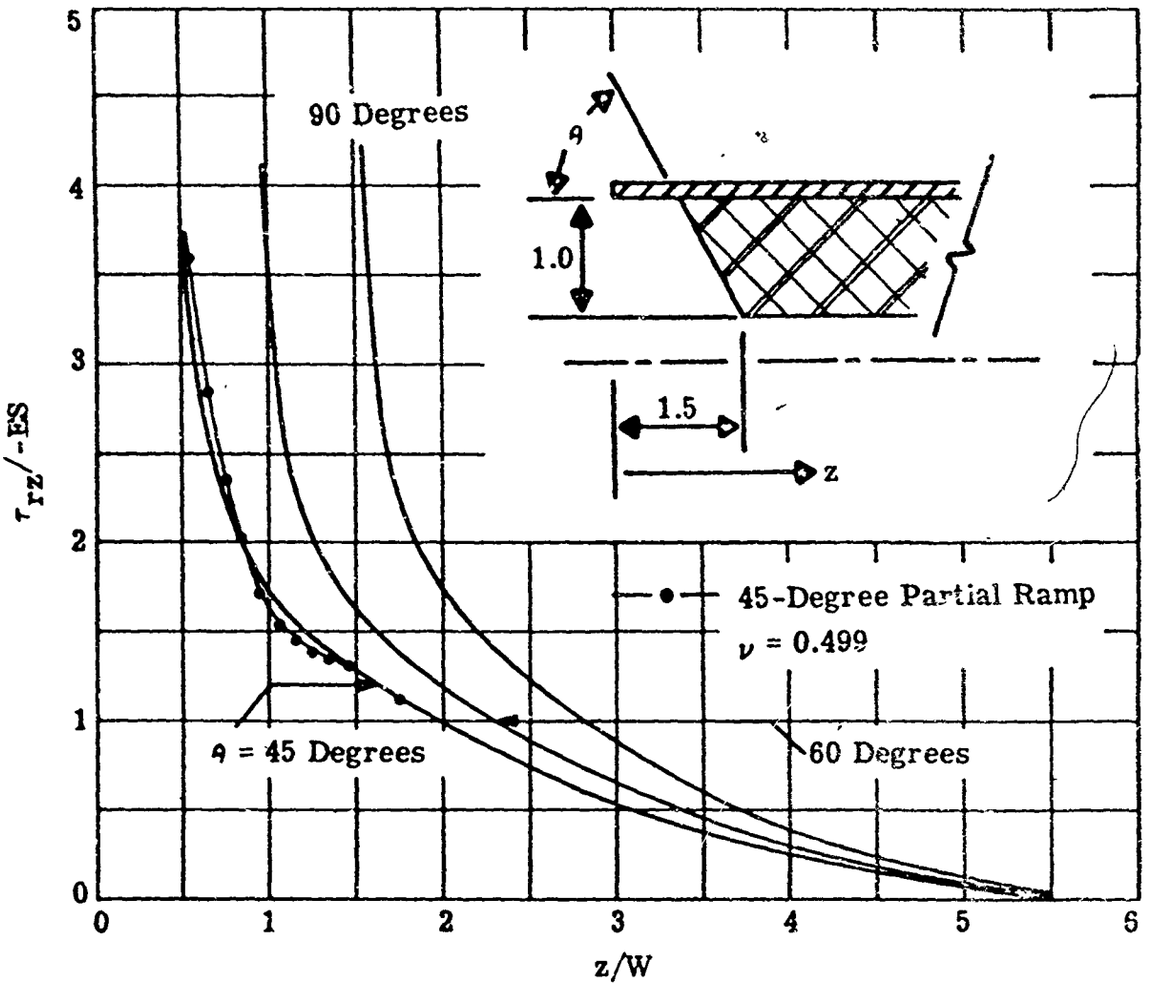

FIGURE 57. CASE BOND SHEAR STRESS FOR CONICAL END TERMINATIONS[23]

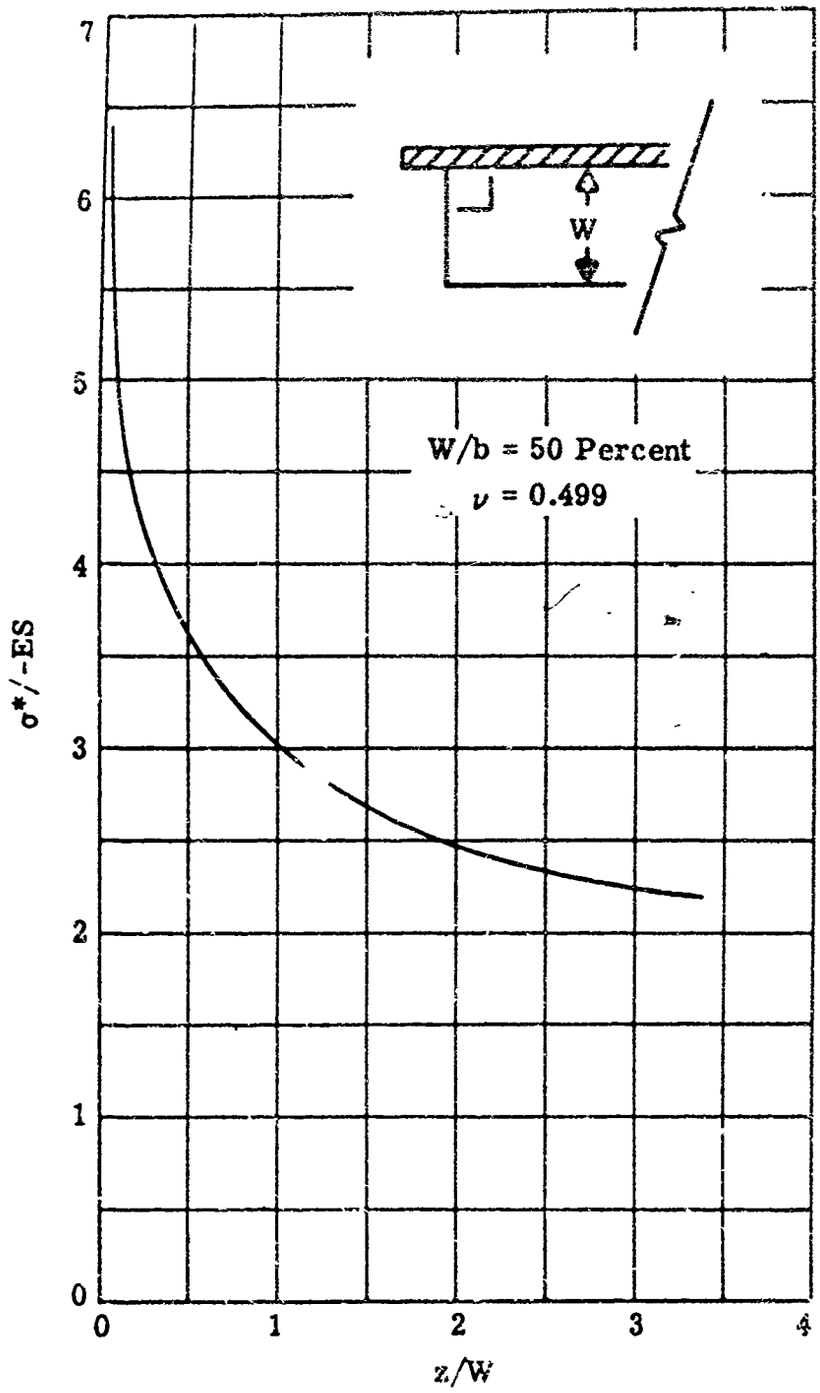

FIGURE 58. EFFECTIVE CASE BOND STRESS FOR THE SQUARE END TERMINATION GRAIN[23]

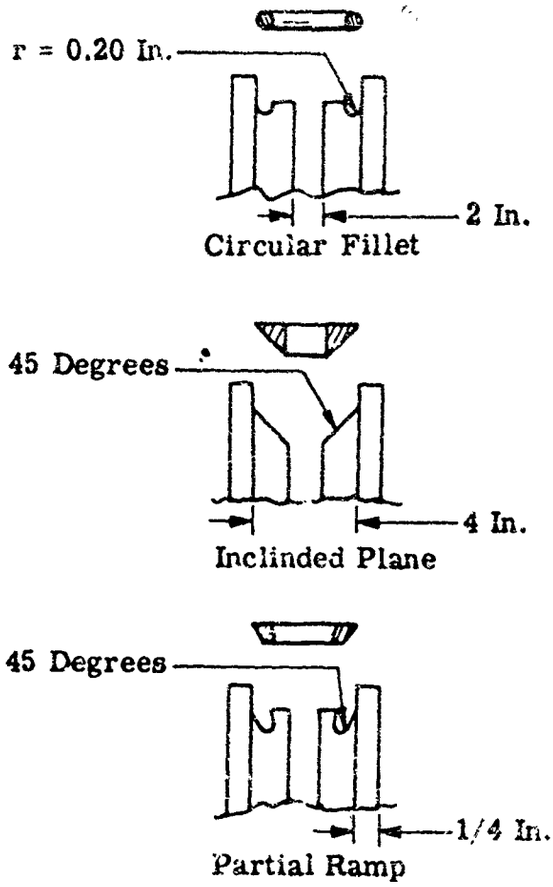

FIGURE 60. CROSS SECTION VIEW OF END GRAIN CONFIGURATIONS[23]

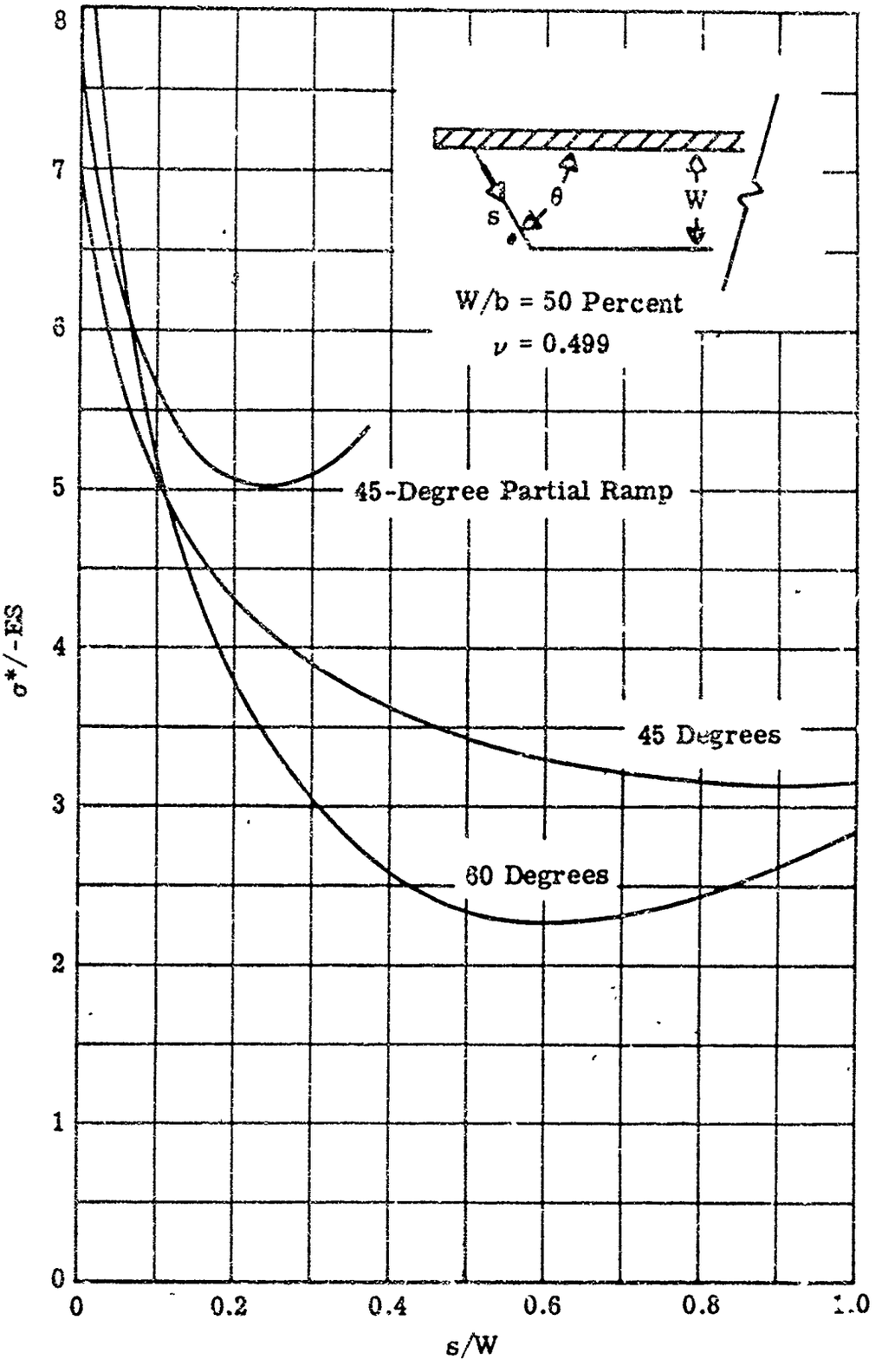

FIGURE 59. EFFECTIVE STRESS DISTRIBUTION AT THE CONICAL END TERMINATIONS[23]

	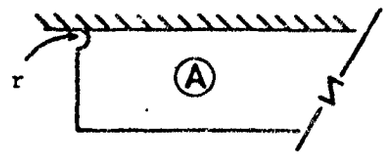 r = 0.05 In.	r = 0.10 In.	r = 0.20 In.	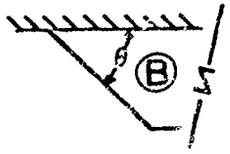 θ = 45°	θ = 60°	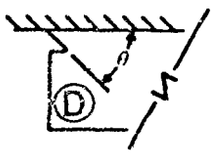 θ = 45°	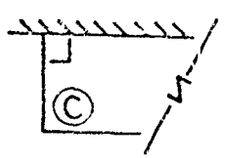 Reference
	(°C)	(°C)	(°C)	(°C)	(°C)	(°C)	(°C)
Temperature at which Failure Initially Noted on X-ray	-70	-70	-82[a]	-82[a]	<-78	-81	-82[a]
	-78	-78	-78	-84	-78	-81	-78
	(b)	-78[c]	-75	<-78	(b)	-81	-75
	-83	-83	-78	-86	-83	-	-78
	-74	-80	-78	-84	-80	-	-78
	-78	-78	-78	-85	-78	-	-
Average Failure Temperature Range	-72	-73	-73	-80	-75	-76	-72
	-77	-78	-78	-85	-80	-81	-77
Predicted Failure	-78	-78	-80	-81	-77	-80	-75
$\sigma^*/-E\delta$	8.55	8.15	7.65	7.00	9.00	7.50	10.0
Calculated Stress Ratio, K_F	1.24	1.18	1.10	1.01	1.30	1.08	1.45

[a] Preliminary Tests

[b] Failed During Accidental Cycling

[c] Accidentally Cycled but Failed Normally

FIGURE 61. FAILURE TEMPERATURES FOR GRAIN-END TERMINATION ANALOGUE MOTORS[23]

determined using linear thermoviscoelasticity theory assuming thermorheologically simple material behavior. Reference temperatures for thermal cooling were obtained from thermocouples embedded in similar analog motors.

The values of the stress ratio K_F presented in Fig. 61 were found to be in excellent agreement with the results of three-dimensional photoelasticity investigations of models having exactly the same dimensions as the propellant analogue motors and end configurations in the form of a 45° inclined plane and a square corner. Three-dimensional photoelasticity tests were also attempted on the model with a natural meniscus; however, the results were inconclusive.

Several interesting features of the failure data presented in Fig. 61 are worth noting. It is first observed that the data for a given grain end configuration exhibit good reproducibility and good agreement with analytical predictions, even though the method of analysis may be open to some question. Considering all of these tests as a group suggests that there is really little difference in behavior between any of these end configurations. Of the differences observed, the two 45° inclined plane configurations failed at temperatures consistently below the others.

The relatively narrow spread in the analogue motor failure temperatures may be explained in a qualitative manner. The data from the two-dimensional photoelastic models indicate that the stress concentration factor for the 45° inclined plane is almost a factor of two greater than that for the circular fillet. It may be expected that these shapes in the three-dimensional analogue motors not only produce higher concentration factors but also tend to be closer together. This result is mainly

attributable to the increased dimensionality of the analogue motors. Secondly, the failure properties of the propellant exhibit significantly increased temperature sensitivity at lower temperatures. Combining these two effects may, in part, explain the closeness of the observed failure temperatures.

Finally, the behavior of the square corner reference configuration, although in agreement with the analytical calculations still suggests somewhat abnormal behavior. This may be attributed to approximations introduced in the analysis and inability of X-rays to detect relatively small defects immediately adjacent to the case wall. Whereas failure was observed in the propellant away from the case wall in the other motors, failure in the square corner reference motor was observed to have occurred very close to and extended along the case wall. In this region the resolution of the radiographic inspection equipment is suspect. Also, analytically this configuration results in a stress singularity and infinite stresses. In analytically calculating the predicted failure temperature, Robinson, et al, [23], used a stress-concentration factor at a point near the grain end. Thus, it is likely that the stresses were higher than analytically predicted.

5.3.3 SUMMARY AND DESIGN GUIDELINES

Before concluding this lengthy section on the design of terminations it is worthwhile to summarize some of the important aspects of the design of grain terminations, and to point out some of the limitations of the analyses presented in the preceeding paragraphs.

The design and analysis of grain terminations represents one of the more difficult problem areas currently facing the designer-analyst. For this reason the previous presentation contained rather in depth discussions of the parametric and specific motor design information presented, including interpretations of some of the research programs. It is hoped that such information will provide the designer with some insight into the thinking processes that go into the design of grain terminations and provide basic guidelines for making rational design decisions.

The discussions on stress relief flaps contains a simple design curve (Figure 6) which experience has proven to be adequate for large diameter solid rocket motors. This curve may also be used for other motor designs if some experience with a similar motor design is available. For low temperature and/or high acceleration applications, the parametric curves obtained from energy balance considerations and grain end contouring studies are better suited.

The use of membrane reinforcing may prove to be a good means for reducing concentrations at grain terminations. However, this approach is not highly recommended at this time. To the authors' knowledge, such an approach has not been investigated in full scale or analogue motor tests; and in view of the probable manufacturing difficulties introduced, this technique should be considered to be only in the research stage at this time.

It has been observed that concave and outward corners are associated with more favorable stress conditions than convex, square or reentrant corners. An included angle less than 45° leads to finite stresses at the grain termination.

Stress concentrations are also decreased as the radius of curvature of an end fillet is increased, however little is gained if the radius is larger than one-half of the grain web.

Length-to-diameter ratio apparently has little effect on the stress concentration for L/D ratios in excess of about 2; and as Poisson's ratio approaches one-half the critical temperature for grain debonding is raised.

The analyses discussed above are subject to the usual limitations of linear elasticity theory. Furthermore, direct application of experimental stress analysis to propellant failure is difficult. Hence, it is recommended that design decisions based on the types of analyses presented herein be corroborated with failure tests of Structural Test Vehicles.

5.4 NOMENCLATURE

A	=	Fracture Surface Area
a	=	Grain Inner Radius
b	=	Grain Outer Radius
c	=	Crack Dimension
c	=	Subscript Referring to Case Properties
E	=	Young's Modulus
e	=	First Strain Invariant
e_2	=	Second Strain Invariant
g	=	Subscript Referring to Grain Properties
K	=	Stress Concentration Factor
k	=	Biaxiality Ratio
k	=	Character of Singularity
K_F	=	Stress Ratio
L	=	Grain Length
R	=	Fillet Radius
s	=	Bond Separation Length
T	=	Temperature
T_0	=	Reference Temperature
U	=	Strain Energy
u, v	=	Displacements
W	=	Strain Energy Density
x,y,z	=	Cartesian Coordinates
r,θ	=	Polar Coordinates
α,β,θ,ϕ	=	Angles
α	=	Free Shrinkage
α	=	Linear Coefficient of Expansion
γ	=	Shear Strain
γ_a	=	Adhesive Fracture Energy
γ_c	=	Cohesive Fracture Energy
ε	=	Normal Strain
λ	=	b/a = Grain Radius Ratio
λ	=	$\frac{\nu E}{(1+\nu)(1-2\nu)}$
λ_n	=	Eigenvalues
ν	=	Poisson's Ratio
μ	=	$\frac{E}{(1+\nu)}$
ρ	=	Star Valley Fillet Radius
σ	=	Normal Stress
τ	=	Shear Stress

5.5 REFERENCES

1. Hoekel, T. and Schapery, R. A., "The Structural Design of Solid Propellants", Report No. 2123, Emerson Electric of St. Louis, Electronics and Space Division, St. Louis, Missouri, (Contract No. N00600-67-C-0081), January 1967.

2. Sampson, R. C. and Campbell, D. M., "Contribution of Photoelasticity to Evaluation of Solid Propellant Motor Integrity", AIAA Journal, Vol. 3, No. 4, April 1966.

3. Jones, J.W., "Engineering Methods for Grain Structural Integrity Analysis", LPC Report No. 578/556-F-3, (Contracts SF04(611)-8013 and DA-04-495-ORD-3260), Lockheed Propulsion Company, Redlands, California, May 1963.

4. Dill, E. H., Deak, A. L., and Schmidt, W. F., "Solid Rocket Structural Integrity Studies: The Grain Termination Problem", MSNW Report No. 67-50-3 (NASA Contract No. NAS7-464), Mathematical Sciences Northwest, Inc., Seattle, Washington, September 1967.

5. Anonymous, "Determination of Optimum Length of End Release for Case Bonded Solid Propellant Rocket Motors", Rocketdyne Special Report No. R-4409 (Contract AF04(611)-11604), Rocketdyne, McGregor, Texas, September 1966.

6. Noel, J. S. and Webb, L. D., "The Role of Fracture Mechanics in the Design of Optimum Grain-Case Terminations", Bulletin of the 5th Meeting of the ICRPG Working Group on Mechanical Behavior, CPIA Publication No. 119, Vol. I, October 1966.

7. Anonymous, "Determination of Optimum Length of End Release for Case Bonded Solid Propellant Rocket Motors", AFRPL-TR-67-72 (Rocketdyne Report No. R-4409-1), (Contract AF04(611)-11604), Rocketdyne, McGregor, Texas, March 1967.

8. Williams, M. L., "Stress Singularities, Adhesion and Fracture," Proceedings of the 5th U.S. National Congress of Applied Mechanics, June 1966.

9. Williams, M. L. and Kunio, T., "An Analysis of Adhesive Debonding in Case-Bonded Solid Propellant Rocket Motors," UTEC DO 69-082, University of Utah, July 1969.

10. Jones, W. B., Jr., "Cohesive and Adhesive Polymer Fracture Investigation," Ph.D. Thesis, University of Utah, June 1970.

11. Leeming, H., et al., "Solid Propellant Structural Test Vehicle and Systems Analysis," LPC Final Report No. 966-F(AFRPL-TR-70-10, Contract F04611-69-C-002), Lockheed Propulsion Company, Redlands, California, March 1970.

12. Durelli, A. J., Parks, V. J., and del Rio, C. J., "Stress Concentration Factors in Bonded Solid Propellant Grains with Difference End Configurations," Catholic University, Special Report, Washington, D.C., April 1966.

13. Durelli, A. J., Parks, V. J., Bhardra, P., and del Rio, C. J., "Study of Stress Concentrations at the Ends of Solid Propellant Grains Subjected to Restrained Shrinkage," Catholic University Final Report, (Contract No. AF-04(611)-10378), Washington, D.C., May 1966.

14. Durelli, A. J., Parks, V. J., and Bhardra, P., "Experimental Determination of Stresses and Strains in a Rectangular Plate Subjected to Biaxial Restrained Shrinkage," Br. J. Appl. Physics, Vol. 17, July 1966.

15. Parks, V. J., and Durelli, H. J., "Stress Distribution in Plates, Bonded on Two Leng Edges with Corners of Seven Different Geometries and Subjected to Restrained Shrinkage," Bulletin of the 5th Meeting of the ICRPG Mechanical Behavior Working Group," CPIA Publication No. 119, Vol. I, October 1966.

16. Durelli, A. J., and Parks, V. J., "Experimental Stress Analysis of Loaded Boundaries in Two-Dimensional Second Boundary Value Problems," Catholic University Report No. 11, (Contract No. NOAV 2249(06), February 1967.

17. Durelli, A. J., Parks, V. J., and Aribe, S., "Optimization of a Slot End Configuration in a Finite Plate Subjected to Uniformly Distributed Load," Catholic University Report No. 13, (Contract No. NONV 2249 (06), Washington, D.C., June 1967.

18. Durelli, A. J., and Parks, V. J., "Photoelastic Analysis in the Neighborhood of Corners of Long Strips Bonded on One Side and Shrunk", Am. Ceramic Soc., Bull., Vol. 46, No. 6, pp. 582-586, June 1967.

19. Durelli, A. J., Parks, V. J., and del Rio, C. J., "Stresses in Square Slabs, with Different Edge Geometries, when Bonded on one Face to a Rigid Plate and Shrunk," Experimental Mechanics, Vol. 7, No. 11, pp. 481-484, November 1967.

20. Durelli, A. J., Parks, V. J., and del Rio, C. J., "Stresses in a Square Slab Bonded on One Face to a Rigid Plate and Shrunk," Acta Mechanica, Vol. III, No. 4, pp. 352-359, 1967.

21. Parks, V. J., Chiang, F. P., and Durelli, A. J., "Maximum Stress at the Angular Corners of Long Strips Bonded on One Scale and Shrunk," Experimental Mechanics, Vol. 8, No. 6, pp. 278-281, June 1968.

22. Durelli, A. J., Parks, V. J., and del Rio, C. J., "Stresses, Strains and Displacements Associated with the Restrained Shrinkage of Cylinder with Tocoidal Cavities," Recent Advances in Engineering Science, Ed. by C. Eringen, Vol. 3, pp. 521-540, 1968.

23. Robinson, C. N., Graham, R. H., and Moore, F. C., "Effect of Grain End Shape on Stress Concentrations at the Case-Propellant Interface," Volume I of Atlantic Research Corporation Final Report on Solid Propellant Mechanical Behavior Studies, AFRPL-TR-69-124-Vol. I., (Contract F04611-68-C-0015), Alexandria, Virginia, May 1969.

VI. EXPERIMENTAL ANALYSIS METHODS

6 1 INTRODUCTION

Experimental stress analyses may serve as the primary analysis tool or confirmatory experimentation of other analysis techniques. Experimental methods are frequently used as the main analysis tool for complex grain configurations when the validity of the results of analytical and numerical analyses is seriously questioned. Experimental methods are also employed for confirmation of analysis and failure predictions with subscale and prototype motor tests used as ultimate verification of grain structural integrity. Properly used, experimental stress analyses represent powerful tools for the designer-analyst, complementing analytical and approximate numerical analysis techniques[1-5].

Presently, experimental methods make considerable use of photoelasticity, displacement measuring devices and Structural Test Vehicles (STV's) which model the essential features of production delivery motors.

6.2 PHOTOELASTICITY

Photoelasticity is an experimental stress analysis method which takes advantage of the birefringence (double refraction property) exhibited by certain isotropic transparent materials when subjected to stress or strain [1-5]. When such a transparent material is viewed in a field of polarized monochromatic light, this optical phenomenon is manifest as interference fringes or alternate dark and light bands known as isochromatics. These fringes are ordered according to the number of darkness-brightness cycles that occur at any given point as the load is increased from zero to its final value. The difference of the principal stresses acting on planes containing the axis of light propagation is related to the fringe order at

a given point and the thickness of the material in the direction of light propagation through the fundamental stress-optic law:

$$\frac{\sigma_1 - \sigma_2}{2} = \tau_{max} = \frac{n f_\sigma}{t} \tag{6.1}$$

where

n = fringe order

t = model thickness

σ_1, σ_2 = principal stresses

τ_{max} = maximum shear stress

f_σ = material fringe constant.

The observed birefringence is not affected by the stress in the direction of light propagation. To obtain stresses with this method of analysis, a model is fabricated from a transparent plastic known to possess the required photoelastic properties. The model is machined so that it is geometrically similar to the prototype and loading. In two-dimensional problems, the loaded model is examined in a field of polarized light. The isochromatic pattern gives the shear stress distribution, and direct visual observation can ordinarily be used to locate regions of high and low normal and shear stresses.

Essentially, two patterns can be obtained. If the polariscope is set to produce maximum darkness in the background outside the model (dark field), then the fringes are ordered $n = 0,1,2,3,\cdots$. If the polariscope is arranged to produce maximum light in the field outside the model (light field), then the fringes have the values of the intermediate orders $n = 1/2, 3/2, 5/2, \cdots$. By the simple process of counting fringes

and multiplying their order by the calibration constant, f_σ the maximum shear stress distributions can be determined throughout the bod, of the model. The model shear stress distribution can then be converted by the use of appropriate scaling laws to the shear stress distribution in the prototype. When the stress field is uniaxial, as on free boundaries, one of the principal stresses is zero and the other can be directly from the photoelastic data. At interior points of the model, additional information is required for determining principal stresses and the evaluation becomes appreciably more complicated.

6.2.1 THREE-DIMENSIONAL PHOTOELASTICITY

For the photoelasticity solution of three-dimensional problems, a somewhat more involved technique is necessary, since the observations of the loaded model in a field of polarized light does not result in a fringe pattern which can be r idily interpreted. Current techniques involve constructing a three-dimensional model and determining the stress state by a "frozen stress"[3-5],"scattered light"[6-20]or "embedded polariscope" photoelastic method. The frozen stress or stress freezing technique in which the isochromatic fringe pattern is locked-in "or frozen into the model by temperature excursions and thin slices then removed wherever the stress distribution is required and viewed in polarized light is probably the most common technique; although the development of the laser has given considerable impetus to scattered light techniques which allow non-destructive time varying measurements without disturbing the model. Embedded polariscope techniques have not found extensive use in solid rocket motor applications and will not be discussed here.

STRESS FREEZING TECHNIQUE

In the frozen stress techniques[3-5]the stress distribution in the three-dimensional model at the time of stress freezing is obtained. The birefringence is frozen into the model by utilizing certain plastics which behave as if they were composed of a mixture of two materials, with different rates of changes in their physical properties under temperature variation. When a model made of such material is heated to a certain "critical" temperature, one component or "phase" becomes soft, while the other is still relatively hard and perfectly elastic. When loaded in this condition and slowly cooled under load, the softened phase rehardens, locking-in or "freezing" the deformation and corresponding fringe pattern permanently into all parts of the model. The load can be removed and slices taken from the model. The removal of slices does not distort or alter the fringe pattern in any manner if the machining operation is carefully performed. This process gives rise to a material with a value of Poisson's ratio very nearly equal to one-half. In other applications this is a serious limitation; however, in solid propellant applications this is usually a desirable trait.

The isochromatic patterns obtained from the slices can be interpreted in much the same manner as the patterns obtained from a two-dimensional model. Shear stress distributions throughout the slice and boundary stress distributions along free boundaries and along surfaces to uniform pressure-type loadings can be determined directly from the patterns. At interior points of the slice, the problem of determining the principal stresses is considerably more difficult. In general, the experimental techniques available for providing the additional information required to

solve completely a two-dimensional problem, are difficult to apply to the three-dimensional case. As a result, a method which utilizes photoelastic data and an integration procedure based on the equations of equilibrium has been developed. The procedure is cumbersome and subject to considerable inaccuracies unless it is applied with extreme care and skill. Fortunately, a complete knowledge of interior stresses is not always required, and a knowledge of boundary stress distributions is sufficient for many design problems.

SCATTERED LIGHT TECHNIQUE

Scattered light photoelasticity[6-20]has several advantages over the technique of transmission photoelasticity discussed above. Firstly, not all photoelastic materials are amenable to stress freezing and birefringent materials more representative of propellant binders cannot be stress frozen. Scattered light photoelasticity does not require the stress freezing process. This method of analysis is nondestructive. Different load conditions can be applied to the same model. This can be a considerable advantage for models with a complex geometry.

The essential data used in the numerical integration of the equations of equilibrium for transmitted light and scattered light are the same, the principal difference being the direction of observations. Observations using the scattered light polariscope are made in the plane transverse to the path of the light. Furthermore, in a transmission polariscope, the direction of the incident light relative to the point of interest is generally constant. However, when using scattered light it is necessary to make observations in different directions. This is

usually accomplished by rotating the model relative to the light[1].

The stress optic law for scattered light is obtained from the basic relation between the fringe order and the secondary principal stress

$$(\sigma_1' - \sigma_2') = C \frac{dn}{ds}$$

where s is the distance the light travels through the stressed mediums, $(\sigma_1' - \sigma_2')$ is the difference in the secondary principal stresses and C is the stress optic coefficient.

The direction of the secondary principal axes may be found by rotating the model until the intensity of the scattered light is constant. With the model in this position the direction of observation is parallel to one of the secondary principal directions, and the intensity of the scattered light, I, is directly proportional to the square of the maximum amplitude of polarized light, A, with proportionality constant ν — a scattering constant (i.e., $I = \nu A^2$).

The basic components of a scattered light polariscope are an intensive monochromatic light source, an optical system, amount for the photoelastic model, and an immersion tank. A common light source is a helium-neon continuous wave gas laser. The immersion fluid is frequently paraffin oil. It is chosen to have the same index of refraction as the

[1] Cheng [15] has described a dual-observation method which does not require rotation of the beam or the model. Only three-dimensional translation of the model is necessary. The method consists of recording simultaneously the intensities of scattered light along two directions of observations making an angle of 45° in a plane normal to the beam.

model material and is used to eliminate refraction and reflection at the surface of the model.

6.2.2 LIMITATIONS OF PHOTOELASTICITY

Although photoelasticity represents an extremely powerful experimental stress analysis tool, some caution must be exercised in applying it to solid propellant structural investigations.

The analyses discussed above are subject to the usual limitations of linear elasticity theory. That is, the photoelastic material is assumed to be isotropic and homogeneous. Deformations are assumed to be small and a linear relation between stress, strain and birefringence is also assumed

The first two limitations are probably not too severe. Furthermore, Sampson [21] has recently postulated a stress-optic law for orthotropic composites based on a Mohi-circle relationship among birefringence components. Although not completely verified at the present time, these results may prove useful in future studies of solid propellants. Large deformations complicates the experimental procedure, but offers no insurmountable difficulties.

The most significant difficulty is associated with high levels of stress in crack-like geometries. In such geometries as the radius of the slot or crack tip becomes smaller, the same load produces higher stress becoming unbonded in the case of a crack and at some point the assumption of a linear relation between stress, strain, and birefringence breaks down. This nonlinear reponse can be avoided to some extent by reducing the load, and in the case of cracks it is necessary to view the stress distribution with approximately one crack width in order to obtain an estimate of the stresses at the tip.

This nonlinear behavior may also be used advantageously. Some of the same nonlinear factors evident in the photoelastic model also exist in the rocket motor prototype. Thus, if one is able to match the nonlinear features, an estimate of the nonlinear stresses and strains in the propellant grain could be made. To the authors' knowledge, this matching has not been attempted. Quantitative determination of the nonlinear stresses and strains requires a nonlinear stress optic law -- presently nonexistent.

The stress state of the photoelastic model is also complicated in studies of narrow slots or cracks. In this situation, the thickness of the model is an order of magnitude or larger than the slot tip radius. The surfaces of the model are in a condition of plane stress. The central portion of the model through the thickness approaches plane strain. The photoelastic analysis gives the result of an integral effect along the path of light. This too, may not be too serious an effect, however, there is some evidence indicating that the difference between the two extremes of plane stress and plane strain may not be too large.

Most birefringeht materials exhibit time dependent or viscoelastic effects. These effects are usually discounted by working in the equilibrium range of the master relaxation curve. Stress freezing procedures, for example, require the dwell time under load to be long enough to obtain equilibrium response and the cooling rate during "freezing" be sufficiently slow to prevent any appreciable thermal gradient in the material.

Dynamic investigations, of course, require consideration of the viscoelastic behavior of the photoelastic model. Photoviscoelasticity constitutive theory describes this behavior. For linear materials, this

theory is completely analogous to linear viscoelasticity theory. Just as time-dependent stresses and strains in viscoelastic materials are related to the variation of the birefringence in a photoviscoelastic material through the time-dependent stress-optic coefficients - the relaxation birefringence-stress and creep birefringence - strain coefficients. The theoretical developments are formally identical to those of linear viscoelasticity theory including time-temperature superposition and power law representations of material behavior [22-31].

6.2.3 APPLICATIONS OF PHOTOELASTICITY TO PROBLEMS OF GRAIN STRUCTURAL INTEGRITY

Two-dimensional photoelastic models have been extensively used for determining stress and strain concentration factors in star shaped propellant grains for pressure and thermal loadings[32-41]. These models are normally subjected to an external boundary pressure and superposition is used to obtain the stress and strain distribution resulting from internal pressure[2]. Concentration factors determined from external pressure loading are also normally applied to the problem of thermal cooling[3]. The stress state in these models is plane stress. In the absence of body forces the governing field equations for plane stress

---

[2] This is only true for relatively thick webs. If the web is thin, the external pressure will not be uniform and shear transfer between the case and grain may be appreciable.

[3] Comparisons of the stress concentration factors determined from plane stress models subjected to external pressure and plane strain and plane stress models subjected to uniform temperature changes has indicated that the concentration factor for plane stress models subjected to external pressure is 5 percent lower than the plane stress uniform temperature factor and is 7 percent higher than the plane strain uniform temperature change factor [42]. Thus, within acceptable engineering accuracy it is conservative to use the plane stress concentration factor determined from external pressure for uniform temperature changes under a condition of plane strain. For thick webs the concentration factors for plane stress external pressure and uniform temperature changes should be in even better agreement.

and plane strain are identical, and the stress distribution is independent of material properties. Thus the results of two-dimensional photoelastic tests are directly applicable to a linearly elastic propellant grain in a state of plane strain. For essentially stress determined boundary conditions the results are also valid for thermorheologically simple, linearly viscoelastic grains.

A large number of parametric photoelastic investigations have been conducted for numerous internal port shapes[32-41]. The results of these studies have been reported and their application to preliminary design analysis discussed elsewhere in this handbook. These investigations have considered simple slot grain geometries, the effect of the slot width and the inverse star point, positive and negative wedge angles and elliptical slot tips. As a general rule-of-thumb, it has been found that an elliptical slot tip with an ellipticity radius ratio of about 2:1 is the optimum star slot tip configuration.

Two dimensional photoelastic tests have also been recently applied to the problem of solid propellant motors under transverse body force loadings[43,44]. Pseudo two-dimensional photoelastic models have been developed for axisymmetric grain geometries[45,46]and two and three dimensional photoelasticity has been applied in studies related to the design of optimum grain end termination configurations[47-58]. The results of these studies are also discussed elsewhere in this report.

Three dimensional photoelasticity has been applied to the analysis of complicated grain geometries and experimental confirmation of three-dimensional finite element computer analyses. For the most part, the finite-element analysis yielded stresses and strains 20-25 percent higher than those measured in photoelasticity tests[59].

6.3 INSTRUMENTATION

Considerable attention in recent years has been directed toward the development of instrumentation suitable for making accurate measurements of deflections strains and stresses in solid propellant grains[40,60]. Currently only measurements of surface strains and deflections can be made reliably. Since propellants exhibit nearly incompressible behavior, strains and deflections can be calculated directly from displacement boundary conditions without direct knowledge of the constitutive relations. The calculation of stresses, on the other hand, requires direct knowledge of the propellant stress-strain behavior, which for modern highly-solids-loaded propellants is strongly nonlinear. Thus, attempts at experimentally measuring stresses in a solid propellant grain with the current (linear) constitutive equations have only been partially successful. This problem of questionable results cannot be resolved by simple calibration of the stress sensing devices since the calibration of such devices in test fixtures requires knowledge of the mechanical properties.

Propellant-instrumentation interaction is another difficult problem which is common to both deformation sensing devices and transducers used to measure stresses. The primary requisite of any instrumentation is that it not distort the quantity being measured. Thus, ideally, the instrumentation used to measure strains should have an infinite compliance so as not to be responsive to stresses, and a stress sensitive device should be mechanically stiff so as not to respond to deformations. Such instrumentation can be devised for surface strain measurements and for case-grain interface bond stresses using through-the-case stress transducers with null displacements maintained by a servo feedback central system. The compliance of gages used to measure internal stresses and strains should match that of the propellant.

This task is not feasible, and thus one must consider gage-grain interaction in attempting to relate gage output in a distorted field to the stress or strain that would exist in the undistorted field. This problem further complicates gage calibration, since it requires a complete solution to the problem posed by the calibration test.

Of the methods proposed and explored for the measurement of surface strains and deflections, surface coatings, moiré grids, linear potentiometers, linear variable differential transformers (LVDT'S), and semiconductor and resistance type strain gages have been the more common. Photoelastic coatings[1,5,40,60] using reflected polarized light have not been completely successful and are not widely used since the reinforcing influence on the propellant surface distorts the free field strain distribution. The Moiré method[61-70]which involves printing a very dense grid of uniformly spaced lines on the propellant surface and observing the displacement of this grid with respect to a separate master grid laid over it is normally used for measuring surface strains over very small areas. Simple grids marked on the propellant surface and photographed before and after loading have also been used to measure surface displacements. These latter two methods require that the propellant surface be essentially flat, although in principle, overlapping grids can be used to measure surface strains on curved surfaces. Linear potentiometers in which displacements cause changes in electrical resistance and LVDT'S in which displacements induce voltage changes have been used for measuring grain slump and dimensional changes of the grain inner bore. Resistance type strain gages and semiconductors are frequently mounted on cantilevered beams used for measuring grain bore dimensional changes. These strain gages have also been externally mounted on fiberglass or thin-walled steel motor cases during firing or

pressurization tests to give an indication of inner bore pressurization strains.

Attempts at measuring strains in the propellant grain interior have only been partially successful due to the interaction between the instrumentation and the propellant grain referred to above. Reasonable success has been demonstrated for measurements of case-grain interfacial shear strains under axial acceleration loadings using a simple shear cube transducer and a bending beam with semiconductor gage elements[71-78]. Capacitance-type conductive rubber gages have also been proposed for internal strain measurements, but these gages have not been explored in any detail yet.

Figure 1 shows the shear cube gage investigated by Lockheed Propulsion Company[75-77]under the Air Force sponsored Structural Test Vehicle program. The gage is a modification of a device developed by Gulton Industries for Hercules[71,73]and consists of two semiconductor gage elements embedded in a cube of compliant material (e.g., propellant binder) with their axes normal to each other and 45° to the mounting surface. The two gage elements form active legs of a bridge circuit. In a pure shear environment one diagonal is subjected to a tensile load and the other to compressive load. In tension or compression both lengthen or shorten, respectively. By considering the difference between the resistance changes of the two elements, the gage responds only to shear. Summing the output allows normal strains to be measured. Presently, the device suffers from an inadequate calibration test method and analysis.

San Miguel[79,80]has investigated the use of a piezoresistive stress transducer for internal measurement of pressurization stresses. The size of the gage is of the order of magnitude of the largest oxidizer particles

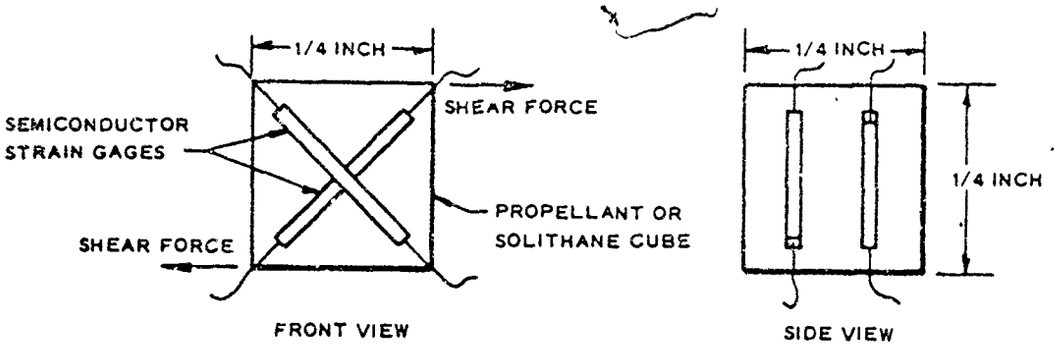

(A) LPC SHEAR STRAIN TRANSDUCER

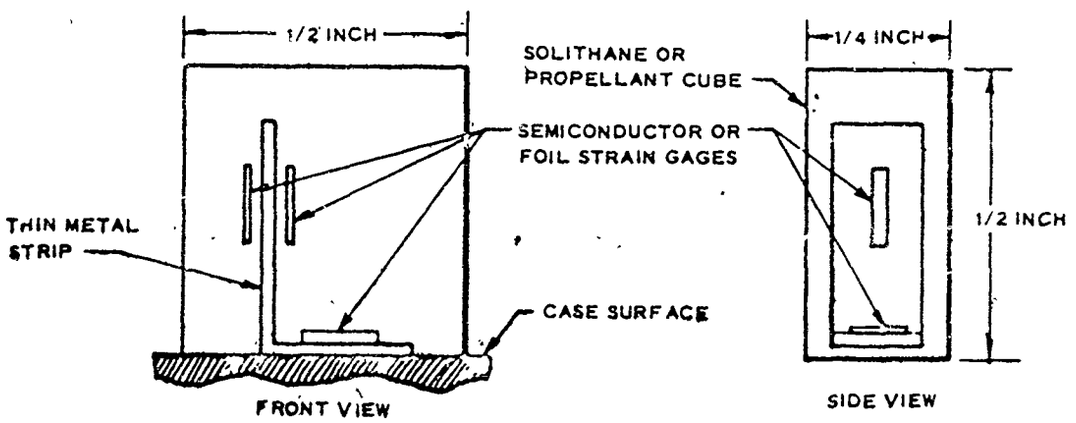

(B) BENDING BEAM SHEAR TRANSDUCER

Figure 1. Embedded Shear Transducers

in solid propellants. Measurements in a 1/4 scale Surveyor motor were approximately fifteen percent lower than predictions based on linear elasticity theory. Considerably worse agreement was obtained during pressurization of unconstrained thick-walled cylinders of polyurethane. This is due to the gage-grain interaction mentioned above. Because of its small size, this interaction is most likely more significant and more severe than in the two normal stress transducers discussed subsequently.

Rocketdyne[72,74,78,81-84] has developed a through-the-case stress transducer for measuring normal case-grain bond stresses. Figure 2 shows the present design which is a modification of a previously developed Rocketdyne transducer. This design incorporates a nulling feature. A cable, which passes through a hole located in the threaded portion of the sensor, is welded to a steel ball which permits the restoring force to be applied between the propellant secondary and the strain gages.

The Rocketdyne gage has also been suggested for use in making shear stress/strain measurements[78]. The major disadvantage of this gage is that it is necessary to drill holes in the case, thus excluding its use on production delivery motors. It is probably the most reliable gage for motor development work however.

Lockheed Propulsion Company[75-77] has developed a diaphragm-type stress transducer for making normal strain measurements,(Figure 3). The use of the gage has been described extensively elsewhere[75-77]. Presently its major drawback is adequate solution to the gage/grain interaction problem and calibration. The interaction problem has been considered by Fitzgerald and Hufferd[75,85] for this gage.

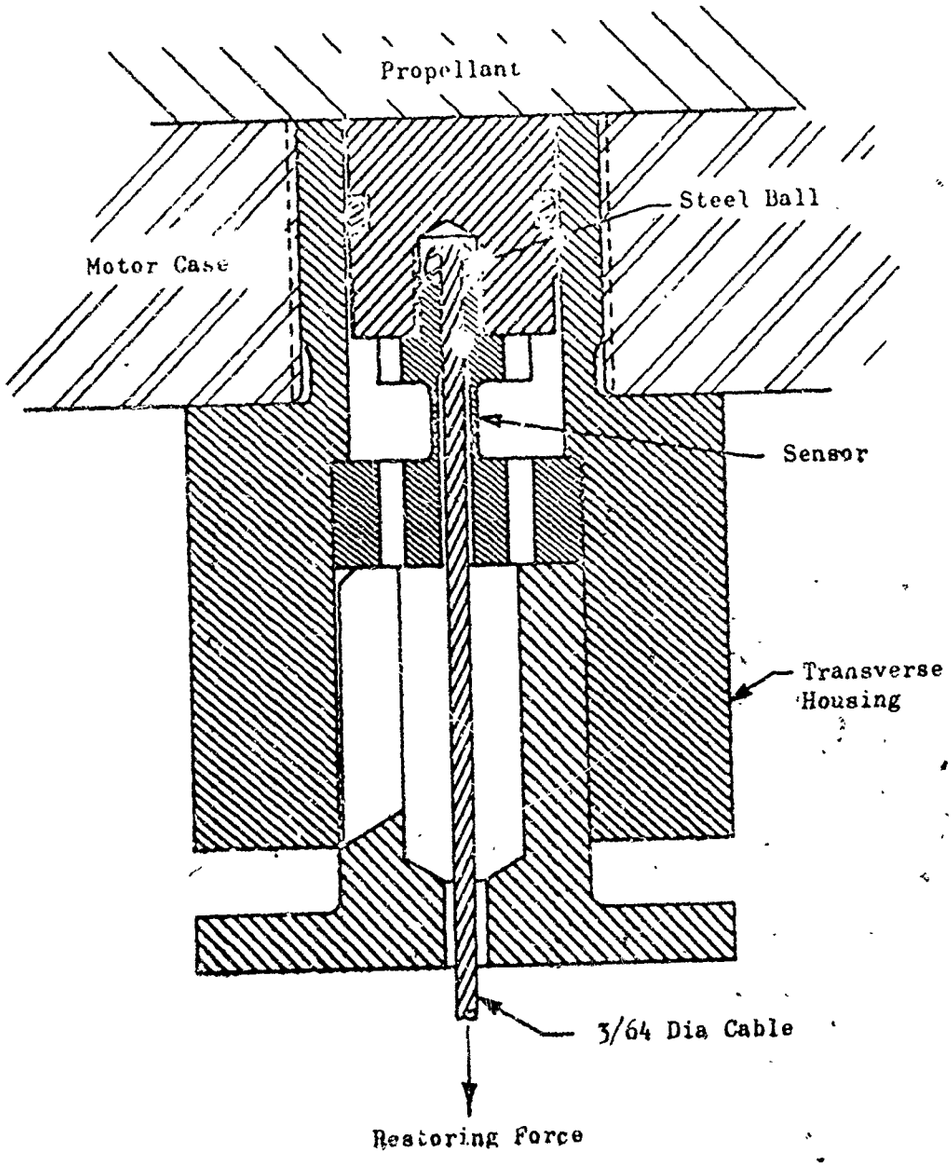

Figure 2. Null Balance Arrangement, Normal Stress Gage

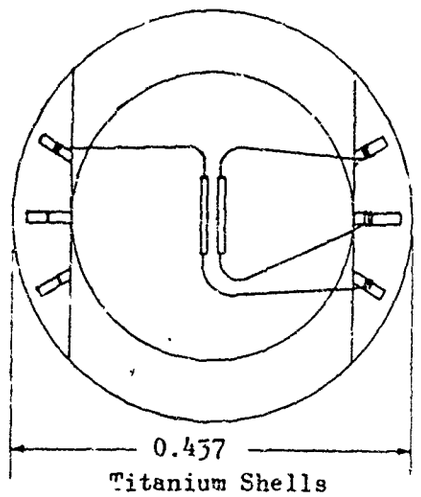

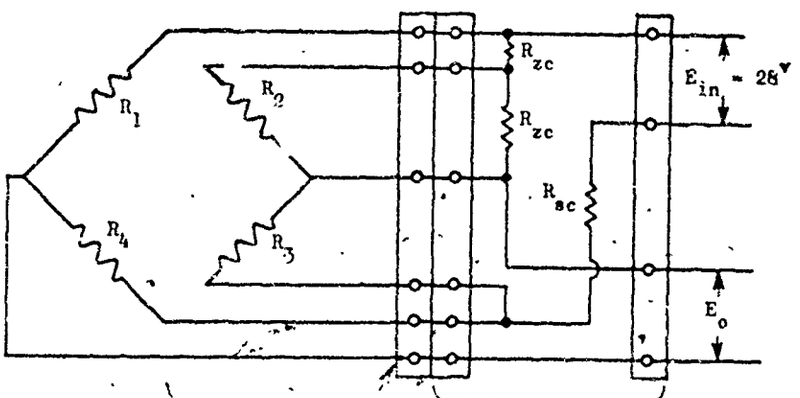

R_1 and R_3 = Outer Diaphragm Gages
R_2 and R_4 = Inner Diaphragm Gages
R_{zc} = Zero Balance Compensation
R_{sc} = Span Compensation

Figure 3. Diaphragm Type Normal Stress Gage

6.4 STRUCTURAL TEST VEHICLES

In view of the discussions throughout the Handbook, it is recognized that extensive use of STV's is the only adequate technique for ultimate verification of grain structural integrity. In addition to the difficulties and uncertainties associated with the calculation of stresses and strains in a solid rocket motor, a universal failure criterion of solid propellants is also currently lacking. Failure testing of an STV provides a means of evaluating overall grain structural integrity in the anticipated motor environment. To avoid scaling difficulties it is desirable to use a full-scale prototype motor as the STV. When economic considerations dictate use of subscale motors, scaling of loading time time as well as geometry must be considered. In such situations it may be necessary to construct several models to adequately scale different loading situations.

Structural Test Vehicles offer a convenient means of studying propellant failure characteristics under loading situations currently not amenable to analysis nor easily duplicated in laboratory testing. In particular, it is noted that an STV is the only method presently available for obtaining reliable information about propellant grain response in thermomechanically coupled environments such as transient heating during thermal cooling or sustained vibration. STV's are also particularly useful for studying damage accumulation in combined or repeated loading situations such as low temperature pressurization or temperature cycling.

Many of the deficiencies associated with current aging programs discussed previously are eliminated by structural testing of aged STV's.

Such tests give an excellent indication of propellant system and subsystem aging characteristics in the full-scale motor.

In addition to providing information on propellant grain failure characteristics subscale STV's can provide basic mechanical property information. Measurement of internal bore dimensional changes at various equilibrium temperatures in two STV's with different web fractions provides sufficient information for calculation of an effective value of Poisson's ratio and the coefficient of thermal expansion for propellant in a multi-axial strained state.

6.5 NOMENCLATURE

C	=	Stress Optic Coefficient
f_σ	=	Material Fringe Constant
I	=	Light Intensity
n	=	Fringe Order
s	=	Distance
t	=	Model Thickness
σ_1, σ_2	=	Principal Stresses
τ	=	Shear Stress
ν	=	Scattering Constant

6.6 REFERENCES

1. Hetenyi, M.: "Handbook of Experimental Stress Analysis," John Wiley & Sons, Inc., N. Y., 1950.

2. Dally, J. W. and Riley, W. F.: "Experimental Stress Analysis," McGraw-Hill, New York, 1965.

3. Durelli, A. J. and Riley, W. F.: "Introduction to Photomechanics," Prentice-Hall, Inc., Englewood Cliffs, N. J., 1965.

4. Durelli, A. J.: "Applied Stress Analysis," Prentice-Hall, Inc., Englewood Cliffs, N. J.

5. Leven, M. M.: (Editor): "Photoelasticity - the Selected Scientific Papers of Max M. Frocht," Pergamon Press.

6. Weller, R.: "A New Method for Photoelasticity in Three-Dimensions," J. Appl. Phys., Vol. 10, No. 4, p. 266, 1939.

7. Weller, R.: "Three-Dimension of Photoelasticity Using Scattered Light," J. Appl. Phys. Vol. 12, No. 8, pp. 610-616, 1941.

8. Drucker, D. C. and Mindlin, R. D.: "Stress Analysis by Three-Dimensional Photoelastic Methods," J. Appl. Phys., Vol. 11, No. 11, pp. 724-732, 1940.

9. Jessop, H. T.: "The Scattered Light Method of Exploration of Stresses in Two and Three-Dimensional Models," Brit. J. Appl. Phys., Vol. 2, pp. 249-260, 1951.

10. Frocht, M. M. and Srinath, L. S.: "A Non-Destructive Method for Three-Dimensional Photoelasticity," Proc. 4th U.S. Nat'l. Congr. Appl. Mech., pp. 329-337, 1958.

11. Srinath, L. S. and Frocht, M. M.: "Scattered Light in Photoelasticity - Basic Equipment and Techniques," Proc. 4th U.S. Nat'l. Congr. Appl. Mech., pp. 775-781, 1962.

12. Srinath, L. S. and Frocht, M. M.: "The Potentialities of the Method of Scattered Light," Symposium on Photoelasticity, (Edited by M. M. Frocht), Pergamon Press, pp. 277-292, 1963.

13. Sampson, R. C.: "A Three-Dimensional Photoelastic Method for Analysis of Differential-Contraction Stresses," Experimental Mechanics, Vol. 3, No. 10, pp. 225-234, 1963. (Discussion by Durelli, A.J., pp. 235-237).

14. Cheng, Y. F.: "Some New Techniques for Scattered-Light Photoelasticity," Experimental Mechanics, Vol. 3, No. 11, pp. 275-278, 1963.

15. Cheng, Y. F.: "A Dual-Observation Method for Determining Photoelastic Parameters in Scattered Light," Experimental Mechanics, Vol. 17, No. 3, pp. 140-144, 1967.

16. Kuske, A.: "Separation of Principal Stresses in the Freezing Method," Experimental Mechanics, Vol. 8, No. 8, pp. 384, 1968.

17. Braswell, D. W., Ranson, W. F., and Swinson, W. F.: "Scattered Light Photoelastic Thermal Stress Analysis of a Solid Propellant Rocket Motor," J. Spacecraft Rockets, Vol. 5, No. 12, pp. 1411-1416, 1968.

18. Cheng, Y. F.: "An Automatic System for Scattered Light Photoelasticity," Experimental Mechanics, Vol. 9, No. 9, pp. 407-412, 1969.

19. Aderholt, R. W., McKinney, J. M., Ranson, W. F. and Swinson, W. F.: "Effect of Rotating Secondary Principal Axes in Scattered Light Photoelasticity," Experimental Mechanics, Vol. 10, No. 4, pp. 160-165, 1970.

20. Aderholt, R. W., Ranson, W. F. and Swinson, W. F.: "Scattered Light Photoelastic Stress Analysis of a Solid Propellant Rocket Motor," Experimental Mechanics, Vol. 10, No. 11, pp. 481-485, 1970.

21. Sampson, R. C.: "A Stress-Optic Law for Photoelastic Analysis of Orthotropic Composites," Experimental Mechanics, Vol. 10, No. 85, 1970.

22. Mindlin, R. P.: "A Mathematical Theory of Photo-Viscoelasticity," J. Appl. Phys., Vol. 20, pp. 206-216, 1949.

23. Dill, E. H.: "On the Phenomenological Rheo-Optic Constitutive Relations," J. Poly. Sci., Pt. C., Vol. 5, p. 67, 1964.

24. Dill, E. H.: "A Theory for Photoviscoelasticity," in Proc. 4th Internat. Congr. on Rheology, N. Y., 1964.

25. Williams, M. L. and Cheng, J.: "The Engineering Analysis of Linear Photoviscoelastic Materials," Experimental Mechanics, Vol. 4, p. 9, 1964.

26. Hackett, R. M., and Krokosky, E. M.: "A Photoviscoelastic Analysis of Time-Dependent Stresses in a Polyphase System," Experimental Mechanics, Vol. 8, No. 12, pp. 539-547, 1968.

27. Johnson, C. V., III, and Goldsmith, W.: "Optical and Mechanical Properties of Birefringent Polymers," Experimental Mechanics, Vol. 9, No. 6, pp. 263-268, 1969.

28. Theocaris, P. S.: "A Review of the Rheo-Optical Properties of Linear High Polymers," Experimental Mechanics, Vol. 5, pp. 105-114, 1965.

29. Brinson, H. F.: "Mechanical and Optical Viscoelastic Characterization of Hysol 4290," Experimental Mechanics, Vol. 8, No. 12, pp. 561-566, 1968.

30. Daniel, I. M.: "Quasi-Static Properties of a Photoviscoelastic Material," Experimental Mechanics, Vol. 5, No. 3, 1965.

31. Arenz, R. J., Ferguson, C. W. and Williams, M. L.: "The Mechanical and Optical Characterization of A Solithane 113 Composition," Experimental Mechanics, Vol. 7, No. 4, pp. 183-188, 1967.

32. Ordall, D. D. and Williams, M. L.: "Preliminary Photoelastic Design Data for Stresses in Rocket Grains," Jet Propulsion, pp. 657-662, 1957.

33. Daniel, I. M. and Durelli, A. J.: 'Photothermoelastic Analyses of Bonded Propellant Grains," Experimental Mechanics, Vol. 1, No. 3, p. 97, 1961.

34. Durelli, A. J., Parks, V. J., and del Rio, C. S.: "Experimental Determination of Stresses and Displacements in Thick-Wall Cylinders of Complicated Shape," Experimental Mechanics, Vol. 8, pp. 319-326, 1968.

35. Durelli, A. J.: "Experimental Means of Analyzing Stresses and Strains in Rocket Propellant Grains," Experimental Mechanics, Vol. 2, No. 4, pp. 102-109, 1962.

36. Durelli, A. J. and Parks, V. J.: "Photoelasticity Methods to Determine Stresses in Propellant-Grain Models," Experimental Mechanics, Vol. 5, No. 2, pp. 33-46, 1965.

37. Fourney, M. E. and Parmerter, R. R.: "Photoelastic Design Data for Pressure Stresses in Slotted Rocket Grains," AIAA Journal, Vol. 1, No. 3, pp. 697-698, 1963.

38. Durelli, A. J. and Parks, V. J.: "Photoelasticity to Determine Strains in Propellant-Grain Models," Experimental Mechanics, Vol. 5, No. 2, pp. 33, 1965.

39. Fourney, M. E. and Parmerter, R. R.: "Parametric Study of Rocket Grain Configurations by Photoelastic Analysis," AFSC Report No. AFRPL-TR-66-52 (Contract No. AF04(611)-1052), Mathematical Sciences Corp., Seattle, Washington, September 1968.

40. Durelli, A. J., and Parks, V. J.: "Survey and Development of Methods for the Determination of Strains in Solid Propellants," Appendix B in Support of Study of Mechanical Properties of Solid Rocket Propellants, Aerojet General Corp. Report No. 0411-10F, (Contract AF 33(600)-40314 S.A. No. 1), Aerojet General Corp., Solid Rocket Plan, Sacramento, Calif., March 1962.

41. Sampson, R. C. and Campbell, D. M.: "Contribution of Photoelasticity to Evaluation of Solid Propellant Motor Integrity," AIAA Journal Vol. 3, No. 4, April 1966.

42. Jenkins, W. C.: "Comparison of Pressure and Temperature Stress-Concentration Factors for Solid Propellant Grains," Experimental Mechanics, Vol. 8, No. 2, pp. 44-96, 1968.

43. Parks, V. J., Durelli, A. J. and Ferrer, L.: "Constant-Acceleration Stresses in a Composite Body," Experimental Mechanics, Vol. 10, No. 2, pp. 49-56, 1970.

44. Parmerter, R. R.: "A Photoelastic Study of Lateral Acceleration in Solid Propellant Rocket Motors," MSNW Report No. 68-50-1 (Contract No. NAS7-464), Mathematical Sciences, Northwest, Inc., October 1968.

45. Fourney, M. E. and Schmidt, W. F.: "Extension of Photoelastic Design Data to Case-Bonded Grains of Axisymmetric Geometries," AFSC Report No. AFRPL-TR-68-136, September 1968.

46. Fourney, M. D.: "A Pseudo Two-Dimensional Photoelastic Method of Testing Axisymmetric Geometries," Experimental Mechanics, Vol. 11, No. 1, pp. 19-25, 1971.

47. Durelli, A. J., Parks, V. J., and del Rio, C. J.: "Stress Concentration Factors in Bonded Solid Propellant Grains with Different End Configurations," Catholic University, Special Report, Washington, D.C., April 1966.

48. Durelli, A. J., Parks, V. J., Bhardra, P., and del Rio, C. J.: "Study of Stress Concentrations at the Ends of Solid Propellant Grains Subjected to Restrained Shrinkage," Catholic University Final Report, (Contract No AF-04(611)-10378), Washington, D.C., May 1966.

49. Durelli, A. J., Parks, V. J., and Bhardra, P.; "Experimental Determination of stresses and Strains in a Rectangular Plate Subjected to Biaxial Restrained Shrinkage," Br. J. Appl. Physics, Vol. 17 July, 1966.

50. Parks, V. J., and Durelli, H. J., "Stress Distribution in Plates, Bonded on Two Long Edges with Corners of Seven Different Geometries and Subjected to Restrained Shrinkage," Bulletin of the 5th Meeting of the ICRPG Mechanical Behavior Working Group," CPIA Publication No. 119, Vol. I, October 1966.

51. Durelli, A. J., and Parks, V. J., "Experimental Stress Analysis of Loaded Boundaries in Two-Dimensional Second Boundary Value Problems," Catholic University Report No. 11, (Contract No. NONV 2249(06), February 1967.

52. Durelli, A. J., Parks, V. J., and Aribe, S., "Optimization of a Slot End Configuration in a Finite Plate Subjected to Uniformly Distributed Load," Catholic University Report No. 13, (Contract No. NONV 2249 (06), Washington, D. C., June 1967.

53. Durelli, A. J., and Parks, V. J., "Photoelastic Analysis in the Neighborhood of Corners of Long Strips Bonded on One Side and Shrunk", Am. Ceramic Soc. Bull., Vol. 46, No. 6, pp. 582-586, June 1967.

54. Durelli, A. J., Parks, V. J., and del Rio, C. J., "Stresses in Square Slabs, with Different Edge Geometries, when Bonded on One Face to a Rigid Plate and Shrunk", Experimental Mechanics, Vol. 7, No. 11, pp. 481-484, November 1967.

55. Durelli, A. J., Parks, V. J., and del Rio, C. J., "Stresses in a Square Slab Bonded on One Face to a Rigid Plate and Shrunk", Acta Mechanica, Vol. III, No. 4, pp. 352-359, 1967.

56. Parks, V. J., Chiang, F. P., and Durelli, A. J., "Maximum Stress at the Angular Corners of Long Strips Bonded on One Scale and Shrunk", Experimental Mechanics, Vol. 8, No. 6, pp. 278-281, June 1968.

57. Durelli, A. J., Parks, V. J., and del Rio, C. J., "Stresses, Strains and Displacements Associated with the Restrained Shrinkage of Cylinde. with Tocoidal Cavities", Recent Advances in Engineering Science, Ed. by C. Eringen, Vol. 3, pp. 521-540, 1968.

58. Robinson, C. N., Graham, P. H., and Moore, F. C., "Effect of Grain End Shape on Stress Concentrations at the Case-Propellant Interface", Vol. I of Atlantic Research Corporation Final Report on Solid Propellant Mechanical Behavior Studies, AFRPL-TR-69-124-Vol. I., (Contract F04611-68-C-0015), Alexandria, Virginia, May 1969.

59. Nelson, J. M., Cook, W. A., and Stibor, G. S., "Comparison of a Three-Dimensional Photoelastic Analysis and a Three-Dimensional Finite Element Analysis of a Propellant Grain Model", Bulletin of the 8th JANNAF Meeting of the Working Group on Mechanical Behavior, CPIA Publication No. 193, Vol. 8, pp. 87-88, March 1970.

60. Durelli, A. J.: "Experimental Strain and Stress Analysis of Solid Propellant Rocket Motors", in Mechanics and Chemistry of Solid Propellants , Edited by A. C. Eringen, H. Liebowitz, S. C. Koh, and J. M. Crowley, pp. 381-442, Pergamon Press, N. Y., 1967.

61. Sampson, R. C. and Campbell, D. M.: "The Grid-Shift Technique for Moiré Analysis of Strain in Solid Propellants", Experimental Mechanics, Vol. 7, No. 11, pp. 449-457, 1967.

62. Morse, S., Durelli, A. J., and Sciammarella, C. A.: "Geometry of Moiré Fringes in Strain Analysis", J. Eng. Mech. Div., Proc. ASCE, Vol. 86, No. EM-4, pp. 105-126, 1960.

63. Sciammarella, C. A. and Durelli, A. J.: "Moiré Fringes as a Means of Analyzing Strains", J. Eng. Mech. Div., Proc. ASCE, Vol. 8, No. EM-1, pp. 55-74, 1961.

64. Sciammarella, C. A. and Chiang, F. P.: "The Moiré Method Applied to Three-Dimensional Elastic Problems", Experimental Mechanics, Vol. 4, No. 11, p. 316, 1964.

65. Theocaris, P. S.:"The Moiré Method in Thermal Fields", Experimental Mechanics, Vol. 4, No. 8, pp. 223-231, 1964.

66. Post, D.: "The Moiré Grid Analyzer Method for Strain Analysis", Experimertal Mechanics, Vol. 5, No. 11, pp. 368-377, 1965.

67. Martin, L. P. and Ju, F. D.: "The Moiré Method for Measuring Large-Plane Nonhomogeneous Deformations", Experimental Mechanics, Vol. 10, No. 12, pp. 521-528, 1970.

68. Martin, L. P. and Ju, F. D.: "The Moiré Method for Measuring Large-Plane Deformations", J. Appl. Mech., Vol. 36, No. 3, pp. 385-391, 1969.

69. Theocris, P. S.: Moiré Fringes in Strain Analysis, Pergamon Press, Oxford, 1969.

70. Hart, W. D.: "Moiré Method for the Measurement of Strains in Solid Propellants", Bulletin of the 3rd ICRPG Meeting of the Working Group on Mechanical Behavior, CPIA Publication No. November 1964.

71. Dicken, G. M. and Thacher, J. H.: "Shear-Strain Measurement in Solid-Propellant Rocket Motors", J. Spacecraft and Rockets, Vol. 2, No. 5, pp. 765-769, 1965.

72. Webb, I. D.: Phase 1 Study and Temperature Transducer Development, Final Report, Volume I, Technical Analysis, AFRPL-TR-69-74, Rocketdyne, A Division of North American Rockwell Corp., McGregor, Texas, March 1969.

73. Anon.: ICRPG Propellant Mechanical Behavior Manual, Chemical Propulsion Information Agency Publication No. 21, February 1968.

74. Anon.: Stress State Transducer Development Program, Phase II, Transducer Designs and Evaluation Acceptance Test Procedures, R-4567, Rocketdyne, A Division of North American Rockwell Corp., McGregor, Texas, September 1969.

75. Leeming, H., et al.: "Solid Propellant Structural Test Vehicle Cumulative Damage and Systems Analysis," Technical Report No. AFRPL-TR-68-130, (Contract No. 404611-67-C-100), Lockheed Propulsion Company, Redlands, Calif., October 1969.

76. Leeming, H.: "Solid Propellant Structural Test Vehicle and Systems Analysis," LPC-Special Report No. 966-S-1, June 1969.

77. Leeming, H., et al.: "Solid Propellant Structural Test Vehicle and Systems Analysis," LPC Final Report No. 966-F(AFRPL-TR-70-10. Contract F04611-69-C-002), Lockheed Propulsion Company, Redlands, Calif., March 1970.

78. Burton, J. D. and Noel, J. S.: "Stress State Transducer Development Programs, Phase III, Transducer Fabrication, Phase IV, Transducer Evaluation," AFRPL-TR-70-102(Contract No. AF04611-68-C-0095), Rocketdyne, McGregor, Texas, October 1970.

79. San Miguel, A. and Siher, R. H.: "A Transducer to Aid in the Structural Design and Application of Plastics," Poly. Engr. Sci., Vol. 7, No. 1, pp. 26-31, 1967.

80. San Miguel, A. and Duran, E. N.: "On the Measurement of Stres in Solid Propellant," Experimental Mechanics, Vol. 10, No. 12, pp. 514-520, 1970.

81. Cousins, T. E.: "A Transducer for Measuring Radial Bond Stresses in Solid Propellant Rocket Motors," Insulation and Cast Bonding Symposium, CPIA Publication No. 159, Sept. 1967, Chemical Propulsion Information Agency, p. 195.

82. Miller, W. H.: "Experimentally Measured Radial Bond Stresses in a Full-Scale Motor," AIAA Paper 68-510,-Atlantic City, N. J., 1968.

83. Miller, W. H.: "Measurement of Solid Rocket Motor Thermally Induced Radial Bond Stresses," J. Spacecraft and Rockets, Vol. 6, No. 11, pp. 1253-1258, 1969.

84. Burton, J. D.: :Solid Propellant Grain-to-Case Bond Stress Measurement." SESA Paper No. 1585, 1969 SESA Fall Meeting, Houston, Texas, October 1969.

85. Fitzgerald, J. E. and Hufferd, W. L.: "Interaction of a Diaphragm Pressure Gage with a Viscoelastic Halfspace," Engineering Mechanics, Vol. 10, No. 7, pp. 257-265.

VII. FAILURE ANALYSIS

7.1 INTRODUCTION

A failure or strength analysis comprises the final stage of a grain structural integrity analysis. The results of a strength analysis are expressed as a factor of safety or margin of safety. Determining a minimum safety factor requires consideration of the statistical variations inherent in the experimental determination of material property data, the loads encountered by the motor (e.g., vibration, acceleration, pressurization, etc.), the physical environment of the motor (e.g., aging conditions, humidity, temperature, etc.), and the inaccuracies inherent in the analysis methods or artifically introduced through simplifying assumptions. The margin of safety determined through proper consideration of these factors is an indication of the overall system reliability. If these factors were precisely known, there would be no real requirement for a margin of safety greater than zero. Inasmuch as this is not the case, and quite often, assumptions or approximations must be made regarding specific information which is unavailable, arbitrary restrictions are placed on an acceptable minimum margin of safety. These restrictions reflect an ignorance factor associated with the structural analysis, the loading environment, propellant behavior and failure criteria as well as the physical environment and mission requirements.

7.1.1 ACCEPTABLE MARGIN OF SAFETY

A factor of safety or safety factor, SF, is defined as the ratio of the capability or allowable response to the induced or calculated load:

$$SF = \frac{\text{CAPABILITY}}{\text{INDUCED}} \qquad (7.1)$$

The margin of safety, MS, is defined by

$$MS = SF - 1 \tag{7.2}$$

Occasionally, a minimum safety factor will be specified by the sponsoring agency and the margin of safety will then be determined from this safety factor. This situation is analogous to most building codes in which factors of 1.15 to 1.25 are applied to the induced loads. In this case

$$MS = \frac{SF(Calculated}{SF(Specified)} - 1 \quad . \tag{7.3}$$

In view of the uncertainties and inadequacies described above, a liberal margin of safety is sought at the present time. As a general rule, a minimum margin of safety of 1.0 based on lower 3-σ unaged propellant properties leads to an acceptable design. The 1-σ standard deviation of propellant properties typically represents about a 10% variation. This variation coefficient is frequently used when such information is unavailable for the proposed propellant formulation. Information on aging degradation indicates that the margin of safety will be reduced to a value between 0.25 and 0.50 under long term ambient storage conditions. As the knowledge of the factors affecting grain structural integrity increases, minimum safety margins may approach 0.10. For the present time, however, lacking accurate descriptions of propellant behavior, and aging degradation, and insufficient knowledge of the statistical distribution of actual grain loads it is necessary to maintain substantial margins of safety in order to continue to produce and deliver

structurally reliable rocket motors; even when such practices are known to exclude grain designs and propellants which may be adequate and considerably less expensive. Even with liberal safety factors proper evaluation of grain structural integrity ultimately requires verification in Structural Test Vehicles.

In the following sections an accounting of some of the more commonly used approaches to propellant failure are presented along with the routine approaches for determining factors of safety. For convenience, the discussion here is separated into three parts: (1) discrete failure analysis, (2) failure criteria and (3) cumulative damage. It will become apparent that this separation is arbitrary and considerable overlapping actually exists.

7.2 DISCRETE FAILURE ANALYSIS

This section is entitled discrete failure analysis because it brings together the routine methods of determining safety factors for the individual loads a solid propellant rocket motor is subjected to rather than attempt to impose a single failure criterion.

To account for the marked time and temperature dependence of propellant behavior one attempts to conduct laboratory tests at loading rates and temperatures representative of the grain loading rate and temperature. In circumstances where this practice is not practiced the time-temperature equivalence principle is used to shift data at other temperatures or loading rates to the desired loading rate and temperature.

The stress state at the inner bore of a long propellant grain under thermal equilibrium or internal pressurization is 2:1 tension-tension. The maximum strain in strip biaxial specimens in constant strain rate tests at the appropriate temperature and strain rate or the constant strain endurance limit is used to evaluate failure by inner bore cracking under thermal equilibrium. Pressurized biaxial tests are used to evaluate port cracking under ignition pressurization. At the preliminary design and analysis state, these data may be estimated assuming propellant incompressibility if the required data are nonexistent. With the assumption of incompressibility the maximum strain in a biaxial specimen is 3/4 that obtained in a uniaxial tension test. Experimental results indicate that this factor may vary from .65 to .75 depending on the particular propellant.

The diametral compression test is often used to evaluate ignition pressure failure by port cracking. This test yields a tensile strain 2.5 times greater than that for uniaxial tension assuming propellant incompressibility. This test may be slightly over conservative, however, and the exact relation between uniaxial and diametral data should be experimentally determined. Experience indicates that uniaxial failure strain in pressurized tests is double that of unpressurized tests at temperatures above 0°F and about 1.5 times as great at lower temperatures. If the observed conversion of uniaxial to diametral data is about 1.5 as much as it is for some propellants, then the diametral test should adequately simulate pressurized biaxial strip failure data for preliminary design purposes.

The bond stress resulting from thermal cooling is evaluated using triaxial tension test data. This data is often approximated by uniaxial, biaxial or bonding data at the preliminary design stage. Failure at case-grain terminations may be evaluated using the blister peel test and the fracture energy considerations discussed in Chapter 5. When this type of data is unavailable, approximate calculations of safety factors make use of uniaxial or biaxial data with multiplicative stress concentration factors as discussed in Chapter 5.

Double-lap shear stress data are normally used to evaluate safety factors for axial acceleration. This stress may be taken to be 70 percent of the uniaxial tension failure stress in preliminary design considerations. Normally a stress concentration of 3 is introduced at the forward case-grain termination.

Separate tests are normally not conducted for excessive propellant deformations. The natural abhorrence of structural designers to large deformations usually prevents slump except for large diameter solid rocket motors. In this situation maximum grain slump is easily calculated using equilibrium propellant properties. Allowance is then made in the design to ensure adequate clearance.

Failure during sustained vibration is normally evaluated from prototype motor tests since irreversible effects such as fracture, degradation or decomposition effects and auto ignition which can result from the combined high temperature and cyclic strain conditions of the vibration environment are extremely difficult to account for. Experience has shown that for the conditions usually encountered in

solid rocket motor vibration, fracture or severe degradation will usually precede and prevent temperature rises to levels at which spontaneous ignition will occur. Propellant susceptibility to fracture, under prescribed vibration conditions is a significant factor in practical situations, however, and is found to vary significantly from propellant to propellant as well as for various transient loading conditions.

7.2 FAILURE CRITERIA

Following Williams [1] we will distinguish between two types of failure criteria. The term failure will be applied to a criterion in which some functional of the stress or strain is exceeded and fracture will denote a condition in which an existing flaw extends according to an energy balance hypothesis. Figure 1 depicts this distinction for a stress failure criterion and fracture of an existing macroscopic flaw.

7.2.1 FAILURE SURFACE CRITERION

A failure criterion defines some particular function of stress or strain which is experimentally evaluated. Failure is indicated when the values of the appropriate function is exceeded. From experience with metals seven such criteria have been investigated for solid propellant applications [2,3].

1) Maximum Principal Stress
2) Maximum Principal Strain
3) Maximum Principal Stress Difference (shear stress)

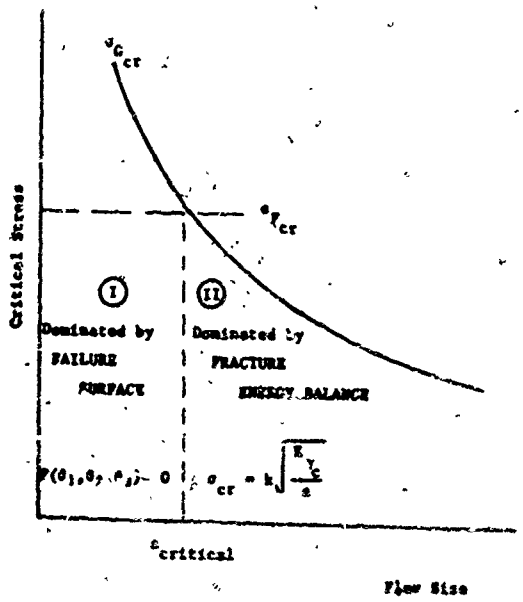

Figure 1. Fracture Regions of Influence

4) Maximum Principal Strain Difference (shear strain)

5) Maximum Total Strain Energy

6) Maximum Distortional Strain Energy

7) Maximum Conserved Distortional Strain Energy

Application of these failure criteria to solid propellants has achieved varying degrees of success. As an aid in visualization of failure, failure surfaces are normally constructed in principal stress (or strain) space. The various combinations of stress states for each of the stress octants are tabulated below:

OCTANT	σ_1	σ_2	σ_3
I	+	+	+
II	+	+	-
III	+	-	+
IV	+	-	-
V	-	+	+
VI	-	+	-
VII	-	-	+
VIII	-	-	-

It is observed that there are four octants characterized by the number of stresses of the same sign. This means that for an isotropic material only four octants need to be tested. These give stress or strain combinations of +++, ++-, +--, and ---.

Various studies aimed at obtaining a general failure criterion for propellants have been conducted, although a unified failure criterie has not yet been found. A few of these approaches are discussed in references 3 through 10.

The establishment of a failure criterion for solid propellants is complicated by the marked rate and temperature sensitivity of propellants. Smith has shown that a time-independent failure envelop may be constructed for uniaxial failure data of polymers. The Smith failure envelope is shown below:

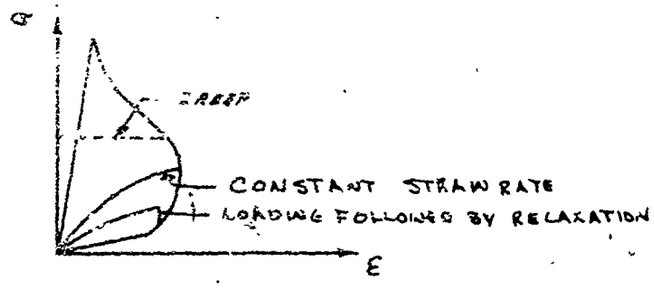

One of the difficulties in applying the Smith failure envelope to propellants is that it does not reflect the path dependent characteristics of propellant failure. Another difficulty is that the extension to multiaxial failure is not well understood.

Anderson and Bennett [9,10] have proposed an energy failure criterion in terms of the first and second stress invariants, and have successfully correlated uniaxial, biaxial and hollow ellipsoid failure data. The hollow ellipsoid test appear to be ideally suited for development of a failure criterion for solid propellants since failure data may be obtained in the four octants of stress space required for the complete description of failure of initially isotropic materials.

7.2.2 FRACTURE

The preceeding discussion has been concerned with failure of materials which do not exhibit flaws or defects. When pre-existing flaws exist Williams [12] has proposed a viscoelastic extension of

Griffith's brittle fracture theory whereby a pre-existing crack will become unstable and propagate when the energy release as a function of crack length and time exceeds a certain critical energy required for creation of a new surface. This approach has been successfully applied to the analysis and design of case-grain termination relief flaps and inner bore failure by port cracking during thermal cooling and pressurization.

7.2.3 CUMULATIVE DAMAGE

Several approaches have been proposed in recent years for assessing damage accumulation in solid propellants based on extension of Miner's linear cumulative damage law. These studies have considered accumulation of energy, stress and strain and have been mainly concerned with repeated temperature cycling and combined temperature and pressure loads.

The most extensive cumulative damage work has been carried out by Bills [12-15] at Aerojet General Corporation. Bills has considered statistical implications in evaluating cumulative damage and failure using a maximum principal stress approach. These studies have resulted in development of criteria for solid propellant screening and preliminary engineering designs. Shift factors have been introduced for pressure and environmental factors which are employed in a manner similar to that of the time-temperature shift factor. Recently, it has been concluded that motor firings generally ignore previous damage. In particular, a set of motors will fire successfully after temperature cycling if none of the motors failed during temperature cycling.

In addition to the studies conducted at Aerojet several other investigations have recently been completed. Rocketdyne [16] approached cumulative damage using fracture mechanics considerations. Atlantic Research Corporation [17] considered applications of the principles of absolute reaction rate theory as derived in the Tobolsky-Eyring expressions. Lockheed Propulsion Company [18] has proposed using volumetric response as a damage index. The general results of these investigations have demonstrated that environmental factors can produce very large changes in the time-to-failure data, and that the statistical aspects of cumulative damage testing are significant and complex; thus requiring the use of extreme value statistics for evaluation of grain reliability.

Hercules [19] has recently completed a cumulative damage study of CMDB propellants. They studied the use of stress cumulative damage, strain failure index, total energy failure index and stress-strain failure envelope, and found that although none of the four criteria accurately accounted for propellant behavior, each of the four were at least qualitatively valid for correlating various aspects of propellant behavior. A nonlinear modification was developed for the strain failure index criterion and used as a measure of the nearness-to-failure during monotonically increasing loading. This approach seems appealing since less nebulus results are expected when a strain failure criterion is applied to grain structural integrity determination.

7.3 REFERENCES

1. Williams, M. L.: "Some General Observations on Failure and Fracture", Lead Article, Solid Rocket Structural Integrity Abstracts, Vol. 7, No. 1, University of Utah, January 1970.

2. Williams, M. L.: "Structural Analysis of Viscoelastic Materials", AIAA Journal, pp. 785-808, 1964.

3. Kruse, R. B.: "Laboratory Characterization of Solid Propellant Mechanical Properties", AIAA Paper No. 65-147, AIAA 6th Solid Propellant Rocket Conference, Washington, D. C., February 1-3, 1965.

4. Jones, T. M. and Kruse, R. B.: "Failure Behavior of Composite Hydrocarbon Fuel Binder Propellants", AIAA Paper No. 65-156, AIAA 6th Solid Propellant Rocket Conference, Washington, D. C., February 1965.

5. Jones, J. W.: "Propellant Failure Mechanisms", LPC Research Division, T.N. 112, Lockheed Propulsion Company, July 1964.

6. Jones, J. W. and Knauss, W. G.: "Propellant Failure Criteria", AIAA Paper No. 65-157, AIAA 6th Solid Propellant Rocket Conference Washington, D. C.

7. Anderson, J. M.: "Rate Dependent Aspects of Failure in Cast Double-Base Propellant, Bulletin of the 8th Meeting of the Jannaf Mechanical Behavior Working Group, CPIA Publication No. 193, Vol. I, March 1970.

8. Swanson, S. R. and Chappell, B. N.: "Development of a Failure Criteria for Double-Base Propellants", Bulletin of the 6th ICRPG Working Group on Mechanical Behavior, CPIA Publication No. 1st, Vol. I, October 1967.

9. Bennett, S. J. and Andersen, G. P.: "Failure Properties of a PBAN Propellant in Multiaxial Stress Fields", Experimental Mechanics, pp. 19-25, September 1968.

10. Anderson, G. P. and Bennett, S. J.: "Fracture of Polymeric Materials in Multiaxial Stress Fields", AFRPL-TR-70-36, Thiokol Chemical Corporation, Wasatch Division, Brigham City, Utah, March 1970.

11. Williams, M. L.: Int. J. Fracture Mechanics, Vol. 1, p. 292, 1965.

12. Bills, K. W., Jr., et al: "A Cumulative-Damage Concept for Propellant-Liner-Bonds in Solid Rocket Motors", J. Spacecraft, Vol. 3, No. 3, p. 408-412, March 1966.

13. Bills, K. W., Jr., et al: "Development of Criteria for Solid Propellant Screening and Preliminary Engineering Design", Report 1159-81F, Aerojet General, December 1968.

14. Bills, K. W., Jr., et al: "Failures in Grains Exposed to Rapid Changes of Environmental Temperature", Aerojet General Report 1236-81F, September 1969.

15. Bills, K. W., Jr., et al: "Applications of Cumulative Damage in the Preparation of Parametric Grain Design Curves and the Prediction of Grain Failures in Pressurization, Report 1341-26F, Aerojet General Corporation, August 1970.

16. Noel, J. S., Burton, J. D. and Harbut, B.C.: "Fracture Mechanics Approach to Cumulative Damage", AFRPL-TR-68-132 (Rocketdyne No. R-4521), Rocketdyne, December 1968.

17. Robinson, C. N., Graham, P. H. and Moore, F.C.: "Application of Reactor Rate to Solid Propellant Mechanical Behavior", Vol. II of Final Report on Solid Propellant Mechanical Behavior Studies, AFRPL-TR-69-124-Vol. II, Atlantic Research Corporation, May 1969.

18. Leeming, H., et al: "Solid Propellant Structural Test Vehicle and Systems Analysis", LPC-Final Report No. 966-F, (AFRPL-TR-70-10; Contract No. F-04611-69-C-002), Lockheed Propulsion Company, Redlands, California, March 1970.

19. Anderson, J. M.: "Cumulative Damage Studies of Conventional-Cast Composite-Modified Double-Base Propellant", AFRPL-TR-69-258, Contract No. F04611-69-C-0016, Hercules, Inc., Magna, Utah, February 1970.

VIII. MATERIAL CHARACTERIZATION

8.1 INTRODUCTION

The material characterization of highly filled solid propellants represents one of the major problems to be resolved before proper structural integrity analyses can be made. Several factors contribute to this problem. The most important consideration is that of representation of propellant mechanical behavior. An adequate description of propellant behavior is required in all areas of grain structural integrity determination. A grain structural analysis is only as valid as the constitutive equations defining the propellant response. The calibration and interpretation of instrumentation for measurement of propellant grain interior stresses and strains is totally dependent upon propellant behavior. Similarly, a failure analysis is of limited value if an inappropriate failure criterion is used; the determination of appropriate failure criteria is likewise dependent on the constitutive equations defining propellant response.

In addition, it is important that the laboratory characterization tests closely simulate the stress state and mechanical and thermal loading history in a solid propellant grain.

It is also noted that in obtaining appropriate descriptions of propellant behavior consideration must be given to the statistical nature of propellant test data resulting from slight, and often subtle, variations in raw material lots, motor casting and curing conditions, and testing conditions and procedures. It is particularly important that nominal unaged propellant properties be quantitatively known in order to properly assess

changes, due to aging. In some situations batch-to-batch variations have been noted which overshadowed changes due to aging and thus complicated service life predictions.

Ideally, a minimum of ten tests from ten different production batches of propellant should be used for determining nominal mechanical and thermal properties. This objective is not always practical, particularly in the case of new propellants in the proposal or early development phase of a solid rocket motor. In such situations it is necessary to rely on past experience. As a rule-of-thumb a value of 10 percent may be used as an indication of the 1-σ standard deviation. In general this level can be maintained in production castings by mixing small batches of propellant as new lots of material are introduced into the production scheme and tailoring quantities such as oxidizer ground/unground ratio, curative ratios, degree of polymerization, crosslink density, etc., to obtain near nominal mechanical and ballistic properties. Determination of nominal propellant behavior from a small propellant casting should be avoided if possible, however.

This chapter presents very brief discussions of the more common mechanical and thermal property tests as well as an assessment of the adequacy of present test procedure for classifying and characterizing nonlinear response. The specific details of sample preparation and test procedures are not discussed here as these are well covered in the "ICRPG Solid Propellant Mechanical Behavior Manual", CPIA Publication No. 21. The material presented here is kept brief since more detailed discussions may be readily found in the literature (e.g., References 1-8). In addition, the Bulletins of recent ICRPG and JANNAF Mechanical Behavior Working Group Meetings, published by CPIA, contain many articles dealing with specific aspects of material characterization.

8.2 MECHANICAL PROPERTY TESTS

The common tests for determining solid propellant mechanical properties are constant elongation rate, stress relaxation, constant strain to failure, creep, constant stress to failure, low cycle fatigue and dynamic modulus measurements. These tests are normally conducted at various temperatures on uniaxial and multiaxial test specimens. Some of the various specimens used in the characterization of solid propellants are shown in Figure 1. Constant elongation rate tests are normally conducted at several loading rates, and stress relaxation and creep tests are conducted at various strain and stress levels, respectively. In addition to providing basic property data for analysis, failure data are also obtained.

Uniaxial tension tests are primarily used for quality assurance testing, and for defining a reduced master stress relaxation modulus curve and associated time-temperature shift function. Normally, the data from stress relaxation tests at several different temperatures are formally shifted horizontally along the time axis to obtain the time-temperature shift function since the WLF equation does not give a particularly good fit for highly solids loaded propellants. Uniaxial tests are also frequently used to obtain constant stress and strain to failure data, creep data and fatigue data.

The double-lap shear specimen with chevron ends yields a simple shear stress field when lateral movement of the outer boundaries is prevented [9-11]. For sufficiently large aspect ratios (approximately greater than 5) a state of near uniform shear exists in the central region of the specimen where failure usually initiates. This test is frequently used to obtain fatigue and dynamic data, and occasionally to determine relaxation moduli in shear.

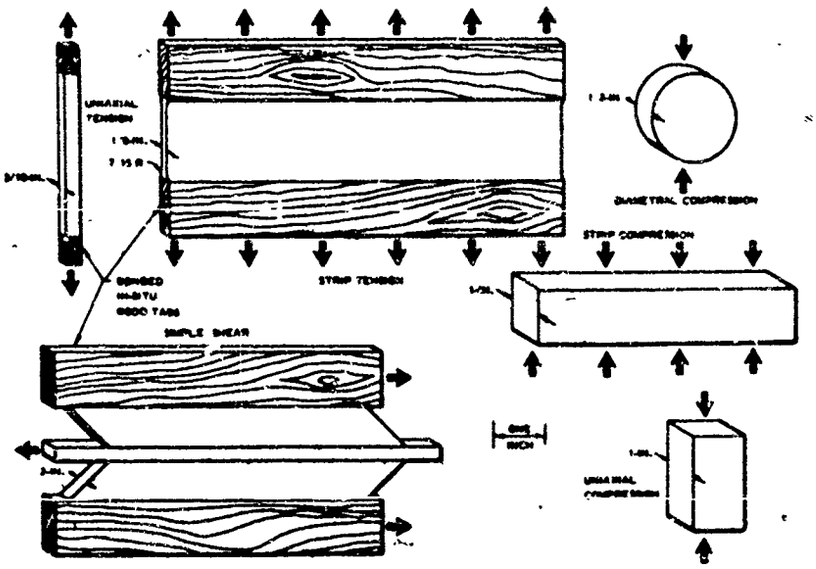

FIGURE 1. VARIOUS SPECIMENS USED IN THE MULTIAXIAL CHARACTERIZATION OF SOLID PROPELLANTS[9]

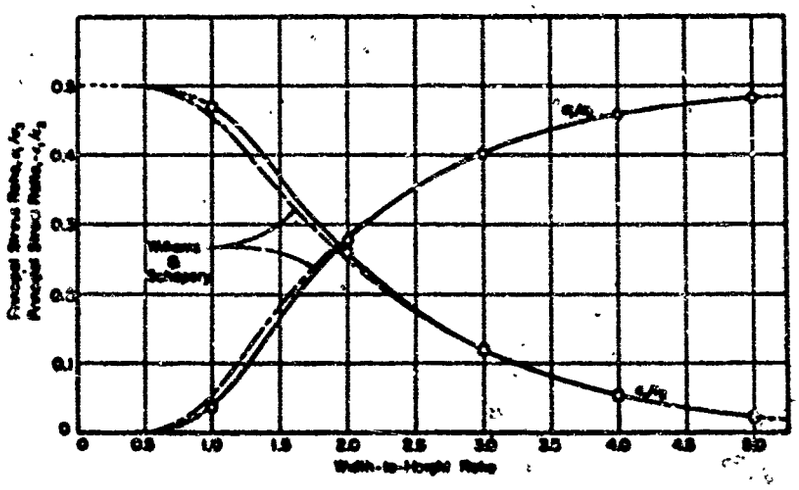

FIGURE 2. PRINCIPAL STRESS AND STRAIN RATIOS AT CENTER OF SPECIMENS FOR POISSON'S RATIO OF 0.5[12]

The biaxial strip specimen yields a 2:1 tension-tension principal stress ratio in the central portion of the specimen for sufficiently large aspect ratios (approximately greater than 5 as shown in Figure 2) assuming incompressible behavior [9-13]. This specimen is normally used for constant strain to failure tests and constant strain rate tests at several strain rates and various temperatures. Stress relaxation tests are also conducted using the biaxial strip specimen. When modifications for multiaxiality are introduced reasonably good agreement between uniaxial and strip biaxial test data is obtained. The strip specimen is used extensively for determining propellant cohesive fracture energy.

The diametral compression test yields a 3:1 compression-tension field at the center of the disk for diameter-to-thickness ratios in excess of about 3 [9, 10, 14-16]. The diametral specimen is mainly used for constant rate tests at several loading rates and temperatures to obtain preliminary or discrete failure data for ignition pressurization loads.

The diametral specimen is ideally suited for investigating the bilinear behavior of solid propellants, inasmuch as the vertical stress component is almost entirely compressive and the horizontal component is almost entirely tension. Figure 3 shows the variation of the ratio of the principal stresses at the center of the specimen as a function of the ratio, γ^2, of compressive modulus, E_c, to tensile modulus, E_T. Most modern highly solids loaded propellants have a value of γ^2 of approximately 2.

The poker chip test (Figure 4) yields a near triaxial tension stress field at the center of the specimen [17-24]. If the shear modulus or tensile modulus is known, this test provides data for determination of

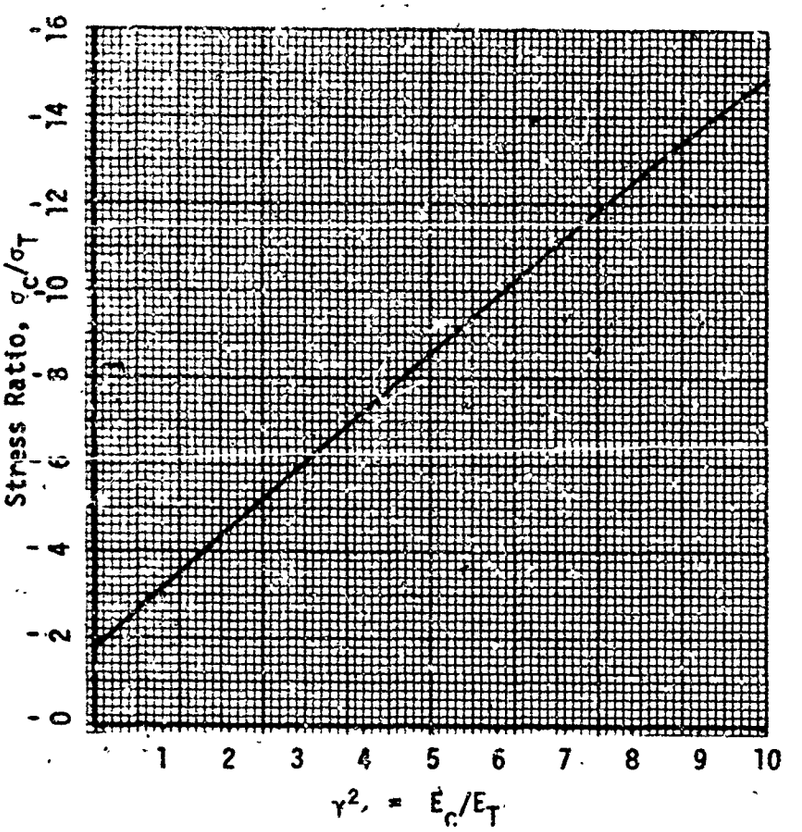

FIGURE 3. VARIATION OF THE RATIO OF PRINCIPAL STRESSES AT THE CENTER OF DIAMETRAL SPECIMEN FOR VARIOUS DEGREES OF BILINEARITY

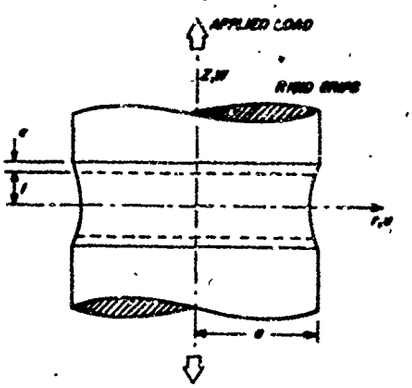

FIGURE 4. TRIAXIAL POKER-CHIP TEST SPECIMEN[24]

the bulk modulus. Inasmuch as the stiffness of this specimen is not normally negligible compared to that of the testing machine, it is usually necessary to use a stiff load transducer with a sensing tip bonded to the propellant at the center of one of the platens to obtain reliable test data.

Dilatometric tests are used for determining dilatation and bulk response; and to evaluate propellant failure properties under superposed pressure [25-37]. Pressure has no noticeable effect on propellant behavior until dewetting is observed.

The hollow ellipsoid test has recently been introduced as an additional multiaxial test for evaluation of propellant properties [38-40]. For linear material behavior this test yields a stress distribution which is independent of material properties. The test method involves suspending a specimen in a test cavity and applying internal and external pressures, or externally bonding the specimen in the test cavity and slowly lowering the temperature until failure is observed. By varying the ratio of major-to-minor axes and the inner and outer pressures acting on the specimen, the stress state at the inner bore of a solid rocket motor may be duplicated. This test may also be used for determining cohesive fracture energy. In some respects this test may adequately serve the purpose of a laboratory STV.

In addition to the tests noted above a wide variety of dynamic tests and specimen configurations have been used to characterize the response of solid propellants to cyclic loading. Some of these tests are summarized in Table I. These tests are useful for measuring viscoelastic behavior and fatigue life. More detailed references to the test procedures may be found in the ICRPG Mechanical Behavior Manual and in References 1 and 8.

TABLE I. SUMMARY OF DYNAMIC TESTS USED FOR SOLID PROPELLANT CHARACTERIZATION[1]

Test	Stress/Strain Application	Frequency Range, c.p.s.	Response Measured By	Data Usually Obtained
Fitzgerald Transducer	Forced sinusoidal nonresonant shear directly applied by pole pieces of electromagnet to sample disk	25-3000	Changes in resistance and capacitance of electrical drive system	$G'(\omega)$ $G''(\omega)$
Oscillating Plate (FIL Tester)	Forced sinusoidal shear strain imposed by mechanical drive of clamped annular plate of propellant	0.1-60	Deflection of center ring, applied force	$G'(\omega)$ $G''(\omega)$
Vibrating Plate	Forced sinusoidal shear strain imposed by vibrating outer ring of annular plate of propellant on an electrodynamic shaker	75-1000	Amplitude ratio, phase angle from two accelerometers, frequency from electrical drive	$G'(\omega)$ $G''(\omega)$
Resonant Weighted Column	Forced sinusoidal uniaxial tension and compression imposed by vibrating weighted rectangular column of propellant on electrodynamic shaker	30-1500	Amplitude ratio, phase angle from two accelerometers, frequency from electrical drive	$E'(\omega)$ $E''(\omega)$
LPC Large Deformation Dynamic Tester	Forced sinusoidal uniaxial tension and shear imposed by mechanical drive to tensile bar or double-lap shear specimen	1-45	Force and displacement by transducers in mounting arrangement	$E'(\omega)$ $E''(\omega)$ $G'(\omega)$ $G''(\omega)$
LPC Small Deformation Dynamic Tester	Forced sinusoidal shear imposed by piezoelectric driver to single-lap shear specimen	20-1000	Driving force from piezoelectric input voltage, transmitted force from piezoelectric monitor on clamped end of specimen	$G'(\omega)$ $G''(\omega)$
Free Vibrating Reed Tester (AGC)	Free damped sinusoidal vibration of clamped thin rectangular specimen, free end set in motion by deflection and release	4-30	Deflection from strain gauge mounted on sample recorded against time, sample dimensions and mass. Time range extended by using time-temperature super-position	$E'(\omega)$ $E''(\omega)$
Forced Vibrating Reed Tester (HPC)	Forced sinusoidal vibration of thin cantilever beam specimen by electrodynamic shaker	10-200	Free end displacement by optical displacement transducers. Input from shaker electrical measurements	$E'(\omega)$ $E''(\omega)$
Dynamic Torsion Tester, Low Range (STL)	Forced sinusoidal oscillatory torsion imposed by mechanical drive to hollow cylindrical specimen through bell-crank arrangement	0.0002-30	Angular displacement sensed by differential transformers; speed indication from electromagnetic sensor on output shaft of drive motor	$G'(\omega)$ $G''(\omega)$
Dynamic Torsion Tester, High Range (STL)	Forced sinusoidal rotary vibration imposed by electrodynamic vibrator to hollow cylindrical specimen through bell-crank arrangement	30-1000	Angular displacement sensed by piezoelectric accelerometers; frequency from vibrator input	$G'(\omega)$ $G''(\omega)$

A schematic of the large deformation dynamic test apparatus used by Lockheed Propulsion Company [41, 42] for investigating heat generation during cyclic loading is shown in Figure 5.

8.3 THERMAL PROPERTY TESTS

A knowledge of propellant density, specific heat and thermal conductivity or thermal diffusivity and coefficient of thermal expansion is required for the ballistic design and structural analysis of solid propellant rocket motors.

Density determinations are normally made using large machined blocks of cured propellant. The density of uncured propellant is determined using a gravimetric technique. There is typically little difference between the two methods.

The specific heat of solid propellants is routinely determined using calorimetry techniques. Apparently, the most accurate determinations of propellant thermal conductivity make use of a guarded hot plate [43, 44]. The determination of the thermal diffusivity of propellants is difficult and is normally calculated after the specific heat, thermal conductivity and density are known. Direct determination of the thermal diffusivity can be made by observing the temperature response of a series of thermocouples accurately positioned in a cured block of propellant subjected to one-dimensional heat conduction [45].

The coefficient of thermal expansion is routinely determined from linear measurements of length-temperature changes using a quartz tube dilatometer. This test also provides information about the glass transition temperature. The coefficient of thermal expansion of most propellants is temperature independent with different values above and below

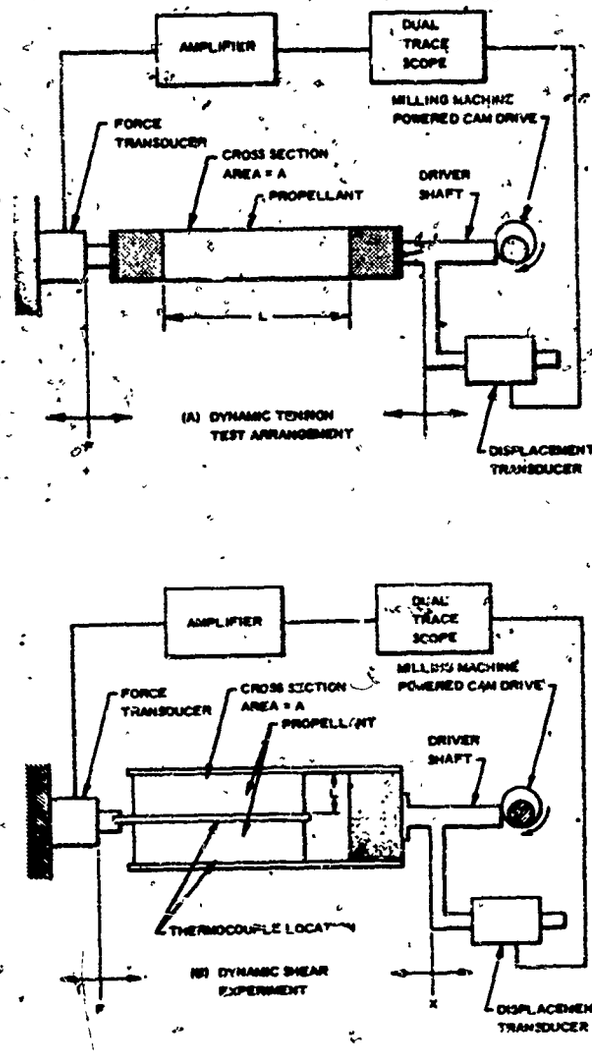

FIGURE 5. SCHEMATIC OF LARGE DEFORMATION DYNAMIC TENSION AND SHEAR APPARATUS[41]

the glass transition temperatures. Different values are also frequently obtained for heating and cooling. Inasmuch as there are indications that the coefficient of thermal expansion may be dependent upon the stress state it is desirable to make measurements in a strained state. Measurement of the dimensional changes of the inner bore at various equilibrium temperatures in two circular port STV's with different web fractions provides sufficient information for calculation of an effective value of Poisson's ratio and the coefficient of thermal expansion for propellant in a multiaxial stress state.

8.4 NONLINEAR CHARACTERIZATION

The use of linear viscoelasticity for a grain structural analysis quite naturally presupposes linear propellant behavior. Specifically, the requirements of additivity (linear superposition of additive outputs and inputs) and homogeneity (e.g., that doubling the rate of strain rate test will double the stress). A rather detailed discussion of the above point is contained in Reference [46]. This reference points out that there arises an all too common failing in carrying out the test procedures given in the ICRPG Mechanical Behavior Manual; namely, neglect of the experimental determination of linearity. In addition, linearity verification is often improperly carried out.

An example of the latter failure is the use of the constant strain rate test as a means of checking linearity. While linear superposition is required for linearity, obedience to the homogeneity condition (i.e., scalar multiplication, $\sigma(a\varepsilon) = a\sigma(\varepsilon)$), is not sufficient to guarantee linearity. Superposition requires that $\sigma(\varepsilon_1+\varepsilon_2) = \sigma(\varepsilon_1) + \sigma(\varepsilon_2)$; that is, the stress produced by the additive superposition of two different

strain histories equals the sum of the stresses produced by each strain history acting alone.

There are three major reasons why propellants fail to obey the linearity rules:

- nonlinearities induced by a basic physical nonlinearity in the propellant
- geometrical nonlinearities induced by large strains, and
- nonlinearities caused by irreversible micro-structural changes in the propellants.

8.41 PHYSICAL NONLINEARITIES

Consider the first cause of nonlinearity, basic physical behavior. For illustrative purposes, consider the rather simple situation of a parallel spring and dashpot - the Kelvin model (no reference is to be drawn that this model represents a solid propellant rather it is one of the simplest reductions of an n^{th} order finite differential operator form for linear viscoelasticity). The governing equation is then

$$\sigma(t) = E\varepsilon(t) + \eta\dot{\varepsilon}(t) \qquad (8\text{-}1)$$

where E is the elastic modulus and η is the viscous coefficient. A constant strain rate input at a rate R_1 can be expressed as

$$\varepsilon_1(t) = R_1 t \qquad (8\text{-}2)$$

Thus from (8-1)

$$\sigma[\varepsilon_1(t)] = ER_1 t + \eta R_1 \tag{8-3}$$

A second test using a rate of strain kR_1 with k an arbitrary constant yields a new input, $\varepsilon_2(t)$;

$$\varepsilon_2(t) = kR_1 t = k\,\varepsilon_1(t) \tag{8-4}$$

$$\dot{\varepsilon}_2(t) = kR_1 = k\,\dot{\varepsilon}_1(t) \tag{8-5}$$

Now (8-1) yields

$$\sigma[\varepsilon_2(t)] = kER_1 t + k\eta R_1 = \sigma[k\varepsilon_1(t)]. \tag{8-6}$$

Comparison of (8-6) with (8-3) and (8-4) then shows that

$$\sigma[k\varepsilon_1(t)] = k\sigma[\varepsilon_1(t)] \tag{8-7}$$

Hence, the homogeneity requirement of linearity holds. This result is implicitly based on both E and η being independent of both strain and strain rate.

If the elastic modulus, E, is strain dependent, say, for example,

$$E = E_0 - E_1\varepsilon \tag{8-8}$$

where E_0 and E_1 are constants, then (8-3) becomes with (8-4)

$$\sigma[\varepsilon_1(t)] = E_0 R_1 t - E_1 R_1^2 t^2 + \eta R_1 . \tag{8-9}$$

Equation (8-6) becomes

$$\sigma[\varepsilon_2(t)] = kE_0 R_1 t - k^2 E_1 R_1^2 t^2 + kn R_1 = k[E_0 R_1 t - kE_1 R_1^2 t^2 + n R_1] \tag{8-10}$$

Inspection of (8-9) and (8-10) then shows that

$$\sigma[k\varepsilon_1(t)] \neq k\sigma[\varepsilon_1(t)] \tag{8-11}$$

because of the multiplier k in the second term of (8-10). Indeed, scalar multiplication holds if and only if $k = 1$; that is, $\varepsilon_1(t) = \varepsilon_2(t)$, identical strain histories or $E_1 = 0$, a linear elastic modulus.

If the viscosity coefficient, η, is nonlinear (non-Newtonian) with a form, say

$$\eta = \eta_0 + \eta_1 \dot{\varepsilon} \tag{8-12}$$

then (8-3) becomes

$$\sigma[\varepsilon_1(t)] = ER_1 t + \eta_0 R_1 + \eta_1 R_1^2 \tag{8-13}$$

and (8-6) becomes

$$\sigma[\varepsilon_2(t)] = \sigma[k\varepsilon_1(t)]$$

$$= kER_1t + kn_0R_1 + k^2n_1R_1^2$$

$$= k[ER_1t + n_0R_1 + kn_1R_1^2] \qquad (8\text{-}14)$$

We again see that from (8-13) and (8-14)

$$\sigma[k\varepsilon_1(t)] \neq k\sigma[\varepsilon_1(t)] \qquad (8\text{-}15)$$

because of the scalar k in the third term of (8-14)

The error or, more properly, deviation from linearity in a constant strain rate test with nonlinearities of the type given by (8-8) in the elastic modulus or (8-12) in the viscous portion is proportional to:

- The ratio of E_1 to E_0, a measure of the intrinsic nonlinear elasticity which vanishes for $E_1 = 0$ (see (8-10))
- The actual value of strain with the nonlinearity increasing at higher strains (compare the term R_1t with $kR_1^2t^2$ in (8-10))

Note that (8-10) may be rewritten as

$$\sigma[k\varepsilon_1(t)] = k\sigma[\varepsilon_1(t)] + k(1-k)E_1\varepsilon_1^2(t) \qquad (8\text{-}16)$$

which for $k > 1$ indicates increased strain rate for the strain $\varepsilon_2(t)$.

Thus, nonlinearity increases proportional to

- $k(1-k)$. At a given time, the "stress softening" effect is more pronounced the greater the rate of strain ratio, k, between the two tests for $k > 1$.
- $\varepsilon_3^2(t)$. The "stress softening" effect increases as the square of the strain value, i.e., the deviation from linearity is greater at the higher strain values and, equivalently, longer times.

Comparison of (8-13) and (8-14) with the latter rewritten as

$$\sigma[k\varepsilon_1(t)] = k\sigma[\varepsilon_1(t)] - k(1-k)\eta_1 R_1^2 \qquad (8\text{-}17)$$

shows that the deviation from homogeneity, for $k > 1$, i.e., increased rate of strain, is

- proportional to $k(1-k)$
- proportional to the basic nonlinear viscosity coefficient, η, and
- proportional to the square of the basic strain rate, R_1.

Quite obviously, both the deviations of (8-16) with respect to the elastic modulus and of (8-17) with respect to the viscous components will only be detectable in a test to the extent that the deviations exceed the data scatter.

Both of the types of deviation become more marked as the ratio of the strain rate of the two tests increases (as k becomes larger).

8.4.2 GEOMETRIC NONLINEARITIES

Assuming a material that is fundamentally linear, one can nevertheless observe, apparent nonlinearities in the stress-strain relation. This phenomena occurs and is observable at large strains, say above 10% in typical solid propellants.

The reasons are purely geometric (or more properly, kinematical) in that the expression for stress is linear in strain and as usually used is referenced to the infinitesimal strain (tensor). As is demonstrated in any text on large deformation elasticity, the use of this infinitesimal strain measure is only an approximation to the correct stress-strain expression. Thus, the large strain nonlinearities result.

As a matter of fact, if one observes actual linearity in the relation of, say, uniaxial stress to the infinitesimal measure of strain, ε, for very large strains, say 20% to 50%, then the material is basically nonlinear. That is, since a basically (physically) linear material should show nonlinearities at large strain with respect to the equations of infinitesimal elasticity the occurrence of linearity in, say, a uniaxial tension, test at these large strain levels will be an indication of basic nonlinear behavior. One would then expect to observe fairly large nonlinearities in, say, a biaxial or other multiaxial test at these same large strain levels.

It should be added that much of the linearity reported in tests above the 10% strain level is because of irreproducibility of the test samples as well as careless control and/or observation of temperature and humidity levels during testing resulting in such large data scatter

that a linear relation may as well be fit to the observed data. This is a proper procedure. Since the data have a large error, one may as well adopt the simplest constitutive equation, a linear one, and obtain questionable analysis results readily and inexpensively. It makes little sense to employ barely tractable nonlinear theories with data of low reliability. The validity of any analysis based upon poor data can only be assured with the concomittant use of large safety factors however, say above 3.0.

8.4.3 IRREVERSIBLE MICRO-STRUCTURAL CHANGES

The third major type of nonlinearity is caused by essentially irreversible microstructural changes such as

- polymer bond breakage
- vacuole formation in the binder
- dewetting vacuole formulation between the binder and solid filler particles.

Unfortunately the single constant strain-rate tests discussed previously in this chapter are not sufficient to detect these irreversible changes. The test does not reverse nor repeat the straining pattern. Thus, a constant strain rate test will show micro-structural changes as physical nonlinearities which were described earlier.

The previously referenced paper by Farris and Fitzgerald [46] has been followed up by extensive work on irreversible changes or permanent memory effects in the doctoral thesis of Farris [47] and the essence of the work with applications has been reported by Fitzgerald and Farris in reference [48]. Currently, further effort along these lines is being

pursued by Farris, now at Aerojet-General Corporation, Sacramento, California, and at the University of Utah.

The essential test procedure for the detection of these microstructural changes is based upon the additivity portion of the linearity law. Two distinct types of tests are generally recommended,

- loading; unloading; reloading, and
- ramp-strain, rest, additional ramp-strain.

For example, Fig. 6 shows the relaxation modulus calculated from tests run at strain levels differing by a factor of two. The results obey the homogeneity rule of linearity in that the resultant modulus is independent of strain.

Thus, if one were to infer from the above that linearity (linear viscoelasticity) held, the predicted results of Fig. 7 would hold. It is observed, however, that quite a different experimental curve results.

A triply repeated ramp strain tests produced the results of Fig. 8 where the calculated curve is based upon a constitutive equation utilizing the ratio of the maximum strain, $||\varepsilon_{11}||_\infty$ to a weighted average $||\varepsilon_{11}||_{21}$, the so-called Lebesgue-21 norm, times the present value of strain, $\varepsilon_{11}(t)$.

For comparison, Figure 9 shows the results of a linear viscoelastic prediction versus a "permanent memory" prediction for a triple ramp strain.

It is thus clear that a different set of nonlinearity is observed with repeated ramp tests. It is thought that the present type of nonlinearity is caused by bond breakage in the propellant binder. Reference [48] discusses this point at length.

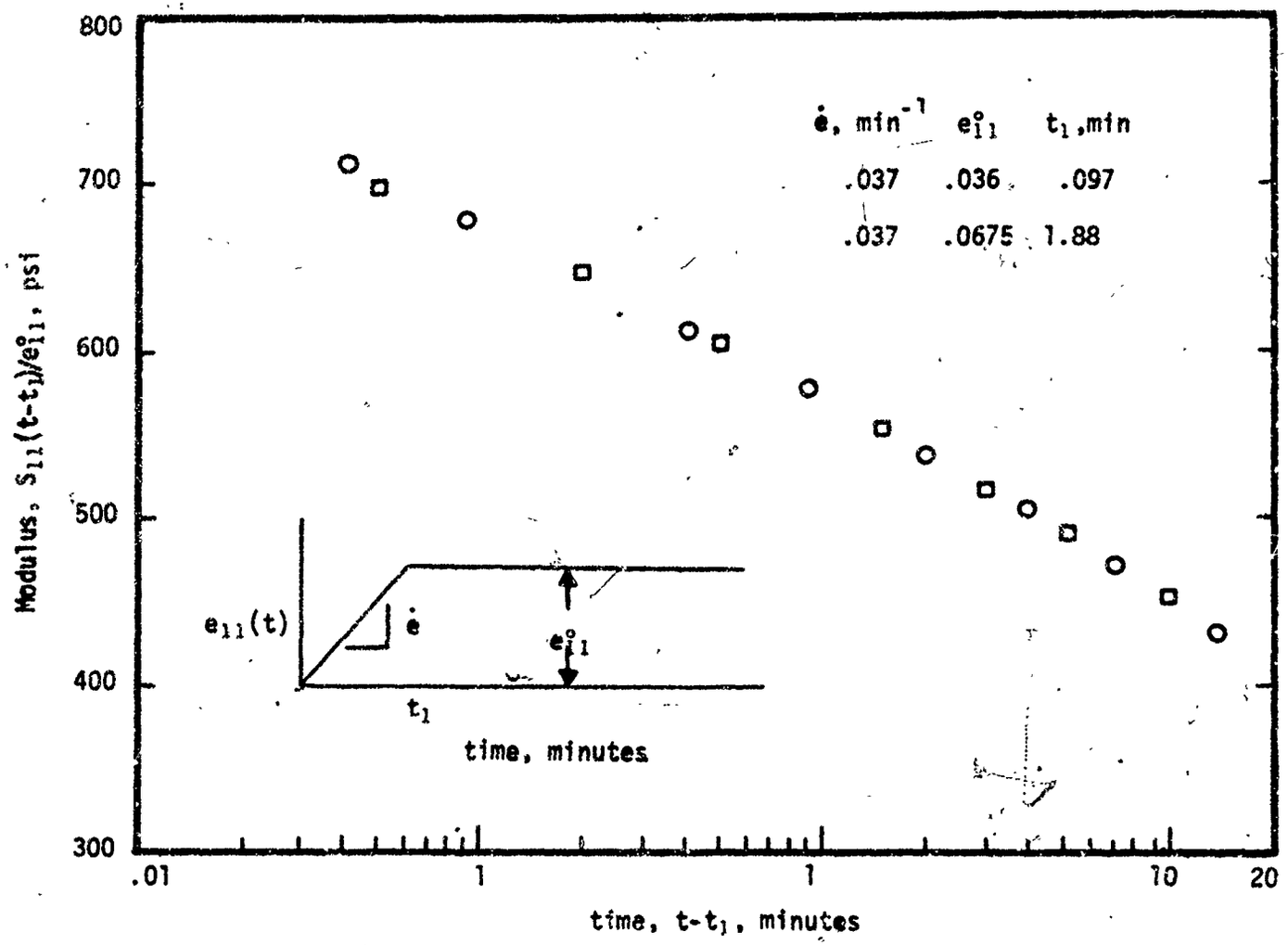

Figure 6. RAMP RELAXATION MODULUS FOR TWO SAMPLES TESTED AT DIFFERENT STRAIN LEVELS [48]

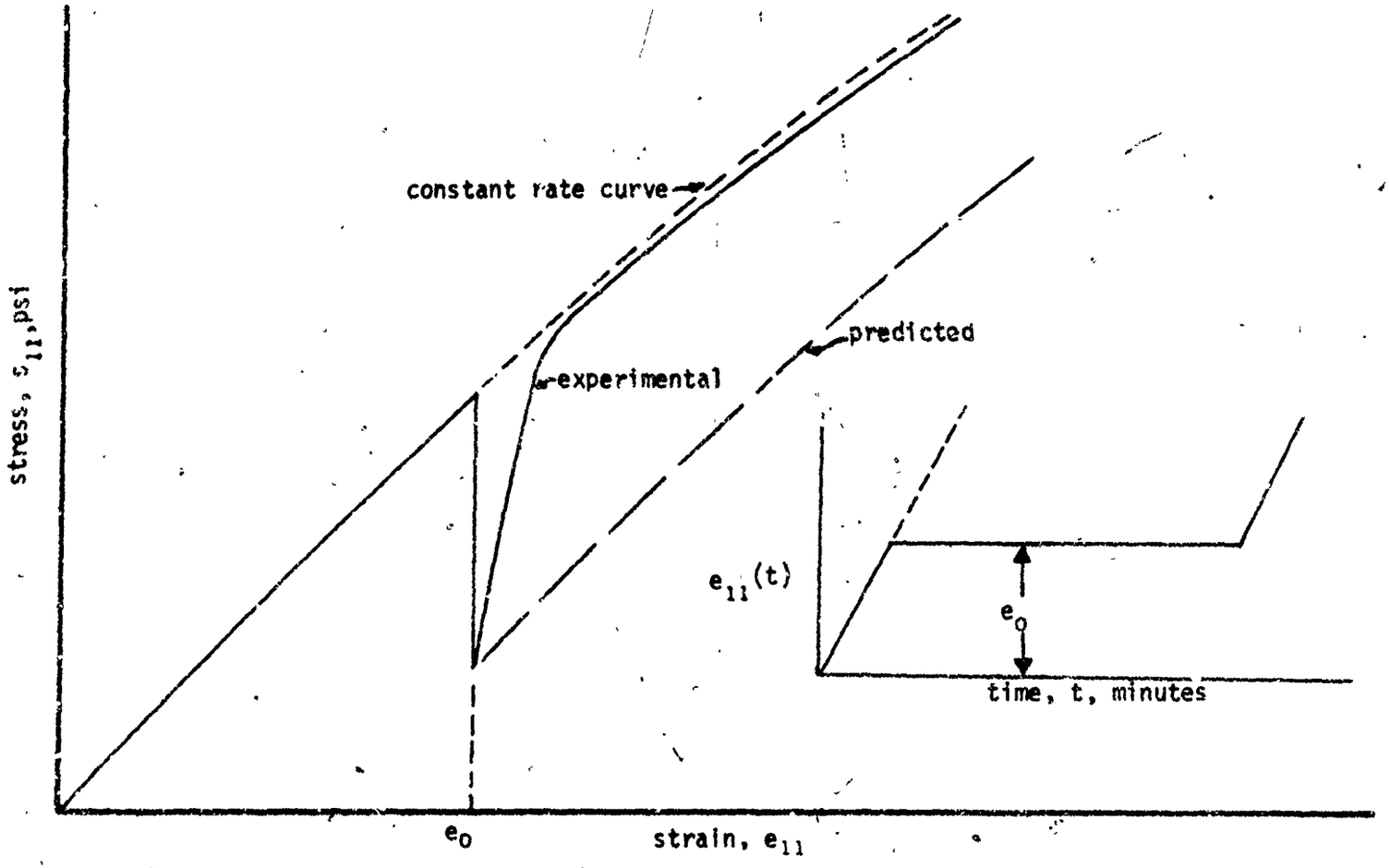

Figure 7. LINEAR VISCOELASTIC STRESS-STRAIN PREDICTION AND EXPERIMENTAL DATA FOR AN INTERRUPTED RAMP STRAIN INPUT ON A TYPICAL COMPOSITE PROPELLANT [48].

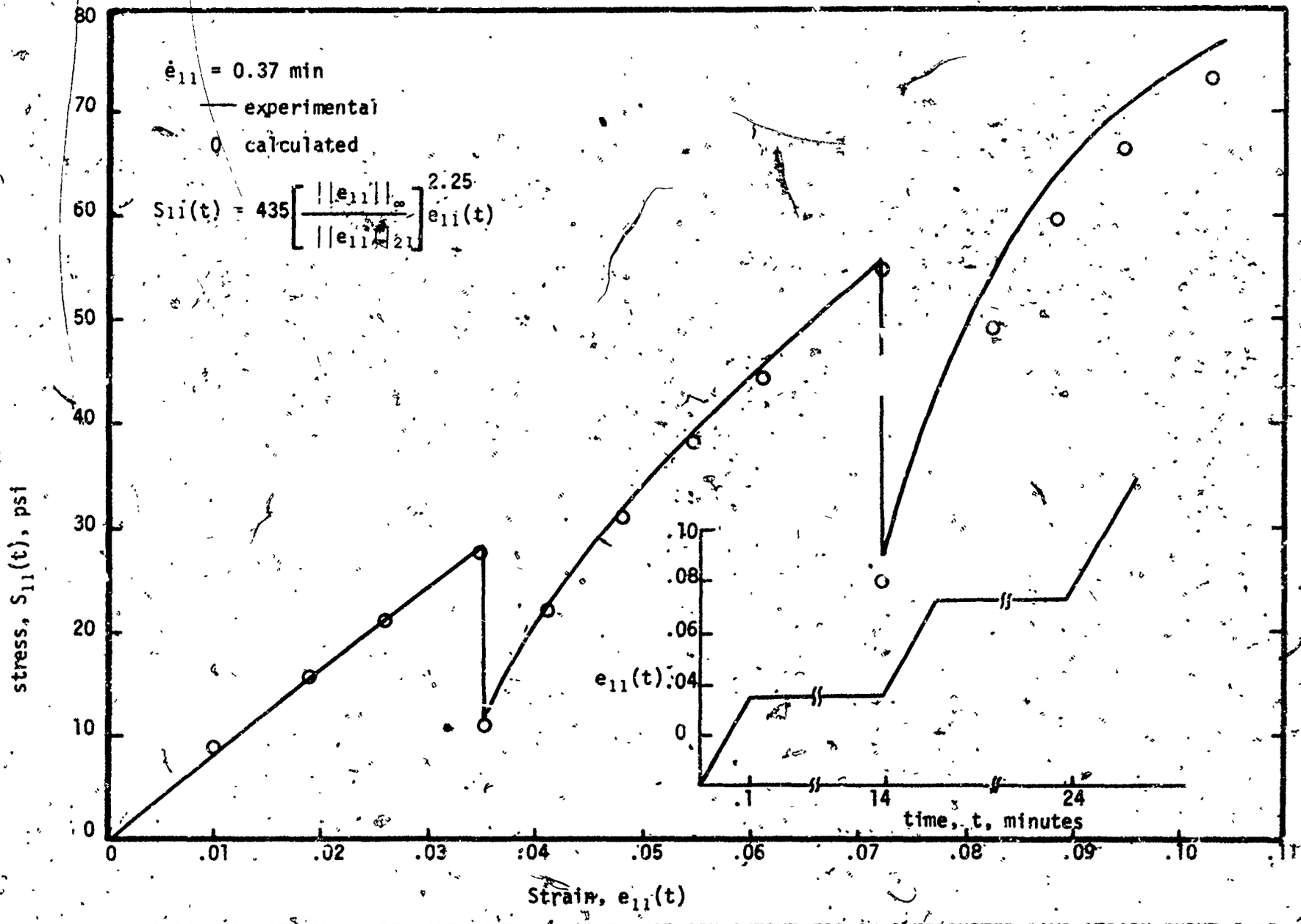

8.22

Figure 9. COMPARISON OF CALCULATED AND OBSERVED STRESS-STRAIN OUTPUT FOR AN INTERRUPTED RAMP STRAIN INPUT [48].

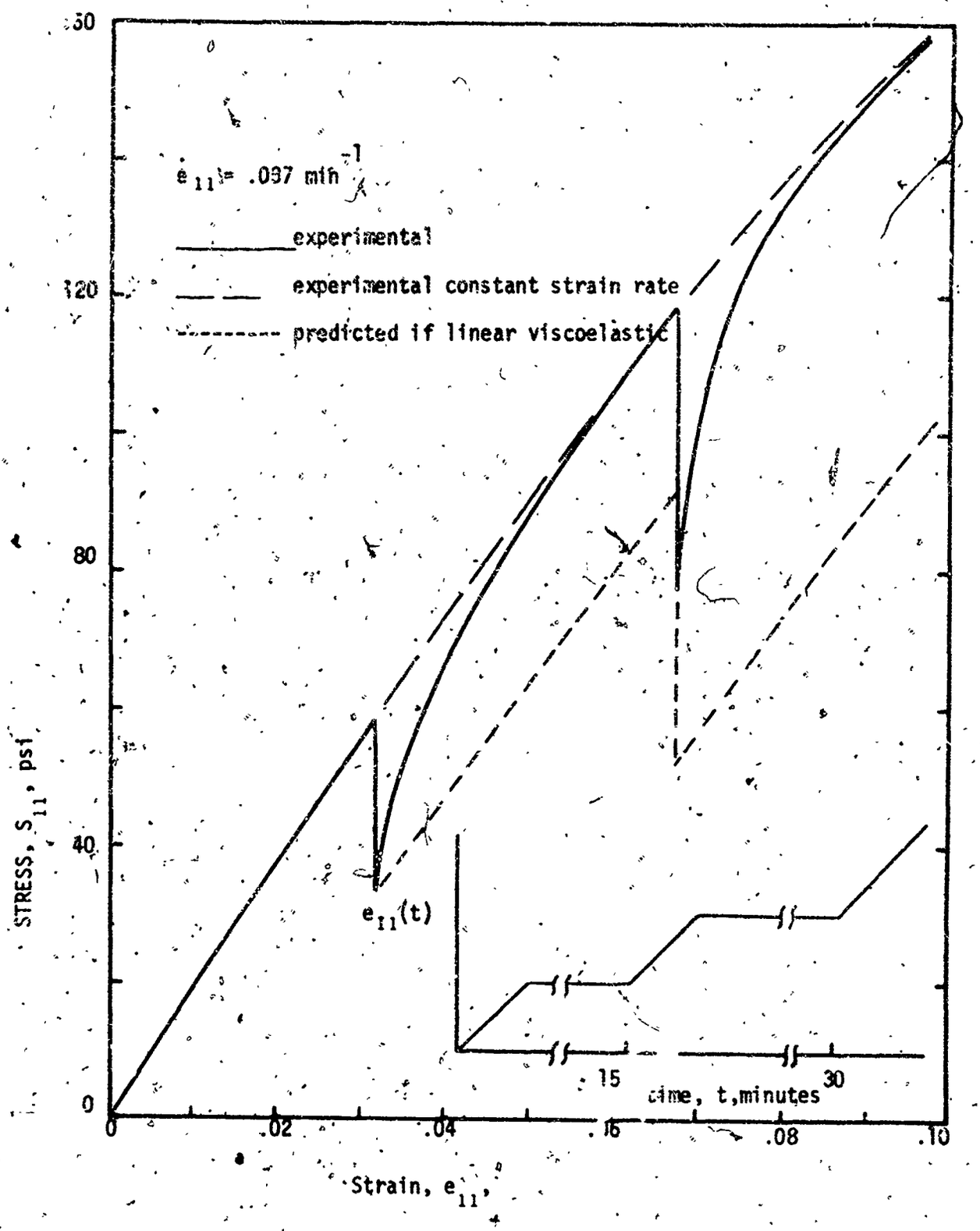

Figure 9. STRESS OUTPUT FOR INTERRUPTED CONSTANT STRAIN RATE TEST [48].

C.1.4 CLOSURE

Several causes of nonlinearity in test results have been pointed out and discussed. It has been shown that one must specify test procedures, (straining histories) involving more extensive tests than simple constant-strain and single ramp-strain in order to detect and distinguish the various nonlinearities.

To the extent that the observed nonlinearities are within acceptable tolerance levels for the intended use, it is recommended that a linear characterization be used.

Where the degree of nonlinearity is large for the intended use, recourse to a nonlinear constitutive relation will be required. This point is dealt with in Chapter II.

Where linearity is indicated for use, linear elasticity and linear viscoelasticity theory may be applied.

One additional point with respect to repeated loading should be mentioned: If tests on a "permanent memory" material exhibiting irreversible changes are conducted after the material has been, say, strained to the maximum anticipated working strain, then the remaining nonlinearities, if any, will fall into the category of basic physical or large strain induced nonlinearities previously discussed. Thus, a "shakedown test" will often be in order prior to test characterization if the ultimate use of the material also involves repeated loadings and unloadings. It is this latter point which provides hope for linear or pseudo-linear characterization and analysis of "permanent memory" type materials.

8.5 NOMENCLATURE

a	=	Constant
E	=	Tensile Modulus
E_0	=	Constant
E_1	=	Constant
E_C	=	Compressive Modulus
E_T	=	Tensile Modulus
k	=	Constant
R_1	=	Strain rate
ε	=	Strain
ε_1	=	Principal Strain
ε_2	=	Principal Strain
$\dot{\varepsilon}$	=	Strain Rate
γ^2	=	E_C/E_T
η	=	Viscosity
η_0	=	Constant
η_1	=	Constant
σ	=	Stress
σ_1	=	Principal Stress
σ_2	=	Principal Stress

8.6 REFERENCES

1. Britton, S. C., "Characterization of Solid Propellants as Structural Materials," Solid Rocket Structural Integrity Abstracts, Vol. 2, No. 4, pp. 1-71, October 1965.

2. Williams, M. L., "Structural Analysis of Viscoelastic Materials," AIAA Journal, Vol. 2, pp. 785-808, 1964.

3. Kruse, R. B., "Laboratory Characterization of Solid Propellant Mechanical Properties," AIAA Paper No. 65-147, 6th Solid Propellant Rocket Conference, Washington, D. C., February 1965.

4. Bollard, R. J. H., et al., "Structural Integrity Analysis of Large Solid Propellant Motor Grains," MSC Report No. 65-21-2, Mathematical Sciences Corporation (Contract No. NAS 7-242), July 1965.

5. Dill, E. H., "The Concept of Constitutive Relations and Failure Criteria and their Essential Role in Design," Paper presented at the ICRPG/AIAA 2nd Solid Propulsion Conference, Anaheim, July 1967.

6. Kruse, R. B., "Propellant Physical Characterization," Paper presented at the 7th Annual Meeting of the ICRPG Mechanical Behavior Working Group, Orlando, November 1968.

7. Dill, E. H., et al., "Structural Integrity Studies," MSNW Report No. 69-50-1, Mathematical Sciences Northwest, Inc. (Contract NAS 7-464), December 1969.

8. Kelley, F. N., "Solid Propellant Mechanical Properties Testing, Failure Criteria, and Aging," Advances in Chemistry, No. 88, "Propellants, Manufacture, Hazards and Testing," pp. 188-243, American Chemical Society, 1969.

9. Jones, J. W. and Knauss, W. G., "Propellant Failure Criteria," AIAA Paper No. 65-157, AIAA 6th Solid Propellant Rocket Conference, Washington, D.C., February 1965.

10. Jones, J. W., "Propellant Failure Mechanisms," Bulletin of the 3rd Meeting of the ICRPG Working Group on Mechanical Behavior, Vol. 8, CPIA Publication No. 611, p. 371, 1964.

11. Cost, T. L., and Parr, C. H., "Analysis of the Biaxial Strip and Shear Lap Tests for Solid Propellant Characterization," Report No. S-73, Rohm & Haas Company (Contract DA-01-021-AMC-11536(Z)), May 1967.

12. Cost, T. L. and Parr, C. H., "Analysis of the Biaxial Strip Test for Polymeric Materials," J. Materials, J MLSA, Vol. 4, pp. 312-323, 1969.

13. Williams, M. L. and Schapery, R. A., "Studies of Viscoelastic Media," ARL 62-356, Aeronautical Research Laboratories (Contract No. AF 33(616)-8399), June 1962.

14. Fitzgerald, J. E., "A Biaxial Test for Solid Propellants," Bulletin of the 19th Meeting of the JANAF Panel on Physical Properties of Solid Propellants, SPIA Publication No. PPI3, p. 155, 1966.

15. Brisbane, J. J., "Stress Distribution in an Elliptical Disk with Concentrated Loads Acting Along the Axes of Symmetry," Quarterly Report on Engineering Research, Rohm & Haas, Co., 1962.

16. Brisbane, J. J., "Further Development of a Bi-Axial Stress Test for Viscoelastic Materials," Bulletin of the 20th Meeting of the JANAF Panel on Physical Properties of Solid Propellants, Vol. I, SPIA Publication No. 144, p. 257, 1961

17. Lindsay, G. H., et al, "The Triaxial Tension Failure of Viscoelastic Materials," ARL 63-152, Aerospace Research Laboratories (Contract No. AF 33(6161-8399), September 1963.

18. Messner, A. M., "Stress Distributions in Poker-Chip Tensile Specimens," Bulletin of the 2nd Meeting of the ICRPG Working Group on Mechanical Behavior, CPIA Publication No. 27, p. 109, 1963.

19. Brisbane, J. J., "Stresses, Strains and Displacements in the Poker Chip Specimen," Bulletin of the 2nd Meeting of the ICRPG Working Group on Mechanical Behavior, CPIA Publication No. 27, p. 337, 1963.

20. Harbert, B. C., "Triaxial Tensile Failure of Solid Propellants," Bulletin of the 3rd Meeting of the ICRPG Working Group on Mechanical Behavior, CPIA Publication No. 61U, p. 357, 1964.

21. Lindsay, G. H., "Stress Distribution in a Poker Chip Specimen Subject to Combined Loads," Bulletin of the 3rd Meeting of the ICRPG Working Group on Mechanical Behavior, CPIA Publication No. 61U, p. 573, 1964.

22. Harbert, B. C., "Triaxial Testing of Solid Propellants," Bulletin of the 4th Meeting of the ICRPG Working Group on Mechanical Behavior, CPIA Publication No. 94U, October 1965.

23. Lindsay, G. H., "Hydrostatic Tensile Fracture of a Polyurethane Elastomer," ARL 66-0029, Aerospace Research Laboratories, (Contract No. AF 33(615)-2217), February 1966.

24. Lindsay, G. H., "Triaxial Fracture Studies," J. Appl. Phys., Vol. 38, pp. 4843-4852, 1967.

25. Sweeny, K. H. and Bills, K. W., "Poisson's Ratios Determination," Bulletin of the JANAF Panel on Physical Properties of Solid Propellants," SPIA Publication No. PPII, pp. 109-113, 1958.

26. Bischel, K., "Measurement of Poisson's Ratio in Tension," Bulletin of the 17th JANAF Panel on Physical Properties of Solid Propellants," SPIA Publication No. PPII, p. 203, 1958.

27. Rainbird, R. W. and Vernon, J. H. C., "An Instrument for the Measurement of Volume Changes Occurring in Tensile Testing," Bulletin of the 19th Meeting of the JANAF Panel on Physical Properties of Solid Propellants, SPIA Publication No. PP13, p. 39, 1960.

28. Kruse, R. B., "Dilatometric Behavior of Composite Solid Propellants under Uniaxial Tension", Bulletin of the 20th Meeting of the JANAF Panel on Physical Properties of Solid Propellants, Vol. I, SPIA Publication No. 140, p. 307, 1961

29. Wogsland, N. C., "An Apparatus for Measuring the Bulk Modulus of Solid Propellants", Bulletin of the 20th Meeting of the JANAF Panel on Physical Properties of Solid Propellants, Vol. I, SPIA Publication No. 140, p. 317, 1961

30. Svob, G. J., et. al., "Volume Changes in Polyurethane Propellants Subjected to Small Strains", Bulletin of the 20th Meeting of the JANAF Panel on Physical Properties of Solid Propellants, Vol. I, SPIA Publication No. 140, p. 295, 1961

31. Fishman, N. and Rinde, J. A., "Dilatation of Composite Propellants", Bulletin of the 2nd Meeting of the ICRPG Working Group on Mechanical Behavior, CPIA Publication No. 27, p. 349, 1963

32. Farris, R. J., "Strain Dilatation in Granular Filled Elastomers", Supplement to the Bulletin of the 2nd Meeting of the ICRPG Working Group on Mechanical Behavior, CPIA Publication No. 27A, p. 55, 1964

33. Fishman, N. and Rinde, J. A., "Development of a Dilatational Equation-of-State", Bulletin of the 3rd Meeting of the ICRPG Working Group on Mechanical Behavior, Vol. I, CPIA Publication No. 61U, 1964

34. Farris, R. J., "Dilatation of Granular Filled Elastomers under High Rates of Strain", J. Appl. Pol. Sci., Vol. 8, p. 23, 1964

35. Surland, C. C., "Compressibility of Elastomers with Crystalline Fillers and Microvoid Inhomogeneities Related to Various Empirical Equations of State for Liquids and Solids", J. Appl. Pol. Sci., Vol. 11, pp. 1227-1249, 1967.

36. Surland, C. C., "Compressibility and Other Thermodynamic Properties of Polymers", J. Appl. Pol. Sci., Vol. 12, pp. 1423-1437, 1968.

37. Farris, R. J., "The Influence of Vacuole Formation on the Response and Failure of Filled Elastomers", Transactions of Soc. Rheology, Vol. 12, pp. 315-334, 1968.

38. Bennett, S. J. and Anderson, G. P., "Mechanical and Failure Properties of Propellant in a Multiaxial Stress Field", Bulletin of the 4th Meeting of the ICRPG Working Group on Mechanical Behavior, CPIA Publication No. 94U, October 1965.

39. Anderson, G. P. and Bennett, S. J., "Mechanical and Failure Properties of an 86 Percent Solids PBAN Propellant in Multiaxial Stress Fields", Exp. Mech., Vol. 8, pp. 411-418, 1968

40. Anderson, G. P. and Bennett, S. J., "Fracture of Polymeric Materials in Multiaxial Stress Fields", AFRPL-TR-70-36, Thiokol Chemical Corp., (Contract F04611-69-C-0036), March 1970.

41. Jones, J. W. and Cantey, D. E., "Investigations of Propellant Dynamic Responses, Viscoelastic Linearity and Thermorheological Behavior", Bulletin of the 3rd Meeting of the ICRPG Working Group on Mechanical Behavior, CPIA Publication No. 61U, pp. 203-243, October 1964.

42. Schapery, R. A. and Cantey, D., "Thermomechanical Response Studies of Solid Propellants Subjected to Cyclic and Random Loading", AIAA Paper No. 65-160, AIAA 6th Solid Propellant Rocket Conference, Washington, D. C., February 1965

43. Allen, E. L. and Willoughby, D. A., "A Simple, Accurate Method for Determining Thermal Conductivity of Solid Propellants", Report S-160, Rohm and Haas Company (Contracts DAAH01-67-C-0655 and DAAH01-68-C-0632), June 1968

44. Allen, E. L. and Willoughby, D. A., "A Simple, Accurate Method for Determining Thermal Conductivity of Solid Propellants", Bulletin of the 7th Meeting of the ICRPG Working Group on Mechanical Behavior (U), CPIA Publication No. 177, pp. 47-53, October 1968

45. Jones, J., Fitzgerald, J. E. and Francis, E. C., "Thermal Stress Investigation of Solid Propellant Grains: Volume I - Theory and Experiment", LPC Report No. 578-F-1, Lockheed Propulsion Company, (Contract HF04(611)-8013), May 1963

46. Farris, R. and Fitzgerald, J. E., "Deficiencies of Viscoelastic Theories as Applied to Solid Propellants", Bulletin of the 8th JANNAF Mechanical Behavior Working Group, CPIA Publication No. 193, Vol. I, March 1970

47. Farris, R. J., "Homogeneous Constitutive Equations for Materials with Permanent Memory", UTEC TH 70-063 Project THEMIS Report AFOSR 70-1962-TR, University of Utah, July 1970

48. Fitzgerald, J. E. and Farris, R. J., "Characterization and Analysis Methods for Nonlinear Viscoelastic Materials", Project THEMIS Report, UTEC TH 70-204, University of Utah, November 1970

IX. LINEAR VISCOELASTICITY

9.1 INTRODUCTION

The literature on linear viscoelasticity is quite extensive; rather than attempt a decidedly incomplete listing, we cite only a few references [1-12], which in themselves contain extensive references to additional works as well as to the original papers.

Certain portions of this chapter have been prepared from lecture notes of classes taught by Dr. W. G. Knauss[1] at the California Institute of Technology, and Dr. M. L. Williams[2] at the University of Utah. We appreciate their permission to include this material.

It is also observed that this discussion is quite abbreviated since the intention here is merely to provide an illustrative introduction to viscoelasticity.

9.2 GENERAL CONSIDERATIONS

When considering the stress-strain relation of an elastic material, it is evident that for a particular value of stress there is associated a particular value of strain, and regardless of the length of time that the stress acts upon the body, or what path was followed in applying it, the strain remains constant. In viscoelastic materials, however, when a stress is applied to the body, the strain state depends upon the manner in which the stress is applied; that is, whether the load is applied

[1] Lecture notes on Theory of Viscoelasticity, California Institute of Technology, Pasadena, California, 1965-1966.

[2] "Engineering Analysis of Viscoelastic Media," University of Utah, Salt Lake City, Utah, March 20-24, 1967.

rapidly or slowly. Thus, the history of loading must be considered as well as the magnitude of the load. In addition, a viscoelastic body will not maintain a constant deformation under a constant stress, regardless of the loading pattern, rather it will deform or creep with time. Also, if such a body is constrained at constant deformation, the stress necessary to hold it gradually diminishes, or relaxes.

Without becoming unnecessarily involved in semantics, one may consider this time dependent effect to be the underlying distinction between viscoelastic materials and elastic materials.

9.3 DESCRIPTION OF A LINEARLY VISCOELASTIC MATERIAL

Material linearity is defined in terms of superposition (additivity) and scalar multiplication (homogeneity) of action and reactions. For illustrative purposes, a simple uniaxial tensile bar will be considered here rather than a general solid under arbitrary loading conditions. Many concepts of viscoelastic material behavior can be demonstrated using this simple stress state, and in most cases, the extension to general three-dimensional considerations is straightforward.

Let the force displacement relation be given in the general form

$$u(t) = [\psi]_t \, F(t) \qquad (9\text{-}1)$$

where $[\psi]_t$ is a time operator characteristic of the material properties of the tensile bar. (For a linearly elastic material, the operator becomes a constant, $\frac{1}{E}$; E being Young's modulus, assuming the bar to have unit dimensions). Equation (1) describes a linear force-displacement relation if the operator $[\psi]_t$ has the properties that

$$[\psi]_t\ [kF(t)] = k[\psi]_t F(t)] \tag{9-2}$$

and

$$[\psi]_t\ [F_1(t) + F_2(t)] = [\psi]_t\ F_1(t) + [\psi]_t\ F_2(t) \tag{9-3}$$

where k is a constant. Equation (2) is an expression of the homogeneity requirement (scalar multiplication) and (3) expresses the addicivity or superposition requirement. These are the only requirements for linearity, and thus

$$k\ u(t) = [\psi]_t\ [k\ F(t)] \tag{9-4}$$

and

$$u(t) = [u_1(t) + u_2(t)] = [\psi]_t\ [F_1(t) + F_2(t)] \tag{9-5}$$

9.4 CONSTITUTIVE EQUATIONS

Consider the special case of an applied time-varying force, a step function of magnitude ΔF_1 at time $t = 0$. Let $H(t)$ denote the Heaviside unit step function and let $c(t) = [\psi]_t\ H(t)$. Then the corresponding displacement Δu is given by

$$\Delta u(t) = c(t)\ \Delta F_1 \tag{9-6}$$

Now let a second force ΔF_2 be applied in a step-like manner at a time τ after the first load, i.e.,

$$F_2(t) = \Delta F_2\ H(t-\tau). \tag{9-7}$$

If the operator $[\psi]_t$ has not changed in the time interval $0 < t < \tau$, or equivalently, if the material characteristics have not changed in this interval (no aging)[3], then the response is only a function of the time interval $t-\tau$, and one finds that

$$[\psi]_t \, H(t-\tau) = c(t-\tau) \quad , \tag{9-8}$$

or

$$\Delta u_2 = \begin{cases} c(t-\tau)\, F_2, & t > \tau \\ 0, & t < \tau \end{cases} \tag{9-9}$$

Linearity permits adding the displacements Δu_1 and Δu_2 to obtain a total displacement after time τ as

$$u = \Delta u_1 + \Delta u_2 = c(t)\Delta F_1 + c(t-\tau)\, \Delta F_2 \tag{9-10}$$

More generally,

$$u = \sum_{i=0}^{N} \Delta u_i(\tau_i) = \sum_{i=0}^{N} c(t-\tau_i)\Delta F_i \quad , \quad (\tau_0 = 0) \tag{9-11}$$

The response (11) is due to the forcing function

$$F = \sum \Delta F_i \, H^*(t-\tau_i) \tag{9-12}$$

---

[3] If the operator changed characteristics then

$$[\psi]_t \, H(t-\tau)F = c(t,\tau)$$

and $\Delta u_2 = c(t,\tau)\Delta F_2$.

Linearity is still not violated with a (linear) aging material.

shown schematically below:

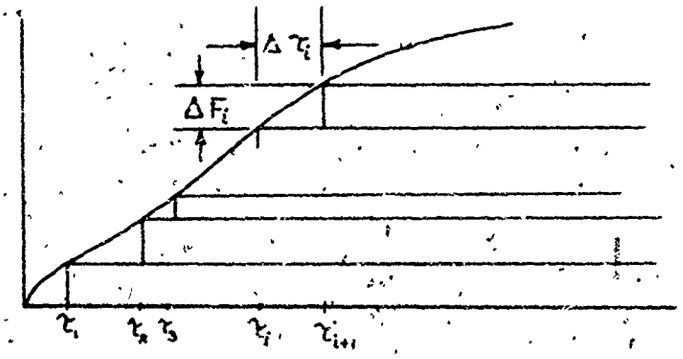

Suppose F is now allowed to approach a continuous function by letting

$$\Delta F_i \to 0 \quad \text{and} \quad \Delta\tau_i = \tau_{i+1} - \tau_i \to 0$$

such that

$$\lim_{\Delta\tau_i \to 0} \frac{\Delta F_i}{\Delta\tau_i} = \left(\frac{dF}{dt}\right)_{t=\tau} \tag{9-13}$$

Then the sum on the right hand side of (11) tends to the integral

$$\lim_{\substack{\Delta\tau_i \to 0 \\ \Delta F_i \to 0}} c(t-\tau_i)\,\frac{\Delta F_i}{\Delta\tau_i}\,\Delta\tau_i = \int_0^t c(t-\tau)\left(\frac{dF}{d\tau}\right)_{t=\tau} d\tau \tag{9-14}$$

This integral is known as Duhamel's integral or Boltzmann's superposition integral. It describes the displacement response of a linearly viscoelastic rod, to an arbitrary load history F(t). If the function F(t) contains a step at t = 0, the response is written more explicitly as

$$u(t) = c(t)F(0) + \int_{0+}^{t} c(t-\tau)\left(\frac{dF}{dt}\right)_{t=\tau} d\tau \tag{9-15}$$

where the integral is interpreted as the limit

$$\lim_{\varepsilon \to 0} \int_{\varepsilon}^{t} c(t-\tau) \left(\frac{dF}{dt}\right)_{t=\tau} d\tau \qquad (9\text{-}16)$$

If F contains further discontinuities, the integral is interpreted in the Lebesgue-Stieltjes sense

$$u(t) \int_{0}^{t} c(t-\tau) \left(\frac{dF}{dt}\right)_{t=\tau} d\tau + \sum_{i=1}^{N} c(t-\tau_i)\, \Delta F_i \qquad (9\text{-}17)$$

In terms of stress $\varepsilon(t)$ and strain $\sigma(t)$, (15) is written

$$\varepsilon(t) = J(t)\sigma(0) + \int_{0+}^{t} J(t-\tau)\dot{\sigma}(\tau)d\tau \qquad (9\text{-}18)$$

where $J(t)$ is normally referred to as the creep function.

If the roles of stress and strain are reversed, the analogous expression

$$\sigma(t) = E(t)\, \varepsilon(0) + \int_{0+}^{t} E(t-\tau)\dot{\varepsilon}(\tau)d\tau \qquad (9\text{-}19)$$

is obtained in which $E(t)$ is the relaxation function.

Taking the Laplace transforms of the appropriate relaxation and creep forms of (15) one obtains the relation between $E(t)$ and $J(t)$; namely,

$$p^2 \bar{E}(p)\, \bar{J}(p) = 1 \qquad (9\text{-}20)$$

The inverse relation of (20) is

$$\int_{0}^{t} E(t-\tau)J(\tau)d\tau = t = \int_{0}^{t} J(t-\tau)E(\tau)d\tau \qquad (9\text{-}21)$$

Equations (20) and (21) are expressions of the fact that the transformed modulus and the transformed compliance are reciprocals of each other. This reciprocity also holds in the t-plane for short time glassy behavior and long time rubbery behavior. For most cases acceptable engineering accuracy is obtained assuming $E(t) = 1/J(t)$ through the transition region also.

The three-dimensional equations may be written by direct analogy with the stress-strain equations of elasticity; viz.,

$$\tau_{ij} = \delta_{ij} \int_0^t \lambda(t-\tau)\dot{e}(\tau)d\tau + \int_0^t \mu(t-\tau)\dot{e}_{ij}(\tau)d\tau \qquad (9\text{-}22)$$

Equation (22) is often written in terms of the spherical and deviatoric components for convenience,

$$\tau_{ij} = S_{ij} + \frac{1}{3}\sigma\,\delta_{ij} \qquad (9\text{-}23)$$

and

$$e_{ij} = \varepsilon_{ij} + \frac{1}{3}e\,\delta_{ij} \qquad (9\text{-}24)$$

where $e = e_{ii}$ and $\sigma = \tau_{ii}$. In this form,

$$S_{ij} = \int_0^t G(t-\tau)\dot{\varepsilon}_{ij}(\tau)d\tau \qquad (9\text{-}25)$$

and

$$\sigma = \int_0^t K(t-\tau)\dot{\varepsilon}(\tau)d\tau \qquad (9\text{-}26)$$

in which G and K denote respectively, the relaxation functions (moduli) in shear and dilatation. This form is found to be particularly convenient,

as will become evident, when the normal assumption of elastic bulk response is assumed.

In addition to the integral formulation previously developed, it is often convenient to consider the differential-operator description of linear viscoelastic behavior

$$P\ \sigma(t) = Q\ \varepsilon(t) \tag{9-27}$$

where q and Q are defined by

$$p = \sum_{i=0}^{N} a_i \frac{\partial^i}{\partial t^i} \tag{9-28}$$

$$Q = \sum_{i=0}^{M} b_i \frac{\partial^i}{\partial t^i} \tag{9-29}$$

in which M = N or is at most greater by one power. This form is convenient for the often used model representation for uniaxial linear viscoelastic response.

9.5 STRESS ANALYSIS

The most straightforward method of obtaining the viscoelastic response for a large class of problems in linear viscoelasticity makes use of the correspondence principle. Through application of the correspondence principle, the time dependent viscoelastic response can be calculated from the solution to an "associated" elastic problem. The basis for the correspondence principle is that, with zero initial conditions, the Laplace or Fourier time-transformed viscoelastic field equations and boundary conditions are formally identical with the equations for an

elastic body with the same geometry. Transformed solutions are calculated by standard elasticity methods, and then inverted to obtain the time-dependent response. The final step of inverting the transforms is often extremely difficult if standard exact or asymptotic methods are used. Two approximate methods of Laplace transform inversion for viscoelastic analysis developed by Schapery are discussed subsequently.

The use of the Laplace or Fourier transforms and the correspondence principle is restricted to that class of problems in which application of the transform results in the replacement of the time dependence by an algebraic dependence on the transform parameter. This means that the correspondence principle will not apply to problems where the boundaries are changing with time, such as in the case of an ablating inner boundary of a burning solid rocket motor, nor will it apply to problems where the boundary conditions are changing from prescribed forces to prescribed displacements or vice-versa, such as in the rolling contact problem.

In the special case of proportional loading (i.e., space and time dependence of prescribed loads and displacements are separable), it has been further observed that the spacial dependence of the transformed viscoelastic solution is the same as that in a geometrically similar elastic body provided the spacial dependence of the prescribed quantities is identical for both problems. This result allows a transformed solution to be derived directly from an elastic solution by replacing the elastic constants by operational moduli (or compliances) and the time dependent prescribed loads and displacements by transformed quantities. It is further observed that for constant stress boundary conditions applied at time $t = 0$, the stress distribution in a viscoelastic body is the same as that in an elastic body of the same geometry with the same loading conditions.

The formal procedure for obtaining a viscoelastic solution using the correspondence principle is now outlined:

(1) Assuming that the material is elastic, obtain the elastic solution for the stresses τ_{ij}, strains e_{ij} and displacements u_i as a function of the geometry, loading and elastic material constants; i.e.;

$$\tau_{ij} = \tau_{ij} (x_k; E, \nu, P) ,$$
$$e_{ij} = e_{ij} (x_k; E, \nu, P) ,$$
$$u_i = u_i (x_k; E, \nu, P) .$$

(2) Replace all time-varying quantities by their Laplace transform equivalents:

$$\tau_{ij} (t) \rightarrow \bar{\tau}_{ij} (p) ,$$
$$e_{ij} (t) \rightarrow \bar{e}_{ij} (p) ,$$
$$u_i (t) \rightarrow \bar{u}_i (p) ,$$
$$P (t) \rightarrow P (p) .$$

(3) Replace the elastic constants by their transform equivalents:

$$K \rightarrow K (p) ,$$
$$E \rightarrow E (p) ,$$
$$G \rightarrow G (p) ,$$
$$\nu \rightarrow \nu (p) .$$

(4) Transform the physical boundary conditions; i.e.,

$$\tau_{ij} (t) \rightarrow \bar{\tau}_{ij} (p) ,$$
$$u_i (t) \rightarrow \bar{u}_i (p) .$$

(5) Solve the associated elasticity problem, now formulated in terms of the transformed field equations and boundary conditions, for the transformed stresses, strains and displacements; i.e.,

$$\bar{\tau}_{ij} = \bar{\tau}_{ij}\,[x_k;\ E(p),\ \nu(p),\ P(p)]\ ,$$
$$\bar{e}_{ij} = \bar{e}_{ij}\,[x_k;\ E(p),\ \nu(p),\ P(p)]\ ,$$
$$\bar{u}_i = \bar{u}_i\,[x_k;\ E(p),\ \nu(p),\ P(p)]\ .$$

(6) Carry out the inversion of the dependent variables; i.e.,

$$\tau_{ij}(x_k, t) = \mathcal{L}^{-1}\,[\bar{\tau}_{ij}(x_k, p)]\ ,$$
$$e_{ij}(x_k, t) = \mathcal{L}^{-1}\,[\bar{e}_{ij}(x_k, p)]\ ,$$
$$u_i(x_k, t) = \mathcal{L}^{-1}\,[\bar{u}_i(x_k, p)]\ .$$

The problems associated with applying the above procedure for obtaining a viscoelastic solution involve the representation of the viscoelastic material constants, and, as mentioned above, the inversion of the transformed quantities. There are several techniques for representing the material behavior. One of the more simple methods makes use of one of the simple model representations. Computational complexities preclude the use of anything more than a four- or five-element model representation of the material, however. Alternately one can use the modified power law representation; e.g.,

$$E_{rel}(t) = E_e + \frac{E_g - E_e}{[1 + t/\tau_o]^n}\ , \qquad (9\text{-}30)$$

where

E_e = Rubbery equilibrium modulus,

E_g = Glassy modulus,

n = Slope of relaxation modulus curve,

τ_o = Characteristic time (which is the time corresponding to a value of the relaxation modulus of $\sqrt{E_g E_e}$).

Equation (30) is useful when considering real time behavior, however, the transformed modulus of (30) is inconvenient to deal with.

Another often used representation which is better suited for transform methods is the Dirichlet or Prony series expansion; e.g.,

$$E_{rel}(t) = E_e + \sum E_k \exp(-t/\tau_k) . \qquad (9\text{-}31)$$

The coefficients E_k are determined by collocating the experimental data over, say, N decades of time. Observing that for vanishingly small times the glassly modulus is recovered, i.e.,

$$E_r(0) = E_g = E_e + \sum E_k . \qquad (9\text{-}32)$$

the collocation in practice is normally carried out over N-1 decades of time which span the transition region. Using the Dirichlet or Prony series representation (Equation (31)), the Laplace transform of the material properties is straightforward, viz.,

$$\bar{E}_{rel}(p) = \frac{E_e}{p} + \sum \frac{E_k}{p+1/\tau_k} \qquad (9\text{-}33)$$

The appropriate transformed modulus required for the analysis is easily demonstrated to be related to (33) through the relation

$$E(p) = p\,\bar{E}(p) = E_e + \sum \frac{p\tau_k E_k}{p\tau_k + 1} \qquad (9\text{-}34)$$

Other required material property parameters can be represented in an identical manner.

Schapery has developed two approximate inversion techniques which greatly simplify computational difficulties associated with using the correspondence principle to obtain viscoelastic solutions. The simplest of the two inversion techniques is called the "direct method" or "inverse double-time rule". This method has been shown to yield good results whenever the derivative of the time dependent solution with respect to logarithmic time, log t, is a slowly varying function of log t. The approximate representation of a viscoelastic response, $\psi(t)$, when the transformed response $\bar{\psi}(p)$ is given by

$$\bar{\psi}(p) = \int_0^\infty \psi(t)\, e^{-pt}\, dt \qquad (9\text{-}35)$$

is given by

$$\psi(t) = [p\,\bar{\psi}(p)]_{p = 2t} \qquad (9\text{-}36)$$

where the factor 2 comes about from the minimization of the error in the approximation for functions which vary slowly as a function of p.

The second approximate method of inversion proposed by Schapery, called the "collocation method", is not as simple as the "direct method", however it is not restricted to functions whose derivative is a slowly varying function of logarithmic time. This method can also be applied directly to an arbitraty input without the difficulties encountered in the direct method. In using the direct method for an arbitrary input, the solution is first obtained for a step input and the Duhamel convolutive integral used to obtain the solution to a general input. That is,

for example, if $\psi(t)$ is an arbitrary input and $\psi_0(t)$ represents the response to a step input $\psi_0 H(t)$, where $H(t)$ is the Heaviside unit step function, then the response $\psi(t)$ to the arbitrary input is given by

$$\psi(t) = \int_0^\infty \psi_0(\tau) \frac{\partial}{\partial \tau} [\psi(t-\tau)] \, d\tau \, . \tag{9-37}$$

In the collocation method, the time dependence is given by a simple series of exponentials which can be readily used in the Duhamel integral for the calculation of responses to other than step function inputs. A third advantage of the collocation method is that the accuracy of the inversion can be improved simply by adding more terms to the series.

To apply the collocation method, the physical response is assumed expressible in the form of a Dirichlet series with unknown coefficients; i.e.,

$$\psi(t) = \gamma_0 + \sum \gamma_k \exp(-t/\tau_k) \, . \tag{9-38}$$

The Laplace transformed solution is then represented in the form

$$\bar{\psi}(p) = \frac{\gamma_0}{p} + \sum \frac{\gamma_k}{p + (1/\tau_k)} \, . \tag{9-39}$$

The assumed transform solution $\bar{\psi}(p)$ given by (39) is then collocated with the known transformed solution, previously determined for the associated elasticity problem, to obtain the unknown coefficients γ_k. Once the γ_k are determined from the p collocation, the desired solution is immediately written down using (38).

The procedure discussed above represents a relatively easy method of determining the viscoelastic response of a solid rocket motor to many loading situations. The inversion techniques are straightforward and can be carried out numerically using a desk calculator or slide rule. For complicated inputs numerical quadrature may be required to evaluate the Duhamel integral (37), however, even this is a simple computer programming task.

For some particular loading situations, the viscoelastic solution may be obtained in an even easier manner by introducing certain simplifying assumptions. In the above discussion all of the material properties (i.e., E, ν, K, G) were at least formally treated as time varying quantities. Simplifications can be introduced in the transformed solution and subsequent inversion by making certain assumptions about the time dependence of these material properties. A typical assumption normally introduced is that the material bulk response is elastic and only the shear response varies with time. This assumption is based on the fact that the measured time dependency of the bulk modulus appears to be small. Another assumption quite often introduced in the structural analysis of solid propellants is that the material is incompressible (i.e., $K \to \infty$, $\nu = \frac{1}{2}$) and only the shear properties are time varying. The rationale for this assumptoon rests on observations that propellants appear to behave nearly incompressible. Also, as the inner bore hoop strains are usually the critical design parameter, at least for conventional motor designs, and since these strains are a maximum as a function of ν at a value of $\nu = \frac{1}{2}$, conservative estimates of the structural capabilities of a motor are obtained when the assumption of incompressibility is made. Proceeding

then with the assumption that only the shear response is time varying, the task of determining the transformed solution and the subsequent inversion is considerably simplified.

With the assumption of incompressibility, one can often obtain quasi-viscoelastic response directly. For example, for rigid or very stiff motor cases ($bE_p/hE_c \ll 1$), the inner bore thermal hoop strain is a function only of the geometry and the temperature loading. Similarly, pressurization strains are a function only of the geometry, case stiffness and internal pressure loading. Approximate time dependent deflections can also be obtained simply by replacing the elastic compliance $1/E_p$ by the viscoelastic creep compliance $D_{crp}(t)$. Thus, for example, the time dependent axial slump of a long hollow cylinder is given by

$$W = \frac{3}{2}\frac{\pi}{a^2} D_{crp}(t) \left[\frac{\lambda^2-1}{2} - \log_e \lambda\right] \qquad (9\text{-}40)$$

The maximum slump is, of course, given when $E_{crp}(t) = D_e = 1/E_e$. Lateral deflections of star points can also be obtained in a similar manner. These approximations for deflection have proved to be quite good.

The quasi-viscoelastic behavior of stresses can also often be determined quite easily. In the case of the lateral acceleration of a star-point the stresses, under the normal strength of materials assumptions, are determined only by the loading and geometry. For this case, because of the prescribed force boundary conditions, the stress distribution is the same as an elastic beam. The time-dependent behavior of radial bond stresses and inner bore hoop stresses can also be approximately determined by substituting the relaxation modulus $E_{rel}(t)$ or the secant modulus $E_s(t)$ defined by

$$E_s(t) = \frac{E_{rel}(t)}{1-n} \qquad (9\text{-}41)$$

for E_p. In these simple approximations the temperature reduced time t/a_T, where a_T is the time-temperature shift factor, is often used in place of the real time t to bring in temperature effects in a simple manner.

These latter approximations, discussed directly above, do not give true viscoelastic behavior, however they can still prove to be useful in a preliminary design analysis in providing a rapid, easy means of estimating general trends of the time dependent viscoelastic response.

9.6 EIGENVALUES OF RELAXATION OPERATORS APPLIED TO LINEAR AND NONLINEAR SOLID PROPELLANT PREDICTIONS

Another interpretation of material behavior is available which provides a basis for estimating nonlinear response deviations from linearity. This method is considered to be highly suited for the novice in helping him to gain "back-of-the-envelope" capability in linear viscoelastic analysis, and providing the linear oriented analyst with a readily used method for nonlinear viscoelastic analysis.

The technique may be used either graphically, numerically on a desk calculator, or numerically on a digital computer. It is also noted that the method encourages (actually almost requires) the analyst both to look at actual experimental data as well as specify the specific tests, rates, and levels of strain at which tests should be conducted.

This method is used in the rocket industry in one form or another by many practitioners who, however, tend to think it not refined enough to publish it. Nevertheless, it is herein presented.

9.6.1 DEVELOPMENT OF EIGENVALUE PROCEDURES

Consider the relaxation operator T defined by

$$T(\varepsilon) = \int_0^t G(t-\tau)d\varepsilon \tag{9-42}$$

with G(t) the time dependent relaxation modulus.

The usual form of (42) in the theory of linear viscoelasticity is

$$\sigma(t) = \int_0^t G(t-\tau)\dot{\varepsilon}(\tau)d\tau \tag{9-43}$$

Thus, we may make the identifications

$$\sigma(t) = T[\varepsilon(t)] = T(\varepsilon)$$

and (9.44)

$$d\varepsilon = \frac{\partial \varepsilon}{\partial \tau}\, d\tau = \dot{\varepsilon}(\tau)d\tau \ .$$

If they exist, the eigenvalues of the operator T are determined from solutions to the equation

$$T\varepsilon = \lambda\varepsilon \tag{9.45}$$

where λ is real valued.

Consider now a sufficiently smooth strain-time input, $\varepsilon(t)$ such that $\varepsilon(t)$ can be represented in a power series as

$$\varepsilon(t) = R_1 t + R_2 t^2 + \cdots + R_n t^n \tag{9.46}$$

with n finite.

Since the representation (42) is linear in $\varepsilon(t)$, we may solve for any of the terms in (46) separately and add the solutions in order to get the complete solution. That is, (44) and (45) become

$$\sigma(t) = \lambda_1\varepsilon_1 + \lambda_2\varepsilon_2 + - - \lambda_n\varepsilon_n \tag{9-47}$$

where we define

$$\begin{aligned} \varepsilon_1 &= R_1 t \\ \varepsilon_2 &= R_2 t^2 \\ \varepsilon_n &= R_n t^n \end{aligned} \tag{9-48}$$

CONSTANT STRAIN RATE INPUT

Let us first look at the solution to the constant strain-rate input ε_1 where $\varepsilon_1 = R_1 t$. Equation (44) yields $\dot{\varepsilon}_1(t) = \frac{\partial \varepsilon_1(t)}{\partial t} = R_1$ so that (43) becomes, with R_1 a constant,

$$\sigma(t) = R_1 \int_0^t G(t-\tau)d\tau \tag{9-49}$$

Reference to Figure 1 shows that the value of the integral in Equation (49) is simply the area under the $G(t)$ relaxation modulus curve from initial time to the present time. The above integral is defined then as $G_1(t)$ where

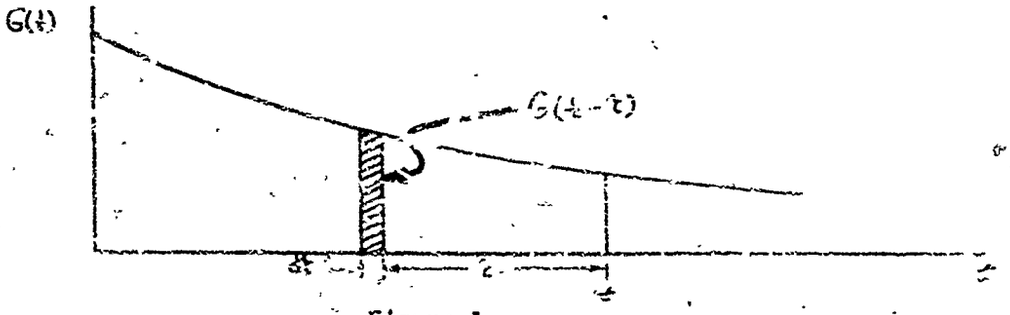

Figure 1

$$G_1(t) = \int_0^t G(t-\tau)d\tau \qquad (9\text{-}50)$$

Thus (44), (45), (49) and (50) yield

$$\sigma_1(t) = T\epsilon_1 = \lambda_1\epsilon_1 = R_1G_1(t) \qquad (9\text{-}51)$$

Multiplying the last term of (51) by unity, here t/t, yields

$$\sigma_1(t) = T(\epsilon_1) = \lambda_1\epsilon_1 = R_1t\,\frac{G_1(t)}{t} \qquad (9\text{-}52)$$

The term $G_1(t)/t$ in (52) is nothing more than the area under the $G(t)$ curve from $t = 0$ to $t = t$ divided by the base length t, or in other words, the average value of $G(t)$ from time zero to the present time,

$$G_{av}(t) = \frac{G_1(t)}{t} \qquad (9\text{-}53)$$

Thus, the eigenvalue λ_1 associated with a constant strain rate test is the average modulus, i.e., from (52) with $\epsilon_1 = R_1t$,

$$\lambda_1 = G_{av}(t) \qquad (9\text{-}54)$$

Thus, the stress, σ_1, produced by a constant strain input, $\epsilon_1 = R_1t$, is given by

$$\sigma_1(t) = \lambda_1\epsilon_1(t) = G_{av}(t)\epsilon_1(t) \qquad (9\text{-}55)$$

The linear, but time dependent, stress strain relation in (55) is identical to the use of the secant modulus as shown in Figure 2.

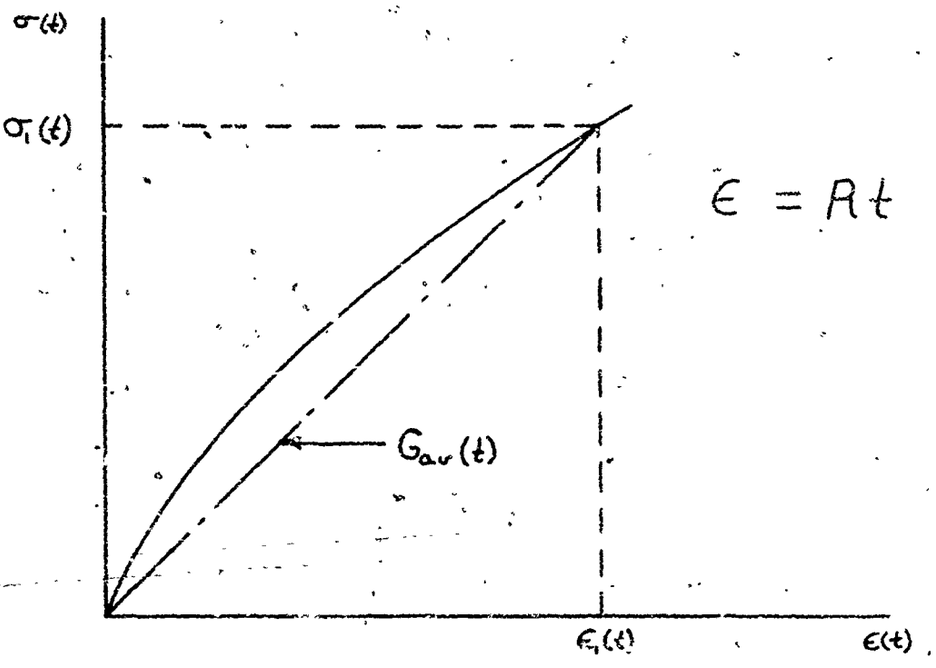

Figure 2

Superposition for Constant Strain Rate Inputs

Consider the ramp strain input of Figure 3

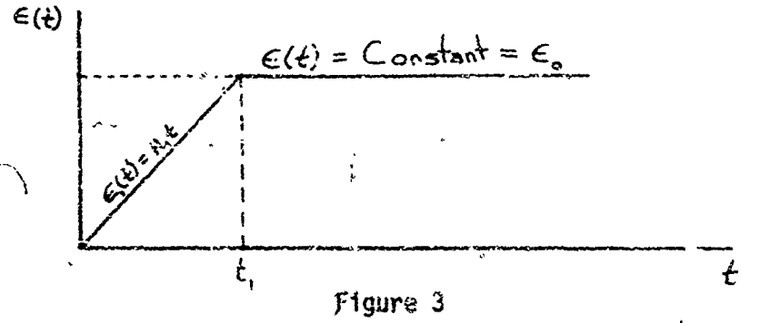

Figure 3

Again, since the stress-strain response is linear, superposition may be used so that the input of Figure 3 results in the input shown in Figure 4.

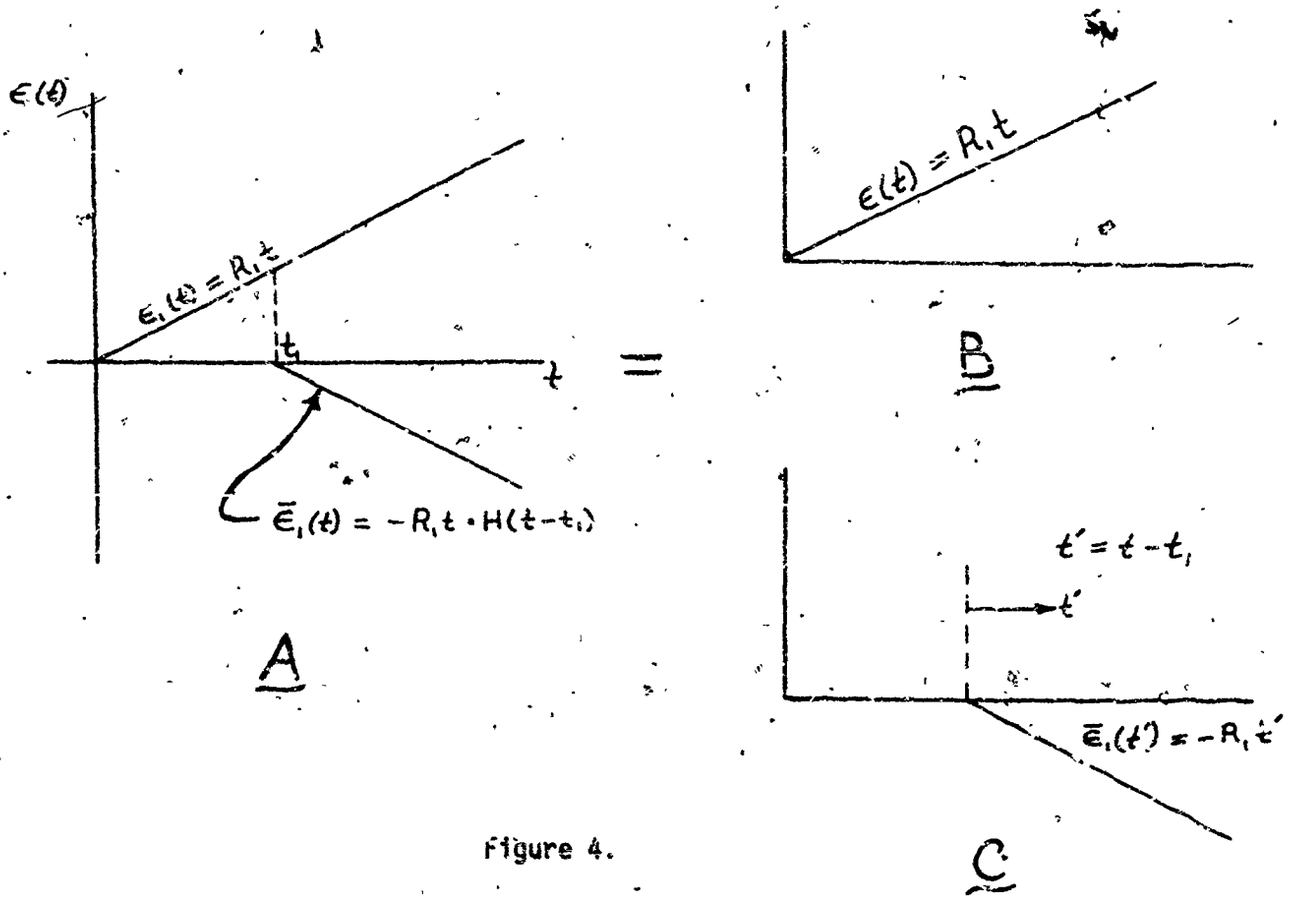

Figure 4.

The solution for the ramp input of Figure 3 is then the sum of the solutions for the constant strain-rate of Figure 4-A plus the solution to the time-shifted negative constant strain rate also shown in Figure 4-A. Superposition then leads to the separation of inputs as shown in Figure 4-B and Figure 4-C.

Equation (45) yields the results for the ramp strain input

$$\sigma(t) = \lambda_1\epsilon_1(t) = G_{uv}(t)\epsilon(t) = G_{av}(t)R_1t \ , \qquad (5\text{-}56)$$

from $t = 0$ to $t = t_1$, and for $t = t_1$ to $t = \infty$ the result

$$\sigma(t) = G_{av}(t)R_1 t - G_{av}(t)R_1 t \cdot H(t-t_1) \qquad (9\text{-}57)$$

where $H(t-t_1)$ is again the Heaviside shifter.

Equation (47) may also be written as

$$\sigma(t) = G_{av}(t)R_1 t - G_{av}(t')R_1 t' \qquad (9\text{-}58)$$

The result is most easily arrived at by first noting that (53) yields

$$G_{av}(t)\, R_1 t = G_1(t)R_1$$

and then (48) becomes

$$\sigma(t) = G_1(t)\, R_1 - G_1(t')R_1 \qquad (9\text{-}59)$$

The computational steps for the above procedure are:

(i) Compute $G_1(t)$, the integral of the relaxation modulus for all values of t. This may be done directly from experimental step-strain relaxation tests or from "quick" ramp strain tests. The integration may be done within sufficient accuracy by use of a planimeter, desk calculator using, say, the trapezoidal rule, or directly on a computer. The result should then be plotted on a curve of $G_1(t)$ versus t and will, of course, be a monotonically increasing function of time (Figure 5).

Quite obviously, if the ramp strain test is recommenced at some later time, t_2 with $t_2 > t_1$, a positive increment will be added to the two previous increments which will simply be the original $G_1(t)R_1$ curve shifted to the right by an amount t_2, as in Figure 7.

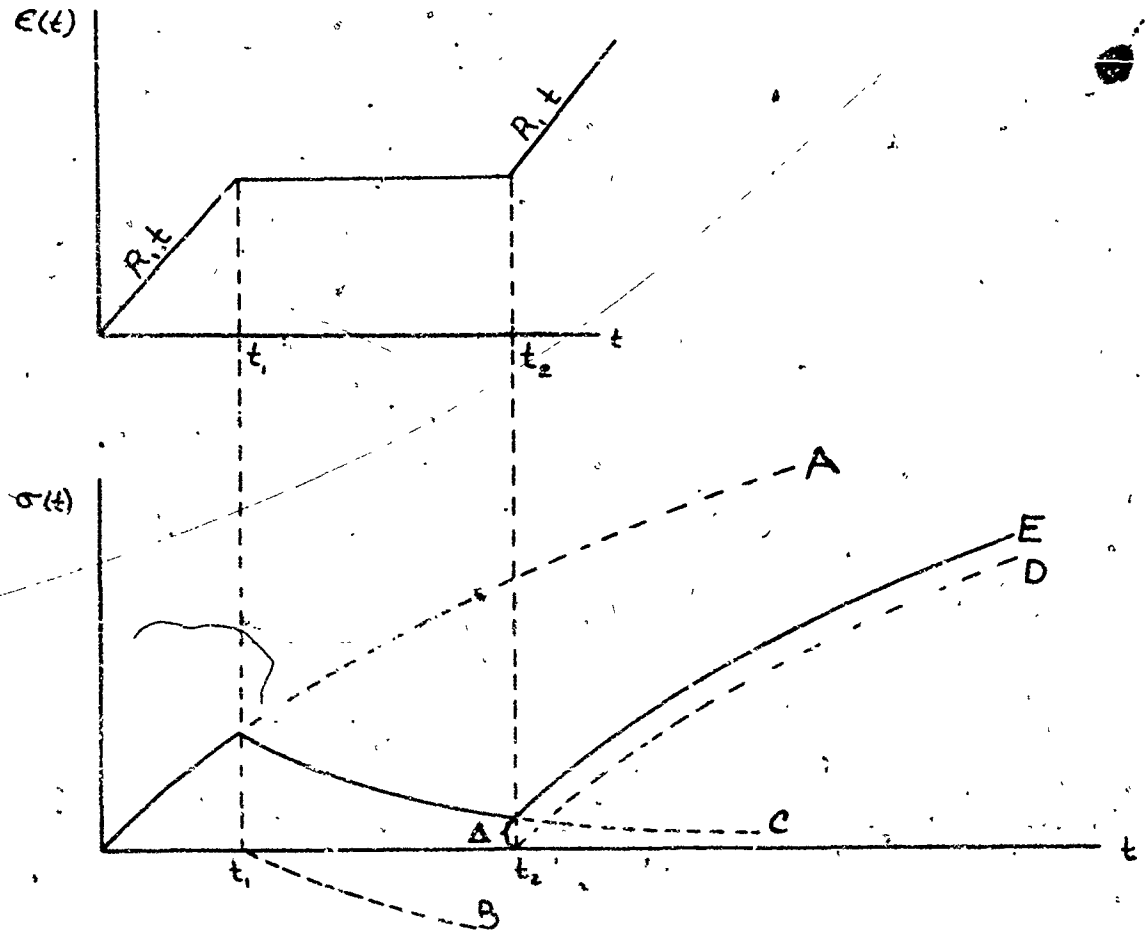

Figure 7

It becomes rather obvious that having a plot of $G_1(t)$ versus t enables the analyst to rapidly and simply plot curves of $\sigma(t)$ versus t for any series of segmented but arbitrary histories of strain. In actual practice, this above described method can be carried out quite rapidly.

In addition to the method described for obtaining stress vs time curves for straight-line segmented strain inputs, the methodology is useful in quantizing trends and instructing the novice in viscoelastic behavior. For example, returning to Figure 7, Curve A, the basic $G_1(t)$ R_1 plot is shown extended beyond time t_1. Curve B is the negative of Curve A shifted to the right an amount t_1. Curve C is the difference, A-B, and as such will always have a smaller negative slope than Curve B since it is Curve B plotted on the base of Curve A which is itself of positive slope rather than being the horizontal abscissia which Curve B is plotted against. Now Curve D, which is Curve A shifted by a distance t_2 is of course plotted relative to the horizontal baseline. But Curve E is Curve D added to Curve C which, as previously noted, has a negative slope which eventually may become horizontal and may also go to zero. We thus see that Curve E, which starts out at time t_2 a distance Δ above Curve D will then come closer to Curve D than Δ and, if Curve C goes to zero, E will be identical to D.

The implication here is that if the "pause" between t_1 and t_2 is very short, Curve E will be almost equal to Curve A. However, if the pause t_2 to t_1 is long (that is, long compared to t_1), then Curve E will approach Curve D to within a distance equal to the long time value of Curve C above the horizontal axis (if C goes to zero, E will to D.) Thus a very long pause will have the effect of "wiping out" the stress caused by the initial loading.

The use of the shifted curves is then useful in quantizing the effects and meanings of "short time", "long time", etc., for any specific material, i.e., a given G(t).

Before proceeding to the solution of second power inputs, i.e., $\epsilon_2(t) = R_2 t^2$, it should be remarked that a fairly good but approximate answer may be obtained by approximating any $\epsilon(t)$ curve by straight line segments as shown in Figure 8.

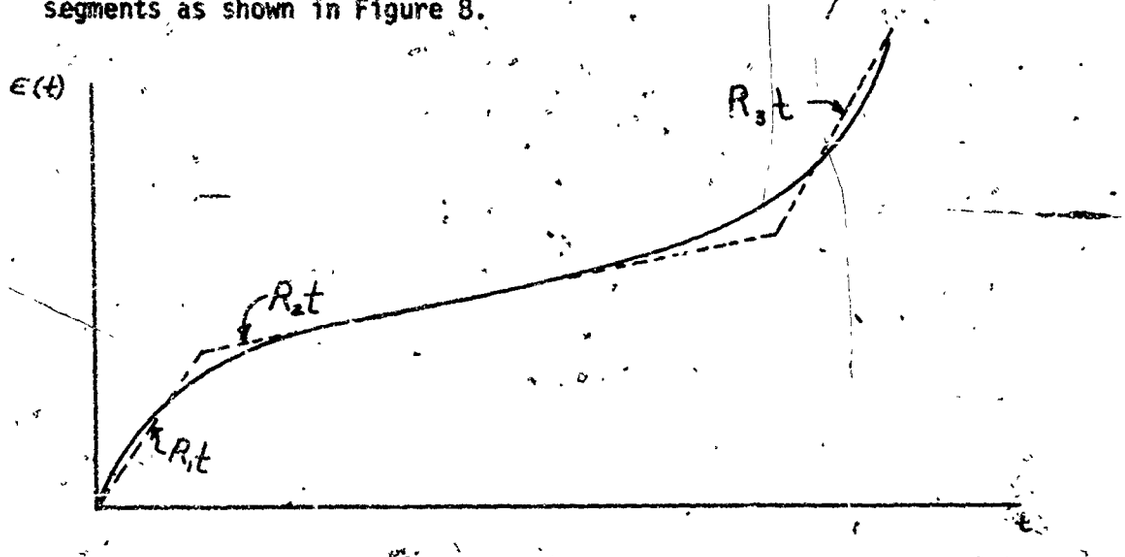

Figure 8

The practicality of this linear approximation is of course dependent on the number of segments needed to reasonably duplicate the actual curve.

Second Order Input

Consider the second term of (46), $\epsilon(t) = R_2 t^2$. Substitution into (53) with $\dot{\epsilon}(t) = 2R_2 t$ yields

$$\sigma(t) = 2R_2 \int_{-\infty}^{t} G(t-\tau)\tau d\tau \qquad (9\text{-}60)$$

Reference to Figure 1 shows that the above expression for the integral is the first moment of the relaxation modulus, i.e.,

$$\int_0^t G(t-\tau)\tau d\tau = G_2(t) = G_1(t)\cdot\bar{t} \qquad (9\text{-}61)$$

where $\bar{t}$ is the "distance" from t to the centroid of the $G(t)$ relaxation modulus curve.

Thus, the associated eigenvalue, λ_2 is from (61), (60) and (59)

$$\sigma(t) = 2R_2G_1(t)\cdot\bar{t} = R_2t^2\cdot G_1(t)\cdot\frac{2\bar{t}}{t^2} = R_2t^2\cdot G_{av}(t)\cdot\frac{2\bar{t}}{t} \qquad (9\text{-}62)$$

or

$$\lambda_2 = \frac{2G_2(t)}{t^2} = G_1(t)\cdot\frac{2\bar{t}}{t^2} = G_{av}(t)\cdot\frac{2\bar{t}}{t} = \lambda_1\cdot\frac{2\bar{t}}{t} \qquad (9\text{-}63)$$

since $\lambda_1 = G_{av}(t) = \frac{G_1(t)}{t}$ from (2.3).

The value of $\bar{t}$ will, for any relaxing material, always be greater than $t/2$ since the curve is "weighted" more heavily toward the $t = 0$ end, and the distance to its centroid measured from time t will then be greater than one-half the distance.

Thus, $2\bar{t}/t \geq 1$ and consequently $\lambda_2 \geq \lambda_1$. Since $G_2(t) = \lambda_2\,\varepsilon(t)$ by definition, we see that a second power strain input will produce higher stresses than a linear strain input at any given value of strain.

Now, since

$$\sigma_2(t) = \lambda_2\varepsilon(t) = R_2t^2\lambda_2 = R_2G_1(t)\cdot 2\bar{t} = R_2t^2\,\frac{G_1(t)}{t} = \qquad (9\text{-}64)$$

$$= \varepsilon_2(t)G_{av}(t)\cdot\frac{2\bar{t}}{t}$$

9.8 REFERENCES

1. Bland, D. R.: "The Theory of Linear Viscoelasticity," Pergamon Press, Inc., New York, 1960.

2. Lee, E. H.: "Viscoelastic Stress Analysis, " in Structural Mechanics, (Proceedings of the First Symposium Naval Structural Mechanics), pp. 456-482, Pergamon Press, New York, 1960.

3. Williams, M. L., Blatz, P. J., and Schapery, R. B.: "Fundamental Stress Studies Relating to the Systems Analysis of Solid Propellants," GALCIT - SM 61-5, February 1961, Also ASTIA (AD-256-905).

4. Anon.: "ICRPG Solid Propellant Mechanical Behavior Manual," CPIA Publication No. 21, 1963.

5. Williams, M. L.: "Structural Analysis of Viscoelastic Materials," AIAA Journal, Vol. 2, pp. 785-808, 1964.

6. Hilton, H. H.: "An Introduction to Viscoelastic Analysis," in Engineering Design for Plastics, Reinhold Publishing Corp., pp. 199-276, 1964.

7. Hilton, H. H.: "A Summary of Linear Viscoelastic Stress Analysis," Feature Article; SRSIA, Vol. 2, No. 2, pp. 1-56, April 1965.

8. Fitzgerald, J. E.: "Propellant Grain Structural Integrity Problems: Engineering Status," Feature Article, SRSIA, Vol. 2, No. 3, pp. 1-44, July 1965.

9. Fitzgerald, J. E.: "Analysis and Design of Solid Propellant Grains," in Mechanics and Chemistry of Solid Propellants-Proceedings of the Fourth Symposium on Naval Structural Mechanics," pp. 19-46, Pergamon Press, New York, 1967.

10. Flügge, W.: "Viscoelasticity," Blaisdell Publishing Co., 1967.

11. Ferry, J. O.: "Viscoelastic Properties of Polymers," (2nd Edition) John Wiley & Sons, Inc., New York, 1970.

12. Christensen , R. M.: "Introduction to the Theory of Viscoelasticity," Academic Press, Inc., New York, 1971.

9.7 NOMENCLATURE

$c(t) = [\psi]_t H(t)$

$e = e_{11} + e_{22} + e_{33}$

e_{ij} = Strain

E = Modulus

$E_{rel}(t)$ = Relaxation Modulus

E_e = Rubbery Modulus

E_g = Glassy Modulus

$G(t)$ = Relaxation Modulus

F = Force

$H(t)$ = Heaviside Unit Step Function $= \begin{cases} 1, & t > 0 \\ 0, & t < 0 \end{cases}$

k = Constant

K = Bulk Modulus

n = Slope of Relaxation Curve

P = Pressure

R = Rate

S_{ij} = Deviatoric Component of Stress

t = Time

T = Relaxation Operator

u = Displacement

δ_{ij} = Kronecker Delta $= \begin{cases} 1, & i = j \\ 0, & i \neq j \end{cases}$

ε = Strain

$\lambda_{\overline{n}}$ = Eigenvalue

λ = Lamé Constant

$[\psi]_t$ = Material Property Characteristics

τ_{ij} = Stress

τ_o = Characteristic Time

τ_k = Time Constant

$\sigma = \tau_{11} + \tau_{22} + \tau_{33}$

ν = Poisson's Ratio

μ = Lamé Constant

X. THERMOVISCOELASTICITY

10.1 INTRODUCTION

The analysis associated with problems in thermoviscoelasticity ranges from the simplicity of linear viscoelastic analysis to the complexity of nonlinear viscoelasticity.

A main reason for this wide range of complexity lies in the physical assumptions relative to the effect of temperature upon the material behavior.

10.2 THERMORHEOLOGICALLY SIMPLE MATERIALS

The essential assumption made in thermoviscoelasticity is that of *thermorheologically simple* behavior, a term coined by Schwarzl and Staverman [1]. Thermorheologically simple behavior implies that the position of a relaxation modulus curve plotted on a logarithmic time scale shifts with temperature change but its shape is unaltered. Thus, there exists an equivalence between time and temperature which was first noted for relaxation and creep by Leaderman [2].

Where T is the temperature, in any convenient units, t the time, and ξ the so-called reduced time, the above defined shift corresponding to thermorheological simplicity means simply that there exists a shift-factor, a_T, such that

$$\log \xi = \log t - \log a_T . \qquad (1)$$

That is, one arbitrarily chooses a reference temperature, T_0, (usually taken as 70°F in the propellant industry) at which a stress-relaxation test is carried out in order to obtain a curve of the relaxation

modulus $G(T_0,t)$ versus the logarithim of time t. Thermorheologically simple materials are those for which, as previously mentioned, the relaxation modulus found at some different temperature, T_1, when plotted versus the logarithm of time is simply shifted horizontally along the log t axis with no change in shape.

Thus, the shift a_T is defined as the distance along the log-time axis between any two identical values of the relaxation modulus for $G(T_0, \log t)$ and $G(T_1, \log t)$.

A master relaxation curve results when the relaxation modulus values for $G(T_1, \log t)$ are replotted as $G(T_0, \log\xi)$ with the definition of Eq. 1 holding.

When applied, as originally intended, to sets of relaxation tests, each of which is at a constant temperature, the concept of thermorheological shifting appears to hold quite well for solid propellants.

The details of time-temperature shifting are quite straightforward and are covered in detail in the ICRPG Mechanical Manual, Section 2.3 and Section 4.3. Section 4.3.6, pages 1 through 11, are reproduced herein as Section 10.3 in order to provide the reader a ready reference to the terms and details of test reduction used for thermorheologically simple materials.

10.3 CALCULATION OF TIME-TEMPERATURE SHIFT FACTOR[1]

Rocket motor strain analysis for many conditions of interest requires accurate specification of the propellant viscoelastic modulus or compliance. While a high degree of precision must be maintained in experimental determination of the viscoelastic properties, the test techniques are not complex. The following describes methods for determination of the relaxation modulus E (t) in uniaxial tensile experiments. It is expedient in these characterizations to use time-temperature superposition techniques in obtaining master representations of the data. Description of simplified methods for obtaining the master or reduced variable representations is included in the discussion. Reference is recommended to the more detailed treatment of linear viscoelastic property specification and reduced variable techniques in Sections 2.4, 2.3 of the manual.

10.3.1 UNIAXIAL TENSILE STRESS RELAXATION MODULUS TEST

SCOPE: a method for laboratory measurement of the stress relaxation modulus E (t) using time-temperature reduced variable techniques is described.

TEST EQUIPMENT REQUIRED: universal tensile tester with temperature conditioning provision. Temperature control capability to within ± 1°F is desirable. Multiple channel fixtures for testing and recording are convenient.

TEST SPECIMEN: machined tab-end tensile specimen as shown schematically in Detail 1:

---

[1] This Section, 10.3, was prepared by J. W. Jones, Lockheed Propulsion Company, 1963.

DETAIL 1

with dimensions

propellant length = l_o (in.), and

cross section area = $h^2 = A_o$ (in.^{2}) in the unstrained state.

Either "in-situ" bonded tab-end or secondary bonded tab-end specimens may be used. Specimens should be precision machined. All specimens should be inspected for flaws or voids, rejecting all samples with visible defects or inhomogeneities. Specimen storage and pretest conditioning should be consistent with test objectives.

TEST METHOD: the tab-end specimen, conditioned at a constant temperature, is clamped in the jaws of the tester and extended at a constant crosshead speed to a predetermined length where the crosshead is stopped. The decay of force at the extended length is measured as time progresses. The conditioning temperature should be maintained within °F during the duration of the test. With reference to Detail 1 and Detail 2, the following constants for the test analysis are defined:

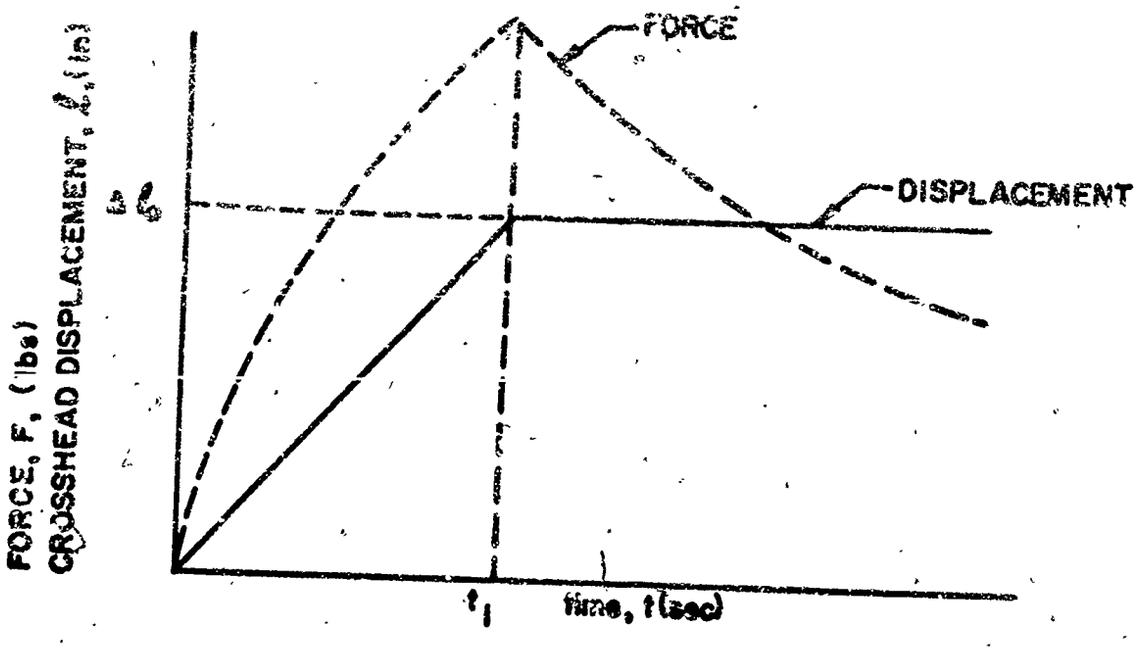

DETAIL 2

Strain at time $t_1 = \varepsilon_0 = \frac{\Delta l_0}{l_0}$ (in/in)

True stress (for $t > t_1$) $= \frac{F(1 + \varepsilon_0)}{A_0}$ (psi)

Relaxation Modulus $= E(t) = \frac{F(1 + \varepsilon_0)}{A_0 \varepsilon_0}$

Strain levels ε_0 between 0.01 and 0.10 are commonly employed in this test. Three to five replicates at each strain level and temperature are advisable. Test durations of the order of 10^3 and 10^4 times t_1 are required to adequately define the relaxation curves.

Isothermal data reduction: the relaxation modulus, averaged from replicate tests at a given temperature,

$$E(t) = \frac{F(1 + \varepsilon_0)}{A_0 \varepsilon_0}$$

four times greater than 10 t_1 only is calculated and plotted on log-log graph paper. Table I illustrates calculation of the relaxation modulus at T = 70°F. Figure 1 depicts the data of Table I in addition to data for several other temperatures.

10.3.2 DETERMINATION OF THE SHIFT FACTOR

The following reduction process does not include the absolute temperature reduction term. For most engineering purposes the effect of such simplification is trivial. An arbitrary reference temperature T_s is selected. Conveniently, the test temperature nearest the ambient laboratory room temperature is chosen (70-80°F). For data at test temperatures T less than T_s, data are shifted to the left. The relative shift a_{tx} necessary to bring adjacent curves into superposition is determined. For example, from Detail 3,

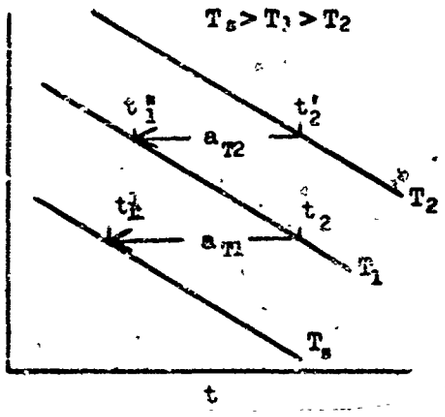

$$a_{T1} = \frac{t_2}{t_1} \text{ or } \log a_{T1} = \log t_2 - \log t_1$$

$$a_{T2} = \frac{t_2'}{t_1'} \text{ or } \log a_{T2} = \log t_2' - \log t_1'$$

DETAIL 3

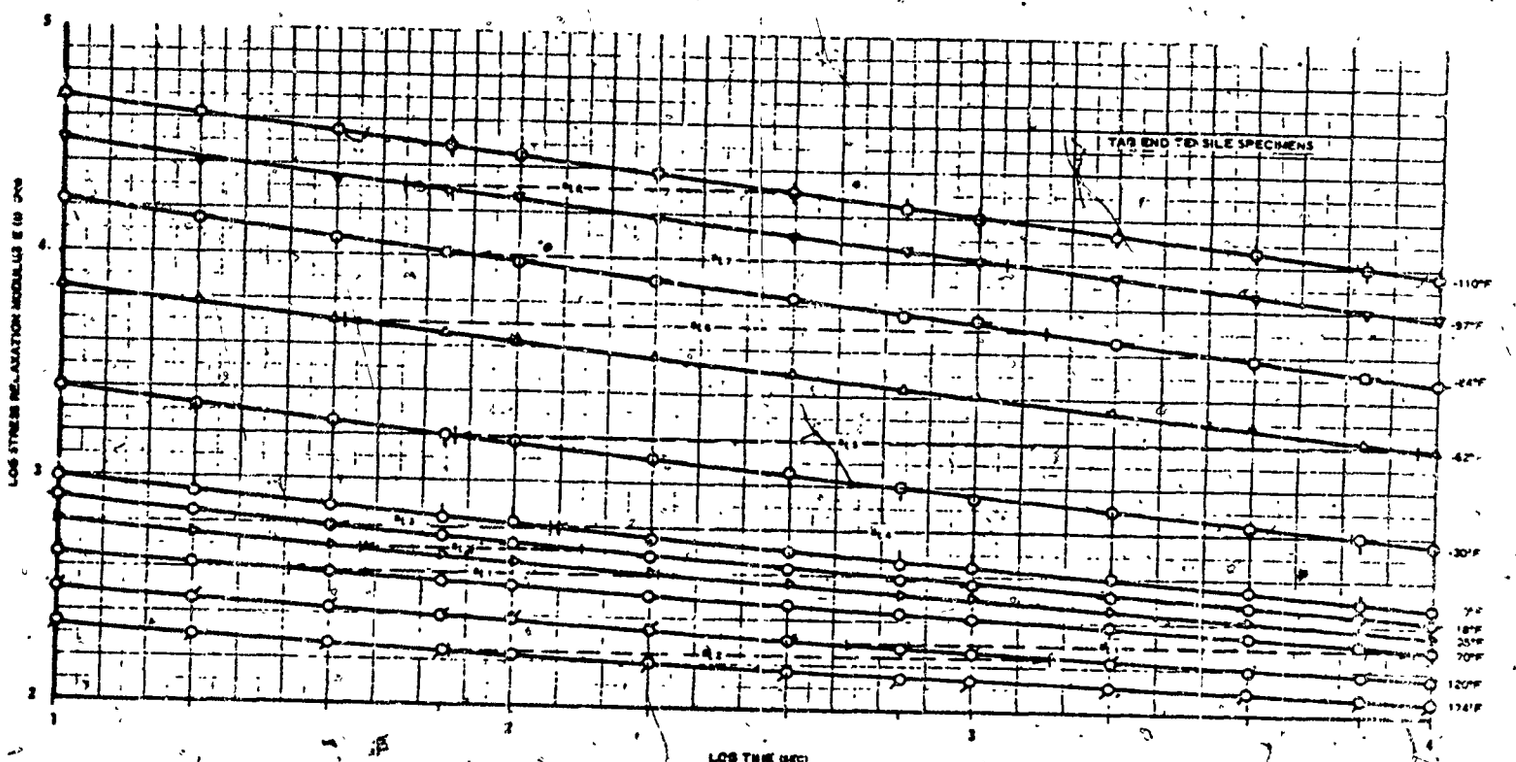

Figure 1. Stress Relaxation Data

TABLE I

PREPARED BY LC
CHECKED BY MLR
APPROVED BY [illegible]

PAGE 1 OF 1
DATE 6-16-63
REPORT NO. 578-F-3

COMPUTATION SHEET - STRESS RELAXATION MODULUS, E (t)

REMARKS _____ PROPELLANT Polycarbutene R
BATCH 7958

TEMPERATURE 70°

SPECIMEN GAGE LENGTH, l_o = 4.00 (IN.)

SPECIMEN X-SECTION AREA, A_o = 6.160 (IN.²)

TESTER X-HEAD DISPLACEMENT, Δl = 0.200 (IN.)

STRAIN LEVEL, $\epsilon_1 = \frac{\Delta l}{l_o} = \frac{0.200}{4.00} = 0.050$ (IN./IN.)

$$E(t) = \frac{F(1+\epsilon_1)}{A_o \epsilon_1}$$

F = FORCE, LBS

$\frac{1+\epsilon_1}{A_o \epsilon_1} = \frac{1.05}{0.008} = 131$; $\text{LOG}\frac{1+\epsilon_1}{A_o \epsilon_1} = 2.117$

TIME t (SEC)	LOG t	LOG t - LOG a_T = LOG a_T	F (LBS)	LOG F	LOG $\frac{1+\epsilon_1}{A_o \epsilon_1}$	LOG E(t)	E (t) (PSI)
10	1.000		3.58	0.554	2.117	2.671	468
20	1.301		3.26	0.513	2.117	2.630	427
40	1.602		2.98	0.475	2.117	2.592	391
70	1.845		2.81	0.449	2.117	2.566	368
100	2.000		2.67	0.427	2.117	2.544	350
200	2.301		2.46	0.391	2.117	2.508	322
400	2.602		2.29	0.358	2.117	2.475	298
700	2.845		2.15	0.328	2.117	2.445	279
1,000	3.000		2.06	0.306	2.117	2.423	265
2,000	3.301		1.88	0.274	2.117	2.391	246
4,000	3.602		1.70	0.231	2.117	2.348	223
7,000	3.845		1.60	0.205	2.117	2.322	210
10,000	4.000		1.53	0.184	2.117	2.301	200

the shift factor a_T for temperature T_1 is a_{T_1} as given. The shift factor for temperature T_2 is given by $a_{T_1} \times a_{T_2}$ (or log a_{T_1} + log a_{T_2}). The process is repeated for each temperature; the shift factor for data at the lowest temperature is given by the product of the a_{T_X} (or the sum of the log a_{T_X}).

For data at test-temperature T greater than T_S, data are shifted to the right. The relative shift a_{T_X} necessary to bring adjacent curves into superposition is determined. For example, with reference to Detail 4,

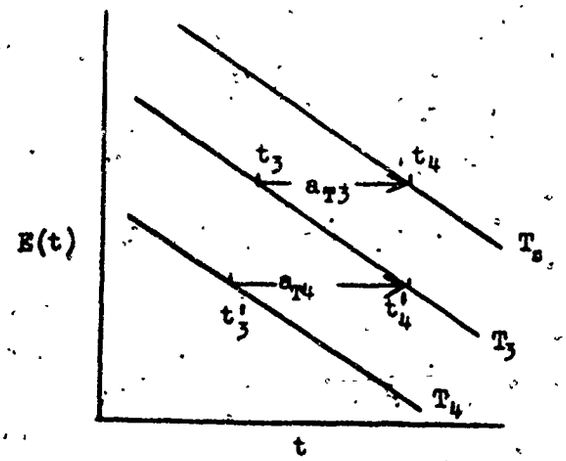

$$a_{T3} = \frac{t_3}{t_4} \text{ or } \log a_{T3} = \log t_3 - \log t_4$$

$$a_{T4} = \frac{t_3'}{t_4'} \text{ or } \log a_{T4} = \log t_3' - \log t_4'$$

DETAIL 4

the shift factor a_T for temperature T_3 is as given. The shift factor for temperature T_4 is $a_{T_3} \times a_{T_4}$ (or log a_{T_3} + log a_{T_4} = log a_T).

The shifts a_{T_X} are shown on Figure 1 and the associated calculations for determination of log a_T are shown in Table II. The circled notation in the "log a_{T_M} column of Table II identify the shifts shown in Figure 1.

TABLE II

PREPARED BY LC
CHECKED BY MB
APPROVED BY [signature]

PAGE 1 OF 1
DATE 6-11-63
REPORT NO. 578-F-3

COMPUTATION SHEET - SHIFT FACTOR a_T

REMARKS _____ PROPELLANT Polycarbutene R

BATCH 7958

T_1	T_2	LOG t_1	LOG t_2	LOG a_{T_B}	LOG a_T for T_1
35	T_B 70	2.32	1.51	-0.81 (1)	= -0.81	35
18	35	2.15	1.66	+0.49 (2)	= 1.30	18
3	18	2.10	1.60	+0.50 (3)	= 1.80	3
-30	3	3.82	2.09	+1.73 (4)	= 3.53	-30
-62	-30	3.96	1.86	+2.10 (5)	= 5.63	-62
-84	-62	3.15	1.64	+1.51 (6)	= 7.14	-84
-97	-84	3.08	1.90	+1.18 (7)	= 8.32	-97
-110	-97	2.60	1.75	+0.84 (8)	= 9.16	-110
				+	=	
				+	=	
				+	=	

$T_x < T_B$

$T_x > T_B$

T_1	T_2	LOG t_2	LOG t_2	LOG a_{T_B}	LOG a_T for T_2
T_B 70	120	273	396	+-1.23 (9)	= -1.23	120
120	174	186	317	+-1.31 (10)	= -2.54	174
				+	=	
				+	=	
				+	=	
				+	=	
				+	=	

Conversion of the data of Figure 1 to master or reduced form is accomplished by performing the shift a_T for the data at each temperature. This corresponds to division of the time scale for the data at each temperature by the value of a_T for that temperature. More conveniently, the operation is conducted logarithmically ($\log t/a_t = \log t - \log a_T$).

The calculation of t/a_T is illustrated in Table III, Col 5. The reduced master relaxation modulus curve is shown in Figure 2 along with the shift factor versus temperature curve. The master relaxation modulus curve displays the modulus versus time behavior of the propellant for three reference temperatures, T_s, 70°F, in the figure.

The relaxation curve for another temperature is obtained by shifting the master time scale. The shift for the temperature of interest is achieved by multiplication along the time scale by the value of a_T for the given temperature or, logarithmically, by adding $\log a_T$ to the master time scale. Shifted time scales for temperatures of 1500°F and -68°F are also shown in Figure 2.

10.4 MATERIAL CHARACTERIZATION

The definition of a thermorheologically simple material is generally restricted, by implication at least, to a linear viscoelastic material. That is, variations in the value of the relaxation modulus, $G(T,t)$ with time are considered to be strain independent.

When the material is indeed linear, the use of the reduced time, $\xi = t/a_T$ is certainly quite proper. Practitioners, however, have extended the concept of time-temperature shifting to the nonlinear

TABLE III

PREPARED BY LC
CHECKED BY MB
APPROVED BY [illegible]

PAGE 1 OF 1
DATE 6-16-63
REPORT NO. 578-F-3

COMPUTATION SHEET - STRESS RELAXATION MODULUS, E (t)

REMARKS _____ PROPELLANT Polycarbutene R
BATCH 795B

TEMPERATURE 174°F

SPECIMEN GAGE LENGTH, l_o = 4.00 (IN.)

SPECIMEN X-SECTION AREA, A_o = 0.160 (IN.²)

TESTER X-HEAD DISPLACEME (T, Δl = 0.200 (IN.)

STRAIN LEVEL, ϵ_1, = $\frac{\Delta l}{l_o} = \frac{0.200}{4.00} = 0.050$ (IN./IN.)

$$E(t) = \frac{F(1+\epsilon_1)}{A_o \epsilon_1}$$

F = FORCE, LBS

$\frac{1+\epsilon_1}{A_o \epsilon_1}$ = $\frac{1.05}{0.008}$ = 131 ; LOG $\frac{1+\epsilon_1}{A_o \epsilon_1}$ = 2.117

TIME t (SEC)	LOG t	LOG t - LOG a_T = LOG a_T	F (LB)	LOG F	+ LOG $\frac{1+\epsilon_1}{A_o \epsilon_1}$ =	LOG E (t)	E (t) (PSI)
10	1.000	3.54	1.72	0.235	2.117	2.352	225
20	1.301	3.841	1.56	0.193	2.117	2.310	204
40	1.602	4.142	1.46	0.165	2.117	2.282	191
70	1.845	4.385	1.36	0.133	2.117	2.250	178
100	2.000	4.54	1.32	0.121	2.117	2.238	173
200	2.301	4.841	1.22	0.086	2.117	2.202	159
400	2.602	5.142	1.14	0.057	2.117	2.175	150
700	2.845	5.385	1.10	0.041	2.117	2.158	144
1000	3.000	5.54	1.07	0.029	2.117	2.146	140
2000	3.301	5.841	1.01	0.003	2.117	2.120	132
4000	3.602	6.142	0.958	-0.019	2.117	2.098	125
7000	3.845	6.385	0.916	-0.038	2.117	2.079	120
10000	4.000	6.54	0.879	-0.054	2.117	2.061	115

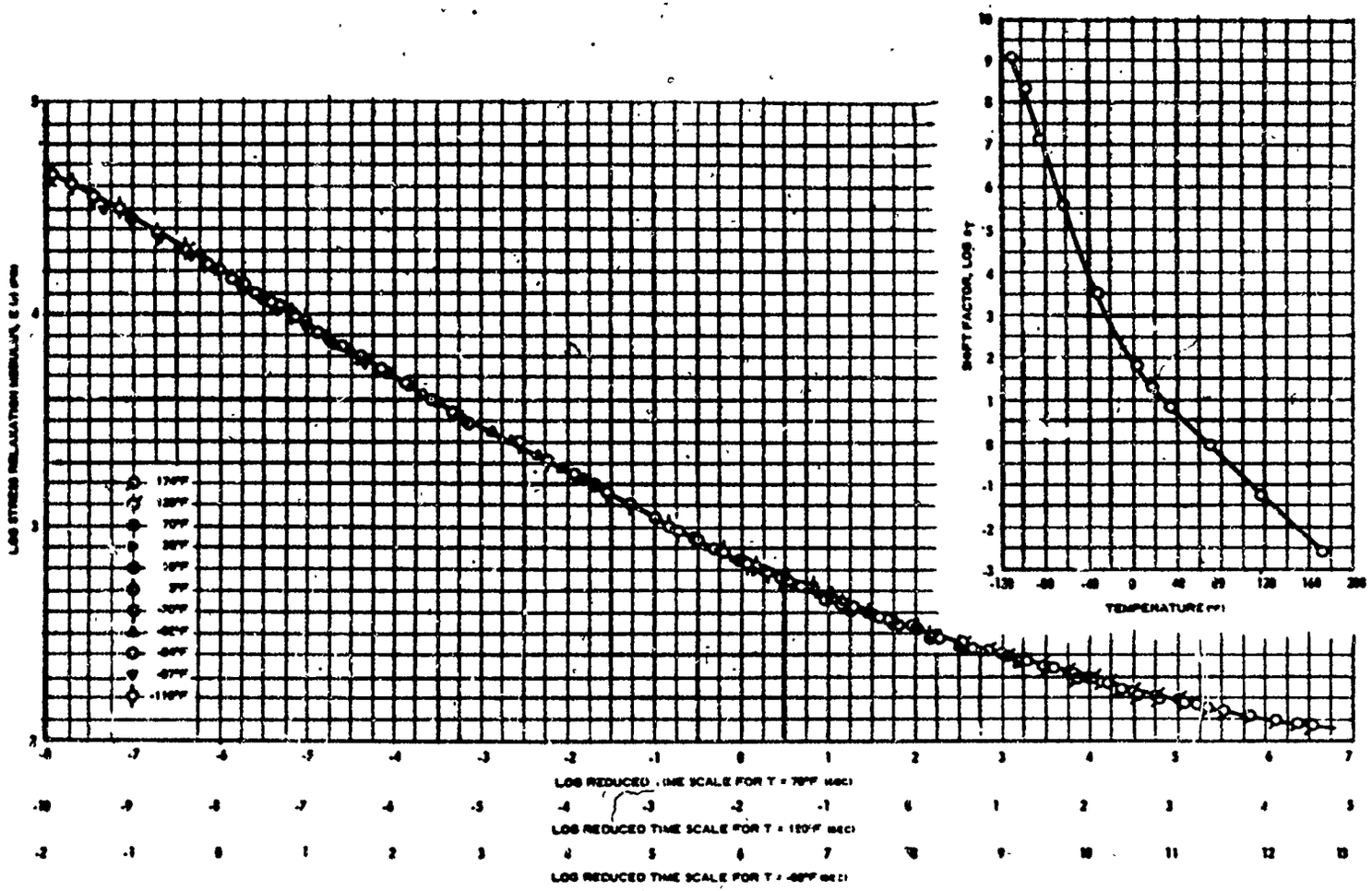

Figure 3. Master Stress Relaxation Modulus at T = 70°F, 150°F, and -68°F.

range. Although this chapter is not going to go into nonlinear behavior which is reserved for Chapter 11, consideration will be given to time-temperature shifting.

One of the earliest attempts at using shift factors for nonlinear materials is essentially implicit in the work of Guth, et al [3]. In Guth's formulation he assumes that the stress, σ, as a function of finite stretch, λ, and time t may be expressed as

$$\sigma(\lambda,t) = F(\lambda)\cdot G(t)$$

where $F(\lambda)$ is some measure of finite deformation. For example, if a Neo-Hookean behavior is assumed

$$F(\lambda) = \lambda^2 - \lambda^{-1} \quad \text{for simple elongation}$$

$$F(\alpha) = \alpha \quad \text{for simple shear}$$

where α is the finite shear deformation.

Stern and Tobolsky [4] found that the above factorization worked quite well when applied to relaxation in the simple elongation of polysulfide rubbers.

Essentially, one defines the relaxation modulus in these cases as

$$G(t) = \sigma(\lambda,t)/F(\lambda)$$

rather than as

$$G(t) = \sigma(t)/\lambda$$

As pointed out by Staverman and Schwarzl [5], any measure of strain which causes the G(t) curves to fall on a single line may be used. It should be noted that for Neo-Hookean and many other materials, the relation between shear deformation and the finite measure of shear strain is linear up to rather large values, say 100% strain.

Where such factorable relations between the measure of strain and the time dependency hold, one may always achieve a single relaxation curve. Thus, in these factorable instances the transition to a different temperature involves the simple substitution of reduced time $\xi = t/a_T$ for the real time t as is done in linear viscoelasticity.

One further remark is in order here. Where the above factorization is possible, one may express the finite strain measure $F(\lambda)$ as

$$F(\lambda) = a_\varepsilon(\lambda - 1) = a_\varepsilon\, \varepsilon$$

where ε is the usual infinitesimal measure of strain. The term a_ε, called herein a strain-shift factor is simply (and obviously) a function of the stretch λ or alternatively, the strain ε. For an ideal Neo-Hookean material in simple tension with, as before

$$F(\lambda) = \lambda^2 - \lambda^{-1}$$

the expression for a_ε will then be

$$a_\varepsilon = \frac{\lambda^3 - 1}{\lambda^3 - \lambda}$$

One may thus follow the following sequence of steps if

$$\sigma(\lambda,t) = F(\lambda)G(t)$$

then for a superposition with respect to $F(\lambda)$

$$\sigma(t) = G(0)F(t) + \int_{\tau=0}^{t} G(t-\tau)\dot{F}[\lambda(\tau)]d\tau$$

where $\dot{G}$, $\dot{F}$ denote time derivatives and $F(t)$ and $F(0)$ denote the value of F for $\lambda(t)$ and $\lambda(0)$ respectively.

Now the use of the strain-shift factor[2]

$$a_\varepsilon \varepsilon = F(\lambda)$$

results in, as above,

$$\sigma(t) = a_\varepsilon \varepsilon G(t)$$

or for superposition

$$\sigma(t) = a_\varepsilon G(0)\varepsilon(t) + a_\varepsilon \int_{\tau=0}^{t} \dot{G}(t-\tau)\varepsilon(\tau)d\tau$$

or

$$\sigma(t) = a_\varepsilon \varepsilon(0)\varepsilon(t) + \bar{a}_\varepsilon \int_{\tau=0}^{t} \dot{G}(t-\tau)\varepsilon(\tau)d\tau$$

Having thus made the transition from linear, to nonlinear (or strain dependent moduli) one may now carry out the time-temperature

---

[2] The term a_ε may differ from $\bar{a}_\varepsilon$ depending upon whether one finds it as defined above or from certain rate tests. As defined here, $a_\varepsilon \neq \bar{a}_\varepsilon$.

superposition by simply substituting the reduced time $\xi = t/a_T$ for real time t yielding

$$\sigma(\xi) = F[\lambda(0)]G(\xi) + \bar{a}_\varepsilon \int_{\xi=0}^{\xi} G(\xi-\tau)\dot{\varepsilon}(\tau)d\tau \ .$$

The first term on the right hand side is simply the elastic response to a step function and the integral is now the strain-shifted, time-temperature shifted usual form of a linear superposition integral. It must be remembered, however, that $\bar{a}_\varepsilon$ is a function of strain ε.

In practice then, one attempts to first reduce all relaxation modulus curves taken at one temperature and several strain levels to a single curve by vertically shifting an amount $\bar{a}_\varepsilon$ for each curve. Where the results are acceptable, factorization may be assumed. Then, one shifts each of these single curves (obtained over a series of different temperatures) horizontally by an amount log a_T on a plot of log G versus log t.

The resultant shift factor curves, $\bar{a}_\varepsilon$ versus strain and a_T versus temperature may then be used to carry out analysis. Again, it must be pointed out that the above method "works when it works". That is, the factorization may not be imposed, rather it must be determined and verified experimentally.

It will be shown in Chapter 11 that the above procedure is the essence of almost all currently used nonlinear methods.

10.5 TRANSIENT PROBLEMS

The previous discussion was confined to tests and analysis run at different but constant temperatures. The major problem in solid rocket grain design relative to thermal effects is, however, a coupled thermomechanical problem. This problem arises in case-bonded grains where the cooling produces shrinkage which leads to self-imposed stresses.

The only currently used method in grain analysis for coping with the transient thermal problem rests on the Moreland-Lee shift hypothesis, wherein the reduced time for a variable temperature is defined as

$$\xi = \int_{\tau=0}^{\tau=t} \frac{d\tau}{a_T}$$

The above integral representation was put forth as a logical possibility. Thus for a material which is factorable, thermorheologically simple and which is subject to a time-varying temperature, the above form for ξ is generally used.

Unfortunately, the results of analysis based upon the above assumptions is rarely in accord with experiment. In general, where experimenters have conducted simple elongation tests at constant cross-head speed while simultaneously cooling the specimen, the predicted results have been in error with respect to the observed data. The difference has been reported as ranging from a factor of 3 to as high as a factor of 8.

The errors observed have occurred at strain levels where the finite deformation alone was considered to contribute little to the results. It thus appears that either

. The Moreland-Lee transient shift expression does not represent the physics of the problem, or

. The coupling between strain and temperature change is a more complex physical relationship in the transient case than can be handled by currently used methods.

Further discussion of the nonlinearities such as the above will be deferred to Chapter 11.

10.6 SOLUTION METHODS

Solution of the linear, reduced time equations of thermoviscoelasticity is in principle identical to the solution of the ordinary linear viscoelastic problem and has been covered elsewhere in this text.

The computer problem, when the temperature field is prescribed, is relatively straightforward. Assuming one has set up one of the finite element problems currently in use which can handle elements with differing moduli, the use then of a reduced time ξ and an available modulus versus ξ tabulation will provide the answers to the transient thermal stress problem. Depending on the time interval used however, restrictions occasioned by numerical stability problems may result if the temperature change imposed is too fast. Only experience on one's computer with a particular algorithm will solve the above trouble, however.

Where the time-temperature field is not specified, but a thermal boundary input is given, the problem is still rather straightforward.

In this case, an uncoupled heat conduction equation is generally specified and its temperature output is used intermittently to specify the resultant temperature field. Depending on the rate of temperature change, the conduction equation will have to be solved at intervals sufficient with respect to the relaxation solution to ensure proper values for the element moduli. In general, one will use some sort of a marching solution.

The use of the Moreland-Lee transient reduced time expression is, to the writers' knowledge, implicit in all current computer programs (e.g.[6]) Where greater precision is desired, one could factor in changes in specific heat and conductivity for the elements as a function of strain and temperature. In the writers' opinion, however, such additional complications are entirely unwarranted as are any other attempts at using coupled thermoviscoelasticity at this time (as in vibration and thermal problems involving the generation of heat through mechanical dissipation), in solving rocket grain design problems.

The reason for the above comment is based on the fact that there is presently no satisfactorily proven nor accepted method for analytically predicting the results of a simultaneous cooling and stretching experiment in simple tension or in biaxial tension in the laboratory.

The use of a strain shift factor, however, is recommended as an aid to obtaining more accurate (physically) results. For example, the paper by Martin [7] which essentially uses such a vertical or a_ε shift should be noted.

10.7 CONCLUSIONS

The use of the concept of thermorheological simplicity coupled with the Moreland-Lee reduced time expression reduces the problem of transient thermal stress analysis to that of ordinary linear viscoelasticity.

Application of the resulting analysis to certain problems involving simultaneous cooling and straining leads to unacceptably large errors in practice. There then remains a pressing need for the development, proof, and acceptance of a usable methodology for transient thermal, viscoelastic problems.

10.8 NOMENCLATURE

A = Area

a_T = Time-Temperature Shift Function

a_ε = Strain Shift Function

F = Finite Strain Measure

G = Relaxation Modulus

h = Specimen Thickness

l = Length

T = Temperature

T_o = Reference Temperature

t = Time

α = Finite Stress Deformation

ε = Strain

λ = Extension Ratio

σ = Stress

ξ = Reduced Time

10.9 REFERENCES

1. Schwarzl, F., and Staverman, A. J., J. Appl. Physics, 23, 838 (1952).

2. Leaderman, H., "Elastic and Creep Properties of Filamentous Materials," Textile Foundation, Washington, D. C., 1943, p. 175.

3. Guth, E., Wack. P. E., and Anthony, R. L., J. Appl. Physics, 17, 347 (1946).

4. Stern, M. D. and Tobolsky, A. V., J. Chem. Physics, 14, 93 (1946).

5. Staverman, A. J. and Schwarzl, F., "Nonlinear Deformation Behavior of High Polymers," in Die Physik Der Hochpolymeren, ad. by H. A. Stuart, p. 139, 140, 1956.

6. Taylor, R. L., Pister, K. S. and Goudreau, G. L., "Thermomechanical Analysis of Viscoelastic Solids," Report No. (68-7) Rept. Civil Engineering, Univ. Calif., Berkeley, California, June 1968.

7. Martin, D. L., Jr., "An Approximate Method of Analysis of Nonlinear Transient Thermoviscoelastic Behavior," Bulletin of the 8th JANNAF Mechanical Behavior Working Group Meeting, CPIA Publication No. 193, Vol. I, pp. 45-51, March 1970.

XI. NONLINEAR VISCOELASTICITY

11.1 INTRODUCTION

The ability to predict analytically the mechanical response of a structure requires as a prerequisite the characterization or mathematical description of the mechanical response of each of the materials in the structure. These mathematical descriptors of the constituent material response, or constitutive equations, as they are called, together with a knowledge of the applied surface loads and displacements and the field equations of engineering mechanics, comprise a system of equations whose solution yields the state of stress and strain for every point within the body. To predict the success or failure of a grain design requires comparing the calculated stress or strain states within the body to some failure criterion. One therefore finds that an analysis of a structure is only as good as the constitutive equations defining material response and also that a failure analysis is of little consequence if the predicted state of stress is largely in error. Also, the determination of general failure criterion for three-dimensional states of stress generally requires the calculation of the stress state in laboratory samples subjected to multiaxial loading conditions. Thus the determination of appropriate failure criteria is also dependent on the constitutive equations defining material response.

While the sequence constitutive equation, loads definition, structural analysis and failure definition are obviously totally interrelated, and the final usable answer to a performance prediction is equally dependent upon the accuracy of each of the above elements in a design, the discussion here is concerned mainly with the development of acceptable constitutive equations.

There seems to be general agreement among practitioners in the field of solid propellant characterization that the primary causes of material nonlinearities are:

- Large strain effects in the polymer occurring at relatively low macro-strains caused by strain magnifications on the microscale resulting from the high solids loading.
- Irreversible or only partially reversible effects both in the polymer and at polymer-particulate interfaces caused by both adhesive and cohesive failure in the polymer or filler.
- Nonlinearities produced by coupled mechanical and thermal effects; e.g., simultaneous cooling and straining.

All of the above effects lead to essentially the same general form of constitutive equation.

The problem at hand is essentially that of

- Determining which of the several possible constitutive forms is most amenable to material characterization and
- Selecting from those amenable to characterization the one which promises to be best suited for future solid rocket grain structural analysis.

It is, of course, extremely important to keep in mind that any type of equation selected for investigation must be of a form suitable for multi-axial use. Secondly, any system of equations selected must inherently contain the elements of nonequilibrium thermodynamics; otherwise it is destined to failure when used in thermo mechanically coupled situations. This latter fact is responsible in part for past failures in attempts to predict the results of simultaneous cooling and straining tests. These failures stem largely from the fact that the time-temperature superposition techniques employed normally assume a common shift factor which is often incorrect under the conditions of interest.

11.1.1 LINEAR VERSUS NONLINEAR ANALYSIS

Attempts to describe the mechanical response of materials have classically taken two paths, (a) the theoretical development of mathematically complete constitutive equations describing the behavior of hypothetical materials and, (b) the experimental determination and subsequent empirical mathematical description of the behavior of real materials to a limited set of loading conditions. Neither approach stands alone and each approach has its merits and difficulties. The complete mathematical description of a hypothetical material is of little value to the engineer if he has no basis upon which to judge whether or not real material response can be described by the theory, and even if it can be, can the parameters in the theory be determined from laboratory tests? On the other hand, the mathematical description of a real material to one loading condition is generally of little value in predicting the response to some completely different loading condition for a nonlinear material. In practice one finds these two approaches must be brought together. This process involves interpreting experimentally based empirical relationships in terms of some complete mathematical description of a hypothetical material. This process represents the means by which one develops a meaningful constitutive theory for modern solid propellants.

In the search for a description of a material response characteristic, it is important to bear in mind that what is needed is a description sufficiently general to permit a meaningful structural analysis of the system, and that it is not necessary to refine the characterization beyond this point. A physically meaningful characterization should be carried out over the same types of loading and thermal histories, and over the same time

scales as the system is expected to experience in actual usage. Hence, the degree of refinement of the material characterization process will depend somewhat upon the loading conditions and the extent of the analysis.

For ideal elastic materials exhibiting no energy dissipation, the state of stress at time t is only a function of the state of strain at time t and is independent of all past states of strain. Viscoelastic materials on the other hand, can dissipate energy and the state of stress at time t in general depends not only on the current state of strain but also on the entire history of the deformation. The material characterization process for viscoelastic materials involves determining this functional dependence of stress on strain in a usable form.

Although viscoelastic materials have been used over the years in many engineering situations, the attempt to accurately determine the state of stress and strain in solid propellant rocket grains has been largely responsible for the recent advances in viscoelastic constitutive theory and reducing to practice viscoelastic stress analysis. In the last decade, for example, the solid rocket industry has progressed to the point where it now has the capability of performing rather sophisticated two dimensional thermal stress analyses of thermorheologically simple, linear viscoelastic materials, including transient thermal analysis. Experience has indicated that for the two major loading conditions of propellant grains, thermal cooling and pressurization, the predicted strains and displacements in case bonded propellant grains are not a strong function of the propellant response characteristics, because of the nearly incompressible behavior of solid propellants. Thus, linear elastic or linear viscoelastic approximations are usually quite adequate for strain and

displacement predictions. Determination of the stresses is not so simple, however, as the highly nonlinear viscoelastic behavior of some modern highly solids loaded propellants appears to produce large errors in predictions for stresses based on linear viscoelastic theory [1-3]. Although some attempts have been made to treat propellants as nonlinear viscoelastic materials, their structural analysis in industrial practice has almost without exception, been based on linear viscoelastic or linear elastic methods. Initial design determination is usually analytical, and design refinements are typically based upon a combination of experience and experiment.

The prime reasons for the continued use of linear theory in analysis are:

- The methods are relatively inexpensive to use.
- The usage is, almost without exception, state-of-the-art in industry.
- There has been no consensus of opinion with respect to alternate nonlinear methods for either characterization or analysis.

The reasons for the aforementioned lack of concensus relative to nonlinear analysis methods stems from:

- Technical disagreements as to the proven validity of currently proposed nonlinear methods of characterization and analysis.
- The rather high cost of laboratory characterization and computer analysis for most proposed methods.
- The generally expressed feeling that nonlinear analyses either provide answers but little different from a linear analysis or, alternatively, linear analyses provides answers on the conservative side.

This latter reason for the continuation of linear analysis methods is based on the fact that the dominant nonlinearity observed of propellants

is a stress softening due to dewetting mechanisms [4,5]. It is thus the feeling of many in the industry that by characterizing the propellant as a linear viscoelastic solid, at small strains in the absence of dewetting, the subsequent stress analysis will provide a conservative estimate for the upper bound of the stresses in any motor configuration. However, recent theoretical and experimental efforts indicate that linear theories based on small strain characterization do not necessarily provide a conservative estimate for the predicted stress states, and that in fact, linear predictions are often substantially lower than experimentally observed [1,2,6].

Stresses two to four fold higher than predicted have been reported by a number of observers [1,2]. Complicating matters is the fact that many of the nonlinear, viscoelastic constitutive theories and analyses used indicate that linear methods should provide a conservative upper bound for the stresses [e.g., 6,7].

Clearly, one of the major problems is providing a physically realistic mathematical description of propellant response. If meaningful stress analyses are to be performed on propellant structures, mathematical representations containing the devices necessary to describe the propellant's response must be found and applied.

The presentation herein is intended to review and extend the theoretical framework for nonlinear thermoviscoelasticity, compare specific applications of most currently used theories, and present in some detail recent efforts not necessarily readily available elsewhere.

Specific step-by-step methods of analysis are not presented at this time. Discussions of the many nonlinear methods of analysis may be readily found in the open literature, and the supplement to this handbook in

preparation under Air Force sponsorship will present details of performing a nonlinear analysis. Our intention here is to provide a background to the subject and a rational basis from which nonlinear constitutive theories for solid propellants may be developed.

11.2 MECHANISMS OF NONLINEAR VISCOELASTIC BEHAVIOR

The source of the nonlinearities in the viscoelastic response of composite solid propellants is not difficult to understand from a microscopic point of view. A general composite solid propellant is composed of a solid oxidizer in a rubbery polymeric material with various other additives to influence burning rate, specific impulse, mechanical properties, and processing characteristics. The mechanical behavior of propellant is most greatly influenced by the polymer and other specific additives for modification of these properties. Although the binder becomes the major load bearing material in the propellant matrix, some bonding to the solid additives and oxidizer causes these materials to become involved in the mechanical behavior of the propellant.

Generally speaking, at low strains propellants are nearly incompressible while at large strains they become highly compressible and exhibit large amounts of volumetric dilatation during uniaxial testing [5]. The yielding behavior is characteristic of these materials and is always coincidental with the increase in volume. This sudden change in modulus is one type of nonlinearity that is well known and recognized by most workers in the field. At these larger strains, the relaxations modulus becomes very strain and dilatation dependent, and this naturally means nonlinear behavior.

On the microstructural scale, failure begins early in the stress-strain history and is first observable as a vacuole in the polymer near the surface of the filler in the direction of stretch [5]. These vacuoles increase in

size and number with increasing strain which causes the volumetric increase. Vacuoles form in the binder at locations of high stress and stress gradients. Once the vacuole forms, the neighboring material is relieved of some of its strain energy which is spent in vacuole growth. This growth reduces stresses and stress gradients in the vicinity of the vacuole and thus reduces its propensity to propagate. Vacuole growth also reduces the influence of filler particles in the neighborhood of the vacuole and results in the yielding observed of the stress-strain behavior and the strain dependence of the relaxation modulus at large strains. Each filler particle is a potential vacuole site, and experimental evidence [5] indicates that 70 to 100% of the filler particles on a volumetric scale have vacuoles immediately adjacent to them in the direction of stretch at large strains.

A measure of the relaxation modulus of the cured binder material shows that relaxation to the rubbery equilibrium modulus occurs very rapidly at room temperature. The relaxation modulus determined on propellant made with the same binder is considerably greater and relaxes at a much slower rate. The equilibrium modulus is not obtained in 10^6 minutes (two years) and may not really exist for propellant although the rate of change becomes so slow that for practical purposes it may be used when the relaxation time is within the time frame of consideration. The relaxation moduli of a polybutadiene acrylic acid/acrylonitule terpolymer (PBAN) binder and a propellant made with this binder (TP-H1011) are presented in Figure 1. The relaxation modulus was measured at three different strain levels (2, 10 and 20%) on the binder material with no change in the relaxation spectrum.

Relaxation in a binder material occurs because the normally coiled polymer chains of which the material structure is composed are being

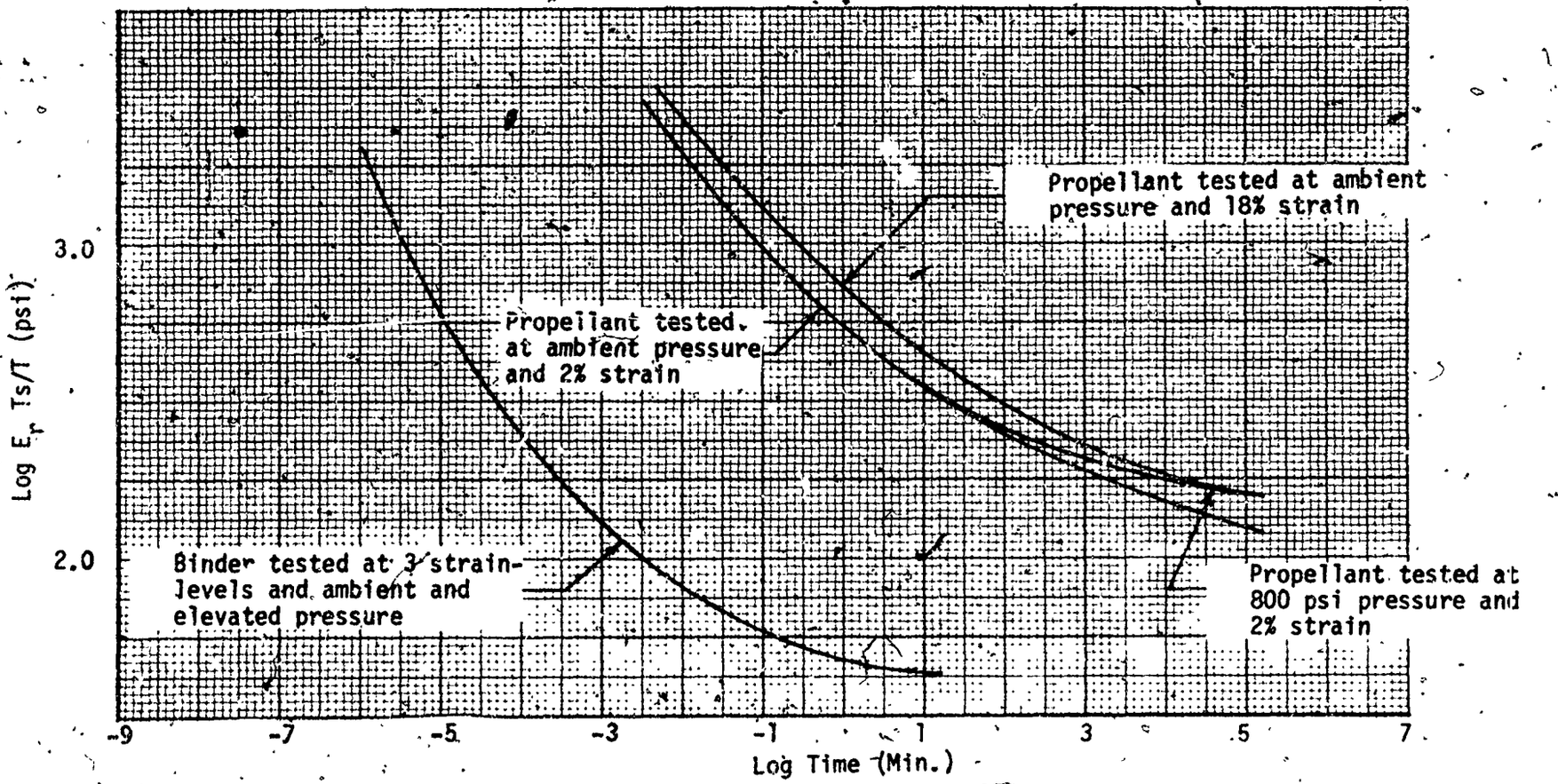

FIGURE I. RELAXATION MODULUS OF TP-H1011 PROPELLANT AND PBAN BINDER

mechanically forced to uncoil. These structural linkages are going to naturally seek the lowest possible energy configuration, and as they do so, the force required to hold them at the new length decays. The time to reach this lowest strain energy condition is a characteristic function of the polymeric material. Although the solids added to the binder to make propellant have some effect upon the chemical reactions forming the polymer crosslink network, the structure is essentially the same when the binder system is made from the same initial chemicals. It is expected that the uncoiling rate of the polymer chains in a propellant will be somewhat similar to those in the binder when subjected to the same strain condition. It is readily seen in Figure 1 that the relaxation times are not the same for binder and propellant. Since the filler materials in a propellant are bearing part of the load due to the binder-particle interfacial bond, it is natural to suspect that part of the load change with time is due to these solids. This suspicion is reinforced in Figure 2, which represents data published by Freudenthal [8] using a sodium chloride filled polyurethane polymer. This is not meant to say that the solids exhibit time dependent characteristics in the same time regime as the polymeric material, but the solids have reinforced the binder and bond failure will result in loss of a pseudo-crosslink (dewetting). Now it is obvious that a distribution of loads occurs on the solid particles throughout the propellant matrix. This causes particulate-polymer interfacial separation to occur at various times resulting in a type of relaxation. This relaxation occurs not only at a different rate from the polymer chain uncoiling mechanism but also is affected differently by temperature and load changes. Whenever two or more reactions are occurring simultaneously and they are dependent to different degrees on external conditions nonlinear response to those conditions will frequently result.

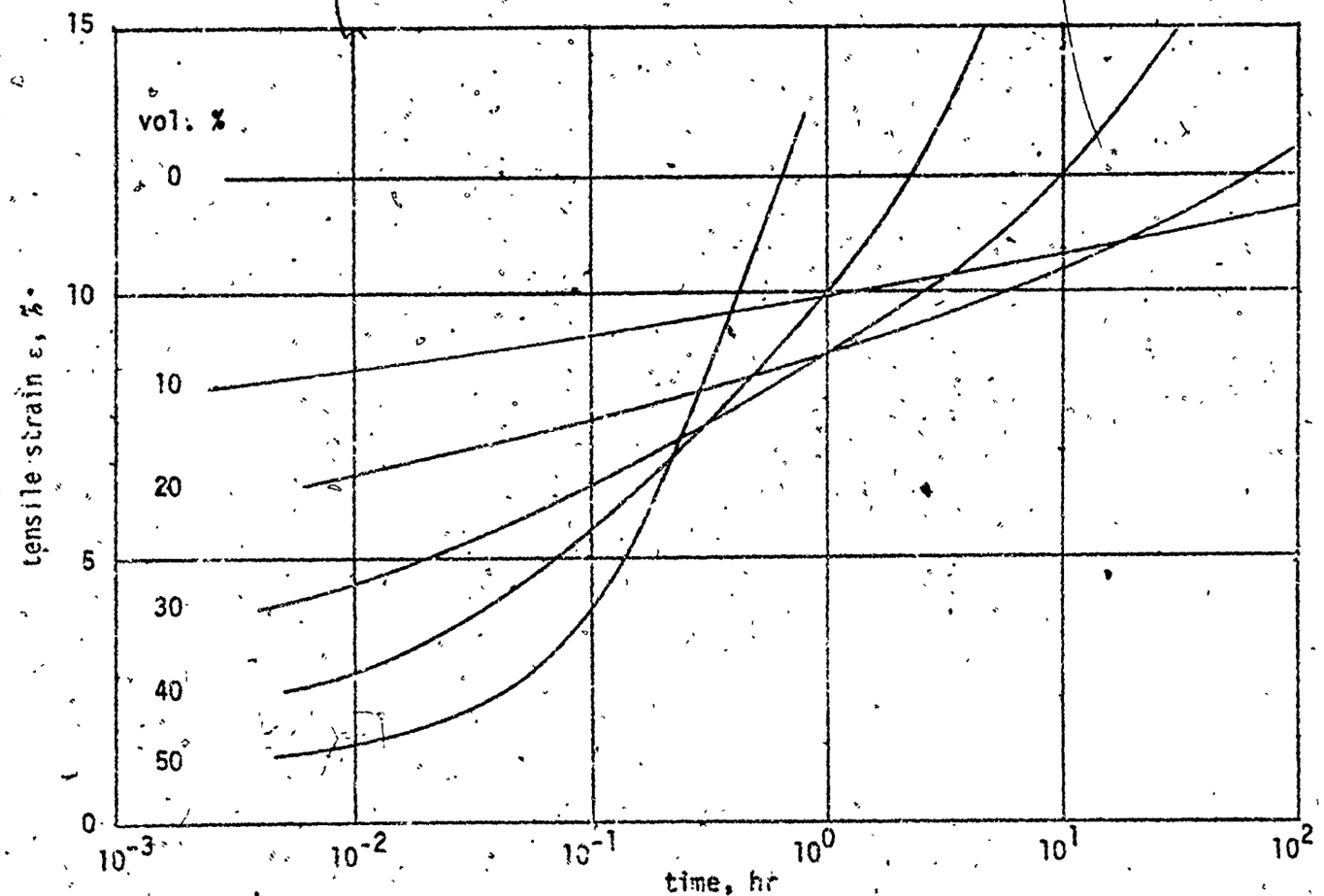

Figure 2. Tensile creep under a tensile stress of 3 kg/cm^2 of polyurethane rubber filled with various percentages of sodium chloride.

Measurement of the relaxation modulus under superimposed hydrostatic pressure shows a smaller relaxation and an earlier approach to an equilibrium modulus (Figure 1). Pressure has no effect on the binder relaxation spectrum. Since pressure reduces the tendency for dewetting, the hypothesis that part of the relaxation is due to binder-filler interfacial separation is substantiated.

It is apparent that polymer chain uncoiling and dewetting are not the only relaxation mechanisms. It is quite likely that particle-particle interactions play a role in the relaxation process. All of these mechanisms create microscopic nonhomogeneities that add up to produce a nonhomogeneous material. Another important source of propellant nonlinearity gives rise to the often observed hysteresis effects. Whereas nonlinearities in the stress-strain behavior for monotonic loading situations have been accounted for using models relating volumetric dilatation to the frequency of vacuole formation, assuming all dilatation may be attributed to vacuole formation, these models, while capable of some irreversible effects, do not properly predict the observed hysteresis many propellants exhibit. Typical hysteresis effects are shown in Figure 3. These hysteresis effects and much of the viscoelastic behavior of propellants has been attributed to time dependent failure of the polymer on a molecular basis [9.-18]. This phenomenon is commonly known as the "Mullins' Effect" and is time-dependent in propellants. Several models have been proposed for modeling this effect [9 -27]. The polymeric chain failure associated with hysteresis effects preceeds volumetric dilatation and is most likely responsible for the nonlinear behavior observed of solid propellants at small strains. The models developed explaining this effect have to date all been one-dimensional. The simplest model [22] is based on the following key assumptions:

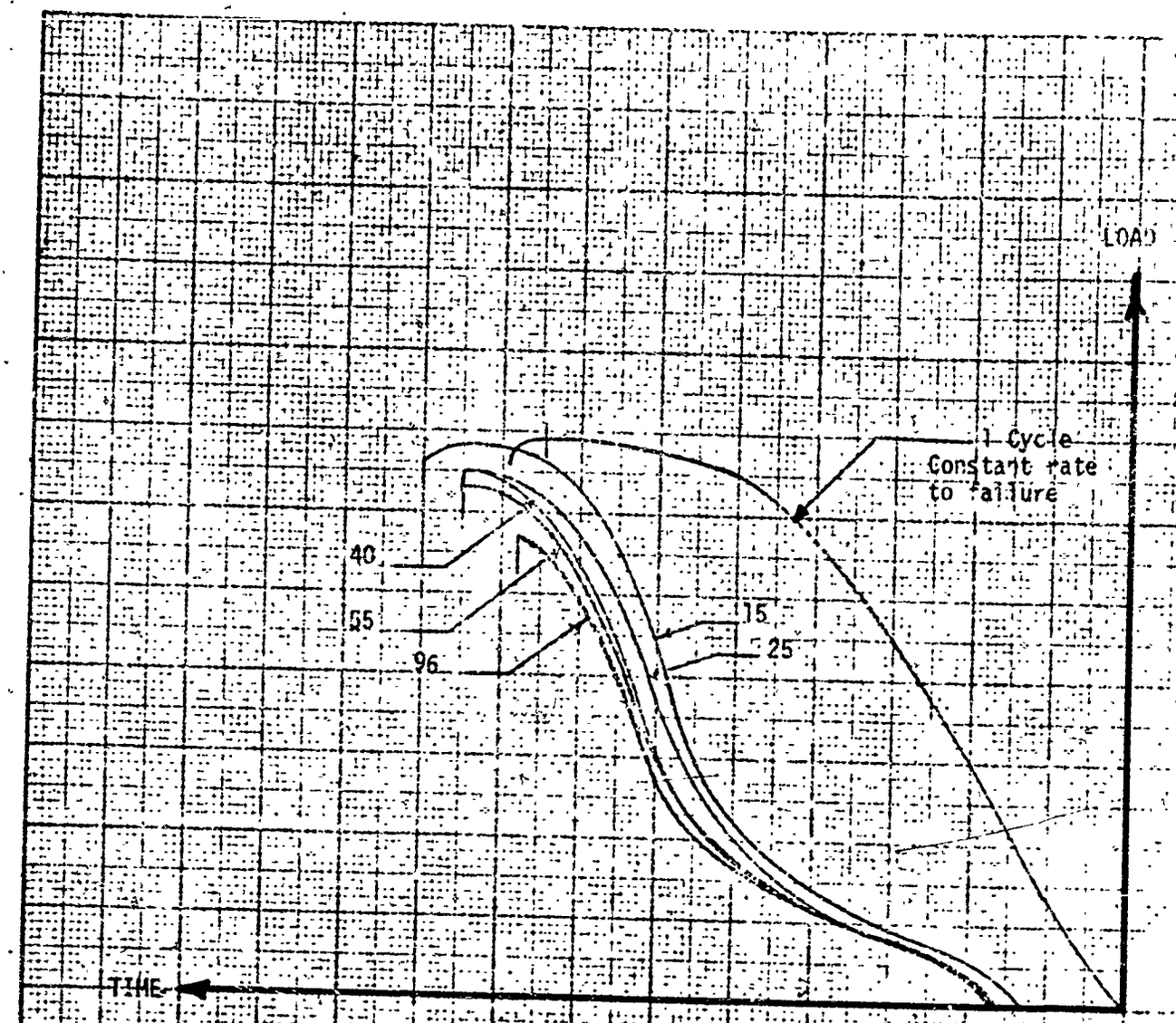

FIGURE 3. UNIAXIAL CONSTANT RATE CYCLING OF TP-H1011 PBAN PROPELLANT. SAMPLES WERE CYCLED TO 90% OF FAILURE STRAIN AND THEN TESTED TO FAILURE ON THE CYCLE SHOWN.

i) A distribution of polymer chain effective lengths or "slackness" between neighboring filler particles.

ii) The microscopic strain in any given chain is proportional to the axial applied strain, the proportionality constant differing from chain to chain.

iii) Each polymer chain has the same elastic stress-strain law.

iv) Each polymer chain ruptures and remains ruptured if at any time in its history its strain exceeds a critical value ε_{max}

Proceeding with this model and a suggested representation of Fitzgerald [23], Farris [8] developed a uniaxial constitutive theory making use of memory function norm which agrees extremely well with experimental results.

There is every indication that dewetting and time dependent chain failure are the dominant mechanisms of nonlinearity in solid propellants. These mechanisms are adequately characterized through the use of memory function norms indtroduced implicitly by Greene and Rivlin [24] and Truesdell and Noll [25] explicitly by Coleman and Noll [26] and Coleman and Mizel [27-29], suggested for solid propellants by Fitzgerald [30], formalized by Hufferd [31] and applied to solid propellant behavior by Farris [9,20,32].

11.3 CLASSIFICATION OF VISCOELASTIC CONSTITUTIVE EQUATIONS

The class of materials termed viscoelastic has different meanings to different groups. Generally speaking, most experimentalists would

classify as viscoelastic all elastic solid materials displaying time dependent response such as relaxation and creep, no matter what the cause. Here, elastic is interpreted in the sense of complete recovery of shape when tractions are removed. Most theorists, on the other hand, restrict the meaning of viscoelastic materials to elastic solids possessing fluid characteristics. These hypothetical viscoelastic materials can have a certain amount of rigidity characteristic of elastic materials, yet can dissipate energy by viscous damping as do some fluids. To the theorist, the elastic solid and the viscous fluid are but two types of viscoelastic materials.

In real materials time dependent response to mechanical disturbances can have many causes only one of which is internal viscosity. Other sources of time effects are aging, thermally activated molecular bond ruptures and formation, and time dependent mechanical degradation of the material's microstructure, such as the previously mentioned dewetting or hysteresis effects. These are a few of possibly many mechanisms that can and do cause time dependency in material response, and in a broad sense, may all be interrupted as viscoelastic.

Generally speaking, viscoelastic response can be characterized as fading memory behavior with different characteristics which distinguish the different types of behavior experimentally observed. The four fading memory characteristics which appear to encompass the majority if not all engineering materials are [31]:

i) Normal Fading Memory

ii) Failing Memory

iii) Finite Memory

iv) Permanent Memory

Normal fading memory constitutive theory represents a time memory mechanism wherein the transient portion of the response decays with time whenever the state of strain is held constant after some initial strain disturbance. For very slow rates of strain, or constant states of strain at long times, the state of stress for a material possessing normal fading memory characteristics is given by a nonlinear elastic stress-strain law, dependent only on the current state of strain and independent of any previous strain states. It is this type of behavior that has received considerable theoretical interest in recent years. Linear elasticity and linear viscoelasticity are often thought of as normal fading memory theories. A normal fading memory can be modeled by an assemblage of (nonlinear) springs and dashpots.

A failing memory material forgets its entire past abruptly, and a finite memory material has no recollection of any event in its history which occurred prior to a certain fixed time.

Permanent memory viscoelastic materials can be simply defined as materials wherein all the effects of past deformation states are not forgotten and therefore still influence the current stress state.

The use of the word "memory" herein is perhaps in need of some clarification. For example, a linear elastic solid whose present response, say the stress field, is dependent only upon the present value of the strain field, is often therefore referred to as a material with no memory, i.e., a material whose response is not dependent upon the specific history of strain. In another sense, however, a linear elastic material possesses a perfect memory with respect to its initial state, i.e., remove all stresses or strains and the material configuration returns to its unique

rest state. Alternatively, a linear elastic material may be interpreted as a failing memory material, i.e., choosing the reference configuration of the body to be a configuration occupied by the body at some fixed time, then the material has no recollection of any experience it has at any other time.

A second category of idealized behavior is contained in the so-called hypoelastic materials in which "the stress at the present time depends only on the order in which the body has occupied its past configurations but not on the time rate at which these past configurations were traversed. It follows that hypoelastic materials need not have a (normal) fading memory"[25]. This class of material, specialized by Truesdell and Noll with respect to stress rates leads to a representation homogeneous in strain rate; that is, a material response which obeys the law of scalar multiplication in strain rate (i.e., homogeneity), but not additivity (i.e., superposition) in the strain itself. Thus, a hypoelastic material is one exhibiting permanent memory characteristics.

A permanent memory theory is necessary to describe time and path sensitive stress states not caused by internal viscosity, such as failure or slippage of the materials microstructure or other time-irreversible microstructural changes like crystallization. The theory of plasticity and viscoplasticity are by necessity permanent memory constitutive theories, as are the aforementioned hypoelastic theories. Permanent memory time and path effects may also be observed in "elastic" materials which recover their original shape when all surface tractions are removed. In contrast to fading memory constitutive theory, little work has been done in reducing permanent memory viscoelastic constitutive theory to practice or developing specific representations for permanent

memory materials. Considerable effort has been spent attempting to describe the behavior of certain permanent memory materials, such as materials exhibiting plastic flow; however, these specialized theories are not applicable to permanent memory viscoelastic materials. There is, of course, a real need for a permanent memory viscoelastic theory, since nearly all viscoelastic materials used as structural materials exhibit permanent memory characteristics. Tire rubber, composite and double base solid propellants, rubber asphalt concrete, rock and masonry materials, most metals and plastics, and nearly all composite materials are, in fact, all permanent memory materials. It is true that the stress states in a few of the above materials at small deformations and at states not approaching failure can be described by fading memory constitutive theory; however, this is of little value if accurate failure predictions or margins of safety are required from an analysis. For some materials such as solid propellants, fading memory viscoelastic predictions are often times greatly in error even at small strains and conditions far below failure [1,2,9,21,22].

11.4 RECENT DEVELOPMENTS IN CONSTITUTIVE EQUATIONS

The most recent University of Utah Project THEMIS report [33] compares and contrasts University developments with previous constitutive theories of Green and Rivlin [24], Coleman and Noll [26,34], Lianis [35-38], Findley and co-workers [39,40], Lockett [41,42], Gottenberg [43], Schapery [44-47], Dong [48,49], Hufferd [31], Fitzgerald [23,30], and Fa ris [9,22 32]. Rather than repeat these comparisons, our intention is to only summarize here those approaches suitable for the development of a usable solid propellant constitutive theory. These developments include the mechanisms required for describing irreversible effects associated with dewetting and polymer chain slippage and failure. These mechanisms are most readily included through introduction of a memory function norm which allows for permanent memory characteristics as well as normal fading memory behavior under certain loading conditions. Green and Rivlin[24] first introduced a constitutive theory for nonlinear materials capable of exhibiting permanent memory characteristics. For initially isotropic materials their representation has the form

$$
\begin{aligned}
\overset{P(\alpha)}{\sim} G_{pq}^{(\mu)} &= \phi^{(0)}(t) + \int_0^t \phi^{(1)}\{t, \tau, g(\tau)\}\, d\tau \\
&+ \int_0^t \int_0^t \phi^{(2)}\{t, \tau_1, \tau_2, g(\tau_1)g(\tau_2)\}\, d\tau_1\, d\tau_2 + \qquad (11\text{-}1) \\
\cdots &+ \int_0^t \int_0^t \cdots \int_0^t \phi^{(n)}\{t, \tau_1, \tau_2, \ldots, \tau_n, g(\tau_1)g(\tau_2)\ldots g(\tau_n)\}\, d\tau_1\, d\tau_2 \ldots d\tau_n
\end{aligned}
$$

where $\phi^{(n)}$ is a homogeneous polynomial scalar invariat of the deformation gradient = $g(\tau_1) \ldots g(\tau_n)$ linear in each of them and a function of t, $\tau_1, \tau_2, \ldots \tau_n$. This representation includes the representations developed

at the University of Utah and those of Farris [8,32]. From a practical point of view, however, the expansion is not too useful. Onat [50] and others have argued that many terms of the expansion may be required to represent constitutive relations which although continuous are not smooth. However, it will be noted in a later section that the accuracy of the functional expansion cannot in general be increased by merely adding higher order integrals since the kernel functions are dependent upon both the order of the expansion and the range of the approximation.

Dong[48,49] has proposed an abstract extension of the multiple integral expansion incorporating various time and strain-memory mechanisms. This formulation is based on the use of several chronological variables for the independent ordering of events, each of which represents a different and independent memory mechanism. If time is the only chronological variable, then the Green-Rivlin equations are recovered. Dong's principle contribution is including more than one type of memory mechanism into a constitutive equation and also the manner in which it must be incorporated. For non-time memory mechanisms, Dong's chronological variables are functionals of the deformation histories. This approach is essentially the same as that used by Schapery[44-47]. The main difference is that the form of Schapery's equation and the reduced time variables were derived from a thermodynamic model and incorporates a single memory mechanism, whereas Dong's approach is purely mathematical which can combine many memory mechanisms. Unfortunately, the multiple integral expansion of Dong's constitutive functional is considerably more complicated than the Green-Rivlin expansion and hence is even more impractical to use for characterizing material response.

Schapery's non-linear constitutive theory [44-47] is derived from thermodynamic principles and its mathematical form is very similar to the Boltzmann superposition integral form of linear viscoelasticity. The one-dimensional equivalent of Schapery's three-dimensional equation has the form

$$\sigma = h_e E_e e + h_1 \int_0^t \Delta E(\rho - \rho') \frac{d(h_2 e)}{d\tau} d\tau \qquad (11\text{-}2)$$

where e is the infinitesimal strain measure and ρ and ρ' are the current value and generic value of a reduced time defined as

$$\rho = \int_0^t \frac{d\tau}{A_e[e(\tau)]} \qquad (11\text{-}3)$$

and

$$\rho' = \int_0^t \frac{d\tau}{A_e[e(\tau')]} \qquad (11\text{-}4)$$

The strain dependent properties in Schapery's equations are h_e, h_1, h_2, and A_e. Variations in the first three are due to higher order strain effects in the Helmholtz free energy while changes in the property A_e arise from similar strong strain influences in both entropy production and free energy. It is only through certain types of strain dependent reduced times that the equation can contain permanent memory behavior. If the function A_e is constant, the equation reduces to a fading memory constitutive equation. For non-isothermal conditions, the functions h_e and A_e are dependent upon temperature as well as strain. In this manner, the often referred to "thermorheologically simple" materials can be included in the representation. The temperature dependent reduced

time produces an "equivalence" between time and temperature observed in many polymeric materials having viscous damping. This equivalence results from the assumption that all hidden coordinates are affected equally by the independent constitutive variables. This assumption implies, for example, a common nonlinearity in all elements of the material model and requires nearly equal relaxation or retardation times. Herein lies the failure of this approach to adequately describe the results of simultaneous cooling and straining tests. For the time scale associated with cooling a solid rocket motor or simultaneous cooling and straining of a propellant test sample, the relaxation times are considerably different and longer, and the assumption of a common shift factor is no longer necessarily valid. Mechanisms do exist within Schapery's approach for introducing discrete shift factors for various portions of the relaxation spectrum (i.e., different nonlinear mechanisms); however, these modifications sacrifice much of the simplicity and appeal of Schapery's constitutive theory by complicating the elimination of hidden variable dependence. Additional integral terms must be added with different material functions.

Like the Lianis fading memory constitutive theory [35-38], Schapery's equation permits fairly straightforward material characterization inasmuch as the same relaxation function appears as in linear viscoelasticity theory. The characterization process can be completed by performing a few multi-step relaxation tests to different strain levels and graphically superposing reduced experimental data. The three dimensional equations for isotropic materials in this type of representation have the same basic form as that given above. Two equations are required however, one expressing deviatoric stress in terms of deviatoric strain,

the other expressing dilatational stress in terms of dilatational strain. These equations have been applied successfully to the nonlinear behavior of fading memory and permanent memory polymeric and metal systems for monotonic loading situations. Because of the single integral nature of his equation, and hence, the fairly simple characterization process, Schapery's constitutive equations are particularly attractive, especially for fading memory materials. For permanent memory behavior, the ability of the researcher to construct shift functions A_e that agree with experimental data makes the approach more complicated; however, this will most likely be true with any permanent memory theory. Because of the broader scope of permanent memory viscoelastic materials, more complex mathematical representations are often needed to describe their response. Schapery has shown that if the shift function $A_e = [\dot{e}(t)]^{-1}$, then rate independent plasticity will result. This observation is not immediately obvious from the constitutive equations which demonstrates that one must develop an intuition for particular nonlinear constitutive representations.

Several workers have proposed the explicit rise of function norms for characterizing the memory response of materials. Coleman and Noll [26] proposed the use of the L_p and L_∞ norms of the deformation gradient, however, without elaboration. Coleman and Mizel [27-29] have since concluded rather penetrating studies exploring the L_2 and L_p norms for fading memory materials. Fitzgerald [30] presented the use of the Chebychev norm as a model for the Mullins' effect. Hufferd [31] has discussed the coupling of a norm representation with fading memory assumptions, and recently Coleman and Owen [51] presented a theory of thermodynamics of materials with permanent memory which is a special case of Hufferd's developments. Whereas these investigations have dealt

with general material behavior from the continuum mechanics point of view, Farris [9,32] has obtained explicit engineering relations for uniaxial loading of materials having mathematically homogeneous constitutive equations. His results, as alluded to before, are contained within the more general theories of Green and Rivlin, Dong, Schapery and Hufferd.

Farris' constitutive theory, as mentioned before, was obtained by modeling the failing microstructure of particulate filled polymeric composites. Farris, like Mullins in 1947, observed that many filled polymeric materials were time dependant in their response to mechanical disturbances even though the filler particles and the polymeric binder were for all practical purposes elastic. Most of these materials are not only time dependent, but exhibit permanent memory response in which stress or strain softening is characteristic. It was also observed that many of these materials obey the homogeneity principle of constitutive linearity (i.e., scalar multiplication) while they do not follow the superposition or additivity principle. He subsequently developed and experimentally verified, a one-dimensional constitutive theory and analysis method valid for nonlinear materials having mathematically homogeneous constitutive equations. He has further demonstrated that for several classes of his constitutive theory a linear solution to a proportional boundary valued problem is admissible for part of the solution, either the stresses or the strains, but not both, while the remaining part of the solution must be obtained by substituting the time dependent linear solutions, into the nonlinear constitutive equation. This approach satisfies the equations of equilibrium, strain compatibility conditions and the proportional boundary conditions and is shown to be a valid solution to the problem. For isotropic materials, Farris' three-dimensional constitutive equations have the form

$$\sigma_{ij}(x_k,t) = \delta_{ij}\int_0^t K_0[I_1(\overset{t}{\underset{\xi=0}{x_k,\xi}}),\ I_2(\overset{t}{\underset{\xi=0}{x_k,\xi}}),\ I_3(\overset{t}{\underset{\xi=0}{x_k,\xi}}),\ t,\tau]\ \dot{e}_k(\tau)d\tau$$

$$+\int_0^t K_1[I_1(\overset{t}{\underset{\xi=0}{x_k,\xi}}),I_1(\overset{t}{\underset{\xi=0}{x_k,\xi}}),\ I_2(\overset{t}{\underset{\xi=0}{x_k,\xi}}),\ I_3(\overset{t}{\underset{\xi=0}{x_k,\xi}}),\ t,\tau]\dot{e}_{ij}(\tau)d\tau \qquad (11\text{-}5)$$

where the kernels are functionals of the histories of the strain invariants as well as functions of the current and generic values of time. To satisfy the homogeneity condition, he has demonstrated that the kernel functions must be homogeneous to degree zero, or equivalently, they must remain invariant to any scalar multiple of the deformation history; that is,

$$K\ [bI_1(\overset{t}{\underset{\xi=0}{x_k,\xi}}),b\ I_2(\overset{t}{\underset{\xi=0}{x_k,\xi}}),b\ \ I_3(\overset{t}{\underset{\xi=0}{x_k,\xi}}),t,\tau]$$

$$= K\ [I_1(\overset{t}{\underset{\xi=0}{x_k,\xi}}),I_2(\overset{t}{\underset{\xi=0}{x_k,\xi}}),I_3(\overset{t}{\underset{\xi=0}{x_k,\xi}}),t,\tau] \qquad (11\text{-}6)$$

where b is an arbitrary scalar. The constitutive equation with this constraint possesses the property that once the stress output to a particular strain input is known, it is also known for any scalar multiple of that input.

For proportional boundary conditions, the equations reduce to the form

$$\sigma_{ij}(x_k,t) = \delta_{ij}\int_0^t k_0[f(\overset{t}{\underset{\xi=0}{\xi}}),t,\tau]\ \dot{e}_{kk}(x_k,\tau)\ d\tau$$

$$+\int_0^t K_2[f(\overset{t}{\underset{\xi=0}{\xi}}),t,\tau]\ \dot{e}_{ij}(x_k,\tau)d\tau \qquad (11\text{-}7)$$

where $f(\xi)$ is the proportional time function . The kernel functionals now contain no spatial measures and it is a simple matter to demonstrate that for certain classes of the constitutive equations, such as the kernels being proportional to each other, a linear solution for the displacement field is valid while the stresses will be nonlinear and can be obtained by substituting the time dependent linear displacement solution into the constitutive equation.

The main difficulty in using Farris' equations is in determining the form of the kernel functionals. These functionals can be any functionals homogeneous to degree zero. Using L_p norms and exponential time functions material characterization can be accomplished without too much difficulty in one-dimension by curve fitting using infinitesimal strain measures. For finite strain measures and a general three-dimensional theory, the curve fitting process is considerably more complicated however. Farris' equations also suffer from the same difficulties as other theories for the problem of simultaneous cooling and straining. Namely, his equations for "thermorheologically simple materials" are based on the questionable assumption of a single common shift factor. Also, not being founded on thermodynamic principles, there is no ready way to introduce multiple shift factor mechanisms.

11.5 EQUATION DEVELOPMENT

From the discussions of the previous sections, one sees then a general form of constitutive equation which will properly include both fading memory effects (such as relaxation caused by internal rearrangements) and permanent memory effects (such as polymer chain failure) is required for solid propellant characterization. Evident in the previous discussions is the fact that published efforts to date have for the most part dealt either entirely with one or the other of the above effects. For example, Schapery's approach considers internal variables of the fading type and curve fits data to account for nonlinearities, and obtains permanent memory characteristics only under restrictive conditions. Conversely, Farris and Fitzgerald have published strictly permanent memory (microfailure and dewetting effects) relations which were also curve fitted.

Just as a shift-factor A_T, may always be obtained by shifting (i.e., curve fitting) isothermal data, so do the above-mentioned approaches always yield a good approximation to the specific tests to which the data is fitted. As previously mentioned, all previously published methods usually fail under thermomechanical coupling (i.e., simultaneous cooling and straining, not heating and straining) and/or extensions to multi-axial conditions. The reason is that real propellants, with the possible exception of certain polyurethanes, are indeed influenced by internal relaxation, internal microfailures (irreversible), and internal microfailures which are only partially reversible (rehealing). Thus, any theoretical equation must contain implicitly the capability to account for these various effective "relaxation" producing mechanisms.

How then to approach the problem when it is known that, based on simultaneous cooling and straining, there is not a common time-temperature

shift factor A_T nor, based on long-term creep data, is there a common A_e shift factor. That is, a common general shift factor A_D does not account for much of the observed data on coupling and long-term creep.

Without being unnecessarily mathematical, let us state that the stress, T, is some functional of the finite deformation gradient history, F_t, the temperature history, θ_t, and some finite number of internal configuration effects, α_t, α_{t_2}, . . . , α_{t_i}, that is

$$T(t) = f\,[F_t, \theta_t, \alpha_{t_i}]. \qquad (11\text{-}8)$$

The above leads to the multiple integral approach; complex, unwieldy, and not including permanent memory effects in the form given here. A second approach, the so-called state variable approach wherein

$$T = f[F(t), \theta(t), \dot{F}(t), \dot{\theta}(t), \alpha_i(t), \dot{\alpha}_i(t)] \qquad (11\text{-}9)$$

allows, with dependent $\dot{\alpha}_i$, a rather straightforward nonlinear viscoelastic approach using only present values of the independent variables. However, by assuming the time dependency of the internal relaxation processes $\dot{\alpha}_i$ as having a common time and strain factor, one obtains the Staverman solution

$$T(t) = \int_{-\infty}^{t} G(t - \tau)\, F(\lambda) d\tau \qquad (11\text{-}10)$$

where $F(\lambda)$ is some finite deformation measure and $G(t - \tau)$ is a common time factor. Schapery's previous publications do exactly this by assuming a common A_T and by assuming that the finite strain measure, $F(\lambda)$, is

$$F(\lambda) = A_e e$$

where e is the infinitesimal, linear strain, and A_e is a common, factorable large strain multiplier obtained experimentally, i.e., by vertical shifting of relaxation curves.

A third approach, originally suggested by Coleman and Truesdell and Noll, then presented by Fitzgerald and finally, made explicit by Fitzgerald

and Farris [22] and Hufferd [31] and more recently by Farris [9] is

$$T = f[||F||_p]$$

where $||F||_p$ is the L_p Lebesque norm. This leads to the Mullins effect, or as shown in recently published works, to a rather nice representation for isothermal variable load histories. The above bases observed relaxation on internal damage. Again, this plus any one of the above methods leads to a combined relaxation-damage representation for isothermal conditions or for non-isothermal conditions where a common A_n exists.

11.6 A GENERAL THEORY OF FADING MEMORY

The conclusion that the current response functionals of a material body are determined by the past history of the body is based on past physical experience with many real materials. In attempting to formulate constitutive theories for general nonlinear materials with memory it is soon realized that arbitrary dependence upon the entire history of the body leads to an extremely cumbersome theory with complex, physically prohibitive experimental difficulties associated with determining the material functions characterizing the material response. Accordingly, simpler mathematical treatments have been introduced which approximate one or more aspects of the behavior of real materials. Thus far the only memory attribute of real material behavior considered in any detail has been that of *fading memory*. The common statement of the *principle of fading memory* is the statement that *events that occurred in the distant past should have less influence in determining the current material response than those that occurred in the recent past.* The difficulties, and deficiencies, associated with this interpretation of fading memory have been discussed above. One of the major criticisms of current fading memory theories is with the restriction that *the memory of a simple material monotonically fades in time.* A more general principle of fading memory is presented here which accomodates more general memory behavior and is more closely related to the observed physical behavior of real materials. The statement of this principle may be given as [31]:

PHYSICAL PRINCIPLE OF FADING MEMORY

Certain events in the long past thermomechanical history of a material body B have less influence in determining the current values of the material response than those in the recent past.

Physically, this principle does not ignore completely the events that occurred in the past history of the body, but rather, allows for certain distant past events to have an appreciable influence on the current material response, while the memory of other events may fade or remain constant in time. This capability is absent from all existing fading memory theories.

From [31] and the above statement of a fading memory principle, it is suggested that all real engineering materials may be treated as fading memory materials. It is shown here that this is indeed the case within the restrictions of thermomechanical constitutive theory. A classification of fading memory characteristics is given, and a short summary of the approaches of previous workers is provided for comparison with the results presented here. The influence of memory on material response is characterized by the formal development of a *memory function norm* which possesses the desirable physical attributes suggested in the following section.

11.6.1. CLASSIFICATION OF FADING MEMORY CHARACTERISTICS

The justification, and reasonability, of the proposition that real materials are fading memory materials is based on an analogy with the behavior of animal intelligence. This analogy suggests consideration of materials with the following types of memory behavior:

i) *Perfect Memory*

ii) *Accelerating Memory*

iii) *Fading Memory*

A *perfect memory material is a material, which remembers totally its entire past.* Thus, the current response of material with perfect memory is influenced by the totality of all past events. There are few, if any, known examples of this class of materials. Some living organism may possess this memory characteristic.

An *accelerating memory material is a material in which disturbances in the past propagate in an unstable manner with time.* Again, examples of these materials are most likely living biological materials such as nerves or muscles. For the purposes of this study these types of materials are excluded by the time-translation invariance requirements of the axiom of frame-indifference.

From the above discussion it appears then that real engineering materials are fading memory materials. Intuitively, this seems reasonable. It is clear that a material should not remember its entire past, but rather, in some sense, should respond less to long past events in its thermomechanical history than to recent ones. It is well known however, that real materials respond differently under different loading situations. Thus, if all engineering materials may be classified as fading memory materials, then there must be different characteristics which distinguish the different types of behavior experimentally observed. Four fading memory characteristics are proposed here, which appear to encompass the majority, if not all, engineering materials:

1) *Normal Fading Memory.*

2) *Failing Memory.*

3) *Finite Memory.*

4) *Permanent Memory.*

A fading memory material with normal fading memory characteristics is a material which responds less to long past events in its thermomechanical history than to recent ones. This definition is analogous to those used by previous workers for fading memory materials. *A failing memory materials forgets its entire past abruptly. A material with finite memory has no recollection of any event in its history which occurred prior to a certain fixed time*[1]. and finally, *permanent memory is characterized by a material which never forgets entirely its past history.* This last characteristic defines a material which recalls part of its thermomechanical history while forgetting other parts[2]. This condition allows certain events in the past history of the material to have a strong influence on the current response functionals of the material. These definitions are motivated physically by materials which may exhibit elastic or inelastic response

[1] Green and Rivlin [ ] introduced the idea of finite memory through the assumption that the material had been at rest for all times before a certain fixed time. Stress relaxation is excluded with this interpretation however. If, on the other hand, arbitrary histories are allowed, but the constitutive functionals have finite memory, in the sense that their values are unaffected by any event prior to a certain fixed time, then materials with finite memory may also exhibit stress relaxation under certain circumstances. This latter interpretation is clearly preferred.

[2] It is to be emphasized that in the interpretation given here a material with permanent memory does not have a perfect memory. A perfect memory material, it is recalled, remembers *totally* its *entire* past history from $\tau = -\infty$ to $\tau = t$.

under certain loading conditions, stress relaxation or creep under other conditions and hysterisis under still anotner loading environment. These ideas provided the motivation for the formulation of the new principle of fading memory stated above.

It is worthwhile to comment briefly on the interpretation of classical theories of materials in relation to the fading memory concepts proposed in this research. The position of elastic materials is the most difficult to state precisely, even though the theory of elasticity is the oldest theory of material behavior. This statement is made because elastic materials are strangely atypical of other materials, and hence, their behavior may be interpreted in a number of different ways which for the most part, although correct, are often misleading. Truesdell [52] has pointed out that the classical theory of (finite) elasticity (or thermoelasticity) occupies four different positions in modern constitutive theory[3]:

1) As the general theory of simple materials in equilibrium.
2) As a theory of special materials in all deformation processes
3) As the common approximation for all simple materials with fading memory if deformed very slowly.
4) As the common approximation for all simple materials with fading memory if deformed very fast.

[3] In terms of the physical theory of fading memory introduced here, items 3) and 4) are valid only for fading memory materials having *normal fading memory* behavior. A material with permanent memory behavior may very well retain its permanent memory characteristics even when deformed very rapidly or very slowly.

With these ideas an elastic material is sometimes interpreted as a *perfect memory material* because it remembers only its reference configuration and does not remember any other. This interpretation does not reflect the arbitrariness of the reference configuration which may be a configuration occupied by the body aeons ago or one nanosecond ago or one not occupied at all by the body. An interpretation which agrees with the memory characteristics proposed here results if the reference configuration of the body is chosen to be a configuration occupied by the body at some fixed time. In this situation an elastic material has no recollection whatsoever of any experience it had at any earlier time, and thus may be characterized as a *fading memory material with failing memory characterization.*

It is also observed that viscous materials such as, for example, classical Newtonian fluids in which the stress is a function of the rate of deformation have failing memory characteristics. In fact, general materials of the differential type (i.e., materials whose response *functionals* are *functions* only of the derivatives of the independent variables at the current time up to some order v) are failing memory materials.

Linear and nonlinear viscoelastic materials as currently formulated are common, well known examples of materials having normal fading memory characteristics.

A perfectly plastic material is the classical example of a material with permanent memory characteristics. Such a material when deformed beyond its yield surface remembers forever the yield point upon further loading or unloading unless annealed, in which case one is then dealing with a new and different material.

The authors are unaware of any material which may be called a typical example of a material having finite memory. If such memory characteristics exist in real materials they are most likely quite difficult to observe and separate from other fading memory characteristics. One can easily visualize coupling between finite memory and normal fading memory characteristics, and between finite memory and permanent memory behavior.

It is obvious that the fading memory characteristics of materials with memory are not mutually exclusive. It is also quite apparent from the above discussions and the statement of a physical fading memory principle that the type of fading memory exhibited by a material is largely determined by the loading environment. Under certain thermomechanical environments a material may display one type of fading memory behavior while under other conditions the same material may display totally different behavior. One example of this phenomena was already been mentioned. Namely, failing memory materials exist as limiting cases of normal fading memory materials. Failing memory behavior is also a limiting case of finite memory. Finite memory-materials may also exhibit permanent memory characteristics. Elastic-plastic materials are examples of materials having failing memory characteristics for all deformations below their yield surface, but which exhibit permanent memory characteristics once yielded. Certain filled polymers, asphalt concretes and solid propellants exhibit normal fading memory characteristics under step and monotonic loading situations, evinced by stress relaxation and creep, and permanent memory characteristics under repeated loading or interrupted loading situations, typically evidenced by hysterisis upon unloading.

The response of certain filled, and unfilled elastomers, polymers, and certain biological materials to monotonic loadings may often be described by large deformation elasticity theory or rubber elasticity theory. These same materials upon unloading exhibit essentially a Mullin's effect which upon further loading is manifest as a permanent memory characteristic. Certain rigid plastics exhibit linear or mildly nonlinear, elastic, or weakly viscoelastic, behavior until deformed to the extent that permanent set is noted. Unless annealed, upon further loading these materials exhibit permanent memory characteristics. These examples reflect this author's experience with certain materials. The reader is most likely able to add to this list from his own experience.

Two important observations may be drawn from the illustrations of memory coupling effects of the previous paragraph:

1) *The fading memory characteristics of a material with memory are essentially determined by the loading environment.*
2) *The secondary memory characteristic of most real materials, and real loading situations, is manifest as permanent memory behavior, almost irrespective of the primary fading memory characteristic.*[4]

[4]The notable exception to this statement is the elastic or elastic-plastic material which is never deformed beyond its yield point. Only *primary* memory characteristics are evident in this exception however.

Although the first statement is implied in the results of previous theories of fading memory; neither of these observations have been explicitly stated for general loading situations. It will be observed in a subsequent discussion that these observations provide the very important physical motivation for the mathematical development of a fading memory measure for real materials subjected to real processes.

11.6.2 POSITION OF PREVIOUS FADING MEMORY THEORIES

A summary of six previous fading memory theories of simple materials is now provided for later illustration of the wider range of applicability of the memory influence measure developed during the course of this research[5]. It will be observed that some of these discussions with the exception of Green and Rivlin's contributions are quite brief since our purpose in reviewing earlier works is to point out only those features of previous theories which are relevant

[5] The recent contributions of Owen and Williams [53] and Owen [54] have been deliberately omitted from consideration here. Neither work allows viscoelastic materials within the class of materials they discuss. In addition, Owen and Williams restrict their attention to rate independent materials with memory whose response functions (functionals) are both differentiable and invariant under static continuations. These materials do not exhibit internal dissipation and are, in essence, hypoelastic materials. On the other hand, the materials considered by Owen need not exhibit fading memory nor is his analysis limited to rate-independent materials. However, the underlying assumptions of his theory, supposedly applicable to elastic-plastic behavior, are physically suspect.

to the developments of this research[6]. The more interested reader is strongly encouraged to seek out the list of works referenced here for a more in-depth analysis and appreciation of the contributions of previous workers.

GREEN-RIVLIN THEORY

The first rigorous treatment of a mechanical constitutive theory of nonlinear materials with memory was presented by Green, Rivlin and Spencer [24,55,56] and will be referred to as the *Green-Rivlin* formulation in this work. Their work has been reviewed and extended by Pipkin [57], Rivlin [58], Smat [50] and Pipkin and Rogers [59], among others.

Assuming that the stress tensor was a continuous functional over the compact space of continuous deformation histories, then using invariance requirements akin to those suggested by Oldroyd [60], assuming non-aging behavior (equivalent to the time-translation invariance requirement of the principle of material frame-indifference), using results from the theory of matrix invariants and firally making use of the Weierstrass theorem on uniform approximation of continuous functions by polynomials, Green and Rivlin [24] derived approximations to the stress functionals for hereditary materials in the form of a *Volterra-Fréchet* multiple integral expansion (i.e., sum of multiple integrals) in which the integrands of the various integrals contain matrix products of the strain tensor and invariants of these matrix products.

[6] The theory of Green and Rivlin is discussed in greater detail since supposedly arbitrary dependence on the deformation history is allowed, and proponents of this approach attempt to apply it to materials and loading processes where its applicability is physically and theoretically suspect.

It is generally believed that the Volterra-Frechet multiple integral representation admits arbitrary dependence on the deformation history and is capable of representing the mechanical behavior of the *most general* nonlinear material with memory. There is insufficient evidence to support such a claim, however. Quite the contrary, there is physical and theoretical evidence which suggests that the multiple integral may be incapable of representing path sensitive phenomena (e.g., inelastic deformations; see, e.g., Wang and Onat [61,62] and Onat [50]), however a rigorous proof of this statement has not yet been obtained. Although a formal proof of the failure of the Green-Rivlin formulation to represent permanent memory behavior or path sensitive behavior is outside the scope of this work, sufficient conditions for such a proof are given which from an intuitive physical point of view appear to be reasonable necessary conditions also.

Obviously, the Green-Rivlin formulation can exhibit failing memory characteristics for certain materials (e.g., nonlinear elasticity). Finite and normal fading memory characteristics are also evident. If it is proposed that the kernel functions in the various multiple integrals vanish if any of time-difference arguments become greater than some fixed time and if this time is interpreted as belonging to the material, then the material physically has strictly finite memory[7].

[7] If, as mentioned in footnote 1 of this section, only that class of deformations that correspond to a state of rest prior to a fixed time is allowed, then the static continuation for such a deformation history generally fails to be of the same class. This implies the physically undesirable result that stress relaxation is excluded, and motivates the preferred, and certainly more physically reasonable association of the *fixed time* with the material itself.

If the kernel functions are monotone strictly-decreasing functions of time, the Green-Rivlin formulation gives rise to strong fading memory behavior. This behavior has been observed for many plastics and polymers in which the kernels behave as exponentially decaying functions of time.

The physical requirement that the constitutive functionals remain bounded as the present time t approaches infinity imposes the requirement that the kernel functions must also be well behaved at sufficiently large times. It is clear that the Green-Rivlin formulation for materials with finite memory and normal fading memory characteristics satisfy this physical requirement. Wang [63] has proved that as a result of this physical requirement the kernels must vanish as the present time variable tends to infinity for materials whose deformations are completely recoverable upon unloading. Several plastics (e.g., polyvinyl chloride, oriented polypropylene) possess this property.

Thus far nothing has been said here which excludes the use of the multiple integral expansion to represent permanent memory behavior or general path sensitive phenomena (e.g., plasticity). It is not clear that the physical requirement of a bounded response at large times excludes representation of permanent memory behavior by a sum of multiple integrals except for certain exceptional cases, such as for example, tertiary creep of metals. There is definite experimental evidence however, which points out the impracticalities of using the Green-Rivlin formulation to represent permanent memory behavior or path sensitive phenomena. Qualitative and intuitively

appealing quantitative arguments can also be presented which suggest that the Volterra-Frechet multiple integral representation may be incapable of representing general path sensitive phenomena.

From their failure to predict the isothermal behavior of commercially pure 1100 aluminum at 300°F under time-dependent uniaxial stress by the first few terms of the multiple integral sum Wang and Onat [62] argued that many terms of the expansion may be required to represent constitutive relations which although *continuous* are not *smooth*. The same argument has been repeated by Onat and Wang [61]. Pipkin [57], Onat [50] and others for constitutive functionals which are continuous but apparently not smooth. However, the accuracy of the functional expansion cannot in general be increased by merely adding higher order integrals since the kernel functions are dependent upon both the order of the expansion and the range of the approximation. It is normally assumed that this situation does not arise in the special case of viscoelastic solids. This assumption is almost sufficient by itself to restrict the multiple integral expansion *a priori* to strong fading memory materials. In particular, it is assumed that the approximation can be treated as an analogy to a Taylor's series expansion of an analytic function. The smaller the strain history is, then the fewer the number of terms needed in the functional power series. Greater accuracy is then obtained by simply adding more higher order integrals, and the kernels are then independent of the number of terms in the expansion.

The validity of the assumption that greater accuracy is obtained by merely adding on more higher order integrals has not been verified because of the enormous experimental difficulties encountered.

Lockett [41] has pointed out that more than 100 independent tests are necessary to define the twelve material functions in even the third order theory. Such an extensive test program has never been undertaken for obvious reasons, and it is totally impractical to seriously consider higher order approximation theories requiring an order of magnitude more difficult test programs to evaluate the material functions. Thus, as a practical matter it is immaterial whether or not the Volterra-Fréchet integral expansion is theoretically capable of representing permanent memory or path sensitive behavior if such a representation is going to require more than three terms of the expansion.

Turning now to slightly more rigorous considerations, there is theoretical evidence which questions the ability of representing path dependent behavior by the Green-Rivlin formulation at any level of approximation. From energy considerations Herrmann [64] was able to derive constitutive relations for materials capable of experiencing instantaneous deformations but not capable of instantaneous energy dissipation which are formally identical to the Volterra-Fréchet integral expansion. Christensen and Naghdi [65], using a representation for the Helmholtz free energy functional (and hence, the stress functional) which essentially followed from the initial assumptions of Green and Rivlin [24], as relaxed by Chacon and Rivlin [66], demonstrated that sufficient conditions for satisfaction of the dissipation inequality (i.e., Clausius-Duhem inequality) are that the material be incapable of exhibiting energy

dissipation. They also noted in the isothermal case that the dissipation inequality is satisfied for all admissible processes and material functions which may be represented as a sequence of decaying exponentials and have a form corresponding to those utilized by Hunter [67] (e.g., $k(2t-\tau_1-\tau_2,)etc$). This latter case is, of course, a special type of normal fading memory behavior.

The above paragraph points out that a sufficient condition for the validity of the Volterra-Fréchet representation of the mechanical behavior of a material with memory is that the material be incapable of energy dissipation. Since this is only a sufficient condition it should be noted that there may be other physical conditions precluding a lack of energy dissipation as a sufficient condition for the Green-Rivlin formulation. However, it seems likely that these other physical conditions, such as direct assumptions regarding the form of the kernel functions (e.g., decaying exponentials), may also exclude representation of permanent memory behavior or general path sensitive phenomena.

In the authors' opinion it seems unlikely that the Volterra-Fréchet multiple integral expansion, as currently formulated and employed, can represent general permanent memory or path dependent behavior, although it is generally accepted as having this capability. This

---

[8]Christensen and Naghdi's development is supposedly for non-isothermal behavior, however the material functions depend only on a reference temperature. A non-isothermal theory in which the material functions depend upon variable temperature as a function of both time and space is outside of the scope of their development mainly as a consequence of the linearization of their theory.

statement gains support from two sources. First, the demonstrated success of the multiple integral sum appears to be mainly due to a fortuitous selection of materials and loading environments. In particular, only the isothermal situation has been considered with polymers and plastics and loading conditions in which only normal fading memory characteristics are apparent. Secondly, for more complicated materials, fading memory characteristics and loading situations the applicability of the Green-Rivlin formulation has not been substantiated. In particular, the isothermal representation has been unsuccessful in representing the behavior of aluminum in the vicinity of its idealized yield surface, and there is insufficient evidence to support the claim that greater accuracy can be obtained by merely adding more higher order integrals. General path sensitive behavior involves internal dissipation of energy and certainly a portion if not all of the energy dissipation goes into raising the temperature of the material. This behavior is evident in the high temperature creep of concrete and metals and the inelastic deformation of materials in general. It is also noted that permanent memory effects are evident in these situations. Thus, it seems unreasonable to expect the Green-Rivlin approach to be capable of representing these kinds of material behavior and loading environments. Certainly one must acknowledge that the thermodynamic approach presented here which allows for non-isothermal environments with coupling between thermal and mechanical effects and physically realistic memory behavior stands a greater chance

of success in describing the behavior of materials and processes involving dissipation of energy.

COLEMAN-NOLL THEORY

Coleman and Noll [26,34 and Coleman [68,69] introduced the physical assumption that *the memory of a simple material fades in time.* This statement of a fading memory principle corresponds to the idea of a fading memory with *normal fading memory characteristics* introduced in this research. Coleman and Noll's assumption of fading memory was given a precise mathematical meaning through the introduction of a *norm* which places greater emphasis on events that occurred in the recent past than those which occurred in the distant past. The physical meaning of their fading memory principle was then interpreted mathematically as an assumption on the continuity of the constitutive functionals with respect to convergence in this norm defining the topology of histories.

For the purposes of this discussion it suffices to consider a constitutive functional equation of the form

$$g(t) = \underset{s=0}{\overset{\infty}{G}} \{f(s)\} , \qquad (11\text{-}13)$$

where G may represent any one of the constitutive functionals, and $f(s)$ may likewise represent the history of any one of the independent constitutive variables for $0 \leq s < \infty$.

To render the mathematical idea of fading memory more precisely, Coleman and Noll introduced the *influence functions* $h(s)$ which

characterizes the rate at which the memory fades. An influence function h of order r ($r > 0$) is required to be a positive monotone-decreasing, continuous function of s which goes to zero rapidly as $s \to \infty$. If the first two conditions hold then a sufficient condition for the last condition to hold is that h(s) decays to zero in such a way that the limit relation

$$\lim_{s\to\infty} s^r h(s) = 0 \qquad (11\text{-}14)$$

monotonically for large s. For example, the function

$$h(s) = (s+1)^{-p} \qquad (11\text{-}15)$$

is an influence function of order r for $r < p$, and the exponential function

$$h(s) = \exp(-\beta s) \ , \ \beta > 0 \qquad (11\text{-}16)$$

is an influence function of arbitrary order.

The *repollection* of a particular history f(s) was first defined analogously to the L_p norms for a given influence function h and a given p;

$$||f(\cdot)||_h = \left[\int_0^\infty [|f(s)|\ h(s)]^p\ ds\right]^{1/p} \quad \text{if } 1 \le p < \infty\ ; \qquad (11\text{-}17)$$

$$||f(\cdot)||_h = \operatorname{ess\,sup}_{s\geq 0} |f(s)|h(s) \quad \text{if } p = \infty \ ; \tag{11-18}$$

where $|f(s)|$ is the magnitude of the history $f(s)$. In later works the norm was simplified to consideration of a fixed value of $p = 2$,

$$||f||_h = \left[\int_0^\infty |f(s)|^2 \, h(s)^2 \, ds\right]^{1/2} . \tag{11-19}$$

Identifying two functions as being equal when they differ only on sets of measure zero, and defining an inner product by the relation

$$\left[f_1(\cdot), f_2(\cdot)\right]_h = \left[\int_0^\infty f_1(s) f_2(s) h(s)^2 \, ds\right]^{1/2} , \tag{11-20}$$

then the space of all histories $f(\cdot)$ for which $||f(\cdot)||_h$ is finite forms a Hilbert space for each influence function of order $r > \frac{1}{2}$. With these definitions the tools of modern analysis were then applied to study various principles of fading memory.

Physically, the memory characteristics of a material, determined by (19) may be interpreted as a *weighted* root-mean-square average of the history $f(\cdot)$ where the weighting function determines the influence of past events upon the current values of the constitutive functionals.

The physical idea of fading memory is now expressed mathematically as the requirement that the material have *small recollection*. Three kinds of histories have small recollection. A history which has deviated little from the rest history throughout the entire past

has small recollection. Secondly, since the influence function assigns little weight to the part of the s-axis where s is large, a history such that $|f(\cdot)|$ is small for the recent past, though perhaps large in the distant past, has small recollection. This example corresponds to the case when the material has been nearly at rest for a long time. Finally, if $|f(\cdot)|$ is large only on a set of small measure, the recollection of f will be small. This case corresponds, for example, to a large deformation during a very brief period of time in the past. From these examples it is seen that histories having small recollection are those histories which have been close to the rest history in the recent past. Coleman and Noll made assumptions and proved theorems concerning materials nearly at rest, which corresponds to a neighborhood of the origin in the space of histories.

In order to construct a family of histories having small recollection, Coleman and Noll introduced the concept of *slow motions*. They made this idea precise through the use of the *retardation* r_α with *retardation factor* α, $0 < \alpha \leq 1$, which is the linear transformation $f \to f_\alpha$ defined for all histories f by

$$(r_\alpha f)(s) = f_\alpha(s) = f(\alpha s) . \qquad (11\text{-}21)$$

The retardation replaces a given history by one which is essentially the same but slower. Any severe deformation is removed further and further into the past, which the material does not remember well, and smooth histories near the present time are given more weight.

With the above ideas Coleman and Noll stated and proved *weak* and *strong* principles of fading memory. Their weak statement of a fading memory principle is essentially the requirement that there exist an influence function h of order $r > 1/2$ such that the constitutive functional G of (13) is Frechet-differentiable at the zero history in the Hilbert space of histories. The nth-order stronger principle of fading memory is the requirement that there exist an influence function of order $r > n + 1/2$ such that the constitutive functional be n-times Frechet differentiable. By sufficiently retarding any given motion one can justify approximating the constitutive functional of the retarded motion by a multilinear function of time derivatives of the given motion at the present time. This theorem gives the result that the nth-order *Rivlin-Ericksen* material may be interpreted as an asymptotic approximation to the theory of general simple materials obeying Coleman and Noll's strong principle of fading memory for sufficiently slow motions.

Several deficiencies may be found in a theory of materials which uses (17) and (18) or (19) to characterize the effects of memory. For one thing, the norm is weighted with a decaying obliviator so that finite and permanent memory characteristics are excluded. It is also noted that there is no unique way of choosing the influence function $h(s)$. The influence function $h(s)$ is not a material function although the existence of an $h(s)$ of the required type is a material property. Further, the arbitrary numbers p in (7) are extremely difficult, if not impossible, to determine experimentally.

WANG'S THEORIES

Wang [70,71] has proposed two fading memory theories. Wang's first theory generalizes the results of Coleman and Noll discussed immediately above. In place of the influence function utilized by Coleman and Noll, Wang formulates a principle of fading memory by means of an obliviating measure. An *obliviating measure* μ on the real time axis $[0,\infty)$ is the Lebesgue-Stieltjes measure associated with a non-decreasing lower semi-continuous real function $\sigma(s)$ with the properties:

i) $\sigma(s) = 0$ for $s \leq 0$;

ii) $\sigma(s)$ is bounded, i.e., $\lim_{s\to\infty} \sigma(s) = M < \infty$.

From condition (ii) $\mu([0,\infty)) = M$. In terms of the obliviating measure μ, the recollection of a history $f(s)$ is defined by

$$||f(\cdot)||_\mu = \left[\int_0^\infty |f(s)|^2 \, d\mu\right]^{1/2} \tag{11-22}$$

If $\sigma(s)$ is continuously differentiable, the function

$$h(s) \equiv \frac{d\sigma}{ds} \tag{11-23}$$

serves the purpose of Coleman and Noll's influence function if it

monotonically decreases when s is large. Alternatively, if $h(s)$ is an influence function as defined above and we set

$$\mu(I) = \int_I h(s)^2 \, ds \tag{11-24}$$

for all Borel sets $I \in [0,\infty)$, then μ is an obliviating measure and (22) reduces to (19). Although the greater generality of an obliviating measure includes a broader class of materials as being endowed with fading memory, Wang's theory suffers from the same deficiencies as Coleman and Noll's theory discussed previously. Permanent and finite memory characteristics are excluded and there is no unique way of determining the functions $d(s)$.

In this same work Wang [70] remarks upon the possibility of extending his formulation of a principle of fading memory to a much bigger class of deformation histories. Considering the class of all deformation histories measurable with respect to a preassigned obliviating measure, Wang introduces a *metric function* d which makes this class a Frechet space. The metric function d, associated with a preassigned obliviating measure, defined by

$$d(D,E) = \int_0^\infty \frac{|D(s)-E(s)|}{1+|D(s)-E(s)|} \, d\mu \; , \tag{11-25}$$

where D and E are two histories, can be shown to give the desired topology on the space of all measurable histories. Namely, a sequence of histories $D_n(s)$ converges in measure to $E(s)$ as

$n \to \infty$ if and only if $d(D_n, E) \to 0$ as $n \to \infty$.

Wang's [71] second theory is based upon the topology of uniform convergence on compact sets rather than the Hilbert-space topology of Coleman and Noll discussed previously. Most of conclusions of the approximation theorems proved by Coleman and Noll [26] remain unchanged; however, the definition of fading memory is different. Wang's formulation is motivated by the desire to satisfy the stress relaxation theorem trivially and to include finite memory as a special case of fading memory.

Before discussing Wang's results for weak and strong fading memory some introductory notions will first be given. Consider the mechanical constitutive relation for a simple material of the form

$$T(t) = \overset{\infty}{\underset{s=0}{T}} \{C(t-s)\} , \qquad (11.26)$$

where $C(t-s)$ is the history of the right Cauchy-Green tensor. The *order* of a simple material is defined to be the smallest integer p $(0 \leq p \leq \infty)$ such that $\mathcal{T}$ does not depend explicitly on $C^{(\gamma)}(\tau)$ if $\gamma > p$. The *domain* of the constitutive functional, denoted by $\mathcal{D}(T)$ is defined to be the class of all C^p positive-definite symmetric tensor-valued functions $C(\tau)$ where $\tau \leq t$ and p is the order of the material. Let T be of the order p, and let $C_n(\tau)$, $n = 1,2,\cdots$, $C(\tau)$ be in $\mathcal{D}(T)$. Then C_n is said to *converge* to $C(\tau)$ if $C_n^{(\gamma)}(\tau) \to C^{(\gamma)}(\tau)$ *uniformly on every finite interval* on $(-\infty,t]$ for all $\gamma \leq p$. Finally a *continuous constitutive functional* T is defined

to be a functional everywhere continuous with respect to the topology on $\mathcal{D}(T)$.

With the above definitions, a simple material is said to obey the *weak principal of fading memory* if its constitutive functional is continuous at every rest history (i.e., $C(t-s) \equiv C(t)$ for all $s \geq 0$) with respect to the topology defined on $\mathcal{D}(T)$. The α-retardation is defined and used in an analogous manner to that of Coleman and Noll discussed above. Wang observes that any linear constitutive functional that has a *linear* dependence on the deformation history near $t = -\infty$, such as the linearly viscoelastic material, cannot satisfy his weak principle of fading memory.

The above definition implies that a simple material obeying the weak principle of fading memory must have two material memory parameters: *the time of sentience* η_0 and *the grade of sentience* δ_0. Briefly the idea behind the time of sentience of a material (for a certain fixed rest history C) is that if a material obeys Wang's principle of fading memory, then for every $\varepsilon > 0$, there exist numbers $\delta > 0$ and $\eta > 0$ such that if $|D^{(\gamma)}(\tau) - C^{(\gamma)}| \leq \delta$ for all $0 \leq \gamma \leq p$ when $\tau \in [t-\eta, t]$, then $|T(\mathcal{D}(\tau) - T(C)| \leq \varepsilon$. Hence if the deviation of $D(\tau)$ from the rest history C is sufficiently small for a sufficiently long period of time, then no matter what happened before the time $t-\eta$ the present stress cannot differ arbitrarily from the static stress. That is, the present stress remains bounded for all possible deformations that occurred before $t - \eta$. If it happens that η is not large enough, then no matter how small the deviation δ is, for

$\tau \in [t-\eta, t]$, the collection of all possible present stresses is unbounded. The least upper bound for all such η's is then defined to be the time of sentience η_0. Thus, η_0 is the number such that if $\eta > \eta_0$, then it is possible to render the collection $\{T(D(\tau))\,|\ |D^{(\gamma)}(\tau) - C^{(\gamma)}| \leq \delta$, for all $0 \leq \gamma \leq$ when $\tau \in [t-\eta, t]\}$ bounded by letting δ be sufficiently small. Roughly speaking, the time of sentience divides the total memory of the material into two parts: the time interval $[t-\eta_0, t]$ may be regarded as the *major memory*, while the interval $(-\infty, t-\eta_0]$ is the *minor memory*. A *finite major memory* means that the present stress can be made to lie in a certain compact set in the tensor space by letting the deviation of the deformation history from the rest history be sufficiently small for a sufficiently long period of time. A simple material thus obeys Wang's weak principle of fading memory if it has finite major memory. It is observed that the idea of a finite memory characteristic introduced in this research generalizes Wang's concept of a finite major memory.

The grade of sentience δ_0 is the largest possible value such that if $\delta < \delta_0$ then it is possible to render the collection of all possible present stresses bounded if $|D^{(\gamma)}(\tau) - C^{(\gamma)}| < \delta$ for all $0 \leq \gamma \leq p$ for a sufficiently long period of time. Roughly speaking, the grade of sentience divides the total deviation of the deformation history from the rest history into two parts. The deviation less than δ_0 is regarded as the *minor* deviation, while the deviation greater than δ_0 is the *major* deviation. A positive grade of sentience corresponds to the fact that the present stress can be made

to lie in a compact set by letting the major deviation vanish for a sufficiently long period of time.

The time of sentience n_0 and the grade of sentience δ_0 can be used as parameters in comparing the memory effects of various simple materials with the same fixed present configuration.

Wang's *strong principle of fading memory* of order n for a simple material is that its constitutive function be n-times continuously Fréchet differentiable.

As mentioned above, Wang defines and uses the α-retardation of a deformation history, in the same sense as Coleman and Noll, to obtain a strong approximation theorem which is equivalent to a Taylor's series expansion of the retardations of a simple material about the zero time of sentience. In an analogous manner, Wang introduces β-relaxations and obtains a Taylor's series expansion of the relaxations of a simple material as the grade of sentience $\delta_0 \to \infty$.

Certain special cases of simple materials excluded in Coleman and Noll's theory obey Wang's weak principle of fading memory; namely, elastic materials, Newtonian fluids and the general Rivlin-Erickson materials. These materials all have time of sentience zero, provided these response functions are continuous and grade of sentience equal to $+\infty$, corresponding to the fact that a continuous function is bounded if its arguments lie in a compact set.

It is noted that even though the elastic materials, linearly viscous fluids and materials of the differential type do not satisfy Coleman and Noll's weak principle of fading memory, but do satisfy

Wang's weak principle of fading memory, Wang's second theory is not a generalization of Coleman and Noll's since the topologies and domains of the response functionals are different for the two theories. Truesdell and Noll [25] point out that even if the domains of the response functionals are restricted such that the concepts of continuity have meaning for both theories there are still materials having fading memory in the sense of Coleman and Noll's theory, but not Wang's second theory and, conversely, there are materials having fading memory in the sense of Wang's theory but not in the sense of Coleman and Noll. This fact represents one serious disadvantage of Wang's second theory. It is clear that a desirable property of new fading memory theories is that they generalize and contain as special cases previous fading memory theories if at all possible. Another deficiency of Wang's second theory, which is common to all existing fading memory theories, is that permanent memory behavior resulting from inelastic deformations is disallowed.

WANG-BOWEN THEORY

Wang and Bowen [72] have supposedly constructed a theory of nonlinear materials with memory more general than that of Coleman [68] which contains Coleman's theory, but not that of Wang. They consider a class of nonlinear materials called *materials with quasi-elastic response*, or more briefly, *quasi-elastic materials*.

Wang and Bowen claim motivation for their development from two major difficulties of Coleman and Noll's theories which turn out to be invalid criticisms. Their first criticism is that to determine

the history of a material particle the local configuration of that particle must be traced back to past infinity (i.e., $s \to \infty$). This is a valid criticism if a theory considers the entire past history of a material (i.e., perfect memory), but in view of Coleman and Noll's fading memory hypotheses this criticism loses most of its validity. Secondly, Wang and Bowen claim that to get a better mathematical model for a nonlinear material with memory, more and more state variables are required to represent the local configuration. This criticism does not apply to a continuum theory. The state variables associated with the internal state variable approach to thermodynamic theories become functions in the continuum approach, and as the previous axiomatic development of Hufferd [31] shows the only functions required are the histories of the deformation, temperature and temperature gradient.

Wang and Bowen base their development on two ideas. First they consider that for any material particle there exists but one fixed 1-parameter family of histories, since whatever has happened in the local configuration of that particle in the past remains fixed in the histories of all future instants. The time parameter t is used as a representation for the past history and the constitutive functionals are replaced by functions. Secondly, it is claimed that a change of the history for a fixed material particle corresponds to a change of the parameter t since the history is a member of a 1-parameter family. Specifically, constitutive equations of the form

$$\phi = f(F,\theta,g,t) \qquad (11\text{-}27)$$

are considered where f is the *instantaneous response function* of the quasi-elastic material and F, θ, g, t denote respectively, the deformation gradient, the temperature, the temperature gradient and the time. It is assumed that the function is continuously differentiable in all four arguments.

Several questions arise about the validity of Wang and Bowen's approach. One can accept the argument that the history of a particle at the current values of F, θ, g and t has already happened. However, it is not at all clear that a different history and even different materials arriving at the same values of the arguments F, θ, g and t will have different response functions. In other words, Wang and Bowen's theory presupposes a knowledge of the response of every material for every deformation-temperature history in order to determine the form of the response function f for a particular material and a particular history. Another point of concern is that Wang and Bowen's application of the requirements of frame-indifference involves only coordinate transformations at the current time t and does not consider time-dependent changes of the reference frame. This result might be interpreted as an indication of the applicability of their results to aging materials, but the applicability to other materials is questioned. Wang and Bowen's theory also excludes the general Rivlin-Ericksen materials since the stress is determined by a number of the time derivatives of F.

The major cricism and deficiency associated with Wang and Bowen's development concerns their resulting thermodynamic constitutive theory. Their theory does not include the concept of equilibrium, and hence consideration of equilibrium thermodynamic processes is outside of the scope of their developments. Clearly a desirable trait of any non-equilibrium thermodynamic theory is that the equilibrium theory be included as a special case.

COLEMAN-MIZEL THEORIES

The last treatment of fading memory theories to be discussed are the recent developments by Coleman and Mizel [27,28]. This discussion will be particularly brief since Coleman and Mizel's [28] latest treatment generalizes their earlier developments and also provides a starting point for the development of the memory influence measure introduced in this research.

Coleman and Mizel [27] first introduced a memory influence measure μ which was absolutely continuous with respect to Lebesgue measure over $(0, \infty)$. Denoting a function in their class of histories by α, and skipping over the details to be discussed later, the memory norm is written

$$||\alpha||^p = |\alpha(0)|^p \mu_0 + \int_0^\infty |\alpha_r(s)|^p k(s) ds \qquad (11\text{-}28)$$

where α_r is the restriction of α to the open interval $(0,\infty)$, $\mu_0 \equiv \mu(\{0\}) > 0$ and k is the *influence function* associated with the influence measure μ, which is actually the Radon-Nikodym

derivative of μ; i.e.,

$$\int_{(a,b)} d\nu \equiv \mu((a,b)) = \int_a^b k(s)ds \qquad (11\text{-}29)$$

for every interval $(a,b) \subset (0,\infty)$. The function k also satisfies the conditions

$$k(s) \geq 0 \quad , \quad \int_0^\infty k(s)\, ds < \infty \qquad (11\text{-}30)$$

and as $s \to \infty$ decays to zero essentially as $o(1/s)$. Thus the influence measure possesses the normal fading memory property. The equation (28) implies that the weight given to the present value $\alpha(0)$ is not negligible when compared to that assigned to the entire past history, but the weight given to any particular past value is. In other words, the present value $\alpha(0)$ of a history α has approximately the same importance to α as its entire past history α_r. The norm given by (28) has been discussed further by Coleman and Mizel [29] in relation to a thermodynamic theory of materials.

Coleman and Mizel's [28] most recent contribution is based on a more general influence measure ν and the norm on the histories is written in the general form

$$||\alpha|| = |\alpha(0)| + \nu(|\alpha_r|) \qquad (11\text{-}31)$$

This result will be observed to be a special case of the developments

here. In this situation Coleman and Mizel admitted only the normal fading memory characteristic however, and did not explicity consider the form of the function $v(|\alpha_r|)$. It is clear that (31) is a generalization of (28)

11.6.3 DEVELOPMENT OF A MEMORY FUNCTION NORM

Mathematically, the statement of the *physical principle of fading* given in §11.6, and the fading memory characteristics of a material in general are interpreted as certain smoothness or continuity requirements on the constitutive functionals with respect to the topology defining the recollection of the material. One of the main criticisms of previous fading memory theories, as illustrated in the above summaries of previous work, is that only those topologies have been considered which give rise to strong fading memory characteristics and occasionally finite memory. In this study a more general memory influence measure than that employed by previous workers is introduced which allows for more physically meaningful memory behavior for a wider class of fading memory materials. The development of this memory function norm is motivated by the mathematical studies of Luxemburg and Zaanen [73,74] on normed Köthe spaces, and generalizes and extends the recent work of Coleman and Mizel [27,28]. The development presented here does not seek maximum generality, but rather anticipates future requirements of subsequent sections.

FADING MEMORY HYPOTHESES

For the purposes of the discussion on memory given here, it suffices to consider a constitutive functional equation of the form

$$g(t) = \overset{\infty}{\underset{s=0}{G}}(f^t) ,$$

where G may represent any one of the material response functionals, and

$$f^t(s) = f(t-s) , \quad 0 \leq s < \infty$$

may likewise represent the history of any of the independent constitutive variables.

Like the axiomatic development of thermomechanical constitutive theory presented in [3] the development of a memory influence measure is also guided by past physical experience. One common attribute of the different memory characteristics is the physical requirement that it should be possible to discuss equilibrium: that is, completely static processes. It is also required that under a static continuation of a given fixed thermomechanical history the values of the response functionals should tend to their equilibrium values as $t \to \infty$, and these equilibrium values should be functions of only equilibrium variables. Furthermore, inasmuch as the function space of admissible histories introduced subsequently may contain histories which assume the value $+\infty$ at some points, it is also required that the memory norm of a given history be finite in the

neighborhood of some time if the norm itself is finite at that particular time. Translating these requirements into slightly more precise statements, the norm $||\cdot||$ assigned to the space of admissible histories f^t is subject to three physical requirements:

1) The *static continuation of the history* f^t *by an amount* σ is the history $f^{t+\sigma}$ of f up to time $t+\sigma$, for $\sigma \geq 0$, in a process for which f has the history f^t up to time t and is then held constant in the interval $[t, t+\sigma]$. We require that *if the norm of* f^t *is finite, then the norm of each static continuation of* f^t *must also be finite,* and moreover, *if the distance between two distinct histories* $||f_1^t - f_2^t||$ is zero, then the distance between their static continuations by any given amount must also be zero.

2) The *σ-section* $f^{t-\sigma}$ of f^t is the history of f up to the earlier time $t-\sigma$, $\sigma \geq 0$, for a process in which f^t is the history of f up to time t. We require that *if* f^t *has finite norm,* then the norm of each σ-section of f^t must also be finite.

3) The equilibrium states must have finite norm; that is, if $f^t(s) \equiv a$, a constant, then it is required that $||f^t|| < \infty$.

These requirements impose restrictions on the space of admissible histories L^+. Namely, if $f^t \in L^+$ then L^+ should contain all static continuations and all σ-sections of f^t. Further, the space L^+ should contain the constant functions and the distance between two distinct constant functions should be nonzero.

DEVELOPMENT OF A MEMORY FUNCTION NORM

We let μ be a non-trivial Σ-finite, positive, regular Borel measure on $[0,\infty)$ and L^+ denote the set of all non-negative functions $f(s)$ on $[0,\infty)$. The notation $\int du$ denotes integration, with respect to μ, over the whole set $[0,\infty)$, and $\chi_E = \chi_E(s)$ stands for the characteristic function of the set $E \subset [0,\infty)$. A function $f \in L^+$ will be allowed to assume a value of $+\infty$ at some (discrete) points $s \in [0,\infty)$, but not at all points. The mapping ρ of L^+ into $[0,\infty)$ is called a *non-trivial function norm* whenever

(i) $0 \leq \rho(f) \leq \infty$ for all $f \in L^+$, and $\rho(f) = 0$ if and only if $f(s) = 0$, μ - *a.e.*[10]

(ii) $\rho(f_1 + f_2) \leq \rho(f_1) + \rho(f_2)$ for all $f_1, f_2 \in L^+$; and $\rho(af) = a\,\rho(f)$ for all $f \in L^+$ and all constants $a \geq 0$.

(iii) $\rho(f_1) \leq \rho(f_2)$ for all $f_1, f_2 \in L^+$ such that $f_1 \overset{\circ}{\leq} f_2$.[9]

---

[9] The notation μ - *a.e.*, or simply *a.e.* or a superposed $^\circ$ (e.g., $f(s) \overset{\circ}{=} 0$) is used to indicate that a given relation holds pointwise *almost everywhere*; that is, for all $s \in [0,\infty)$ except for a set E with $\mu(E) = 0$.

(iv) There exists at least one $f \in L^+$ such that $0 \leq \rho(f) < \infty$.

Properties (i) - (iii) are standard defining characteristics of a norm. Property (iv) assures the non-triviality of the function norm ρ. This property is introduced to exclude the trivial case that $\rho(f) = \infty$ for every $f \in L^+$ which is not almost everywhere equal to zero. As a consequence, $\mu([0,\infty)) > 0$. The function norm ρ is said to have the *sequential Fatou property* when the following property holds:

(v) if $f_0, f_1, f_2, \cdots \in L^+$ and if $f_n \uparrow f_0$ pointwise μ - *a.e.*, then $\rho(f_n) \uparrow \rho(f_0)$

If all five of these properties hold, then ρ is called a *non-trivial function norm, relative to* μ, *with the sequential Fatou property.* For the most part, this discussion will consider only functions satisfying properties (i) - (v) enumerated above.

The set of all $f \in L^+$ satisfying $\rho(f) < \infty$ is denoted by $L_\rho = L_\rho([0,\infty),\mu)$. If ρ is a function norm and μ-almost equal functions are identified in the usual way, L_ρ is a normed linear space with respect to the norm

$$||f||_\rho = \rho(f) . \qquad (11\text{-}34)$$

Spaces of this type are sometimes call *normed Kothe spaces.* Since ρ has been required to possess the Fatou property L_ρ is norm complete, and is actually a *Banach function space.*

It is evident that the L_ρ-spaces are a generalization of the more familiar L_p-spaces ($1 \leq p \leq \infty$), where

$$\rho_p(f) = \left[\int |f|^p d\mu\right]^{1/p} , \quad 1 \leq p < \infty ; \qquad (11\text{-}35)$$

and

$$\rho_\infty(f) = ess\ sup\ |f|, \quad p = \infty , \qquad (11\text{-}36)$$

A theory of fading memory which is based upon more general Banach function spaces than the L_p-spaces has several advantages which become apparent from a review of the previous discussion in §11.6.2 of L_p-norms of the form

$$||f||^p = \int_{[0,\infty)} |f|^p \, d\mu , \quad 1 \leq p < \infty , \qquad (11\text{-}37)$$

with μ a positive, regular Borel measure on $[0,\infty)$. The obvious observation is the greater generality available than in the L_p-spaces. More importantly, however, the arbitrary numbers p, are eliminated, and the importance of the experimentally non-determinable influence function k, used extensively by Coleman and Mizel, is de-emphasized.

Luxemburg and Zaanen [74] point out that the hypotheses do not exclude the existence of a measurable subset $B \subset [0,\infty)$ of positive measure such that not only $\rho(\chi_B) = \infty$ for the characteristic function χ_B of B, but even $\rho(\chi_C) = \infty$ for every $C \subset B$ of any set of positive

measure. They call any set having this property a *ρ-purely infinite set* or an *unfriendly set*. If B is an unfriendly set, then any $f \in L_\rho$ vanishes on B. In this investigation these sets will not be admitted. It can be shown [74] that there is a largest unfriendly set B_{max}, determined modulo null sets, which may be removed from consideration with the measure of the remaining set still positive since ρ is non-trivial. A function norm ρ such that there exists no ρ-purely infinitely subsets is called *saturated*. All of the function norms introduced and discussed here, including those discussed previously in §II.6.2 are saturated norms. Physically, this situation means that the history $f^t(s)$ is not allowed to become unbounded (i.e., infinite) over a *finite* interval (distance) of the non-negative real (time) axis $[0,\infty)$. The history $f^t(s)$ is allowed, however, to exhibit jump discontinuities, characterized by step function loading situations, at discrete isolated points $s \in [0,\infty)$. The history $f^t(s)$ is also allowed to assume infinite values on sets of measure zero (i.e., isolated points), characterized by Dirac delta function inputs, although the ρ-norm for such a loading situation will remain finite.

One of the methods to construct new function norms from known ones is based on the fact that the collection of all function norms, with the set (in our case $[0,\infty)$) and the measure μ fixed is partially ordered with respect to the natural ordering:

$$\rho_1 \leq \rho_2 \text{ whenever } \rho_1(f) \leq \rho_2(f) \text{ for all } f \in L^+.$$

Given the arbitrary collection of non-trivial function norms ρ_τ, satisfying (i) - (v), such that $\rho_\tau \leq \rho_0$ for a fixed nontrivial ρ_0 and all τ, then

$$\rho(f) = \sup_\tau \rho_\tau(f) \quad . \tag{11-38}$$

is also non-trivial and satisfies (i) - (v). This result continues to hold if all the ρ_τ are semi-norms instead of norms, provided the collection $\{\rho_\tau\}$ is total in the sense that $f = 0$ whenever $\rho_\tau(f) = 0$ for all τ simultaneously.

Further properties and more detailed mathematical analyses on the L_ρ-spaces, and general Banach spaces, are contained in the penetrating studies of Luxemburg and Zaanen [73,74].

Since the L_ρ-spaces generalize the L_p-spaces it is clear that the function norm $\rho(f)$ includes the memory norms of Coleman and Noll and Wang's results for an obliviating measure. The close connection between $\rho(f)$ and the memory semi-norms (28) and (31) of Coleman and Mizel is also evident. Thus, the previous fading memory theories discussed in 11.6.2 which involved the use norms or semi-norms to measure the memory characteristics of a material may be regarded as memory function norms for materials exhibiting normal fading memory characteristics. Memory function norms (semi-norms) may also be written for materials exhibiting other memory characteristics. For example, the function norm

$$\rho(f) = |f(0)| \tag{11-39}$$

may be used to indicate that the memory of the material is determined by the present value of the history implying failing memory characteristics. Permanent memory characteristics may be characterized by

$$\rho(f) = \operatorname*{ess\,sup}_{s\in[0,\infty)} |f(s)| \quad . \tag{11-40}$$

In order to introduce the types of memory characteristics discussed in §11.6.1, the function norm will be written in the form

$$\rho(f) = \rho_0(f) + \rho_r(f) \quad , \tag{11-41}$$

where the subscript o refers to a value of $s = 0$ and the subscript r denotes the restriction to the open interval $(0,\infty)$. In particular, the memory function norm

$$\rho(f) = |f(0)| + \operatorname*{ess\,sup}_{s\in(0,\infty)} |f(s)|\, k(s) \tag{11-42}$$

will be employed. The first term $|f(0)|$ introduces the influence of the present value of the history, and the second term introduces

---

[10] Like Coleman and Mizel's [27,28] developments there is an atom in measure at the current time in this decomposition.

[11] The motivation for consideration of a memory norm in this form stems from the earlier work of Coleman and Noll [26] and Coleman and Mizel [27-29].

memory characteristics. The function k is a preassigned positive function which is bounded and measurable on $(0,\infty)$. It can be shown through an extension of an argument given by Coleman and Mizel [28] that if k is essentially monotone decreasing on $(0,\infty)$, then this last term gives rise to normal fading memory characteristics. This proof will not be given here since it is quite complicated and very lengthy. In physical theories it quite often turns out that fading memory is characterized by decaying exponentials. Thus, the function k may be assumed to be of the form

$$k(s) = \exp(-\beta s) \ , \ \beta > 0 \qquad (11\text{-}43)$$

to exhibit normal fading memory behavior. Permanent memory behavior is obtained when $k(s) = 1$ for all s, and elastic response may result when k(s) is chosen sufficiently small.

A further discussion of the memory semi-norm (42) with respect to the thermodynamic developments of this research is presented in the following sections.

11.7 FURTHER DEVELOPMENT OF A THERMODYNAMIC CONSTITUTIVE THEORY

In this section some of the pertinent results of the previous sections are summarized, and a more compact notation is introduced to simplify subsequent formalism. Admissible thermomechanical and thermodynamic processes are defined precisely and the Clausius-Duhem inequality is used to obtain an admissible thermodynamic constitutive theory for thermomechanical materials obeying the fading memory principle proposed in the previous section. Although certain portions of this development parallel those of previous workers, it will be observed that distinct and substantial differences exist between our results and those of earlier workers. In particular, it will be noticed that in most cases the constitutive theory developed here generalizes and combines various aspects of Coleman's [68,69,29] thermodynamics into a single unified theory which allows for more general, and more meaningful, physical behavior which has heretofore been excluded in continuum thermodynamic theories proposed for materials with memory.

11.7.1 THERMODYNAMIC PRELIMINARIES

This research is concerned with simple material bodies which are subjected to thermomechanical processes only. That is, a nonpolar body B (body couples and couple stresses are assumed absent) is considered which is subjected to only combined thermal and mechanical loading situations. The specific free energy ψ, the specific

entropy η, the symmetric stress tensor T and the heat flux vector q have been introduced as the dependent mechanical and thermal constitutive variables. The deformation gradient F (equivalently the right Cauchy-Green tensor C) and the absolute temperature θ are treated as the independent variables.

The mechanical forces acting on a simple material body $\mathcal{B}$ are always resolvable into a body force field and a field of symmetric stresses. The mass density ρ has been assumed to be continuous at all points of $\mathcal{B}$ for all times t, and it has been further assumed that there is no mass diffusion in $\mathcal{B}$, however the body is allowed to deform and conduct heat. A material point in $\mathcal{B}$ is denoted by X and is identified with its position vector X relative to a fixed local reference configuration κ_C.[12] The spatial position of the material point X at time t is described by the motion, or deformation, of the particle at X with respect to the reference configuration κ_C,[12]

$$x = \chi(X,t) \tag{11-44}$$

A thermomechanical process in $\mathcal{B}$ is characterized by eight functions of X and t:

[12] We use the notation X for both the material particle X and its position vector relative to the reference configuration κ_C. It is supposed that the context will prevent any undue confusion.

1) The *spatial position* in $\mathcal{B}$, $x = \chi(X,t)$.

2) The *absolute temperature*, $\theta = \theta(X,t)$, (assumed positive; $\theta > 0$).

3) The *symmetric Cauchy stress tensor*, $T = T(X,t)$.

4) The *specific energy* per unit mass, $\varepsilon = \varepsilon(X,t)$.

5) The *specific entropy* per unit mass, $\eta = \eta(X,t)$.

6) The *heat flux vector*, $q = q(X,t)$.

7) The *specific body force*, $b = b(X,t)$, (exerted on $\mathcal{B}$ by bodies not in contact with $\mathcal{B}$).

8) The *heat supply* per unit mass and time, $r = r(X,t)$, (absorbed by $\mathcal{B}$ at X through radiation from the external world).

Under the assumption of no mass diffusion, the above set of eight functions constitutes a *local thermomechanical process* for a nonpolar body $\mathcal{B}$ if and only if the local forms of the laws of balance of energy are satisfied at all material points X in $\mathcal{B}$.[13] Actually only the first six functions above need to be specified to determine the process. Once χ, θ, T, ε, η and q have been specified for

[13] The laws of conservation of mass and balance of moment of momentum are trivially satisfied for the bodies and motions considered here. In particular, conservation of mass yields $(\rho/\rho_0)^{-1} = \det F$ and the balance of moment of momentum requires that $T = T^T$.

all X and t then the body force vector b and the scalar heat supply are uniquely determined by the requirement that the process satisfy the laws of balance of momentum and balance of energy.

Under suitable smoothness assumptions in a sufficiently small neighborhood about the interior point X, the local law of balance of linear momentum has the form[14]

$$div\ T + \rho b = \rho \ddot{x}, \tag{11-45}$$

and the local law of balance of energy is written

$$\rho \dot{\varepsilon} = T \cdot L - div\ q + \rho r\ . \tag{11-46}$$

The *deformation gradient* at X relative to the reference configuration κ_0 has been previously defined as the gradient of the deformation function $\chi(X,t)$,

$$F = F(X,t) \equiv \nabla \chi(X,t)\ . \tag{11-47}$$

The motion $\chi(X,t)$ has been assumed to be a smooth homeomorphism so that F is always continuously invertible in B. This means that the

[14] In the event surfaces of discontinuity exist across which certain quantities may exhibit jump discontinuities (45) and (46) are replaced by the appropriate jump equations at these surfaces.

jacobian of χ with respect to X is non zero in B, and the inverse F^{-1} of F exists and is continuous in the interior of B. Thus, as mentioned previously, the mass density ρ in the current configuration at time t is related to the mass density κ_0 in the reference configuration ρ_0 through the relation

$$(\rho/\rho_0)^{-1} = det\ F\ , \tag{11-48}$$

where the reference configuration mass density ρ_0 is constant in time. Since the inverse F^{-1} of F exists, (47) may be used to write the *velocity gradient* L in the form

$$L = \dot{F}\ F^{-1}\ . \tag{11-49}$$

The *right Cauchy-Green strain tensor* C is defined in terms of the deformation gradient by

$$C = F^T F\ . \tag{11-50}$$

Consider the specific internal entropy, η, as composed of a part η_e representing the result of entropy flux to the material particle, X, and of a part η_i representing the result of internal entropy evolution at the material particle X, so $\eta = \eta_e + \eta_i$.

The statement of Duhem [75], and others, that

$$dS = \frac{dQ}{\theta} + dN \tag{11-51}$$

with $$dN \geq 0 \tag{11-52}$$

was intended to be applicable to the difference between two equilibrium states, A and B, with the identifications

- dS, the total change in entropy S of a macroscopic body at temperature θ ,
- dQ, the total net heat change in the body and
- dN, the "transformation noncompensée" or evolution of entropy occasioned by internal irreversible processes within the body.

Assuming that natural processes require a finite time for their completion, t_A is defined to be the time at which the process being investigated begins, and t_B is the time at which the final equilibrium state, B, is reached. Then (51) and (52) may be written

$$\int_{\tau=t_A}^{t_B} \dot{S} d\tau = \int_{\tau=t_A}^{t_B} \dot{(Q/\theta)}\, d\tau + \int_{\tau=t_A}^{t_B} \dot{N} d\tau \tag{11-53}$$

and

$$\int_{\tau=t_A}^{t_B} \dot{N} d\tau \geq 0 \tag{11-54}$$

It is understood in (53) and (54) that t_A is independent, that is, the process may be started at any given time, and hence the above definitions are objective with respect to time. Furthermore, when the initial equilibrium state, A, is the initial rest-state, the lower limit of integration may be

set equal to $t_A = 0$ or $t_A = -\infty$ without loss of generality. However, the upper limit of integration, or more specifically, the interval of integration is not necessarily an independent variable. That is, a finite time is required for the body to respond to a stimulus and $[t_B - t_A]$ is a dependent interval. This dependent delay occurs, for example, when finite conductivity and finite specific heat require a finite interval for thermal equilibrium to be reached. Similarly, mechanical and chemical relaxation processes require finite intervals of time for equilibrium to occur after an initial disturbance.

Equations (53) and (54) are global, applying to the entire body. For use in continuum mechanics, it is desirable to express the above equations in local form. Thus, analogously to (53), we define

$$\dot{n}_e = \frac{r}{\theta} - \frac{1}{\rho} \operatorname{div}\left(\frac{q}{\theta}\right) \tag{11-55}$$

Carrying out the divergence operation results in

$$\dot{n}_e = \frac{r}{\theta} - \frac{\operatorname{div} q}{\rho\theta} + \frac{q \cdot g}{c\theta} \tag{11-56}$$

where $g \equiv \operatorname{grad} \theta$, the spatial temperature gradient.

The Duhem relations now become, defining $\dot{n}_i$ as the specific rate of internal entropy evolution analogously to $\dot{N}$,

$$\int \rho \dot{n}\, d\tau = \int \rho \dot{n}_e\, d\tau + \int \rho \dot{n}_i\, d\tau$$

$$= \int \frac{\rho r}{\theta} d\tau - \int \theta^{-1} \operatorname{div} q\, d\tau + \int \frac{q \cdot g}{\theta^2} d\tau$$

$$+ \int \rho \dot{n}_i\, d\tau \tag{11-57}$$

with all integrals evaluated over the interval $[t_A, t_B]$.

Similarly, relation (54) becomes

$$\int_{\tau=t_A}^{t_B} \rho \dot{\eta}_i \, d\tau \geq 0 \qquad \text{(II-58)}$$

The above relation will be termed the weak postulate of entropy evolution. The relation (58) permits the specific rate of internal entropy to assume negative values so long as the integral per se is non-negative over all allowable time intervals.[15]

POSTULATE 1 (Weak Principle of Entropy Evolution).

The local change in internal entropy between any two equilibrium states shall be non-negative, that is

$$\int_{\tau=t_A}^{t_B} \rho \dot{\eta}_i \, d\tau \geq 0 \qquad \text{(II-58)}$$

The above may readily be written so as to include state discontinuities with respect to time wherein

$$[\eta_i] \geq 0 \qquad \text{(II-59)}$$

implies that the internal entropy discontinuity is also non-negative.

Recent publications in continuum mechanics have put forth the so-called Clausius-Duhem (C-D) inequality as a postulate in thermomechanics. As generally published, the C-D inequality is not the same as (58), which is directly derivable from the works of Duhem and other classical thermodynamicists.

[15] If (58) is formulated in global form, the implication results that the internal entropy change may be negative for portions of the body, but not for the entire body. However, the relation must hold for any portion of the body, and thus the local form holds.

The C-D inequality as generally published is identical to the following strong entropy evolution postulate [76][16]

POSTULATE 2 (Strong Principle of Entropy Evolution)

The local rate of change of specific internal entropy shall be non-negative, that is

$$\dot{\eta}_i \geq 0 \qquad (11\text{-}60)$$

It is obvious that the strong principle (60) implies the weak principle (58), but that the weak principle does not imply the strong for dependent time of reaction intervals, $[t_B - t_A]$.

It will be noticed that the term adiabatic has not been used in defining the two alternate forms of the second law of thermodynamics, (58) and (60). The reason is that whereas adiabatic has useful meaning for global bodies, the equivalent to adiabatic for a local formulation would be

- $\frac{r}{\theta} = 0$, no energy supply from external sources
- $\operatorname{div}\left(\frac{q}{\theta}\right) = 0$, no conductive heat flux.

The above, on a local level, imply no energy transfer by heat at a material point X which will later be seen to imply a material with

- opaqueness to radiation and
- zero thermal conductivity.

It should be noted that all phenomenological relations in classical (linearized) thermodynamics obey both the strong and the weak postulates of

[16]The C-D inequality, for example in Coleman's work [68], uses $\gamma \geq 0$ which, on comparison with the later relations developed herein, is seen to be identical to (60).

entropy evolution. In addition, all published phenomenological relations in the thermodynamics of irreversible processes (T.I.P.) also obey both postulates. However, the basic inequality used by Prigogine [77], or especially the fundamental inequality used by Meixner [78], are actually weak postulates that anticipate the possibility in far from equilibrium processes that η_i may be negative for certain times.

Both Clausius in his 1865 work in which he stated

$$dS \geq \frac{dQ}{\theta} \tag{11-61}$$

and Duhem in 1888 where he stated

$$dS = \frac{dQ}{\theta} + dN \tag{11-62}$$

$$dN \geq 0$$

could be said to have anticipated our strong principle of entropy evolution. However, it was Coleman [66], who first precisely set it down as a postulate in continuum mechanics.

Before concluding this section, we set down a lemma to Postulate 2

LEMMA 1 (Strong Principle of Entropy Evolution)

The internal specific entropy η_i is a weakly monotonically increasing function of time.

The proof is straightforward from (60) :

Now, with appropriate smoothness assumptions, the decomposition

$$\eta = \eta_e + \eta_i \tag{11-63}$$

leads to the rate equation

$$\dot{\eta} = \dot{\eta}_e + \dot{\eta}_i \tag{11-64}$$

$$\dot{\eta}_i = \dot{\eta} - \dot{\eta}_e \tag{11-65}$$

which, with (56), yields

$$\eta_i = \dot{\eta} - (r/\theta) + (\rho\theta)^{-1} \operatorname{div} q - (\rho\theta)^{-1} q \cdot g \qquad (11\text{-}66)$$

Introducing the *first Piola-Kirchhoff stress tensor* S, defined by

$$S = (\rho/\rho_0)^{-1} T(F^T)^{-1} \qquad (11\text{-}67)$$

the local balance law (46) may be written in the alternate form

$$\rho\dot{\varepsilon} = (\rho/\rho_0)\, S \cdot \dot{F} - \operatorname{div} q + \rho r . \qquad (11\text{-}68)$$

Inserting (68) into (66) the strong form

$$\theta\dot{\eta}_i = \theta\dot{\eta} - \dot{\varepsilon} + \rho_0^{-1} S \cdot \dot{F} - (\rho\theta)^{-1} q \cdot g \geq 0 \qquad (11\text{-}69)$$

of the local rate of entropy production is obtained.

The *specific free energy* ψ (Helmholtz free energy per unit mass) is defined by

$$\psi = \varepsilon - \theta\eta . \qquad (11\text{-}70)$$

Noting that $\dot{\psi} = \dot{\varepsilon} - \dot{\theta}\eta - \theta\dot{\eta}$, (69) may be written in still another form;

$$\theta\eta_i = -(\dot{\psi} + \dot{\theta}\eta) + \rho_0^{-1} S \cdot \dot{F} - (\rho\theta)^{-1} q \cdot g \geq 0 . \qquad (11\text{-}71)$$

This inequality, known as the *Clausius-Duhem inequality*, is of prime importance in determining restrictions on the acceptable forms of the constitutive functionals for admissible processes.

A local *thermomechanical process in B* is said to be an *allowable local thermomechanical process* if it is compatible with the local balance laws (45) and (46) and if it satisfies the postulate of positive rate of entropy production expressed by (71). Evidently, then, an *allowable thermomechanical process* is a *thermodynamic process*. A thermodynamic process is said to be an *admissible thermodynamic process* if it is compatible with the constitutive equations at each point X of B for all times t. From previous discussions it is observed that for every choice of the deformation function χ and the absolute temperature θ, as functions of X and t, there corresponds a unique admissible thermodynamic process in B. The spatial position $x = \chi(X,t)$ and the temperature $\theta = \theta(X,t)$ determine the independent constitutive variables. The constitutive equations then yield ψ, η, T (or S), and q, from which the internal energy $\varepsilon = \psi + \theta\eta$ may be calculated. The body force vector b and the heat supply σ may then be uniquely determined from the local balance laws (45) and (46) or (68) Although the body force b and the heat supply σ determined in this manner appear to be somewhat artificial in nature, in studying the restrictions imposed on the constitutive functionals by the Clausius-Duhem inequality this result allows arbitrary specification of certain independent variables with the knowledge that there will exist one admissible thermodynamic process corresponding to this choice.

11.7.2 CONSTITUTIVE ASSUMPTIONS

The axiomatic development of [31] leads to the following forms for the constitutive equations[17]:

$$\psi = \overset{\infty}{\underset{s=0}{p}} \{C^t(s),\ \theta^t(s),\ (F^t(s))^T g^t(s);\ X\}\ , \qquad (11\text{-}72)$$

$$S = \overset{\infty}{\underset{s=0}{S}} \{C^t(s),\ \theta^t(s),\ (F^t(s))^T g^t(s);\ X\}\ , \qquad (11\text{-}73)$$

$$\eta = \overset{\infty}{\underset{s=0}{h}} \{C^t(s),\ \theta^t(s),\ (F^t(s))^T g^t(s);\ X\}\ , \qquad (11\text{-}74)$$

$$q = \overset{\infty}{\underset{s=0}{Q}} \{C^t(s),\ \theta^t(s),\ (F^t(s))^T g^t(s);\ X\}\ , \qquad (11\text{-}75)$$

where S and Q are respectively tensor and vector-valued functionals and p and h are scalar-valued functionals defined over the field of real-valued functions C^t, θ^t, F^t, and g^t of s for $0 \leq s < \infty$ and for each fixed X in B. In these equations the independent variables

---

[17] Even though thermomechanical and thermodynamic processes have been formally defined in terms of the symmetric Cauchy stress tensor T, it turns out to be simpler in applications to employ one of the Piola-Kirchoff stress tensors. This result follows, from the fact that the stress tensor T is referred to the current deformed configuration whereas the strain measure employed here (i.e., C) is referenced to the undeformed reference configuration κ_0, and, in developing a constitutive theory using the right Cauchy-Green tensor C it is more appropriate to also use a stress tensor which is referred to the undeformed reference configuration. The first and second Piola-Kirchoff stress tensors satisfy this requirement, however, for our purposes here we will proceed with only the first Piola-Kirchoff stress tensor S.

$C^t(s)$, $\theta^t(s)$, $F^t(s)$ and $g^t(s)$ denote respectively the histories of the right Cauchy-Green strain tensor C, the absolute temperature θ, the deformation gradient F and the gradient of the temperature in the current deformed configuration up to time t. That is, for example,

$$C^t(s) \equiv C(t-s) \ , \ 0 \leq s < \infty \ . \tag{11.76}$$

The other histories θ^t, F^t and g^t are defined in an identical manner.

The constitutive equations (72) through (75) satisfy the fundamental axioms of thermomechanical constitutive theory, however in the sequel the intervening manipulations are considerably simplified if the following slightly different set of constitutive assumptions is employed:

$$\psi = \overset{\infty}{\underset{s=0}{p}} \{F^t, \theta^t; g\} \ , \tag{11-77}$$

$$S = \overset{\infty}{\underset{s=0}{S}} \{F^t, \theta^t; g\} \ , \tag{11-78}$$

$$\eta = \sum_{s=0}^{\infty} \underset{s}{h} \{F^t, \theta^t; g\} , \qquad (11\text{-}79)$$

$$q = \sum_{s=0}^{\infty} \underset{s}{Q} \{F^t, \theta^t; g\} . \qquad (11\text{-}80)$$

The main difference between this set of constitutive equations and the previous set (72) through (75) is a result of relaxing the frame-indifference requirements with respect to arbitrary orthogonal changes of reference frame. Space and time translation invariance is still observed however. Relaxing the requirements for invariance under arbitrary rotations allows use of the deformation gradient F in place of the right Cauchy-Green tensor C and g in place of $F^T g$. As a result, however, the response functionals in (77) through (80) are different from those in (72) through (75) even though we continue to use the same notation for convenience. The constitutive equations may be rephrased in an objective form rather easily following our study of the consequences of the Clausius-Duhem inequality.

A physical restriction has also been introduced into the set of constitutive equations (77) through (80) which is not a direct consequence of the axiomatic development. Namely, it is supposed that the response functionals are functions of only the current

value of the temperature gradient at the material point X.[18]

In writing the constitutive equations (77) - (80) explicit dependence on the material point X has also been omitted for notational convenience. In the discussions that follow it is immaterial whether or not the body $\mathcal{B}$ is materially homogeneous or inhomogeneous. All of

[18] The justification for this assumption is based on the fact that there is presently no physical evidence which suggests that the respons functionals should be influenced by the history of the temperature gradien.. Mathematically, this assumption is equivalent to assuming that the history of the temperature gradient is sufficiently smooth to allow a Taylor's series representation in time about the current time, and then neglecting all terms beyond the first term. Although this assumption appears physically reasonable, it is in direct contradiction to the formal axiomatic development [31]. If dependence on the entire history g^t is initially assumed then it can be shown that dependence on the past history g^t_r of g^t must be retained in the free energy functional ρ. In a previous result the author [79] demonst ted that the restrictions imposed on the constitutive equations by the Clausius-Duhem inequality are quite sensitive to the initial constitutive assumptions. It was further argued that the *formal* development of a thermomechanical constitutive theory required a consistent set of constitutive assumptions. In accord with this idea one may argue that the history of the temperature gradient should be included in the list of independent constitutive variables. If this argument is accepted then one must look elsewhere for thermodynamic restrictions. One possible source of obtaining thermodynamic restrictions which has not as yet been fully explored, has been suggested by Fitzgerald [30] extended slightly by Hufferd and Fitzgerald [79] and recently put on a more rigorous foundation by Fitzgerald [23]. On the other hand, however, great care must be exercised in the formal development of constitutive theories which are not sufficiently guided by physical experience. Such theories will always be extremely cumbersome to work with and may not relate substantially to physical reality. The approach adopted in this study, as noted, has been to introduce formalism only when physical experience is unavailable.

the arguments used subsequently are valid in either case. Each of the arguments of the response functionals depends on the material position X and hence on the reference configuration κ_0. If a reference configuration can be chosen such that all of the response functionals are independent of X, then the body is said to be *materially homogeneous* and all points X in B are equivalent. If no such configuration can be found then B is said to be *materially inhomogeneous* and the position of the material particle X must be explicitly considered.

For notational convenience the arguments of the response functionals in (77) - (80) will be replaced by the set

$$\{F_r^t,\ \theta_r^t;\ F,\ \theta,\ g\}$$

where the subscript r denotes the restriction to the open interval $s \in (0,\infty)$, and where

$$F \equiv F^t(0) = F(t)\ , \tag{11-81}$$

$$\theta \equiv \theta^t(0) = \theta(t)\ . \tag{11-82}$$

The functions

$$F_r^t(s) = F^t(s)\ ,\quad 0 < s < \infty\ ; \tag{11-83}$$

and

$$\theta_r^t(s) = \theta^t(s)\ ,\quad 0 < s < \infty \tag{11-84}$$

are called the *past histories* up to time t of the deformation gradient F and the temperature θ, respectively. It is required that the histories have a limit at $s = 0$, typically defined by

$$F_r = \lim_{s=0} F_r^t(s)\ . \tag{11-85}$$

In general, $F_r \neq F$ and $\theta_r \neq \theta$. Thus introducing the past histories F_r^t and θ_r^t allows for a jump discontinuity in the deformation gradient and the temperature at the current time t. Had we continued to use the total history (eg., $F^t(s) = F(t-s)$, $0 \leq s < \infty$) or the *difference history* defined, for example by

$$F_d^t(s) = F^t(s) - F(t) \ , \quad 0 \leq s < \infty, \tag{11-86}$$

jumps in the recent history would not be allowed without the introduction of auxilliary histories. Evidently, for smooth recent histories, $F_r = F$ and $\theta_r = \theta$.

Subsequent notation can be further simplified by introducing the notation Λ to denote the ordered pairs (L,λ) with L a second order tensor and λ a scalar. With the definitions

$$\alpha\Lambda_1 + \beta\Lambda_2 = \alpha(L_1,\lambda_1) + \beta(L_2,\lambda_2) = (\alpha L_1 + \beta L_2, \ \alpha\lambda_1 + \beta\lambda_2) \tag{11-87}$$

and

$$\Lambda_1 \cdot \Lambda_2 = (L_1,\lambda_1) \cdot (L_2,\lambda_2) = tr(L_1 L_2^T) + \lambda_1\lambda_2 \tag{11-88}$$

the collection of all Λ's forms a Euclidean vector space $V_{(10)}$ of dimension 10 with the natural norm

$$|\Lambda| = (\Lambda\cdot\Lambda)^{\frac{1}{2}} = (tr LL^T + \lambda^2)^{\frac{1}{2}} \tag{11-89}$$

The set of vectors of the form

$$\Gamma = (F,\theta) \tag{11-90}$$

with F, the deformation gradient, an invertible tensor, and θ, the temperature, a positive number form a cone C in $V_{(10)}$. The history up to time t of the deformation gradient and the temperature in a local process is denoted by the function

$$\Gamma^t = (F^t, \theta^t) \qquad (11\text{-}91)$$

mapping the extended non-negative real axis $[0,\infty)$ into C:

$$\Gamma^t(s) = [F^t(s), \theta^t(s)] \in C\ , \quad s \in [0,\infty)\ . \qquad (11\text{-}92)$$

The restriction to the open interval $(0, \infty)$ is denoted by the subscript r:

$$\Gamma_r^t(s) = [F_r^t(s), \theta_r^t(s)] \in C_r,\ s \in (0,\infty)\ , \qquad (11\text{-}93)$$

where C_r is a cone in the space of past histories. The *stress-entropy* pair

$$\Sigma(t) = [\rho_0^{-1} S(t), -\eta(t)] \qquad (11\text{-}94)$$

at time t is also an element of $V_{(10)}$.

With the above shorthand notations, the constitutive equations (77) through (80) may be written in the simplified form

$$\psi = \overset{\infty}{\underset{s=0}{P}} \{\Gamma_r^t;\ \Gamma,\ g\}\ , \tag{11-95}$$

$$\Sigma = \overset{\infty}{\underset{s=0}{\Xi}} \{\Gamma_r^t;\ \Gamma,\ g\}\ , \tag{11-96}$$

$$q = \overset{\infty}{\underset{s=0}{Q}} \{\Gamma_r^t;\ \Gamma,\ g\}\ , \tag{11-97}$$

where the functional Ξ has the components

$$\Xi = (\rho_0^{-1} S, - h)\ . \tag{11-98}$$

In terms of the above definitions the Clausius-Duhem inequality (66) may be written in the form

$$\dot{\psi} - \Sigma \cdot \dot{\Gamma} + (\rho\theta)^{-1} q \cdot g \leq 0\ . \tag{11-99}$$

Equations (95) - (97) are the form of the constitutive equations, and (99) is the form of the Clausius-Duhem inequality which will be employed in subsequent discussions.

Some of the concepts and requirements of the fading memory semi-norm introduced in §11.6.3 will now be recalled and discussed in relation to the smoothness of the constitutive functionals P, Ξ and Q.

The Banach function space of Lebesgue-measurable functions mapping $(0,\infty)$ into $V_{(10)}$ will be denoted by B_r. The norm on B_r will be denoted by $||\cdot||_r = \rho_r(\cdot)$. In particular we will be interested

in the set of elements of B_r mapping $(0,\infty)$ into the cone C_r discussed above;

$$C_r = \left[\Gamma = (F,\theta) | \Gamma \in V_{(10)}, \det F > 0, \theta > 0\right] \qquad (11.100)$$

The set of elements of B_r corresponding to functions mapping $(0,\infty)$ into C_r forms, in turn, a cone C_r in B_r.

The properties of the memory function norm have been discussed in §1.6.3. It is recalled that space B_r is required to have the following properties:

i) The constant functions are in B_r; i.e., if Ω is in $V_{(10)}$ then the function $\omega(s) = \Omega$ for $s \in (0,\infty)$ is in B_r.

ii) The space B_r contains all right and left translates of its elements. If ψ is in B_r, then for each $\delta \geq 0$ the right translate $T^{(\delta)}\psi$ and the left translate $T_{(\delta)}\psi$ defined by

$$T^{(\delta)}\psi(s) = \begin{cases} 0, & 0 \leq s \leq \delta, \\ \psi(s-\delta), & \delta < s < \infty; \end{cases} \qquad (11.101)$$

and

$$T_{(\delta)}\psi(s) = \psi(s+\delta) \quad 0 \leq s \leq \infty \qquad (11.102)$$

are also in B_r.

The set of all Lebesgue measurable functions Λ^t which map $[0,\infty)$ into $V_{(10)}$ and satisfy

$$||\Lambda^t_r||_r < \infty \tag{11.103}$$

is denoted by B and is called the *space of total histories*. The elements of B are functions which take on values in $V_{(10)}$ with the property

$$|\Lambda^t(0)| < \infty \tag{11.104}$$

Introducing the function norm

$$||\Lambda^t|| = |\Lambda^t(s)| + ||\Lambda^t_r||_r \,, \tag{11.105}$$

with the usual identification of equal functions B is a Banach space. Thus the norm (105) may be taken to be of the form given by (42); viz:

$$||\Lambda^t|| = |\Lambda^t(0)| + \underset{s\,\in(0,\infty)}{ess\ sup}\ |\Lambda^t_r(s)|k(s) \,. \tag{11.106}$$

The elements of B corresponding to functions r^t mapping $[0,\infty)$ into the cone C form a cone $\mathcal{C}$ in B and it is assumed that for each fixed value of g in $V_{(3)}$ the domain of the functionals $p \equiv$ and Q are this cone.

The constitutive functionals p, Ξ and Q are assumed to be continuous over their entire domain of definition $C \oplus V_{(3)}$ relative to the norm $||\cdot||$, (905), on the total histories and the usual norm $|\cdot|$ on $V_{(3)}$. It is further assumed that the free-energy functional p is continuously Fréchet-differentiable. That is, whenever ϕ and v are such that $r^t + \phi$ is in C and v is in $V_{(3)}$

$$p(r^t + \phi;\, g + v) = p(r^t;\, g) + \delta p(r^t;\, g|\phi) \tag{11-107}$$

$$+ \partial_g p(r^t;\, g)\cdot v + o(||\phi|| + |v|)\,, \tag{11-108}$$

where $\delta p(r^t;\, g|\cdot)$ is a linear functional defined on $\mathcal{B}$ and such that $\delta p(r^t;\, g|\phi)$ is jointly continuous in r^t, g and ϕ for all $r^t \in C$, $g \in V_{(3)}$ and $\phi \in \mathcal{B}$, while $\partial_g p(r^t,\, g)$ is jointly continuous in $r^t \in C$ and $g \in V_{(3)}$ with values in $V_{(3)}$, and

$$\lim_{||\phi||+|v|\to 0} \frac{o(||\phi|| + |v|)}{||\phi|| + |v|} = 0\,. \tag{11-109}$$

The function $\dot{r}^t$ is defined by

$$\dot{r}^t(s) = -\frac{d}{ds}\, r^t(s) = \frac{d}{d\tau}\, r(\tau)\Big|_{\tau=t-s} \tag{11-110}$$

for almost all $s \in [0,\infty)$. The function $\dot{r}^t_r$ is defined by

$$\dot{\Gamma}_r^t(s) = \frac{d}{d\tau}\,\Gamma(\tau)\Big|_{\tau=t-s} \qquad (11\text{-}110)$$

for almost all $s \in (0,\infty)$; $\dot{\Gamma}_r^t$ is just the restriction of $\dot{\Gamma}^t$ to $(0,\infty)$. Finally $\dot{\Gamma}$ is defined by

$$\dot{\Gamma}(t) = (\dot{F}(t), \dot{\theta}(t)) \triangleq -\frac{d}{ds}\,\Gamma^t(s)\Big|_{s=0} \qquad (11\text{-}111)$$

11.7.3 THERMODYNAMIC RESTRICTIONS ON CONSTITUTIVE FUNCTIONALS

It follows from the smoothness assumption for p that the time derivative of ψ exists at t and is given by

$$\dot{\psi}(t) = \delta p(\Gamma^t;\, g|\dot{\Gamma}^t) + \partial_g p(\Gamma^t;\, g)\cdot\dot{g} \quad , \qquad (11\text{-}112)$$

with $\dot{\Gamma}^t$ given by (109). The assumed differentiability of p implies the existence and continuity of the partial derivative operators $\delta_\Gamma p$ and $D_\Gamma p$ defined by [31]

$$p(\Gamma_r^t + \theta;\, \Gamma, g) = p(\Gamma_r^t;\, \Gamma,\, g) + \delta_\Gamma p(\Gamma^t,\, g|\psi) + o(||\psi||_\Gamma), \qquad (11\text{-}113)$$

$$p(\Gamma_r^t;\, \Gamma + \Omega, g) = p(\Gamma_r^t;\, \Gamma, g) + D_\Gamma p(\Gamma^t;\, g)\cdot\Omega + o(|\Omega|) \quad . \qquad (11\text{-}114)$$

These equations hold throughout the domain of p. Using (113) and (114) the Clausius-Duhem inequality (99) may be written in the form

$$[\Xi(r^t;\, g) - D_r p(r^t;\, g)]\cdot\dot{r} - \delta_{\dot{r}} p(r^t;\, g|\dot{r}_r^t)$$

$$- (\rho\theta)^{-1} Q(r^t;\, g)\cdot g - \partial_g p(r^t;\, g)\cdot\dot{g} \geq 0 \,. \qquad (11\text{-}115)$$

Recalling previous comments, $r^t = (F^t, \theta^t) \in C$ and $g(t) \in V_{(3)}$ may be arbitrarily selected with the assurance that there will exist at least one admissible local thermodynamic process corresponding to this choice. Furthermore $\dot{g}$ may be chosen independently of r^t and g. Thus from (115) it is deduced

$$\partial_g p = 0 \,. \qquad (11\text{-}116)$$

Thus the free energy functional p is independent of the (current) value of the temperature gradient. The inequality (115) may thus be written

$$[\Xi(r^t;\, g) - D_r p(r^t)]\cdot\dot{r} - \delta_{\dot{r}} p(r^t|\dot{r}_r^t) - (\rho\theta)^{-1} Q(r^t;\, g)\cdot g \geq 0 \,. \qquad (11\text{-}117)$$

The procedure followed from this point on by previous workers has been to claim that $\dot{r}$ may be arbitrarily selected and then to require the generalized stress functional Ξ to be independent of g. This procedure, as we shall note subsequently, creates difficulties for certain processes. An alternate, equally acceptable and possibly more useful approach in describing real material behavior is outlined here which removes some of these difficulties. A detailed discussion

and intrapretation of the assumption introduced and the results obtained here, as well as a comparison with previous thermodynamic theories is delayed until the following section.

It is first noted that the generalized stress functional may be decomposed in the following manner [31]:

$$\Xi(\Gamma^t;\, g) = \Xi_o(\Gamma^t) + {}_o\Xi(\Gamma^t;\, g) \tag{11-118}$$

where Ξ_o is a functional of Γ^t, independent of g, and ${}_o\Xi$ is a functional of Γ^t and a function of g. Next, in analogy with previous thermodynamic theories the association

$$\Xi_o = D_\Gamma p \tag{11-119}$$

is *assumed*. Introducing (118) along with (119) into (116) it is concluded that

$${}_o\Xi(\Gamma^t;\, g)\cdot\dot{\Gamma} - \delta_{\dot{\Gamma}} p(\Gamma^t|\dot{\Gamma}^t_r) - \rho\theta^{-1}\, Q(\Gamma^t;\, g)\cdot g \geq 0. \tag{11-120}$$

The quantity δ defined by

$$\delta = [{}_o\Xi(\Gamma^t;\, g)\cdot\dot{\Gamma} - \delta^t_{\dot{\Gamma}} p(\Gamma^t|\dot{\Gamma}^t_r)] \tag{11-121}$$

is called the *internal dissipation*. Thus, (120) simplifies to

the *reduced dissipation inequality*.

$$\rho\theta\delta \geq q\cdot g \qquad (11\text{-}122)$$

11.7.4 DISCUSSION OF RESULTS AND COMPARISON WITH PREVIOUS THEORIES

The restrictions imposed on the constitutive functionals and admissible processes by the requirement that the local rate of entropy production be non-negative are embodied in the assumption (119) and the dissipation inequality (122).

In order to demonstrate the motivation for the development of the last paragraph in the previous section and to demonstrate the limited applicability of previous thermodynamic theories we return to (117) and explore in greater detail the restrictions imposed on admissible processes and the resulting constitutive functionals. Equation (117) is interpreted as imposing restrictions on admissible processes as well as constitutive functionals. The space of histories (processes) for which (117) is postulated to be valid includes histories that are smooth at the current time as well as histories that exhibit jump discontinuities at the present time. For histories that possess jumps at the present time it is argued that Γ may be specified independently of Γ^t and g. One then concludes that the generalized stress functional Ξ_o is independent of g and is determined from the free energy functional through functional differentiation; i.e.,

$$\Xi_o(\Gamma^t) = D_\Gamma p(\Gamma^t) \qquad (11\text{-}123)$$

The internal dissipation δ is then defined by

$$\delta = - \delta_{\dot{r}} p(r^t | \dot{r}_r) \tag{11-124}$$

and the dissipation inequality

$$\rho\theta\delta \geq q \cdot g \tag{11-125}$$

results. Since δ is independent of g, we may set $g = 0$ and obtain

$$\delta \geq 0 . \tag{11-126}$$

That is, the internal dissipation is non-negative. This latter inequality is interpreted as a statement that the Clausius-Duhem inequality implies the Clausius-Planck inequality [31].
From (124) it is noted that histories with jumps at the present time are incapable of exhibiting instantaneous dissipation.

The above argument is supposedly valid for all histories. However, it is not applicable for histories which are smooth at the present time. For histories which are smooth at the current time r may not be selected independently of r_r^t. In particular it is required that $\dot{r}$ be the limit of the restriction $\dot{r}_r^t$ as $s \to 0$. In this case one cannot conclude that Ξ is independent of g, and hence the subsequent arguments are not valid.

Returning now to (118) we explore the validity of the arguments leading to (122) for histories which are smooth at the current time. The decomposition (118) is motivated by experience with simpler theories of materials of the differential type. These materials have been studied by several workers including a recent in-depth study by the authors [79]. In this work the author noted that a decomposition such as (118) may be obtained for the stress for general nth-order Rivlin-Ericksen materials with one component of the stress derivable from a (non-equilibrium) potential, while the other component, called the *extra stress*, may be associated with higher order dissipative mechanisms. In the situation here, the generalized stress functional Ξ has one component Ξ_0 which is derivable from the non-equilibrium free energy functional p, while the remaining component ${}_0\Xi$ gives rise to instantaneous dissipation. The assumption embodied in (119) is motivated by two sources; first, (119) is a result of application of the Clausius-Duhem inequality for histories with jumps at the present time, and secondly, a similar expression is obtained in studies of materials of the differential type. The association (119) leads to the definition of the internal dissipation given by (121) In contrast to (124) it is observed that histories which are smooth at the present time give rise to instantaneous dissipation. This is clearly a desirable property for viscous materials and general inelastic deformations such as, for example, plasticity. It is noted that the dissipation inequality (122) is formally identical to (125) with the exception that δ is given by (121) in place of (124) It is

also observed that for smooth histories at the present time δ, given by (122), is not independent of g and hence (126) cannot be concluded. Thus, the internal dissipation may be negative in histories smooth at the present time. The internal dissipation is the amount by which internal working exceeds the rate of growth of internal energy less heat storage, or alternatively δ/θ is the amount by which the entropy growth $\rho\eta$ exceeds the quotient of non-mechanical power by temperature. Roughly speaking, a negative internal dissipation then means that energy can be added to a body at rate faster than it can be dissipated by internal stress working or heat storage. This result is not physically unreasonable. Thus, the requirement of strictly non-negative dissipation is not implied by the Clausius-Duhem inequality (except in a homothermal field) for histories continuous at the current time. This requirement may be met if the less restrictive and less general Clausius-Planck inequality is assumed to hold (see [31]).

From the above discussion, (118) through (122) give reasonable restrictions on the constitutive functionals for histories smooth at the current time, whereas the approach and arguments of Coleman and others are inapplicable. It is easily shown that these results also reduce to previous results (123) through (126) for histories with jumps at the present time. For histories with a jump at the present time Γ is independent of Γ_r^t in (123) and the inequality (123) holds only if

$$_{o}\Xi = 0 \, . \qquad (11\text{-}127)$$

Hence, (121) reduces to (124) and (119) follows as a result, as well as (126).

In conclusion, it is apparent that the development presented here, which is based on the reasonable assumption (119) generalizes Coleman's results to include smooth histories at the present time, and also contains his results for histories with jumps at the present time. This development leads also to the physically desirable result that instantaneous dissipation is allowed.[19] Finally, it is noted that in practical physical situations jump discontinuities do not occur.

Before closing this discussion, the results of (118) through (121) will be assimilated in terms of the more familiar quantities ψ, S, n and q:

$$\psi(t) = \sum_{s=0}^{\infty} p_s(F^t,\theta^t) \, , \qquad (11\text{-}128)$$

$$n(t) = \sum_{s=0}^{\infty} h_s(F^t,\theta^t) \, , \qquad (11\text{-}129)$$

$$S(t) = S_o(t) + {}_{o}\Sigma(t) = \sum_{s=0}^{\infty} S_s(F^t,\theta^t) + \sum_{s=0}^{\infty} {}_{o}S_s(F^t,\theta^t;g) \, , \qquad (11\text{-}130)$$

$$q(t) = \sum_{s=0}^{\infty} c_s(F^t,\theta^t;g) \qquad (11\text{-}131)$$

[19] Truesdell [80] has independently arrived at similar conclusions.

In addition, the stress S_o and the entropy n are derivable from the free energy functional p;

$$S_o(t) = \rho_0 \, D_F \, p(F^t, \theta^t) \, , \tag{11-132}$$

$$n(t) = D_\theta \, p(F^t, \theta^t) \, . \tag{11-133}$$

11.7.5 EQUILIBRIUM THERMODYNAMICS

The results of the previous section may be easily shown to reduce to the proper results for equilibrium processes.

The *isothermal static continuation of* Γ^t *by amount* σ is defined by

$$\Gamma^{t+\sigma}(s) = \begin{cases} \Gamma^t(s) \, , & 0 \le s \le \sigma \, ; \\ \Gamma^t(s-\sigma) \, , & \sigma < s < \infty \, . \end{cases} \tag{11-134}$$

The quantity $\Gamma^{t+\sigma}$ is regarded as the history up to time $t+\sigma$ of the history Γ^t up to time t which is then held constant in the interval $[t,t+\sigma]$. Thus, for $\tau \in [t,t+\sigma]$

$$\dot{\Gamma} = (\dot{F},\dot{\theta}) = (0,0) \, . \tag{11-135}$$

The past history $\Gamma_r^{t+\sigma}$ of $\Gamma^{t+\sigma}$, i.e., the restriction $\Gamma^{t+\sigma}$ to the open interval $(0,\infty)$, obeys the relation

$$\Gamma_r^{t+\sigma} = \Gamma_r^t - T^{(\sigma)} \, \Gamma_r^t + T^{(\sigma)} \, \Gamma_r^t \, , \tag{11-136}$$

where $R^{(\delta)}$ is the translation operator defined by (101) and Γ_r^+ is the constant function on $(0,\infty)$ with value

$$\Gamma_r^+(s) = \Gamma_\sigma = \Gamma^t(0) \ , \quad 0 < s < \infty \ . \tag{11-137}$$

During the static part $t < \tau < t + \delta_1$ of an isothermal static continuation, the rate of change of the free energy is given by

$$\dot{\psi}(\tau) = - \delta_{\dot{r}} p(\Gamma^t | \Gamma_r^t) \tag{11-138}$$

which is just the expression for the internal dissipation obtained by previous workers. According to (126) this dissipation is non-negative implying

$$\dot{\psi}(\tau) \leq 0 \ , \tag{11-139}$$

in accordance with previous results. If we do not insist on an *isothermal* continuation, then

$$\dot{\psi}(\tau) = - (\rho^{-1}\delta + \eta\dot{\theta}) \ , \tag{11-140}$$

which form (122) requires

$$\dot{\psi}(\tau) \leq - [\eta\dot{\theta} + (\rho\theta)^{-1} \, q \cdot g] \ . \tag{11-141}$$

This result indicates that dissipation is possible in a stress-relaxation test.

All of the usual results obtained by previous workers still hold in the development introduced here. The history corresponding to constant values of Γ^t for all times has the least free energy. As a continuation is extended to $\sigma \to +\infty$ the familiar equilibrium relations result however, it is noted that these equilibriums values may depend upon a maximum value of the history attained in the past history of the body as well as the value of the history when the continuation was initiated. Coleman and Owen[51] have recently concluded an investigation of equilibrium thermodynamics of materials with permanent memory attributes similar to those discussed here.

11.8 APPROXIMATE THEORIES AND DISCUSSION OF APPLICATIONS

A discussion of the application of the results of this research to the behavior of various classes of materials is presented in this section. A brief discussion is also included which points out the difficulties associated with both conducting an acceptable experimental program and interpreting the results of such a program. The position of classical theories is pointed out along with indications of methods for obtaining representations of the constitutive functionals.

11.8.1 PRELIMINARIES

Two extensions have been introduced into the thermodynamic constitutive theory developed in the previous sections which have been noticably absent from previous theories. First, we have introduced a memory function norm in the explicit form

$$||\Gamma^t(s)|| = |\Gamma^t(0)| + \operatorname{ess\,sup}_{s\in(0,\infty)} |\Gamma_r^t(s)|k(s) \qquad (11-142)$$

which allows for different fading memory characteristics, whereas previous theories have dealt only with materials having normal fading memory characteristics. Secondly, Coleman's thermodynamic theory of materials has been generalized to include deformation-temperature histories which are smooth at the present time through decomposition of the generalized stress functional into two components, one of which is associated with instantaneous dissipation. These two ideas extend the

classes of processes and materials significantly beyond those allowed in previous theories. However, it is noted that certain difficulties are attendant with these benefits. The major difficulties arise in representation of the constitutive functionals and in the description and conduction of adequate experimental programs. Before discussing these difficulties, we first review the constitutive functionals that must be determined and the coupled energy equation to be solved. From (128) through (133) it is observed that the free energy functional p determines the stress S_o and the entropy η. Thus, given

$$\psi(t) = \overset{\infty}{\underset{s=0}{p}}\,(F_r^t,\ \theta_r^t;\ F,\ \theta) \tag{11-143}$$

one can then determine S_o and η from the relations

$$S_o(t) = D_F p(F_r^t,\ \theta_r^t;\ F,\theta), \tag{11-144}$$

$$\eta(t) = D_\theta p(F_r^t,\ \theta_r^t;\ F,\theta). \tag{11-145}$$

It is noted that although S_o and η are dependent upon the past history of the deformation-temperature pair $(F,\ \theta)$, the current values of S_o and η are obtained through functional differentiation with respect to the present values of F and θ.

The coupled energy equation to be solved has the form

$$-q\cdot g = \rho\theta\dot{\eta} - \rho r - \delta\ . \tag{11-146}$$

If Fourier's law of heat conduction is assumed then

$$K\nabla^2\theta = \rho\theta\dot{\eta} - \rho r - \delta \ , \qquad (11\text{-}147)$$

where K is thermal conductivity of the material,[20] r is the radiant heat supply and δ is the internal dissipation given by

$$\delta = (\rho/\rho_0)\, S\cdot\dot{F} - \rho(\dot{\psi} + \eta\dot{\theta}). \qquad (11\text{-}148)$$

In addition, the first Piola-Kirchoff stress tensor satisfies Euler's first law of motion in the form

$$DIV\ S + \rho_0 b_0 = \rho_0 \ddot{x} \qquad (11\text{-}149)$$

Equations (146) through (148) represent the set of coupled equations to be solved for general nonlinear thermomechanical materials with memory. For materials or processes which do not give rise to instantaneous dissipation, the procedure for solving these equations, although extremely complicated is still nonetheless straightforward. For materials which exhibit instantaneous dissipation however, the solution of these equations is considerably more difficult. This difficulty arises from the decomposition of the stress S,

$$S(t) = S_\infty(t) + {}_0S(t). \qquad (11\text{-}150)$$

Inserting (149) and (150) the internal dissipation may be written

[20] It should be mentioned that if Fourier's Law is assumed and if $K>0$, then $q\cdot g\leq 0$ and $\delta\geq 0$. In this situation the Clausius-Duhem inequality does imply the Clausius-Planck inequality even though the dissipation δ is not independent of g.

$$\delta = (\rho/\rho_0)\, S_o \cdot \dot{F} + (\rho/\rho_0)\, {}_oS \cdot \dot{F} - \rho(\dot{\psi} + \eta\dot{\theta}) \qquad (11\text{-}151)$$

Assuming that the free energy ψ is known, the stress S_o may be determined from (144) and the entropy η determined from (145), however, the *extra* dissipative stress ${}_oS$ remains unspecified. The difficulty is thus associated with determining the stress ${}_oS$.

It appears that the best technique for determining ${}_oS$ is to assume a functional representation for ${}_oS$ and p, determine S_o and η using ((144) and (145), and then conduct a sufficient number of independent experimental tests to determine the material functions appearing in the functional representations requiring that the material functions be such that (146) is in agreement with experimentally measured temperature distributions. Such an extensive test program has not been carried out for general materials; polymers and plastics in particular, because of the significant financial expense and difficulties associated with obtaining *accurate* temperature measurements. Such a program is considerably simplified in the case of metals. Dillon [81 - 83] and Dillon and Tauchert [84]have experimentally measured the stress, strain and temperature in aluminum and copper bars and tubes under static and cyclic loading conditions in both the elastic and plastic regions. Their results indicated that the linear theory of coupled thermoelasticity is in general agreement with experimental results, and vividly demonstrated that plasticity cannot be treated as an isothermal process.

11.8.2 REPRESENTATION OF CONSTITUTIVE FUNCTIONALS AND APPROXIMATE THEORIES

From the previous discussion it is observed that a knowledge of the free energy ψ and the extra stress ${}_{o}S$ is required for solution of (146) through (148). Thus only a knowledge of the functionals p and ${}_{o}S$ is required. Since permanent memory behavior has been allowed for in the developments presented here, the approximation theories of Coleman and Noll [26,34], Coleman [68,69] and Coleman and Mizel [27] will not in general be applicable. Their approximation theories will apply when the influence function k(s) in (142) is a decaying exponential and for slow motions corresponding to only normal fading memory behavior. Coleman's [69] approximation for rapid deformations will apply when the material exhibits normal fading memory characteristics (i.e., $k(s)=e^{-\beta s}$) or under monotonic loadings, or when the instantaneous deformation impulse is larger in magnitude than the supremum of any deformation in the past history of the body. The approximate theories of Lianis [35-31] McGuirt and Lianis [38] and Cost [85] will also be applicable when the material exhibits only normal fading memory behavior.

For deformation-temperature processes and material behavior more general than those indicated in the above paragraph new representations must be found. There are a number of representation theorems for linear functionals, however, the literature does not seem to contain a great deal about such theorems for nonlinear functionals. Martin and Mizel Chacon and Friedman [87] Friedman and Katz [88] and Mizel and

Sundaresan [89] have investigated the possibility of obtaining integral representations of additive and biadditive nonlinear functionals on function spaces of measurable functions. Although the results of these workers are of a general interest, the abstract nature of these studies and lack of in-depth investigations makes their results impractical to apply at the present time. Another approach to obtaining representations is to assume applicability of the Stone-Weierstrass approximation theorem and then expand the functionals p and ${}_{o}S$ in a Volterra-Frechet sum of multiple integrals. This approach seems equally impractical to apply in view of the comments made previously regarding the experimental difficulties associated with the isothermal application of even a third order approximation.

Adopting the pragmatic point of view of an engineer, the most practical and straightforward approach is to assume forms for the representations of p and ${}_{o}S$ of a simple nature at first; increasing the complexity only as dictated by comparison with experimental results. In view of the practical desire to represent the history of the deformation-temperature pair (F,θ) in as simple a form as possible, a starting point is to assume that the functionals p and ${}_{o}S$ may be written in the form

$$\psi(t) = \sum_{s=0}^{\infty} p \left[||F_r^t(s)||_\infty k(s), ||\theta_r^t||_\infty h(s); F, \theta \right] , \qquad (11\text{-}152)$$

$${}_{o}\psi(t) = \sum_{s=0}^{\infty} {}_{o}S \left[||F_r^t(s)||_\infty k(s), ||\theta_r^t||_\infty h(s); F, \theta, g \right] , \qquad (11\text{-}153)$$

where the notation $||\cdot||_\infty$ has been introduced for the quantity

$$\underset{s\in(0,\infty)}{ess\ sup}\ |\cdot|$$

for notational convenience; and the additional influence function $h(s)$ has been introduced to allow for different memory response for the temperature θ and the deformation gradient F.

Two particularly simple approaches to representing (152) and (153) appear to be worth consideration. First, a direct dependence upon the history may be assumed. For example, one may assume explicit functions for $k(s)$ and $h(s)$ and treat the influence of the history as, say, a weighted integral of the form

$$\int_0^\infty ||\cdot||_\infty k(s)\, ds \quad (< \infty) \,. \tag{11-154}$$

The functionals p and ${}_oS$ then become functions and one may attempt a Taylor's series expansion in several variables exploring the error associated with the remainder term through a series of experimental tests.

A second apprach is to follow the suggestion of Bernstein, Kearsley and Zapas [114] and assume single integral constitutive equations of the form

$$\psi = \underset{s=0}{\overset{\infty}{p}} = \int_0^\infty L\left[||F_r^t||_\infty k(s),\ ||\theta_r^t||_\infty h(s);\ F,\ \theta\right] ds, \tag{11-155}$$

$$S = \underset{s=0}{\overset{\infty}{{}_oS}} = \int_0^\infty M\left[||F_r^t||_\infty k(s),\ ||\theta_r^t||_\infty h(s);\ F,\ \theta, g\right] ds. \tag{11-156}$$

These two representations can be further simplified if additional assumptions are introduced. A common assumption which has been justified experimentally for certain materials relates to the idea of *thermorheologically simple solids*. The main feature of the constitutive relations of such materials is a temperature-time equivalence postulate with the property that the mechanical response of the material is affected by a uniform temperature change through a uniform expansion or contraction of the time scale. The constitutive equations of thermorheologically simple solids obeying Coleman and Noll's fading memory hypotheses have been investigated by Lianis [35,37], McGuirt and Lianis [38], Crochet and Naghdi [91, 92] and Cost [85]. In the above representations this assumption involves replacing the time t (or s) by the (temperature) reduced time $\xi(t)$ (or $\xi(s)$) defined by

$$\xi(\tau) = \int_0^\tau \phi[\theta^t(\sigma)]d\sigma \qquad (11\text{-}157)$$

where the function ϕ represents the *temperature-time shift factor* which is a monotone decreasing function of τ. Other simplifying assumptions may also be introduced. Simplifications resulting from particular choices of the influence functions $k(s)$ and $h(s)$ are discussed in the following section.

In applying (155), the function L should be determined in terms of the invariants of the strain measures C or B to satisfy objectivity and simplify its representation, and likewise any Taylor's series expansion should be made in terms of the invariants of C or B.

This discussion has considered mainly the Chebychev norm (*see sup* 1.1). General L_p norms have been further studied by Farris [9], Fitzgerald and Farris [33] and Fitzgerald [30]. An illustration of the application of the L_p norm to a specific problem is presented in Section 11.9.

11.8.3 SPECIAL THEORIES OF MATERIAL BEHAVIOR

The relation of certain special theories of material behavior is summarized in relation to the thermodynamic constitutive theory developed in this chapter.

If k(s) is chosen sufficiently small in (142) the classical theory of (finite) thermoelasticity results. Under isothermal, homothermal conditions the classical theory of finite elasticity results.

Spatially homologous uniform temperature changes with k(s) a decaying exponential and h(s) vanishingly small in (152) and (153) leads to (finite) thermoviscoelasticity. The same restrictions under isothermal conditions yields (finite) viscoelasticity.

The relation of previous approximate thermodynamic theories has been indicated in the previous section. Under these conditions Rivlin-Ericksen materials represent an asymptotic approximation to the constitutive equations developed here.

Selecting $k(s)=1$ in (142) provides a means of describing viscoplasticity or plasticity. Setting $k(s)=1-k'(s)$ in (142) allows consideration of viscoplasticity or plasticity in which the material response is also dependent upon the temperature history. This capability does not currently exist in any thermodynamic theory even through Dillon [82 - 86] has obtained evidence of temperature history effects in experimental studies with aluminum.

One final comment is in order regarding (154). Equation (154) appears to be a reasonable technique for weighting memory effects. It is noted, however, that this requires that

$$\int_0^\infty k(s)ds < \infty \qquad (11.158)$$

since $||\cdot||_\infty$ is independent of s. Several types of memory characteristics may be introduced satisfying (158) through different choices of the influence functions k(s) or h(s). For example, choosing k(s) to be a decaying exponential gives rise to normal fading memory with respect to the supremum attained in the history of F. This behavior may also be interpreted as an indication that a kind of rehealing phenomenon is taking place. Permanent memory behavior results if the choice

$$k(s) = (1 + s)^{-2} \qquad (11.159)$$

is inserted in (154). It is evident that this discussion applies equally well to the influence function h(s) in (152) and (153), and that there are obviously many more weighting factors that may be obtained through different choices of k(s) satisfying (158).

II.8.4 CLOSURE AND CONCLUSIONS

A thermodynamic constitutive theory applicable to non-aging thermomechanical materials has been presented which extends previous theories to include more physically realistic material behavior.

It is first noted that the time-translation invariance requirements of the principle of material frame-indifference exclude consideration of aging materials. In one sense this is a serious limitation, but in another sense, this limitation is not too significant. On the one hand, the response of many materials; polymers, plastics and biological materials in particular, is known to be, in general, quite sensitive to the age of the material. On the other hand, however, the aging behavior of most polymers and plastics can be de-emphasized in controlled environments. The demonstrated inability of predicting the thermomechanical response of these materials under non-aging conditions justifies and provides the motivation for research studies such as the one reported here.[21]

The second and more significant contribution of this program has been the development of an explicit means of characterizing the influence of the memory of materials which is more closely related to the observed physical behavior of real materials. A *memory norm* has been introduced which allows for fading memory, finite memory and most importantly, permanent memory. Allowing for permanent memory response enables

[21] An alternate approach to the study of aging materials which deserves consideration involves weighting the history of the body by a factor which characterizes aging effects.

consideration of general inelastic deformations (e.g., plasticity, viscoplasticity) from a general continuum thermodynamic viewpoint. This result has important implications when coupled with the resulting thermodynamic developments. First, the continuum treatments of inelastic deformations, and plasticity in particular which consider only the isothermal situation (e.g., Onat [50]) have been experimentally demonstrated by Dillon [82-85] to be invalid. Secondly, the thermodynamic development of a theory of plasticity from the internal state variable approach (e.g., Dillon [82], Green and Naghdi [93-94], Valanis [95]) although allowing for dependence upon the current temperature does not include explicit influence of the temperature history. Again, Dillon [82-85] has experimentally demonstrated that the history of the temperature does influence the current response.

The final development was the extension of Coleman's [68-69] theory of thermodynamics to allow consideration of materials capable of instantaneous dissipation. This development is of critical importance in applying continuum thermodynamic constitutive theories to the description of general inelastic deformations such as plasticity are viscoplasticity in which, along with the permanent memory behavior discussed above, instantaneous dissipation is observed.

The extension of previous continuum thermodynamic theories to allow for instantaneous dissipation raises again the question of the status of the Onsagerist theories. Valanis [96] demonstrated an equivalence between Coleman's theory and Onsagerist theories for viscoelastic materials (i.e., normal fading memory) with instantaneous

elastic response but incapable of instantaneous dissipation. In view of the results of this research it is apparent that Valanis's conclusions must be reinvestigated from a different point of view.

As a final comment, we remark on the definition of nonequilibrium entropy. In this development, it has been required that the temperature be non-negative and that entropy be defined. There is seldom if ever, any serious question regarding the assumption of the existence of a non-negative temperature. There has been, however, in recent times questions raised regarding the definition of non-equilibrium entropy. Meixner [97-99] in particular, has claimed that one cannot define entropy in non-equilibrium processes and has proceeded to develop a *fundamental inequality* which supposedly circumvents the necessity of a definition for non-equilibrium entropy. Meixner's question on the definition of non-equilibrium entropy has been partially answered in recent years by Coleman and Mizel [100 -102], Coleman and Dill[103], Coleman and Greenberg [104] and Hofelich [105]. For finite degree of freedom systems using stability arguments under conditions far from equilibrium, these persons have demonstrated the existence of Liapunov functions which have properties that are formally identical to entropy. Fitzgerald, in the discussion to [23], has proposed a further concept of nonequilibrium entropy which promises, under his restrictions, to provide uniqueness. The extension of these results to the coupled thermomechanical response of continua has not been accomplished as yet, however.

11.9 IDEALIZED THERMOVISCOELASTIC CYLINDER PROBLEM

This section presents a sample problem as illustration of the means of conducting a nonlinear analysis using the ideas of permanent memory discussed previously.

Utilizing models of the failing microstructure of propellant materials, Farris [9] has shown that ratios of p^{th} order Lebesque norms, L_p, are not only excellent measures for use in constitutive equations but that they have a physical relationship to microscopic behavior parameters. These norms have the form

$$||f||_p = \left\{ \int_0^t |f(\xi)|^p d\xi \right\}^{1/p} \qquad (11\text{-}160)$$

and have certain properties that allow close approximation of real propellants. Using L_p norms and exponential time functions, uniaxial material characterization can be accomplished without too much difficulty using infinitesimal strain measures.

In order to demonstrate the applicability and relative ease in which Farris' nonlinear constitutive theory can be applied to proportional boundary valued problems, the example of a cylindrical propellant grain with inner diameter 2a and outer diameter 2b, bonded to rigid case at its outer boundary and slowly cooled will be analyzed. For simplicity, it will be assumed that (1) the propellant is incompressible and obeys the time temperature superposition principle, (2) the grain is sufficiently long that plane strain conditions prevail, and (3) the cooling process is so slow that no thermal gradients exist in the grain. With these restrictions, the strains are statically determinant and of the form

$$e_{rr}(r,T(t)) = \Delta T(t) e^{\circ}_{rr}(r), \qquad (11\text{-}161)$$

$$e_{\theta\theta}(r,T(t)) = \Delta T(t) e^{\circ}_{\theta\theta}(r), \qquad (11\text{-}162)$$

where
$$\Delta T(t) = T(t) - T_0, \qquad (11\text{-}163)$$

and
$$e^{\circ}_{rr}(r) = (3/2)\alpha_p - (\alpha_c - (3/2)\alpha_p)(b^2/r^2), \qquad (11\text{-}164)$$

$$e^{\circ}_{\theta\theta}(r) = (3/2)\alpha_p + (\alpha_c - (3/2)\alpha_p)(b^2/r^2) \qquad (11\text{-}165)$$

In the above equations $T(t)$ is the grain temperature, α_p and α_c are the linear thermal expansion coefficients of the propellant and case materials, and T_0 is the stress free temperature. For this simple problem one finds the strains are proportional to $\Delta T(t)$. Therefore, the conditions needed for the constitutive equations to be simplified for proportional problems are satisfied. The constitutive equations for the material therefore become from (5) and (7)

$$\sigma_{rr}(r,t) = P(r,t) + \int_0^t K\left[\Delta T(\xi'), t'-\tau'\right]_0^{t'} e^{\circ}_{rr}(r)\dot{\Delta T}(\tau)d\tau \qquad (11\text{-}166)$$

$$\sigma_{\theta\theta}(r,t) = P(r,t) + \int_0^t K\left[\Delta T(\xi'), t'-\tau'\right]_0^{t'} e^{\circ}_{\theta\theta}(r)\dot{\Delta T}(\tau)d\tau \qquad (11\text{-}167)$$

In the above equation $P(r,t)$ is an arbitrary pressure which results from the incompressible nature of our problem and t', ξ', and τ' are reduced times defined by

$$t' = \int_0^t d\rho/A_T(\tau), \qquad (11\text{-}168)$$

$$\tau' = \int_0^{\tau} d\rho/A_T(\tau) \qquad (11\text{-}169)$$

and
$$\xi' = \int_0^{\xi} d\rho/A_T(\tau), \qquad (11\text{-}170)$$

where A_T is a temperature dependent shift function.

It can be simply shown that these stress-strain equations satisfy the equilibrium equations providing $\partial P/\partial r = 0$. One also finds that since the radial stress at the inner boundary is zero, the pressure term becomes

$$P(r,t) = P(t) = e^{\circ}_{rr}(a) \int_0^t K\left[\Delta T(\xi'), t'-\tau'\right] \Delta T(\tau) d\tau \qquad (11\text{-}171)$$

The solution for the radial and hoop stresses then becomes

$$\sigma_{rr}(r,t) = (e^{\circ}_{rr}(r) - e^{\circ}_{rr}(a))\, F\left[\Delta T(\xi')\right]_0^{t'} \qquad (11\text{-}172)$$

$$\sigma_{\theta\theta}(r,t) = (e^{\circ}_{\theta\theta}(r) - e^{\circ}_{rr}(a))\, F\left[\Delta T(\xi')\right]_0^{t'} \qquad (11\text{-}173)$$

where

$$F\left[\Delta T(\xi')\right]_0^{t'} = \int_0^t K\left[\Delta T(\xi')_0^{t'}, t'-\tau'\right] \dot{T}(\tau) d\tau \qquad (11\text{-}174)$$

Now these equations are valid for all homogeneous constitutive equations, linear or nonlinear. If, for example, the propellant were linearly elastic, the functional would reduce to,

$$F\left[\Delta T(\xi')\right]_0^{t'} = 2G\Delta T, \qquad (11\text{-}175)$$

where G = shear modulus.

If the material were linear viscoelastic the functional would become

$$F\left[\Delta T(\xi')\right]_0^{t'} = \int_0^t K(t'-\tau')\dot{\Delta T}(\tau) d\tau. \qquad (11\text{-}176)$$

where K(t') = the time dependent relaxation modulus.

At this point one can draw some insight into Farris' constitutive theory. This insight can best be obtained by comparing the features of linear elastic, linear viscoelastic, and nonlinear homogeneous elastic or viscoelastic constitutive equations. For linear elastic materials the moduli are independent of strain magnitude and time. For linear viscoelastic materials the moduli are independent of strain magnitude but depend upon time, the time dependency being dictated by the convolution integral of the relaxation modulus and the strain rate history. For nonlinear homogeneous constitutive materials, the moduli are independent of strain magnitude and can depend upon time or strain history in an almost arbitrary manner. One sees that with respect to the history dependency of the moduli, linear viscoelastic and linear elastic materials are subclasses of homogeneous constitutive theory which is a subclass of the general permanent memory theory developed previously.

For the purpose of comparison, the radial bond stress and the inner bore hoop stress have been computed for two different materials and two different thermal inputs. The first material is a linear viscoelastic material with relaxation moduli Kt^n and the second material a nonlinear homogeneous material also with relaxation moduli Kt^n. For the second material the functional appearing in the stress-strain equation will be of the same form which Farris' found predicted accurately the response of propellants for monotonic inputs [9]

$$F\left[\int_0^{t'} \Delta T(\xi')\right] = K\left[\frac{||\Delta T||_\infty}{||\Delta||_p^r}\right]^q \Delta T(t) \qquad (11\text{-}177)$$

where $||\Delta T||_\infty = \max_{\tau=0} |\Delta t(\tau)|$ (11-178)

$$||\Delta T||_p = \left\{ \int_0^{\xi} (|\Delta T(\xi)|^p / a_T(\xi)) d\xi \right\}^{1/p} \quad (11\text{-}179)$$

Note that this last norm is with respect to reduced time.

The values of the parameters used in the analysis are summarized below.

Linear and Nonlinear Analysis

$$\text{Log } A_T = \frac{-8.86\ (T - T_s)}{183 + (T - T_s)}$$

$\alpha_p = 5 \times 10^{-5}\ ^\circ F^{-1}$

$\alpha_c = 5 \times 10^{-6}\ ^\circ F^{-1}$

K = 1500

b = 4

a = 1

Relaxation modulI = $1500.\ (t/A_T)^{-.2}$

Linear Viscoelastic Analysis

$$F\left[\Delta T(\xi')\right]_0^{t'} = \int_0^t (t'-\xi')^{-0.2}\ \dot{T}(\tau) d\tau$$

Nonlinear Homogeneous Analysis

$$F\left[\Delta T(\xi')\right]_0^{t'} = \left(\frac{||\Delta T||_\infty^q}{||\Delta T||_p^r} \right) \Delta T(t) \qquad q/p = 0.2$$

Figure 4 compares the two different thermal inputs considered in this analysis. The first, a simple ramp input, and the second an interrupted ramp input. In Figure 5, the inner bore hoop strain is given vs. time. It should be emphasized that the strains for the simple case investigated depend only on grain temperature and are independent of time. Also, the strain distribution within the cylinder is given exactly by linear elastic methods even though the constitutive equations used in the analysis could have been any linear or nonlinear representation. In Figures 6 through 9, the radial bond stresses and the inner bore hoop stresses are compared for the two different thermal histories. For comparative purposes, several values of p-q pairs were used, $p = 10,20,50$ and $q = 2,4,10$. From these computations we find that the nonlinear theory predicts much higher stresses than does the linear theory even though all materials have the same relaxation moduli and the same temperature shift function. Also, the time dependency of the stress decay is more marked in the nonlinear theory. These computations are in agreement with the data of Leeming [1] and Bornstein [2,3] which indicate that linear viscoelastic predictions fall far below observed propellant behavior in certain simultaneous cooling and straining tests.

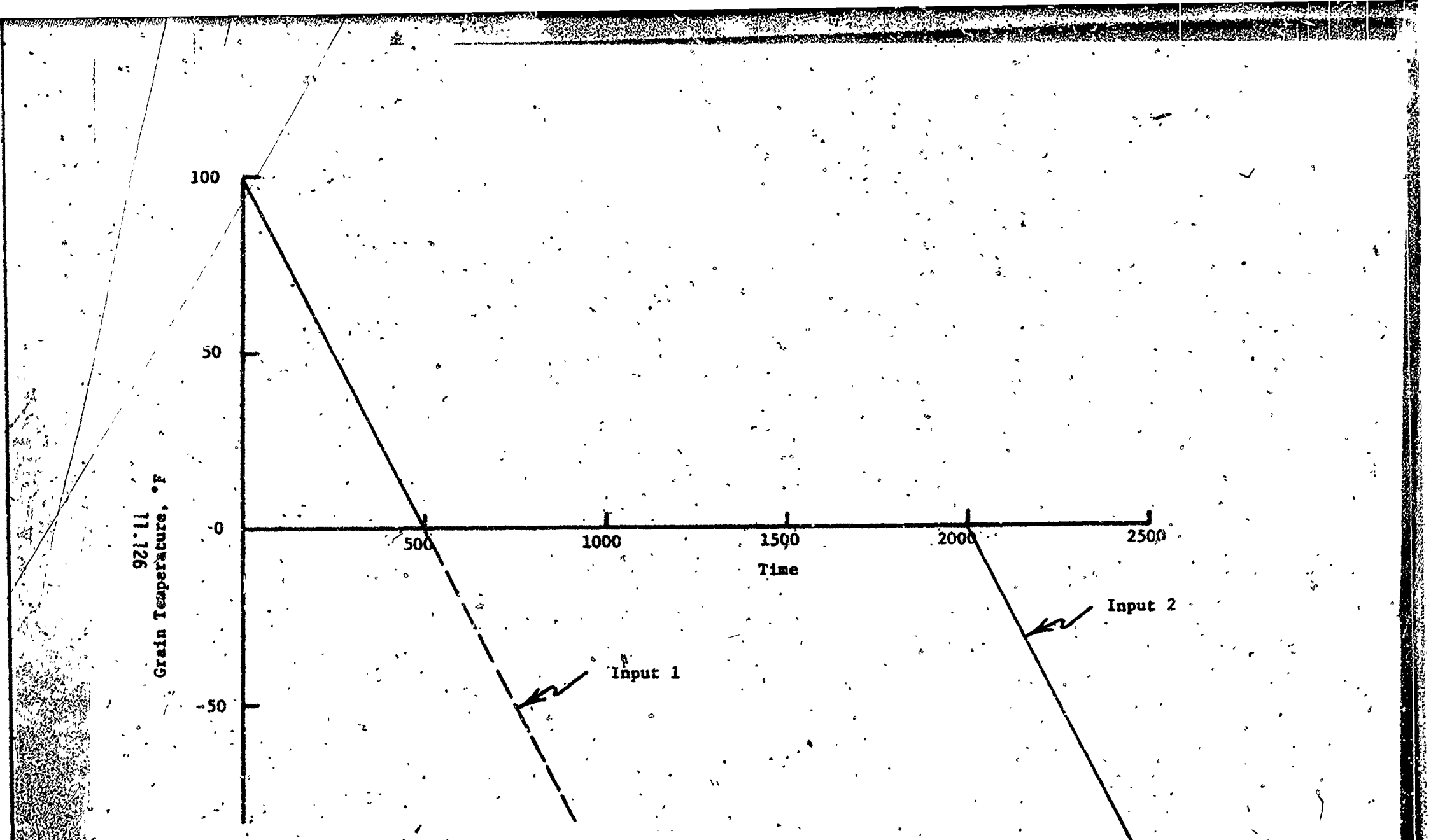

Figure 4. COMPARISON OF THERMAL HISTORIES USED IN STRESS ANALYSIS

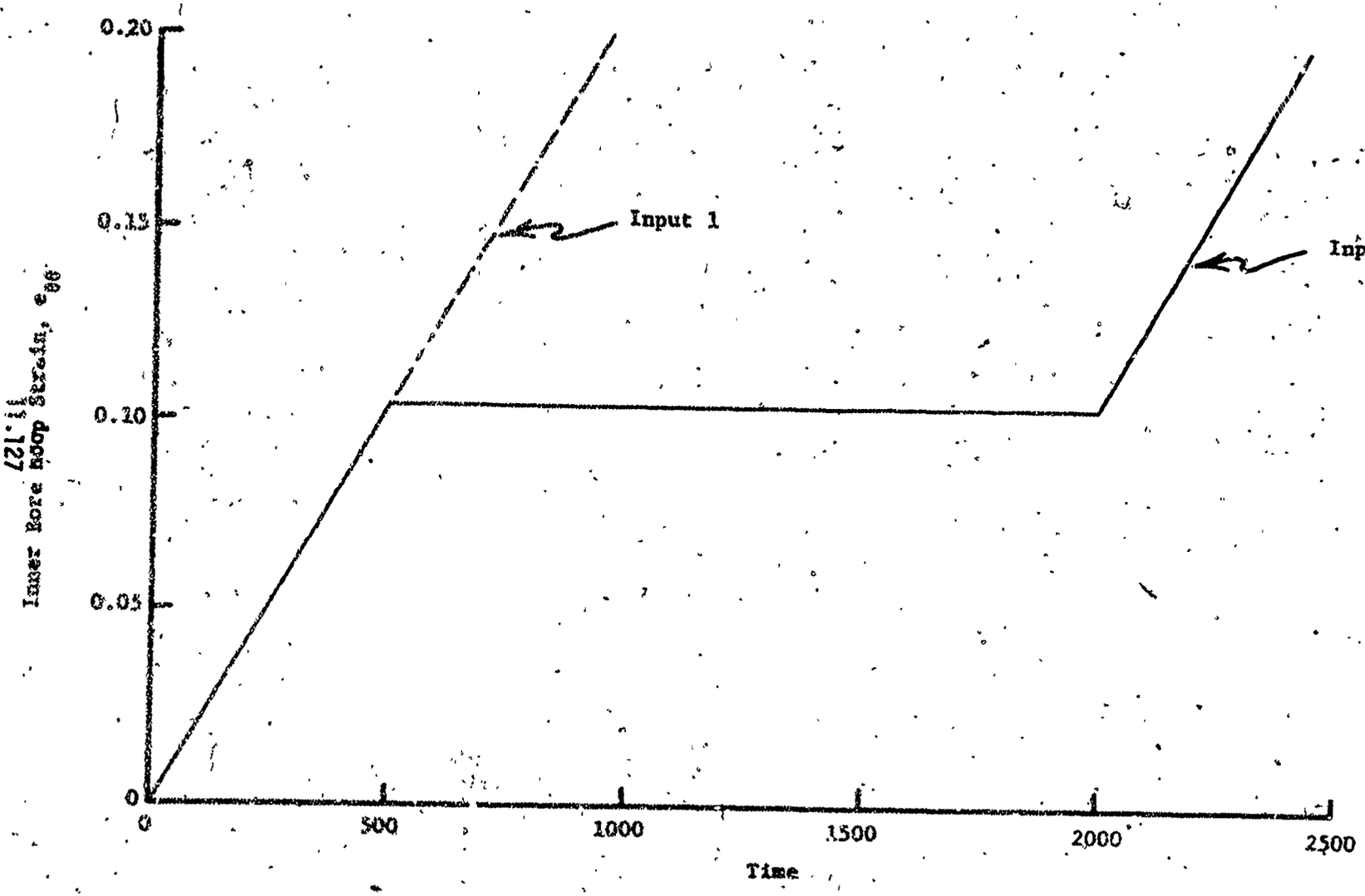

Figure 5. COMPARISON OF INNER BORE HOOP STRAIN FOR THERMAL HISTORIES USED IN STRESS ANALYSIS

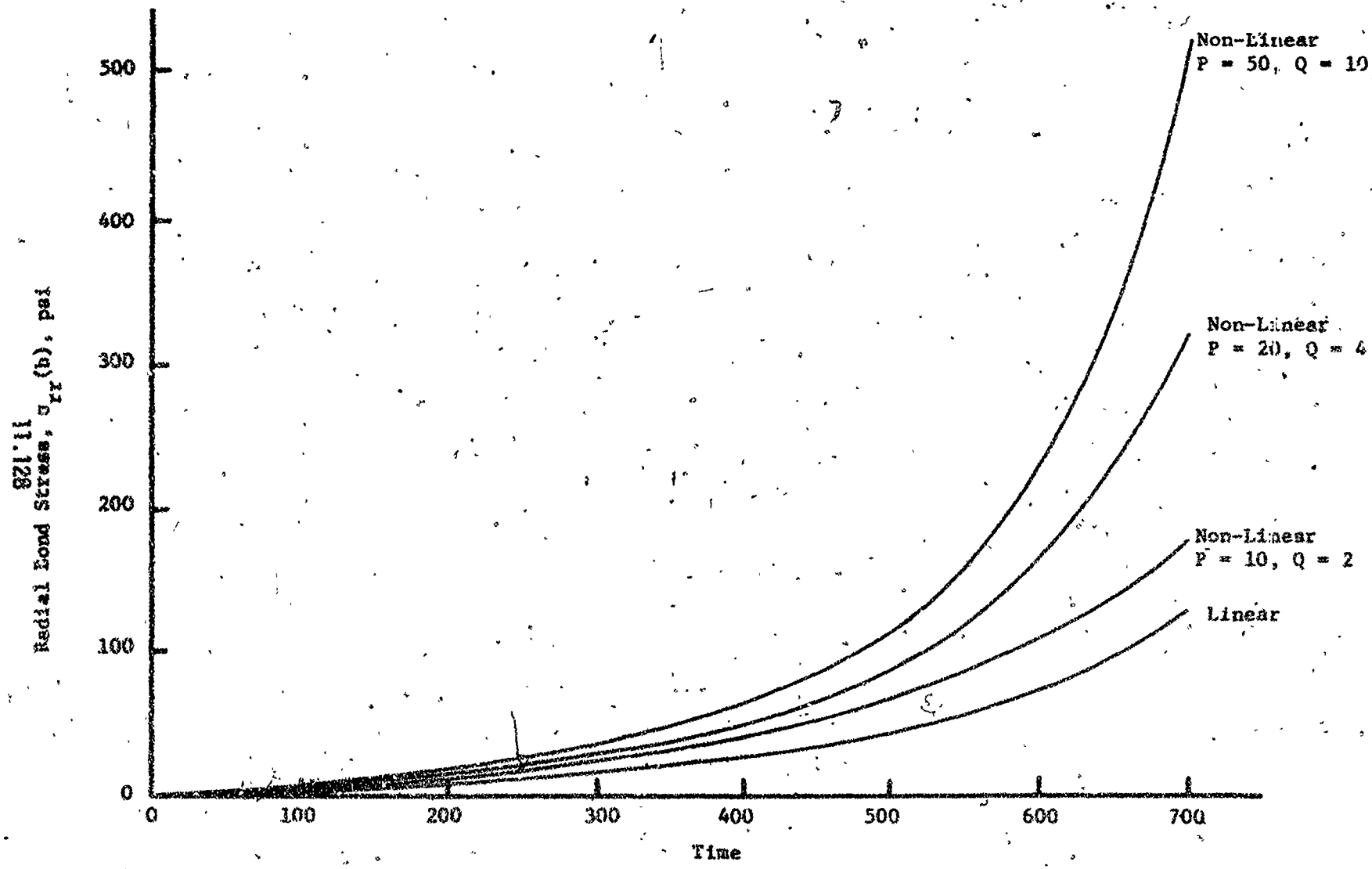

Figure 6. COMPARISON BETWEEN LINEAR AND NON-LINEAR VISCOELASTIC PREDICTIONS FOR RADIAL BOND STRESS USING THERMAL HISTORY 1

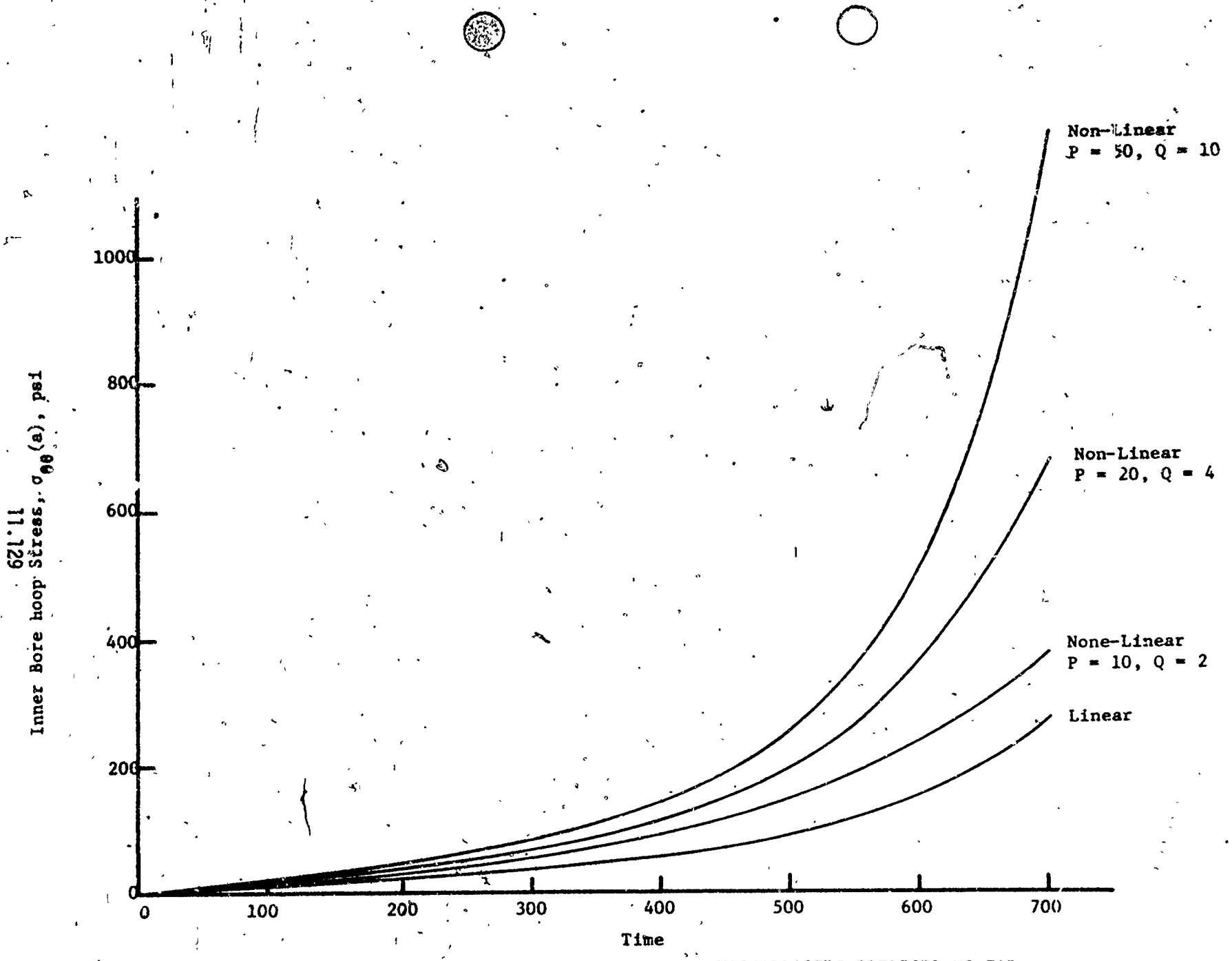

Figure 7. COMPARISON BETWEEN LINEAR AND NON-LINEAR VISCOELASTIC PREDICTIONS FOR INNER BORE HOOP STRESS USING THERMAL HISTORY 1

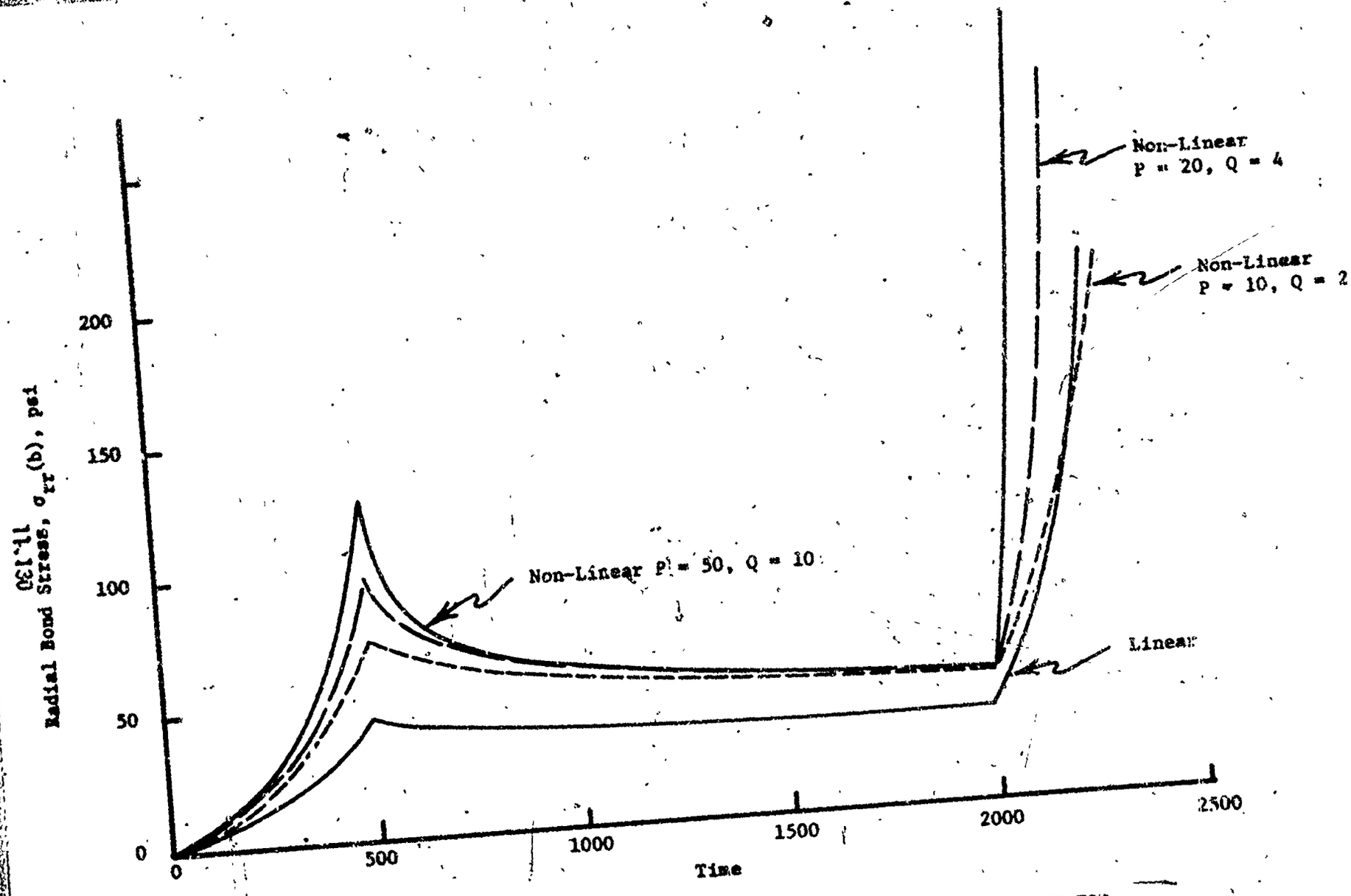

Figure 8. COMPARISON BETWEEN LINEAR AND NON-LINEAR VISCOELASTIC PREDICTIONS FOR RADIAL BOND STRESS USING THERMAL HISTORY 2

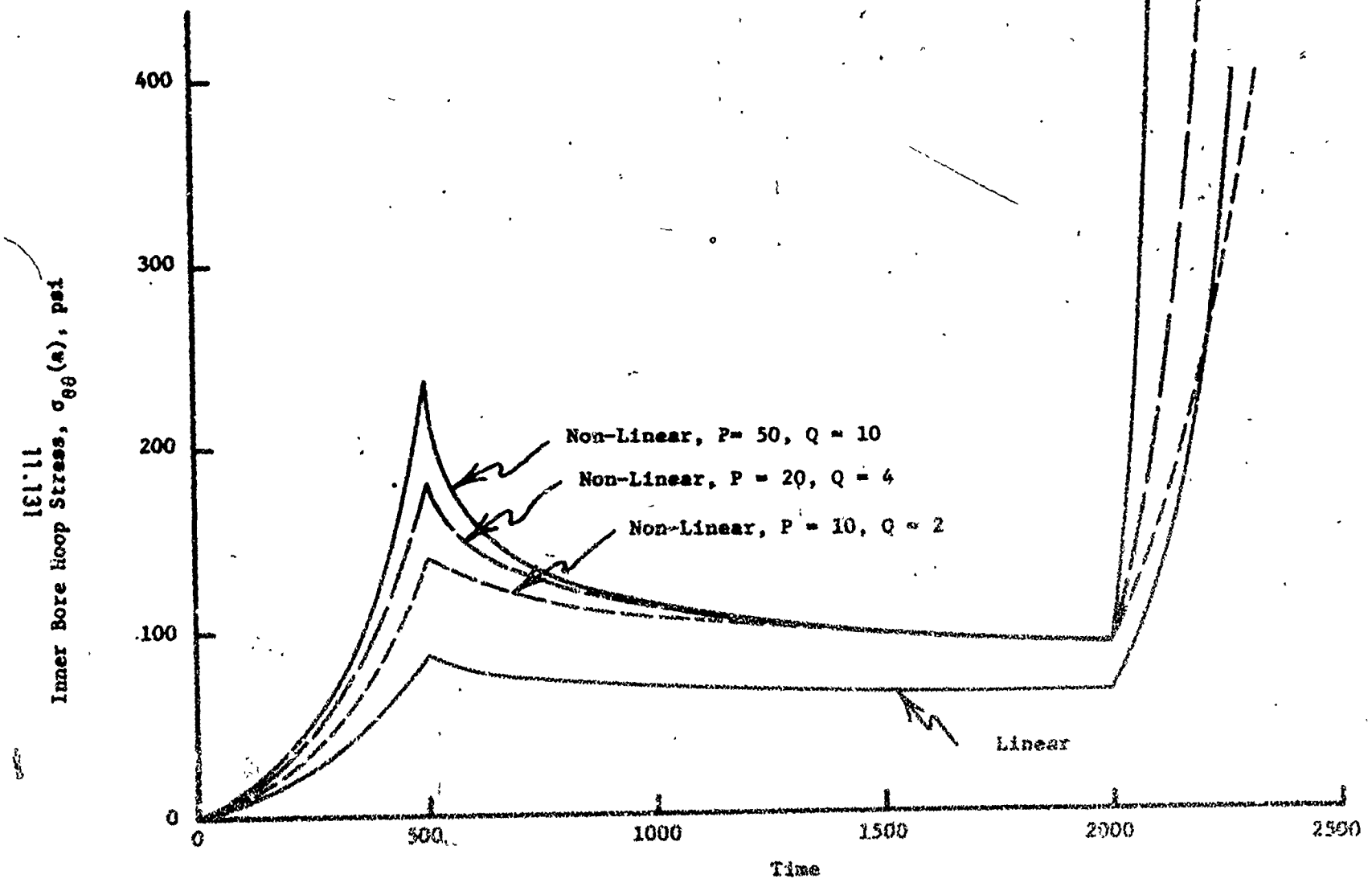

Figure 9. COMPARISON BETWEEN LINEAR AND NON-LINEAR VISCOELASTIC PREDICTIONS FOR INNER BORE HOOP STRESS USING THERMAL HISTORY 2

11.10 COMPARISON OF VARIOUS NONLINEAR METHODS OF ANALYSIS

While it is obviously clear that there exists no unique nonlinear representation for the nonlinear response of solid propellants. There are several specific methods being proposed.

The permanent memory method using norms appears to offer promise in the deformation zone, below which dewetting appears. Further comparisons are needed for this method.

Several of the other methods have, fortunately, been compared and evaluated by Stafford at the National Physical Laboratory in England [109]. Stafford's article is reproduced here as an appendix (11A) to this chapter in its entirety since it is an excellent review and rewriting it would not improve its concise sytle.

In this publication it becomes apparent as pointed out herein that strain and temperature shifting of one form or another constitutes the essence of the application of the various fading memory theories.

11.11 NOMENCLATURE

A_D = General shift factor
Ae = Strain shift factor
A_T = Temperature-time shift factor
B = Material body
b = Specific body force
b = Grain outer diameter
C = Right Cauchy-Green Tensor
e = Strain measure
F = Deformation gradient
f(t) = Proportional time function
f = General constitutive functional
f = General constitutive variable history
G = General constitutive function
G = Strain measure
g = Gradient of temperature
h(s) = Influence function
h_e = Material constant
h_1 = Material constant
h_2 = Material constant
h = Entropy functional
I_1 = First strain invariant
I_2 = Second strain invariant
I_3 = Third strain invariant
K = Kernal function
K_0 = Kernel function
K_1 = Kernel function
k(s) = Influence function
L = Velocity gradient
Lp = Lebesgue Norm = $||\cdot||_p = [\int_0^\infty ||\cdot||^p d\tau]^{1/p}$
L_∞ = Chebychev Norm = $||\cdot||_\infty$ = ess sup $|\cdot|$
M = Irreversible component of entropy
P = Pressure
P = Material response
p = Free entropy functional
Q = Heat flux vector
Q = Heat flux vector functional
q = Heat flex vector
r = Order of influence function
r = Heat supply per unit time and unit in ess
S = Total entropy
S = Piola-Kirchoff stress tensor
S = Stress functional
S = Dummy time
T = Symmetric Cauchy Stress Tensor
T = Temperature
t = time
X = Material position
x = Spatial position
r_θ = Polar coordinates
α_{10} = Linear coefficient of expansion of propellant
α_c = Linear coefficient of expansion of case
α_i = Internal state variables
α_{ξ_i} = Internal configuration variables
σ_{ij} = Kronecher delta
δ = Dissipation
ε = Strain
ε = Specific entropy
T_α = Retardation of a history
η = Specific entropy
κ_0 = Local reference configuration
θ = Temperature
ϕ = Kernal function
ξ = Reduced time
ψ = Specific free energy
ρ_0 = Reference configuration density
ρ, ρ' = Dummy time
ρ = Density
$\rho(f)$ = Function norm of f
σ = Stress
τ = Dummy time
μ = Lebesgue measure
χ = Deformation

11.12 REFERENCES

1. Lemming, H., et al.: "Solid Propellant Structural Test Vehicle and Systems Analysis", LPC Final Report No. 966-F(AFRPL-TR-70-10), Lockheed Propulsion Company, Redlands, California, March 1970.

2. Bornstein, G. A.: "Transient Thermoviscoelastic Analysis of An Uniaxial Bar","Bulletin of Subcommittee on Numerical Analysis of Solid Rocket Systems", Bulletin of 8th Mechanical Behavior Working Group, Vol. 1, CPIA Pub. 193, March 1970.

3. Bornstein, G. A.: "Structural Integrity of Air-Launched Solid Propellant Motors (U)", Indian Head Technical Report 297, Naval Ordnance Station, February 1970.

4. Farris, R. J.: "The Character of the Stress-Strain Function for Solid Propellants", Trans. Soc. Rheol., 12, pp. 281-301, 1968.

5. Farris, R. J.: "The Influence of Vacuole Formation on the Response and Failure of Highly Filled Polymers", Trans. Soc. Rheol., 12, pp. 315-534, 1968.

6. Huang, N. C. and Lee, E. H.: "Nonlinear Viscoelasticity for Short Time Ranges", J. Appl. Mech., Trans. ASME, p. 313, June 1966.

7. Martin, D. L.: "An Approximate Method of Analysis of Nonlinear Transient Thermoviscoelastic Behavior", Bulletin of the 8th JANNAF Mechanical Behavior Working Group Meeting, CPIA, Publ. 193, Vol. 1, p. 45, March 1970.

8. Fruendenthal, A. M.: "Strain-Sensitive Response of Filled Elastomers", Technical Report No. 24, Department of Civil Engineering and Engineering Mechanics, Columbia University, New York, December 1968.

9. Farris, R. J.: "Homogeneous Constitutive Equations for Materials with Permanent Memory", UTEC TH 70-083, PROJECT THEMIS Report AFOSR 70-1962 TR, University of Utah, June 1970.

10. Mullins, L. J.: "Effect of Stretching on the Properties of Rubber", J. Rubber Res., 16, pp. 275-289, 1947.

11. Mullins, L. J.: "Studies in the Absorption of Energy by Rubber", J. Rubber Res., 16, pp. 180-185, 1947.

12. Oberth, A. E.: "Principle of Strength Reinforcement in Filled Elastomers", Rub. Chem. S. Tech., 40, 5, pp. 1347-1363, December 1967.

13. Bueche, F.: "Molecular Basis for the Mullins Effect", J. Appl. Polymer Sci., 4, pp. 107-114, 1960.

14. Bueche, F.: "Mullins Effect and Rubber-Filler Interaction", J. Appl. Polymer Sci., 5, pp. 271-281, 1961.

15. Bueche, F.: "Mechanical Degradation of High Polymers", J. Appl. Polymer Sci., Vol. IV, No. 10, pp. 101-106, 1960.

16. Bueche, F. and Halpin, J. C.: "Molecular Theory for the Tensile Strength of Gum Elastomers", J. Appl. Phys., Vol. 35, No. 1, pp. 36-41, 1964.

17. Hsiao, C. C., Moghe, S. R., and Kausch von Schmeling, H. H. "Time-Dependent Mechanical Strength of Oriented Media", J. Appl. Phys., Vol. 39, No. 8, pp. 3857-3861, 1968.

18. Moghe, S. R., Kawatate, K., Cheung, J. B., and Hsiao, C. C.: "Mechanical Breakdown of Oriented Solids under Time Dependent Loads", Proceedings of the Fifth International Conference on Rheology, Kyoto, Japan, 1968.

19. DeVries, K. L. and Farris, R. J.: "The Effect of Strain in Homogeneities on Deformation and Fracture", UTEC DO 69-027 (Appendix to UTEC DO 69-029), University of Utah, March 1969.

20. Farris, R. J.: "Applications of Viscoelasticity to Filled Materials", Master's Thesis, Department of Civil Engineering, University of Utah, June 1969.

21. Fitzgerald, J. E.: "High Solids Loading in Solid Propellers", UTEC TH 69-073e, TASK V of PROJECT THEMIS ANNUAL REPORT UTEC TH 69-073, University of Utah, September 1969.

22. Farris, R. J. and Fitzgerald, J. E.: "Deficiencies of Viscoelastic Theories as Applied to Solid Propellants", Bulletin JANNAF Mechanical Behavior Working Group, 8th Meeting 1969, CPIA Publication No. 193, Vol. 1, March 1970.

23. Fitzgerald, J. E.: "Thermodynamic Restrictions in Non-Linear Rate Type Materials", Pure and Appl. Chem., Vol. 22, pp. 357-368 (Discussion to above), 1970.

24. Green, A. E. and Rivlin, R. S.: "The Mechanics of Non-Linear Materials with Memory, Part One", Arch. Rat. Mech. Anal., 1, pp. 1-21, 1959.

25. Truesdell, C. A. and Noll, W.: "The Nonlinear Field Theories of Mechanics", Encyclopaedia of Physics, Vol. 3, Part 3 (Edited by S. Flügge), Springer-Verlag, Inc., Berlin, 1965.

26. Coleman, B. D. and Noll, W.: "An Approximation Theorem for Functionals, with Applications in Continuum Mechanics", Arch. Rational Mech. Anal., Vol. 6, pp. 355-370, 1960.

27. Coleman, B. D. and Mizel, V. J.: "Norms and Semi-Groups in the Theory of Fading Memory", Arch. Rational Mech. Anal., Vol. 23, pp. 87-123, 1966.

28. Coleman, B. D. and Mizel, V. J.: "On the General Theory of Fading Memory", Arch. Rational Mech. Anal., Vol. 29, pp. 18-31, 1968.

29. Coleman, B. D. and Mizel, V. J.: "A General Theory of Dissipation in Materials with Memory", Arch. Rational Mech. Anal., Vol. 27, pp. 255-274, 1969.

30. Fitzgerald, J. E.: "Thermomechanical Coupling in Viscoelastic Materials", Discussion portion of above, International Conference on Structure, Solid Mechanics, and Engineering Design in Civil Engineering Materials, Southampton, England, April 1969, to be published by John Wiley and Sons, 1971.

31. Hufferd, W. L.: "Thermodynamics of Materials with Memory", UTEC TH 70-076, PROJECT THEMIS Report AFOSR 70-1961 TR, University of Utah, May 1970.

32. Farris, R. J.: "Applications of Non-Linear Viscoelasticity and Cumulative Damage (A Realistic Evaluation of Real Propellant Behavior)", Second Quarterly Report, 1565-26-Q-2, Aerojet Solid Propulsion Company, October 1970.

33. Fitzgerald, J. E. and Farris, R. J.: "Characterization and Analysis Methods for Nonlinear Viscoelastic Materials", PROJECT THEMIS Report, UTEC TH 70-204, University of Utah, November 1970.

34. Coleman, B. D. and Noll, W.: "Foundations of Linear Viscoelasticity", Rev. Modern Physics, Vol. 33, pp. 239-249, 1961.

35. Lianis, G.: "Nonlinear Thermorheologically Simple Materials", Proceedings of the Fifth International Congress on Rheology, Kyoto, Japan, 1968.

36. Lianis, G.: "Application of Thermodynamics of Viscoelastic Materials with Fading Memory - Integral Constitutive Equations", Int. J. Nonlinear Mechanics, Vol. 5, No. 1, pp. 23-34, 1970.

37. Lianis, G.: "Integral Constitutive Equations of Nonlinear Thermo-Viscoelasticity", Purdue University Report A & ES 65-1, January 1965.

38. McGuirt, C. W. and Lianis, G.: "Experimental Investigation of Nonlinear, Non-Isothermal Viscoelasticity", Int. J. Engng. Sci., Vol. 7, pp. 579-599, 1969.

39. Lai, J. S. Y. and Findley, W. N.: "Stress Relaxation of Nonlinear Viscoelastic Material Under Uniaxial Strain", Trans. Soc. Rheol., 12, p. 259, 1968.

40. Onaran, K. and Findley, W. N.: "Combined Stress-Creep Experiments on a Nonlinear Viscoelastic Material to Determine the Kernel Functions for a Multiple Integral Representation of Creep", Trans. Soc. Rheol., 1, pp. 299-327, 1965.

41. Lockett, F. J.: "Creep and Stress-Relaxation Experiments for Nonlinear Materials", Int. J. Engng. Sci., Vol. 3, pp. 59-75, 1965.

42. Lockett, F. J. and Stafford, R. O.: "On Special Constitutive Relations in Nonlinear Viscoelasticity", Intern. J. Engng. Sci., 7, pp. 917-930, 1969.

43. Gottenberg, W. G., Bird, J. O., and Agrawal, G. L.: "An Experimental Study of a Nonlinear Viscoelastic Solid in Uniaxial Tenston", J. Appl. Mech. Trans. ASME, 1, 1969.

44. Schapery, R. A.: "A Theory of Nonlinear Thermoviscoelasticity Based on Irreversible Thermodynamics", Proc. Fifth U. S. Nat. Cong. of Appl. Mech., ASME, pp. 511-530, 1966.

45. Schapery, R. A.: "On the Characterization of Nonlinear Viscoelastic Materials", Polymer Eng. Sci., 9, pp. 295-310, 1969.

46. Schapery, R. A.: "Further Development of a Thermodynamic Constitutive Theory: Stress Formulation", Purdue University Report AA S ES 69-2, February 1969.

47. Schapery, R. A.: "On a Thermodynamic Constitutive Theory and Its Application to Various Nonlinear Materials", Proceedings of the IUTAM Symposium, East Kilbride, June 1968.

48. Dong, R. G.: "Studies in Mechanics of Nonlinear Solids", Ph.D. Dissertation, University of California, Livermore, Lawrence Radiation Lab, 1964.

49. Dong, R. G.: "Constitutive Equations Involving Chronological Variables", University of California Radiation Laboratory Report 12228, Livermore, California, December 1964.

50. Onat, E. T.: "Description of Mechanical Behavior of Inelastic Solids", Proceedings of the 5th U. S. National Congress on Applied Mechanics, pp. 421-434, 1966.

51. Coleman, B. D. and Owen, D. R.: "On the Thermodynamics of Materials with Memory", Arch. Rat. Mech. Anal., Vol. 36, No. 4, pp. 245-269, 1970.

52. Truesdell, C.: Six Lectures on Modern Natural Philosophy, Springer-Verlag, Inc., New York, 1966.

53. Owen, D. R. and Williams, W. O.: "On the Time Derivatives of Equilibrated Response Functions", Arch. Rational Mech. Anal., Vol. 33, pp. 288-306, 1969.

54. Owen, D. R.: "Thermodynamics of Materials with Elastic Range", Arch. Rational Mech. Anal., Vol. 31, pp. 91-112, 1968.

55. Green, A. E., Rivlin, R. S. and Spence, A. J. M.: "The Mechanics of Non-linear Materials with Memory, Part II", Arch. Rational Mech. Anal., Vol. 3, pp. 82-90, 1959.

56. Green, A. E. and Rivlin, R. S.: "The Mechanics of Non-linear Materials with Memory, Part III", Arch. Rational Mech. Anal., Vol. 4, pp. 387-404, 1960.

58. Rivlin, R. S.: "Nonlinear Viscoelastic Solids", SIAM Review, Vol. 7, pp. 323-340, 1964.

57. Pipkin, A. C.: "Small Finite Deformations of Viscoelastic Solids", Rev. Modern Physics, Vol. 36, pp. 1034-1041, 1964.

59. Pipkin, A. C. and Rogers, T. G.: "A Non-linear Integral Representation for Viscoelastic Behavior", J. Mech. Phys. Solids, Vol. 16, pp. 59-72, 1968.

60. Oldroyd, J. G.: "On the Formulation of Rheological Equations of State", Proc. Roy. Soc. (London), Series A200, pp. 523-541, 1950.

61. Onat, E. T. and Wang, T. T.: "Integral Representation of Creep and Rate Sensitivity in Metals", Brown University Technical Report Nonr 562(20)39, March 1965.

62. Wang, T. T. and Onat, E. T.: "Non-linear Mechanical Behavior of 1100 Aluminum at 300°F", Acta Mechanica, Vol. 5, pp. 54-70, 1968.

63. Wang, T. T.: "Explicit Forms of the Material Functions for Certain Non-linear Materials with Memory", Polytechnic Institute of Brooklyn Report Nonr 839(32)(PIBAL912), February 1966.

64. Herrmann, L. R.: "On A General Theory of Viscoelasticity", J. Franklin Institute, Vol. 280, pp. 244-255, 1965.

65. Christensen, R. M. and Naghdi, P. M.: "Linear Non-isothermal Viscoelastic Solids", Acta Mechanica, Vol. 3, pp. 1-12, 1967.

66. Chacon, R. V. S. and Rivlin, R. S.: "Representation Theorems in the Mechanics of Materials with Memory", Z. angew. Math. Phys., Vol. 15, pp. 444-447, 1965.

67. Hunter, S. C.: "Tentative Equations for the Propagation of Stress, Strain and Temperature Fields in Viscoelastic Solids", J. Mech. Phys. Solids, Vol. 9, pp. 39-51, 1961.

68. Coleman, B. D.: "Thermodynamics of Materials with Memory", Arch. Rational Mech. Anal., Vol. 17, pp. 1-46, 1964.

69. Coleman, B. D.: "On Thermodynamics, Strain Impulses, and Viscoelasticity", Arch. Rational Mech. Anal., Vol. 17, pp. 230-254, 1964.

70. Wang, C. C.: "Stress Relaxation and the Principle of Fading Memory", Arch. Rational Mech. Anal., Vol. 18, pp. 117-126, 1965.

71. Wang, C. C.: "The Principle of Fading Memory", Arch. Rational Mech. Anal., Vol. 18, pp. 343-366, 1965.

72. Wang, C. C. and Bowen, R. M.: "On the Thermodynamics of Non-linear Materials with Quasi-elastic Response", Arch. Rational Mech. Anal., Vol. 22, pp. 79-99, 1966.

73. Luxemburg, W. A. J. and Zaanen, A. C.: "Compactness of Integral Operators in Banach Function Spaces", Math. Annalen, Vol. 149, pp. 150-180, 1963.

74. Luxemburg, W. A. J. and Zaanen, A. C.: "Some Examples of Normed Köthe Spaces", Math. Annalen, Vol. 162, pp. 337-350, 1966.

75. Duhem, M. P.: "De L'Aimantation par Influence", 1re Thése á la faculté des sciences de Paris, Gauthier-Villars et fils, Paris, p. 3, 30 October 1888.

76. Fitzgerald, J. E.: MSC Thesis, University College, Cork, Ireland, May 1970.

77. Prigogine, I.: "Etude thermodynamique des phénomenes irréversibles", Dunod, Paris-Liége, 1947. or "Introduction to Thermodynamics of Irreversible Processes", 3rd. Edition, John Wiley and Sons, New York, 1967.

78. Meixner, J.: "T. I. P. Has Many Faces", Proc. I.V.T.A.M. Symposia, Vienna, H. Parkus, L. I. Sedov, Springer-Verlag, Wien, New York.

79. Hufford, W. L. and Fitzgerald, J. E.: "Thermodynamic Restrictions in Simple Rate Materials", University of Utah Report UTEC TH 70-020, January 1970.

80. Truesdell, C. A.: Rational Thermodynamics, McGraw-Hill Book Co., New York, 1970.

81. Dillon, O. W., Jr.: "An Experimental Study of the Heat Generated During Torsional Oscillations", J. Mech. Phys. Solids, Vol. 10, pp. 235-244, 1962.

82. Dillon, O. W., Jr.: "Coupled Thermoplasticity", J. Mech. Phys. Solids, Vol. 11, pp. 21-33, 1963.

83. Dillon, O. W., Jr.: "The Heat Generated During the Torsional Oscillations of Copper Tubes", Int. J. Solid Structures, Vol. 2, pp. 181-204, 1966.

84. Dillon, O. W., Jr. and Tauchert, T. R.: "The Experimental Technique for Observing the Temperatures Due to the Coupled Thermoelastic Effect", Int. J. Solid Structures, Vol. 2, pp. 385-391, 1966.

85. Cost, T. L.: "Thermomechanical Coupling Phenomeno in Non-isothermal Viscoelastic Solids", Rohm and Haas Company Report S-226, August 1969.

86. Martin, A. D. and Mizel, V. J.: "A Representation for Certain Non-linear Functionals", Arch. Rational Mech. Anal., Vol. 15, pp. 353-367, 1964.

87. Chacon, R. V. and Friedman, N.: "Additive Functionals", Arch. Rational Mech. Anal., Vol. 18, pp. 230-240, 1965.

88. Friedman, N. and Katz, M.: "A Representation Theorem for Additive Functionals", Arch. Rational Mech. Anal., Vol. 21, pp. 49-57, 1966.

89. Mizel, V. J. and Sundaresan, K.: "Representation of Additive and Biadditive Functionals", Arch. Rational Mech. Anal., Vol. 30, pp. 102-126, 1968.

90. Berstein, B., Kearsley, E. A. and Zapas, L. J.: "A Study of Stress Relaxation with Finite Strain", Trans. Soc. Rheology, Vol. 7, 1963.

91. Crochet, M. J. and Naghdi, P. M.: "A Class of Simple Solids with Fading Memory", University of California, Berkeley, College of Engineering Report No. AM-68-9, December 1968.

92. Crochet, M. J. and Naghdi, P. M.: "On Thermorheologically Simple Solids", University of California, Berkeley, College of Engineering Report No. AM-69-3, January 1969.

93. Green, A. E. and Naghdi, P. M.: "A Thermodynamic Development of Elastic-Plastic Continua", Irreversible Aspects of Continuum Mechanics and Transfer of Physical Characteristics in Moving Fluids, (edited by H. Parkus and L. I. Sedov), pp. 132-145, Springer-Verlag, Inc., New York, 1968.

94. Green, A. E. and Naghdi, P. M.: "A Class of Viscoelastic-Plastic Media", University of California, Berkeley, College of Engineering Report No. AM-67-2, March 1967.

95. Valanis, K. C.: "On the Thermodynamic Foundation of Plasticity", Iowa State University, Engineering Research Insitute Report No. 67, May 1968.

96. Valanis, K. C.: "The Viscoelastic Potential and Its Thermodynamic Foundations", J. Math. Phys., Vol. XLVII, pp. 262-275, 1968.

97. Meixner, J.: "On the Foundation of Thermodynamics of Processes", Paper presented at the International Symposium "A Critical Review of the Foundations of Relativistic and Classical Thermodynamics", University of Pittsburgh, 7-8 April 1969.

98. Meixner, J.: "Consequences of an Inequality in Nonequilibrium Thermodynamics", J. Appl. Mech., pp. 481-488, 1966.

99. Meixner, J.: "Processes in Simple Thermodynamic Materials", Arch. Rational Mech. Anal., Vol. 33, pp. 33-53, 1969.

100. Coleman, B. D. and Mizel, V. S.: "Existence of Entropy as A Consequence of Asymptotic Stability", Arch. Rational Mech. Anal., Vol. 25, pp. 243-270, 1967.

101. Coleman, B. D. and Mizel, V. J.: "On Thermodynamic Conditions for the Stability of Evolving Systems", Arch. Rational Mech. Anal., Vol. 29, pp. 105-113, 1968.

102. Coleman, B. D. and Mizel, V. J.: "On the Stability of Solutions of Functional - Differential Equations", Arch. Rational Mech. Anal., Vol. 30, pp. 173-196, 1968.

103. Coleman, B. D. and Dill, E. H.: "On the Stability of Certain Motions of Incompressible Materials with Memory", Arch. Rational Mech. Anal., Vol. 30, pp. 197-224, 1968.

104. Coleman, B. D. and Greenberg, J. M.: "Thermodynamics and the Stability of Fluid Motion", Arch. Rational Mech. Anal., Vol. 25, pp. 321-341, 1967.

105. Hofelich, F.: "On the Definition of Entropy for Non-equilibrium States", Z. Physik, Vol. 226, pp. 395-408, 1969.

APPENDIX 11A

ON MATHEMATICAL FORMS FOR THE MATERIAL FUNCTIONS IN NONLINEAR VISCOELASTICITY

By

R. O. Stafford

Division of Numerical and Applied Mathematics
National Physical Laboratory
Teddington, Middlesex

Reproduced from the

Journal of Mechanics and Physics of Solids

Vol. 17, pp. 339 to 358, 1969

With permission of the copyright

owner, -- Pergamon Press,

and the author.

J. Mech. Phys. Solids, 1969, Vol. 17, pp. 339 to 358. Pergamon Press. Printed in Great Britain.

ON MATHEMATICAL FORMS FOR THE MATERIAL FUNCTIONS IN NONLINEAR VISCOELASTICITY

By R. O. Stafford
Division of Numerical and Applied Mathematics, National Physical Laboratory
Teddington, Middlesex

(*Received* 18*th December* 1968)

Summary

Three special forms of material functions are introduced into the Green–Rivlin constitutive equations of nonlinear viscoelasticity. Two of these reduce the third-order equations to single integral forms, rationally and experimentally derived by others. Published creep and stress-relaxation data are analysed using both the proposed and previously published constitutive equations, particular attention being given to multi-step data. Specific results show the limits of applicability of the third-order constitutive relations for the materials considered.

1. Introduction

During the last decade a number of general constitutive relations have been formulated to represent the mechanical behaviour of nonlinear viscoelastic materials. In particular, the rational theories listed by Truesdell and Noll (1965), as well as those derived by Schapery (1966) from irreversible thermodynamics, are capable of representing a large variety of real materials under quite general deformations.

However, these general theories are too complicated for practical applications; even the determination of material parameters may be beyond present testing procedures. Thus, simplification or specialization is a prerequisite to practical applicability. A number of writers have given some attention to simplifications. Huang and Lee (1966) have developed forms applicable to very short times, and Pipkin and Rogers (1968) developed an integral series arranged so that experimental data may be incorporated directly. The present paper is intended as an additional step in the area of simplifications. Particular attention is directed to reducing the evaluation of material functions to simple (one-step) creep or stress-relaxation tests. Additional tests are considered which partly determine the ability of a constitutive equation to predict general deformations of a specific material.

We shall consider primarily the isothermal theory of (initially) isotropic simple materials in the explicit form of a third-order integral polynomial. This formulation is chosen because it includes the effects of physical and geometric nonlinearity in a general fashion, and is the lowest order nonlinear theory applicable to general deformations. Recently these integral polynomial equations have received considerable attention. Lockett (1965) has shown that in principle all twelve material functions can be determined by experiment, but Lifshitz and Kolsky (1966) have found these tests exceedingly difficult to perform accurately.

Reprinted with the kind permission of the copyright owner, Pergamon Press, and the author.

11.145

One may divide simplifications into two not-unrelated areas of kinematic and physical limitations. In a previous paper, Lockett and Stafford (1969) restricted the constitutive relations to certain classes of deformation fields, and specific results were given for creep and stress-relaxation formulations of plane stress and plane strain of an incompressible material. Considered here are some physical restrictions obtained by making bold assumptions on the mathematical form of the material functions, assumptions which reduce the experimental programs to single-step tests. Some justification is attempted by providing some explanation of the limitations, and the connection to other constitutive relations is indicated. However, the final justification is applicability, so creep and stress-relaxation data from several sources is analysed in Sections 4 and 5. For reasons developed in Section 3.4, particular attention is given to multi-step data.

2. Review of Previous Results

The equations below presume that there is an initial configuration for which the material is isotropic, homogeneous, unstressed and unstrained. Also, the material is assumed to be simple, i.e. the stress σ_{ij} at a given particle at time t depends only upon the history of the displacement gradients $F_{ij} = \partial y_i(\mathbf{X}, \tau)/\partial X_j$ at that particle. Coordinates $X_i\ (i = 1, 2, 3)$ denote the initial position with respect to a fixed cartesian system, and $y_i(\mathbf{X}, \tau)$ is the particle position at time τ. In functional form the constitutive relation can be written as

$$\mathbf{Q}(t) = \underset{\tau=-\infty}{\overset{t}{\mathbf{D}}}\{\mathbf{F}(\tau)\}, \tag{2.1}$$

where matrices $\mathbf{Q}$ and $\mathbf{F}$ represent a stress measure $\boldsymbol{\Sigma}$ and strain $\mathbf{E}$ and $\mathbf{D}$ is a matrix functional which depends on the definition chosen. Stress and strain are defined by

$$\boldsymbol{\Sigma} = \begin{cases} \mathbf{R}^T \boldsymbol{\sigma} \mathbf{R} \\ \mathbf{F}^T \boldsymbol{\sigma} \mathbf{F} \end{cases}, \quad \mathbf{F} = \mathbf{R}\mathbf{U}, \quad 2\mathbf{E} = \mathbf{U}^2 - \mathbf{I} = \mathbf{F}^T\mathbf{F} - \mathbf{I}. \tag{2.2}$$

The decomposition of $\mathbf{F}$ expresses the idea that the deformation may be considered to be a pure stretch $\mathbf{U}$ followed by a rigid rotation $\mathbf{R}$.

An explicit form may be given to (2.1) (Green and Rivlin, 1957) by assuming that it can be expressed as an integral polynomial, and the most general form for an initially isotropic material is, to third order,

$$\begin{aligned}\mathbf{Q}(t) = &\int_{-\infty}^{t} \{\mathbf{I}\,\psi_1 T_1 + \psi_2 \mathbf{M}_1\}\, d\tau_{(1)} \\ &+ \int_{-\infty}^{t}\int \{\mathbf{I}\,\psi_3 T_1 T_2 + \mathbf{I}_4\,\psi\, T_{12} + \psi_5 T_1 \mathbf{M}_2 + \psi_6 \mathbf{M}_1 \mathbf{M}_2\}\, d\tau_{(2)} \\ &+ \int_{-\infty}^{t}\int\int \{\mathbf{I}\,\psi_7 T_{123} + \mathbf{I}\,\psi_8 T_1 T_{23} + \psi_9 T_1 T_2 \mathbf{M}_3 + \psi_{10} T_{13} \mathbf{M}_3 + \\ &\qquad + \psi_{11} T_1 \mathbf{M}_2 \mathbf{M}_3 + \psi_{12} \mathbf{M}_1 \mathbf{M}_2 \mathbf{M}_3\}\, d\tau_{(3)}. \end{aligned} \tag{2.3}$$

In this relation,

$$M_\alpha = \dot{\mathbf{P}}(\tau_\alpha), \quad T_\alpha = \mathrm{tr}(M_\alpha), \quad T_{\alpha\beta} = \mathrm{tr}(M_\alpha M_\beta),$$

$$T_{\alpha\beta\gamma} = \mathrm{tr}(M_\alpha M_\beta M_\gamma), \quad d\tau_{(N)} = d\tau_1 d\tau_2 \ldots d\tau_N,$$

where the superposed dot denotes a material time derivative. Material functions ψ_1 and ψ_2 are functions of one variable s_1; $\psi_3, \ldots, \psi_6$ are functions of s_1, and s_2, $\psi_7, \ldots, \psi_{12}$ are functions of s_1, s_2 and s_3; where $s_\alpha = t - \tau_\alpha$. It has been shown by LOCKETT (1965) that the following symmetries may be assumed without loss of generality:

$$\left.\begin{aligned} &\psi_3, \psi_4, \psi_5, \psi_9, \psi_{10} = s(1, 2), \quad \psi_7 = s(1, 2, 3), \\ &\psi_6, \psi_{11} = s(2, 3), \quad \psi_{12} = s(1, 3), \end{aligned}\right\} \tag{2.4}$$

where $s(i, j)$ denotes symmetry in the ith and jth arguments. A creep formulation is given by defining $\mathbf{P} = \boldsymbol{\Sigma}$ and $\mathbf{Q} = \mathbf{E}$; and a stress relaxation formulation is given by setting $\mathbf{P} = \mathbf{E}$ and $\mathbf{Q} = \boldsymbol{\Sigma}$.

In a one-dimensional deformation which depends on one spatial coordinate X, and the displacement vector is in the x-direction, the constitutive equation reduces to

$$Q = \int_{-\infty}^{t} J(s_1) \dot{P}_1 \, d\tau_{(1)} + \int_{-\infty}^{t}\int K(s_1, s_2) \dot{P}_1 \dot{P}_2 \, d\tau_{(2)} + \int_{-\infty}^{t}\int\int L(s_1, s_2, s_3) \dot{P}_1 \dot{P}_2 \dot{P}_3 \, d\tau_{(3)}. \tag{2.5}$$

Note that Lagrangian and classical strain are related by

$$E = \epsilon + \tfrac{1}{2}\epsilon^2,$$

and either may be used in (2.5); of course, the material functions are different in each case, and a third-order theory in E is not identical with one in ϵ.

In addition to (2.5) we will use one other simplification of (2.3), originally developed by PIPKIN (1964). By employing a geometrical condition of zero volume change, he developed a four-function stress-relaxation formulation for incompressible materials. The two alternative forms are

$$\left.\begin{aligned} \mathbf{R}^T \sigma \mathbf{R} \\ \mathbf{F}^T \sigma \mathbf{F} \end{aligned}\right\} = \int_{-\infty}^{t} \psi_2 \mathbf{M}_1 \, d\tau_{(1)} + \int_{-\infty}^{t}\int \psi_8 \mathbf{M}_1 \mathbf{M}_2 \, d\tau_{(2)} + \int_{-\infty}^{t}\int\int (\psi_{10} T_{12} \mathbf{M}_3 + \psi_{12} \mathbf{M}_1 \mathbf{M}_2 \mathbf{M}_3) \, d\tau_{(3)}. \tag{2.6}$$

The material functions are different for each form, and

$$\mathbf{P} = \mathbf{E}, \quad \sigma = \mathbf{s} + p\mathbf{1},$$

where $\mathbf{s}$ and p denote deviatoric stress and hydrostatic pressure.

In a recent paper, LOCKETT and STAFFORD (1969) have shown that an equation similar to (2.6) could be derived for the creep formulation, and the conditions of plane strain and plane stress reduced these constitutive equations to relations involving only three material functions. Experimental programs for evaluating the 'plane' equations were described; however, the number of tests required

indicates that these equations may still be too complex for routine practical application. Additional kinematic restrictions would yield a result only applicable to very special deformations. Hence, we are led to suspect that the representation of physical behaviour contained in the theories may be too general, and the response of many real materials may be described by less general material functions.

Also, it should be emphasized that third-order equations like (2.3), (2.5) and (2.6) are restricted *a priori* to small strain (or stress) rates and to nonlinear materials which do not differ greatly from their linear counterparts. Since an equation connecting shear stress and shear strain must be an odd-order relation, these third order approximations are the lowest order theories which contain nonlinear shear behaviour.

3. Special Forms of Material Functions

Considered in the following are three simplifications named for their effect. They may be applied to either the creep or the stress-relaxation formulation. The criterion for selection is that the resulting equation can be experimentally determined from one-step tests. Present experimental techniques for multi-step tests cannot accurately determine the second- and higher-order material functions, particularly at short times. Although these simplifications impose no explicit additional restrictions, the effect may be to limit deformation further than is implied by the third-order expansion.

3.1. *Physical linearity*

A physically linear viscoelastic material is such that the response is a linear functional of history. One method of reducing the multiple integrals to single integrals is to assume that the material functions may be expressed as a sum of single argument functions, viz.,

$$\psi_i(\alpha_1, \alpha_2, \ldots, \alpha_n) = \frac{1}{n}\left[f_i^{(1)}(\alpha_1) + f_i^{(2)}(\alpha_2) + \ldots + f_i^{(n)}(\alpha_n)\right]. \quad (3.1)$$

Some of these functions will be related by the symmetry conditions (2.4); for example, $f_3^{(1)} = f_3^{(2)}$.

This approximation produces a response which is linearly dependent on the history of the input, but is nonlinearly dependent on the present value of the input. The resultant constitutive equation is directly related to the theory of finite viscoelasticity developed by Coleman and Noll (1961). Working from mechanical considerations, they derived a stress relaxation equation for isotropic compressible materials under isothermal conditions which contained twelve relaxation functions. By expanding the various strain measures in terms of E [see (2.2)] and polynomials in E, it is readily shown that, to third order in E, Coleman and Noll's result is identical to the 'linear' stress relaxation form of (2.8). Dunoff and Lianis (1965) and McGuirt and Lianis (1967) have found for several incompressible materials that Coleman and Noll's result can follow one- and two-step data with only three or four relaxation functions. In the following, it is shown that (2.8) can follow data of Lianis and also some data developed by Zapas and Craft (1965).

3.2. *Superposition*

A second type of simplification is to define a multiple-argument material function in terms of a single function of one argument in the following manner:

$$\left.\begin{aligned}\psi_1(x, y) &= f_1(x)\, H(y-x) + f_1(y)\, H(x-y),\\ \psi_2(x, y, z) &= f_2(x)\, H(y-x)\, H(z-x) + f_2(y)\, H(x-y)\, H(z-y)\\ &\quad + f_2(z)\, H(x-z)\, H(y-z).\end{aligned}\right\} \tag{8.2}$$

Dependence on $x, y, z, \ldots$ has been given the same functional form in order that the ψ_i should be continuous at $x = y = z = \ldots$; this results in completely symmetric forms. H denotes the Heaviside step function

$$H(x) = \begin{cases} 1, \text{ if } x \geqslant 0 \\ 0, \text{ if } x < 0. \end{cases}$$

Equations (8.2) produce a response in which each term has a linear dependence on the history of an input measure; however, each measure is a nonlinear function of the input. Hence, the resulting constitutive equation is in the form of a convolution integral and is sometimes considered to be a Boltzmann superposition theory for large deformations. FINDLEY and LAI (1967) and LAI and FINDLEY (1968) have also considered a type of nonlinear superposition. Although they did not explicitly define the material functions as in (8.2), their resultant equations are equivalent.

A special form of (8.2), which is related to strain-dependent modulus theory, is obtained by assuming that certain functions f_i are related. For compressible materials,

$$f_i(x) = \begin{cases} A_i\, \psi_1(x), & i = 3, 4, 7, 8, \\ A_i\, \psi_2(x), & i = 5, 9, 10, \\ A_i\, f_6(x), & i = 11, \end{cases} \tag{8.3}$$

where the constants A_i are found from experiment. For incompressible materials, some simplification is obtained from the introduction of the condition of no volume change (see LOCKETT and STAFFORD, 1969).

8.3 *Product nonlinearity*

Finally, we discuss one form which may be considered to be an analytic approximation to the material functions. In view of the one-step test requirement, we suppose that second- and higher-order material functions are separable and expressible as the products

$$\psi_i(x_1, x_2, \ldots, x_n) = f_i^{(1)}(x_1)\, f_i^{(2)}(x_2) \ldots f_i^{(n)}(x_n), \tag{8.4}$$

where functions $f_i^{(j)}$ are related by the symmetry conditions (2.4), e.g. $f_6^{(1)} = f_6^{(2)}$, etc. LAI and FINDLEY (1968) and FINDLEY and ONARAN (1968) have proposed forms similar to (8.4). However, they considered only completely symmetric forms, an unnecessary limitation in three dimensions.

The effect of this approximation cannot be evaluated quantitatively, as none of the second- or higher-order terms have ever been completely determined. Qualitatively, there is experimental evidence to support the assumption that ψ can be represented by a series. Then (8.4) is an approximation to ψ by a product of series, and this is acceptable only when ψ contains a very small number of terms,

or for small excursions about the axis $\sigma_1 = \sigma_2 = \ldots = \sigma_n$. In practice this may be acceptable as linear behaviour is dominant in the range of finite small strains applicable to the theory. Also, by the definition of *strong oblivion* (decaying memory), the essential aspects of physical (as opposed to geometrical) nonlinearity occur in the recent past, near the axis $\sigma_1 = \sigma_2 = \ldots = \sigma_n$.

8.4 *Discussion*

Before dealing with quantitative comparisons, we make some general remarks on features which can be observed in the numerical results. The essential characteristics are illustrated by a one-dimensional constitutive equation, and application of the approximations to (2.5) leads to the following results. A physically linear material implies that

$$Q = \int_0^t \{\psi_1(t-\tau) + f_2(t-\tau)\,P(t) + f_3(t-\tau)\,P^2(t)\}\,\dot{P}(\tau)\,d\tau. \qquad (8.5)$$

The superposition approximation produces the result

$$Q = \int_0^t \{\psi_1(t-\tau) + f_2(t-\tau)\,2^{\frac{1}{2}}P(\tau) + f_3(t-\tau)\,3P^2(\tau)\}\,\dot{P}(\tau)\,d\tau. \qquad (8.6)$$

The assumption of product nonlinearity yields

$$Q = \int_0^t \psi_1(t-\tau)\dot{P}(\tau)\,d\tau + \left\{\int_0^t f_2^{\frac{1}{2}}(t-\tau)\dot{P}(\tau)\,d\tau\right\}^2 + \left\{\int_0^t f_3^{\frac{1}{3}}(t-\tau)\dot{P}(\tau)\,d\tau\right\}^3, \qquad (8.7)$$

where the square and cube roots of f_2 and f_3 are introduced to make the equations identical for one-step tests. Thus, for $P = P_0\,H(t)$,

$$Q = P_0\,\psi_1(t) + P_0^2 f_2(t) + P_0^3 f(t). \qquad (8.8)$$

However, the response of (8.8) to (8.7) to general loads is quite different. It should be emphasized that for nonlinear superposition the response to each new load level is identical and independent of the previous history. This is readily observed for step loadings:

$$P = AH(t) + (B-A)\,H(t-k),$$

$$Q[P] = Q[A]\,H(t) + Q[B]\,H(t-k).$$

Hence, the nonlinearity is entirely confined to the magnitude of the load and no interaction of loads or coupling effect occurs.

The physically linear equation (8.5) shows an unrealistic effect in recovery tests. The response to an input is a nonlinear function of the current value $P(t)$. During recovery, $P(t) \equiv 0$, $t > k$, and the response is a linear relaxation

$$Q = \int_0^k \psi_1(t-\tau)\,\dot{P}(\tau)\,d\tau.$$

A linear recovery may be acceptable for special materials or small inputs, but, generally, nonlinear materials will have a nonlinear recovery.

Although one-step tests may be sufficient for determining the material functions, it is well known that such tests are incapable of assessing the degree of applicability of a specific constitutive equation to general deformations. This is readily illustrated by result (3.8), as one may use the functions determined therefrom in any of the three constitutive equations (3.5), (3.6) or (3.7). Hence, the selection of a constitutive equation must be guided by additional information, and we believe that a multiple-step test can provide criteria for selecting a constitutive equation.

Pipkin and Rogers (1968) observed that multi-step inputs are a more critical test of a constitutive equation's ability to describe the response, particularly in comparison with constant rate inputs. A brief inspection of the limited multi-step data available (Pipkin and Rogers, 1968; McGuirt and Lianis, 1967; Zapas and Craft, 1965; and Findley and Lai, 1968) shows that in general both creep and stress–relaxation equations predict a lower response than measured. This seems particularly marked in unloading tests which are shown in Figs. 1 and 2. Hence, it is desirable to be able to predict, from a knowledge of the material functions, which type of constitutive equation will give the better (and usually larger) response prediction.

Since we shall test the constitutive equations using step inputs, these are applied to the one-dimensional equations to obtain algebraic equations from which inequalities may be readily established. Let PROD_i, SUP_i and LIN_i denote respectively the product nonlinear form (3.7), the superposition form (3.6) and physically linear form (3.5), where the subscript $i = 2, 3$ denotes a second- or third-order term. The comparison of SUP with PROD and LIN gives the same result for both second and third-order terms and is independent of the sign of the material function:

$$\left.\begin{matrix}(\mathrm{SUP}_i - \mathrm{PROD}_i)\\ (\mathrm{SUP}_i - \mathrm{LIN}_i)\end{matrix}\right\} \times \operatorname{sgn}(P_{n+1} - P_n) \begin{cases} < 0, & f_i > 0 \\ > 0, & f_i < 0 \end{cases} \tag{3.9}$$

The comparison of PROD with LIN varies with order:

$$(\mathrm{PROD}_i - \mathrm{LIN}_i) \times \operatorname{sgn}[f_i(t)] \times \operatorname{sgn}(P_{n+1} - P_n) \begin{cases} < 0, & i = 2, \\ > 0, & i = 3. \end{cases} \tag{3.10}$$

Here, $\operatorname{sgn}(P_{n+1} - P_n)$ is the *sign* of the difference in two steps. The statement (3.10) is not completely independent of f_i, but holds (for all materials investigated) provided that $|P_{n+1}| \geqslant 0{\cdot}03\,|P_n|$. It should be remembered that the fully nonlinear equations (2.5) will (in principle) follow the first three steps exactly, and thereafter may be expected to produce a better prediction than any of the approximations. This conclusion was partially confirmed by Nees and Sackman (1967) in the one-dimensional seven-step creep tests on polyethylene.

The term $\operatorname{sgn}(P_{n+1} - P_n)$ makes the inequalities dependent on the input. This implies that if one approximation is best for decreasing loads another may be best for increasing loads. Unfortunately, there are insufficient data to test this conclusion. Hence, these inequalities can only serve as a guide; however, it seems that a large step followed by several unloading steps is a more critical test than several loading steps.

These inequalities also apply to two- and three-dimensional constitutive equations like (2.3). They can be extended to continuous inputs by replacing $\operatorname{sgn}(P_{n+1} - P_n)$ by $\operatorname{sgn}[\dot{P}(t)]$, provided that $\operatorname{sgn}[\dot{P}(\tau)] = \operatorname{sgn}[\dot{P}(t)]$, $0 < \tau < t$. This, in turn, is limited justification for using multi-step tests to evaluate the applicability of a constitutive equation to general deformations.

4. One-Dimensionsional Data: Creep Formulations

Findley and others obtained some interesting multi-step creep data on two different materials: unplasticized PVC (Findley and Lai, 1966) and polyurethane foam (Findley and Stanley, 1966). The maximum strain was less than 2 per cent, well within the limits of applicability of all theories, and the one-step response was clearly nonlinear. Hence, these data are an excellent check for the various equations and the results are reported in detail.

In the original papers, the one-step response of both materials was modelled by

$$\epsilon = a(\sigma) + b(\sigma)\, t^p, \; p = 0{\cdot}155. \tag{4.1}$$

The elastic term $a(\sigma)$ is nearly linear, and $b(\sigma)$ can be approximated by a cubic:

$$a(\sigma) = a\sigma, \quad b(\sigma) = b_1\sigma + b_2\sigma^2 + b_3\sigma^3, \tag{4.2}$$

with a relative error less than 3 per cent. By comparison with (3.8), we define $P = \sigma$, $Q = \epsilon$, and

$$\psi_1 = a + b_1 t^p, \quad f_2 = b_2 t^p, \quad f_3 = b_3 t^p, \tag{4.3}$$

where the constants used herein* are given in Table 1.

Table 1. *Single-step test results*

	a	b_1	b_2	b_3
PVC $\times 10^6$	2·22457	5·96009 $\times 10^{-2}$	8·78509 $\times 10^{-5}$	$-$ 8·75795 $\times 10^{-9}$
FOAM $\times 10^6$	27·333	2·1282	2·5342 $\times 10^{-3}$	4·8749 $\times 10^{-6}$

Using (4.3), one may write out directly the response to multi-step loads. Let the input be defined with use of the Heaviside step function:

$$\sigma(t) = \sum_{i=1}^{n} (\sigma_i - \sigma_{i-1})\, H(t - t_i), \quad t_n \leqslant t < t_{n+1}, \tag{4.4}$$

with initial values $\sigma_0 = t_1 = 0$. Then the three approximations (3.5) to (3.7) yield the responses

$$\epsilon_{\text{LIN}} = a(\sigma_n) + \frac{b(\sigma_n)}{c_n} \sum_{i=1}^{n} (t - t_i)^p (\sigma_i - \sigma_{i-1}), \tag{4.5}$$

$$\epsilon_{\text{SUP}} = a(\sigma_n) + \sum_{i=1}^{n} [b(\sigma_i) - b(\sigma_{i-1})]\, (t - t_i)^p, \tag{4.6}$$

$$\epsilon_{\text{PROD}} = a(\sigma_n) + b_1 \sum_{i=1}^{n} (t - t_i)^p (\sigma_i - \sigma_{i-1}) + b_2 \left\{ \sum_{i=1}^{n} (t - t_i)^{p/2} (\sigma_i - \sigma_{i-1}) \right\}^2 + b_3 \left\{ \sum_{i=1}^{n} (t - t_i)^{p/3} (\sigma_i - \sigma_{i-1}) \right\}^3. \tag{4.7}$$

*As in Findley and Rogers (1963), the PVC data has been slightly modified to fit the multi-step test of Findley and Lai (1967).

To provide an additional comparison we include a one-dimensional equation derived from the thermodynamics of irreversible processes. Following M. A. Biot's linear analysis, SCHAPERY (1966) has developed explicit equations for nonlinear materials wherein the physical nonlinearity is contained in a 'reduced time,' where this reduction is an implicit function of strain. In a recent paper, SCHAPERY (1968) has considered a more general entropy production inequality which may depend on functions of stress as well as (his previously considered) functions of strain. Hence, for a stress-relaxation formulation, one may choose the reduced time to be a function of strain, and for the creep formulation choose a function of stress. Schapery's one-dimensional creep formulations may be written as

$$\epsilon = a(\sigma) + f(\sigma)\int_0^t D[\rho(t) - \rho(\tau)]\frac{d}{d\tau}\left(\frac{\sigma}{A_G}\right)d\tau, \qquad \rho(t) = \int_0^t \frac{A_S(\sigma)}{A_D(\sigma)}dt', \quad (4.8)$$

where D is the viscoelastic component of the linear creep compliance. It is probable that creep and recovery data for several stress levels and times are the most convenient data for evaluating functions A_G, A_D and $f(\sigma)$ as well as $a(\sigma)$ and D. However, to enable comparison with the previous results, a special form of (4.8) is chosen which can be evaluated from one-step tests.

The response to step input $\sigma = \sigma_0 H(t)$ is

$$\epsilon = a(\sigma_0) + f(\sigma_0) D[t A_G(\sigma_0)/A_D(\sigma_0)] \frac{\sigma_0}{A_G(\sigma_0)}. \quad (4.9)$$

By comparison with (4.1), let

$$D\{t A_G/A_D\}\frac{f}{A_G} = \psi^p b(\sigma_0)/\sigma_0. \quad (4.10)$$

Equation (4.8) can take on a number of forms; setting $A_D = A_G = 1$ yields a 'linear' equation like (3.5), and $f = 1$ with $A_G = A_D$ produces a 'superposition' equation like (3.6). We are interested in forms employing reduced time, and the most successful form (for the data investigated) is that which includes all of the nonlinearity in the reduced time. Thus, let $f(\sigma) = A_G(\sigma) = 1$; hence,

$$D(t/A_D) = b_1 (t/A_D)^p, \quad \frac{1}{A_D} = \left(1 + \frac{b_2\sigma + b_3\sigma^2}{b_1}\right)^{1/p}. \quad (4.11)$$

The response to multi-step loading (4.4) is

$$\left.\begin{aligned} \epsilon_{MP} &= a(\sigma_n) + b_1 \sum_{i=1}^{n} \{\rho(t) - \rho(t_i)\}^p (\sigma_i - \sigma_{i-1}), \\ \rho(t) - \rho(t_k) &= \frac{t - t_k}{A_D(\sigma_n)} + \sum_{i=k}^{n-1} \frac{t_{i+1} - t_i}{A_D(\sigma_i)}. \end{aligned}\right\} \quad (4.12)$$

When (4.12) is unsatisfactory, the next level of approximation is to include either $f(\sigma)$ or $A_G(\sigma)$; the latter choice gives somewhat better results. To be specific, let one-step tests define the relationship between A_D and A_G, and then express A_G as a polynomial, viz. $1 + k_1\sigma + k_2\sigma^2 + \ldots$. Hence, a linear A_G is defined by one two-step test, a quadratic A_G by one three-step test, and so forth. Since this

paper is limited to equations defined by one-step tests, only brief remarks on these results are included.

Given (4.8) and Table 1, the inequalities (3.9) and (3.10) may be evaluated directly. For a large step followed by several unloading steps, $P_{s+1} < P_s$ and the results are as follows:

	Second-order terms	Third-order terms
PVC	SUP > PROD > LIN	PROD > LIN > SUP
FOAM	SUP > PROD > LIN	SUP > LIN > PROD

(4.13)

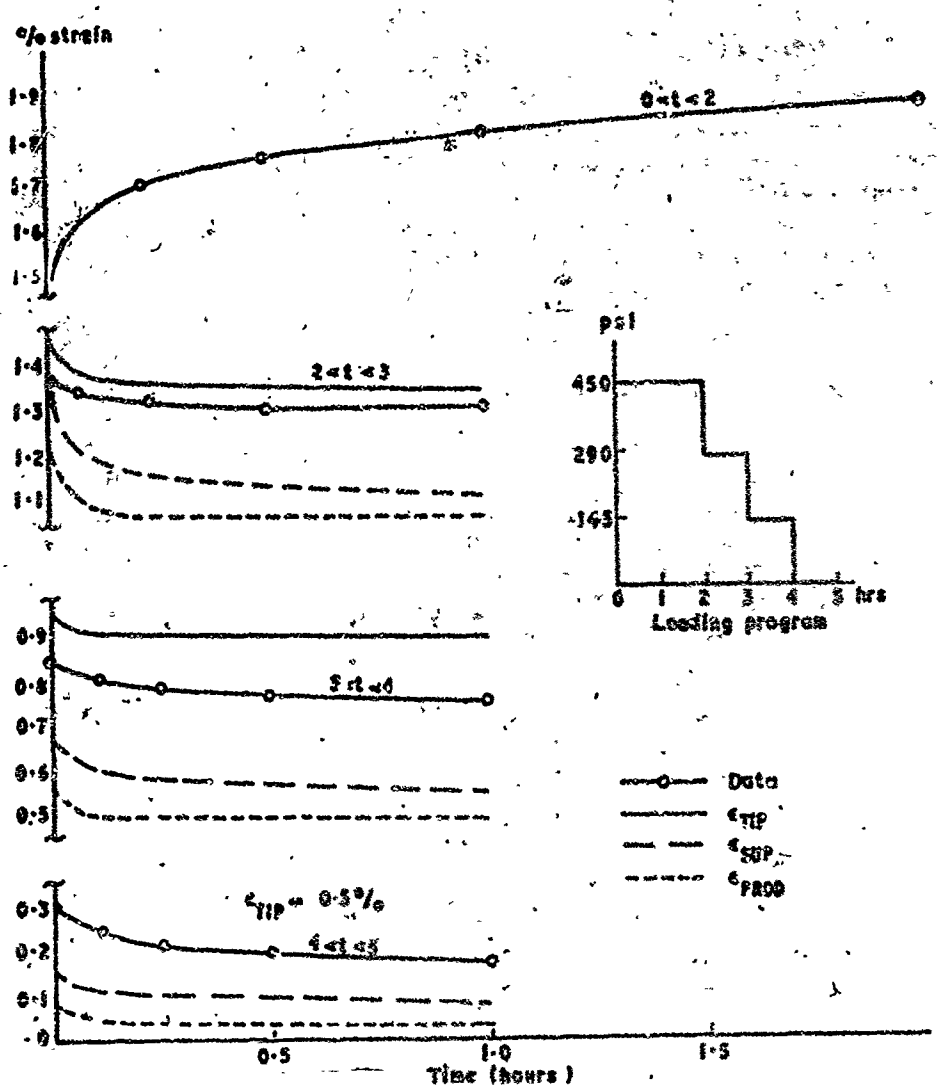

FIG 1. Creep of polyurethane foam (FINDLEY and STANLEY, 1965).

The predictions for the FOAM material are shown in Fig. 1, and clearly none of the constitutive equations follow the data in a satisfactory manner. From inequalities (4.18) the superposition theory is superior to the others, and this is readily observed. The linear form is not shown as it was almost uniformly 98 per cent of the product form. The reduced-time equation (4.12) gave a good prediction of the second step. However, the error increased very rapidly to 0·5 per cent strain at the fourth step. Evidently the function A_σ is needed to characterize this material; a quadratic A_δ was found to give excellent results.

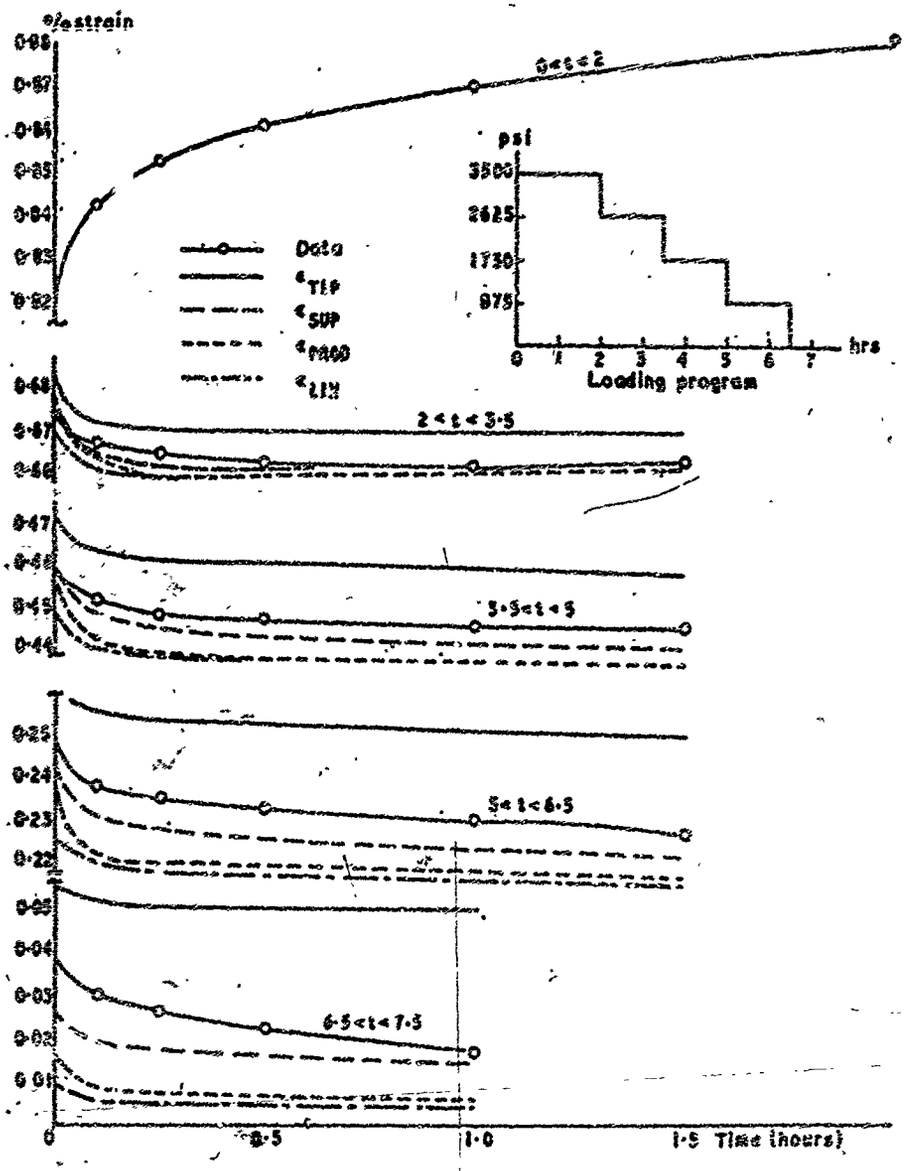

FIG. 2. Creep of polyvinylchloride (FINDLEY and LAI, 1966).

Figure 2 shows that all three approximations can follow the PVC data rather well. To evaluate inequalities (4.13) one must determine which term dominates. From (4.2) one finds that the second-order term is larger (for $\sigma < 10^4$); this is clearly observed in the fourth and fifth steps where the superposition form is larger than the product form, the latter being slightly greater than the linear form. The error in the reduced-time equation increased from 0·01 per cent strain to 0·05 per cent strain, and this cannot be ascribed to experimental variation. However, a linear A_0 was found to give slightly better results than the superposition form.

LARSKITZ and KOLSKY (1956) made a specific experimental study of the multiple-integral creep formulation for polyethylene. They were able to evaluate the functions J, K and L of (2.3) along the axis $x_1 = x_2 = x_3$, and their results are shown in Fig. 3. They also reported a number of two-step tests in an attempt to evaluate K and L for unequal arguments; however, the scatter in their data precluded quantitative results.

Although their two-step tests were inconclusive, these data provide a direct means by which one may partly check the assumption of product separability over a wide range of times. Following (3.4), let

$$\left.\begin{aligned} K(x, y) &= [K(x, x)]^{\frac{1}{2}} [K(y, y)]^{\frac{1}{2}}, \\ L(x, y, z) &= [L(x, x, x)]^{\frac{1}{3}} [L(y, y, y)]^{\frac{1}{3}} [L(z, z, z)]^{\frac{1}{3}}, \end{aligned}\right\} \qquad (4.14)$$

where the values of the functions under the radicals are taken directly from Fig. 3. Using (4.14) in (2.5), with the definitions

$$P = \sigma(t), \quad Q = E(t), \quad \epsilon = (1 + 2E)^{\frac{1}{2}}, \qquad (4.15)$$

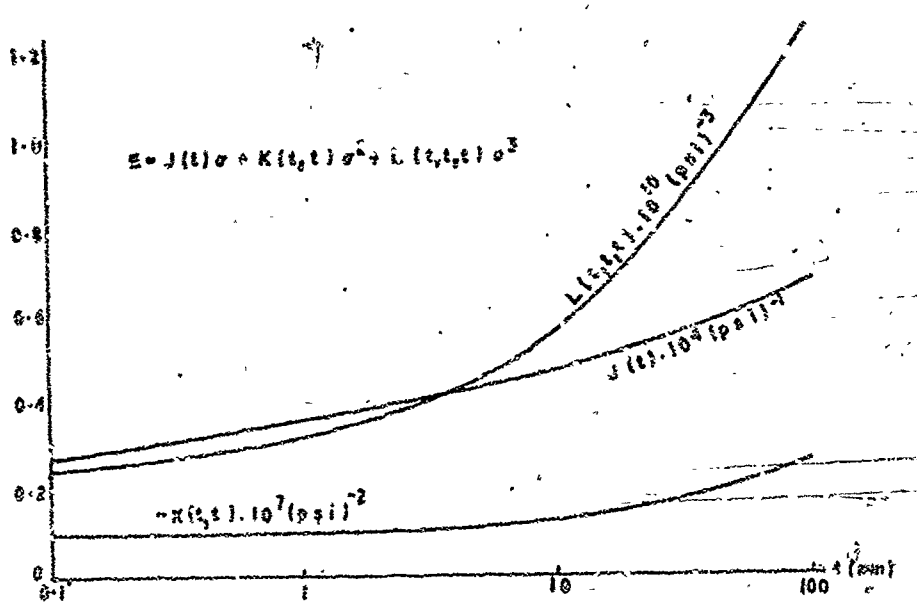

FIG. 3. Kernels for polyethylene (LARSKITZ and KOLSKY, 1956).

an equation like (8.7) is obtained. This result can be used for comparison with five different two-step tests reported by Lifshitz and Kolsky; typical results are shown in Fig. 4.

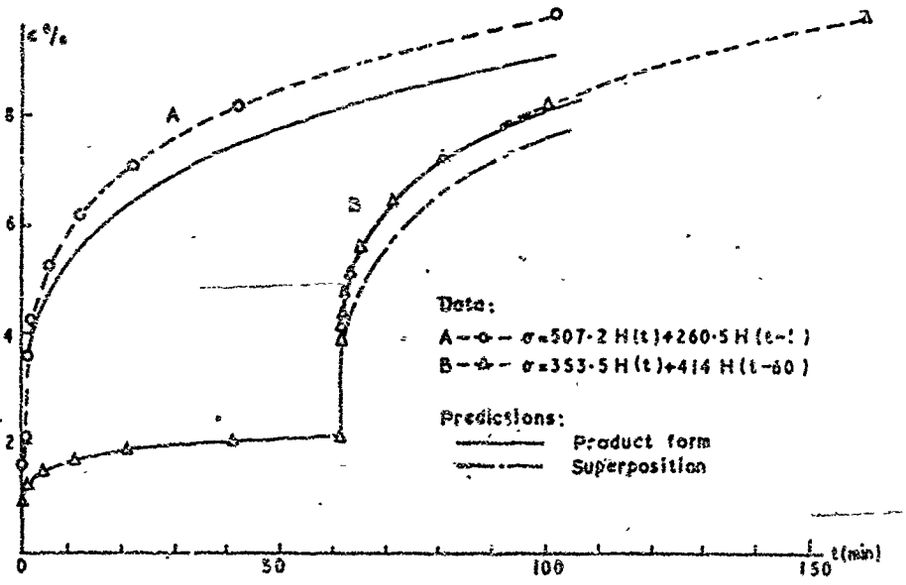

FIG 4. Creep of polyethylene (Lifshitz and Kolsky, 1966).

Curve B of Fig. 4 is typical of the data which has an initial step of 353·5 psi. The product approximation followed the data exactly except at very long times, where a small error begins to appear. When the initial step was increased to 507·2 psi, all of the predictions were significantly low, as shown by curve A of Fig. 4. However, this error was a constant 0·74 per cent strain along the entire second-step, and shifting the curves upward yields very good agreement. Hence, this error seems to be of an elastic nature, and therefore it does not invalidate the assumption of product separability for the viscoelastic response. Evidently, the product form is valid for some materials over a fairly wide range of time.

The question of which approximation will give the best fit to multi-step data is partly answered by the previously derived inequalities. Using Fig. 3 in (4.13) yields

Second-order terms	Third-order terms	
SUP > PROD > LIN	PROD > LIN > SUP	(4.16)

Thus, we know *a priori* that only the superposition form can improve on the product form. However, the third-order term dominates, particularly at high stresses, and the superposition prediction is observed to have a significant error.

5. Uniaxial Data: Stress-Relaxation Formulation

Here, the third-order integral polynomial theory is compared with two sets of uniaxial data which were previously analysed with two quite different three-dimensional constitutive equations for incompressible materials. McGuirt and Lianis (1967) used a simplification of Coleman and Noll's finite linear viscoelasticity theory to analyse styrene butadiene rubber; Zapas and Craft (1965) used the BKZ elastic fluid theory to analyse polyisobutylene. Both dealt with very large strains (80 to 100 per cent); however, experiments were limited to one- or two-step tests where good agreement was obtained, although predictions tended to be less than the measured stresses.

For uniaxial loadings in the X_1-direction of an incompressible material, let

$$y_1 = \lambda X_1, \quad y_2 = X_2/\lambda^{\frac{1}{2}}, \quad y_3 = X_3/\lambda^{\frac{1}{2}}. \tag{5.1}$$

Then the McGuirt-Lianis equation reduces to

$$\sigma(t) = f(\lambda)\left(\lambda^2 - \frac{1}{\lambda}\right) + 2\int_0^t \phi_1(s)\frac{d}{d\tau}\left[\lambda^2(\tau) - \frac{1}{\lambda(\tau)}\right]d\tau + 2\int_0^t \{\phi_0(s) + (I_2 - 3)\,\Phi_0(s)\}\frac{d}{d\tau}\left\{\frac{\lambda^2(\tau)}{\lambda^3} - \frac{\lambda}{\lambda(\tau)}\right\}d\tau, \tag{5.2}$$

where

$$\left.\begin{aligned} s &= t - \tau, \quad I_2 = 2\lambda + 1/\lambda^2, \\ f(\lambda) &= a + \frac{b}{(I_2 - 2)^2} + \{c + d\,(I_2 - 3)\}\frac{1}{\lambda}. \end{aligned}\right\} \tag{5.3}$$

Note that functions involving the integration variable τ are shown explicitly. The BKZ elastic fluid theory becomes

$$\left.\begin{aligned} \sigma(t) &= \int_0^t \left[\frac{\lambda^2(\tau)}{\lambda^2} - \frac{\lambda(\tau)}{\lambda}\right] h\left(\frac{\lambda}{\lambda(\tau)},\ s\right)d\tau, \\ h(\lambda, t) &= -\frac{\partial H(\lambda, t)}{\partial t}. \end{aligned}\right\} \tag{5.4}$$

Although starting from very different standpoints, both investigations ended with similar one-step test results. Let $\lambda = 1 + (\lambda - 1)H(t)$, then (5.2) and (5.4) become

$$\frac{\sigma_{REL}}{\lambda^2 - 1/\lambda} = f(\lambda) + 2\,\phi_1(t) + 2\,[\phi_2(t) + (I_2 - 3)\,\Phi_2(t)]\frac{1}{\lambda}, \tag{5.5}$$

$$\frac{\sigma_{REL}}{\lambda^2 - 1/\lambda} = H(\lambda, t) = \alpha(t)(\lambda^2 - 1) + \beta(t)/\lambda + \gamma/(t). \tag{5.6}$$

Both investigations revealed that three material functions were sufficient to describe the one-step response, and all can be well represented by elementary functions like t^n or $\ln t$.

An equivalent third-order integral polynomial theory can be developed from the R-formation of (2.6). By subtracting $\frac{1}{3}$ tr σ (to eliminate the hydrostatic pressure) and expressing $\bar{\mathbf{M}}$ in terms of λ_i where $\lambda_i = \lambda(\tau_i)$, one obtains

$$\sigma(t) = \tfrac{1}{2}\int_0^t \psi_2 \frac{d}{d\tau_{(1)}}\left(\lambda_1^2 - \frac{1}{\lambda_1}\right) d\tau_{(1)}$$
$$+ \tfrac{1}{4}\int_0^t\int_0^t \psi_8 \frac{d^2}{d\tau_{(2)}}\left[(\lambda_1^2-1)(\lambda_2^2-1) - \left(\frac{1}{\lambda_1}-1\right)\left(\frac{1}{\lambda_2}-1\right)\right] d\tau_{(2)}$$
$$+ \tfrac{1}{8}\int_0^t\int_0^t\int_0^t \psi_{10}\frac{d^3}{d\tau_{(3)}}\left\{\left[(\lambda_1^2-1)(\lambda_2^2-1) + 2\left(\frac{1}{\lambda_1}-1\right)\left(\frac{1}{\lambda_2}-1\right)\right]\left(\lambda_3^2 - \frac{1}{\lambda_3}\right)\right\} d\tau_{(3)}$$
$$+ \tfrac{1}{8}\int_0^t\int_0^t\int_0^t \psi_{12}\frac{d^3}{d\tau_{(3)}}\left[(\lambda_1^2-1)(\lambda_2^2-1)(\lambda_3^2-1) - \left(\frac{1}{\lambda_1}-1\right)\left(\frac{1}{\lambda_2}-1\right)\left(\frac{1}{\lambda_3}-1\right)\right] d\tau_{(3)}. \qquad (5.7)$$

For one-step tests, (5.7) reduces to

$$\frac{\sigma}{\lambda^2 - 1/\lambda} = \tfrac{1}{2}\psi_2(t) + \tfrac{1}{4}\psi_8(t,t)\left(\lambda^2 + \frac{1}{\lambda} - 2\right) + \frac{1}{8}\psi_{10}(t,t,t)\left[(\lambda^2-1)^2 + 2\left(\frac{1}{\lambda}-1\right)^2\right]$$
$$+ \frac{1}{8}\psi_{12}(t,t,t)\left(\lambda^4 - 3\lambda^2 + \lambda + 3 - \frac{3}{\lambda} + \frac{1}{\lambda^2}\right). \qquad (5.8)$$

Since (5.8) is restricted to small finite strains, we write

$$\lambda = 1 + \epsilon,$$

and expand the terms in the equations in powers of ϵ. Equation (5.8) can be made to coincide with (5.5) and (5.6) to third order in ϵ by choosing the following definitions for the ψ' s:

	McCurdy and Lianis (1957)	Zapas and Craft (1965)
$\frac{1}{2}\psi_2$	$2\phi_2 + 2\phi_1$	$\beta + \gamma$
$\frac{1}{4}\psi_8$	$-2\phi_6$	$2\alpha - \beta$
$\frac{1}{8}\psi_{10}$	$5/3\,(\phi_5 + 2\Phi_6)$	$-5/3(\alpha - \beta)$
$\frac{1}{8}\psi_{12}$	$-2/3\,(2\phi_5 + 7\Phi_6)$	$2/3\,(\alpha - \beta)$

The error induced by ignoring fourth and higher terms can be readily estimated for one-step tests:

$$|\sigma - \sigma_{ML}| \leqslant \left|2.7\,\phi_0 \sum_{n=6}^{\infty}(-1)^n \epsilon^n\right|, \qquad (5.9a)$$

$$|\sigma - \sigma_{BKZ}| \leqslant \left|\frac{5}{3}(\alpha - \beta)\sum_{n=4}^{\infty}(-1)^n n\,\epsilon^n\right|. \qquad (5.9b)$$

The question of multi-step loads is an open one. Neither of the papers presented more than two-step data, none of which was in the range of strains *supposedly* applicable to (3.7). Equations (3.9) and (3.10) may be used to determine which approximation

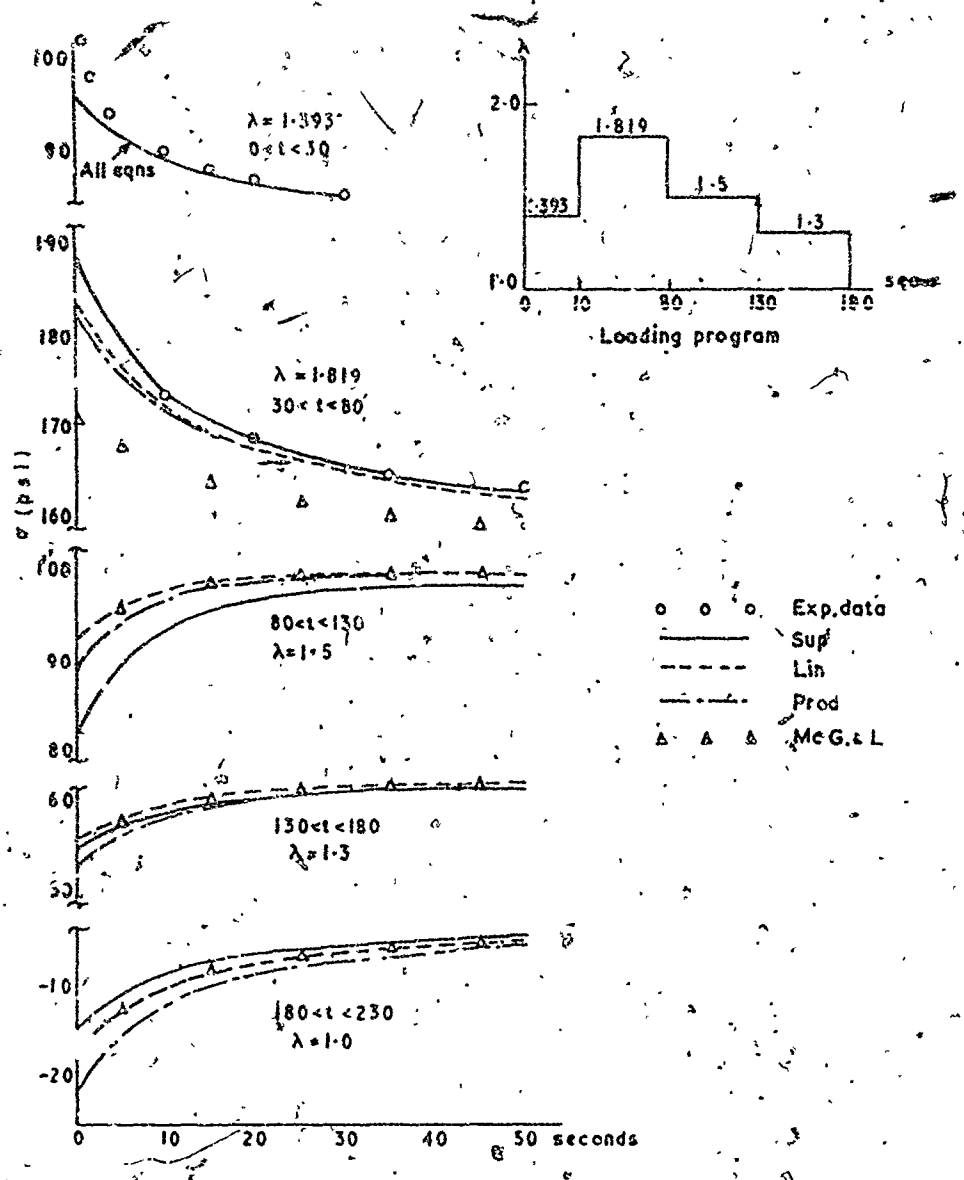

FIG. 5. Stress–relaxation of SBR (McGUIRT and LIANIS, 1967).

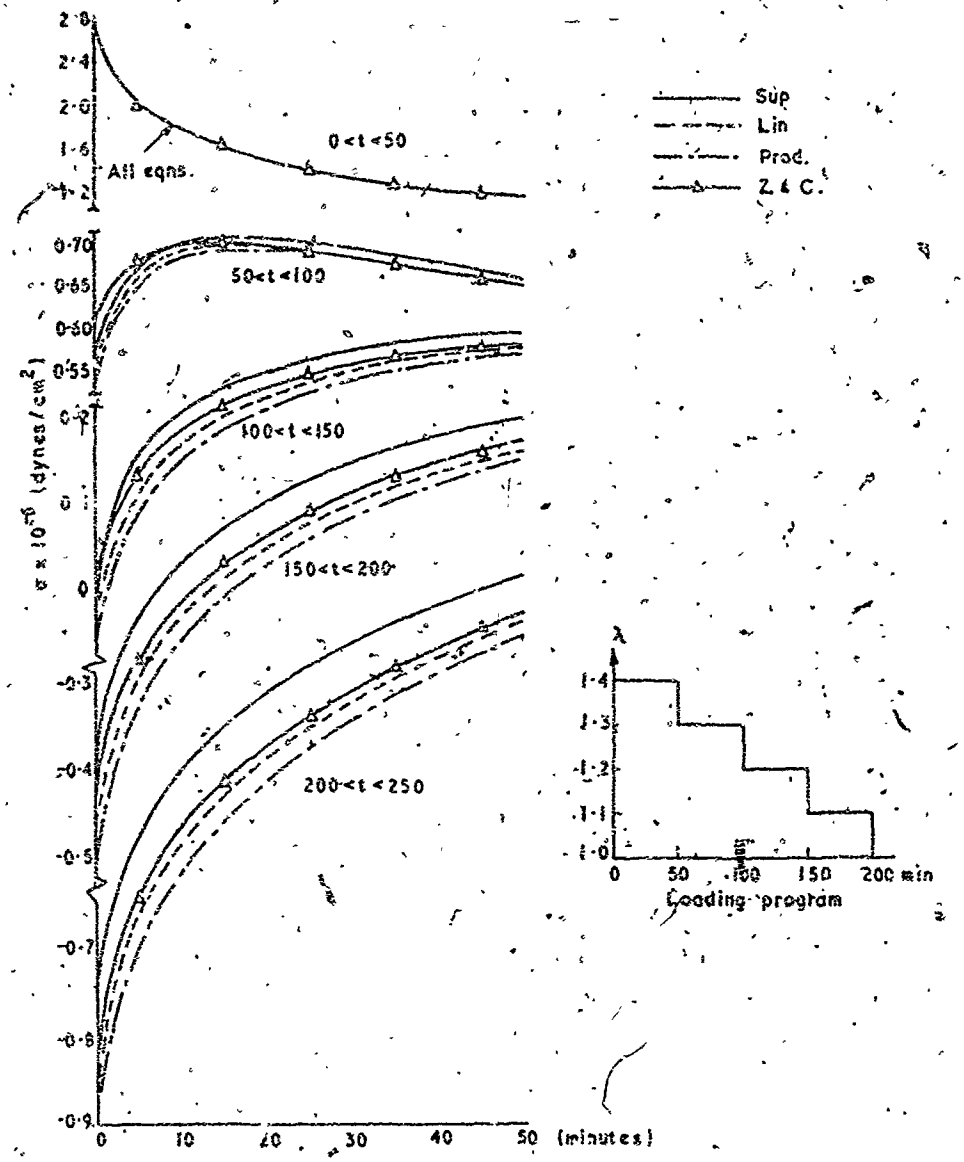

FIG 6. Stress-relaxation of PIB (ZAPAS and CRAFT, 1965).

will predict the larger response. For decreasing steps, both materials yield the results:

ψ_8	ψ_{10}	ψ_{12}
SUP > LIN > PROD	LIN > PROD > SUP	SUP > PROD, ≶ LIN.

By evaluating relative magnitudes, one finds;

$\lambda < 1{\cdot}4$	$\lambda > 1{\cdot}4$	
SUP > LIN > PROD	LIN > PROD > SUP	(5.10)

These inequalities are reversed for increasing steps.

The three approximations of Section 3 may be applied to (5.7) and the multi-step response written down, just as in Sections 3.4 and 4; the multi-step response of (5.2) and (5.4) is developed in an analogous way. The results are shown in Figs. 5 and 6, and in both cases the superposition form of (5.7) yields a larger response in successive steps, as predicted by (5.10).

Surprisingly, the Green–Rivlin theory [see (5.7)] will follow the McGuirt–Lianis equation (5.2) for all λ. Hence, the first two steps shown in Fig. 5 were taken from their report, and all three approximations are observed to yield a better prediction of the second-step data, with the superposition form having no measurable error. At low strain levels ($\lambda < 1{\cdot}5$) the linear form of (5.7) equals (5.2) to the fourth or fifth digit. Unfortunately, there is a significant error in the first step for $t < 10$. This error was also apparent (but less obtrusive) in the original semi-log plot (McGuirt and Lianis, 1967, Fig. 2). This may be only experimental variation, but it is possible that the representation of one-step response, equation (5.5), is somewhat in error.

The Zapas–Craft equation (5.4) shown in Fig. 3 is a counter-example, as the Green–Rivlin equation (5.7) will not follow (5.4) when $\lambda > 1{\cdot}4$. Zapas and Craft (1965) ran tests with input levels similar to the first two steps of Fig. 5, and (5.4) gave very good results. However, all forms of the Green–Rivlin theory, equation (5.7), gave a poor prediction of the second step (26 percent too high at $\lambda_2 = 1{\cdot}698$). This sort of disagreement at large strains is to be expected of a third-order theory, and was indicated by the error estimates as (5.9b) is much more slowly convergent than (5.9a). When the strains are restricted to $\lambda \leqslant 1{\cdot}4$, as in Fig. 6, good agreement is obtained.

6. Concluding Remarks

Although the proposed simplifications reduce the multiple integrals so that one-step tests are sufficient to evaluate material functions, a multi-step test is required to indicate the applicability to general deformations. Evidently, tests like those performed by Findley and Stanley (1966) may be satisfactory. The tests required for two- and three-dimensional equations offer additional complications.

It has been noted by LOCKETT and STAFFORD (1969) that when the material functions are completely symmetric only uniaxial tests are required. Thus, only the superposition form can be determined from uniaxial tests, while the product and linear forms require biaxial tests.

In a recent paper, PIPKIN and ROGERS (1968) proposed an integral series representation of a different form. The first term represents exactly the response to single-step inputs, the second term generalizes the exact representation to two-step inputs, and so forth. By noting that some multi-step data (see Fig. 2) was well represented by the first term of their series, they concluded that their form was preferable to (2.6); their first term being

$$E_1(t) = \int_0^t d_1 C_1\{\sigma(\tau),\ t-\tau\}, \tag{6.1}$$

where $d_1 C \equiv (\partial C/\partial\sigma)\cdot\dot{\sigma}(\tau)\,d\tau$ for continuous loading histories.

Although the term (6.1) itself is not exactly a superposition form, nearly all published one-step data will force it to become one, as the usual experimental result seems to be a separable function of time and input, like (4.1), (5.5) and (5.6). Hence, the superposition curves in Figs. 1 and 2 are identical to the results reported by Pipkin and Rogers. Their second-order function $C_2(\sigma_1,\ t-t_1,\ \sigma_2,\ t-t_2)$ requires the evaluation of a function of four variables. However, LIANIS and KOLAKY (1966) were unable to evaluate a function of two variables $K(t_1, t_2)$; hence, the complete evaluation of C_2 appears impractical. Also, Lifshitz and Kolsky's results indicate that the two-step response is a separable function of time(s) and strain(s). If this separability were to hold for all step-tests, the constitutive equation would again reduce to a superposition form.

The demonstration that the incompressible third order theory, equation (2.6), can fit the forms derived by Lianis, and by Zapas and Craft, is not particularly meaningful. It may be argued that almost any relation will fit one- or two-step data for sufficiently small stresses and strains. Rather, this should be viewed as providing some justification for the use of δ-function and δ-function theories of LOCKETT and STAFFORD (1969) to describe incompressible three- and two-dimensional deformations. The final criteria of applicability should include multi-step tests, and on the basis of Section 5 one may expect the superposition form to yield more accurate predictions.

An important question is how to proceed when none of the equations derivable from one-step tests will follow multi-step data. No complete answer can be proposed, but it appears that the next level of sophistication would be the reduced-time equations like (5.8) developed by Schapery. Here, evaluation of, say, A_0, requires only one two-step test, one three-step test, etc., while an integral polynomial theory requires at least n two-step tests, $\frac{1}{2}n^2$ three-step tests, etc. For example, it found that choosing A_0 to be linear in σ gave excellent results for PVC. However, it must be remembered that reduced-time equations will only follow data in which the functional form of the response is unchanged by additional steps. If it does change, one must resort to the more general integral polynomial theories.

Although the applicability of the various one-dimensional constitutive relations has been discussed in detail, there remain open a number of questions in the general

three-dimensional case. For example, the ability of the approximate equations to describe strain-induced anisotropy has not been investigated. Clearly, more experimental data are required before nonlinear constitutive equations can be applied to general deformations with a high degree of confidence.

ACKNOWLEDGMENT

The work reported in this paper was done as part of the research programme of the National Physical Laboratory.

REFERENCES

COLEMAN, B. D. and NOLL, W.	1961	*Rev. mod. Phys.* 33, 239.
ERICKSEN, P. H. and LEIGHTON, G.	1965	Purdue Univ. Report AA & ES 65-6.
FICHERA, W. N. and LAI, J. S. Y.	1963	Brown Univ. Report EMRL-27.
	1967	*Trans. Soc. Rheol.* 11, 361.
FICHERA, W. N. and CARMAN, K.	1968	*Trans. Soc. Rheol.* 12, 217.
FICHERA, W. N. and STAFFORD, C. A.	1968	Brown Univ. Report EMRL-81.
GURTIN, M. E. and ERINGEN, A. C.	1967	*Archs. rat. mech. Anal.* 1, 1.
HUANG, N. C. and LEE, E. H.	1966	*J. appl. Mech.* 33, 313.
LEE, J. S. Y. and FICHERA, W. N.	1966	*Trans. Soc. Rheol.* 12, 259.
LEVINSON, J. M. and KLASKY, H.	1966	Brown Univ. Report AM-22.
LEIGHTON, F. J.	1965	*Int. J. Engng. Sci.* 3, 59.
LEIGHTON, F. J. and STAFFORD, R. O.	1969	*Int. J. Engng. Sci.* 7, 917.
McGUIRT, C. W. and LEIGHTON, G.	1967	Purdue Univ. Report AA & ES 67-14.
NOLL, W. and SACHSE, J. J.	1967	*Trans. Soc. Rheol.* 11, 507.
PIPKIN, A. C.	1964	*Rev. mod. Phys.* 36, 1034.
PIPKIN, A. C. and ROGERS, T. G.	1968	*J. Mech. Phys. Solids* 16, 59.
SCHAEFFER, R. A.	1966	*Proc. 5th U.S. Nats. Congr. Appl. Mech.*, p. 511.
	1968	Purdue Univ. Report AA & ES 68-6.
TRUESDELL, C. and NOLL, W.	1965	*The Nonlinear Field Theories of Mechanics. Encyclopedia of Physics* (Edited by FLÜGGE, S.), Vol. III/3. Springer, Berlin.
ZAPAS, L. J. and CRAFT, T.	1965	*NBS J. Res.* 69A, 6, 541.

XII. RESEARCH NEEDS

12.1 INTRODUCTION

Examination of the previous eleven chapters reveals the fact that there exist several areas wherein less than satisfactory predictive analysis methods are currently being used.

These problem areas are primarily occasioned by either or both of two fundamental reasons

- lack of a sufficiently meaningful physical model of the phenomenon in question and/or
- lack of suitable analysis techniques for solving the pertinent boundary value problem.

Secondary reasons for the existance of problem areas are

- lack of credible instrumental data for confirmation of analysis methods and
- insufficient application of instrumental measurements under broad spectrum field use conditions.

Recent developments in instrumentation technology indicate that there now exist gauges and, most importantly, gauge calibration methods applicable to a restricted range of environmental conditions. Thus, increased field use measurements are in order. Two or three programs along this latter line have in fact recently been initiated by the services.

Because of the rather high cost and long lead time needed for both instrument development and field use application and observation, it will probably require sustained effort over the next five years to bring this phase of research to an acceptance level wherein it will have the design and analysis impact necessary to effect meaningful improvements.

The first two major problem areas, physical modeling and mathematical analysis are, of necessity, closely interdependent - a physical model for material behavior that is non-analyzable or an analysis based upon an overly restricted physical model are equally inapplicable. The important basic theoretical research of the 1950's followed by the extensive laboratory characterization of the 1960's have laid the basis for a broad ranging coupled theoretical - experimental effort during the 1970's upon the problem of nonlinear, coupled thermomechanical behavior of high solids loaded propellants (chemical and aging effects implied). In spite of the previous time and money expended upon this problem, the fact remains that the solution will require a disperse, broadly based attack over the next decade involving industry, government, and university participation.

The comments and needs set forth in this chapter are those of the authors. The specific items have been influenced by the discussions and recommendations of the JANNAF S/I Committee. It is intended that future revisions of this chapter will be reviewed and approved by the S/I Committee in order that the recommendations reflect the ideas of all interested groups.

12.2 SPECIFIC RESEARCH NEEDS

(1) Development of inexpensive, reliable, readily usable stress and strain transducers which do not interfere with grain integrity.

(2) Non-isothermal viscoelastic analysis including re-evaluation of the Moreland-Lee shift hypothesis.

(3) Nonlinear material characterization.

(4) Computer analysis of boundary value problems utilizing (2) and (3).

(5) Aging effects in (2) and (3)

(6) Coupled thermomechanical characterization experiments including aging and thermal property determination.

(7) Failure characterization for both cohesive and adhesive conditions.

(8) Chemical and microstructural effects on behavior and synthesis of improved materials.

(9) Loads definition improvement with emphasis on statistical inputs.

(10) Mechanical-ballistic interaction optimization routines.

(11) Determination and definition of methods for grain figure of merit.

(12) Multi-dimensional thermomechanical routines with emphasis on vibration

(13) More extensive STV and prototype verification of the above items.

More extensive discussion of the above points may be found in the "Structural Integrity Committee CY 1970 Report" by S. C. Browning.

APPENDIX A

SUMMARY OF LINEAR ELASTICITY EQUATIONS

APPENDIX A

SUMMARY OF LINEAR ELASTICITY EQUATIONS

A.1 CYLINDRICAL EQUATIONS:

EQUATIONS OF MOTION:

$$\frac{\partial \sigma_r}{\partial r} + \frac{1}{r}\frac{\partial \tau_{r\theta}}{\partial \theta} + \frac{\partial \tau_{rz}}{\partial z} + \frac{\sigma_r - \sigma_\theta}{r} + R = \rho \frac{\partial^2 u}{\partial t^2}$$

$$\frac{\partial \tau_{r\theta}}{\partial r} + \frac{1}{r}\frac{\partial \sigma_\theta}{\partial \theta} + \frac{\partial \tau_{\theta z}}{\partial z} + \frac{2\tau_{r\theta}}{r} + \Theta = \rho \frac{\partial^2 v}{\partial t^2}$$

$$\frac{\partial \tau_{rz}}{\partial r} + \frac{1}{r}\frac{\partial \tau_{\theta z}}{\partial \theta} + \frac{\partial \sigma_z}{\partial z} + \frac{\tau_{rz}}{r} + Z = \frac{\partial^2 w}{\partial t^2}$$

STRESS-STRAIN:

$$\varepsilon_r = \frac{1}{E}[\sigma_r - \nu(\sigma_\theta + \sigma_z)] + \alpha(T - T_o)$$

$$\varepsilon_\theta = \frac{1}{E}[\sigma_\theta - \nu(\sigma_r + \sigma_z)] + \alpha(T - T_o)$$

$$\varepsilon_z = \frac{1}{E}[\sigma_z - \nu(\sigma_r + \sigma_\theta)] + \alpha(T - T_o)$$

$$\gamma_{r\theta} = \frac{\tau_{r\theta}}{\mu}, \quad \gamma_{rz} = \frac{\tau_{rz}}{\mu}, \quad \gamma_{\theta z} = \frac{\tau_{\theta z}}{\mu}, \quad \mu = \frac{E}{2(1+\nu)}$$

DISPLACEMENT:

$$\varepsilon_r = \frac{\partial u}{\partial r}, \quad \varepsilon_\theta = \frac{u}{r} + \frac{1}{r}\frac{\partial v}{\partial \theta}, \quad \varepsilon_z = \frac{\partial w}{\partial z}$$

$$\gamma_{r\theta} = \frac{1}{r}\frac{\partial u}{\partial \theta} + \frac{\partial v}{\partial r} - \frac{v}{r}, \quad \gamma_{rz} = \frac{\partial u}{\partial z} + \frac{\partial w}{\partial r}, \quad \gamma_{\theta z} = \frac{\partial v}{\partial z} + \frac{1}{r}\frac{\partial w}{\partial \theta}$$

COMPATIBILITY:

$\nabla^4\phi = 0$, ϕ = stress function

$$\nabla^2 = \frac{\partial^2}{\partial r^2} + \frac{1}{r}\frac{\partial}{\partial r} + \frac{1}{r^2}\frac{\partial^2}{\partial \theta^2} + \frac{\partial^2}{\partial z^2}$$

A.2 AXIALLY SYMMETRIC EQUATIONS

EQUATIONS OF MOTION:

$$\left.\begin{aligned} \frac{\partial \sigma_r}{\partial r} + \frac{\partial \tau_{rz}}{\partial z} + \frac{\sigma_r - \sigma_\theta}{r} + R &= \rho \frac{\partial^2 u}{\partial t^2} \\ \frac{\partial \tau_{rz}}{\partial r} + \frac{\partial \sigma_z}{\partial z} + \frac{\tau_{rz}}{r} + Z &= \rho \frac{\partial^2 w}{\partial t^2} \end{aligned}\right\}$$ No dependence on θ, $\tau_{r\theta} = \tau_{\theta z} = 0$

STRAIN-DISPLACEMENT:

$$\epsilon_1 = \frac{\partial u}{\partial r}, \quad \epsilon_\theta = \frac{u}{r}, \quad \epsilon_z = \frac{\partial w}{\partial z}, \quad \gamma_{rz} = \frac{\partial u}{\partial z} + \frac{\partial w}{\partial r}$$

(Stress-strain relation unchanged from above)

STRESS FUNCTIONAL APPROACH (NO BODY FORCES; EQUILIBRIUM)

$$\nabla^4\phi = 0 , \quad \nabla^2 = \frac{\partial^2}{\partial r^2} + \frac{1}{r}\frac{\partial}{\partial r} + \frac{\partial^2}{\partial z^2}$$

$$\sigma_r = \frac{\partial}{\partial z}\left[\nu\nabla^2\phi - \frac{\partial^2\phi}{\partial r^2}\right]$$

$$\sigma_\theta = \frac{\partial}{\partial z}\left[(2-\nu)\nabla^2\phi - \frac{\partial^2\phi}{\partial r^2}\right]$$

$$\sigma_z = \frac{\partial}{\partial z}\left[(2-\nu)\nabla^2\phi - \frac{\partial^2\phi}{\partial z^2}\right]$$

$$\tau_{rz} = \frac{\partial}{\partial r}\left[(1-\nu)\nabla^2\phi - \frac{\partial^4\phi}{\partial z^2}\right]$$

$$\varepsilon_r = -\frac{(1+\nu)}{E}\frac{\partial^3\phi}{\partial r^2\partial z}$$

$$\varepsilon_\theta = -\frac{(1+\nu)}{E}\frac{1}{r}\frac{\partial^2\phi}{\partial r\partial z}$$

$$\varepsilon_z = \frac{(1+\nu)}{E}\frac{\partial}{\partial z}\left[(1-2\nu)\nabla^2\phi + \frac{\partial^2\phi}{\partial r^2} + \frac{\partial\phi}{\partial r}\right]$$

$$u = -\frac{(1+\nu)}{E}\frac{\partial^2\phi}{\partial r\partial z}$$

$$w = \frac{(1+\nu)}{E}\left[(1-2\nu)\nabla^2\phi + \frac{\partial^2\phi}{\partial r^2} + \frac{1}{r}\frac{\partial\phi}{\partial r}\right]$$

A.3 AXIALLY SYMMETRIC EQUATIONS - TWO-DIMENSIONAL:

EQUATIONS OF MOTION:

$$\frac{\partial\sigma_r}{\partial r} + \frac{\sigma_r - \sigma_\theta}{r} + R = \rho\frac{\partial^2 u}{\partial t^2}$$

STRAIN-DISPLACEMENT:

$$\varepsilon_r = \frac{\partial u}{\partial r}, \quad \varepsilon_\theta = \frac{u}{r}, \quad \varepsilon_z = \frac{\partial w}{\partial z}$$

PLANE STRESS:

$$\sigma_z = 0$$

$$\varepsilon_r = \frac{1}{E}(\sigma_r - \nu\sigma_\theta) + \alpha(T - T_o)$$

$$\varepsilon_\theta = \frac{1}{E}(\sigma_\theta - \nu\sigma_r) + \alpha(T - T_o)$$

$$\varepsilon_z = -\frac{\nu}{E}(\sigma_r + \sigma_\theta) + \alpha(T - T_o)$$

PLANE STRAIN:

$$\varepsilon_z = 0$$

$$\varepsilon_r = \frac{1}{E}\left[\sigma_r - \nu(\sigma_\theta + \sigma_z)\right] = \left(\frac{1-\nu^2}{E}\right)\left[\sigma_r - \left(\frac{\nu}{1-\nu}\right)\sigma_\theta\right] + \alpha(T - T_o)$$

$$\varepsilon_\theta = \frac{1}{E}\left[\sigma_\theta - \nu(\sigma_r + \sigma_z)\right] = \left(\frac{1-\nu^2}{E}\right)\left[\sigma_\theta - \left(\frac{\nu}{1-\nu}\right)\sigma_r\right] + \alpha(T - T_o)$$

Hence, to change plane stress into plane strain, substitute:

$\frac{E}{1-\nu^2}$ for E and $\frac{\nu}{1-\nu}$ for ν.

STRESS FUNCTIONAL APPROACH (NO BODY FORCES AND EQUILIBRIUM):

$$\nabla^4\phi = 0$$

$$\nabla^2 \equiv \frac{\partial^2}{\partial r^2} + \frac{1}{r}\frac{\partial}{\partial r}$$

$$\sigma_r = \frac{1}{r}\frac{\partial\phi}{\partial r} = \frac{A}{r^2} + 2c$$

$$\sigma_\theta = \frac{\partial^2\phi}{\partial r^2} = -\frac{A}{r^2} + 2c$$

$$\phi = A \ln r + c\, r^2$$

A.4 ENERGY THEOREMS

MINIMUM POTENTIAL ENERGY THEOREM:

Of all displacements satisfying compatibility and the displacement boundary conditions, those which satisfy the equilibrium equations and the boundary conditions make the potential energy, V, an absolute minimum.

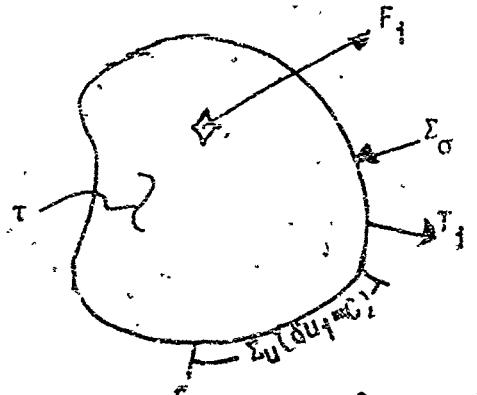

$$V = \int_\tau W(e_{ij})d\tau - \int_{\Sigma_\sigma} T_i u_i d\sigma - \int_\tau F_i u_i d\tau$$

$$W(e_{ij}) = \frac{1}{2}\left\{(\lambda + 2\mu)e^2 - 4\mu e_2\right\} - (3\lambda + 2\mu)\alpha(T - T_0)e$$

$$= W^{(T=T_0)}_{(e_{ij})} + W^{(T)}_{(e_{ij})}$$

$$e = e_{11} + e_{22} + e_{33}$$

$$e_2 = \frac{1}{2}\delta^{ij}_{pq} e_{pi} e_{qj}$$

$$\lambda = \frac{\nu E}{(1+\nu)(1-2\nu)} \quad ; \quad \mu = \frac{E}{2(1+\nu)}$$

LEMMA:

If the potential energy is an absolute minimum, then the displacements are such as to satisfy equilibrium and stress conditions.

MINIMUM COMPLEMENTARY ENERGY THEOREM:

Of all stress tensor fields τ_{ij} that satisfy the equations of equilibrium and the boundary conditions where stresses are prescribed, those which satisfy compatibility and displacement boundary conditions make the complementary energy, V^*, an absolute minimum.

$$V^* = \int_\tau W(\tau_{ij})d\tau - \int_{\Sigma_u} T_i \bar{u}_i \, d\sigma$$

$$W(\tau_{ij}) = \frac{1+\nu}{2E} \tau_{ij} \tau_{ij} - \frac{\nu}{2E} (\tau_{\alpha\alpha})^2$$

CONVERSE THEOREM:

If the complementary energy V^* is an absolute minimum, then the strasses are such as to satisfy compatibility and displacement boundary conditions.

REISSNER'S MIXED PRINCIPLE:

Elastic equilibrium is distinguished by a stationary value of the functional J_R when τ_{ij} and u_i are varied independently, provided that the tensor τ_{ij} is symmetric.

$$J_R = \iint_\tau \left\{ -\hat{W}(\tau_{ij}) - F_i u_i + \frac{1}{2} \tau_{ij} (u_{i,j} + u_{j,i}) \right\} d\tau$$

$$- \int_{\Sigma_\sigma} T_i u_i \, d\sigma - \int_{\Sigma_u} \tau_{ij} \nu_j \, u_i \, d\sigma .$$

A.5 RELATIONS BETWEEN ELASTIC CONSTANTS

$$\lambda = \frac{E\nu}{(1+\nu)(1-2\nu)} = \frac{(E-2\mu)}{3\mu-E} = K - \frac{2}{3}\mu = \frac{3\nu K}{1+\nu} = \frac{3K(3K-E)}{9K-E}$$

$$\nu = \frac{E}{2(1+\nu)} = \frac{\lambda(1-2\nu)}{2\nu} = \frac{3}{2}(K-\lambda) = \frac{3K(1-2\nu)}{2(1+\nu)}$$

$$\nu = \frac{3K-E}{6K} = \frac{\lambda}{(\lambda+\mu)} = \frac{\lambda}{3K-\lambda} = \frac{E}{2\mu} - 1 = \frac{3K-2\mu}{2(3K+\mu)}$$

$$K = \frac{E}{3(1-2\nu)} = \lambda + \frac{2}{3}\mu = \frac{\lambda(1+\nu)}{3\nu} = \frac{2\mu(1+\nu)}{3(1-2\nu)} = \frac{\mu E}{3(3\mu-E)}$$

APPENDIX B

FINITE ELEMENT ANALYSIS

APPENDIX B

FINITE ELEMENT ANALYSIS

B.1 INTRODUCTION

In chapter four of this handbook the fundamental (elasticity) equations of the finite element method were developed, and their application to grain structural analyses discussed briefly. In this appendix, the finite element method of analysis is further discussed. The emphasis of this discussion is on the use of a finite element computer program instead of upon the theory of the technique or the mechanics of computer programs. Thus, this appendix reflects the attitude of the user rather than the producer. Those persons desiring to pursue the theory in greater detail than presented herein are referred to the many text books and survey articles. In particular, reference 1 is an excellent introduction to the subject and [2-4]contain particularly lucid, thorough descriptions of the application of the finite element method to grain structural analysis problems.

A sample computer program listing is included here for illustrative purposes. Listings of computer programs for particular analyses are also contained in the reports referenced in [5] through [18].

B.2 SUMMARY OF THEORY

As mentioned in chapter four, finite element solutions normally begin with the statement of a variational principle. A functional is defined which has as its arguments the relevant physical variables of the problem. It is then shown that the particular functions (among certain admissible types) which minimize the functional are in fact the ones that satisfy the governing differential equations of the problem. For example, the Theorem of Minimum

Potential Energy states that the potential energy assumes an absolute minimum for those displacements satisfying the equilibrium equation, provided that classes of admissible functions are limited to those satisfying the boundary conditions.

It is obvious, then, that one could (1) guess an approximate solution to a problem, (2) calculate the potential energy, and (3) compare to another approximate solution. Of the two, the one with the minimum energy is chosen as the better. We then search for another approximation to compare. By such a process, the solution will eventually be reached, if it is possible to reach a solution. A more systematic process, akin to the Rayleigh-Ritz method,* is to assume an approximate solution, with unknown parameters. We then determine the unknown parameters in such a manner as to minimize the functional. Then, we know that the solution we have is the best of the type with which we started. The finite element method is essentially such a process.

The origin of the name of the "finite element" arises from the fact that, to perform the process of minimization discussed above, the body being analyzed is divided into small subregions, over which expressions for the displacement are assumed. For example, suppose we wish to analyse the body shown in Figure 1. This body which is axisymmetric, is subjected to axisymmetric loads, e.g., axial acceleration.

We could suppose that this body may be represented by a collection of rings of triangular cross-section as in Figure 2.

This is, in fact, the type element used for such problems. However, the triangles usually are combined into quadrilaterals within the program, and we need only concern ourselves with the quadrilateral. Thus, we might

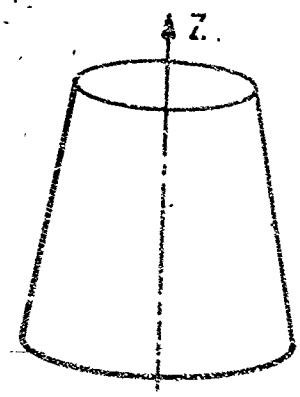

Figure 1. Representative Axisymmetric Solid

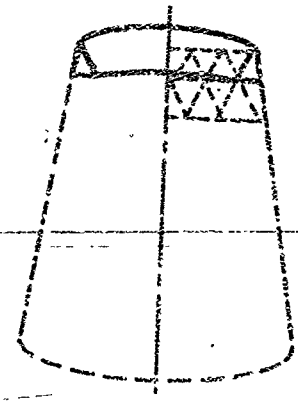

Figure 2. Typical Idealization of Axisymmetric Solid

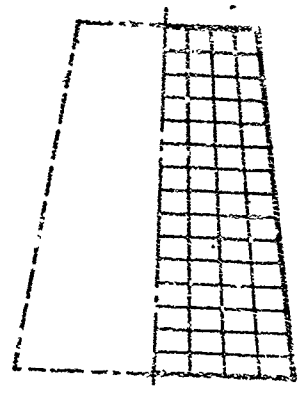

Figure 3. Quadrilateral Idealization of Solid

break up the body into the subregions such as shown for simplicity only in Figure 3. The right hand section of the body is shown subdivided.

In the axisymmetric case, these elements are each actually rings. If this were a plane problem, they would be prisms with axis perpendicular to the plane of the paper.

The displacement field is now assumed in some form for each element. This introduces several unknown parameters. These parameters can be solved for in terms of the displacements at particular points in the elements, usually the corners which are known as the nodal points. Hence, we have a set of subregions, for each of which we have an assumed displacement shape depending upon the unknown nodal point displacements. The functional for each region now can be calculated and minimized with respect to the unknown displacements. This leads to a system of algebraic equations in the nodal point displacements. Solution of these equations yields the displacement field which minimizes the functional and from which the stresses can be calculated.

In actual practice, the above is not carried out as easily as it is described. The handling of the large amount of data and solution of the resulting system of equations are problems which must be solved in an efficient manner. However, this capability has been built into the computer program and as such is not the user's problem.

One point which is significant to a user is the form of the displacement assumption. If the function is linear in each element, then the displacements along the edges of each element will coincide. This appears desirable, and is frequently used. Higher order assumptions will lead to

different results. The linear assumption also lends itself to approximation of arbitrary fields as the elements become smaller. The point to be noted is that in areas of bodies where the actual displacement field is linear, a linear approximation is adequate with large elements. In areas where the displacement is more complex, smaller elements will be required to approximate the actual displacements. In particular, in areas where the displacements are progressively more nonlinear, the elements must be progressively smaller. In addition, errors in the displacement approximation produce even larger errors in stress calculations because stress is related to the derivatives of displacements.

6.3 APPLICATION OF THE FINITE ELEMENT METHOD

This and the next subsection will show in detail the steps involved in using a finite element program and will include some numerical examples. This is undoubtedly the simplest way to discuss the practical use of the finite element method. Because the actual use of a program is dependent on the program, one must sacrifice some generality by reference to a particular program. However, we shall assume the available program similar to the one given in Section 6.5. Specific details may change from program to program but the general ideas remain the same.

6.3.1 INPUT DATA

Broadly speaking, the data that must be input to a computer program can be separated out into several categories: control information, nodal point data, element data, material properties, and load data. These categories are not unique and some programs may combined one or more into a single category. For example, it is quite natural to lump the last three together because for any element we must associate the material of which it consists and the

loads to which it is subjected. We shall discuss the type of data in each category as though they were separate, and indicate the conventions wherever possible.

Control information

(a) Title: usually the first item of information required is the title, etc., or any identification the user desires
(b) Number of nodal points
(c) Number of rows of nodal points
(d) Number of materials
(e) Axisymmetric or plane problem
(f) Number of cards of same type to be read

Data of this type refers to the problem in general and/or to the process of input to the computer. Load information that is relevant to the whole problem may also be input to this category. In this case, either item (b) or (c) information will be required, not both - the program details determine which. Also, Item (e) will not be needed for a program that is specifically either plane or axisymmetric.

Nodal point data

(a) Nodal point number - either a single number or two (I, J) coordinates if the nodal point array is associated with a matrix
(b) Coordinates of the nodal point
(c) Indication of whether forces or displacements, or neither, are specified in each coordinate direction
(d) Specified forces and/or displacement, if any
(e) Any other relevant information, e.g., temperature, if it is associated with nodal points, or special types of control information

Element data

(a) Element number

(b) Nodal points to which element is connected

(c) Material identification

All this information may be absorbed into other areas. The element number may be associated with a particular nodal point to which the element is connected; this eliminates Item (a) and Item (b); Item (c) can be handled by a request to read the data while reading nodal point information.

Material properties

(a) Mechanical properties - modulus, etc.

(b) Thermal properties - expansion coefficient

(c) Physical properties - density, etc.

(d) Identification

Load data

(a) Element to which load is applied

(b) Magnitude of load - pressure, temperature change, etc.

These data and material properties may be associated with element data, and hence to specific nodal points under some sort of nodal point-element correspondence. It is not necessary to do so, however.

Final comments on the input data

In general, it is necessary to define the position of every nodal point, the elements connected to that nodal point, the material properties for each element, as well as nodal point and element loads. Because a given problem might involve close to 1000 nodal points, with somewhat fewer elements, the amount of data would be prohibitative if each nodal point and element was treated separately. This is not done, of course. A program will incorporate some sort of self-generating feature. For example, if two nodal points are separated by several for which no data is specified, the program might generate the required intermediate points along a straight line joining the given points, with uniform spacing. Similarly, the elements left out would be generated.

By this self-generating process, the number of input data is considerably reduced. The only nodal points and elements that require specification are those along the boundary of the object, as well as interior points for

which changes from previous data occur. For example, when two different materials are adjacent, the transition from the first to the second must be specified.

B.3.2 OUTPUT DATA

At the conclusion of an analysis, a great deal of information has been created - stresses, displacements, strains. etc. All this information is output. At this point, there is no convenient way to reduce the volume unless the analyst knows that only certain results are needed. In general, the analysis will yield hundreds of pages of results. Provision can be made, however, to write the results on a tape, and then to have this information presented graphically in terms of stress and strain contours, etc.

The user must be cautioned against placing total confidence in the results of the analysis. The finite element method is a useful tool, but still is not a panacea for the analyst. Results will be dependent on the ability of the analyst to capture the essential features of the problem by proper layout of the nodal points and elements describing the object of concern. There is no substitute for intelligent engineering consideration of the problem.

B.4 EXAMPLE PROBLEMS

This subsection makes more specific the comments of the preceding subsection by presenting a group of examples of finite element analyses, including the whole process of solving the problem. For additional examples, the reader is referred to the references listed at the end of the appendix.

The program used to solve the examples is the Rohm and Haas AMGO32A, suitably modified for use on a Univac 1108 computer. The program listed in a following section [7] is due to Wilson and is similar in operation to the Rohm and Haas program used for these examples.

B.4.1 UNIAXIAL COMPRESSION OF A RIGHT CIRCULAR CYLINDER

The first example is the simplest problem that one can formulate - uniaxial compression of a circular cylindrical sample. The setup of the

problem is shown in Figure 4. Figure 4(A) shows the physical problem with the necessary defining quantities. As shown in Figure 4(B), it is possible to reduce the problem to one of smaller proportions by taking into account symmetry. This is in a form that can be analyzed by an axisymmetric program, i.e., a body of revolution loaded by axisymmetric forces. We note that points on the axis of the body can only deform in the z-direction, while points on the r-axis can only move in the r-direction, this from the symmetry of the problem. Thus, we have established displacement boundary conditions along the z- and r-axes. On the top surface, the pressure is known, while the side is free. The grid is added and nodal points defined in Figure 4(C). The grid is the simple, obvious one - an array of squares 0.5 inch x 0.5 inch covering the section of the cylinder, a total of 50 elements and 66 nodal points. The nodal points now have (I, J) coordinates associated with them as shown.[1] The displacement conditions are indicated by rollers. The nodal points on the two axes can roll along those axes, except that the (1, 1) nodal point cannot move at all.

This figure defines the problem in enough detail to generate the input data, which is shown in Figure 5. For convenience in discussing the data, we have numbered the columns in groups of 10, 1-9 and blank.

The first line of data is simply a title in the required format.

The second line of data gives the number of nodal point cards to be read (34), and number of rows (11).

The next 34 cards are nodal point cards, followed by 12 cards giving element properties and loads, and finally a card ending the data.

[1] Note that I = column number, J = row number.

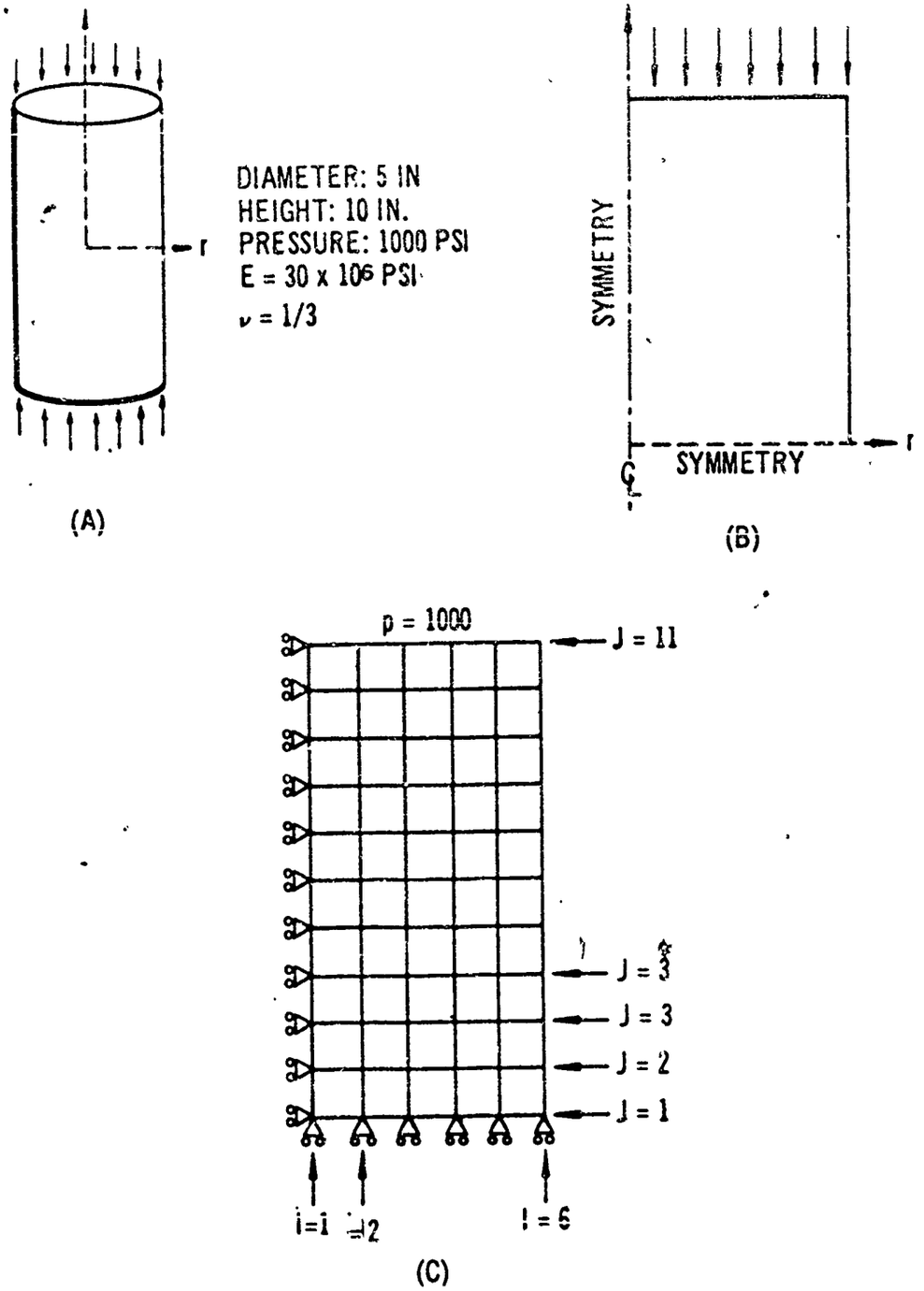

Figure 4. Setup of Simple Compression Problem

```
12345678912345678912345678912345678912345678912345678912345678912345678912345678
AM0042A SIMPLE COMPRESSION
   34   11
    1    1    11100        0.0         0.0
    2    1    00100        0.5         0.0
    3    1    00100        1.0         0.0
    4    1    00100        1.5         0.0
    5    1    00100        2.0         0.0
    6    1    50100        2.5         0.0
    1    2    01000        0.0         0.5
    6    2    50000        2.5         0.5
    1    3    01000        0.0         1.0
    6    3    50000        2.5         1.0
    1    4    01000        0.0         1.5
    6    4    50000        2.5         1.5
    1    5    01000        0.0         2.0
    6    5    50000        2.5         2.0
    1    6    01000        0.0         2.5
    6    6    50000        2.5         2.5
    1    7    01000        0.0         3.0
    6    7    50000        2.5         3.0
    1    8    01000        0.0         3.5
    6    8    50000        2.5         3.5
    1    9    01000        0.0         4.0
    6    9    50000        2.5         4.0
    1   10    11000        0.0         4.5
    2   10    10000
    3   10    10000
    4   10    10000
    5   10    10000
    6   10    50000        2.5         4.5
    1   11    51000        0.0         5.0
    2   11    50000        0.5         5.0
    3   11    50000        1.0         5.0
    4   11    50000        1.5         5.0
    5   11    50000        2.0         5.0
    6   11    50000        2.5         5.0
3000000.00.35333333330.0      0.0         0.0         0.0         0.0         0.0
11111111
00000101                                                1000.0                      3
00000101                                                1000.0                      3
00000101                                                1000.0                      3
00000101                                                1000.0                      3
00000101                                                1000.0                      3
END OF DATA
```

Figure 5. Input for Simple Compression Problem

In the system used in the program here, the number of an element is associated with the nodal point of smallest (I, J) connected to it. As nodal points are input, we then specify whether an element is to be associated or not, and what to do about the element properties. This is probably most easily seen by reference to the data. As the computer reads the nodal point cards, the following data is found: I, J, element type, four boundary condition codes, r - coordinate, z - coordinate, four loads and/or displacements. For example, Card 1 reads as follows:

Column	Data	Meaning
5	1	I = 1
10	1	J = 1
15	1	read element data
16	1	u_r specified
17	1	u_z specified
18	0	no moment or rotation specified
19	0	no slope specified
21-30	0.0	r - coordinate
31-40	0.0	z - coordinate
41-50	0.0	u_r
51-60	0.0	u_z
61-70	0.0	moment/rotation
71-80	0.0	slope

if the number in Column 15 were 0, the program assumes the same data as for the previous element; if it were 5, no element is associated with this point; 2, 3, and 4 also have specific meanings. If the number in Columns 16-18 is zero, no data is specified; if 1, displacement/rotation data; if 2, force/moment data. Column 19 has a 1 if displacement is along a slope, 0 otherwise. Column 20 is blank. The remaining columns, by 10's, contain r, z, u_r, u_z, moment of rotation, and displacement slope. If the data in a given field is zero, it may be left blank.

Thus, the first six cards refer to nodal points (1, 1) to (6, 1), for all of which the z-displacement is zero, the r-displacement specified (as zero) for only (1, 1). Each nodal point has an element associated with it, except (6, 1). The element data is read for (1, 1), and the same for the rest. No slope or moment is specified. Coordinates are given and applied forces or

displacements are zero. Note that all the nodal points in Row 1 are specified since it is part of the boundary.

For nodal point (1, 1), element data is to be read, and the same data holds until nodal point (1, 10) because only 1 in Column 15 requests data. The first element card is 27, on which is read, by 10's, the following: E; ν; thermal load, $\int \alpha dT$; radial body force; axial body force; pressure; shear; and a number to indicate where the pressure and/or shear acts. Card 28 is also read, and indicates what information is new by a 1 in the appropriate column. For all the elements up to (1, 10), $E = 30 \times 10^6$ psi, $\nu = 1/3$.

Note that all the boundary nodal points are entered as data; and on the left, an element is entered with each nodal point.

Starting with (1, 10), the lower left corner of the left element, we must indicate the pressure load on the top of this element. Thus, we request element data to be read as Cards 29 and 30, where p = 1000.0 psi and a 3 indicates the pressure and face on which it acts (according to a standard scheme). Since we don't change E or ν, these values carry on. For element (2, 10) we again read the pressure, since the program does not carry on the pressure from element to element. This process continues to nodal (6, 10), with which no element is assocated.

Nodal points (1, 11) through (6, 11) finish the regions boundary. No element is associated with these, and only (1, 11) has a specified force or displacement ($u_r = 0$).

While the above description is somewhat tedious, it gives a detailed illustration of data requirements, both in kind and arrangement.

Output for this problem is shown in Figure 6.

Not all the output is shown, for it is too voluminous. It consists of the following:

(1) Boundary condition information for verifying the boundary conditions

(2) Coordinates of all nodal points-includes all the interior points for which no coordinates were specified

(3) Displacements of all nodal points

(4) Stresses and strains in each element - radial, hoop, axial, and shear stress and strain; and maximum and minimum stresses and strains

I J/ ANGLE	COORDINATES R	Z	STRESSES / STRAINS RADIAL R	HOOP THETA	AXIAL Z	SHEAR R-Z	MAXIMUM	MINIMUM	MAX SHEAR
1 1 .00	.250	.250	-1.3097-03 8.6667-04	-1.6371-03 8.6667-04	-1.9500+04 -1.0674-10	3.5384-04 3.1453-11	-1.4734-03 8.6667-04	-1.9500+04 9.1225-11	9.7500+03 8.6667-04
2 1 .00	.750	.250	-2.6193-03 8.6667-04	-2.7831-03 8.6667-04	-1.9500+04 -1.5307-10	5.3481-04 4.7539-11	-2.7831-03 8.6667-04	-1.9500+04 -1.4916-10	9.7500+03 8.6667-04
3 1 .00	1.250	.250	-2.7831-03 8.6667-04	-4.4201-03 8.6667-04	-1.9500+04 -1.8230-10	3.8674-04 3.4377-11	-2.9468-03 8.6667-04	-1.9500+04 -1.7826-10	9.7500+03 8.6667-04
4 1 .00	1.750	.250	-2.9468-03 8.6567-04	-4.0927-03 8.6667-04	-1.9500+04 -1.8228-10	1.6628-04 1.4780-11	-3.1105-03 8.6667-04	-1.9500+04 -1.3643-10	9.7500+03 8.6667-04
5 1 .00	2.250	.250	-1.8008-03 8.6667-04	-3.1105-03 8.6667-04	-1.9500+04 -8.3680-11	1.3724-03 1.2199-10	-1.9645-03 8.6667-04	-1.9500+04 -7.6398-11	9.7500+03 8.6667-04
1 2 -.00	.250	.750	1.6371-04 8.6667-04	-1.6371-04 8.6667-04	-1.9500+04 -1.3930-10	-3.2961-04 -2.9299-11	0.0000 8.6667-04	-1.9500+04 -1.3461-10	9.7500+03 8.6667-04
2 2 -.00	.750	.750	-2.1282-03 8.6667-04	-1.3097-03 8.6667-04	-1.9500+04 -9.9746-11	-8.4509-04 -7.5119-11	-2.2919-03 8.6667-04	-1.9500+04 -9.0949-11	9.7500+03 8.6667-04
3 2 -.00	1.250	.750	-3.2742-03 8.6667-04	-4.0927-03 8.6667-04	-1.9500+04 -7.6725-11	-4.0864-04 -3.6041-11	-3.4379-03 8.6667-04	-1.9500+04 -6.9122-11	9.7500+03 8.6667-04
4 2 -.00	1.750	.750	-4.4201-03 8.6667-04	-4.2564-03 8.6667-04	-1.9500+04 -5.4282-11	-1.01[illegible]-03 -9.028[illegible]-11	-4.5839-03 8.6667-04	-1.9500+04 -4.7294-11	9.7500+03 8.6667-04
5 2 -.00	2.250	.750	-2.7831-03 8.6667-04	-4.9113-03 8.6667-04	-1.9500+04 -3.3305-11	-1.2371-03 -1.0997-10	-2.9468-03 8.6667-04	-1.9500+04 -2.5466-11	9.7500+03 8.6667-04
1 3 -.00	.250	1.250	-4.9113-04 8.6667-04	-8.1855-04 8.6667-04	-1.9500+04 -4.4774-11	-3.6250-04 -3.2222-11	-6.5484-04 8.6667-04	-1.9500+04 -4.0018-11	9.7500+03 8.6667-04
2 3 -.00	.750	1.250	-2.4554-03 8.6667-04	-2.1282-03 8.6667-04	-1.9500+04 -3.4753-11	-9.5028-04 -8.4469-11	-2.6193-03 8.6667-04	-1.9500+04 -2.5466-11	9.7500+03 8.6667-04
3 3 -.00	1.250	1.250	-3.6016-03 8.6667-04	-4.5839-03 8.6667-04	-1.9500+04 -2.0663-11	-8.6843-04 -7.7192-11	-3.7653-03 8.6667-04	-1.9500+04 -1.0914-11	9.7500+03 8.6667-04
4 3 .00	1.750	1.250	-4.7476-03 8.6667-04	-4.4201-03 8.6667-04	-1.9500+04 -1.4734-11	2.5420-04 2.2595-11	-4.9113-03 8.6667-04	-1.9500+04 -1.0914-11	9.7500+03 8.6667-04
5 3 .00	2.250	1.250	-3.4379-03 8.6667-04	-4.[illegible]029-03 8.6667-04	-1.9500+04 -3.2465-11	8.0571-04 7.1641-11	-3.4379-03 8.6667-04	-1.9500+04 -2.9104-11	9.7500+03 8.6667-04
1 4 -.00	.250	1.750	-1.6371-03 8.6667-04	-1.9645-03 8.6667-04	-1.9500+04 1.3895-11	-1.3184-04 -1.1719-11	-1.8008-03 8.6667-04	-1.9500+04 1.0914-11	9.7500+03 8.6667-04
2 4 -.00	.750	1.750	-3.4379-03 8.6667-04	-3.1105-03 8.6667-04	-1.9500+04 2.2268-11	-1.9639-04 -1.7457-11	-3.6016-03 8.6667-04	-1.9500+04 2.5466-11	9.7500+03 8.6667-04
3 4 -.00	1.250	1.750	-4.6201-03 8.6667-04	-5.4024-03 8.6667-04	-1.9500+04 2.3319-11	-2.2414-04 -1.9923-11	-4.5839-03 8.6667-04	-1.9500+04 2.5466-11	9.7500+03 8.6667-04
4 4	1.750	1.750	-5.4024-03	-5.4024-03	-1.9500+04	-2.6645-04	-5.5661-03	-1.9500+04	9.7500+03

Figure 6. Output for Simple Compression Problem

Only data for elements (1,1) through (4,4) is shown. There is no need to show more, as the values are the same for each row, changing only in r - a phenomenon we should have anticipated, due to symmetry. (We could have saved considerable labor by only using one row of elements.) Notice that $\sigma_z = -1000$ psi, $\sigma_r \simeq 0$, $\sigma_\theta \simeq 0$, as is correct. Also $\epsilon_z = \sigma_z/E = 1/3 \times 10^{-4}$; $\epsilon_r = \epsilon_\theta = -\nu\epsilon_z = 0.111 \times 10^{-4}$, as is correct. In this very simple problem, the displacement field is linear, with consequent good results.

B.4.2 THERMAL EXPANSION OF A RIGHT CIRCULAR CYLINDER

This example uses the same shape as Example 1, a circular cylinder, but the loading and boundary conditions are different. In this example we subject the cylinder to a temperature rise of 100°F so that $\int \alpha \, dT = 6.5 \times 10^{-4}$, and restrain the expansion which would normally occur. This requires removal of the input cards specifying the applied pressure, and addition of a 1 to Column 17 of each card for Row 11 to indicate that $u_z = 0$ for these points. Note that both the nodal point cards for the interior nodes of Row 10, and the material cards corresponding to those nodal points are removed. On the first material card the thermal load is then added. The input is shown in Figure 7. The results are shown in Figure 8 in the form of the output for Elements (1, 1) - (4, 4). Again the displacement field is linear, and the resulting stresses are exactly correct.

B.4.3 CENTRIFUGAL LOADING OF A RIGHT CIRCULAR CYLINDER

Example 3 uses the same data as Example 2, except that the thermal load is replaced by a radial body force, $r\omega^2 = 1000$. This gives the stresses set up by rotation with angular velocity ω. The results for this case are summarized in Figure 9. The stresses σ_r, σ_θ, σ_z and displacement u_r are shown. The exact solutions are given as solid lines and the results from the finite element program as points. Again, the agreement is excellent.

```
123456789 123456789 123456789 123456789 123456789 123456789 123456789 12345678

AMG032A  RESTRAINED THERMAL EXPANSION
   50    11
    1     1     11100          0.0          0.0
    2     1     00100          0.5          0.0
    3     1     00100          1.0          0.0
    4     1     00100          1.5          0.0
    5     1     00100          2.0          0.0
    6     1     50100          2.5          0.0
    1     2     01000          0.0          0.5
    6     2     50000          2.5          0.5
    1     3     01000          0.0          1.0
    6     3     50000          2.5          1.0
    1     4     01000          0.0          1.5
    6     4     50000          2.5          1.5
    1     5     01000          0.0          2.0
    6     5     50000          2.5          2.0
    1     6     01000          0.0          2.5
    6     6     50000          2.5          2.5
    1     7     01000          0.0          3.0
    6     7     50000          2.5          3.0
    1     8     01000          0.0          3.5
    6     8     50000          2.5          3.5
    1     9     01000          0.0          4.0
    6     9     50000          2.5          4.0
    1    10     01000          0.0          4.5
    6    10     50000          2.5          4.5
    1    11     51100          0.0          5.0
    2    11     50100          0.5          5.0
    3    11     50100          1.0          5.0
    4    11     50100          1.5          5.0
    5    11     50100          2.0          5.0
    6    11     50100          2.5          5.0
30000000.00.33333330.00065    0.0          0.0          0.0          0.0          0.0
11111111
END OF DATA
```

Figure 7. Input for Restrained Thermal Expansion Problem

I J/ ANGLE	Coordinates R	Z	STRESSES / STRAINS RADIAL R	HOOP THETA	AXIAL Z	SHEAR R-Z	MAXIMUM	MINIMUM	MAX SHEAR
1 1 .00	.250	.250	7.9297-05 1.1111-05	7.9297-05 1.1111-05	-1.0000+03 -3.3333-05	6.2995-06 5.5996-13	6.9065-05 1.1111-05	-1.0000+03 -3.3333-05	5.0000+02 4.4444-05
2 1 .00	.750	.249	5.8833-05 1.1111-05	8.4412-05 1.1111-05	-1.0000+03 -3.3333-05	3.2093-05 2.8527-12	8.8601-05 1.1111-05	-1.0000+03 -3.3333-05	5.0000+02 4.4444-05
3 1 .00	1.250	.249	3.3253-05 1.1111-05	7.1623-05 1.1111-05	-1.0000+03 -3.3333-05	3.3352-05 2.9646-12	2.8137-05 1.1111-05	-1.0000+03 -3.3333-05	5.0000+02 4.4444-05
4 1 .00	1.750	.249	-5.1159-06 1.1111-05	8.6970-05 1.1111-05	-1.0000+03 -3.3333-05	3.8959-05 3.4630-12	-1.2790-05 1.1111-05	-1.0000+03 -3.3333-05	5.0000+02 4.4444-05
5 1 .00	2.250	.249	-2.8137-05 1.1111-05	2.0464-05 1.1111-05	-1.0000+03 -3.3333-05	3.6304-05 3.2271-12	-3.3253-05 1.1111-05	-1.0000+03 -3.3333-05	5.0000+02 4.4444-05
1 2 .00	.250	.750	1.0743-04 1.1111-05	9.4644-05 1.1111-05	-1.0000+03 -3.3333-05	1.9691-05 1.7503-12	9.9760-05 1.1111-05	-1.0000+03 -3.3333-05	5.0000+02 4.4444-05
2 2 .00	.750	.749	7.9297-05 1.1111-05	8.9528-05 1.1111-05	-1.0000+03 -3.3333-05	7.4894-05 6.6572-12	7.4181-05 1.1111-05	-1.0000+03 -3.3333-05	5.0000+02 4.4444-05
3 2 .00	1.250	.749	1.2790-05 1.1111-05	6.9065-05 1.1111-05	-1.0000+03 -3.3333-05	1.0140-04 9.0488-12	2.5560-06 1.1111-05	-1.0000+03 -3.3333-05	5.0000+02 4.4444-05
4 2 .00	1.749	.748	-1.5348-05 1.1111-05	7.1623-05 1.1111-05	-1.0000+03 -3.3333-05	8.3951-05 7.4624-12	-2.8137-05 1.1111-05	-1.0000+03 -3.3333-05	5.0000+02 4.4444-05
5 2 .00	2.249	.749	-3.3253-05 1.1111-05	-5.1159-06 1.1111-05	-1.0000+03 -3.3333-05	4.0564-05 3.6057-12	-4.0927-05 1.1111-05	-1.0000+03 -3.3333-05	5.0000+02 4.4444-05
1 3 .00	.250	1.250	8.9528-05 1.1111-05	8.4412-05 1.1111-05	-1.0000+03 -3.3333-05	2.8354-05 2.5203-12	8.1855-05 1.1111-05	-1.0000+03 -3.3333-05	5.0000+02 4.4444-05
2 3 .00	.750	1.249	5.3717-05 1.1111-05	7.1623-05 1.1111-05	-1.0000+03 -3.3333-05	1.0725-04 9.5332-12	4.1601-05 1.1111-05	-1.0000+03 -3.3333-05	5.0000+02 4.4444-05
3 3 .00	1.249	1.248	-5.1159-06 1.1111-05	7.6739-05 1.1111-05	-1.0000+03 -3.3333-05	1.7516-04 1.5570-11	-1.2790-05 1.1111-05	-1.0000+03 -3.3333-05	5.0000+02 4.4444-05
4 3 .00	1.749	1.248	-7.6739-06 1.1111-05	7.1623-05 1.1111-05	-1.0000+03 -3.3333-05	1.0758-04 9.5627-12	-1.7906-05 1.1111-05	-1.0000+03 -3.3333-05	5.0000+02 4.4444-05
5 3 .00	2.250	1.249	3.5811-05 1.1111-05	7.1623-05 1.1111-05	-1.0000+03 -3.3333-05	4.2679-05 3.7937-12	2.8137-05 1.1111-05	-1.0000+03 -3.3333-05	5.0000+02 4.4444-05
1 4 .00	.250	1.750	8.6970-05 1.1111-05	7.9297-05 1.1111-05	-1.0000+03 -3.3333-05	5.5196-05 4.9063-12	8.1855-05 1.1111-05	-1.0000+03 -3.3333-05	5.0000+02 4.4444-05
2 4 .00	.750	1.749	2.0464-05 1.1111-05	5.6833-05 1.1111-05	-1.0000+03 -3.3333-05	1.6026-04 1.4246-11	1.0232-05 1.1111-05	-1.0000+03 -3.3333-05	5.0000+02 4.4444-05
3 4 .00	1.249	1.748	-5.6275-05 1.1111-05	1.7906-05 1.1111-05	-1.0000+03 -3.3333-05	2.5679-04 2.2826-11	-6.9065-05 1.1111-05	-1.0000+03 -3.3333-05	5.0000+02 4.4444-05
4 4	1.749	1.748	-2.0464-05	6.9065-05	-1.0000+03	1.0309-04	-3.0695-05	-1.0000+03	5.0000+02

Figure 8. Output for Restrained Thermal Expansion Problem

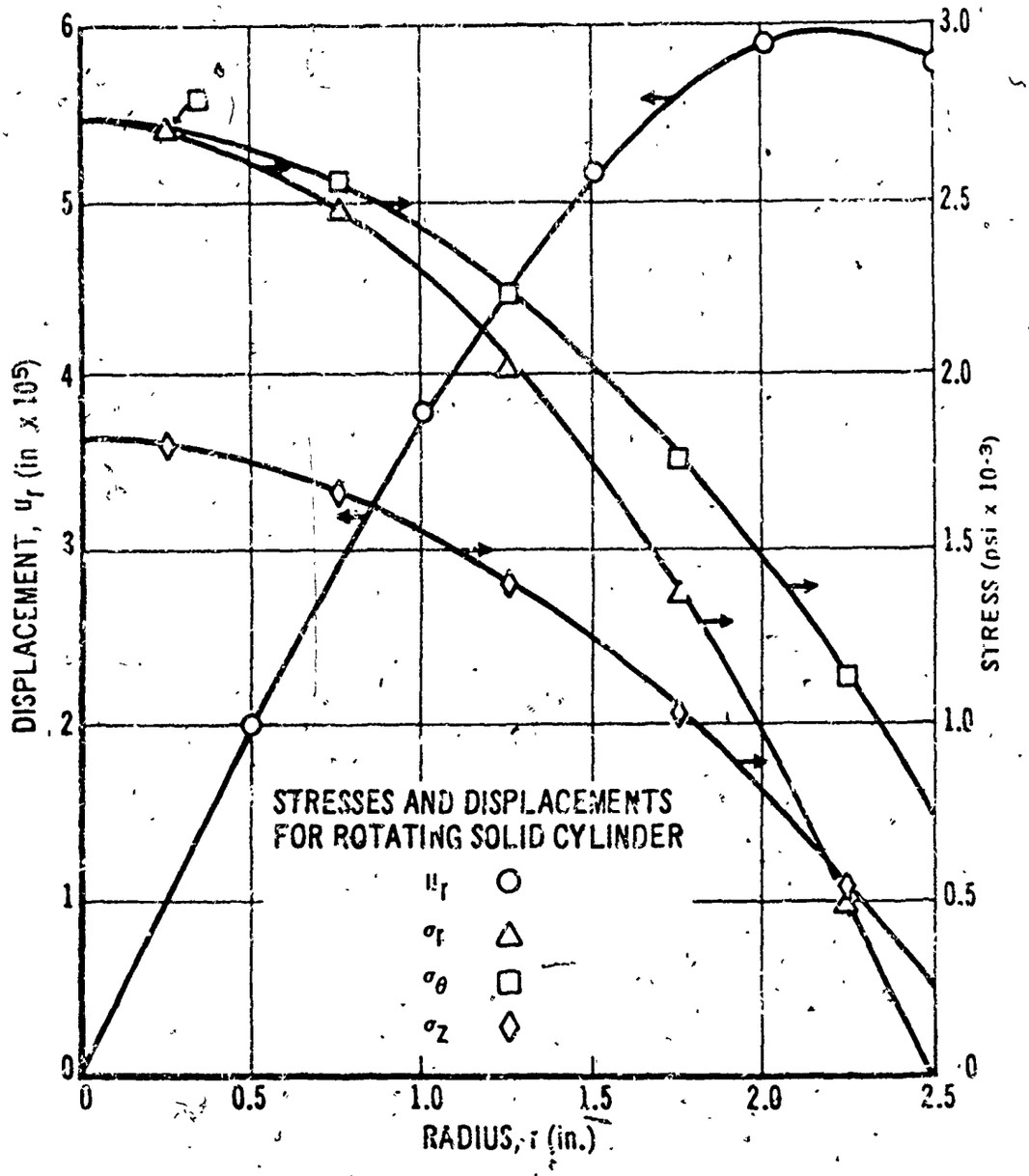

Figure 9. Stresses and Displacements for Rotating Solid Cylinder

B.4.4 INTERNAL PRESSURIZATION AND ROTATION OF A HOLLOW CYLINDER

In the next two examples the geometry is changed to a hollow cylinder. The inner radius is 0.5 inch and the outer 3.0 inches so that the wall thickness is 2.5 inches, as was the radius of the original cylinder. In both examples, the longitudinal deformation is restrained, creating a problem in plane strain. For Example 4, an internal pressure of 1000 psi is applied; and for Example 5, radial body force is applied, with $r\omega^2 = 1000$. The results of the analyses are shown in Figures 10 and 11.

B.4.5 INTERNAL PRESSURIZATION OF A COMPOSITE CYLINDER

To illustrate the ability of the program to handle problems with multiple materials, consider the problem of a composite cylinder subjected to internal pressure. The loading is again an internal pressure of 1000 psi magnitude. The cylinder is now composed of two materials: an inner portion ($r = 0.5$ inch to $r = 1.5$ inches) of copper, and an outer portion ($r = 1.5$ inches to $r = 3.0$ inches) of steel. The result of the finite element analysis and exact solution are shown in Figure 12. Note that discontinuities exist in the displacement gradient and gradient of σ_r, as well as in σ_θ and σ_z. In this particular example an analysis with a mesh of one-half the original size (0.25 inch compared to 0.5 inch) was performed. The solid points for σ_θ are from the second analysis to demonstrate the accuracy with which the discontinuity is captured.

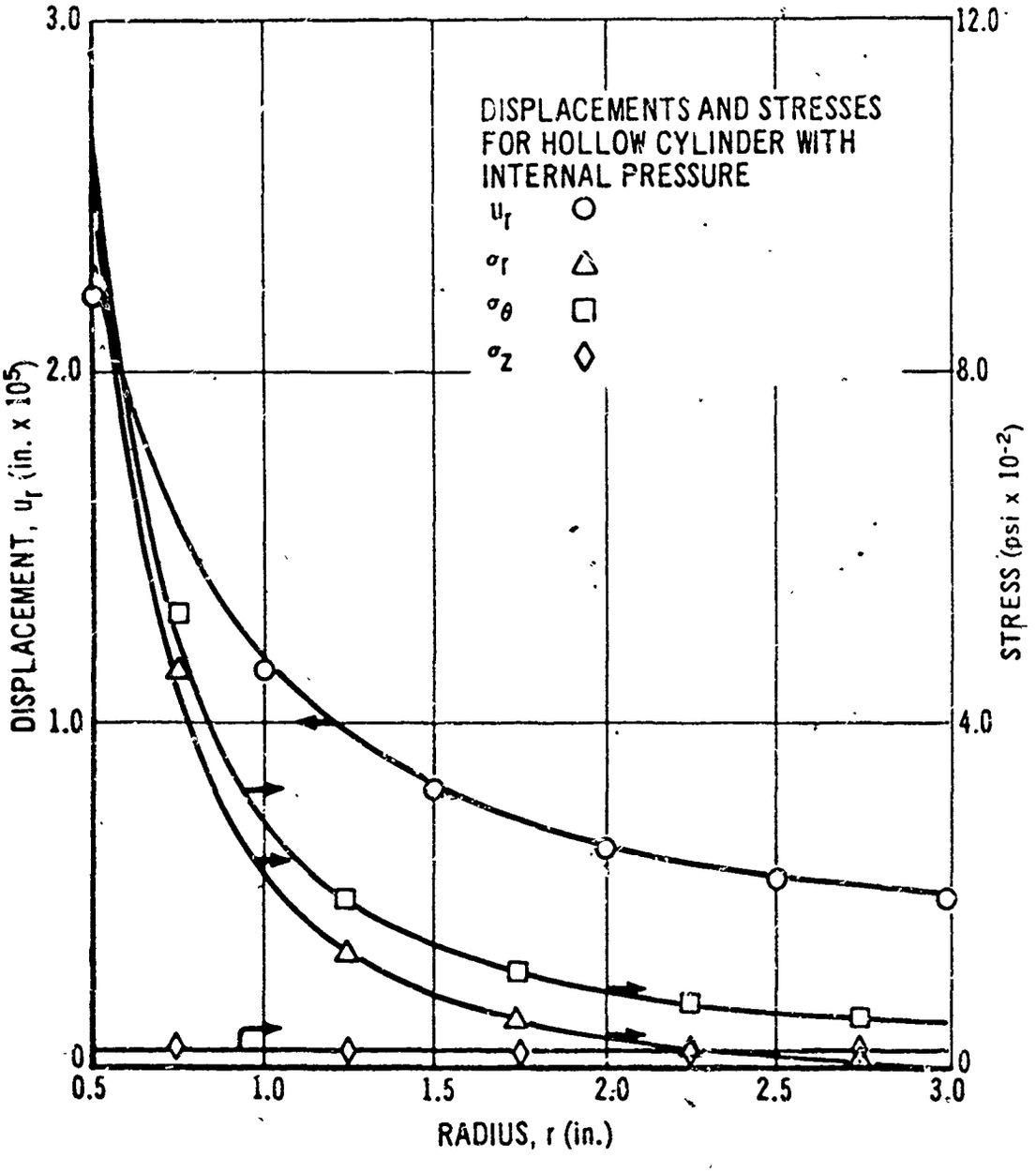

Figure 10. Displacements and Stresses for Hollow Cylinder with Internal Pressure

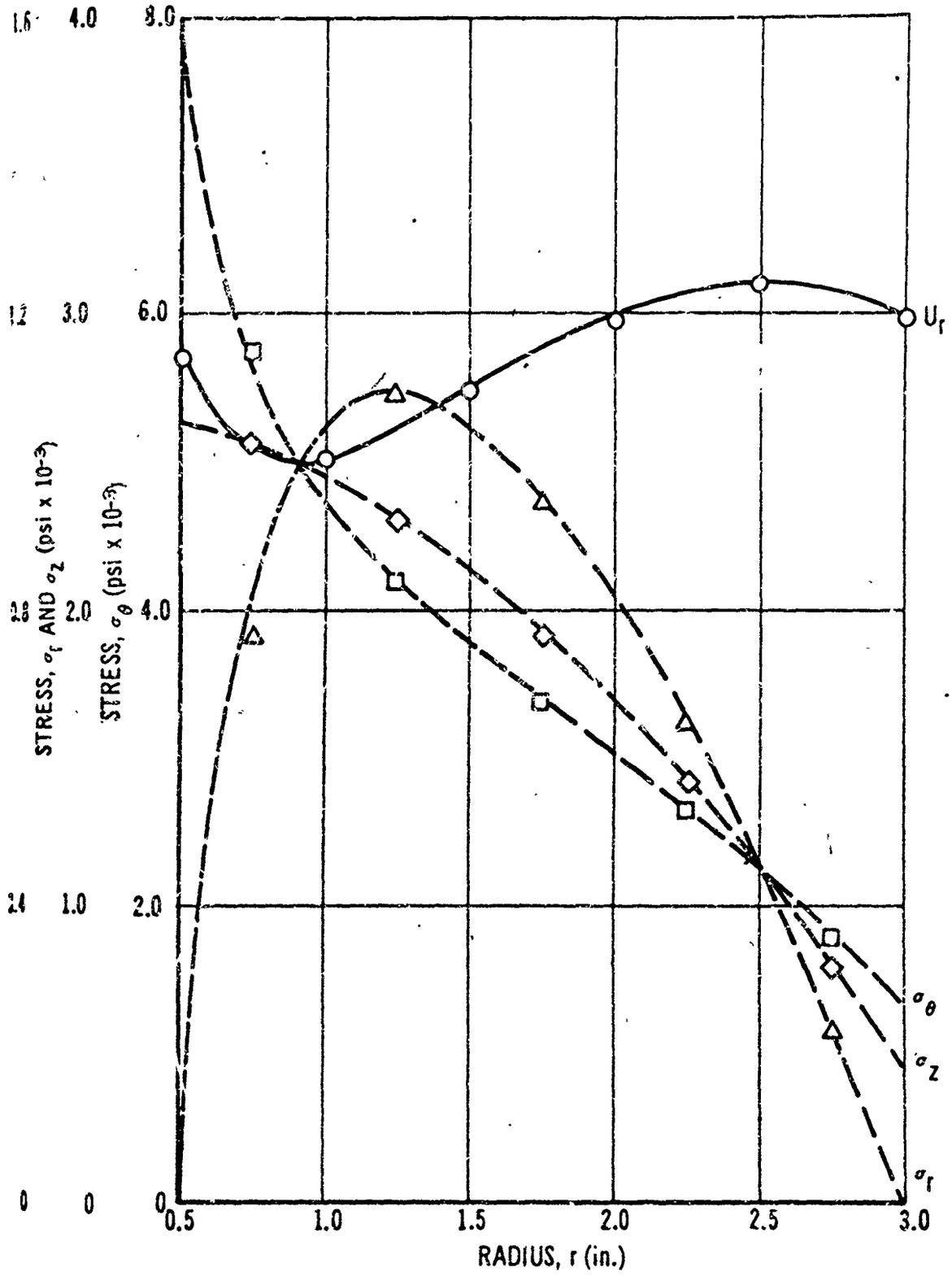

Figure 11. Displacements and Stresses in Rotating Hollow Cylinder

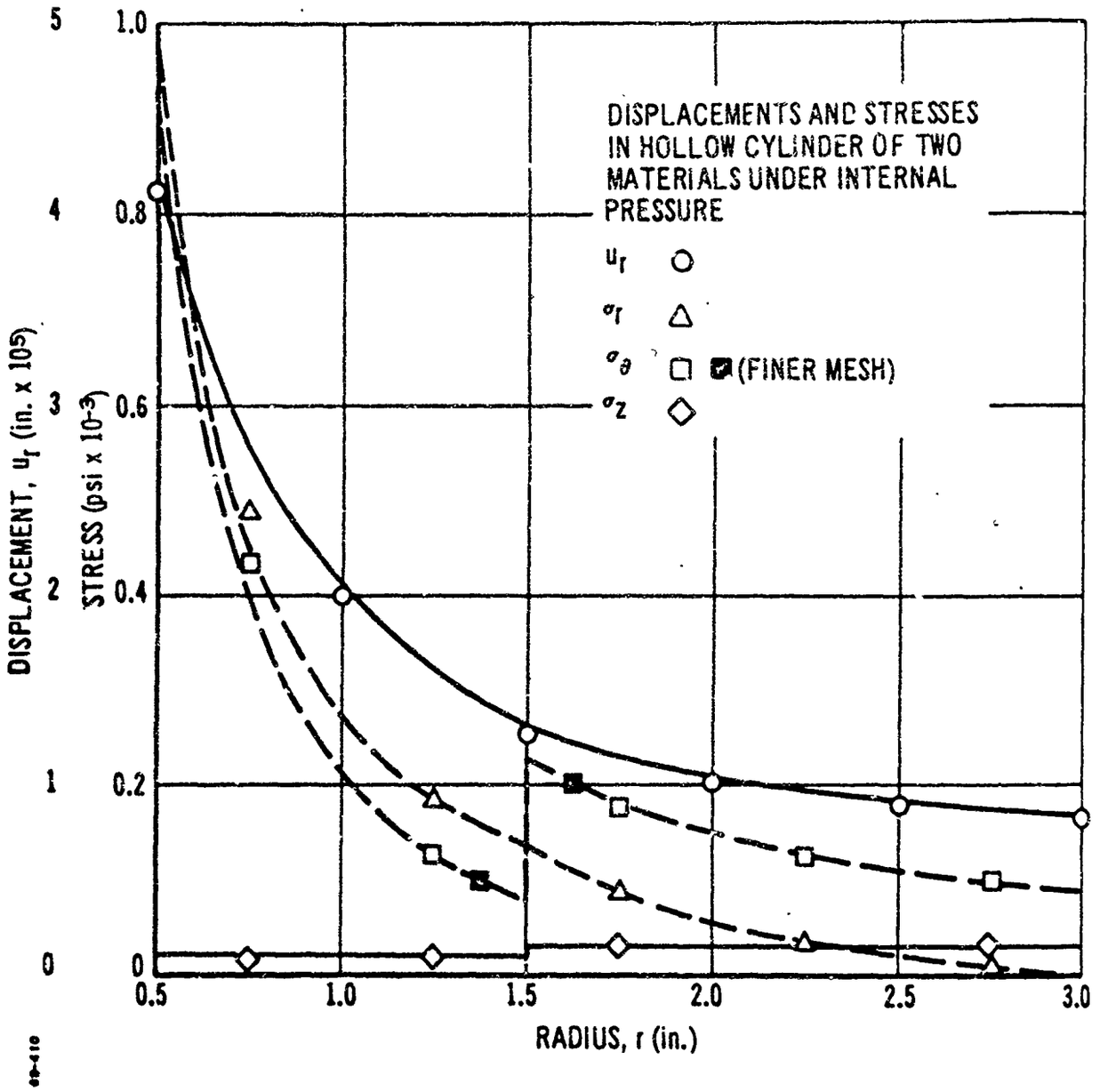

Figure 12 . Displacements and Stresses in Hollow Cylinder of Two Materials Under Internal Pressure

G.5 SAMPLE FINITE ELEMENT COMPUTER PROGRAM

PART A - PROGRAM LISTING (UNIVAC 1108, FORTRAN IV)

```
@ON FOR WILSON
C      ARBITRARY AXISYMMETRIC SOLIDS
       COMMON NUMNP,NUMEL,NUMMAT,NUMPC,ACELZ,ANGFO, BAND,TEMP,MTYPE,Q,NP,
      1 HED(12),E(8,8,12),R0(12),XXNN(12),R(900),Z(900),UR(900),UZ(900),
      2 CODE(900),T(900),IC(200),JRC(200),PR(200),ANGLE(4)
       COMMON /ARG/ RRR(5),ZZZ(5),S(10,10),P(10),TT(4),LM(4),DD(3,3),
      1 HH(6,16),RR(4),ZZ(4),C(4,4),H(6,10),D(6,6),F(6,10),TP(6),XI(10)
      2 ,EE(7),IX(800,5),EPS(800)
       COMMON /BANARG/ MBAND,NUMBLK,B(108),A(108,54)
       COMMON /PLANE/ NPP
C      READ AND PRINT OF CONTROL INFORMATION AND MATERIAL PROPERTIES
   50 READ  (5,1000) HED,NUMNP,NUMEL,NUMMAT,NUMPC,ACELZ,ANGFO,Q,NP,NPP
      WRITE (6,2000) HED,NUMNP,NUMEL,NUMMAT,NUMPC,ACELZ,ANGFO,Q,NP
      IF (NPP) 54,56,54
   54 WRITE (6,2008)
   56 DO 59 M=1,NUMMAT
      READ (5,1001) MTYPE,NUMTC,RO(MTYPE),XXNN(MTYPE)
      WRITE (6,2011) MTYPE,NUMTC,RO(MTYPE),XXNN(MTYPE)
      READ (5,1005) ((E(I,J,MTYPE),J=1,8),I=1,NUMTC)
      WRITE (6,2010) ((E(I,J,MTYPE),J=1,8),I=1,NUMTC)
      DO 58 I=  NUMTC,6
      DO 58 J=1,8
   58 E(I,J,MTYPE)=E(NUMTC,J,MTYPE)
   59 CONTINUE
C      READ AND PRINT OF NODAL POINT DATA
      WRITE (6,2004)
      L=0
   66 READ(5,1002) N,CODE(N),R(N),Z(N),UR(N),UZ(N),T(N)
      NL=L+1
      ZX=N-L
      DR=(R(N)-R(L))/ZX
      DZ=(Z(N)-Z(L))/ZX
      DT=(T(N)-T(L))/ZX
   70 L=L+1
      IF(N-L) 100,90,80
   80 CODE(L)=0.0
      R(L)=R(L-1)+DR
      Z(L)=Z(L-1)+DZ
      UR(L)=0.0
      UZ(L)=0.0
      T(L)=T(L-1)+DT
      GO TO 70
   90 WRITE(6,2002)(KK,CODE(KK),R(KK),Z(KK),UR(KK),UZ(KK),T(KK),KK=NL,N)
      IF(NUMNP-N) 100,110,60
  100 WRITE (6,2009) N
      CALL EXIT
  110 CONTINUE
C       READ AND PRINT OF ELEMENT PROPERTIES
      WRITE (6,2005)
      N=0
  130 READ (5,1003) M,(IX(M,I),I=1,5)
  140 N=N+1
      IF (M-N) 170,170,150
  150 IX(N,1)=IX(N-1,1)+1
      IX(N,2)=IX(N-1,2)+1
      IX(N,3)=IX(N-1,3)+1
      IX(N,4)=IX(N-1,4)+1
      IX(N,5)=IX(N-1,5)
```

```
  170 WRITE (6,2003) N,(IX(N,I),I=1,5)
      IF (N-N) 180,180,140
  180 IF (NUMEL-N) 190,190,130
  190 CONTINUE
C     READ AND PRINT OF PRESSURE BOUNDARY CONDITIONS
      IF (NUMPC) 200,310,200
  200 WRITE (6,2005)
      DO 300 L=1,NUMPC
      READ  (5,1004) IBC(L),JBC(L),PP(L)
  300 WRITE (6,2007) IBC(L),JBC(L),PP(L)
  310 CONTINUE
C     DETERMINE BAND WIDTH
      J=0
      DO 340 N=1,NUMEL
      DO 340 I=1,4
      DO 325 L=1,4
      KK=IABS(IX(N,I)-IX(N,L))
      IF (KK-J) 325,325,320
  320 J=KK
  325 CONTINUE
  340 CONTINUE
      MBAND=2*J+2
C     SOLVE NON-LINEAR STRUCTURE BY SUCCESSIVE APPROXIMATIONS
      DO 350 N=1,NUMEL
  350 EPS(N)=0.0
      DO 500 NNN=1,NAP
C     FORM STIFFNESS MATRIX
      CALL STIFF
C     SOLVE FOR DISPLACEMENTS
      CALL BANSOL
      WRITE (6,2006) (N,B(2*N-1),B(2*N),N=1,NUMNP)
C     COMPUTE STRESSES
      CALL STRESS
  500 CONTINUE
      GO TO 50
 1000 FORMAT (12A6/4I5,3F10.2,2I5)
 1001 FORMAT (2I5,2F10.0)
 1002 FORMAT (I5,F5.0,5F10.0)
 1003 FORMAT (6I5)
 1004 FORMAT (2I5,F10.0)
 1005 FORMAT (8F10.0)
 2000 FORMAT (1H1,12A6/
     1 30H0 NUMBER OF NODAL POINTS------ I3 /
     2 30H0 NUMBER OF ELEMENTS---------- I3 /
     3 30H0 NUMBER OF DIFF. MATERIALS--- I3 /
     4 30H0 NUMBER OF PRESSURE CARDS---- I3 /
     5 30H0 AXIAL ACCELERATION---------- E12.4/
     6 30H0 ANGULAR VELOCITY------------ E12.4/
     7 30H0 REFERENCE TEMPERATURE------- E12.4/
     8 30H0 NUMBER OF APPROXIMATIONS---- I3)
 2001 FORMAT (49H1ELEMENT NO.      I     J     K     L    MATERIAL  )
 2002 FORMAT (I12,5I2,2F12.3,2E24.7,F12.3)
 2003 FORMAT (1I13,4I6,1I12)
 2004 FORMAT (10AH)NODAL POINT        TYPE  R-ORDINATE  Z-ORDINATE  R LO
     1AD OR DISPLACEMENT  Z LOAD OR DISPLACEMENT TEMPERATURE )
 2005 FORMAT (29H0PRESSURE BOUNDARY CONDITIONS/ 24H     I     J    PRESS
     1URE )
 2006 FORMAT (12HIN.P. NUMBER 1X 2HUR 18X 2HUZ / (1I12,2E20.7))
```

```
 2007 FORMAT (2I6,F12.2)
 2008 FORMAT ('20H0PLANE STRESS STRUCTURE ')
 2009 FORMAT (25H0NODAL POINT CARD ERROR IN *5)
 2010 FORMAT (15H0  TEMPERATURE 10X 5HE(RZ) 9X 6HNU(RZ) 11X 4HE(T)
     1, 10X 5HNU(T) 6X 6HG(RZ) 7X 6HALPHA(T) *5H   YIELD STRESS /
     2 (F15.2,7E15.5))
 2011 FORMAT (17H0MATERIAL NUMBER= I3, 30H, NUMBER OF TEMPERATURE CARDS=
     1 I3, 15H, MASS DENSITY= E12.4 ,16H,MODULUS RATIO= E12.4 )
C
      END
@N FOR STIFF
      SUBROUTINE STIFF
      COMMON NUMNP,NUMEL,NUMAT,NUMPC,ACEL2,NGEO, RAND,TEMP,MTYPE,Q,NP,
     1 MED(12),E(8,8,12),CC(12),XXNU(12),R(900),Z(900),UR(900),UZ(900),
     2 CODE(900),T(900),IFC(200),JRC(200),PR(200),ANGLE(4)
      COMMON /ARG/ RRE(5),ZZ(5),S(10,10),P(10),TT(4),LM(4),DD(3,3),
     1 HH(6,10),RR(4),ZZ(4),C(4,4),H(6,10),D(6,6),F(6,10),TP(6),XI(10)
     2 ,EE(7),IX(800,5),EPS(800)
      COMMON /BANARG/ NBAND,NUMBLK,B(108),A(108,54)
      COMMON /PLANE/ NPE
C     INITIALIZATION
      REWIND 11
      NP=27
      ND=2*NP
      ND2=2*ND
      STOP=0.0
      NUMBLK=0
      DO 50 N=1,ND2
      B(N)=0.0
      DO 50 M=1,ND
   50 A(N,M)=0.0
C     FORM STIFFNESS MATRIX IN BLOCKS
   60 NUMBLK=NUMBLK+1
      NH=NP*(NUMBLK+1)
      NV=NH-NP+1
      NL=NP-NP+1
      KSHIFT=2*NL-2
      DO 210 N=1,NUMEL
      IF (IX(N,5)) 210,210,65
   65 DO 80 I=1,4
      IF (IX(N,I)-NL) 80,70,70
   70 IF (IX(N,I)-NH) 90,80,80
   80 CONTINUE
      GO TO 210
   90 CALL QUAD(N,VOL)
      IF(VOL) 142,142,144
  142 WRITE (6,2003) N
      STOP=1.0
  144 IF(IX(N,3)-IX(N,4)) 145,145,145
  145 DO 150 II=1,8
      CC=S(II,10)/S(10,10)
      P(II)=P(II)-CC*P(10)
      DO 150 JJ=1,8
  150 S(II,JJ)=S(II,JJ)-CC*S(10,JJ)
      DO 160 II=1,8
      CC=S(II,8)/S(8,8)
      P(II)=P(II)-CC*P(8)
      DO 160 JJ=1,8
```

```
  160 S(II,JJ)=S(II,JJ)-CC*S(9,JJ)
C
C          ADD ELEMENT STIFFNESS TO TOTAL STIFFNESS
  169 DO 166 I=1,4
  166 LY(I)=2*IX(N,I)-2
      DO 200 I=1,4
      DO 200 K=1,2
      II=LY(I)+K-KSHIFT
      KK=2*I-2+K
      B(II)=B(II)+P(KK)
      DO 200 J=1,4
      DO 200 L=1,2
      JJ=LY(J)+L-II+1-KSHIFT
      LL=2*J-2+L
      IF(JJ) 200,200,175
  175 IF(ND-JJ) 180,195,195
  180 WRITE (6,2004) N
      STOP=1.0
      GO TO 210
  195 A(II,JJ)=A(II,JJ)+S(KK,LL)
  200 CONTINUE
  210 CONTINUE
C     ADD CONCENTRATED FORCES WITHIN BLOCK
      DO 250 N=NL,NM
      K=2*N-KSHIFT
      B(K)=B(K)+UZ(N)
  250 B(K-1)=B(K-1)+UR(N)
C     BOUNDARY CONDITIONS
C       1. PRESSURE B.C.
      IF (PUMPC) 260,310,260
  260 DO 300 L=1,NUMPC
      I=IBC(L)
      J=JBC(L)
      PP=PR(L)/6.
      DZ=(Z(I)-Z(J))*PP
      DR=(R(J)-R(I))*PP
      RX=2.0*R(I)+R(J)
      ZX=R(I)+2.0*R(J)
      IF (NPP) 262,264,262
  262 RX=3.0
      ZX=3.0
  264 II=2*I-KSHIFT
      JJ=2*J-KSHIFT
      IF (II) 280,280,265
  265 IF (II-ND) 270,270,280
  270 SINA=0.0
      COSA=1.0
      IF (CODE(I)) 271,272,272
  271 SINA=SIN(CODE(I))
      COSA=COS(CODE(I))
  272 B(II-1)=B(II-1)+RX*(COSA*DZ+SINA*DR)
      B(II)=B(II)-RX*(SINA*DZ-COSA*DR)
  280 IF (JJ) 300,300,285
  285 IF (JJ-ND) 290,290,300
  290 SINA=0.0
      COSA=1.0
      IF (CODE(J)) 291,292,292
  291 SINA=SIN(CODE(J))
```

```
      COSA=COS(CODE(JJ))
  292 B(JJ-1)=B(JJ-1)+ZX*(COSA*DZ+SINA*DR)
      B(JJ)=B(JJ)-ZX*(SINA*DZ-COSA*DR)
  300 CONTINUE
C       Z. DISPLACEMENT B.C.
  310 DO 400 M=NL,NN
      IF (M-NUMNP) 315,315,400
  315 U=UR(M)
      N=2*M-1-KSHIFT
      IF (CODE(M)) 390,400,316
  316 IF (CODE(M)-1.) 317,370,317
  317 IF (CODE(M)-2.) 318,390,318
  318 IF (CODE(M)-3.) 390,380,390
  370 CALL MODIFY(A,B,ND2,MBAND,N,U)
      GO TO 400
  380 CALL MODIFY(A,B,ND2,MBAND,N,U)
  390 U=UZ(M)
      N=N+1
      CALL MODIFY(A,B,ND2,MBAND,N,U)
  400 CONTINUE
C     WRITE BLOCK OF EQUATIONS ON TAPE AND SHIFT UP LOWER BLOCK
      WRITE (11) (B(N),(A(N,M),M=1,MBAND),N=1,ND)
      DO 420 N=1,ND
      K=N+ND
      B(N)=B(K)
      B(K)=0.0
      DO 420 M=1,ND
      A(N,M)=A(K,M)
  420 A(K,M)=0.0
C       CHECK FOR LAST BLOCK
      IF (L-NUMNP) 60,480,480
  480 CONTINUE
      END FILE 11
      IF(STOP) 490,500,490
  490 CALL EXIT
  500 RETURN
 2003 FORMAT (26HONEGATIVE AREA ELEMENT NO. I4)
 2004 FORMAT (29HOBAND WIDTH EXCEEDS ALLOWABLE I4)
      END
$ENTRY QUAD
      SUBROUTINE QUAD(N,VOL)
      COMMON NUMNP,NUMEL,NUMAT,NUMPC,ACEL2,NGEO,MBAND,TEMP,MTYPE,O,NP,
     1 NED(12),E(6,6,12),RO(12),XSND(12),R(900),Z(900),UR(900),UZ(900),
     2 CODE(900),T(900),IBC(200),JBC(200),PR(200),ANGLE(6)
      COMMON /ARG/ PRR(5),ZZ(5),S(10,10),P(10),TT(4),LM(4),ND(3,3),
     1 HH(6,10),RR(4),ZZ(4),C(4,4),H(6,10),D(6,6),F(6,10),TP(6),XI(10)
     2 ,EE(7),IX(900,5),EPS(600)
      COMMON /BANDNG/ ND,NUMBLK,A(108),A(108,54)
      COMMON /PLANE/ NPP
   90 I=IX(N,1)
      J=IX(N,2)
      K=IX(N,3)
      L=IX(N,4)
      MTYPE=IX(N,5)
      IX(N,5)=-IX(N,5)
C           FORM STRESS-STRAIN RELATIONSHIP
      TEMP=(T(I)+T(J)+T(K)+T(L))/4.0
      DO 103 M=2,8
```

```
      IF (E(M,1,MTYPE)-TEMP) 103,104,104
  103 CONTINUE
  104 RATIO=0.0
      DEN=E(M,1,MTYPE)-E(M-1,1,MTYPE)
      IF (DEN) 70,71,70
   70 RATIO=(TEMP-E(M-1,1,MTYPE))/DEN
   71 DO 105 KK=1,7
  105 EE(KK)=E(M-1,KK+1,MTYPE)+RATIO*(E(M,KK+1,MTYPE)-E(M-1,KK+1,MTYPE))
      TEMP=TEMP-0
      EPSR=EE(7)/EE(1)
      IF (EPSR-EPS(N)) 10,,108,106
  108 RATIO=(EE(7)/(EPS(N)*EE(1)))*(1.0-XXN(MTYPE))+XXNN(MTYPE)
      EE(1)=EE(1)*RATIO
      EE(5)=EE(5)*RATIO
  109 CONTINUE
      IF (NPP) 86,86,84
   86 XX=EE(1)/EE(3)
      COMM=EE(1)/(XX-EE(2)**2)
      C(1,1)=COMM*XX
      C(1,2)=COMM*EE(2)
      C(1,3)=0.0
      C(2,1)=C(1,2)
      C(2,2)=COMM
      C(2,3)=0.0
      C(3,1)=0.0
      C(3,2)=0.0
      C(3,3)=0.0
      C(4,4)=.5*EE(1)/(XX+EE(2))
      GO TO 88
   84 C(1,1)=1.0/EE(1)
      C(1,2)=-EE(2)/EE(1)
      C(1,3)=-EE(4)/EE(3)
      C(2,1)=C(1,2)
      C(2,2)=C(1,1)
      C(2,3)=C(1,3)
      C(3,1)=C(1,3)
      C(3,2)=C(2,3)
      C(3,3)=1.0/EE(3)
      CALL SYMINV(C,3)
      C(4,4)=EE(5)/(2.0+2.0*EE(2))
   88 DO 110 M=1,3
  110 TT(M)=((C(M,1)+C(M,2))*EE(5)+C(M,3)*EE(6))*TEMP
C          FORM QUADRILATERAL STIFFNESS MATRIX
      RPP(5)=(R(I)+R(J)+R(K)+R(L))/4.0
      ZZZ(5)=(Z(I)+Z(J)+Z(K)+Z(L))/4.0
      DO 94 M=1,4
      MM=IX(N,M)
      IF(NPP) 91,89,91
   89 IF (R(MM)) 93,91,93
   91 R(MM)=.01*RPP(5)
      IF (CODE(MM)) 93,92,93
   92 CODE(MM)=1.0
   93 RPP(M)=R(MM)
   94 ZZZ(M)=Z(MM)
      DO 100 II=1,10
      P(II)=0.0
      DO 95 JJ=1,6
   95 HH(JJ,II)=0.0
```

```
      DO 100 JJ=1,10
  100 S(II,JJ)=0.0
      DO 110 II=1,4
      JJ=IY(N,II)
  110 ANGLE(II)=COOF(JJ)/57.3
      IF (ANGLE(II)) 125,120,125
  120 CALL TRISTF(1,2,3)
      RRR(5)=(RRR(1)+RRR(2)+RRR(3))/3.0
      ZZZ(5)=(ZZZ(1)+ZZZ(2)+ZZZ(3))/3.0
      VOL=XI(1)
      GO TO 130
  125 VOL=0.0
      CALL TRISTF(4,1,5)
      VOL=VOL+XI(1)
      CALL TRISTF(1,2,5)
      VOL=VOL+XI(1)
      CALL TRISTF(2,3,5)
      VOL=VOL+XI(1)
      CALL TRISTF(3,4,5)
      VOL=VOL+XI(1)
      DO 140 II=1,6
      DO 140 JJ=1,10
  140 HH(II,JJ)=HH(II,JJ)/4.0
  130 RETURN
      END
ON FOR TRISTF
      SUBROUTINE TRISTF(II,JJ,KK)
      COMMON NUMNP,NUMEL,NUMMAT,NUMPC,ACCLZ,ANGFO,MBAND,TEMP,MTYPE,O,NP,
     1 NED(12),E(9,8,12),RO(12),XXMN(12),R(900),Z(900),UR(900),UZ(900),
     2 COOF(900),T(900),IPC(200),JPC(200),PR(200),ANGLE(4)
      COMMON /ARG/ RRR(5),ZZ(5),S(10,10),P(10),TT(4),LM(4),DD(3,3),
     1 HH(6,10),RR(4),ZZ(4),C(4,4),H(6,10),D(6,6),F(6,10),TP(6),XI(10)
     2 ,EE(7),IX(800,5),EPS(900)
      COMMON /PLANE/ IPP
C       1. INITIALIZATION
      LM(1)=II
      LM(2)=JJ
      LM(3)=KK
      RR(1)=RRR(II)
      RR(2)=RRR(JJ)
      RR(3)=RRR(KK)
      RR(4)=RRR(II)
      ZZ(1)=ZZZ(II)
      ZZ(2)=ZZZ(JJ)
      ZZ(3)=ZZZ(KK)
      ZZ(4)=ZZZ(II)
   85 DO 100 I=1,6
      DO 90 J=1,10
      F(I,J)=0.0
   90 H(I,J)=0.0
      DO 100 J=1,6
  100 D(I,J)=0.0
C       3. FORM INTEGRAL(C)T*(C)*(G)
      CALL INTER(XI,RR,ZZ)
      D(2,6)=XI(1)*(C(1,2)+C(2,3))
      D(3,5)=XI(1)*C(4,4)
      D(5,5)=XI(1)*C(4,4)
      D(6,6)=XI(1)*C(2,2)
```

```
      IF (NPP) 104,106,104
  104 D(2,2)=XI(1)*C(1,1)
      D(5,5)=XI(1)*C(4,4)
      GO TO 108
  106 D(1,1)=XI(3)*C(3,3)
      D(1,2)=XI(2)*(C(1,3)+C(3,3))
      D(1,5)=XI(5)*C(3,3)
      D(1,6)=XI(2)*C(2,3)
      D(2,2)=XI(1)*(C(1,1)+2.0*C(1,3)+C(3,3))
      D(2,5)=XI(4)*(C(1,3)+C(3,3))
      D(3,3)=XI(6)*C(3,3)+XI(1)*C(4,4)
      D(3,6)=XI(4)*C(2,3)
  108 DO 110 I=1,6
      DO 110 J=I,6
  110 D(J,I)=D(I,J)
C       4. FORM  COEFFICIENT-DISPLACEMENT TRANSFORMATION MATRIX
      COMM=RR(2)*(ZZ(3)-ZZ(1))+RR(1)*(ZZ(2)-ZZ(3))+RR(3)*(ZZ(1)-ZZ(2))
      DD(1,1)=(RR(2)*ZZ(3)-RR(3)*ZZ(2))/COMM
      DD(1,2)=(RR(3)*ZZ(1)-RR(1)*ZZ(3))/COMM
      DD(1,3)=(RR(1)*ZZ(2)-RR(2)*ZZ(1))/COMM
      DD(2,1)=(ZZ(2)-ZZ(3))/COMM
      DD(2,2)=(ZZ(3)-ZZ(1))/COMM
      DD(2,3)=(ZZ(1)-ZZ(2))/COMM
      DD(3,1)=(RR(3)-RR(2))/COMM
      DD(3,2)=(RR(1)-RR(3))/COMM
      DD(3,3)=(RR(2)-RR(1))/COMM
      DO 120 I=1,3
      J=2*LM(I)-1
      H(1,J)=DD(1,I)
      H(2,J)=DD(2,I)
      H(3,J)=DD(3,I)
      H(4,J+1)=DD(1,I)
      H(5,J+1)=DD(2,I)
  120 H(6,J+1)=DD(3,I)
C     ROTATE UNKNOWNS IF REQUIRED
      DO 125 J=1,2
      I=LM(J)
      IF (ANGLE(I)) 122,125,125
  122 SINA=SIN(ANGLE(I))
      COSA=COS(ANGLE(I))
      IJ=2*I
      DO 124 K=1,6
      TEM=H(K,IJ-1)
      H(K,IJ-1)=TEM*COSA+H(K,IJ)*SINA
  124 H(K,IJ)= -TEM*SINA+H(K,IJ)*COSA
  125 CONTINUE
C       5. FORM ELEMENT STIFFNESS MATRIX (H)T*(D)*(H)
      DO 130 J=1,10
      DO 130 K=1,6
      IF (H(K,J)) 128,130,128
  128 DO 129 I=1,6
  129 F(I,J)=F(I,J)+D(I,K)*H(K,J)
  130 CONTINUE
      DO 140 I=1,10
      DO 140 K=1,6
      IF (H(K,I)) 138,140,138
  138 DO 139 J=1,10
  139 S(I,J)=S(I,J)+H(K,I)*F(K,J)
```

```
  140 CONTINUE
C       6. FORM THERMAL LOAD MATRIX
      IF (NPP) 145,150,145
  145 TT(3)=0.0
      COMM=XI(1)*EE(4)
      S(9,9)=S(9,9)+COMM
      S(10,10)=S(10,10)+COMM
  150 COMM=RO(MTYPE)*ANGFQ**2
      TP(1)=COMM*XI(7) + XI(2)*TT(3)
      TP(2)=COMM*XI(9) + YI(1)*(TT(1)+TT(3))
      TP(3)=COMM*XI(10)+ XI(6)*TT(3)
      COMM=-RO(MTYPE)*ACELZ
      TP(4)=COMM*XI(1)
      TP(5)=COMM*XI(7)
      TP(6)=COMM*XI(3) +XI(1)*TT(2)
      DO 160 I=1,10
      DO 160 K=1,6
  160 P(I)=P(I)+H(K,I)*TP(K)
C     FORM STRAIN TRANSFORMATION MATRIX
  400 DO 410 I=1,6
      DO 410 J=1,10
  410 HH(I,J)=HH(I,J)+H(I,J)
      RETURN
      END
ON FOR SYMINV
      SUBROUTINE SYMINV(A,NMAX)
      DIMENSION A(4,4)
      DO 200 N=1,NMAX
      D=A(N,N)
      DO 100 J=1,NMAX
  100 A(N,J)=-A(N,J)/D
      DO 150 I=1,NMAX
      IF(N-I) 110,150,110
  110 DO 140 J=1,NMAX
      IF(N-J) 120,140,120
  120 A(I,J)=A(I,J)+A(I,N)*A(N,J)
  140 CONTINUE
  150 A(I,N)=A(I,N)/D
      A(N,N)=1.0/D
  200 CONTINUE
      RETURN
      END
ON FOR INTER
      SUBROUTINE INTER(XI,RR,ZZ)
      DIMENSION RR(3),ZZ(3),XI(10),XM(6),R(6),Z(6),XX(6)
      COMMON /PLANE/ NPP
      DATA (XX(I),I=1,6)/3*1.0,3*3.0/
      COMM=RR(2)*(ZZ(3)-ZZ(1))+RR(1)*(ZZ(2)-ZZ(3))+RR(3)*(ZZ(1)-ZZ(2))
      COMM=COMM/24.0
      R(1)=RR(1)
      R(2)=RR(2)
      R(3)=RR(3)
      R(4)=(R(1)+R(2))/2.
      R(5)=(R(2)+R(3))/2.
      R(6)=(R(3)+R(1))/2.
      Z(1)=ZZ(1)
      Z(2)=ZZ(2)
      Z(3)=ZZ(3)
```

```
      Z(4)=(Z(1)+Z(2))/2.
      Z(5)=(Z(2)+Z(3))/2.
      Z(6)=(Z(3)+Z(1))/2.
      IF (IPP) 10,30,10
   10 DO 20 I=1,6
   20 XM(I)=XX(I)
      GO TO 40
   30 DO 35 I=1,6
   35 XM(I)=XX(I)*R(I)
   40 DO 50 I=1,10
   50 XI(I)=0.0
      DO 100 I=1,6
      XI(1)=XI(1)+XM(I)
      XI(7)=XI(7)+XM(I)*P(I)
      XI(8)=XI(8)+XM(I)*Z(I)
      XI(9)=XI(9)+XM(I)*R(I)**2
      XI(10)=XI(10)+XM(I)*P(I)*Z(I)
      IF(R(I).LT.1.E-10) GO TO 100
      XI(2)=XI(2)+XM(I)/R(I)
      XI(3)=XI(3)+XM(I)/(R(I)**2)
      XI(4)=XI(4)+XM(I)*Z(I)/R(I)
      XI(5)=XI(5)+XM(I)*Z(I)/(R(I)**2)
      XI(6)=XI(6)+XM(I)*Z(I)**2/(R(I)**2)
  100 CONTINUE
      DO 150 I=1,10
  150 XI(I)=XI(I)*COMM
      RETURN
      END
ON FOR MODIFY
      SUBROUTINE MODIFY(A,B,NEQ,MBAND,N,U)
      DIMENSION A(108,54),B(108)
      DO 250 M=2,MBAND
      K=N-M+1
      IF(K) 235,235,230
  230 B(K)=B(K)-A(K,M)*U
      A(K,M)=0.0
  235 K=K+M-1
      IF(NEQ-K) 250,240,240
  240 B(K)=B(K)-A(N,M)*U
      A(N,M)=0.0
  250 CONTINUE
      A(N,1)=1.0
      B(N)=U
      RETURN
      END
ON FOR BANSOL
      SUBROUTINE BANSOL
      COMMON /BANARG/ NN,NUMBLK,B(108),A(108,54)
      NN=54
      NL=NN+1
      NH=NN+NN
      REWIND 11
      REWIND 12
      NB=0
      GO TO 150
C     REDUCE EQUATIONS BY BLOCKS
C     1. SHIFT BLOCK OF EQUATIONS
  100 NB=NB+1
```

```
      DO 125 N=1,NN
      NN=N+1
      B(N)=B(NM)
      B(NM)=0.0
      DO 125 M=1,MM
      A(N,M)=A(NM,M)
  125 A(NM,M)=0.0
C     2. READ NEXT BLOCK OF EQUATIONS INTO CORE
      IF (NUMBLK-NB) 150,200,150
  150 READ (11) (B(N),(A(N,M),M=1,MM),N=1,NM)
      IF (NB) 200,200,200
C     3. REDUCE BLOCK OF EQUATIONS.
  200 DO 300 N=1,NN
      IF(A(N,1)) 225,300,225
  225 B(N)= B(N)/A(N,1)
      DO 275 L=2,MM
      IF(A(N,L)) 230,275,230
  230 C=A(N,L)/A(N,1)
      I=N+L-1
      J=0
      DO 250 K=L,MM
      J=J+1
  250 A(I,J)=A(I,J)-C*A(N,K)
      B(I)=B(I)-A(N,L)*B(N)
      A(N,L)=C
  275 CONTINUE
  300 CONTINUE
C     4. WRITE BLOCK OF REDUCED EQUATIONS ON TAPE 2
      IF (NUMBLK-NB) 375,400,375
  375 WRITE(12) (B(N),(A(N,M),M=2,MM),N= 1,NN)
      GO TO 100
C     BACK-SUBSTITUTION
  400 DO 450 M=1,NN
      N=NN+1-M
      DO 425 K=2,MM
      L=N+K-1
  425 B(N)=B(N)-A(N,K)*B(L)
      NN=N+NN
      B(NM)=B(N)
  450 A(NM,NB)=B(N)
      NB=NB-1
      IF (NB) 475,500,475
  475 BACKSPACE 12
      READ (12) (B(N),(A(N,M),M=2,MM),N= 1,NN)
      BACKSPACE 12
      GO TO 400
C     ORDER UNKNOWNS IN B ARRAY
  500 K=0
      DO 600 NB=1,NUMBLK
      DO 600 N=1,NN
      NM=N+NN
      K=K+1
  600 B(K)=A(NM,NB)
      RETURN
      END
ON FOR STRESS
      SUBROUTINE STRESS
      COMMON NUMNP,NUMEL,NUMMAT,NUMPC,ACELZ,ANGFQ,MBAND,TEMP,NTYPE,Q,NP,
```

```
     1 PED(12),E(8,8,12),PO(12),XX(N(12),R(900),Z(900),UR(900),UZ(900),
     2 CODE(900),T(900),IBC(200),JBC(200),PR(200),ANGLE(4),SIG(10)
      COMMON /ARG/ RRR(5),ZZZ(5),S(10,10),P(10),TT(4),LM(4),ND(3,3),
     1 HH(6,10),RR(4),ZZ(4),C(4,4),H(6,10),D(6,6),F(6,10),TP(6),XI(10)
     2 ,EE(7),IX(800,5),EPS(800)
      COMMON /BANDARG/ NO,IJMPLX,B(108),A(108,54)
      COMMON /PLANE/ NPP
C     COMPUTE ELEMENT STRESSES
      XKE=0.0
      XPE=0.0
      MPRINT=0
      DO 300 M=1,NUMEL
      N=M
      IX(N,5)=IABS(IX(N,5))
      MTYPE=IX(N,5)
      CALL QUAD(N,VOL)
      IX(N,5)=MTYPE
      DO 120 I=1,4
      II=2*I
      JJ=2*IX(N,I)
      P(II-1)=B(JJ-1)
  120 P(II)=B(JJ)
      DO 150 I=1,2
      RR(I)=P(I+8)
      DO 150 K=1,8
  150 RR(I)=RR(I)-S(I+8,K)*P(K)
      COMM=S(9,9)*S(10,10)-S(9,10)*S(10,9)
      IF (COMM) 155,160,155
  155 P(9)=(S(10,10)*RR(1)-S(9,10)*RR(2))/COMM
      P(10)=(-S(10,9)*RR(1)+S(9,9)*RR(2))/COMM
      GO TO 165
  160 P(9)=0.0
      P(10)=0.0
  165 DO 170 I=1,6
      TP(I)=0.0
      DO 170 K=1,10
  170 TP(I)=TP(I)+HH(I,K)*P(K)
      RR(1)=TP(2)
      RR(2)=TP(6)
      RR(3)=(TP(1)+TP(2)*RRR(5)+TP(3)*ZZZ(5))/RRR(5)
      RR(4)=TP(3)+TP(5)
  175 DO 180 I=1,3
      SIG(I)=-TT(I)
      DO 180 K=1,3
  180 SIG(I)=SIG(I)+C(I,K)*RR(K)
      SIG(4)=C(4,4)*RR(4)
C     CALCULATE ENERGY TERMS
      DO 250 I=1,10
      COMM=0.0
      DO 200 K=1,10
  200 COMM=COMM+S(I,K)*P(K)
  250 XPE=XPE+COMM*P(I)
      XKE=XKE+VOL*PO(MTYPE)*(P(9)**2+P(10)**2)
C
C     CALCULATE EFFECTIVE STRAIN
      IF (NPP) 251,252,251
  251 RR(3)=-(SIG(1)+SIG(2))*EE(2)/EE(1)
  252 CC=(RR(1)+RR(2))/2.0
```

```
      CR=SQRT( ((RR(2)-RR(1))/2.0)**2 + (RR(4)/2.0)**2 )
      RR(1)=CC+CR
      RR(2)=CC-CR
      EPS(I)=SQRT((RR(1)-RR(2))**2+(RR(1)-RR(3))**2+(RR(2)-RR(3))**2)
     1 *.707/(1.0+EE(2))
C     OUTPUT STRESSES
C     CALCULATE PRINCIPAL STRESSES
      CC=(SIG(1)+SIG(2))/2.0
      CR=SQRT(((SIG(2)-SIG(1))/2.0)**2 + SIG(4)**2 )
      SIG(5)=CC+CR
      SIG(6)=CC-CR
      SIG(7)=28.648*ATAN2(2.*SIG(4),(SIG(1)-SIG(2)))
C     STRESSES PARALLEL TO LINE I-J
      I=IX(N,1)
      J=IX(N,2)
      ANG=2.*ATAN2(Z(J)-Z(I),R(J)-R(I))
      COS2A=COS(ANG)
      SIN2A=SIN(ANG)
      CX=.5*(SIG(1)-SIG(2))
      SIG(8)=CX*COS2A+SIG(4)*SIN2A+CC
      SIG(9)=2.*CC-SIG(8)
      SIG(10)=-CX*SIN2A+SIG(4)*COS2A
      IF (UPP) 103,104,103
  103 SIG(9)=EE(4)*P(9)
      SIG(10)=EE(4)*P(10)
  104 IF (MPRINT) 110,105,110
  105 WRITE (6,2000)
      MPRINT=50
  110 MPRINT=MPRINT-1
  305 WRITE (6,2001)  N,RR(5),ZZ(5),(SIG(I),I=1,10)
  306 CONTINUE
      IF (XKE) 310,320,310
  310 W=SQRT(XPE/XKE)
      WRITE (6,2006) W
  320 RETURN
 2000 FORMAT (7H1EL.NO.  7X 1HR  7X 1HZ 4X 8HR-STRESS 4X 8HZ-STRESS 4X
     1 8HT-STRESS 3X 8HRZ-STRESS 2X 10HMAX-STRESS 2X 10HMIN-STRESS
     2 37H  ANGLE IJ-STRESS JK-STRESS      SHEAR )
 2001 FORMAT (I7,2F8.2,1P6E12.4,0P1F7.2,1P3E10.2)
 2006 FORMAT (36H0APPROXIMATE FUNDAMENTAL FREQUENCY = E12.5)
      END
```

PART B - INPUT DATA

The following is a description of the input data used to describe the problem to the computer:

A. IDENTIFICATION CARD - (72H)

Columns 1 to 72 of this card contain information to be printed with results.

B. CONTROL CARD - (415, 3F10.2, 215)

Columns 1 - 5 Number of nodal points (900 maximum)
6 - 10 Number of elements (800 maximum)
11 - 15 Number of different materials (12 maximum)
16 - 20 Number of boundary pressure cards (200 maximum)
21 - 30 Axial acceleration in the Z-direction
31 - 40 Angular velocity
41 - 50 Reference temperature (stress free temperature)
51 - 55 Number of approximations
56 - 60 = 0 Axisymmetric analysis
= 1 Plane stress analysis

C. MATERIAL PROPERTY INFORMATION

The following group of cards must be supplied for each different material:

First Card - (215, 2F10.0)

Columns 1 - 5 Materials identification - any number from 1 to 12.
6 - 10 Number of different temperatures for which properties are given - 8 maximum
11 - 20 Mass density of material
21 - 30 Ratio of plastic modulus to elastic modulus

Following Cards - (8F10.0) One card for each temperature

Columns 1 - 10 Temperature

11 - 20 Modulus of elasticity - E_r and E_z

21 - 30 Poisson's ratio - ν_{rz}

31 - 40 Modulus of elasticity - E_θ

41 - 50 Poisson's ratio - $\nu_{\theta r}$ and $\nu_{\theta z}$

51 - 60 Coefficient of thermal expansion - α_r and α_z

61 - 70 Coefficient of thermal expansion - α_θ

71 - 80 Yield stress - σ_y

D. NODAL POINT CARDS - (215, F5.0, 5F10.0)

One of the first steps in the structural analysis of a two-dimensional solid is to select a finite element representation of the cross-section of the body. Elements and nodal points are then numbered in two numerical sequence each starting with one. The following group of punched cards numerically define the two-dimensional structure to be analyzed. There is a card for each nodal point and each card contains the following information:

Columns 1 - 5 Nodal point number

6 - 10 Number which indicates if displacements or forces are to be specified

11 - 20 R - ordinate

21 - 30 z - ordinate

31 - 40 XR

41 - 50 XZ

51 - 60 Temperature

If the number in column 10 is

0 - XR is the specified R-load and
XZ is the specified Z-load.

1 - XR is the specified R-displacement and
XZ is the specified Z-load.

2 - XR is the specified R-load and
XZ is the specified Z-displacement.

3 - XR is the specified R-displacement and
XZ is the specified Z-displacement.

All loads are considered to be total forces acting on a one radian segment (or unit thickness in the case of plane stress analysis). Nodal point cards must be in numerical sequence. If cards are omitted, the omitted nodal points are generated at equal intervals along a straight line between the defined nodal points; the necessary temperatures are determined by linear interpolation; the boundary code (column 10), XR and XZ are set equal to zero.

E. ELEMENT CARDS - (615)

One card for each element

Columns 1 - 5 Element number
6 - 10 Nodal Point I
11 - 15 Nodal Point J
16 - 20 Nodal Point K
21 - 25 Nodal Point L
26 - 30 Material Identification

1. Order nodal points counter-clockwise around element.
2. Maximum difference between nodal point I. D. must be less than 27

Element cards must be in element number sequence. If element cards are omitted, the program automatically generates the omitted information by incrementing by one the preceding I, J, K and L. The material identification code for the generated cards is set equal to the value given on the last card. The last element card must always be supplied.

Triangular elements are also permissible, they are identified by repeating the last nodal point number (i.e., I, J, K, L).

F. PRESSURE CARDS - (2I5, 1F10.0)

One card for each boundary element which is subjected to a normal pressure.

Columns 1 - 5 Nodal Point I
6 - 10 Nodal Point J
11 - 20 Normal Pressure

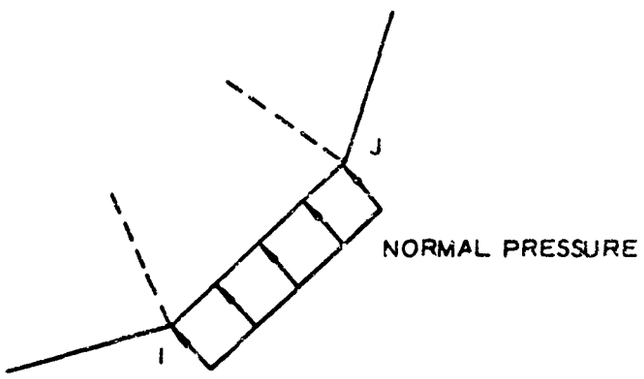

As shown above, the boundary element must be on the left as one progresses from I to J. Surface tensile force is input as a negative pressure.

PART C - ADDITIONAL REMARKS AND OUTPUT DATA

A. MATERIAL PROPERTIES

Material properties vs. temperature are input for each material in tabular form. The properties for each element in the system are then evaluated by interpolation. The mass density of the material is required only if acceleration loads are specified or if the approximate frequency is desired. Listing of the coefficients of thermal expansion are necessary only for thermal stress analysis. The plastic modulus ratio and the yield stress are specified only if nonlinear materials are used.

B. SKEW BOUNDARIES

If the number in columns 5-10 of the nodal point cards is other than 0, 1, 2 or 3, it is interpreted as the magnitude of an angle in degrees. This angle is shown below.

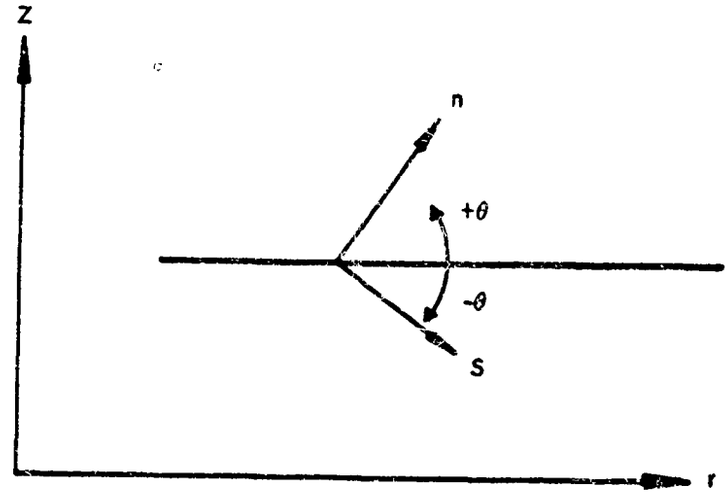

The terms in columns 31-50 of the nodal point card are then interpreted as follows:

XR is the specified load in the s-direction

XZ is the specified displacement in the n-direction

The angle θ must always be input as a negative angle and may range from -0.001 to -180 degrees. Hence, + 1.0 degree is the same as -179.0 degrees. The displacements of these nodal points which are printed by the program are:

u_r = the displacement in the s-direction

u_z = the displacement in the n-direction

C. USE OF THE PLANE STRESS OPTION

A one punch in column 60 of the control card indicates the body is a plane stress structure of unit thickness. In the case of plane stress analysis, the material property cards are interpreted as follows:

Columns 11 - 20 Modulus of elasticity - E_r

21 - 30 Poisson's ratio - ν

31 - 40 Modulus of elasticity - E_z

The corresponding stress-strain relationship used in the analysis is:

$$\begin{bmatrix} \sigma_r \\ \sigma_z \\ \tau_{rz} \end{bmatrix} = \frac{E_r}{\mu-\nu^2} \begin{bmatrix} \mu & \nu & 0 \\ \nu & 1 & 0 \\ 0 & 0 & \frac{\mu-\nu^2}{2(\mu+\nu)} \end{bmatrix} \begin{bmatrix} \epsilon_r \\ \epsilon_z \\ \gamma_{rz} \end{bmatrix}$$

where

$$\mu = \frac{E_r}{E_z}$$

D. OUTPUT DATA

The following information is developed and printed by the program:

1. Reprint of input data
2. Nodal point displacements

3. Stresses at the center of each element
4. An approximate fundamental frequency. (The displacements for the given load condition are used as an approximate mode shape in the calculation of a frequency by Raleigh's procedure. A considerable amount of engineering judgement must be used in the interpretation of this frequency.)

E. PLOT OF FINITE ELEMENT MESH

The program automatically develops a plot of the outline of each element in the system. This serves as an excellent check on the input data. In order to obtain the plot from AGC's computer operation, an additional charge card must be submitted with the job. If only a plot of the mesh is desired, the calculation of displacements and stresses may be eliminated by specifying more pressure cards than actually exist. The first 30 columns of the identification card are used as a title for the plot.

REFERENCES

1. Zienkiewicz, O. C., The Finite Element Method in Structural and Continuum Mechanics, McGraw-Hill Book Company, New York, 1967.

2. Anderson, J. M., "A Review of the Finite Element Stiffness Method as Applied to Propellant Grain Stress Analysis Feature Article, SRSIA, (AFRPL-TR-69-220), Vol. 6, No. 4, pp. 1-54, October 1969.

3. Pau, C. H., "The Application of Numerical Methods to the Solution of Structural Integrity Problems of Solid Propellant Rockets," SRSIA, Vol. 1, No. 2, October 1964.

4. Pau, C. H., "The Application of Numerical Methods to the Solution of Structural Integrity Problems of Solid Propellant Rockets II", SRSIA, Vol. 4, No. 1, January 1967.

5. Becker, E. B. and Brisbane, J. J., "Application of the Finite Element Method to Stress Analysis of Solid Propellant Rocket Grains," Technical Report S-76, Rohm Haas Company, Redstone Research Laboratories, November 1965.

6. Pister, K. S., Taylor, R. L. and Dill, E. H., "A Computer Program for Axially Symmetric Elasticity Problems," Mathematical Sciences Corporation Report No. 65-21-3, December 1965.

7. Wilson, E. L., "A Digital Computer Program for the Finite Element Analysis of Solids with Nonlinear Material Properties," Aerojet-General Corporation Report TM-23, July 1965.

8. Wilson, E. L., "A Computer Program for the Dynamic Stress Analysis of Underground Structures," Structural Engineering Laboratory Report 67-3, University of California, Berkeley, February 1967.

9. Hermann, L. R., Taylor, R. L. and Green, D. R., "Finite Element Analysis for Solid Rocket Motor Cases," Report No. 67-4, Structural Engineering Laboratory, University of California, Berkeley, March 1967.

10. Brisbane, J. J. and Becker, E. B., "Stress Analysis of Solid Propellant Grains Under Transverse Acceleration Loads," Technical Report S-116, Rohm and Haas Company, Redstone Research Laboratories, March 1967.

11. Dunham, R. S. and Taylor, R. L., "Finite Element Analysis of Axisymmetric Solids with Arbitrary Loading," Structures Report 67-5, University of California, Berkeley, June 1967.

12. Nickell, R. E., "Stress-Wave Analysis in Layered Thermoviscoelastic Materials by the Extended Ritz Method," Technical Report S-175, Rohm and Haas Company, Redstone Research Laboratories, October 1968.

13. Becker, E. B. and Pau, C. H., "Application of the Finite Element Method to Heat Conduction in Solids," Technical Report S-117, Rohm and Haas Company, Redstone Research Laboratories, November 1968.

14. Leeming, H., et al, "Solid Propellant Structural Test Vehicle Cumulative Damage and Systems Analyses," Appendix, Final Technical Report AFRPL-TR-68-130, October 1968.

15. Cost, T. L., "Thermomechanical Coupling Phenomena in Non-Isothermal Viscoelastic Solids, Technical Report S-226, Rohm and Haas Company, Redstone Research Laboratories, August 1969.

16. Becker, E. B., Brisbane, J. J. and Schkade, A. F., Jr., "Investigation of Techniques of Three-Dimensional Finite Element Stress Analysis," Technical Report S-250, Rohm and Haas Company, Redstone Research Laboratories, March 1970.

17. Duham, R. S., "Dynamic Stress Analysis of One-Dimensional Thermorheologically Simple Viscoelastic Solids with Nonlinear Heat Conduction Analysis," Report No. RK-JR-70-13, U. S. Army Missile Command, Redstone Research Laboratories, July 1970.

18. Taylor, R. L., Goudreau, G. L., and Pister, K. S., "Thermomechanical Analysis of Viscoelastic Solids, Structural Engineering Laboratory Report 68-7, University of California, Berkeley, June 1968.

APPENDIX C

PARAMETRIC DESIGN CURVES

FOREWORD

The parametric design data presented in this Appendix has been compiled from the following two references:

1) LOCKHEED PROPULSION COMPANY STRUCTURES MANUAL, December 1969

2) Messner, A. M. and Schiessmann, D.: "Barameter Calculation of Simple Propellant Grains for Temperature Cycling, Pressurization, and Acceleration", Appendix D, Study of Mechanical Properties of Solid Rocket Propellants, Aerojet-General Report No. 0411-10F, March 1962.

Permission to publish this material is greatly appreciated.

.1 General

Curves are presented to aid in making preliminary stress and strain analyses of propellant grains. Inner bore hoop strain, interface radial stress and interface shear stress values may be obtained for a wide range of b/a and L/b ratios. Linear interpolation may be used as required for problems in which intermediate values of the governing parameters exist. The primary loading conditions associated with propellant grain structural problems are a function of pressure, temperature and acceleration. Results of a stress analysis for each of the three loading conditions may be superimposed to obtain total stresses and strains resulting from a combined loading condition.

Analysis was performed based on the infinitesimal theory of elasticity and subject to all of the associated limitations and assumptions. In particular, the assumptions are made that the propellant is a homogeneous, isotropic, elastic solid and that the magnitudes of the strains, rotations and displacements are small.

Actual grain configurations consist of a concentric hollow cylinder with square ends. The analytical solutions are thus valid only for the axisymmetrical case. Mechanical properties and load levels used in the analyses are as follows:

Linear Coefficient of Thermal Expansion	Case $\alpha_c = 5.89 \times 10^{-6} \frac{in}{in°F}$
Linear Coefficient of Thermal Expansion	Propellant $\alpha_p = 63 \times 10^{-6} \frac{in}{in°F}$
Poisson's Ratio	Case $\nu_c = 0.3$
Poisson's Ratio	Propellant $\nu_p = 0.5$
Modulus of Elasticity	Case $E_c = 30 \times 10^6$ psi
Modulus of Elasticity	Propellant $E_p = 1000$ psi
Thickness of Case to Diameter Ratio	$t/D = 0.00195$
Pressure Loading	P = 500 psi
Axial Acceleration	A = 10 g

.2 Recommended Analysis Procedure

All of the design curves are based on analytical solutions of a concentric hollow cylinder with square ends. Consequently, a star bore configuration must be converted to an equivalent hollow cylinder.

Absolute magnitude of the stresses and strains may be obtained from the design curves as follows:

A. Determine the dimensions and loading conditions to be considered

1.	Outer radius of propellant	b
2.	Inner radius of propellant	a
3.	Length of propellant	L
4.	Pressure	p
5.	Cure temperature - storage	ΔT
6.	Acceleration in number of g's	n
7.	Poisson's Ratio of propellant is 0.5	ν_p
8.	Modulus of propellant	E_p

B. Find appropriate solutions for specified geometry and end bonding condition. Linear interpolation may be used as required.

C. Multiply solutions found in B by the applicable factors listed in Table -1.

D. Determine strain concentration factor at the star tip and multiply inner bore hoop strain by this factor.

For original grain design, consideration should be given to the following recommended design practices.

TABLE -1

MULTIPLICATION FACTORS

Quantity to be Determined	Type of Loading	Multiplication Factor
Shear Stress	Pressure	$\frac{\text{Modulus}}{1000}$
Shear Stress	Temperature	$\frac{\text{Modulus}}{1000} \times \frac{\text{Temp. Change } ^{\circ}F}{-79}$
Shear Stress	Acceleration	g's $\frac{\text{Acceleration}}{10} \times \frac{b}{13}$
Radial Stress	Pressure	$\frac{\text{Pressure}}{500}$
Radial Stress	Temperature	$\frac{\text{Modulus}}{1000} \times \frac{\text{Temp. Change } ^{\circ}F}{-79}$
Radial Stress	Acceleration	g's $\frac{\text{Acceleration}}{10} \times \frac{b}{18}$
Hoop Strain	Pressure	1
Hoop Strain	Temperature	$\frac{\text{Temperature Change } ^{\circ}F}{-79}$
Hoop Strain	Acceleration	g's $\frac{\text{Acceleration}}{10} \times \frac{1000}{\text{Modulus}} \times \frac{b}{18}$

.3 Recommended Design Practices

A. In addition to ensuring that strain levels are kept down to a minimum it is necessary to achieve a high strength bond between the propellant and the case. In general it is good practice to keep the bond stress lower than 10 percent of the propellant modulus.

B. A compromise must be made between star tip fillet radius and sliver loss. Structurally, a star tip that subtends the maximum angle is the best and the ideal tip geometry is a 2:1 ellipse. *

C. Structural reliability decreases as grain constraints increase. Highly bonded grains with small inner bores are poor structurally. Free surfaces and unbonded regions tend to relieve the stresses and strains in the system.

D. There are several basic characteristics of the propellant grain systems that can be assumed.

1. While deformations of the motor case have a direct influence on the propellant-grain, the grain is incapable of causing any case deformation effects.

2. All strains and stresses generated by independent loads can be added to obtain results for combined loads.

3. Steady state thermal conditions are always more severe than the transients between the steady state condition.

If a motor is to be placed in a low temperature storage box until steady state conditions prevail and then moved to a high temperature storage, the most severe structural conditions will occur in the low temperature environment.

* This statement is true within the limitations of elastic theory, however, for the case of viscoelastic materials there is evidence to the fact that actual tip geometry is not important

.4 Sample Problem

Use of the design curves is best illustrated by a sample problem. The problem shown in Figure 1 is solved for the following combination of loads and material properties:

LOADING CONDITIONS

1. Temperature Cycling to +35°F, $\Delta T = -85°F$
2. Pressure Loading, $p = 1290$ psi
3. Axial Acceleration, $A = 30$ g

MATERIAL PROPERTIES

1.	Poisson's Ratio of Propellant	$\nu_p = 0.5$
2.	Poisson's Ratio of Case	$\nu_c = 0.3$
3.	Modulus of Elasticity of Propellant	$E_p = 3500$ psi
4.	Modulus of Elasticity of Case	$E_c = 30 \times 10^6$ psi
5.	Linear Coefficient of Thermal Expansion for Propellant	$\alpha_p = 63 \times 10^{-6} \frac{in}{in-°F}$
6.	Linear Coefficient of Thermal Expansion for Case	$\alpha_c = 5.9 \times 10^{-6} \frac{in}{in-°F}$
7.	Density of Propellant	$\rho_p = 0.063 \frac{lb}{in^3}$
8.	Cure Temperature of Propellant (Stress Free Condition)	$T_{cure} = 120°F$

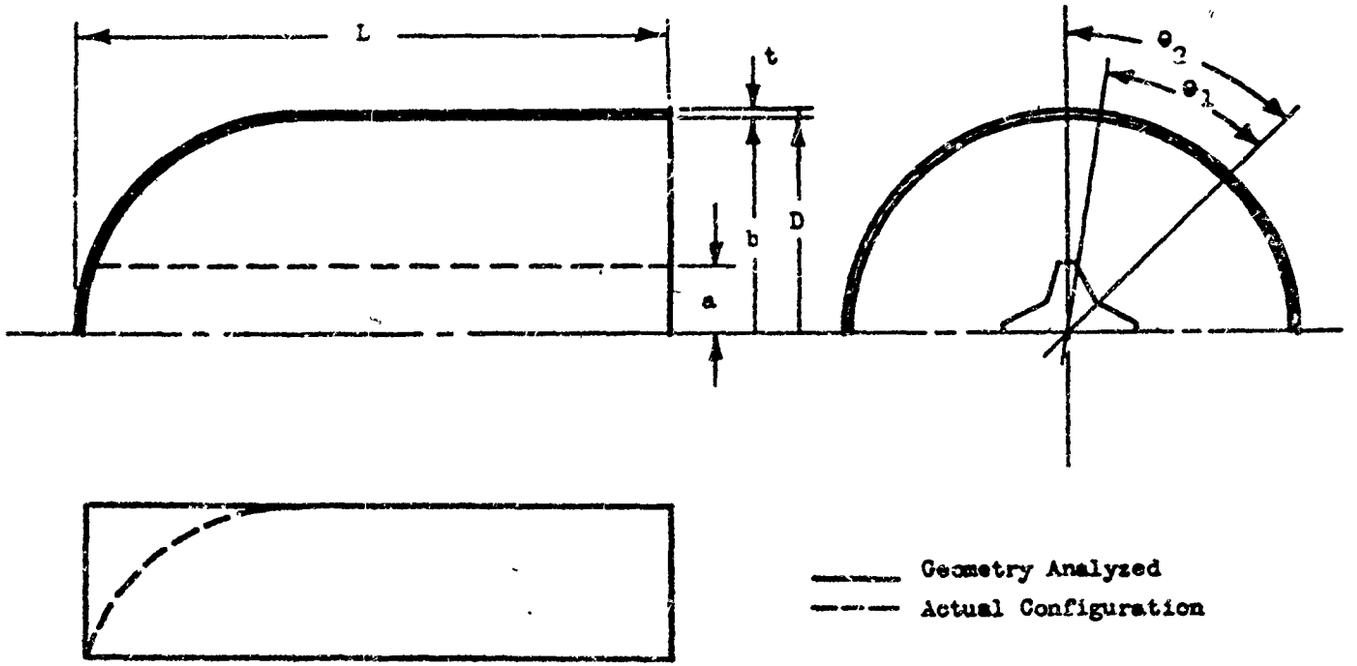

Geometrical Approximation

Configuration of Sample Problem

Figure 1

CALCULATIONS

L = 35 in.

b = 10 in.

a = 3 in.

$$\varepsilon_{\theta_{max}} = \varepsilon_{\theta_{bore}} \left[\frac{2\theta_2 - \theta_1}{2(\theta_2 - \theta_1)} \right]$$

L/b = 3.50

b/a = 3.33

t/D = 0.00195

where: $\theta_1 = 37°$ and

$\theta_2 = 45°$

$$\varepsilon_{\theta_{max.}} = 3.31\ \varepsilon_{\theta_{bore}}$$

One End is Bonded

Pressurization

Interface Radial Stress

$$\text{Stress} = \text{Value shown} \times \frac{\text{Actual Pressure}}{500 \text{ psi}}$$

Interpolate between Figures 10,11 and 13,14

$$\text{Stress} = \sigma_r = -492 \left[\frac{1290}{500} \right] = \underline{-1268 \text{ psi}}$$

Location near free end

Inner Bore Hoop Strain

Strain = Value shown x Strain Concentration Factor

Interpolate between Figures 10,11 and 13,14

Strain = $\varepsilon_{\theta_{max}}$ = 4.20 x 3.31

Strain = ε_{max} = 13.90%

Location Near Bonded End

Interface Shear Stress

Stress = Value shown x $\frac{\text{Propellant Modulus}}{1000}$

Interpolate between Figures 17 and 15

Stress = σ_z = 18.2 x $\frac{3500}{1000}$ = 63.8 psi

Location: Near Inner Bore Surface

Temperature Cycling

Interface Radial Stress

Stress = Value shown x $\frac{\text{Propellant Modulus}}{1000 \text{ psi}}$ x $\frac{\text{Actual Temp Difference}}{-79°F}$

Interpolate between Figures 32,33 and 37,38

Stress = 82 x $\left[\frac{3500}{1000}\right]$ x $\frac{-85}{-79}$

Stress = σ_r = 310 psi

Location at Free End

Inner Bore Hoop Strain

Strain = Value shown x $\frac{\text{Strain Concentration Factor}}{}$ x $\frac{\text{Actual Temp. Difference}}{-79°F}$

Interpolate between Figures 34,35 and 37,38

Strain = $\varepsilon_{\theta_{max}}$ = 6.1 x 3.31 x $\frac{-85}{-79}$

Strain = $\varepsilon_{\theta_{max}}$ = 21.6%

Location Near Bonded End

Interface Shear Stress

$$\text{Stress} = \text{Value shown} \times \frac{\text{Propellant Modulus}}{1000 \text{ psi}} \times \frac{\text{Actual Temp. Difference}}{-79°F}$$

Interpolate between Figures 34, 35 and 39

$$\text{Stress} = 23.5 \times \left[\frac{3500}{1000}\right] \times \frac{-85}{-79}$$

$$\text{Stress} = \sigma_s = \underline{88.5 \text{ psi}}$$

Location near Inner Bore

Acceleration.

Interface Radial Stress

$$\text{Stress} = \text{Value shown} \times \frac{\text{Actual Acceleration}}{10} \times \frac{b}{18}$$

Interpolate between Figures 60 and 63

$$\text{Stress} = 19 \times \frac{30}{10} \times 0.555$$

$$\text{Stress} = \sigma_r = \underline{31.8 \text{ psi}}$$

Location at Free End

Interface Shear Stress

$$\text{Stress} = \text{Value shown} \times \frac{\text{Actual Acceleration}}{10} \times \frac{b}{18}$$

Interpolate between Figures 60 and 63

$$\text{Stress} = 4.8 \times \frac{30}{10} \times 0.555$$

$$\text{Stress} = \sigma_s = \underline{8.0 \text{ psi}}$$

Location Near Free End

Inner Bore Hoop Strain

$$\text{Strain} = \text{Value shown} \times \frac{\text{Strain Concentration Factor}}{} \times \frac{\text{Actual Acceleration}}{10}$$

$$\times \frac{1000}{\text{Propellant Modulus}} \times \frac{b}{28}$$

Interpolate between Figures 60 and 63

$$\text{Strain} = 0.58 \times 3.31 \times \frac{30}{10} \times \frac{1000}{3500} \times 0.555$$

$$\text{Strain} = {}^{c}\varepsilon_{max} = -0.92\%$$

Location Near Bonded End

.5 Parametric Curves

Structural problems commonly encountered in solid propellant grains can best be described by illustrations which show the grain deformations under load.

The propellant solidifies at its cure temperature and is then stress free as shown in Figure 2A When the motor is cooled to an operating or storage temperature level, the propellant tries to assume the configuration shown in Figure 2B Figure 2C shows the low temperature configuration that results because the propellant is bonded to the case and cannot assume the unbonded geometry of Figure 2B Inner bore hoop strain is a measure of the percent increase in inner bore radius from Figure to Figure 2C It is important to note that strains are measured from the stress free configuration 2B and not from initial dimensions shown in Figure 2A A plot of inner bore hoop strain, since it represents percent change in radius will have the same shape as the inner bore of the grain.

The deformed grain shapes obtained by pressurization and acceleration loading conditions are shown by Figures 2D and 2E respectively.

Mechanical properties, constants, and loading conditions which were used throughout the analyses, to prepare the design curves, are presented in section .1.

Configurations of geometries analyzed are shown by Figure 3F and a list of solutions are presented by Table -2. Reference to the list of solutions will facilitate use of the design curves and permit the rapid solving of problems. The design curves are grouped by type of loading and classified within each group by geometry, type of stress or strain and definitive dimensionless ratios. Each design curve thus catalogued is referenced to the appropriate figure and page number.

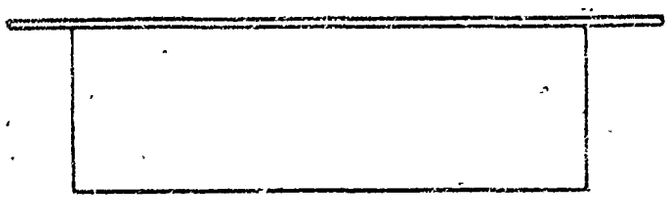

Propellant at Cure Temperature
Figure 2a

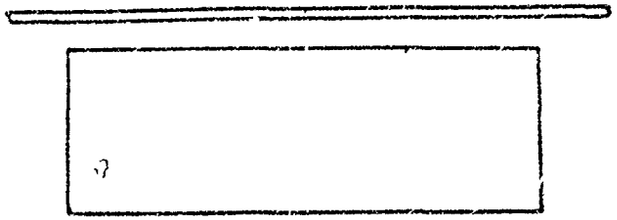

Unbonded Propellant at Lower than Cure Temperature
Figure 2b

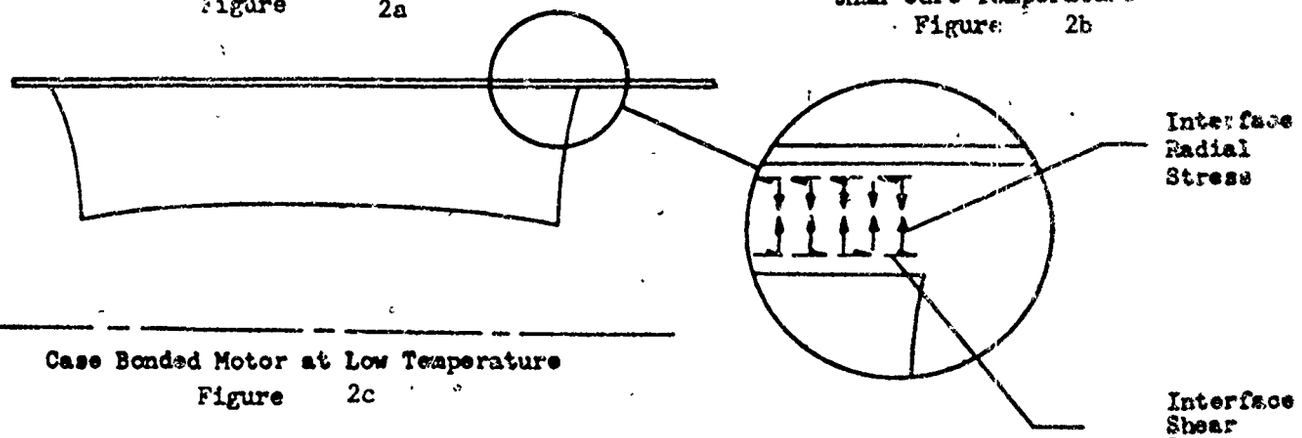

Case Bonded Motor at Low Temperature
Figure 2c

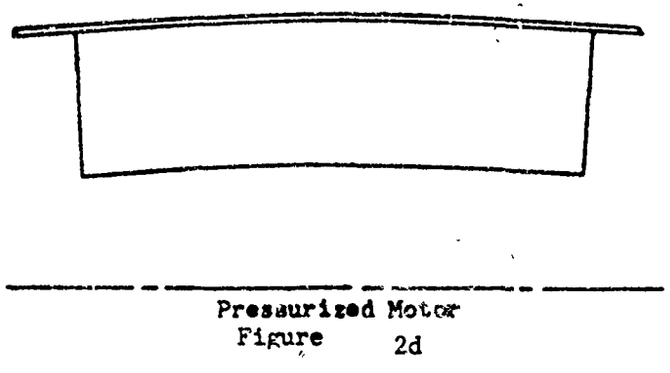

Pressurized Motor
Figure 2d

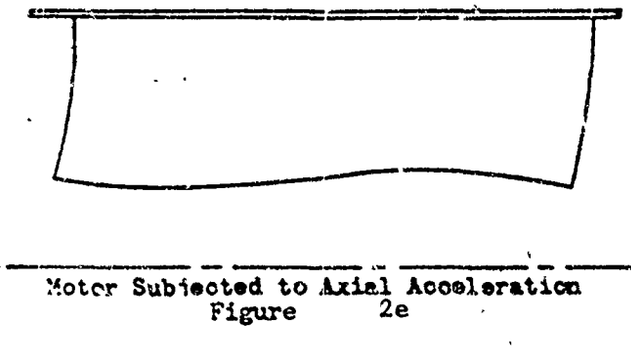

Motor Subjected to Axial Acceleration
Figure 2e

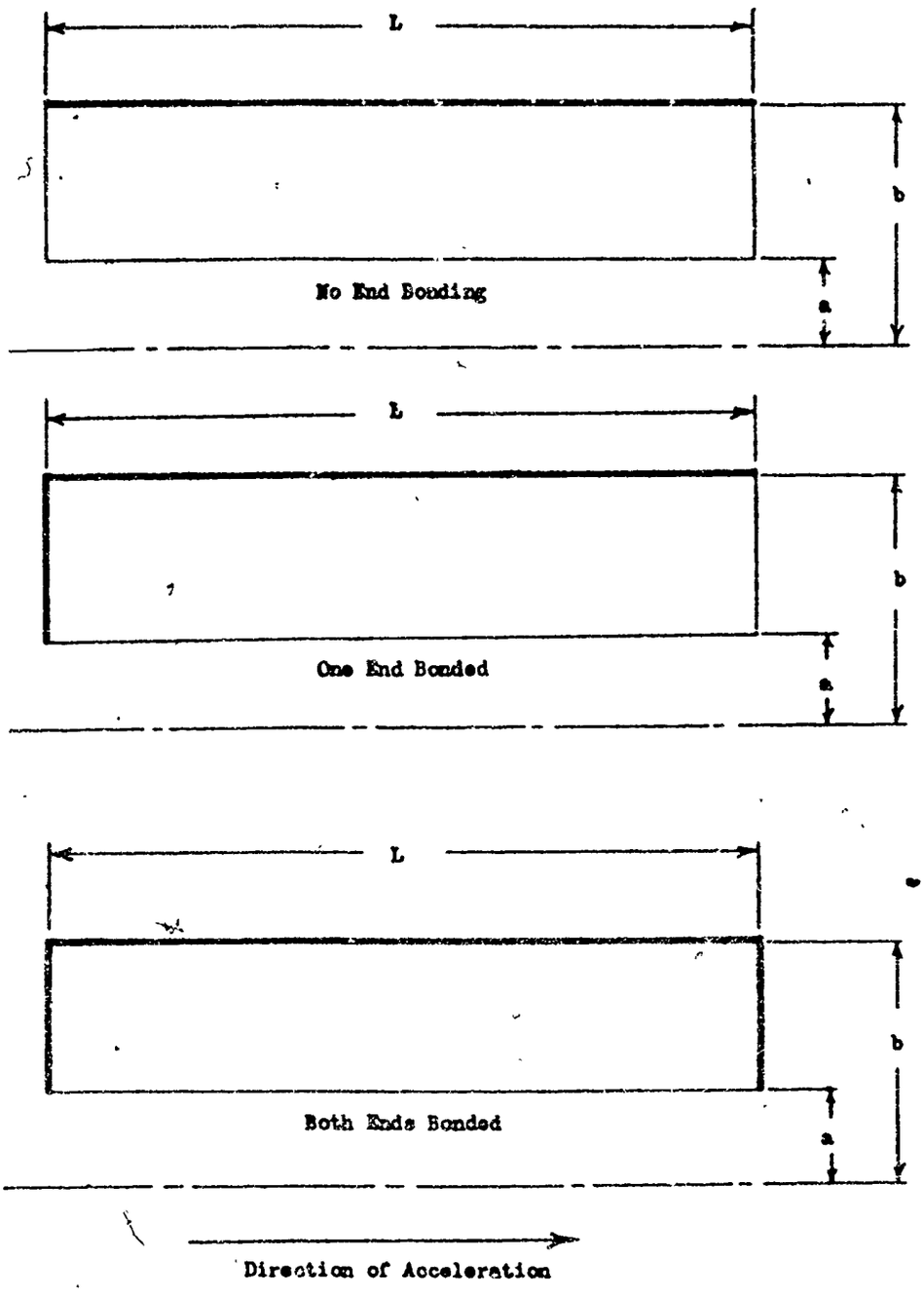

Configuration of Geometries Analyzed

Figure 3

TABLE -2

LIST OF SOLUTIONS

LOAD CONDITION	GEOMETRY	L/b	STRESSES	b/a	FIGURE
Pressurization	No end bonding	2	Interface	2,3,4,6	4,5
↑	No end bonding	4	↕	↑	6,7
↕	No end bonding	8	↓	↕	7,8
↕	One end bonded	2	Interface	↕	8,9
↕	↑	2	End	↕	10,11
↕	↕	4	Interface	↕	12
↕	↕	4	End	↕	13,14
↕	↕	8	Interface	↕	15
↕	One end bonded	8	End	↕	16,17
↕	Both ends bonded	2	Interface	↕	18
↕	↑	2	End	↕	19,20
↕	↕	4	Interface	↕	21
↕	↕	4	End	↕	22,23
↓	↓	8	Interface	↓	24
Pressurization	Both ends bonded	8	End	2,3,4,6	25,26,27
Temp. Cycling	No end bonding	2	Interface	2,3,4,6	28,29
↑	No end bonding	4	↕	↑	30,31
↕	No end bonding	8	↓	↕	32,33
↕	One end bonded	2	Interface	↕	34,35
↕	↑	2	End	↕	36
↕	↕	4	Interface	↕	37,38
↕	↕	4	End	↕	39
↕	↕	8	Interface	↕	40,41
↕	One end bonded	8	End	↕	42
↕	Both ends bonded	2	Interface	↕	43,44
↕	↑	2	End	↕	45
↕	↕	4	Interface	↕	46,47
↕	↕	4	End	↕	48
↓	↓	8	Interface	↓	49,50
Temp. Cycling	Both ends bonded	8	End	2,3,4,6	51
Acceleration	No end bonding	2	Interface	2,3,4,6	52,53
↑	No end bonding	4	↕	↑	54
↕	No end bonding	8	↓	↕	56,57
↕	One end bonded	2	Interface	↕	58,59
↕	↑	2	End	↕	60
↕	↕	4	Interface	↕	61,62
↕	↕	4	End	↕	63
↓	↓	8	Interface	↓	64,65
Acceleration	One end bonded	8	End	2,3,4,6	64

List of Solutions (Cont'd)

LOAD CONDITION	GEOMETRY	L/b	STRESSES	b/a	FIGURE
Acceleration	Both ends bonded	2	Interface	2,3,4,6	67,68
		2	Fwd end		69
		2	Aft end		70
		4	Interface		71,72
		4	Fwd end		73
		4	Aft		74
		8	Interface		75,76
		8	Fwd end		77
Acceleration	Both ends bonded	8	Aft end	2,3,4,6	78

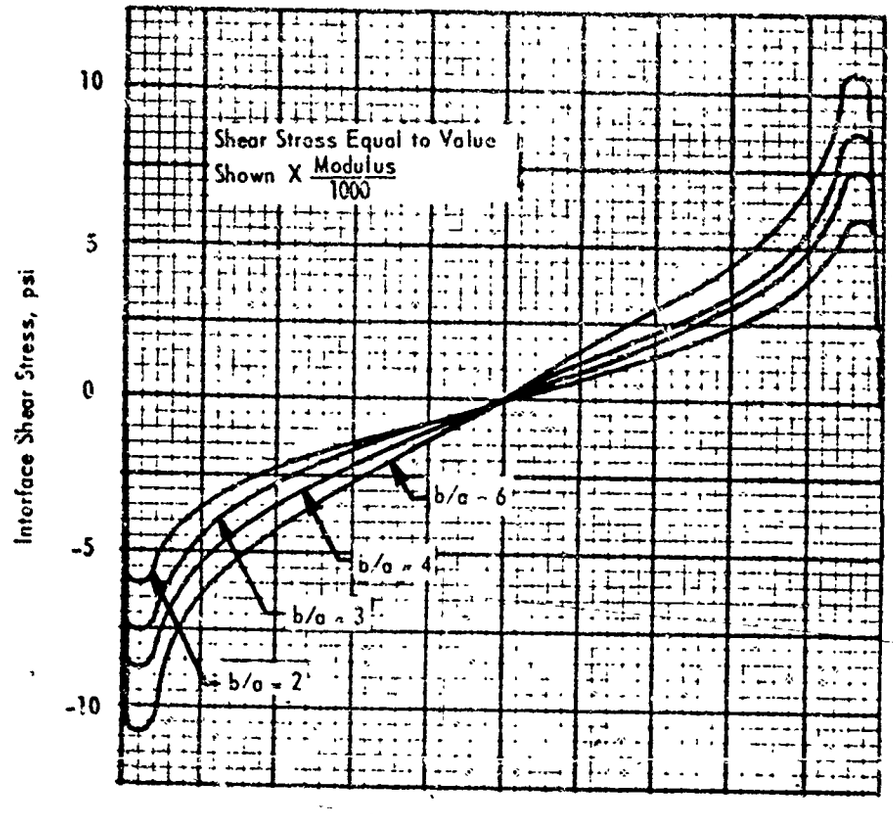

P = 500 psi
L/b = 2

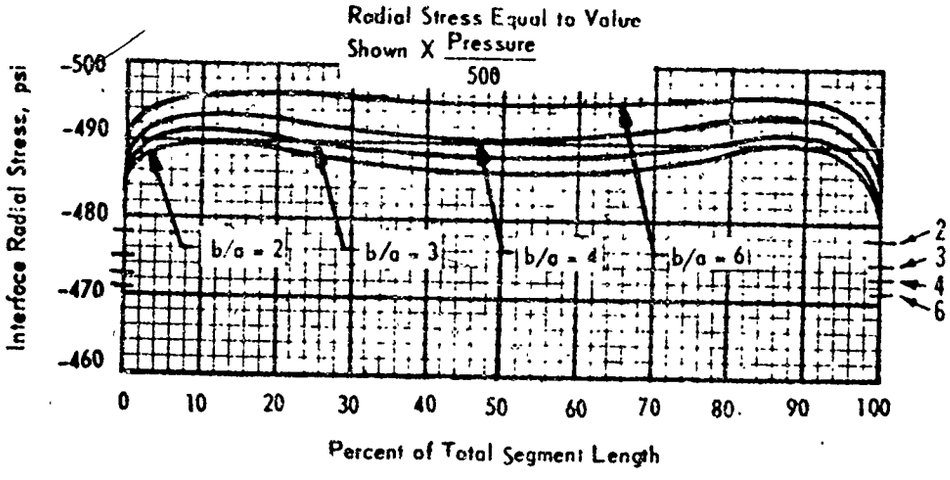

Interface Stresses Caused by Pressure
No End Bonding

Figure 4

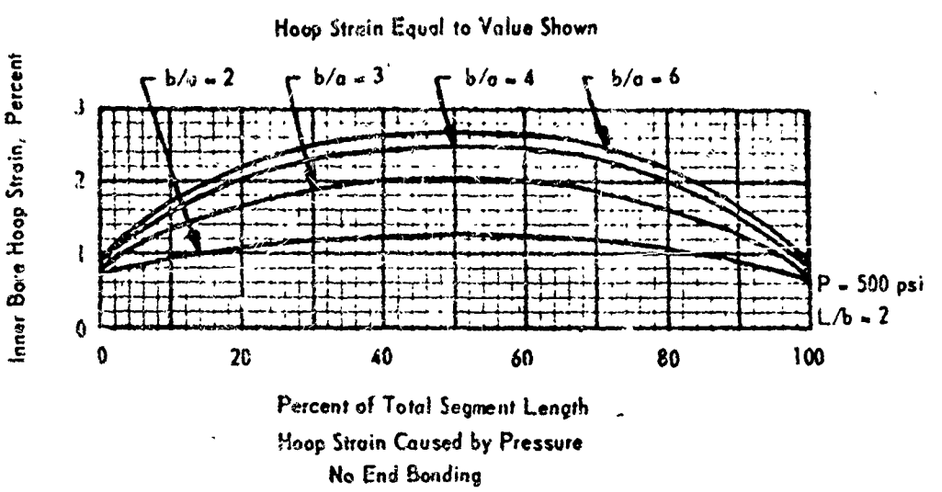
Hoop Strain Equal to Value Shown
b/a = 2
b/a = 3
b/a = 4
b/a = 6
Inner Bore Hoop Strain, Percent
3
2
1
0
0
20
40
60
80
100
P = 500 psi
L/b = 2
Percent of Total Segment Length
Hoop Strain Caused by Pressure
No End Bonding

Figure 5

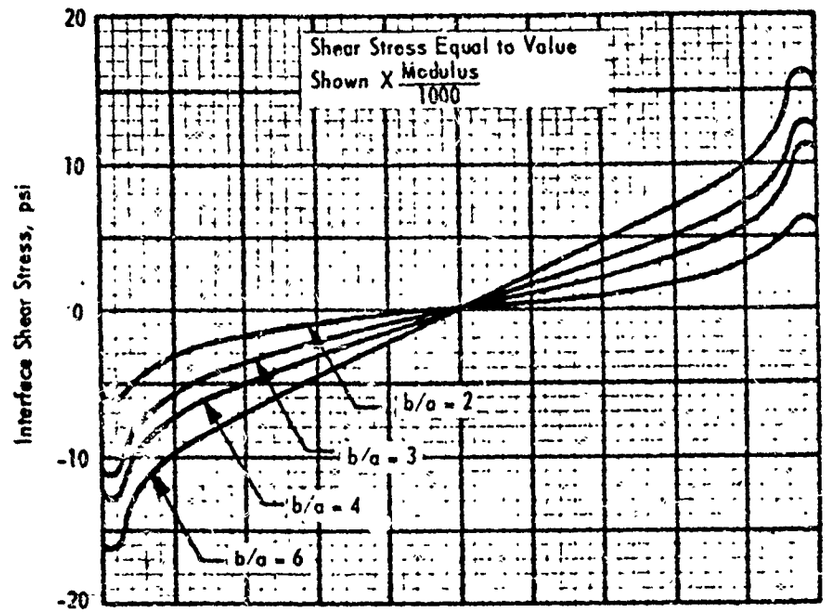

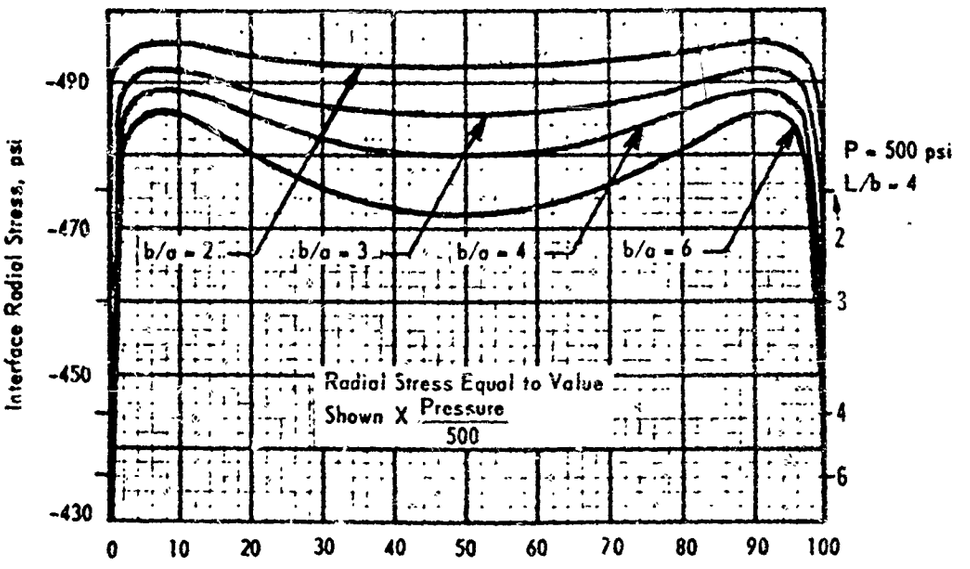

Interface Stresses Caused by Pressure
No End Bonding

Figure 6

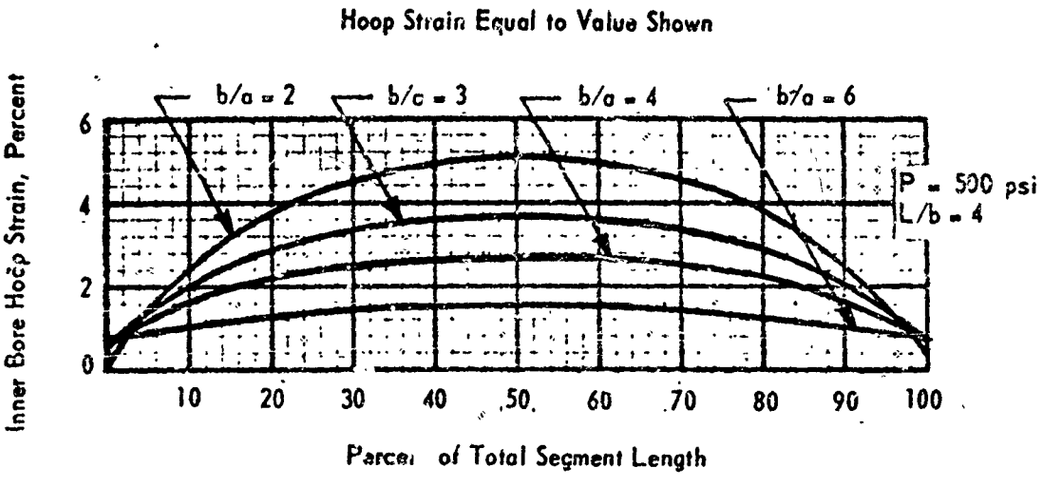

Hoop Strain Caused by Pressure
No End Bonding

Figure 7

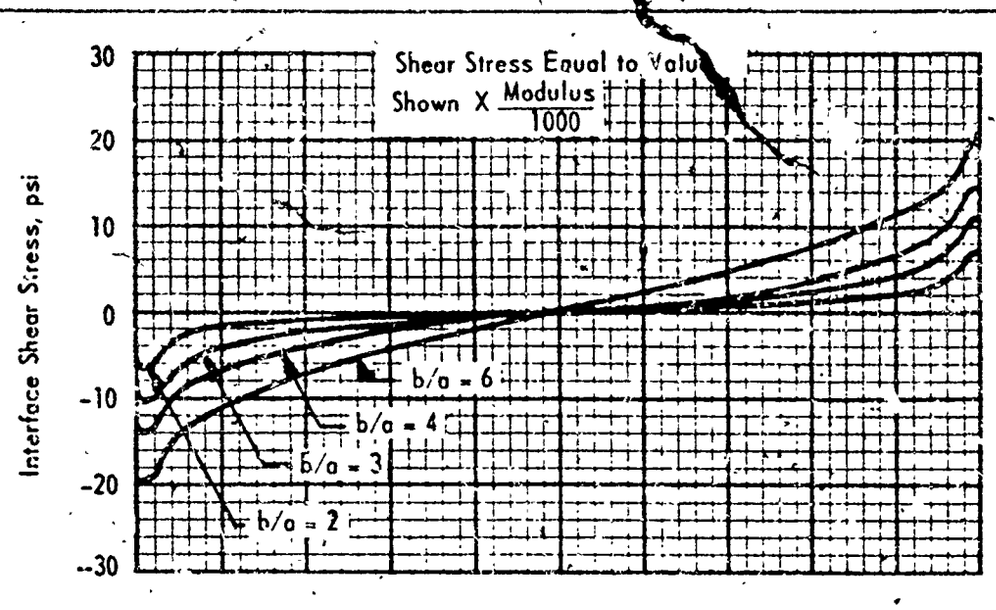

P = 500 psi
L/b = 8

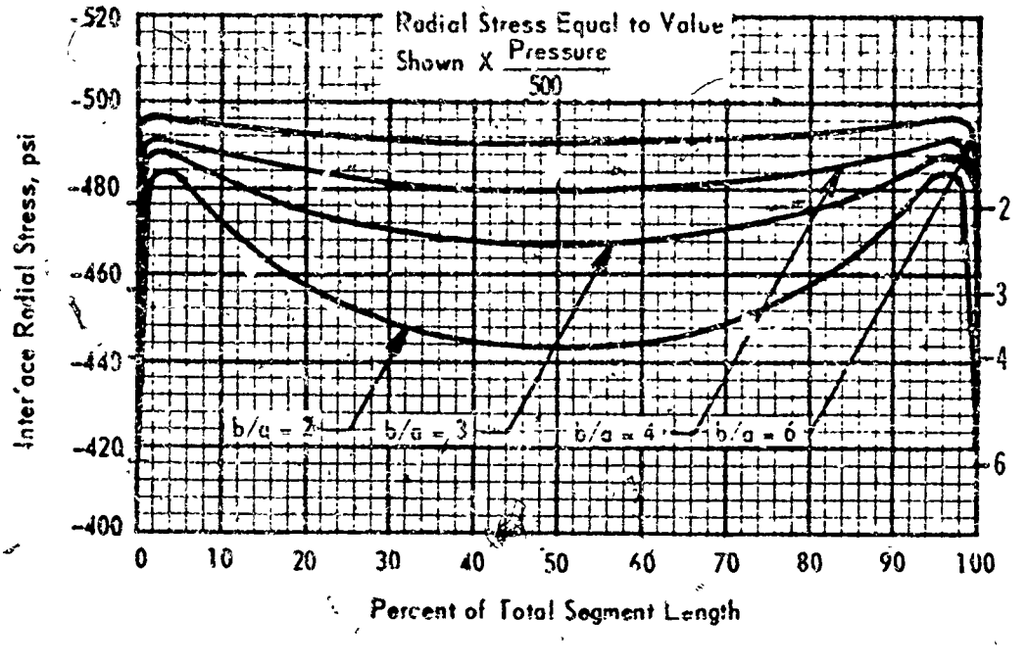

Interface Stresses Caused by Pressure
No End Bonding

Figure 8

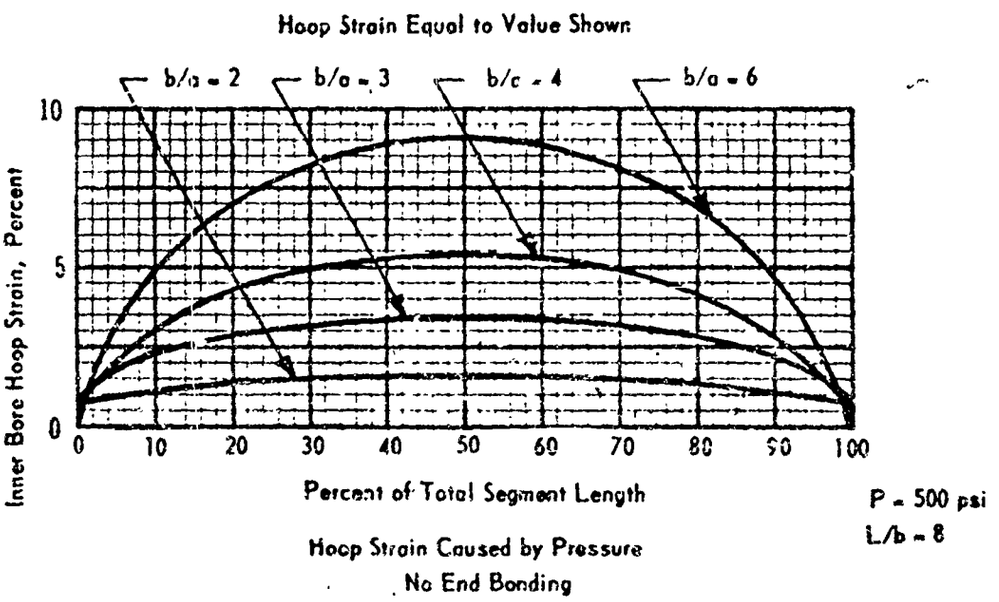
Hoop Strain Equal to Value Shown
b/a = 2
b/a = 3
b/c = 4
b/a = 6
10
5
0
0
10
20
30
40
50
60
70
80
90
100
Inner Bore Hoop Strain, Percent
Percent of Total Segment Length
P = 500 psi
L/b = 8
Hoop Strain Caused by Pressure
No End Bonding

Figure 9

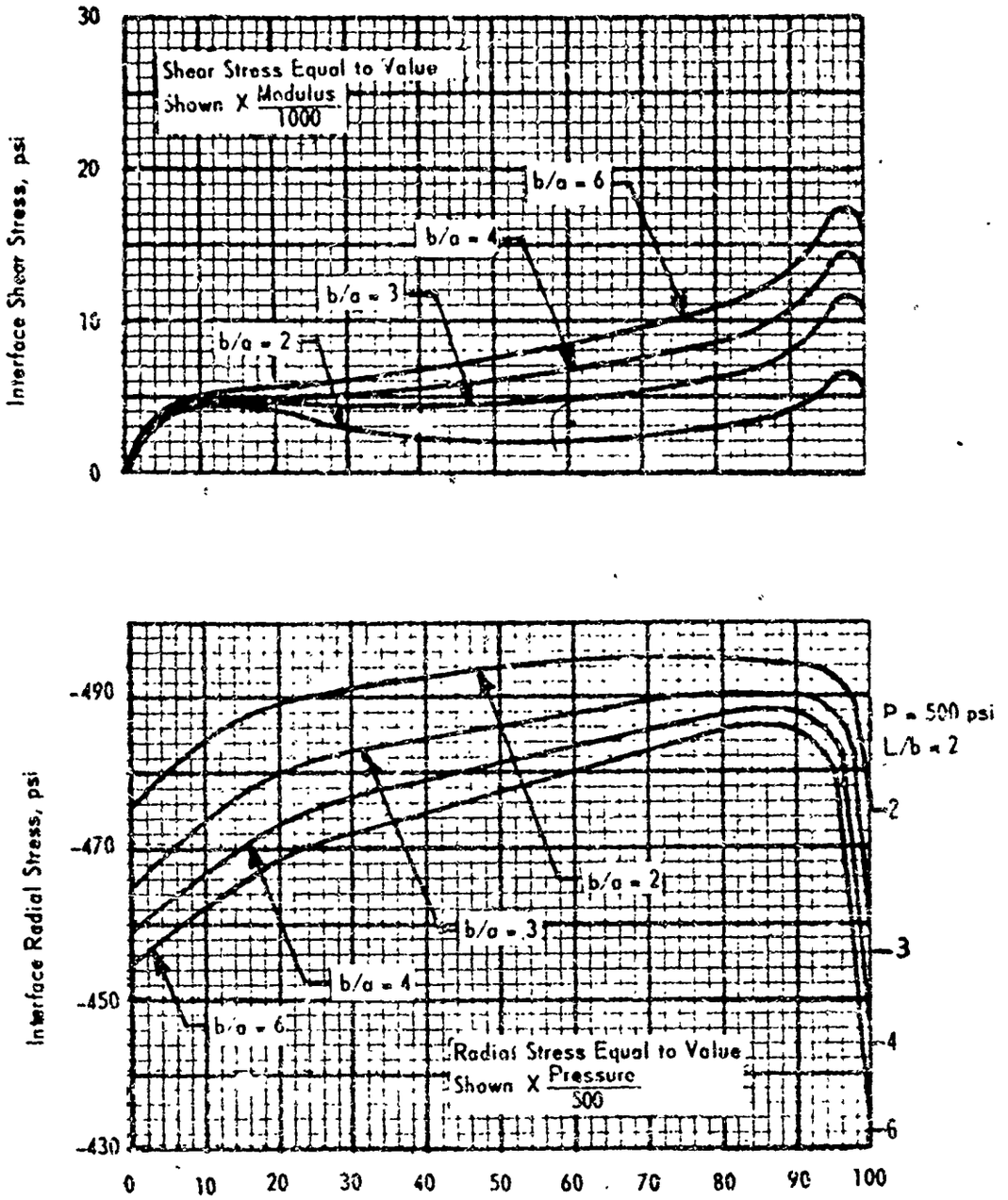

Interface Stresses Caused by Pressure
One End Bonded

Figure 10

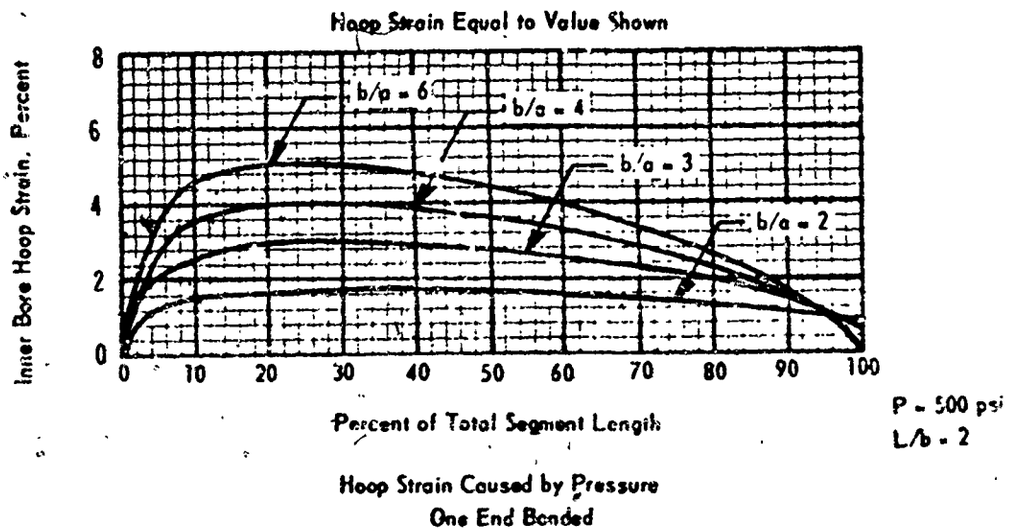
Hoop Strain Equal to Value Shown
Inner Bore Hoop Strain, Percent
8
6
4
2
0
b/a = 6
b/a = 4
b/a = 3
b/a = 2
0
10
20
30
40
50
60
70
80
90
100
Percent of Total Segment Length
P = 500 psi
L/b = 2
Hoop Strain Caused by Pressure
One End Bonded

Figure 11

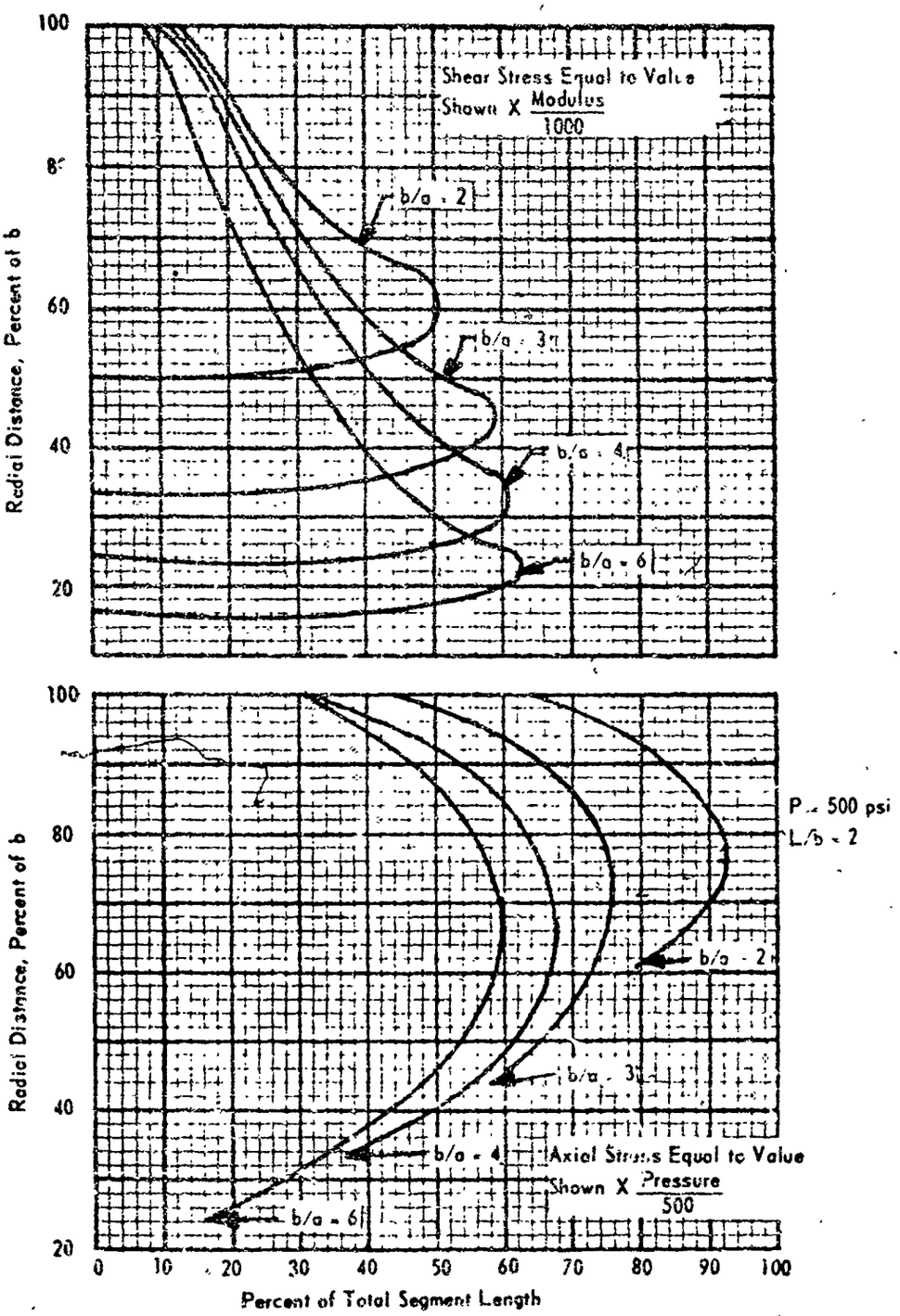

Interface Stresses Caused by Pressure
One End Bonded

Figure 12

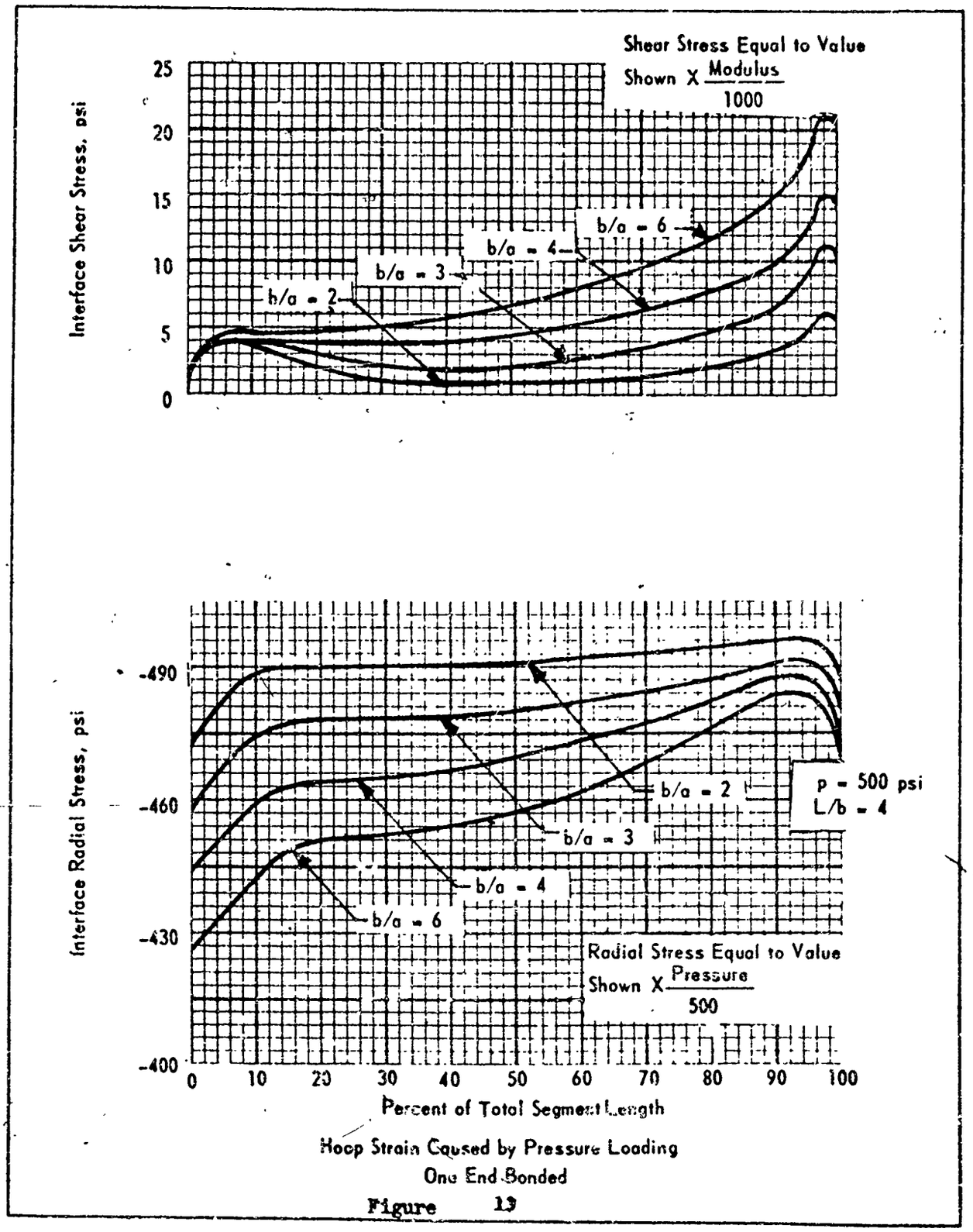

Hoop Strain Caused by Pressure Loading
One End Bonded

Figure 13

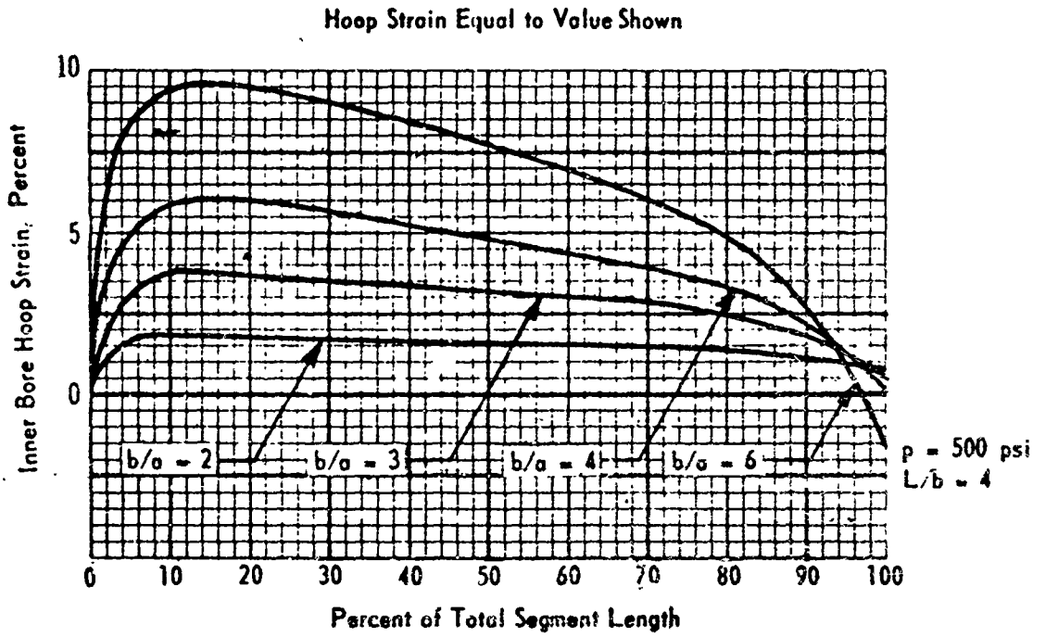

Hoop Strain Caused by Pressure Loading
One End Bonded

Figure 14

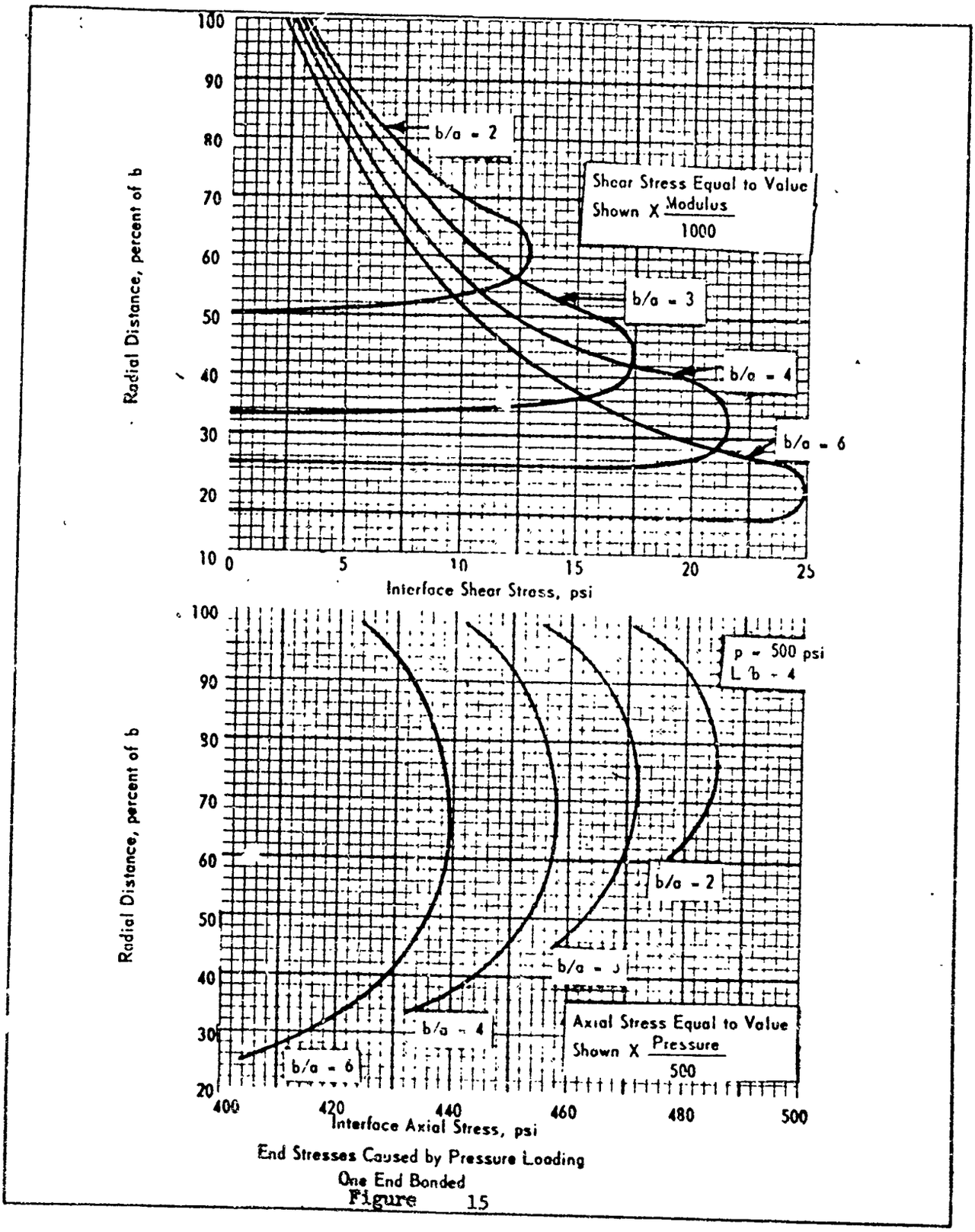

End Stresses Caused by Pressure Loading
One End Bonded

Figure 15

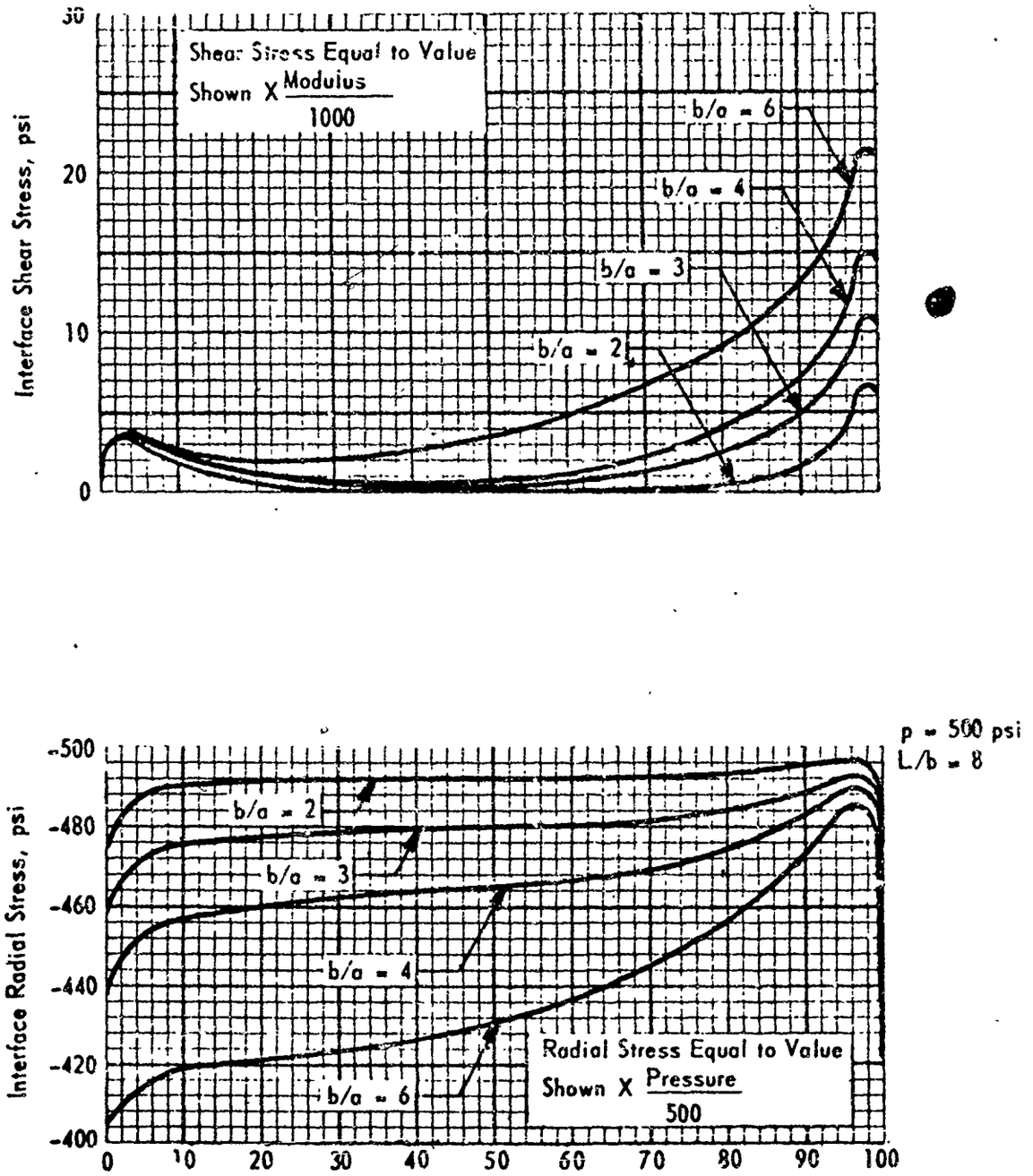

Stresses Caused by Pressure Loading
One End Bonded

Figure 16

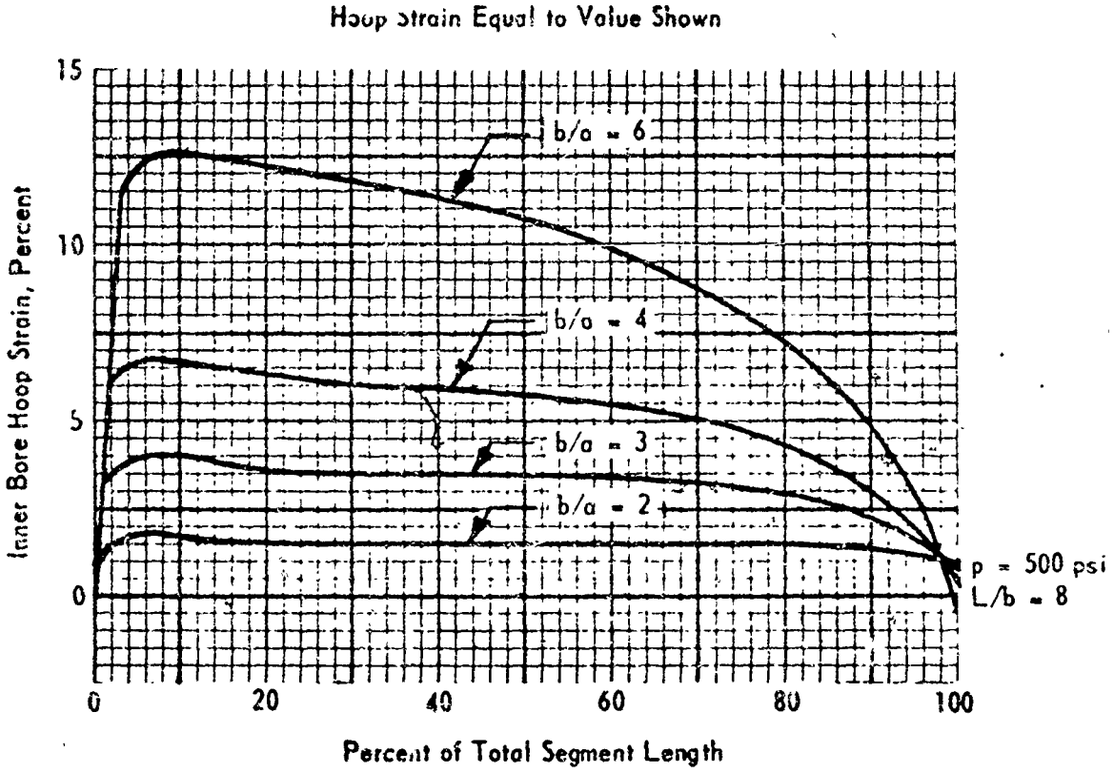

Hoop Strain Caused by Pressure Loading
One End Bonded

Figure 17

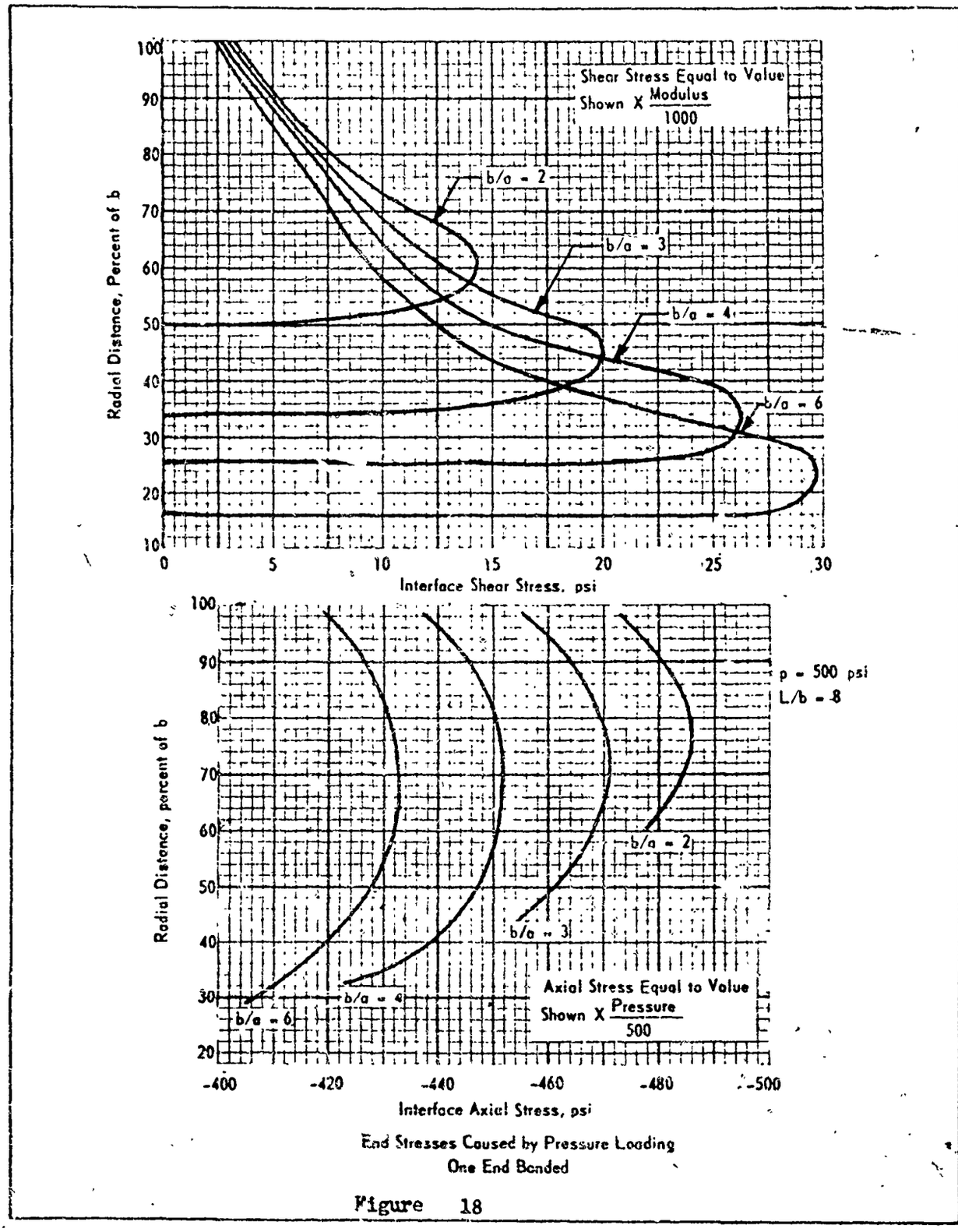
Shear Stress Equal to Value Shown X Modulus / 1000
b/a = 2
b/a = 3
b/a = 4
b/a = 6
Radial Distance, Percent of b
Interface Shear Stress, psi
p = 500 psi
L/b = 8
Axial Stress Equal to Value Shown X Pressure / 500
Radial Distance, percent of b
Interface Axial Stress, psi
End Stresses Caused by Pressure Loading
One End Bonded

Figure 18

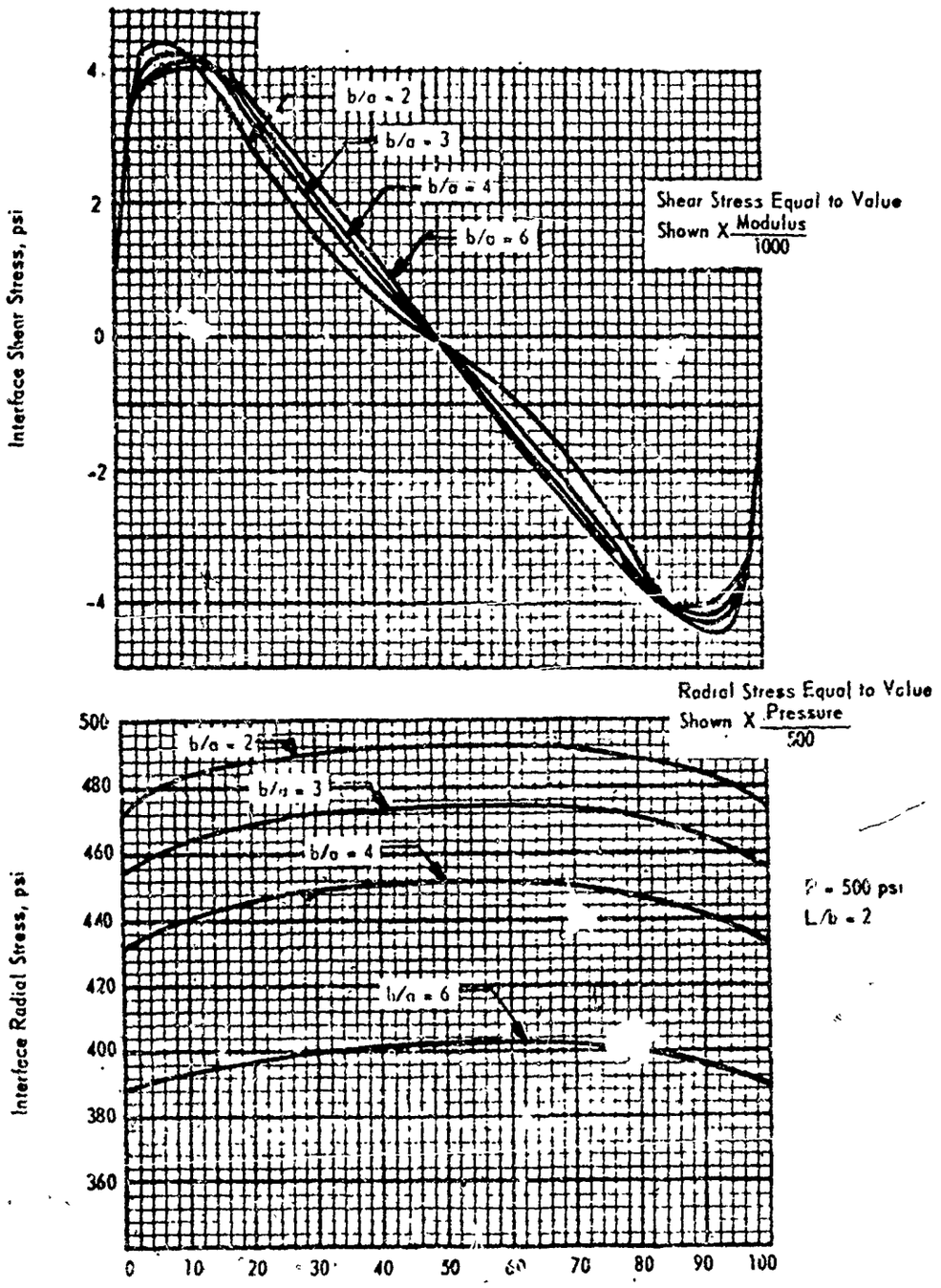

Stresses Caused by Pressure Loading
@ Both Ends Bonded

Figure 19

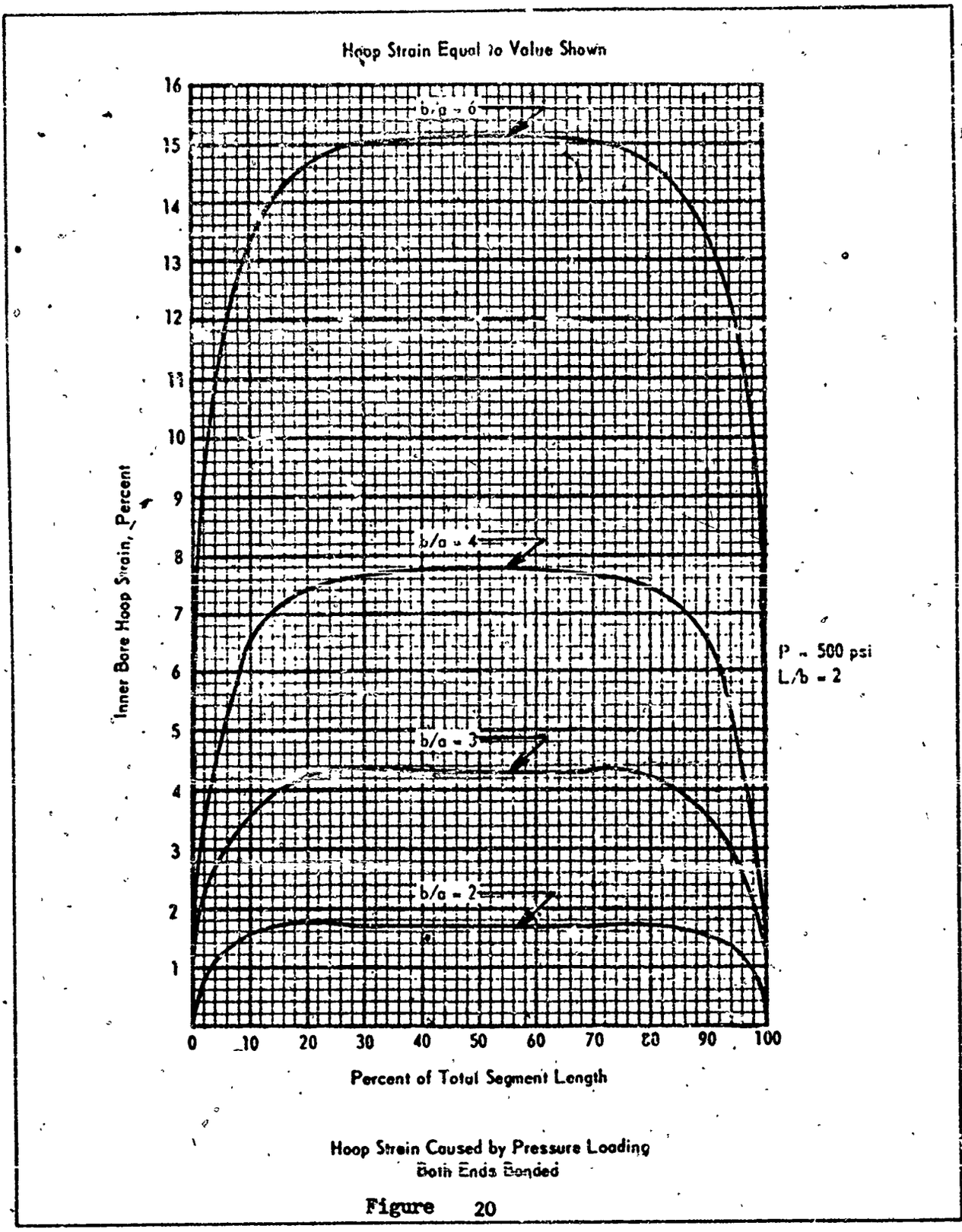

Hoop Strain Caused by Pressure Loading
Both Ends Bonded

Figure 20

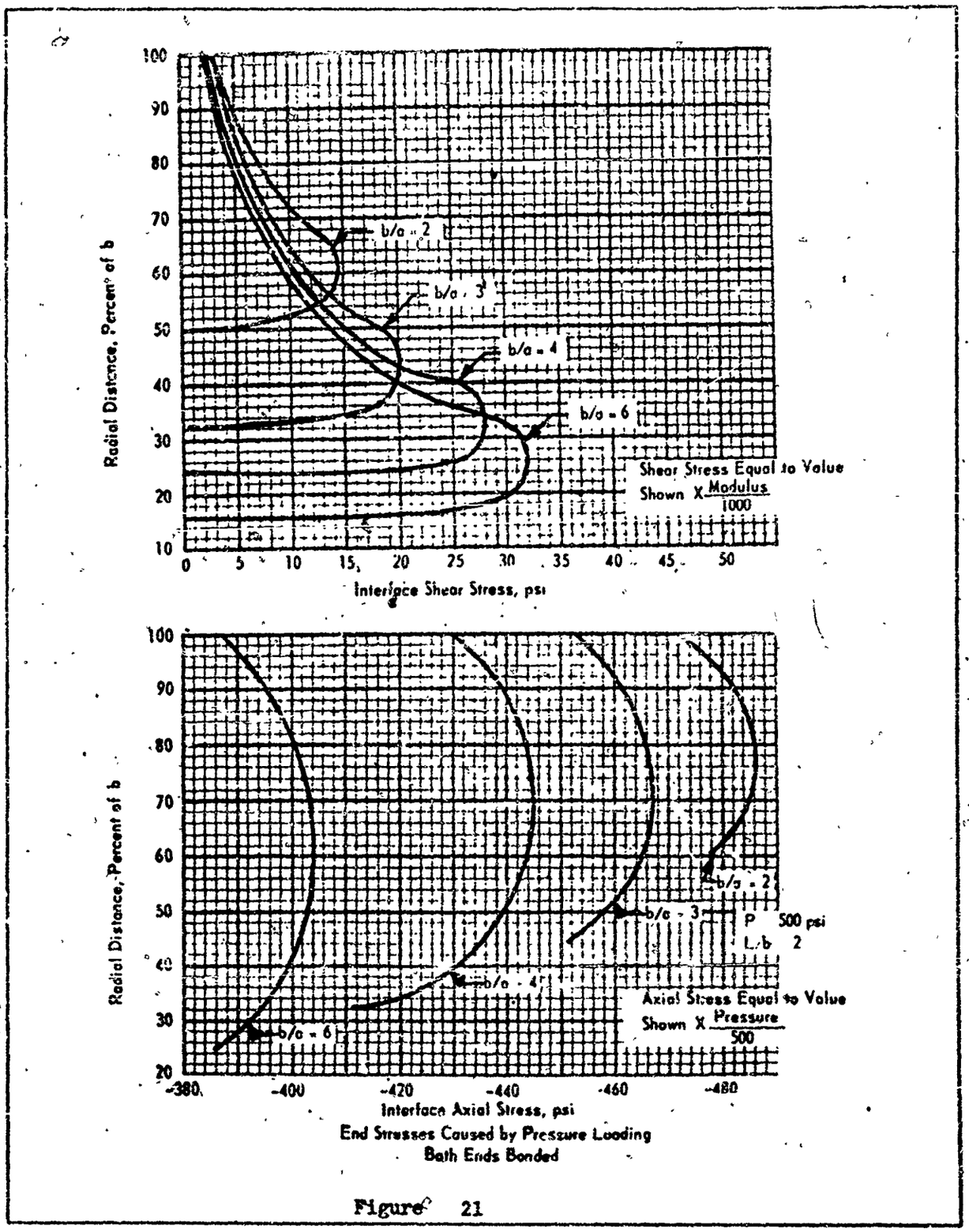
Radial Distance, Percent of b
100
90
80
70
60
50
40
30
20
10
0
5
10
15
20
25
30
35
40
45
50
b/a = 2
b/a = 3
b/a = 4
b/a = 6
Shear Stress Equal to Value Shown X Modulus / 1000
Interface Shear Stress, psi
Radial Distance, Percent of b
100
90
80
70
60
50
40
30
20
-380
-400
-420
-440
-460
-480
b/a = 2
b/a = 3
b/a = 4
b/a = 6
P 500 psi
L/b 2
Axial Stress Equal to Value Shown X Pressure / 500
Interface Axial Stress, psi
End Stresses Caused by Pressure Loading
Both Ends Bonded

Figure 21

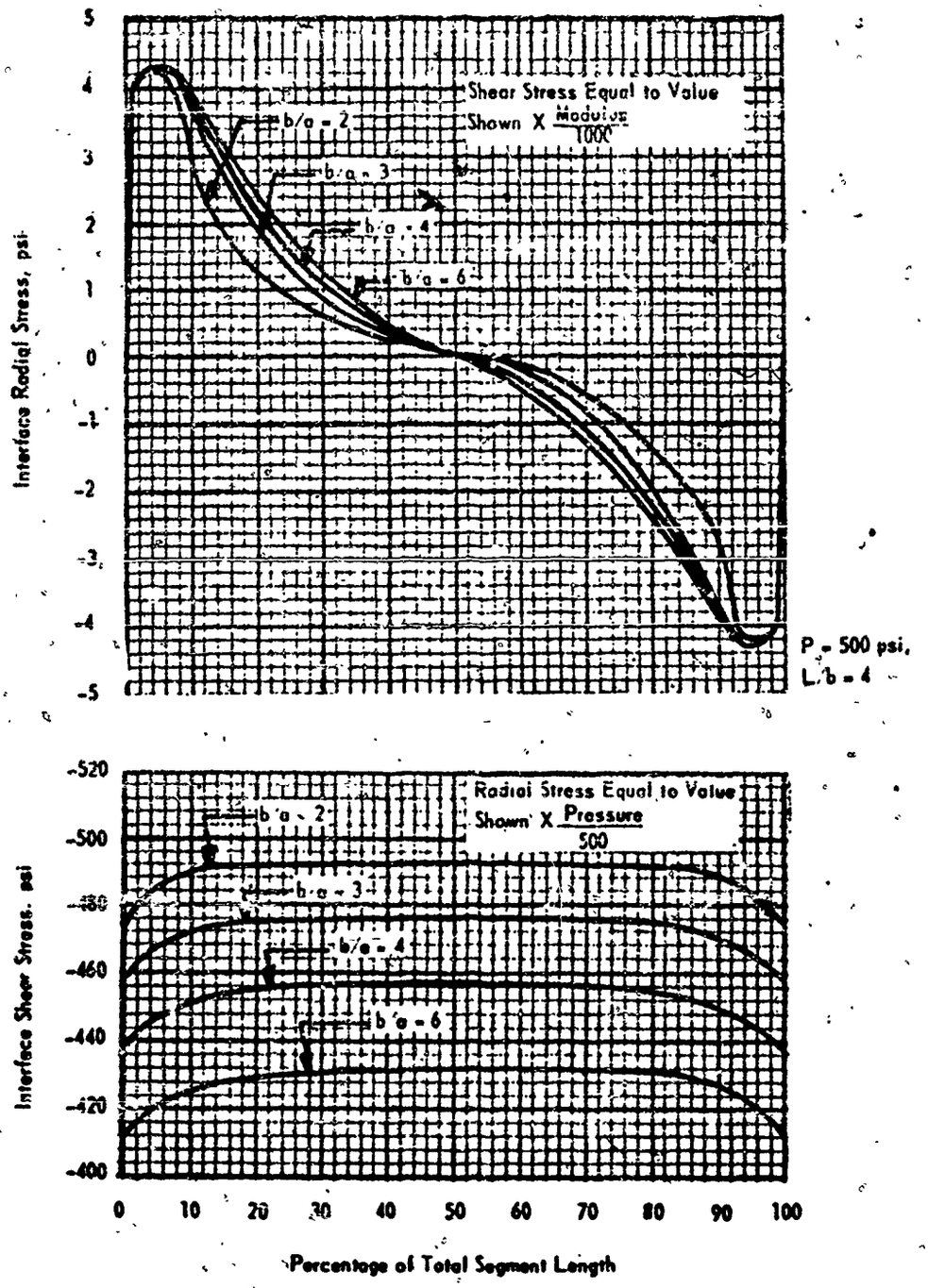

Interface Stresses Caused by Pressure Loading
Both Ends Bonded

Figure 22.

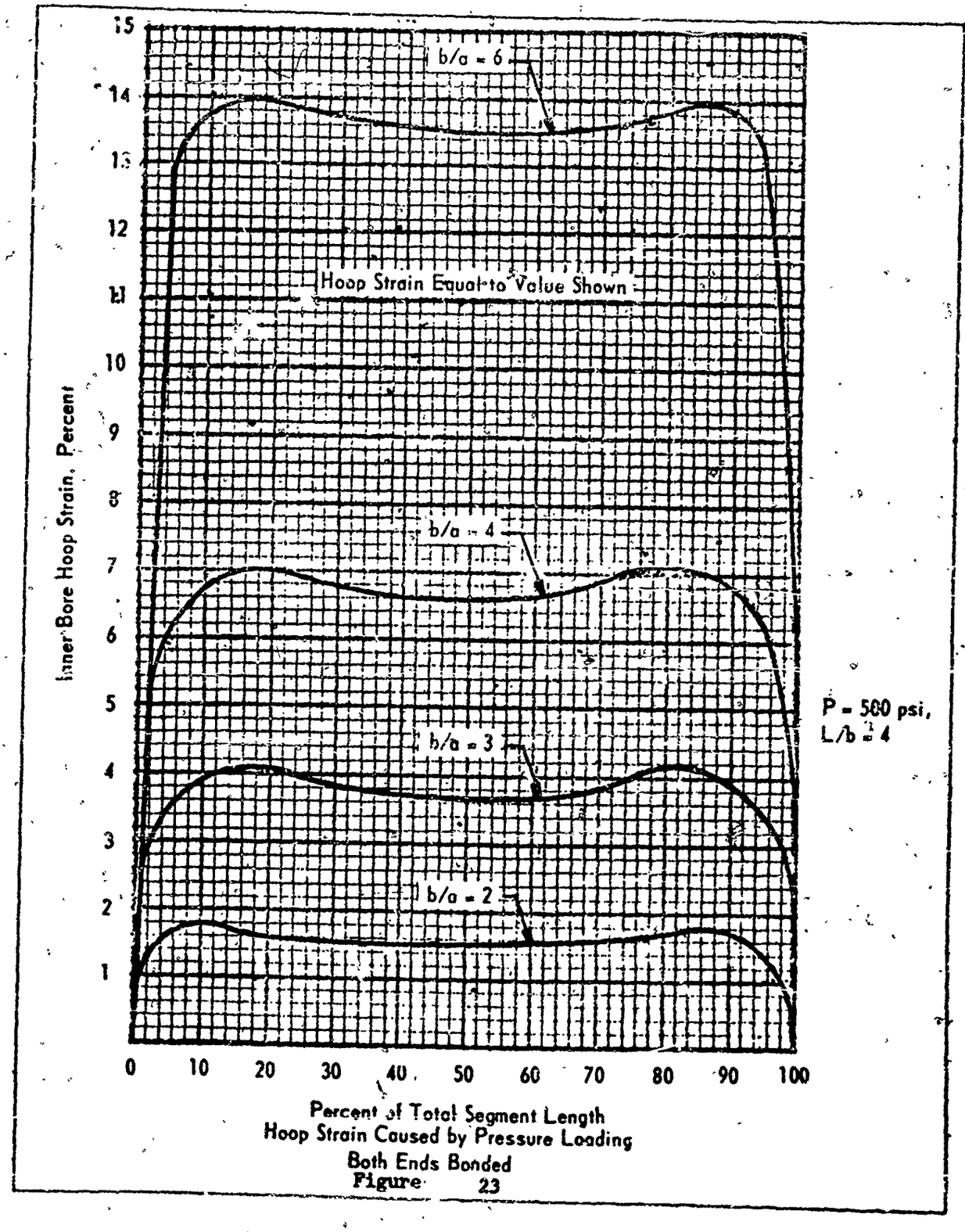
Inner Bore Hoop Strain, Percent
15
14
13
12
11
10
9
8
7
6
5
4
3
2
1
b/a = 6
Hoop Strain Equal to Value Shown
b/a = 4
b/a = 3
b/a = 2
P = 500 psi,
L/b = 4
0
10
20
30
40
50
60
70
80
90
100
Percent of Total Segment Length
Hoop Strain Caused by Pressure Loading
Both Ends Bonded
Figure 23

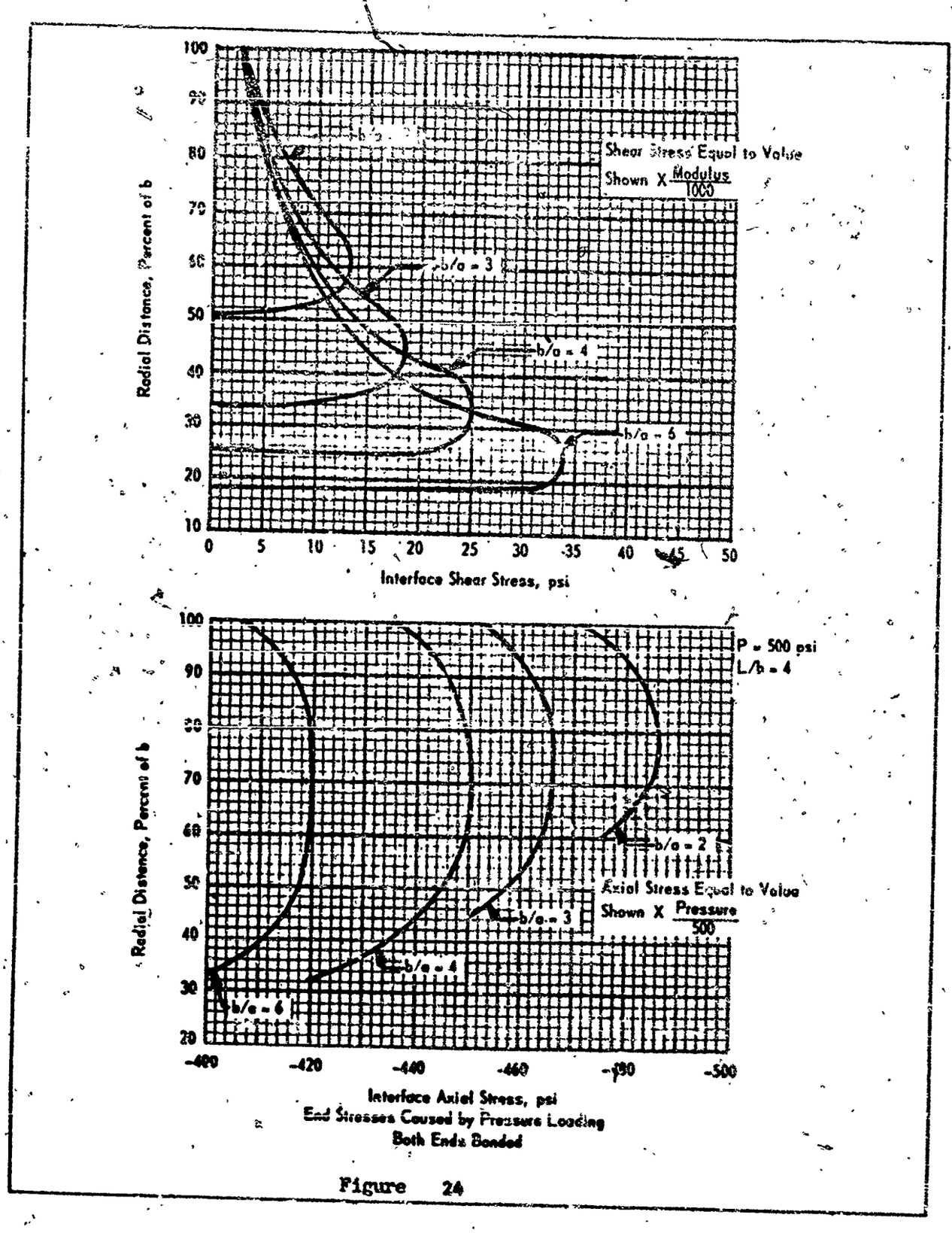
Radial Distance, Percent of b
Shear Stress Equal to Value Shown X Modulus / 1000
b/a = 3
b/a = 4
b/a = 6
Interface Shear Stress, psi
P = 500 psi
L/b = 4
b/a = 2
b/a = 3
b/a = 4
b/a = 6
Axial Stress Equal to Value Shown X Pressure / 500
Interface Axial Stress, psi
End Stresses Caused by Pressure Loading
Both Ends Bonded

Figure 24

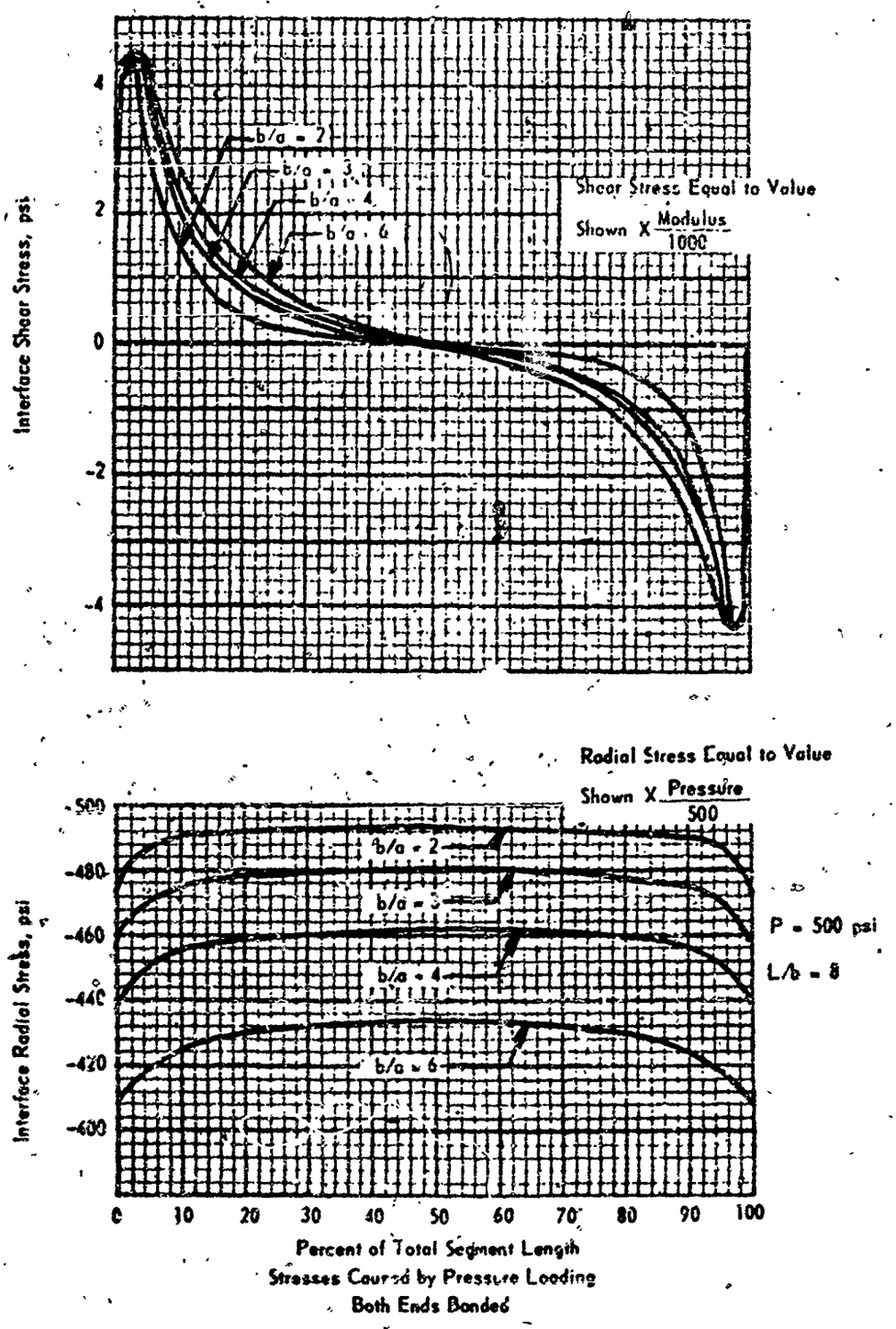
Interface Shear Stress, psi
4
2
0
-2
-4
b/a = 2
b/a = 3
b/a = 4
b/a = 6
Shear Stress Equal to Value Shown X Modulus / 1000
Interface Radial Stress, psi
-500
-480
-460
-440
-420
-400
b/a = 2
b/a = 3
b/a = 4
b/a = 6
Radial Stress Equal to Value Shown X Pressure / 500
P = 500 psi
L/b = 8
0
10
20
30
40
50
60
70
80
90
100
Percent of Total Segment Length
Stresses Caused by Pressure Loading
Both Ends Bonded

Figure 25

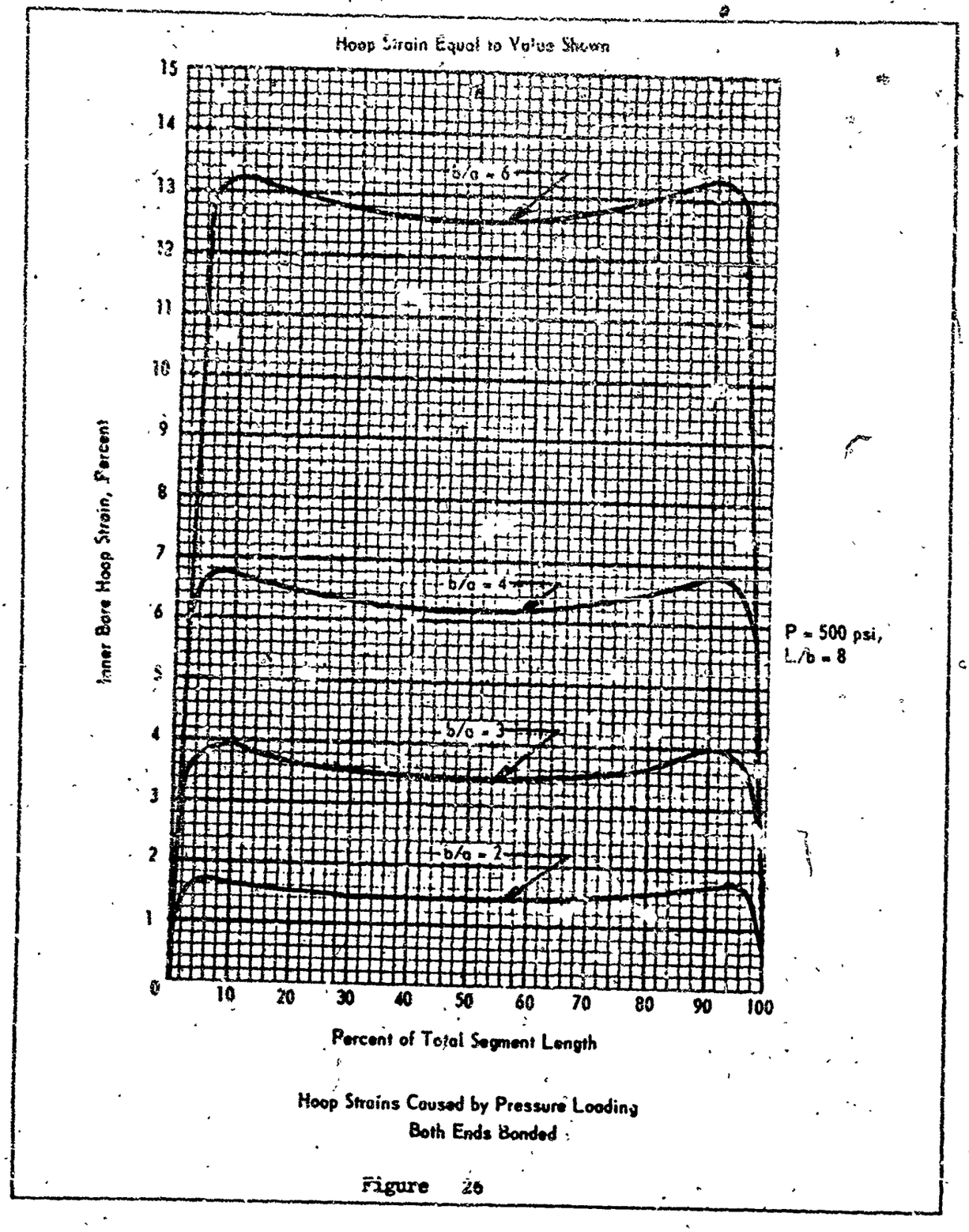

Hoop Strains Caused by Pressure Loading
Both Ends Bonded

Figure 26

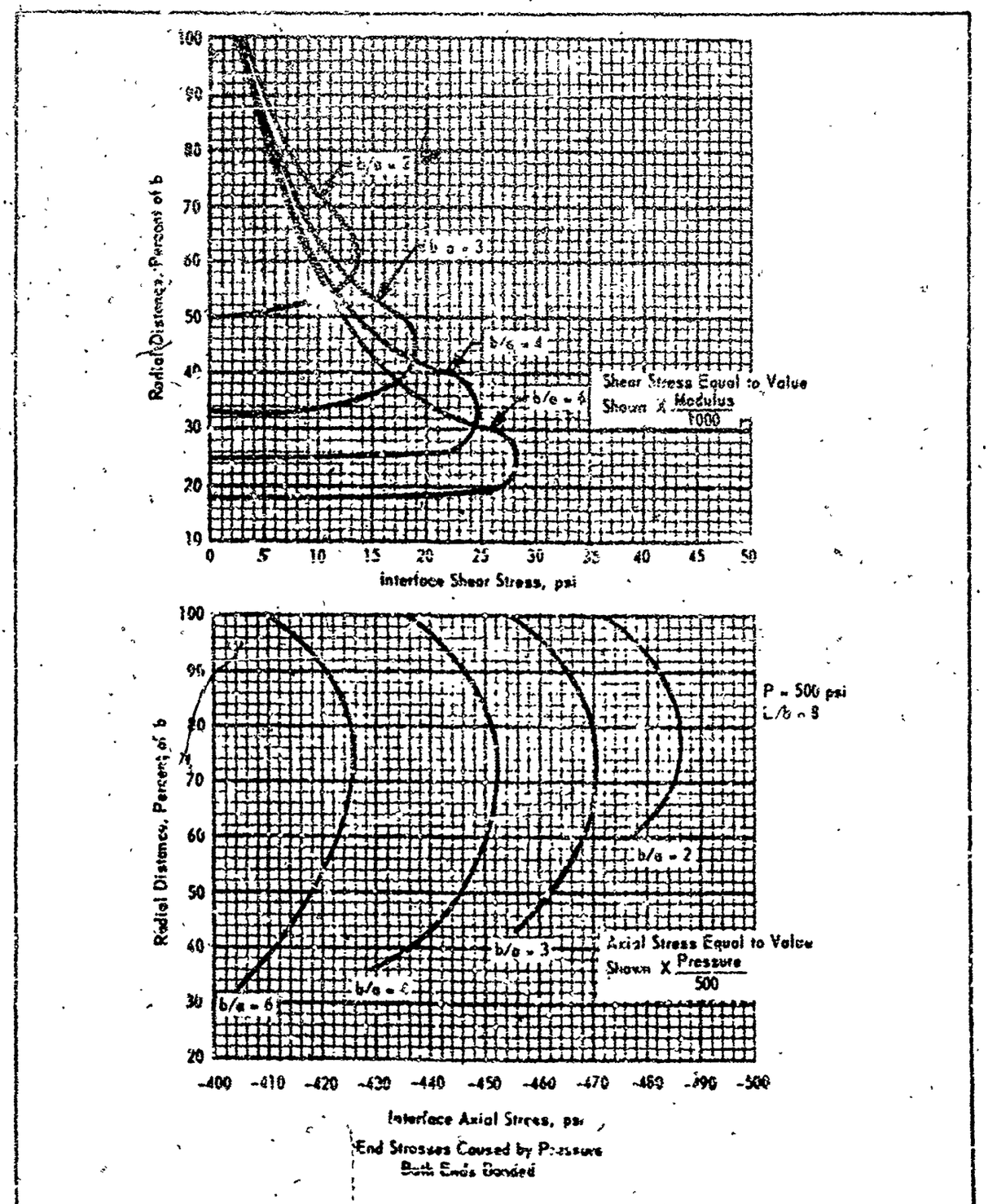
Radial Distance, Percent of b
b/a = 2
b/a = 3
b/a = 4
b/a = 6
Shear Stress Equal to Value Shown X Modulus / 1000
Interface Shear Stress, psi
Radial Distance, Percent of b
P = 500 psi
L/b = 8
b/a = 2
b/a = 3
b/a = 4
b/a = 6
Axial Stress Equal to Value Shown X Pressure / 500
Interface Axial Stress, psi
End Stresses Caused by Pressure
Both Ends Bonded

Figure 27

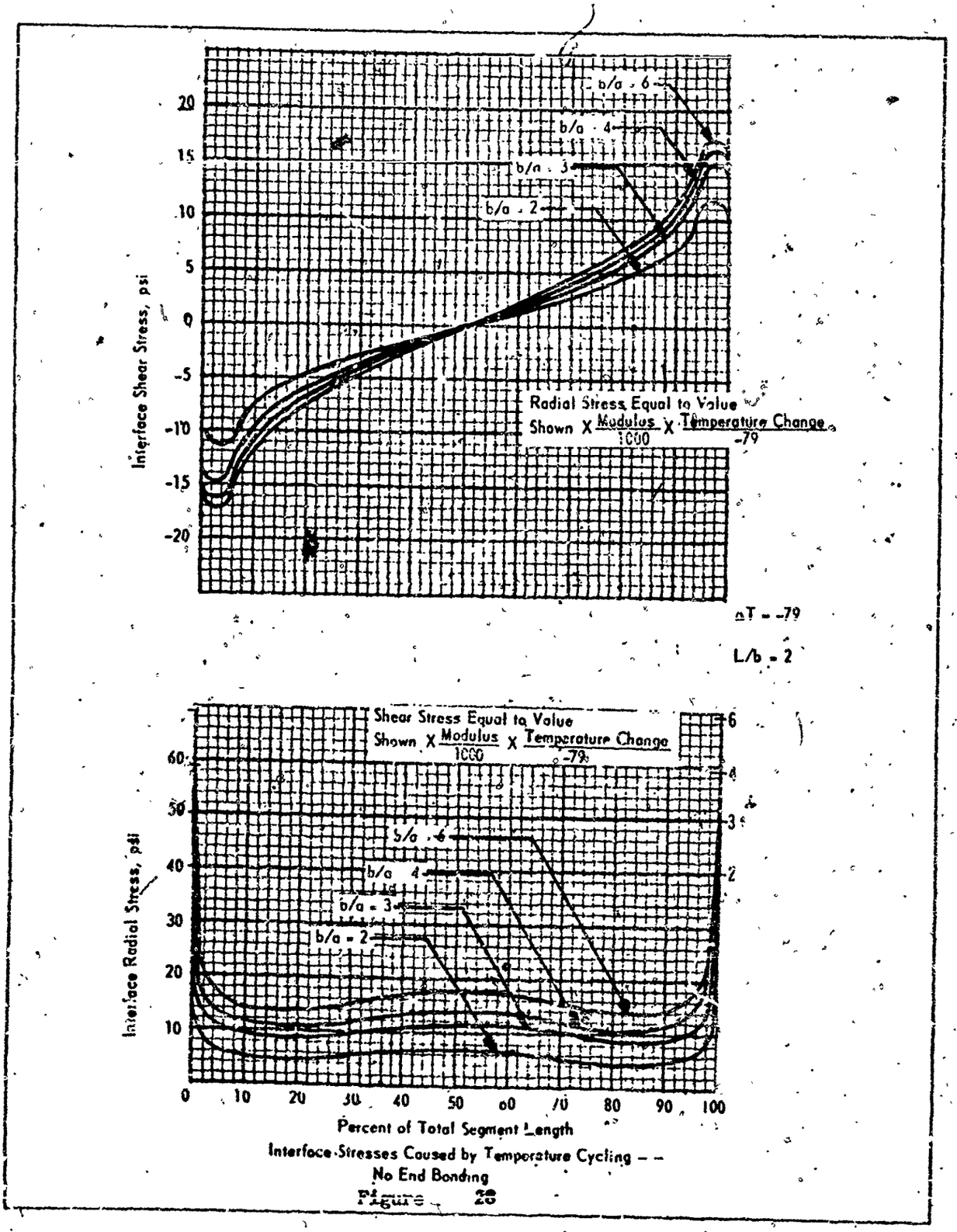

Interface Stresses Caused by Temperature Cycling – –
No End Bonding

Figure 20

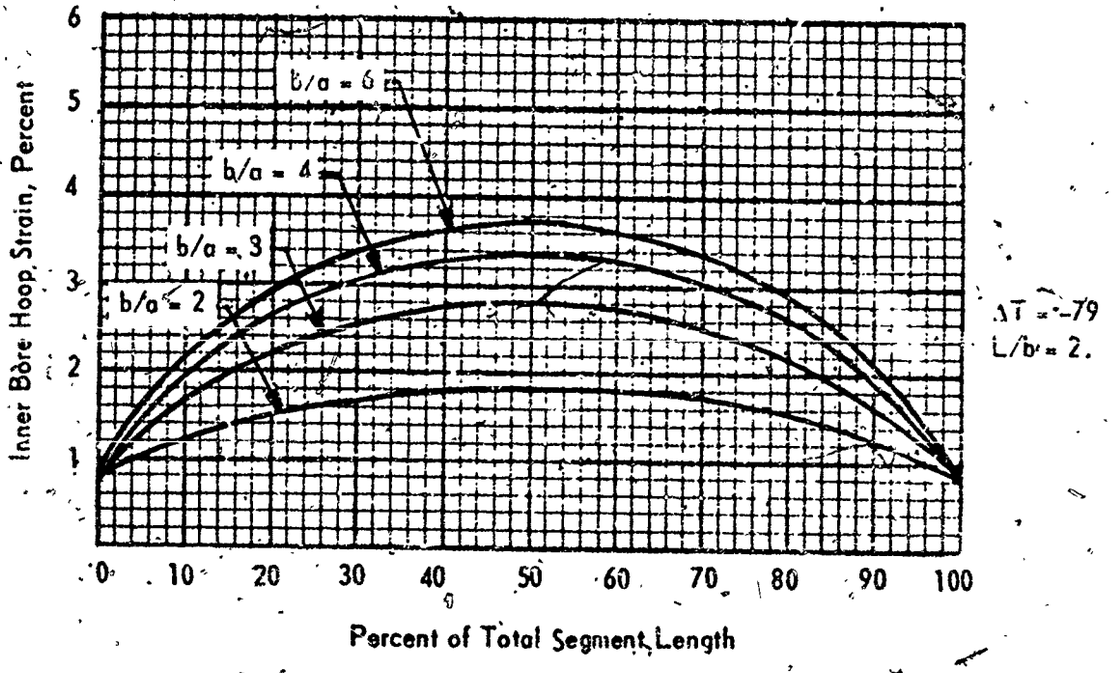

Hoop Strain Caused By Temperature Cycling – No End Bonding

Figure 29

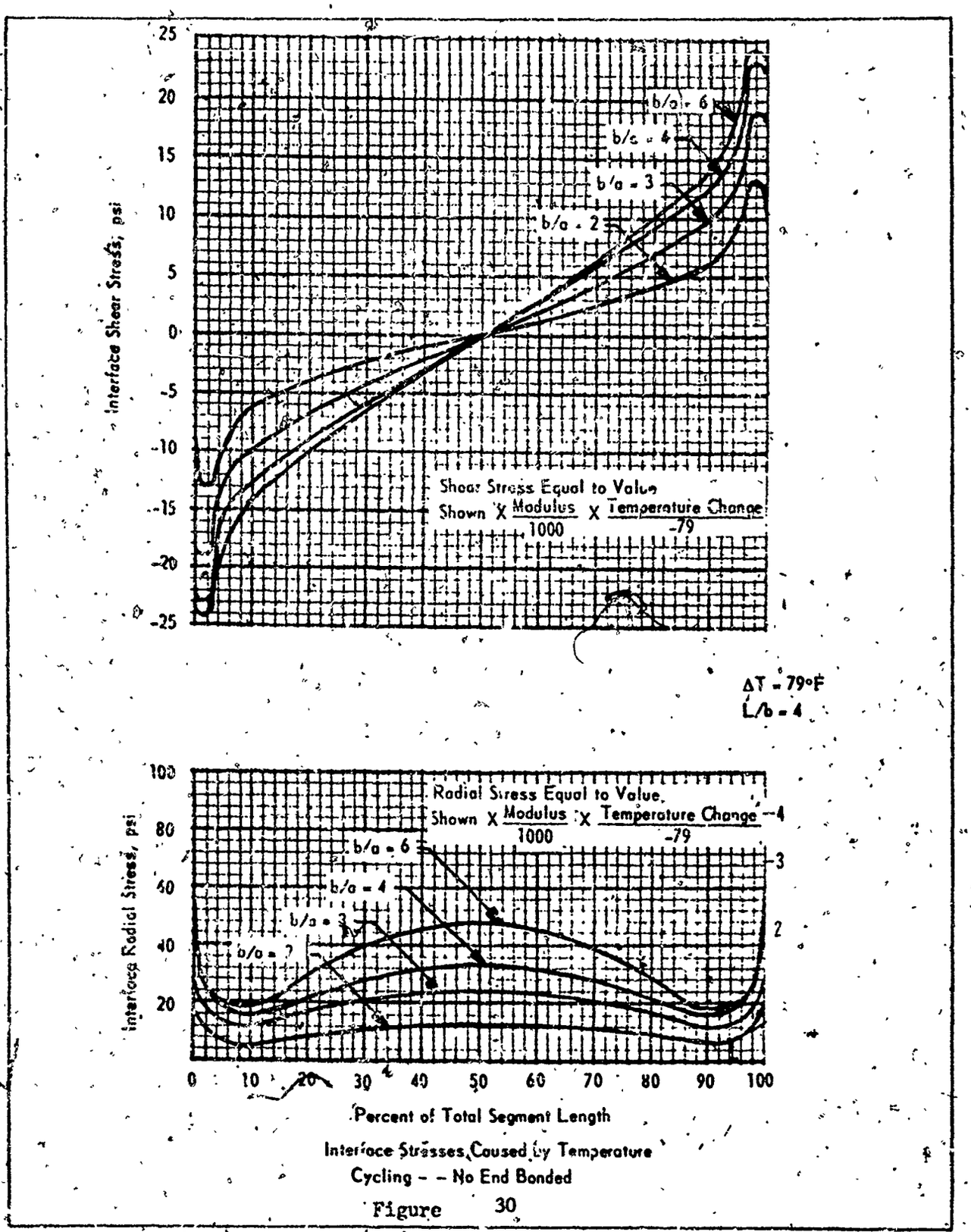

Interface Stresses Caused by Temperature Cycling – – No End Bonded

Figure 30

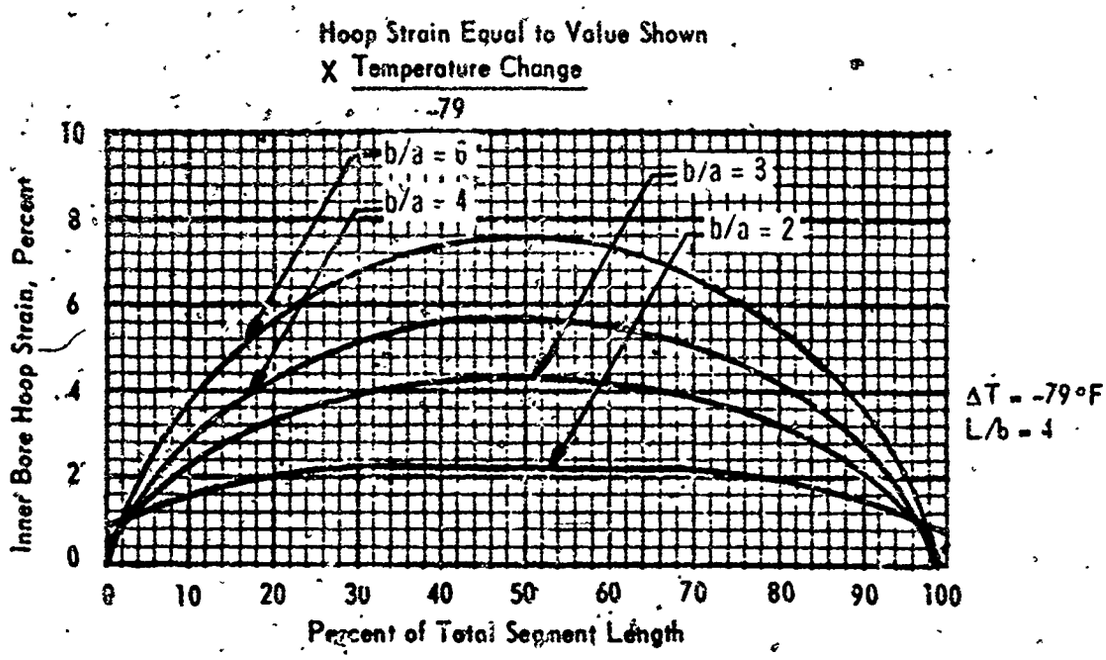

Hoop Strain Caused by Temperature Cycling -- No End Bonding

Figure 31

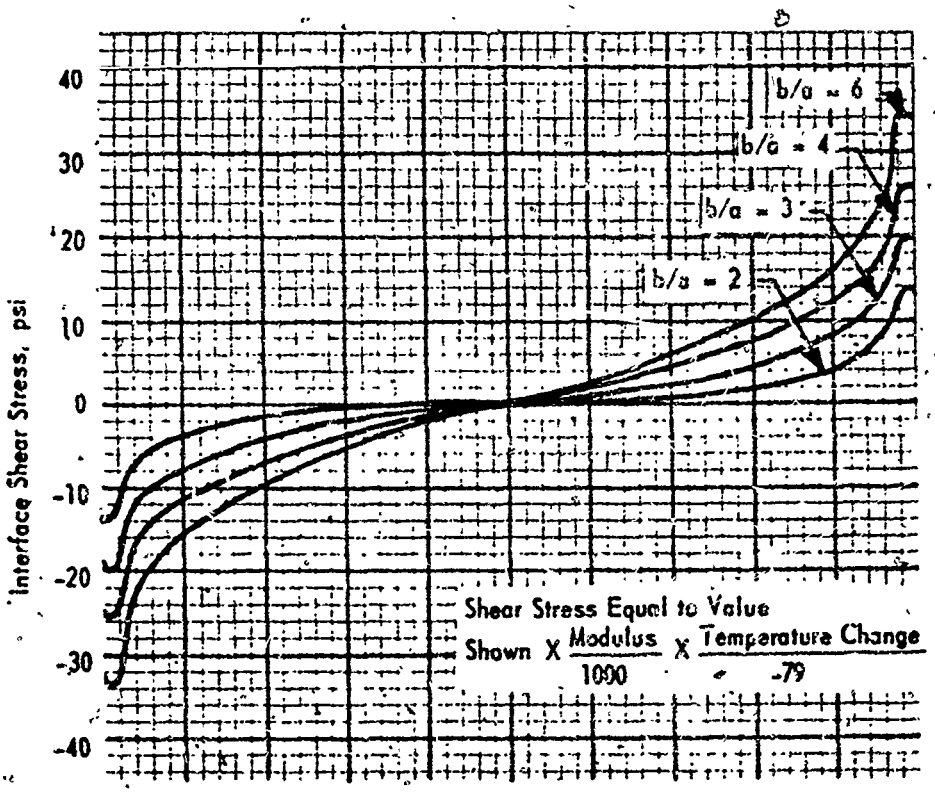

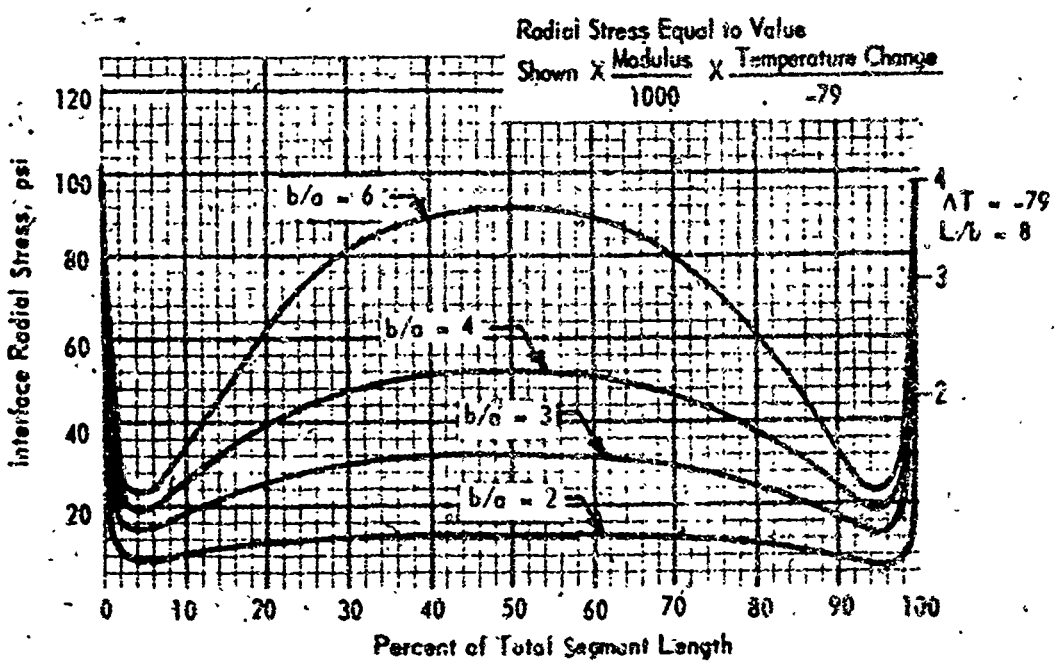

Interface Stresses Caused by Temperature Cycling - No End Bonding

Figure 32

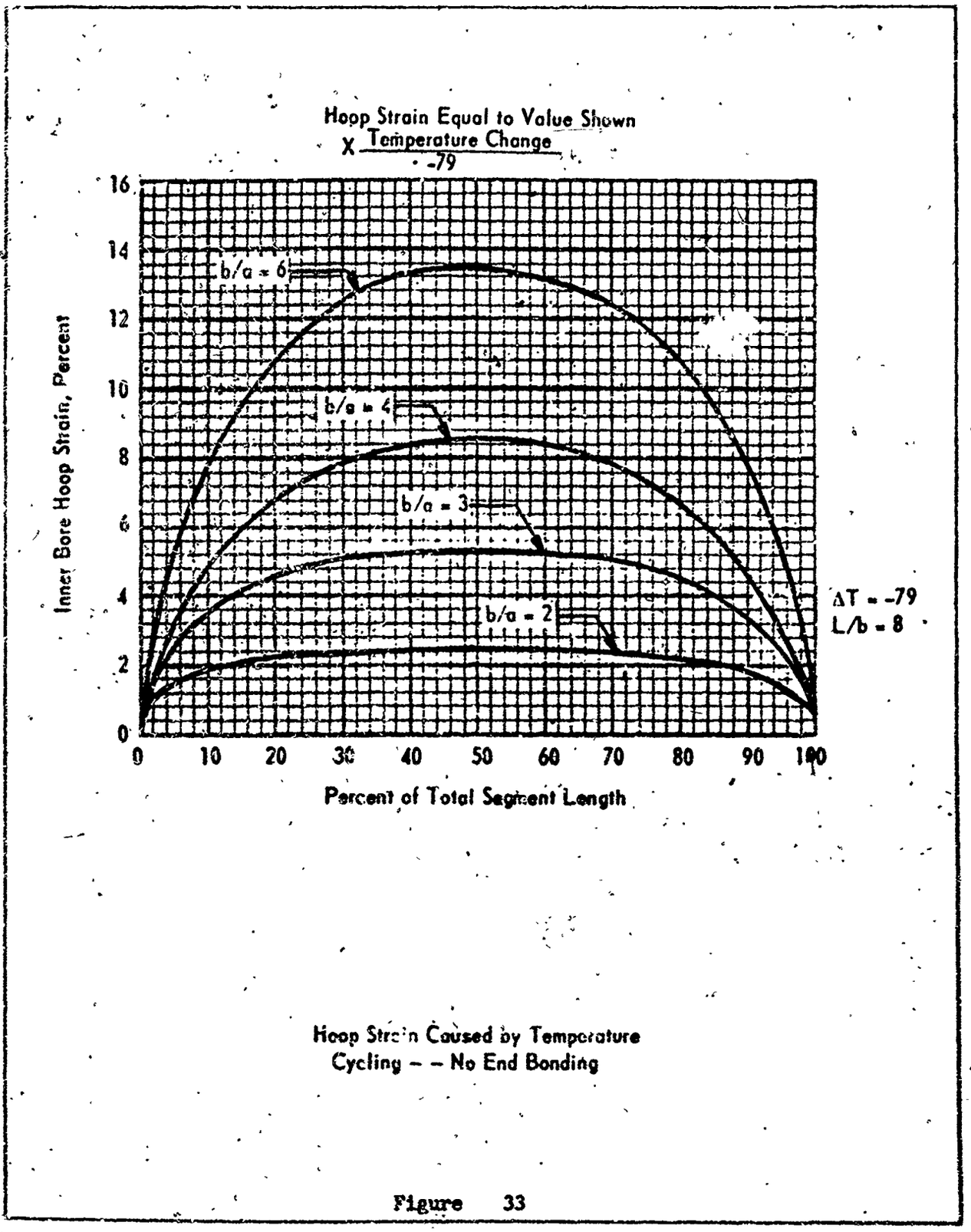
Hoop Strain Equal to Value Shown
X Temperature Change / -79
Inner Bore Hoop Strain, Percent
16
14
12
10
8
6
4
2
0
b/a = 6
b/a = 4
b/a = 3
b/a = 2
0
10
20
30
40
50
60
70
80
90
100
Percent of Total Segment Length
ΔT = -79
L/b = 8
Hoop Strain Caused by Temperature Cycling – – No End Bonding

Figure 33

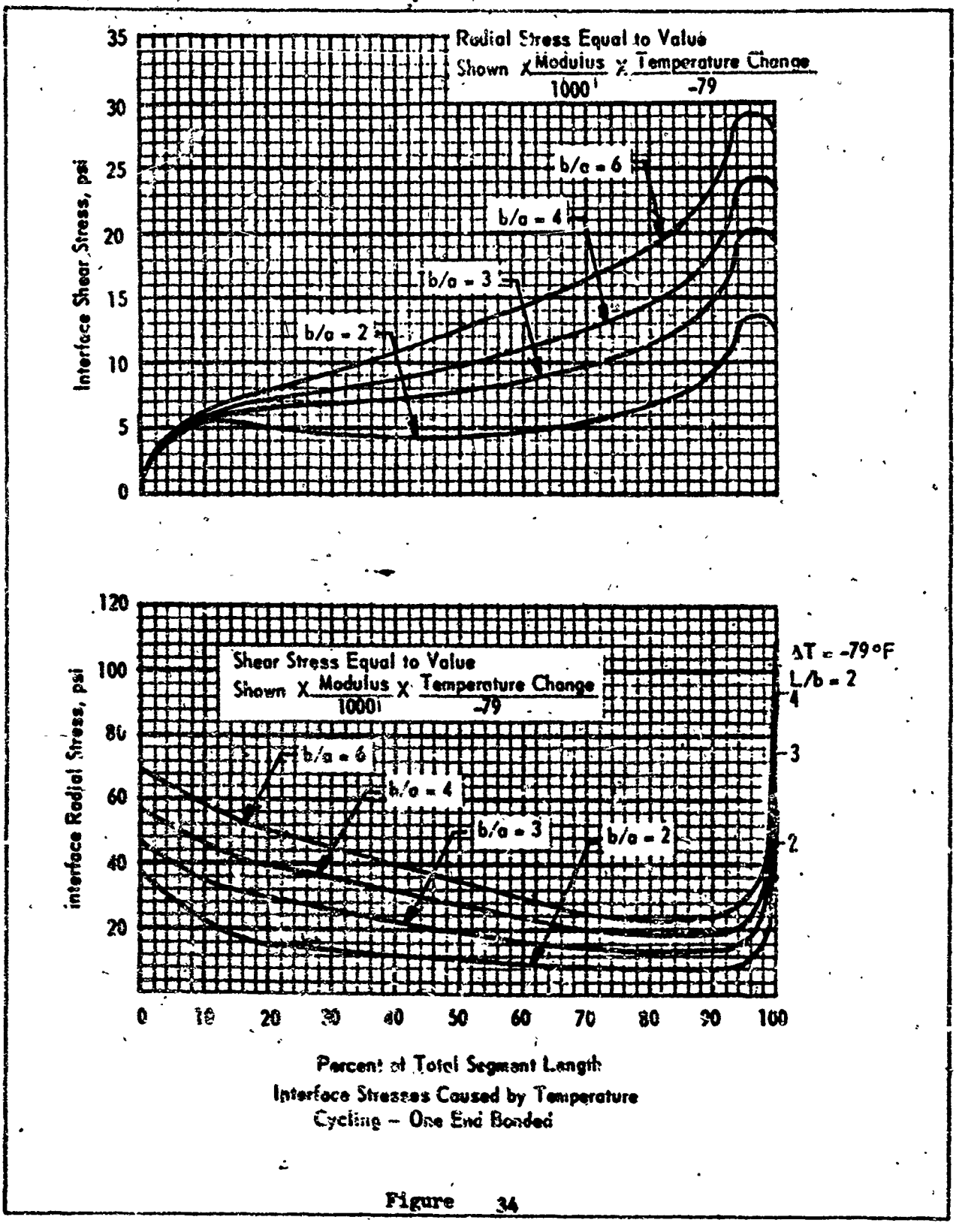

Interface Stresses Caused by Temperature Cycling – One End Bonded

Figure 34

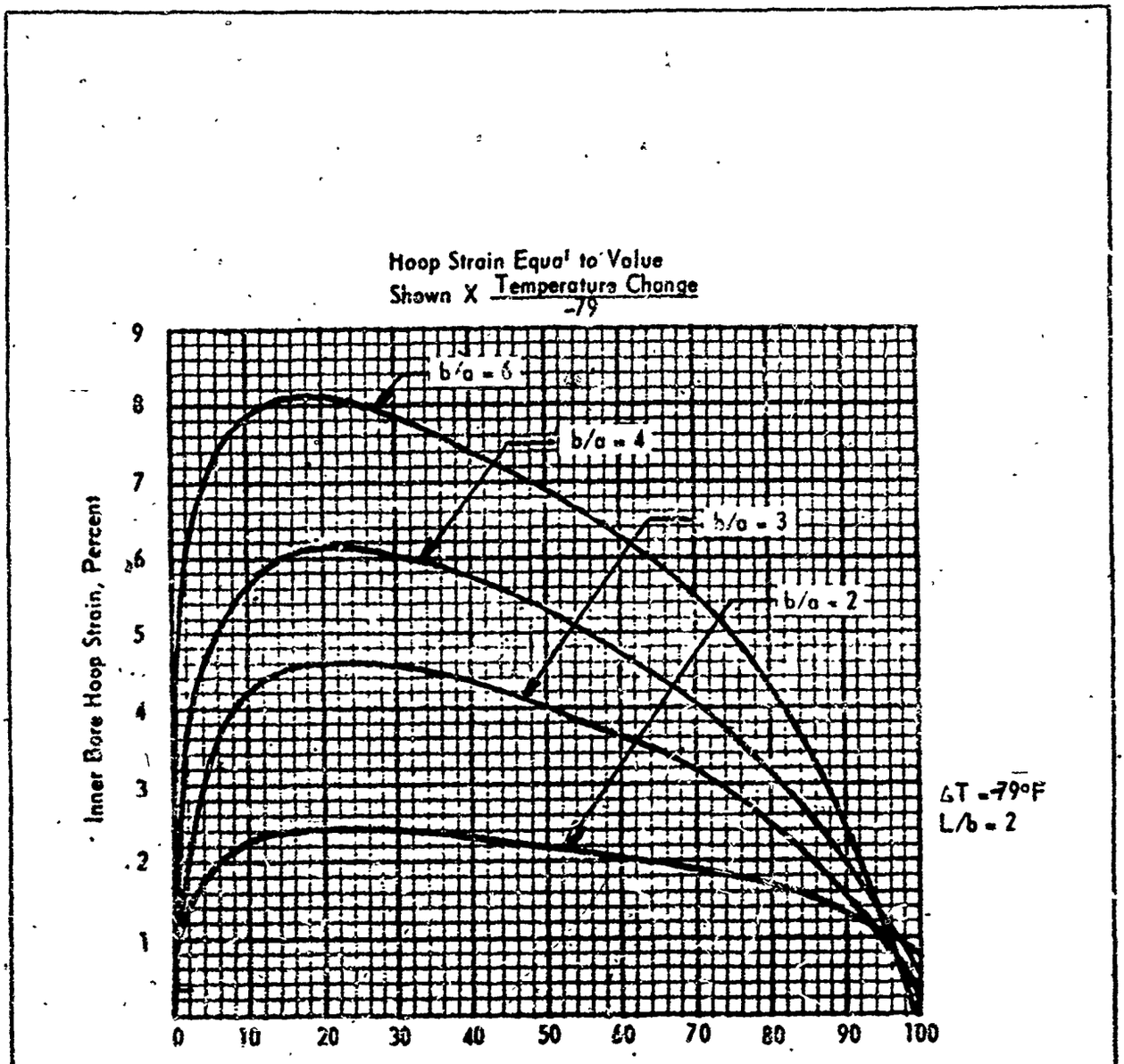
Hoop Strain Equal to Value Shown X Temperature Change / -79
Inner Bore Hoop Strain, Percent
9
8
7
6
5
4
3
2
1
b/a = 6
b/a = 4
b/a = 3
b/a = 2
0
10
20
30
40
50
60
70
80
90
100
Percent of Total Segment Length
ΔT = -79°F
L/b = 2
Hoop Strain Caused by Temperature Cycling – –
One End Bonded

Figure 35

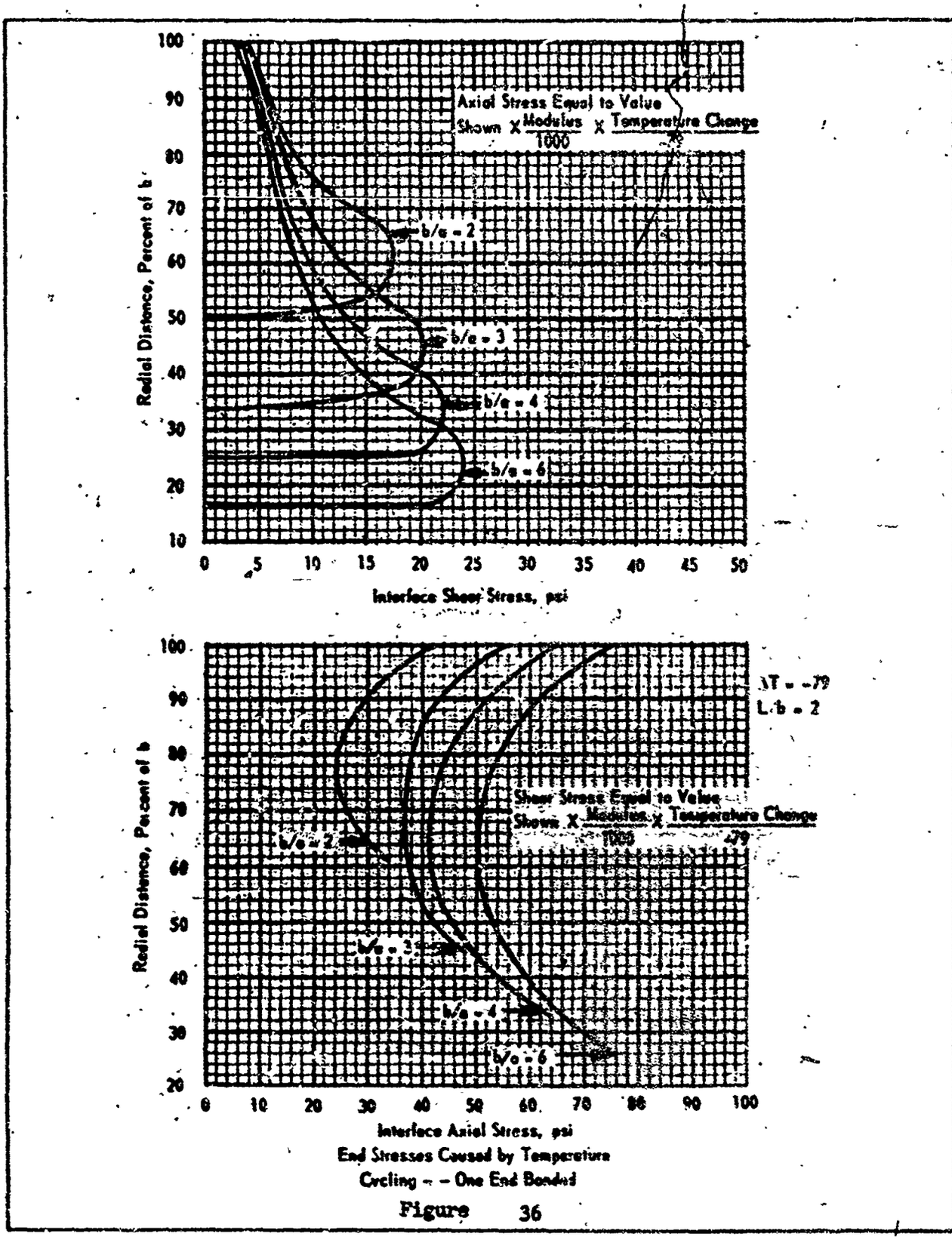

End Stresses Caused by Temperature Cycling - - One End Bonded

Figure 36

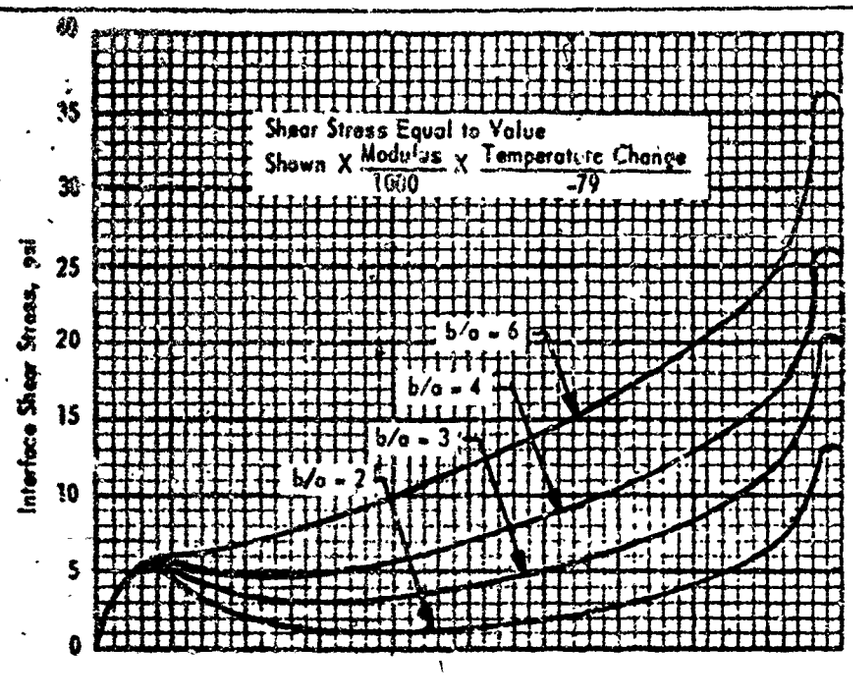

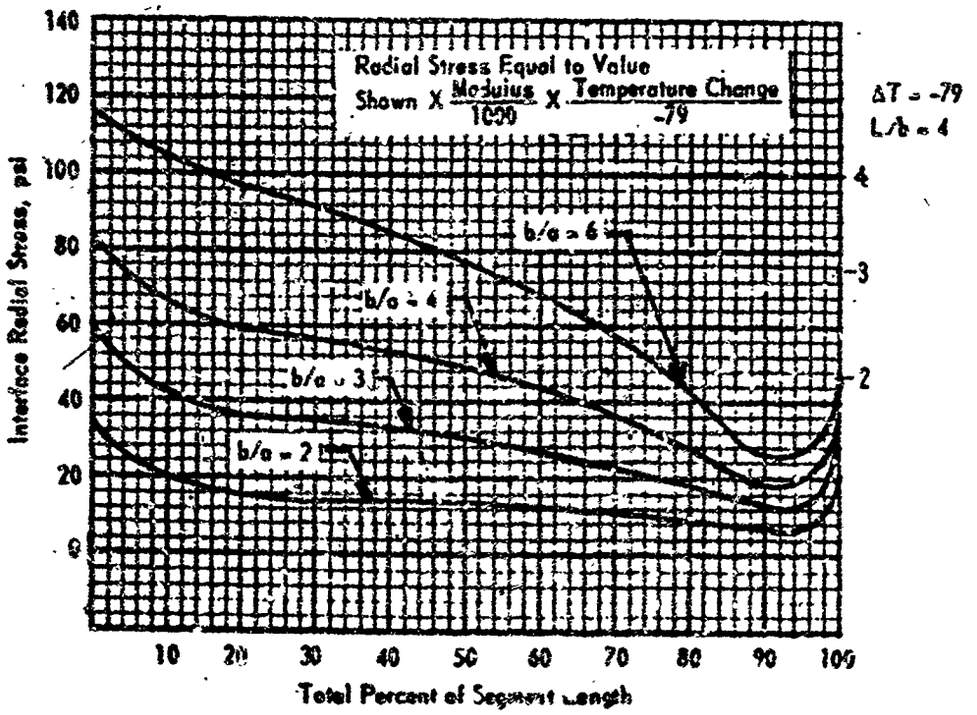

Interface Stresses Caused by Temperature Cycling – – One End Bonded

Figure 37

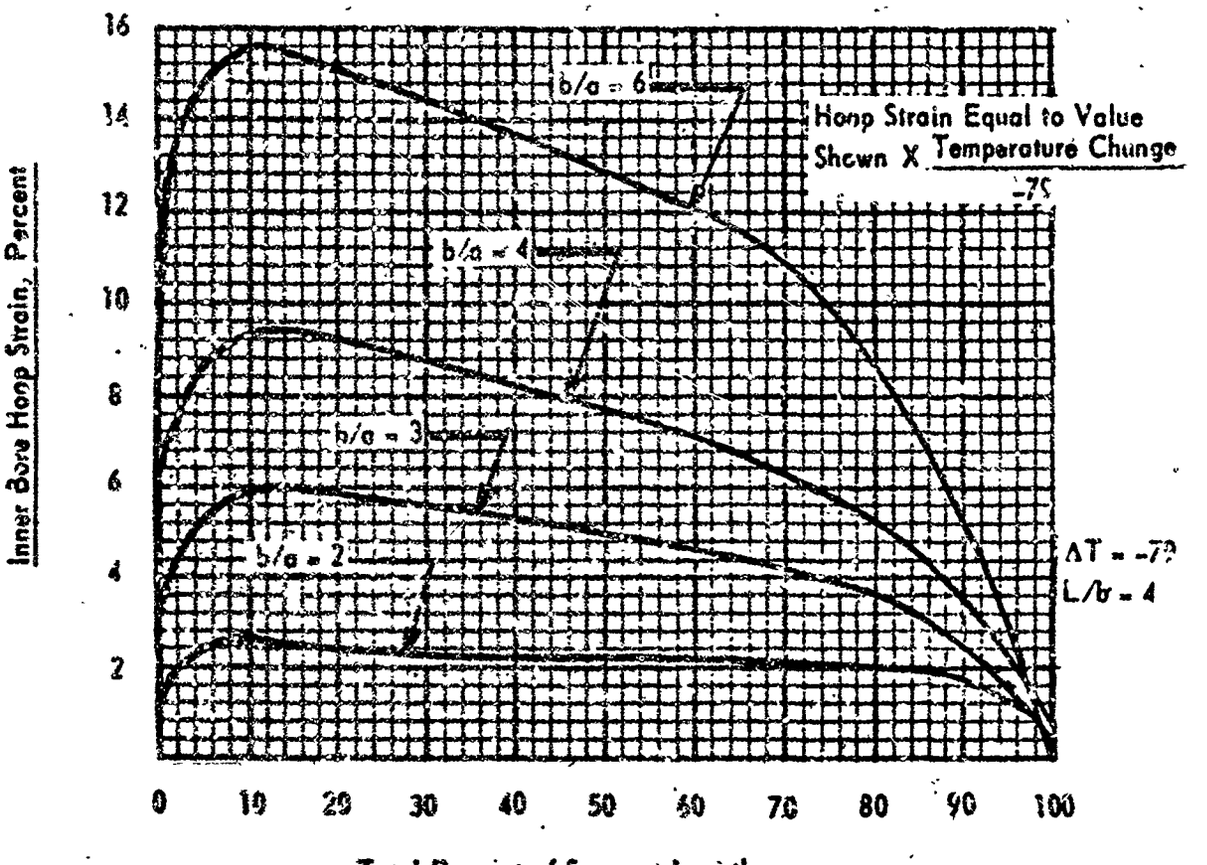

Hoop Strain Caused by Temperature Cycling -- One End Bonded

Figure 30

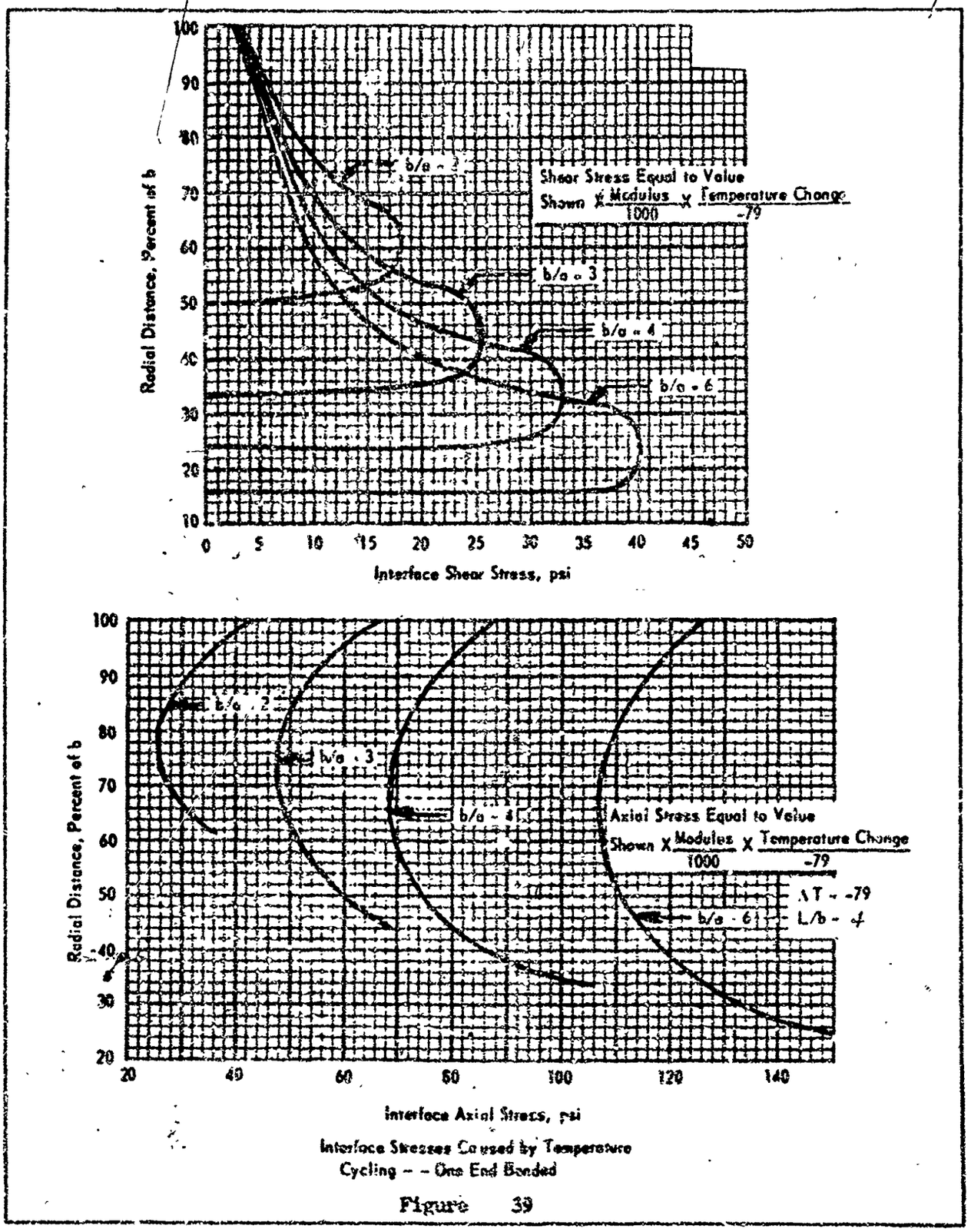

Interface Stresses Caused by Temperature Cycling -- One End Bonded

Figure 39

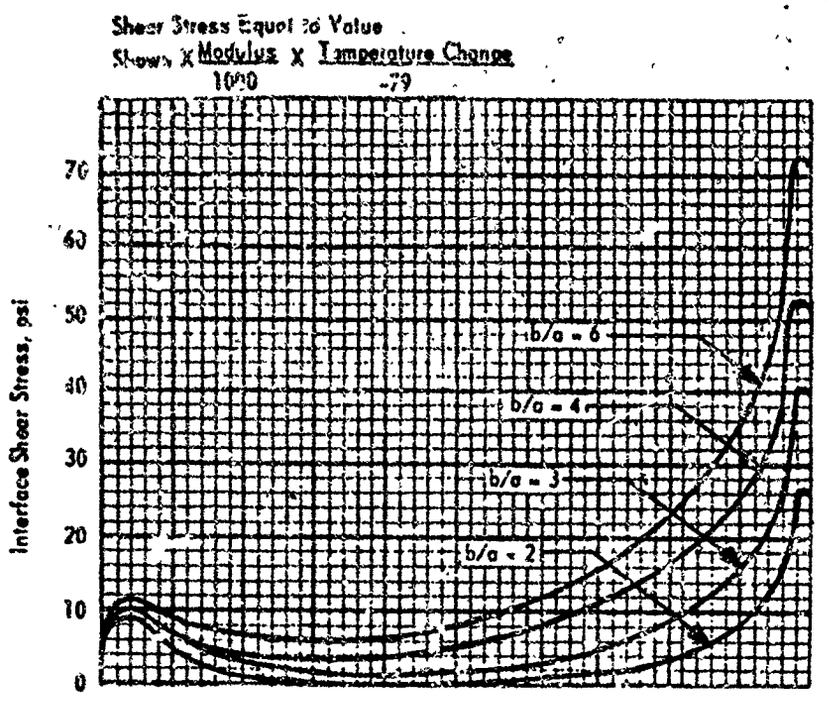

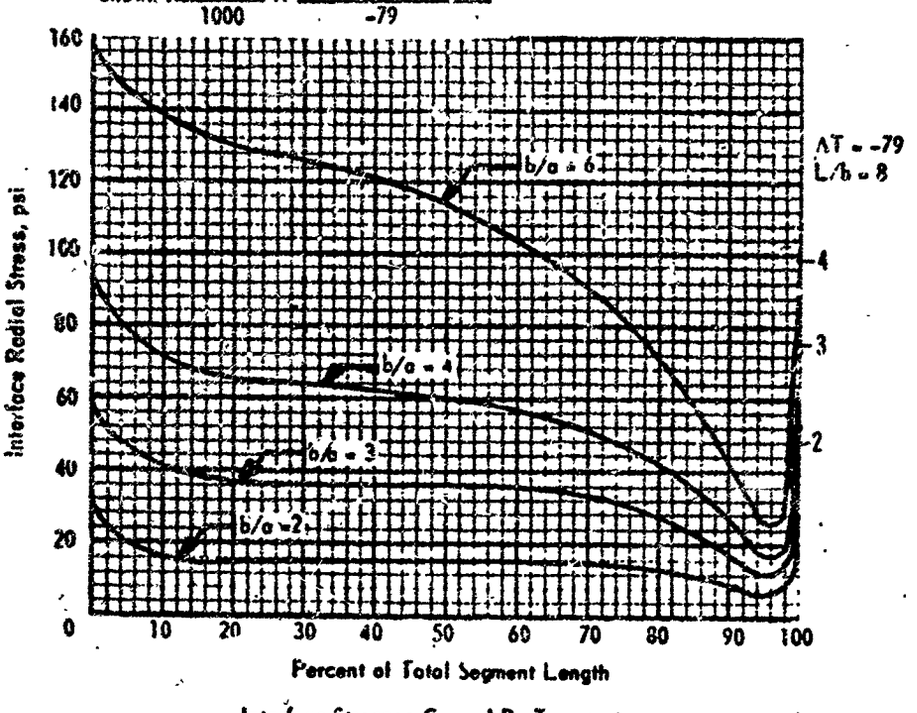

Interface Stresses Caused By Temperature Cycling – One End Bonded

Figure 40

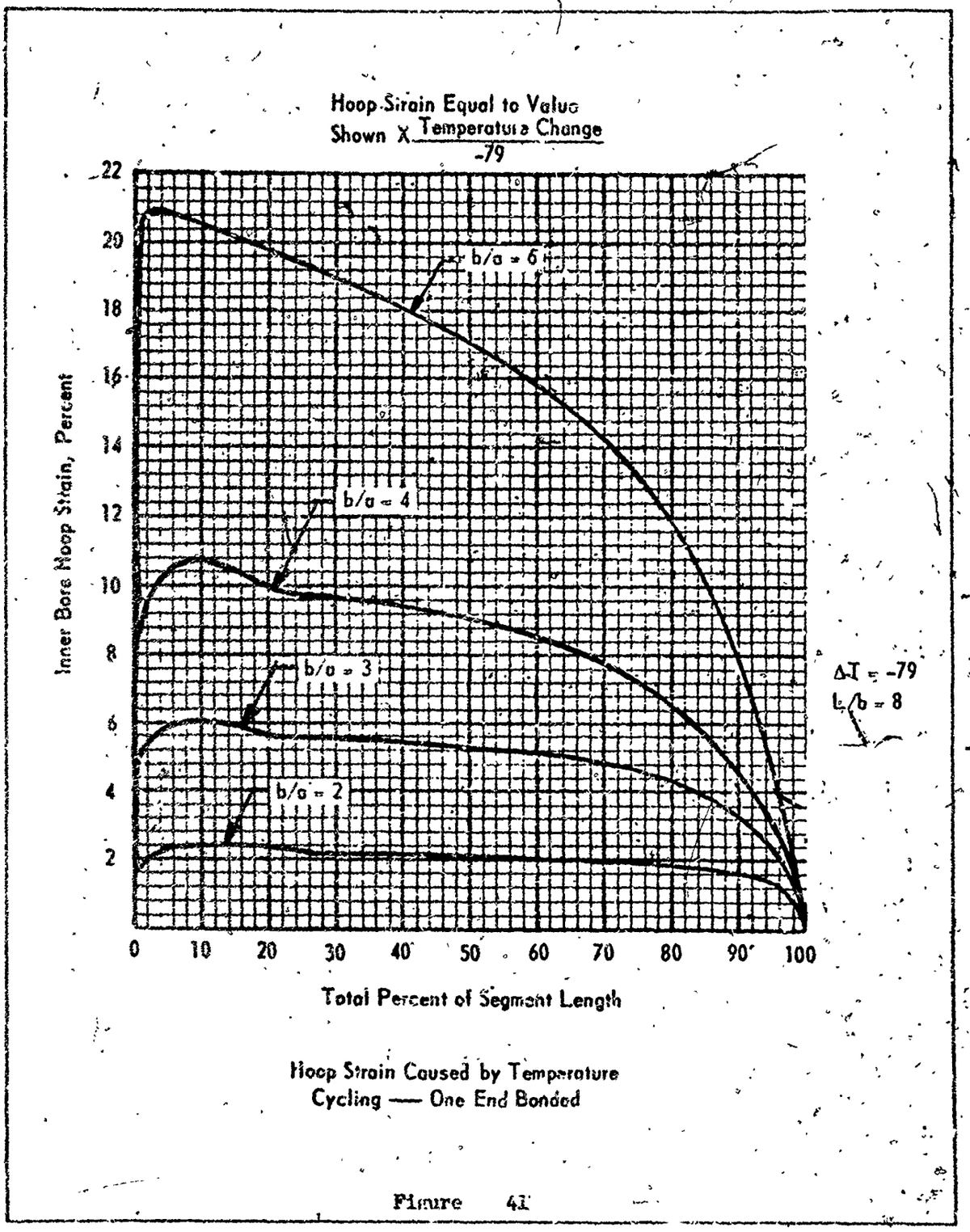

Hoop Strain Caused by Temperature Cycling — One End Bonded

Figure 41

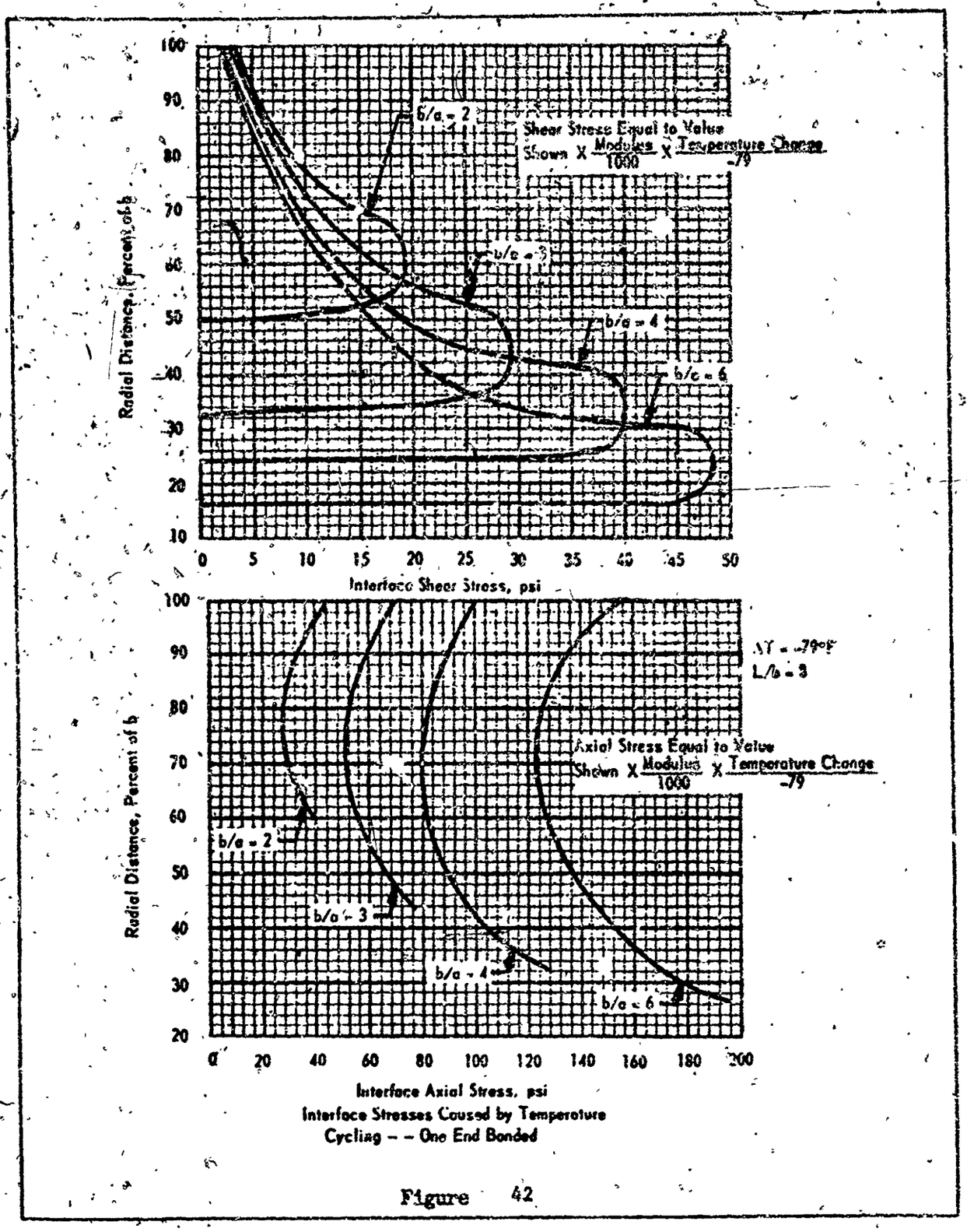

Figure 42

Interface Stresses Caused by Temperature Cycling -- One End Bonded

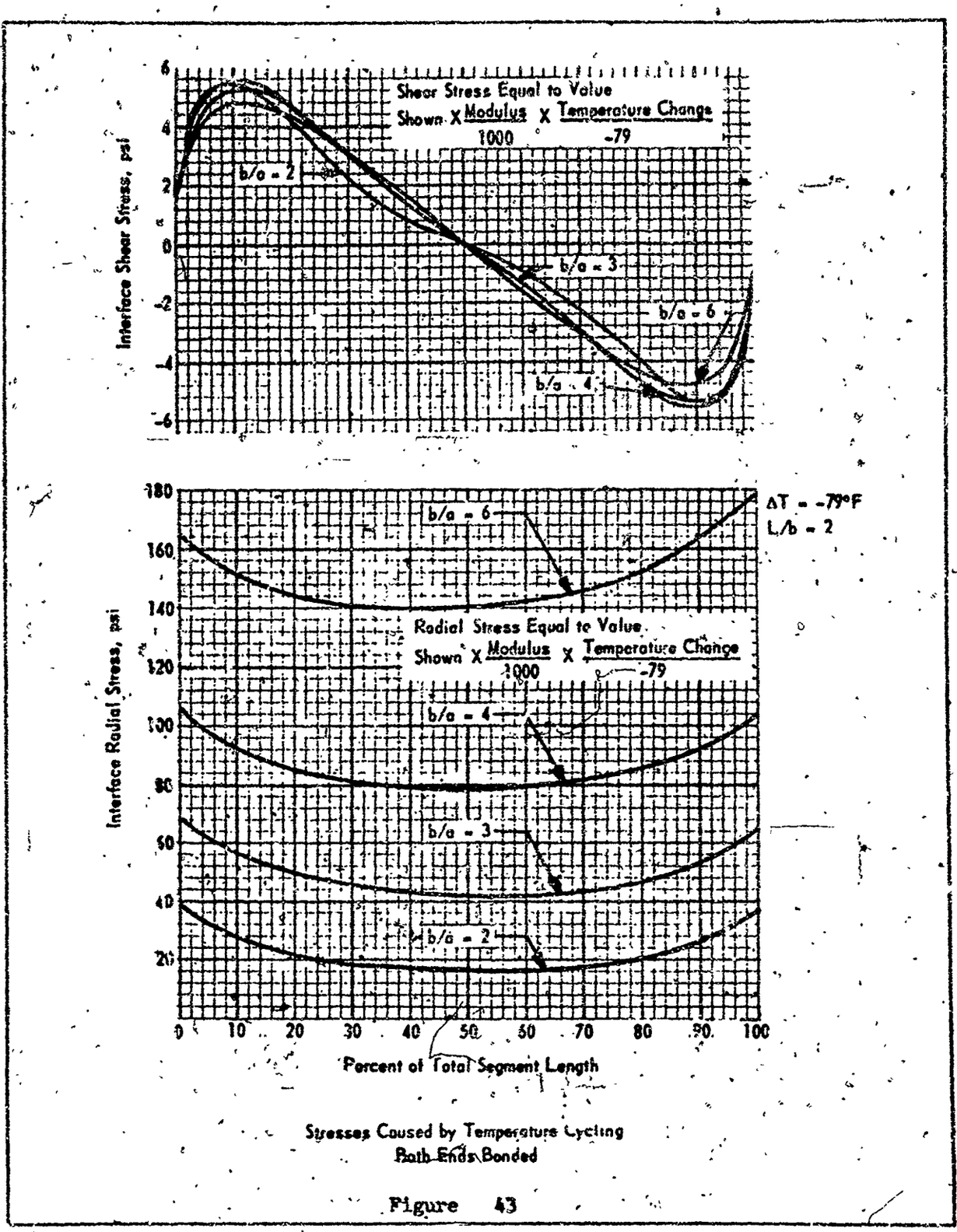

Stresses Caused by Temperature Cycling
Both Ends Bonded

Figure 43

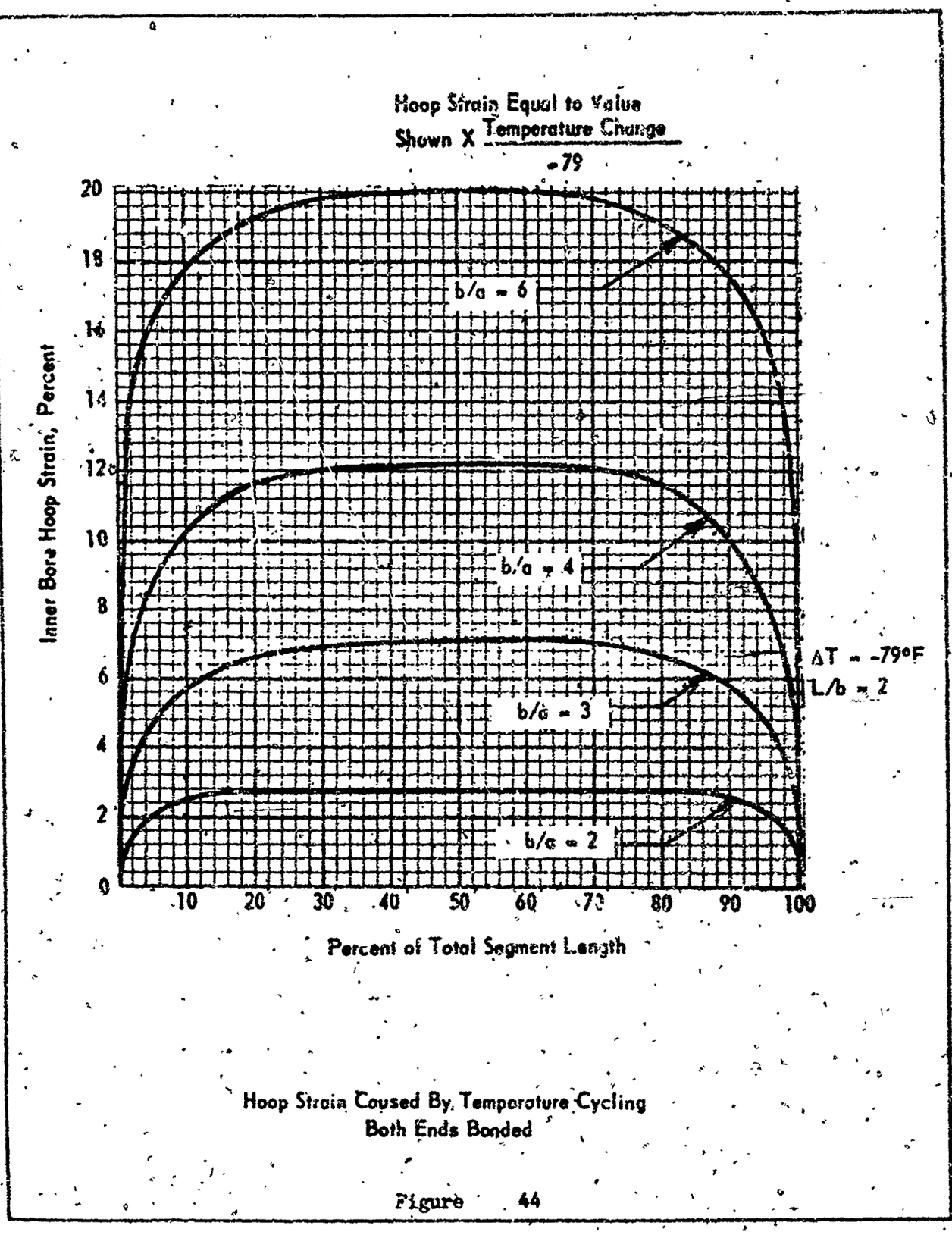

Hoop Strain Caused By Temperature Cycling
Both Ends Bonded

Figure 44

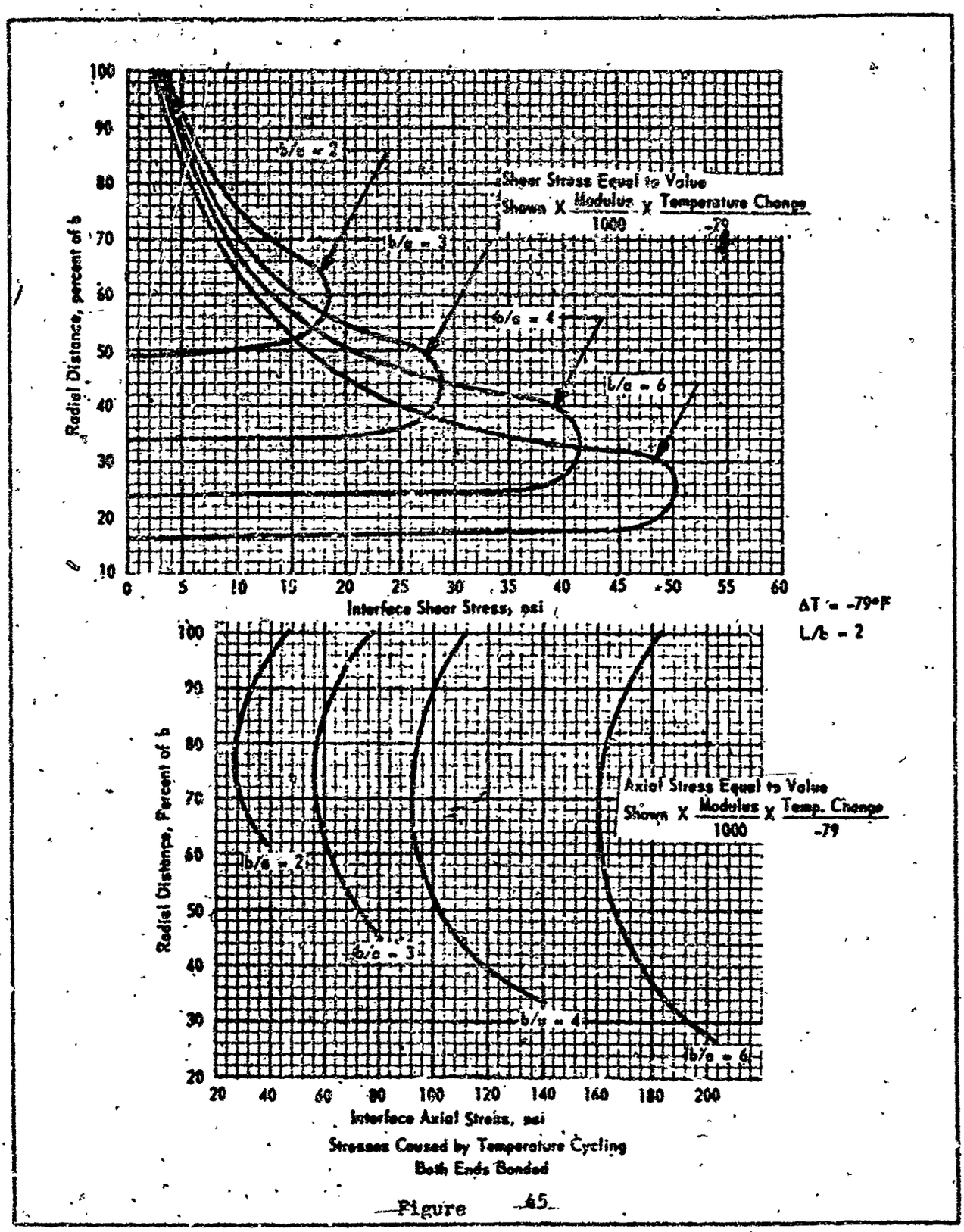
Radial Distance, percent of b
Interface Shear Stress, psi
Shear Stress Equal to Value Shown X Modulus / 1000 X Temperature Change / -79
b/a = 2
b/a = 3
b/a = 4
b/a = 6
ΔT = -79°F
L/b = 2
Radial Distance, Percent of b
Interface Axial Stress, psi
Axial Stress Equal to Value Shown X Modulus / 1000 X Temp. Change / -79
b/a = 2
b/a = 3
b/a = 4
b/a = 6
Stresses Caused by Temperature Cycling
Both Ends Bonded

Figure 45

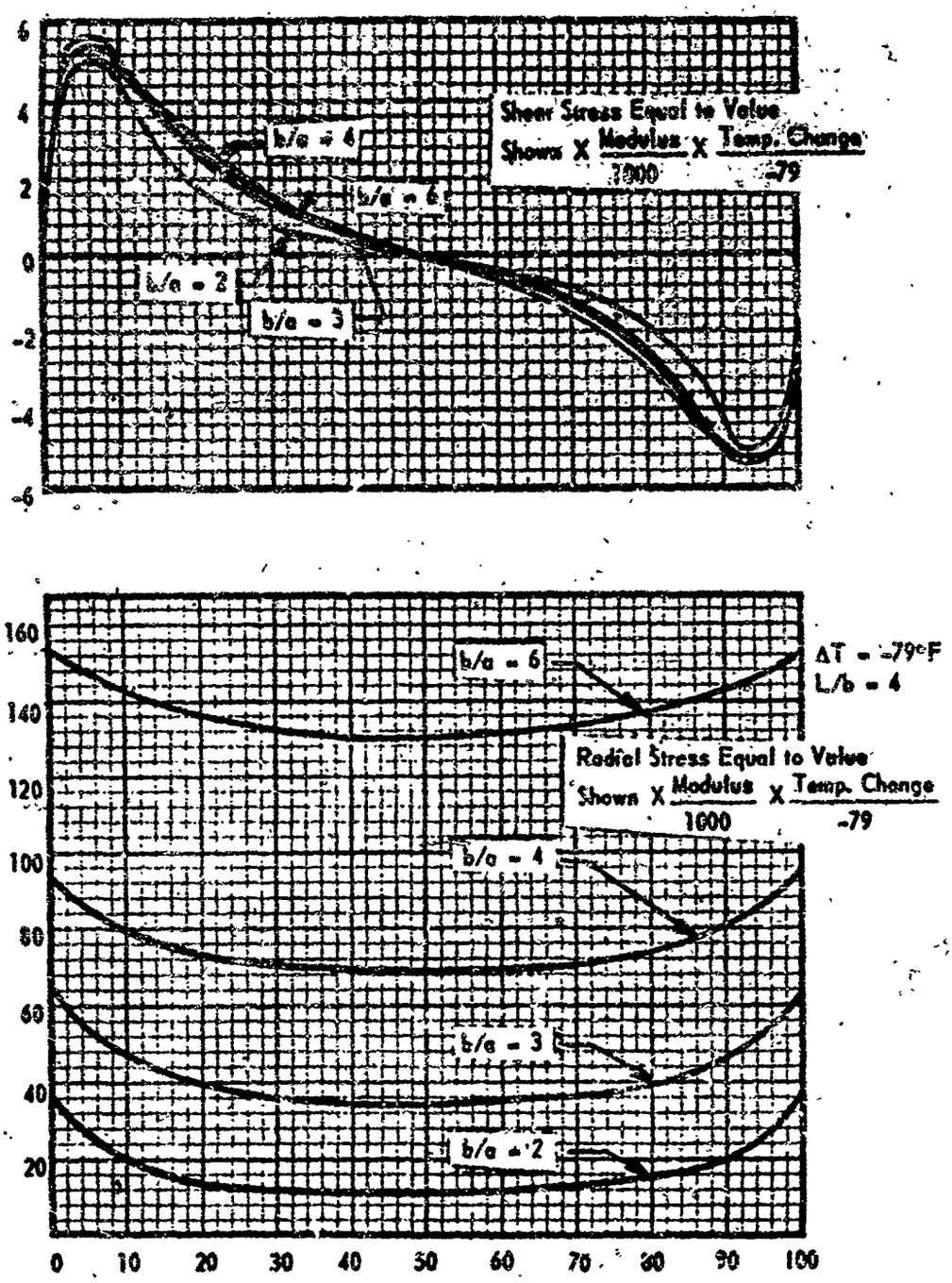

Stresses Caused by Temperature Cycling
Both Ends Bonded

Figure 46

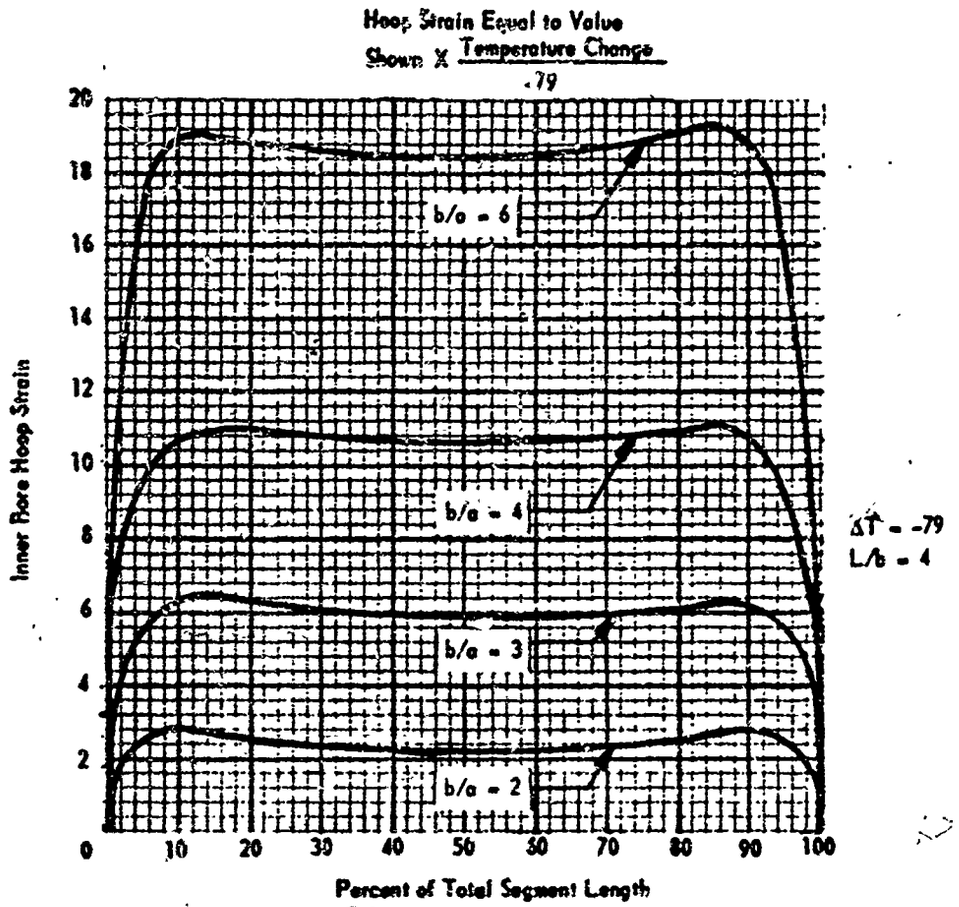

Hoop Strain Caused by Temperature Cycling
Both Ends Bonded

Figure 47

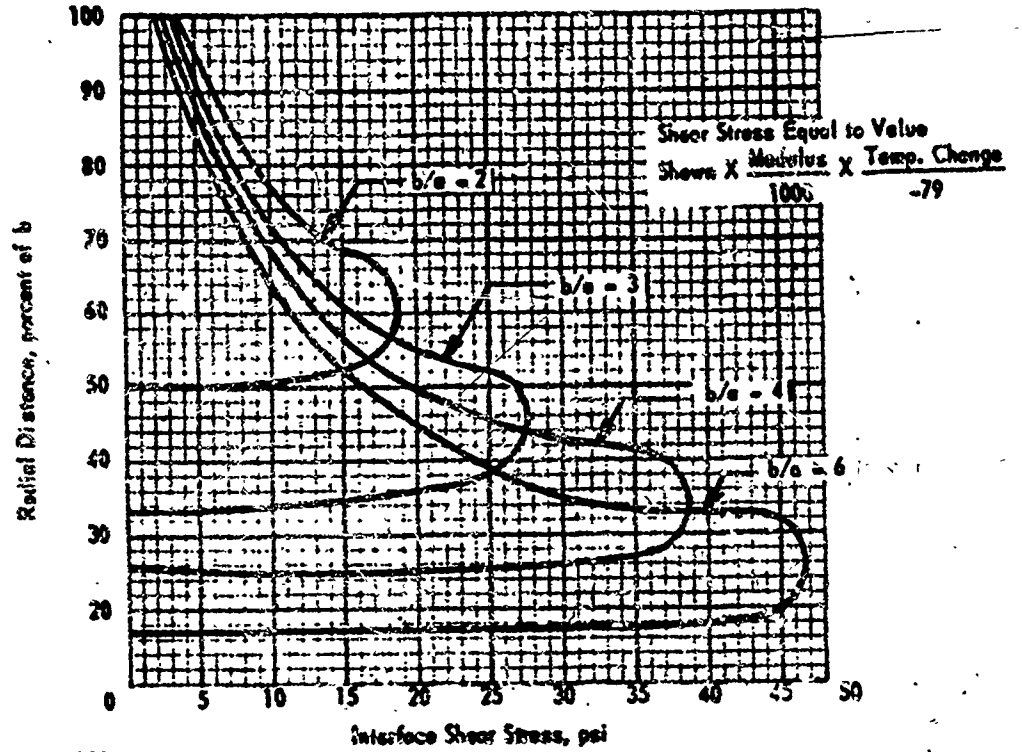

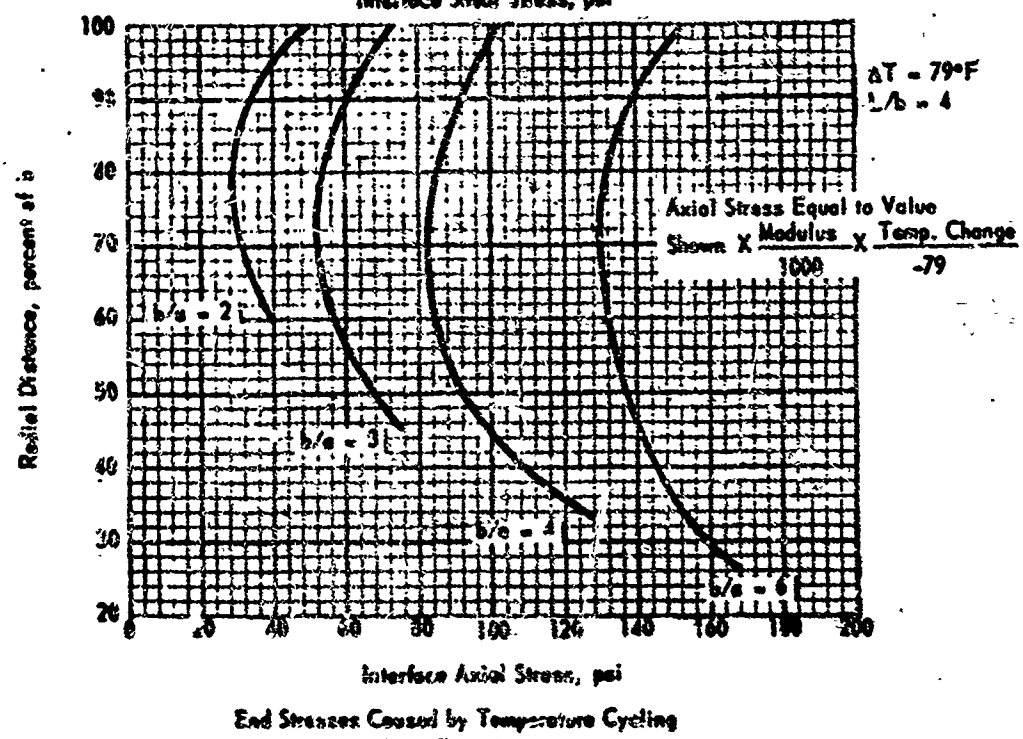

End Stresses Caused by Temperature Cycling
Both Ends Bonded

Figure 48

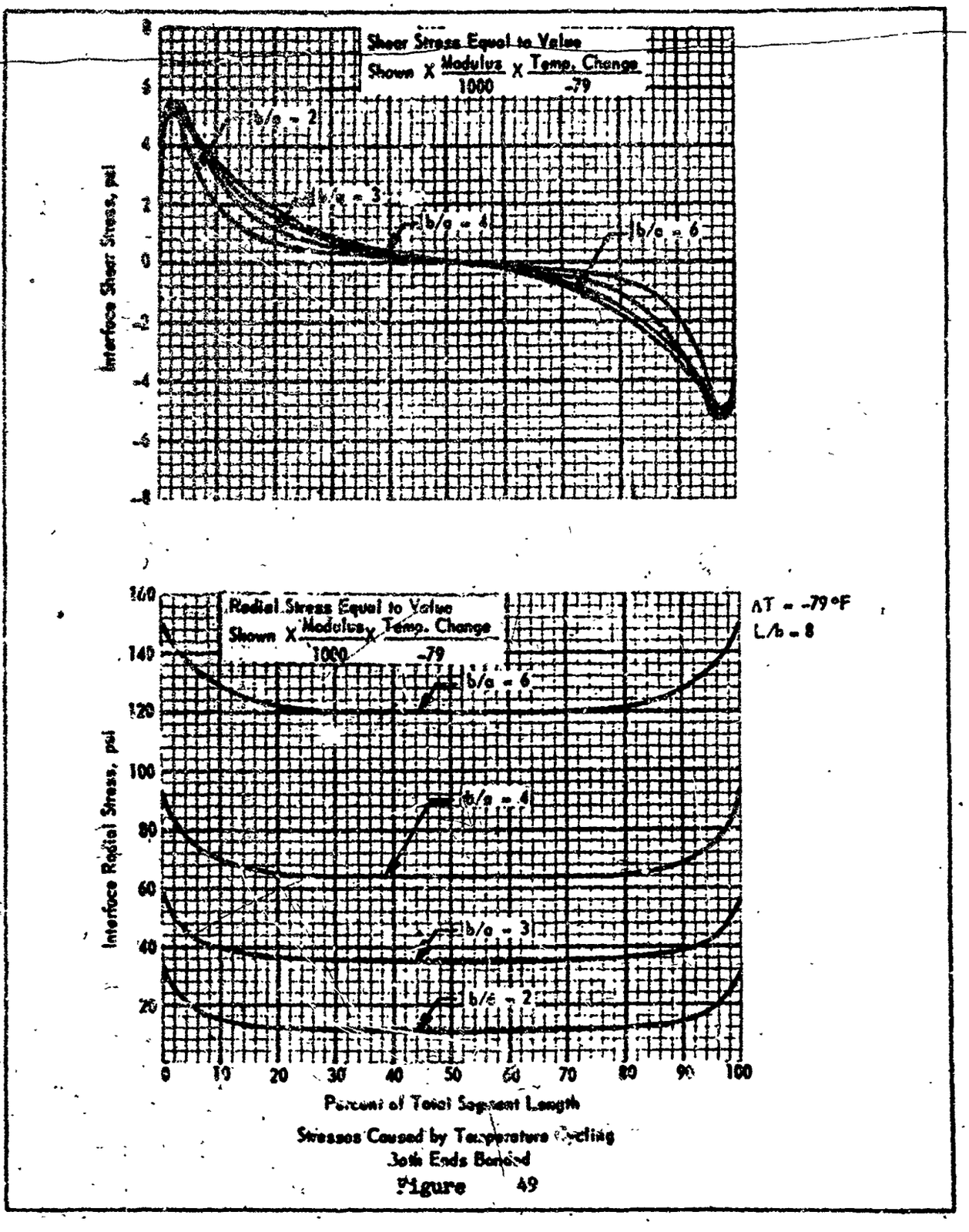

Stresses Caused by Temperature Cycling
Both Ends Bonded

Figure 49

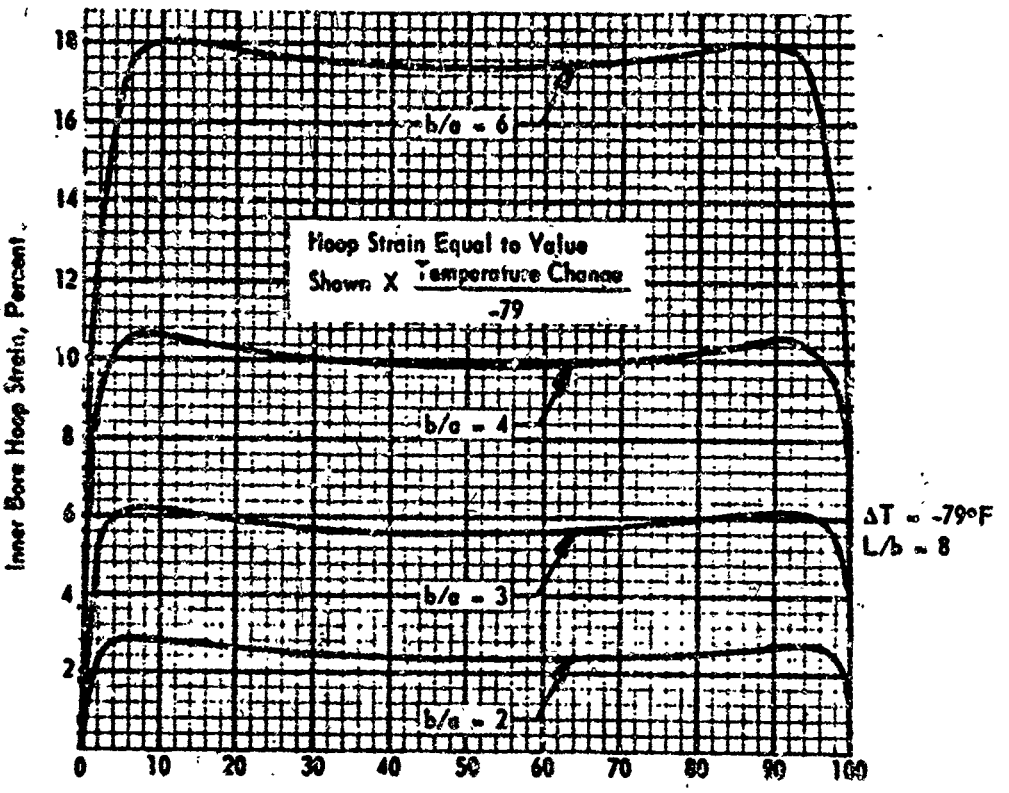

Hoop Strain Caused by Temperature Cycling
Both Ends Bonded

Figure 50

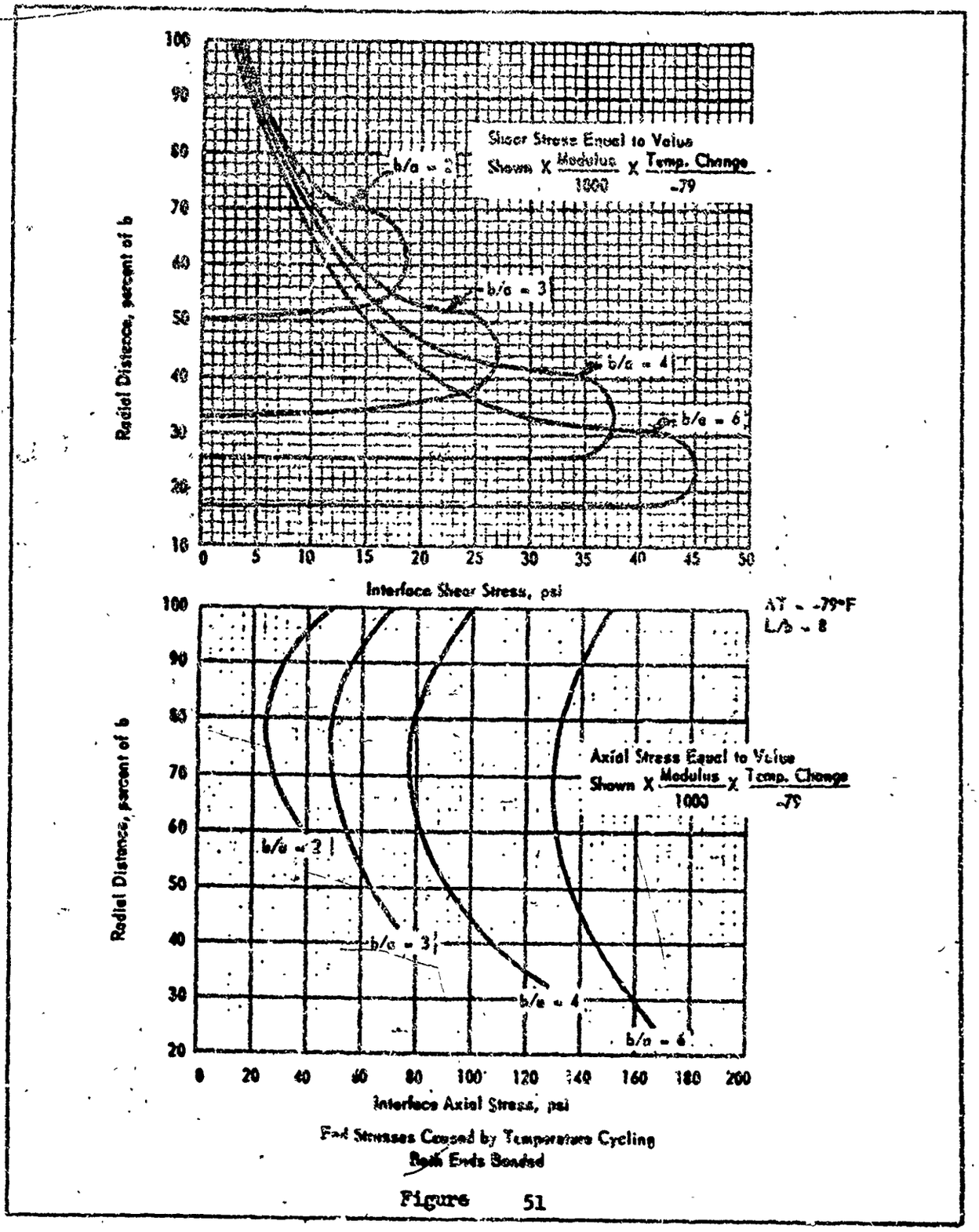

End Stresses Caused by Temperature Cycling
Both Ends Bonded

Figure 51

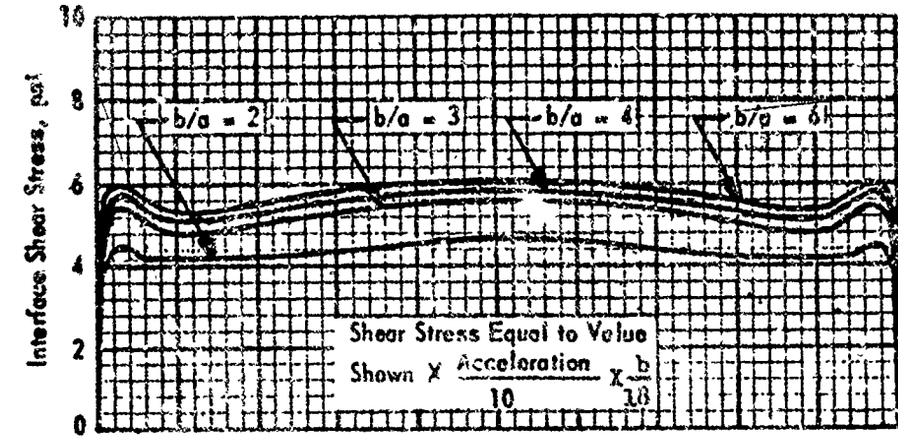

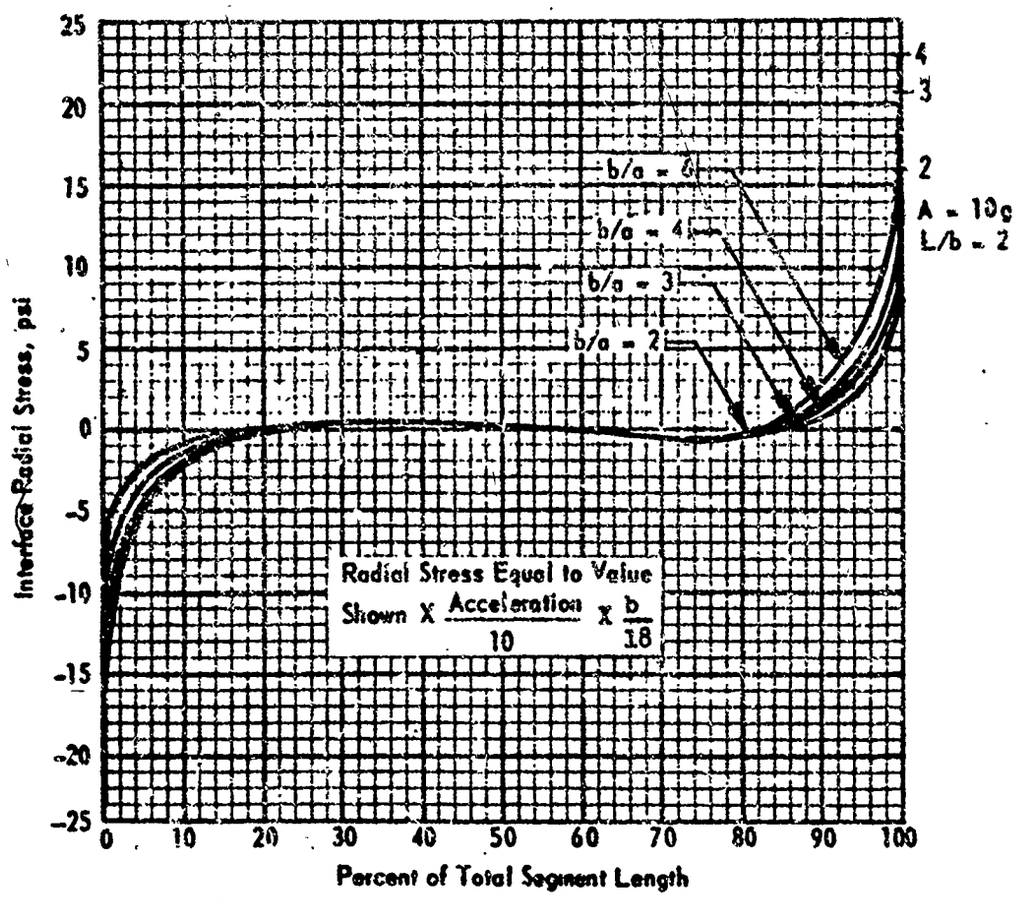

Stresses Caused by Axial Acceleration
No End Bonding

Figure 52

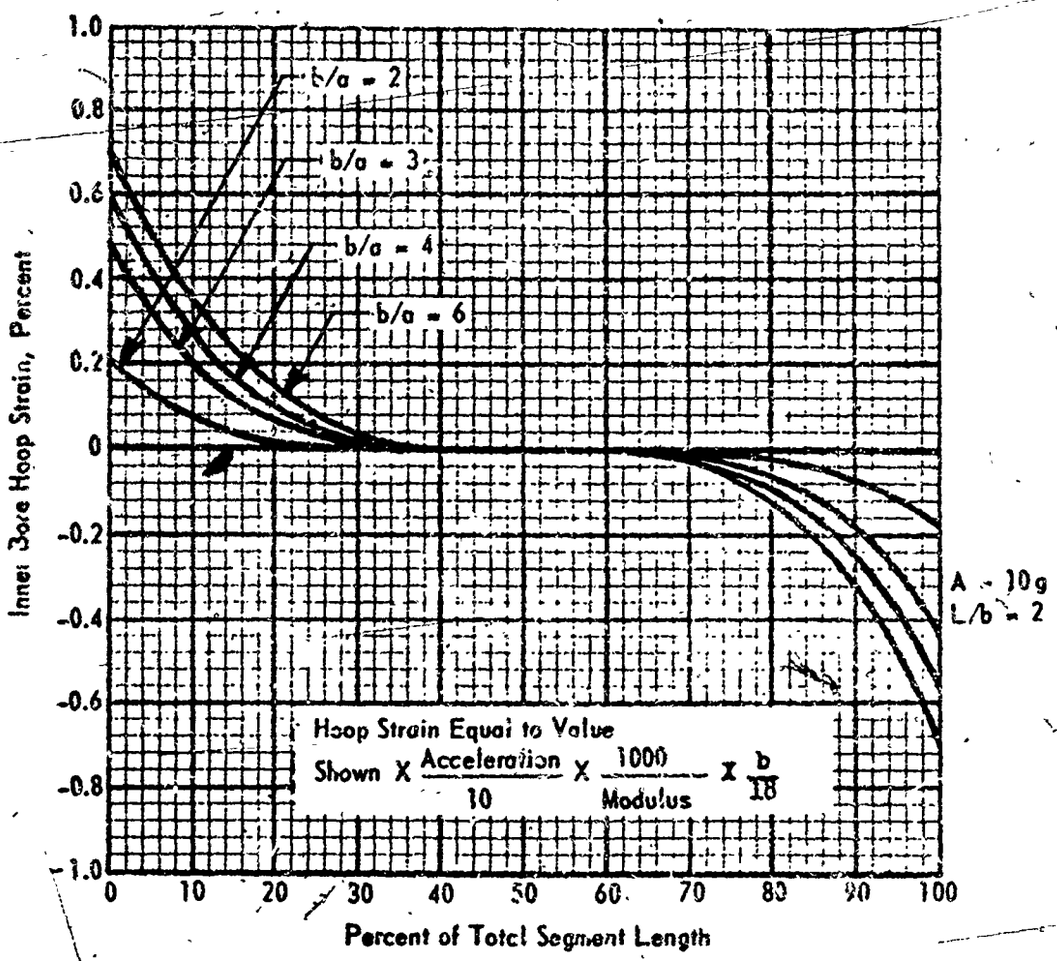
1.0
0.8
0.6
0.4
0.2
0
-0.2
-0.4
-0.6
-0.8
-1.0
b/a = 2
b/a = 3
b/a = 4
b/a = 6
Inner Bore Hoop Strain, Percent
A = 10g
L/b = 2
Hoop Strain Equal to Value Shown X Acceleration / 10 X 1000 / Modulus X b/18
0
10
20
30
40
50
60
70
80
90
100
Percent of Total Segment Length

Figure 53

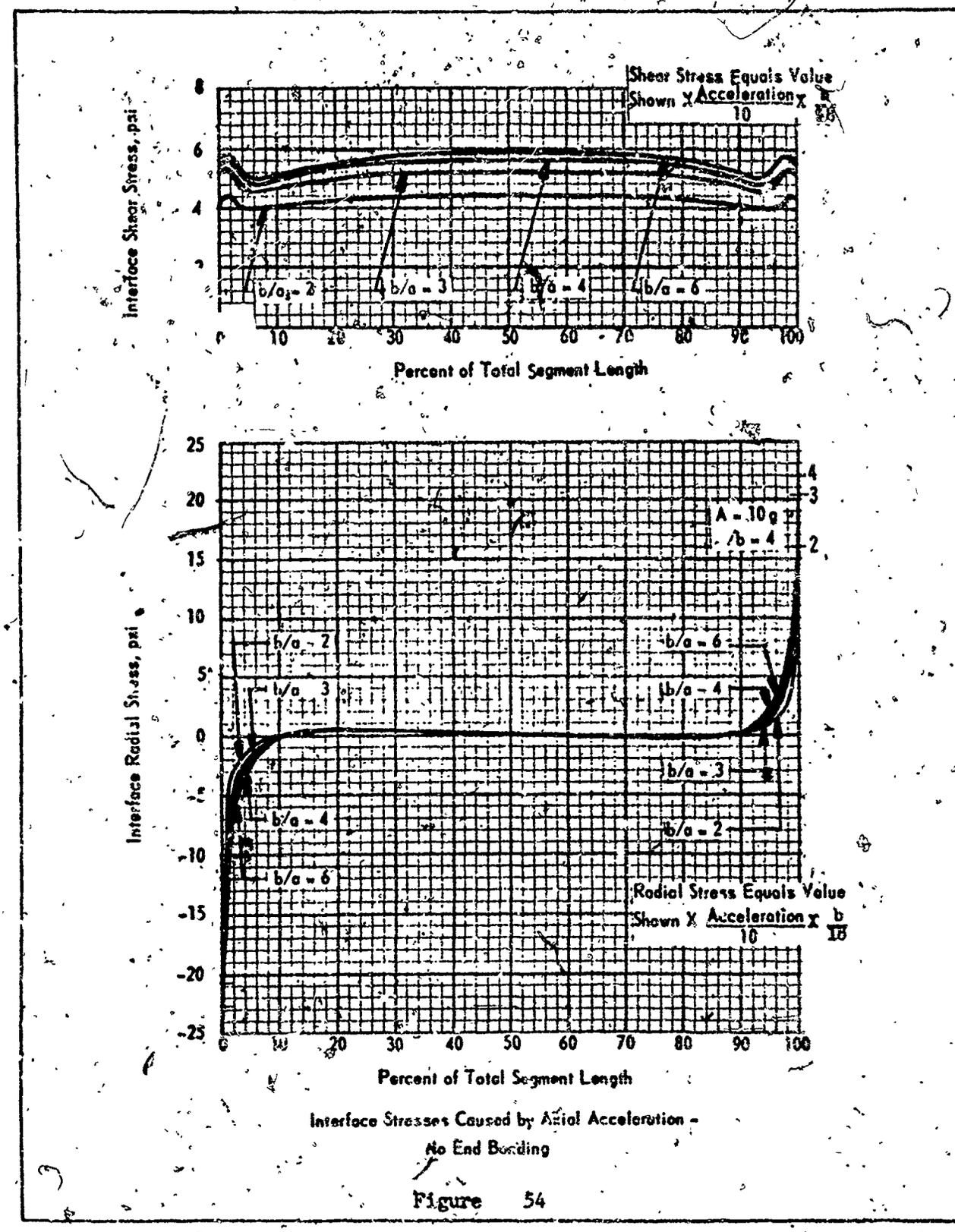

Interface Stresses Caused by Axial Acceleration - No End Bonding

Figure 54

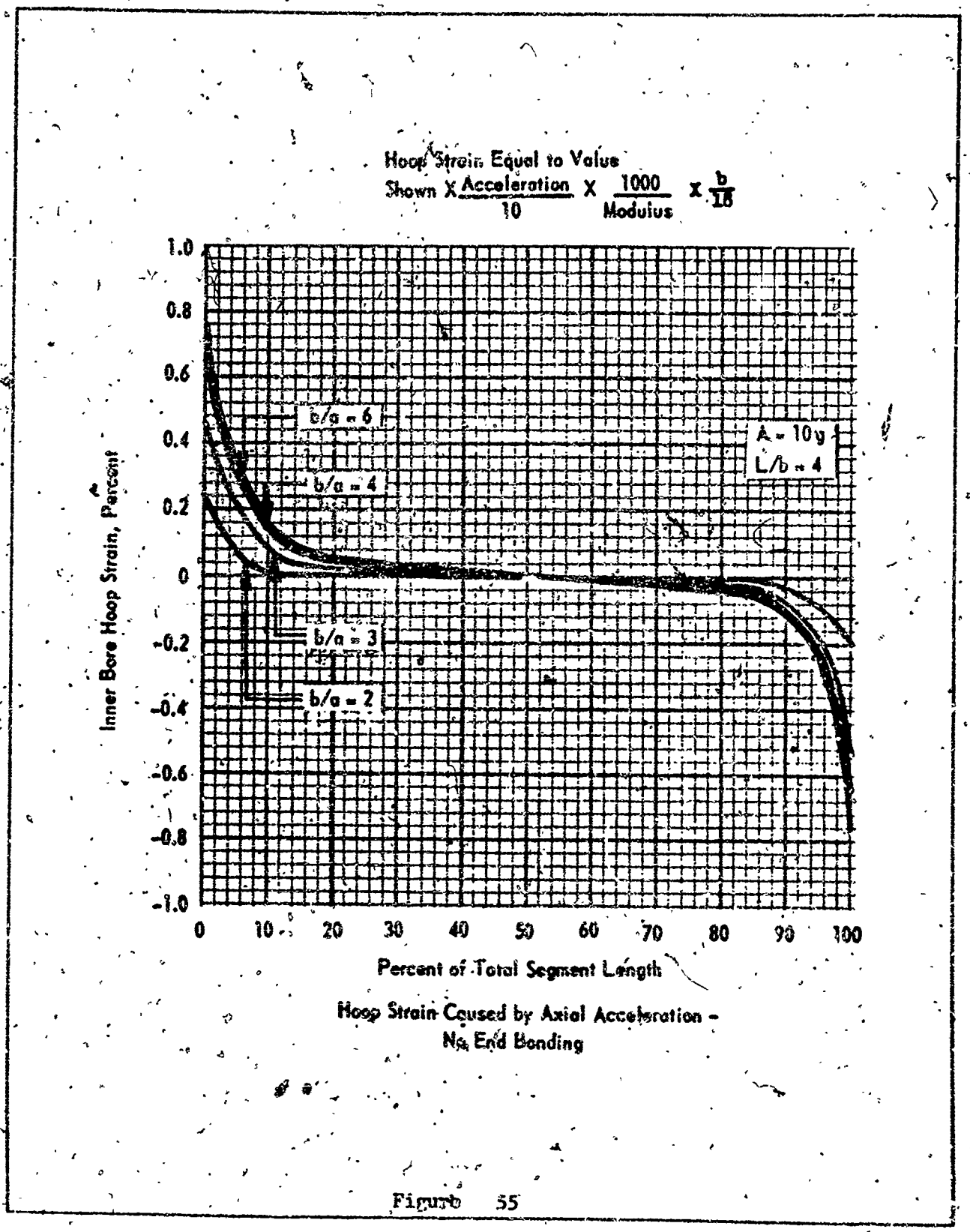
Hoop Strain Equal to Value Shown X Acceleration/10 X 1000/Modulus X b/18
Inner Bore Hoop Strain, Percent
1.0
0.8
0.6
0.4
0.2
0
-0.2
-0.4
-0.6
-0.8
-1.0
b/a = 6
b/a = 4
b/a = 3
b/a = 2
A = 10g
L/b = 4
0
10
20
30
40
50
60
70
80
90
100
Percent of Total Segment Length
Hoop Strain Caused by Axial Acceleration - No End Bonding

Figure 55

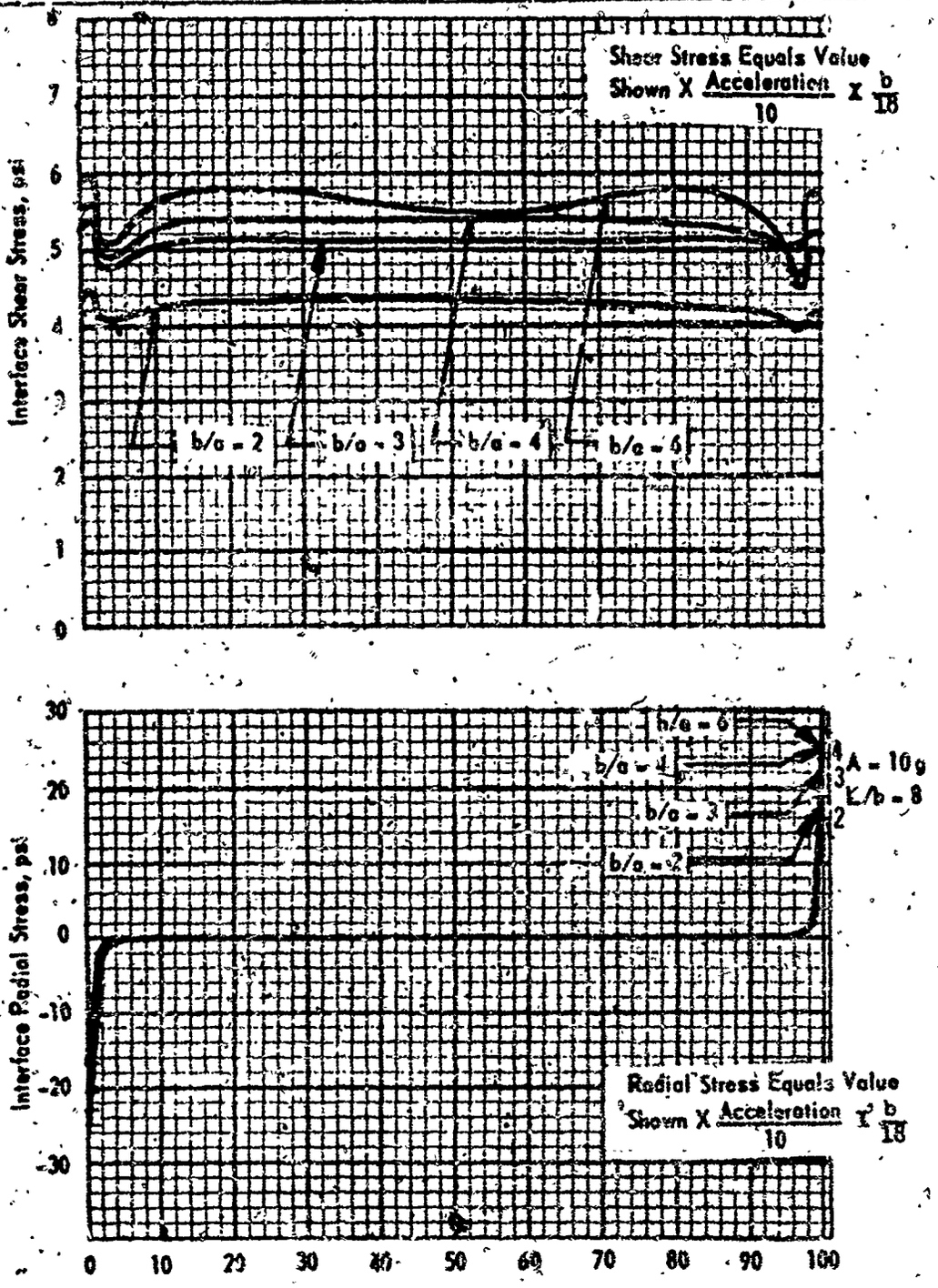

Interface Stresses Caused by Axial Acceleration - One End Bonded

Figure 36

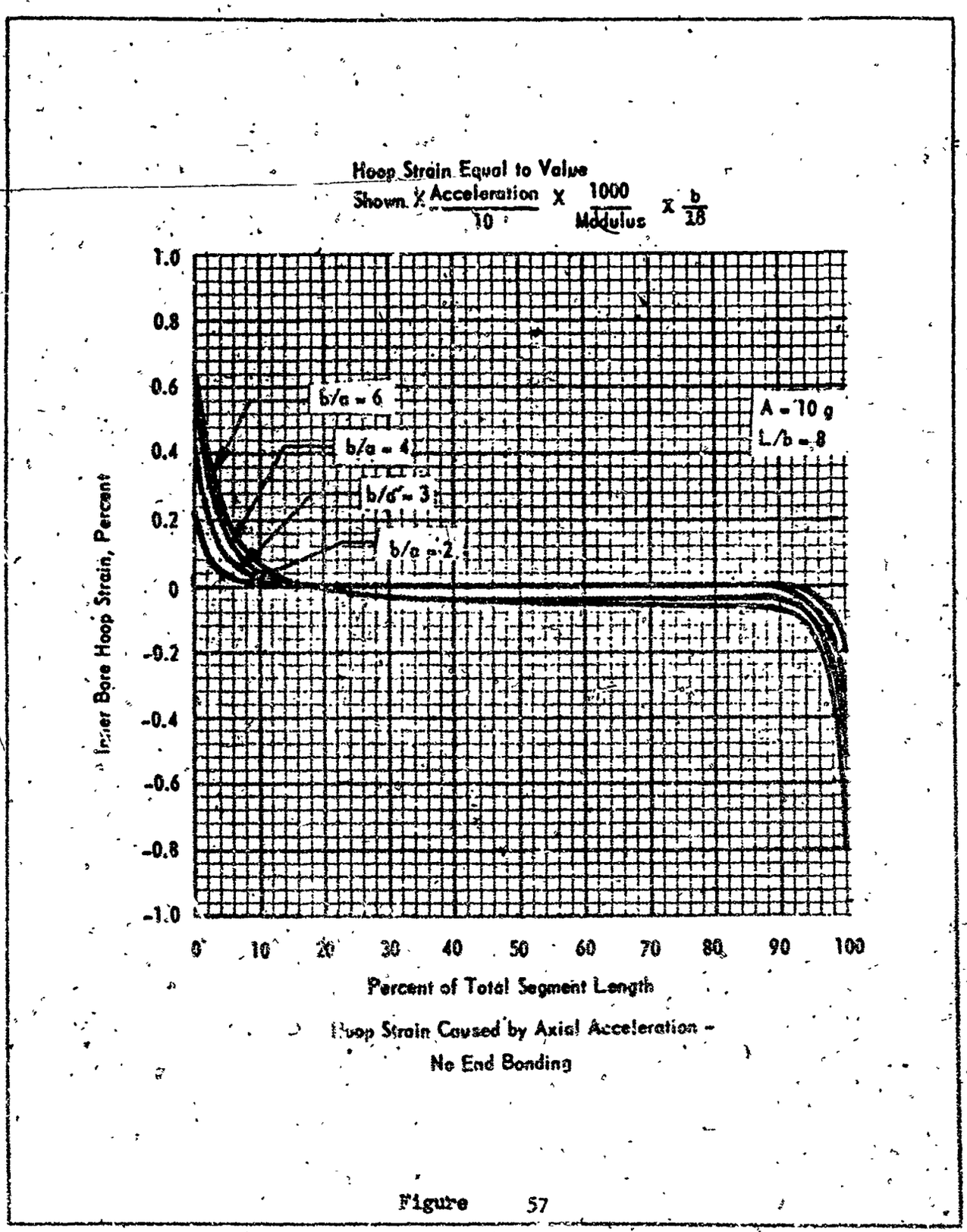
Hoop Strain Equal to Value Shown X Acceleration / 10 X 1000 / Modulus X b/18
1.0
0.8
0.6
0.4
0.2
0
-0.2
-0.4
-0.6
-0.8
-1.0
Inner Bore Hoop Strain, Percent
b/a = 6
b/a = 4
b/a = 3
b/a = 2
A = 10 g
L/b = 8
0
10
20
30
40
50
60
70
80
90
100
Percent of Total Segment Length
Hoop Strain Caused by Axial Acceleration - No End Bonding

Figure 57

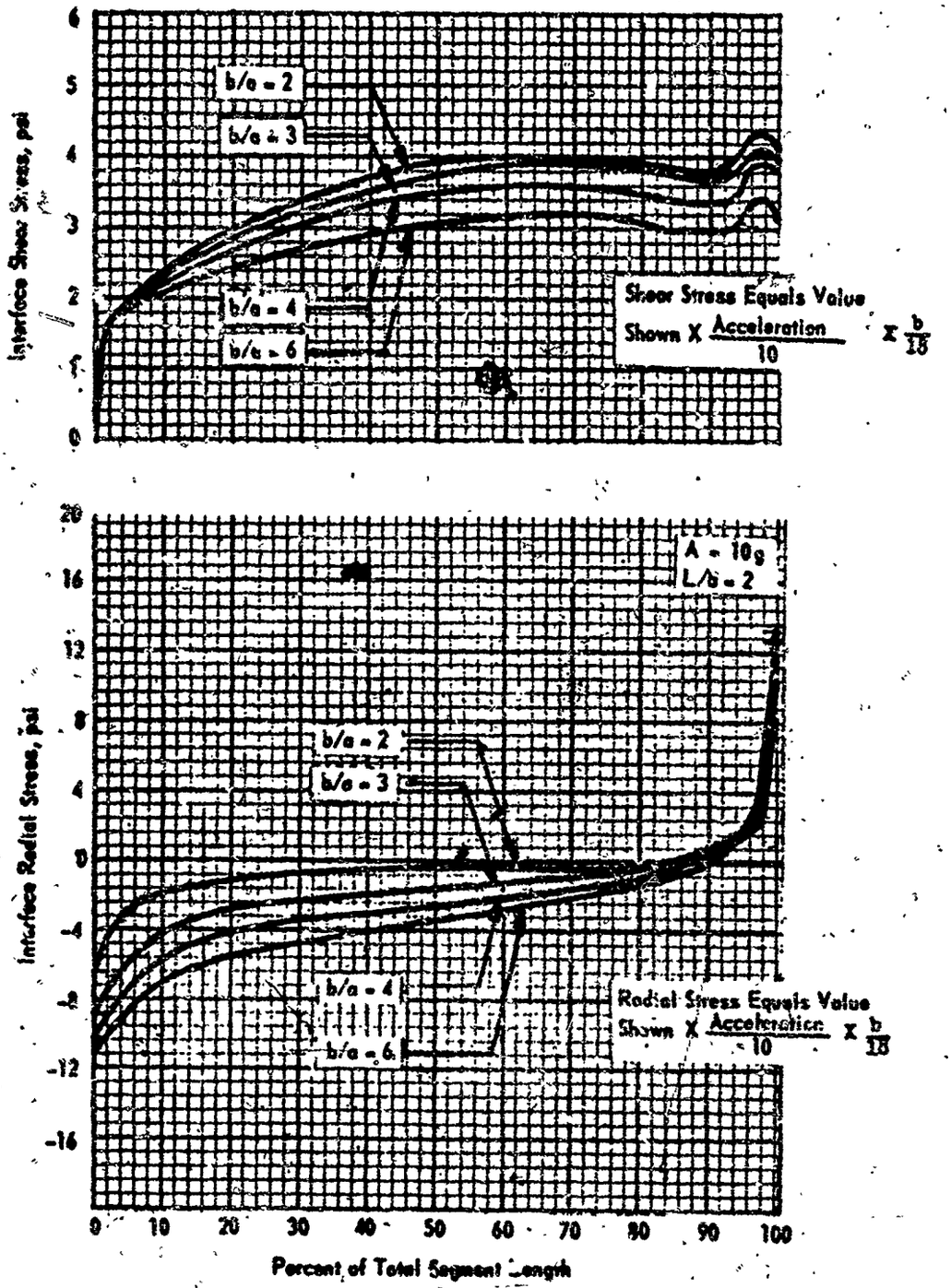

Interface Stresses Caused by Axial Acceleration -
One End Bonded

Figure 58

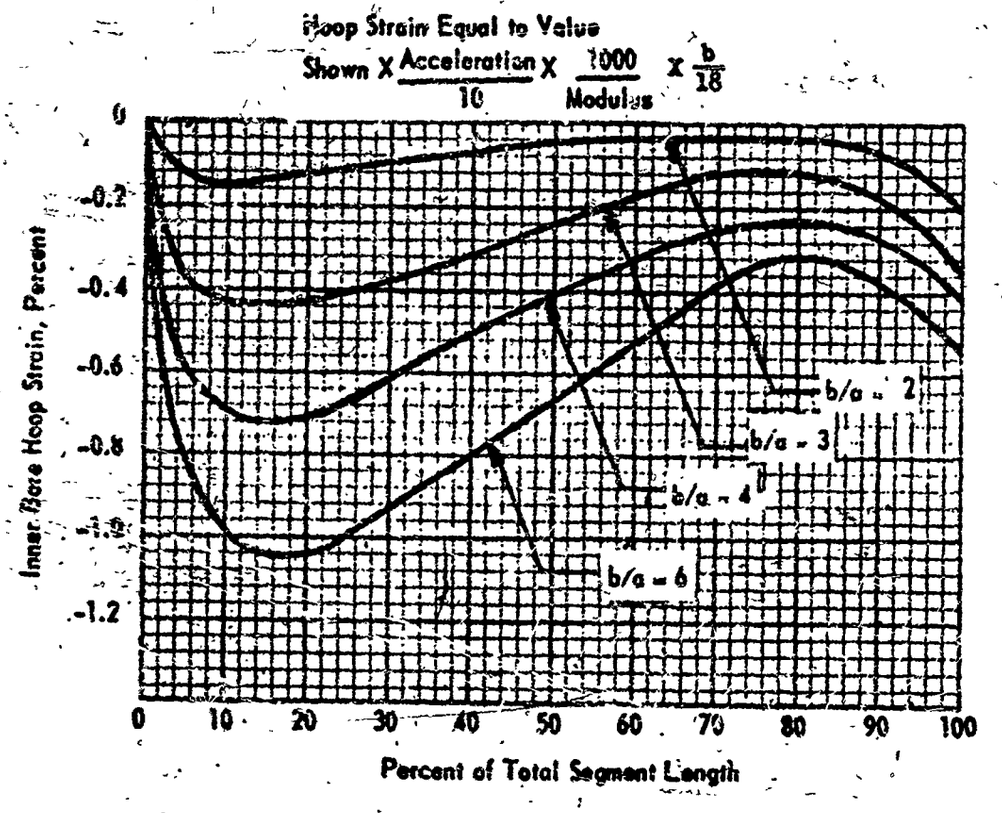

Hoop Strain Caused by Axial Acceleration –
One End Bonded

Figure 59

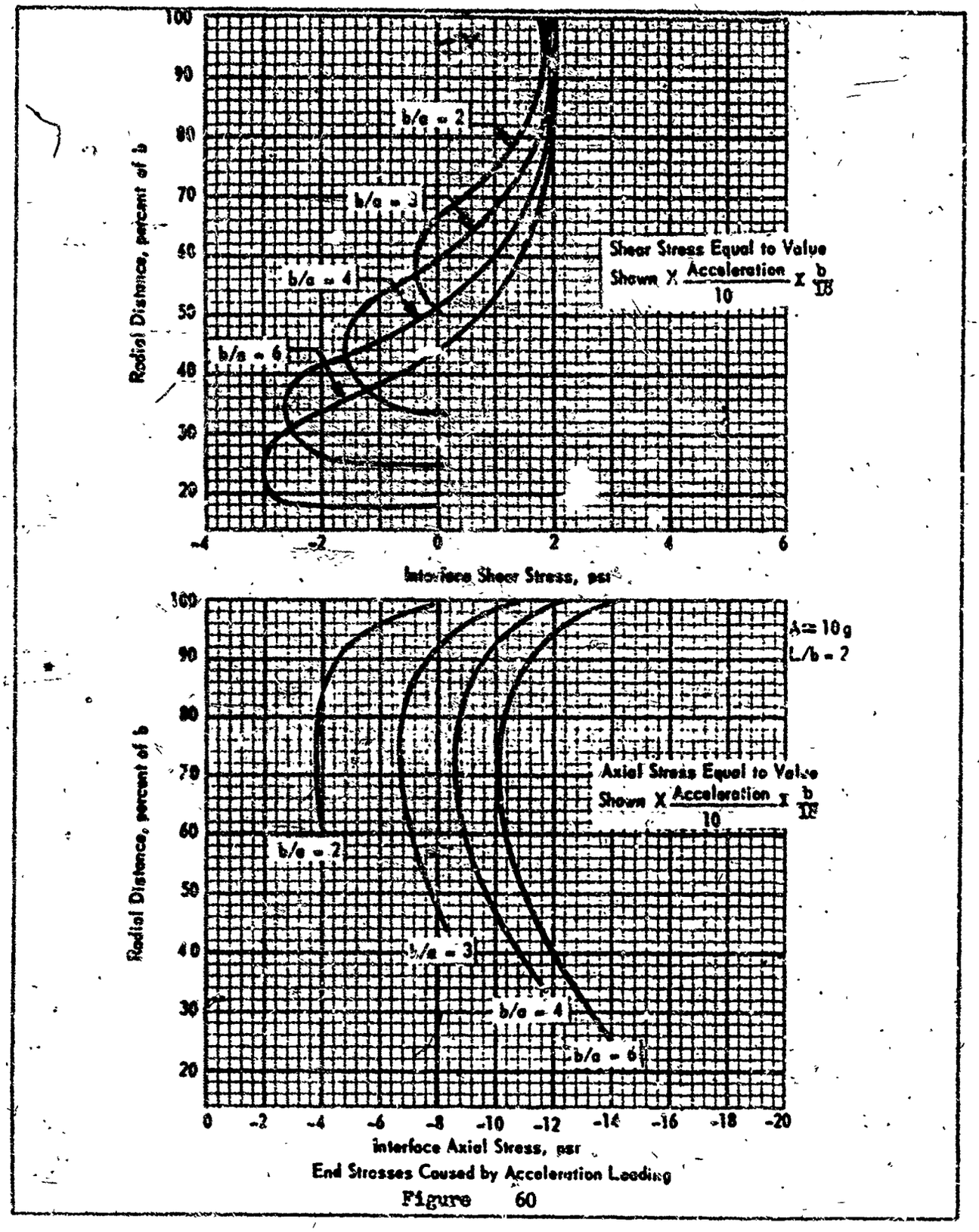
Radial Distance, percent of b
b/a = 2
b/a = 3
b/a = 4
b/a = 6
Shear Stress Equal to Value Shown X Acceleration / 10 X b/18
Interface Shear Stress, psi
A = 10 g
L/b = 2
Axial Stress Equal to Value Shown X Acceleration / 10 X b/18
Interface Axial Stress, psi
End Stresses Caused by Acceleration Loading

Figure 60

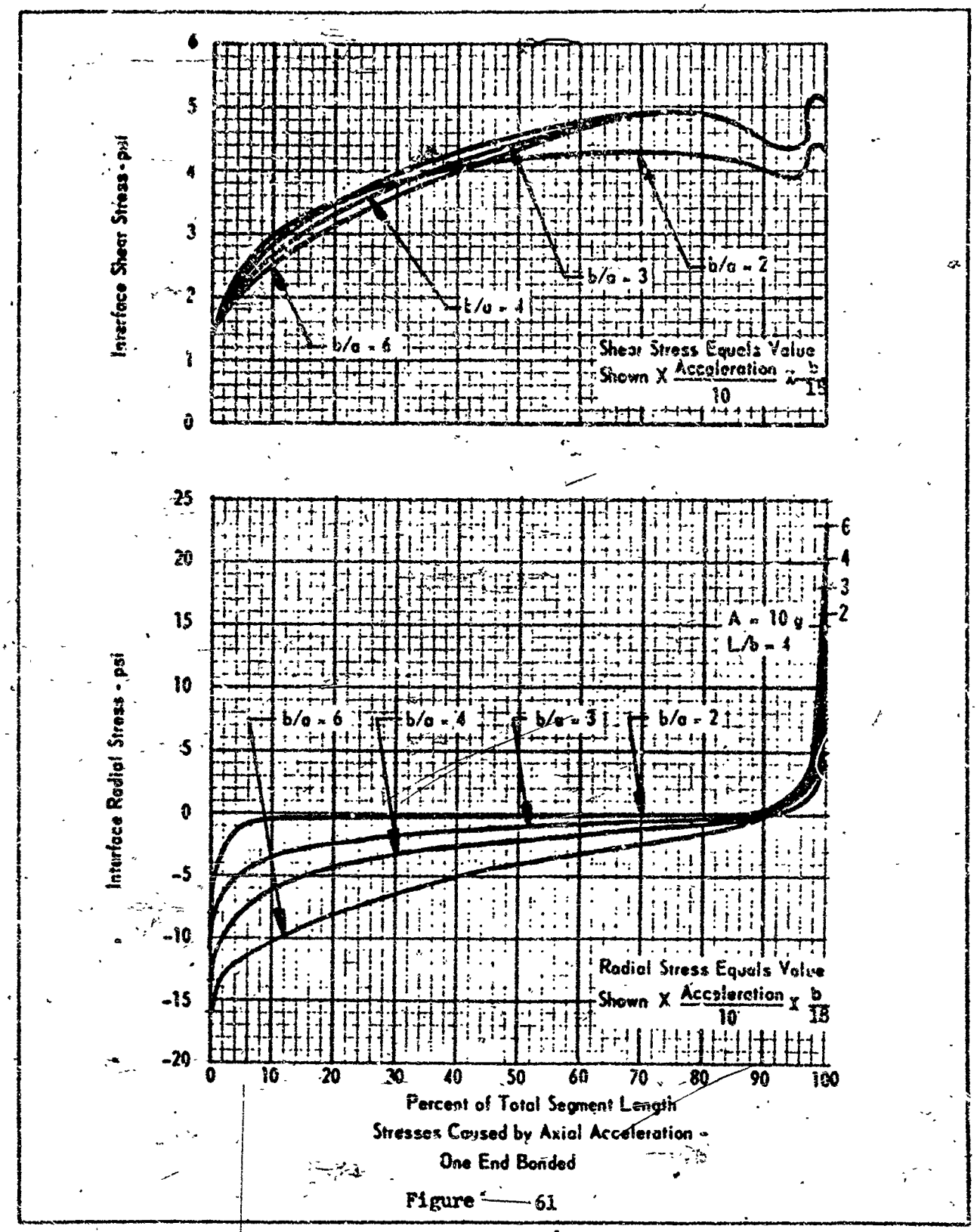

Stresses Caused by Axial Acceleration - One End Bonded

Figure 61

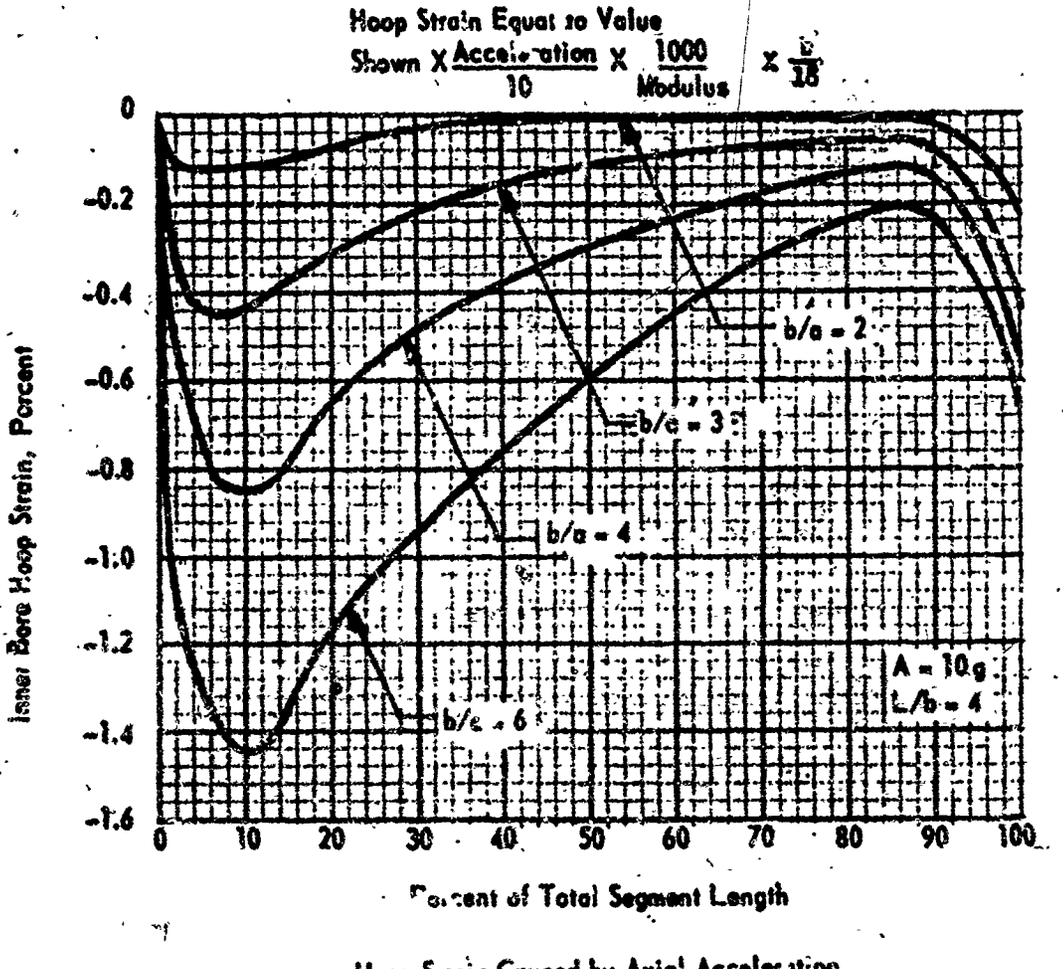

Hoop Strain Caused by Axial Acceleration
One End Bonded

Figure 62

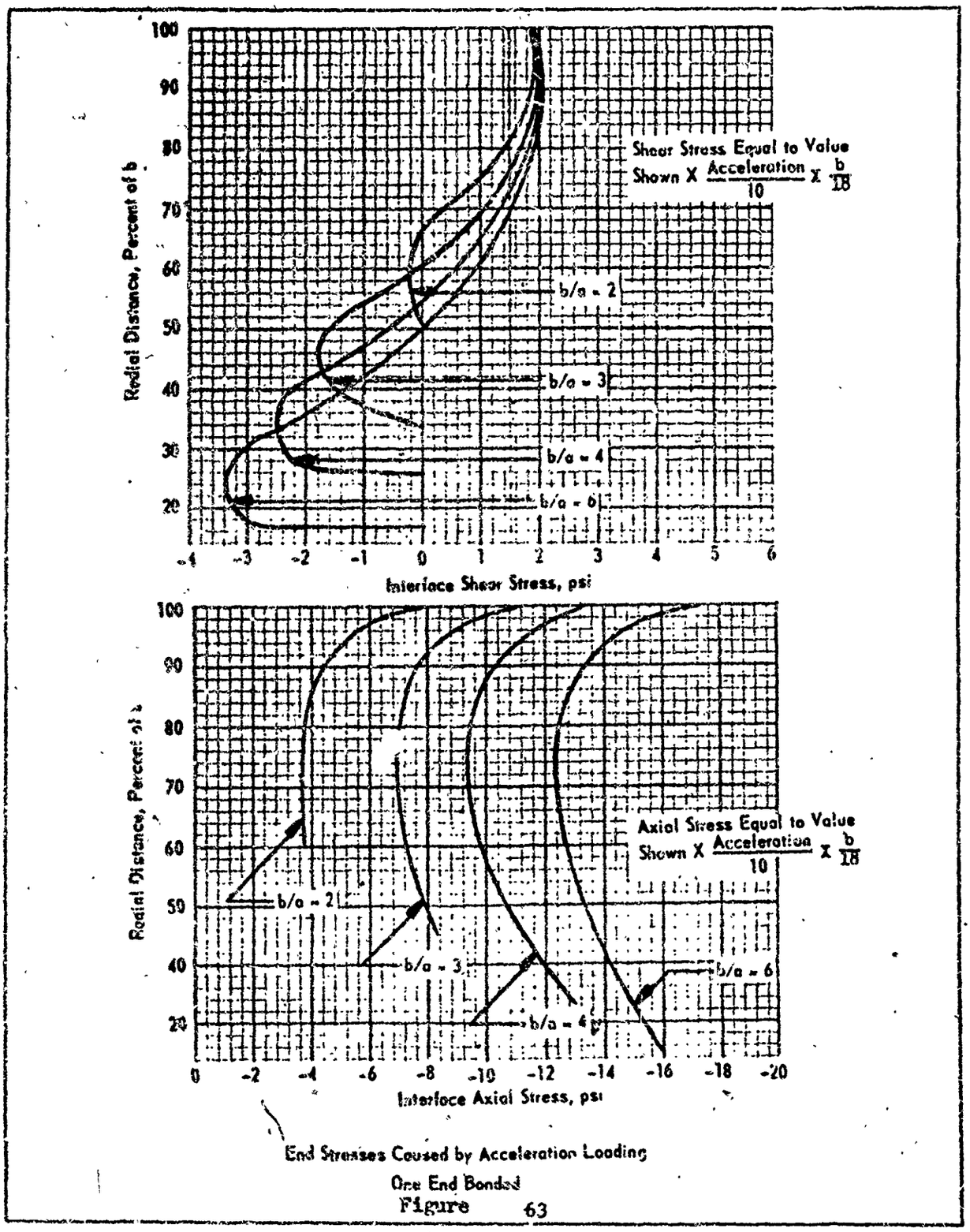

End Stresses Caused by Acceleration Loading

One End Bonded

Figure 63

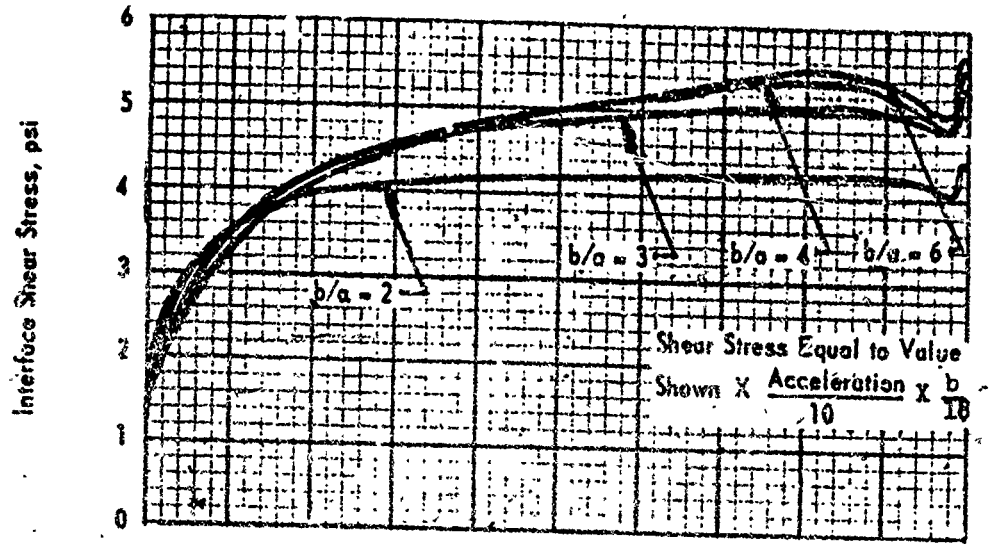

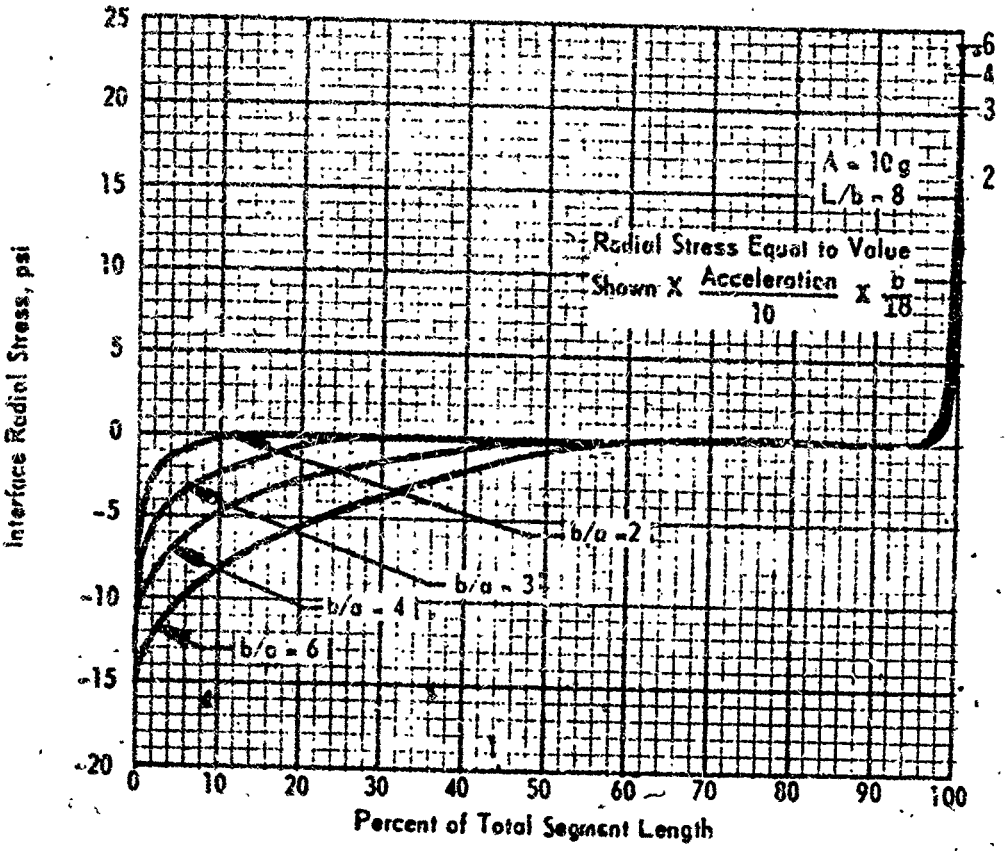

Stresses Caused by Axial Acceration –
One End Bonded

Figure 64

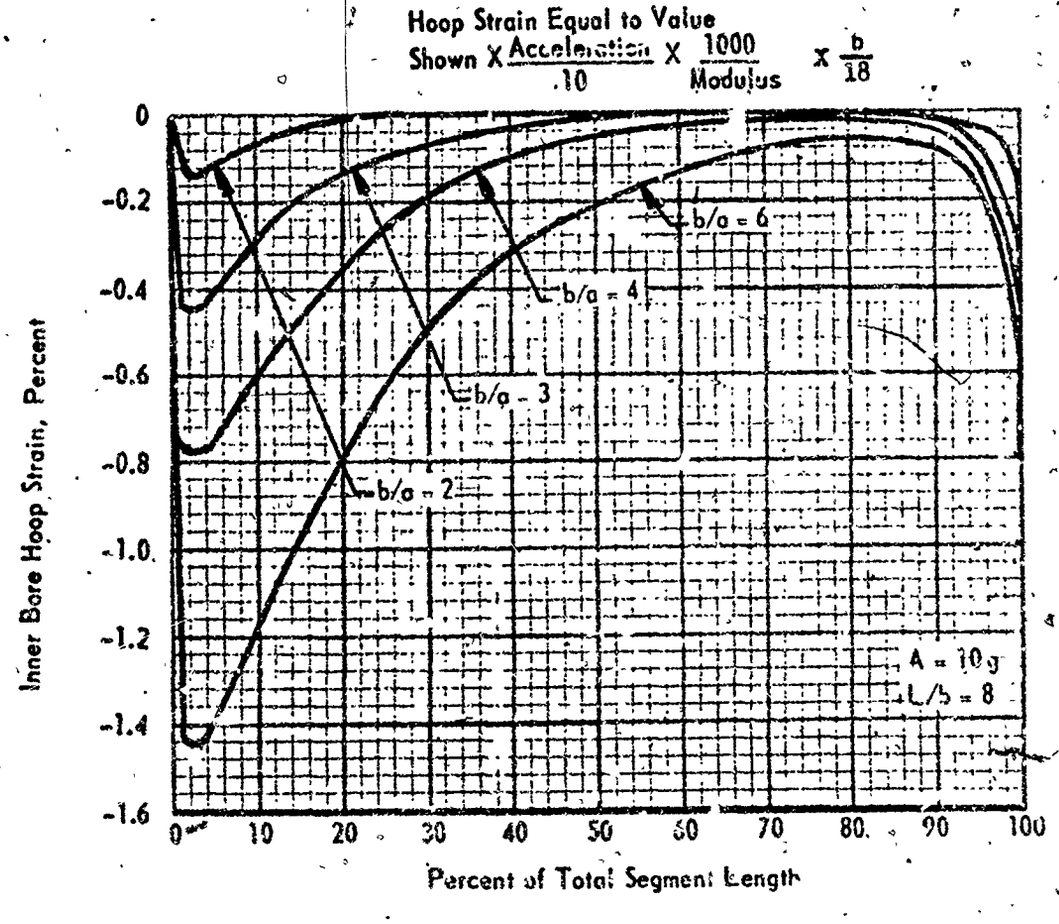

Hoop Strain Caused by Axial Acceleration - One End Bonded

Figure 55

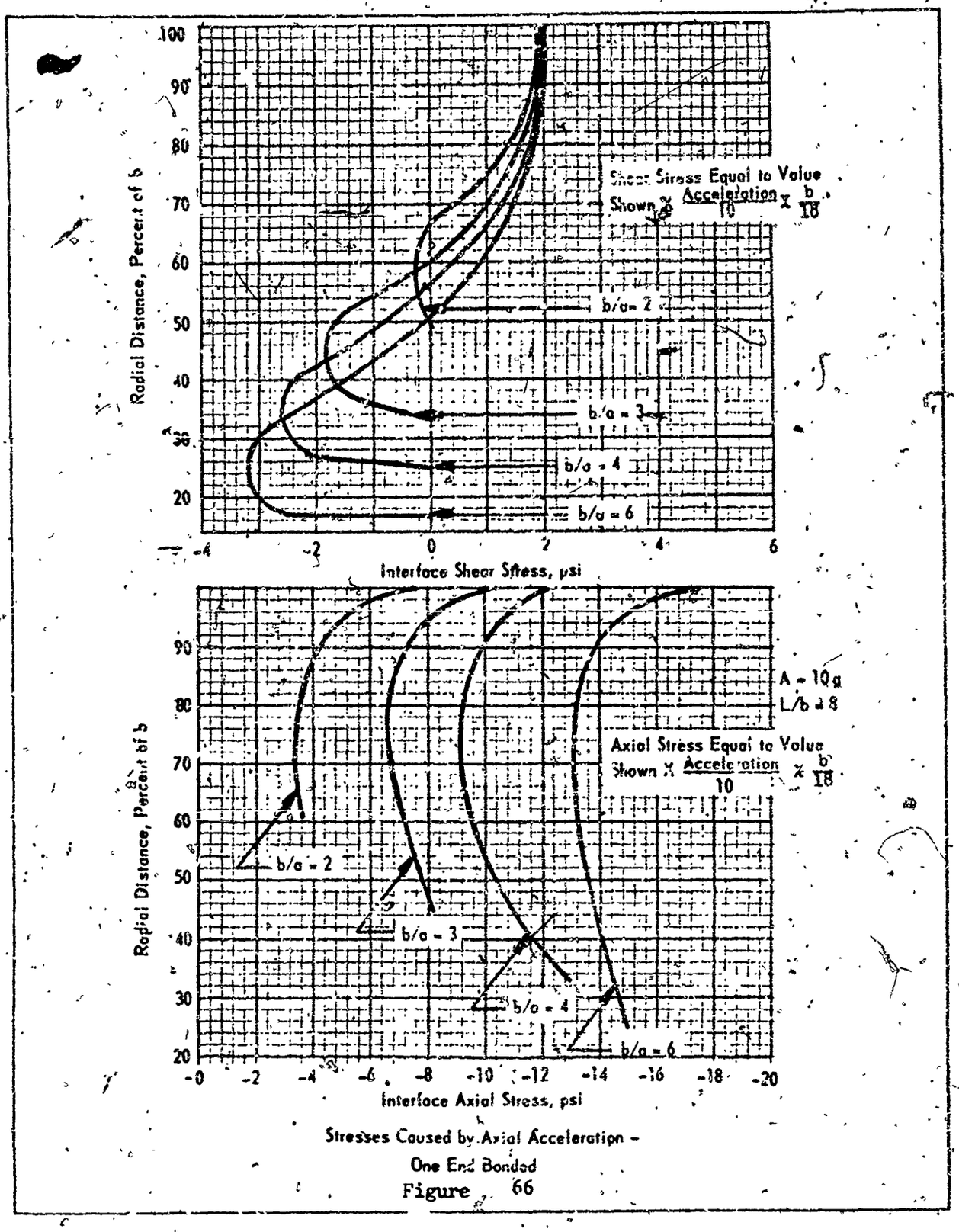

Stresses Caused by Axial Acceleration - One End Bonded

Figure 66

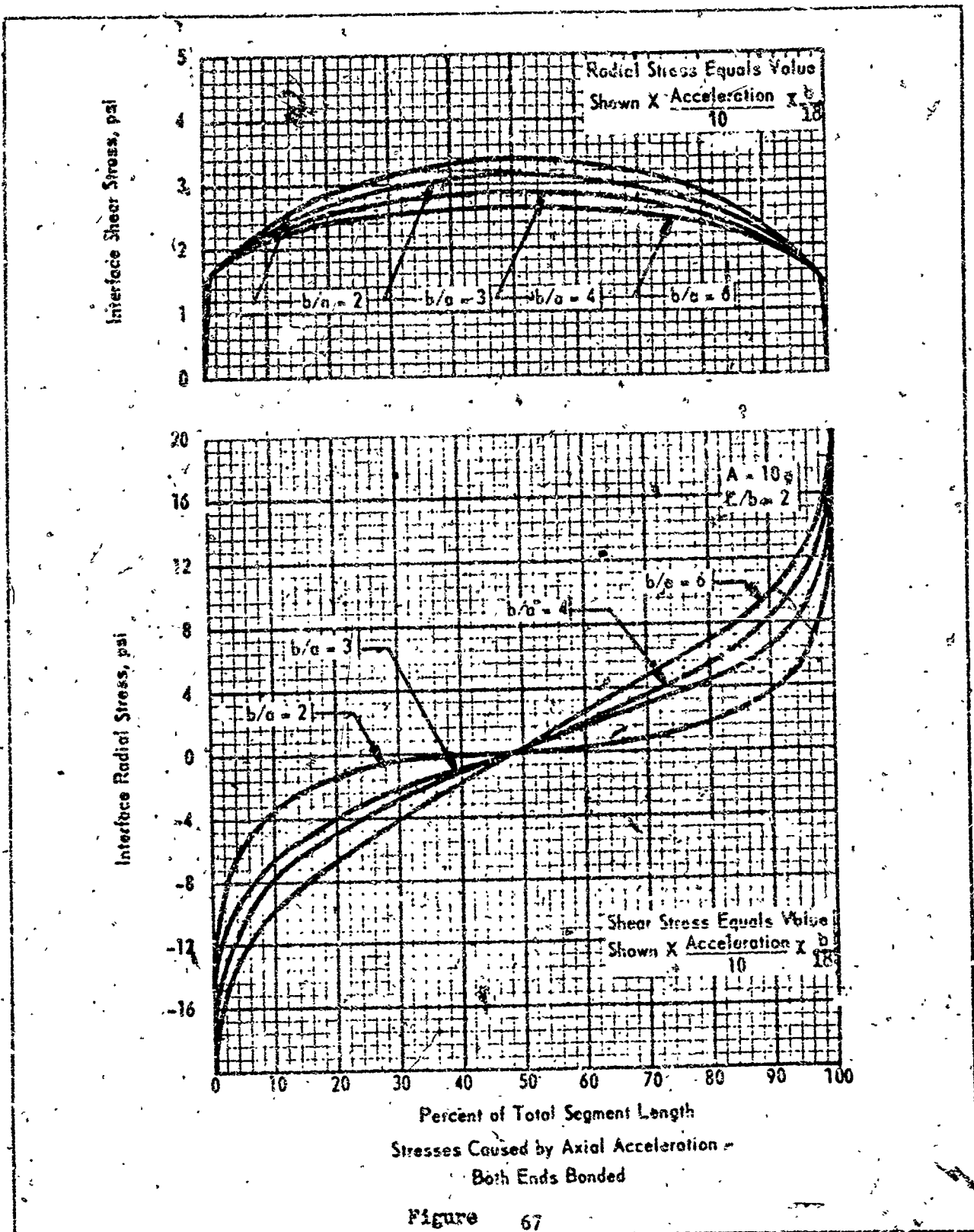

Stresses Caused by Axial Acceleration -
Both Ends Bonded

Figure 67

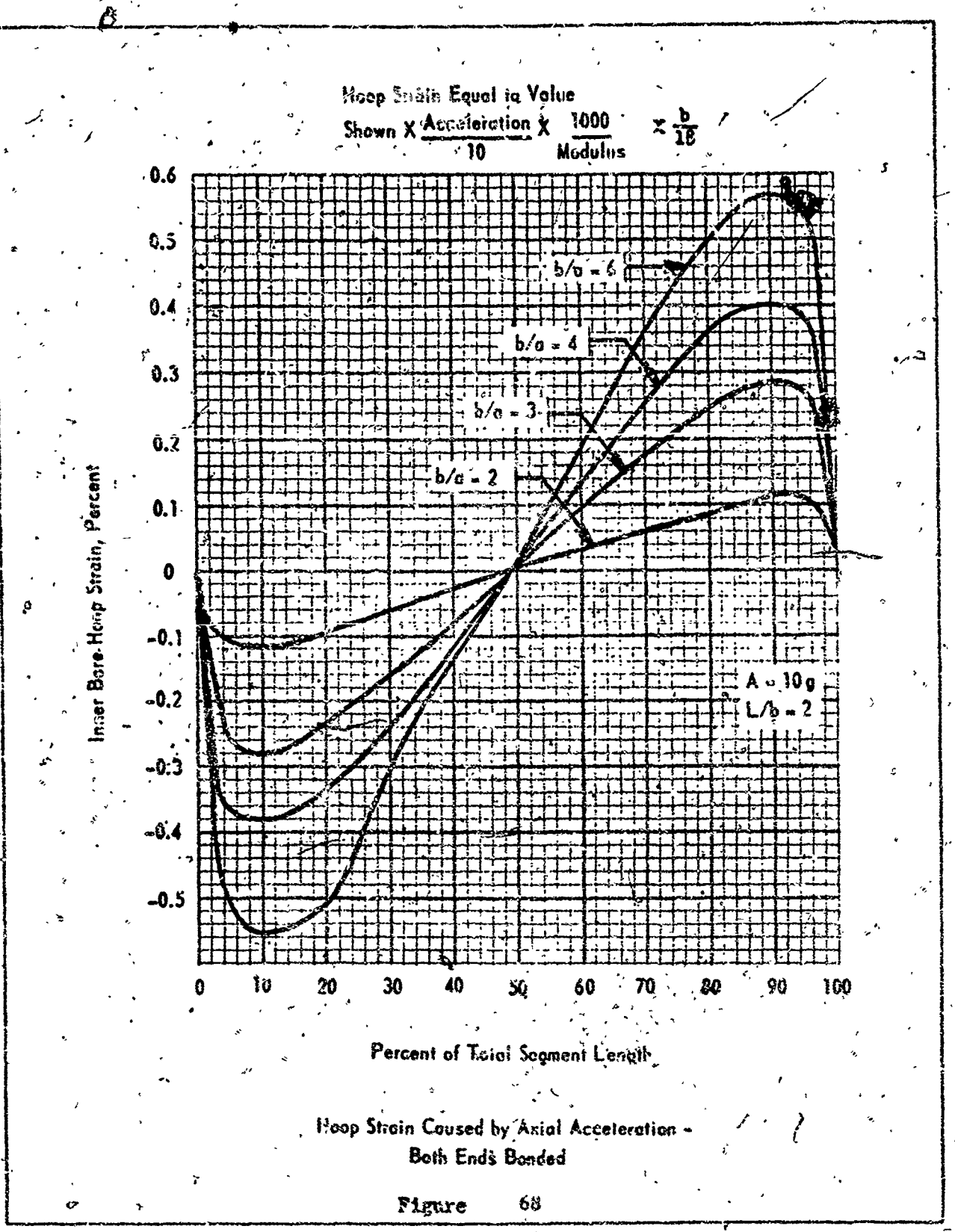

Hoop Strain Caused by Axial Acceleration -
Both Ends Bonded

Figure 68

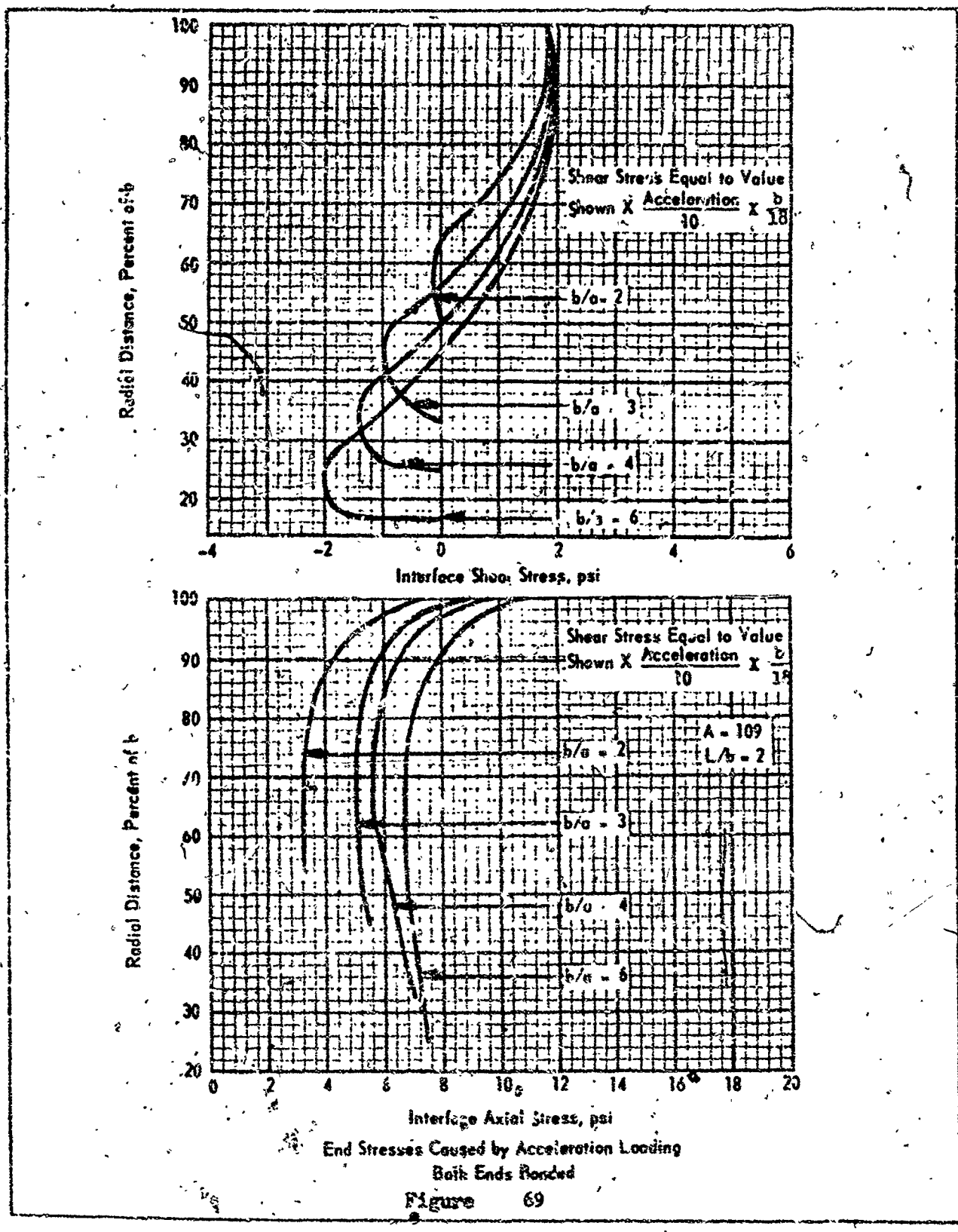

End Stresses Caused by Acceleration Loading
Both Ends Bonded

Figure 69

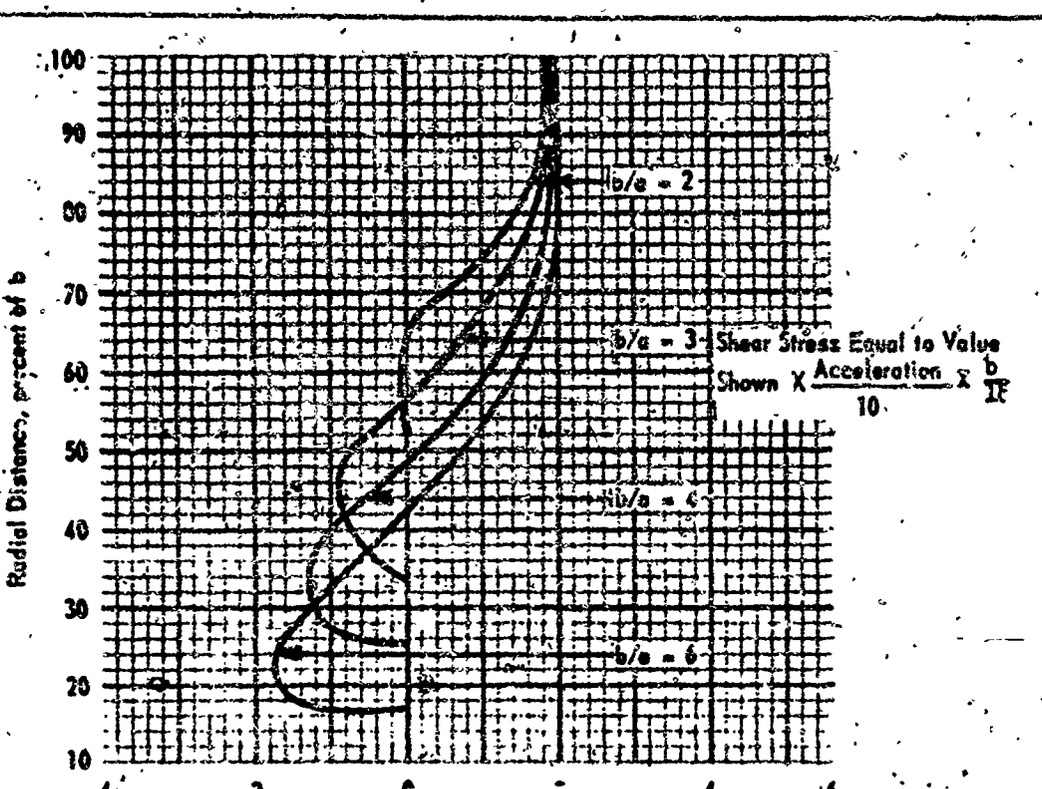

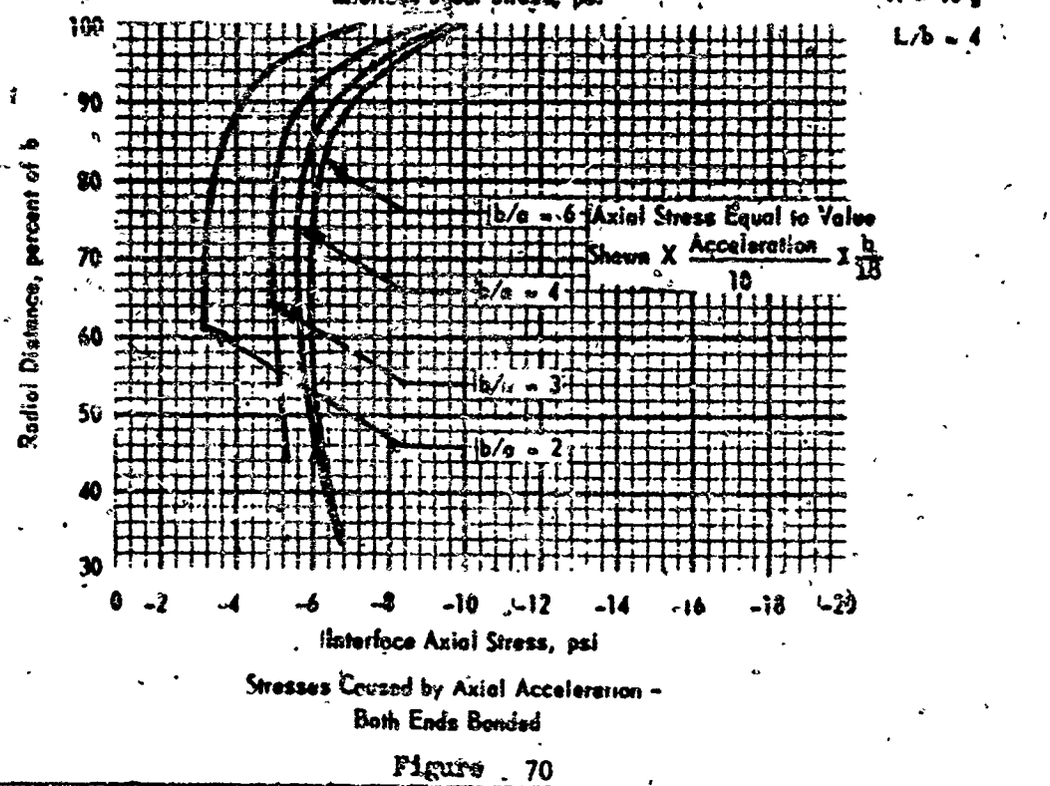

Stresses Caused by Axial Acceleration -
Both Ends Bonded

Figure 70

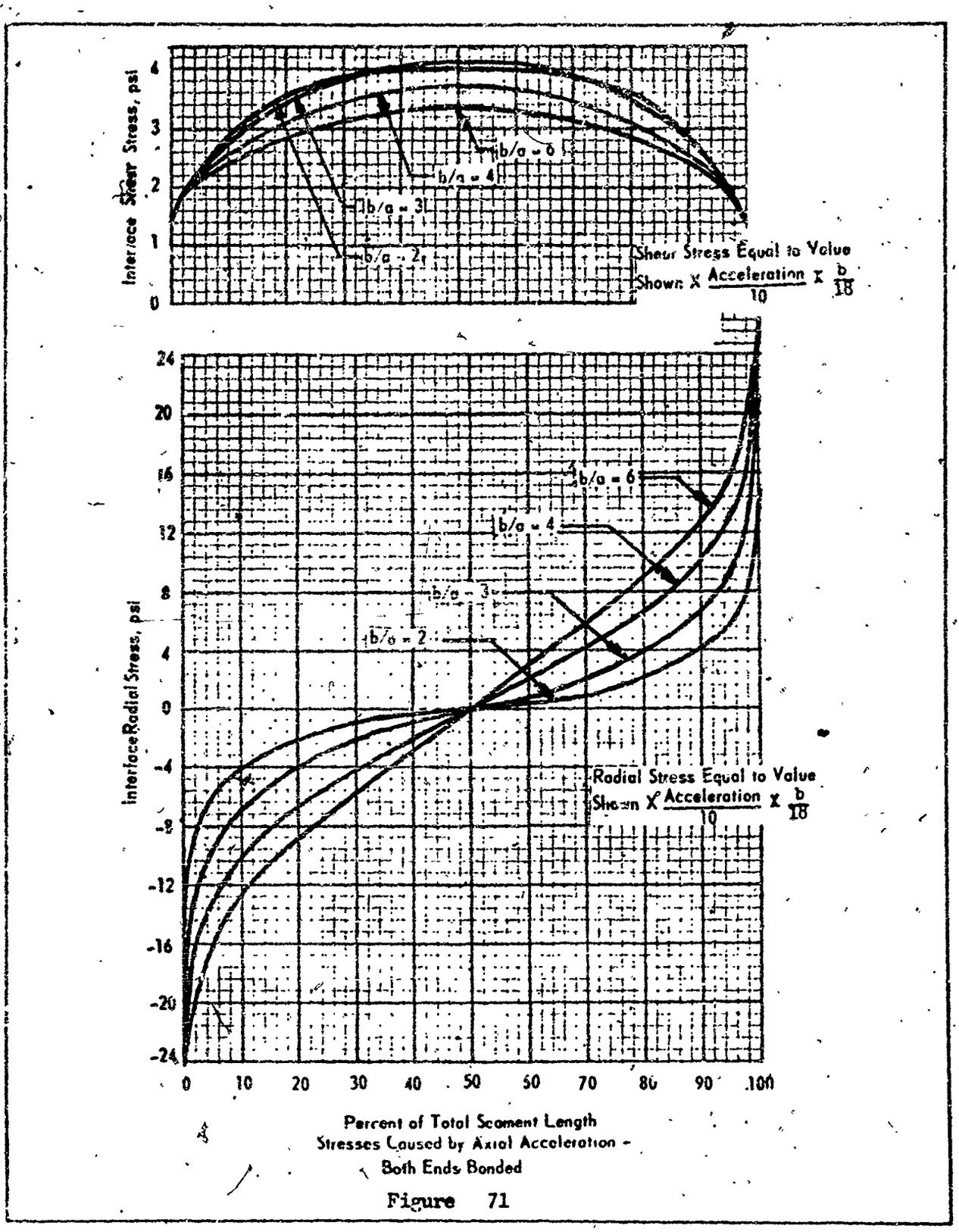

Stresses Caused by Axial Acceleration - Both Ends Bonded

Figure 71

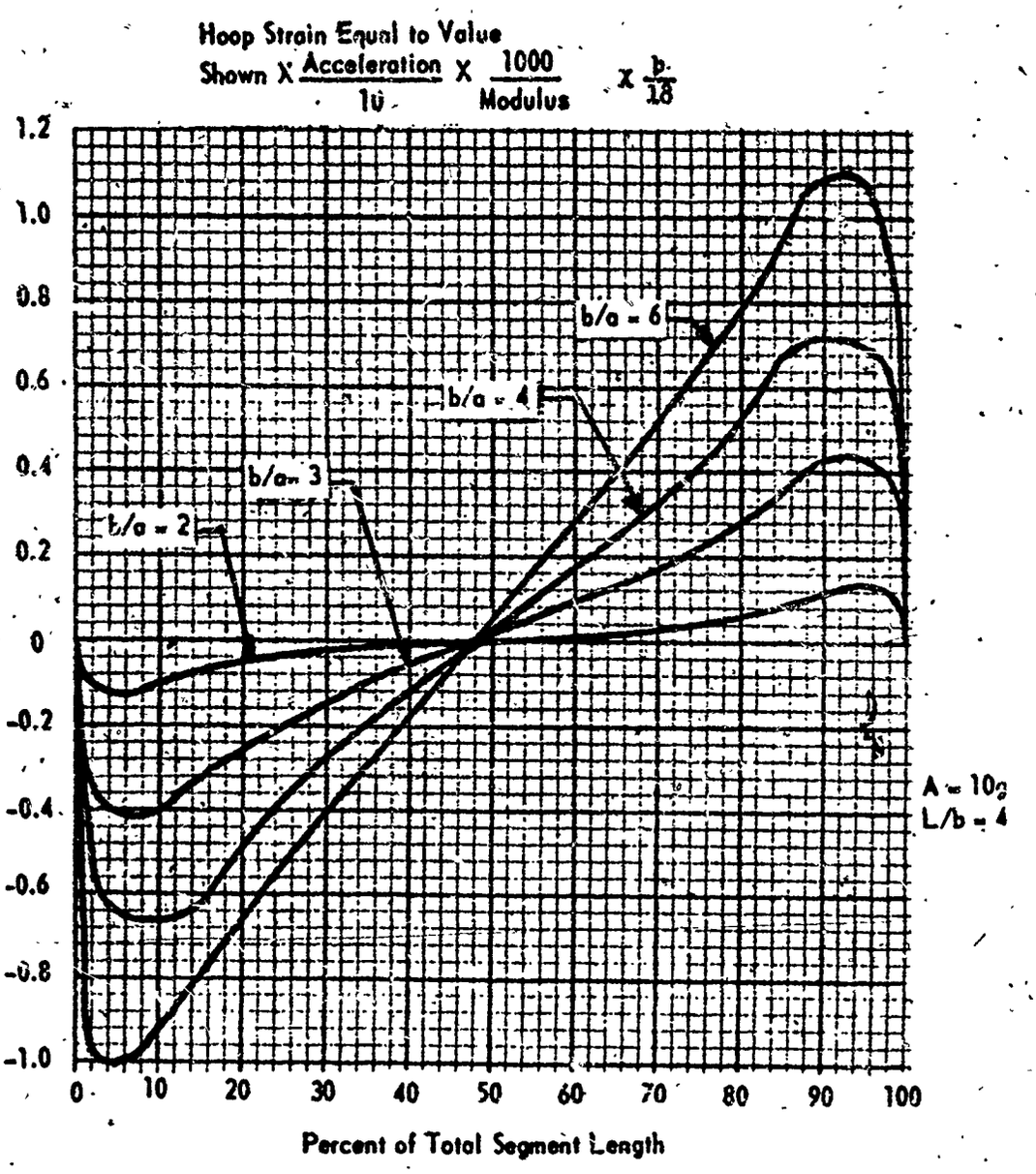

Hoop Strain Caused by Axial Acceleration
Both Ends Bonded

Figure 72

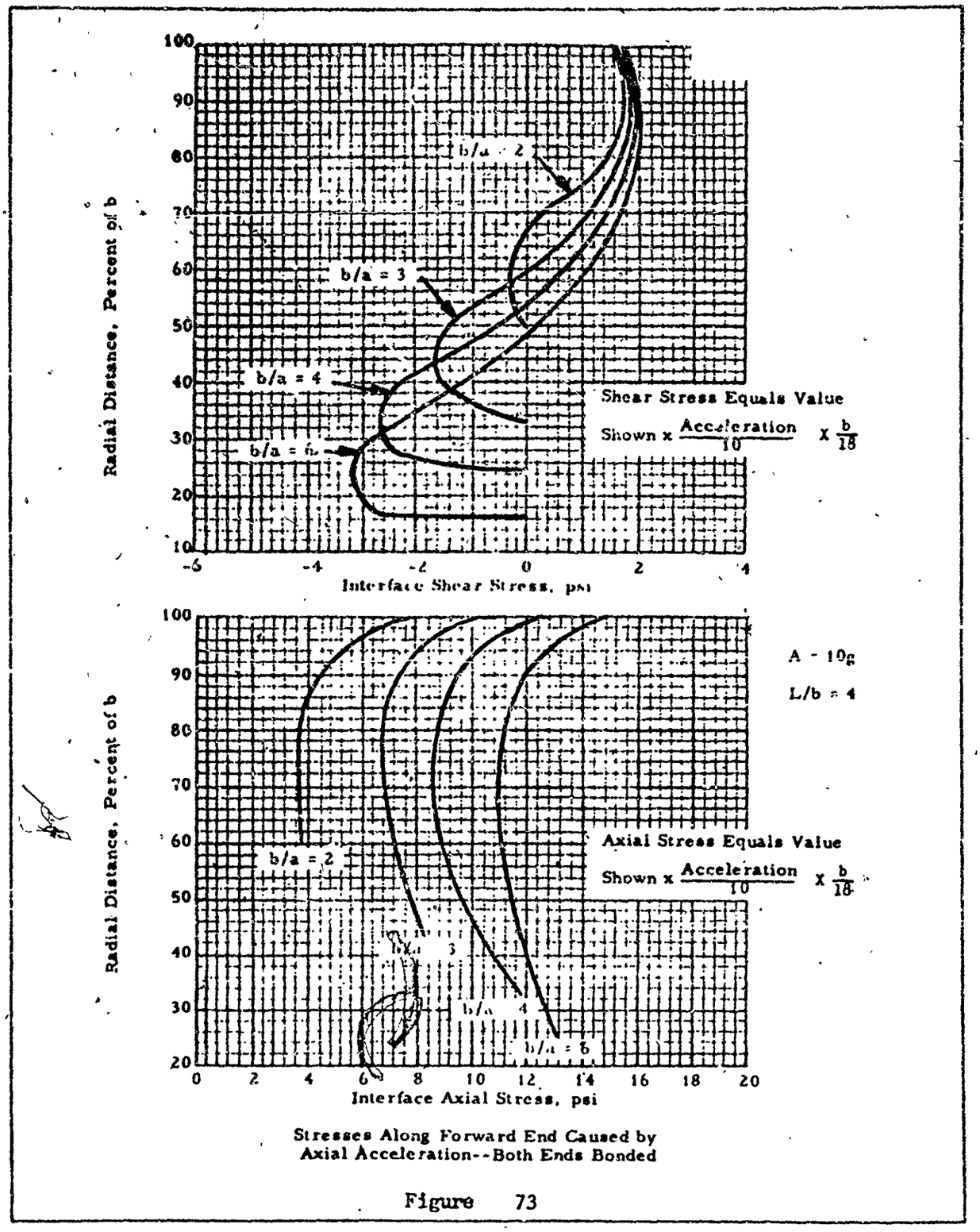

Stresses Along Forward End Caused by Axial Acceleration--Both Ends Bonded

Figure 73

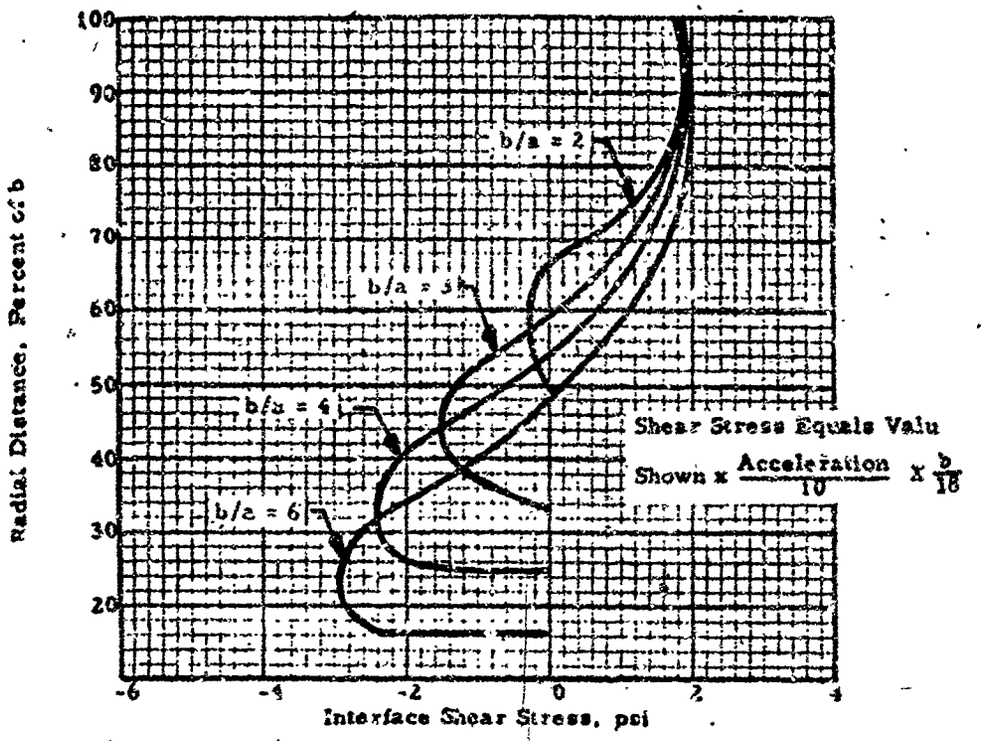

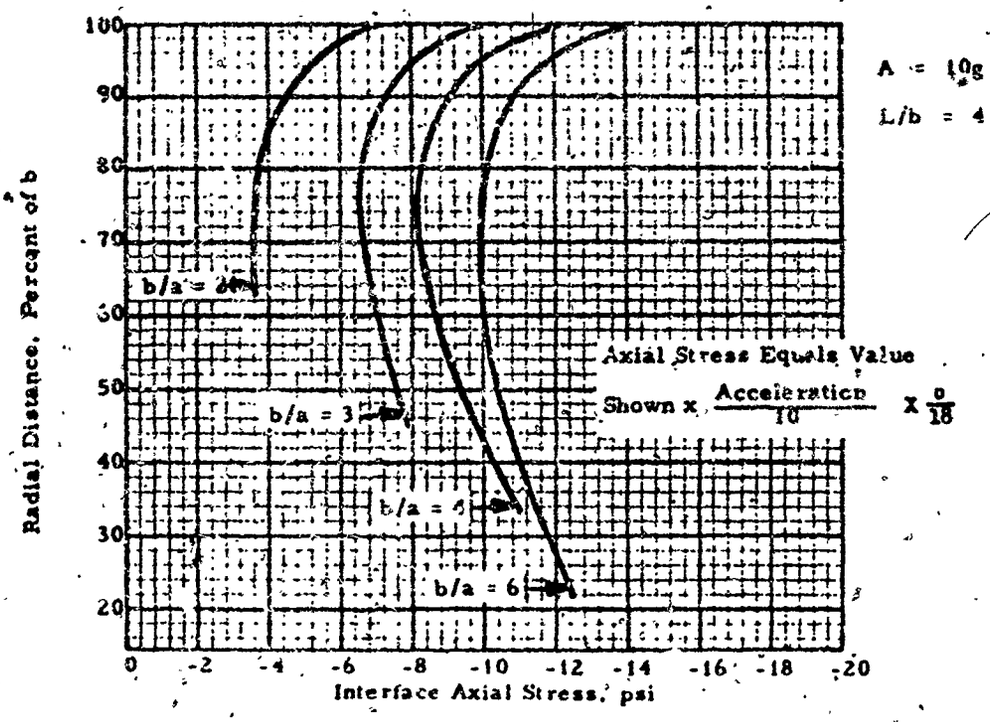

Stresses Along Aft End Caused by Axial Acceleration--Both Ends Bonded

Figure 74

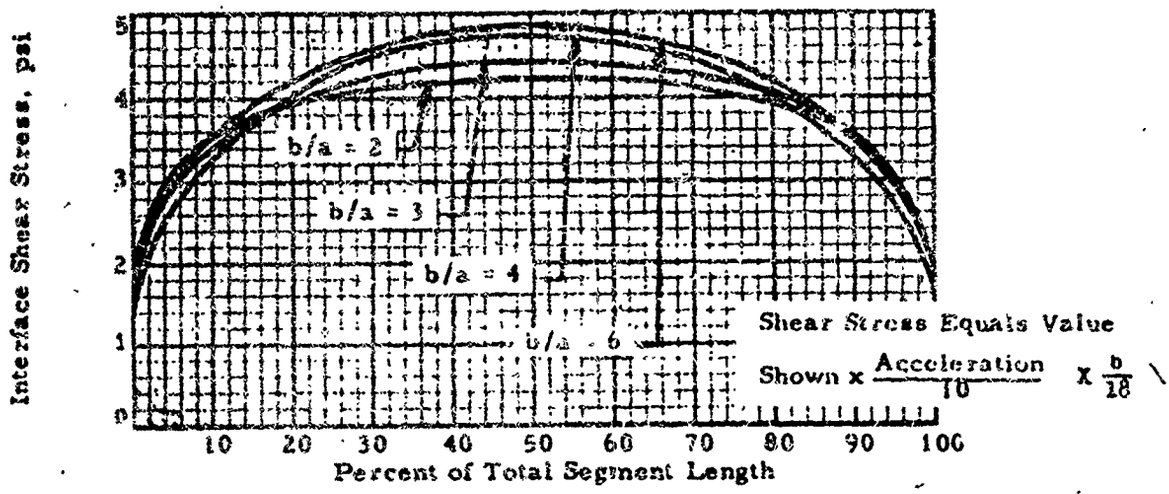

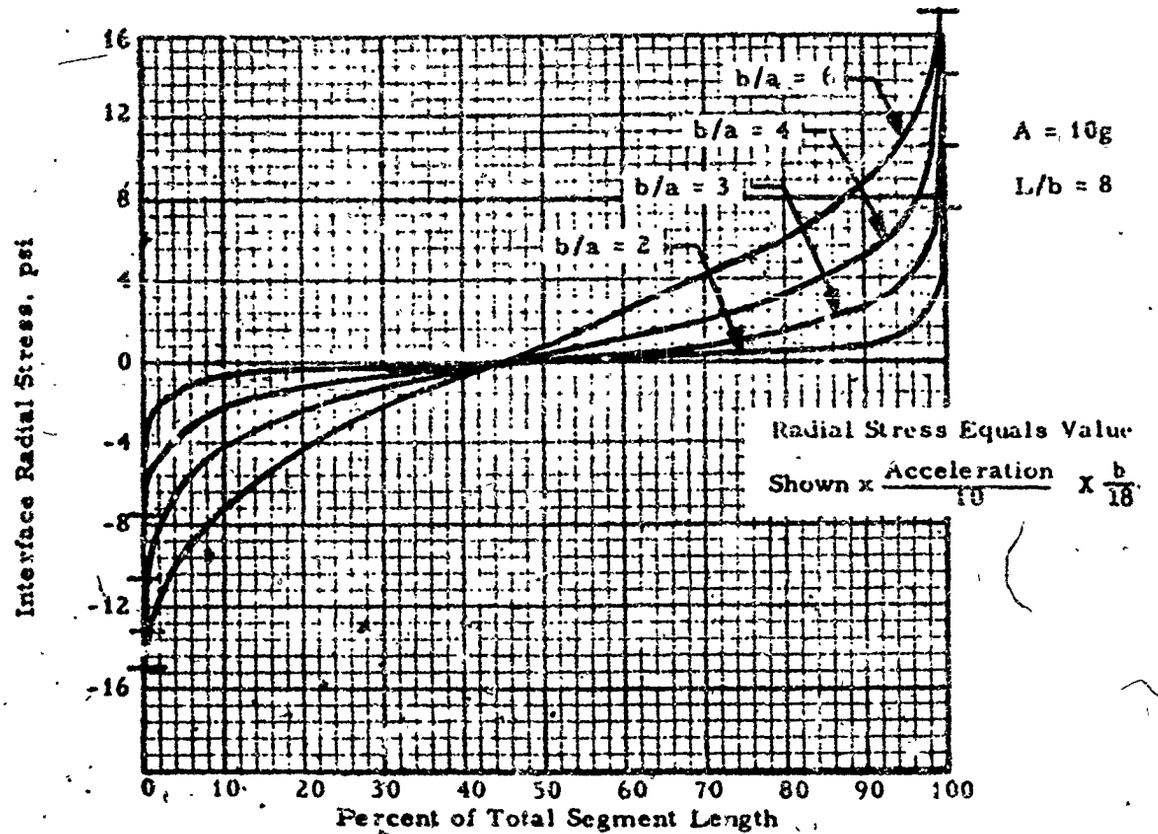

Interface Stresses Caused by Axial Acceleration - Both Ends Bonded

Figure 75

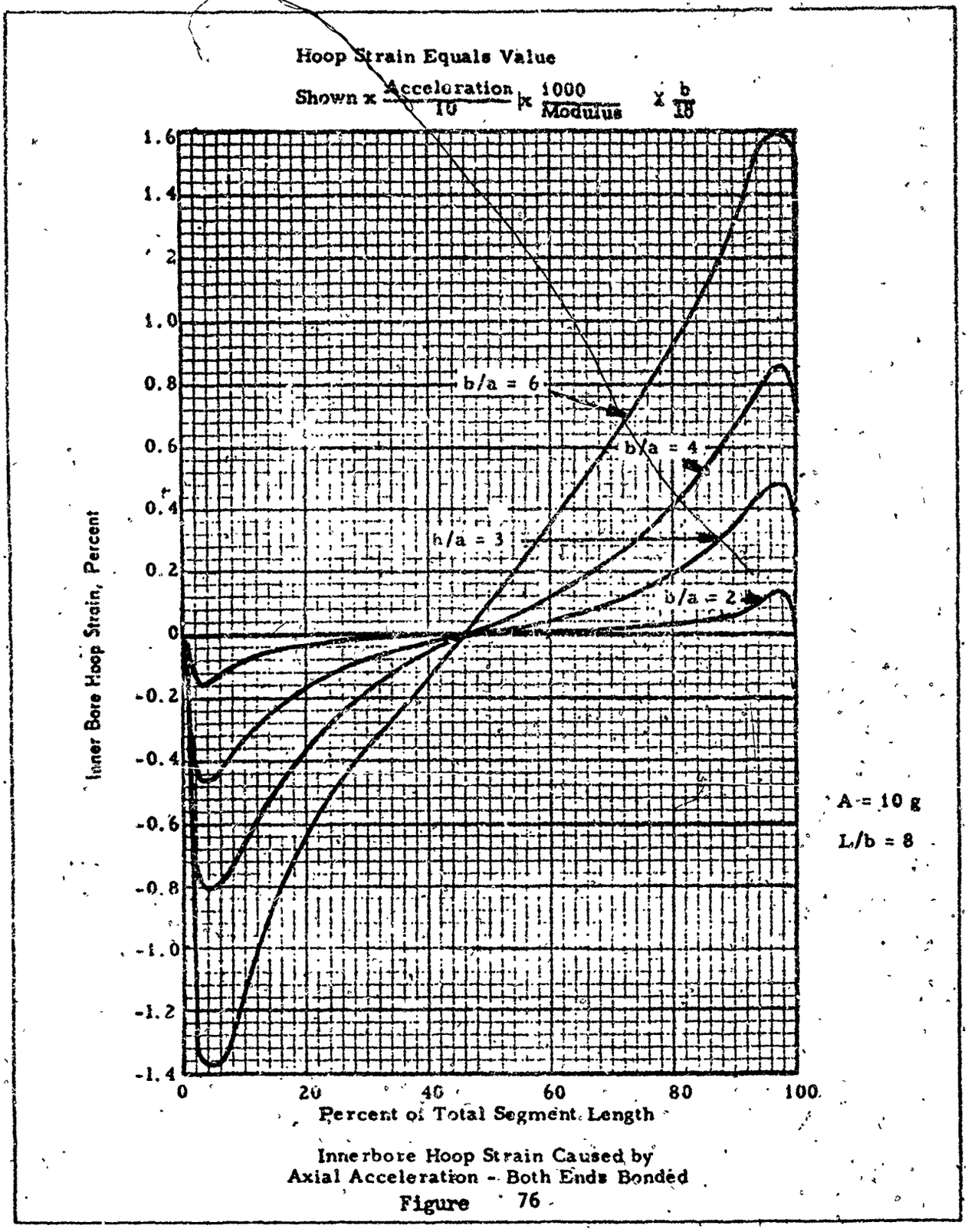

Innerbore Hoop Strain Caused by
Axial Acceleration - Both Ends Bonded

Figure 76

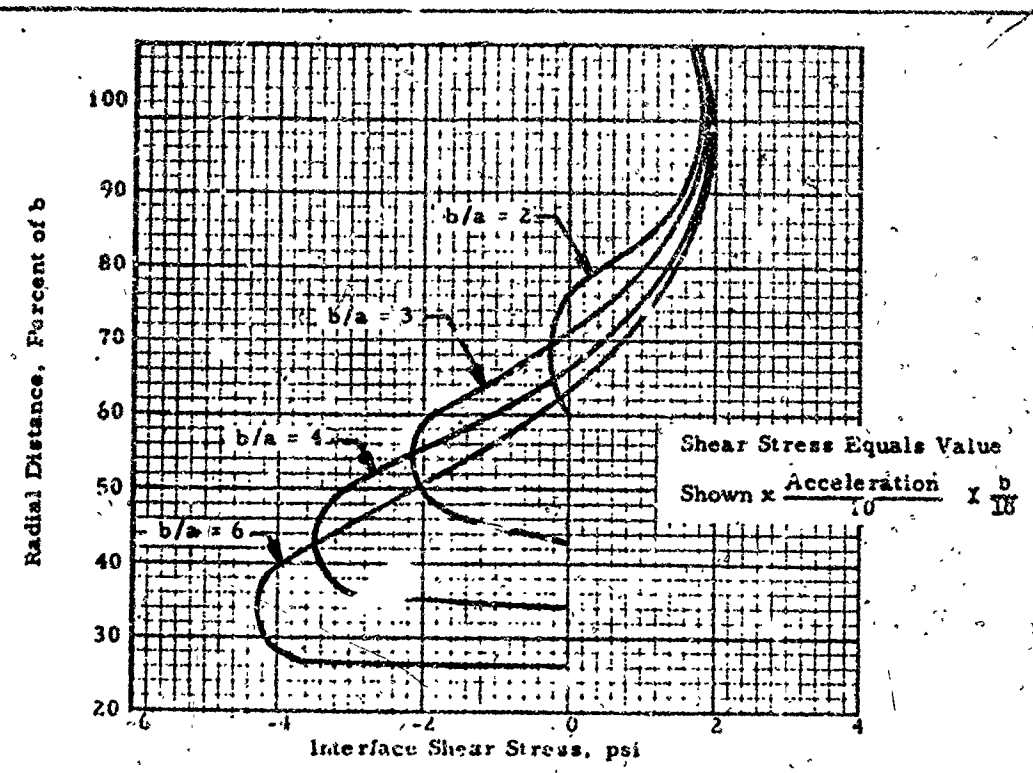

A = 10 g

L/b = 8

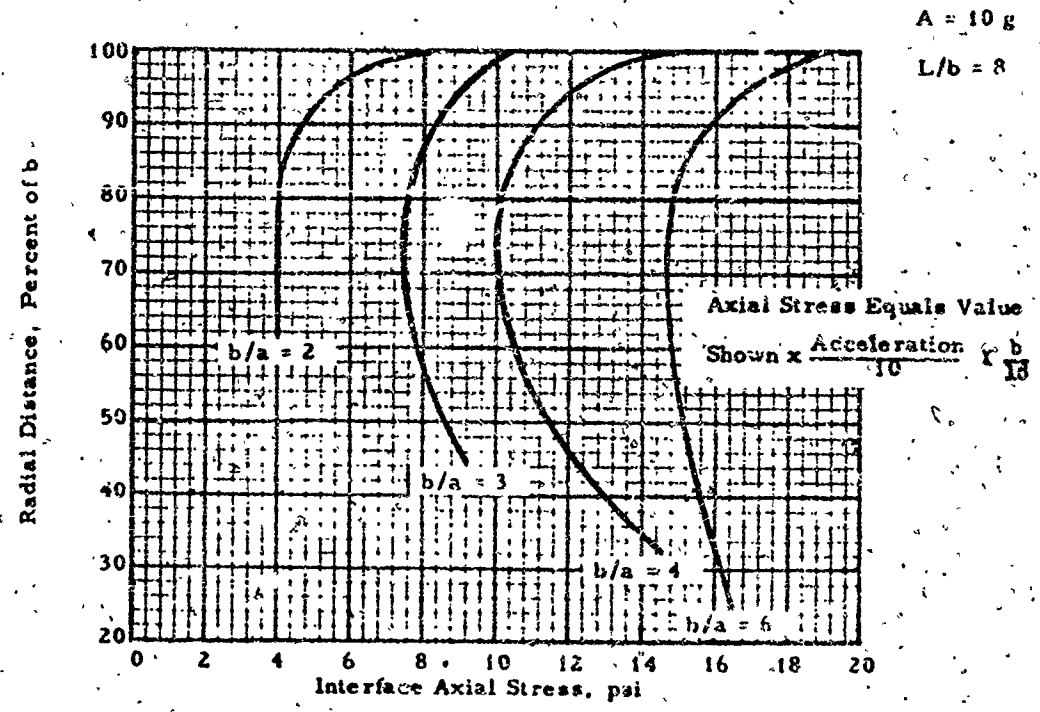

Stress Along Forward End Caused By Axial Acceleration--Both Ends Bonded

Figure 77

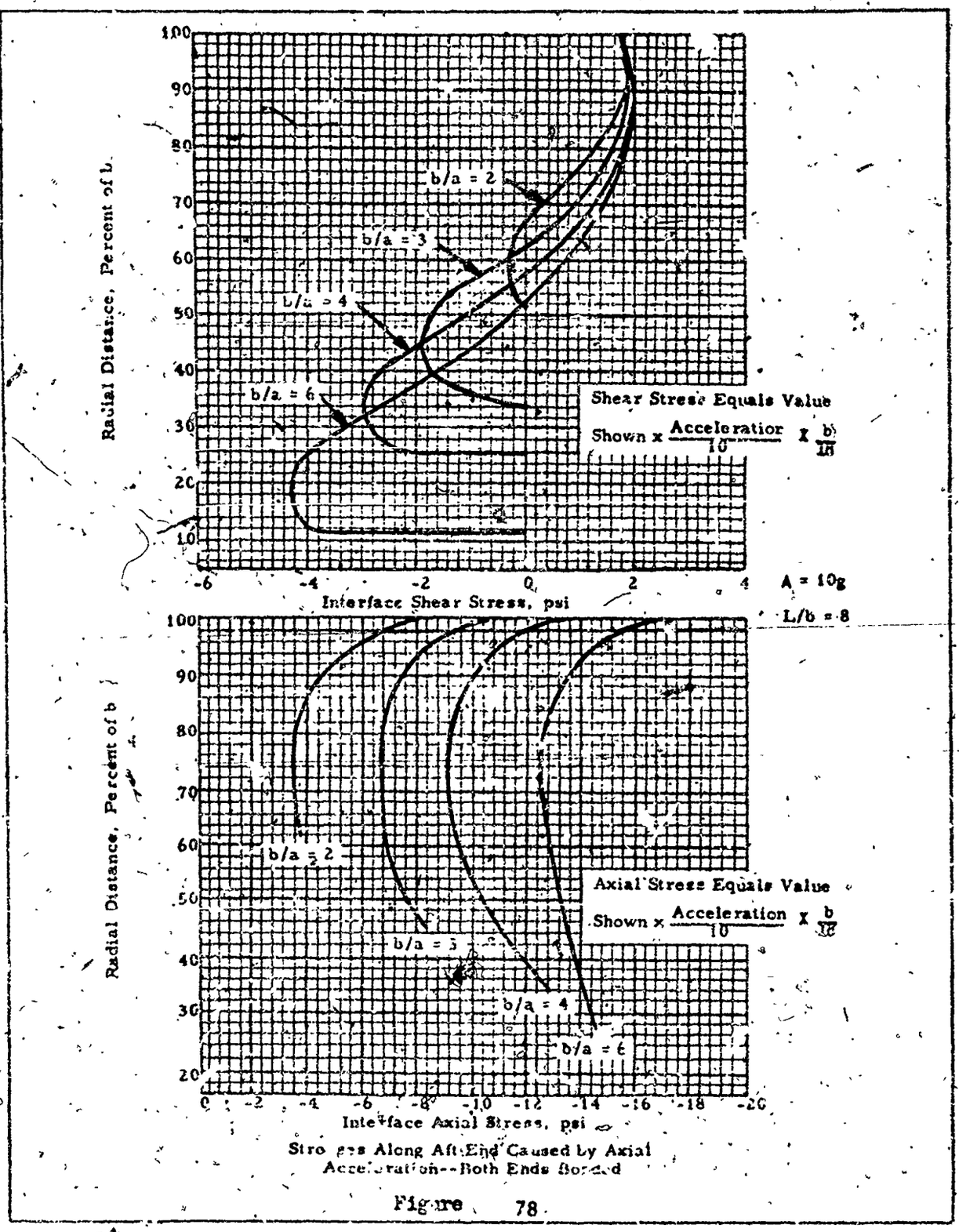

Stresses Along Aft End Caused by Axial Acceleration--Both Ends Bonded

Figure 78

APPENDIX D

PHOTOELASTIC STRESS/STRAIN CONCENTRATION FACTORS

FOR

STAR SHAPED PROPELLANT GRAINS

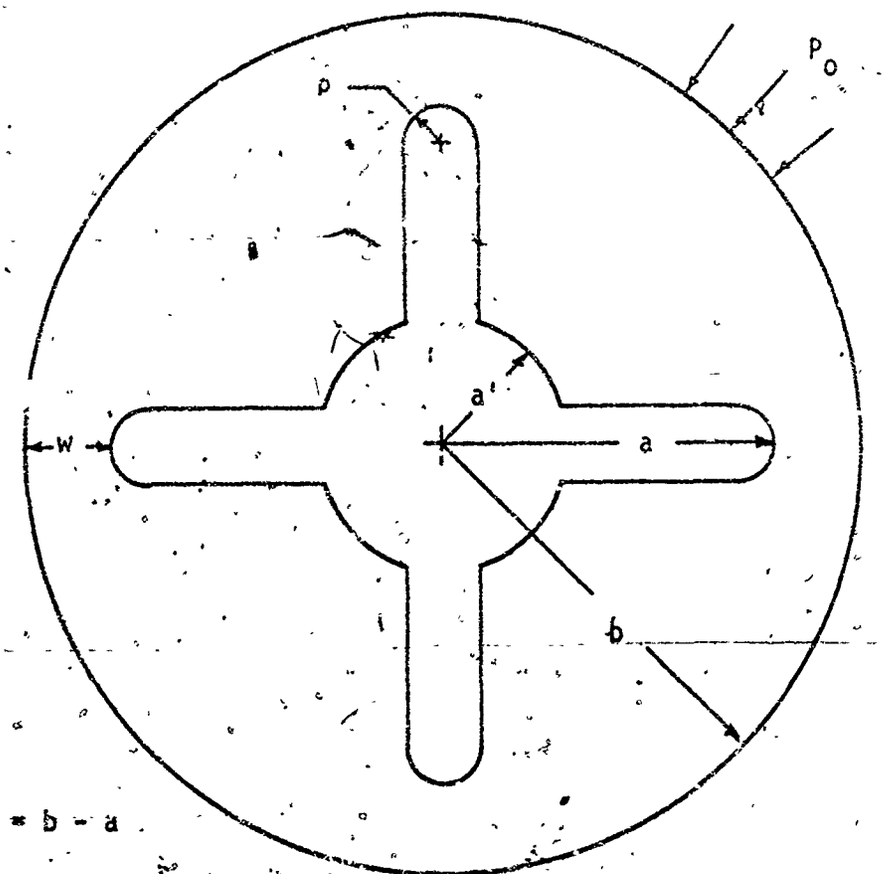

Figure D-1. Geometry of Typical Cross-Section, Simple Slot Configuration

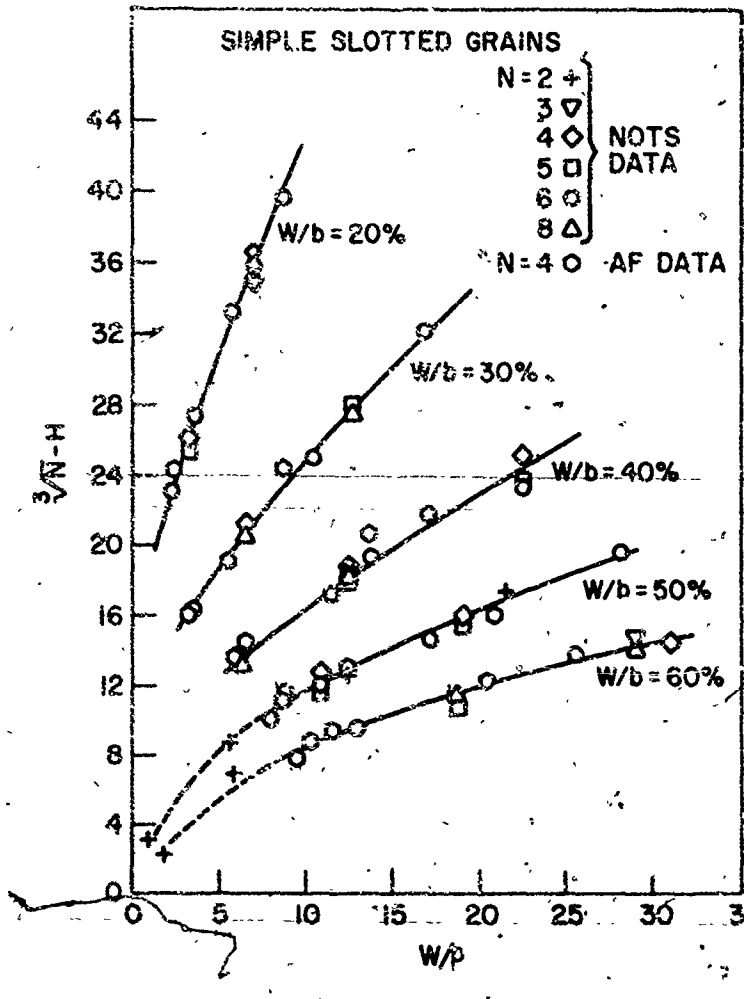

Figure D-2

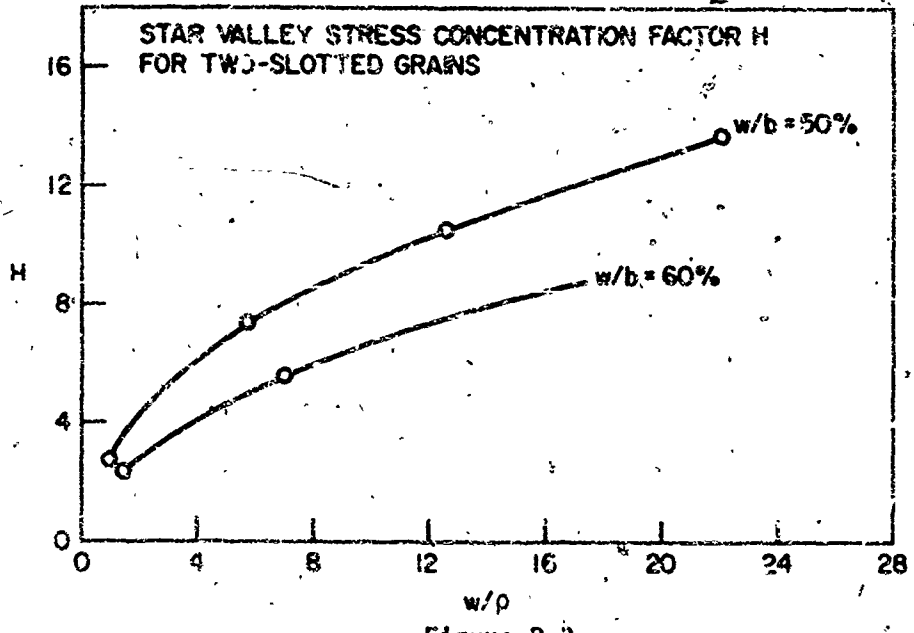

Figure D-3

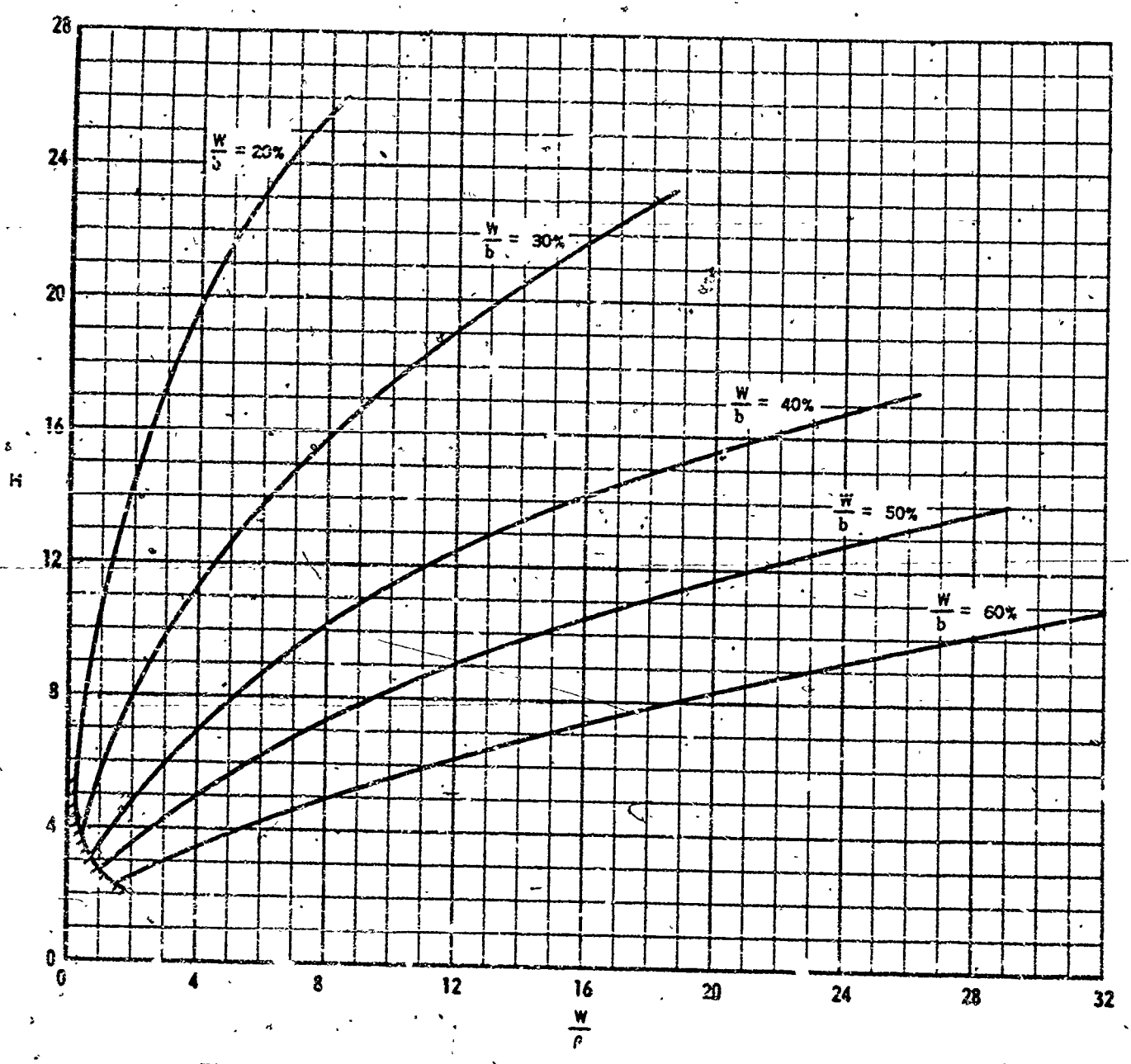

Figure D-4. Star Valley Stress Concentration Factor H for Three-Slotted Grains

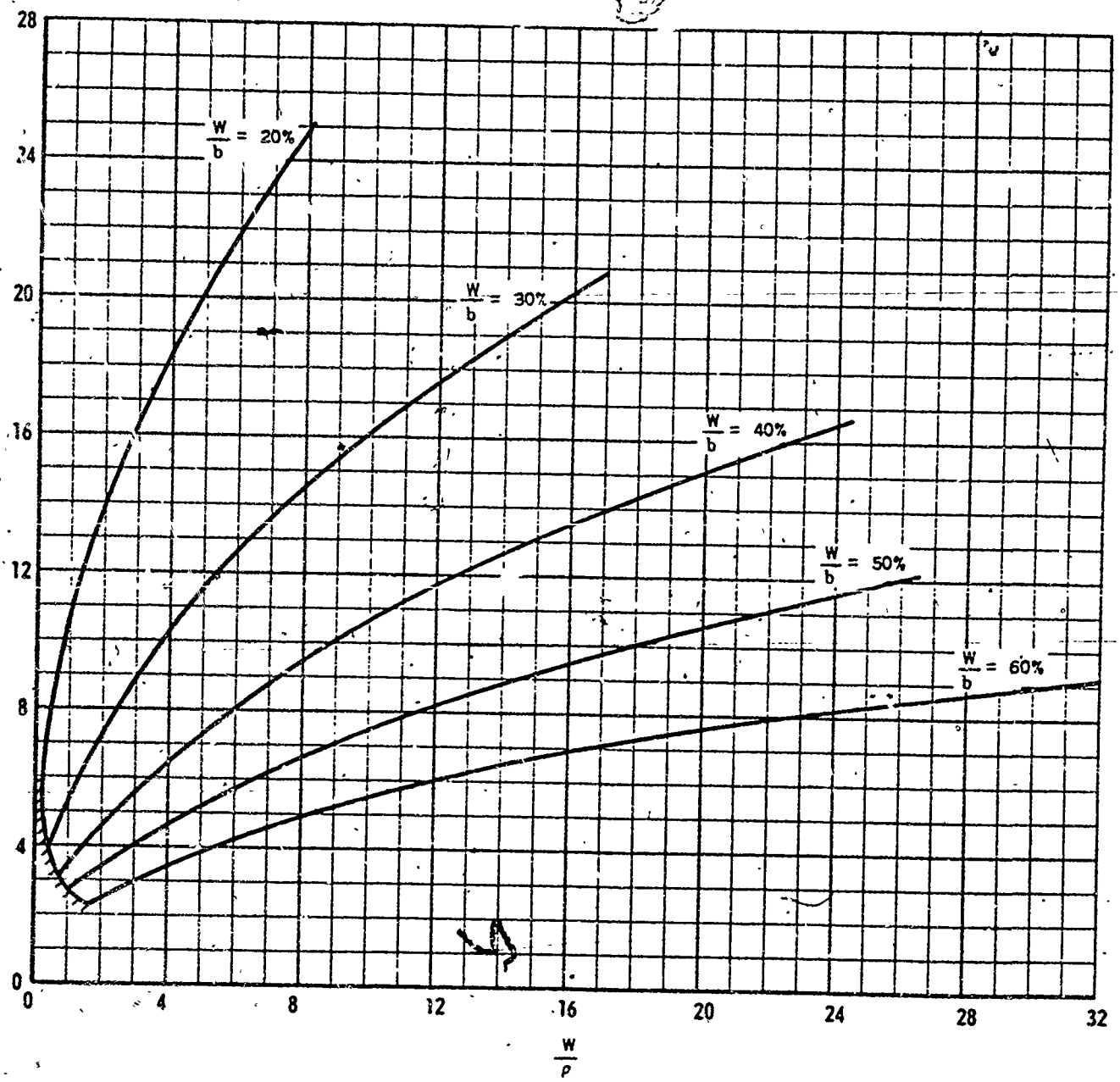

Figure D-5. Star Valley Stress Concentration Factor H for Four-Slotted Grains

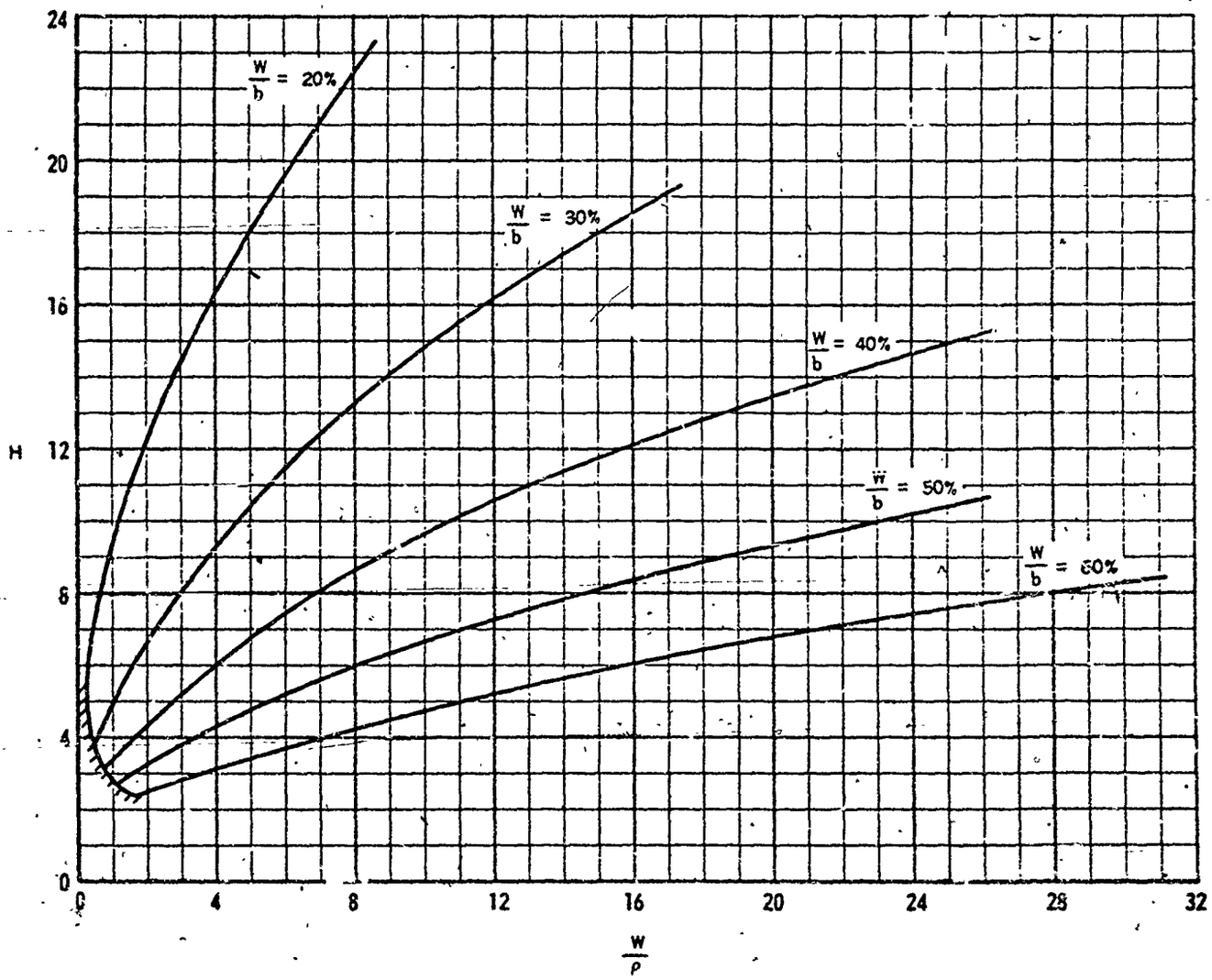

Figure D-6. Star Valley Stress Concentration Factor H for Five-Slotted Grains

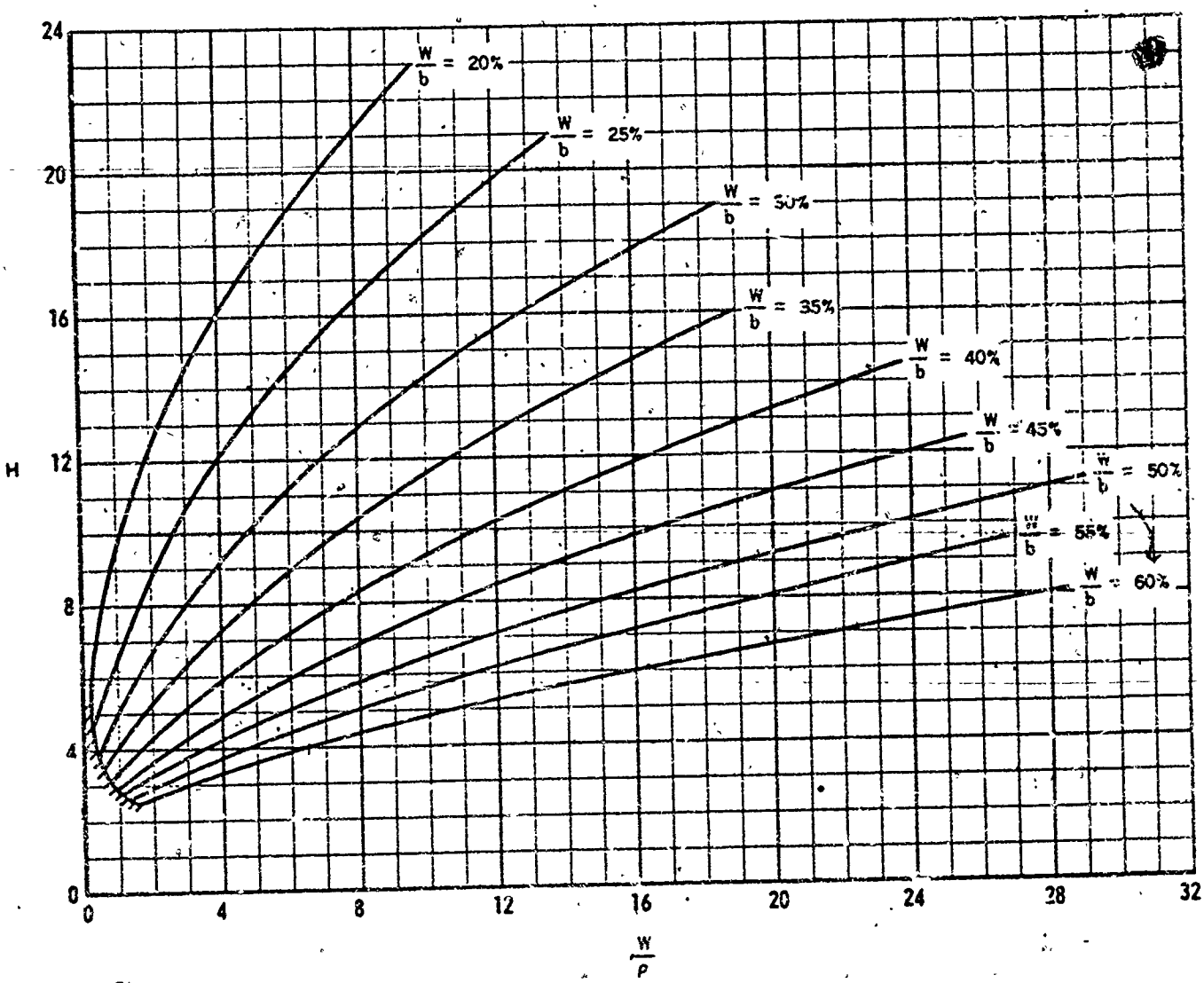

Figure D-7. Star Valley Stress Concentration Factor H for Six-Slotted Grains

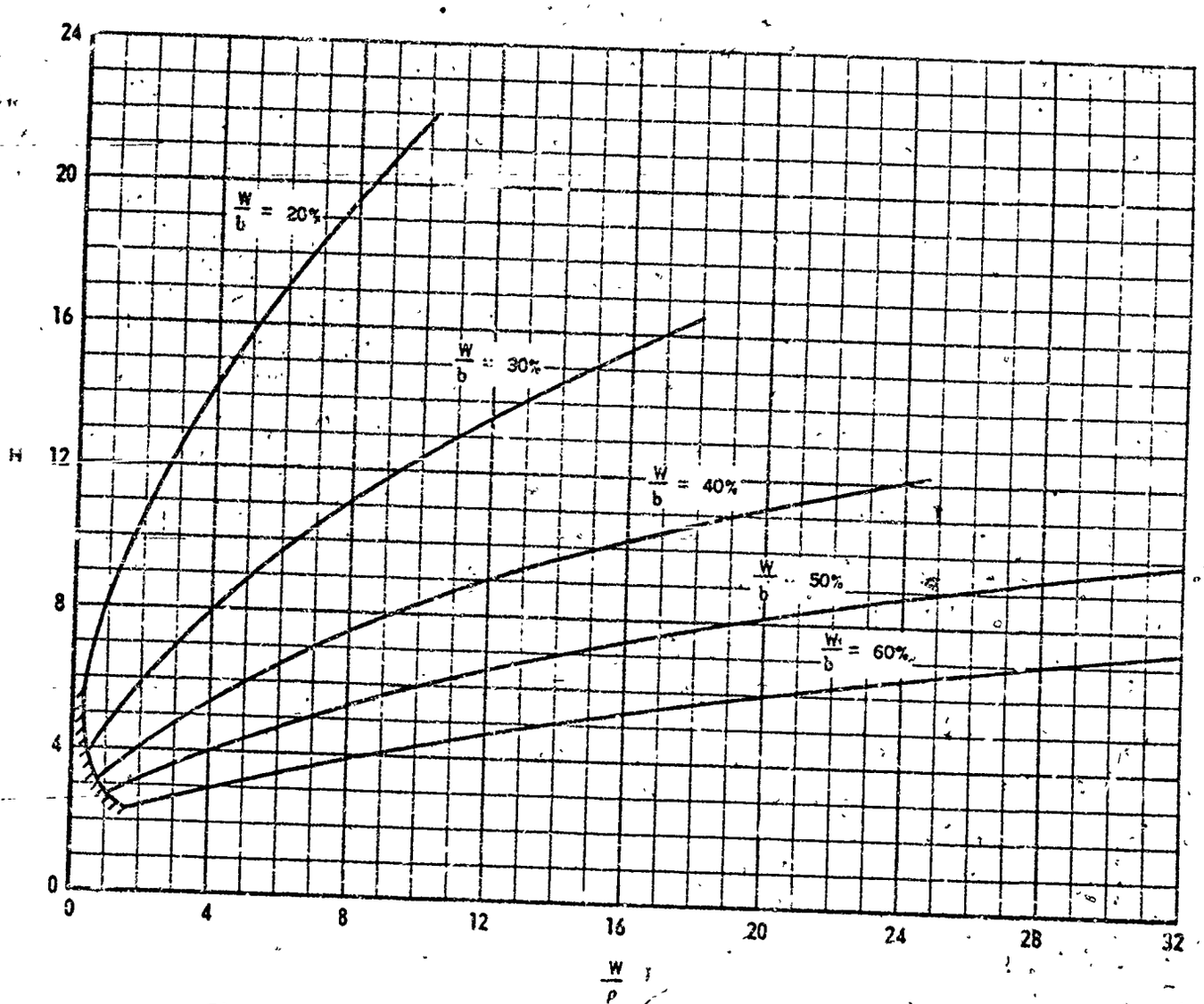

Figure D-8. Star Valley Stress Concentration Factor H for Eight-Slotted Grains

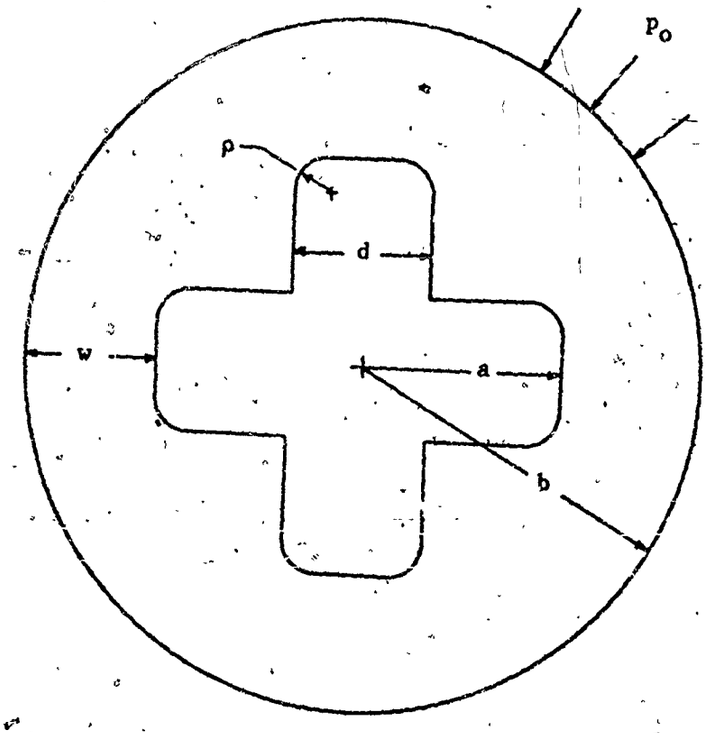

GEOMETRY OF TYPICAL CROSS SECTION

FOR SLOT WIDTH EFFECT

Figure D-9.

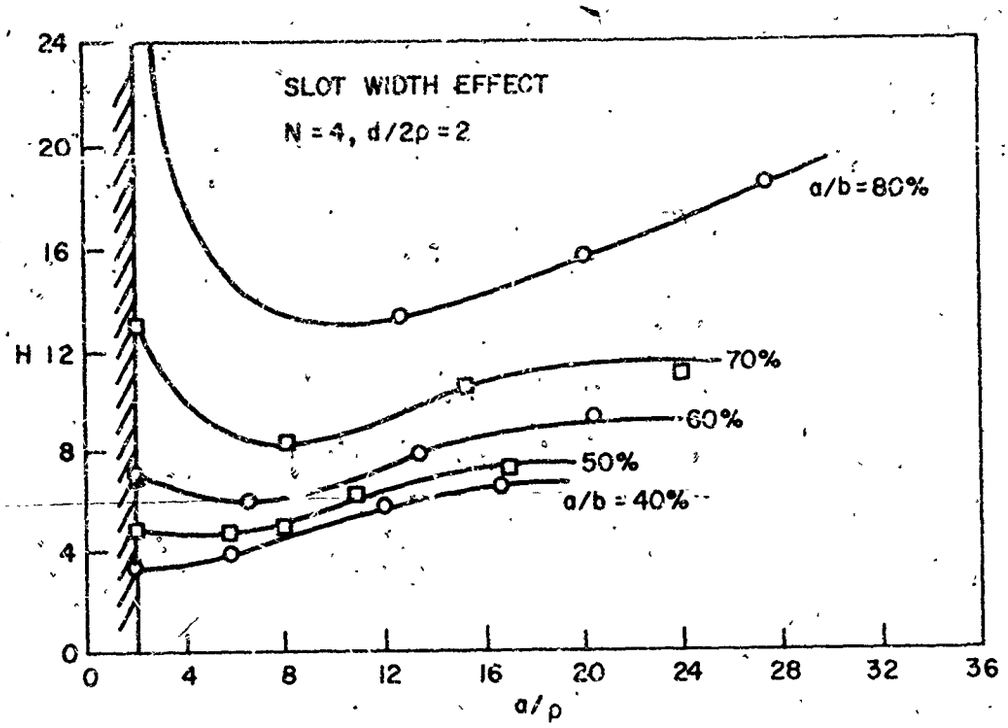

Figure D-10

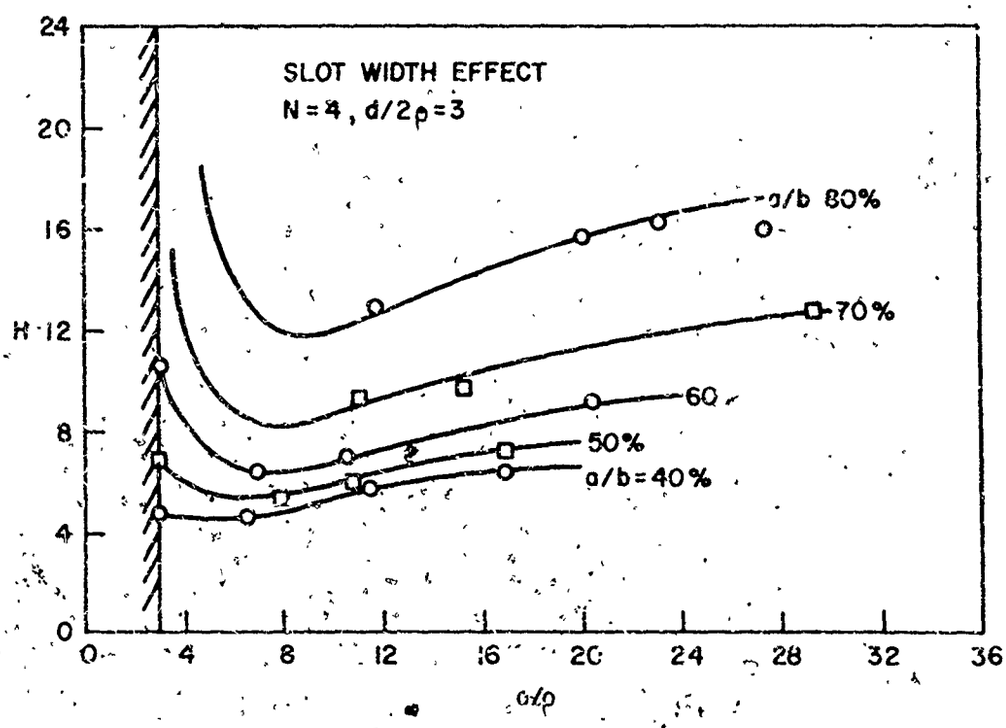

Figure D-11

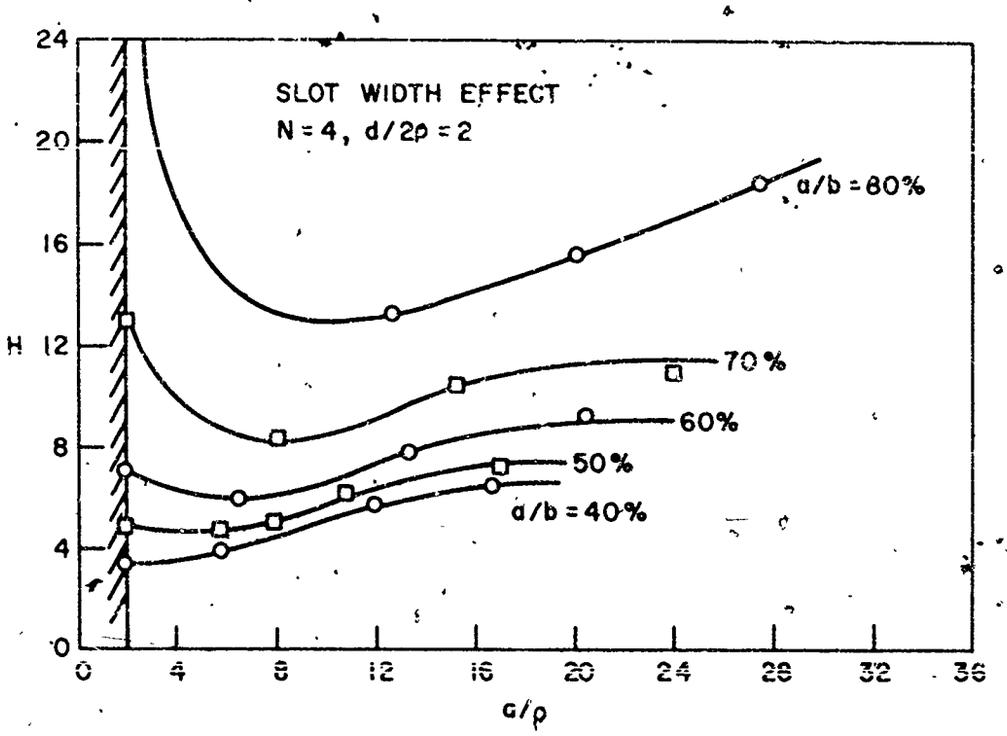

Figure D-12

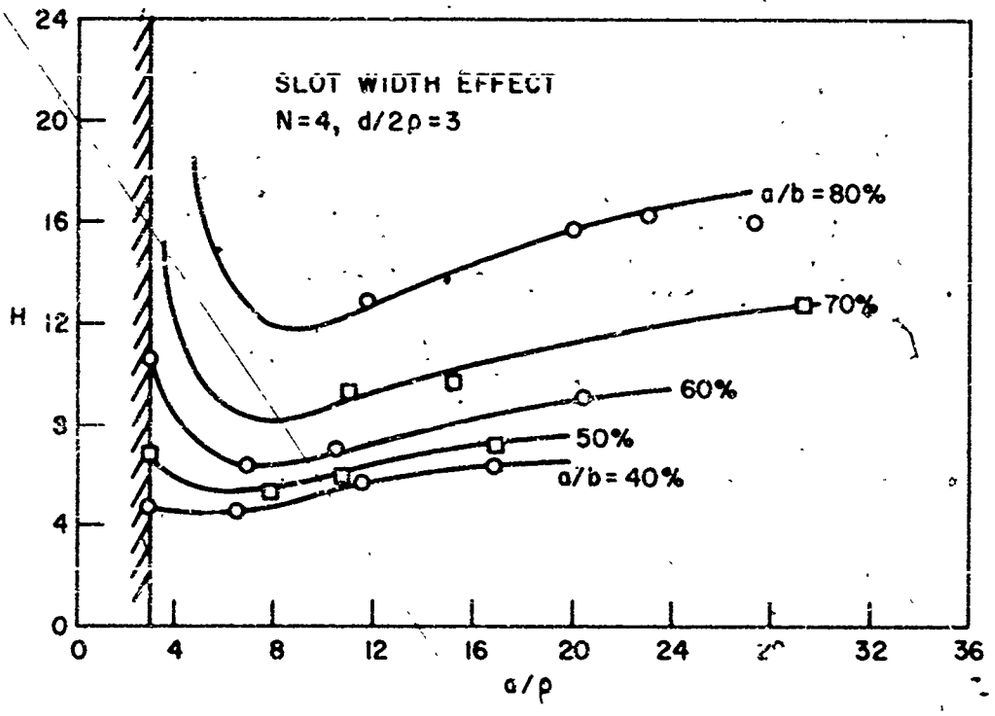

Figure D-13

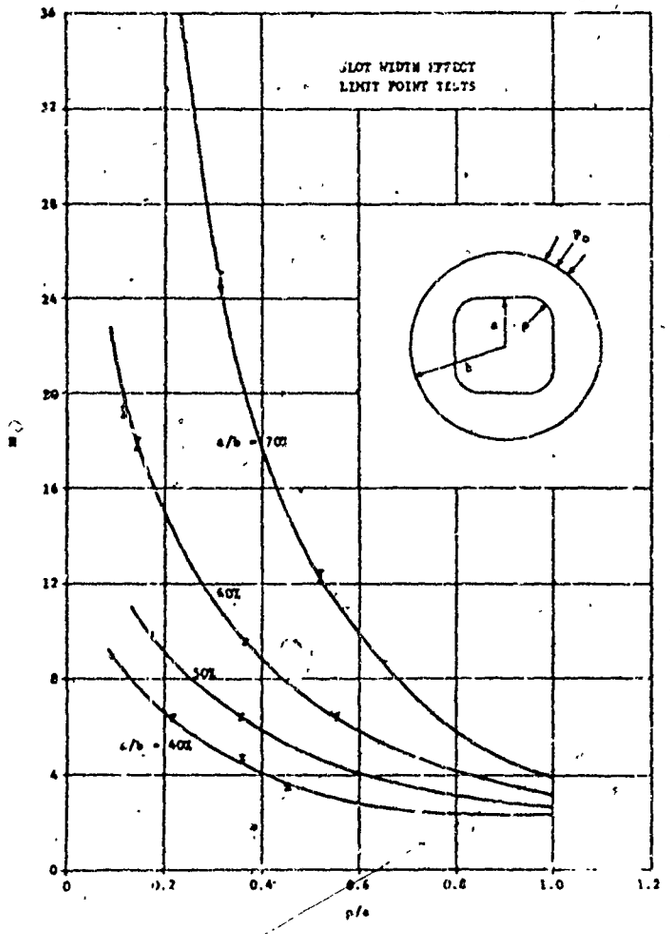

Figure D-14

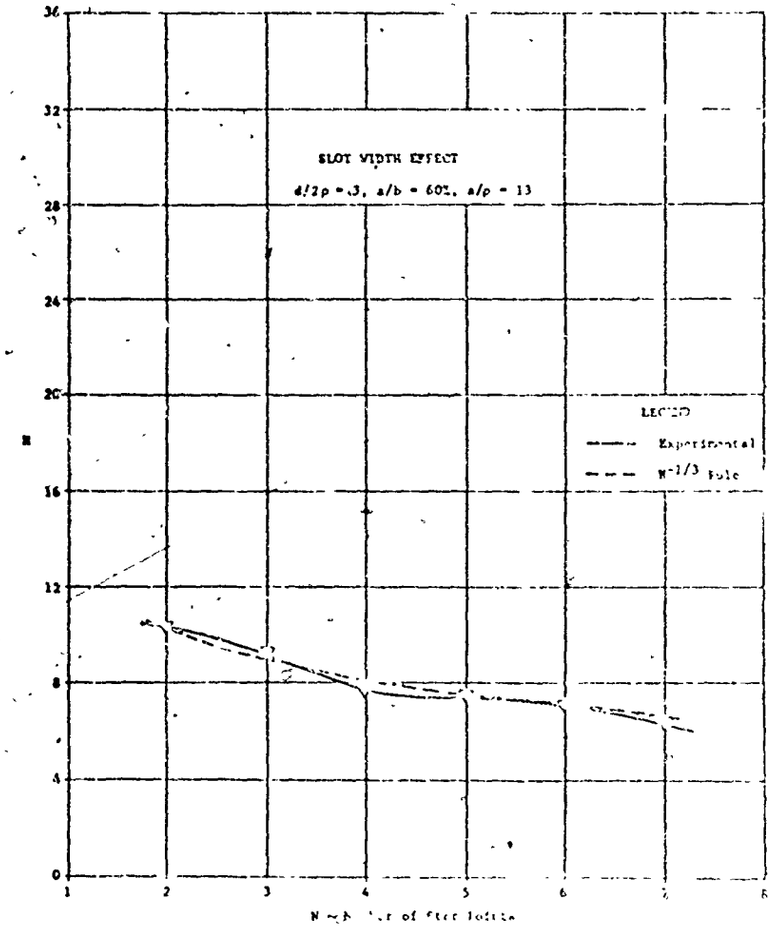

Figure D-15

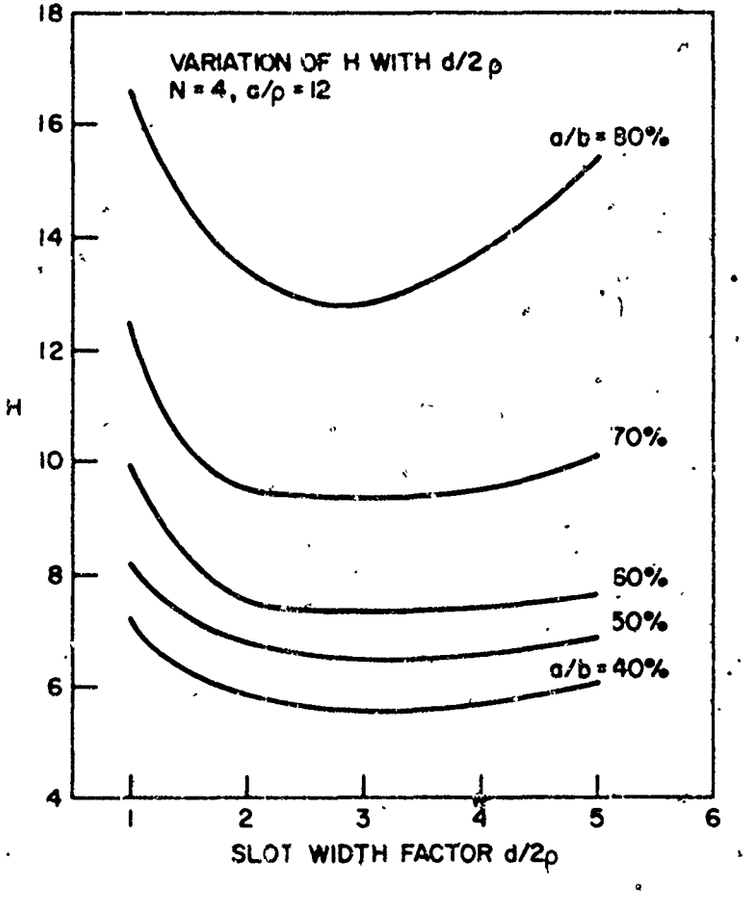

Figure D-16.

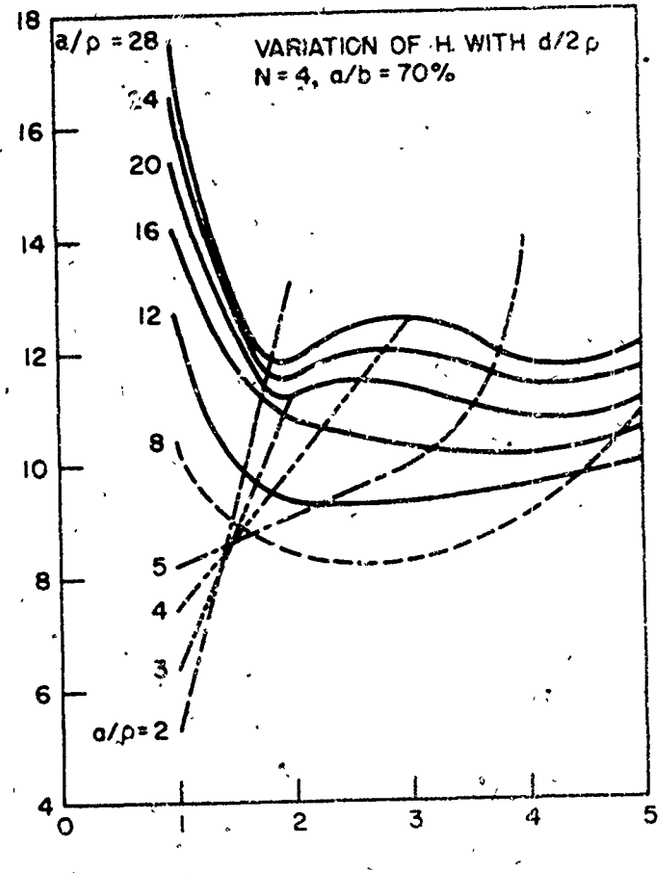

Figure D-17.

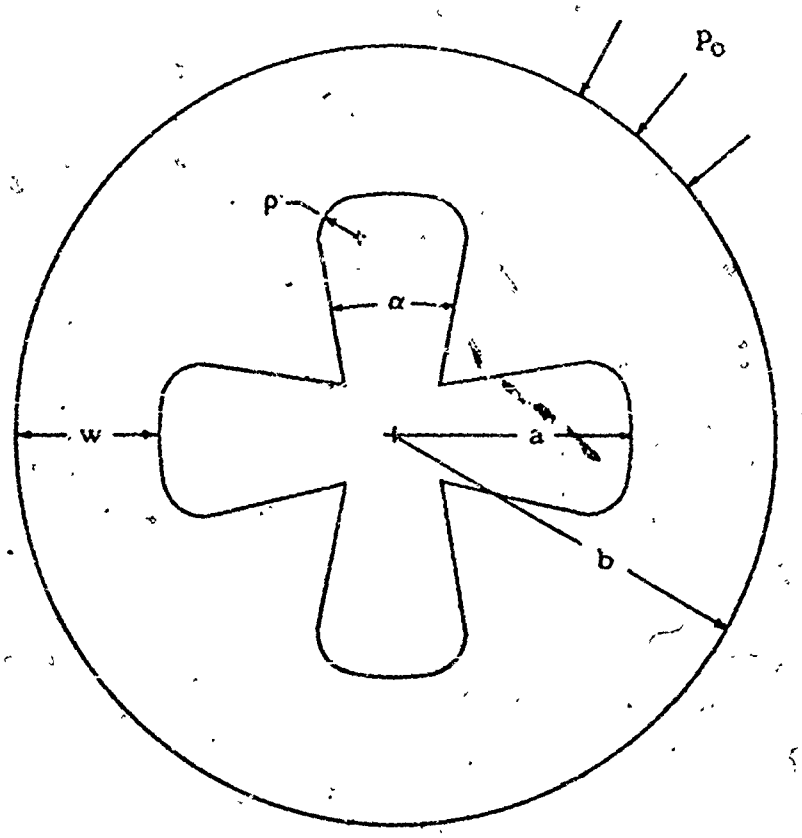

GEOMETRY OF TYPICAL CROSS SECTION

FOR POSITIVE WEDGE ANGLE TESTS

Figure D-18.

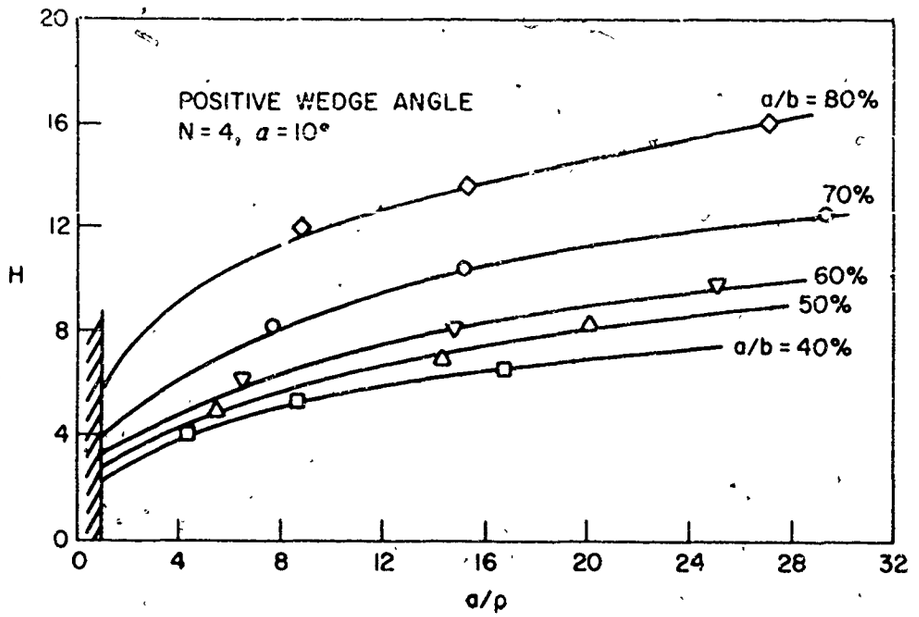

Figure D-19

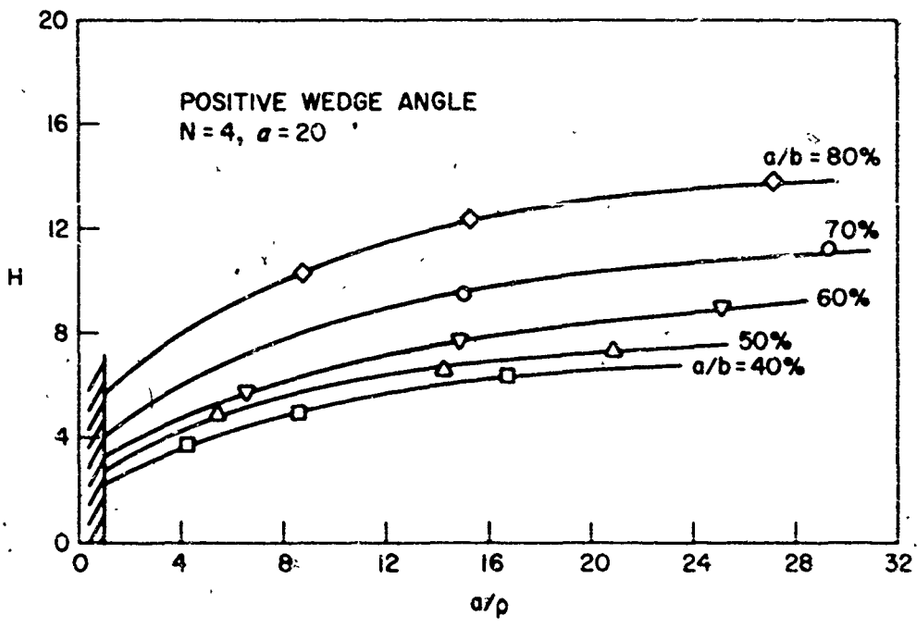

Figure D-20

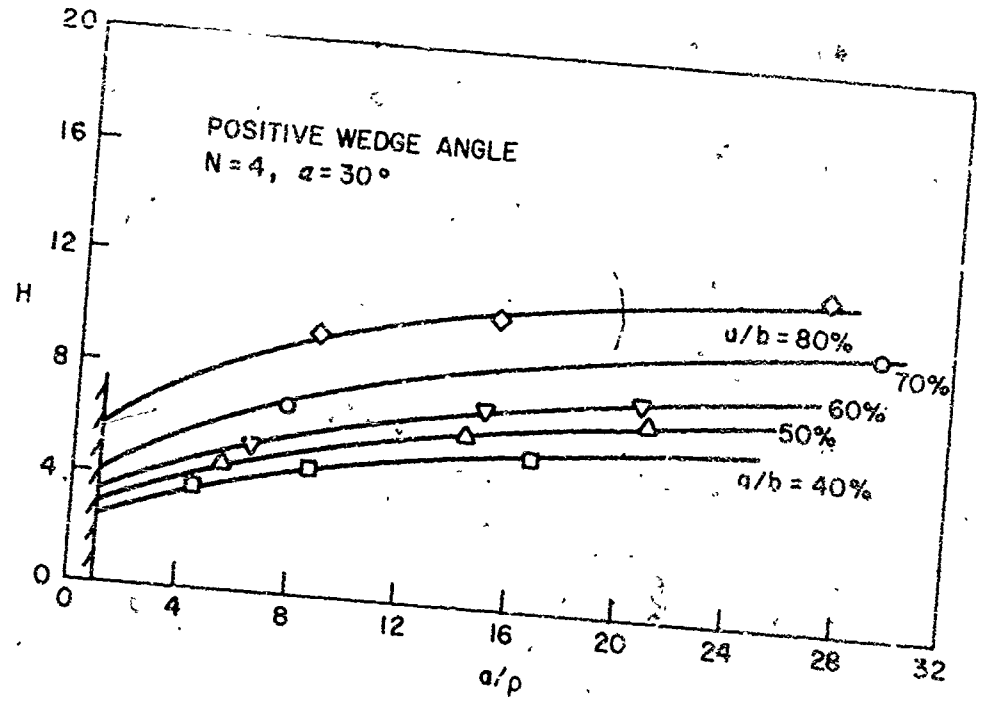

Figure D-21

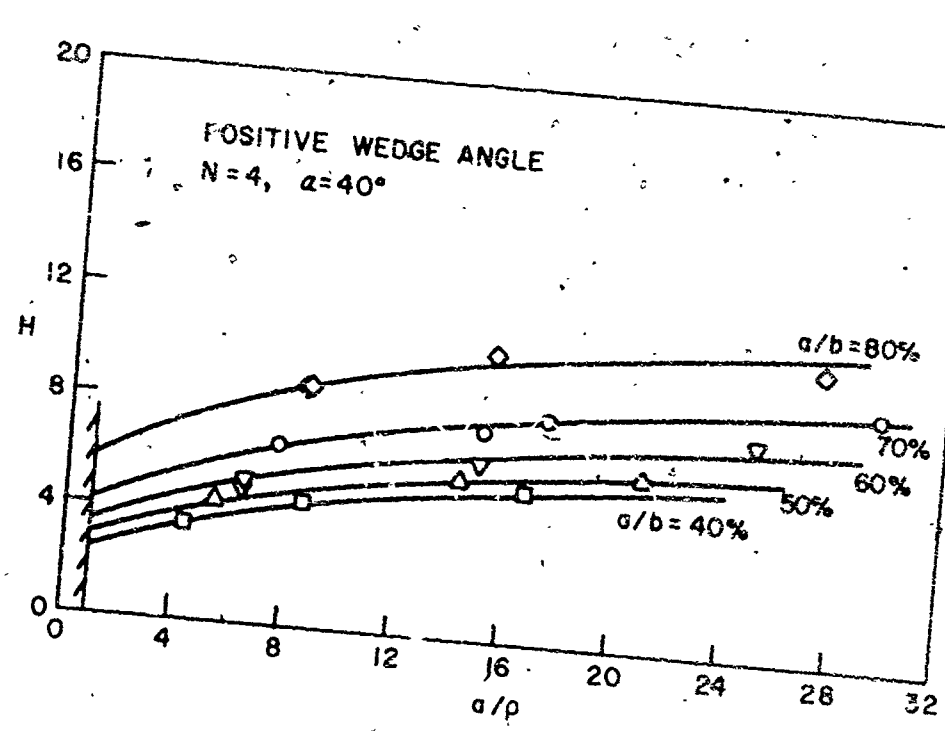

Figure D-22

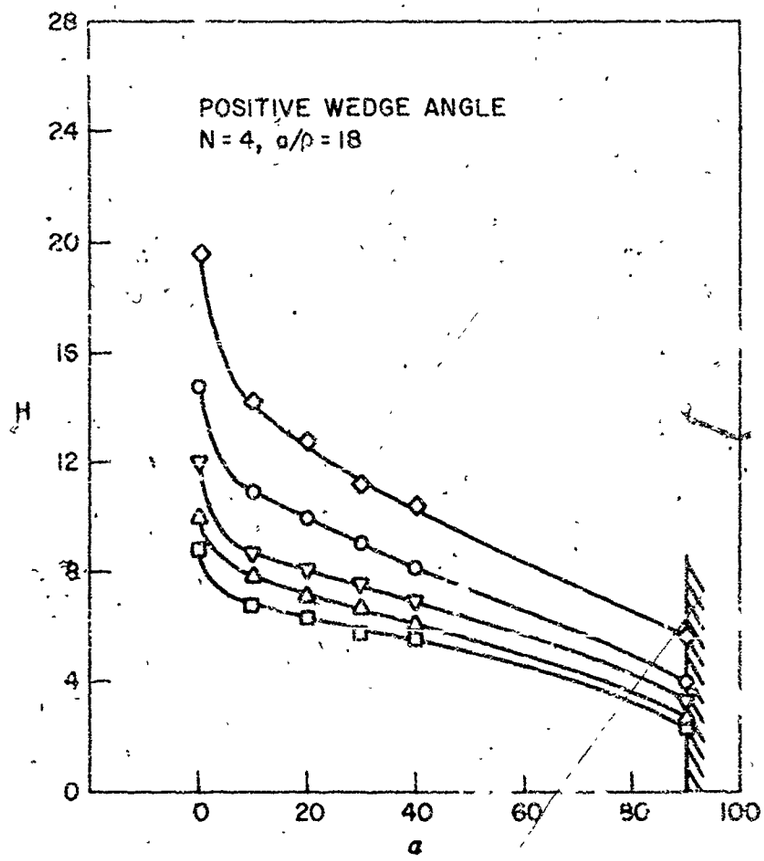
POSITIVE WEDGE ANGLE
N = 4, a/ρ = 18
H
a
0
4
8
12
16
20
24
28
0
20
40
60
80
100

Figure D-23

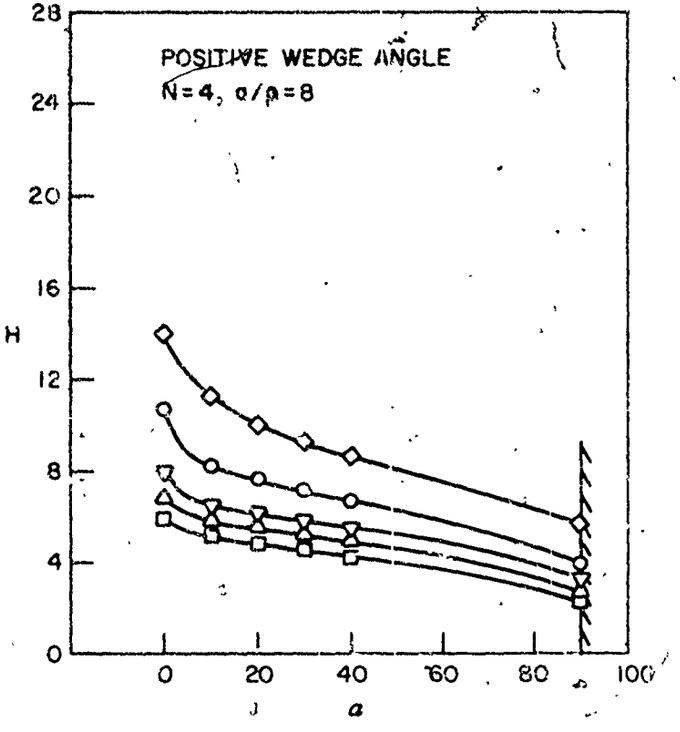

Figure D-24

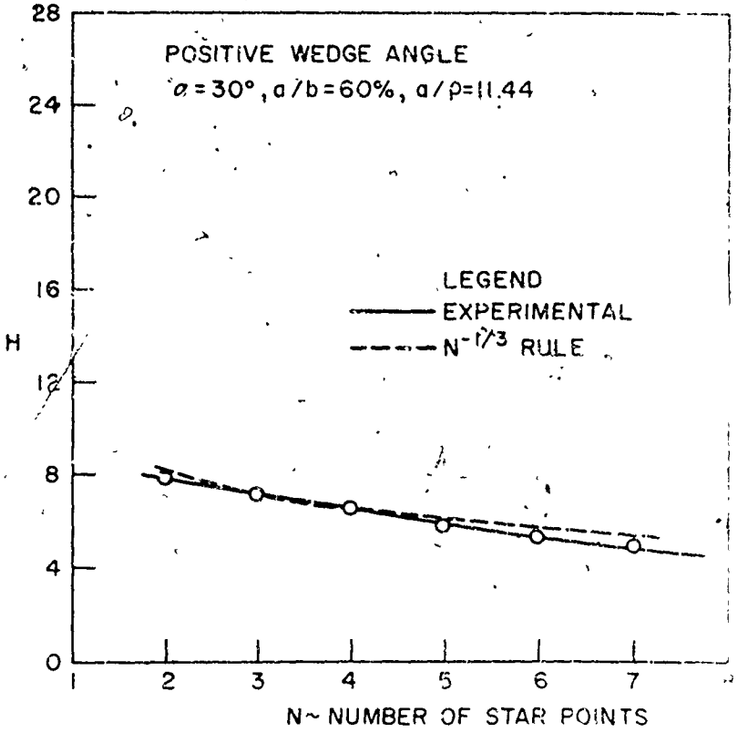

Figure D-25

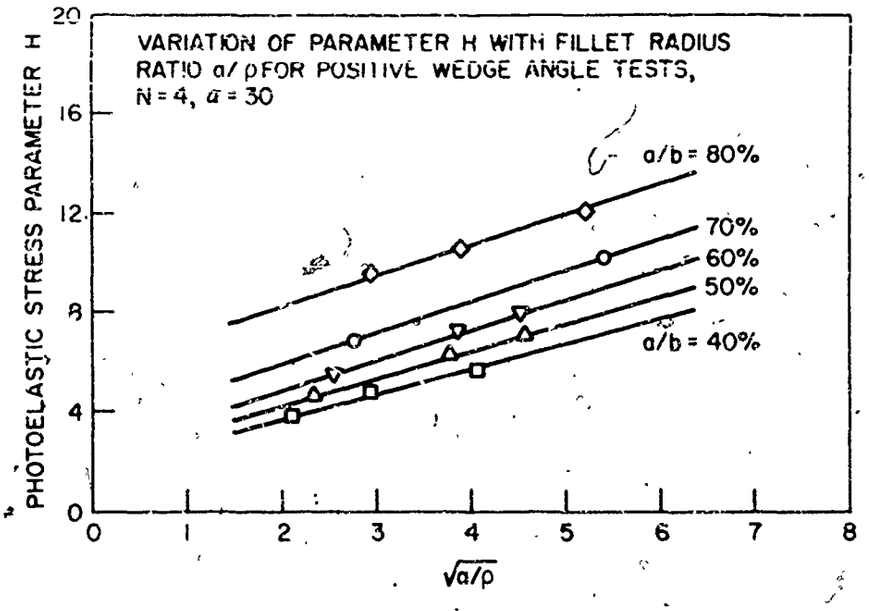

Figure D-26.

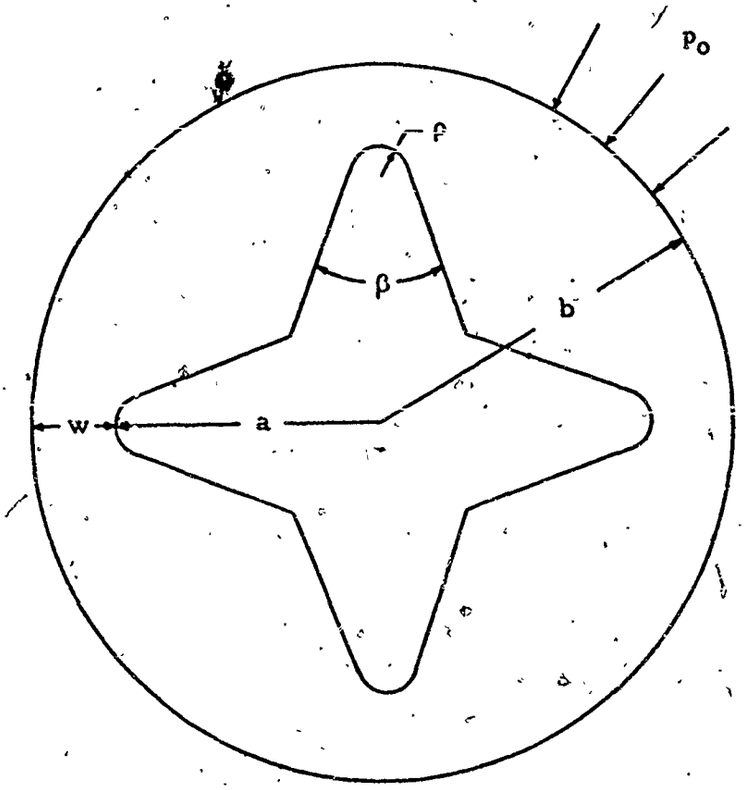

Figure D-27. GEOMETRY OF TYPICAL CROSS SECTION FOR NEGATIVE ANGLE TESTS.

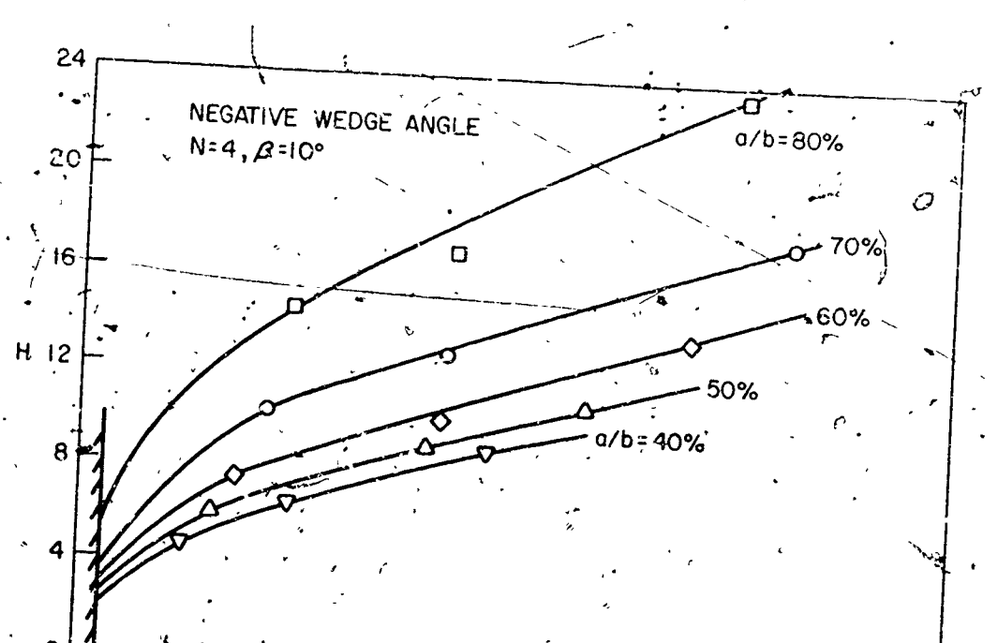

Figure D-28

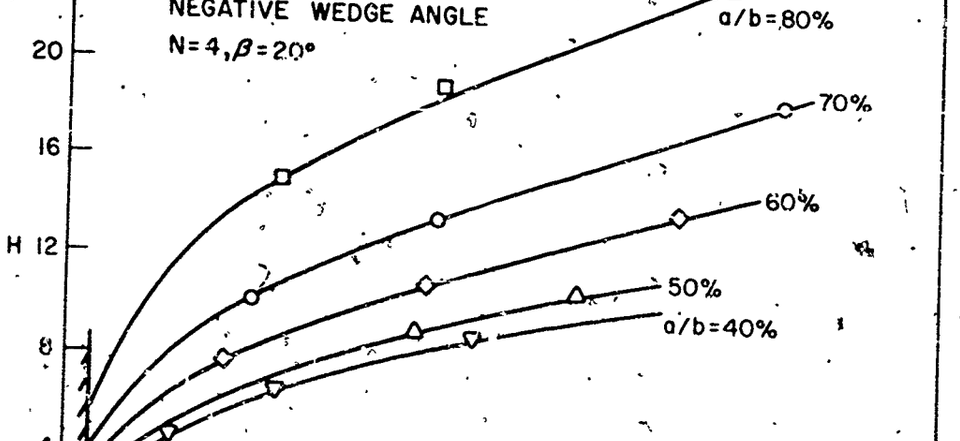

Figure D-29

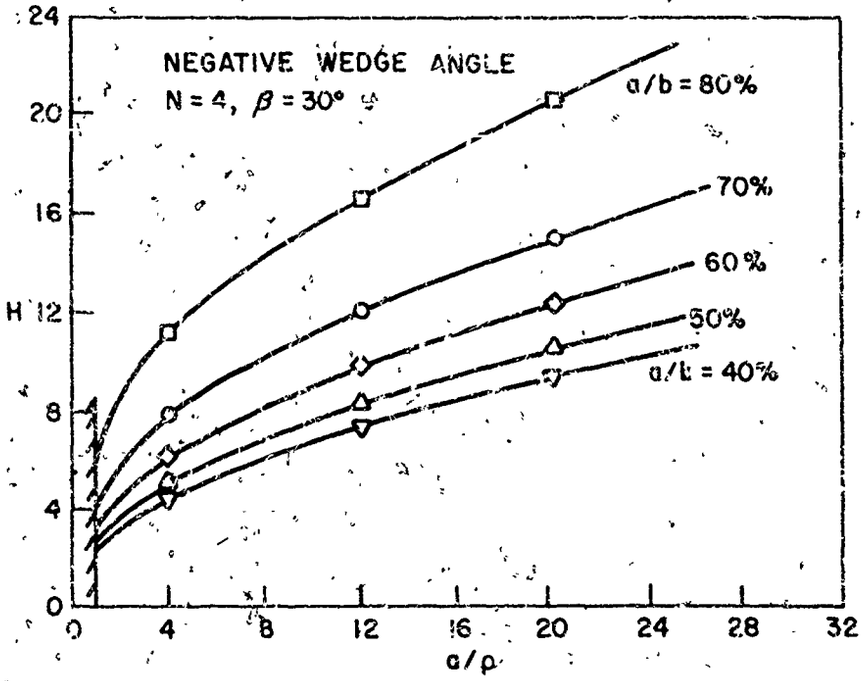

Figure D-30.

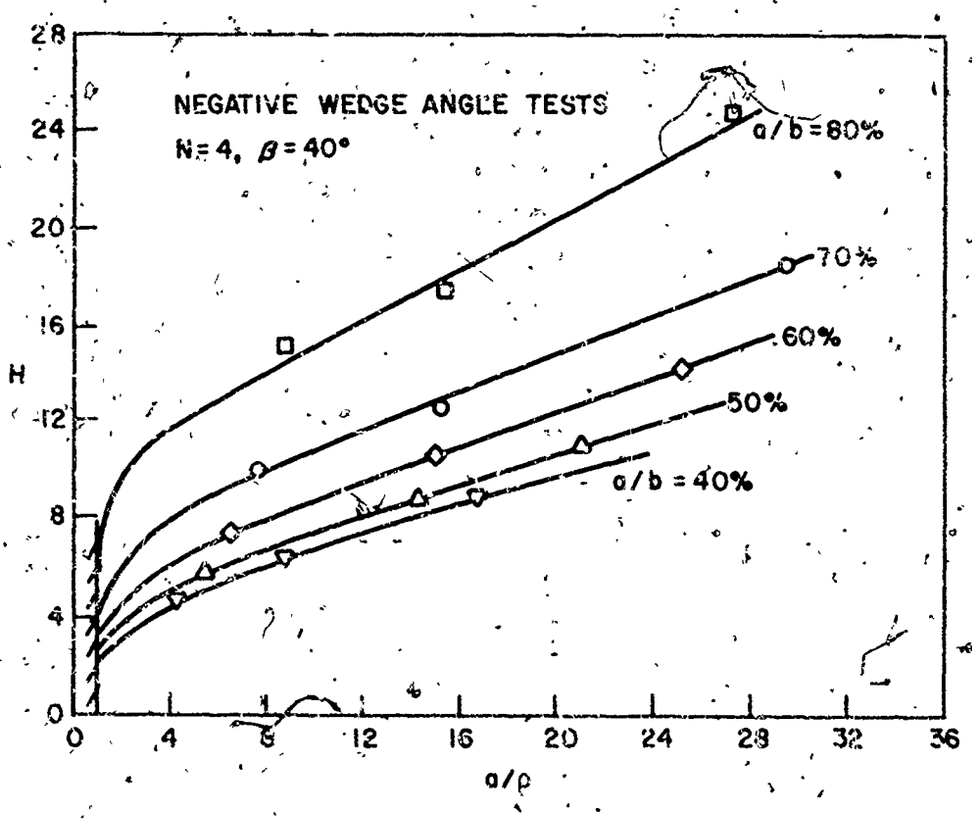

Figure D-31

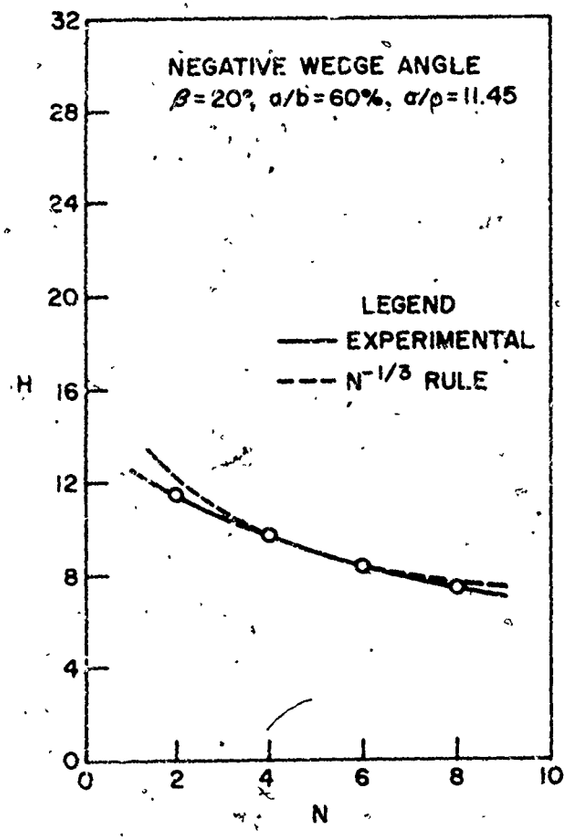

Figure D-32

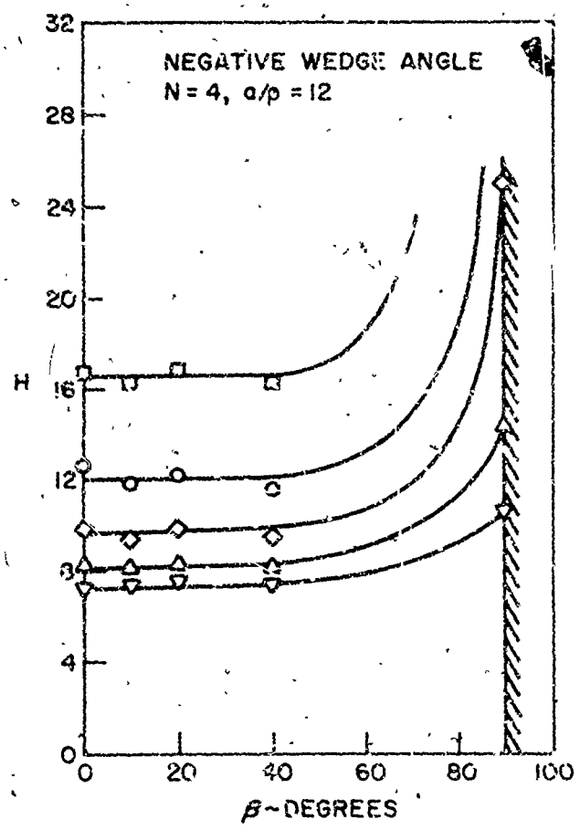

Figure D-33

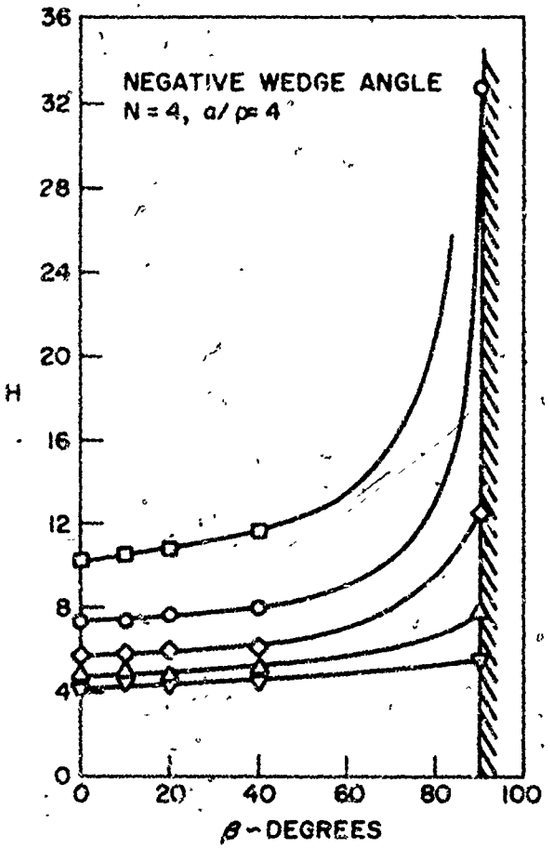

Figure D-34

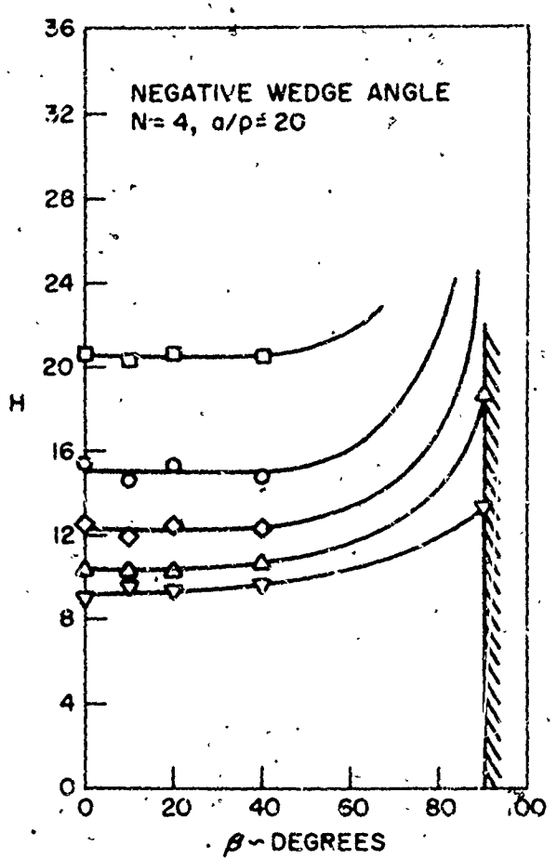

Figure D-35

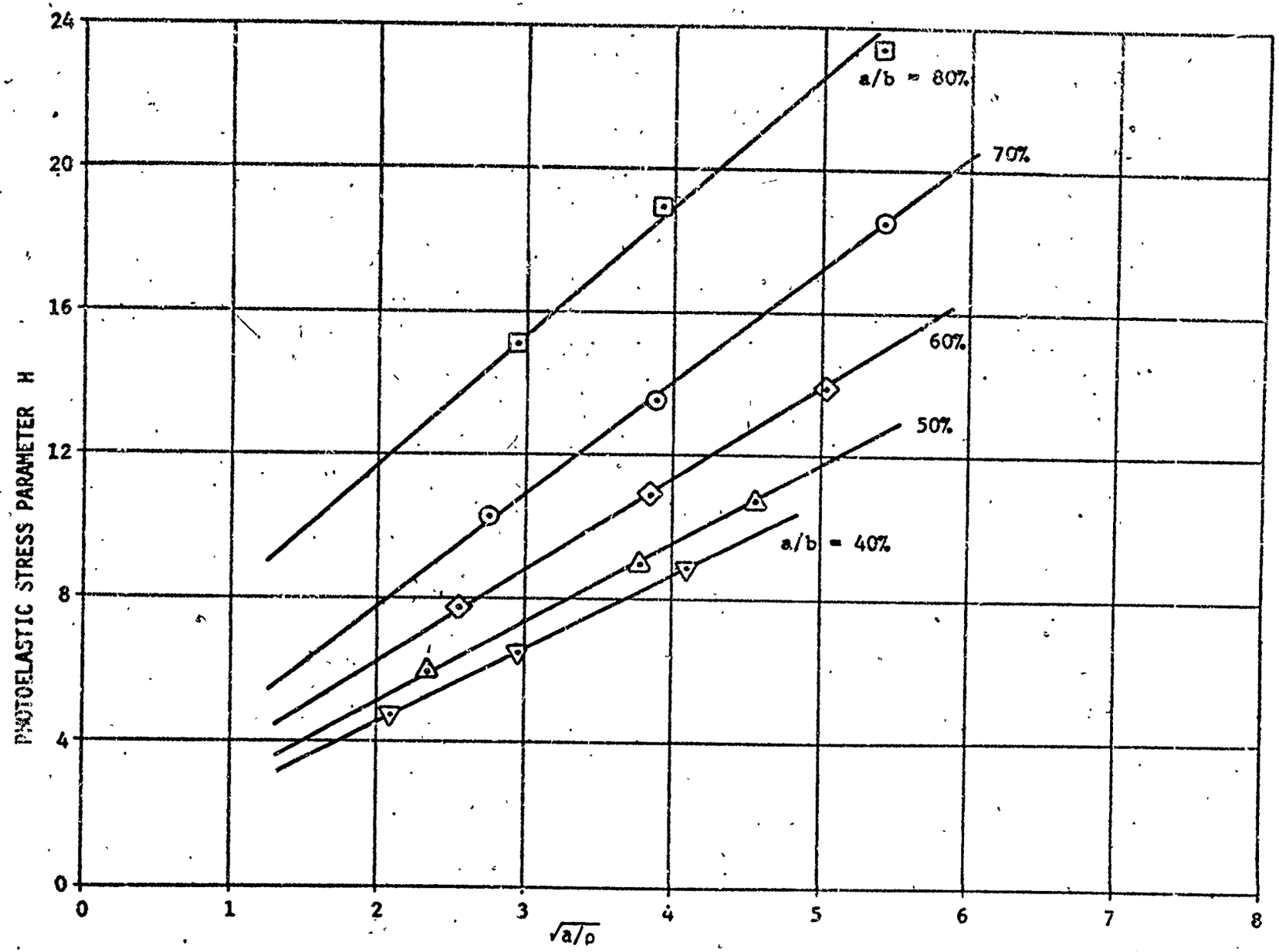

Figure D-36. Variation of Parameter H With Fillet Radius Ratio a/ρ For Negative Wedge Angle Tests, N = 4, β = 20.

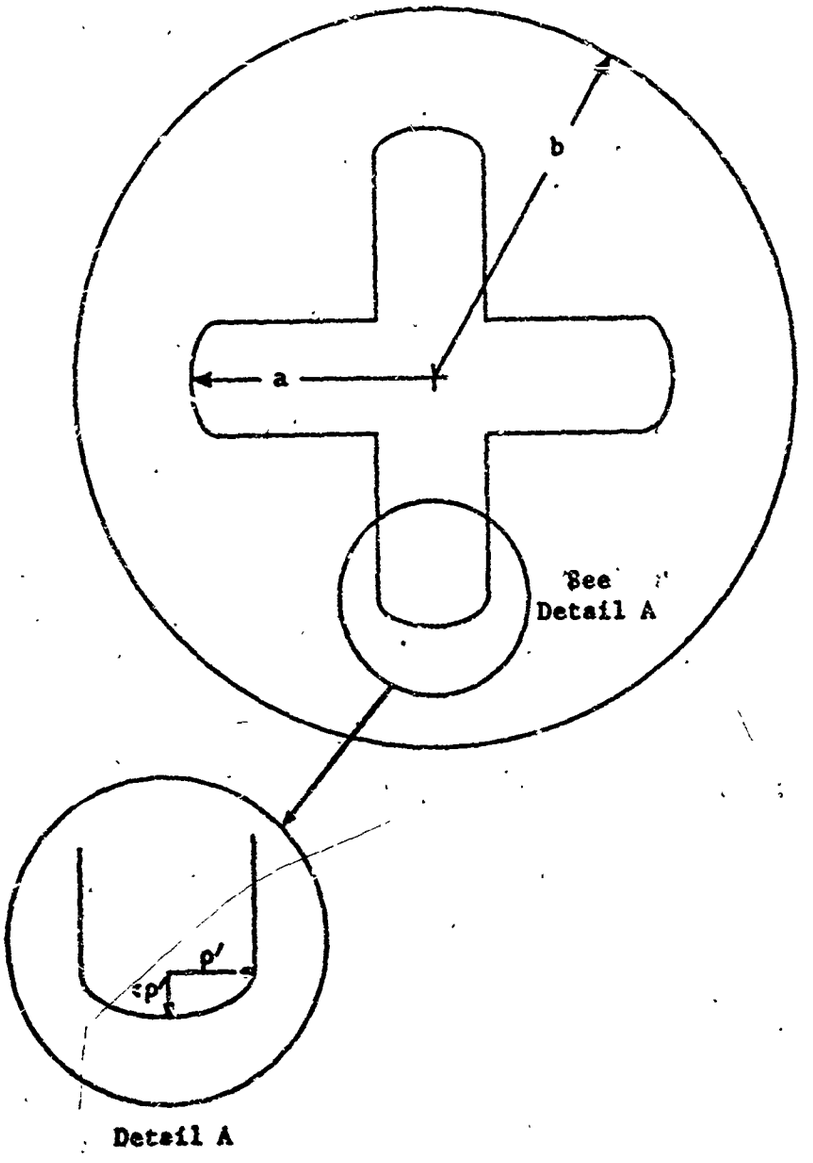

Figure D-37. GEOMETRY OF TYPICAL CROSS SECTION FOR ELLIPTICAL SLOT TIP TESTS

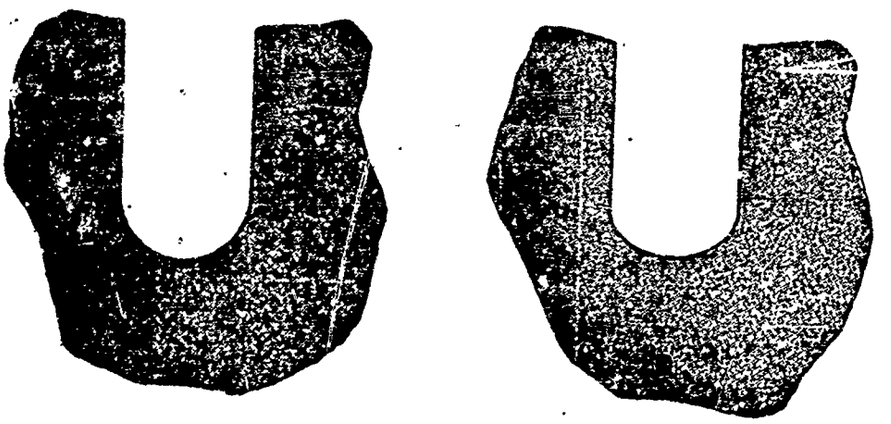

$\epsilon = 1.0, \quad 2\rho = 0.753$

$\epsilon = 0.8, \quad 2\rho = 0.753$

$\epsilon = 0.6, \quad 2\rho = 0.753$

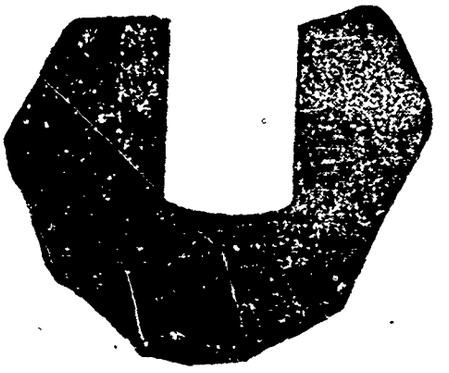

$\epsilon = 0.4, \quad 2\rho = 0.753$

Figure D-38. DETAIL OF ELLIPTICAL SLOT TIP GEOMETRY FOR VARIOUS ECCENTRICITIES

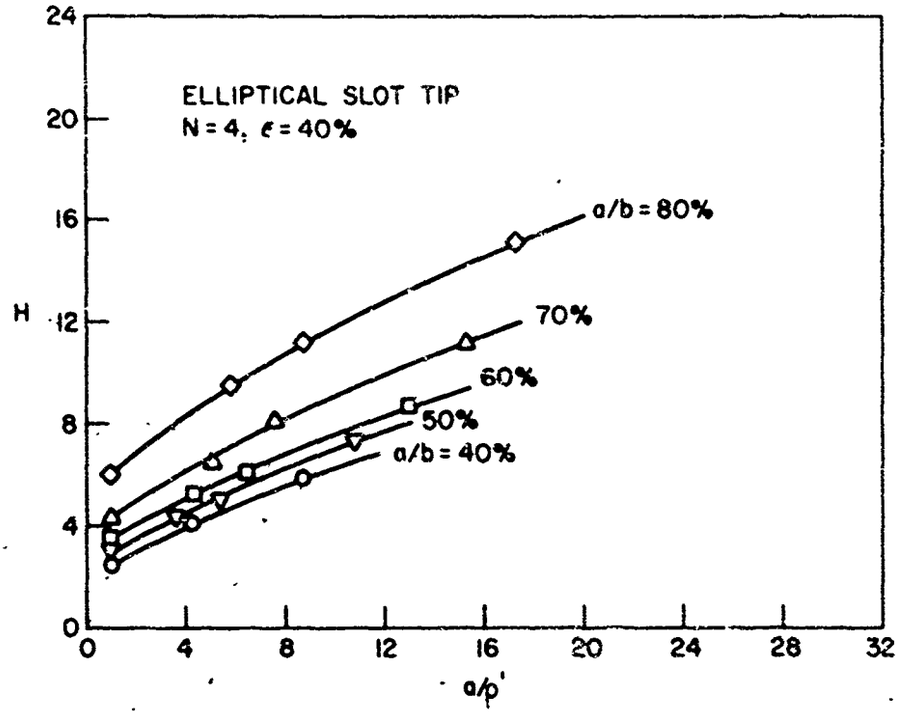

Figure D-39

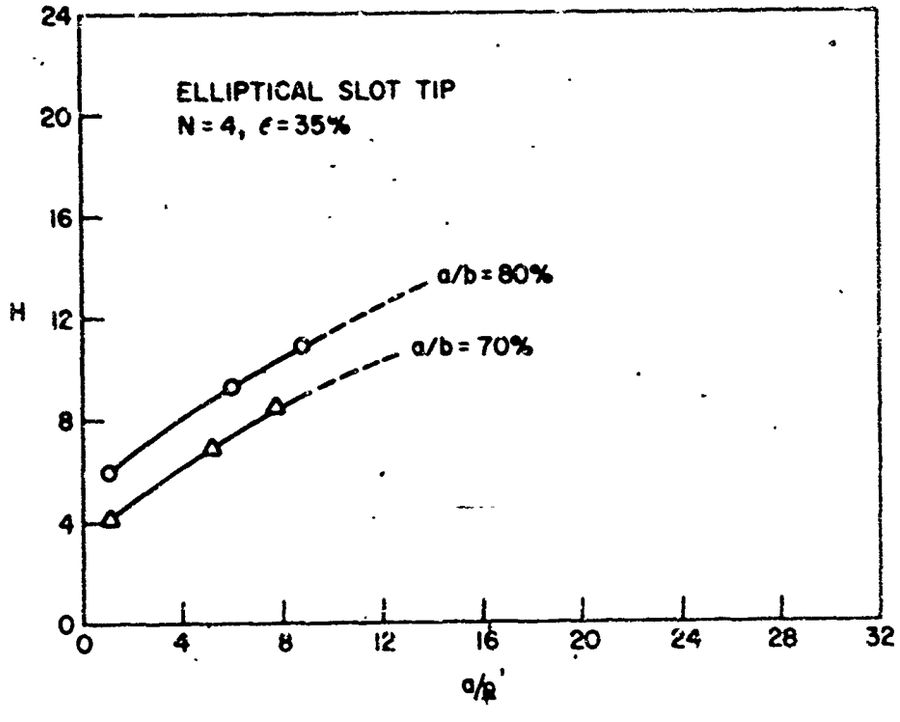

Figure D-40

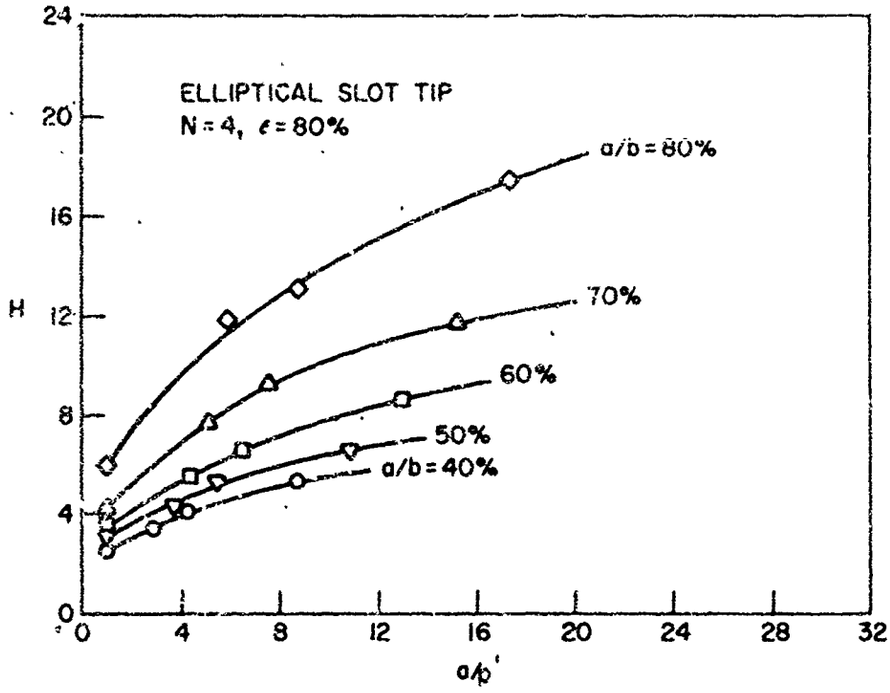

Figure D-41

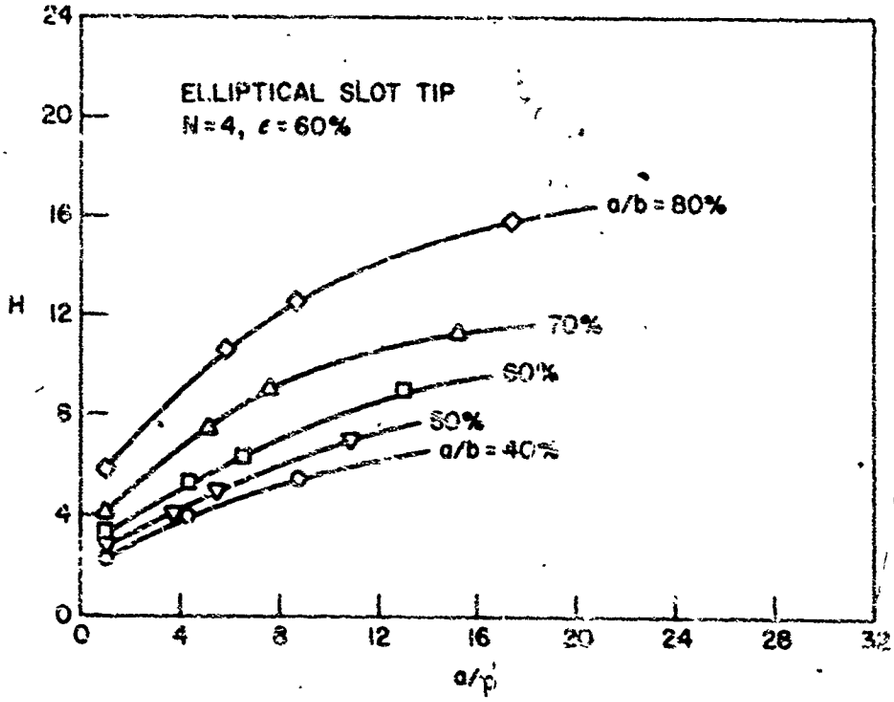

Figure D-42

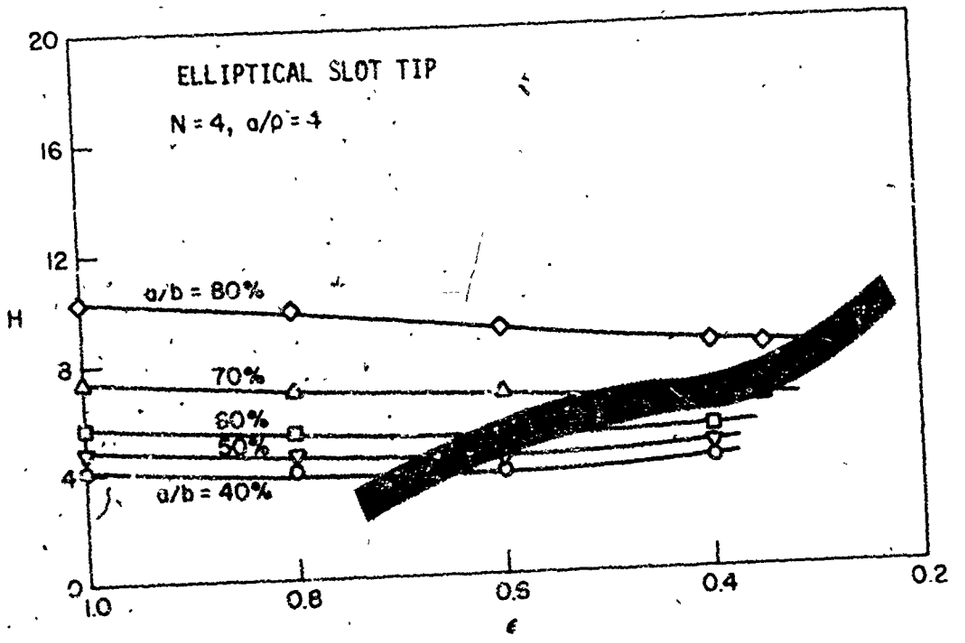

Figure D-43

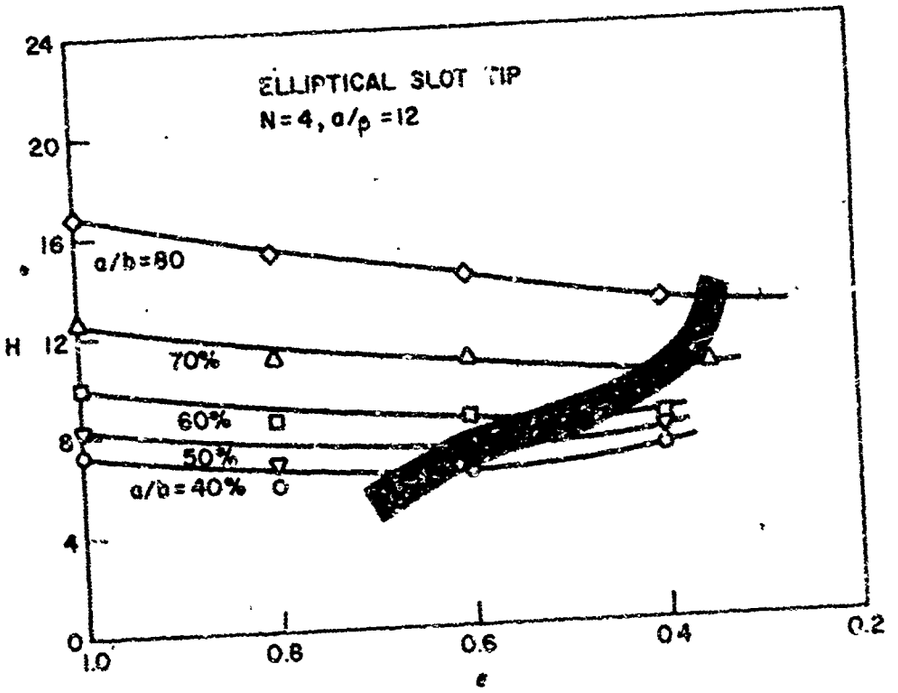

Figure D-44

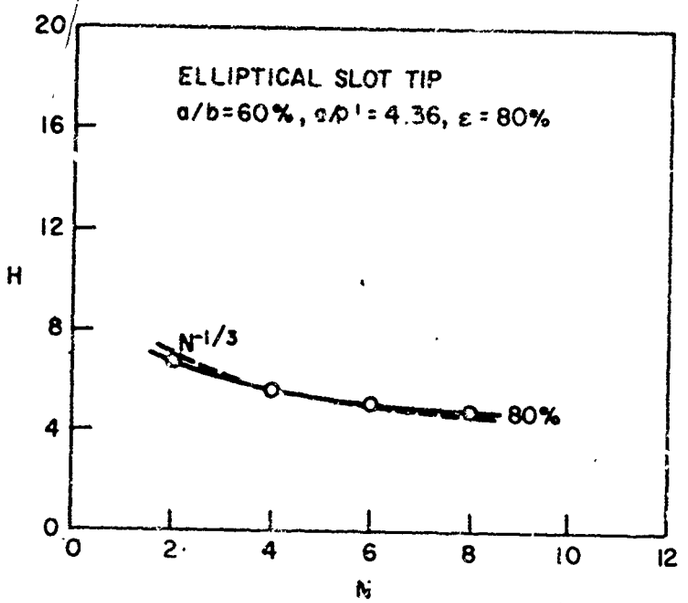
ELLIPTICAL SLOT TIP
a/b=60%, a/t = 4.36, ε = 80%
H
N
$N^{-1/3}$
80%
0
4
8
12
16
20
0
2
4
6
8
10
12

Figure D-45

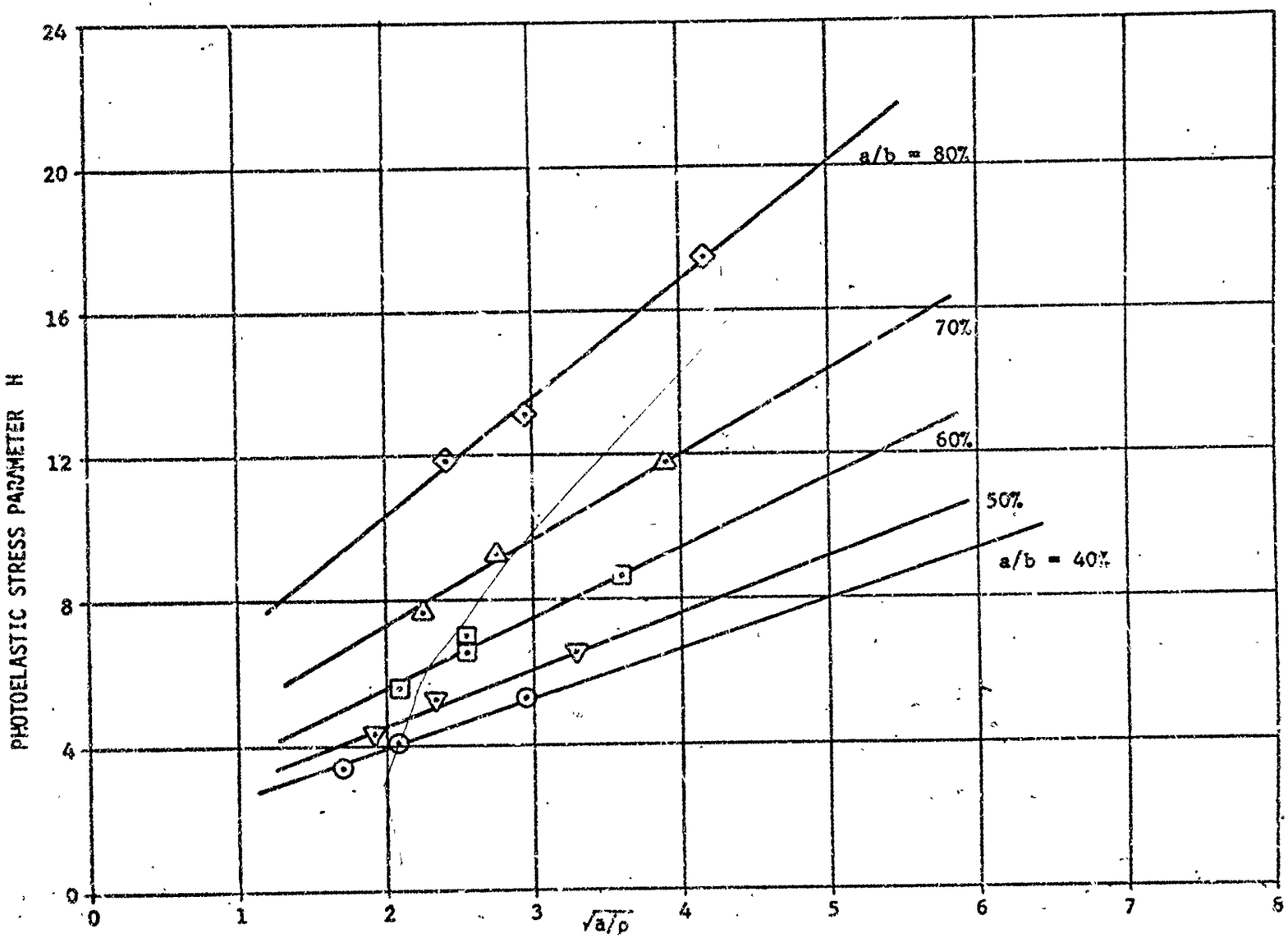

Figure D-46. Variation of Parameter H With Fillet Radius Ratio a/ρ For Elliptical Slot Tip Tests, N = 4, ε = 0.8.

APPENDIX E

SAMPLE MOTOR STRUCTURAL INTEGRITY ANALYSIS

FOREWORD

This appendix presents a sample rocket motor structural analysis to illustrate the use of the methods discussed in the handbook. Rather than attempt a complicated problem here, it was felt that more benefit would be derived by the novice designer/analyst from a relatively straightforward motor design. For this purpose, the feature article of Volume 4, November 3, of the Solid Rocket Structural Integrity Abstract, (UTEC SI-67-028, July 1967), "The Structural Design of a Large Solid Rocket Motor Grain", (UTEC SI-67-050) by Dr. Harold Leeming, is reprinted in its entirety herein.

THE STRUCTURAL DESIGN OF A LARGE SOLID ROCKET MOTOR GRAIN

by

H. Leeming
Lockheed Propulsion Company
Redlands, California

INTRODUCTION

The purpose of this article is to describe the methods used at Lockheed Propulsion Company to ensure the structural integrity of a large solid rocket motor (LSM). The analysis methods and experimental techniques described are, of course, used for all solid propellant structural analyses and their application to a specific design of rocket motor will serve to illustrate the approach. The particular LSM design described and analyzed in this article was successfully fired at LPC on 15 January 1965. It is a monolithic 156-inch diameter motor containing a circular port grain design, with a radial slot near the aft end to give an increased initial burning area and produce a satisfactory pressure-time record.

Most of the LSMs made to date have been multi-segment designs but they will not be considered in this article since the structural design of one segment is identical with that used for the monolithic LSM and the environmental loads encountered are the same.

Before structural analysis, ballistic parameters such as impulse, thrust and burn time, together with anticipated propellant burning rate have dictated a circular port geometry with an additional radial slot. Since at this early stage the grain dimensions are not precisely known, the structural analysis proceeds in two phases. Initially, only the most significant environmental loads are considered and a preliminary analysis is performed to ensure that the design is feasible and safety factors adequate.

During this phase, propellant and bond properties are estimated from relatively few tests performed on early development propellant batches. Once the feasibility of the design has been established and a propellant has been formulated, a large batch is cast for characterization of its physical properties and the second structural analysis phase is initiated. This comprises a detailed analysis of the specific grain design making use of numerical computer programs to ascertain, as accurately as possible, the maximum stresses and strains existing within the grain. These maxima are then compared to allowable propellant and bond system properties determined from the characterization propellant batch to determine safety factors. Design details such as the lengths of the boots or flaps are also investigated at this stage of the analysis.

When a very large motor is involved in which numerous batches of propellant are cast into a single grain, a further review of the analysis is required. Test data are obtained from each batch of propellant used in the LSM casting and statistical propellant physical properties are determined enabling a realistic assessment of the structural safety of the motor to be made, prior to firing.

Many assumptions and approximations are necessary in a structural analysis of any solid rocket motor. These will be discussed subsequently and a still later section will consider methods of improving the whole structural analysis procedure.

MOTOR DESIGN PARAMETERS

The particular motor design considered in this article is illustrated in Figure 1. It consists of a monolithic circular port grain with a radial slot at the aft end. The dimensions shown in the sketch are those adopted in the final motor design.

A summary of the key design parameters is given below:

Grain Length	L	=	288 inches
Grain Outer Diameter	2b	=	156 inches
Grain Inner Diameter	2a	=	55.7 inches
Case Wall Thickness	h	=	0.5 inches
Propellant Thermal Expansion Coefficient	α_p	=	4.4×10^{-5} inch/inch/°F
Case Thermal Expansion Coefficient	α_c	=	0.63×10^{-5} inch/inch/°F
Case Material Modulus	E_c	=	27×10^6 psi
Equivalent Propellant Modulus	E_p	=	(Various, see text)
Poisson's Ratio, Case Material	ν_c	=	0.3
Poisson's Ratio, Propellant	ν_p	=	0.5
Propellant Bulk Modulus	K_p	=	5×10^5 psi

Motor Operating Pressure	=	650 psi
Pressure Rise Time	=	0.406 seconds
Minimum Storage Temperature	=	40°F
Maximum Storage Temperature	=	100°F
Minimum Firing Temperature	=	60°F
Maximum Firing Temperature	=	100°F

Propellant

The propellant used in the LSM, designated LPC-580 is based on a polybutadiene-acrylic acid-acrylonitrile (PBAN) binder which contains 87 percent total solids content, by weight.

GRAIN ANALYSIS TECHNIQUES AND PROBLEM AREAS

The structural analysis of a propellant grain has become increasingly sophisticated in recent years. The use of large digital computers has enabled analyses to be made of complex grain shapes with reasonable accuracy. However, many assumptions are still inherent in the computer analyses and in the methods used to correlate experimental propellant physical properties with the parameters required in the analysis programs.

Almost all currently available computer programs are based on infinitesimal elastic theory with the assumption that the propellant, insulation and case materials are isotropic and homogeneous. These assumptions are for the most part valid for motor cases but not true for propellants and elastomeric insulation materials. These are known to exhibit properties which depend strongly on temperature and strain rate, which is typical of viscoelastic rather than elastic materials. The theory of linear viscoelasticity is commonly used to describe such behavior.

A further assumption frequently made is that propellant is incompressible with a Poisson's ratio of 0.5. This assumption is valid for the majority of propellants under loading conditions removed from failure. Many rubber based propellants containing large quantities of ammonium perchlorate and aluminum fillers exhibit filler-binder pullaway or dewetting when failure is approached. When dewetting occurs, the apparent volume of the propellant increases due to the production of minute voids so that the propellant is no longer incompressible and Poisson's ratio is much less than 0.5. However, with current analysis methods, the assumption of incompressible behavior enables one to adopt simplified analysis procedures.

In deriving physical properties from experimental test data for use in grain analyses, it is assumed that propellant is not only linearly viscoelastic but thermorheologically simple. This assumption which again is usually good at small strain levels enables data derived at one strain rate and temperature to be correlated with other different strain rate and isothermal data by means of the principle of time-temperature equivalence. Considerable experimental data at small strain levels, support the view that propellants are thermorheologically simple materials. A commonly used extrapolation of this principle is its application to failure data obtained at different strain rates and temperatures. By this means failure properties may be estimated and used in motor calculations for conditions which cannot be determined experimentally, e.g., failure under the very low strain rates (10^{-7} inch/inch/minute) obtained during thermal cooling of a large motor. A review of failure property determination will be given in a later section of this article.

The simplifying assumptions described briefly in this section enable grain stresses and strains to be calculated using only one intrinsic physical property parameter; the relaxation modulus of the propellant. From the relaxation modulus - reduced time curve, its associated shift factor - temperature curve and knowing the motor history, an equivalent modulus may be determined (References (1) and (2), and inserted in the grain analysis program.

It should be stressed that even if the grain analysis is carried out by means of simple equations derived from closed form analytical solutions, the aforementioned approximations and assumptions still have to be made. In fact, to arrive at a closed form solution it is usually necessary to simplify the equations even further by assuming, for example, either a plane strain or plane stress condition exists. Thus the problem is reduced in complexity from a three dimensional to a two dimensional stress state.

Since a detailed grain analysis program is both costly to run and time consuming to set up, the simpler equations are usually adopted during the preliminary design phases when ballistic and physical properties may interact causing many design changes before a final grain geometry is adopted.

Figure 2 illustrates the iterative approach which must be adopted in motor design. The motor specification describes the essential ballistic, geometric and environmental conditions which must be achieved. Using assumed ballistic and physical properties various design geometries are considered until a satisfactory compromise is achieved. During this phase, many small scale development propellant mixes are made and tested to tailor a formulation for the specific application. From these test data a final propellant formulation and design geometry are established. Large scale propellant batches are then cast for ballistic and physical property characterization.

A detailed design analysis is then performed using a computer program based on the specific design geometry and realistic safety factors are established to guarantee satisfactory motor operation.

PHYSICAL PROPERTY TESTING

In contrast to the early days of motor design analysis, characterization of the physical properties of a propellant requires an extensive program of tests designed to measure the uniaxial and biaxial response over a wide range of temperatures to simulate the stress-strain states existing at critical locations within a grain. Lockheed Propulsion Company adopts the experimental procedures described in the ICRPG Solid Propellant Mechanical Behavior Manual (3), whenever standardized test procedure exists. In the case of the strip biaxial, tension-tension tests, an agreed specimen type and test procedure is not yet available. The specimen and procedure adopted at LPC for this important test condition are described briefly in the text.

Test types conducted as part of a propellant characterization program are as follows:

1) Uniaxial stress relaxation tests using tab-end specimens over the environmental temperature range.

2) Uniaxial constant strain rate tests using JANAF specimens at a 2.0-inch/minute crosshead speed, over the environmental temperature range.

3) Strip biaxial, tension-tension tests at a 0.1-inch/minute crosshead speed, over the environmental temperature range.

4) Simple shear tests, using the chevron shear specimen at a crosshead speed of a 0.05-inch/minute over the environmental temperature range.

5) Diametral compression tests at a crosshead speed of 0.2-inch/minute over the required temperature range.

6) Bond-in-tension tests at a crosshead speed of 0.2-inch/minute over the required temperature range.

A brief description of the test samples, experimental results for the LSM propellant LPC-580, and the loading conditions to which the data are applied, are given next.

Uniaxial Stress Relaxation Tests

A sketch of a tab-ended uniaxial tensile specimen of the type used for stress relaxation testing is given in Figure 3. The specimen has a square cross section, constant across its whole length, and therefore the gage length is known very closely as 4.0-inches.

In stress relaxation tests, the tab-end tensile specimens are elongated to a strain level ε_o and the decay of stress in the specimen with time is observed. Tests are conducted at a series of temperatures spaced sufficiently close that an overlap exists between the 1000-second duration relaxation modulus curves as shown in Figure 4. The master stress relaxation versus reduced time curve and the logarithmic shift factor versus temperature curve are then obtained by translating the individual modulus curves horizontally along the log time axis to coincide with the 70°F relaxation modulus curve. Figure 5 shows the resulting master relaxation modulus curve and the shift factor curve log a_T versus temperature for LPC-580 propellant.

Uniaxial Constant Rate Tests

A sketch of a JANAF uniaxial tensile specimen is given in Figure 6. Such specimens are generally used to determine standard failure properties at a specified crosshead speed of 2.0-inch per minute. The failure point is most conveniently taken as the maximum in the load-time record, from which the stress at maximum load and the strain at maximum load are determined. Experimental failure data for LPC-580 propellant are shown in Figure 7 against a scale of temperature.

There is no state of uniaxial tension anywhere within a grain so that uniaxial tensile failure data are not used for design purposes. JANAF uniaxial test data are accepted industry-wide as a standard and are mainly used in comparative evaluations of different propellants.

Strip Biaxial, Tension-Tension Tests

A strip biaxial specimen shown schematically in Figure 8 consists of a filleted plate of propellant, with a width five times its height, bonded to rigid wooden supports along its width. The specimen is clamped along the wooden support members and elongated in a testing machine at a constant rate as shown in Figure 9. The direct force applied by the testing machine produces a stress σ in the direction of the force, i.e., along the length of the specimen. The restraint applied to the propellant by the wooden supports produces a secondary tensile stress equal to $\sigma/2$ (for an incompressible propellant) across the width of the specimen. The resulting stress-strain field closely approximates that occurring at the middle of the port of a long circular port grain. Thus, strip biaxial failure data is used as a measure of the capability of propellant at the ports of circular port or star center grains under thermal and axial acceleration loadings.

Ultimate true stress and strain curves for LPC-580C propellant tested in strip biaxial tests at a crosshead speed of 0.1-inch/minute are given in Figure 10. Typically, it is found that failure stresses are similar to uniaxial failure stresses, but failure strains are lower than those obtained in uniaxial tension.

Chevron Shear Tests

A sketch of the double lap Chevron shear specimen adopted at LPC is shown in Figure 11. Early experiments with square-ended specimens showed that it was necessary to cut the ends of the specimens to the 45° angle, producing the Chevron shape, to eliminate failure initiation at the highly stressed corners. In test, the shear specimen is rigidly clamped to a metal fixture restraining the deformation under load to simple shear Testing is carried out at a constant crosshead speed of 0.05-inch/minute and measurements are made of maximum shear stress and corresponding shear strain. Experimental data obtained with LPC-580 propellant are shown in Figure 12 as a function of temperature. Maximum shear stress and shear strain data are used as a motor failure criterion under conditions of axial acceleration.

Diametral Compression Tests

The diametral compression specimen, shown in Figure 13, consists of a thin circular disc of propellant, the diameter of which is three times its thickness. The specimen is tested by applying a load across a diameter in a testing machine at a constant crosshead speed as shown in Figure 14. The geometry of the specimen produces a tensile stress normal to the applied compressive stress at the center of the specimen. Failure occurs at the center of the specimen and either a tensile failure (vertical fracture) or a shear failure may be obtained.

Diametral compression failure data obtained with LPC-580 is shown in Figure 15. These data are used as a criterion of failure under pressurization conditions upon ignition and firing because the stress-strain state resembles that existing at the port of a long grain under pressurization loads (principal failure stress and strain are both tensile with a large normal compressive stress).

Bond-in-Tension Tests

The bond-in-tension test specimen is illustrated in Figure 16. Specimens are prepared by casting propellant into the steel cylinders onto end plates prepared with the insulation-liner substratum to be used in the LSM. After propellant cure they are tested in tension at a constant crosshead speed of 0.2-inch/minute over the temperature range of interest. The measured tensile strength at failure and the type of failure, e.g., adhesive, or cohesive in the propellant, are recorded to define the strength of the weakest component. Measured strength values lower than the failure stresses obtained in strip biaxial tests supersede the use of the strip failure data as the applicable failure criterion, when the failure is observed at a substrate interface (adhesive failure) in the bond-in-tension specimen.

The bond-in-tension failure strengths observed with LPC-580C propellant are shown in Figure 17. Cohesive failure was obtained so that the strip biaxial failure stress was retained as the critical failure criterion.

Additional Tests

In addition to the standard types of tests described so far, two additional experimental investigations were required because of the method of casting the LSM from numerous propellant batches, and because of the lack of controlled conditioning facilities for storage of the LSM prior to firing.

The first test series was designed to investigate the effects of an interruption to the casting schedule due to possible equipment failure. JANAF uniaxial tensile specimens were machined from cartons in which half the propellant had been put in place initially, and the remainder had been cast after a series of delays up to 48 hours. Half the cartons were coated with a layer of liner material prior to casting the second half of the propellant and the remaining cartons were untreated prior to the second casting of propellant. The cartons were maintained at the casting temperature 145°F before casting the second half of the propellant.

The failure stresses and strains resulting from this series of experiments are shown in Figure 18. It was determined that a casting delay of up to 24 hours could be tolerated with no detrimental effects. Furthermore, the data implied that the propellant surface need not be treated with liner prior to continuing casting operations.

In another series of experiments, JANAF tensile specimens were tested after exposure to 0, 30, 60, and 100 percent R.H. for periods of 7, 14, 28, 55, and 100 days. The results of these tests are shown in Figure 19 through 22. Examination of these curves shows that LPC-580 propellant shows no degradation in physical properties under 0 and 30 percent R.H. storage for 100 days. Exposure to 60 percent and 100 percent R.H. environment produces a marked loss in tensile strength which occurs most rapidly at the 100 percent R.H. storage condition. It was determined from these data that a maximum continuous storage humidity level of 30 percent R.H. could be tolerated by the LSM propellant.

PRELIMINARY GRAIN STRUCTURAL ANALYSIS

The equations for determining critical stresses and strains within the LSM and the means of calculating the propellant and bond system failure properties used during a preliminary structural analysis are given in detail in LPC Report No. 578/566-F-3 "Engineering Methods for Grain Structural Integrity Analysis" (Ref. 4).

The following loading conditions were investigated during this analysis phase:

1. Storage at a uniform temperature of 40°F.
2. Firing at 60°F temperature.
3. Slump and shear stresses under vertical storage conditions at 100°F.
4. Transportation with maximum loading of 3g, 10 cps sinusoidal, at 100°F.

The environmental loading conditions are first examined separately in this section and later, safety factors are determined using the linear cumulative damage concept (Ref. 5 and 6).

Thermal Storage at 40°F

Under thermal equilibrium conditions, the thermal hoop strain ϵ_θ (a), at the port is given by:

$$\epsilon_\theta(a) = \log_e (1 + \frac{3}{2} \alpha_R \lambda^2 \bar{F} K_t \Delta T) \quad (1)$$

where $$\alpha_R = \alpha_P - \frac{1 + \nu_c}{1 + \nu_p} \alpha_c \quad (2)$$

α_p = propellant linear coefficient of thermal expansion

α_c = case linear coefficient of thermal expansion

ν_c = Poisson's ratio of the case material

and

ν_p = Poisson's ratio of the propellant

λ = ratio of grain O.D. to grain I.D.

ΔT = temperature decrement below zero stress/strain temperature

K_t = star valley stress/strain concentration factor (equal to one for a cylindrical port grain)

$\bar{F}$ = Parr correction factor for finite lenth grain

The value of ΔT is measured from an equivalent stress and strain free temperature T_i which is higher than the curve temperature (145°F) because of shrinkage of the propellant during cure. A value of T_i = 160°F has been determined experimentally for PBAN propellants of the LPC-580 type cured at 145°F, and this figure has been adopted in the analysis.

The values of the constants used in the LSM analysis are given above, from which

$$\alpha_R = 4.4 \times 10^{-5} - \frac{1 + 0.3}{1 + 0.5} \times 0.63 \times 10^{-5} \qquad \text{From (2)}$$

$$= 4.4 \times 10^{-5} - 0.546 \times 10^{-5}$$

$$= 3.85 \times 10^{-5} \text{ inch/inch/°F}$$

$$\lambda = b/a = 156/55.7 = 2.8$$

$$L/D = 288/56 = 1.85$$

Thus $\bar{F} = 0.73$

$$\epsilon_\theta(a) = \log_e \left\{ 1 + 1.5 \times 3.85 \times 10^{-5} \times 7.84 \times .73 \Delta T \right\} \qquad \text{From (1)}$$

$$= \log_e \left\{ 1 + .000331 \ \Delta T \right\}$$

for T = 60°F , ΔT = 100 and

$$\epsilon_\theta(a) = \log_e 1.0331 = 3.27\%$$

for T = 40°F , ΔT = 120 and

$$\epsilon_\theta(a) = \log_e 1.0398 = 3.9\%$$

Under thermal equilibrium conditions, the maximum bond stress at the propellant-case interface is given by

$$\sigma_{(b)} = \frac{2}{3} \alpha_R E_p K_p (\lambda^2 - 1) \Delta T \qquad (3)$$

where

K_p is the stress concentration factor at the case/grain termination, taken equal to 2.0, and E_p is the equivalent elastic modulus of the propellant at the end of cooldown. To determine E_p, a cooldown time of 80,000 minutes (56 days) was used based on experience gained during earlier LSM manufacture at LPC. Although this cooldown time is insufficient to arrive at a nearly uniform grain temperature distribution as discussed by Fitzgerals in Ref. 7.

The equivalent modulus is obtained from the equation

$$E_{eq} = \frac{1}{t} \int_0^t E_{rel} (\psi - \psi^*) \frac{d\epsilon}{d\tau} \, d\tau$$

where $$\psi = \int_0^t \frac{d\tau}{a_T}$$

A method of determining an exact viscoelastic solution to this equation is given in Ref. (2). For many materials including propellants, an acceptable equivalent modulus may be defined by

$$E_{eq} = E_{rel} (t/a_T)$$

and this equation is frequently adopted at LPC to arrive at quasi viscoelastic solutions. For LPC-580 propellant when $t = 8 \times 10^4$ minutes $= 4.8 \times 10^6$ seconds and $T = 60°F$, from Figure 5, $\log a_T = 0.25$. Hence $\log_{10} t/a_T = 6.68 - 0.25 = 6.43$ and the value of the relaxation modulus E_{eq} at $\log t = 6.43$ seconds is estimated to be 110 psi.

Thus $\sigma_r(b) = \frac{2}{3} \times 3.85 \times 10^{-5} \times 110 \times 2\,(7.84-1) \times 100$ From (3)

$= 3.9$ psi

When T = 40°F, log a_T = 1.0 and log t/a_T = 5.68

Thus E_{eq} = 130 psi and

$\sigma_r(b) = \frac{2}{3} \times 3.85 \times 10^{-5} \times 130 \times 2\,(7.84-1) \times 120$ From (3)

$= 5.5$ psi

Determination of Allowable Failure Stress and Strain

The methods for determining allowable stress and strain values from the experimental data are fully described in Ref. (4). However, as an illustration, the limiting thermal strain at the port of the motor and the limiting bond stress at the case-propellant interface will be determined.

The relevant failure data are the strip-biaxial tension-tension obtained experimentally at a strain rate of 0.067-inch/inch/minute. Making the assumption that the strain rate during cooling is a constant, we find that the port hoop strain rate = $\frac{3.9}{100 \times 8 \times 10^4}$ inch/inch/minute $\approx 5 \times 10^{-7}$ inch/inch/minute.

It is required therefore to determine the strip biaxial failure stress and strain at this low thermal cooling strain rate. Strain rate-temperature equivalence shows that testing at a low strain rate at 70°F is equivalent to testing at the normal strain rate but at a high temperature. The temperature shift may be determined from the log a_T versus temperature curve, Figure 5, using the strain rate ratio $R_c/R_T = 5 \times 10^{-7}/0.067 = 7.5 \times 10^{-6}$ giving a log shift factor = $\log_{10} 7.5 \times 10^{-6} = -5.125$. The allowable failure stress and strain is obtained therefore by determining the temperature equivalent to a log a_T shift of -5.125 from the starting temperature, 40°F, (initial shift factor = 1.0) and taking the failure stress and strain values at this temperature. For example, the temperature equivalent to a shift log a_T value of -5.125 + 1.0 = -4.125 is 190°F; the strip biaxial failure strain at this temperature is 13.5 percent and the failure stress is 36.0 psi. Assuming that statistical data are not available at this time to give lower 2σ failure values, values of 80 percent of the measured stresses and strains may be used, based on considerable data with similar propellants. Therefore the lower 2σ strip biaxial failure strain = 0.8 x 13.5 = 10.8 percent and the lower 2σ failure stress = 0.8 x 36 = 29.0 psi. Thus the strain damage increment D_ϵ due to storage at 40°F and defined by the ratio, calculated stress or strain / allowable stress

or strain, is equal to $\frac{3.9}{10.8}$ = 0.36 and the bond stress damage increment D is equal to $\frac{5.5}{29.0}$ = 0.19. Thus for the storage alone, the thermal port hoop strain safety factor is given by $\frac{1}{D}$ = $\frac{1}{0.36}$ = 2.8 and the interface bond stress safety factor = $\frac{1}{0.17}$ = 5.9.

Pressurization on Ignition

Ignition of the motor produces a pressurization port hoop strain additional to that obtained during thermal cooldown to firing temperature. Assuming a finite propellant compressibility and free or stress-relieved ends to the grain, the following expression gives the critical hoop pressurization strain $\epsilon_{\theta p}$ (a) occurring during ignition at the grain port:

$$\epsilon_{\theta p}(a) = \frac{3.4 h \lambda^2 P_i K}{E_c (3 + \lambda^2)} + \frac{(\lambda^2 - 1)}{2} \left(\frac{P_i}{K}\right) \qquad (4)$$

where P_i = MEOP psi

h = case wall thickness-inches

E_c = case material modulus

K = propellant bulk modulus

and the other symbols have the meaning previously assigned them. (A finite bulk modulus, K, is used in this expression since the change in propellant volume under high pressures can produce significant increases in hoop strains in some motor designs).

Hence, $\epsilon_{\theta p}(a)$ = $\frac{3.4 \times 78 \times 7.84 \times 650 \times 1}{0.5 \times 27 \times 10^6 \times (3 \times 7.84)} \left(\frac{7.84 - 1}{2}\right) \left(\frac{650}{5 \times 10^5}\right)$ from (4)

= 0.92 + 0.435 %

= 1.36%

The allowable port hoop strain is determined in a similar manner to that illustrated for thermal cooldown but in this case, the applicable failure data are those determined in the diametral compression test. Assuming again a uniform strain rate during ignition, the mean strain rate is given by

ε (p) (a)/ pressure rise time = $\frac{1.36 \times 60}{100 \times .406}$ inch/inch/minute = 2.0 inch/inch/minute. Since the test strain rate is equal to 0.067 inch/inch/min., the strain rate ratio = 2.0/.067 = 30, giving a log shift factor of $\approx$ 1.48. The equivalent temperature for the ignition rate of strain for firing at 60°F is found from Figure 5 to be 25°F. The measured failure strain from Figure 15 is therefore 28.0 percent giving an estimated lower 2σ value of 28 x 0.8 = 22.4 percent. The damage increment sustained under pressurization loading is given by 1.36/22.4 = 0.061.

Using the linear cumulative damage concept, the safety factor under pressurization after cooldown to 60°F may be evaluated as follows. If D_T is the damage increment due to thermal cooldown and D_p is that increment sustained under pressurization then total damage sustained = $\Sigma D_i = D_T + D_p$ and safety factor = $\frac{1}{\Sigma D_i} = \frac{1}{D_T + D_p}$

For the LSM, the strain damage at the port is then

$$D_{TOT} = \frac{3.27}{10.8} + 0.061 = 0.302 + 0.061$$

$$= 0.363$$

and the firing safety factor at 60°F is equal to $\frac{1}{0.363} = 2.76$

A safety factor is not calculated here for firing at 100°F but Figure 23 shows the relationship between thermal and pressurization hoop strain requirements at the LSM port and the allowable lower 2σ failure strains for these conditions against a base of temperature. Safety factors for firing at the various temperatures are also plotted showing the reduction in safety factor with lower operating temperature. At a temperature of -45°F, the firing safety factor is calculated to be 1.0 and theoretically, the motor should fire satisfactorily at this temperature. It is common practice to include a minimum safety factor of 1.5 in the design calculations making the lower safe firing temperature equal to -30°F.

Slump and Shear Stresses Under Vertical Storage at 100°F

The radial and axial defections of a grain under vertical storage conditions are given by the equation

$$U_{r,z} = (\overset{*}{P}) \frac{\rho n g b^2}{E(\tau)} \qquad (5)$$

where $\overset{*}{P}$ = a constant determined from Figures D-10 through D-14, Ref. (1)

ρ = propellant density lb/in^3

ng = acceleration in gravities

$E_{(\tau)}$ = equivalent elastic modulus at time considered

From the reference curves for a free-free ended grain $\overset{*}{P}$ = 0.48 for axial displacement U_z, and = 0.13 for radial displacement U_r.

The value of $E_{(\tau)}$ = 80 psi may be estimated from Figure 5 using a storage period of three months $\approx 8 \times 10^6$ seconds and a log a_T of -0.5 corresponding to a 100°F storage temperature.

Thus $U_z = \frac{0.48 \times 0.064 \times 1 \times 78^2}{80}$ from (5)

$= 2.34$ inches

and $U_r = \frac{0.13 \times 0.064 \times 1 \times 78^2}{80}$ from (5)

$= 0.64$ inch

The additional hoop strain at the bottom end of the port due to vertical storage is calculated to be $\frac{0.64}{27.85} \times 100 = 2.3$ percent. Fortunately this strain occurs at the end of the grain where the hoop strain due to thermal cooling is zero, or slightly compressive and the additional hoop strain due to vertical storage does not produce a critical condition.

The propellant-case interfacial shear stresses under vertical storage conditions may be calculated from the equation

$$\tau_z(b) = \frac{ngb\rho K_b}{2}\left(\frac{\lambda^2-1}{\lambda^2}\right) \qquad (6)$$

where all the terms have been defined.

Substituting $K_b = 2.0$ one has then from equation (6)

$$\tau_z(b) = \frac{1 \times 78 \times 0.064 \times 2}{2}\left(\frac{7.84 - 1}{7.84}\right)$$

$$= 4.35 \text{ psi}$$

Measured shear failure data under constant load conditions are the correct values to compare with this storage shear stress. Since these data were not available, an estimate of the probable minimum failure shear stress was made from the curve given in Figure 12. A minimum value of 30 psi was taken which implies a lower 2σ failure stress of 27.0 psi giving a shear stress safety factor of 27/4.35 = 6.2.

Transportation Stresses at 100°F

The same equation given for vertical storage may be used to determine the maximum shear stress under a 3g sinusoidal acceleration transportation load, as the motor was transported in the vertical condition.

hence $$\tau_z(b) = \frac{ngb\rho K_b}{2}\left(\frac{\lambda^2-1}{\lambda^2}\right)$$

and $$\tau_z(b) = \frac{3 \times 78 \times 0.064 \times 2}{2}\left(\frac{7.84 - 1}{7.84}\right)$$

$$= 13.0 \text{ psi}$$

To determine a mean strain rate, an equivalent modulus is calculated using Schapery's approximation (Ref. 8) that frequency and time are related by the equation $\omega \approx 1/2t$. For a frequency of 10 cps = 63 radians/second the equivalent time = 1/126 = .008 second. Thus, log t/a_T = -1.1, and the modulus value from Figure 5 is found to be 700 psi. The dynamic strain level corresponding to 13.0 psi stress is then 1.85 percent and the mean strain rate is approximately = $\frac{1.85 \times 60}{100 \times 0.1 \times 0.25} \approx 45$ inch/inch/minute.

The allowable failure stress is determined from Figure 12 using the strain rate ratio of 45/0.067 = 670, giving a log shift of 2.83 from the value at 100°F, -0.5.

The temperature corresponding to the high strain rate at 100°F is therefore 15°F and the measured shear failure stress is then 150 psi. The lower 2σ allowable shear stress is therefore 0.8 x 150 = 120 psi giving a safety factor under the 3g transportation vibration of $\frac{120}{13.0}$ = 9.2. The higher safety factor when compared to the static case is due to the higher failure strength of the propellant under dynamic loads. Clearly it is better to compare dynamic stress and strain values with failure data determined in a dynamic test mode. However, the low level of the stresses and strains obtained in the LSM design and the consequent high safety factor estimates lead to the conclusion that the transportation vibration problem is not critical for short time periods. If the loading is sustained for a considerable time, then measured fatigue data should be obtained and used to calculate allowable failure stresses.

Conclusions of Preliminary Structural Analysis

Table I details the estimated stress and strain maxima calculated in the preliminary structural analysis phase. Also tabulated are the estimated failure stresses and strains and the resulting factors of safety, based on the linear cumulative damage concept where more than one type of loading is involved. The analysis shows clearly that the design is structurally sound and contains no obvious weaknesses. Consequently a detailed computer analysis of the specific LSM grain may now be made.

DETAILED STRUCTURAL ANALYSIS OF LSM DESIGN

The detailed computer analysis of the LSM grain was carried out using the motor geometry shown in Figure 1. The axisymmetric, finite difference computer program devised by A. Messner while at Aerojet General Corporation, and described in Ref. 9 through 11, was used to perform the grain structural analyses. Three

loading conditions were investigated, thermal storage, pressurization, and axial acceleration. The resulting stress and strain distributions calculated along the grain are shown in Figures 24 through 30. Also given on these Figures are the numerical parameters used to obtain these results.

The stress and strain curves for the three loading conditions will be discussed briefly in the next sections.

Thermal Storage

Figure 24 shows the port hoop strain developed during thermal cooldown to 60°F from a stress free temperature of 150°F. The curve shows a maximum port hoop strain equal to 3.4 percent at a point approximately 100-inches from the head end of the grain. This value is very close to that obtained during the preliminary analysis phase, i.e., 3.27 percent.

Figure 25 shows the normal tensile stresses at the propellant-case interface after cooldown to 60°F and a peak of 4.6 psi is obtained near the aft end of the grain. A peak value of 2.7 psi is obtained near the head end and a level of 2.1 psi occurs from approximately 20 inches to 120 inches from the motor head end. The peak normal stress value estimated during the preliminary analysis for a 60°F storage temperature was 3.9 psi, somewhat less than the 4.6 peak given in Figure 25.

The propellant-case interface shear stress distribution is shown in Figure 26 and shows a peak propellant-case interface shear stress value of 3.4 psi occurs near the head end of the grain. A smaller peak value of 2.75 psi occurs near the aft end of the grain.

Pressurization Loading

Port hoop strain and propellant-case interface shear stress curves are given against axial position along the motor in Figures 27 and 28. A maximum pressurization hoop strain of 2.3 percent is obtained which is higher than the 1.36 percent calculated in the preliminary analysis. Figure 28 shows a peak pressurization shear stress value of 18.7 psi at the head end of the motor and a lower peak value of 8 psi at the aft end.

Axial Acceleration

On computer solution derived for a steady state acceleration load was used to obtain Figures 29 and 30. Figure 29 shows the port hoop strain resulting from motor storage in a vertical position for a period of 3 months at 100°F. The peak deformations are found at the ends of the grain and a maximum tensile hoop strain of 3.1 percent is obtained. This value must be compared with the 2.3 percent strain value calculated in the preliminary analysis.

Figure 30 shows the propellant-case interface stresses obtained under a 3g axial acceleration at a temperature of 100°F. Once again the shear stresses peak at the grain ends with a maximum value of 10.5 psi at the aft end. This value compares favorably with the 13.0 psi calculated during the preliminary analysis.

Effects of Variation in Boot Length

Preliminary estimates of the minimum length of boots or flaps required to prevent propellant-case unbonding at the grain terminations are made on the basis of experimental data shown in Figure 4-2, Ref. (4). This curve shows measured crack depths for motors of various diameter up to 120 inches. For a motor 156 inches diameter, a crack depth of 4 to 5 inches would be anticipated and conservatively a flap or boot length of twice the crack depth, i.e., 8 to 10 inches may be used.

A computer analysis was made to determine the effects of using different boot lengths from 10 inches to 37 inches at the head end of the grain. Figure 31 shows the normal tensile stresses as a function of axial position for thermal storage at 60°F and Figure 32 shows the shear stress distributions. The normal stress curves show small differences in peak tensile stress $\approx$ 2.75 (psi) at the head end for boot lengths from 10 to 29 inches, but the tensile stress peak increases to 3.4 psi with the longest boot length of 37 inches. The interface shear stresses, on the other hand, are maximum at the shortest boot length and decrease from 3.5 psi to 2.3 psi as the boot length increases from 10 inches to 37 inches. The results of the analysis confirmed that a boot length of 10 inches was adequate for the LSM design and that nothing would be gained by using a greater length.

Determination of Allowable Failure Stresses and Strains

The methods used for determining allowable stress and strain values are exactly the same as those described during the preliminary analysis phase. It is not necessary to estimate lower 2σ failure stresses and strains since the strip biaxial test data obtained from a series of LPC-580 propellant batches during casting of the LSM and shown in Table II enables realistic standard deviations to be calculated. The standard deviation for the stresses is 15.4 psi = 15 percent of the mean value, whereas the standard deviation for the strain is 1.6 percent = 13 percent of the mean failure strain value. Thus a lower 2σ failure stress of 0.70 of the measured value and a lower 2σ failure strain = 0.74 of the measured value may be used.

Conclusions of Computer Structural Analysis

The calculated maximum stresses and strains obtained from the computer analysis are given in Table III together with the allowable values and the resulting safety factors. A review of these figures shows that although in some instances safety factors are lower than those obtained from the simpler analysis, no design weakness is evident and the motor should perform satisfactorily.

SUMMARY AND CONCLUSIONS

Existing design analysis techniques to ensure the structural integrity of a large solid motor have been described in this article. The analysis techniques and physical property interpretation procedures are certainly adequate but only when mature judgment is exercised.

The use of digital computer programs has enabled a realistic assessment to be made of stresses and strains occurring within a specific motor design. The particular motor considered in this article has a simple grain configuration which can be analyzed using axisymmetric computer programs with no approximation. Other configurations such as star shaped perforated grains require additional analyses, usually based on a generalized plane strain approximation, to investigate the effects of port shape. The results of the axisymmetric and the plane strain analyses must then be combined to give a single set of maximum stress and strain values occurring within the grain.

At this time, the accuracy of computer analyses is limited principally by the fact that real materials are not isotropic, homogeneous and incompressible. Furthermore, propellants are not perfectly linear viscoelastic materials, especially at the higher filler levels currently being used. As a consequence, major improvements to the analyses may be made by generalizing the fundamental equations to include nonlinear (elastic) behavior and finite compressibility. Since a solution for a completely general material description is clearly insolvable, the experimentalist must first describe the essential features of the real materials occurring in solid rocket motors. In this context, the nonlinear viscoelastic theory of Schapery (12) appears a very promising approach to a difficult problem. By making assumptions compatible with thermodynamics and practical experience with propellant, a nonlinear material description may be devised.

Although analysis techniques need improvement before a complex three-dimensional grain problem can be handled with ease, the greatest uncertainty with any grain structural integrity analysis remains the determination of allowable failure stresses and strains. No unifying failure theory is yet defined which can describe the failure properties of propellant under the commonly occurring stress and strain conditions. Consequently, various failure criteria are adopted for

different regions of the same grain, e.g., maximum principal strain criterion for port failure and maximum principal stress criterion for propellant-case interface bond failure.

The maximum principal strain theory of failure is widely used in propellant grain analyses, although it has proved unreliable for metal failure prediction. Its chief advantage is the fact that port strains are measurable quantities which may be compared directly with laboratory test values. On the other hand, stresses cannot be observed but have to be inferred using an equivalent modulus value. Thus in reality propellant may fail because a limiting stress is exceeded, but the uncertainties of calculating the maximum stress values within the grain may make the application of this failure criterion very unreliable.

Current effort to devise a usable failure theory includes the strain energy approach adopted by Williams (13), the failure envelope concept due to Smith (14) and the multiaxial stress "constraint parameter" suggested by Siron and Duerr (15). Clearly there is no lack of theories of failure which can be demonstrated to apply to certain propellants under well defined experimental test conditions. There is, however, very little data verifying the applicability of any one failure theory in a realistic motor environment. In this context the recently initiated Air Force program to investigate failure and cumulative damage theories using one propellant type between several contractors should prove of great value. A closely allied program using the identical propellant is the Structural Test Vehicle work in which experimental measurements will be made of bond stresses and port strains of simple circular port grains. The objective of this program is an experimental investigation of the accuracy of currently available structural analysis techniques.

Considering the results of the structural analysis described in this article, the maximum stresses and strains obtained in the preliminary analysis phase are generally close to those obtained from the computer analysis. The chief advantage of the more detailed analysis procedure is that variations in stress and strain throughout the grain can be observed and possible sources of trouble identified which are not obvious at first glance.

It should be mentioned that in many instances the absolute magnitude of a stress peak is a function of geometric grid size, since theoretically an infinite stress is obtained at a singularity. For these cases, experience dictates an approach similar to that discussed in Ref. 16. The grid system selected is such that the shear and tensile stress maxima are determined at a distance of one-percent of the outer radius (b).

The axisymmetric computer program is capable of handling a more complex analysis of a grain than those described in this article. Layers of insulating material and elastomeric boot materials can be incorporated in a more detailed motor description. In the case of motors which have lower safety factors or which may be marginal in certain aspects, a more thorough analysis of this kind is performed. The motor design considered here is considered sufficiently safe that no more detailed analysis was necessary. Similarly, it is known that the analysis of a grain under transient rather than steady state temperature conditions may produce higher interface normal and shear stresses. However, in the case of a

larger motor, rates of cooling and heating are so low that significant stress increases are not obtained.

The analysis and experimental work described in this article was supported by 36-inch diameter subscale firing of the LSM grain design using LPC-580 propellant before the large motor was cast and fired.

Finally, there is one key point which should be borne in mind in which the design and manufacture of an LSM is very different from any other (smaller) motor; the LSM has to fire successfully the first time, there is no second chance. The normal proving and qualification series of tests just cannot be carried out. Therefore, almost any depth of analysis required to prevent structural failure during firing is justifiable.

REFERENCES

1. H. M. Darwell, A. Parker and H. Leeming, "The Mechanical Behavior of Cast-Double-Base Propellants in Rocket Motors", AIAA 6th Solid Propellant Rocket Conference, Paper No. 65-161 (February 1965).

2. R. A. Schapery, " A Method of Viscoelastic Stress Analysis Using Elastic Solutions", Journal of the Franklin Institute, Vol. 279, pp 268-289, (April 1965).

3. ICRPG " Solid Propellant Mechanical Behavior Manual", CPIA Publication No. 21, (September 1963).

4. Lockheed Propulsion Company Report No. 578/556-F-3, "Engineering Methods for Grain Structural Integrity Analysis", (May 1963).

5. M. L. Williams, P. J. Blatz and R. A. Schapery, "Fundamental Studies Relating to Systems Analysis of Solid Propellants", GALCIT SM 61-5 (February 1961).

6. K. W. Bills, Jr., "Study of Cumulative Damage Techniques for the Prediction of Motor Failure", First Quarterly Report, 1 July 1966 - 28 August 1966, Aerojet General Corporation, Sacramento, California.

7. J. E. Fitzgerald, "Analysis and Design of Solid Propellant Grains", Lockheed Propulsion Company Report No. 6-3523 presented at Internation Conference on the Mechanics and Chemistry of Solid Propellants, Purdue University (April 65)

8. R. A. Schapery, "Irreversible Thermodynamics and Variational Principles with Applications to Viscoelasticity" PhD Thesis, California Institute of Technology, 1962.

9. A. M. Messner, "Propellant Grain Stress Analysis,""Proceedings 17th JANAF-ARPA-NASA Solid Propellant Group Meeting, pp 149-166, (1961).

10. A. M. Messner and R. N. Shearly, "Stress Analysis of Axisymmetrical Propellant Grains with Arbitrary End Geometries" Aerojet-General Structures Technical Memorandum 201 SRP, (October 1962) Confidential.

11. A. M. Messner and A. O. Rock, "Thermal Stresses in Cylinders of Finite Length" Aerojet General Structures Technical Memorandum 213 SRP, (1963).

12. R. A. Schapery, "A Theory of Nonlinear Thermoviscoelasticity based on Irreversible Thermodynamics, "Proceedings 5th U.S. National Congress of Applied Mechanics, ASME, pp 511-530 (June 1966).

13. M. L. Williams, "Initiation and Growth of Viscoelastic Fracture", International Journal of Fracture Mechanics, Vol. 1 No. 4, (December 1965) pp 292 - 310.

14. T. L. Smith, "Current Research on Mechanical Properties of Elastomeric Materials at Stanford Research Institute," Bulletin of the First Meeting JANAF-ARPA-NASA Working Group on Mechanical Behavior, (1963).

15. R. E. Siron, T. H. Duerr, "An Engineering Approach to Multiaxial Failure in Solid Propellants", ICRPG Bulletin of the 5th Meeting of the Mechanical Behavior Working Group, CPIA No. 119 Vol. 1, (November 1965).

16. R. N. Shearly and A. M. Messner, "Stresses in Propellant Grain Bond Systems", CPIA Publication No. 61U, Bulletin of the Third ICRPG Working Group on Mechanical Behavior, Vol. 1, pp 103-118 (October 1964).

TABLE I

PRELIMINARY STRUCTURAL ANALYSIS RESULTS

ATTACHMENT	CRITICAL STRESS/STRAIN	LOWER BY ALLOWABLE STRESS/STRAIN	SAFETY FACTOR
Storage at [illegible] Thermal Insulation			
• Fort Steele	3.9%	10.0%	2.6
• Mind Topside Forces	.5 psi	25.0 psi	5.3
2. Piping (Pressurization and Thermal) at [illegible]			
• Thermal Fort Steele	3.2%	10.0%	3.1%
• Pressurization Fort Steele	1.1%	22.5%	
3. Structural Loads			
• Storage Room Induction Forces after Insertion at 1000'	4.2% psi	24.0 psi	5.5
• Transportation Shock Induction Forces (Up, 15 cps Sinusoidal at 1000')	13.0 psi	120 psi	9.2

NOTE: Allowable stresses and strains incorporate the a reliability factor of [illegible]

TABLE II

DATA-TO-LAG CORRELATION IN THE FIELD STATIC STRAIN-GAGGED PROPELLER OF LPC-420 AIRPLANE (Root Temperature 70°F)

Blade Station	Measured Maximum Stress (psi)	Margin of Maximum Error (%)
Blade 1/R=0.5	116.0	12.4
-0.5	118.0	12.0
-0.5	120.0	11.3
-0.0	99.1	13.0
-0.5	112.0	12.4
-0.0	94.0	13.4
-0.5	109.0	12.6
-1.0	97.3	13.1
-0.5	84.3	12.2
-0.0	116.0	13.1
-0.5	118.0	13.7
-0.0	87.3	13.0
-0.5	71.5	9.7

Mean Failure Stress = 102.5 psi

Standard Deviation = 13.6 psi = 15% of Mean Value

Mean Failure Strain = 14.5%

Standard Deviation = 1.6% = 12% of Mean Value

TABLE III

REVISED STRUCTURAL ANALYSIS RESULTS

ATTACHMENT	CRITICAL STRESS/STRAIN	LOWER BY ALLOWABLE STRESS/STRAIN	SAFETY FACTOR
1. STORAGE AT -65°F THERMAL INSULATION			
• Fort Steele	4.2%	2%	2.1
• Interface Principal Stress, Mind Top	7.1 psi	25 psi	3.5
• Structure Principal Stress, Aft End	5.25 psi	25 psi	5.0
2. PIPING (PRESSURIZATION AND THERMAL) AT -65°F			
• Thermal Fort Steele	3.5%	10%	2.7
• Pressurization Fort Steele	2.5%	12%	
3. AERODYNAMIC LOADS			
• Average Air Jet Force Induction Stress/Strain 3 Hours at 500°F	3.5 psi	25 psi	6.0
• Transportation Shock Induction Forces (Up, 10 cps Sinusoidal at 1000')	10.5 psi	100 psi	10.0

NOTE: Allowable stresses and strains incorporate the a reliability factor of [illegible]

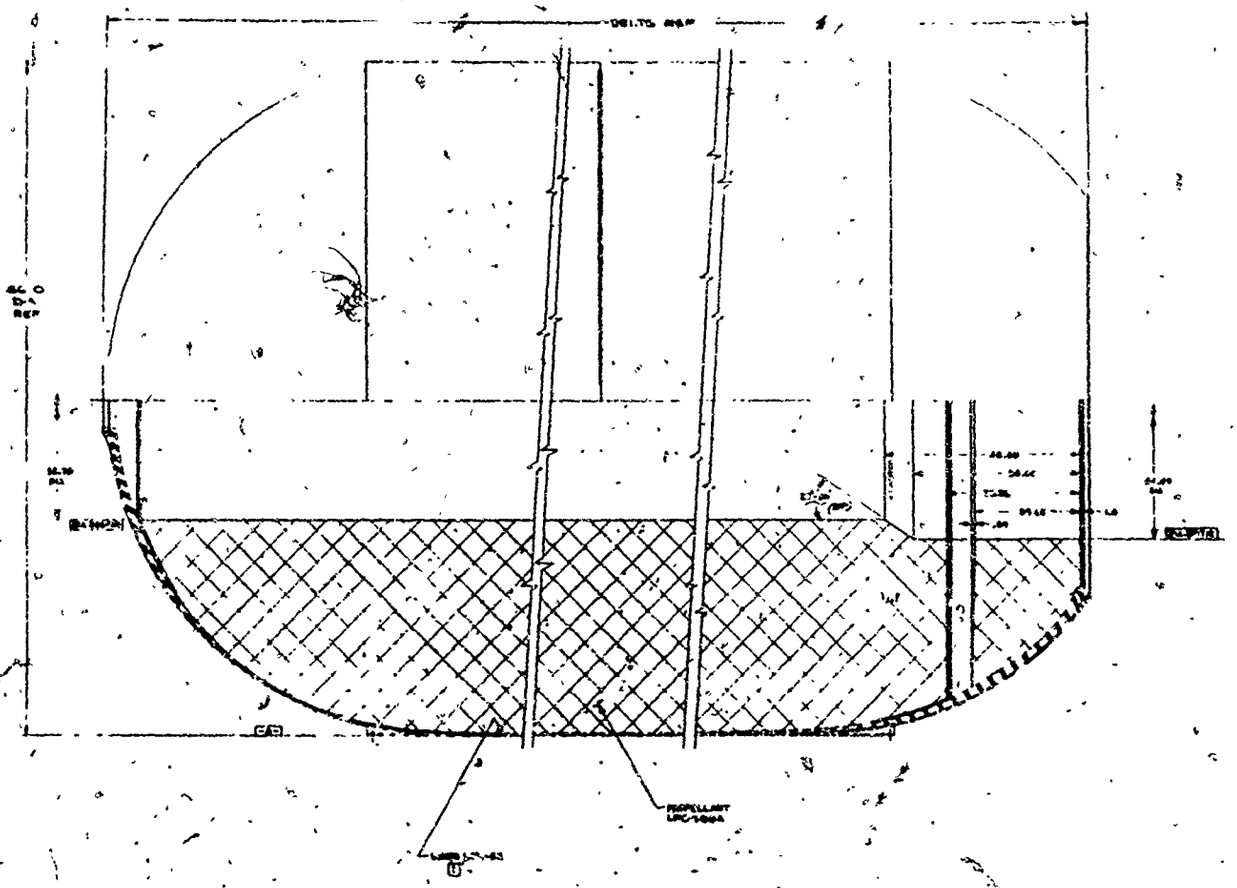

Figure 1 156-inch Diameter Monolithic Motor

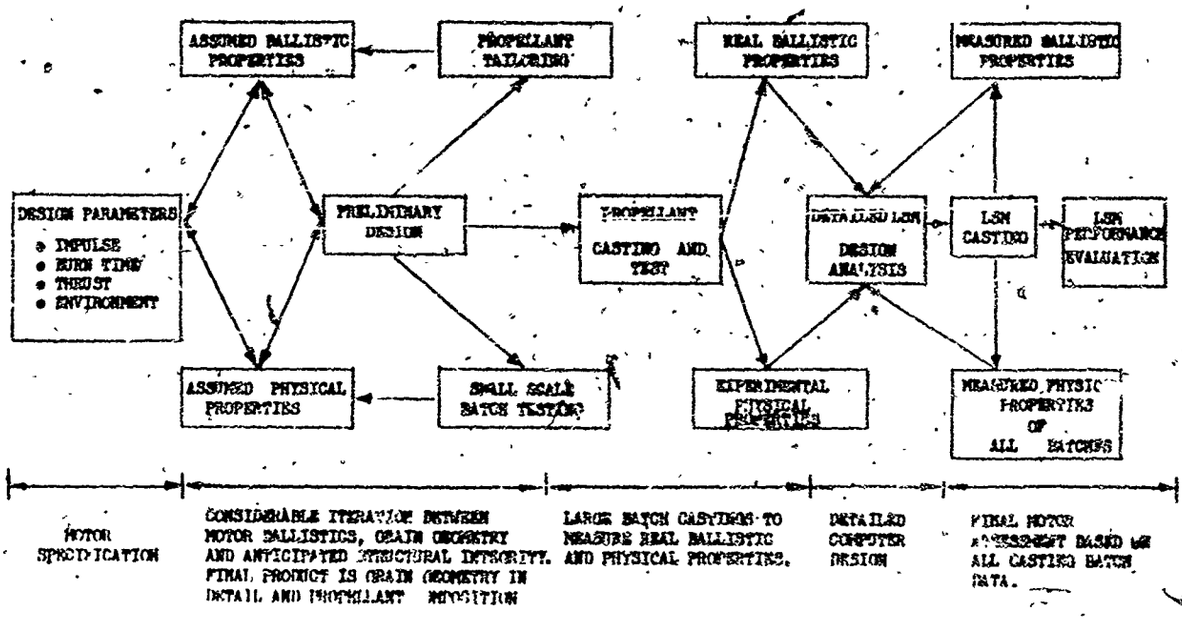

Figure 2. Motor Design Chart

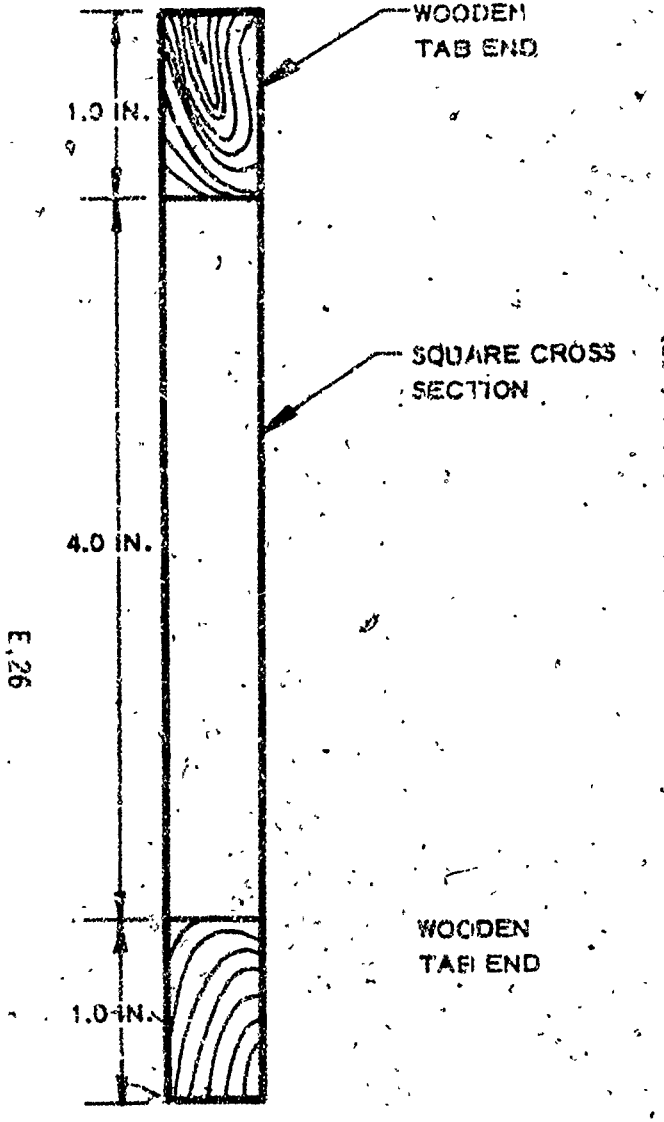

Figure 3 Tab End Tensile Specimen

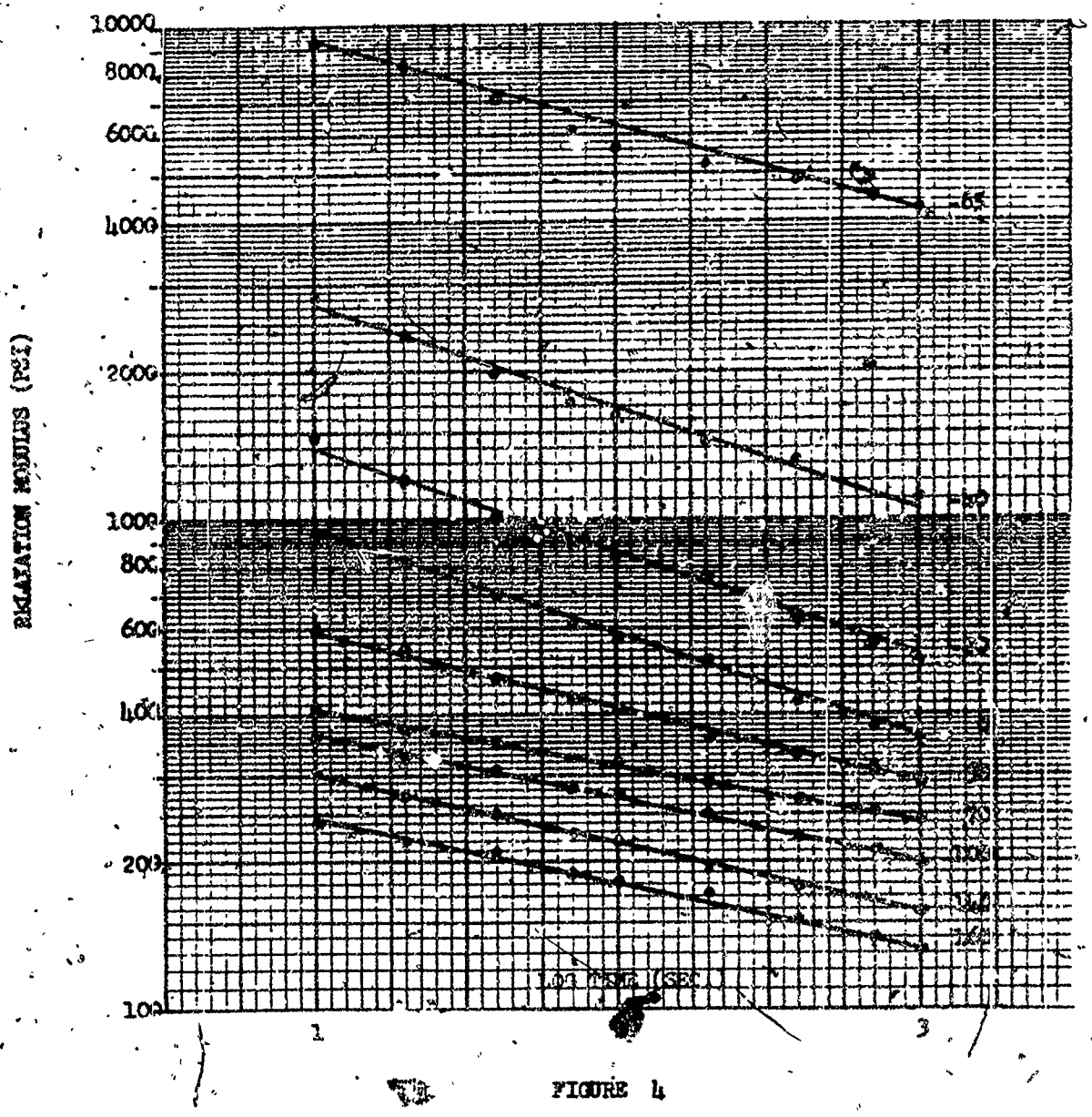

FIGURE 4

LPC-580 RELAXATION MODULUS-TIME DATA

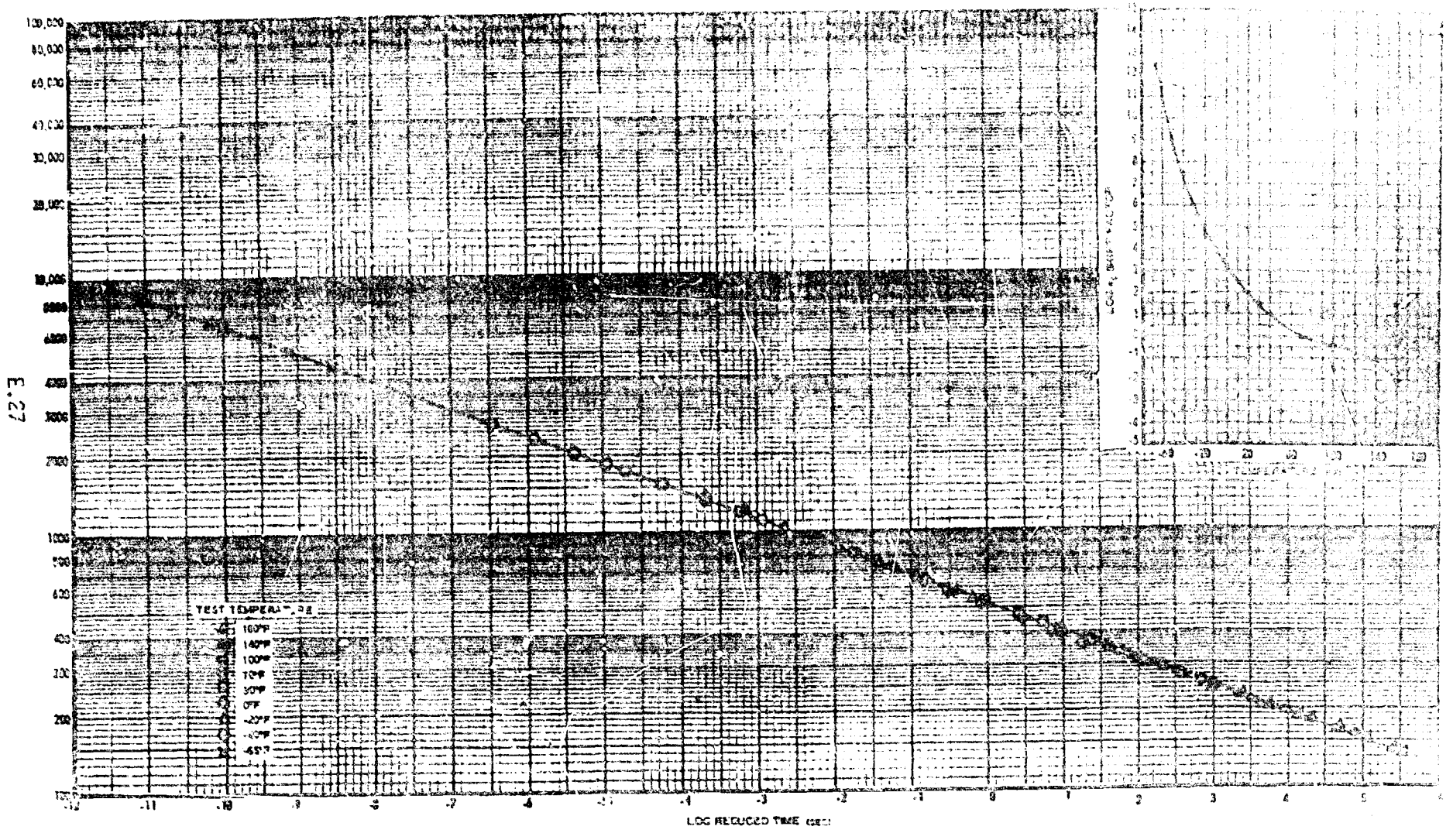

Figure 5. Master Stress Relaxation Modulus and Shift Factor of LPC-380 Propellant (Temperature = 70°F).

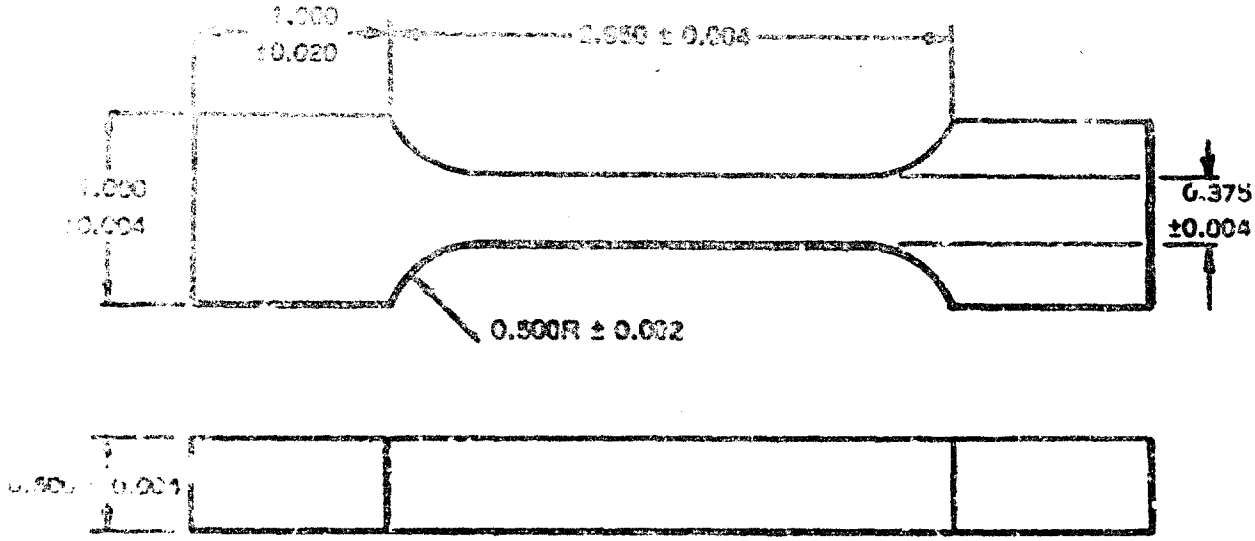

Figure 6 JANAF Tensile Specimen

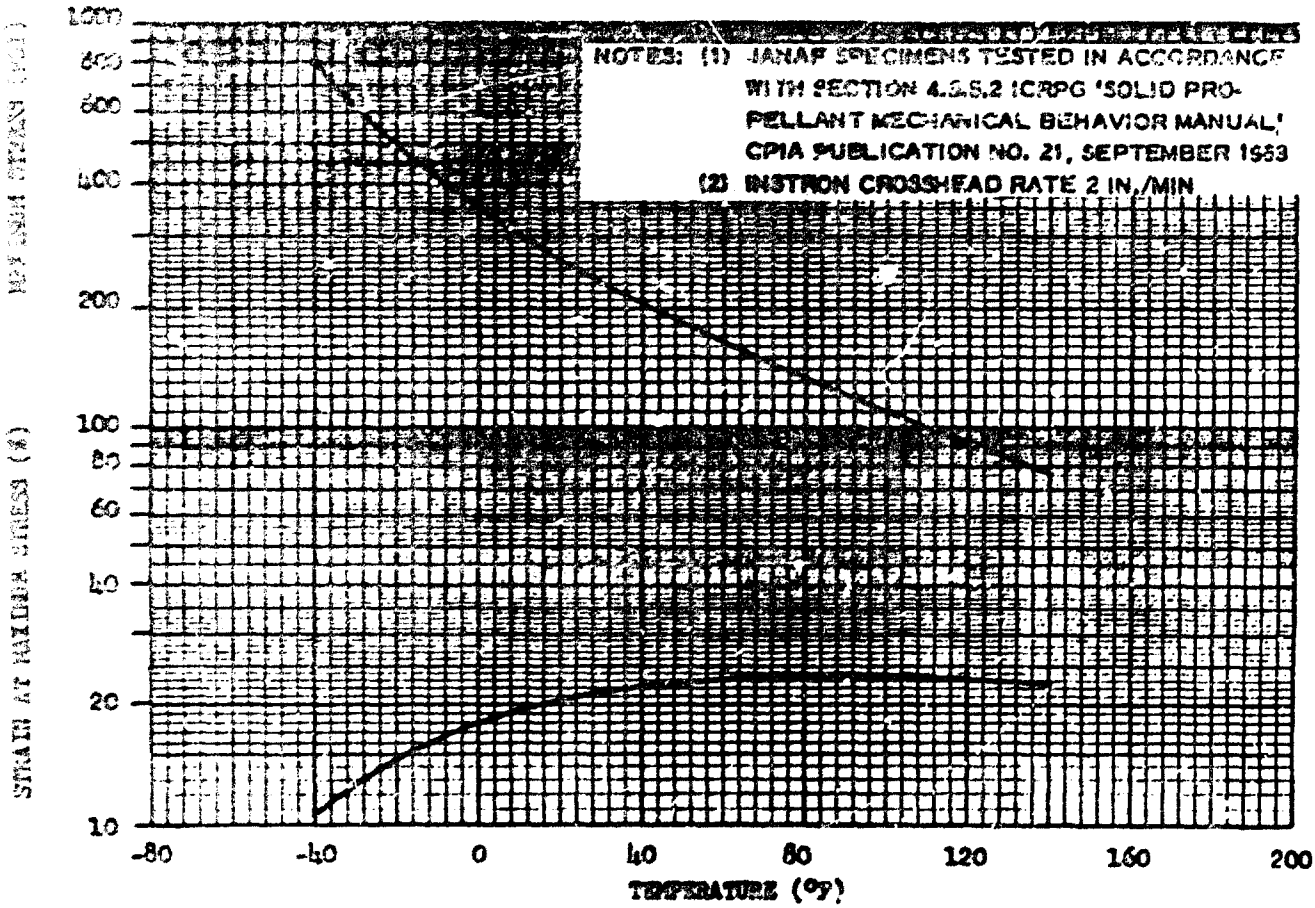

FIGURE 7

UNIAXIAL CONSTANT ELONGATION RATE PROPERTIES OF LPC-580 PROPELLANT

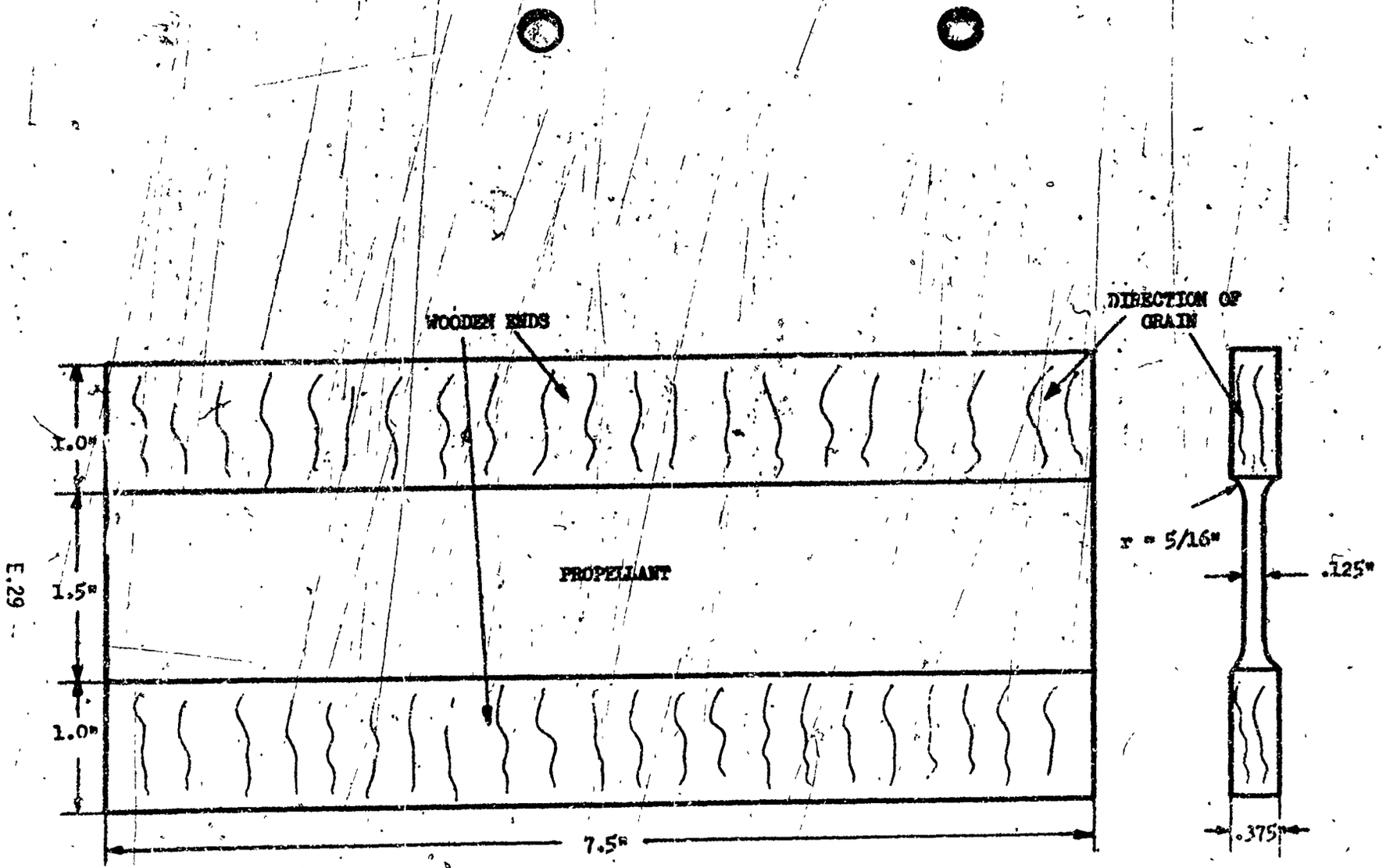

FIGURE 8

STRIP BIAXIAL SPECIMEN

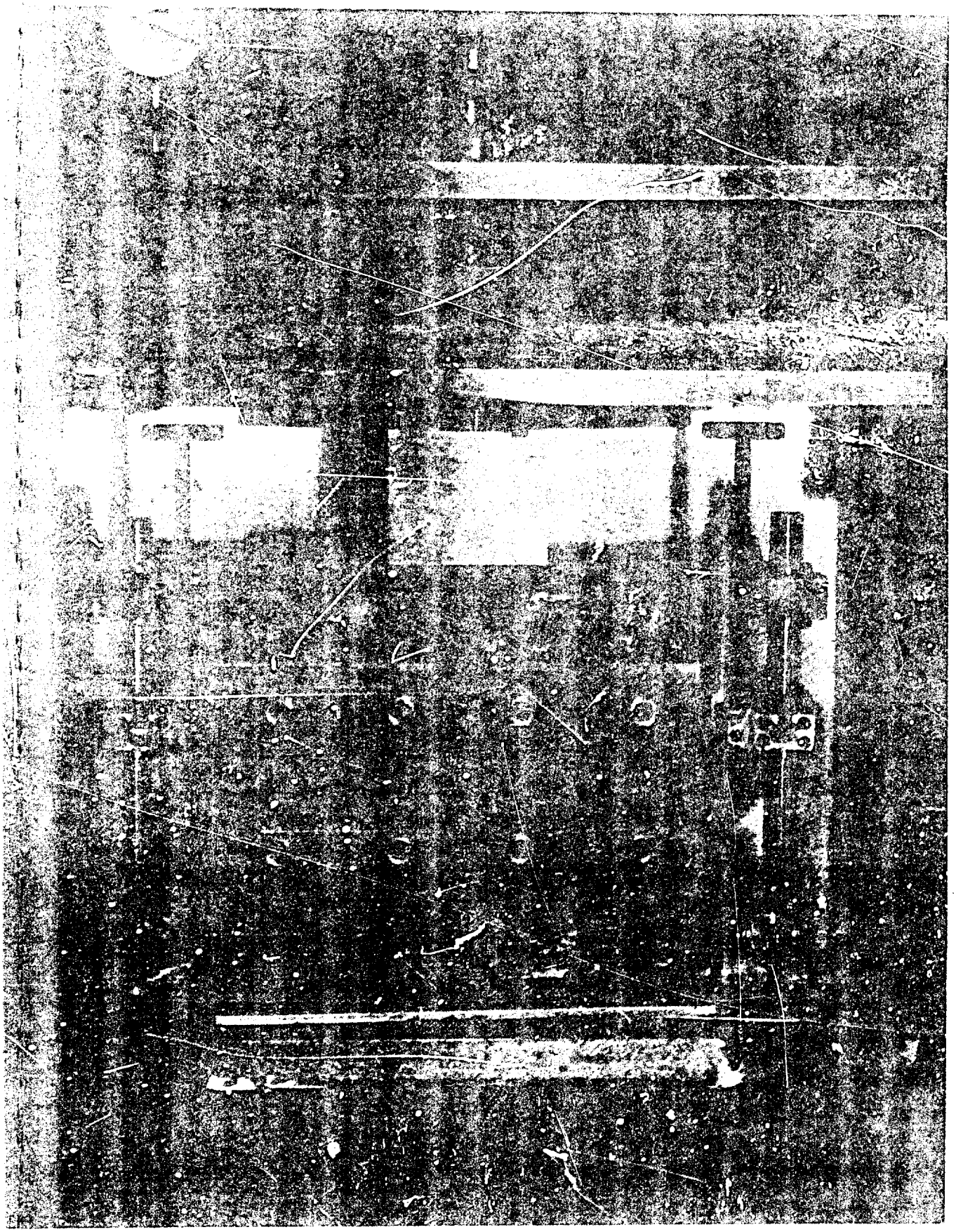

Figure 9 Biaxial Tension Test Specimen Under Test in Instron Apparatus

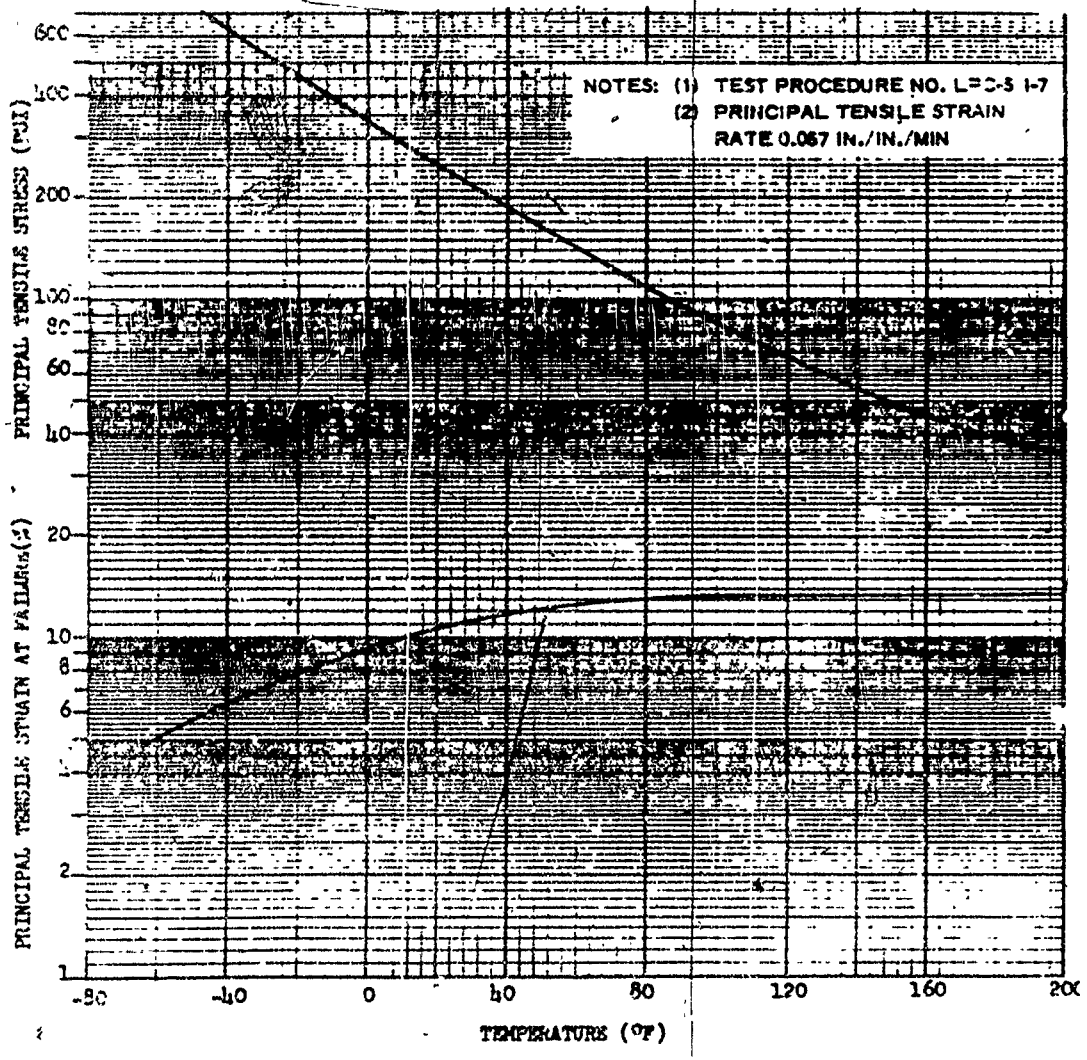

Figure 10. Strip Biaxial Tension-Tension Ultimate Properties of LPC-580 Propellant

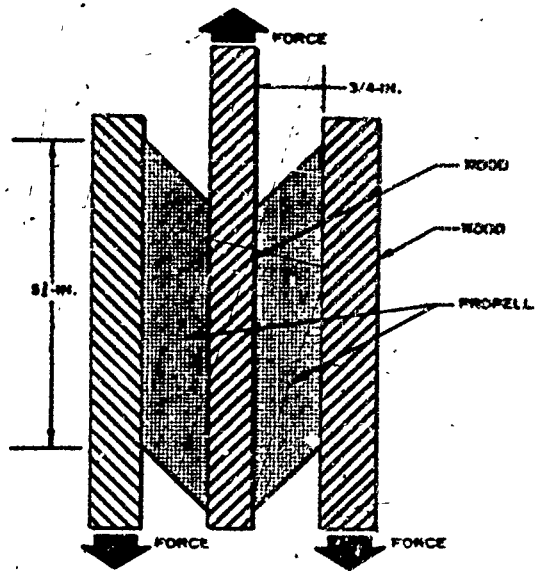

Figure 11 3-Arm Double-Lap Simple Shear Specimen

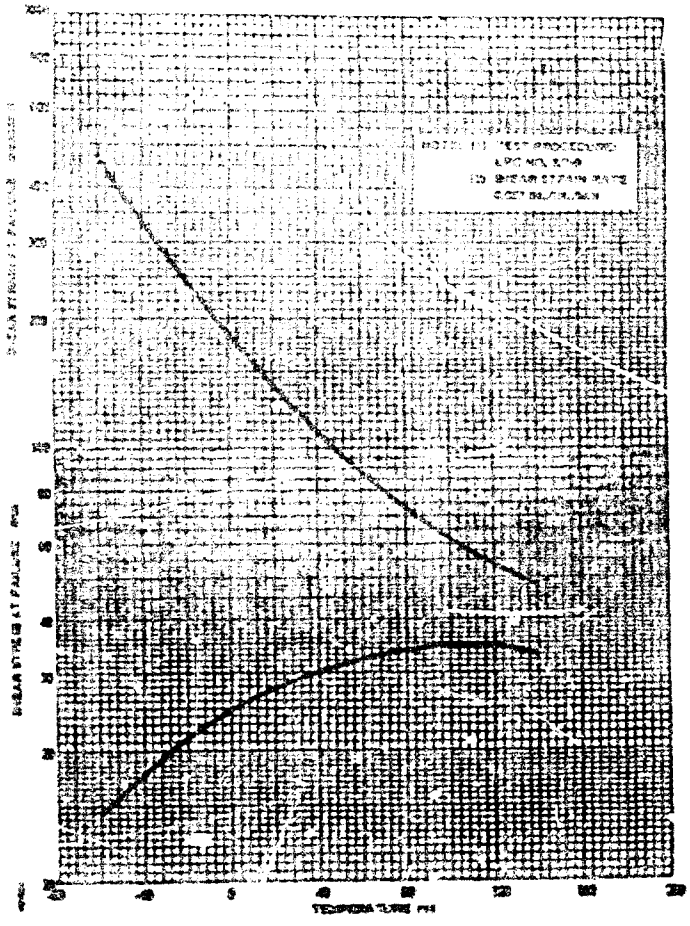

Figure 12 Cleavo - Shear Failure Properties of LPC-500 Propellant

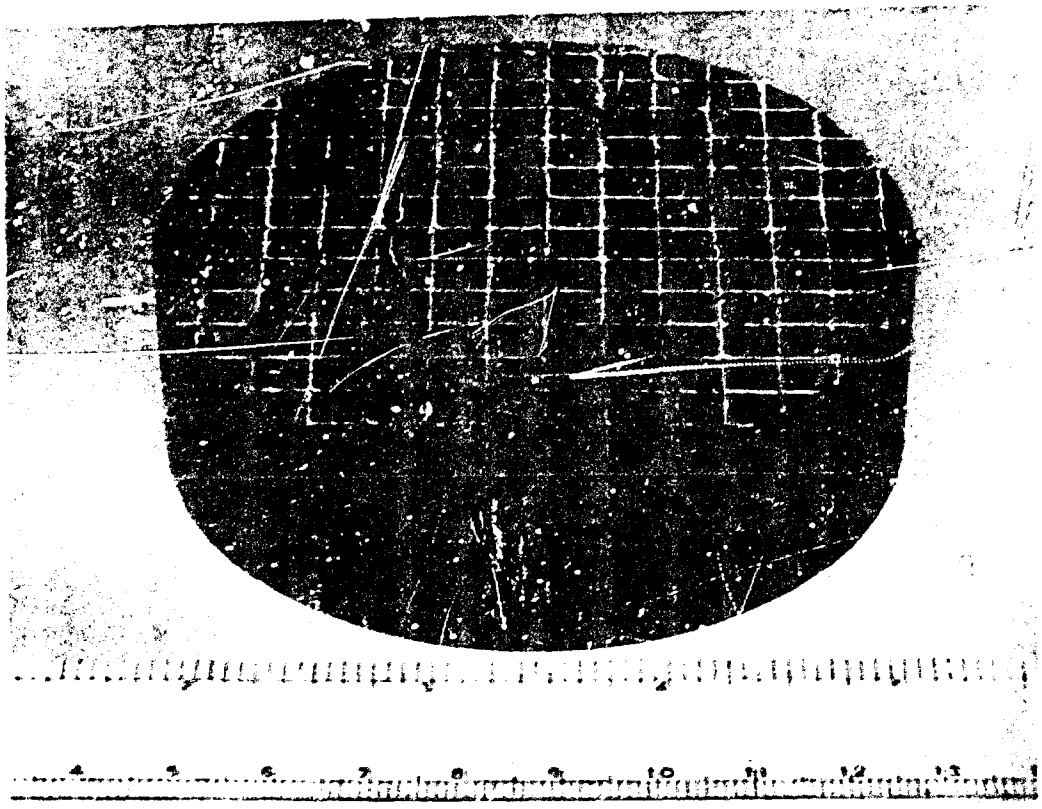

Figure 13 Diametral Compression Test Specimen

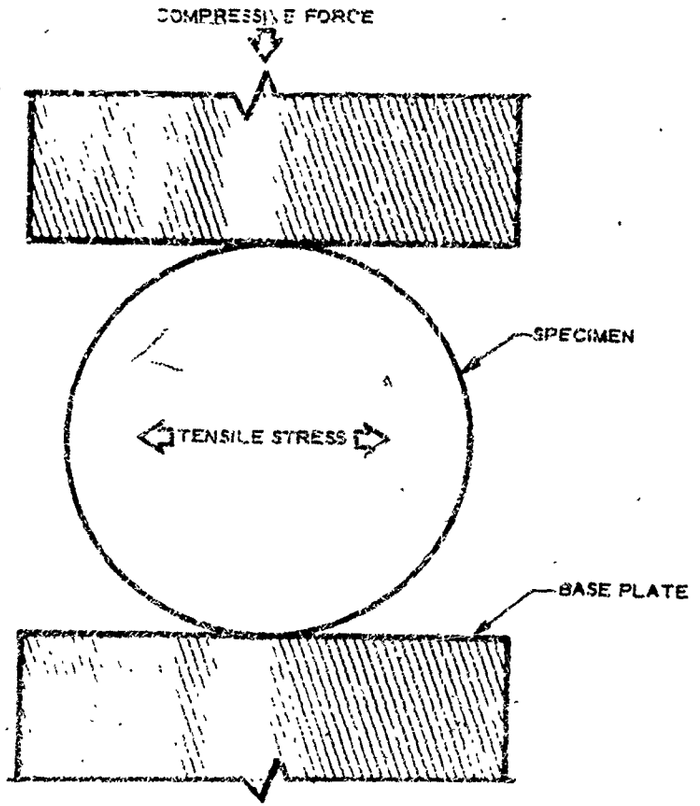

Figure 14 Diametral Compression-Tension Test

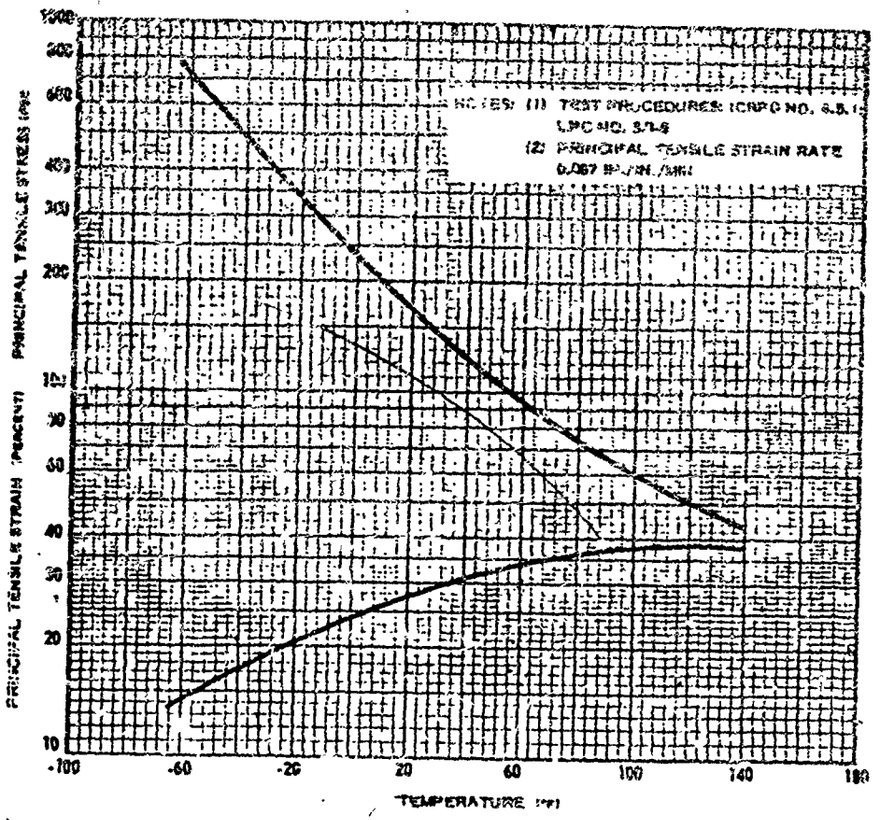

Figure 15 Diametral Compression-Tension Failure Properties of LPC-580 Propellant

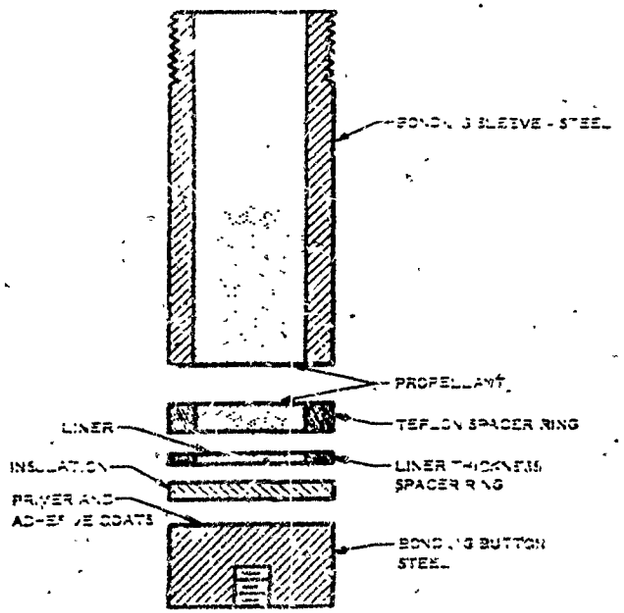

FIGURE 16 BOND IN TENSION SPECIMEN

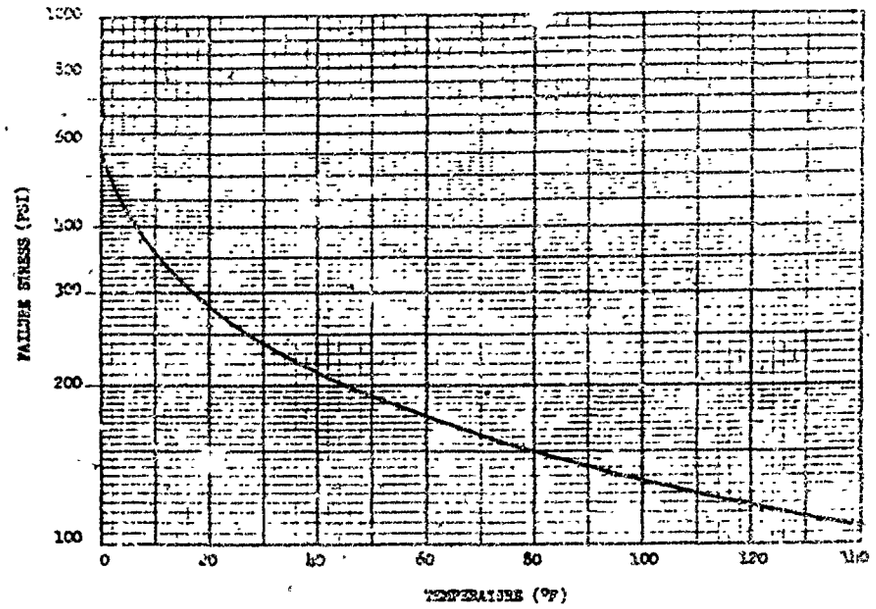

FIGURE 17

BOND-IN-TENSION FAILURE STRESSES LPC-580 PROPELLANT

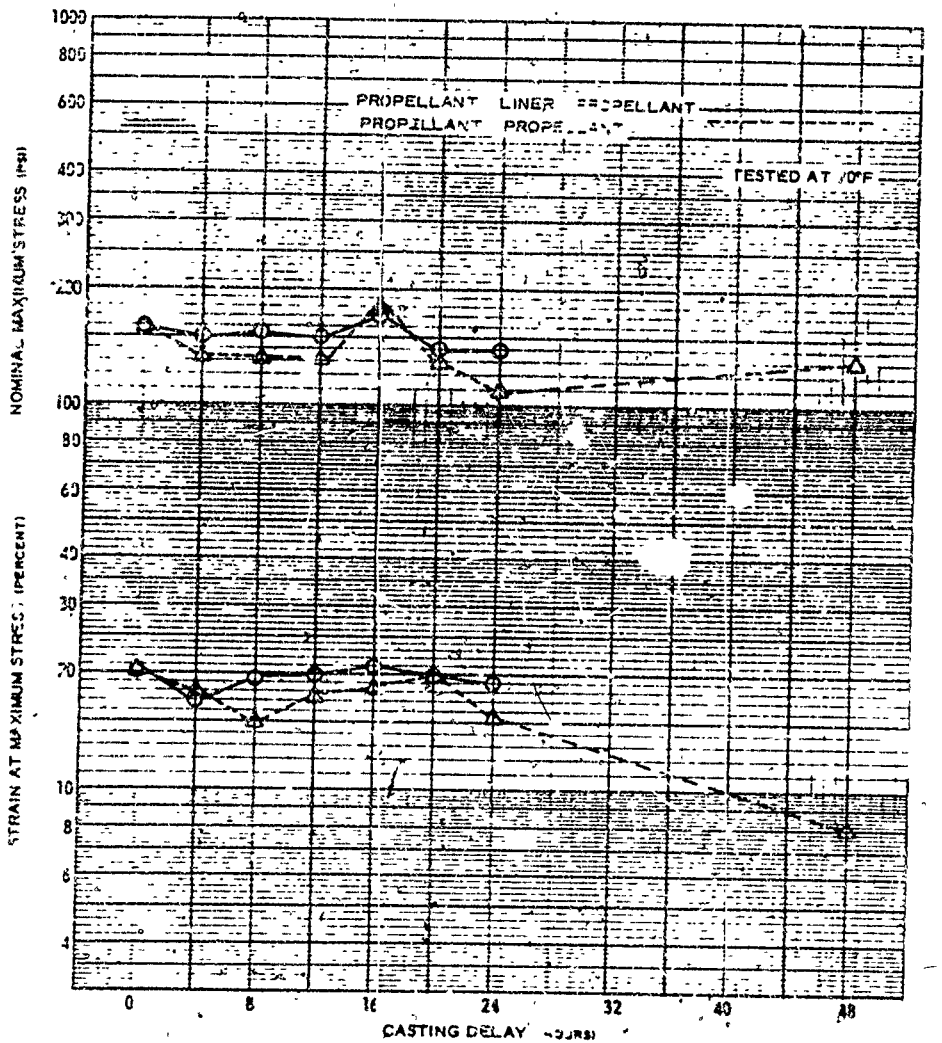

Figure 18. Measured Batch-to-Batch Bondability, Uniaxial Constant Elongation Rate Properties versus Casting Delay, LPC-580 Propellant at 70°F

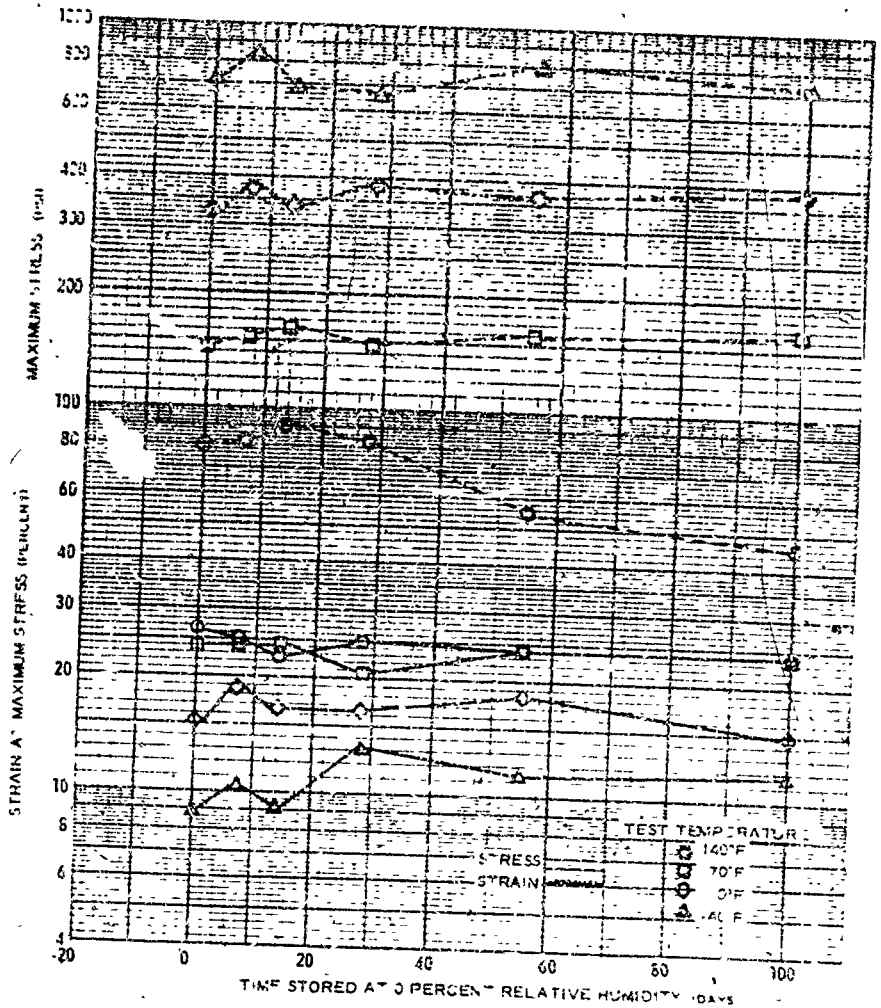

Figure 19. Effects of Zero-Percent Relative Humidity on LPC-55 Propellant, Batch 2817

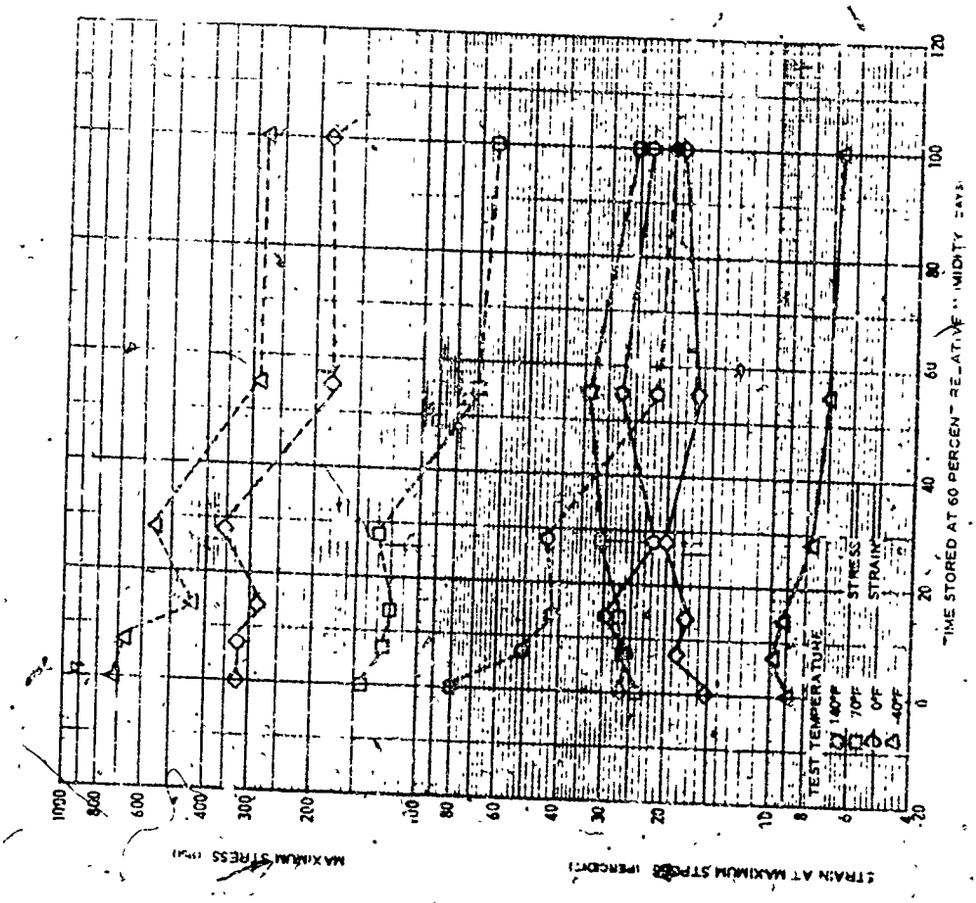
TEST TEMPERATURE
140°F
70°F
0°F
-40°F
STRESS
STRAIN
TIME STORED AT 60 PERCENT RELATIVE HUMIDITY, DAYS
STRAIN AT MAXIMUM STRESS, PERCENT
MAXIMUM STRESS, PSI

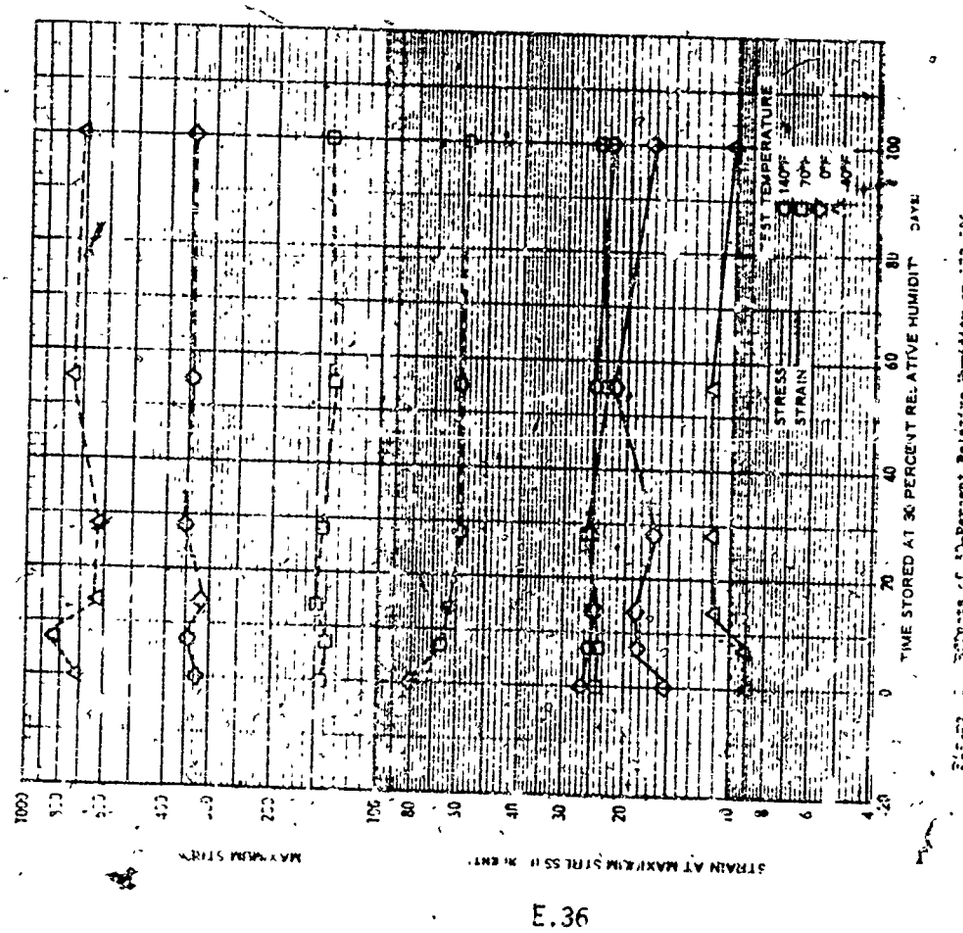
TEST TEMPERATURE
140°F
70°F
0°F
-40°F
STRESS
STRAIN
TIME STORED AT 30 PERCENT RELATIVE HUMIDITY, DAYS
STRAIN AT MAXIMUM STRESS, PERCENT
MAXIMUM STRESS, PSI

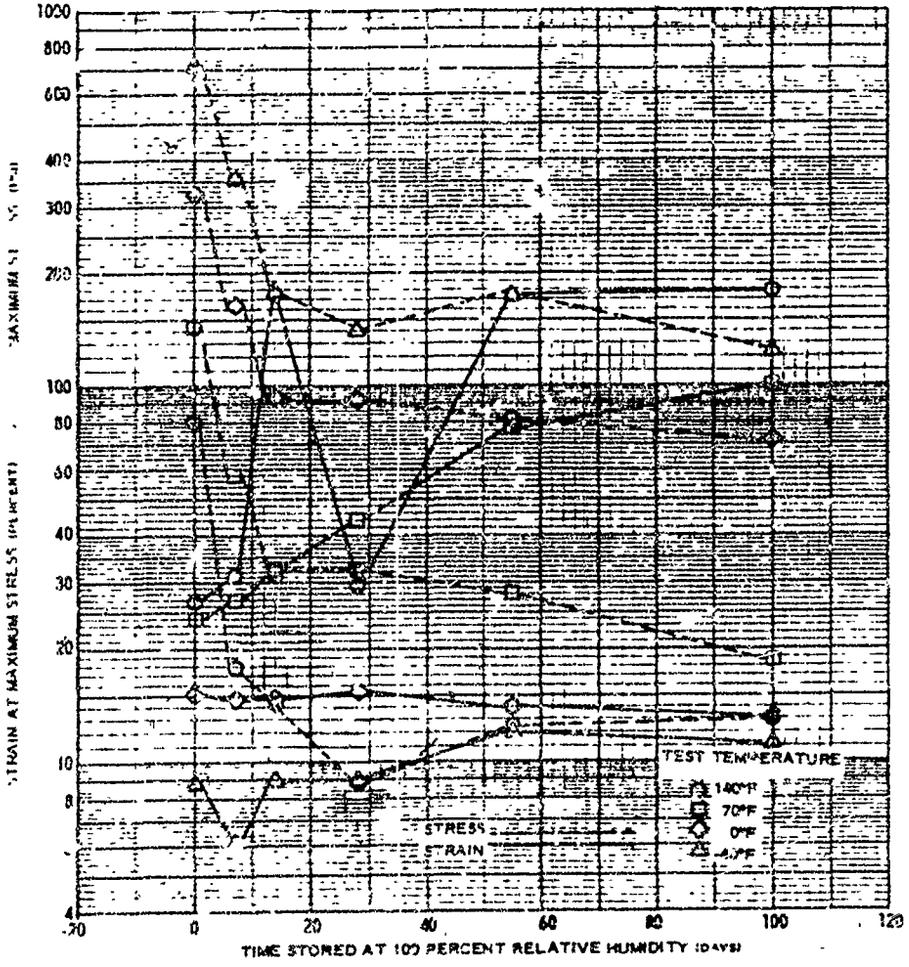

Figure 22. Effects of 100-Percent Relative Humidity on LPC-580 Propellant

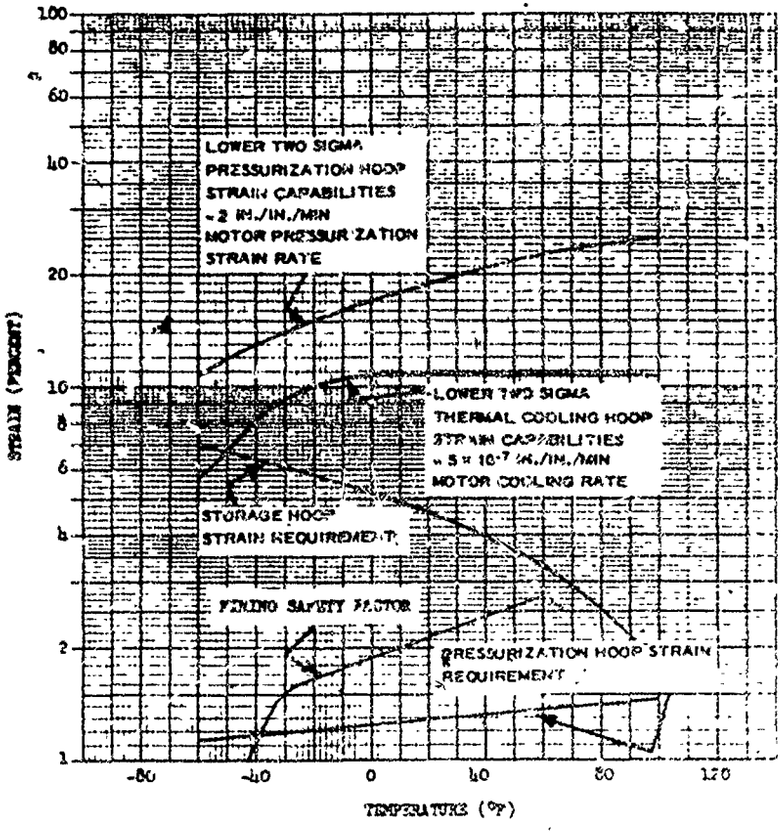

Figure 23. Storage and Firing Requirements Versus LPC-580 Propellant Capabilities.

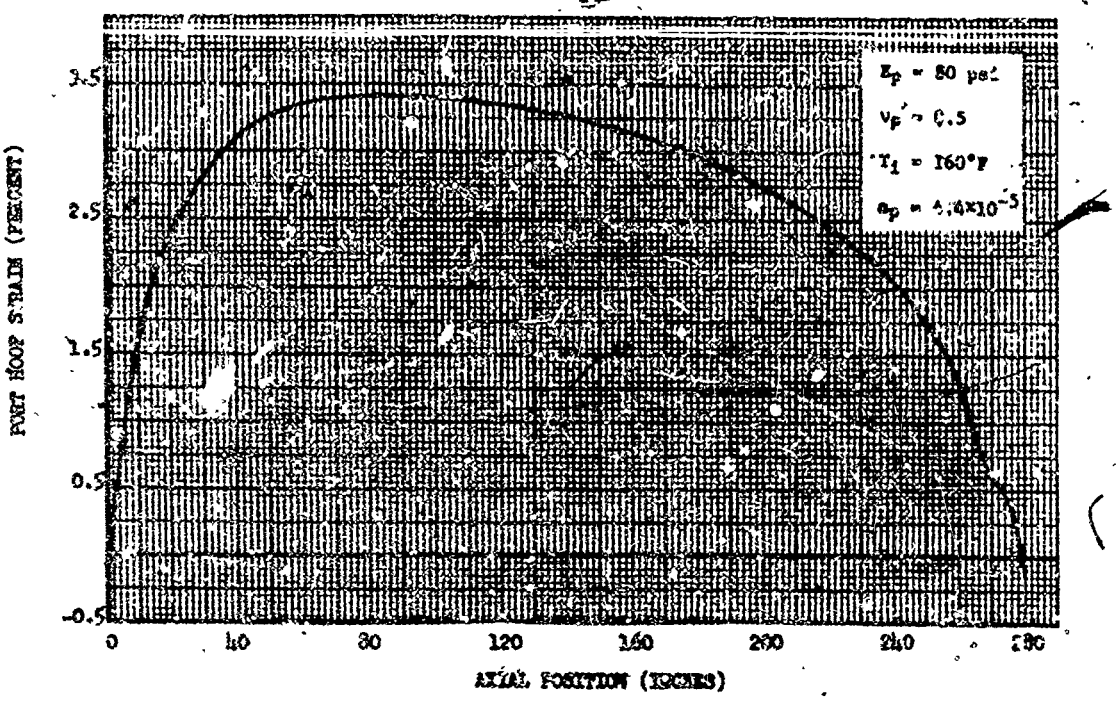

Figure 24. 156 inch diameter Motor Port Hoop Strain versus Axial Position from Head End - Storage Temperature = 60°F.

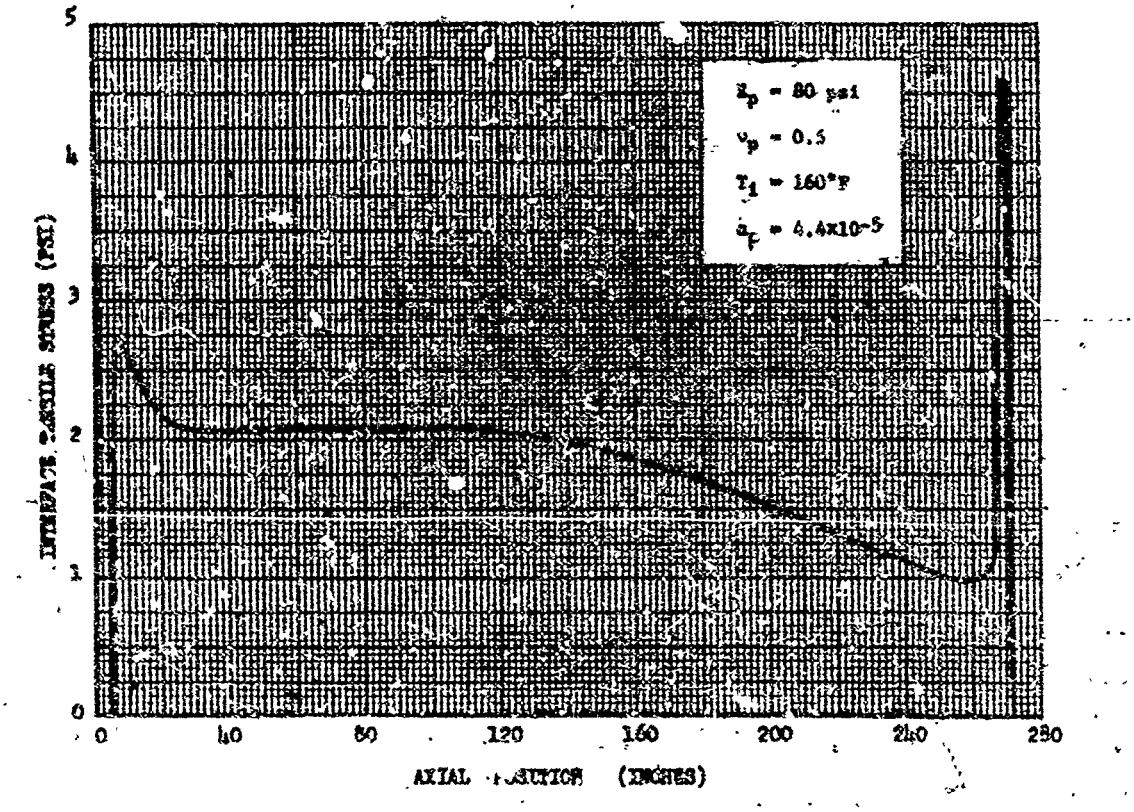

Figure 25. 156 inch diameter Motor Interface Tensile Stress versus Axial Position from Head End - Storage Temperature = 60°F.

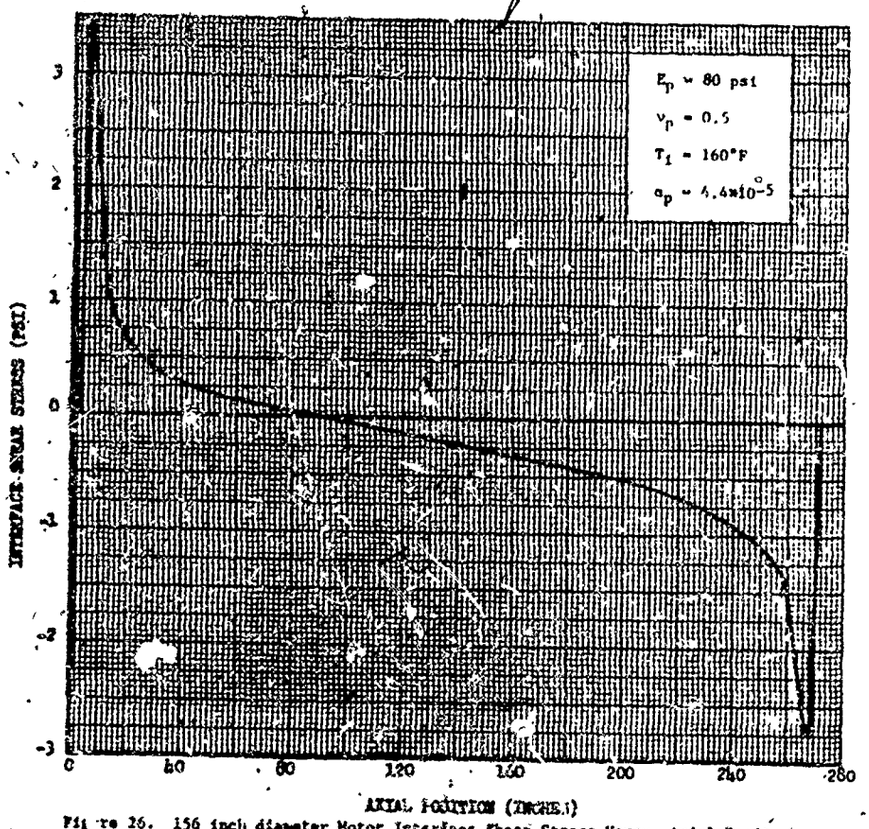

Figure 26. 156 inch diameter Motor Interface Shear Stress Versus Axial Position from Head End - Storage Temperature = 60°F.

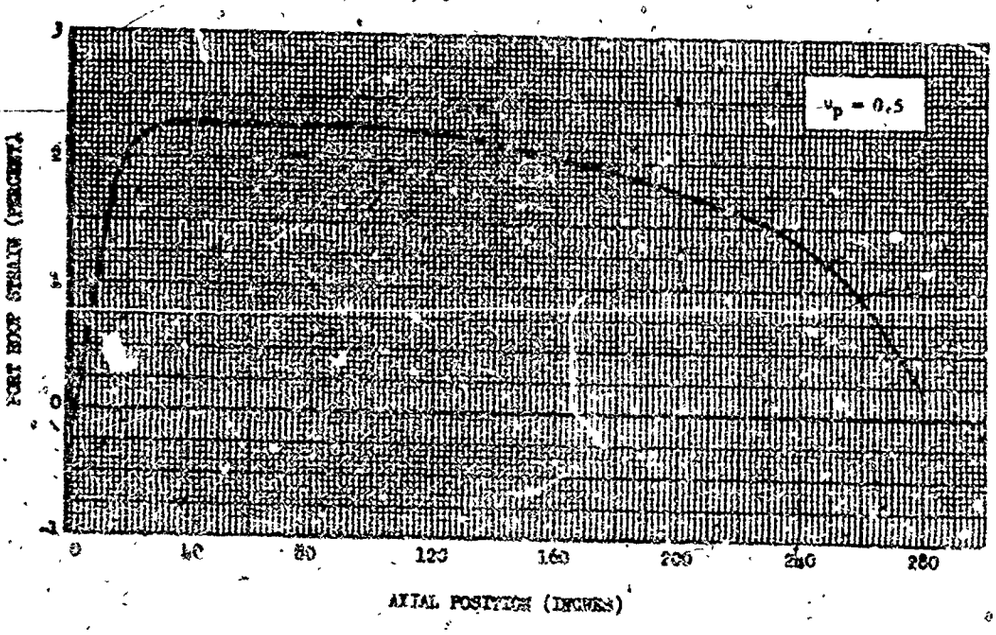

Figure 27. 156 inch diameter Motor Pert Hoop Strain versus Axial Position from Head End - 650 psi Pressure Loading.

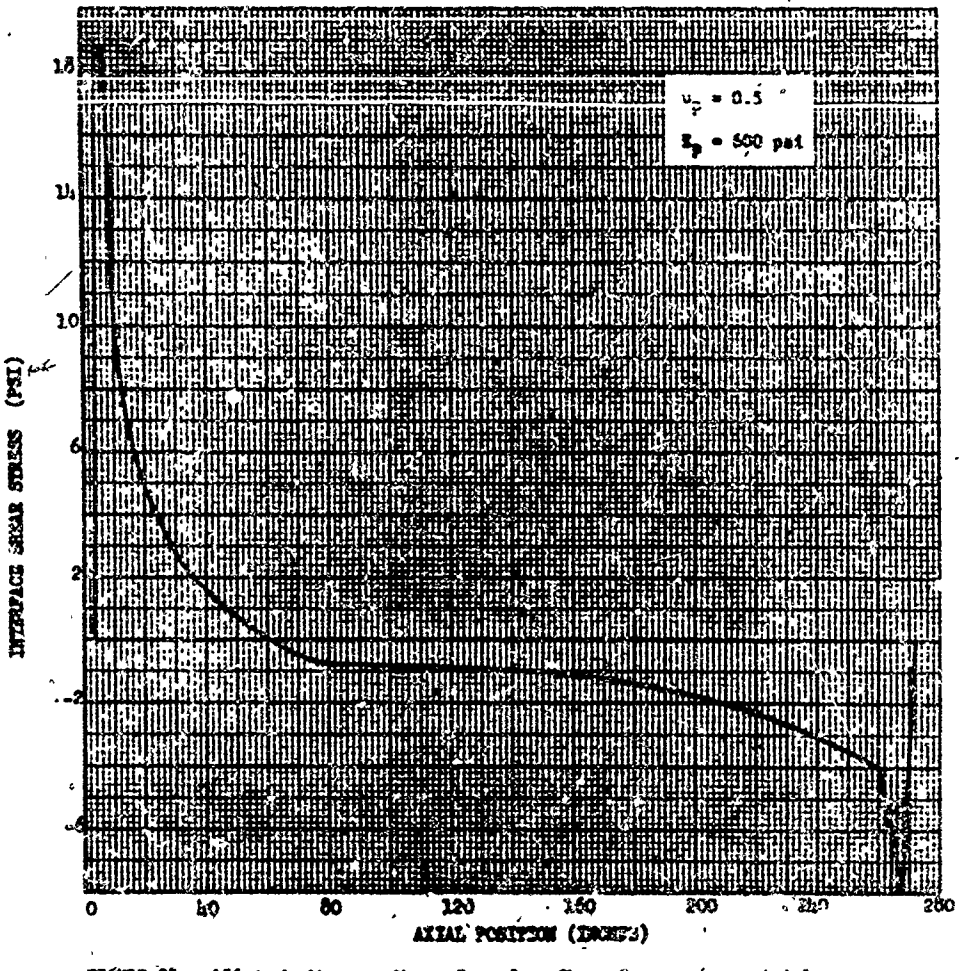

FIGURE 28. 156 inch diameter Motor Interface Shear Stress versus Axial Position from Head End - 650 psi Pressure Loading.

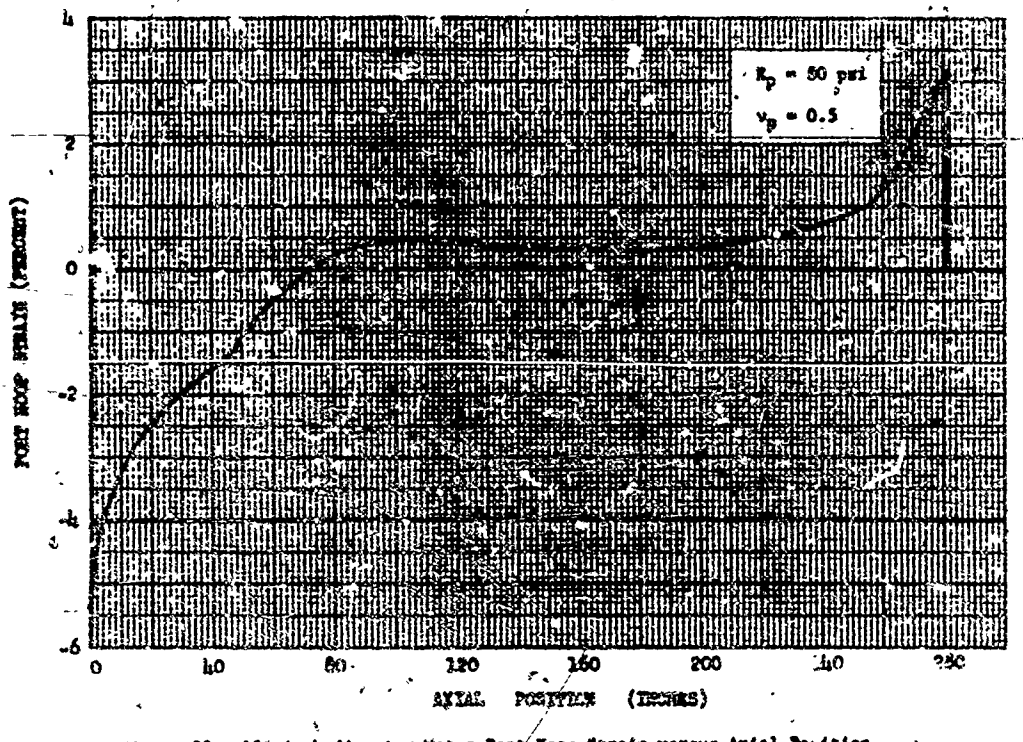

Figure 29. 156 inch diameter Motor Fore Hoop Strain versus Axial Position from Head End - Vertical Storage (1g) at 100°F.

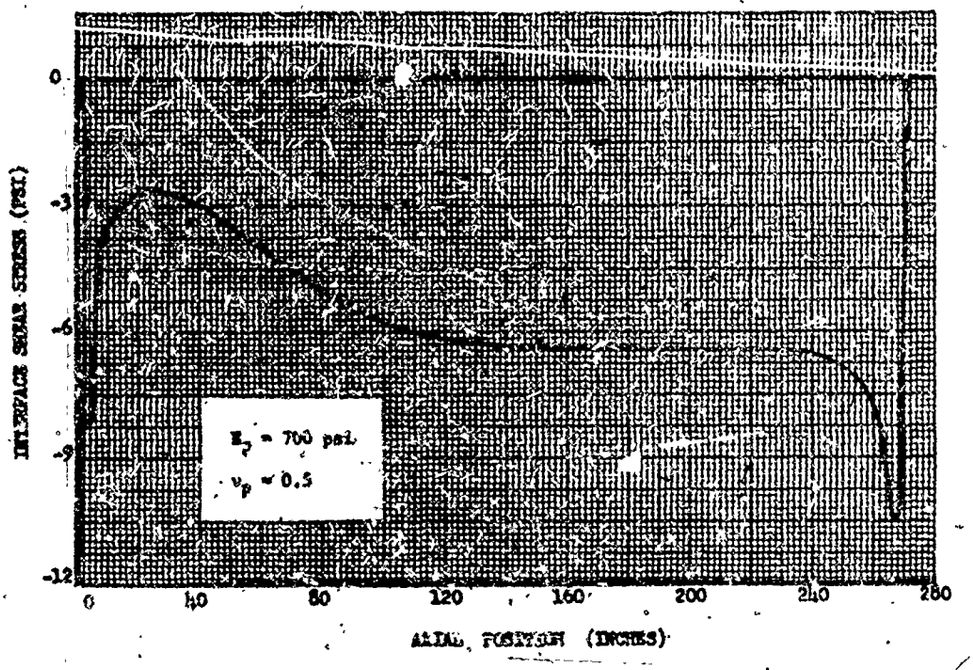

Figure 30. 156 inch diameter Motor Interface Shear Stresses versus Axial Position from Head End - 3g Sinusoidal Vertical Acceleration at 100°F.

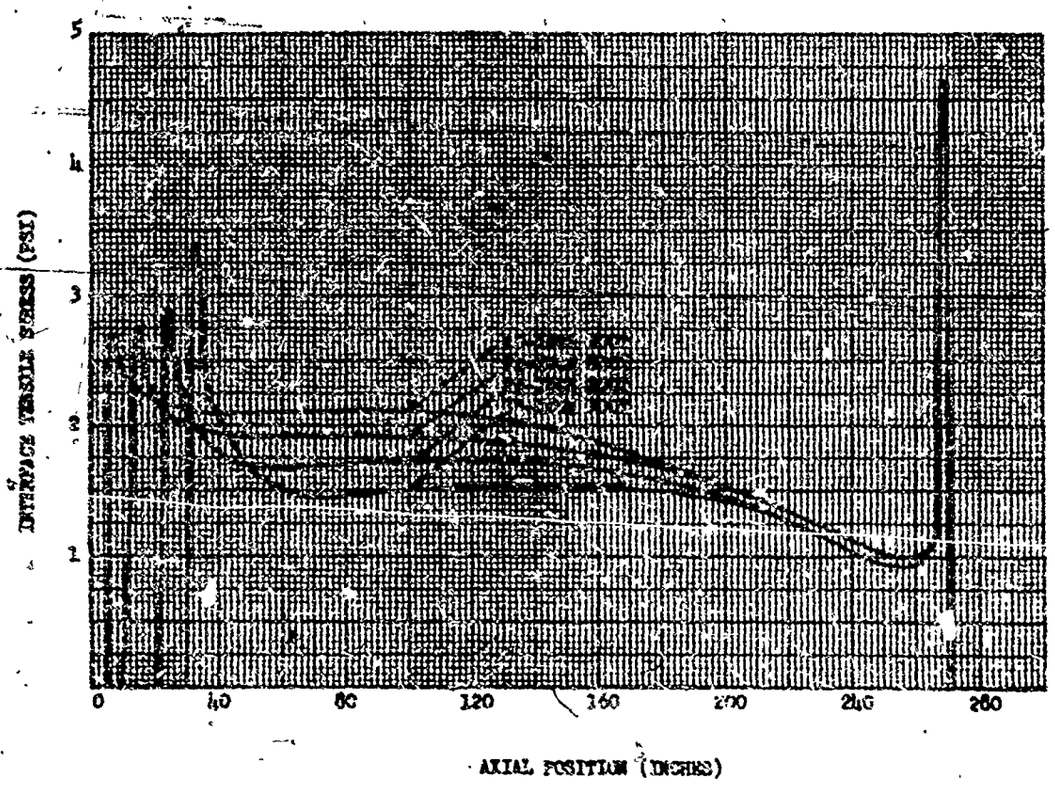

Figure 31. Normal Interface Stresses for Various Boot Lengths.

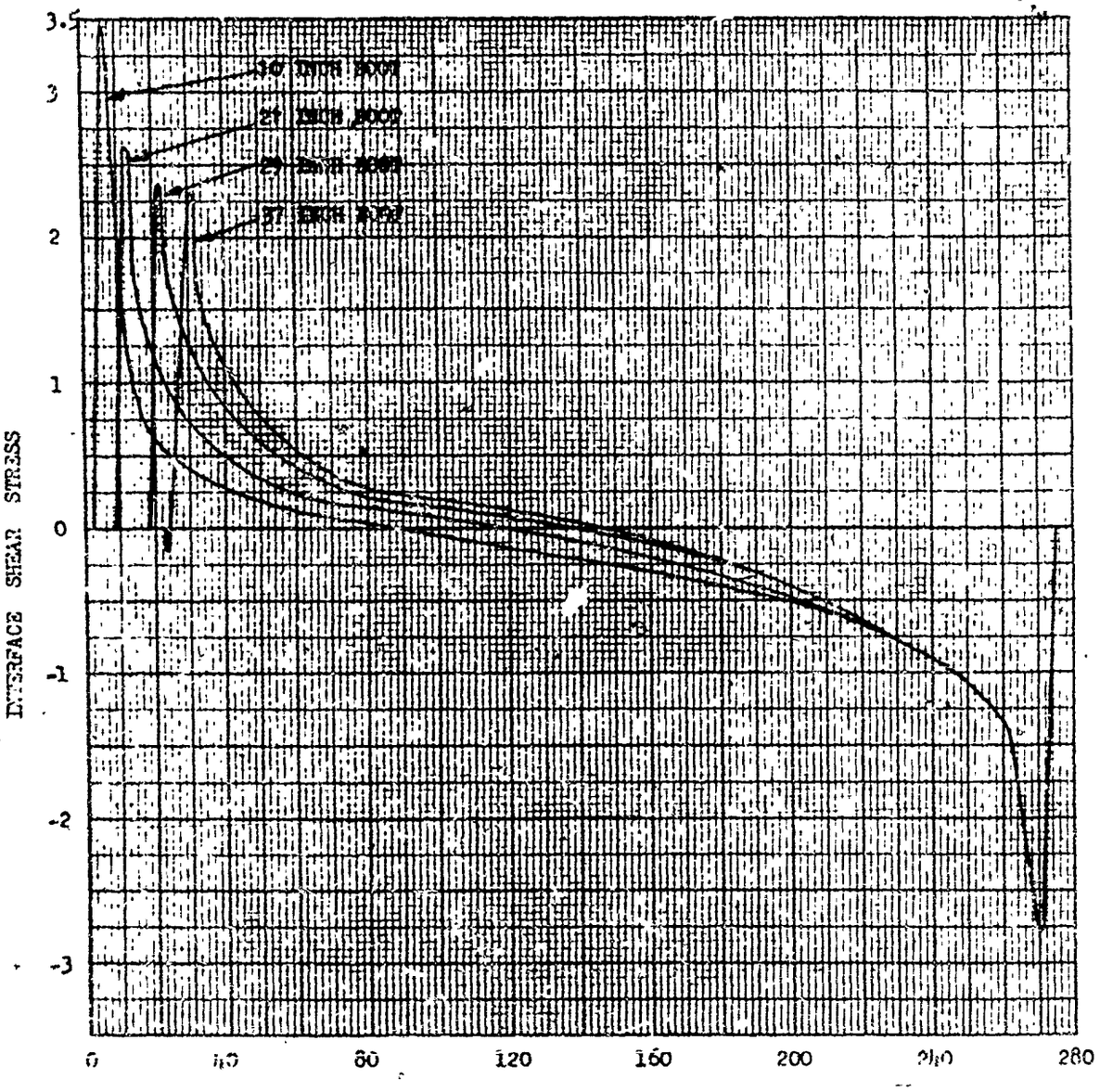

Figure 32. Interface Shear Stresses for Various Boot Lengths.

APPENDIX F

MOTOR EXPERIENCE

APPENDIX F

MOTOR EXPERIENCE

F.1 INTRODUCTION

This appendix presents a compendium of motor experience gained throughout the solid propellant industry during the past decade. Motor failures and subsequent corrective action taken are discussed in the hope that such information might benefit the entire industry in preventing similar type failures in the future. Inasmuch as the greatest effort has been made to avoid compromising the proprietorship of the various companies or causing embarrassment to any compary or presenting material of a classified nature, these discussions take on a rather general form in which the specific details relating to motor programs, mission objectives and propellant type are for the most part omitted. It is still felt that this material will benefit the new engineer entering the solid propellant industry.

F.2 MOTOR FAILURES

The first two motor failures discussed below were reported in the open literature by Rocketdyne [1]. The following motor failures are reported anonymously for the reasons cited above.

F.2.1. BOOST-SUSTAIN DEMONSTRATION MOTOR

This particular development motor had a grain geometry consisting of a partially restricted two-slot sustain and a six-slot boost. A conicyl (radial slot) was used in the transition zone between these two geometries. After a period of aging and during a

series of temperature cycles, a fracture was noted by radiographic inspection at the liner propellant interface in the sustain grain near the conicyl (section V of figure F-1). After reviewing the analyses, material properties and processing techniques, it was hypothesized that the material properties had to be significantly different from the control properties used in the analyses. This hypothesis was supported by the fact that the failure did not occur in the area previously shown to be most critical by conventional failure analyses, and later substantiated from tests conducted on samples obtained from the motor after dissection.

To provide a basis for grain structural integrity reassessment the motor was dissected using a remotely operated, TV monitored lathe at several judiciously selected longitudinal stations (see figure F-1). Propellant, propellant-restrictor and/or -liner specimens were removed; and mechanical properties were determined for material from various locations within the motor. Considerable variation in properties across the grain webs were reflected in the comparison of these specimen tests. The additional comparison with properties from control samples cast from the same propellant mix showed a significant difference and provided an assessment of the combined effects of propellant/restrictor, -/liner, -/insulation and -/mandrel compatibility; chemical migration, processing techniques; thermal cycling; vibration and high temperature aging.

Figure F-2 depicts Rex hardness distributions measured following motor dissection. These readings gave initial insight into the propellant mechanical property variational trends across the grain web. Based

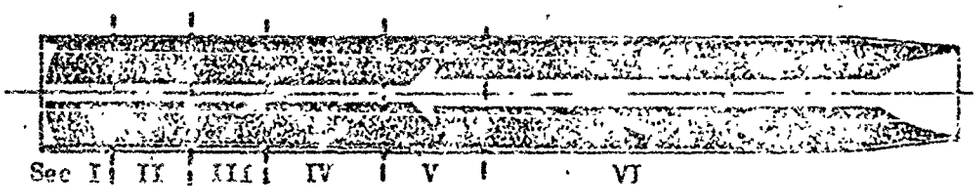

Boost-Sustain Demonstration Motor

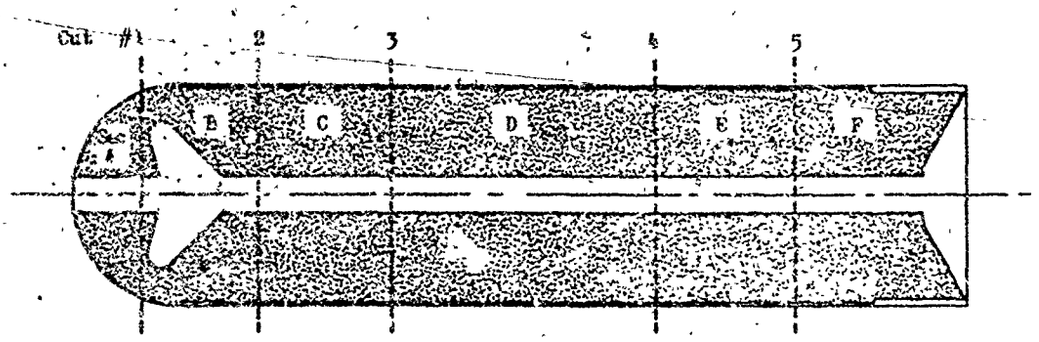

Development Motor

FIGURE F-1 MOTOR DISSECTION PLAN

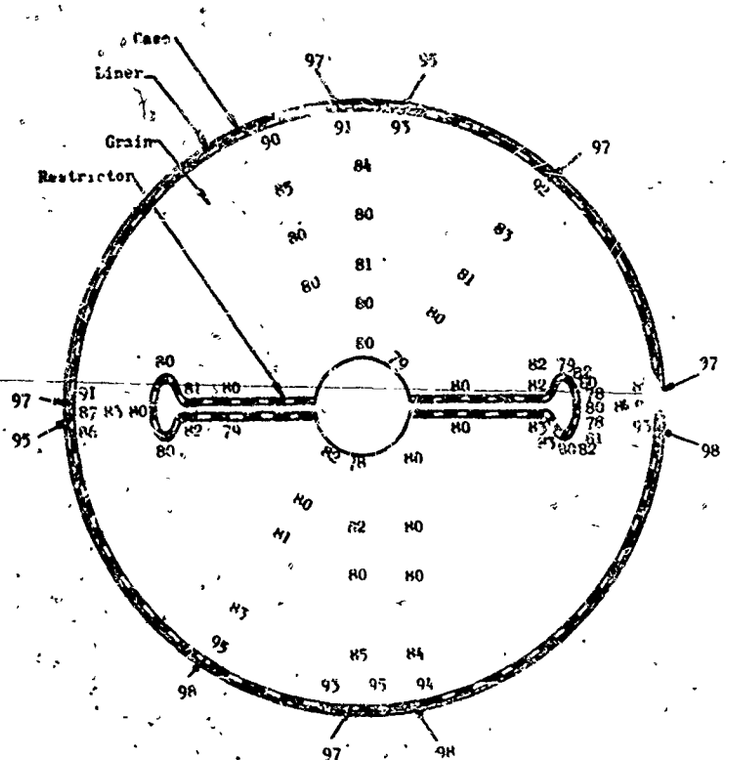

FIGURE F-2 A SUMMATION OF REX HARDNESS READINGS TAKEN ON CROSS SECTION OF SUSTAIN GRAIN SEGMENTS [1]

on this distribution, each motor section was segmented into a series of pie-shaped pieces, and peel test and numerous mechanical property specimens were removed as illustrated in figure F-3. The latter were cut with their longitudinal axis parallel to that of the motor and at various radial distances from the liner-propellant interface. The graphical representation of the mechanical properties of these specimens, presented in figures F-4, F-5, F-6, illustrates the degree of heterogeneity across the grain web. These properties and the associated distributions were analytically considered in a reassessment of the grain's structural capability under various loading conditions.

A two-dimensional model of the central region of the grain (figure F-7) was used in a finite element analysis to reassess the structural capability of this grain design. The simulation of the propellant modulus variation shown in figure F-4 is also depicted in this figure. Inasmuch as the 2-D model assumes the grain to be axisymmetric, it was necessary to assume equivalent web fractions for the slotted boost and sustain grains. The basis for this assumption was to utilize a web fraction which for a cylindrical grain would predict a radial bond stress under a plane strain loading condition which was equal to the maximum value predicted in the plane strain analyses of the actual slotted grain cross sections. The web fractions were 68 and 50% for the sustain and boost grains, respectively. A thermal analysis was carried out considering this model with the modulus distribution shown in figure F-7.

Figure F-8 illustrates the analytically determined maximum principle stress distributions in the propellant at the liner interface

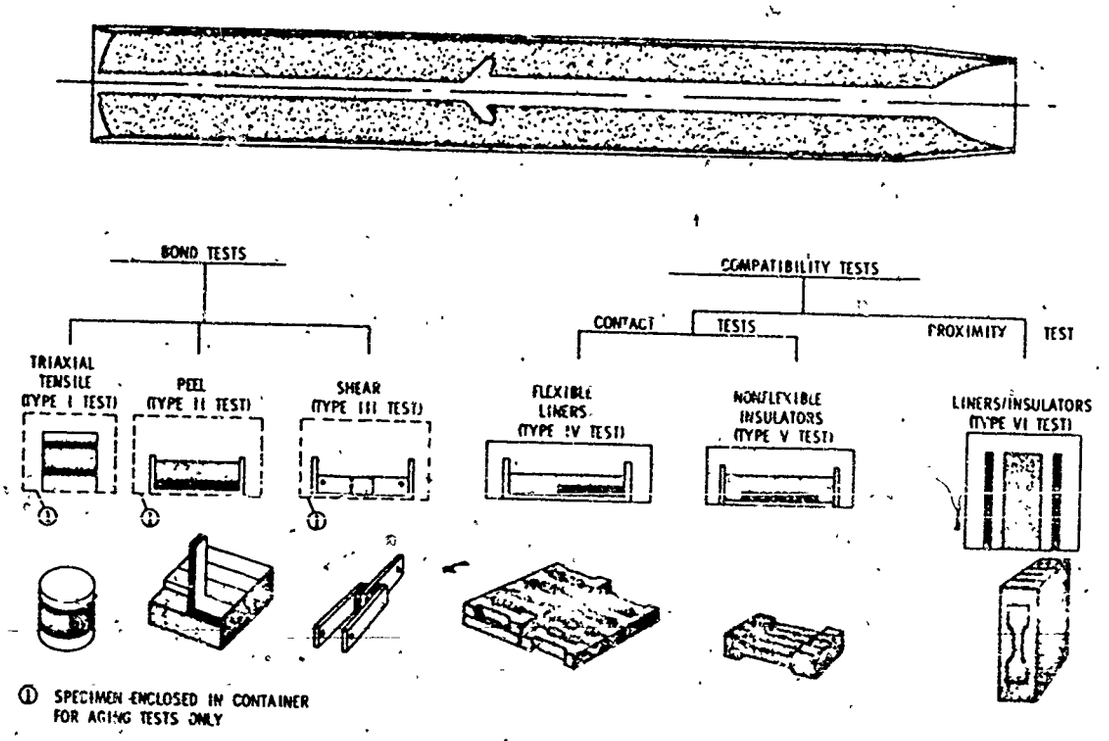

FIGURE F-3 LINER-PROPELLANT BOND AND SYSTEM COMPATIBILITY TESTS [1]

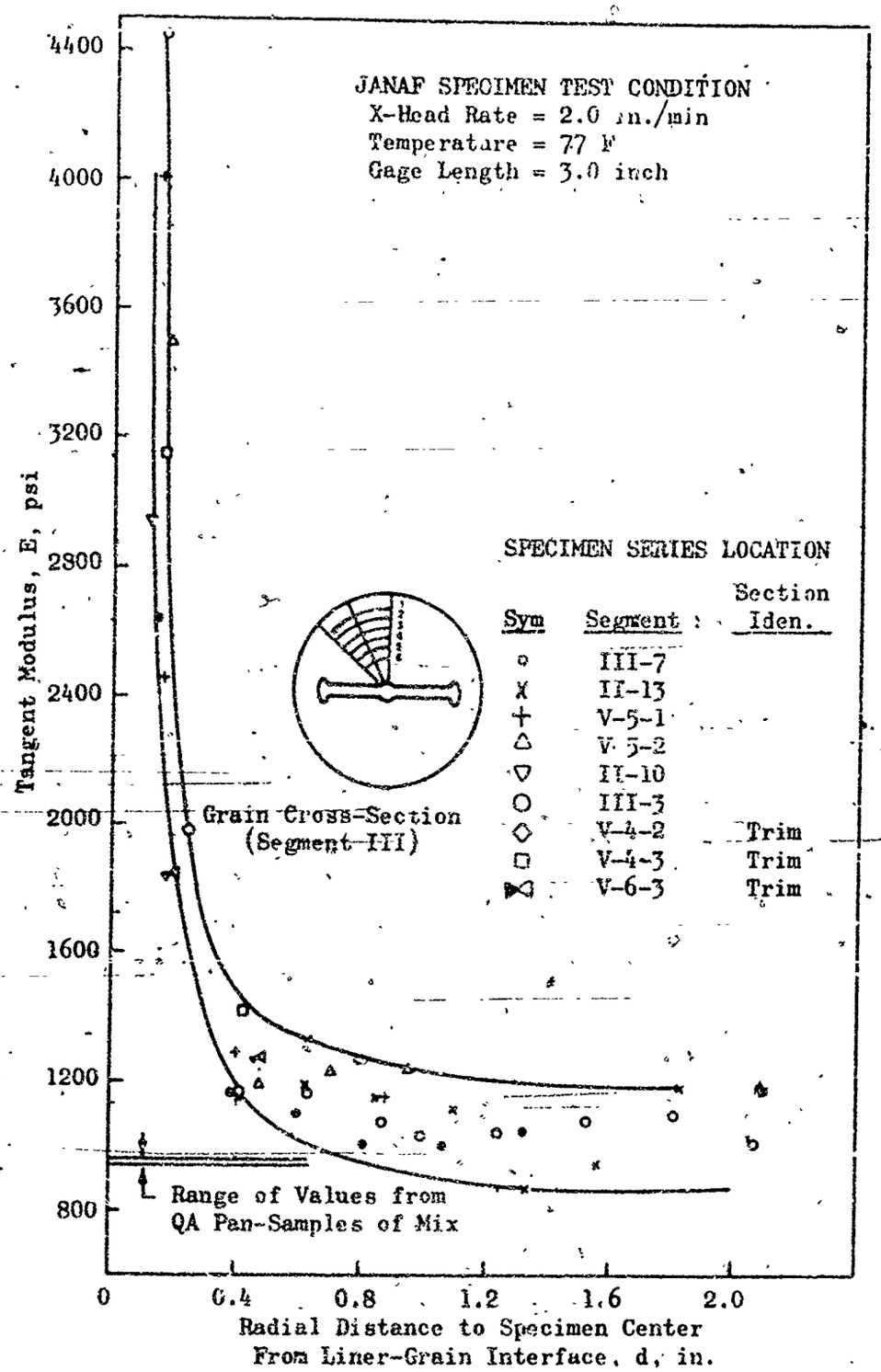

FIGURE F-4 MODULUS VS SPECIMEN LOCATION [1]

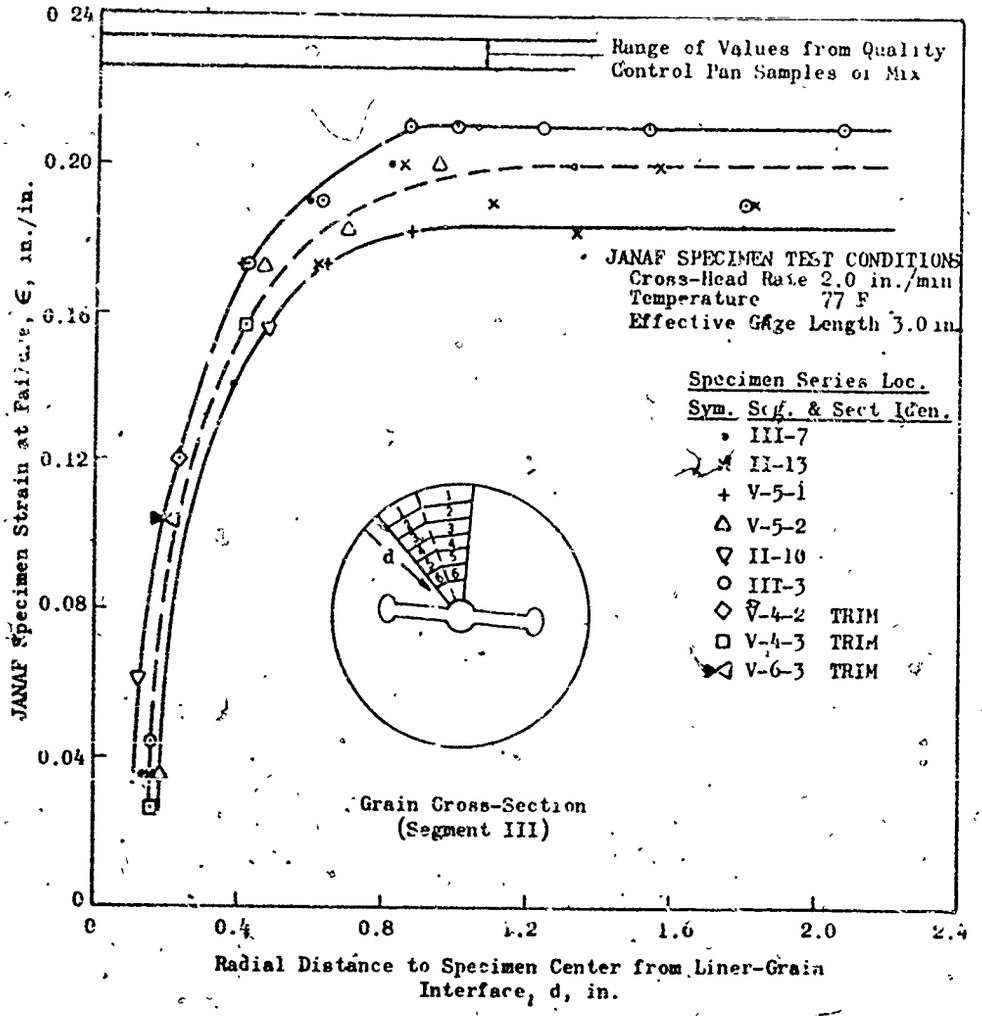

FIGURE F-5. GRAIN ALLOWABLE--UNIAXIAL STRAIN VARIATION WITH DISTANCE FROM LINER-GRAIN INTERFACE [1]

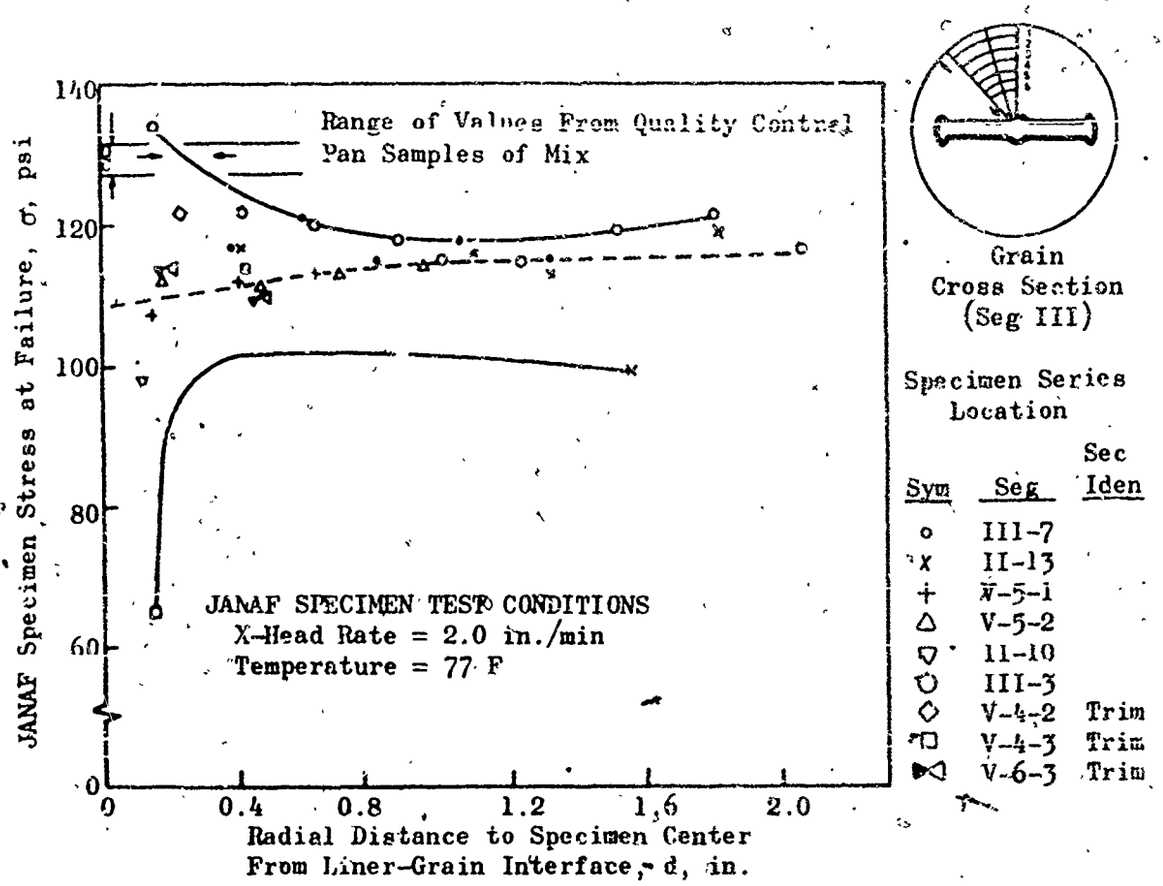

FIGURE F-6, GRAIN ALLOWABLE--UNIAXIAL STRESS VARIATION WITH DISTANCE FROM LINER-GRAIN INTERFACE[1]

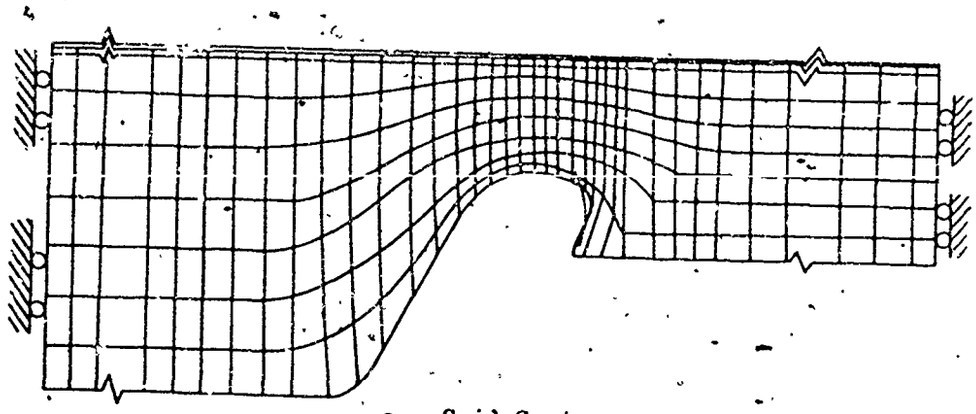

a. Grid System

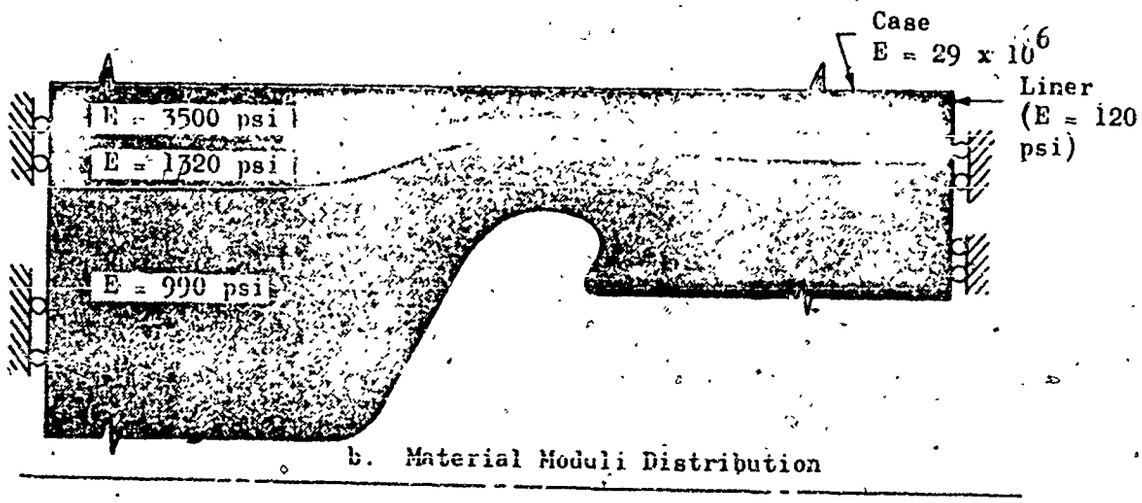

b. Material Moduli Distribution

FIGURE F-7 MATHEMATICAL MODEL FOR BOOST-SUSTAIN GRAIN MOTOR[1]

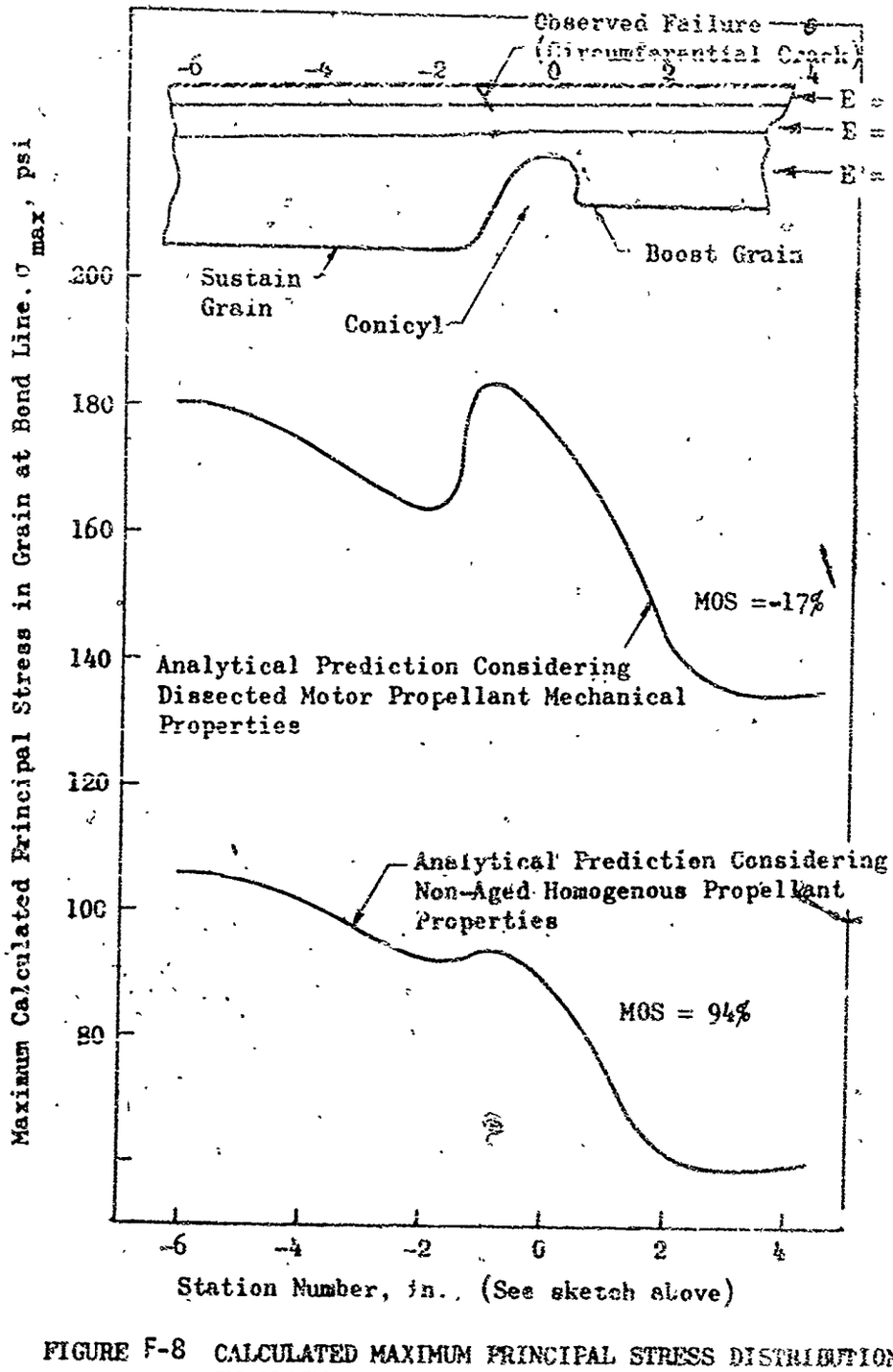

FIGURE F-8 CALCULATED MAXIMUM PRINCIPAL STRESS DISTRIBUTION IN GRAIN ADJACENT TO LINER IN CENTRAL REGION OF MOTOR[1]

in the central region of this grain using homogeneous propellant properties as determined from unaged control samples, and employing the heterogeneous propellant modulus distribution indicated at the top of figure F-8 and in figure F-7. Using the data from the dissected motor, a negative margin of safety of 17% was calculated at the propellant/liner bond. Considering the conventional laboratory control data a positive margin of safety of 94% was predicted. The circumferential crack, schematically illustrated in figure F-8, was observed during radiographic inspection of the temperature cycled motor and confirmed by visual inspection of the dissected grain.

Figure F-9 illustrates the associated significance of heterogeneity at the inner bore of the restrictor portion of this slotted grain design. The uniaxial strain at failure of specimens taken across the dissected grain web give a relative assessment of the local-immediate vicinity of restrictor-reduction in propellant allowable elongation.

The failure in this demonstration motor was attributed to a curative imbalance between the propellant and liner which caused a hardening of the propellant and reduction of elongation at the propellant liner interface.

This failure and subsequent structural integrity reassessment program illustrates the importance and usefulness of motor dissection as a means of assessing grain structural integrity. The curves of mechanical property data obtained from the dissected motor superposes cumulative damage effects resulting from aging and temperature cycling. Thus, comparison of such data with un-aged control sample data should provide the grain structural integrity engineer with a higher confidence

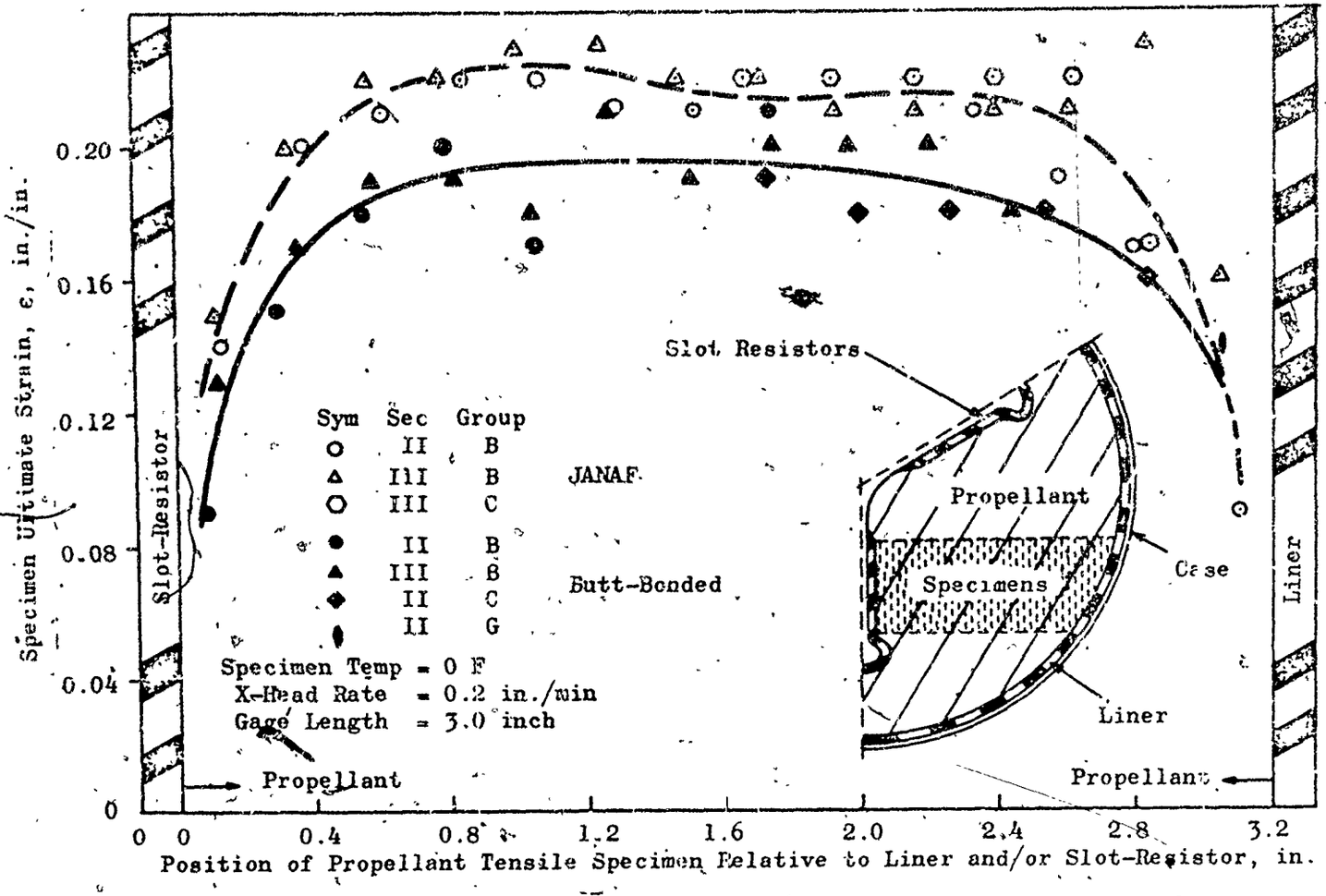

FIGURE F-9 PRIMED LINER/SLOT-RESTRICTOR INFLUENCE ON PROPELLANT ULTIMATE ELONGATION CAPABILITY[1]

level in the propellant mechanical property capabilities.

This failure also points out that it is possible to experience failures in areas which are not thought to represent the most critical regions by conventional analyses.

F.2.2. DEVELOPMENT MOTOR

As a result of the successful dissection and grain structural integrity reassessment program for the boost-sustain demonstration motor described in F.2.1. above, and the observed significant differences between motor and control propellant properties, a similar program was carried out by Rocketdyne when they experienced a propellant structural failure during another development motor program. A schematic view and the five cuts used in dissecting this motor are shown in figure F-1. This motor is approximately 12 inches in diameter, 90 inches long and contains 300 pounds of propellant. After high temperature aging followed by temperature cycling, the propellant separated from the liner at the aft end in the region of the glass phenolic insulator, and several small cracks were noted at the forward end of the igniter bore. These latter cracks extended around the forward dome near the propellant/liner interface. These failures were not expected since previous stress analysis showed the area with the minimum margin of safety was the tip radius of the conicyl.

Rex hardness readings for propellant taken from sections A and B are shown in figure F-10. Uniaxial JANAF specimens were cut from pie-shaped segments of propellant removed from the various sections, and tensile testing of the JANAF specimens was done at several crosshead rates and temperatures. Typical results of this testing for section B

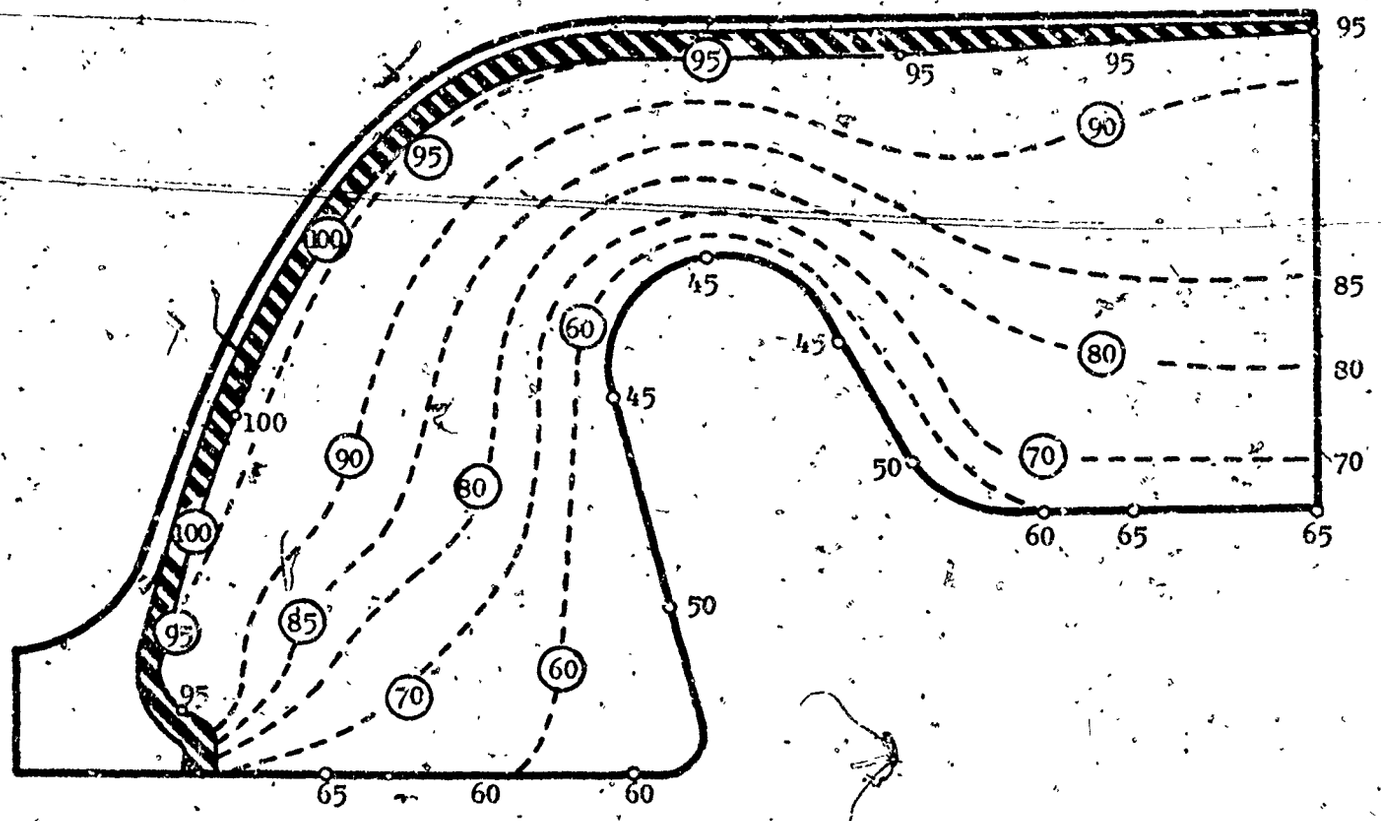

FIGURE F-10 REX HARDNESS DISTRIBUTION—FORWARD END OF DEVELOPMENT MOTOR [1]

are shown in Table F-I. These data were plotted as a function of the radial distance from the propellant/liner interface to the center of the specimen as shown in figures F-11 through F-13. Control sample properties for the same propellant mix are also presented in these figures for comparative purposes.

The original grain structural analysis, based on control properties, showed a minimum margin of safety of 170% at the conicyl tip. The mathematical model the analysis of sections A and B is shown in figure F-14. The modulus distribution based on dissected properties is also shown in this figure. When heterogeneous properties and allowable propellant values from figure F-11 and F-12 were used in a finite element computer analysis, this margin of safety decreased to 112%. However, strain in the igniter bore became the critical item and the resulting margin of safety for this area as shown in figure F-14 was -20% indicating that the observed propellant cracking should have occurred.

The liner and propellant in section F was significantly different from the remainder of the motor. Because of the presence of the glass phenolic insulator in section F, the propellant and liner in this area were softened instead of hardened as in section B. The softening of the propellant and resulting changes in tensile strength and elongation are shown in figures F-15 through F-17. The margin of safety at the aft tip of section F was 180% in the original analysis; however, the margin of safety became negative, when the dissected motor properties of figures F-15 through F-17 were used.

Although some changes in material properties were anticipated for the motor after high temperature aging and temperature cycling, based

TABLE F-I JANAF UNIAXIAL TENSILE PROPERTIES FROM GRAIN SEGMENT**

TEST CONDITIONS	SECTION B			
	Distance* (Liner Interface Inward)	ε, in./in.	σ, psi	E, psi
		Section B-1		
	0.150	0.05	187	5500
	0.389	0.17	183	1587
	0.587	0.19	169	1293
	0.804	0.17	130	1016
		Section B-2		
	0.134	0.04	190	6332
	0.377	0.17	192	1646
	0.606	0.19	164	1262
	0.843	0.18	133	1039
Temp = 77°F	1.071	0.16	105	875
		Section B-3		
Gage Length = 3.0 in.	0.159	0.04	163	5094
	0.436	0.17	182	1551
Crosshead Rate =	0.673	0.21	159	1109
2.0 in./min	0.903	0.20	134	944
	1.141	0.16	88	746
		Section B-4		
	0.155	0.04	174	5327
	0.421	0.16	184	1542
	0.652	0.21	180	1330
	0.881	0.17	125	972
	1.081	0.15	84	724
		Section B-5		
	0.150	0.05	194	5087
	0.395	0.17	189	1549
	0.600	0.19	162	1197
	0.819	0.18	138	995
	1.013	0.19	116	845

*Radial Distance from Liner-Propellant Interface to JANAF Specimen

**Information taken from Reference 1.

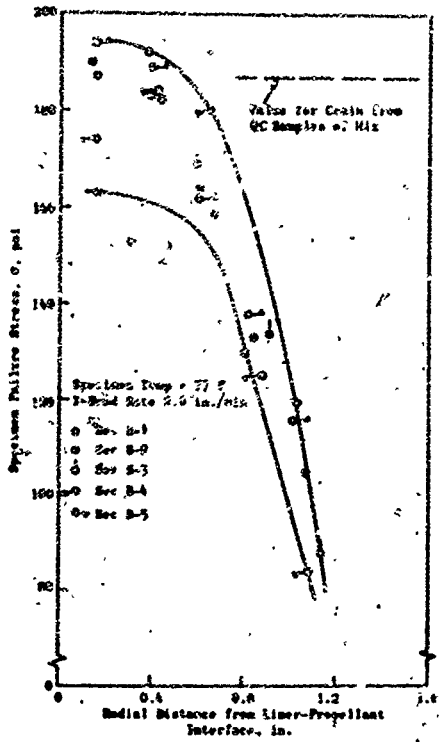

FIGURE F-11 PROPELLANT UNIAXIAL STRESS[1]

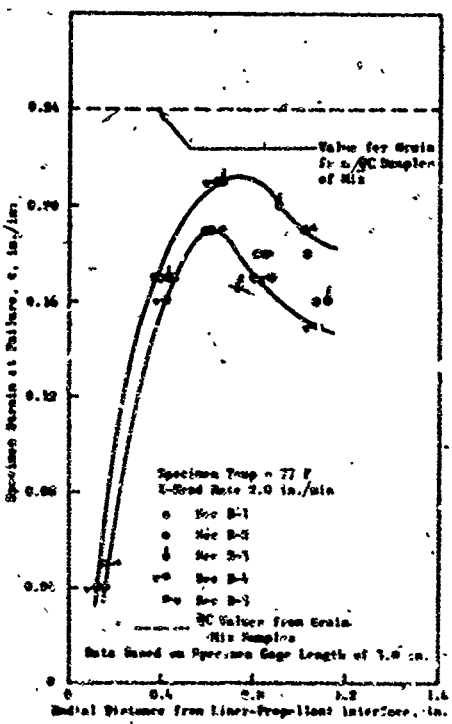

FIGURE F-12 PROPELLANT ELONGATION, UNIAXIAL[1]

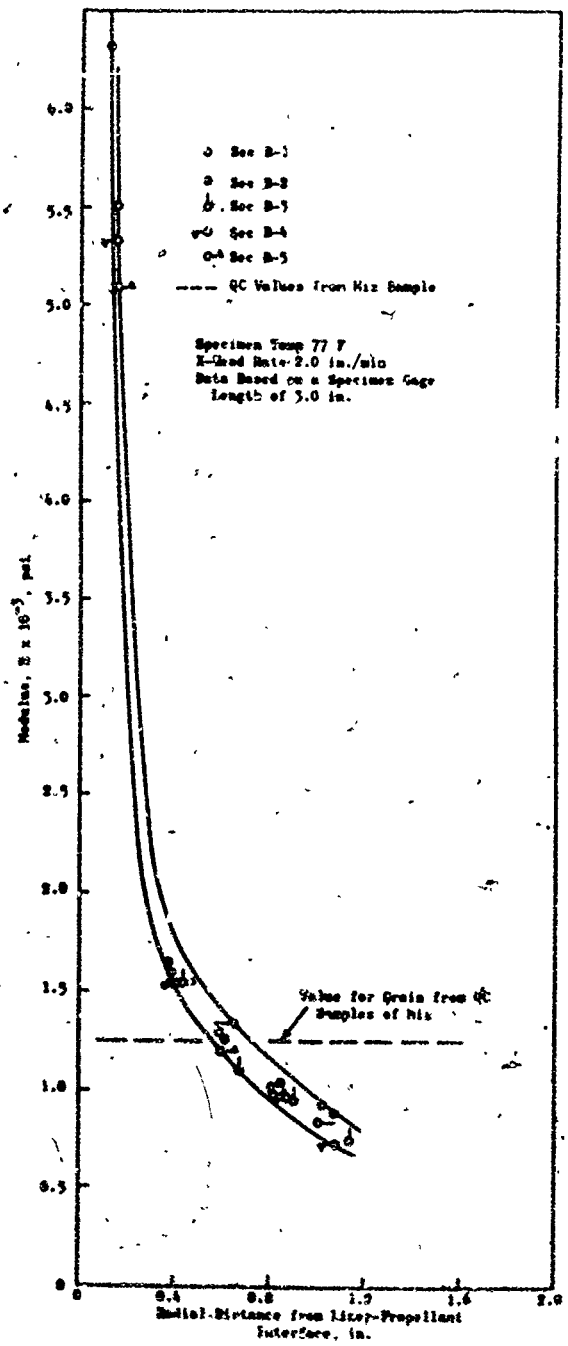

FIGURE F-13 PROPELLANT UNIAXIAL MODULUS[1]

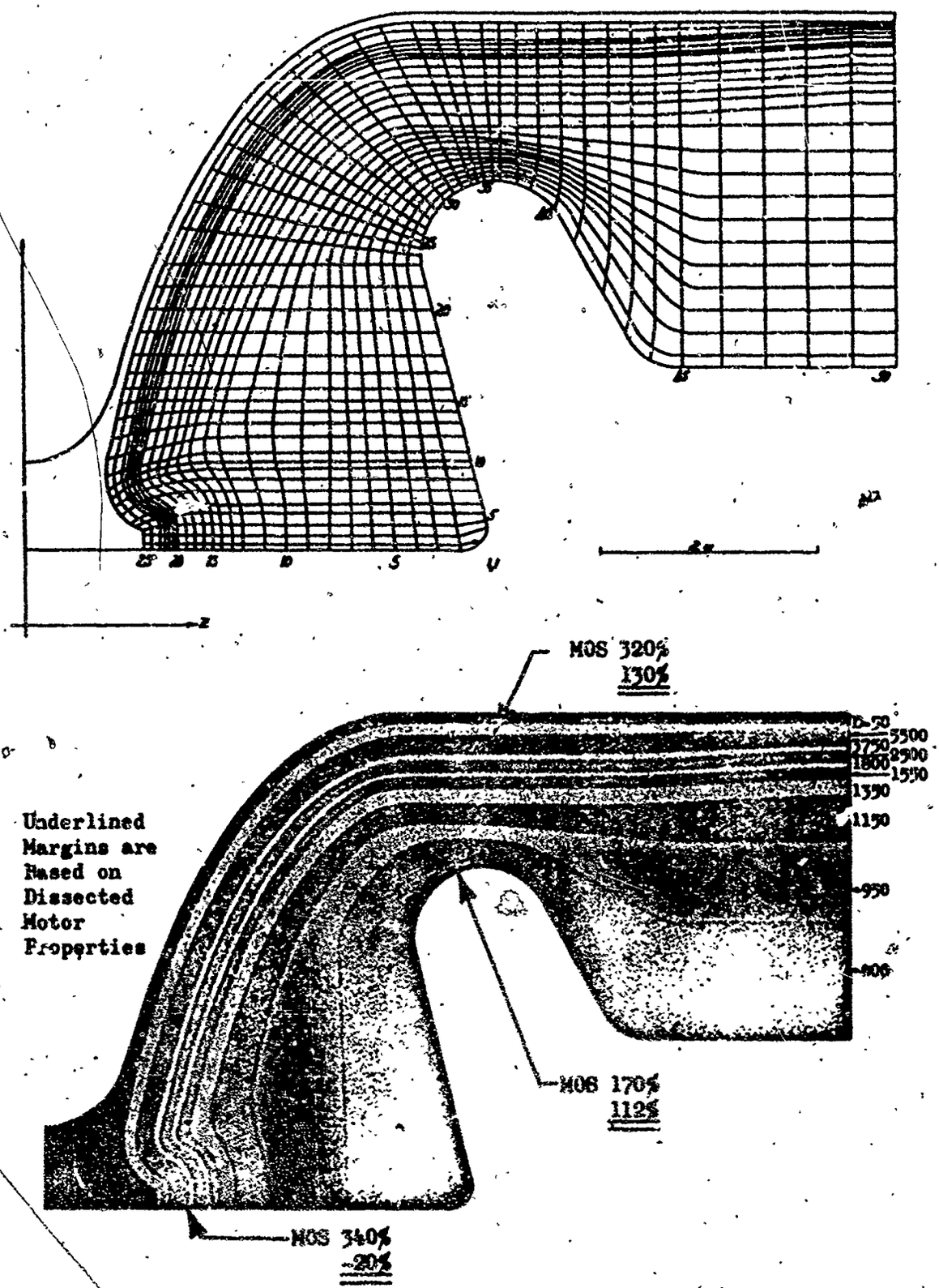

FIGURE F-14 FORWARD END AXISYMMETRIC GRID SYSTEM [1]

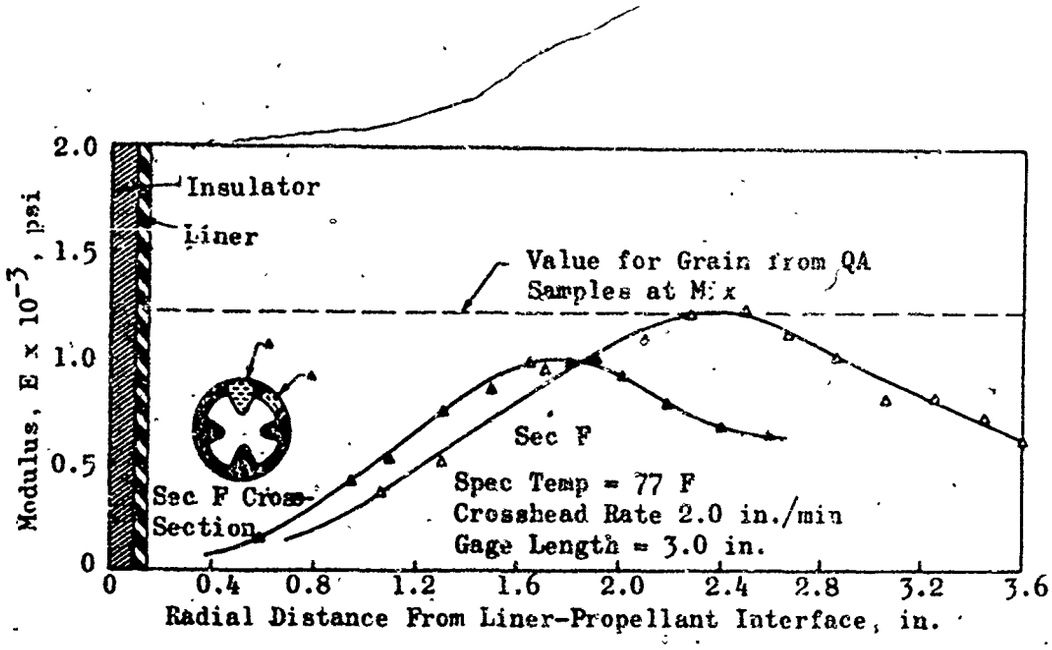

FIGURE F-15 PROPELLANT UNIAXIAL MODULUS[1]

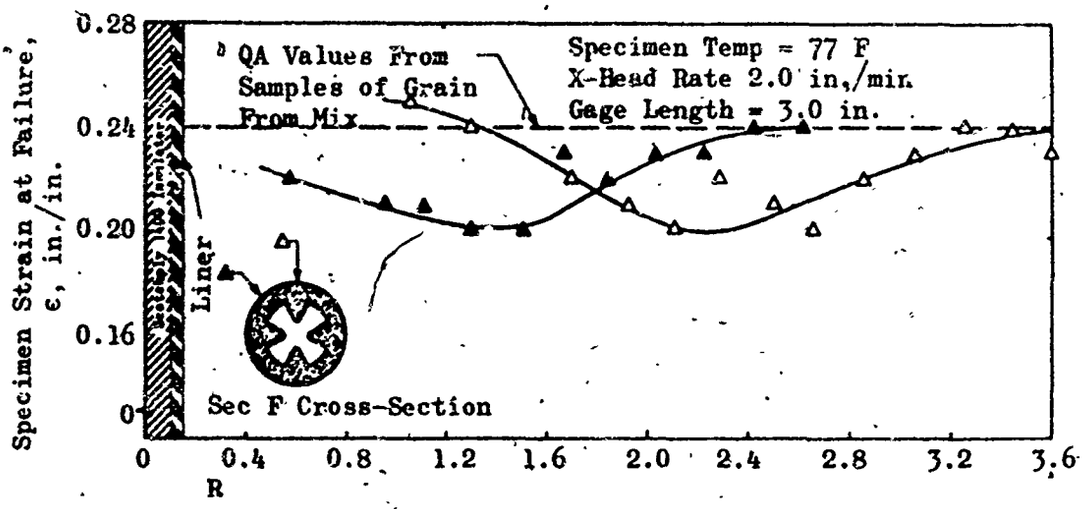

FIGURE F-16 PROPELLANT UNIAXIAL ELONGATION[1]

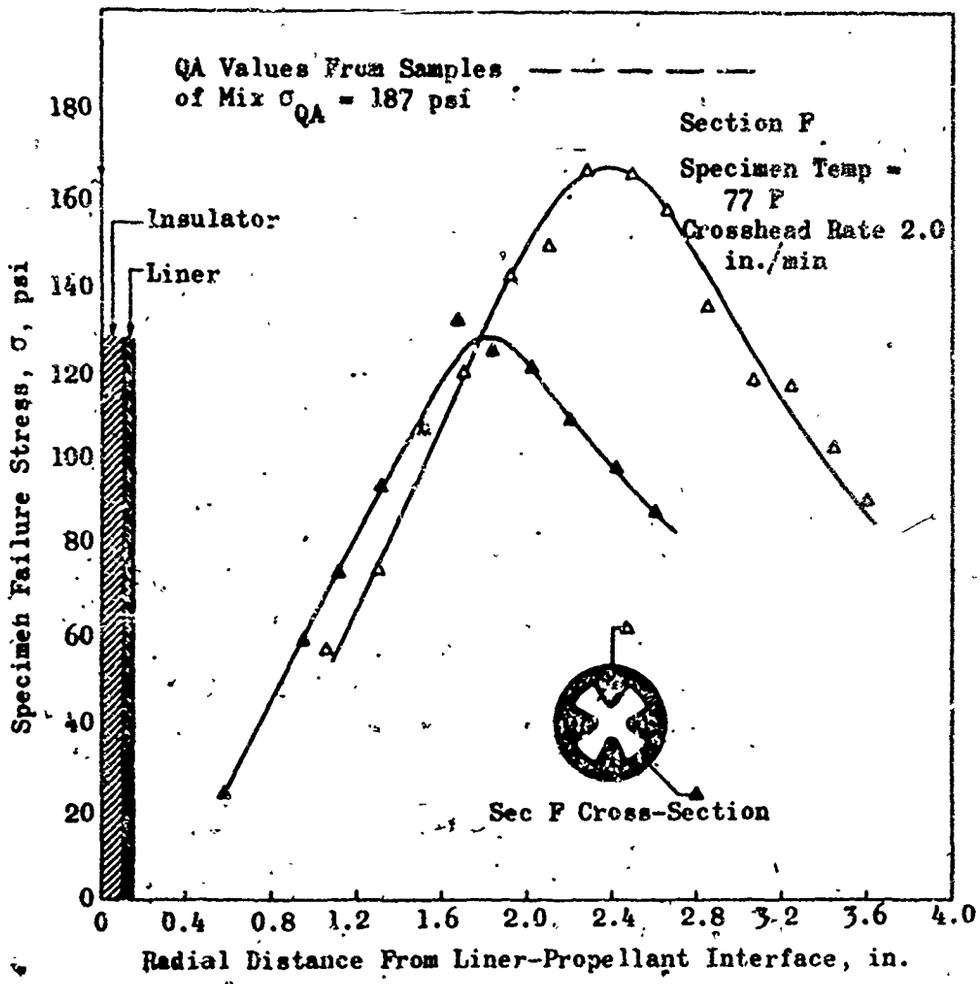

FIGURE F-17 PROPELLANT UNIAXIAL STRESS[1]

on previous motor experience and laboratory testing, the changes were not anticipated to be as significant as shown by the dissection results. The softening of the propellant at the inner bore and resulting decrease in tensile strength and elongation shown in figures F-10, F-11, and F-12 was traced to a conicyl mandrel coating material/propellant incompatibility which became evident after high temperature aging. Hardening of the propellant and reduction of elongation at the propellant liner interface shown in figures F-10 and F-12 was caused by a Mapo curative imbalance between the propellant and liner. These problems were solved by changing the conicyl mandrel coating material, and balancing the propellant-liner curative. The softening of the propellant at the aft end and resulting decrease in tensile strength as shown in figures F-15 through F-17 were traced to out gassing of the glass phenolic insulator during high temperature aging. This problem was solved by changing the insulator material, and changing the aft end propellant contour to make a 30° angle with the case, instead of the 60° angle the previous motor had.

F.2.3. CASE 3

A catastrophic failure occurred during endurance vibration of an essentially rod and tube grain design at high temperature. The rod was supported at 6 locations - 3 forward and 3 rear - by sponge pads. The failure was attributed to excessive temperature rises under the sponge pad supports. The problem was satisfactorily corrected in subsequent motors by increasing the number of support pads to 9 and by using a stiffer sponge material.

F.2.4. CASE 4

During 170°F endurance vibration cracks were observed at the base of some star points in this motor program as illustrated below. Initially heavy accelerometers were attached to the star points that cracked. These accelerometers were replaced by smaller, lightweight accelerometers; however, the problem still persisted. It had been reasoned, that the large mass of the original accelerometer had acted to greatly increase the amplitude of the deflections. When the problems still persisted, however, it was apparent that the accelerometers did not represent the real problem. The problem was corrected by providing support for the star points. The real problem was probably associated with the large deflections that long slender star points may undergo during sustained vibration; however, it is unusual that cracks developed rather than excessive temperature rises being observed.

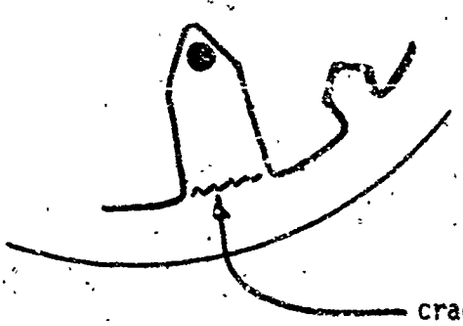

F.2.5. CASE 5

This grain design was essentially a cantilever grain supported on a plastic tube which burned on inner and outer surfaces.

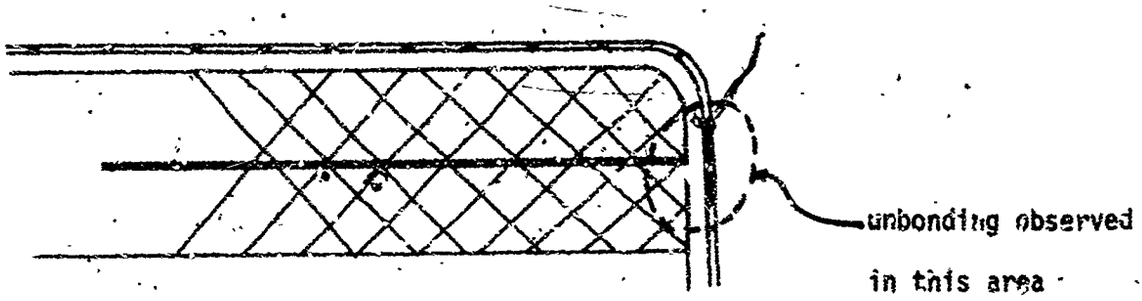

Grain unbonding during temperature cycling followed by propellant peeling from the grain support during firing was observed. This problem was corrected by introducing fiberglass reinforced floaters (i.e., flaps) at the head end of the motor.

F.2.6. CASE 6

Cracking of this motor during temperature cycling was observed under the locations where clamp-on type aircraft hangers were attached. The problem was attributed to the large amount of induced case ovality. The problem was corrected by a redesign of the hanging fixtures.

The problems of grain cracking directly under hanging lugs during low temperature drop tests also occurred. The sponsoring government agency had supplied the original design configuration and hanging fixtures, and the propulsion contractor had already redesigned the hanging fixtures once to correct the temperature cycling problem. Rather than invest the effort required for another redesign of the hanging fixtures, the sponsor chose to raise the low temperature extreme for drop testing. No further problems were observed at this new temperature; however, the original problem was not satisfactorily solved either analytically or experimentally.

The above problem was observed in another motor program by this same company. Again, the problem was circumvented by the sponsor raising the low temperature requirements for drop testing.

F.2.7. CASE 7

During temperature cycling and low temperature vibration grain/case separation at the forward end of a high mass fraction motor was observed. A three-dimensional photoelastic analysis was performed, and the head end

configuration was changed slightly with the released area extended slightly.

F.2.8. CASE 8

This failure is a good example of the interaction between a grain stress analysis and ballistics. A schematic of the aft end of the motor is shown below.

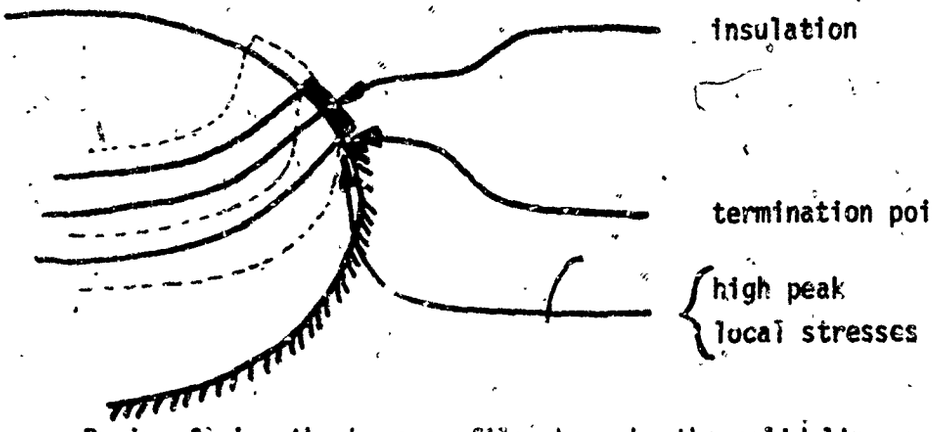

During firing the burn profile shown by the solid line was obtained. The angle at which the burn surface reached the termination point was such that high local stresses and grain/case unbonding resulted. The situation was corrected by extending the insulation as shown by the dotted line which slightly changed the burn shape and at which the burn surface reached the termination point. This example points out that critical stresses do not necessarily occur at motor ignition, but may develop during motor burning.

F.2.9. CASE 9

This failure involved a demonstration motor using a submerged nozzle and a full diameter radial slot separating the main grain and a small "doughnut" shaped aft grain. The design is shown schematically below. Shortly after ignition a failure characterized by a distinct increase in motor pressurization followed by ejection of the nozzle assembly was observed. Following an extensive failure investigation,

it was concluded that the design of aft grain and cavity with the restricted flow passages resulted in preferential ignition in the aft cavity. The slot opening was wider than the entrance to the aft cavity so that a substantial pressure differential existed between the slot and the furthermost aft cavity. This pressure differential was of sufficient magnitude to rupture the small aft grain. The additional pressures generated by the additional burning area resulting from the rupture of the aft grain and the restriction of gas flow from the aft cavity were of sufficient magnitude to cause failure of the nozzle attachment bolts.

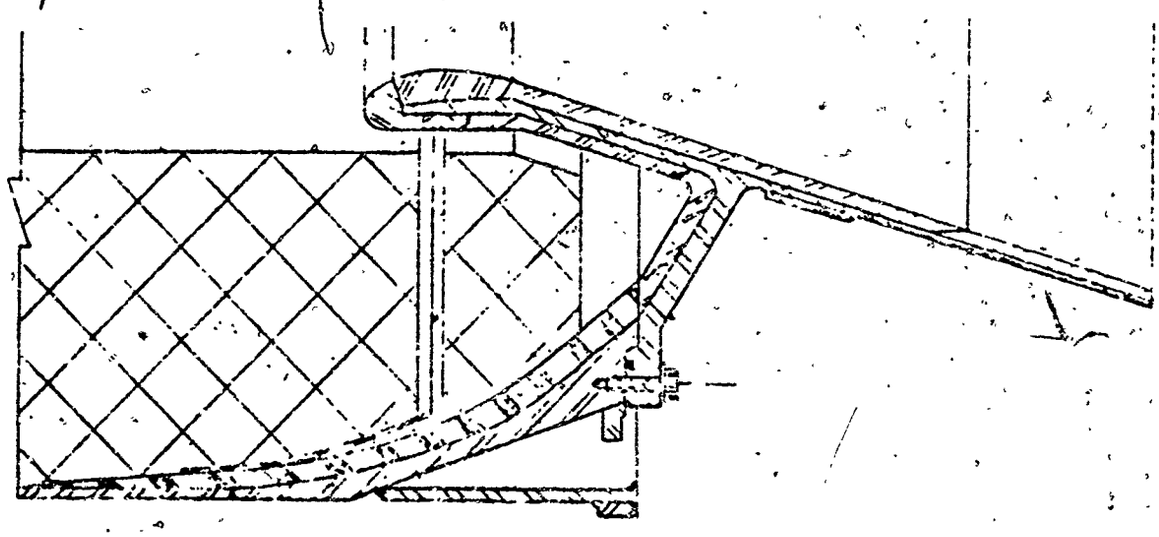

This problem was corrected by increasing the width of the entrance to the aft cavity; thus allowing an equal pressure on all faces of the aft grain.

F.2.10. CASE 10

This next example involves the structural failure of several motors due to the presence of moisture. The failure investigation program is discussed in some detail since it vividly illustrates the structural

damage that may be incurred due to the presence of moisture, and it brings out several important facets of propellant behavior and processing controls that should be considered in a production motor program.

Inspection upon completion of various tests revealed that five qualification motors exhibited cracks in the propellant grain web valleys. Investigation showed that all five motors had undergone, among the various tests, temperature cycling between the high and low temperature environmental limits. In all instances, inspection of the grains indicated that moisture had been present.

Probing the cracks and the areas where moisture had been present revealed darkened areas which were indicative either of oxidized propellant binder or penetration of the grain by a carrier of the oxidized surface material of phenylene diamine. Because phenylene diamine is soluble in water, it was initially assumed, and later substantiated, that the propellant had absorbed water.

The mechanical properties of the particular propellant involved are highly sensitive to moisture content. Laboratory tests on cut propellant samples showed that the physical properties of propellant are degraded when exposed to humid atmospheres (figure F-8). Therefore, it was conjectured that if the propellant was exposed to moisture and then subjected to a low temperature, the grain would not have sufficient low temperature elongation to survive the exposure.

Consideration of all other possibilities resulted in no assignable cause which could have caused the cracks. Although the original premise of moisture degradation could be supported quite well, the source of the moisture could not be determined. The motors were closed during cycling

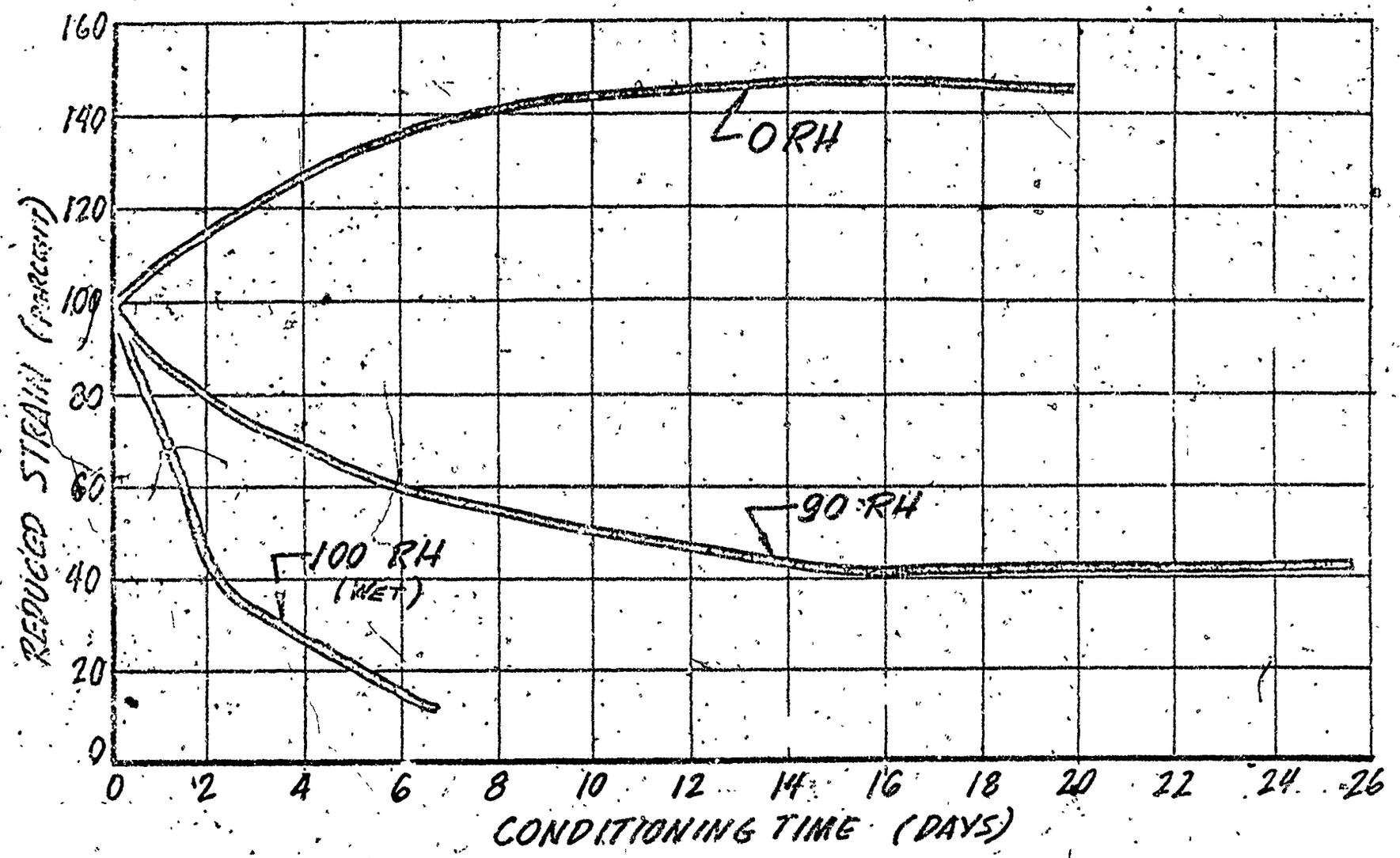

Figure F-18 Constant Elongation Rate Properties of Propellant, Humidity Level at 70°F, Test Temperature 70°F

with a semi-rigid, polyethylene over-caps on both the igniter boss and the aft closure flange. In addition, the normal breathing of the motor cavity as the temperature changed could not account for the large amounts of moisture found in the motors. It was determined analytically that eight changes of air at 50 percent relative humidity and 70°F temperature were necessary to bring in one fluid ounce of water; however, nearly one pint was drained from one motor, and the desiccant bags in another motor had gained one pound when the motor was inspected. Analysis of the propellant raw ingredients revealed the possibility for six pounds of water to be present in the grain, not including the additional 2.88 pounds which is added as a processing aid. If as little as 10 percent of this water could migrate to the grain surface, it would account for the amount of moisture which was found.

A comprehensive failure investigation was undertaken to isolate the source of the moisture, to verify that moisture can cause grain failure, and to eliminate any other possible causes of failure. This program was divided into three sections:

(1) Propellant Laboratory Tests

(2) Structural Integrity Laboratory Tests

(3) Full-Scale Motor Tests

A plant scale batch of propellant was mixed and cast to provide all of the samples for the propellant investigation.

PROPELLANT LABORATORY TESTS

ANALYSIS OF RAW MATERIALS AND PROPELLANT

To determine the amount of moisture carried through the mixing and deaeration cycles, moisture analyses were made on the raw materials and on the propellant at the end of the mix cycle, after the vacuum casting operation, and at end of cure. The results follow.

Material	H_2O(%)	Analysis method
Unground ammonium perchlorate	0.02	Karl Fischer reagent
Ground ammonium perchlorate	0.03	Karl Fischer reagent
Magnesium oxide	0.29	Oven drying
Fuel slurry	0.59	Azeotropic distillation
Propellant mix*	0.13	Calculated
Propellant:		
end of mix	<0.04	Azeotropic distillation
vacuum cast	<0.05	Azeotropic distillation
cured in sealed container	0.07	Desiccation

*Based on H_2O content of ingredients added.

Since the theoretical quantity of water resulting from curing reactions has been calculated as 0.19 percent, it is apparent that the postulated reactions are incomplete, or part of the water is tied up irreversibly by reactions with MgO or $Mg(ClO_4)_2$.

The value of 0.07 percent for moisture in the cured propellant is appreciably less than anticipated at the start of the investigation.

SPECIAL STUDIES

Equilibrium moisture content. Many materials, including solid propellants, exhibit an equilibrium moisture content which is a function of relative humidity. Thus, at a specified relative humidity,

propellant having a moisture content greater than the equilibrium moisture value will lose water until the equilibrium moisture value will lose water until the equilibrium value is attained, while propellant at a lower than equilibrium value will gain moisture.

From these data it is concluded that practically all unbound or unoccluded water present in raw materials is eliminated during the mixing process. Most of the water released from the cure reactions after completion of the mix cycle is retained by the propellant. Knowledge of the propellant equilibrium moisture relationship is essential to an understanding of processes involving the drying or wetting of propellant. Since the relationship can vary somewhat with temperature, measurements were carried out at both 25°C and 60°C. The experimental procedure was as follows.

Samples of propellant were prepared in the form of cuttings and dried by desiccation until no further loss in weight occurred, and the samples in weighing dishes were then placed into desiccators containing saturated salt solutions which maintain a known constant relative humidity, as indicated below.

Solution	Relative Humidity at 25°C (%)	Solution	Relative Humidity at 60°C
$LiNO_3$	47	NaBr	50
NaCl	76	NaCl	74
KCl	85	KNO_3	82
KNO_3	93	$CuSO_4$	94

Dishes were weighed periodically over a period of 260 hours, after which time all weights had stabilized except those over 90 percent relative humidity which were continuing to gain weight. For comparative purposes, samples of ammonium perchlorate were also exposed and weighed.

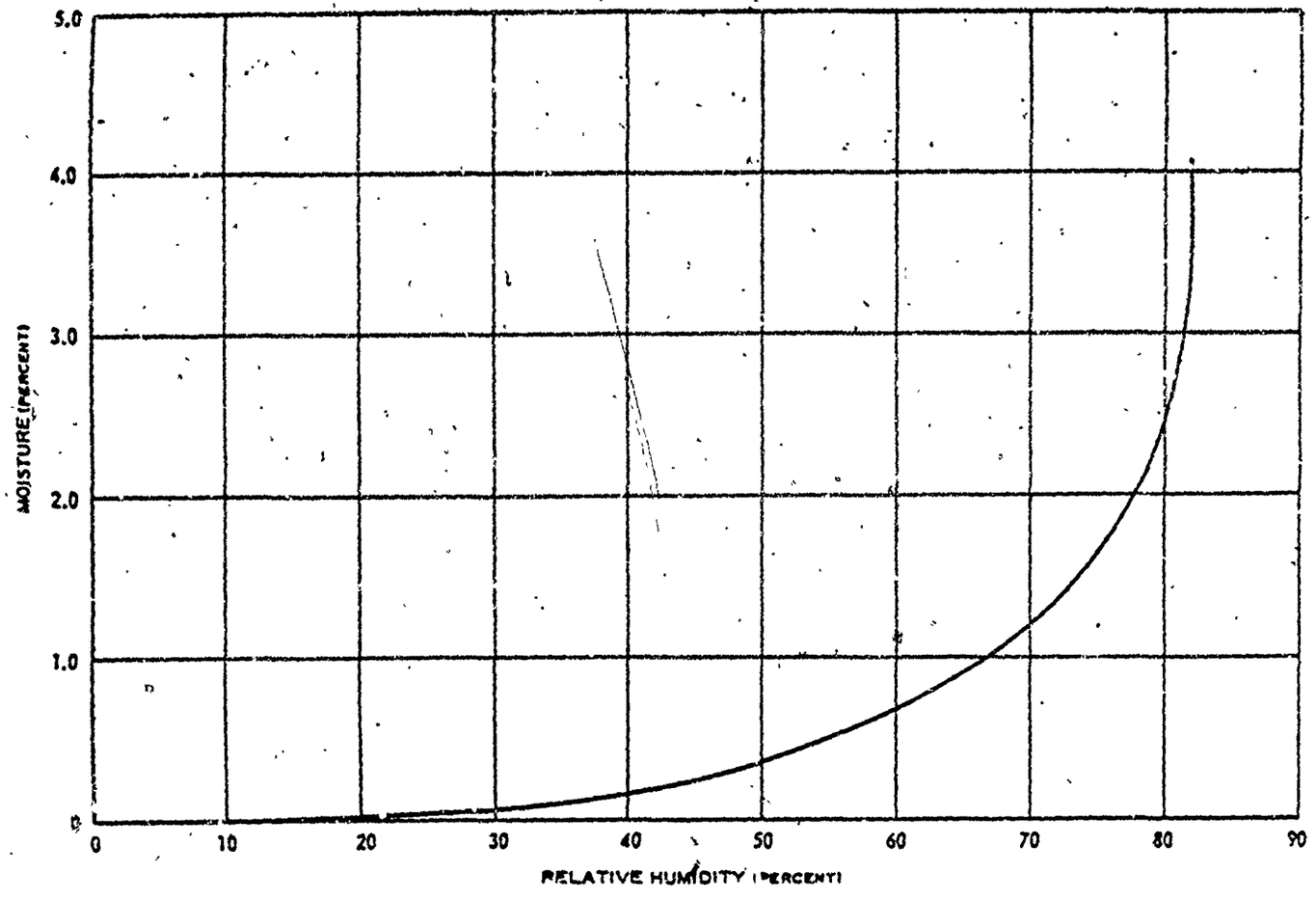

Figure F-19 Equilibrium Moisture versus Relative Humidity at 60°C for Propellant

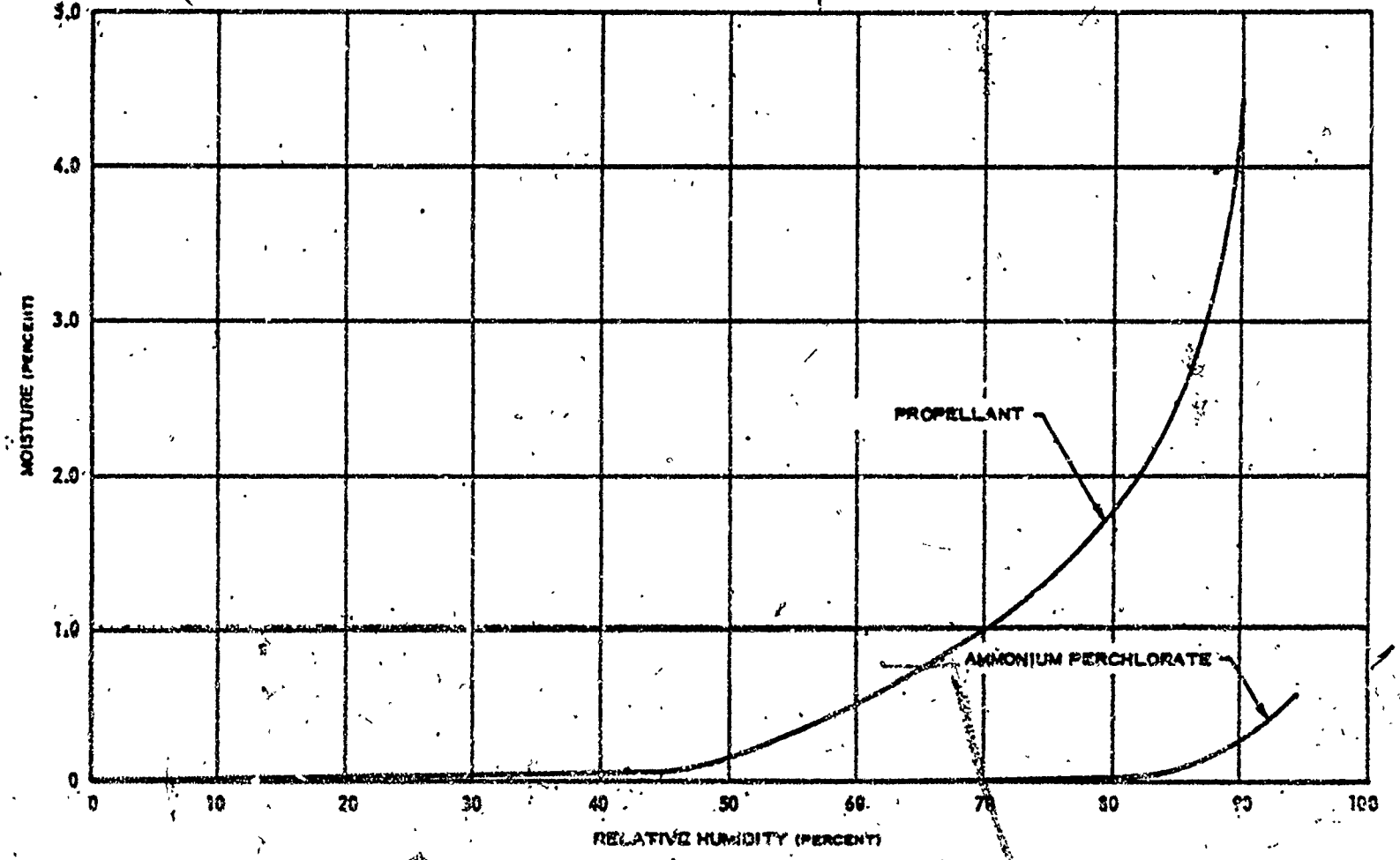

Figure F-20 Equilibrium Moisture versus Relative Humidity at 25°C for NH_4ClO_4 and Propellant

Weight gains after 260 hours were calculated to moisture content on a dry basis.

The data obtained are plotted in figures F-19 and F-20. The following conclusions may be drawn.

- There is a significant difference in the relationship of equilibrium moisture to percent relative humidity as a function of temperature. At a given percent relative humidity, the equilibrium moisture increases with increasing temperature.
- At normal ambient temperature, the equilibrium moisture content is less than 0.1 percent at values of relative humidity below 57 percent. Since the moisture content of the cured propellant is approximately 0.07 percent, there is negligible driving force for gain or loss of moisture in the 30 to 50 percent relative humidity span.
- The equilibrium moisture of propellant is substantially above that of NH_4ClO_4. However, above about 94 percent relative humidity, the oxidizer exhibits deliquescence; i.e., it continues to take up water until completely in solution. In this region no equilibrium moisture is attained by the propellant. There is evidence that the percent relative humidity for NH_4ClO_4 deliquescence is lower at higher temperatures.

Diffusion rates of moisture in propellant. Data on rates of change of propellant moisture content as a function of temperature were desired in order to estimate the possibilities of drying grains and the degree to which propellant moisture might contribute to the accumulation of water during the cycling process.

Propellant was cast into a series of pint jars to a depth of approximately 2-1/2 inches (comparable to the web thickness of the motor grain). The jars were sealed tightly and subjected to the normal curing cycle, then cooled to room temperature. An epoxy-versamide resin was used to seal cracking at the glass propellant interface. Moisture content of the cured propellant, as previously noted, was found to be only 0.07 percent. The samples were then exposed to essentially zero percent relative humidity in desiccators over Drierite at 40°F, 75°F, and 140°F, and loss in weight was measured periodically over a period of 300 hours.

Because of the low initial moisture content, drying rates were low and essentially constant over the 300-hour period. Expressed as percent loss in H_2O per 100 hours, results were as follows:

Temperature (0°F)	ΔH_2O (%/100 Hours)
40	0.0018
75	0.0023
140	0.0060

Prolonged drying would, of course, result in a decrease in rate with time. It may be concluded that any significant drying of the propellant grain below its initial low water content would be an extremely time-consuming process, and that there can be only negligible contributions of H_2O from the propellant grain to the substantial amount of water noted in some motors during cycling. Nevertheless, prolonged exposure of the grain to the dry atmosphere resulting from the presence of a desiccant pack in the motor will result in transfer of water from the grain to the desiccant, and will gradually reduce the capacity of the dasiccant.

Following termination of the above tests at 300 hours, jars were transferred to desiccators at >90 percent relative humidity to observe the rate of moisture adsorption. The data obtained follow:

Temperature (0°F)	Relative Humidity (%)	Time (hr)	H_2O Gain (%)
75	93	66	0.026
75	93	135	0.061
140	94	66	0.39
140	94	135	0.85

The percent of moisture gained refers to the propellant mass as a whole; surface layers, of course, would be much higher. The higher rates reflect the greater driving force due to the high equilibrium moisture of the propellant at these relative humidities.

Simulated cycling test. The purpose of this study was to estimate by a laboratory-scale experiment the moisture which would accumulate in the part of a grain under the following specified set of cycling conditions:

- 2-1/2 high-to-low temperature cycles
- No desiccant present
- System free to "breathe" (i.e., to maintain atmospheric pressure during temperature changes) but not to be otherwise exposed during the duration of the test.

Each of the two test units consisted of propellant cast to a 2-1/2 inch depth (web thickness) in 4-inch diameter steel pipes capped at both ends. Propellant liner was applied to the bottom cap and sidewalls to minimize the chances of unbonding during cycling. A free volume above the top surface of the propellant was maintained to simulate the ratio of propellant volume to port volume existing in the motor.

The propellant was cured with the units tightly sealed to prevent loss of moisture generated during cure. After cooling to ambient temperature, the cap on each unit was fitted with a "Bunsen valve" (section of rubber tubing approximately 2 inches long with a 3/4-inch slit lengthwise) to allow breathing. The units were then subjected to the following cycling history:

(1) Heated to 120°F over 24-hour period, then to 140°F over 24-hour period

(2) Cooled to 80°F over 24-hour period, then to 30°F over 12-hour period, then to -20°F over 36-hour period

(3) Heated to 80°F over 24-hour period, then to 110°F over 12-hour period, then to 140°F over 36-hour period

(4) Cooled to 80°F over 72-hour period, then to -20°F over 72-hour period

(5) Warmed to ambient over 36-hour period

It was recognized that this experiment would fail to simulate the conditions on cycling of any given motor in at least two respects. First, rates of heating and cooling of the test units would not be the same as an actual motor because of the gross difference in size; to minimize differences, heating and cooling was conducted stepwise, as noted. Secondly, the relative humidity of the air in the conditioning chambers was not controlled. Not only would this be difficult, but the history of external relative humidity during previous motor cyclings was not known. However, a general similarity in these conditions is a reasonable assumption.

Following the cycling, the units were assembled so that a current of dry nitrogen could be passed through the free volume and thence

through a tared drying tube containing anhydrous $Mg(ClO_4)_2$. After two hours purging, weight gains of the drying tubes were 0.047 and 0.066 grams respectively for the two units. The headcaps were then removed and the units inspected. There was no free moisture present and no visible evidence that liquid water had been present on the propellant surface at any time. No unbonding at the propellant-liner-case interface was visible.

Expressed as percent of propellant weight, the quantities of H_2O measured correspond to 0.0051 and 0.007 percent. On this basis water in the amount of 86 and 102 cubic centimeters respectively, was expected to be presented in the propellant grain. Analysis of the propellant for moisture content following the above treatment gave results of 0.099 and 0.093 percent for the two samples.

STRUCTURAL INTEGRITY LABORATORY TESTS

PHYSICAL PROPERTY TESTS

The propellant samples and analog motors obtained from the casting of propellant were divided into three pretest groups:

(1) Undesiccated and tested as received

(2) Desiccated with Drierite for seven days at 70°F

(3) Postdried for seven days at 140°F

Data obtained in uniaxial tensile tests, together with comparable physical property test data obtained from other motor propellant batches, are presented below.

Constant elongation rate uniaxial tests. Uniaxial constant elongation rate tests were performed on machined JANAF samples over a temperature range of 140°F to -75°F. Samples were prepared from

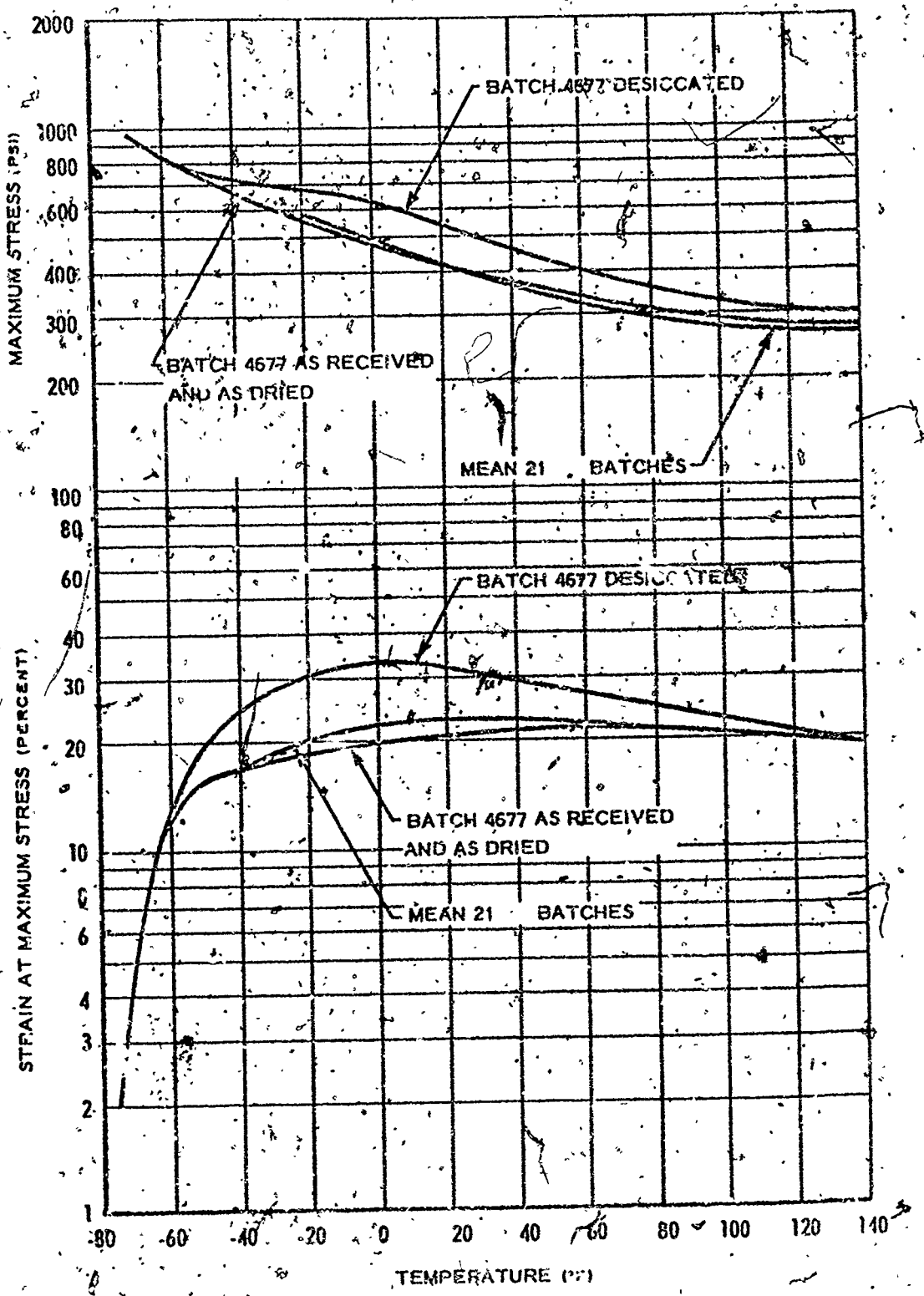

Figure F-21 Constant Elongation Characteristics of Propellant

randomly selected half-gallon amounts of propellant from the three basic pretest conditions. The measured strain data were obtained using a plastic extensometer.

Data presented in figure F-21 indicate a marked improvement in physical properties for propellant which has been desiccated for one week at 70°F. No significant difference between the physical properties of propellant in the "as received" and "postdried" condition was apparent.

Data obtained from the other motor propellant batches also appear in figure F-21. The properties from this batch of propellant (P-4677) were significantly higher, especially in the strain at maximum stress parameter, then the properties of the other batches; the significance of this finding is discussed in subsequent paragraphs.

Constant strain endurance. Constant strain tests were performed on JANAF test specimens desiccated one week prior to testing exhibited a slight increase in constant strain characteristics except for the temperature range below -60°F. Below -60°F, the propellant's physical properties appeared similar to the physical properties of the "as cast" and "postdried" propellant samples. In all instances, the constant strain data were comparable with the strain at maximum stress data obtained from constant elongation rate tests.

Humidity Study

Humidity levels of 0, 32, 66, and 100 percent relative humidity were established by using large glass desiccant jars. Relative humidities (RH) of 32 and 56 percent were obtained by adjusting the density of an aqueous solution of calcium chloride and sodium nitrite; the zero-humidity condition was established by using Drierite; and the

100 percent condition was established by conditioning the specimen over a water solution. The propellant samples used in the humidity study were in the "as cast", undesiccated condition. Uniaxial constant elongation rate tests were conducted at three test temperatures to define a standard or control for physical properties of the propellant. The remaining samples were then randomly selected, placed in the four desiccant jars, and humidity-conditioned at a constant temperature of 70°F. At intervals of 3, 7, 14, and 28 days conditioning time, samples were removed from the desiccant jars and subjected to the standard constant elongation rate tests at three temperatures.

Effect of humidity on the physical properties. The effect of humidity on the constant elongation rate properties of the propellants at 70°F is shown in figure F-22. In the figure, changes in maximum stress and in strain at maximum stress are quoted as the ratio, in percent, of the standard physical properties as defined for the test condition under consideration to the physical properties at the corresponding temperature. At a test temperature of 70°F, storage at zero percent RH increased the constant elongation rate properties of the propellant. After 28 days storage at 70°F, the strain at maximum stress increased 39 percent, while the maximum stress increased approximately 20 percent. At levels of 32 and 66 percent RH, the propellant exhibited a slight change in constant elongation rate properties. Exposure to 100 percent RH produced a significant and rapid decrease in physical properties. After three days, the strain had decreased to 50 percent of the initial properties, while the maximum stress properties were only 70 percent of the original properties. After 28 days at 100 percent RH, these properties were 26 and 35 percent of the original physical properties respectively.

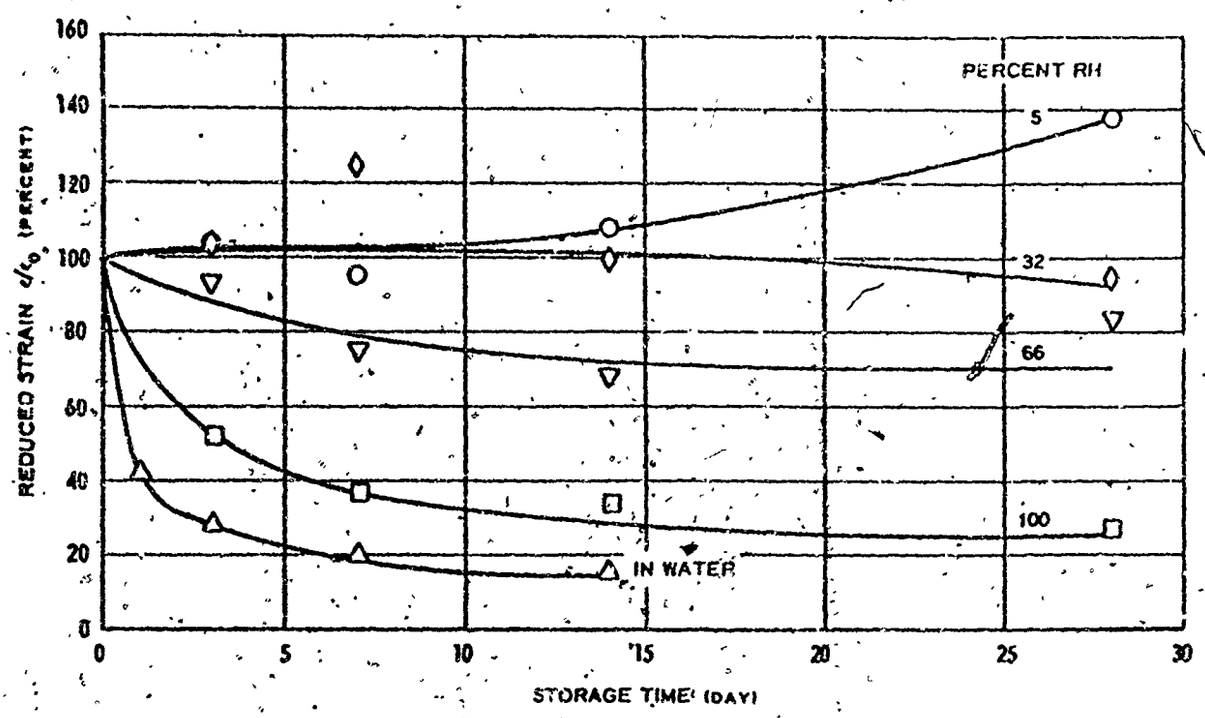

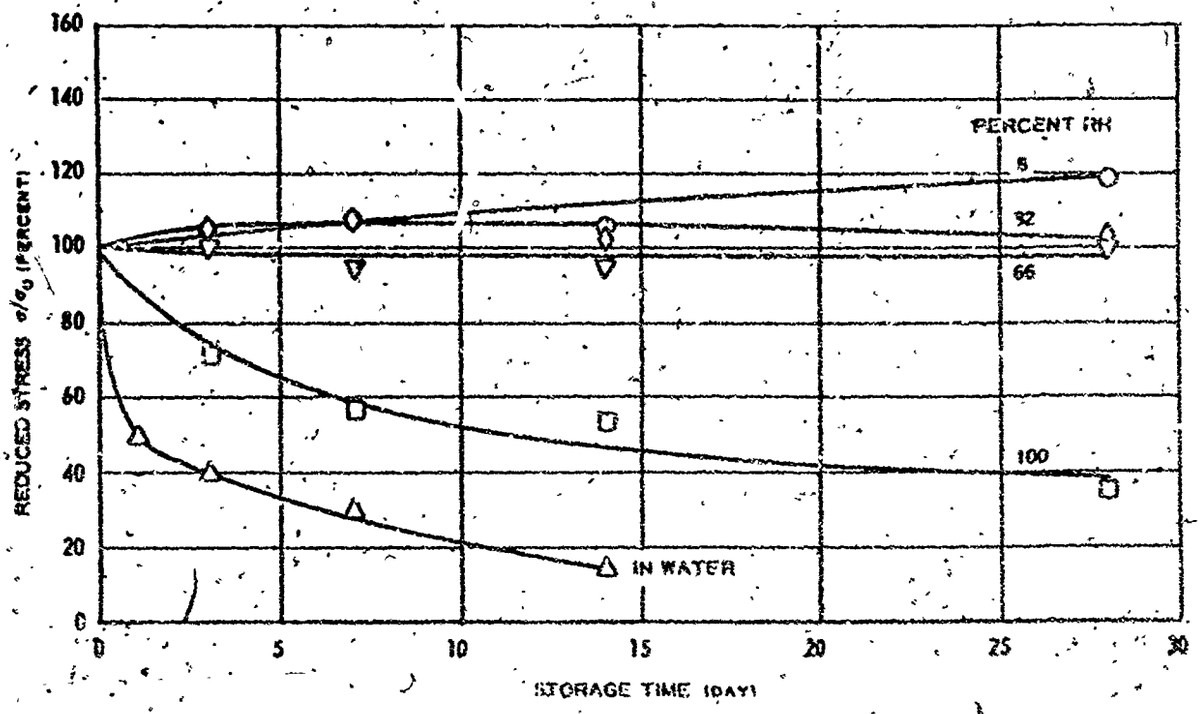

Figure F-22. Constant Elongation Rate Properties versus Humidity Storage at 70°F, Test Temperature 70°F

Similar rapid decreases in constant elongation rate properties were obtained at the other two test temperatures.

Physical properties of wet propellant. The results of constant elongation rate tests performed on JANAF samples which had been immersed in water and tested at periodic intervals is also depicted in figure F-22. After one day, the properties deteriorated to 40 percent of the initial strain and 50 percent of the initial stress values. Further degradation in physical properties was such that, after 14 days, the 70°F physical properties are 15 percent of the initial strain and 14 percent of the initial stress.

Effects of humidity on prestrained JANAF specimens. A series of tests was conducted in which machined JANAF specimens were prestrained to 4 to 9 percent strain exposed to humidity levels of zero and 100 percent for a period of seven days, and subjected to a constant elongation rate test. The results indicated that the one-week storage of prestrained propellant samples at zero percent RH produced a measurable increase in constant elongation rate properties. Storage of prestrained samples at 100 percent RH for one week degraded the properties catastrophically. All of the prestrained samples stored at 100 percent RH for one week failed before any additional tests could be performed.

Effect of low temperature storage on propellant. The low temperature storage capabilities of propellant were investigated in a series of uniaxial constant elongation rate tests. JANAF specimens in a desiccated condition were stored at the low temperature extreme for periods of time up to 28 days. The data showed a small decrease in strain at maximum stress capabilities at the maximum 28 days. However, 28-day storage at this temperature was beyond the motor requirements;

since the magnitude of the reduction was small, it was concluded that the degradation was not detrimental to full-scale motor operation.

Investigation into flow defects. The casting flow pattern in a typical motor casting was duplicated by a specially designed sample. The sample was designed to duplicate the condition at the root of the star valley and was cast and cured using the standard process techniques. JANAF specimens were then prepared with the suspected defect area located in the central constant cross section of the specimen. Constant elongation rate tests showed no evidence of structural defect; the maximum true stress and associated strain data were identical, within experimental error, with the original control propellant physical properties.

Investigation of skin effects. JANAF specimens were also prepared so that one side of the specimen had a cast surface similar to that of the motor port. Constant elongation rate tests on the specimens showed no evidence of a surface or skin effect; the physical property stress-strain data were again identical with the original control propellant data. The specimen failure mode was also standard: no prime failure was observed in, or directly connected with, the surface condition.

ANALOG MOTOR TESTS

By suitable choice of internal grain dimension, cylindrical case-bonded analog motors are used as convenient test vehicles to simulate the motor thermal hoop strain versus temperature conditions. Based upon previous theoretical investigations, a 4-inch diameter by 10-inch long, 50 percent web fraction motor was chosen for testing.

Thermal cycling. Three analog motors were subjected to thermal cycling tests between the environmental temperature extremes. The propellant in these three motors was subjected to pretest conditions as follows:

Motor	Condition
No. 1	As cast, desiccated
No. 2	Post-dried at 140°F
No. 3	As cast, motor port with free water

With all three motors at ambient conditions, the grain temperature was elevated to 140°F, then rapidly cooled and subsequently returned to ambient. Visual inspection of the motor, utilizing a borescope, revealed several small longitudinal cracks on the bottom surfac of Motor No. 3. The other two motors displayed no evidence of grain cracks or case/grain end-separation. These two motors were then twice subjected to the temperature cycle and no cracks or end separation was observed. Since the analog motors were specifically designed to reproduce the motor critical thermal hoop strain characteristics, the failure of Motor No. 3 after one cycle was considered significant.

Analog motor thermal failure tests. A thermal condition-to-destruction test was performed on three 4 by 10-inch analog motors. The propellant grain in each motor was subjected to pretest conditions as follows:

Motor	Condition
No. 4	As cast, undesiccated
No. 5	Desiccated one week at 70°F
No. 6	Conditioned at 100 percent RH for one week

After each successively lower grain temperature was established, the motor bore diameter was measured and the motor was inspected. At a temperature of -98°F, grain inspection revealed no cracks or case/grain end-separation.

The superior low temperature capabilities of these motors was attributed to the superior strain at maximum true stress characteristic of propellant Batch P-4677. Based on uniaxial data, failure at -80°F was predicted; the deviation between predicted and actual failure temperature being attributed to the analog motor deficiencies at low temperatures.

EFFECT OF MOISTURE DEGRADATION

The drastic reduction in the physical properties of this propellant due to high relative humidity and liquid moisture, discussed above, and its effect on the operation of the motor was examined in detail. Constant strain endurance capability was used as the propellant failure criterion governing the failure temperature of a thermally cooled grain with the hoop strain at the root of the star valley being the critical location.

Shown in Figure F-23 are the degradation in propellant physical properties, applied to the lower two-sigma values of the strain-at-maximum-stress data from 21 motor batches of the propellant, and the motor maximum hoop strain under thermal cooling. The maximum motor hoop strains were derived analytically and corroborated previously in a condition-to-destruction test on a full scale motor. This figure illustrates the extreme deleterious effects of moisture on this propellant grain.

The effect of moisture in liquid form is catastrophic. A subsequent cycling test performed on a full scale motor demonstrated the validity of this analysis.

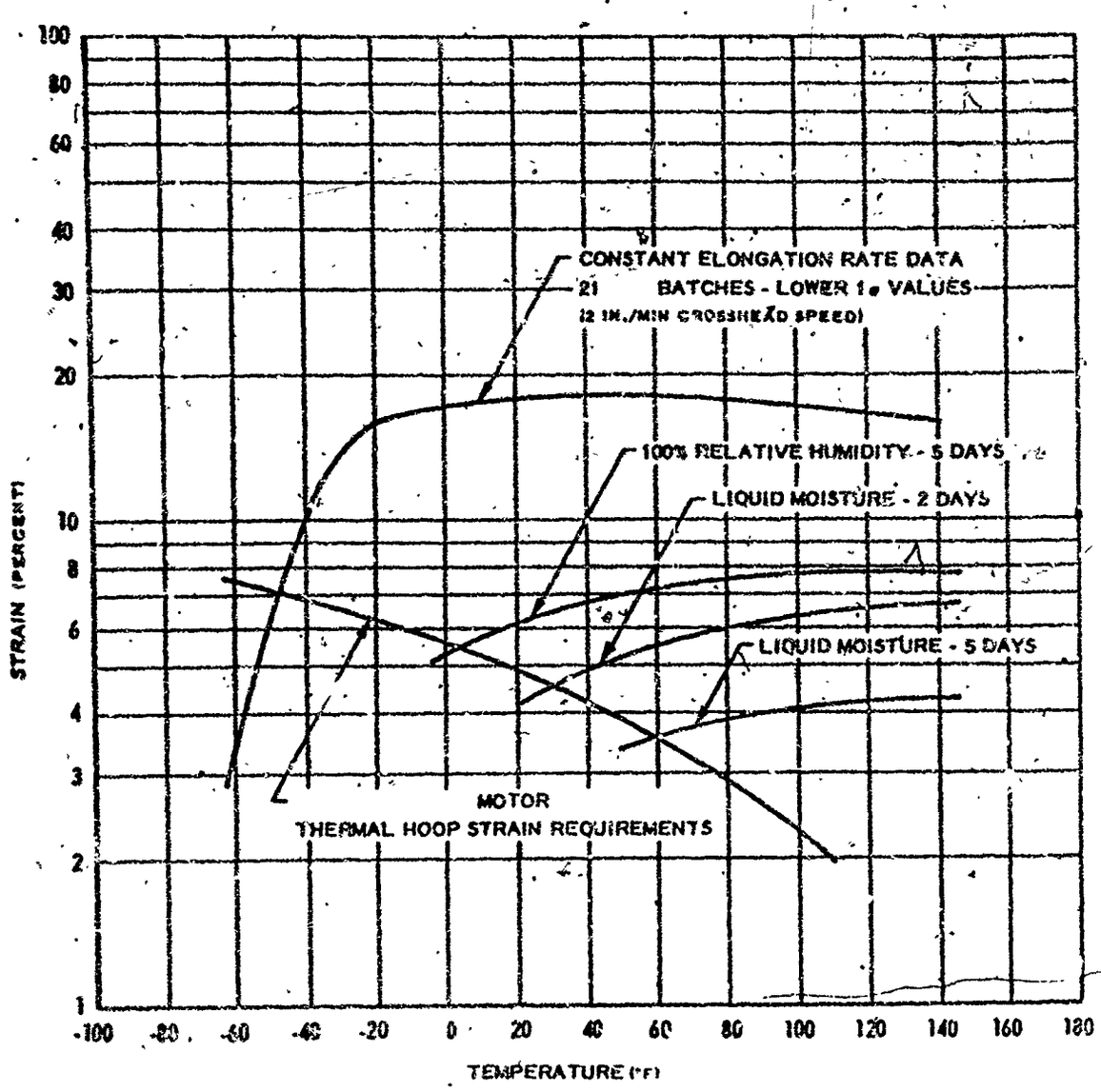

Figure F-23 Thermal Hoop Strain Requirements versus Propellant Capabilities

FULL-SCALE MOTOR TESTS

Motor drying. One motor was installed in a circulating air oven with 50 pounds of desiccant. The oven temperature was set at 140°F, and air was circulated through the motor and the desiccant packs. After 24 hours, the desiccant was weighed and was found to have gained six pounds. The desiccant was changed, and during the second 24-hour period the desiccant gained an additional six pounds. Because of the similarity in these two weights, a second oven was set up without a motor and air was circulated in essentially the same manner as before. After one day of operation, the desiccant gained nearly six pounds also. The ovens were kept in operation three more days with similar weight gains, and it was concluded that the air was not extracting moisture from the motor. These data were later substantiated by laboratory testing.

Evaluation cylinder. Another drying test was conducted on a 36-inch evaluation cylinder which contained an 18-inch port. The drying rig used for the evaluation cylinder was thought to be a closed loop except for the valve which was permitted to open for charging of the system. The desiccant packs were weighed continuously during the test and the data recorded. It was found that the desiccant gained one pound in the first two hours and then leveled off to a constant moisture gain of 0.15 pounds per hour. The test was continued for three days with the desiccant changed every 24 hours; the motor was then removed from the drying loop and test conducted for an additional 24-hour period. It was found that the weight gain was essentially the same without the motor as with the motor, and it was concluded that moisture was being introduced from the atmosphere and no significant drying of the motor resulted.

Temperature cycling tests. One motor, which had previously failed in temperature cycling, was cleaned with a solvent to remove the moisture deposits from the grain surface, sealed with an igniter headcap and aft closure assembly, and pressurized to 50 psi with dry nitrogen. The motor was temperature conditioned through one cycle, opened, and inspected at 70°F. Inspection showed no signs of moisture on the grain surface. The motor was reassembled, pressurized, and cycled a second time; inspection showed no moisture after this second cycle.

Another motor, which had also failed, was rotated 180° from the attitude first used to test the motor, and sealed with a polyethylene sheet which was taped around the outer periphery of the aft flange. The motor was undesiccated and subjected to temperature cycling. Without opening the motor, an inspection was conducted at 70° following the first cycle. The inspection showed no additional moisture deposits on the surface. The motor was then conditioned to -3°F, and inspection through the polyethylene sheet showed no additional signs of moisture. The polyethylene sheet was removed from the motor with the conditioning chamber box open and the grain surface immediately began to frost over. The motor was left open and the air permitted to circulate into the cavity, entering on the top side of the motor, exiting on the bottom, and extending about halfway over the length of the motor. The box door was closed and the temperature reset to 70°F. Upon reinspection at ambient conditions, the motor displayed an appearance and degree of moisture content similar to that of the motors in which cracks had been found.

A full-scale motor was cast to demonstrate the results of the propellant investigation. The motor was assembled with 48 units (4 pounds) of desiccant installed and was temperature cycled twice over the environmental temperature extremes. The motor was disassembled at ambient temperature and inspected by the contractor and propulsion company personnel. The grain was sound and free of moisture and oxidizer deposits.

The motor was reassembled without desiccant, using the semi-rigid polyethylene covers to seal the cavity. The motor was again temperature cycled twice and inspected at ambient temperature. The grain cavity contained free moisture and heavy oxidizer deposits, and the lower web valleys were cracked. The cracks were identical with those previously observed in the motors which failed.

Conclusions. From the described tests and the data obtained in the laboratory, it was concluded that the cause of the failure of the five motors was the introduction of atmospheric moisture into the grain cavity of those motors during inspections conducted routinely at low temperature, and leakage past the semi-rigid plastic covers used to close the motors during conditioning. Although the covers themselves were considered to be tight fitting, a seal was not effected because the bolt holes in the aft flange of the chamber were open to the atmosphere which permitted moisture to bypass the cover seal.

These conclusions were supported by the following events:

- Successful temperature cycling, prior to occurrence of grain cracking in the five motors, of two motors which did not have bolt holes open.

Successful conditioning, subsequent to the grain defect investigation of four motors which were sealed.

On the basis of the collected data generated by the investigation, and in consideretion of program data accumulated previous to and subsequent to the investigation, the corrective action described below was instituted.

- Desiccant packs were incorporated into the motors to maintain the cavity at the desired humidity level.
- The grain cavity of the motor was purged with dry nitrogen during assembly to provide a dry atmosphere.
- Inspection and handling instructions was issued which prohibited opening of the motors at temperatures below 60°F.
- All testing was conducted with the motors fully assembled.
- The motors were shipped completely assembled and purged to protect them from the atmosphere.

No further grain failures were noted during the remainder of the program after this corrective action was instituted.

F.2.11. CASE 11

This next example points out the seriousness of inadequate quality control on motor processing hardware. The particular motor involved was a workhorse sled rocket motor which was also used as an upper stage vehicle in a sounding rocket. The motor is approximately 10 feet long and 9 inches in diameter. The forward section of the grain had a cylindrical port configuration with a very high web fraction. The aft section of the grain had a star perforated configuration. Upon

cooldown to ambient temperatures following propellant cure cracking in the star valleys in the vicinity of the transition region from the star to circular port configuration in eight out of nine motors cast from a single batch of propellant was observed. The one motor which did not crack was found to be unbonded in the cylindrical section of the grain for eighteen inches by radiographic inspection. In addition, these units also had head and aft end unbonds. These failures were totally unexpected since a large number of these motors had been produced in the past on several different programs with no difficulties. The propellant, used on many different programs, was a low solids filled PBAA with excellent physical propellants.

Propellant samples were removed from one unit to provide specimens for structural integrity and chemical analysis. During removal of these samples it was noted that there appeared to be a physical difference in samples taken from the head and aft end locations. The general conditions appeared to be tacky and sticky; suggestive of propellant undercure. Test specimens taken from the aft and head end of the motor gave the following results:

	Aft	Head
stress	133 psi	126 psi
strain @ max. stress	28%	21%

It was subsequently determined that the propellant cure schedule had recently been changed from a nominal 108 hours at 140°F to 72 hours at 140°F. This particular propellant casting was the first to employ the new cure cycle. It was further noted that other programs had previously used a 120 hour cure at 140°F.

At the time that the cracking of these motors was observed, an additional casting of nine motors was taking place. These motors showed no visual signs of cracking at the end of the 72 hour cure; however, they were placed in an oven at 140°F and cured for an additional 36 hours, for reasons discussed below, followed by a slow cooldown to 80°F. Visual inspection of four of these motors revealed that all four motors were cracked. Thus, it was concluded that the additional post cure of the motor was not effective in retarding cracking. The additional post cure probably did more harm than good. Inner bore cracking is governed mainly by propellant elongation. It has been demonstrated on many propellants that normally propellant strain capabilities are higher in a slightly undercured state than in a more fully cured state. Thus, it should not have been expected that the additional post cure would have alleviated the cracking problem.

In addition to the short cure time, a known high humidity condition was known to have existed during either final processing of these last two motor castings. Two specimens taken from the aft end of the motor from which previous propellant samples were removed were subjected to 50% relative humidity for 22 hours and 42 hours. The test results were as follows.

	22 Hours	42 Hours
max. stress	95 psi	70 psi
strain @ max. stress	25%	13%

Although none of these values or the previous physical property data were sufficiently low to analytically predict failure at the temperature environment the motors had experienced, the results did

indicate that a difference in the propellant existed between the aft and head end of the motor; and exposure of specimens to humidity results in significant degradation physical properties. Based on this latter information and the fact that high humidity conditions were known to have existed during either final processing or motor casting the decision was made to post cure the motors from the second casting an additional 36 hours at 140°F. This decision was based on past experience which seemed to indicate that moisture had a more severe effect on undercured propellant than on fully cured propellant. Subsequent failures on motor cooldown, however, indicated that the extended cure probably did more harm than good.

In order to support the customer flight test schedules it was necessary to consider casting another group of nine motors based on the limited failure analysis data present at that time. Stress relief flaps were introduced at the head end of the motor to alleviate the head end unbonding problem. A new batch of liner was prepared for these motors and a step cure cycle consisting of 16 hours at 120°F 12 hours at 135°F and 92 hours at 140°F was introduced and the cooldown period was extended to 15 hours. In addition, dessicant bags were placed in the motors immediately after mandrel removal. Of these nine motors, one exhibited head end unbonding and one motor had a large void area near the propellant surface in the cylindrical section of the grain which later gave use to a crack in the port. No other anomalies were observed in the remaining motors.

At the same time the above motors were being cast for the customer, a comprehensive failure investigation was initiated. This program was

aimed at investigating (1) the moisture content in the insulation and all components of the propellant and liner, (2) determining effect of humidity on propellant physical properties, (3) evaluation of liner/propellant bond system and (4) evaluation of propellant cure cycle.

Midway through the above failure investigation program the structural integrity engineer had the occasion to inspect the casting mandrels. It was noted that the star valley radii appeared to have a smaller radius than called for on the engineering drawings. Subsequent measurements showed the configuration shown on the right below. Prior to the casting of the first group of motors the grain design had been changed slightly for ballistic reasons and new mandrels had been fabricated supposedly with a 3/8" radius on the star valleys in the transition region as shown on the left below.

The mandrels were observed to have offsetting curves of 3/8" radii such that a much smaller radius was present at the star valley. A subsequent grain analysis showed that the motors should have cracked at ambient temperature.

New mandrels of the proper configuration were fabricated; the stress relief flaps were introduced, the liner thickness and liner precure were altered slightly and the 120 hour step cure on subsequent motors was maintained with the grain interior dessicated during handling, transportation and storage. No subsequent failure problems were noted.

The above discussion illustrates how expected sensitivity to events such as, for example, cure cycle and the presence of moisture may mask another real problem. This also points the need for a close association between manufacturing personnel and the structural integrity engineer. In particular it is important for the structural integrity engineer to be quite familiar with actual motor processing equipment and procedures in contrast to those specified on engineering drawings since quite often deviations will exist which may seem acceptable to individuals not fully aware of the importance of grain structural integrity considerations.

F.2.12. CASE 12

This example involved a high energy propellant demonstration motor. The motor was approximately 36 inches long and 18 inches in diameter, and consisted of an end-burning grain loaded in a thick rubber insulation cartridge which was head end bonded only. These motors were cast and fired at ambient temperature in an altitude chamber. The first motor fired failed during the firing. Inspection of the drawings and remaining motors led to the supposition that the rubber cartridge, which extended about 4 inches past the end of the grain, had been deformed against the case before pressure had been equalized between the cartridge and the case; and subsequently had peeled away from the grain exposing sufficient additional burning surface to cause an overpressurization failure. The cartridge was trimmed to within 1/4" of the grain end and the remaining two motors were fried successfully.

F.2.13. CASE 13

Unbonding and bubbling of a mastic insulation was observed in this motor during cure of a layer of liner coating. The problem was attributed to outgassing of hydrophobic components in the mastic. The mastic was removed and replaced with a commercially purchased insulation material.

This same motor had aft end stress relief flaps which were secondarily bonded together and then bonded to the motor case. During cure of the motor the secondary bond between the flaps failed and the propellant adhered to the mandrel. When the mandrel was removed a deep circumferential crack propagating radially inward from the port was observed. This crack was attributed to the propellant "washing" off the mandrel surface coating during the motor casting and allowing the propellant to "slump" against the mandrel when the bond between the flaps failed. The propellant aft of this crack was removed for a demonstration firing. In a subsequent demonstration motor the mandrel surface coating material was changed, and the flaps were internally vulcanized together and secondarily bonded to the motor case. No problems were observed in this motor.

F.2.14. CASE 14

After high temperature endurance vibration of this high mass fraction motor grain/insulation unbonding was found by radiographic inspection near the forward tangent point. The head end dome of this motor was free floating with a stress relief flap. It was concluded that insufficient "free volume" had been left at the head end for grain expansion during the high temperature vibration. As a result high shear stresses developed

near the cylindrical/dome transition region which resulted in the observed failure. In subsequent motors, care was taken to insure that an adequate free volume at the head end of the motor was available for grain expansion during high temperature vibration.

F.3. CLOSURE

The examples of motor failures discussed in the previous section illustrate some of the structural integrity problems that may be encountered. Although this list is not complete, it is indicative of the nature of the problems causing the greatest concern to structural integrity engineers. Numerous other problems, mainly associated with grain unbonding, poor processing methods, and adverse effects of humid environments may be cited. In these situations, a closer association between the structural integrity engineer and the motor manufacturing personnel must be encouraged if careless motor failures are to be avoided. This is particularly true of grain unbonding problems and deleterious effects of moisture or solvents. As a good general practice, the greatest effort should be made to prevent contamination of any bonding surfaces and adhesives or liners by moisture or solvents. It has been remarked in an earlier chapter that most adhesive bond failures may be attributed to poor processing controls. These failures, for the most part, can be avoided if greater caution is exercized. The responsibility for implementing more careful processing techniques lies with the structural integrity engineer who is aware of the seriousness of the problems that may develop from carelessness.

F.4 REFERENCES

1. Fulbright, J. L.; and Miller, W. H.: "Failure Analysis of Solid Propellant Grains Based on Dissected Motor Properties," Bulletin of the 6th ICRPG Mechanical Behavior Working Group Meeting, CPIA Publication No. 158, Vol. 5, Oct. 1967.